

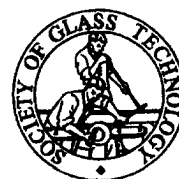
Reproduced From
Best Available Copy

19990126 103

Extended Abstracts

11th International Symposium on Non-Oxide & New Optical Glasses

6-10 September 1998
Sheffield, UK



DISTRIBUTION STATEMENT A

Approved for public release;
Distribution Unlimited

Blank Preceding Pages

FOREWORD

11th International Symposium on Non-Oxide Glasses and New Optical Glasses

IS(NOG)² '98

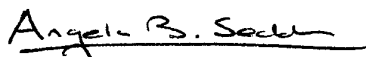
The 11th International Symposium, formerly known as *the International Symposium on Non-Oxide Glasses*, and held about every two years since 1981, is the premier conference for discussion of the latest developments in synthesis, structure, properties, processing and applications of non-oxide glasses and new optical glasses. An important objective of the Symposium is to bridge the gap between scientific understanding and technical requirements so that the enormous future potential of special glasses, including for innovative photonic materials technologies, is realised effectively. For the first time the title of the Symposium has been extended so that it encompasses special oxide glasses, hence making the conference the forum for discussion of all types of non-traditional inorganic glasses. About 100 delegates are attending the 11th Symposium from 21 different countries.

IS(NOG)² '98 is taking place at Taptan Conference Centre, University of Sheffield. Sheffield is the fourth largest city in England and is world famous for its steel and cutlery industries. The University founded the first department of Glass Technology in 1915 and the 11th Symposium is being co-organised by the Centre for Glass Research, which is a direct descendant of the Department of Glass Technology. The City is on the edge of the magnificent Peak District National Park.

The 11th Symposium comprises one oral session running 6-10 September 1998. The invitation keynote lecture will be given by Professor David N. Payne of the Optoelectronics Research Centre (ORC), University of Southampton, England, and there are 11 invited papers and 46 oral papers in total. There are three separate poster sessions with 74 poster papers in total. Full manuscripts submitted at the Symposium will be refereed for publication in a special volume of the *Journal of Non-Crystalline Solids*.

I should like to thank: my Deputy Chairman, Dr Dan W. Hewak (ORC, University of Southampton) and the Local Organisation Committee for their hard work; Jill Costello, Christine Brown, Sara Lindley and David Moore of the Society of Glass Technology for the splendid conference administration and the International Advisory Board for awarding me the honour of bringing the 11th Symposium to Sheffield. I am especially grateful to the financial Sponsors, who are listed herewith, for making the Symposium possible.

I bid you a very warm welcome to Sheffield.



Angela B. Seddon, Chairman of IS(NOG)² '98

LOCAL ORGANISING COMMITTEE

Chairman: Angela B. Seddon

Centre for Glass Research
Department of Engineering Materials
University of Sheffield
Sheffield S1 3JD, UK

Deputy Chairman: Dan W. Hewak

Optoelectronics Research Centre
University of Southampton
Southampton SO17 1BJ, UK

Symposium Administrator: Jill Costello

Society of Glass Technology (SGT)
20 Hallam Gate Road
Sheffield S10 5BT
Tel: +44 (0) 114 266 3168
Fax: +44 (0) 114 266 5252
e-mail: jill@glass.demon.co.uk

Local Organisation Committee Members

Miss J. Costello	(SGT, UK)
Dr D. Furniss	(University of Sheffield, UK)
Dr R. Li	(University of Sheffield, UK)
Dr A. Jha	(University of Leeds, UK)
Dr M. G. Pellatt	(Merck Ltd, UK)

INTERNATIONAL ADVISORY BOARD

I. D. Aggarwal	(USA)	J. Illinger	(USA)
R. M. Almeida	(Portugal)	T. Kanamori	(Japan)
R. Bartholomew	(USA)	J. Lucas	(France)
A. Bruce	(USA)	D. MacFarlane	(Australia)
A. G. Clare	(USA)	D. N. Payne	(UK)
G. H. Frischat	(Germany)	M. Poulain	(France)
Fuxi Gan	(China)	A. B. Seddon	(UK)
D. W. Hewak	(UK)	G. H. Sigel	(USA)

LIST OF SPONSORS OF IS(NO²G)²

- **Corning SA, France.**
- **Galileo Corporation, USA.**
- **Hoya Co. Ltd., R & D Centre, Japan.**
- **Merck Ltd., UK.**
- **European Commission,
Directorate General XII,
Science, Research & Development.
Directorate C:
Industrial and Materials Technologies.**
- **USARDSG,
United State Army,
European Research Office.**
- **ONREUR,
United States Navy,
European Office of Naval Research.**
- **Society Of Glass Technology.**
- **Sheffield City Council.**
- **University of Sheffield.**

INVITED SPEAKERS

KEYNOTE Professor David Payne (Optoelectronics Research Centre, University of Southampton, UK)

"The Glass Ceiling"

A1 T. Kanamori (NTT Opto-electronics Laboratory, Ibaraki, Japan)

"Non-silica glass fibre amplifiers"

A2 A. J. Faber (TNO Institute of Applied Physics, Eindhoven, The Netherlands)

"Fabrication of glass based optical amplifiers for telecommunication applications"

A4 J. S. Sanghera (Naval Research Laboratory, Washington D.C., USA)

"Active and passive chalcogenide glass optical fibres for IR applications"

C1 H. Eckert (Institut für Physikalische Chemie, Westfälische Wilhelms University, Germany)

"Quantitative NMR studies of the local structure in chalcogenide glasses"

E1 F. Gan (Shanghai Institute of Optics and Fine Mechanics, China)

"Crystallisation dynamics of chalcogenide glass thin films under non-equilibrium conditions"

F1 S. W. Martin (Department of Materials Science and Engineering, Iowa State University of Science and Technology, USA)

"Structure and dynamics of fast ion conducting chalcogenide glasses"

G1 R. S. Quimby (Department of Physics, Worcester Polytechnic Institute, USA)

"Spectroscopy and applications of low phonon energy glasses doped with rare earth ions"

H1 F. Wise (Department of Applied Physics, Cornell University, USA)

"Studies of optical nonlinearities of chalcogenide and heavy metal oxide glasses"

H5 V. Tikhomirov (Department of Materials, University of Leeds, UK)

"Photoinduced effects in rare-earth doped and undoped chalcogenide glasses"

I4 P. Tick (Corning Incorporated, USA)

"Ultra-transparent glass ceramics, a photonic materials for the 21st century"

**11th International Symposium on Non-Oxide Glasses and
New Optical Glasses**

IS(NOG)² '98

EXTENDED ABSTRACTS

		Oral	Poster
Keynote	The Glass Ceiling	3	
A	Glass Photonic Devices	5-19	-
B	Glass Synthesis	20-51	223-272
C	Glass Structure	52-68	273-326
D	Glass Physicochemical Properties	69-87	327-357
E	Glass Processing	88-124	358-390
F	Glass Electronic and Ionic Properties	125-136	391-404
G	Rare Earth Doping	137-173	405-444
H	Optical Properties	174-202	445-501
I	New Glasses/Glass Systems and New Directions	203-219	502-543
	Author Index		547-550

11th International Symposium on Non-Oxide Glasses and New Optical Glasses

IS(NOG)²

6-10 September 1998

Sheffield, UK

SCIENTIFIC PROGRAMME

Sunday 6 September

2.00 pm: Registration

6.00 pm: Wine and cheese reception

6.45 pm: Informal dinner at Tapton Hall of Residence

Monday 7 September

8.50-9.10 Opening Ceremony - PROFESSOR M HOLCOMBE, Deputy
Dean, Faculty of Engineering, University of Sheffield

Chairman: **D MacFARLANE** (Monash University, Australia)

9.10-10.10 **KEYNOTE LECTURE: "The Glass Ceiling"**
D N PAYNE
*Optoelectronics Research Centre, University of
Southampton, UK*

SESSION A GLASS PHOTONIC DEVICES

10.10-10.50 **A1(I) INVITED PAPER**
"Non-silica glass fibre amplifiers"
**T KANAMORI¹, Y NISHIDA¹, A MORI¹, K KOBAYASHI¹,
M YAMADA², T SHIMADA¹, M SHIMIZU¹ & Y OHISHI²**
¹ *NTT Opto-Electronics Laboratories, Ibaraki, Japan*
² *NTT Electronics Corporation, Ibaraki, Japan*

10.50-11.30 Coffee

12.10 **A2(I) INVITED PAPER**
"Fabrication of glass based optical amplifiers"
A J FABER
TNO, Eindhoven, The Netherlands

- 12.10-12.30 **A3** "Pr³⁺-doped InF₃/GaF₃ based fluoride glass fibres and Ga-Na-S glass fibres for light amplification around 1.3μm"
K ITOH, H YANAGITA, H TAWARAYAMA, K YAMANAKA,
 E ISHIKAWA, K OKADA, H AOKI, Y MATSUMOTO,
 Y MATSUOKA & H TORATANI
HOYA Corporation, Tokyo, Japan
- 12.30-1.50 Lunch
 MEETING OF THE INTERNATIONAL ADVISORY BOARD
Authors to put up posters AP, BP & CP
- 1.50-2.30 **A4(I) INVITED PAPER**
"Active and passive chalcogenide glass optical fibres for IR applications"
J S SANGHERA & I D AGGARWAL
Naval Research Laboratory, Washington DC, USA

SESSION B GLASS SYNTHESIS

- Chairman: **P A TICK** (Corning Inc, USA)
- 2.30-2.50 **B1** "Towards low optical loss gallium-lanthanum-sulphide glass fibres"
R LI & A B SEDDON
Centre for Glass Research, University of Sheffield, UK
- 2.50-3.10 **B2** "Sol-gel processing of germanium sulphide based films"
O MARTINS, J XU & R M ALMEIDA
INESC Instituto Superior Técnico, Lisbon, Portugal
- 3.10-4.10 Tea and **POSTER SESSION [AP, BP, CP]**
- 4.10-4.30 **B3** "Catalysed gelation of amorphous sulphides"
J S SANGHERA¹, C SCOTTO², S BAYYA² & I D AGGARWAL¹
¹ *Naval Research Laboratory, Washington DC, USA*
² *Virginia Polytechnic Institute, Blacksburg, USA*
- 4.30-4.50 **B4** "In-situ generation of Eu²⁺ in glass-forming melts"
D R MacFARLANE¹, P J NEWMAN¹, J D CASHION² & A EDGAR³
¹ *Department of Chemistry, Monash University, Australia*
² *Department of Physics, Monash University, Australia*
³ *School of Chemical & Physical Sciences, Victoria University, New Zealand*

- 4.50-5.10 **B5** "Measurements, procedures and results from investigations into heavy metal fluoride glasses for electromagnetic calorimetry in particle physics"
 K W BELL³, R M BROWN¹, D J A COCKERILL¹,
P S FLOWER¹, P R HOBSON², D C IMRIE², B W
 KENNEDY¹, A L LINTERN¹, J M PARKER³ & M SPROSTON¹
¹ Rutherford Appleton Laboratory, Didcot, UK
² Department of Physics, Brunel University, UK
³ Centre for Glass Research, University of Sheffield, UK
- 5.10-5.30 **B6** "Incorporation of lanthanum oxybromide in fluorophosphate glasses"
J B DENIS & M POULAIN
*Laboratoire des Matériaux Photoniques, Université de
 Rennes, France*
- 6.30 **Coaches depart for the Mappin Museum and Peak
 Caverns**

Tuesday 8 September

SESSION C GLASS STRUCTURE

- Chairman: **S W MARTIN** (Iowa State University of Science &
 Technology, USA)
- 8.30-9.10 **C1(I) INVITED PAPER**
"Quantitative nuclear magnetic resonance (NMR) studies of
 the local structure in chalcogenide glasses"
H ECKERT, G REGELSKY, P MUTOLO, J SCHMEDT,
 M WITSCHAS
*Institut für Physikalische Chemie, Westfälische Wilhelms
 University, Germany*
- 9.10-9.30 **C2** "Neutron diffraction studies of the structure of Ge-based
 multi component sulphide glasses"
A C HANNON¹ & B AITKEN²
¹ ISIS Facility, Rutherford Appleton Laboratory, Didcot, UK
² Corning Incorporated, Corning, USA

- 9.30-9.50 **C3** "Smeared first order phase transition in chalcogenide semiconductor melts"
YU S TVER'YANOVICH & O V IL'CHENKO
Department of Chemistry, St Petersburg State University, Russia
- 9.50-10.10 **C5** "EXAFS studies of possible clustering of thulium ions in tellurite glasses"
D B HOLLIS¹, D P TURNER¹, L D FIRTH¹ & F W MOSSELLMANS²
¹ *Department of Electronic Engineering & Physics, University of Paisley, Scotland*
² *SRS Laboratory, Daresbury, England*
- 10.10-11.10 Coffee and Conference Photograph

SESSION D GLASS PHYSICOCHEMICAL PROPERTIES

- Chairman: **J S SANGHERA** (Naval Research Laboratory, USA)
- 11.10-11.30 **D1** "Initial corrosion stages of a heavy metal fluoride glass in water"
B HUEBER¹, G H FRISCHAT¹, A MALDENER², O DERSCH² & F RAUCH²
¹ *Institut für Nichtmetallische Werkstoffe, Technische Universität Clausthal, Germany*
² *Institut für Kernphysik, Universität Frankfurt/Main, Germany*
- 11.30-11.50 **D2** "Viscosity of fluoride glasses near the fibre drawing temperature"
G ZHANG^{1,2}, J JIANG^{1,2}, M POULAIN², A S DELBEN¹ & J R DELBEN¹
¹ *Laboratoire des Matériaux Photoniques, Université de Rennes, France*
² *Departamento de Física, Universidade Federal de Mato Grosso do Sul, Brazil*
- 11.50-12.10 **D3** "Physical properties and Raman spectroscopy of GeAs sulphide glasses"
B G AITKEN & C W PONADER
Corning Incorporated, Corning, USA

12.10-12.30 **D4** "Crystallisation in 70Ga₂S₃-30 La₂S₃ glasses as a function of oxide/hydroxide concentration"
S P MORGAN, I M REANEY, R BUCKLEY, D FURNISS &
A B SEDDON
Centre for Glass Research, University of Sheffield, UK

Authors to put up posters DP, EP, FP & GP

1.45 **COACHES DEPART FOR TRIP TO BRONTE COUNTRY**

Wednesday 9 September

SESSION E GLASS PROCESSING

Chairman: **A JHA** (University of Leeds, UK)

8.30-9.10 **E1(I) INVITED PAPER**
"Crystallisation dynamics of chalcogenide glass thin films under extra non-equilibrium conditions"

FUXI GAN

Shanghai Institute of Optics and Fine Mechanics, China

9.10-9.30 **E2** "Photoinduced active and passive integrated-optic elements in rapid thermally annealed chalcogenide glasses"
S RAMACHANDRAN & S G BISHOP

Microelectronics Laboratory, University of Illinois, USA

9.30-9.50 **E3** "Design and fabrication of PZG fluoride glass channel waveguides. The state of the art"

Y GAO¹, B BOULARD¹, M LEMITI², R RIMET³, P LOEFFLER⁴ & H POIGNANT⁵

¹ *Laboratoire des Fluorures, Université du Maine, France*

² *INSA, Villeurbanne, France*

³ *Laboratoire d'électromagnétisme micro-onde et optoélectronique, Grenoble, France*

⁴ *Robert Bosch GmbH, Stuttgart, Germany*

⁵ *France Télécom, CNET Lannion, France*

9.50-10.10 **E4** "Planar and channel waveguides on fluoride glasses"

R SRAMEK, G FONTENEAU & J LUCAS

Laboratoire Verres et Céramiques, Université de Rennes, France

- 10.10-10.30 **E5** "Physical vapour deposition of rare earth doped ZrF₄-based glass planar waveguides"
P J MORAIS, M C GONCALVES & R M ALMEIDA
INESC Instituto Superior Técnico, Lisbon, Portugal
- 10.30-11.10 Coffee
- 11.10-11.30 **E6** "Chemical etching of AlF₃-based glasses"
Y D WEST, E R TAYLOR, R C MOORE & D N PAYNE
Optoelectronics Research Centre, University of Southampton, UK
- 11.30-11.50 **E7** "Compositional investigation of Yb³⁺ doped heavy metal fluoride glasses for laser-induced fluorescent cooling applications"
M T MURTAGH, G H SIGEL Jr, J C FAJARDO,
 B C EDWARDS & R I EPSTEIN
Fibre Optic Materials Research Programme, Rutgers University, USA

SESSION F GLASS ELECTRONIC & IONIC PROPERTIES

- Chairman: **A C HANNON** (Rutherford Appleton Laboratory, UK)
- 11.50-12.30 **F1(I) INVITED PAPER**
"Ionic conductivity in optimised chalcogenide FIC glasses"
S W MARTIN
Department of Materials Science & Engineering, Iowa State University of Science and Technology, USA
- 12.30-12.50 **F2** "Glass-forming ability and cationic transport in gallium-containing chalcogenide glasses"
YU S TVER'YANOVICH, V V ALEKSANDROV, I V MURIN & E G NEDOSHOVENKO
Department of Chemistry, St Petersburg State University, Russia
- 12.50-2.10 Lunch
 MEETING OF THE INTERNATIONAL ADVISORY BOARD

SESSION G RARE EARTH DOPING

Chairman: J H SIMMONS (University of Florida)

2.10-2.50 G1(I) INVITED PAPER

"Comparison of low-phonon hosts for 1300 nm optical amplifier"

R S QUIMBY¹ & B G AITKEN²

¹ Department of Physics, Worcester Polytechnic Institute, USA

² Corning Incorporated, USA

2.50-3.10 G2 "Spectroscopic properties of Nd³⁺ in fluoroaluminate glasses for an efficient 1.3µm optical amplifier"

M NAFTALY¹, A JHA¹, B N SAMSON² & E R TAYLOR²

¹ Department of Materials, University of Leeds, UK

² Optoelectronics Research Centre, University of Southampton, UK

3.10-3.30 G3 "Role of the Urbach edge and host glass defects in broad band excitation of rare earth dopants in chalcogenide glasses"

D A TURNBULL¹, V KRASTEVA², J S SANGHERA³,
G H SIGEL JR² & S G BISHOP¹

¹ Microelectronics Laboratory, University of Illinois, USA

² Fibre Optics Materials Research Programme, Rutgers University, USA

³ Naval Research Laboratory, Washington DC, USA

3.30-4.30 Tea & POSTER SESSION [DP, EP, FP, GP]

4.30-4.50 G4 "New rare earth doped selenide and telluride glasses and fibres"

B COLE, L B SHAW, J S SANGHERA, B B HARBISON,
P C PUREZA, R MIKLOS, V Q NGUYEN, R MOSSADEGH,
D T SCHAAFSMA & I D AGGARWAL

Naval Research Laboratory, Washington DC, USA

4.50-5.10 G5 "Mid-infrared emissions and non-radiative relaxation in Ge-Ga-S glasses doped with Dy³⁺"

J HEO & Y B SHIN

Department of Materials, Science & Engineering, Pohang University of Science and Technology, Korea

- 5.10-5.30 **G6** "Synthesis and optical properties of the Ge-Sb-S:PrCl₃ system glasses"
 B FRUMAROVA¹, P NEMEC², **M FRUMAR**² & J OSWALD³
¹ *Joint Lab of Solid State Chemistry of the Academy of Science and of University of Pardubice, Czech Republic*
² *Department of General Inorganic Chemistry, University of Pardubice, Czech Republic*
³ *Institute of Physics of the Czech Academy of Sciences, Prague, Czech Republic*
- 5.30-5.50 **G7** "Site-selective spectroscopy of Nd³⁺ ions in heavy metal oxide glasses"
R BALDA¹, J FERNANDEZ¹, M SANZ¹, L M LACHA¹, A DE PABLOS² & J M FERNANDEZ-NAVARRO²
¹ *Dpto de Fisica Aplicada 1, ETSII, y Telecom, Universidad del Pais Vasco, Bilbao, Spain*
² *Institute de Ceramica y Vidrio, Madrid, Spain*
- 7.00 **COACHES DEPART FOR CONFERENCE DINNER**

Thursday 10 September

Authors to put up posters HP & IP

SESSION H OPTICAL PROPERTIES

- Chairman: **R M ALMEIDA** (Instituto Superior Tecnico, Portugal)
- 8.30-9.10 **H1 (I) INVITED PAPER**
"Studies of optical nonlinearities of chalcogenide and heavy metal oxide glasses"
F WISE¹, I KANG¹, S SMOLORZ¹, B G AITKEN² & N F BORRELLI²
¹ *Department of Applied Physics, Cornell University, USA*
² *Corning Incorporated, USA*
- 9.10-9.30 **H2 (Substituted paper)**
"Broadband 1.5µm emission spectroscopy of Er³⁺-doped tellurite glasses"
S SHEN, M NAFTALY & A JHA
Department of Materials, University of Leeds, UK

- 9.30-9.50 **H3 "Recent developments in As-S glass fibres"**
 G G DEVYATYKH¹, M F CHURBANOV¹, I V SCRIPACHEV¹,
 G E SNOBATIN¹, E M DIANOV² & V G PLOTNICHENKO²
¹ *Institute of Chemistry of High Purity Substances, Russian Academy of Sciences*
² *Scientific Centre of Fibre Optics, General Physics Institute, Russian Academy of Sciences*
- 9.50-10.10 **H4 "Light scattering from coated dielectric particles in fluoro-zirconate glass"**
A EDGAR
School of Chemical & Physical Sciences, Victoria University of Wellington, Australia
- 10.10-11.10 Coffee and **POSTER SESSION [HP, IP]**
- 11.10-11.50 **H5(I) INVITED PAPER**
"Photoinduced effects in rare-earth doped and undoped chalcogenide glasses"
V TIKHOMIROV
Department of Materials, University of Leeds, UK
- 11.50-12.10 **H6 "Bragg gratings inscription in rare earth doped fluoro-zirconate glasses"**
R SRAMEK¹, F SMEKTALA¹, J LUCAS¹, W X XIE², P BERNAGE² & P NIAY²
¹ *Laboratoire des Verres et Céramiques, Université de Rennes, France*
² *Laboratoire de Dynamique Moléculaire et Photonique, Université des Sciences et Technologies de Lille, France*
- 12.10-1.10 Lunch

SESSION I NEW GLASSES/GLASS SYSTEMS AND NEW DIRECTIONS

Chairman: **J M PARKER** (University of Sheffield, UK)

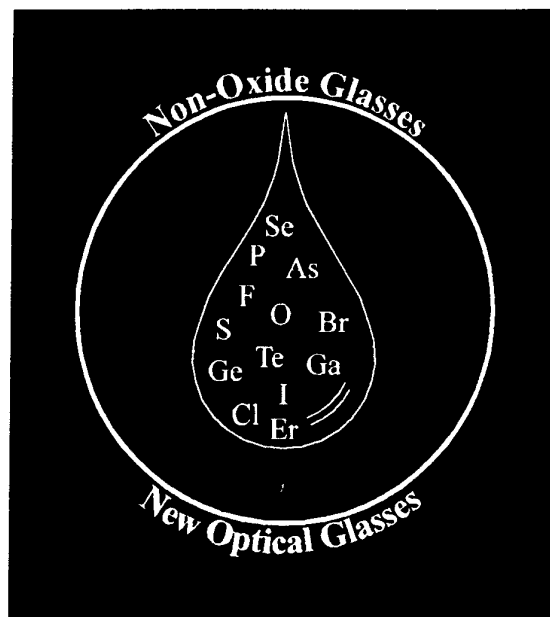
- 1.10-1.30 **I1 "Rare earth doped transparent glass-ceramics with high cross-sections"**
M MORTIER & F AUZEL
Groupe d'Optique de Terres Rares CNRS, Meudon & France Telecom CNET, Bagneux,

France

- 1.30-1.50 **I2** "Nano-crystalline fluorescence in fluoride glasses"
D R MacFARLANE¹, J JANVORNIEZKY¹, P J NEWMAN¹ &
D J BOOTH²
¹ *Department of Chemistry, Monash University, Australia*
² *Department of Physics, Victoria University of Technology,
Australia*
- 1.50-2.10 **I3** "Tungsten-tellurite glass: a new candidate medium for Yb³⁺
doping"
X FENG, C QI, F LIN & H HU
Shanghai Institute of Optics & Fine Mechanics, China
- 2.10-2.50 **I4(I) INVITED PAPER**
"Ultra-transparent glass ceramics for photonic applications"
P A TICK
Corning Incorporated, Corning, USA
- 2.50 Tea and Departure

LIST OF SPONSORS OF IS(NOG)²

- **Corning SA, France.**
- **Galileo Corporation, USA.**
- **Hoya Co. Ltd., R & D Centre, Japan.**
- **Merck Ltd., UK.**
- **European Commission,
Directorate General XII,
Science, Research & Development.
Directorate C:
Industrial and Materials Technologies.**
- **USARDSG,
United State Army,
European Research Office.**
- **ONREUR,
United States Navy,
European Office of Naval Research.**
- **Society Of Glass Technology.**
- **Sheffield City Council.**
- **University of Sheffield.**



ATTENDANCE LIST

11th International Symposium on Non-Oxide & New Optical Glasses

6-10 September 1998
Sheffield, UK



Dr Jean-Luc Adam

Universite de Rennes 1
Lab des Verres & Ceramiques
Campus de Beaulieu
35042 Rennes Cedex
France

☎ +33 299 28 6262

☎ +33 299 28 1600

✉ jean-luc.adam@univ-rennes1.fr

Dr Ishwar Aggarwal

National Research Laboratory
Code 5606
Washington DC 20375-5000
USA

☎ +1 202 767 9316

☎ +1 202 767 9311

✉ ish.aggarwal@nrl.navy.mil

Dr Bruce Aitken

Corning Incorporated
SP-FR-05-1
Corning
NY 14831
USA

☎ +1 607 974 3111

☎ +1 607 974 3675

✉ aitkenbg@corning.com

Dr Rui Almeida

INESC
R Alves Redol 9-3D
1000 Lisbon
Portugal

☎ +351 1 3100371

☎ +351 1 3145843

✉ rmaa@inesc.pt

Dr Luise Anselm

Inst f Hochfrequenztechnik
TU-Braunschweig
Bienroderweg 53
Aubenstelle
38018 Braunschweig
Germany

☎ +49 531 391 9450

☎ +49 531 391 9452

✉ l.anselm@tu.bs.de

Dr Graham R Atkins

University of Sydney Australian
Photonics CRC
Australian Technology Park
Everleigh
NSW 1430
Australia

☎ +61 2 9351 1923

☎ +61 2 9351 1910

✉ g.atkins@oftc.usyd.edu.au

Prof Rolindes Balda

Universidad del Pais Vasco
Dept Fisica Aplicada I
ETSII y Telecom
Alameda Urquijo s/n
Bilbao 48012
Spain

☎ +34 944 278055

☎ +34 944 414041

✉ wupbacrr@bi.ehu.es

Dr Roger F Bartholomew

Corning Incorporated
Sullivan Park FR-5
Corning
NY 14831
USA

☎ +1 607 974 3181

☎ +1 607 974 3675

✉ bartholomew@corning.com

Profesor Stephen Bishop

University of Illinois
127 Microelectronics Lab
208 North Wright Street
Urbana
IL 61801
USA

☎ +1 217 333 3097

☎ +1 217 244 6375

✉ sgbishop@uiuc.edu

Miss Stephanie Blanchandin

LMCTS Faculte des Sciences
123 Avenue Albert Thomas
87060 Limoges Cedex
France

☎ +33 5 55 45 74 96

☎ +33 5 55 45 72 70

✉ pthomas@unilim.fr

Mr Valentin K Bogdanov

Optical Technology Research Lab
Victoria University
PO Box 14428
Melbourne City
Victoria 8001
Australia

☎ +61 3 9688 4297

☎ +61 3 9688 4698

✉ valentinebogdanov@vut.edu.au

Dr Brigitte Boulard

Universite du Maine
Laboratoire des Fluorures
72085 Le Mans Cedex 9
France

☎ +33 2 43 83 33 50

☎ +33 2 43 83 35 06

✉ brigitte.boulard@fluor.univ-lemand.fr

Dr Marco Braglia

CSELT
Via G Reiss Romoli 274
10148 Torino
Italy

☎ +39 11 22 85 619

☎ +39 11 22 85 840

✉ marco.braglia@cse.lt.it

Mrs Maria Brekhovskikh

Kurnakov Inst of Gen & Inorg Chem
Russian Academy of Sciences
Leninsky pr 31
Moscow 117907
Russia

☎ +7 095 955 4853

☎ +7 095 954 1279

Dr Tomaz Catunda

Universidade de Sao Paulo
Inst de Fisica de Sao Carlos
Caixa Postal 369
SP 13560-970
Brazil

☎ +55 16 273 9861

☎ +55 16 271 3616

✉ tomaz@if.sc.usp.br

Prof Mikhail F Churbanov

Institute of Chemistry
Russian Academy of Sciences
49 Tropinin Street
GSP-75
Nizhny Norgozod 603600
Russia

☎ +7 8312 66 86 66

☎ +7 8313 66 91 62

✉ sen@hp.nnov.su

Miss J Costello

Society of Glass Technology
20 Hallam Gate Road
Sheffield S10 5BT
UK

☎ +44 114 266 3168

☎ +44 114 266 5252

✉ jill@glass.demon.co.uk

AFTER 14 SEPTEMBER

Don Valley House
Savile Street East
S4 7UQ

☎ +44 114 263 4455

☎ +44 114 263 4411

Dr Gary Dale

Dept of Electrical Engineering
University of Edinburgh
Kings Buildings
Mayfield Road
Edinburgh EH9 3JL
Scotland

☎ +44 131 650 5638

✉ gd@ee.ed.ac.uk

Mr Jean B Denis

University of Rennes 1
CEMA Lab Matériaux Photoniques
Campus de Beaulieu
F-35042 Rennes Cedex
France

☎ +33 2 99 286263

☎ +33 2 99 286972

Dr Leonid Dmitruk

General Physics Institute
Russian Academy of Sciences
Vavilov Street 38
Moscow 117947
Russia

☎ +7 095 132 8275

☎ +7 095 135 0270

Dr Hellmut Eckert

Inst für Physikalische Chemie
Westfälische Wilhelms Univ
Scholssplatz 7
D-48149 Münster
Germany

☎ +49 251 832 9161

☎ +49 251 832 9159

✉ eckert@uni-muenster.de

Dr Andrew Edgar

Victoria University
School of Chem & Phys Sciences
Kelburn Parade
Wellington
New Zealand

☎ +64 4 472 100

☎ +64 4 495 5237

✉ andy.edgar@vuw.ac.nz

Dr Peter Ewen

Dept of Electrical Engineering
University of Edinburgh
Kings Building
Mayfield Road
Edinburgh EH9 3JL
Scotland

☎ +44 131 650 5651

☎ +44 131 650 6554

✉ pjse@ee.ed.ac.uk

Mr A J Faber

TNO Inst of Applied Physics
PO Box 595
NL 5600 AN Eindhoven
The Netherlands

☎ +31 40 265 0260

☎ +31 40 244 9350

✉ faber@tpd.tno.nl

Dr Xian Feng

Shanghai Inst of Optics & Fine Mechanics
Adacemica Sinica
PO Box 800-216
Shanghai 201800
China

☎ +86 21 595 34890 564

☎ +86 21 595 28885

Prof Joaquin Fernandez

Universidad del Pais Vasco
ETSII y Telecom
Alameda Urquijo s/n
Bilbao 48013
Spain

☎ +34 944 278055

☎ +34 944 414041

✉ wupferoj@bi.ehu.es

Dr Paul S Flower

Rutherford Appleton Laboratory
Didcot
Oxon OX11 0QX
UK

☎ +44 1235 446264

☎ +44 1235 446733

✉ p.s.flower@rl.ac.uk

Prof Gunter H Frischat

TU Clausthal
Inst für Nichtmetallische Werkstoffe
We AG-Glas
Zehntnerstr 2A
38678 Clausthal-Zellerfeld
Germany

☎ +49 5232 722463

☎ +49 5232 723119

✉ gunther.frischat@tu-clausthal.

Prof Miloslav Frumar

University of Pardubice
Dept of Inorganic Chemistry
53210 Pardubice
Czech Republic

☎ +420 40 6037161

☎ +420 40 514530

✉ miloslav.frumar@upce.cz

Dr David Furniss

University of Sheffield
Centre for Glass Research
Hadfield Building
PO Box 600
Mappin Street
Sheffield S1 3JD
UK

☎ +44 114 222 5921

☎ +44 114 222 5943

✉ d.furniss@sheffield.ac.uk

Professor Fuxi Gan

Shanghai Inst of Optics & Fine Mechanics
Adacemica Sinica
PO Box 800-211
Shanghai 201800
China

☎ +86 21 5952 8814
☎ +86 21 5952 8812
✉ fxgan@fudan.ac.cn

Mr Marie Pierre Glemot

University of Rennes 1
CEMA Lab Materiaux Photoniques
Campus de Beaulieu
F-35042 Rennes Cedex
France

☎ +33 2 99 286263
☎ +33 2 99 286972

Mr Laurent Griscom

Universite de Rennes 1
Lab des Verres & Ceramiques
Campus de Beaulieu
35042 Rennes Cedex
France

☎ + 33 2 992 86734
☎ +33 2 9928 1600
✉ laurent.griscom@univ-rennes1.fr

Dr Yann Guimond

Universite de Rennes 1
Lab des Verres & Ceramiques
Campus de Beaulieu
35042 Rennes Cedex
France

☎ + 33 2 992 86734
☎ +33 2 9928 1600
✉ guimond@univ-rennes1.fr

Dr Alex Hannon

ISIS Facility
Rutherford Appleton Laboratory
Chilton
Didcot
Oxon OX11 0QX
USA

☎ +44 1235 445358
☎ +44 1235 445720
✉ a.c.hannon@rl.ac.uk

Prof Olav Gaute Helleso

Dept of Physics
University of Tromso
N-9037 Tromso Norway

☎ +47 77 64 52 97
☎ +47 77 64 55 80
✉ ogh@phys.uit.no

Dr Jong Heo

Dept of Mater Sci & Eng
POSTECH
Pohang Univ of Science & Tech
San 31, Hyoja-dong
Pohang
Kyungbuk 790-784
Korea

☎ +82 562 279 2147
☎ +82 562 279 2399
✉ jheo@postech.ac.kr

Mr Peter Hertogen

Katholieke Univ Leuven
Semiconductor Physics Lab
Celestijnenlaan 200
B-3001 Heverlee-Leuven
Belgium

☎ +32 16 32 7100
☎ +32 16 32 7987
✉ peter.hertogen@fys.kuleuven.ac.be

Dr Dan Hewak

University of Southampton
Optoelectronics Res Centre
Southampton SO17 1BJ
UK

☎ +44 1703 593 164
☎ +44 1703 593 149
✉ dh@orc.soton.ac.uk

Dr David B Hollis

Dept of Physics
University of Paisley
High Street
Paisley PA1 2BE
Scotland

☎ +44 141 848 3606
☎ +44 141 838 3616
✉ holl-ph0@paisley.ac.uk

Dr Joyce Illinger

Chief, Materials Sci Branch
European Res Office US Army
223 Old Marylebone Road
London NW1 5TH
UK

☎ +44 171 514 4930

☎ +44 171 724 1433

✉ jillinger@army.ehis. navy.mil

Dr Katsihisa Itoh

Hoya Corporation
Technology Development Lab
3-3-1 Musashino
Akishima-shi
Tokyo 196-8510
Japan

☎ +81 42546 2721

☎ +81 42546 2746

✉ ito@sngw.rdc.hoya.co. jp

Dr Animesh Jha

University of Leeds
Dept of Materials
Leeds LS2 9JT
UK

☎ +113 233 2342

☎ +113 242 2531

✉ a.jha@leeds.ac.uk

Dr Terutoshi Kanamori

NTT Opto-electronics Lab
Tokai-Mura, Naka-gun
Tokai
Ibaraki 310
Japan

☎ +81 29 287 7519

☎ +81 29 287 7193

✉ kanamori@iba.iecl.ntt. co.jp

Dr Jens Kobelke

Inst für Physikalische Hochtechnologie
IPHTe v Jena
Helmholtzweg 4
D-07743 Jena
Germany

☎ +49 3641 302818

☎ +49 3641 302850

✉ kobelke@main.ipht- jena.de

Mr Joerg Kraus

CSELT
Via G Reiss Romoli 274
10148 Torino
Italy

☎ + 39 11 228 7311

☎ +39 11 228 5840

✉ joerg.kraus@cse.lt.it

Ms Liv Kukkonen

University of Sheffield
Dept of Engineering Materials
Hadfield Building, Mappin Street
Sheffield S1 3JD
UK

☎ +114 222 5983

Dr Irina Kuznetsova

Kurnakov Inst of Gen & Inorg Chem
Russian Academy of Sciences
Leninsky pr 31
Moscow 117907
Russia

☎ +7 095 5 48 53

☎ +7 095 4 12 79

Dr Giles Le Flem

ICMCB
Ave du Dr A Schweitzer
33608 Pessac Cedex
France

☎ +33 56 84 62 94

☎ +33 56 84 27 61

✉ leflem@chimsol.icmbc.u- bordeaux

Dr Ronan Lebullenger

IFSC Univ de Sao Paulo
Grupo de Materials
PO Box 369
13560-250 Sao Carlos SP
Brazil

☎ +55 16 273 9828

☎ +55 16 261 5440

✉ lebullen@if.sc.usp.br

Dr Ruihua Li

University of Sheffield
Centre for Glass Research
Hadfield Building, Mappin Street
Sheffield S1 3JD
UK

☎ +44 114 222 5957

☎ +44 114 222 5943

✉ r.li@shef.ac.uk

Mr Xiaobo Liu
University of Leeds
Dept of Materials
Leeds LS2 9JT
UK

☎ +44 113 233 2366
☎ +44 113 233 2531
✉ liu@leeds.ac.uk

Professor Jacques Lucas
Universite de Rennes 1
Lab des Verres & Ceramiques
Campus de Beaulieu
35042 Rennes Cedex
France

☎ +33 299 28 6262
☎ +33 299 28 1600
✉ j.lucas@univ-rennes1.fr

Miss Hongli Ma
University of Rennes 1
Lab des Verres & Ceramiques
Campus de Beaulieu
35042 Rennes
France

☎ +33 299 286262
☎ +33 299 281600

Dr Douglas MacFarlane
Monash University
Dept of Chemistry
Clayton
Victoria 3168
Australia

☎ +61 3 9905 4540
☎ +61 3 9905 4597
✉ d.macfarlane@sci.monash.edu.au

Dr Inge Irma Maes
UM Research
Kasteelstraat 7
B-2250 Olen
Belgium

☎ +32 14 24 50 31
☎ +32 14 24 57 16
✉ inge.maes@um.be

Dr Steve W Martin
Iowa State University of Science
& Technology
Dept of Mater Sci & Engineering
Ames
Iowa 50011
USA

☎ +1 515 294 0745
☎ +1 515 294 5444
✉ swmartin@iastate.edu

Mr Orlando Martins
INESC/IST
Rua Alves Redol 9-3D
Lisbon 1000
Portugal

☎ +351 1 3100 369
☎ +351 1 314 5843
✉ omartins@eniac.inesc.pt

Miss K J McKinlay
57 Trickett Road
Hillsborough
Sheffield S6 2NP
UK

☎ +44 114 268 6201
☎ +44 114 268 1073
✉ j.mckinlay@britglass.co.uk

Professor Mikhail Mikhailov
Corning Scientific Centre in St
Petersburg
Westpost PO Box 109
Lappeenranta
Fin 53101
Finland

☎ +7 812 329 2074
☎ +7 812 329 2061
✉ corning@infopro.spb.su

Eng Paulo J Morais
INESC
Rua Alves Redol 9-3D
Lisbon 1000
Portugal

☎ +351 1 3100000 ext 2369
☎ +351 1 3145843
✉ hjgdm@email.inesc.pt

Dr Michel Mortier
CNRS-UPR 211
1 Place A Briand
92190 Meudon Bellevue
France
☎ +33 1 4507 53 00
📠 +33 1 4507 5107
💻 mortier@cnrs/bellevue.fr

Dr Sabrina Mosso
CSELT
Via G Reiss Romoli 274
10148 Torino
Italy
☎ +39 11 228 5619
📠 +39 11 228 5840
💻 sabrina.mosso@cse.lt

Dr A Murali
Sri Venkateswara University
Senior Research Fellow
Dept of Physics
Tirupati 517 502
India
☎ +91 8574 50666
📠 +91 8574 27499
💻 cybernet@cyberservices.com

Mr Michael Murtagh
Rutgers University
Dept of Ceramic & Materials Eng
607 Taylor Road
Piscataway
NJ 08854-8065
USA
☎ +1 732 445 4526
📠 +1 732 445 3258
💻 murtagh@rei.rutgers.edu

Dr Mira Naftaly
University of Leeds
Dept of Materials
Leeds LS2 9JT
UK
☎ +44 113 233 2551
📠 +44 113 242 2531
💻 naftaly@leeds.ac.uk

Dr Francesco Negrisola
Vile Sarca 222
Milano
Italy
☎ +39 266 423872
📠 +39 264 425466

Professor Gerard Palavit
Bat C5 2^e etage
UFR de Chimie USTL
59655 Villeneuve d'Ascq Cedex
France
☎ +33 3 204 34186
📠 +33 3 203 37246
💻 gerard.palavit@univ-lille1

Dr John M Parker
University of Sheffield
Dept of Engineering Materials
Hadfield Building
Mappin Street
Sheffield S1 3JD UK
UK
☎ +44 114 222 5514
📠 +44 114 222 5943
💻 j.m.parker@sheffield.ac.uk

Dr David Payne
University of Southampton
Fibre Optics Institute
Dept Electronics & Info
Southampton SO9 5NH
UK
☎ +44 1703 594521
📠 +44 1703 593142
💻 dnp@orc.soton.ac.uk

Dr Martin G Pellatt
Merck Ltd
Merck House
Poole
Dorset BH15 1TD
UK
☎ +44 1202 664565
📠 +44 1202 666530
💻 martin.pellatt@merck-ltd.co.uk

Dr Marcel Poulain
University of Rennes 1
CEMA Lab Matériaux Photoniques
Campus de Beaulieu
F-35042
Rennes Cedex
France

☎ +33 2 99 286263
☎ +33 2 99 286972
✉ poulain@univ-rennes1.fr

Dr Michel Poulain
University of Rennes 1
CEMA Lab Matériaux Photoniques
Campus de Beaulieu
F-35042 Rennes Cedex
France

☎ +33 2 99 286263
☎ +33 2 99 286972
✉ poulain@univ-rennes1.fr

Dr Antonina Provorova
Russian Inst of Chem Tech
Kashizskoe Shosse 33
Moscow 115230
Russia

☎ +7 095 324 8884
☎ +7 095 324 5441

Dr Jianrong Qiu
Hirao Active Glass Project
ERATO JST
Super-Lab 206 Keihanna Plaza
Kyoto 619-02
Japan

☎ +81 774 95 5205
☎ +81 774 05 5206
✉ jrj@hap.jst.go.jp

Miss Carine Quemard
Universite de Rennes 1
Lab des Verres & Ceramiques
Campus de Beaulieu
35042 Rennes Cedex
France

☎ +33 2 9928 1610
☎ +33 2 9928 1600
✉ carine.quemard@univ-rennes1.fr

Prof Richard Quimby
Dept of Physics
Worcester Polytechnic Inst
100 Institute Road
Worcester
MA 01609-2280
USA

☎ +1 508 831 5490
☎ +1 508 831 5886
✉ rsquimby@wpi.edu

Dr Ian M Reaney
University of Sheffield
Centre for Glass Research
Hadfield Building
Mappin Street
Sheffield S1 3JD
UK

☎ +44 114 222 5471
☎ +44 114 222 5943
✉ i.m.reaney@sheffield.ac.uk

Dr Kathleen Richardson
University of Central Florida
CREOL
PO Box 162700
4000 Central Florida Blvd
Orlando
FL 32765
USA

☎ +1 407 823 6822
☎ +1 407 823 6880
✉ kcr@creol.ucf.edu

Professor Subhash Risbud
Univ of California at Davis
Dept Chemical Eng and Mater Sci
One Shields Avenue
Davis
CA 95616
USA

☎ +1 530 752 5132
☎ +1 530 754 6350
✉ shrisbud@ucdavis.edu

Dr Mohammed Saad
Institut National d'Optique
369 rue Franquet
Sainte Foy
Quebec
Canada G1P 4N8
☎ +1 418 657 7006
☎ +1 418 657 7009
✉ saad@ino.qc.ca

Dr Jas Sanghera

Naval Research Laboratory
Code 6505 2
Washington DC 20375
USA

☎ +1 202 767 5836

☎ +1 202 404 6355

✉ sanghera@ccf.nrl.navy.mil

Dr Michael Scheffler

Inst für Physikalische Hochtechnologie
IPHTe v Jena PF 100 239
D-0743 Jena
Germany

☎ +49 3641 302 868

☎ +49 3641 302 850

✉ scheffler@main.ipht-jena.de

Mr Ronald C Schimmel

TNO Inst of Applied Physics
PO Box 595
NL 5600 AN Eindhoven
The Netherlands

☎ +31 40 2660 262

☎ +31 40 244 9350

✉ r.c.schimmel@tpd.tno.nl

Mr Adam Schrader

NYS College of Ceramics
Alfred University
2 Pine Street
Alfred
NY 14802
USA

☎ +1 607 562 8689

☎ +1 607 871 2392

✉ schrader@bigvax.alfred

Dr Igor Scripachev

Russian Academy of Sciences
Inst of Chemistry of High Purity Substances
GSP-75
603600 Nizhny Norgozod
Russia

☎ +7 8312 66 8542

☎ +7 8312 66 8666

✉ sen@hp.nnov.su

Dr Angela B Seddon

University of Sheffield
Centre for Glass Research
Hadfield Building
Mappin Street
Sheffield S1 3JD
UK

☎ +44 114 222 5516

☎ +44 114 222 5943

✉ a.b.seddon@sheffield.ac.uk

Mr Shaoxiong Shen

85 Oatland Heights
Leeds LS7 1SQ
UK

☎ +44 113 242 1046

✉ mssess@leeds.ac.uk

Mr Jonathan D Shephard

University of Sheffield
Dept of Engineering Materials
Hadfield Building
Mappin Street
Sheffield S1 3JD
UK

☎ +44 114 222 5990

☎ +44 114 222 5943

✉ mtp95jds@sheffield.ac.uk

Dr Yutaka Shimizugawa

1-8-31 Midorigaoka
Ikeda
Osaka 563 8577
Japan

☎ +81 727 51 9537

☎ +81 727 51 9631

✉ shimizug@onri.go.jp

Ms Catherine Simmons

University of Florida
Department of Materials
Box 116400
Gainesville
FL 32611-6400
USA

☎ +1 352 392 6679

☎ +1 352 392 1756

✉ cjs@silica.mse.ufl.edu

Prof Joseph H Simmons

Dept of Mater Sci & Eng
University of Florida
PO Box 116400
Gainesville
FL 32611
USA

☎ +1 352 392 6679

☎ +1 352 392 1751

✉ simmons@silica.mse.ufl.edu

Dr Frederic Smehtala

Universite de Rennes 1
Lab des Verres & Ceramiques
Campus de Beaulieu
35042 Rennes Cedex
France

☎ +33 2 9928 1610

☎ +33 2 9928 1600

✉ smehtala@univ-rennes1.fr

Dr David J Sparrowe

Merck Ltd
Merck House
Poole
Dorset BH15 1TD
UK

☎ +44 1202 493565

☎ +44 1202 670153

✉ david.sparrowe@merck-ltd.co.uk

Miss Ruth Sramek

Universite de Rennes 1
Lab des Verres & Ceramiques
Campus de Beaulieu
35042 Rennes Cedex
France

☎ +33 2 9928 1610

☎ +33 2 9928 1600

✉ ruth.sramek@univ-rennes1.fr

Professor Martin Stickley

USAF European Office of Aerospace R&D
223 Old Marylebone Road
London NW1 5TH
UK

☎ +44 171 514 4354

☎ +44 171 514 4960

✉ mstickley@eoard.af.mil

Dr Kiyoharu Tadanaga

University of Sheffield
Centre for Glass Research
Hadfield Building
Mappin Street
Sheffield S1 3JD
UK

☎ +44 114 222 5921

☎ +44 114 222 5943

✉ mt4kt@sheffield.ac.uk

Dr Setsuhisa Tanabe

Faculty of Integrated Studies
Kyoto University
Sakyo-ku
Kyoto 606-8501
Japan

☎ +81 75 753 6821

☎ +81 75 753 6844

✉ tanabe@chem.h.kyoto-u.ac.jp

Dr Philippe Thomas

LMCTS Faculte des Sciences
123 Avenue Albert Thomas
87060 Limoges Cedex
France

☎ +33 5 55 45 74 96

☎ +33 5 55 45 72 70

✉ pthomas@unilim.fr

Dr Paul Tick

Corning Incorporated
AR218N
Sullivan Park
Corning
NY 14831
USA

☎ +1 607 974 3251

☎ +1 607 974 3675

Dr Victor Tikhomirov

University of Leeds
Dept of Materials
Leeds LS2 9JT
UK

☎ +44 113 233 2551

☎ +44 113 242 2531

✉ v.tikhomirov@leeds.ac.uk

Prof Dr Yuriy S Tver'yanovich

Dept of Chemistry
St Petersburg University
Prospekt 2
St Petersburg 198904
Russia

☎ +7 812 428 69 33

☎ +7 812 428 74 79

✉ yuratver@yt2461.spb.edu

Professor Norimasa Umesaki

Osaka National Res Inst
AIST
1-8-31 Midoriga-oka
Ikeda
Osaka 563 8577
Japan

☎ +81 727 51 9536

☎ +81 727 51 9631

✉ umesaki@onri.go.jp

Dr Natalya Vinogradova

General Physics Institute
Vavilov Street 38
Moscow 117947
Russia

☎ +7 095132 82 75

☎ +7 095 135 0279

Dr Yvonne West

University of Southampton
Optoelectronics Res Centre
Southampton SO17 1BJ
UK

☎ +44 1708 592825

☎ +44 1703 593149

✉ yw@orc.soton.ac.uk

Professor F Wise

Dept of Applied Physics
Cornell University
Ithaca
New York 14853
USA

☎ +1 607 255 1184

☎ +1 607 255 7658

✉ fwise@msc.cornell.edu

Professor Ling Zan

IR MAT Lab
Wuhan University
Wuhan 430072
China

☎ +86 27 8749 4524

☎ +86 27 8679 4019

✉ zhanlin@public.wh.hb.cn

Dr Jia-cheng Zhong

IR MAT Lab
Wuhan University
Wuhan 430072
China

☎ +86 27 8749 4524

☎ +86 27 8679 4019

✉ zhong@public.wh.hb.cn

11th International Symposium on
Non-Oxide Glasses and New Optical Glasses

6 to 10 September 1998, University of Sheffield, UK

SUPPLEMENTARY BOOKLET

of

EXTENDED ABSTRACTS

An Investigation of the Complex Upconversion Energy Transfer between two and three kinds of the TR^{3+} Ions in a Fluorozirkonate Glass.

A.A.Andronov, I.A.Grishin, V.A.Guryev and A.P.Savikin

Quantum Radiophysics Department, University of Nizhny Novgorod,
Gagarin av., 23, 603600 Nizhny Novgorod, Russia
e-mail: laser@rf.unn.runnet.ru

INTRODUCTION Heavy-metal fluoride glass is very attractive medium for active optics: lasers and amplifiers when doped with trivalent Rare-Earth (TR^{3+}) ions. It was shown that optical properties of most part TR^{3+} such as Er^{3+} , Pr^{3+} , Yb^{3+} , Tm^{3+} , Ho^{3+} etc in fluoride host (for example, in fluorozirkonate glass ZBLAN) are sufficiently better than in silica. This caused by relatively low phonon energy of the host: $\sim 550 - 590 \text{ cm}^{-1}$ for various ZBLAN compositions and strong ion-host and ion-ion interactions which lead to inhomogenous broadening of energy levels and specific energy transfer between ions. Due to this, the effect of upconversion luminescence in the near-VU, blue-green and red bands excited with near-IR through stepwise and cooperative processes, is much more effective in fluoride glasses than in silica, phosphate and other glasses. It is well known that the efficiency of laser emission can be increased by addition of another kind of active ions which absorb pump radiation and transfer the excitation energy to the working ions. This method of *sensibilization* of laser media is suitable for upconversion applications too. The most popular donor ion for upconversion applications is Ytterbium which absorbs IR light near 975nm with $\Delta\lambda \approx 7\text{nm}$ ($^2F_{7/2} \rightarrow ^2F_{5/2}$ manifolds transition in ZBLAN glass) and transfer this excitation to another kind of ions: Er^{3+} , Pr^{3+} , Tm^{3+} , Ho^{3+} via cross-relaxation and cooperative processes. An infrared emission can be also sensibilized in pairs such as Pr^{3+} / Nd^{3+} , Tm^{3+} / Nd^{3+} , Er^{3+} / Ho^{3+} etc. We also shown that Rare-Earth «triplet» $Er^{3+} / Ho^{3+} / Yb^{3+}$ in fluoride glass has increased upconversion efficiency and very interesting for low-threshold fiber lasers applications.

EXPERIMENTAL We have studied an upconversion luminescence from 2mm thick samples of synthetic fluorozirkonate glass ZBLAN composed as shown in Table (in molar %):

	ZrF ₄	BaF ₂	AlF ₃	LaF ₃	YbF ₃	ErF ₃	HoF ₃	NaF
1	52	20	4	3	-	1	-	20
2	52	20	4	1	-	3	-	20
3	52	20	4	-	3	1	-	20
4	52	20	4	-	3	-	1	20
5	51.75	20	4	-	3	1	0.25	20
6	51.5	20	4	-	3	1	0.5	20
7	51	20	4	-	3	1	1	20

The InGaAs/GaAs quantum-well CW diode-laser ($\lambda_{\text{pump}} = 970 \div 985 \text{ nm}$, $P \leq 1500 \text{ mW}$) was used as a pump source, focused into samples with 85mm objective. For low temperature measurements we mounted samples on a copper sink with a thermocouple and put them into Dewar with optical windows. Luminescence emission was analyzed with home-made automated spectrofluorimeter based on DFS-12 double monochromator of 0.01nm spectral

resolution. Photon counting technique was used to detect and analyze pulses from S20 PMT FEU-79.

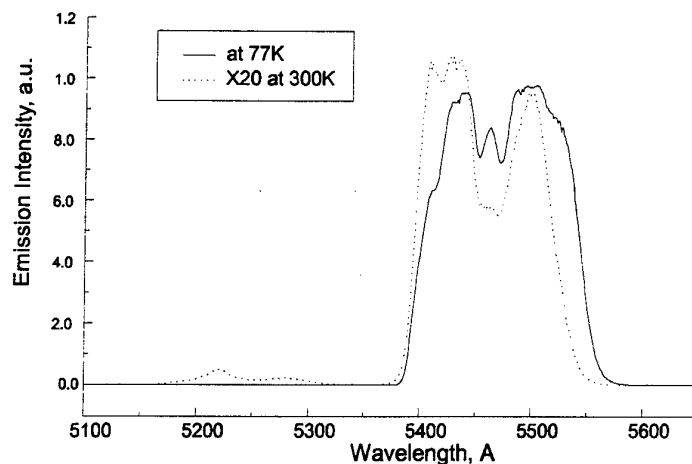


Fig. 1.

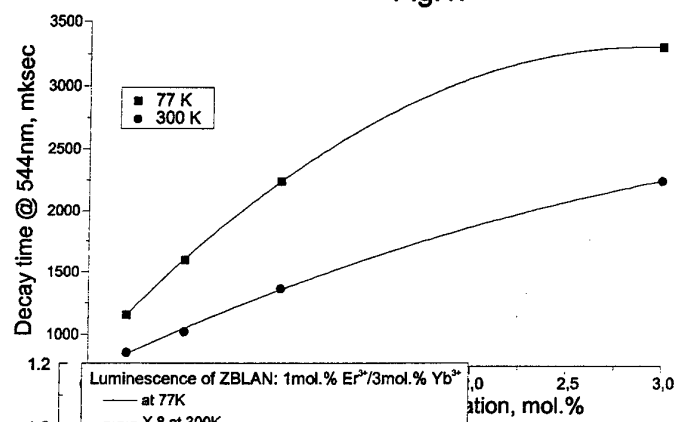


Fig. 2.

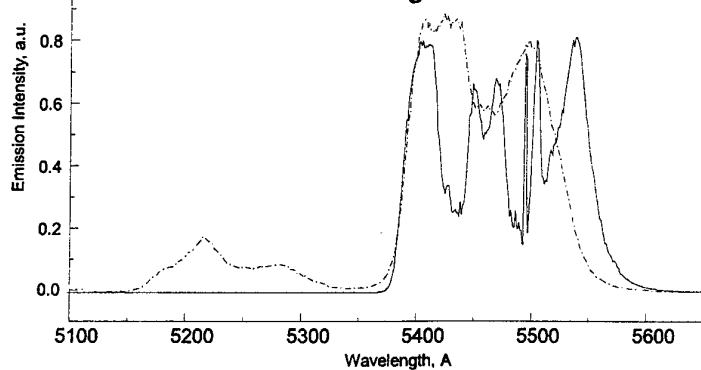


Fig. 3.

RESULTS AND DISCUSSION

Spectra of an upconversion luminescence of sample 1 (1mol.% Er^{3+} :ZBLAN) at room (dotted curve, scaled in 20 times) and nitrogen temperatures (solid curve) are shown in Fig. 1.

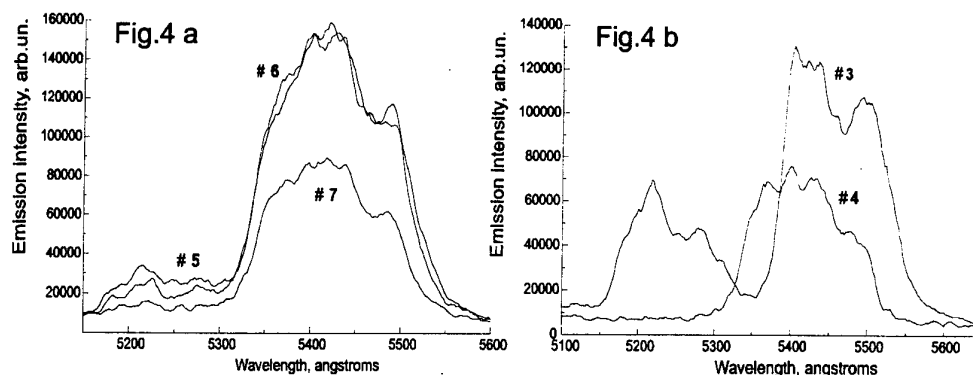
Dependencies of the luminescence decay time on erbium concentration at these temperatures are shown on Fig. 2. Additional doping with Yb^{3+} (sample 3) lead the increasing the overall green luminescence at least in 3.5 times in comparison with sample 1 (single erbium of the same concentration).

But at 77K the growth of the upconversion efficiency in $\text{Er}^{3+}/\text{Yb}^{3+}$ pair is only 8 times, Fig. 3. Decay times of green luminescence at 544nm (the gravity center of the $^4\text{S}_{3/2} \rightarrow ^4\text{I}_{15/2}$ transition) in pair at room and nitrogen temperatures become 1091 and 1452 mksec correspondingly, that is considerably smaller than in the single erbium of 1mol.% (see Fig. 2).

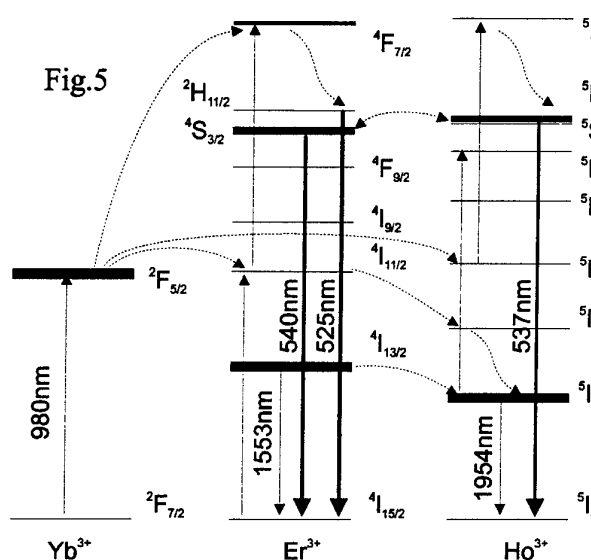
It can be seen from Fig. 1 and 3, that the luminescence in band $\lambda \approx 520 \div 530\text{nm}$ ($^2\text{H}_{11/2} \rightarrow ^4\text{I}_{15/2}$ transition) hasn't appear at 77K neither in Er^{3+} nor in $\text{Er}^{3+}/\text{Yb}^{3+}$ -doped samples. This fact can be explained if we suppose that level $^2\text{H}_{11/2}$ populates from lower

energy level, $^4\text{S}_{3/2}$ with phonons ($h\nu_{\text{ph}} \approx 576\text{ cm}^{-1}$) absorption.

An idea of three (and even four) kinds of ions in the same host is old enough. The such doping was used to increase the efficiency (sensibilize) of solid-state IR lasers due to ion-ion energy transfer: typically, $\text{Er}^{3+}/\text{Tm}^{3+}/\text{Ho}^{3+}$, $\text{Er}^{3+}/\text{Tm}^{3+}/\text{Yb}^{3+}$, $\text{Nd}^{3+}/\text{Tm}^{3+}/\text{Cr}^{3+}$ etc. It was found in [1], that triply-doped fluorozirconate glass $\text{Yb}^{3+}/\text{Er}^{3+}/\text{Ho}^{3+}$:ZBLAN (samples 5-7) has improved



characteristics of upconversion luminescence: overall intensity, shape smoothing and lower power density threshold. Spectra of upconversion luminescence of triply doped ZBLAN and, for comparison, those of pairs $\text{Yb}^{3+}/\text{Er}^{3+}$ and $\text{Yb}^{3+}/\text{Ho}^{3+}$ - **Figs. 4a** and **b** correspondingly. At present time we're going to explain the discussed phenomena as follows (see **Fig.5**).



First: the Ho^{3+} ion provides upconversion such as Er^{3+} one, with similar pump/luminescence wavelengths and comparable efficiency. The second goal of co-doping the $\text{Yb}^{3+}/\text{Er}^{3+}$ pair with Ho^{3+} is well-known: ion-ion energy transfer between lower levels of these ions, (including phonon-assisted transitions) i.e. $\text{Er}^{3+} : ^4\text{I}_{11/2} \rightarrow \text{Ho}^{3+} : ^5\text{I}_6$; $\text{Er}^{3+} : ^4\text{I}_{13/2} \rightarrow \text{Ho}^{3+} : ^5\text{I}_7$ leads to depopulation of metastable erbium levels, which slow down the speed of upconversion process. There are also some energy transfer processes between higher levels of this system, which also improving its upconversion characteristics: $\text{Er}^{3+} : ^2\text{H}_{11/2} \rightarrow \text{Ho}^{3+} : ^5\text{F}_4$ (the presence of this transition is follows from

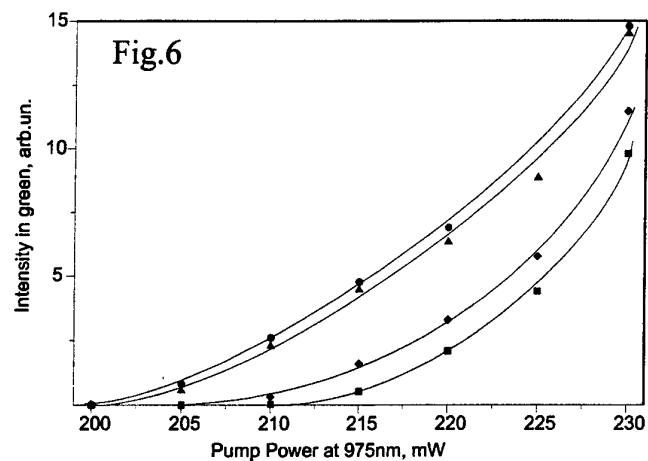
luminescence spectra near 525nm, Fig.4a); $\text{Ho}^{3+} : ^5\text{S}_2 \leftrightarrow \text{Er}^{3+} : ^4\text{S}_{3/2}$ - this transfer is expected to be reciprocal, $\text{Ho} \rightarrow \text{Er}$ because of positive ΔE of corresponding levels and $\text{Er} \rightarrow \text{Ho}$ (from experimental data). The promising of triply-doped ZBLAN for low-threshold upconversion fiber lasers is also illustrated with the results of measurement of pump power dependence of green luminescence intensity [2], **Fig.6**, there circles correspond to 0.25mol.% of Ho^{3+} , triangles - 0.5, diamonds - 1 and squares - to sample without holmium.

Results of our just performed experiments with spectra and kinetics of triply-doped ZBLAN samples at room and liquid nitrogen temperatures, which aren't presented here, also give us a reason to consider these compositions and the idea of triple doping as very interesting and attractive for further research.

The Research project is supported by Russian Foundation for Basic Research Grant No. 96-02-16996a

REFERENCES

- [1] I.A.Grishin, V.A.Guryev, V.L.Mart'yanov, and A.P.Savikin //Tech.Phys.Lett.- 23 (1997), No.1, pp. 70-72
- [2] A.A.Andronov, I.A.Grishin, V.A.Guryev, and A.P.Savikin //Proc. LEOS 10th Meeting, v.2, (1997), p. 387



TEM STUDIES OF 70Ga₂S₃-30La₂S₃ GLASSES

I. M. Reaney, S. P. Morgan[#], R. Li and A. B. Seddon.

Centre for Glass Research,
Department of Engineering Materials, University of Sheffield, Sheffield, S1 3JD, UK.

ABSTRACT

The crystallisation of 70Ga₂S₃-30La₂S₃ glasses after isothermal reheating for 3h just above the glass transformation range (T_g), and then rapid quenching to ambient, has been studied using transmission electron microscopy (TEM). Glasses prepared from sulphides (supplied by Merck Ltd., UK, before June 1996) were melted under vacuum in a vitreous carbon crucible, sealed inside a silica tube. Low oxide content glasses devitrified slightly on quenching. On reheating close to T_g, low oxide glasses formed barrel shaped crystallites composed of laths of a new monoclinic phase, with inter-lath crystals which were gallium-rich and may be Ga₂S₃. On reheating glass samples containing greater levels of oxide, barrel shaped crystals formed composed of laths of melilite-structured La_{3.33}Ga₆S₁₄ and the new phase in an eutectic or eutectoid-like microstructure.

INTRODUCTION

100-xGa₂S₃-xLa₂S₃ (GLS) based glasses were investigated quite extensively in the 1970's by Loireau-Lozac'h *et al.*^{2,3} who mapped out the glass forming region³ and identified crystalline phases. According to these authors, slow cooling produced a mixture of α-Ga₂S₃ and a hexagonal phase, LaGaS₃. On reheating a glass of 64Ga₂S₃:36La₂S₃ (mol%), LaGaS₃, hexagonal La₆Ga_{3.33}S₁₄, and tetragonal La_{3.33}Ga₆S₁₄ were produced. When the Ga₂S₃ content was increased, heat treatment resulted in La_{3.33}Ga₆S₁₄.

More recent investigations^{4,5} have revealed glass formation and crystallisation behaviour that contradicts the work of Loireau-Lozac'h *et al.*^{2,3}. Morgan *et al.*⁴ found that glass formation, using the same sulphide precursors and melting schedule described below, was difficult from precursor sulphides containing less than about 0.5 wt % oxygen.⁴ Furthermore, X-ray diffraction patterns from reheated crystallized samples produced by Morgan^{4,5} did not correspond to the phases and phase evolution reported by Loireau-Lozac'h *et al.*^{2,3}.

To investigate the discrepancy between recent results^{4,5} and those reported previously^{2,3}, two glasses of composition 70Ga₂S₃:30La₂S₃ have been produced using precursors with different oxygen concentrations. These were isothermally reheated for 3h not far above the glass transformation range T_g for 3h and then rapidly quenched to ambient. Phase growth was investigated in detail using transmission electron microscopy.

EXPERIMENTAL PROCEDURES

5g glass batches of composition 70Ga₂S₃:30La₂S₃ (mol%) were melted under vacuum from gallium and lanthanum sulphides (4N supplied before June 1996, by Merck Ltd., UK) inside a vitreous carbon crucible within a sealed silica tube. Glass 1 contained less than about 0.5 wt% oxygen whereas glass 2 contained very approximately 1 wt % oxygen, as defined using the information supplied by the raw material manufacturer and assuming that the batch oxide

[#] now at, British Nuclear Fuels, Sellafield, Seascale, Cumbria, CA20 1PG, UK.

level persists in the as-prepared glasses. In order to study crystallisation behaviour, glasses 1 and 2 were heat treated under dry, white spot, flowing nitrogen (BOC,UK) in a carbon boat for 3 hours at 590°C for glass 1 and 600°C for glass 2, respectively.

Infrared (IR) spectra were collected on a Perkin-Elmer series 2000 Fourier transform infrared (FTIR) spectrophotometer using as-prepared glasses which were polished to a few mm pathlength. Absorbance spectra were normalised to a 1mm sample pathlength and then converted to % transmission. A Philips 1700 diffractometer was used for powder X-ray diffraction (XRD). Cu K α radiation was used to scan samples through the range 20 to 80 °2 θ at 2°2 θ minute⁻¹.

Samples, no smaller than 4mm diameter, were prepared by grinding to ~30 microns thick, at which point a copper ring was stuck to the sample using epoxy resin. The sample was then ion beam milled using a GATAN Dual Ion Mill, Model 600, at an angle of 15°, whilst rotating, until a hole had been produced. JEOL 3010 and Philips 420 transmission electron microscopes equipped with Oxford instruments Link eXL EDS (energy dispersive spectroscopic) detectors and workstations were used to image and to analyse the composition of samples.

RESULTS AND DISCUSSION

The low oxide GLS glasses were difficult to prepare crystal-free and hence usually contained low levels of crystals within a substantially glassy matrix. Having closely examined these crystals under different orientations in the transmission optical microscope, we suggest that they are barrel shaped rather than octahedral, as previously reported by Morgan *et al.*⁵.

Figure 1 shows infrared spectra of as-prepared glasses 1 and 2. Typical background transmission was 70-72% and spectra contained common absorption bands at 2.94 μ m (3400cm⁻¹), 5.50 μ m (1817cm⁻¹), 8.63 μ m (1158cm⁻¹) with an IR edge composed of two bands at 10.71 μ m (933cm⁻¹) and 12.63 μ m (792cm⁻¹). It should be noted that, as the oxygen content of the glass precursors increased, the intensity of the band at 8.63 μ m also increased. Madeiros-Neto (1995)⁶ and Hewak (1994)⁷ have suggested that this band is associated with SO₄²⁻ in the GLS system and its increase in glass 2 is consistent with a higher O-concentration.

After heat treatment, XRD patterns of the quenched samples clearly showed that, although the morphologies of the crystals remained similar according to optical microscopy, the crystallisation product changed as the oxygen increased, Fig. 2. Several of the peaks associated with crystallised glass 2 could be indexed according to the phase La_{10/3}Ga₆S₁₄ which has a melilite structure and was first observed in the GLS system by Loireau-Lozazh *et al.*^{2,3}. The peaks in the spectra obtained from crystallized glass 1 and several major ones from glass 2, which matched each other, did not match any known phase in the JCPDS data files. However, Morgan *et al.*⁸, in their study of the crystallisation of 70:30 GLS glass suggest that this phase has a monoclinic Bravais lattice, $a = 0.58$, $b = 1.02$, $c = 0.94$ nm and $\beta = 86^\circ$.

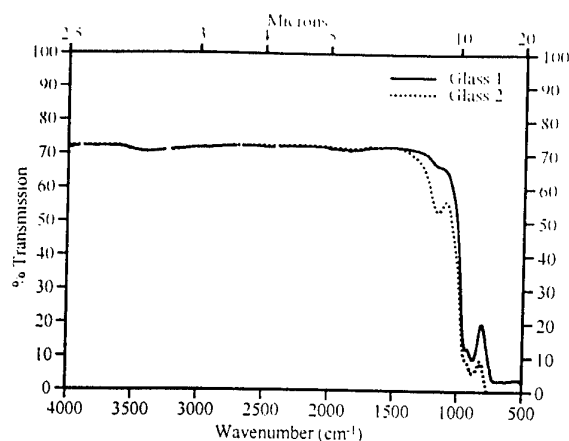


Figure 1. Fourier transform infrared spectra of glass 1 and 2.

Figure 3 is a TEM image showing the internal morphology of the barrel shaped crystallites found on quenching and heat treatment of glass 1. The crystals consist of lamellae separated by an inter-lath phase. The laths are around 1 μm in diameter and have approximately a 2:1 Ga_2S_3 : La_2S_3 ratio according to EDS analysis.⁸ The inter-lath phase was shown by EDS to be Ga-rich and it is suggested that this might be α - Ga_2S_3 .

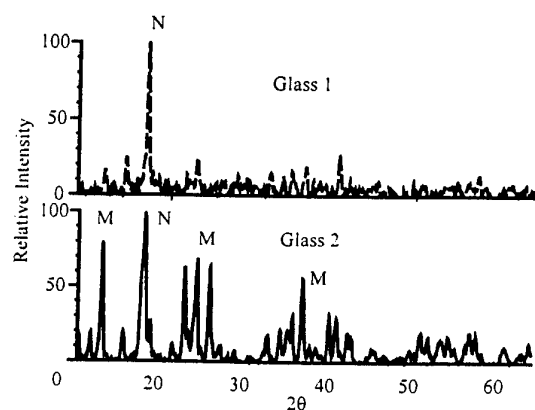


Figure 2. X-ray patterns of glasses 1 and 2, heat treated at 590°C and 610°C, respectively, for 3h. M=melilite; N=new phase.

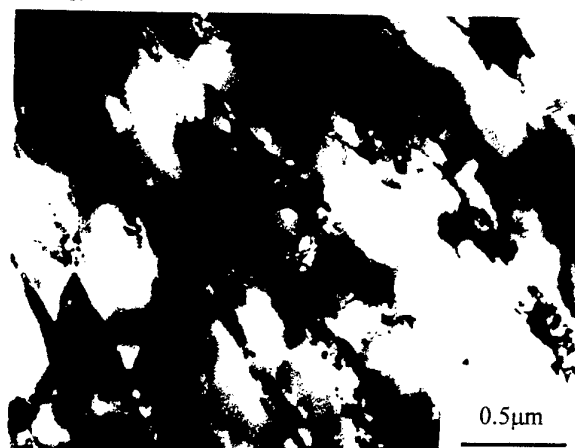


Figure 3. TEM image showing the internal morphology of crystallites in glass 1 (low oxide) which have grown during melt-quenching and/or reheating at 590°C/3h.

TEM images from heat treated glass 2 appeared to indicate that the crystals have a different internal microstructure from those observed in glass 1. Fig. 4. The diffraction contrast suggests an intergrowth of either two orientations of the same phase or two different phases. In addition, the laths are narrower and less linear than observed in glass 1, resembling an eutectic or eutectoid microstructure. EDS spectra from adjacent laths, typified by Fig. 5, were virtually identical and contained significant amounts of La. Therefore, the Ga_2S_3 phase, proposed to exist between laths in crystallised glass 1, was not considered to be present as one of the intergrowth phases.

Morphologically identical crystals to those in Fig. 4 have been studied in great detail (Figs 6 and 7). These crystals were found to grow (accompanied by other phases which will be discussed in a future paper) during the melt-cooling of more recent samples of GLS: specifically, $65\text{Ga}_2\text{S}_3\text{-}35\text{La}_2\text{S}_3$ made from component sulphides ('standard' supplied by Merck after June 1996) melted inside a vitreous carbon crucible, held inside a silica tube; the batch contained 0.44wt% total oxygen according to LECO analysis. Melt-cooling of $65\text{Ga}_2\text{S}_3\text{-}35\text{La}_2\text{S}_3$ was achieved by cooling from the liquidus at 1°C min^{-1} to 785°C , immediately followed by fast quenching to ambient. TEM of the intergrowth type crystals gave many spots on the electron diffraction patterns from the intergrowth itself. Fig. 6, which could be indexed according to the $[001]$ zone axis of the new monoclinic phase found in glass 1.⁸ The extra reflections could be indexed according to the $[001]$ zone axis of the melilite-structured compound, $\text{La}_{3.33}\text{Ga}_6\text{S}_{14}$. Figure 7 is an end-on view of the same kind of intergrowth as observed initially in plan view in Fig. 4 for glass 2. Two sets of lattice fringes are apparent.

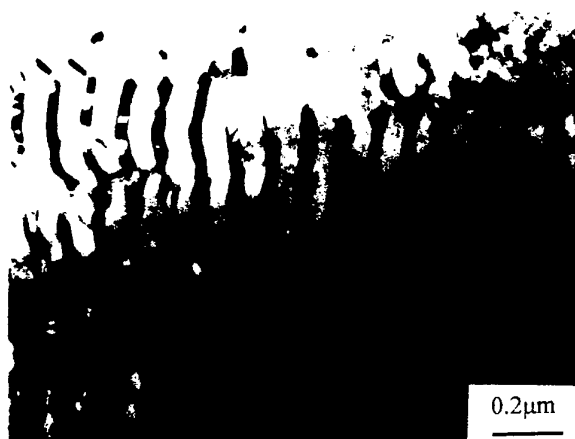


Figure 4. Transmission electron micrograph of the internal structure of the crystallites in the heat treated glass 2 at $610^\circ\text{C}/3\text{h}$.

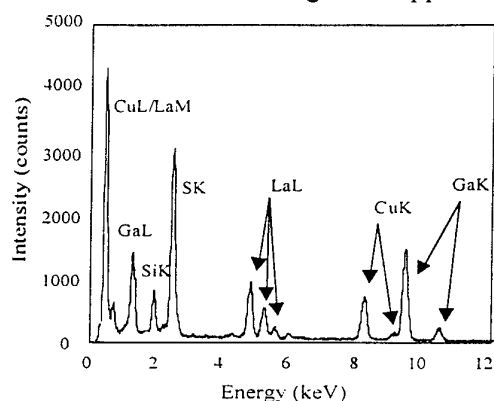


Figure 5. Energy dispersive X-ray spectra from phases shown in Fig. 4.

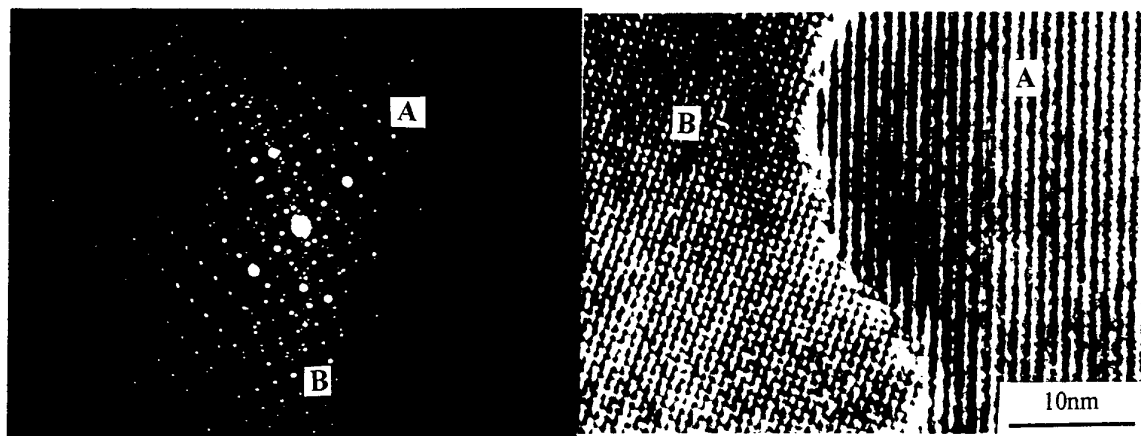


Figure 6. Electron diffraction pattern from laths, one phase found in $65\text{Ga}_2\text{S}_3\text{-}35\text{La}_2\text{S}_3$ which had been cooled from the liquidus at 1°C min^{-1} to 785°C , followed by fast quenching to ambient. The crystals appear morphologically identical to those observed in Glass 2 (Fig 5). A = $[001]_{\text{new phase}}$ after ref[8] and B = $[001]_{\text{melilite}}$ after refs [2,3].

Figure 7. End-on lattice image of the laths found in Fig. 6 and morphologically identical to laths shown in plan view in Fig. 4 for glass 2. A = region of new phase and B = melilite.

These are marked A and B in the image. The region marked A arises from the new monoclinic phase whereas B corresponds to a second phase with a different d-spacing, compatible with melilite-structured, $\text{La}_{3.33}\text{Ga}_6\text{S}_{14}$. If EDS traces from the two sets of laths are compared then they appear virtually coincident, Fig. 5, indicating that the new GLS phase and the second phase have similar $\text{Ga}_2\text{S}_3:\text{La}_2\text{S}_3$ ratios.

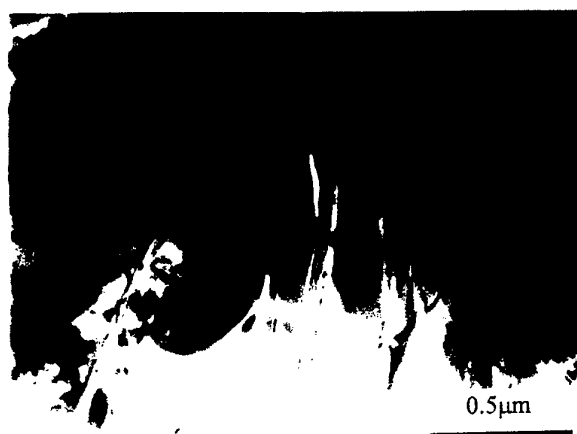


Figure 8. TEM micrograph showing region of residual glass between barrel shaped crystals in heat treated glass 2.

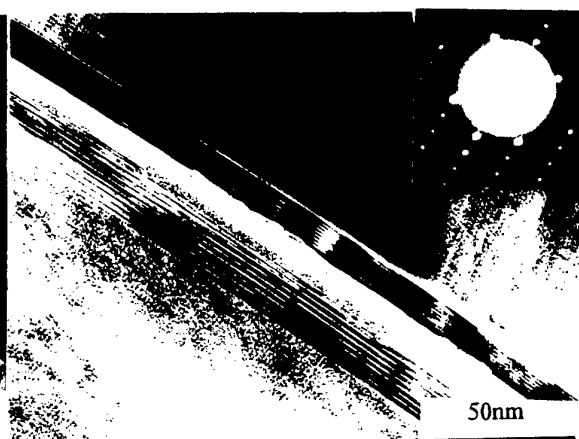


Figure 9. TEM image of the interface between the residual glass and showing the presence of Ga sulphide. Inserted is a streaked electron diffraction pattern from the Ga-sulphide phase

Peaks arising from $\text{La}_{3.33}\text{Ga}_6\text{S}_{14}$ are present in X-ray diffraction patterns and this phase has a $\text{Ga}_2\text{S}_3 : \text{La}_2\text{S}_3 = 1.8 : 1.0$, close to that of the new monoclinic phase which is approximately 2:1. The above evidence for the crystals morphologically identical to those found in reheated glass 2 strongly supports the view that the barrel shaped crystals in glass 2 are composed of intergrowths of the melilite-structured, $\text{La}_{3.33}\text{Ga}_6\text{S}_{14}$ and the new monoclinic phase.

The extent to which the melilite-structured, $\text{La}_{10/3}\text{Ga}_6\text{S}_{14}$ phase (with respect to the new monoclinic phase) occurs in any given region of an barrel shaped crystal, within reheated glass 2, varies but further work in this system has shown that it eventually dominates the X-ray and TEM diffraction patterns if the oxide or hydroxide content is increased in the precursor sulphides.⁹ Glass 1 which has a very low oxide content only contains the new monoclinic phase first discussed by Morgan *et al.*⁸ As crystallisation proceeds in glass 2, the residual glass becomes enriched in Ga sulphide. This phase nucleates and grows as 'whiskers' in-between the barrel shaped crystals and can also be observed to surround them, Figs 8 and 9. In effect, the barrel shaped crystals become encapsulated in Ga sulphide. The whiskers exhibit planar defects parallel with their length and diffraction patterns exhibit streaking associated with this phenomenon, insert in Fig 9. The whisker-like formation is unique to the growth of melilite/new phase barrel shaped crystals and is not a typical morphology. More commonly, isolated dendrites of $\alpha\text{-Ga}_2\text{S}_3$ have been observed in GLS glass.¹⁰

CONCLUSIONS

For the $70\text{Ga}_2\text{S}_3$ - $30\text{La}_2\text{S}_3$ glasses:

- 1) FTIR indicated that oxide-associated bands at the glass IR edge increased as oxide content increased in the glass precursors.
- 2) The new monoclinic GLS phase observed by Morgan *et al.* formed as the major phase on reheating, only when the oxide content of the as-batched glass was low (as-batched total oxygen less than 0.5 wt%).
- 4) $\text{La}_{3.33}\text{Ga}_6\text{S}_{14}$ growth did not occur on reheating unless the oxide content of the material was higher ((as-batched total oxygen very approximately 1 wt%).
- 5) Barrel shaped crystals in samples containing about 1 wt % total oxygen exhibited an eutectic or eutectoid-like microstructure, being composed of alternate laths of the new monoclinic GLS phase and $\text{La}_{3.33}\text{Ga}_6\text{S}_{14}$.

REFERENCES:

1. Hewak D W, Deol R S, Wang J, Wylangowski G, Medeiros Neto J A, Samson B, Laming R I, Brocklesby W S, Payne D N, Jha A, Poulain M, Otero S, Surinach S and Baro M D, *Electronic Letts.*, **29**, 237 (1993).
2. Loireau-Lozac'h A M, Guittard M and Flahaut J, *Mat. Res. Bull.*, **12** (1977).
3. Loireau-Lozac'h A.M. and Guittard M, *Mat. Res. Bull.*, **11**, 1489 (1976).
4. Morgan S P, Furniss D, Seddon A B and Moore M W, *J. Non-Cryst. Solids*, **213 & 214** 72 (1996).
5. S P Morgan, I M Reaney, R Buckley, D Furniss and A B Seddon, *J. Am. Ceram. Soc.* in press
6. D. W. Hewak, R I. Laming, J. A. Medeiros Neto, E. Taylor, B. Samson, J. Wang, D. W. Hewak, R. I. Laming, D. N. Payne, E. Tarbox, P. D. Maton, C. M. Loba, B. E. Kinsman and R. J. Hanney, *J. Non-Cryst. Solids*, **184**, 292 (1995).
7. D. W. Hewak, R I. Laming, J. A. Medeiros Neto, B. Samson, J. Wang, B. Dussardier, E. Taylor, G. Wylangowski, *IEE Colloquium Digest* **072** 3/1-3/6 (1994).
8. I. M. Reaney, R. Buckley, D. Furniss and A. B. Seddon. *J. Am Ceram. Soc.*, in press 1998.
9. S. P. Morgan, I. M. Reaney, R. Buckley, D. Furniss and A. B. Seddon. Submitted to *J. Am Ceram. Soc.*, 1998.
10. R. Li, I.M. Reaney and A.B. Seddon, in preparation (1998).

TOWARDS MONOMODE PROPORTIONED FIBREOPTIC PREFORMS BY EXTRUSION.

David Furniss and Angela B Seddon

Centre for Glass Research,
Department of Engineering Materials, University of Sheffield,
Sheffield, S1 3JD, UK. Email d.furniss@sheffield.ac.uk

1. ABSTRACT

Extrusion of inorganic glass melts is demonstrated as a helpful approach for making fibreoptic preforms. Thus rods, and fine bore tubes, of good dimensional control and surface finish have been made of sodium borosilicate glasses and gallium lanthanum sulphide glasses. One-step extrusion of core/clad preforms is also demonstrated, and optimisation of the extruder die design described to minimise taper of the core/clad ratio within the constant outside diameter preform.

2. INTRODUCTION.

Silica glass optical fibres for telecommunications have proved dramatically successful, particularly due to the development of the 1.5 micron erbium doped fibre amplifier. The EDFA has enabled the replacement of slower electronic methods of amplification. However there exists a considerable length of older 1.3 micron silica fibre in for which no photonic amplifier is available. Silica has not proved to be a suitable host for 1.3 micron optical amplifiers due to a high phonon energy and hence considerable non-radiative decay competing with the desired stimulated emission. For efficient optical amplification a low phonon energy glass host must be found.

One of the most promising glass types is the gallium-lanthanum-sulphide, (GLS) system. (Becker *et al*¹) However the GLS glasses present difficulties in fabrication of optical fibre preforms. There is presently no chemical vapour deposition route. The rotational casting route successfully used with fluoride glasses has not proved effective due to the higher liquidus temperatures, and temperature/viscosity characteristics, of the GLS glasses.

Preforms have been made by machining of glass billets into rods and tubes, but this is a wasteful process and can result in a poor core/clad interface due to the surface quality of the machined tube bore. Also the tube can not be made into monomode proportions in one step, so over-cladding is required, resulting in greater opportunity for crystallisation of the preform.

In this paper the method of extrusion for making GLS preforms is proposed and initial experiments with both water soluble oxide glass and GLS are described.

3. EXTRUSION.

3.1 Introduction.

Extrusion is commonly used in the industrial forming of plastics and metals. In inorganic glasses extrusion has been demonstrated by Roeder²⁻⁴, for various systems including soda-lime-silica, lead silicates and boric oxide. Complex rod and tube sections

have been produced. Roeder and Miura *et al*⁵ have extruded fluoroaluminozirconate glasses into core/clad preforms in a single operation. In this work we have considered both methods for use with the GLS glasses. Extrusion is carried out in a high viscosity region, typically 10^8 Pas. Crystal growth is generally slow in this region.

3.2 Extruder.

Figure 1 shows a side view of the extrusion equipment. A three zone electric resistance furnace provides heating for the extruder barrel. The glass billet is placed in the preheated stainless steel barrel which was used unlined or with a liner of graphite or high carbon cast iron. A stainless steel bobbin, which is a close fit in the barrel, is driven by the punch, which is in turn driven by customised hydraulics. This forces the glass melt out through the die assembly. The die geometry gives the glass its shape as it is force through. Temperature in the die wall is monitored by a thermocouple and the load applied is measured by a load cell. Extrusion velocity is measured by timing the position of the punch via an LVDT. The die and bobbin are sleeved in bronze to reduce wall friction to the barrel and the die can be graphite lined to reduce friction to the glass melt.

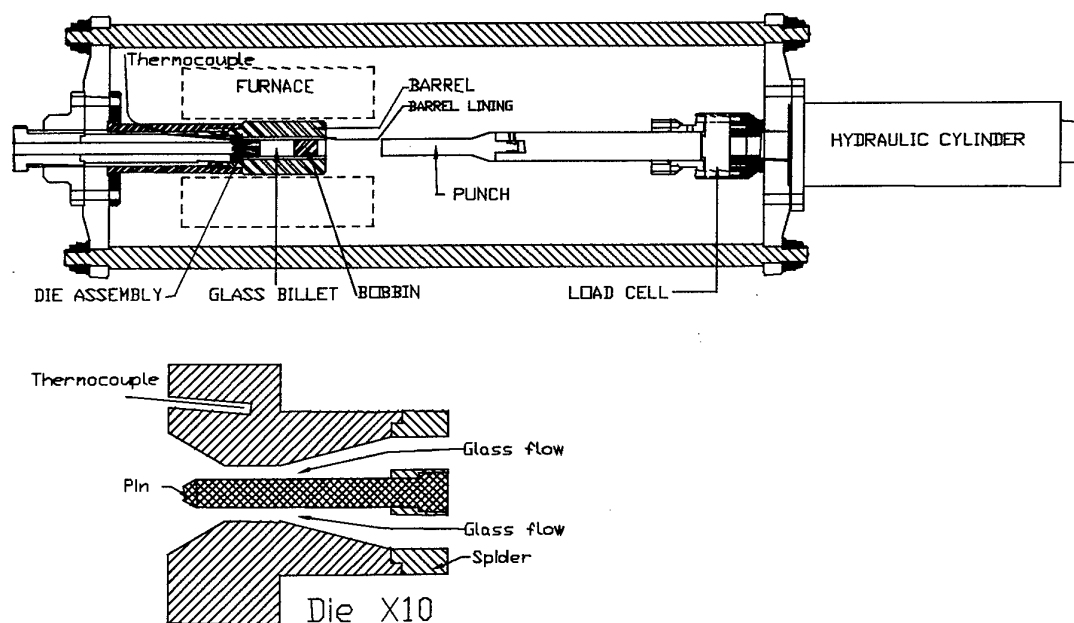


Figure 1. The extruder is shown in the horizontal position with the punch withdrawn. The end-to-end dimension is about 1.75m. The furnace is shown schematically in place around the barrel. The measuring thermocouple is located close to the die. for clarity, the extruder support frame, water cooling and optional inert gas flow have been omitted. The die assembly is also shown enlarged.

4. ROD AND TUBE EXTRUSION.

4.1 Monomode tube.

To produce a monomode proportioned fibre by the rod in tube method requires that the rod diameter be in the order of 0.05x that of the tube outer diameter, for a fibre around 100 to 200 μ m. For a 10mm OD preform we must achieve a rod diameter of 0.5mm, requiring a tube of less than 1mm ID. To produce a 0.5mm rod the most appropriate approach is to stretch a larger diameter rod in a process similar to fibre drawing. This is a well proven method so here we concentrate on the extrusion of the tube.

4.2. Oxide glass

In order to determine the design for the die an oxide glass 5Na₂O-75B₂O₃-20SiO₂ (mol%) has been chosen which is water soluble, so aiding the cleaning of the extruder and allowing further machining to be carried out on the die geometry. This glass was melted from Na₂CO₃ and the other oxides, 0.5 mol% of CoO could be added in order to give a colour contrast between core and cladding. The batch was melted at 1400°C in Pt for 5 hours, stirring for the last 3 hours before casting into graphite moulds to produce correctly sized billets and annealing at 320°C.

Initially the pin in the die was 5mm diameter with the die bore 10mm. Extrusion was carried out both in the horizontal and vertical positions. When horizontal the outgoing extruded glass was supported in a graphite "vee" cradle beyond the die. In the vertical position, straightness of the tube was improved compared with the horizontal. However there is a tendency for the weight of the rod so far extruded to stretch the part of the tube still being extruded. This results in a slight taper over the length of the tube. The die bore was either plain stainless steel or graphite lined. Due to the friction between the glass melt and the die wall the glass moved more slowly at the wall than in the centre of the glass. As the glass leaves the die this velocity profile must come to an end, the result is the radial expansion of the glass, die swell. The stainless steel die can exhibit up to 20% linear swell. Using a graphite lining reduced the friction and hence the die swell and also improved the surface finish of the extruded glass (Roeder¹⁻³). However the physical strength of graphite is insufficient to allow its use on the pin, and it is here on the inside of the tube where the surface finish is most important. So for tube extrusion the graphite lined die was not frequently used.

Table 1. The dimensions of extruded tubes of the water soluble glass for different die pin diameters.

Run	Load /kN	Furnace temp. /°C	Die temp /°C	Die dimensions as constructed /mm		Mean tube dimensions /mm		Die OD/ ID	Tube OD/ ID	For tube length /mm
				ID	OD	ID	OD			
A	7.0	420	385	2.5	12.0	2.84 ±0.10	11.63 ±0.32	4.8	4.1	200
B	6.0	440	405	1.5	12.0	1.66 ±0.13	11.76 ±0.12	8.0	7.1	160
C	10.2	425	390	1.0	12.0	1.15 ±0.19	12.59 ±0.26	12.0	11.0	190

A typical result for the 10mm/5mm graphite lined die over 250mm of length was OD/ID $9.75 \pm 0.06 \text{ mm} / 3.95 \pm 0.10 \text{ mm}$, with a maximum out-of-round for both OD and ID of 0.05mm. The diameter of the pin was steadily reduced to 1.0mm giving the results shown in Table 1 [6]. When pin sizes below 1mm were tried the tensile strength of the stainless steel proved to be inadequate and the pin snapped.

4.3 GLS extrusion.

The GLS glasses were prepared by melting from the standard sulphides (Merck Ltd) at 1150C in a vitreous carbon crucible inside a silica tube, then remelting into 30mm diameter billets. Extrusion was carried out under flowing argon at 604C. Initially rods were extruded in a graphite lined die at a load of 10kN in the horizontal position. With a die bore of 4.9mm the resulting rod had a good surface finish with a diameter of $4.914 \text{ mm} \pm 0.004 \text{ mm}$, the out of round was $< 0.004 \text{ mm}$, over a length of 250mm [7].

Tube extrusion of the GLS glass was carried out vertically with a plain stainless steel die with a 1mm pin which resulted in a good bore surface. However at present tubes are very short and we are working on improving this

5. CORE/CLAD EXTRUSION.

5.1 Oxide glass.

Billets of the water soluble sodium-borosilicate glass were prepared 30mm diameter and 15mm long, one with 1% CoO and the other undoped, with one end of each polished flat. A stainless steel die with a tapering lead in (figure 2a) was used. With the extruder at 385°C the clear undoped billet was placed into the extruder barrel first, followed by the Co doped billet with the polished ends together. They were then extruded vertically downward at 5kN load. The resulting rod started off clear, then the coloured core appeared, increasing in diameter as the extrusion progressed. Figure 3 shows the core diameter increasing at the expense of the cladding thickness. Figure 4 shows the core/clad ratio produced.

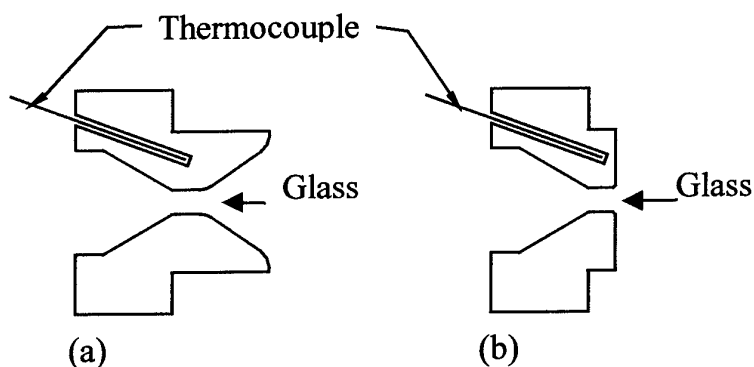


Figure 2. Cross sections of the two die profiles used for the cord/clad extrusion.

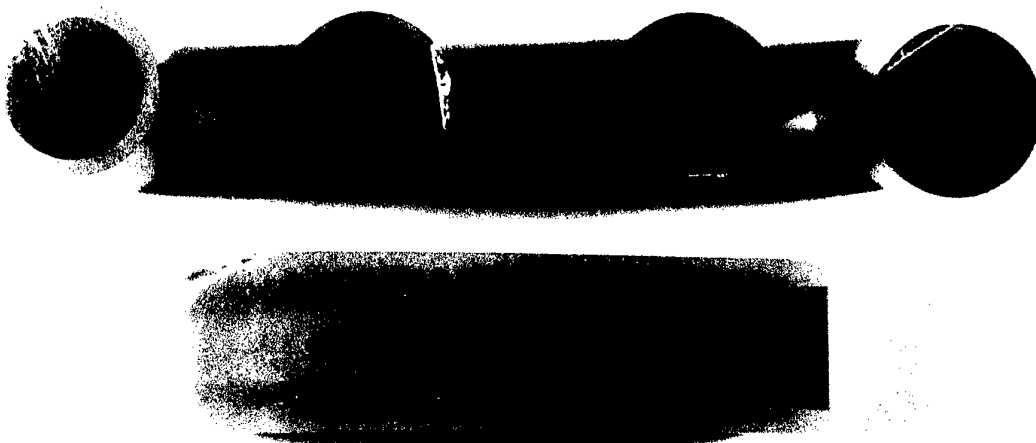


Figure 3. Core/clad extruded samples of $2.5\text{Na}_2\text{O}-87\text{B}_2\text{O}_3-10.5\text{SiO}_2$ (mol%) glass, undoped, and doped with 1 wt% cobalt oxide to give the purple coloration. The overall outside diameter is constant $10.9\text{mm} \pm 0.1\text{mm}$ over 150mm but the core/clad. diameter ratio has become larger as the extrusion proceeded giving a tapered core/clad interface.

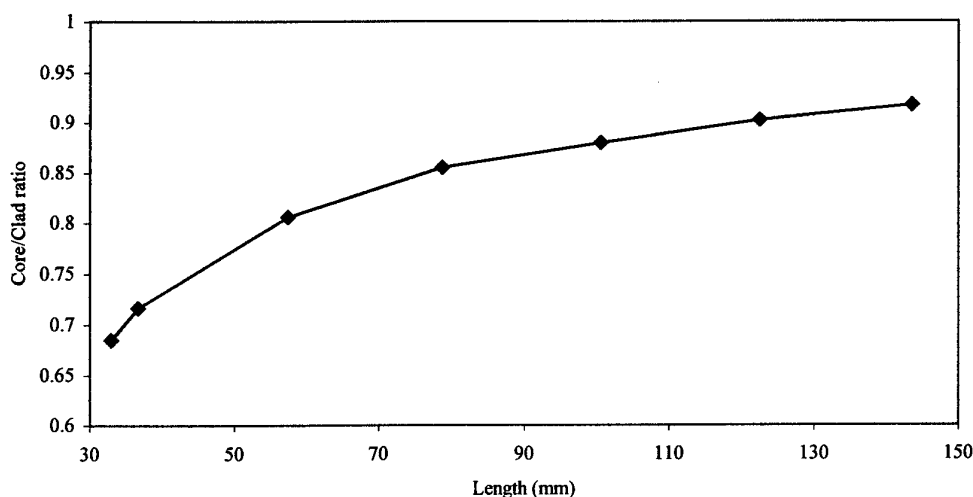


Figure 4. Plot of core diameter / clad diameter versus distance along the core/clad extruded sample for the die in figure 2a. Cladding diameter 10.9mm The same sample is pictured in figure 3 and is $2.5\text{Na}_2\text{O}-87\text{B}_2\text{O}_3-10.5\text{SiO}_2$ (mol%) glass, coloured purple with 1wt% cobalt oxide.

To attempt an improvement in the core/clad ratio the extrusion was repeated with a plain flat die (Figure 2b). Clear and cobalt doped glass billets of 12.5mm length and 30mm diameter were used This resulted in an improved core clad ratio over a greater length (Figure 5). The OD is $5.4\text{mm} \pm 0.1\text{mm}$ with an out-of-round for the core and the clad of less than 0.1mm over 300mm length. However this is still not monomode and would need over cladding.

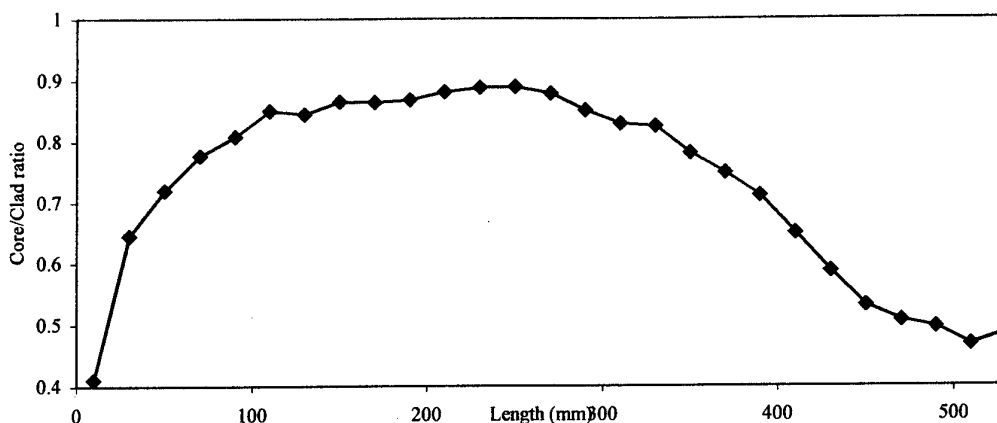


Figure 5. Plot of core diameter / clad diameter versus distance along the core/clad extruded sample for the die in figure 2b. Cladding diameter 5.4mm

6 SUMMARY.

GLS rods of good surface quality, with a diameter of 5mm have been extruded with very good diameter variation and circularity along the rods. Tubes of oxide and GLS glass with a 1mm bore and 12mm OD have been produced with a good internal surface quality. At present we are working to extend the GLS tube length which can be successfully extruded for subsequent rod-in-tube fibre drawing

7 ACKNOWLEDGEMENTS.

The Engineering and Physical Sciences Research Council, UK have supported this work on grants GR/J47583 and GR/L36932. The Authors thank D.W. Hewak and J. Wang of the ORC, Southampton University, UK for providing the raw Ga-La-S glass.

8. REFERENCES

1. P.C. Becker, M.M. Broer, V.C. Lambrecht, A.J. Bruce and G. Nykolak, "Pr³⁺:Ga-La-S : a promising material for 1.3 μ m amplification", *Technical Digest of Topical Meeting: Optical amplifiers and their applications* Optical Society of America, Washington DC, 1992 (Post-deadline paper PDP5).
2. E. Roeder, "Extrusion of glass", *J. Non-Cryst. Solids*, **5** pp. 377-388, 1971.
3. E. Roeder, "Flow behaviour of glass during extrusion", *J. Non-Cryst. Solids*, **7** pp203-220, 1972.
4. W. Egel-Hess and E. Roeder, "Extrusion of glass melts-influence of wall friction effects on the die swell phenomenon", *Glasstech. Ber.* **62** pp279-284, 1989.
5. K. Miura, I. Masuda, K. Itoh and T. Yamashita, "Fluorozirco-aluminate glass fibre", *Mater. Sci. Forum.* **67&68** pp335-340, 1991.
6. A.B. Seddon, D. Furniss and A. Moteshari, "Extrusion method for making fibreoptic preforms of special glasses", SPIE(The International Society for Optical Engineering) Vol 3416 "Infrared Glass Optical Fibres and Their Applications", Quebec, 1998 Ed. M. Saad.
7. D. Furniss and A.B. Seddon, "Extrusion of gallium lanthanum sulphide glasses for fibreoptic preforms", *J. Mater Sci.* (Accepted for publication).

SECTION 1

**ORAL
PRESENTATIONS**

THE GLASS CEILING

D. N. Payne

**Optoelectronics Research Centre, University of Southampton,
Southampton, SO9 5NH, UK**

ABSTRACT NOT AVAILABLE

NON-SILICA GLASS FIBER AMPLIFIERS

**T. Kanamori, Y. Nishida, A. Mori, K. Kobayashi, M. Yamada*, T. Shimada,
M. Shimizu, and Y. Ohishi***

NTT Opto-Electronics Laboratories, Tokai, Ibaraki, 319-1193 Japan

***NTT Electronics Corporation, Tokai, Ibaraki, 319-1193 Japan**

ABSTRACT

We report our current progress in the development of non-silica glass fiber amplifiers. We describe the fabrication of low-loss Pr^{3+} -doped InF_3 -based fibers and low-loss Er^{3+} -doped TeO_2 -based fibers, and their use in constructing an efficient 1.3- μm band PDFA and a low-noise 1.5- μm broadband EDFA. High gain coefficients of 0.36, 0.30, 0.26, and 0.18 dB/mW are realized for the PDFA using fibers with Δn values of 6.6, 4.6, 3.7, and 2.5 %, respectively. The EDFA provides an extremely wide amplification bandwidth of 83 nm with a signal gain of over 20 dB and a noise figure of < 6.5 dB.

1. INTRODUCTION

Optical fiber amplifiers are key devices for increasing the transmission distance, speed and capacity of optical communication systems. Recent trends, such as the development of wavelength-division multiplexing (WDM) systems, has meant that fiber amplifiers must meet a variety of requirements. These include high gain, high output power, a low noise figure, a broad and flat gain spectrum, high reliability, low cost, and compactness. Non-silica glass fiber amplifiers have the potential to meet these requirements.

Since the first demonstration of 1.3 μm amplification using a Pr^{3+} -doped ZrF_4 -based fiber, low phonon energy glasses have generated great interest as efficient hosts [1, 2]. This is because the $^1\text{G}_4$ level in Pr^{3+} suffers a multi-phonon relaxation which leads to a reduction in the quantum efficiency of the $^1\text{G}_4$ to $^3\text{H}_5$ transition. There has been a considerable amount of research on new glass hosts for efficient Pr^{3+} -doped fiber amplifiers (PDFAs). The suggested hosts are InF_3 -based fluoride glasses such as the InF_3 -based system [3], the $\text{InF}_3/\text{GaF}_3$ -based system [4], the $\text{PbF}_2/\text{InF}_3$ -based system [5], mixed-halide glasses [6], chalcogenide glasses such as Ga-La-S [7], Ga-Na-S [8], and As-S [9]. The InF_3 -based fluoride glass family is the most promising candidate as the glass host for the next generation of PDFAs in terms of meeting many of the above requirements. The key issue as regards developing efficient

InF_3 -based PDFAs for practical use is to reduce the losses of the high- Δn fibers to the level of ZrF_4 -based fiber.

A significant broadening of the amplification bandwidth has been achieved in the 1.5 μm band by using Er^{3+} -doped TeO_2 -based fiber [10, 11]. Its bandwidth is 80 nm with a signal gain of over 20 dB. However, it is necessary to reduce the noise figure to make practical TeO_2 -based Er^{3+} -doped fiber amplifiers (EDFAs). This can be also achieved by developing low-loss TeO_2 -based fiber.

This paper describes the development of low-loss Pr^{3+} -doped InF_3 -based fibers and low-loss Er^{3+} -doped TeO_2 -based fibers, and efficient 1.3- μm band PDFAs and a low-noise 1.5- μm broadband EDFA using these non-silica glass fibers.

2. EXPERIMENTAL

2.1 Single-mode fiber fabrication

We fabricated single-mode fibers by using a modified jacketing method [12]. The preforms were prepared by the conventional suction-casting method. The jacketing tubes for elongation and fiber drawing were produced by the rotational casting method using molds with a cylindrical hole and a tapered hole, respectively.

a) Melting and casting: InF_3 -based glasses [3, 5]: InF_3 and GaF_3 were purified by solvent extraction with acetylacetone in benzene. Fluorides with a high purity of much better than 99.99 % were used as the glass materials. Mixtures of the core and cladding materials and NH_4F were melted at 850 $^\circ\text{C}$ in vitreous carbon crucibles. The melts were cast into metal molds to produce preforms and jacketing tubes.

TeO_2 -based glasses: High-purity TeO_2 was prepared from Te metal whose purity exceeded 6 N. The raw materials, which were more than 99.9% pure, were weighed and mixed in gold crucibles. They were then melted at 900 $^\circ\text{C}$, and cast into metal molds using the above mentioned methods.

b) Fiber drawing: A preform prepared by suction-casting, which had a tapered core, was elongated together with a straight jacketing tube into a secondary preform. To eliminate the tapered core structure in the secondary preform, a tapered jacketing tube was used for the fiber drawing process. The secondary preform was inserted into the tapered jacketing tube and drawn into a single-mode optical fiber coated with UV-curable acrylate.

2.2 Measurements

The transmission loss spectra were measured using the cutback technique.

The signal gain dependence on pump power was measured using the fabricated Pr^{3+} -doped fiber. The fiber was butt-jointed to wavelength-division-multiplexing couplers and forward pumped using a Ti: sapphire laser. The pumping wavelength was 1.015 μm , and the signal wavelength and signal level were 1.30 μm and -30 dBm, respectively.

We measured the gain characteristics of a TeO_2 -based EDFA with a cascade configuration. Each fiber was pumped by a $1.480\text{ }\mu\text{m}$ LD module coupled through a bulk-type WDM coupler in the signal line. Optical isolators were inserted in the post-input and pre-output ports and between the TeO_2 -based fibers. The TeO_2 -based fiber and high- Δn silica fiber were connected by using the thermally-fused expanded core (TEC) technique and the tilted V-groove connection technique. The insertion loss and reflection at the tilted V-groove connection were 0.3 dB and $< -50\text{ dB}$, respectively.

3. RESULTS AND DISCUSSION

3.1 InF_3 -based PDFA

a) Single-mode fiber characteristics

Single-mode fibers with Δn values of 2.5 and 3.7% were fabricated using the InF_3 -based system [3] and those values 4.6 and 6.6 % using the $\text{PbF}_2/\text{InF}_3$ -based system [5]. A typical transmission loss spectrum is shown in Fig. 1. The large peaks around wavelengths of 0.6 and $1.0\text{ }\mu\text{m}$ are caused by Pr^{3+} . The small peak at $0.8\text{ }\mu\text{m}$ is due to the cutoff of the first higher-order mode. Table 1 lists the parameters and transmission losses of the Pr^{3+} doped fibers we obtained. Low loss values of 0.04, 0.05, 0.18 and 0.20 dB/m

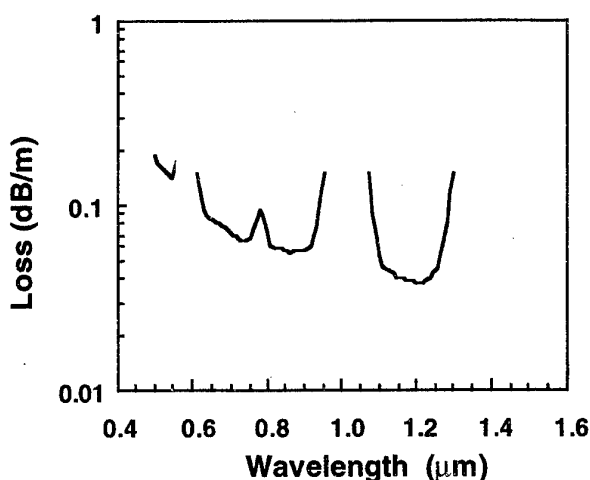


Fig. 1. Transmission loss spectrum of InF_3 -based fiber with Δn of 2.5% and Pr^{3+} content of 500 ppm.

were obtained at $1.2\text{ }\mu\text{m}$ in the single-mode fibers with Δn values of 2.5, 3.7, 4.6 and 6.6%, respectively. The transmission losses of the fibers with Δn values of 2.5 and 3.7 %, which we fabricated using the InF_3 -based system, were effectively reduced to the level of ZrF_4 -based single-mode fiber by

using purified InF_3 and GaF_3 raw materials. These loss characteristics indicate that the losses of the InF_3 -based fibers with Δn values of 2.5% and 3.7 % approach the practical level

Table 1. Characteristics of Pr^{3+} -doped InF_3 -based single-mode fibers.

Δn (%)	Glass system	Core diameter (μm)	Cutoff wavelength (μm)	Loss (dB/m, $1.2\text{ }\mu\text{m}$)
2.5	InF_3 -based glass	2.0	0.9	0.04
3.7	InF_3 -based glass	1.8	1.0	0.05
4.6	$\text{PbF}_2/\text{InF}_3$ -based glass	1.6	1.0	0.18
6.6	$\text{PbF}_2/\text{InF}_3$ -based glass	1.2	1.0	0.20

Pr^{3+} content is 500 ppm.

required for fiber amplifiers. By contrast, the fibers with Δn values of 4.6 and 6.6%, fabricated from the $\text{PbF}_2/\text{InF}_3$ -based system, exhibit a slightly high loss value. The difference in the loss levels indicates that the thermal stability of the $\text{PbF}_2/\text{InF}_3$ -based system must be slightly improved.

b) Amplification characteristics

Figure 2 shows the internal small signal gain dependence on the pump power for 20 m long and 19 m long single-mode fibers with Δn values of 3.7 and 6.6%, respectively [13]. The dependence with the most efficient ZrF_4 -based fluoride fiber with a Δn of 3.7 % is also shown for comparison [14]. An internal small signal gain of 28.2 dB, corresponding to a net gain of 20 dB, for a fiber with a Δn of 6.6 % was achieved at a pump power of 100 mW. This net gain is nearly double that of the most efficient ZrF_4 -based Er^{3+} -doped fiber. Table 2 summarizes the gain coefficients of fluoride fibers. The gain coefficient was increased from 0.18 to 0.36 by increasing the Δn from 2.5 to 6.6 % for InF_3 -based fibers. It is clear that InF_3 -based fiber achieves gain coefficients about 1.3 times higher than ZrF_4 -based fiber with the same Δn value.

We used these low loss fibers to construct two efficient PDFA modules: a high power PDFA module with a Nd-YLF laser and a fiber with a Δn of 2.5%, and a plug-in type PDFA module with $1.017 \mu\text{m}$ LDs and fibers with a Δn of 6.6% for rack-mounted shelves [15, 16]. In the former module, as shown in Fig. 3, we achieved an output power of 15.6 dBm,

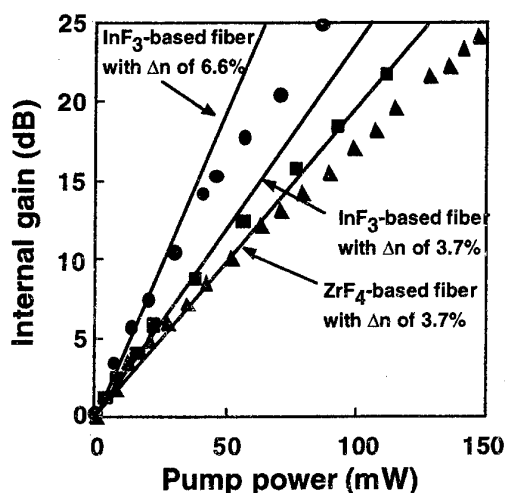


Fig. 2. Pump power dependence of gain at $1.3 \mu\text{m}$.
Input signal level: -30 dBm
 Pr^{3+} content: 500 ppm

Table 2. Gain coefficients of Pr^{3+} -doped fluoride fibers

Δn (%)	Gain coefficient of InF_3 -based fiber (dB/mW, $1.3 \mu\text{m}$)	Gain coefficient of ZrF_4 -based fiber (dB/mW, $1.3 \mu\text{m}$)
2.5*	0.18	0.14
3.7	0.26	0.21
4.6	0.30	-
6.6	0.36	-

Pr^{3+} content is 500 ppm except for 2.5 % Δn fiber;
*: Pr^{3+} content is 1000 ppm.

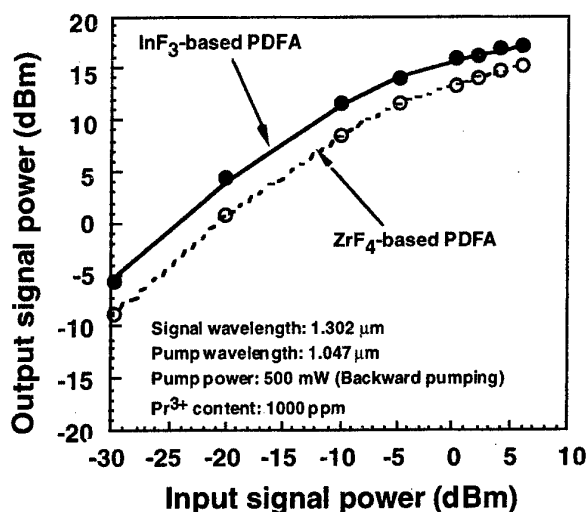


Fig. 3. Output signal power dependence on input signal power.

which is 2.4 dBm more than that of a ZrF_4 -based PDFA, with an input signal power of 0 dBm. The latter module exhibited a small signal gain of 24 dB and an output power of 10 dBm with an input signal power of 0 dBm. This output power level satisfies the ITU-T standards for STM-64 systems [17]. The high gain and high output power characteristics of these PDFAs increases the feasibility of using PDFAs in practical 1.3 μm transmission systems.

3.2 TeO_2 -based EDFA

a) Single-mode fiber characteristics

We fabricated a low loss TeO_2 -based fiber using synthesized high-purity TeO_2 , which was white because it contained no yellow or gray TeO_3 and no black TeO . The transmission loss spectrum of the fiber is shown as a solid line in Fig. 4. The Δn of the fiber was 1.5%. The cutoff wavelength and the Er^{3+} concentration were 1.15 μm and 500 ppm, respectively. The broken line shows the loss spectrum of a fiber obtained using commercial TeO_2 raw material for comparison. The Δn , the cutoff wavelength, and the Er^{3+} concentration of the fiber were 1.5%, 1.3 μm , and 4000 ppm, respectively. The absorption peaks observed around 1.0 and 1.4 μm were caused by Er^{3+} . The fiber prepared using the high purity TeO_2 exhibited a low loss of 0.05 dB/m at 1.2 μm . By contract, the loss of a fiber obtained using commercial TeO_2 was 0.9 dB/m at 1.2 μm . The difference between the losses is attributed to the purity of the TeO_2 raw material.

b) Amplification characteristics

Figure 5 shows the small signal gain and noise figure spectra of a TeO_2 -based EDFA with a cascade configuration using low-loss fibers. The fiber were 4 and 10 m in length

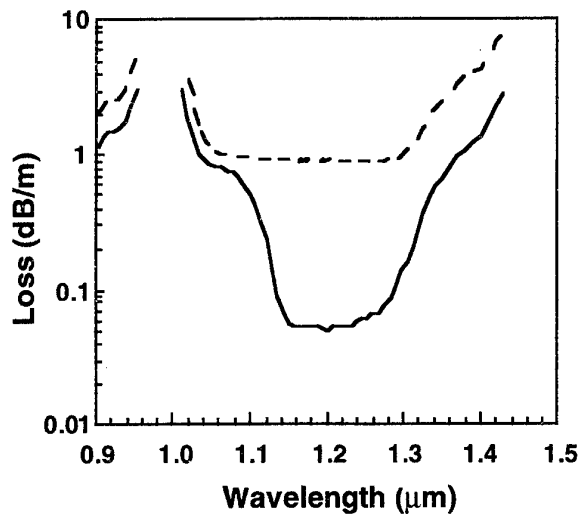


Fig. 4. Transmission loss spectra of Er^{3+} -doped TeO_2 -based fiber.

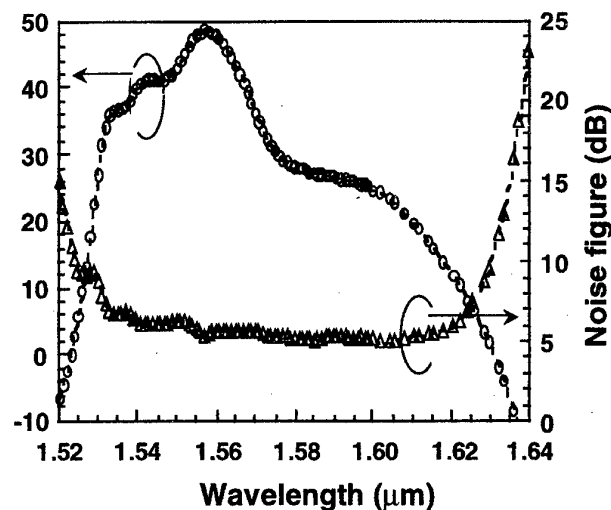


Fig. 5. Small signal gain and noise figure spectra of TeO_2 -based EDFA.

and the pump powers launched into each fiber were 150 and 200 mW, respectively. The input signal power was -30 dBm. The peak gain was 49 dB at 1.557 μm , and we obtained gains exceeding 20 dB over an 83 nm bandwidth of 1.528-1.611 μm . The minimum noise figure was 4.8 dB at 1.602 μm , and we obtained a noise figure of < 6.5 dB over an 85 nm bandwidth of 1.539-1.624 μm . The noise figure in the short wavelength region below 1.535 μm was improved by more than 10 dB [11]. The gain difference between the peak and the flat region, which was about 20 dB, can be suppressed by using gain equalizing techniques [18]. A TeO_2 -based EDFA with both a broad gain bandwidth and a low flat noise figure will facilitate the development of WDM network systems with high transmission capacity.

CONCLUSION

We have successfully fabricated low-loss InF_3 -based Pr^{3+} -doped single-mode fibers as efficient 1.3 μm band amplification hosts, and low-loss TeO_2 -based Er^{3+} -doped single-mode fiber for low noise 1.5 μm broadband amplification. We achieved high gain coefficients of 0.36, 0.30, 0.26, and 0.18 dB/mW for PDFAs using fibers with Δn value of 6.6, 4.6, 3.7, and 2.5 %, respectively, and an extremely wide amplification bandwidth of 83 nm with a signal gain of over 20 dB and a noise figure of < 6.5 dB for a TeO_2 -based EDFA. We believe that this newly developed PDFA and EDFA using non-silica fibers will be highly promising for upgrading the current optical transmission systems.

ACKNOWLEDGMENTS

The authors thank K. Nakagawa, K. Hoshino, Y. Terunuma, K. Oikawa, K. Shikano, and K. Kato for fiber preparation, and H. Kozawaguchi and S. Sudo for their encouragement.

REFERENCES

- [1] Y. Ohishi, T. Kanamori, T. Kitagawa, S. Takahashi, E. Snitzer, and G.H. Sigel; Opt. Lett., 16(1991)1747.
- [2] Y. Ohishi, T. Kanamori, T. Nishi, Y. Nishida, and S. Takahashi; Proc. Int. Cong. Glass, Madrid, 1992, p. 73.
- [3] Y. Nishida, Y. Ohishi, T. Kanamori, Y. Terunuma, K. Kobayashi, and S. Sudo; Proc. 19th Euro. Conf. Optical Communication, Montreux, vol. 1, 1993, p. 34.
- [4] H. Yanagita, K. Itoh, E. Ishikawa, H. Aoki, and H. Toratani; Tech. Dig. of OFC'95, Washington DC, 1995, PD2.
- [5] Y. Nishida, T. Kanamori, Y. Ohishi, M. Yamada, K. Kobayashi, and S. Sudo; Tech. Dig. of OAA'96, Washington DC, 1996, PD3.
- [6] M.A. Newhouse, B.G. Aitken, R.F. Bartholomew, L.J. Button, and N.F. Borrelli; Tech.

- Dig. of OAA'93, Washington DC, 1993, p. 248.
- [7] P.C. Becker, M.M. Broer, V.G. Lambrecht, A.J. Bruce, and G. Nykolak; Tech. Dig. of OAA'92, Washington DC, 1992, PD5.
 - [8] H. Tawarayama, E. Ishikawa, K. Itoh, H. Aoki, H. Yanagita, K. Okada, K. Yamanaka, Y. Mastuoka, and H. Toratani; Tech. Dig. of OAA'97, Washington DC, 1997, PD1.
 - [9] Y. Ohishi, A. Mori, T. Kanamori, K. Fujiura, and S. Sudo; Appl. Phys. Lett., 65(1994)13.
 - [10] A. Mori, Y. Ohishi, M. Yamada, H. Ono, Y. Nishida, K. Oikawa, and S. Sudo; Tech. Dig. of OFC'97, Washington DC, 1997, PD1.
 - [11] Y. Ohishi, A. Mori, M. Yamada, H. Ono, Y. Nishida, and K. Oikawa; Opt. Lett., 23(1998) 274.
 - [12] T. Kanamori, Y. Terunuma, Y. Nishida, K. Hoshino, K. Nakagawa, Y. Ohishi, and S. Sudo; J. Non-Cryst. Solids, 213&214(1997)121.
 - [13] T. Shimada, Y. Nishida, K. Kobayashi, T. Kanamori, K. Oikawa, M. Yamada, and Y. Ohishi; Electron. Lett., 33 (1997)1972.
 - [14] Y. Ohishi, T. Kanamori, Y. Terunuma, M. Shimizu, M. Yamada, and S. Sudo; IEEE Photon Tech. Lett., 6(1994)195.
 - [15] M. Yamada, Y. Nishida, T. Kanamori, K. Kobayashi, T. Shimada, and Y. Ohishi; Tech. Dig. of CLEO/Pacific Rim'97, Chiba, 1997, p. 48.
 - [16] Y. Nishida, M. Yamada, J. Temmyo, T. Kanamori, and Y. Ohishi; IEEE Photon Tech. Lett., 9(1997)1096.
 - [17] Draft new ITU-T recommendation G.691, ITU-T SG15-Rep. R 55, COM 15-R 55-E, June 1996.
 - [18] M. Yamada, A. Mori, K. Kobayashi, H. Ono, T. Kanamori, K. Oikawa, Y. Nishida, and Y. Ohishi; Tech. Dig. of OFC'98, Washington DC, 1998, PD7.

FABRICATION OF GLASS BASED OPTICAL AMPLIFIERS

A.J. Faber

TNO Institute of Applied Physics, P.O. Box 595,
5600 AN Eindhoven, NL, email faber@tpd.tno.nl

ABSTRACT

Different techniques for the fabrication of glass planar optical waveguides, including ion exchange, ion implantation, flame hydrolysis, sol-gel and RF sputtering, have been reported in the literature. In this paper the advantages and disadvantages of these techniques for preparing rare earth-doped waveguide amplifiers are evaluated.

Most attention is focused on recent work at TNO-TPD, in which RF sputtering is used as method for depositing Er-doped thin film glass waveguides. The importance of the fabrication method for realising efficient waveguide amplifiers is illustrated for the case of an Er-doped phosphate glass waveguide amplifier. The advantages of multicomponent phosphate glasses as host for Er will be presented, as well.

Critical fabrication process parameters are discussed, including: (1) melting conditions of the sputter target phosphate glass, (2) sputtering parameters like sputter gas composition and pressure, (3) post-deposition thermal annealing conditions and (4) etching process parameters for patterning of channel waveguides. The influence of the above process parameters on the relevant waveguide properties, i.e. optical loss, refractive index and Er luminescence properties, are outlined.

More recently, work has started to prepare phosphate glass optical waveguides by sol-gel methods. Up to now, 0.7 μm thick sodium-aluminum-phosphate glass films have been prepared on silicon by dipping in the coating solutions. For densification of the as-deposited films, the films can be heat treated up to 450 $^{\circ}\text{C}$. At higher annealing temperatures the films tend to crystallize.

By optimisation of the sputtering process parameters, an optical gain at 1.535 μm of 4.1 dB over a 1 cm channel waveguide was achieved for 980 nm pumping with a power of about 21 mW. Using simple modelling calculations, optical gain figures of more than 10 dB are predicted for 4 cm long Er-waveguides.

Pr³⁺-DOPED InF₃/GaF₃ BASED FLUORIDE GLASS FIBERS AND Ga-Na-S GLASS FIBERS FOR LIGHT AMPLIFICATION AROUND 1.3 μm

**K. Itoh, H. Yanagita, H. Tawarayama, K. Yamanaka, E. Ishikawa, K. Okada,
H. Aoki, Y. Matsumoto, A. Shirakawa, Y. Matsuoka and H. Toratani**

**Technology Development Laboratory, R&D Center, HOYA CORPORATION
3-3-1 Musashino, Akishima-shi, Tokyo, 196-8510 Japan
email ito@sngw.rdc.hoya.co.jp**

INTRODUCTION

Recently, efficient amplifiers working around 1.3 μm have been requested in optical telecommunication networks. Pr³⁺-doped non-oxide glass fibers have been expected as the most suitable amplifier at 1.3 μm. The efficiency of PDF is critically dependent on the radiative efficiency of the ¹G₄ level. To reduce multi-phonon relaxation from this level a low phonon host is needed. Furthermore, the host glass needs to be stable enough against the thermal stress it suffers during fiber manufacturing. Considering these requirements, we have selected two non-oxide glass hosts, namely InF₃/GaF₃ based fluoride system and chalcogenide system, Ga-Na-S(GNS).

The InF₃/GaF₃ based glass has a lower phonon energy than ZrF₄ based fluoride glass, such as ZBLAN; which is now a major glass system for Pr³⁺ doped fibers, which should result in a relatively high RQE of the Pr³⁺ ion[1]. And Pr³⁺-doped chalcogenide glasses have much higher RQE(≅56%) and are potentially much more efficient PDFs [2]. However, because of low thermal stability against crystallization or poor solubility of Pr³⁺ ions efficient PDFs using chalcogenide glasses had not been obtained. To overcome these difficulties, we selected a Ga-Na-S (GNS) glass system from reported sulfide glasses as a host glass for Pr³⁺ ion [3]. GNS glasses are thermally stable and can be doped with large amounts of rare-earth ions[4].

We have been able to fabricate relatively low loss single-mode glass fibers using both glass systems, and we have demonstrated obtained highly-efficient amplification characteristics from these PDFs. We report on the development of the PDFs using these non-oxide glasses.

EXPERIMENTS AND RESULTS

InF₃/GaF₃ BASED GLASS SYSTEM

High purity fluoride raw materials (but still of commercial grade) for Pr³⁺:1000 ppmwt doped InF₃/GaF₃ glass were mixed, melted in a carbon crucible in an inert-gas atmosphere, and quenched. The RQE of Pr³⁺ ions in the InF₃/GaF₃ glass was estimated from Judd-Ofelt analysis and lifetime measurement[1]. The RQE was 1.6 times higher than that of Pr³⁺ in ZBLAN[1].

In order to fabricate a high NA(numerical aperture) single-mode fiber using $\text{InF}_3/\text{GaF}_3$ glass as a core glass, a ZBLAN glass was used as a cladding glass. This core/cladding combination, resulted in a NA of 0.54-0.56 at 0.6 μm . We prepared preforms for single-mode fibers by the extrusion method[5].

Pr^{3+} :1000 ppmwt doped $\text{InF}_3/\text{GaF}_3$ glass single-mode fibers were drawn to a cladding diameters of 110-130 μm and core diameters of 1.2-1.4 μm . The fibers were in-line-coated by UV curable polyurethan-acrylate polymer. The background losses of these fibers were 0.15-0.25 dB/m at 1.2 μm . The tensile strength of one of these fibers was measured and the result is shown in Figure 1.

The amplification characteristics of this fiber was measured in bi-directional pumping configuration. A gain coefficient of 0.29 dB/mW has been obtained for a small-signal input of -30 dBm[6]. This gain coefficient is higher than the 0.24 dB/mW of Pr^{3+} : 500ppmw -doped ZBLAN fiber [7]. However, it has been reported that a Pr^{3+} :500ppmw doped PDF was able to offer a slightly higher gain coefficient than a Pr^{3+} :1000 ppmwt doped PDF for small signal input [7].

Figure 2 shows the fiber length dependence of the signal output power for a Pr^{3+} :1000 ppmwt doped $\text{InF}_3/\text{GaF}_3$ glass single-mode fiber. The optimum fiber length was less than 7 m for an input signal level and a total pump power of +1.6 dBm and 260 mW, respectively.

We have assembled PDF-modules(PDFMs) using the $\text{InF}_3/\text{GaF}_3$ based glass single-mode fibers connected to silica fibers[6]. The modules have been sealed against environmental atmosphere. The reliability tests of these PDFMs is now almost completed, and so far our modules are providing to conform to the standards of Bell-Core, GR-1211-CORE-CORE series.

We now illustrate some optical

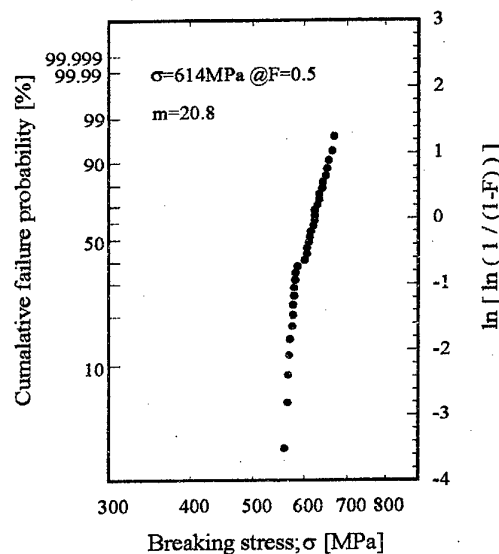


Figure 1. Tensile strength of an $\text{InF}_3/\text{GaF}_3$ based PDF

Sample span length was 200 mm. Measured under 25 °C , 60 % RH.

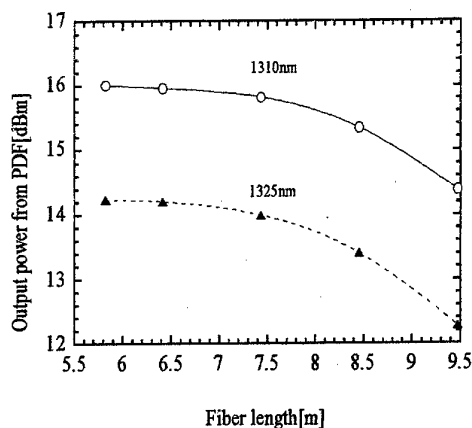


Figure 2. Fiber length dependence of signal output power for the Pr^{3+} :1000ppmw doped $\text{InF}_3/\text{GaF}_3$ glass single-mode fiber.

The input signal level was +1.6 dBm. Bi-directional pumping configuration with pump wavelength of 1012 nm.

The core diameter of this PDF was 1.2 μm . The background loss was 0.15 dB/m at 1.2 μm .

amplification properties of our recently developed $\text{InF}_3/\text{GaF}_3$ based PDFMs :

Figure 3 shows the pump power dependence of the signal output power at $1.305 \mu\text{m}$ based PDFM. The input signal level was $+2.1 \text{ dBm}(=1.62 \text{ mW})$;

Figure 4 shows the input signal power dependence of the net gain for 220 mW of pump power,

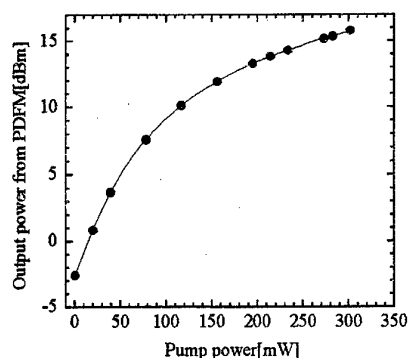


Figure 3. Pump power dependence of the signal output power of $\text{InF}_3/\text{GaF}_3$ based PDFM.

The input signal level was $+2.1 \text{ dBm}$. Bi-directional pumping configuration with pump wavelength of 1012 nm . The PDF length was 5.8 m long with core diameter of $1.2 \mu\text{m}$. The background loss of the PDF was 0.15 dB/m at $1.2 \mu\text{m}$.

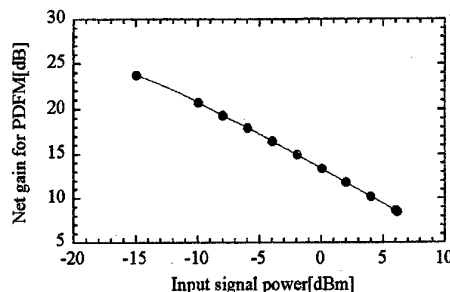


Figure 4. Input signal power dependence of net gain of the $\text{InF}_3/\text{GaF}_3$ based PDFM.

The pump power was 220 mW . The PDF and pump configurations were the same as in Figure 3.

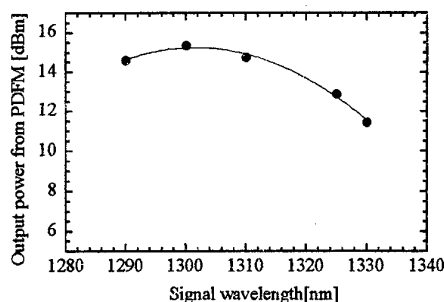


Figure 5. Signal wavelength dependence of output power of a $\text{InF}_3/\text{GaF}_3$ based PDFM

The input signal level was $+2.1 \text{ dBm}$. The pump power was 282 mW . The PDF and pump configurations were the same as in Figure 3.

Figure 5 shows the signal wavelength dependence of the output power for 282 mW of pump power.

For the relatively large input signal power of $+2.1 \text{ dBm}$, an output power of $15.2 \text{ dBm}(=33 \text{ mW})$ has been obtained with a total launched pump power of 272 mW . The noise figure was 5.7 and 6.3 dB at 1310 and 1325 nm , respectively.

CHALCOGENIDE GLASS SYSTEM

Pr^{3+} :750 ppmwt doped GNS glasses were prepared by a melt-quenching method. We used the extrusion method to make the preform for single-mode fiber. The numerical aperture

was 0.31. We used a Dy^{3+} doped GNS glass as an over-cladding glass to strip cladding modes.

The Pr^{3+} :750 ppmwt doped GNS glass single-mode fibers were drawn into cladding diameters of 110-130 μm , core diameters of 2.0-2.5 μm . The fibers were in-line-coated by

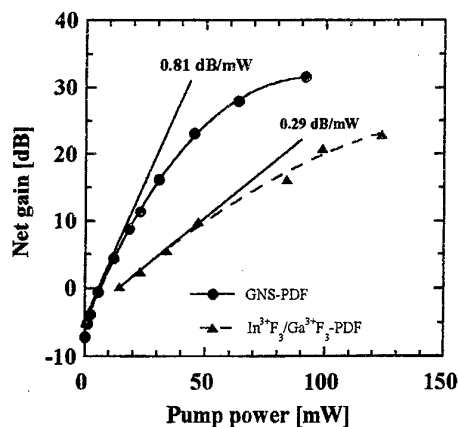


Figure 6. Pump power dependence of the net gain of the Pr^{3+} :750 ppmwt doped fiber at 1340 nm.

The input signal level was -30 dBm. Bi-directional configuration with pump wavelength of 1017 nm. The PDF length was 6.1 m and the core diameter of 2.5 μm . The numerical aperture was 0.31.

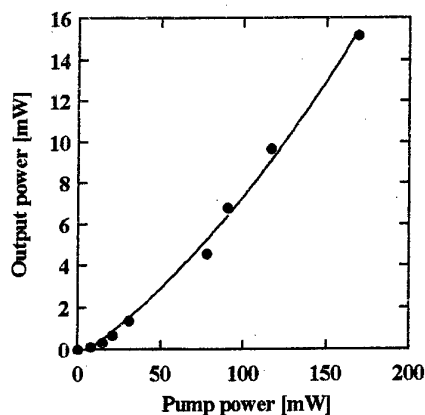


Figure 7. Pump power dependence of output power at 1340 nm.

The input signal level was -8 dBm. Pump and fiber configurations were the same as in Figure 6.

UV curable polyurethan-acrylate polymer. The background losses at 1.3 μm of these fibers were 1.2-1.5 dB/m. No GSA(ground state absorption) of Pr^{3+} ions around 1.3 μm could be observed in this glass system. A gain coefficient of 0.81 dB/mW at 1.34 μm and a net gain of 30dB at a pump power of less than 100mW were obtained[4].

Figure 6 shows the pump power dependence of the net gain at 1.34 μm for a Pr^{3+} :750

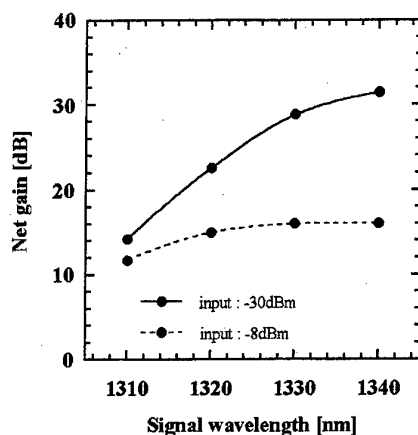


Figure 8. Input signal wavelength dependence of net gain of GNS-PDF

The pump power was 90mW. Bi-directional pumping configuration.

ppmw/doped GNS glass single-mode fiber for the input signal level of -30 dBm. Figure 7 shows the pump power dependence of the output power at $1.34 \mu\text{m}$ for an input signal power level -8 dBm. Figure 8 shows the signal wavelength dependence of the net gain of a GNS-PDF for a pump power of 90 mW.

DISCUSSIONS

At present, a higher output level of optical amplifier is requested in the optical communication network. One of the issues of $\text{InF}_3/\text{GaF}_3$ based glass single-mode fibers is the low light conversion efficiency at high output signal level (over 10 dBm) compared with Er^{3+} doped fiber amplifier (EDF). We have studied on numerically, simulated a $\text{InF}_3/\text{GaF}_3$ based PDF. This simulation suggests that the fairly large ESA (excited state absorption) from $^1\text{G}_4$ to $^1\text{D}_2$ level might significantly reduce the output power of amplified signal in the $\text{InF}_3/\text{GaF}_3$ based PDF. But we can expect that the $\text{InF}_3/\text{GaF}_3$ based PDFs will be able to amplify with higher efficiency than high NA ZBLAN PDFs. Figure 9 shows the extrapolated for output power of the $\text{InF}_3/\text{GaF}_3$ based PDFM in a high pump power region. This extrapolation is based on the measured pump-output power characteristics. An output power over $+20$ dBm ($=100$ mW) is expected for a pump power of 800 mW and an initial input level of $+2.0$ dBm.

The GNS glass single-mode fiber yields a much higher gain coefficient around wavelength of 1340 nm. However, the gain coefficient becomes lower in a shorter wavelength region. At 1310 nm, the gain coefficient for small input signals was 0.51 dB/mW. GNS-PDFs are best suited for

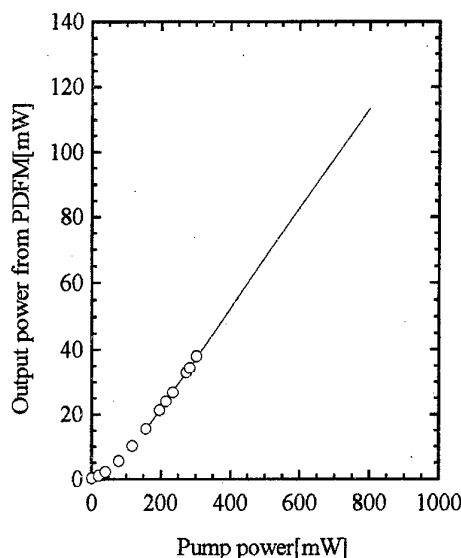


Figure 9. An extrapolation for output power of the $\text{InF}_3/\text{GaF}_3$ based PDFM in high pump power region based on measured property.

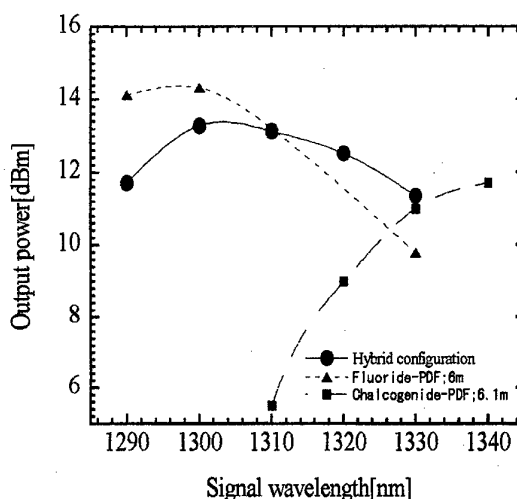


Figure 10. Signal wavelength dependence of output power for hybrid PDF.

For the hybrid PDF, the input signal level was -6 dBm, the pump power was 200 mW, the fiber length was 5.1 and 4.8 m for the GNS PDF and the $\text{InF}_3/\text{GaF}_3$ PDF respectively.

amplify in the wavelength range 1325 – 1350 nm when the input power is excess of –8 dBm. On the other hand, the output power of the $\text{InF}_3/\text{GaF}_3$ based PDF falls in the signal wavelength range 1330 – 1350 nm. The available signal wavelength region for the $\text{InF}_3/\text{GaF}_3$ based PDF is 1290 – 1330 nm. A flat and broad gain spectrum is required in WDM systems, in which several optical channels must be amplified simultaneously. However, the flatness of $\text{InF}_3/\text{GaF}_3$ based PDF in the signal wavelength of 1290-1330 nm was not sufficient for WDM use. To flatten and broaden the signal wavelength dependence of 1290 – 1330 nm region, we have proposed a novel PDF amplifier using a hybrid configuration of $\text{InF}_3/\text{GaF}_3$ glass PDF / GNS PDF[8]. Figure 10 shows the gain spectrum of this hybrid PDF.

We believe that those highly efficient PDFs and PDFM such as $\text{InF}_3/\text{GaF}_3$ glass based, GNS glass based or hybrid configuration will extend the capability of optical telecommunication fiber cable at 1.3 μm , which is the operating wavelength of most optical network and of CATV.

CONCLUSION

We have developed three types of highly-efficient Pr^{3+} doped fiber amplifiers around 1.3 μm . The $\text{InF}_3/\text{GaF}_3$ based fluoride glass PDF has a relatively high gain coefficient and a high power signal output compared with ZBLAN PDF. The chalcogenide system, GNS PDF has particularly high gain coefficient: 0.81 dB/mW at signal wavelength of 1340nm for small signal input of –30 dBm. The hybrid PDF using $\text{InF}_3/\text{GaF}_3$ based fluoride glass PDF and GNS PDF has the flattest gain spectrum in 1.3 μm wavelength region and will be able to extend a region of WDM usage.

REFERENCES

- [1] H. Yanagita, K. Itoh, E. Ishikawa, H. Aoki and H. Toratani, in Technical Digest of Conference on Optical Fiber Communication, (1995) paper PD2.
- [2] P.C. Becker, M. M. Broer, V. G. Lambrecht, A.J. Bruce and G. Nykolak, in Technical Digest of Topical Meeting on Optical Amplifiers and their Applications, (1993) paper PDP5.
- [3] M. Palazzi, C.R. Acad. Sc. Paris, **299** (1984) 529-532.
- [4] H. Tawarayama, E. Ishikawa, K. Itoh, H. Aoki, H. Yanagita, K. Okada, K. Yamanaka, Y. Matsuoka and H. Toratani, OSA TOPS Optical Amplifiers and their Applications, **16** (1997) 141-143.
- [5] K. Itoh, K. Miura, I. Masuda, M. Iwakura, and T. Yamashita, J. Non-Cryst. Solids, **67** (1994) 112-116.
- [6] H. Aoki, K. Itoh, E. Ishikawa, H. Yanagita, and H. Toratani, TECHNICAL REPORT OF IEICE. LQE. **96-28** (1996) 49-54.
- [7] Y. Ohishi, T. Kanamori, M. Shimizu, M. Yamada, Y. Terunuma, J. Temmyo, M. Wada and S. Sudo, IEICE TRANSC. COMMUN., **E77-B** [4] (1994) 421-440.
- [8] E. Ishikawa, H. Tawarayama, K. Yamanaka, K. Itoh, K. Okada, H. Aoki, H. Yanagita, Y. Matsuoka and H. Toratani, 1998 OSA Technical Digest Series "OFC '98", **2** WG7 (1998) 140.

Active and Passive Chalcogenide Glass Optical Fibers for IR Applications

J.S. Sanghera and I.D. Aggarwal

Naval Research Laboratory, Code 5606, Washington, DC 20375

While chalcogenide glasses have been studied for several decades, it is only in this last decade that we have seen a significant effort to utilize these glasses and especially the fibers in actual systems and applications. The applications can be divided into two groups, namely passive and active. In the passive applications, the fiber is used as a light conduit from one location to another and does not change the light other than that due to the fiber scattering and absorption losses and end face reflection losses. In active applications, the light signal is modified, for instance by the presence of dopants or by non-linear effects.

The tables below, summarizes a review of the information obtained from the literature and other unpublished work pertaining primarily to applications of chalcogenide glass fibers. The motivation behind these applications and results obtained to-date will be discussed in more detail in the presentation and final manuscript.

Passive Applications	Active Applications
Laser Power Delivery <ul style="list-style-type: none"> • 5.4 μm (CO) • 10.6 μm region • Atmospheric 2-5 μm region • Medical Free Electron Laser (2-10 μm) • Anti-reflection (AR) coatings 	Rare Earth Doped Fibers <ul style="list-style-type: none"> • Fiber Lasers - 1.08 μm (Nd) • Amplifiers - 1.08 μm (Nd) - 1.34 μm (Pr) - 1.34 μm (Dy) • Infrared Scene Simulation (IRSS) emission in 2-5 μm and 8-11 μm region • Chemical Sensing – Toluene detection • Gratings - 1.5 μm
Chemical Sensing <ul style="list-style-type: none"> • Aqueous, non-aqueous, toxic chemicals • Polymers, paints, pharmaceuticals • Condition Based Maintenance (CBM) • Cone Penetrometer System • Active Coatings • Bio-medical 	Non-linear <ul style="list-style-type: none"> • Optical switching • Second Harmonic Generation • Frequency mixing • Electrical Poling
Temperature Monitoring <ul style="list-style-type: none"> • Grinding ceramics 	
Thermal Imaging & Hyperspectral Imaging <ul style="list-style-type: none"> • Coherent fiber bundles 	
Near Field Microscopy <ul style="list-style-type: none"> • Imaging and spectroscopy 	
Fiber Multiplexing <ul style="list-style-type: none"> • Fiber couplers 	
Refractive/Diffractive Elements <ul style="list-style-type: none"> • Micro-Lenses 	

Towards Low Optical Loss Gallium-Lanthanum-Sulphide Glass Fibres

Ruihua Li and Angela B. Seddon

Centre for Glass Research, Department of Engineering Materials
The University of Sheffield, Sheffield, S1 3JD, UK

ABSTRACT

Gallium-lanthanum-sulphide (GLS) glasses have been proposed as potential rare-earth hosts for 1.3 μ m optical amplification. To develop thermally stable GLS glasses, and thus facilitate production of monomode low optical loss GLS glass fibre, a series of fundamental studies has been carried out and the key results are presented here. These include: the critical role of oxide content played in glass formation; phase identification during the crystallisation of GLS glasses; nucleation and crystallisation behaviour of GLS glasses; the effects of enhanced oxide content and other sulphide and chloride additives on glass stability.

INTRODUCTION

Gallium-lanthanum-sulphide (GLS) glasses have been proposed as potential rare-earth hosts for 1.3 μ m optical amplifiers¹. GLS glasses have a considerably lower characteristic phonon energy (by about 200-300 cm⁻¹), and thus significantly lower non-radiative decay rates, than ZBLAN fluoride glasses². Hence GLS glasses exhibit longer emission lifetimes of rare-earth dopants, such as Pr³⁺. GLS glasses show superior solubility for rare earth ions compared to other sulphide glasses such as Ge-S glasses. However, so far monomode low optical loss fibre has still to be made from GLS glasses for efficient devices. To this end, it has been essential that fundamental studies be carried out to optimise the properties of this material for fibre making.

In-depth studies at the Centre for Glass Research (CGR), University of Sheffield, working in parallel with the Optoelectronics Research Centre (ORC), Southampton University, have involved a programme of development, characterisation and optimisation of GLS glasses by using a combination of analytical techniques: thermal analysis, analytical electron microscopy, x-ray diffractometry, infrared and UV/visible spectroscopy. This report will focus on the research work carried out recently in the CGR. Previously published results will also be reviewed and critically compared.

GLASS FORMATION IN Ga₂S₃-La₂S₃ SYSTEM

The formation of glasses in the system Ga₂S₃-La₂S₃ was reported in the 1970s^{3,4}. It was claimed that the extent of the glass forming region depended on the melt-quenching temperature: from 1100°C, the glass region extending from $n=0.50$ to 0.75; at 1200°C, from $n=0.50$ to 0.85, where $n=\text{Ga}/(\text{Ga}+\text{La})$ is cationic mole fraction³.

Recently, studies carried out in both the ORC⁵ and CGR⁶ have revealed that the level of oxide content in sulphide precursors plays a decisive role in the formation of GLS glasses (ref). Importantly, when low oxide content sulphide precursors were used, no crystal-free glasses could be made in this system. When quenching from 1150°C a batch of $n=0.70$ and "oxygen" content [O]=0.13wt% crystallised on fast melt quenching. Only after the oxide level was increased to [O]=0.21wt% could crystal-free glass be made on fast quenching⁶. Therefore, the

oxide levels of the sulphide precursors have since been carefully monitored and the "oxygen" content ([O]) of precursor sulphides was measured by the supplier (Merck Limited, UK) using LECO. As oxide was introduced the visible absorption edge of GLS glasses was observed to blue-shift and the multiphonon edge was impaired⁶.

Attention has been paid not only to monitoring the purity of chemical precursors but also to minimising the contamination during the glass preparation procedure. To reduce absorption loss due to OH, the purging nitrogen used in the batching glovebox was circulated through a drying column containing molecular sieves, frequently regenerated by vacuum baking. GLS glasses containing from 500ppm to 10000ppm Pr_2S_3 dopant have been made. Figure 1 shows IR absorption spectra collected for two glasses of $n=0.70$ and $[\text{O}]=1\text{wt}\%$, one undoped and the other doped with 5000ppm Pr_2S_3 . Bands due to Pr^{3+} dopant are evident but the OH absorption band at around $2.9\mu\text{m}$ is negligible for optical pathlength of approximately 5mm.

PHASES DETERMINATION DURING CRYSTALLISATION

Two intermediate phases appear in the phase diagram established by Loireau-Lozac'h et al⁴: $\text{Ga}_{10/3}\text{La}_6\text{S}_{14}$ of hexagonal structure and LaGaS_3 of monoclinic structure. Another crystal phase $\text{Ga}_6\text{La}_{10/3}\text{S}_{14}$ of melilite type tetrahedral structure was also identified and it was only well formed in presence of slight excess of Ga_2S_3 ³. It was reported by Loireau-Lozac'h et al.³ that in an $n=0.64$ GLS glass, three phases $\text{Ga}_6\text{La}_{10/3}\text{S}_{14}$, $\text{Ga}_{10/3}\text{La}_6\text{S}_{14}$ and LaGaS_3 formed in varying proportions on reheating. When the heat treatment temperature was raised, a decrease of phase LaGaS_3 and an increase of phase $\text{Ga}_6\text{La}_{10/3}\text{S}_{14}$ was observed, whereas the concentration of $\text{Ga}_{10/3}\text{La}_6\text{S}_{14}$ kept practically constant. When $n>0.64$ then phase $\text{Ga}_6\text{La}_{10/3}\text{S}_{14}$ was alone appeared in the GLS glasses on heating.

A comprehensive crystallisation study has been carried out when reheating glasses in the Ga_2S_3 - La_2S_3 system, with $n=0.75, 0.72, 0.70, 0.68, 0.65, 0.62$, over a sufficiently wide range of temperature⁷. A new phase (phase A) was identified to be among the first phases to appear in all the six heat treated GLS glasses. Phase A has been claimed to have a monoclinic structure and an approximate composition of $2\text{Ga}_2\text{S}_3\cdot\text{La}_2\text{S}_3$ ⁸. Also identified was phase B, which showed a similar XRD profile to that of $\text{Ga}_6\text{La}_{10/3}\text{S}_{14}$ but slightly smaller d-spacings. It was demonstrated that phase B could form in all six glass compositions instead of only in the glasses of excess Ga_2S_3 . A La-rich gallium lanthanum sulphide phase (phase C) was detected in the heat treated GLS glasses with increasing heat treatment temperature or La_2S_3 concentration in the composition. Phase C has its major diffraction peaks close to, but distinguished from, those of phase B. Figure 2 shows the XRD pattern of phase C, which cannot be identified on the basis of available information. With increase of heat treatment temperature, phase C became more dominant while phase A and phase B disappeared gradually. $\alpha\text{-Ga}_2\text{S}_3$ (phase D) also appeared in the $n=0.75$ glass on fast melt quenching and in the heat treated $n=0.72, 0.75$ glasses. These results highlight significant differences when compared with those reported by Loireau-Lozac'h et al.³. We suggest that a different oxide level in the starting materials may have contributed to the different crystal phases obtained in our laboratory compared with those obtained previously by Loireau-lozac'h et al.^{3,4}. To help clarify this difference, detailed investigation of the effects of oxide content on the crystallisation behaviour of GLS glasses have been carried out^{6,9}.

NUCLEATION AND CRYSTALLISATION BEHAVIOUR

The fibre making process, which normally includes preform manufacturing and fibre drawing, is practically also a multi-step heat treatment process. The process will invite devitrification as

the glass is cycled in the temperature region between the glass transition temperature and the onset of crystallisation temperature. Both the conventional two-step heat treatment method and isothermal and non-isothermal DSC were used to investigate the nucleation and crystallisation behaviour of the GLS glasses¹⁰.

Bulk crystallisation was found to be dominant during the devitrification of GLS glasses. In an $n=0.70$ and $[O]=0.49\text{wt}\%$ glass nucleation was observed at temperatures $\geq 550^\circ\text{C}$. Figure 3 shows crystals formed in this glass after it was (i) heat treated at 640°C for 15 minutes; (ii) heat treated at 580°C for 10 hours and then 640°C for 15 minutes. The increased number of crystals in figure 3(ii) reveals the number of nuclei formed during the nucleation heat treatment at 580°C . Crystal growth was detected when the heat treatment temperature was $\geq 590^\circ\text{C}$. Above 590°C the crystal growth rate increased rapidly with increasing temperature. At temperatures between 620°C and 660°C both isothermal DSC analysis and microscopy observation have revealed that this glass has a very high overall crystallisation rate.

EFFECTS OF ENHANCED OXIDE CONTENT

The existence of oxide content is critical for the formation of GLS glasses. However this does not mean that the higher the level of oxide content the more stable the glasses.

A series of GLS glasses was prepared based on $n=0.70$ with La_2O_3 substituted at the expense of La_2S_3 ⁶. When the batches prepared contained less than $\leq 0.13\text{wt}\%$ oxygen melts devitrified on quenching. As La_2O_3 was added and $[O]$ gradually increased from $0.21\text{wt}\%$ to $2.12\text{wt}\%$, rather unusual behaviour occurred. Figure 4 shows the values of T_x-T_g , which is often used as criterion of glass stability, as a function of oxide content. Firstly, the value of T_x-T_g increased dramatically with the increase of oxide level $[O]$ from 0.21 to $0.49\text{wt}\%$. The glass stability plateaued from 0.49 to $0.97\text{wt}\%$ and from 0.97 to $2.12\text{wt}\%$ decreased. Further increase in oxide content from $[O]=2.12\text{wt}\%$ led to glass stability starting to increase again. Heat treatment and subsequent XRD and microscopy studies confirmed this dependence of the thermal stability of GLS glasses on the oxide concentration, except for the revelation that the glass thermal stability had already started to fall when $[O]$ was increased from $0.65\text{wt}\%$ to $0.97\text{wt}\%$. The conclusion is that the level of oxide is a decisive factor for Ga-La-S glass stability.

Studies further revealed that when $n=0.70$ GLS glasses were reheated at 630°C , if the oxygen content $[O]$ of the batches was less than $0.49\text{wt}\%$ "oxygen", phase A was the only crystal phase formed on reheating. When $[O]$ was between 0.49 and $2.12\text{wt}\%$, both phases A and B formed. When a sufficient amount of "oxygen" was introduced, $[O] \geq 2.12\text{wt}\%$, phase B was the only crystalline phase to form. Indeed, phase B was the only phase claimed to appear in the GLS glasses of $n>0.64$ by Loireau-lozac'h et al. in their work³. The results obtained here support the suggestion that a different oxide level in the starting materials may have led to the formation of the different crystal phases. On the basis of the dependence of the formation of phase B on oxide content, and its smaller d-spacings compared with those of $\text{Ga}_6\text{La}_{10/3}\text{S}_{14}$ (JCPDF card no. 27-0229), we suggested that phase B might be $\text{Ga}_6\text{La}_{10/3}\text{S}_{14}\text{O}_2$ (JCPDF card no.39-0767).

The true nature of the stabilising mechanism of certain amounts of oxide in the glass composition could well depend on eutectic crystal growth of phase A and phase B^{9,11}. Thus, addition of a certain amount of oxide could lead to the total glass composition approaching the eutectic point of phase A and phase B. The formation of either of the two phases would inhibit

the formation of the other; this competition for growth would be exacerbated by the closeness of composition of phases A and B. As a matter of fact, as the oxide concentration was changed, then a greater amount of one crystalline phase formed at the expense of the other.

DEVITRIFICATION DURING MELT-COOLING

To achieve a better understanding of this system and further clarify the different results, a series of GLS glasses with varying cationic ratio and oxide contents was prepared. The glasses were remelted and their devitrification behaviour during melt-cooling from above the liquidus was studied¹².

When three glasses of $n=0.65$, 0.70 and 0.75 and $[O]<0.45\text{wt}\%$ were remelted and cooled at $1^\circ\text{C}/\text{min}$ to 785°C , 750°C , or 700°C and then immediately quenched the same four crystalline phases: phase A, phase B, phase C and phase D were identified as were found for the glasses on reheating. When melt $n=0.65$ was cooled to 785°C phase C was identified by XRD, if it was cooled to 750°C or 700°C then phase D and phase B also formed. When melt $n=0.70$ was cooled to 750°C phase C, phase B and phase D were identified and only tiny amounts of phase A appeared. When melt was cooled to 700°C then the amount of phase A increased. When glass melt $n=0.75$ was cooled, to 750°C phase C, phase D and phase A were identified, to 700°C then phase A increased and at the same time phase B appeared. $\alpha\text{-Ga}_2\text{S}_3$, phase D, displayed a dendrite structure when crystallised in a slowly cooled melt.

Keeping the n value at 0.70 , the glasses of different levels of oxide content were remelted and cooled at $1^\circ\text{C}/\text{min}$ to 700°C and then quenched. The results showed that with the increase of oxide content in the glass composition, phase A initially increased ($[O]$ from $0.21\text{wt}\%$ to $0.97\text{wt}\%$) and then decreased ($[O]$ from $0.97\text{wt}\%$ to $2.12\text{wt}\%$) in its relative diffraction intensity. Phase B increased in its diffraction intensity progressively with the increase of oxide content. Phase B was the only phase identified in the devitrified glass containing $2.12\text{wt}\%$ $[O]$, which was indeed the same as in the case of reheating. Phase C and phase D decreased in diffraction intensity when oxide content increased from $[O]=0.21\text{wt}\%$ to $0.65\text{wt}\%$ and disappeared when the oxide level was further increased to $0.97\text{wt}\%$. The results have shown that both phase A and phase C only formed in low oxide content GLS glasses. This evidence might have explained why Loireau-lozac'h et al did not identify these two phases in their work^{3,4}.

THE EFFECTS OF ADDITIVES

Zn, Pb, Bi, Cd, Sr, and Ba sulphides were added to $n=0.70$ glass at the expense of La_2S_3 respectively to identify any improvement in glass stability. The results showed that without the presence of a critical amount of oxide then the glasses devitrified on melt-quenching. The effects of these additives seemed to be overshadowed by those of the oxide content. Due to the variation of oxide content in these sulphide additives from one to another, no sulphide has been identified as a helpful additive for improving glass stability. However all additives were successfully incorporated when a sufficient amount of oxide content was introduced and could act as refractive index modifiers or for adjustment of T_g s. Oxide tends to shorten excited state lifetimes of rare earth dopants and therefore a compromise in oxide level must be struck.

Alkali and alkaline-earth chlorides (MCl_x , $x=1$ or 2) were also introduced into the GLS glasses in the form of $(100-y)(0.70\text{Ga}_2\text{S}_3 \cdot 0.30\text{La}_2\text{S}_3) \cdot y\text{MCl}_x$ (mol). The y value, equivalent to the mole fraction of halide which could be introduced into the composition to make crystal-free glass, largely depended on the oxide concentration in the sulphide precursors. The more oxide

present, the more halide could be incorporated. To increase the oxide content, La_2O_3 was used to substitute for La_2S_3 while n was kept constant at 0.70. When the overall oxide content $[\text{O}]$ was 0.57wt%, then up to 5mol% CsCl could be added. A further increase of CsCl added led to the formation of crystals in the glass on melt-quenching. When $[\text{O}]$ was 1.00wt%, then up to 10mol% CsCl could be added before the glass stability started decreasing. If BaCl_2 was used instead of CsCl then only half the equivalent mole fractions could be added, possibly due to BaCl_2 supplying double the Cl. When compared with the original GLS glasses these chloride incorporated glasses have higher Tgs and larger Tx-Tg. With increasing chloride content, the colour of the glasses changed from dark red to pale yellow suggesting that the visible absorption edge had blue shifted.

SUMMARY

The formation and crystallisation of gallium-lanthanum-sulphide glasses have been proved far more complicated than previously believed. To make low loss GLS glass fibres more fundamental studies, such as viscosity behaviour etc., yet to be carried out,

ACKNOWLEDGEMENT

We gratefully acknowledge financial support from the UK Engineering and Physical Science Research Council under Grant number GR/K78928. We thank Mr. H. Bagshaw for his technique support and Dr. D. Furniss of CGR, Sheffield University, Dr. D.W. Hewak of ORC, Southampton University, and Dr. M. G. Pellatt and Mr. D. Sparrowe of Merck Limited, UK for helpful discussion.

REFERENCES

1. P. C. Becker, M. M. Broer, V. G. Lambrecht, A. J. Bruce and G. Nykolak, Tech. Dig. Topical Meeting Optical Amplifiers and Their Applications, 1993, Post-deadline paper PDP5.
2. Y. Ohishi, T. Kanamori, T. Kitagawa, S. Takahashi, E. Snitzer, H. Sigel, Optics Letters, 1991, 16, pp1747-1749.
3. A. M. Lozac'h, M. Guittard and J. Flahaut, Mat. Res. Bull., 11, 1489-1496, 1976
4. A. M. Lozac'h, M. Guittard and J. Flahaut, Mat. Res. Bull., 12, 881-886, 1977.
5. D. W. Hewak, Progress report, 1997.
6. R. Li, D. Furniss, H. Bagshaw, and A. B. Seddon, J. Mat Res. submitted.
7. R. Li, and A. B. Seddon, J. Am. Ceram. Soc., submitted.
8. S.P. Morgan, I.M. Reaney, R. Buckley, D. Furniss and A.B. Seddon, J. Am. Ceram. Soc., in press.
9. R. Li, and A. B. Seddon, to be submitted.
10. R. Li, and A. B. Seddon, to be submitted.
11. S.P. Morgan, I.M. Reaney, R. Buckley, D. Furniss and A.B. Seddon, J. Am. Ceram. Soc., submitted.
12. R. Li, I. M. Reaney, and A. B. Seddon, to be submitted.

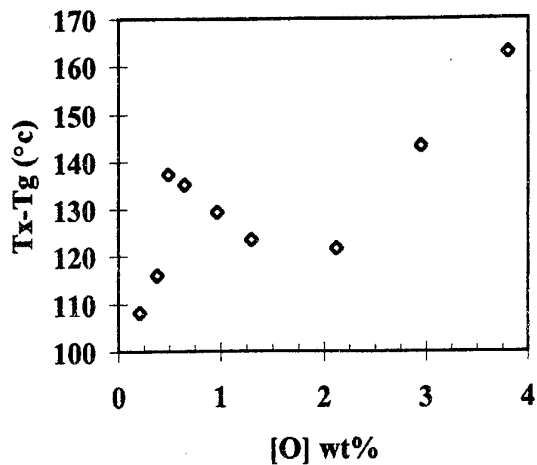
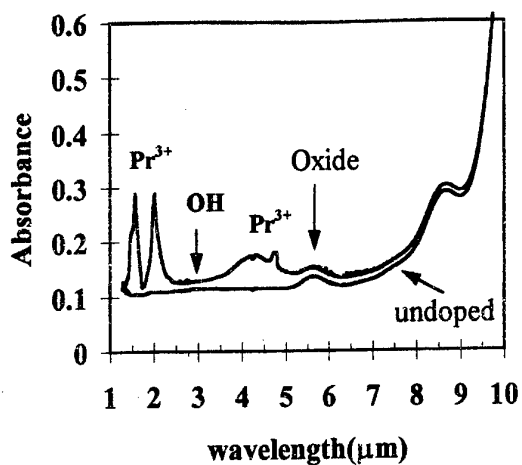


Figure 1 IR absorption spectra of GLS glasses. Figure 4 Tx-Tg as a function of oxide content.

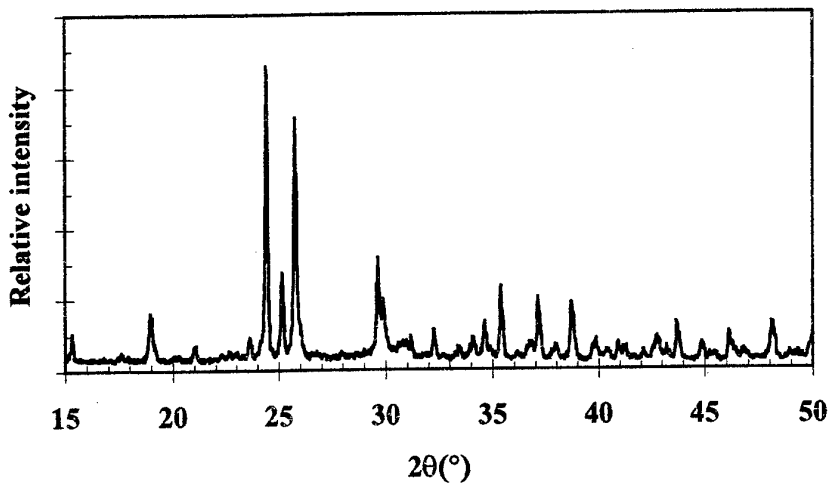


Figure 2 X-ray diffraction pattern of phase C.

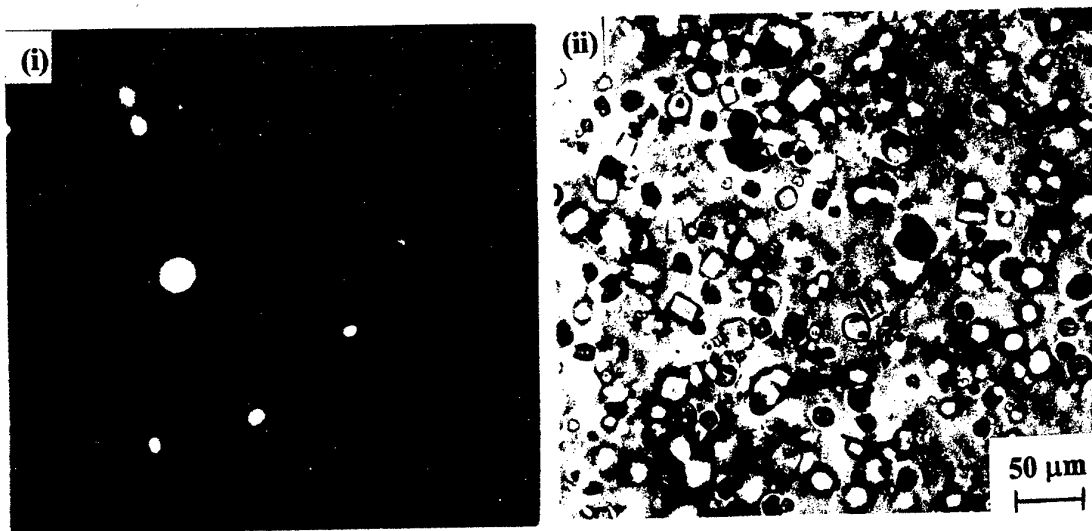


Figure 3 Crystals formed in heat treated GLS glasses

SOL-GEL PROCESSING OF GERMANIUM SULFIDE BASED FILMS

Orlando Martins, Jian Xu and Rui M. Almeida

Departamento de Engenharia de Materiais / INESC

Instituto Superior Técnico, Av. Rovisco Pais, 1000 Lisboa, Portugal

Email : omartins@eniac.inesc.pt

ABSTRACT

Germanium sulfide is a well known optical material, which is transparent in the 0.5-10 μm wavelength region and the possibility of preparing germanium sulfide glass films by sol-gel processing is of great interest for applications such as planar waveguides for integrated optics. The present paper describes possible alternative ways of using sol-gel processing for the liquid phase deposition of germanium sulfide based films. The Ge precursors used were germanium tetrachloride (GeCl_4) and germanium ethoxide ($\text{Ge}(\text{OC}_2\text{H}_5)_4$), while the different sources of S utilized were thiourea, thioacetamide and hydrogen sulfide. Special precautions were necessary to protect the reaction mixture from water contamination, which produced GeO_2 . The films obtained were characterized by ellipsometry, IR and XPS spectrometries. Although some oxide contamination was evident in most films prepared, refractive indices close to that expected for dense GeS_2 glass were usually obtained. In some cases, the film composition contains germanium sulfide without oxide impurities.

I. INTRODUCTION

Fiber optic and integrated optics (IO) amplifiers for the 1.3 μm telecommunications window may be developed by doping suitable glass host materials with praseodymium ions (Pr^{3+}). This ion is optically active near 1.3 μm , based on the radiative transition from the metastable $^1\text{G}_4$ state to the $^3\text{H}_5$ state. This transition is quenched by non-radiative multiphonon relaxation from the $^1\text{G}_4$ to the $^3\text{F}_4$ level, through the excitation of lattice vibrations and this makes the fluorescence lifetimes unacceptably low in high phonon energy oxide glasses [1-2]. In the case of Pr^{3+} , it is especially important that the glass host is a material with low phonon energies and the non-radiative multiphonon relaxation rate is reduced. Chalcogenide glasses, with low phonon energies compared with oxide and fluoride glasses and high refractive indices, should be efficient host materials with low non-radiative relaxation rates. However, the presence of O and H impurities in such glasses has also a serious fluorescence quenching effect and such species must be removed very carefully.

Sulfide glasses based on GeS_2 are promising hosts [1,3]. Germanium sulfide is a well known optical material, which is transparent in the 500 nm to 10 μm wavelength region. Most germanium sulfide glasses reported in the literature, either undoped [4,5] or doped with Pr^{3+} [1,3], were made by melting ; sol-gel fabrication of these materials has been little investigated [6-8]. In these cases, the material composition was not pure, but it was a mixture of GeS_2 and GeO_2 . The authors proposed that water impurity was the reason for GeO_2 formation during GeS_2 synthesis. Special precautions are necessary to protect the reaction from water contamination.

The objective of this work is to assess the feasibility of fabricating germanium sulfide glass planar waveguides by the sol-gel process, by using different germanium and sulfur precursors, with special precaution to protect the reaction mixture from exposure to any water impurity, in order to obtain pure germanium sulfide glass.

II. EXPERIMENTAL PROCEDURE

II.1) Film fabrication

For the preparation of GeS_2 sol-gel films, several different experiments were carried out, varying the different parameters which have an influence on the properties of the final solution, namely :

- the nature of the germanium precursor : germanium ethoxide, TEOG ($\text{Ge}(\text{OC}_2\text{H}_5)_4$), or germanium tetrachloride (GeCl_4) ;
- the different sources of sulfur : thiourea ($\text{SC}(\text{NH}_2)_2$), thioacetamide ($\text{CH}_3\text{CS}(\text{NH}_2)$), or hydrogen sulfide (H_2S) ;
- the nature of the solvent : ethanol, or toluene ;
- the nature of the catalyst : HCl , H_2SO_4 , or propionic acid ($\text{CH}_3\text{CH}_2\text{COOH}$).

All reactions and manipulations were carried out inside a N_2 -filled glove-box, or under dry nitrogen, using standard schlenk techniques.

II.1.1) Reaction between thiourea and Ge precursors

When thiourea is used, it is difficult to obtain a clear, transparent solution. In most cases (with germanium tetrachloride), a white precipitate is formed immediately and the liquid becomes milky. After testing different experimental conditions, the best solution was obtained by the reaction of thiourea with germanium ethoxide (TEOG) in ethanol, containing sulfuric acid (final $\text{pH}=1.3$). The solution thus prepared is kept at a temperature near 70°C and it remains stable for at least one week, as a transparent liquid. Only ethanol was used as solvent, because it is not possible to dissolve thiourea in toluene.

Suitable sols were used for depositing films in a glove box filled with dry N_2 . These were prepared on silicon wafers, by dip-coating (30 cycles, at a rate of 6 cm/min), followed by heat-treatment inside the glove-box at 250°C , for 5 hours.

II.1.2) Reaction between thioacetamide and Ge precursors

Thioacetamide was easily dissolved in ethanol (but not in toluene), yielding a clear solution. GeCl_4 was added to this solution very slowly. The reaction between thioacetamide and GeCl_4 (there was no reaction with TEOG), was observed by the changing color : the solution becomes yellow and, after 3 minutes, it slowly becomes milky. Films were prepared before precipitation, on Si substrates, by spin-coating (speed of 2000 rpm, for 30 seconds) inside the glove-box, and they were heat-treated at 250°C during 5 hours. However, these films tend to be slightly opalescent and this does not disappear with the heat-treatment.

II.1.3) Reaction between H_2S and Ge precursors

After testing different experimental conditions, the direct reaction between H_2S and TEOG did not give good results. Only GeCl_4 appears to give good results in the preparation of germanium sulfide sol-gel films, using the following method. Inside a N_2 -filled glove-box, GeCl_4 is easily dissolved in toluene, containing propionic acid catalyst (this was found to be preferable to HCl or H_2SO_4), inside a schlenk glass vessel, which is then closed, withdrawn from the dry box and placed in a nitrogen gas line. After purging the system for a few minutes, hydrogen sulfide is admitted, until a molar ratio $\text{H}_2\text{S}/\text{GeCl}_4 \sim 4$ is achieved. The solution thus prepared is kept at a temperature near 40°C and it is aged for about 1 ~ 4 weeks. Some sols were clear and yellowish, but some had a few milky lumps as well.

Films were prepared on Si substrates by dip-coating or by spin-coating and they were heat-treated at 250°C during 5 hours. These films were usually still slightly opalescent (lossy waveguides).

II.2) Film characterization

The films were characterized by IR spectroscopy, ellipsometry and X-ray photoemission spectroscopy (XPS). IR absorption spectra were measured with Nicolet 5 DXC and 20 F Fourier transform spectrometers, in the range of 50-4400 cm^{-1} . XPS measurements were carried out in a ultra high vacuum chamber, using a Mg $K\alpha$ X-ray source. Refractive index and thickness measurements were performed with an ellipsometer (Rudolph Research, $\lambda=633$ nm).

III. RESULTS and DISCUSSION

III.1) Films prepared by the reaction between thiourea and Ge precursors

The following results were obtained with the best solution prepared, using TEOG as a precursor, in ethanolic medium.

III.1.1) IR spectra

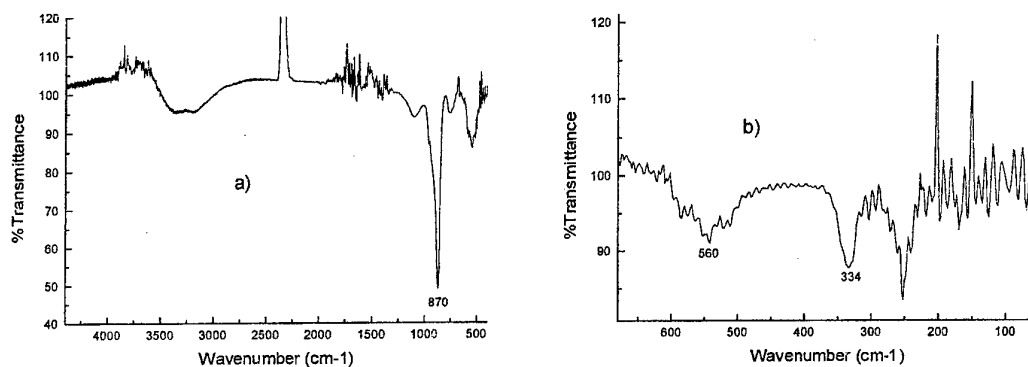


Figure 1 : Infrared absorption spectra of germanium sulfide containing film, prepared from TEOG and thiourea, dried at 250°C, during 5 hours : a) middle IR ; b) far IR spectrum.

In the IR spectrum of a germanium sulfide containing film (figure 1), the presence of Ge-O bonds is indicated by the peaks at 870 cm^{-1} and at 560 cm^{-1} , the same as found in germanium oxide by several authors [9-11] ; most of these films appear to be composed of GeO_2 , containing appreciable amounts of OH, at 250°C, revealed by the broad band near 3300 cm^{-1} . A positive identification of Ge-S bonds at ~334 cm^{-1} [3-5] was only possible in the best cases, where the solution became clear and transparent. But even these films were still composed of a mixture of sulfide and oxide.

III.1.2) Ellipsometric measurements

The films where the presence of Ge-S bonds was positively observed by IR had a refractive index of 1.79 ± 0.04 at 633 nm. The refractive indices of GeO_2 and GeS_2 glasses are, at 633 nm, 1.60 [12] and 2.30 [3], respectively. For a film index of 1.79, the relative volume fractions (%) of GeS_2 and GeO_2 would be approximately 33:67, based on the Lorentz-Lorentz equation [13] :

$$\frac{n_f^2 - 1}{n_f^2 + 2} = V_s \frac{n_s^2 - 1}{n_s^2 + 2} + V_o \frac{n_o^2 - 1}{n_o^2 + 2} \quad \text{with } V_o = 1 - V_s$$

with V_s and V_o : volume fractions of GeS_2 and GeO_2 respectively

n_s , n_o and n_f : refractive index of GeS_2 glass (2.30), GeO_2 glass (1.60) and the film (1.79)

This result was consistent with the presence of a mixture of oxide and sulfide.

III.1.3) XPS spectra

The X-ray photoemission spectroscopy (XPS) measurement on a germanium sulfide containing film clearly shows the presence of Ge, S and O atoms (table 1). One must be careful about the very large oxygen concentrations detected, since adventitious oxygen species may be preferentially concentrated at the surface of the films. Two different positions for the S 2p peaks were observed : one position corresponds to the presence of S-H bonds at 169 eV and the other to the presence of S-Ge bonds at 165 eV. It can be estimated that the maximum and minimum S/Ge ratios in the films prepared were 1.18 and 0.09 respectively. The corresponding O/Ge ratios were higher, 8.33 and 2.56, respectively. The present films always appear to contain a mixture of germanium oxide and sulfide, plus some OH groups.

Table 1 : XPS data for germanium sulfide based film prepared from TEOG and thiourea, dried at 250°C during 5 hours

Peak assignment	Binding energy (eV) ± 1 eV	At %	Possible chemical Environment
O 1s	532	73 ± 7.3	GeO ₂ + adventitions
S 2p	165	5 ± 0.5	GeS ₂
	169	3 ± 0.3	H ₂ S
Ge 3d	33	18 ± 1.8	GeO ₂ and GeS ₂

III.2) Films prepared by the reaction between thioacetamide and Ge precursors

The best results were obtained by reacting thioacetamide with germanium tetrachloride.

III.2.1) IR spectra

The IR absorption spectrum of a germanium sulfide based film (figure 2) shows absorption bands at 375 cm⁻¹ and a shoulder at 435 cm⁻¹, corresponding to the presence of Ge-S bonds. The absorption band of Ge-O bonds at 870 cm⁻¹ is now absent from this film. Thus, it appears that the reaction of thioacetamide with germanium tetrachloride, dissolved in ethanol, is a good way for essentially eliminating the presence of oxide from the films and to obtain only germanium sulfide (only Ge-S bonds are present in the IR spectrum).

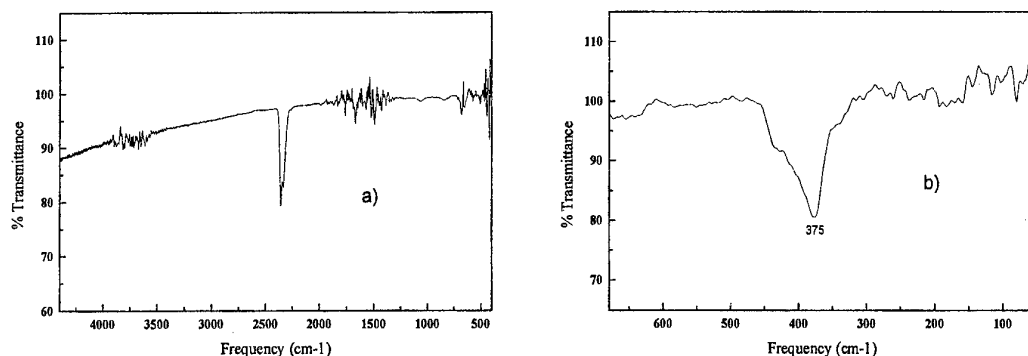


Figure 2 : Infrared absorption spectra of germanium sulfide containing film, prepared from GeCl₄ and thioacetamide, dried at 250°C, during 5 hours : a) middle IR ; b) far IR spectrum

III.2.2) Ellipsometric measurements

The refractive index values found for different germanium sulfide based films, at 633 nm, are all around 2.3 ± 0.1 , the same as the index found in the literature for GeS_2 glass [3].

III.2.3) XPS spectra

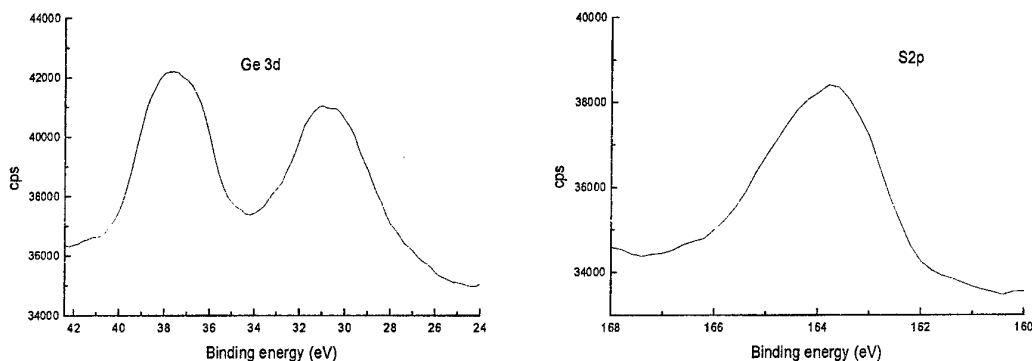


Figure 3 : XPS spectra of germanium sulfide based film prepared with GeCl_4 and thioacetamide, dried at 250°C , during 5 hours.

In the XPS spectra of a germanium sulfide based films (figure 3), two different positions for the Ge 3d peaks were observed : one position corresponds to the presence of Ge-S bonds at 31 eV and the other to the presence of Ge-Cl bonds at 38 eV. On the otherhand, only one position was found for the S 2p peak at 164 eV, corresponding to the presence of S-Ge bonds. The Cl 2p peak was found at 192 eV. For this film, it can be estimated that the Cl/Ge ratio is ~ 3.35 and the S/Ge ratio is ~ 2.07 . Therefore, the films made by the reaction of thioacetamide and germanium tetrachloride appear to consist basically of a germanium thiochloride chalcoholide glass, containing appreciable amounts of Cl even after hours at 250°C . The presence of Ge-Cl bonds, however, was not detected by IR spectroscopy.

III.3) Films prepared by the reaction between H_2S and Ge precursors

The best quality germanium sulfide based films were obtained when using GeCl_4 as a precursor and they were also characterized by several methods.

III.3.1) IR spectra

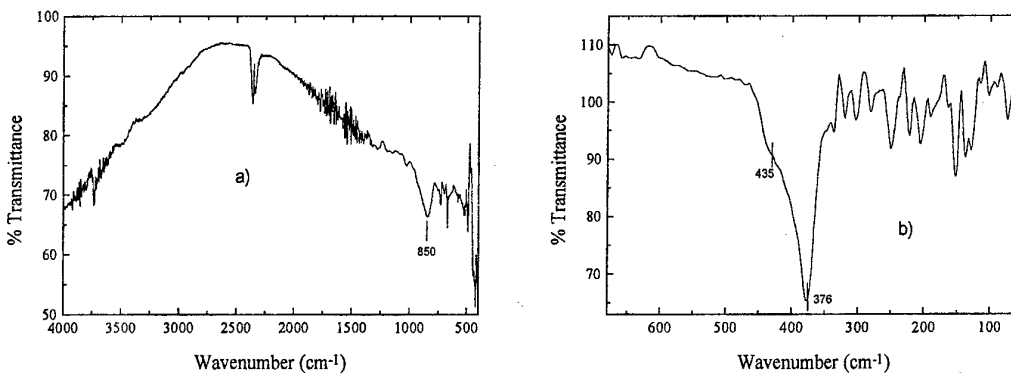


Figure 4 : Infrared absorption spectra of germanium sulfide based film, prepared with GeCl_4 and H_2S , dried at 250°C during 5 hours : a) middle IR ; b) far IR spectrum

In the middle IR spectrum, there is an absorption peak due to Ge-O species at 850cm^{-1} , but no other significant absorption peaks due to solvent or catalyst existed after heat treatment (250°C during 5 hours), as shown in figure 4. The far IR spectrum shows absorption peaks near 376 cm^{-1} and 435 cm^{-1} , both due to Ge-S vibrations [3-5]. It appears that the reaction of hydrogen sulfide with germanium tetrachloride always yields films containing a mixture of GeS_2 and some residual GeO_2 . Although special precautions were taken by using the N_2 -filled glove-box and the schlenk technique under dry nitrogen, there was still some water contamination during processing, responsible for the GeO_2 formation.

III.3.2) Ellipsometric measurements

The refractive index values of different germanium sulfide based films at 633 nm are near ~ 1.9 , probably due to the residual oxide and, perhaps, to some optical (band tail) absorption at 633 nm.

IV. CONCLUSIONS

The germanium sulfide based films prepared so far have an acceptable optical quality, but not sufficiently good to qualify them as planar waveguides (their propagation losses have not yet been measured). Their composition appears to contain, in most cases, a mixture of sulfide and oxide (or chloride) in variable proportions. In terms of elimination of residual oxide species for possible active applications (e.g. Pr^{3+} doping), the best results so far have been achieved with films prepared by the reaction of GeCl_4 and thioacetamide, dissolved in ethanol. In this case, the films appear to be composed of a thioclchloride chalcohalide glass and they have a high refractive index of 2.3 (which is the same as the index of GeS_2 glass).

At this point, the fabrication of GeS_2 planar waveguides by sol-gel processing appears feasible. Their optical quality will still be further improved and optical propagation loss measurements will be performed. The optimized films will then be doped with Pr^{3+} .

REFERENCES

- [1] D.R. Simons, A. J. Faber, H. Waal, J. Non-Crystalline Solids **185** (1995) 283.
- [2] W. J. Miniscalco, in : Rare-earth doped fiber lasers and amplifiers, ed. by Michel J. F. Digonnet (Marcel Dekker, Inc., New York, 1993), ch.2, pp. 19-133.
- [3] A. Jha, P. Sapp, G. Kakarantzas, *ibid.* p391.
- [4] G. Lucovsky, J. P. de Neufville, F. L. Galeener, Phys. Rev. B **9** (1974) 1591.
- [5] G. Lucovsky, F. L. Galeener, R. C. Keezer, R. H. Geils, H. A. Six, Phys. Rev. B **10** (1974) 5134.
- [6] P. J. Melling, Am. Cer. Soc. Bull. **63** (1984) 1427.
- [7] A. B. Seddon, S. N. B. Hodgson, M. G. Scott, J. Am. Ceram. Soc. **26** (1991) 2599.
- [8] V. Stanic, A. C. Pierre, T. H. Etsell, J. Mater. Res. **11** (1996) 363.
- [9] W. Kaiser, P. H. Keck, C. F. Lange, Phys. Rev. **101** (1956) 1264.
- [10] V. V. Obukhov-Denisov, N. N. Sobolev, V. P. Cheremisinov, Opt. Spectry. USSR, English Transl. **8** (1960) 267.
- [11] M. K. Murthy, E. M. Kirby, Phys. Chem. Glasses **5** (1964) 144.
- [12] K. D. Simmons, G. I. Stegeman, B. G. Potter, J. Non-Crystalline Solids **179** (1994) 254.
- [13] Mc Born, E. Wolf, Principles of optics (Oxford, Pergamon, 1975), p.87.

Catalyzed Gelation of Amorphous Sulphides

J.S. Sanghera, C. Scotto¹, S. Bayya¹ and I. D. Aggarwal

Naval Research Laboratory, Code 5606, Washington, DC 20375

¹ Virginia Polytechnic Institute, Blacksburg, VA 24061

The Sol-Gel route is typically a low temperature solution route for making either crystalline or amorphous inorganic materials. There is a plethora of work in the literature pertaining to oxide gels and perhaps the most extensively studied material is silica glass in the form of bulk monoliths and films. Since it is a low temperature process, it is also possible to make organic/inorganic hybrid materials. Other advantages of this solution route include high purity and homogeneous products.

Very little work has been published in the area of non-oxide gels, especially chalcogenides. These materials are of technological interest for many applications in the infrared. Some of these include passive fibers for laser power delivery or chemical sensing, as well as active fibers containing rare earth ions for lasers and amplifiers. Another exciting area is the development of compact devices based on thin film planar waveguides based on chalcogenide glasses.

One problem facing many researchers working in the field of chalcogenide glasses lies in the lack of availability of high quality precursors leading to extrinsic scattering and absorption. Furthermore, there are concerns that traditional melting for prolonged times at elevated temperatures in quartz ampoules may lead to contamination and therefore higher optical losses and possibly poor glass stability. Therefore, there is a need to investigate alternative low temperature processing techniques to make the chalcogenide precursors and glasses. Such a technique may also be useful for making thin films for planar waveguide devices.

We describe a process for making amorphous sulphide based gels and rare earth doped sulphide gels. The role of catalysts to speed up the gelation time from about 1 day to less than 30 minutes is discussed. The catalysts not only speeden up the reaction time, but also increase the degree of gelation so that the amount of unreacted precursor is significantly reduced. We will report the infrared, DSC/DTA and fluorescence data for both undoped and doped gels. The gelation mechanism will be discussed.

IN-SITU GENERATION OF Eu^{2+} IN GLASS-FORMING MELTS B4

D. R. MacFarlane¹, P. J. Newman¹, J. D. Cashion² and A. Edgar³

¹ Department of Chemistry, Monash University, Clayton, Vic., Australia

² Department of Physics, Monash University, Clayton, Vic., Australia

³ School of Chemical and Physical Sciences, Victoria University
Wellington, New Zealand

We report on the efficacy of in-situ reduction of Eu^{3+} to Eu^{2+} in a fluoride melt by a variety of chemical reductants and by bulk electrochemical reduction. The Eu^{2+} content of the resultant glasses was determined by a combination of EPR and magnetic susceptibility measurements. Addition of LiH or use of a hydrogen atmosphere produced near-complete reduction, whilst the electrochemical technique produced only around 30% conversion. None of the fluorozirconate glasses produced showed luminescence from Eu^{2+} ions, although a fluoroaluminate glass made using the LiH reduction technique showed strong luminescence.

1) INTRODUCTION

The optical properties of trivalent rare earth ions in fluorozirconate glass form the basis for several useful applications such as fibre lasers, three dimensional displays, and optical refrigerators, and so have received considerable attention in the literature. Divalent ions in the same glasses have been less intensively studied, even though these species also have potential applications in optoelectronics. For example, Sm^{2+} -doped borate glass [1] has been investigated as an information storage material, whilst Eu^{2+} doped glass is a potential Faraday rotator material [2] and a photostimulated X-ray phosphor [3]. The photostimulation effect occurs when a thin film of an appropriate material, such as crystalline BaClBr doped with Eu^{2+} ions, is exposed to X-rays. When subsequently scanned by a red laser beam, those areas exposed to X-rays emit blue light and so an X-ray image can be developed. The precise mechanism of the photostimulation is still a topic of discussion [4]; in the simplest model, the incident X-ray ionises an Eu^{2+} ion to Eu^{3+} , and the liberated electron is trapped at a fluorine vacancy, forming an F centre. Subsequent irradiation by laser light can liberate this electron, which then recombines with an Eu^{3+} ion, resulting in blue Eu^{2+} luminescence from a $4f^65d^1$ to $4f^7$ transition. A problem with the existing crystalline phosphors is that scattering of the red laser light by the micro-crystalline phosphor powder limits the spatial resolution. This could be improved if a suitable glass phosphor could be found.

Qiu et al [3] have recently reported that fluoroaluminate glass doped with Eu^{2+} ions shows a small but measurable photostimulated phosphor effect. Europium is commonly available only as the trivalent fluoride, and therefore it is usually necessary to have some method of reducing it to the divalent state in the glass preparation; Qiu et al [3] achieved this using a hydrogen atmosphere in the preparation process. The fluorozirconates are an alternative well-known family of fluoride glasses, but as far as we are aware they have not yet been investigated with a view to Eu^{2+} doping for X-ray phosphor applications. However, fluorozirconate glasses present a particular problem for low valence dopants due to the ease with which Zr^{4+} can be itself reduced. We have therefore undertaken a study of processes by which Eu^{2+} ions can be introduced into the fluorozirconate hosts using a variety of techniques to reduce trivalent to divalent europium. The Eu^{2+} content is assayed principally by an EPR/magnetic susceptibility technique.

The EPR spectra of Eu^{2+} and Gd^{3+} ions in fluorozirconate glass has been previously reported by Furniss et al [5]. The spectra we observe for these ions in ZBLAN fluorozirconate glass are very similar in appearance to those described earlier [5], and indeed to the EPR spectra for these ions in many other glasses (see for example the review by Brodbeck and Iton [6]). Both Eu^{2+} and Gd^{3+} have an f^7 electronic configuration with an $^8S_{7/2}$ ground state, which is split in a crystal field into four closely spaced doublets. The application of a magnetic field splits the doublets, and EPR transitions are seen between the individual states. In a glass, the crystal field is quasi-random from one site to the next, and so a sharp-line spectrum is not observed, but rather a broad absorption with some sharper features at particular g-values.

Eu^{3+} ions have a non-magnetic ${}^7\text{F}_0$ singlet ground state which does not contribute to the EPR spectrum or the magnetic susceptibility; the ${}^7\text{F}_1$ first excited state has a small thermal population at room temperature and so makes a minor contribution to the susceptibility, but any EPR signal is unobservable due to strain broadening and fast relaxation.

2) EXPERIMENTAL METHODS

All the metal fluorides of the base glass and europium trifluoride were obtained from either BDH or Morita. The metal hydrides and borohydrides were obtained from Aldrich (highest possible purity) and used as received. H_2 gas was instrument grade (99.9%) from BOC and mixed with high purity argon to give 5, 10 and 25 vol% mixtures. Fluorozirconate ($53\text{ZrF}_4\text{-}20\text{BaF}_2\text{-}1.5\text{LaF}_3\text{-}1.5\text{YF}_3\text{-}3\text{AlF}_3\text{-}20\text{NaF-}1\text{EuF}_3$) and fluoroaluminate ($35\text{AlF}_3\text{-}10\text{BaF}_2\text{-}20\text{CaF}_2\text{-}10\text{SrF}_2\text{-}14\text{YF}_3\text{-}10\text{MgF}_2\text{-}1\text{EuF}_3$) glasses were batched in a nitrogen filled drybox and melted in graphite or vitreous carbon crucibles fitted with platinum lids using a quartz lined electrically heated furnace attached to the back of the drybox. InF_3 was deliberately omitted from all but one formulation. The atmosphere over the melt was highly purified argon except when H_2 mixtures were used for reduction. The platinum lids were removed when a hydrogen atmosphere was used. Electrochemical reduction was achieved using the method described by MacFarlane et al [7]. In all cases, small slabs ($20\times 10\times 3$ mm) were poured, annealed at 260°C for fluorozirconates and 350°C for fluoroaluminates and then cooled slowly to room temperature.

Magnetic susceptibilities were measured at room temperature using a transformer-based system which has been described by Edgar and Quilty [8]. The magnetic susceptibility was determined relative to a standard sample of gadolinium sulphate hydrate.

EPR spectra were recorded at room temperature using Varian X-Band (9 GHz) spectrometers. To determine the Eu^{2+} content in our glass samples, we compared the amplitude of the broad EPR absorption line at $\sim 0.1\text{T}$ (shown in figure 1) with the equivalent line in a ZBLAN sample doped with 1% Gd^{3+} . We assume that all of the gadolinium occurs in the trivalent state; observations of other oxidation states for this ion are extremely rare. Our measurement is done by comparing the peak-to-peak amplitude of the line at 0.1T for the Eu^{2+} doped glass with the EPR spectrum of a Mn^{2+} -based transfer standard and then repeating the process for the Gd^{3+} doped glass. Spectra were recorded at power levels at or below one milliwatt to minimise any power broadening of the spectra and considerable care was taken to ensure that the geometry of the microwave cavity, glass sample, and reference sample was always the same, and the mass of the samples was taken into account. The reproducibility of the measurement was tested by measuring the apparent concentration of the same Eu-doped glass sample on six different occasions in the two different spectrometers. The standard deviation of the measurement was 5%.

The bare EPR signal amplitude ratios underestimate the relative concentrations of $\text{Eu}^{2+}/\text{Gd}^{3+}$ because unresolved ${}^{151}\text{Eu}$ and ${}^{153}\text{Eu}$ hyperfine splitting broadens the Eu^{2+} line by around 15% compared to that for Gd^{3+} . This would require a correction factor of ~ 1.3 to be applied to the bare amplitude ratios, since line intensities are proportional to the square of linewidths for first-derivative EPR spectra. To estimate this factor more precisely, we have measured the magnetic susceptibilities of those samples with the largest EPR amplitude ratios, and which show no Eu^{3+} fluorescence: we therefore take these to contain almost entirely divalent europium. For this group of glasses only, the magnetic susceptibility can be used to derive an absolute Eu^{2+} concentration by comparing with the gadolinium sulphate standard. Averaging over this group, we arrive at a scaling factor of 1.34, which is consistent with the estimate from the linewidth ratios. This scaling factor has then been applied in Table 1 to the EPR ratios for other samples which contain non-negligible quantities of Eu^{3+} , and for which the analysis of the magnetic susceptibility is complicated by the two charged states.

Optical fluorescence spectra were recorded at room temperature using a 0.25 meter focal length Spex spectrometer with 254 nm narrow-line or 350 nm broad-band excitation sourced from a mercury lamp. The resolution was 2 nm. Mossbauer spectra at room temperature were recorded using a conventional, constant acceleration spectrometer system.

3) RESULTS

The X-band EPR spectra for two samples of ZBLYN glass, one containing 1% Gd^{3+} and the other, by our assay, 0.91% Eu^{2+} , are shown in Figure 1. The spectrometer gain for the Eu^{2+} spectrum is 1.6 times greater than for the Gd^{3+} spectrum, so that the low-field line shapes can be directly compared. It is evident from the figure that the 0.1T line, used in this work for assay purposes, is of similar shape for both types of dopant. We show in Table 1 the calculated percentages of Eu^{2+} calculated by the method described in section 2 for a variety of ZBLYN glasses which contain 1 mol percent of europium, introduced in all but two cases by the addition of europium trifluoride.

The simple use of a graphite crucible is partially effective in achieving reduction, but results in a glass covered with a thin carbon film and which is of poor transparency, possibly due to carbon inclusions or to reduced zirconium. Addition of indium fluoride to minimise the latter problem results in a substantially smaller fraction of Eu^{2+} ions, suggesting that the indium is reduced before the europium. Electrochemical reduction produces a glass of high transparency and up to 0.28 mol% Eu^{2+} . The results with hydrogen depend upon the ratio of hydrogen to argon used in the furnace atmosphere, and upon the processing time. Essentially complete conversions were obtained for argon atmospheres containing 10% and 25% hydrogen, but lower conversions were achieved when the hydrogen concentration was reduced to 5%. The samples were of good transparency to the eye; most but not all showed orange fluorescence.

We examined several glass samples containing between 0.5 and 2% LiH as a reductant, and found that this additive is very effective, resulting in a stoichiometric reduction of Eu^{3+} to Eu^{2+} . None of the three samples produced with 1 mol% LiH showed any orange fluorescence, implying complete conversion of Eu^{3+} to Eu^{2+} . Glasses with 1 mol% of both EuF_3 and LiH were of low transparency with a greyish tinge, but glasses containing a smaller concentration of LiH were clear. A glass which was over-doped with 2 mol% LiH was green in colour, and contained black flecks which had a silvery surface, presumably corresponding to a metallic or semiconducting compound containing reduced zirconium. Glasses with lower concentration of LiH did show weak orange fluorescence. Sodium hydride appeared to be slightly less effective than LiH , but gave a clear glass. One glass was produced with no europium content but 1% LiH ; this glass had the same green/black appearance as that described earlier. To check for the presence of Zr^{3+} , an EPR spectrum of this glass was recorded but no signals were seen.

Single glass samples were produced with LiBH_4 and $\text{ZrH}_{1.9}$. These reductants appeared to be almost as effective as LiH in reducing the Eu^{3+} . We have also examined glasses containing 1 mol% EuF_3 which had 1 mol% of CeF_3 , MnF_2 , or ZrO_2 added. The two former additives have higher oxidation states available for any redox reaction with the europium, whilst the latter has been previously shown to have a reducing effect for iron in fluorozirconate glass [9]. None of the resulting glasses showed Eu^{2+} concentrations of more than 0.05%, and so we find this group of additives is not effective in achieving reduction. Towards the end of this work, some europium difluoride became available from Cerac Inc. and Prof. M. Spaeth donated some nominally EuF_2 sourced from Agfa AG. We include results for this material in Table 1. The Agfa material does not lead to a significant concentration of Eu^{2+} ions, suggesting that it does in fact contain only a small fraction of europium in the divalent state, but use of the Cerac material results in almost as much divalent europium as the most effective reduction procedures. Mossbauer spectra of the nominally two divalent fluorides confirmed that the Cerac material was more than 94% divalent europium, whilst no divalent europium could be observed in the Agfa material. This difference between the two sources of nominally EuF_2 is also apparent when they are introduced into the fluoroaluminates, as described below. Possibly the difluoride is subject to some oxidation during storage.

In Figure 2 we show the optical fluorescence spectra of fluoroaluminate glasses produced using the Cerac and Agfa europium difluoride starting material and from EuF_3 using the LiH reductant process. EPR assays of the relative Eu^{2+} content in these glasses showed that the glass made from the Agfa europium fluoride contained approximately one-fifth the Eu^{2+} concentration of the other two glasses. The fluoroaluminate spectra show a broad Eu^{2+}

luminescence centred at around 415 nm, as reported by Qiu et al [3], which is strongest for the glass prepared using LiH reductant. The broad emission corresponds to a $4f^65d$ to $4f^7$ transition, whilst a narrow line at 360 nm is the $^6P_{7/2}$ to $^8S_{7/2}$ transition within the $4f^7$ configuration [3]. This glass was of good optical quality. Neither the glass doped with Cerac EuF_2 or the one treated with LiH showed any luminescence due to Eu^{3+} , but the glass produced with Agfa starting material showed Eu^{3+} luminescence peaks near 600 nm.

The Mossbauer spectrum of a fluorozirconate glass produced using 5% EuF_3 and 5% LiH was similar to that reported earlier for a fluoride glass with the composition $61\text{ZrF}_4\text{-}2\text{EuF}_2\text{-}12\text{BaF}_2\text{-}7\text{ThF}_4$ [11]. The isomer shifts, line widths (FWHM), and relative areas of the single absorption lines observed for each valence in the present case were -14.2(2) mm/s, 10.6(4) mm/s and 87(7)% for Eu^{2+} and -0.3(2) mm/s, 3.0(4) mm/s and 13(2) % for Eu^{3+} . The linewidth for Eu^{2+} is anomalously large [10].

4) DISCUSSION

We have not observed Eu^{2+} luminescence in any of our fluorozirconate samples, despite proving quite conclusively that they contain significant quantities of Eu^{2+} ions. This is surprising, given that the heavy-metal fluorozirconates with their low phonon energies generally result in very efficient fluorescence from trivalent rare earth ions, and in the present case luminescence from Eu^{3+} ions is observed in all of the glasses (provided only that a significant fraction of Eu^{3+} remains in the reduced glass). Furthermore, the same Eu^{3+} to Eu^{2+} reduction processes lead to very efficient luminescence in the closely related fluoroaluminates. Efficient Eu^{2+} emission is also observed in many crystalline fluorides such as CaF_2 . The fluorozirconates therefore appear to be a special case. A small crystal field splitting of the $4f^65d$ lowest term might leave the lowest level of this configuration above the first excited state $^6P_{7/2}$ of the $4f^7$ configuration, but no luminescence corresponding to the latter transition, which is clearly visible in the fluoroaluminates (Figure 2), is apparent either.

We suggest that the absence of luminescence is associated with de-excitation involving nearby zirconium ions. The optical absorption spectrum between 200 and 400 nm, described elsewhere [11], is complicated by the superposition of absorptions due to Eu^{2+} , and some reduced zirconium species which may be Zr^{3+} or Zr^{2+} . We see no evidence for Zr^{3+} in any of our EPR spectra; Zr^{2+} is an even electron system and is EPR inactive. It is possible that the Eu^{2+} ions are being de-excited by energy transfer to a reduced zirconium site, which itself loses energy through radiationless transitions. However, this effect should be dependent on the concentration of the reduced zirconium, and it might be expected that in the large number of glasses investigated that there would be at least some which had a sufficiently low concentration of reduced zirconium that luminescence would be observed. Thus it appears that the $4f^65d$ excited state for europium in fluorozirconate glass is substantially different from that in other fluorides in some way which is specifically related to zirconium. It is possible that the multiple valence states associated with zirconium lead to hybridisation, with an excited state corresponding to an admixture of $\text{Eu}^{2+} - \text{Zr}^{4+}$ and $\text{Eu}^{3+} - \text{Zr}^{3+}$ configurations.

5) CONCLUSIONS

Reduction of Eu^{3+} to Eu^{2+} in fluorozirconate glass can be achieved by addition of LiH, NaH, LiBH_4 or $\text{ZrH}_{1.9}$ to the starting materials, by use of a hydrogen containing atmosphere, or less effectively by electrochemical reduction. The former processes, at least in the case of LiH, have the advantage that the degree of reduction can be predicted, but electrochemical reduction and treatment in a hydrogen atmosphere result in glasses of better optical quality. The LiH process applied to fluoroaluminate glasses produces material of good quality with strong Eu^{2+} luminescence. No Eu^{2+} luminescence could be observed from any of the large number of fluorozirconate glasses produced, most of which demonstrably contained a significant Eu^{2+} content. We conclude that the absence of Eu^{2+} luminescence is an intrinsic feature of this material, and precludes the use of this material in X-ray phosphor applications. However, since Eu^{2+} is known to contribute a strong Faraday rotation effect, further work will characterize the magnitude of this effect in these glasses.

6) REFERENCES

- [1] K. Hirao, J. Non-Cryst. Solids 196, (1996) 16
- [2] J. Qiu, K Tanaka, and K Hirao, J. Amer. Ceramic Soc. 80 (1997) 2696.
- [3] J. Qiu, Y. Shimizugawa, Y. Iwabuchi and K. Hirao, Appl. Phys Lett. 71 (1997) 759.
- [4] S. Schweizer, P. Willens, P J R Leblans, L. Struye and J M Spaeth, J. Appl. Phys 79 (1996) 4157.
- [5] D. Furniss, E.A. Harris, D.B. Hollis, J. Phys. Chem (Solid State Phys.) 20 (1985) L147.
- [6] C M Brodbeck and L E Iton, J. Chem. Phys 83 (1985) 4285.
- [7] D.R. MacFarlane, J. Javorniczky and P.J. Newman, These Proceedings.
- [8] A. Edgar and J.W. Quilty, Amer. J. of Phys. 61 (1993) 944.
- [9] S. Aasland, T. Grande, and S. Julsrund, J. Non-Cryst. Solids 184 (1995) 297.
- [10] J. M. D. Coey, A. McEvoy, and M. W. Shafer, J. Non-Cryst. Solids 43 (1981) 387.
- [11] P. J. Newman, D. R. MacFarlane, and A. Edgar, to be published.

Table 1: Preparation procedures and Eu^{2+} assay results for ZBLYAN:Eu glasses. Glassy carbon crucibles are denoted by gc.

<u>Crucible</u>	<u>Atmosphere</u>	<u>Additives or Process</u>	<u>$\text{Eu}^{2+}/\text{Gd}^{3+}$ EPR Signal Ratio</u>	<u>Estimated Eu^{2+} Concentration (mol%)</u>	<u>Luminescence (350 nm excitation)</u>
graphite	Ar	-	0.23	0.29	orange
graphite	Ar	0.25% InF_3	0.04	0.05	orange
gc	Ar	e/chemical	0.22	0.28	orange
gc	Ar, 5% H_2	-	0.52	0.66	orange
gc	Ar, 5% H_2	-	0.81	1.03	nil
gc	Ar, 5% H_2	-	0.74	0.94	nil
gc	Ar	1% LiH	0.74	0.94	nil
gc	Ar	1% NaH	0.66	0.84	weak orange
gc	Ar	0.25% LiBH_4	0.78	0.99	nil
gc	Ar	0.5% ZrH_2	0.86	1.09	nil
gc	Ar	1% EuF_2 (Agfa)	0.05	0.06	orange
gc	Ar	1% EuF_2 (Cerac)	0.67	0.85	nil

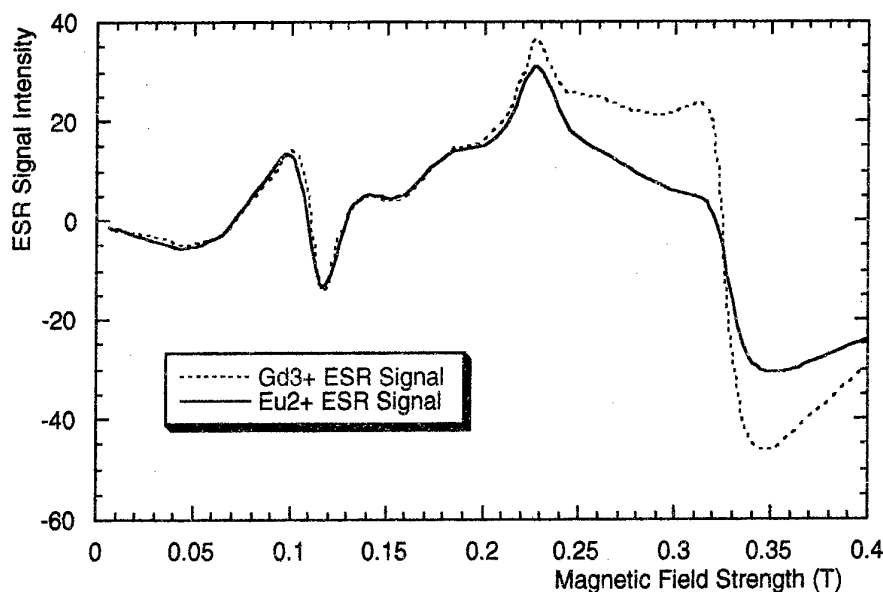


Figure 1. Room temperature EPR spectra at 9.1 GHz for ZBLYAN glasses containing 1% Gd^{3+} (dashed line) and 0.91% Eu^{2+} (solid line).

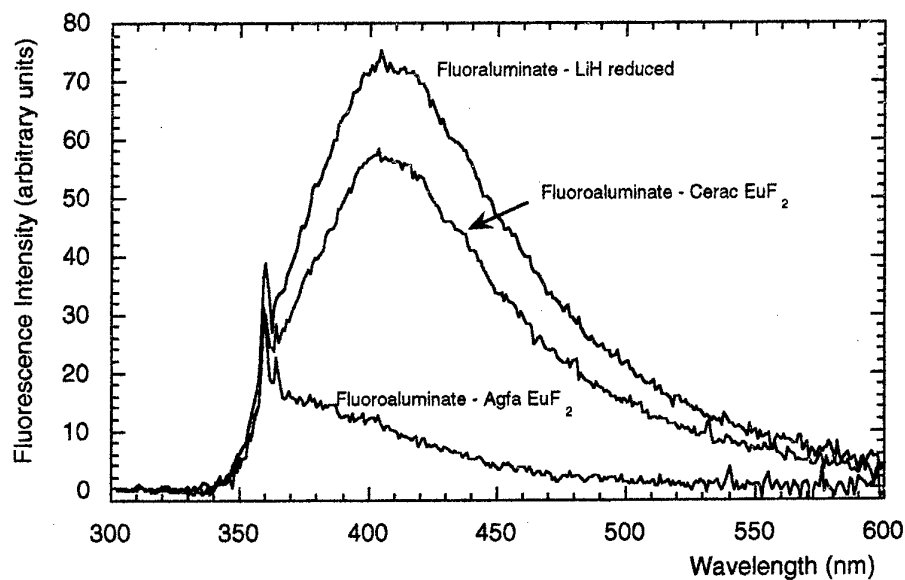


Figure 2: Luminescence spectra for three samples of fluoroaluminate glass containing 1 mol% europium. The weak sharp line at 363 nm is due to a residual emission from the nominally 254 nm mercury lamp used for excitation, whilst the stronger sharp line at 360 nm is the $^6\text{P}_{7/2}$ to $^8\text{S}_{7/2}$ transition of Eu^{2+} .

MEASUREMENTS, PROCEDURES AND RESULTS FROM INVESTIGATIONS INTO HEAVY METAL FLUORIDE GLASSES FOR ELECTROMAGNETIC CALORIMETRY IN PARTICLE PHYSICS

K.W. Bell¹, R.M. Brown¹, D.J.A. Cockerill, P.S. Flower¹, P.R. Hobson²,
B.W. Kennedy¹, K.J. McKinlay³, A.L. Lintern¹, J.M. Parker³, M. Sproston¹

1. Rutherford Appleton Laboratory,
Chilton, Didcot, OXON OX11 0QX, UK. e mail: p.s.flower@rl.ac.uk
2. Institute for Physical & Environmental Sciences, Brunel University,
Uxbridge, UB3 4PH, UK
3. Department of Engineering Materials, University of Sheffield,
Sheffield, UK

ABSTRACT

Studies carried out into the production of large blocks of scintillating fluoride glass for use as a material for electromagnetic calorimetry in high energy particle physics experiments have found variations of light yield between samples. By studying the light yield from excited samples as a function of time, and comparing this with the samples' optical transmission, the relative contributions of quenching and absorption to yield can be separated. Data will be presented showing the influence of temperature, cerium concentration, indium concentration and different chemical feedstocks on light yield and decay time.

INTRODUCTION

An extensive program of research has been undertaken into the development of heavy fluoride glasses as a calorimetric material in high energy physics. The glasses used were developed and produced at Sheffield University. The glass mixture was based on a standard ZBLAN mix but the zirconium fluoride was replaced by hafnium fluoride to increase density, and lanthanum fluoride was replaced by cerium fluoride to give a scintillation emission. Results on the glass mixtures used, the glass manufacturing techniques, and the yields achieved, have been presented in previous papers[1,2,3]. Recent work has concentrated on the production of large blocks of glass (620g). This has necessitated the use of different batches of HfF_4 and significant variations in scintillation properties were found between different blocks.

The techniques used to measure the scintillation yields of these samples gave very accurate information on light yield as a function of time and it was found that variations in yield could be independently attributed to absorption or quenching by studying variations in transmission and pulse shape. The technique was also sufficiently sensitive to identify variations in quenching as a function of temperature and to detect low levels of scintillation emission.

METHOD

The glasses were manufactured as described in a previous paper [2], but particular care was taken over the annealing procedure to minimise the levels of stress present in the sample in order to facilitate subsequent cutting of the specimens.

The principal tests on yield and decay time were made at the CLRC Rutherford Appleton Laboratory using a 770MeV/c proton beam. These particles were of sufficient energy to give a uniform and prompt excitation of the test samples, which scaled linearly with thickness. Small test samples (20mm x 6.3mm x 10mm) were placed in the proton beam in a thin walled sample holder and coupled by an air light guide to a UV sensitive 50mm phototube (EMI9814QB). Sensors upstream and downstream of the sample provided a precise timing signal $\pm 1\text{ns}$ (the proton takes less than 0.1ns to traverse the sample). The signal from the phototube was fed to a LeCroy 7200 digital oscilloscope and the charge digitised in 1ns time bins over a 500ns time gate.

These data were summed for 5000 events and analysed off-line to determine yield and time structure. Data were also taken with a pure CeF_3 crystal of similar thickness (5mm) and yields were expressed as a percentage of CeF_3 yield, as this has been widely reported in literature. For data at different temperatures, the sample holder was mounted on a Peltier cooled support structure.

The large blocks were measured in two ways. First off cuts 20mm x 6.3mm x 10mm were taken to provide direct comparison with the small sample data. Then the remaining sections of the blocks (now 30mm x 21mm x 138mm) were measured by scanning them longitudinally with a 10mm diameter proton beam of 405MeV/c. This beam was stopped by the glass enabling an estimate to be made of the uniformity of response of the glass as a function of position.

For these measurements a 19mm Hamamatsu R1166 phototube was used and the beam trigger was modified to allow for the fact that protons stopped in the sample. Data acquisition was by a computer controlled system which digitised charge in 0.25pC bins over a 300ns time gate.

In order to highlight trends in changes in pulse shape, different analytical techniques were used. The data were fitted using a cascade function analogous to that used in calculating radioactive decays. This however proved difficult to fit as the initial rise time was dominated by the response of the photodetector circuit.

In order to avoid biasing the interpretation by assuming a decay mechanism, the peak was normalised to 100% and the area under the decay curve was estimated for a specific time gate. This was found to give a good indication of trends and was sensitive to small changes.

Comparing the full width half maximum of the decay curves was sufficient to indicate trends

RESULTS

Temperature

Measurements of changes in yield with temperature showed, as reported in a previous paper [1], a steady fall in yield of -0.36% per $^{\circ}\text{C}$ with temperature for an HBCeA glass. There was also a decrease in the pulse width as the temperature increased. Fig. 1 shows the variation of pulse width against temperature expressed in terms of the normalised, integrated yield over 130ns.

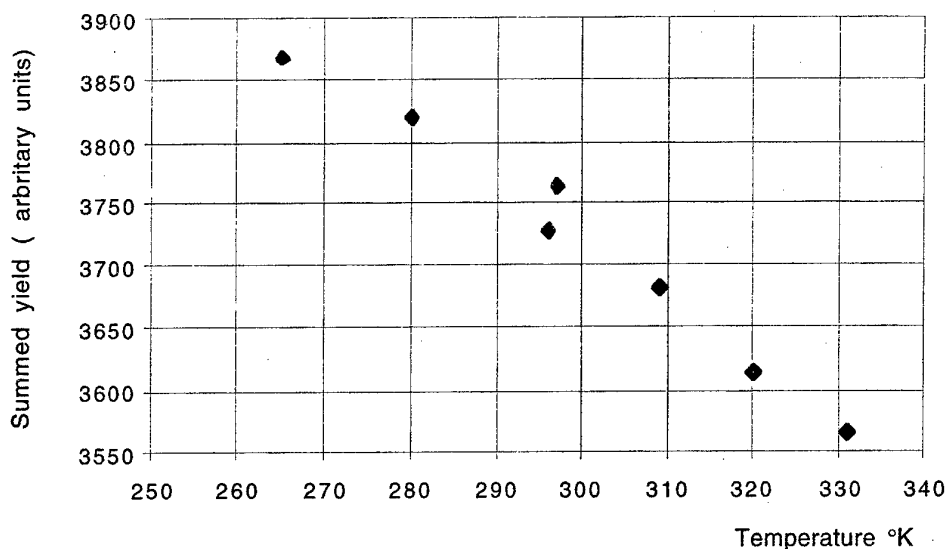


Fig.1 Integrated light yield within a 130ns time interval, as a function of temperature.

Indium addition

There was a very strong fall in yield with increasing InF_3 concentration, but measurements of the UV transmission at the CeF_3 edge showed no significant change in transmission. In addition, there was a very strong reduction in pulse width with even small additions of indium fluoride. Fig. 2 shows the change in pulse width as a function of indium fluoride concentration expressed in terms of integrated yield over 130ns.

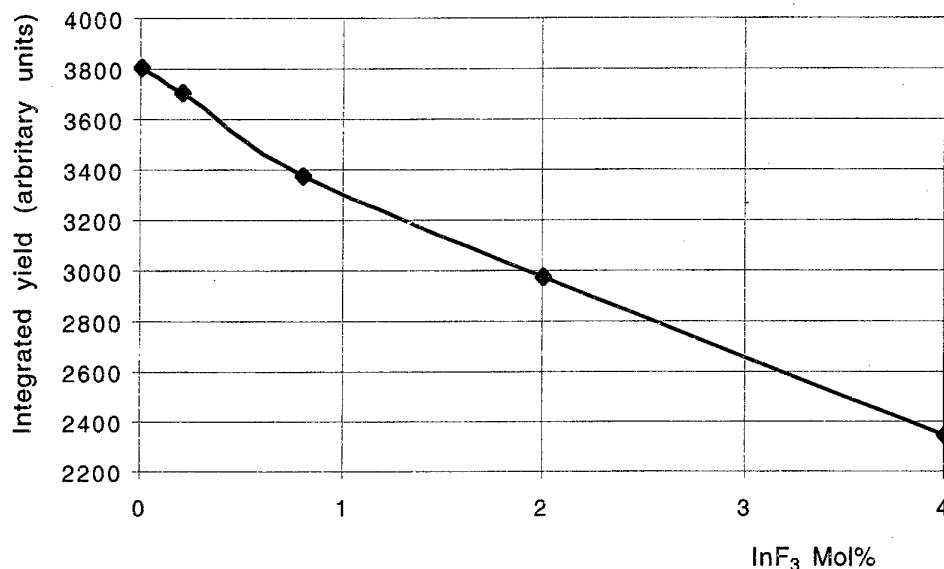


Fig.2 Integrated light yield within a 130ns time interval, as a function of indium concentration

Cerium addition

The addition of cerium increased yield. The effect saturated at higher concentrations. Fig.3 shows that the pulse also becomes narrower.

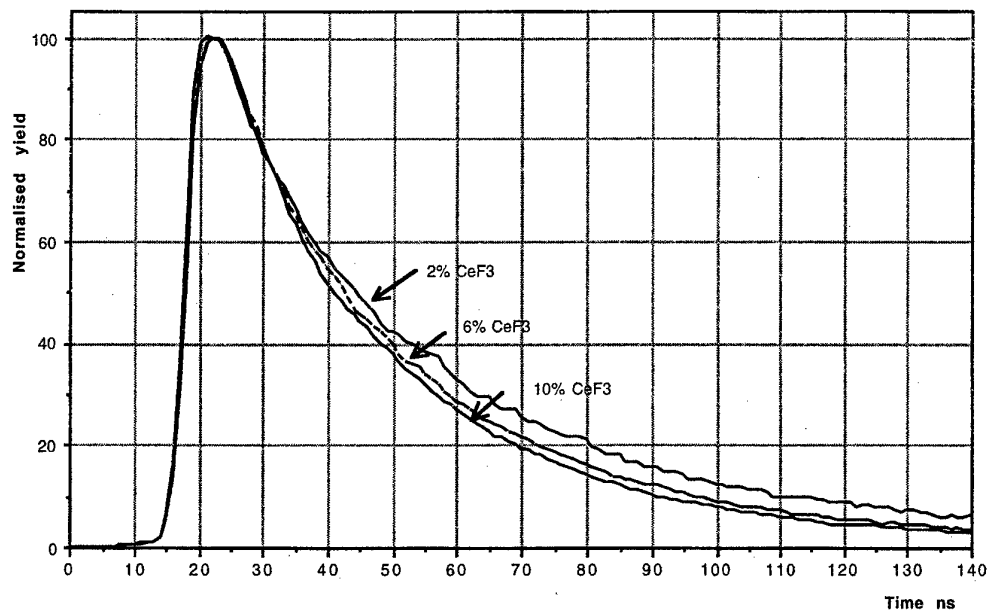


Fig.3 The effect of increasing cerium concentration on decay time

Zirconium addition

The substitution of HfF_4 with ZrF_4 caused a gradual fall-off in yield with 100% substitution giving no significant signal. Fig.4 compares the pulse shapes for different ZrF_4 concentrations.

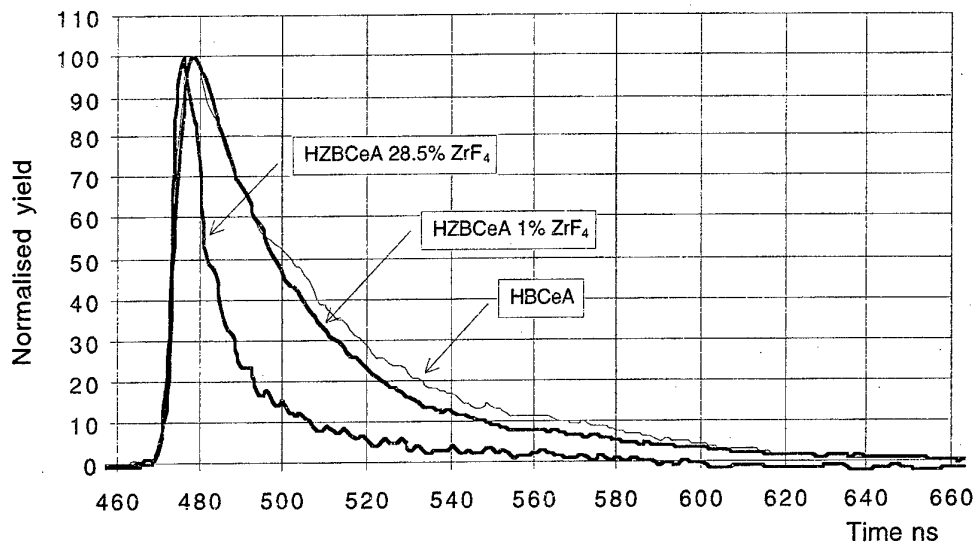


Fig.4 The effect of zirconium on decay time

Large blocks

Measurements on large blocks prepared under similar conditions showed a very wide range of behaviour with most of the large blocks giving a poor yield (Fig. 5).

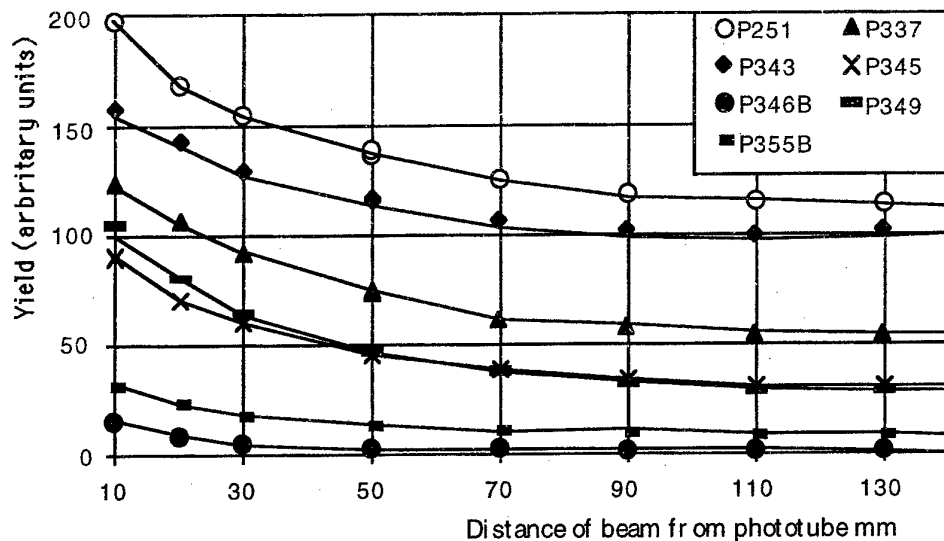


Fig.5 Yield as a function of excitation position

Measurements of relative decay times (Fig.6) showed small variations with only P346 showing signs of significant quenching.

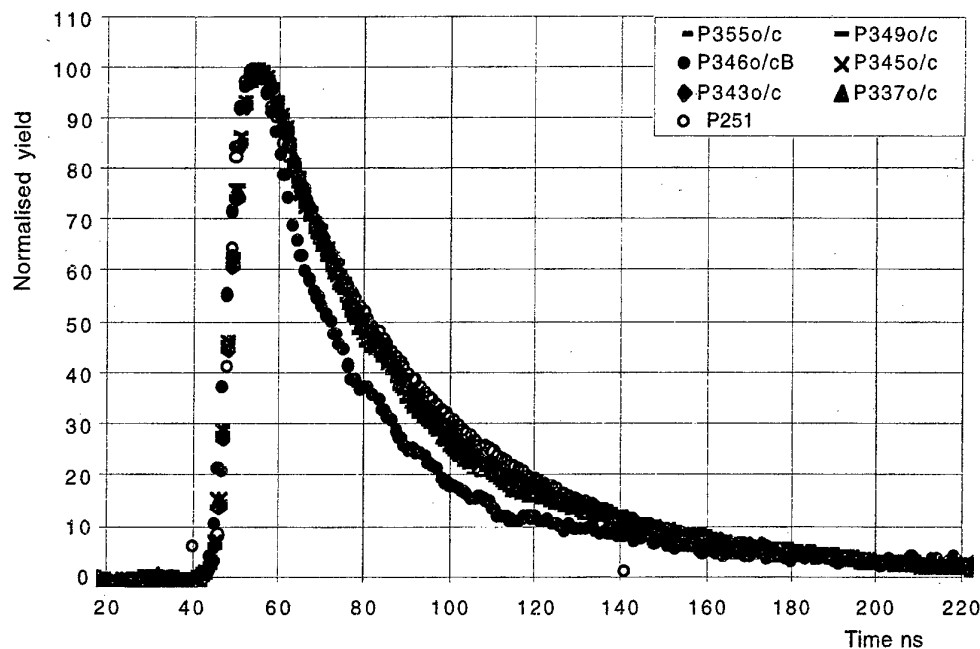


Fig.6 The decay times for various large glass blocks

There were however significant variations in transmission (Fig.7). P346B, the block that exhibited most quenching showed the poorest transmission, but P355B which also showed poor transmission did not show significant quenching.

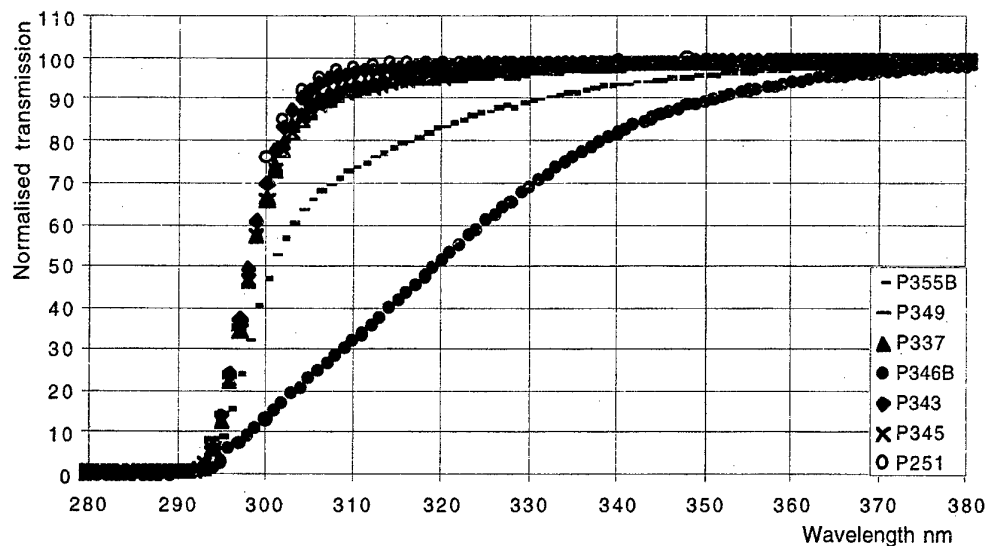


Fig.7 Internal transmission of large block offcuts (6.3mm) normalised to 100% at 500nm.

DISCUSSION

The use of a particle beam to excite a scintillating glass gives information on scintillation yield and the time structure of the yield. The manner in which the pulse width and yield fall with temperature (Fig.1) indicate that more of the shallower traps holding excited

electrons are emptying non radiatively at higher temperature, truncating the emission curve.

A similar but much more pronounced quenching process (Fig.2) occurs when InF_3 is added. Measurement of the transmission of InF_3 doped glass samples showed no significant increase in absorption near the UV edge suggesting that all attenuation in the yield must be due to a quenching rather than an absorptive effect.

Devitsin et al [4] first reported the reduction in the rate of rise in yield at higher CeF_3 additions. We have been able to confirm this result [1]. We also find that pure CeF_3 has a yield of about 10 times the yield of 5% CeF_3 in an HBCeAN glass. We have observed, that saturation in light yield is associated with a reduction in pulse width (Fig.3). This could be attributed to clustering, causing an increase in the non radiative decay modes.

The onset of quenching with the substitution of ZrF_4 for HfF_4 (Fig.4) is surprisingly slow given that there is no significant scintillation yield with pure ZrF_4 . This result is very significant from the point of view of calorimetry since the performance is insensitive to ZrF_4 impurity.

The production of large blocks has proved difficult. The tests carried out in the beam line indicate that most of the blocks so far produced do not give a sufficiently uniform response to be used in a calorimeter experiment (Fig.5). Measurements on small samples (Fig.6) and the characteristic attenuation of the signal with position suggest that quenching is not the primary cause of signal loss and the problems are associated with poor UV transmission (Fig.7).

Detailed measurements of one block showed strong absorption bands of chromium and nickel. It was later found that the HfF_4 used had, at one stage in its production, been processed in a stainless steel vessel. The cause of the problem in other samples has not yet been identified

CONCLUSIONS

The best blocks of glass produced indicate that adequate quality is achievable given suitable raw materials and optimal processing. However, in order for a large calorimeter (tonnes of glass) to be constructed at an affordable cost, low cost raw material must be used. The successful production of a few blocks demonstrates that this is indeed possible. However the variability of the results shows that further work is required to make this a realistic process.

ACKNOWLEDGEMENTS

We would like to thank E.G. Devitsin, V.A. Kozlov, V.N. Makhov and S.U. Potashov from the Lebedev Institute and L.N. Dimitruk from the General Physics Institute and V. Fedorov of the All-Russian Institute of Chemical Technology in Moscow for many helpful discussions and for supplying some the HfF_4 used in these tests.

We thank the Particle Physics and Astronomy Research Council for their support of this work.

REFERENCES

- [1] P.R. Hobson et al., Dense, Fast, Radiation-tolerant Fluorohafnate Glass Scintillators for Electromagnetic Calorimeters in High Energy Physics. Proc of the Int Conf on Inorganic Scintillators and Their Applications, SCINT 95, Ed by P. Dorenbos and C.W.E. van Eijk (Delft University Press, 1996) 317.
- [2] P.R. Hobson et al., The industrial production of large, inexpensive blocks of scintillating fluoro-hafnate glass. Proc of the Int Conf on Inorganic Scintillators and Their Applications, SCINT 95, Ed by P. Dorenbos and C.W.E. van Eijk (Delft University Press, 1996) 505
- [3] P.R. Hobson et al., The development of dense scintillating hafnium fluoride glasses for the construction of homogeneous calorimeters in particle physics. Journal of Non-Crystalline Solids 213&214 (1997) 147-15
- [4] E.G. Devitsin et al., Heavy Scintillators for Scientific and Industrial Applications Edited by F. de Notaristefani et al. (Editions Frontiere, Gif-sur-Yvette, 1993) 401.

INCORPORATION OF LANTHANUM OXYBROMIDE IN FLUOROPHOSPHATE GLASSES

J. B. Denis, M. Poulain

Laboratoire Matériaux Photoniques, Université de Rennes1, F-35042 Rennes

ABSTRACT

New fluorophosphate glasses containing LaOBr were synthesized. LaOBr was prepared at 450°C by the chemical reaction of the bromine gas on the La₂O₃ powder. The vitreous areas in the NaPO₃-LiF-LaOBr and NaPO₃-BaF₂-LaOBr ternary systems are reported. Glass samples were characterized by DSC. The incorporation of lanthanum oxybromide was found to increase the glass stability against devitrification. Two series of glasses were prepared with the composition (55-x/2)NaPO₃ (45-x/2)BaF₂ xLaOBr and 49NaPO₃ 39BaF₂ (xLaOBr+yLa₂O₃) in order to assess the influence of lanthanum and bromide on refractive index and density. The IR transmission is reported and discussed.

KEYWORDS: Fluorophosphate glasses, lanthanum oxybromide, refractive index, density

INTRODUCTION

Non linear optical materials are extensively used in laser systems and integrated optics. While crystalline materials make the basis of most practical devices, glasses offer attractive possibilities. Because they can be manufactured in large volumes, under a variety of shapes and at low cost, their global figure of merit is high [1].

Non linear properties are usually correlated to refractive index, molar refractivity and density [2,3]. These basic properties depend directly on chemical composition, and especially the concentration in large and heavy ions. This paper reports attempts to incorporate lanthanum oxybromide in fluorophosphate glasses in order to assess its influence on physical properties.

EXPERIMENTAL

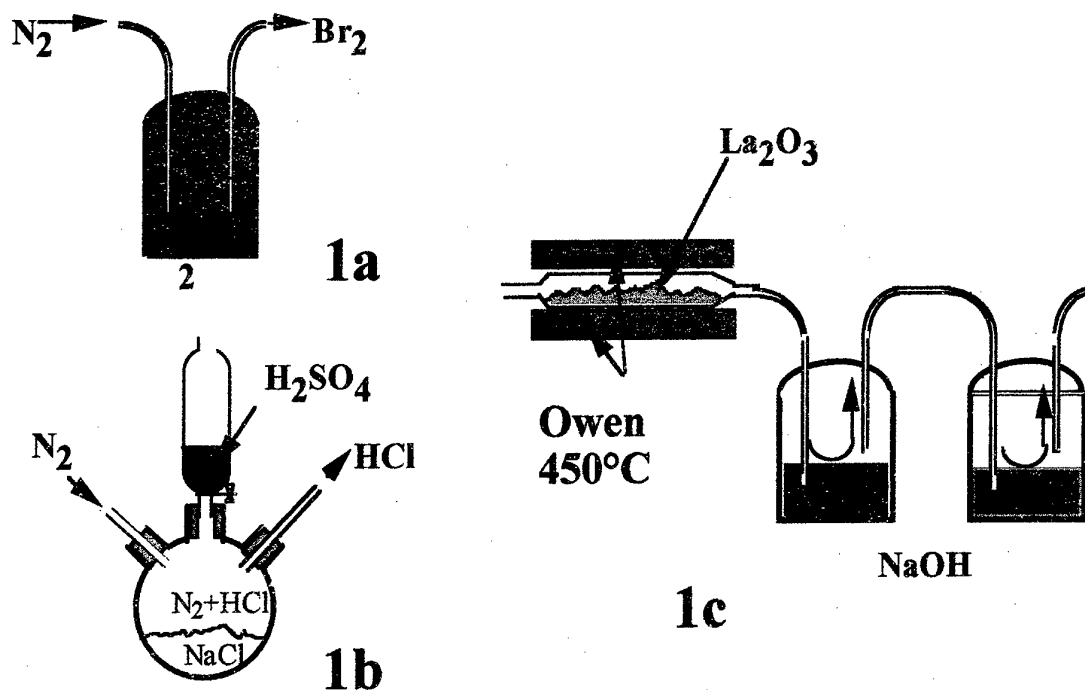
Starting materials are sodium polyphosphate (NaPO₃)_n from Strem, LiF and BaF₂ from Merck and La₂O₃ 4N from Rhone Poulenc .

Lanthanum oxybromide is synthesized by flowing gaseous Br₂ over La₂O₃ at 450 °C for 3 hours. Experimental set-up is described at figure 1. Prior to treatment, lanthanum oxide was fired at 700 °C to remove water and carbon dioxide.

Lanthanum oxychloride LaOCl was prepared by reaction between La₂O₃ and gaseous HCl at 450 °C, while solid state reaction between La₂O₃ and LaF₃ was used for LaOF (15 hours at 950 °C, platinum crucible and dry atmosphere)

X-Ray diffraction and gravimetric control were used to assess material purity. The DTA/TG analysis shows that LaOBr does not melt below 1000 °C, but some weight loss occurs above 900 °C. This may arise from the formation of volatile LaBr₃. There may be also the chemical action of the water and oxygen traces in the cell atmosphere.

Glass samples, usually 3 grams in weight are prepared in the following way: calculated amounts of starting materials are mixed and heated up to melting at 600 °C in a long platinum tube. Melt is maintained at this temperature for fining during a short time - 3 to 5 minutes - to minimize halogen loss. Then melt is poured onto a brass mold heated around 250 °C. After solidification samples are annealed for 1 hour at 250 °C or 10 °C below T_g when T_g is known.



Figures 1- Set-up for the bromination or the chlorination of La₂O₃ including source of Br₂ (1a), HCl (1b) and reaction enclosure (1c)

Glasses are colorless, even at high LaOBr content. They are free of crystals and bubbles. They are stable at room atmosphere, but should be polished with ethanol rather than water because they have limited chemical durability in aqueous solutions.

Characteristic temperatures, T_g, T_x and T_p, are the glass transition temperature, the onset and peak temperatures of the crystallization. They were measured using SEIKO DSC 220. The experimental uncertainties are < ±1°C. Glass forming ability was estimated from the value of the thermal stability range $\Delta T = T_g - T_x$. The glass density was obtained by Archimedean method with an uncertainty 0.02 using CCl₄ as the immersion liquid.

RESULTS

A first set of preparations has been implemented in the NaPO₃-LiF-LaOBr ternary system. Vitreous area is drawn in figure 2. Only a limited amount of LaOBr could be introduced in

glass composition and devitrification occurred when LaOBr content was in excess of 3.5 mol %. Vitreous binary range NaPO_3 -LaOBr is very narrow and a third component seems necessary to ease LaOBr incorporation.

After several attempts we concentrated on the NaPO_3 - BaF_2 -LaOBr system. Barium fluoride is the most common modifier in fluoride glasses and previous works implemented in our group showed that stable barium and sodium fluorophosphate glasses could be obtained [4]. The corresponding vitreous area is reported in figure 3. Maximum lanthanum concentration is observed between 45 and 55 mol % NaPO_3 . It may reach 15 % as in the 48NaPO_3 - 37BaF_2 - 15LaOBr glass.

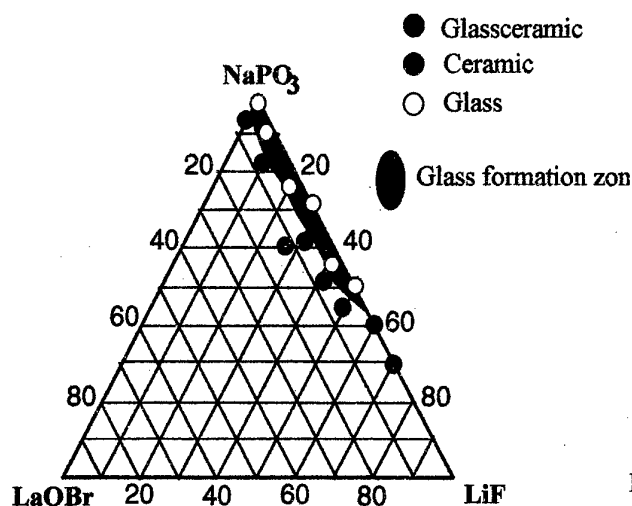


Figure 2 - Glass formation range (mol%) in the NaPO_3 -LaOBr-LiF system

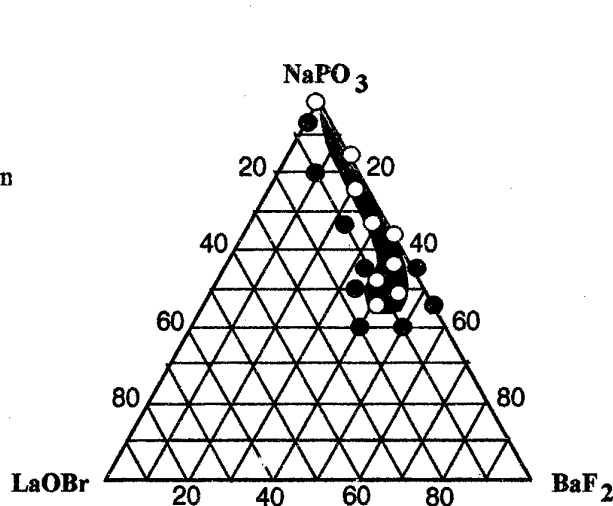


Figure 3 - Glass formation range (mol%) in the NaPO_3 - BaF_2 -LaOBr system

CHARACTERISTIC TEMPERATURES

A Set of samples was synthesized with the general composition:
 $(55 - x) \text{NaPO}_3$, $(45 - x) \text{BaF}_2$, $2x \text{LaOBr}$ with $x = 1, 2, 3, 4, 5$

Characteristic temperatures are reported in table 1 and figure 4 for visualization. Thermal stability range T_x - T_g increases versus LaOBr concentration. It is expected to drop beyond 12 % LaOBr as crystallized samples are obtained at high LaOBr content. Melting starts near 500 °C for most of these glasses.

Table 1. Characteristic temperatures and thermal stability range of $(55 - x) \text{NaPO}_3$, $(45 - x) \text{BaF}_2$, $2x \text{LaOBr}$ glasses.

x	$T_g(^{\circ}\text{C})$	$T_x(^{\circ}\text{C})$	$T_p(^{\circ}\text{C})$	$T_f(^{\circ}\text{C})$	$T_x - T_g(^{\circ}\text{C})$
0	268	396	411	523	128
1	243	327	334	554	84
2	246	350	355	502	104
3	264	385	393	503	121
4	266	387	394	498	121
5	278	404	409	493	126

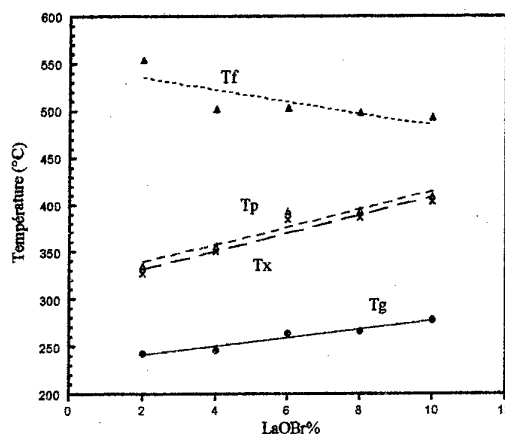


Figure 4 - Characteristic temperatures as a function of LaOBr content. Lines are drawn as guides for the eye

REFRACTIVE INDEX

Lanthanum oxybromide is expected to increase refractive index. Two groups of samples were used for this study, one with an increasing concentration in LaOBr and the second one with a variable bromine content and a constant cationic composition:

- 1) $(55-x/2) \text{ NaPO}_3 - (45-x/2) \text{ BaF}_2 - x \text{ LaOBr}$ ($4 \leq x \leq 12$)
- 2) $49 \text{ NaPO}_3 - 39 \text{ BaF}_2 - x \text{ LaOBr} - (6-x/2) \text{ La}_2\text{O}_3$ ($0 \leq x \leq 12$)

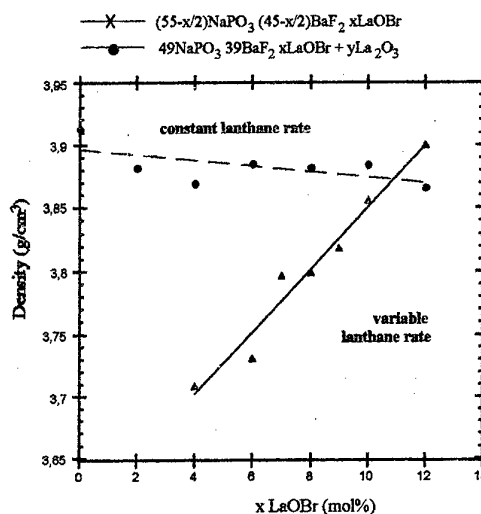
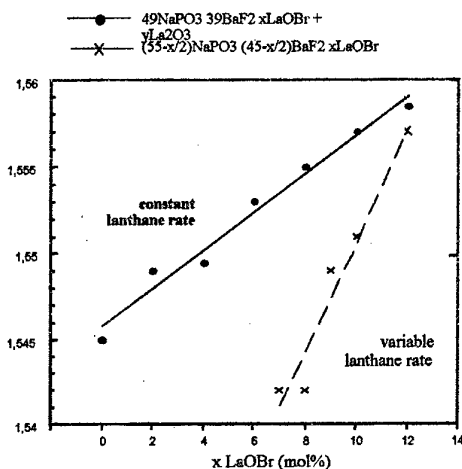


Figure 5. Refractive index versus LaOBr content Figure 6. Density versus LaOBr content
Lines are drawn as guides for the eye

The evolution of refractive index with respect to composition is plotted in figure 5. As expected n_D increases with composition index x . The slope of the straight line is $2.6 \cdot 10^{-3} \text{ mol}^{-1}$ for LaOBr and $1.3 \cdot 10^{-3} \text{ mol}^{-1}$ for Br alone, i.e. when La content is constant. This shows that Br and La have the same influence on refractive index.

DENSITY

The same samples were used for density measurements. Results are exemplified by figure 6. Density increases with LaOBr concentration. However it is nearly constant when only bromine concentration is changed. As it will be discussed below, bromine incorporation has two opposite influences on density.

INFLUENCE OF HALOGEN NATURE

For assessing the influence of the halogen on the physical properties, we have synthesized three glasses with the same nominal composition:



Characteristic temperatures and densities are given in table 2. As one could expect, glass transition temperature is higher for lighter halogens, but density is smaller. The chlorine-containing glass has a larger thermal stability range and appears more stable against devitrification.

Table 2. Characteristic temperatures and density of lanthanum oxyhalide glasses

LaOX	T _g (°C)	T _x (°C)	T _p (°C)	T _f (°C)	T _x -T _g (°C)	Density
LaOBr	266	387	394	498	121	3,76
LaOCl	270	399	410	500	129	3,84
LaOF	272	388	392	548	110	3,87

INFRARED TRANSMISSION

Figure 7 shows the infrared transmission curve of the 51 NaPO₃ - 41 BaF₂ - 8 LaOBr glass between 400 and 4000 cm⁻¹. A large absorption band centered on 2100 cm⁻¹ limits strongly the optical transmission. It corresponds to the first overtone of the PO₄ ν₃ vibration mode, for which the fundamental mode is located around 1020 cm⁻¹. As in most fluorophosphate glasses, the OH absorption is very small as hydroxyls decompose in fluoride melts to form gaseous HF.

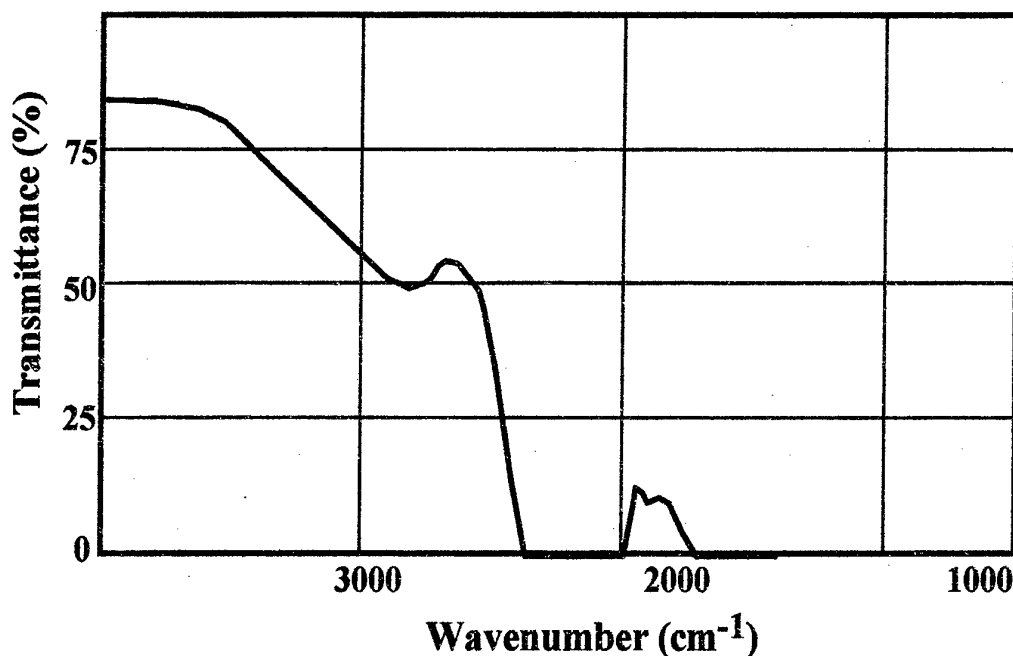


Figure 7 - Infrared transmission of a 51 NaPO₃ - 41 BaF₂ - 8 LaOBr glass sample, 5 mm in thickness

DISCUSSION

Barium fluoride make possible incorporation of lanthanum oxybromide in a sodium metaphosphate glass. While LaOBr is expected to be a modifier, there is not clear reason why barium cations could limit the nucleating effect of the oxyhalide. Vitreous network should consist in PO₄, PO₃F and PO₂F₂ tetrahedra, and it is unlikely that bromine anions are linked to phosphorous.

The influence of bromine on density involves two factors: atomic weight and ionic radius. The large ionic radius of the Br⁻ anion leads to the increase of the molar volume which, in turns, limits the increase of the density which results from the larger molecular weight. This may also explain why the change in refractive index is not larger with bromine than with lanthanum.

Further optical measurements, especially non linear refractive index, will quantify the respective contributions of halogen and lanthanide. Halogen incorporation may be an interesting way to induce optical changes, and this could achieved directly by a chemical reaction in the glass melt.

CONCLUSION

Lanthanum oxybromide could be incorporated in fluorophosphate glasses, using BaF₂ in association with sodium polyphosphate. Stable glasses containing up to 15 mol % LaOBr have been prepared. Density and refractive index increase with oxybromide concentration. It was observed that Br and La have an equal influence on refractive index. But bromine content

does not change much the density. These glasses could be used for further experiments for the measurements of the contribution of LaOBr to the non linear optical properties.

REFERENCES

- [1] S.R. Friberg & P.W. Smith IEEE J. Quantum Electron. QE-23, n°12 (1987) 2089
- [2] R.C.Miller. Appl. Phys. Lett. 5 (1964) 17
- [3] N.L. Boling, A.J. Glass & A. Owyong, IEEE J. Quantum Electron. QE-14, n°8 (1978) 601
- [4] M. Matecki and M. Poulain, J. Non Cryst. Solids 56 (1983) 111

QUANTITATIVE NUCLEAR MAGNETIC RESONANCE (NMR) STUDIES OF THE LOCAL STRUCTURE IN CHALCOGENIDE GLASSES

Hellmut Eckert, Guido Regelsky, Paul Mutolo, Jörn Schmedt
auf der Gönne, Michael Witschas

Institut für Physikalische Chemie, Westfälische Wilhelms-Universität
Münster, Schlossplatz 7, D48149 Münster, Germany, email
eckerth@uni-muenster.de

ABSTRACT

An overview is given on recent nuclear magnetic resonance (NMR) structural studies of phosphorus chalcogenide glasses and melts. The detailed structural speciation of these systems has been derived on the basis of ^{31}P dipolar spin echo decay spectroscopy, magic angle spinning (MAS), and variable temperature liquid state NMR above the glass transition temperature. A specific feature in the phosphorus-selenium system is the competition between homo- and heteropolar bond formation, which can be quantitatively characterized by means of these complementary NMR approaches. The influence of various elemental glass constituents upon these equilibria has been studied in detail in a variety of ternary systems. Finally, MAS in combination with double-quantum (DQ)-NMR provides detailed quantitative information on the network structural features present in a variety of ionically conducting thiophosphate glasses.

INTRODUCTION

Nonoxide chalcogenide glasses, which are based on the sulfides, selenides and tellurides of Main group III-V elements have gained much interest as optical and electronic materials with prospective applications as infrared-transparent optical fibers, reversible conductivity switching devices, photoresists, and solid electrolytes. While during the past three decades the experimental studies have been concerned with the measurement of bulk physical properties, more recent work has concentrated on the atomic scale structural organization of these systems, using modern spectroscopic and computational techniques. In particular, solid state nuclear magnetic

resonance (NMR) methods have proven useful to determine the local environments and the spatial distributions of the various atomic constituents in chalcogenide glasses [1]. In recent years, the research area has benefitted greatly from the influx of new powerful selective averaging, spectral editing, and multi-dimensional correlation techniques, resulting in a significantly advanced understanding of the medium-range order in the glassy state. Using these advanced „third-generation“ experiments, significant progress has been made in the structural understanding of binary phosphorus chalcogenide glass systems [2,3], using the favorable NMR properties of the ^{31}P isotope.

TERNARY GLASSES IN THE SYSTEM PHOSPHORUS-SULFUR-SELENIUM

Previous experiments have shown that the structural characteristics of P-Se and P-S glasses differ from each other fundamentally: while the structure of P-Se glasses can be described as a two-dimensional infinite network with competitive P-P and P-Se bonding, P-S glasses exhibit a pronounced tendency to produce zero-dimensional P_4S_x molecular clusters. This tendency persists even in the ternary P-S-Se system, resulting in pronounced segregation effects, which have been characterized by solid state MAS and high-resolution liquid state NMR [4]. In particular cases, mixed P-S-Se clusters have also been identified.

TERNARY PHOSPHORUS TELLURIDE GLASSES

While binary P-S and P-Se glasses are easily prepared, all attempts to prepare phosphorus-tellurium glasses have been unsuccessful. Indeed, examples of inorganic compounds having phosphorus-tellurium bonds are extremely scarce. In spite of this obvious lack of chemical reactivity phosphorus can be introduced as a third component into the binary glass systems silicon-tellurium and germanium-tellurium [5]. ^{31}P MAS and spin echo decay data reveal that in the P-Si-Te glass system the extent of P-P bonding is approximately that expected from statistical probability and the tendency for Si-P bonding is quite pronounced [6]. In contrast, the phosphorus environment in Ge-P-Te glasses is entirely dominated by phosphorus-phosphorus bonding, producing molecular P_4 upon heating above the glass transition temperature.

THIOPHOSPHATE GLASSES AND CRYSTALS

Recently high resolution double-quantum ^{31}P NMR spectroscopy has been shown to provide a lot of structural information on glassy and crystalline thiophosphates [7]. The homonuclear dipolar interaction is reintroduced under MAS-conditions to excite double quantum coherences. A pulse sequence known under the acronym C7 [8] was found to be particularly useful. The development of the double quantum coherence as a function of the excitation time is determined by the strength of the homonuclear dipolar interaction. As demonstrated on various crystals, thiophosphate anions PS_4^{3-} , $\text{P}_2\text{S}_7^{4-}$ and $\text{P}_2\text{S}_6^{4-}$ can thus be identified by characteristic excitation profiles. This approach is applied to ionically conductive glasses in the system $\text{Li}_2\text{S-P}_2\text{S}_5$. In the case of glassy $\text{Li}_4\text{P}_2\text{S}_7$, DQ-MAS reveals a structural transformation on crystallization to $\text{Li}_4\text{P}_2\text{S}_6$ [9] and offers information on the positionally disordered x-ray structure of the latter.

REFERENCES

- [1] H. Eckert, (invited review), NMR Basic Principles and Progress 33 (1994) 125.
- [2] D. Lathrop, H. Eckert, Phys. Rev. B 43 (1991) 7279.
- [3] C.M. Lyda, J.M. Leone, M.A. Bankert, Y. Xia, H. Eckert, Chem. Mater. 6 (1994) 1934.
- [4] P. Mutolo, H. Eckert, in preparation.
- [5] A.R. Hilton, C.R. Jones, M. Brau, Infrared Phys. 4 (1964) 213.
- [6] M. Witschas, G. Regelsky, H. Eckert, Journal of Non-Crystalline Solids 215 (1997) 226.
- [7] J. Schmedt auf der Gönne, H. Eckert, Chemistry - A European Journal 1998, in press.
- [8] Y.K. Lee, N.D. Kurur, M. Helmle, O.G. Johannessen, N.D. Nielsen, M.H. Levitt, Chem. Phys. Lett. 242 (1995) 304.
- [9] R. Mercier, J.P. Malugani, B. Fahys, J. Douglade, G. Robert, J. Solid State Chem. 43 (1982) 151.

NEUTRON DIFFRACTION STUDIES OF THE STRUCTURE OF Ge-BASED MULTICOMPONENT SULPHIDE GLASSES

A.C. Hannon^a and B.G. Aitken^b

^a ISIS Facility, Rutherford Appleton Laboratory, Chilton, Didcot, Oxon,
OX11 0QX, UK. email a.c.hannon@rl.ac.uk

^b SP-FR-05, Corning Incorporated, Corning, NY 14831, USA.

ABSTRACT

We have used high real-space resolution pulsed neutron diffraction to investigate the structure of fibre-forming Ge-based multicomponent sulphide glasses. Diffraction patterns were measured up to a maximum momentum transfer of 40\AA^{-1} for a series of seven samples from the stoichiometric system $\text{Ge}_{25}(\text{As,Ga})_{10}\text{S}_{65}$, with Ga contents from 0 to 10 atomic percent. The correlation functions all show three principal peaks at 2.23\AA , 2.97\AA and 3.49\AA . The first principal peak in the correlation functions is predominantly due to Ge-S bonds, together with smaller contributions from As-S and Ga-S bonds. The second principal peak is due to cation-cation distances between edge-sharing structural units. The third principal peak is due mostly to S-S distances within structural units. There is also fine structure around the first peak of the correlation functions, consisting of a small 'pre-peak' at about 2.0\AA and a larger and broader shoulder at about 2.5\AA . The pre-peak does not show detectable changes with composition, whilst the shoulder grows steadily as gallium is added to the glass. The position of the pre-peak, 2.0\AA , is consistent with either S_2^{2-} disulphide groups within a structural unit, or with S-S bonds in the network, due to chemical disorder. According to the chemical disorder model, the peak at 2.5\AA is due to Ge-Ge bonds in the network. If gallium is tetrahedrally coordinated then the number of these bonds must increase as gallium replaces arsenic. Such an increase is observed in the experimental data and hence the chemical disorder model is preferred over the disulphide model.

1. INTRODUCTION

Fibre amplifiers are becoming a key component of optical communications systems as the transition is made from electro-optical systems to purely optical systems. The quantum efficiency for the transition used in a fibre amplifier is restricted by multiphonon mediated decay to nearby levels. The probability of multiphonon decay between two energy levels is inversely related to the number of phonons required to bridge the energy gap [1], and an improvement in quantum efficiency would be expected through the use of a host material with lower phonon energies. This has lead to a considerable interest in the past in fibre-forming glass systems based on the relatively heavy glass former Ga_2S_3 . More recent work [2], however, has been drawn towards glasses containing As_2S_3 because these have much better thermal stability and hence have a much improved fibre drawability. Nevertheless gallium is still an essential component for fibre amplifier applications because it is found to be required in a small amount in order to have efficient luminescence. The addition to a GeAs glass of a very small amount of gallium (less than 1 atomic %) causes a rapid decrease in the density and a rapid redshift of the absorption edge [2]. This indicates the occurrence of a major structural rearrangement, the nature of which is as yet unknown. We report the first use of neutron diffraction to investigate the structure of these complex multicomponent fibre amplifier glasses.

2. THEORY

The quantity measured in a neutron diffraction experiment [3,4] is the differential cross-section

$$\frac{d\sigma}{d\Omega} = I^s(Q) + i(Q), \quad (1)$$

where Q is the magnitude of the momentum transfer, $I^s(Q)$ is the self scattering and $i(Q)$ is the distinct scattering. $I^s(Q)$, which can be calculated approximately, is subtracted from the data to give $i(Q)$. Structural information may then be obtained by using a Fourier transform to obtain the total correlation function

$$T(r) = T^0(r) + \frac{2}{\pi} \int_0^\infty Q i(Q) M(Q) \sin(rQ) dQ, \quad (2)$$

where $T^0(r) = 4\pi r g^0 \left(\sum_l c_l \bar{b}_l \right)^2$ is the average density contribution, g^0 is the atomic number density, and $M(Q)$ is a modification function. The correlation function is a weighted sum of partial correlation functions $t_{ll'}(r)$;

$$T(r) = \sum_{ll'} c_l \bar{b}_l \bar{b}_{l'} t_{ll'}(r), \quad (3)$$

where c_l and \bar{b}_l are respectively the atomic fraction and coherent scattering length for element l , and the l, l' summations are each over the elements of the sample.

3. EXPERIMENTAL PROCEDURE

Seven samples of $\text{Ge}_{25}(\text{As}, \text{Ga})_{10}\text{S}_{65}$ were made by melt quenching as described in detail in reference 2. The individual sample compositions are given in Table 1, together with the density values. The sample compositions are stoichiometric and can also be expressed in the form $5(\text{GeS}_2) \cdot (\text{As}_{1-x}\text{Ga}_x)_2\text{S}_3$, as shown in figure 1.

Table 1. Densities of the $\text{Ge}_{25}(\text{As}, \text{Ga})_{10}\text{S}_{65}$ neutron diffraction samples.

Ga content (atomic %)	density (gcm ⁻³)	atomic number density (atoms Å ⁻³)
0	2.885	0.03738
1.4	2.904	0.03768
2.8	2.908	0.03780
4.25	2.9125	0.03792
6	2.908	0.03793
8	2.906	0.03799
10	2.879	0.03772

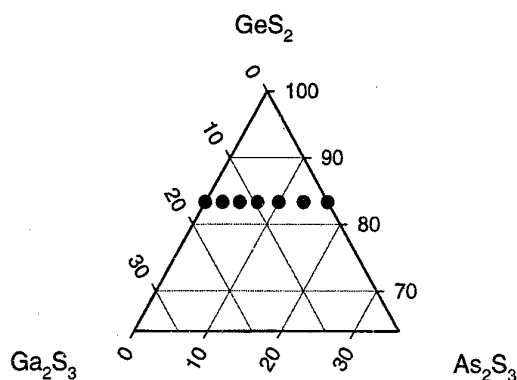


Figure 1. Compositions of the neutron diffraction samples.

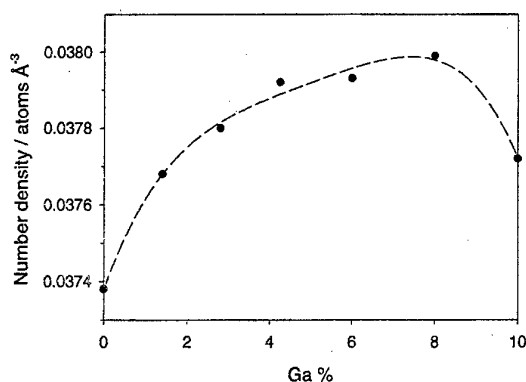


Figure 2. Atomic number densities of the neutron diffraction samples.

The LAD diffractometer [5] at the ISIS pulsed neutron source at the Rutherford Appleton Laboratory was used to make a high real-space resolution neutron diffraction measurement for each of the samples. For the measurements the samples were broken into pieces with maximum dimension $\sim 5\text{mm}$ and were placed in containers made of thin (25 micron) vanadium foil so as to minimise the experimental corrections.

4. RESULTS

Oscillations were discernible in the diffraction data up to a maximum momentum transfer of 40\AA^{-1} . Experimental corrections were made to the data, as described in reference 3. Figure 3a shows the corrected distinct scattering, $i(Q)$, for the $5(\text{GeS}_2) \cdot (\text{As}_2\text{S}_3)$ sample, whilst Figure 3b shows the lower Q region of the data for this sample together with the data for the $5(\text{GeS}_2) \cdot (\text{Ga}_2\text{S}_3)$ sample. The diffraction patterns show small changes, mostly in the region below about 8\AA^{-1} , as gallium replaces arsenic in the glass. For instance the first sharp diffraction peak moves to a lower position, Q , as the Ga content increases. The relatively slight changes seen in the diffraction pattern are consistent with the expectation that both Ga_2S_3 and As_2S_3 easily enter the GeS_2 random network as glass formers with only a slight modification of the short and medium range order.

The data were Fourier transformed according to equation (2) and using the Lorch modification function [6] with a maximum Q of 40.0\AA^{-1} . Figure 4a shows the correlation functions, $T(r)$,

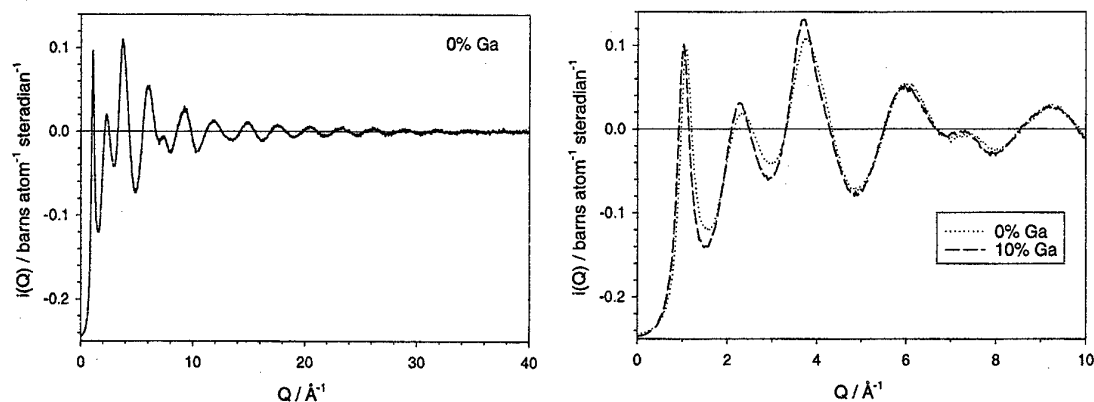


Figure 3. The distinct scattering $i(Q)$ a) for the 0% Ga sample covering the full Q -range, and b) for both the 0% Ga and 10% Ga samples in the region below 10\AA^{-1} .

for the $5(\text{GeS}_2) \cdot (\text{As}_2\text{S}_3)$ and $5(\text{GeS}_2) \cdot (\text{Ga}_2\text{S}_3)$ samples in the region up to 6\AA where the most significant features were observed. The correlation function has three principal peaks at 2.23\AA , 2.97\AA and 3.49\AA . The first and second principal peaks show very little change with composition, whilst the high r side of the third principal peak grows steadily as the Ga content increases.

Figure 4b shows the 'fine structure' observed near the first peak of the correlation function for all seven of the samples studied. A small 'pre-peak' is observed at about 2.0\AA which does not show any definite trend with glass composition. Also a larger and broader shoulder is observed at about 2.5\AA which increases in area as the Ga content of the glass increases.

5. DISCUSSION

5.1 THE PRINCIPAL PEAKS IN THE CORRELATION FUNCTIONS

The first principal peak in the correlation functions at 2.23\AA may be identified as being due to X-S bonds, where X represents any cation, Ge, Ga or As. In crystalline GeS_2 , which has a tetrahedral structure [7], the mean Ge-S bond length is 2.218\AA . In crystalline Ga_2S_3 , in which Ga is tetrahedrally coordinated by S [8], the mean Ga-S bond length is 2.255\AA . In crystalline As_2S_3 , in which As are at the vertex of an AsS_3 trigonal pyramid [9], the mean As-S bond length is 2.283\AA . The three X-S bond lengths in these glasses are thus much too close to be observed as separate peaks in the correlation functions (for the Lorch modification function with a Q_{max} of 40\AA^{-1} the real-space resolution has a full width at half maximum of 0.136\AA).

The second principal peak in the correlation functions at 2.97\AA arises from X-X distances between cations which are not bonded but are in two structural units which are connected by edge-sharing. In the high temperature crystalline form of GeS_2 [10] the Ge-Ge distance between edge-sharing tetrahedra is 2.919\AA . It is not clear whether in the glass this edge-sharing distance can occur for cations other than Ge.

The third principal peak in the correlation functions at about 3.49\AA includes a contribution from S-S distances between two sulphurs which are not bonded to each other, but are members of the same structural unit. For an ideal XS_4 tetrahedron with an X-S distance of 2.23\AA (the position of the first principal peak) the corresponding S-S distance would be 3.64\AA . This is somewhat longer than the observed position of the third principal peak. However, we note firstly that the edge-sharing configuration involves a distortion of the tetrahedra so that the two sulphurs on the shared edge are closer than for the ideal tetrahedral

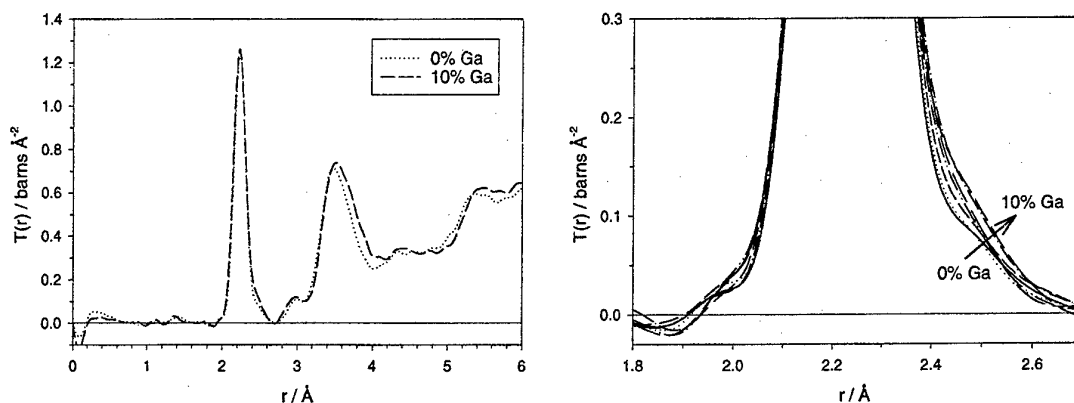


Figure 4. The total correlation function $T(r)$ a) for the 0% Ga and 10% Ga samples, and b) showing the first peak fine structure for all of the samples.

geometry. (If the edge-sharing Ge-Ge distance is 2.97Å then the S-S distance for the shared edge is 3.33Å or less.) Secondly we note that there will also be some additional contribution to the correlation function in this region due to X-X distances between corner-sharing units. This contribution is likely to affect the observed position of the third principal peak.

5.2 THE FINE STRUCTURE IN THE FIRST PEAK OF THE CORRELATION FUNCTIONS

The most intriguing aspect of the correlation functions of these glasses concerns the fine structure observed around the first principal peak, as shown in Figure 4b, which can only be observed with the high real-space resolution of pulsed neutron diffraction. The pre-peak at about 2.0Å can only arise from one possible pairing of atoms in these samples; a distance this short can only be due to a bond between two sulphur atoms. However, there are at least two possible ways in which such a S-S distance could arise. For amorphous MoS₃ we have observed a small peak in the correlation function at 1.99Å which is due to disulphide S₂²⁻ groups within an octahedral MoS₆ structural unit [11]. It may thus be suggested that the pre-peak observed in the present data at about 2.0Å could also be due to disulphide groups within structural units. The other possible explanation for the S-S pre-peak is that, despite their stoichiometric compositions, the glasses we have studied may have a small degree of chemical disorder. According to this model the network includes a small number of S-S bonds between structural units (supersulphide S₂⁻ bridges), and also a balancing number of X-X bonds. In the crystalline forms of sulphur the S-S bonds are typically about 2.05Å long, although there is some variation with bond- and dihedral-angles [12]. Thus there is not a sufficient difference between the expected S-S bond lengths for the two models (disulphide and chemical disorder) to be able to use the observed position of the small S-S pre-peak to discriminate between them. Note that the S-S pre-peak in the correlation function has a very small area compared to the first principal peak for two reasons; firstly sulphur has a small neutron scattering length compared to the other elements in the glasses, and secondly only a minority of the sulphur atoms are involved in this type of bond. Within the accuracy and reliability of our data, it appears that the number of S-S bonds remains constant as the Ga content of the glass changes.

The shoulder at about 2.5Å is an additional observation that must be explained by any structural model. In the disulphide model this shoulder is difficult to explain. It may be proposed that there could be a longer X-S distance from X cations to the sulphurs which are in disulphide groups. However, a S-S distance as short as 2.0Å would lead to severely distorted GeS₄ tetrahedra. (The S-Ge-S bond angle would be about 47° which differs greatly from the ideal tetrahedral value of 109.47°.) Furthermore we have been able to find no evidence in model systems (crystals or molecules) to support the idea of a longer bond from Ge to the S in S₂²⁻ groups.

In the chemical disorder model the 2.5Å shoulder is clearly explained as being due to X-X bonds (probably these are mostly or all Ge-Ge). In crystalline Ge, which has a tetrahedral structure, the Ge-Ge bond length is 2.45Å [13] and this is similar to the position of the shoulder in the correlation functions of the sulphide glasses. Furthermore the chemical disorder model can explain the growth in the shoulder as the Ga content is increased: It is expected that gallium atoms are tetrahedrally coordinated, but Ga₂S₃ itself has insufficient sulphur to satisfy this coordination requirement. Hence for Ga to be tetrahedrally coordinated, the addition of Ga₂S₃ to the glass must be accompanied by either a decrease in the number of S-S bonds or an increase in the number of X-X bonds. However, our results indicate that the number of S-S bonds remains constant and hence the number of X-X bonds must increase as the Ga content of the glass increases. This is what is observed. In fact the addition of one unit

of Ga_2S_3 to the glass requires that the number of X-X bonds increase by one so that one sulphur atom is made available to satisfy the tetrahedral coordination requirement for gallium. Note that the incorporation of As_2S_3 into the glass structure does not require a change in the number of X-X bonds because As is expected to be three-coordinated and As_2S_3 has sufficient sulphur to satisfy this coordination requirement.

An alternative explanation for the S-S pre-peak in the correlation functions would be the presence in the samples of a small amount of some form of elemental sulphur. However, we do not believe that this explanation is correct. We have not observed any Bragg peaks in the data, such as would be observed if a crystalline form of sulphur were present. The formation of amorphous sulphur requires rapid quenching into liquid nitrogen [14] and so its presence is unlikely. Furthermore, such an explanation would then require a further explanation for the X-X shoulder and it is most unlikely that the samples would contain germanium as a second impurity phase.

Finally, we note that a very similar pre-peak and shoulder have recently been observed in a neutron diffraction experiment on pure As_2S_3 glass [15]. This suggests that a small degree of chemical disorder may be a common structural feature of sulphide glasses.

6. CONCLUSIONS

Our results show that there is a small amount of chemical disorder in stoichiometric $\text{Ge}_{25}(\text{As,Ga})_{10}\text{S}_{65}$ glasses. The neutron correlation functions show a small pre-peak at about 2.0\AA and a shoulder at about 2.5\AA . These are due to small numbers of S-S bonds and Ge-Ge bonds in the network.

ACKNOWLEDGEMENTS

Thanks are due to Simon Hibble (University of Reading) and Joohee Lee (Cambridge University) for illuminating discussions.

REFERENCES

- [1] L.A. Riseberg and M.J. Weber, in: Progress in Optics, ed. E Wolf, 14 (1976) 91.
- [2] B.G. Aitken and R.S. Quimby, J. Non-Cryst. Solids 213 & 214 (1997) 281.
- [3] A.C. Hannon, W.S. Howells and A.K. Soper, IOP Conf. Series 107 (1990) 193.
- [4] A.C. Hannon, J.M. Parker and B. Vessal, Trans. Amer. Cryst. Assoc. 27 (1991) 293.
- [5] W.S. Howells, Rutherford Appleton Laboratory Report RAL-80-017 (1980).
- [6] E.A. Lorch, J. Phys. C 2 (1969) 229.
- [7] G. Dittmar and H. Schäfer, Acta Cryst. B 32 (1976) 1188.
- [8] A. Tomas, M.P. Pardo, M. Guittard, M. Guymont and R. Famery, Mat. Res. Bull. 22 (1987) 1549.
- [9] D.J.E. Mullen and W. Nowacki, Z. Kristallogr. 136 (1972) 48.
- [10] G. Dittmar and H. Schäfer, Acta Cryst. B 31 (1975) 2060.
- [11] S.J. Hibble, R.I. Walton, D.M. Pickup and A.C. Hannon, J. Non-Cryst. Solids 232-234 (1998) in press.
- [12] N.N. Greenwood and A. Earnshaw, Chemistry of the Elements (Pergamon, Oxford, 1984) p. 774.
- [13] J.F.C. Baker and M. Hart, Acta Cryst. A 31 (1975) 364.
- [14] R. Winter, W.-C. Pilgrim, P.A. Egelstaff, P. Chieux, S. Anlauf and F. Hensel, Europhys. Lett. 11 (1990) 225.
- [15] J.H. Lee, private communication, 1998.

SMEARED FIRST-ORDER PHASE TRANSITION IN CHALCOGENIDE SEMICONDUCTOR MELTS

Yu.S. Tver'yanovich, O.V. Il'chenko

St.-Petersburg State University, Department of Chemistry, St.-Petersburg, 198904, Russia. email yuratver@yt2461.spb.edu

ABSTRACT

The semiconductor-metal transition in chalcogenide glassforming melts is accompanied by endothermic effect and structural transformation. It should be referred to as a smeared first-order phase transition with the micro-regions of co-operative structural transformations involving several dozens of atoms. Apparently, this mechanism of the semiconductor-metal transition reflects the structure of glass-forming melts and glasses themselves, which are characterised by the existence of structurally self-consistent regions, i.e., by the medium-range order.

INTRODUCTION

Temperature dependencies of physical-chemical properties of chalcogenide glassforming melts at the semiconductor - metal transition (SMT) are rather well investigated [1]. However till now there is no standard microscopic model of this phenomenon. Cohen and Jortner have assumed [2], that at SMT the melt consists of semiconductor and metal microregions, volumetric shares of which (but not the sizes) vary at changing of temperature. Mott believed that melts at SMT are homogeneity microscopically [3]. The question of microscopic nature of SMT gets a special importance in connection with development of idea

of the medium range order in glasses and melts. The idea of the medium range order reflects crisis of the modern theory of liquid state, based in the account of inter-atomic interactions only in limits of the first co-ordination sphere. Not only electrical properties of melts transformed at SMT, but Mott model and Cohen-Jortner model were used for discussion of electrical properties only.

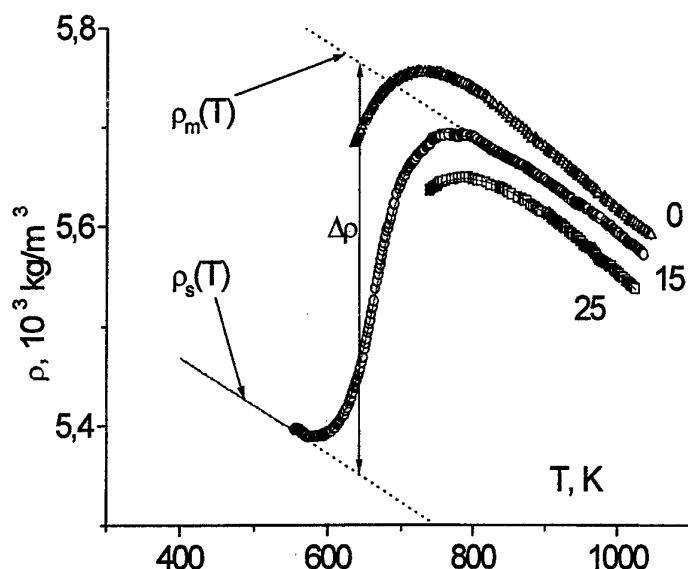


Fig. 1. Examples of temperature dependencies of density of melts $x\text{Ge}-(100-x)\text{Te}$. Points are the experimental datum. Lines are the results of fitting (equation 4). Figures mean the x .

EXPERIMENTAL RESULTS

It was shown in the previous papers, that in the

interval of temperatures of SMT not only respective alterations of

electrical properties of chalcogenide melts occurs, but also significant change of magnetic susceptibility down to change of its sign and increase of density of melts (ρ) occurs also [4]. It was shown on the example As_2Te_3 , that wide endothermic effect is observed also [5].

Dependencies of density of melts in the system Ge - Te (fig. 1) on temperature are investigated with the help of the method of thermometer. The device STA429 (Netzsch) was used for studying the dependencies of heat capacity of these alloys on temperature (fig. 2). The received results are similar with the effects observed earlier for the melt of As_2Te_3 [4,5]. The temperatures of maxima of heat capacity and of minima of factor of thermal expansion coincide with each other and with the temperatures of SMT, which are determined earlier from the data on a magnetic susceptibility and electrical conductivity [4,6]. The half-widths of these effects coincides also for each particular composition of melt. It convincingly testifies, that these effects (C_p and ρ) concern the same phenomenon of SMT. The effects are convertible on temperature.

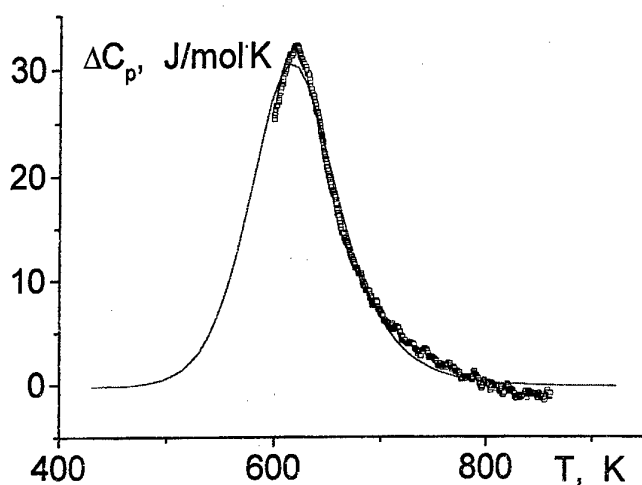


Fig. 2. Temperature dependence of excess heat capacity of Te melt. Points are the experimental datum. Lines are the results of fitting (equation 3).

MODEL

Thus, convertible on temperature SMT in the melts is accompanied with the endothermic effect, with the change of nature of chemical bonds and with the chemical structure. The latter is expressed not only in increase of density on a few percents, but also in increase of average coordination number of atoms [7]. Told testifies that this effect should be attributed to the phase transitions. At the same time it cannot be

considered as classical phase transition, occurring under isothermal conditions. It is necessary to attribute the SMT to so-called smeared phase transitions, distinctive feature of which is coexistence of both phases in a rather wide interval of temperatures [8]. The presence of maximum $C_p = f(T)$ is an attribute of smeared phase transition of the first order.

The dependence $C_p(T)$ in case of classical phase transitions of the first order is described, as it is known, by the δ -function. If the first order phase transition is a so-called, λ -transition (the dependence $C_p(T)$ reminds the Greek letter λ), it means, that the process of transition begins at temperatures below the temperature of phase transition and covers the micro-regions of small sizes. But the sizes of these regions become in infinity at temperature of phase transition. In case of smeared phase transitions the micro-regions have limited sizes and at the temperature of transition. The smeared phase transitions consist of numerous elementary acts, each of which covers only insignificant part of a phase - micro-region of co-operative structural transformations (RCST).

The reason of existence of smeared phase transitions is deviations of internal parameters of system from average value. Thus the system can be divided in to elementary

regions, so, the phase transition can be considered as classical in the limits of these elementary regions. The sizes of such RCST have essential meaning for the explanation the degree of smearing of the phase transition. The less the RCST are, the more the deviations of local values of parameters of various micro-regions from average value are [9] and therefore the appropriate phase transition is more smeared. The degree of smearing of phase transition decreases at growth of the size RCST and at last, when its volume is equal to the volume of considered system, the classical phase transition will be observed.

The following expression for the estimation number of (n) atoms included in RCST is offered using these representations [8]

$$n = \frac{4k_B T_{tr}^2 \Delta C_p}{Q_{tr}^2} \quad (1)$$

Where ΔC_p is excess heat capacity at temperature of transition, T_{tr} and Q_{tr} - are temperature and heat of transition accordingly. The use of this expression allows to come to a conclusion that the mentioned micro-regions in the investigated melts consist of several tens of atoms.

The interrelation between the sizes of particles, possible statistical deviations of their properties from average values and the degree of smearing of phase transition is also discussed in [9]. The offered expression for the estimation of sizes RCST give similar result for n.

If RCST are so small (10 - 100 atoms), the heat of the elementary acts of transformation is about of the heat of thermal fluctuations. There is one more reason of smearing of phase transition. Really, in this case, even if all elementary regions are identical, will be observed smearing of phase transition, caused by thermal fluctuations. At any temperature there will be the final probability that the part of RCST is in non-ground state for given temperature. If the sizes RCST are so small, the nature of smeared phase transition becomes close to the nature of chemical equilibrium. Its movement at a change of temperature is convertible.

Let us estimate the size of RCST on the basis of this idea. Accordingly with [4]: $\rho(T) = (1-\zeta)\rho_s(T) + \zeta\rho_m(T)$, where ζ is the degree of transformation, $\rho_s(T)$ and $\rho_m(T)$ are hypothetical meanings of density of melt at semiconductor state and at metal state corresponding. The values of these parameters are obtained by extrapolations of real linear dependencies on temperature of density before and after the temperatures of transition region. Accordingly it is possible to enter a constant of equilibrium of transition $K = \zeta/(1-\zeta)$; [4]. In that case

$$\frac{d(\ln K)}{dT^{-1}} = \frac{E_{tr}}{R} \quad (2)$$

where: E_{tr} is the enthalpy of the SMT for Avogadro number of RCST. It can be possible to right the following expression for ΔC_p and ρ :

$$\Delta C_p = Q_{tr} \frac{d\zeta}{dT} = \frac{Q_{tr} E_{tr} \exp\left[\frac{E_{tr}}{R} \left(\frac{1}{T} - \frac{1}{T_{tr}}\right)\right]}{RT^2 \left\{1 + \exp\left[\frac{E_{tr}}{R} \left(\frac{1}{T} - \frac{1}{T_{tr}}\right)\right]\right\}^2}; \quad (3)$$

$$\rho = \rho_{tr} - 0.5\Delta\rho + \alpha(T_{tr} - T) + \frac{\Delta\rho}{1 + \exp\left[\frac{E_{tr}}{R}\left(\frac{1}{T} - \frac{1}{T_{tr}}\right)\right]}; \quad (4)$$

where: ρ_{tr} is the density of melt at T_{tr} ; α is the factor of thermal expansion; $\Delta\rho$ is the increase of density of melt as the result of SMT (Fig. 1). The following suppositions are used in last equations. The semiconductor and the metal melts have the same values of C_p and of α . In other words, SMT is the first order smeared phase transition without any participant of the

second order smeared phase transition. It is supposed as well, that RCST have the size, which does not depend on temperature.

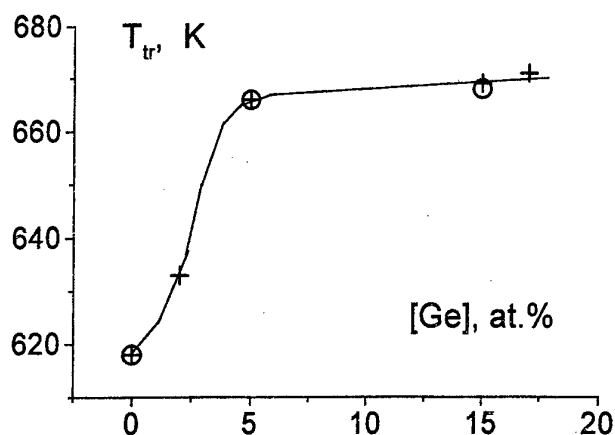


Fig. 3. Dependence of temperature of SMT on Ge content:

+ - the datum obtained from $C_p(T)$ dependencies;
O - the datum obtained from $\rho(T)$ dependencies.

DISCUSSIONS

The results of fitting of experimental datum on $C_p(T)$ and $\rho(T)$ with the use of equations (3) and (4) are presented on Fig. 1 and 2. It can be seen, that experimental datum are described by equations (3) and (4) sufficiently. The temperature of SMT can be defined as the temperature, at which the equilibrium constant K is equal to 1 [4]. The T_{tr} obtained in such manner from $C_p(T)$ has the same value as

obtained from $\rho(T)$ (fig. 3). The strong changing of T_{tr} occurs at small amount of Ge. The reason of this phenomena may be the distinction of co-ordination numbers of Te and of Ge.

The number of atoms involved in RCST is equal, according to the model, to relation $n = E_{tr}/Q_{tr}$. For all investigated melts n is equal to 25-45 atoms. Both reasons of transformation of classical phase transition into smeared phase transition acted simultaneously in investigated melts. So, the value of size of RCST obtained when only one of these reasons are taken into account must be smaller then the real size.

CONCLUSIONS

It is concluded from the temperature dependencies of heat capacity and density of melts in the Ge-Te system, that semiconductor - metal transition is the smeared first order phase transition. This transition in chalcogenide melts consists of numerous elementary acts. Each of them includes several tens of atoms.

ACKNOWLEDGEMENTS

This work has been supported by the Russian Fund of Basic Researches (Grant N98-03-32114a), by the Russian Programme "Integration" (Grant N 589) and by the Competition Centre of S.-Petersburg State University (Grant N97-92-66).

REFERENCES

1. M.Cutler. Liquid Semiconductor. Academic Press. 1977.
2. M.H.Cohen, J.Jortner. Phys. Rev. Letters. 30 (1973) 699.
3. N.F.Mott. Phyl. Mag. B. 37 (1978) 377.
4. Yu.S.Tver'yanovich, Z.U.Borisova. V.A.Funticov. Neorganicheskie Materialy. 22 (1986) 1546.
5. Tver'yanovich Yu.S., Ushakov V.M., Tverjanovich A.S. J.of Non-Cryst. Sol. 197 (1996) 235.
6. Yu.S.Tver'yanovich, M.S.Gutenev. Magneto-chemistry of glassy semiconductors. St.-Petersburg Univ. 1997.
7. B.Cabane, J.Friedel. J. de Physique. 32 (1971) 73.
8. B.N.Rolov. Fizika tverdogo tela. 10 (1968) 3441.
9. Bal'makov M.D., Tver'yanovich Yu.S., Tver'yanovich A.S. Glass Physics and Chemistry, 20 (1994) 381.

COMPARISONS OF NEODYMIUM DOPED FLUOROALUMINATE AND FLUOROZIRCONATE GLASSES FOR OPTICAL COMPONENTS

Adam B. Schrader and Alexis G. Clare
New York State College of Ceramics
2 Pine St., Alfred, NY USA

There are many different types of fluoride glasses such as fluorozirconates, fluoroaluminates, fluoroberyllates, and fluoroindates. Each of these subsets is named after the most abundant base component. Fluoride glasses have a wide window of transmission into the infrared region (typically from 200nm to 7 μ m) which make them candidate materials for IR telecommunications. Two of the most commonly used fluoride glasses of interest are the fluorozirconate and fluoroaluminate systems. Fluorozirconate glasses such as ZBLAN (ZrF_4 - BaF_2 - LaF_3 - AlF_3 - NaF) compositions with different rare-earth dopant levels have been thoroughly studied and put into practical use in the telecommunications industry, however fluoroaluminate compositions have also shown potential for similar applications and exhibit a number of advantages over their fluorozirconate counterparts. Fluoroaluminate (AlF_3 - BaF_2 - CaF_2 - SrF_2 - MgF_2 - YF_3) glasses, which have a higher glass transition temperature and are more chemically and mechanically durable than fluorozirconate glasses, may be a better option for both passive and active optical components. Previous work at several institutions, including Alfred University has shown that the absorption and fluorescence spectra for rare-earth ions in fluorozirconate glasses differ in intensities and fluorescence efficiencies from those in fluoroaluminate glasses. Given that fluorine atoms surround the rare-earth ion in both systems, it is believed that these differences arise from structural arrangements around the rare-earth ion beyond the first coordination shell which affect the electronic structure of the ion. There is considerable interest in broadening the range of transitions available for amplifying and lasing in rare earths. Understanding the dependence of the electronic structure and spectra in these glasses on extended coordination may help elucidate some of the observed differences. The focus of this study was to investigate the source of these observed differences by characterizing Neodymium doped fluorozirconate and fluoroaluminate glasses using a combination of techniques including Extended X-ray Absorption Fine Structure (EXAFS) and Electron Spin Resonance Spectroscopy (ESR). The host glass compositions chosen were a standard YABCSM for the fluoroaluminate and ZBLAN for the fluorozirconate with varying additions (0-5 mol%) of Nd^{3+} substituting for Y^{3+} or La^{3+} .

respectively. Neodymium was chosen as the rare-earth ion because it is a spectrally well studied ion in many different host glasses. The EXAFS and ESR results will be correlated to the absorption and fluorescence spectroscopy of the same glasses.

**EXAFS studies of possible clustering of
thulium ions in alkali tellurite glasses.**

D.B. Hollis, D.P. Turner, L.D. Firth
Department of Electronic Engineering and Physics
University of Paisley
Paisley PA1 2BE

F.W. Mossellmans
SRS Laboratory
Daresbury
Warrington WA4 4AD

Thulium, when doped into glasses at concentrations over 0.5 mole %, exhibits concentration quenching of the fluorescence around $1.8\mu\text{m}$ far greater than that for the thulium ions in crystals. Structural studies by density measurements and optical energy gap observations, reported elsewhere in this conference lead us to suspect inhomogenetics with alkali rich areas in the glasses we have chosen. Fluorescence under C.W. and pulsed excitation at 705 nm also reported elsewhere in this conference, shows, for the emission centred around $1.8\mu\text{m}$, that dipole-quadrupole interactions, rather than the usual dipole-dipole interactions are occurring. This evidence is again suggestive of clustering of the thulium ions.

These glasses were of type $\text{XRO}_2 \cdot (1-X) \text{TeO}_2$, where x runs from 0 to 30 mole%, and R is Li, Na. or K. They were made from alkali metal carbonates and tellurium oxide, with extra additions of 0.1 to 5.0 molar% of Tm_2O_3 . After melting in recrystallised alumina crucibles for 30 minutes, they were annealed at 250°C for 30 minutes and cooled at 1°C per minute to room temperature.

We have taken Tm^{3+} $\text{K}\alpha$ EXAFS spectra on station 8.1 of the Daresbury synchrotron radiation source. The pre-edge and EXAFS backgrounds were energy calibrated and subtracted out using the Daresbury program packages EXCALIB and EXBACK. The EXAFS data were then compared to synthetic data generated using the package EXCURV97 and various selections of first and second shell coordination of atoms around the thulium ions. We find that it is possible to produce a close match between the experimental EXAFS and the theoretically synthesised EXAFS, when we assume that thulium ions are present in the second coordination shell around the central thulium ion. This result leads us to believe that the thulium ions are clustered. Further more, we obtain acceptable matches between theory and experiment if we assume that alkali ions, but not tellurium ions are present in the second coordination shell. This result leads us to believe that the thulium ions cluster in the alkali rich part of the glass structure.

INITIAL CORROSION STAGES OF HEAVY METAL FLUORIDE GLASS IN WATER

Brigitte Hueber, Günther Heinz Frischat

Inst. f. Nichtmetallische Werkstoffe, Technische Universität Clausthal, Zehntnerstr. 2a,
D-38678 Clausthal-Zellerfeld, Germany. email guenther.frischat@tu-clausthal.de
and

Achim Maldener, Oliver Dersch, Friedrich Rauch

Inst. f. Kernphysik, Universität Frankfurt/Main, August-Euler-Str. 6,
D-60486 Frankfurt/Main, Germany

ABSTRACT

A ZrF_4 - BaF_2 - YF_3 - AlF_3 presputtered glass was corroded in H_2O for durations between 1 and 50 min at 20, 40, 60 and 80 °C. The profiles of Zr, Ba, Y and Al were measured by secondary neutral mass spectrometry, H was measured by nuclear reaction analysis, whereas O was monitored using Rutherford backscattering spectrometry. On the basis of these results it is shown that the corrosion zone approaches a composition near that of the BaZrF_6 phase. Further, a modified corrosion model for the initial stages of the glass attack is proposed, where H_2O is the initiating species.

1. INTRODUCTION

Since their discovery in 1975 the group of heavy metal fluoride glasses belongs to one of the most investigated materials [1-3]. Originally, they were considered as candidates for long distance low-loss fibers, however, interest has now shifted to their application in sensors, optical waveguides, lasers, etc. There have been many attempts to study the corrosion resistance of heavy metal fluoride glasses in water or aqueous media [4-6]. They were found to be much less resistant compared to technical silicate glasses. This strongly restricts their potential applicability.

Until recently, the corrosion resistance studies have been done using commonly available methods, e. g. by monitoring changes in surface morphology, weight, corrosion solution or infrared transmission [6]. During such mostly long-time water corrosion processes different mechanisms overlap, e. g. $\text{OH}^- \leftrightarrow \text{F}^-$ ion exchange, incongruent dissolution, layer formation by redeposition from the solution, and crack formation on the surface. Elucidation of the specific mechanisms is very difficult in such a case.

This study focuses on the short-time corrosion processes of a heavy metal fluoride glass. This offers the possibility to propose a modified corrosion model. However, since only thin reaction layers have to be analyzed, surface-sensitive methods with nm depth resolution have to be used.

2. EXPERIMENTAL

The composition of the glass used in this study was 50 ZrF_4 , 33 BaF_2 , 10 YF_3 , 7 AlF_3 (m%). Various physical properties of this glass can be found in Ref. [7]. High purity fluoride materials (BDH Laboratory Supplies, Poole, Dorset, England) were melted for 1 h at 850 °C in a Pt crucible. The melt then was poured into a brass mould, preheated to 240 °C. After

annealing for 4 h at 320 °C, 4 mm thick 7 x 7 mm² glass slabs were prepared by sawing, grinding and polishing.

From corrosion studies on silicate glasses it is known that the zone near the surface of this type of glass is strongly altered, i.e. some of the components appear to be depleted, others show an increase in concentration [8]. This zone may be as thick as 100 nm. The reason for this may originate from sample preparation such as grinding and polishing, or from weathering of the glass surface during storage. Since heavy fluoride glasses are more hygroscopic than silicate glasses, it is to be expected that this distortion process may be even stronger. In order to overcome this effect, the glasses were presputtered for a depth of about 350 nm. The samples then displayed a concentration distribution of all components close to that in the bulk of the glass.

The short-time corrosion on these samples with the presputtered areas was done in 200 ml of distilled water in polyethylene vessels. Corrosion temperatures were between 20 and 80 °C for times between 1 and 50 min, respectively. The glass samples were then rinsed in acetone and placed either in the high vacuum transfer system or in a desiccator.

The depth profiling of Zr, Ba, Y and Al was performed using an SNMS apparatus (Ions and Neutrals Analyzer, INA 3, Leybold AG, Köln, Germany), which makes possible the analysis of sputtered neutrals by post-ionisation in a krypton plasma [9]. Sputtering was done at liquid nitrogen temperature, and the use of the high frequency mode (HFM, Specs GmbH, Berlin, Germany) enabled charge compensation by electrons from the plasma. This is especially useful for the analysis of non-conductive materials. The intensity-time profiles obtained were subsequently converted into concentration-depth profiles. From the depth of the sputter craters (P1 Long Scan Profiler, TENCOR Instruments GmbH, München, Germany) a sputter rate of 0.35 ± 0.05 nm/s was calculated which was used to convert the sputter times into depths. The proper conversion of the intensities is more difficult. A detailed description for silicate glasses can be found in [9] and for heavy metal fluoride glasses in [10]. The quantification was done on the basis of the molar compounds ZrX_4 , BaX_2 , YX_3 and AlX_3 , respectively, where $X = aF^- + bOH^- + c(1/2O^{2-})$, with the partition factors a , b and c . In the bulk of the glass $a = 1$, and $b = c = 0$.

Hydrogen depth profiles were obtained using the ¹⁵N nuclear reaction analysis (NRA), which is based on the resonant reaction $^1H(^{15}N, \alpha\gamma)^{12}C$. This technique has been used in glass hydration studies before and the reader is referred to [11] for details of the technique and the equipment. Oxygen depth profiles were obtained using a special version of Rutherford backscattering spectrometry (RBS) in which the strongly increased $^{16}O + ^4He$ scattering cross section at $E(^4He) = 3.045$ MeV is utilized, compare [11,12]. H and O depth profiling was done at the Institut für Kernphysik, Universität Frankfurt/Main, Germany.

3. RESULTS

Fig. 1 shows typical SNMS reaction profiles after corrosion for 15 min at 80 °C. The statistical significance of the data is given by the fact that for a time of 300 s about 50 data points were gathered. Three regions can be seen, denoted by A, B and C. After having reached the sputter equilibrium (at ≈ 15 nm), region A displays a strong depletion in Ba. This is in agreement with earlier results which showed that this cation is hydrated most easily [13]. Region B is a corrosion layer and an analysis of the profiles for all temperatures and times shows a practically constant final composition of $(43 \pm 2) ZrF_4 - (39 \pm 3) BaF_2 - (11 \pm 1) YF_3 - (5 \pm 1) AlF_3$ (m%), see Fig. 2. This composition approaches the glass forming boundary according to [14] and it is also not very far from the stable composition of the crystal phase $BaZrF_6$. Region C describes the bulk of the unaltered glass. For temperature-time regimes exceeding

those that were studied, a different mechanism occurs, wherein parts of the attacked layers peel off and the corrosion starts at the fresh glass surfaces again.

In order to obtain a deeper insight into the hydration process, it became necessary to determine the profiles of hydrogen and oxygen in the leached layers, too. Fig. 3 compares the profiles of H and O after corrosion for 2 and 10 min at 80 °C, respectively. The H/O ratio changes both as a function of time and of depth. While for short times $H/O \leq 1$ for all depths - this probably implies an $F^- \leftrightarrow OH^-$ ion exchange as the dominating mechanism -, a crossover in the H/O ratio can be found for longer times. Near the surface (zone A) much more O than H is found, whereas with the beginning of zone B the ratio H/O changes to > 1 .

4. DISCUSSION

The long-time corrosion model by Tregoe et al. [13] serves as a basis for the modified model proposed in this work. These authors considered H^+/H_3O^+ ions as the initiator of the corrosion process. Bridging fluorine ions are removed into the solution as HF. Because of its high hydration energy the Ba^{2+} ions react with H_2O and leave the surface as $Ba(OH)_2$. Crack and crystal formation at the glass surface is the consequence. Fig. 4 displays our model, which - for simplicity - considers a glass composition of the $BaF_2 - ZrF_4$ system. It is believed to be valid for zone A, in which the attack starts.

Step 1: The glass network prior to the attack, with Ba^{2+} ion bonding between the ZrF_x chains.

Step 2: H_2O molecules attack the glass surface, break bridging fluorine bonds and form Zr-O-Zr bridges. The F^- ions react with the H^+ ions from the water molecules and leave the glass surface as HF. This mechanism is supported by the fact that for longer reaction times a major part of the oxygen is not bound to hydrogen, see Fig. 4. Of course, the $F^- \leftrightarrow OH^-$ exchange still occurs, however, with less priority.

Step 3: Ba^{2+} ions are also involved in the reaction. This may occur in two ways:

- The SNMS profiles of Fig. 1 displayed an enrichment of Ba in zone B and the tendency towards forming there a composition near $BaZrF_6$. For that Ba^{2+} ions must diffuse from zone A into zone B, possibly together with OH^- ions. When this layer becomes too thick, it peels off, allowing again an attack at a fresh glass surface [10]. This process is diffusion-limited.
- As described in the model by Tregoe et al. [13], the Ba^{2+} ions may react with H_2O and can leave then the glass surface as $Ba(OH)_2$, possibly together with HF. This results in a dissolution of the network.

In principle, both mechanisms of step 3 may occur simultaneously. The first mechanism may predominate at higher temperatures, where a \sqrt{t} change of the overall reaction depth was found [10], whereas at lower temperatures this change occurred proportional to t , possibly an indication for the second mechanism.

5. CONCLUSIONS

A ZrF_4 - BaF_2 - YF_3 - AlF_3 presputtered glass was corroded in H_2O for times between 1 and 50 min and at temperatures from 20 to 80 °C. The Zr, Ba, Y, Al profiles were measured by SNMS, H was measured by NRA and O by RBS. All intensity-time profiles could be converted into concentration-distance dependencies. In zone B, the corrosion zone, all reaction profiles merge to a final composition near that of the BaZrF_6 phase. In zone A, where the reaction between glass and water starts, a mechanism prevails with H_2O as an initiating species. Details of this modified mechanism are discussed.

ACKNOWLEDGEMENTS

The authors gratefully acknowledge financial support of this work by the Deutsche Forschungsgemeinschaft (DFG), Bonn.

REFERENCES

- [1] M. Poulain, M. Poulain, J. Lucas and P. Brun, *Mat. Res. Bull.* 10 (1975) 243.
- [2] A.E. Comyns, *Fluoride Glasses*, Critical Reports on Applied Chemistry 27, John Wiley & Sons, New York 1989.
- [3] I.D. Aggarwal and G. Lu, *Fluoride Glass Fiber Optics*, Academic Press, Inc., San Diego 1991.
- [4] C.J. Simmons and J.H. Simmons, *J. Am. Ceram. Soc.* 69 (1986) 661.
- [5] Y. Dai, K. Takahashi and I. Yamaguchi, *J. Am. Ceram. Soc.* 78 (1995) 182.
- [6] G.H. Frischat and I. Overbeck, *J. Am. Ceram. Soc.* 67 (1984) C-238.
- [7] S.Y. Choi and G.H. Frischat, *J. Non-Cryst. Solids* 129 (1991) 133.
- [8] H.J. Franek, G.H. Frischat and H. Knödler, *Glastechn. Ber.* 56 (1983) 165.
- [9] R. Schmitz, G.H. Frischat, H. Paulus and K.-H. Müller, *Fresenius J. Anal. Chem.* 358 (1997) 42.
- [10] B. Hueber, PhD dissertation, TU Clausthal (1998).
- [11] M. Laube, PhD dissertation, U Frankfurt (1996).
- [12] M. Laube and F. Rauch, *Fresenius J. Anal. Chem.* 353 (1995) 408.
- [13] D. Tregoeat, M.J. Liepmann, G. Fonteneau, J. Lucas and J.D. Mackenzie, *J. Non-Cryst. Solids* 83 (1986) 282.
- [14] A. Lecoq and M. Poulain, *J. Non-Cryst. Solids* 41 (1980) 209.

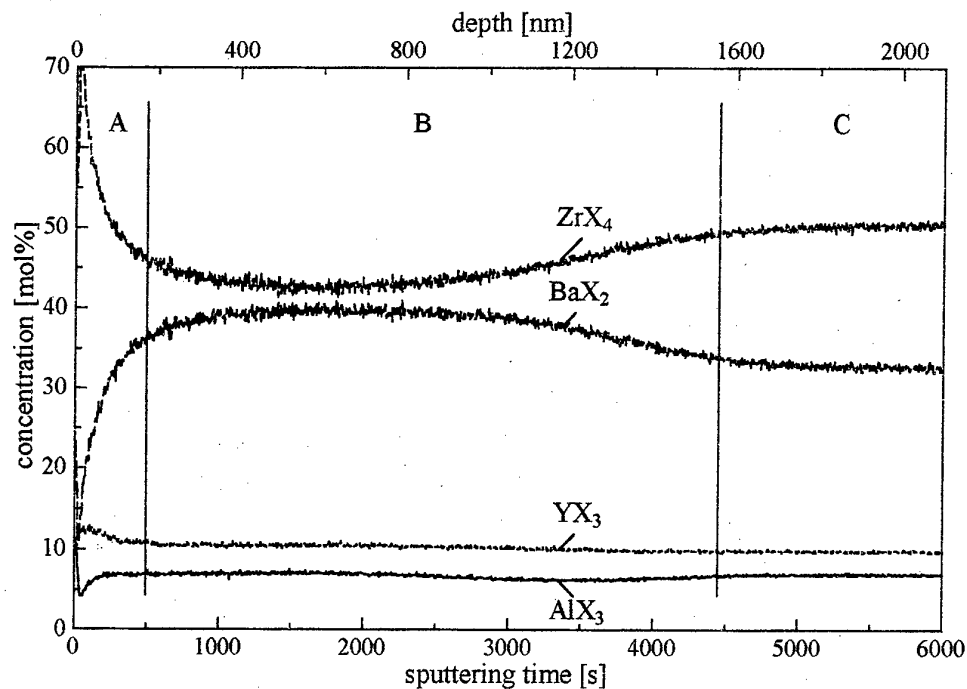


Fig. 1. Concentration-distance profiles of heavy metal fluoride glass after corrosion for 15 min at 80 °C

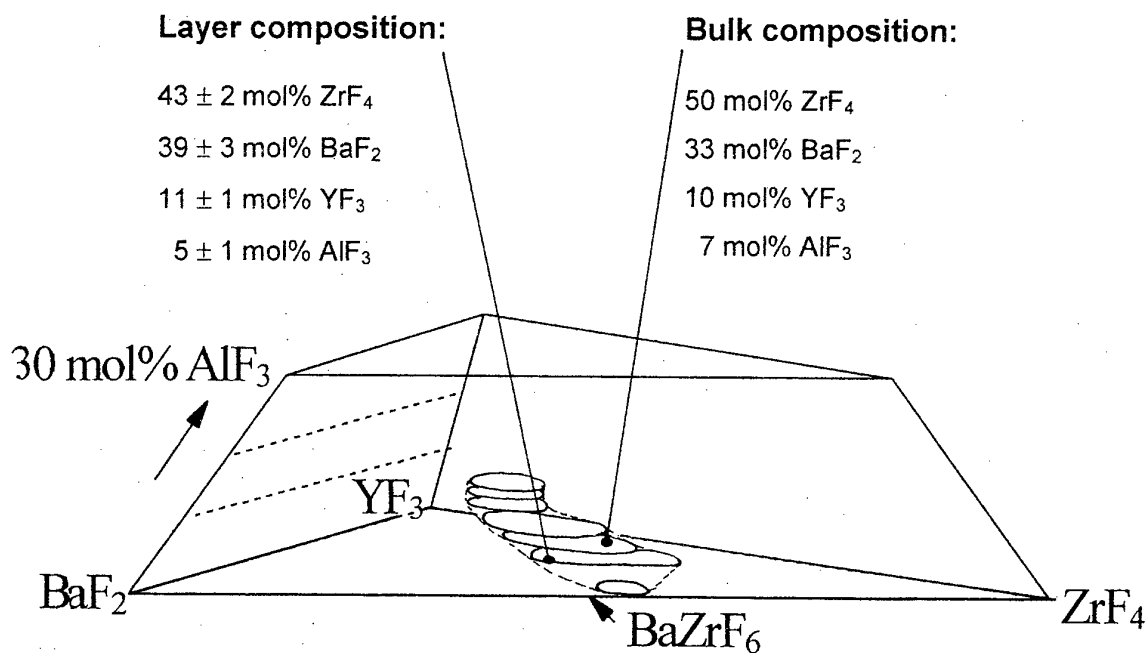


Fig. 2. General view of the domain in the ZrF₄-BaF₂-YF₃-AlF₃ quaternary system according to Lecoq and Poulain [14]

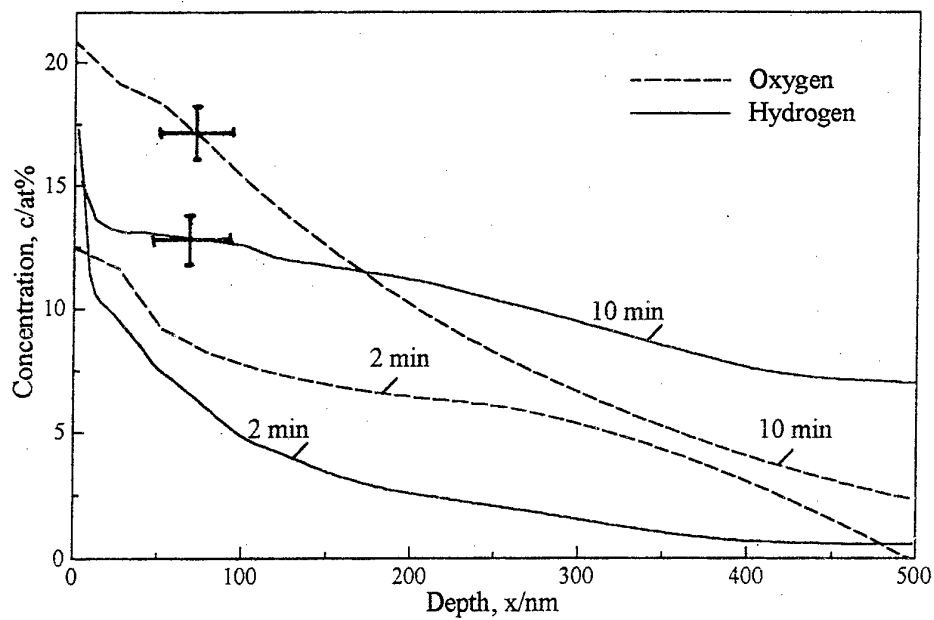


Fig. 3. Concentration-depth profiles of O and H after corrosion for 2 and 10 min at 80 °C

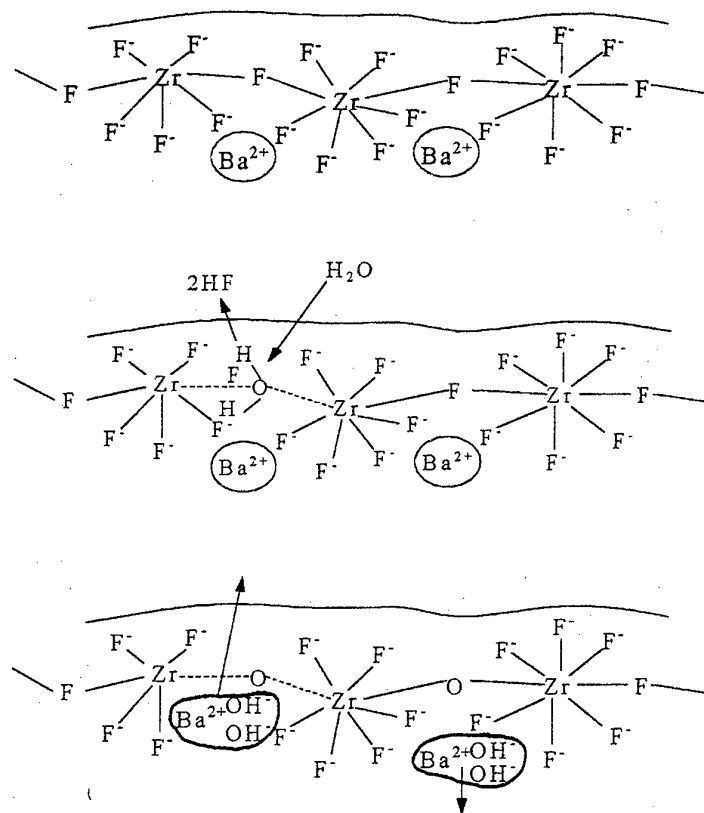


Fig. 4. Modified corrosion model for the initial stage

VISCOSITY OF FLUORIDE GLASSES NEAR FIBER DRAWING TEMPERATURE

G. Zhang # *, J. Jiang # *, M. Poulain#, A.S. Delben *, J.R. Delben *,

#Laboratoire des Matériaux Photoniques, Université de Rennes 1, Rennes-35042, France

*Dept. de Física, Univ. Federal de Mato Grosso do Sul, 79070-900, Campo Grande, Brazil

ABSTRACT

The temperature-viscosity dependence of ZrF_4 -, SnF_4 - and CdF_2 -based fluoride glasses was obtained by two methods. The first one is from Moynihan's relation based on the DSC data considering the width of glass transition region e.g. T_g and T_g' , the beginning and ending temperatures of glass transition. We defined a factor $G = (T_g'/T_g)(T_g' - T_g)$ in the relation because it does determine the viscosity at a temperature $(T - T_g')$. The slope of the calculated $\log \eta - T$ decreases following a regularity: fluorozirconate glass (0.11) > fluoroindate glasses (0.08) > cadmium fluorochloride glass (0.05). The second method is the Parallel-Plate technique. The same order of $(\log \eta - T)$ slope was observed in the measured results, e.g. 0.12, 0.09 and 0.08 respectively for the tetra-valence, the tri-valence and the di-valence fluoride glasses. The Arrhenius activation energies of the shear viscosity are 27.4 for PGICZ and 15.3 kcal/mole for $CdFCl$. The influence of the viscosity difference between the studied glasses on glass crystallization and on fiber drawing is discussed.

1. INTRODUCTION

Fluoride glasses are promising for many applications, such as infrared optical signal and energy transmission, amplification in telecommunication, hosting materials of laser optics, due to their wider IR transmitting range, lower phonon energy of glass network and lower intrinsic losses. However most of their uses based on these excellent properties is in fiber form. Fluoride optical fiber is mainly obtained by drawing preforms at a temperature well above glass transition at which the viscosity should be in the range 10^3 - 10^6 Pa.s. The low enough rate of crystallization at this temperature is the key factor to get high optical quality fiber. So the characteristic of $\log \eta - T$ and thermal stable range ($T_x - T_g$) are the most important factors for fiber drawing and subsequently the understand of their viscosity characteristics is essential. Some methods, such as Beam bending (10^9 - 10^{11} , viscosity in Pa.S), Penetration (10^7 - 10^{11}) and Parallel plate (10^5 - 10^{10}) [1], have been applied to measure the viscosity above glass transition temperature T_g . Among these techniques, parallel-plate process has advantages in small and simple sample required and capability measuring viscosity range near to fiber drawing temperature. However the relatively high tendency of crystallization of some fluoride glasses often restrain the measurement in low viscosity region. Based on the DSC data considering the width of glass transition region, e.g. the beginning and ending temperatures T_g and T_g' , Moynihan proposed an equation [2] which can estimate the temperature dependence of viscosity for predicate fiber drawing.

The viscosity characteristics of fluorozirconate and fluoroaluminate glasses had been studied [3,4]. Their viscosity-temperature behaviors are more far from Arrhenian melt such as classic silicate glass melt, e.g. the fluoride melts are more ionic fragmentary. Meanwhile the similar $\log \eta - T$ gradients were observed for all the studied ZBLA, ZBLA, ABCMY and ZBLALi and ZBLALiPb compositions (for abbreviation $Z = ZrF_4$, $B = BaF_2$, $L = LaF_3$, $A = AlF_3$, $C = CaF_2$, $M = MgF_2$ and $Y = YF_3$). Although some of them have been successfully drawn in fiber, the new fluoride, heavy halide and chalcogenide glasses which have much lower phonon energy than current ZrF_4 - and AlF_3 -based systems, are required for the applications in optical fiber amplifier and fiber lasers. Some fluoroindate [5-7] and cadmium fluorochloride [8-9] glasses exhibit similar thermal stable range like the standard ZBLAN glass, but the fiber drawing on these systems is associated always with some difficulties. The aim of this work is to investigate the composition dependence of viscosity in various sorts of fluoride glasses, and also to discuss the possibility in fiber drawing for some glasses with low phonon energy which are interested to active applications.

2. EXPERIMENTAL

2.1. Sample preparation and characteristic temperatures

The glass compositions used in this work are: ZBLAN(53 ZrF_4 -20 BaF_2 -4 LaF_3 -3 AlF_3 -20 NaF), ZBLA[2](57 ZrF_4 -36 BaF_2 -3 LaF_3 -4 AlF_3), IZnBS[5](34 SnF_4 -6 GaF_3 -20 ZnF_2 -16 BaF_2 -20 SrF_2 -2 GdF_2 -

2NaF), $\text{BiZnYbT}[2](30\text{BaF}_2\text{-}30\text{InF}_3\text{-}20\text{ZnF}_2\text{-}10\text{YbF}_3\text{-}10\text{ThF}_4)$, $\text{GIPCdZn}[7](22\text{GaF}_3\text{-}13\text{InF}_3\text{-}30\text{PbF}_2\text{-}18\text{CdF}_2\text{-}13\text{ZnF}_2\text{-}2\text{GdF}_3\text{-}2\text{NaF})$, $\text{CdFCI47}[9](30\text{CdF}_2\text{-}18.5\text{CdCl}_2\text{-}8\text{NaF}\text{-}25\text{NaCl}\text{-}12.5\text{BaF}_2\text{-}2\text{KF}\text{-}4\text{LiF})$.

The ZBLAN, GIPCdZn and IZnBS glasses were prepared by the typical NH_4HF_2 process. The reagent grade oxides and/or fluorides were used as raw materials. 0.1-0.3 mole glass batches were placed in platinum tube for fluorination at 350 °C and 500 °C for a few hours. The fluorochloride glasses are melted from unhydrate fluorides and chloride. After the normal melting, casting and annealing processes the glass bulks or rods could be obtained.

The glass characteristic temperatures of bulk samples were measured under N_2 flow by using a DSC-220 SEIKO. The heating rate was 10°C/min. The uncertain values of characteristic temperatures are $\pm 1^\circ\text{C}$ for glass transition (T_g), end of glass transition (T_g'), the onset and peak temperatures of crystallization (T_x and T_p), and $\pm 2^\circ\text{C}$ for melting point (T_m) and liquidus temperature (T_l).

2.2. Estimation of T - η from DSC data

By C.T. Moynihan's relation[2], we can simulate the viscosity nearing fiber drawing range from DSC or DTA data, T_g and T_g' :

$$\log \eta = -5 + \frac{14.2}{\frac{0.147(T - T_g')}{T_g'^2(\frac{1}{T_g} - \frac{1}{T_g'})} + 1} = -5 + \frac{14.2}{\frac{G}{T_g'^2(\frac{1}{T_g} - \frac{1}{T_g'})} + 1} \quad (1)$$

We defined a factor $G = (T_g'/T_g)(T_g' - T_g)$ in the relation because it does determine the gradient of $\log \eta$ - T curve at a temperature ($T - T_g'$). For high T_g glasses, fiber drawing temperature T_d can be easily obtained by:

$$T_d = [T - T_g'] \log \eta + T_g' \approx [T - T_g'] \log \eta + T_g + G. \quad (2)$$

This method makes an appropriate information about fiber drawing possibility based on the minimal experimental input (T_g and T_g' only) for the viscosity unknown well glass systems.

2.3. Determination of T - η by parallel-plate method

The cylindrical samples are slices cut from annealed glass rods and roughly polished. The dimension of sample are typically with 6-8 mm in diameter and 3-4 mm in thickness. The parallelism of the two surfaces of the sample is better than 0.02 mm. The samples are sandwiched between two platinum foils or between two silica plates and then put into a Viscometer from Theta Industries Inc. and a modified commercial TMA/SS-220 from Seiko company, respectively. The applied load is ranged from 10 to 200 g. By measuring the deformation rate with the temperature, we can have the temperature-viscosity relationship by using Gent's equation[10]:

$$\eta = 2\pi M g h^5 / [3V (dh/dt) (2\pi h^3 + V)]. \quad (3)$$

It has been indicated that the measured viscosity could be effected by the remained stress when heating rate is about 10 °C/min. in dynamic measurement [11]. In order to diminish this effect and also to get the temperature dependence of viscosity more close to the real fiber drawing condition, we measured viscosity at low heating rate, 2 °C/min. This value is based on the empiric parameters used in fiber drawing that: the highest temperature in heating zone is 60-80 °C above T_g , while the temperature of preform 30-40 mm far from the highest temperature point should be preheated at a temperature near T_g , and the preform feeding rate is 1-2 mm/min. If the temperature changes linearly in the heating zone, the heating rate of preform is in range 2 - 4 °C/min. In fact the temperature profile is normally more smooth in the high temperature area for pulling fiber than in the low temperature area. So the supposed heating rate in fiber drawing zone is about 2 °C/min., which should be not far from the real case.

3. RESULTS

3.1. Calculated temperature dependence of viscosity

As the $\log \eta$ - T gradient is depended to G value, the determination of $G = (T_g'/T_g)(T_g' - T_g)$ is very important. T_g and T_g' could vary with the glass annealing and heating rates [12]. In normal

DSC/DTA heating rate range, 5-10°C/min, T_g and T_g' change only 1-2°C. But they may change evidently with the cooling rate. Table 1 represents the T_g and T_g' values and the induced G values for the samples undergone different annealing processes.

Table 1. Determination of viscosity characteristics of some fluoride glasses by DSC data.

Glass	Cooling rate (°C/min)	T_g (K)	T_g' (K)	G (K)	Selected G	$d\log\eta/dT$ (at T_g')	$\Delta\log\eta/\Delta T$ ($\log\eta=7-9$)
ZBLAN	As made	537.0	554.6	18.18	16	0.130	0.108
	0.99 in DSC	537.2	552.7	15.95			
	1.97 in DSC	536.4	554.2	18.39			
	6.28 in DSC	535.0	554.7	20.42			
GIPCdZn	As made	521.0	541.2	20.98	21	0.11	0.084
	0.99 in DSC	520.2	541.6	22.28			
IZBS	As made	565.3	588.8	24.78	24	0.098	0.073
	0.99 in DSC	565.1	587.0	22.74			
	4.92 in DSC	563.0	587.8	25.89			
CdFCl47	As made	399.4	431.4	34.56	32	0.072	0.055
	0.99 in DSC	399.1	431.7	35.26			
	4.93 in DSC	398.7	432.6	36.78			

We can see that the induced G values decrease more evidently with the lowering of cooling rate in the higher T_g fluoride glasses than in the low T_g CdFCl glass. It is not suitable to get T_g and T_g' values directly from the as made samples because the cooling rate of the annealing furnace with a given heat capacity should be large when it is cooled from a high temperature. By compare the G values obtained at different condition, the annealing rate of the as made samples is about 2-4 °C/min for fluorindate glasses and less than 1 °C/min for CdFCl glass respectively. In order to compare the G determined $\log\eta$ - T dependence, a pre-annealing treatment at low cooling rate (1-2 °C/min.) is preferred for high T_g systems. In fact the difference of G value resulted from the variation of the cooling rate is much smaller than that between the different glass systems. It is clear that this G difference reflects the different temperature dependence of viscosity.

Table 1 listed also the calculated $\log\eta$ - T gradient in the viscosity range 10^{7-9} Pa.s. based on the selected G values. The slope of the calculated $\log\eta$ - T decrease following the order : ZBLAN (0.108) > GIPCdZn (0.084) > IZnBS (0.073) > CdFCl47 (0.055). This regularity will be consisted by the experimental data by Parallel-plate method presented in next section.

We think that the difference of $\log\eta$ - T gradient is probably related to glass' ionic character. By comparison with silicate glasses, fluorides glasses have high ionic nature and exhibit steep $\log\eta$ - T relation. Among the studied systems in this work, ZrF_4 -based glasses contain much tetra-valence Zr ions which result in high ionic characteristic and therefore the highest viscosity-temperature gradient. In same way the tri-valence fluorides (GaF_3 and InF_3) based glasses have higher $\log\eta$ - T gradient than the di-valence fluoride glasses (CdFCl47).

3.2. Determination of $\log\eta$ - T relationship by parallel-plate method

The careful choice of the process parameters, e.g. the heating rate and applied load, wide viscosity range could be measured by parallel-plate method. For the viscometer from Theta Industries Inc., large sample and high load can be used due to its large silica probe (12 mm in diameter), which allow the viscosity near T_g could be obtained as the deformation occurs at low temperature under the heavy pressure. Meanwhile smaller sample and light load should be employed for the modified Seiko's TMA/SS-220, because its silica probe is thin (2 mm) and the diameter of the sandwiching silica plates is 10 mm in diameter. Another limit of the modified TMA is its small available probe fall down distance for sample's deformation (less than 1.5 mm). Figure 1 shows the deformation curves recorded on TMA/SS-220 under different loads. The estimated temperature dependence of viscosity is presented in figure 2.

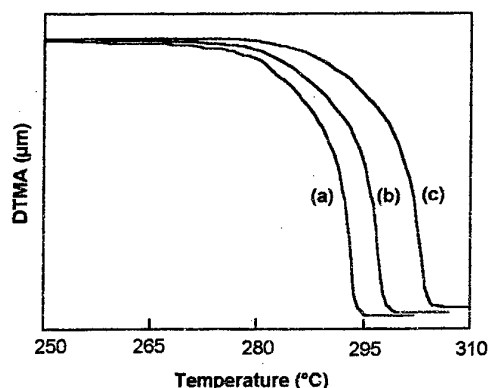


Fig. 1. Deformation curves of GIPCdZn glass under load (a) 100g, (b) 50g and (c) 10 g.

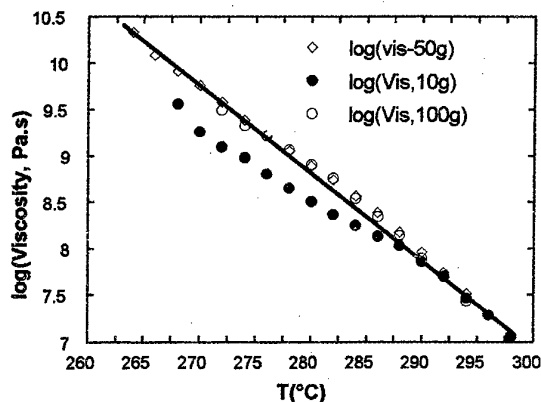


Fig.2. $\log\eta$ -T curves of GIPCdZn glass determined under different load (10, 50, 100 g).

From figure 2, we can see that the deformation curve applied with a load of 100 g begins and ends at lower temperatures. Meanwhile with a load of 10g the curve ends at a temperature 10 C higher than that of with load of 100 g. So light load will be beneficial to obtain the viscosity at high temperature, e.g. more near to fiber drawing range. However the $\log\eta$ -T curve obtained under 10g load in figure 4 appears stronger non-linear character, by comparing with that obtained under heavy loads (50 and 100 g), at high viscosity range. This maybe is due to the not very good contact between the silica plate and the sample under the light load, which is could make evident influence on deformation rate especially at low temperature before glass being soft. As the applied load increase (50-200g), the experimental data has good linearity in viscosity range of 10^{7-9} Pa.s in both two equipments. Same results is observed in the calibration by using the standard glass 711 from National Bureau of Standards (NBS). Table 2 reports the $\log\eta$ -T gradient in 10^{7-9} Pa.s. Similar to the viscosity-temperature dependence estimated in previous section, the measured data show again that $\log\eta$ -T slope decreases with the ionic character decreasing from ZBLAN glass, to GIPCdZn glass and then to CdFCI47 glass.

Table 2. Determination of viscosity characteristics by parallel-plate method.

glass	$\Delta\log\eta/\Delta T$ ($\log\eta=7-9$) (by TMA-220 Seiko, Inc.)	$\Delta\log\eta/\Delta T$ ($\log\eta=7-9$) (by Viscometer Theta Industries Inc.)
ZBLAN20	0.12 (50g, 2C/min)	0.14 (200g, 2C/min)
GIPCdZn	0.093 (100g, 2C/min) 0.090 (50g, 2C/min) 0.085 (50g, 1C/min)	0.12 (200g, 2C/min)
CdFCI47	0.080 (50g, 2C/min)	0.11 (200g, 2C/min)

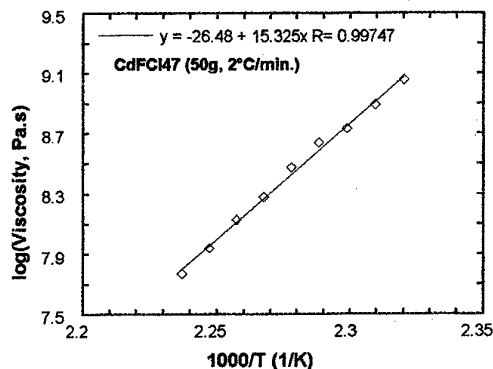
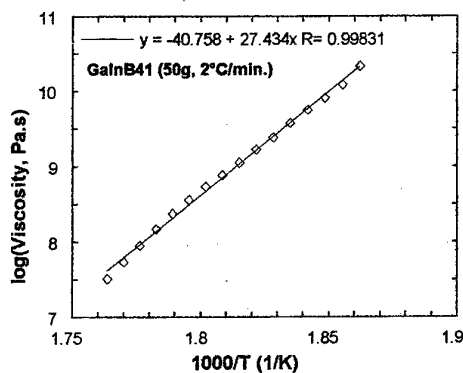


Fig.4. Activation energies of viscous flow of GIPCdZn and CdFCI47 glasses.

The activation energies of viscous flow of GIPCdZn and CdFCI47 glasses are obtained by plotting $\log \eta$ vs $1000/T$ and presented in figure 3. Large difference, 27.4 kcal/mole for GIPCdZn and 15.3 kcal/mole for CdFCI47 respectively, is observed. These values also should be related to the difference of ionic nature between them.

3.3. Predication of fiber drawing possibility

Based on the properties of viscosity and thermal stability obtained previously, fiber drawing possibility could be evaluated. We defined T_0 here the starting crystallization temperature at which the detectable exothermic deviation from the baseline could be observed. It is evidently that fiber drawing temperature should be lower than T_0 instead of T_x because the crystallization rate at T_x is really high to get low loss fiber. A little large sample will be beneficial to observe this temperature, although it is also depended to the DSC's sensibility. Table 3 lists the T_0 temperature obtained by DSC measurement on the sample of 40 mg in weight. The heating rate is $2^\circ\text{C}/\text{min}$, the same heating rate used in viscosity measurement. The temperatures, $T_{d\text{cal}}$ and $T_{d\text{meas}}$, are respectively the calculated and measured fiber drawing temperatures at which $\log \eta = 5$ (Pa.s). They are obtained by calculating from the relation (2) and by extra-plotting the measured viscosity curve to $\log \eta = 5$ (Pa.s).

Table 3. Evolution of fiber drawing possibility in fluoride glasses.

Glass	T_0 ($^\circ\text{C}$)	$T_{d\text{cal}}$ ($^\circ\text{C}$)	$T_{d\text{meas}}$ ($^\circ\text{C}$)	$T_0 - T_{d\text{cal}}$ ($^\circ\text{C}$)	$T_0 - T_{d\text{meas}}$ ($^\circ\text{C}$)
ZBLAN	344	326	320	+18	+24
GIPCdZn	322	331	321	-9	+1
IZBS	345	384	353	-39	-8
CdFCI	205	258	235	-53	-30

The conclusion of the table 3 is that fiber drawing from preform is easy for ZBLAN glass, but some what difficult for GIPCdZn and IZnBS glasses and maybe impossible for CdFCI glass. This evaluation agrees well to the practical fiber drawing efforts. ZBLAN fiber had been fabricated with a loss less than 1 dB/km. Meanwhile GIPCdZn and other Pb-containing $\text{GaF}_3/\text{InF}_3$ based glasses can be drawn into experimental fiber with a loss two orders higher than that of ZBLAN, and CdFCI fiber is not yet up to date.

4. DISCUSSION

From the current view of fluoride glass formations, the lower activation energy in crystallization and/or in viscous flow is associated with higher thermal stability of glass. Some times this assume is not valid. The crystallization activation energy of ZBLAN and ZBLALi glasses are 196[13] and 168[14] kJ/mole respectively, which seems ZBLALi is better in the resistance of devitrification. In fact ZBLAN are more stable than ZBLALi both in glass forming and fiber drawing. Although the crystallization activation energy (E_a) and viscous flow activation energy (E_η) of ZBLAN are much higher than InF_3 -containing ZBLANI[15], but there is not evident difference on isothermal DSC crystallizations at 20 and 30°C below T_x , even at $T_x - 10^\circ\text{C}$ the DSC curve of ZBLAN is somewhat better than ZBLANI. So the relation between glass stability and activation energy shows paradox.

From the formulae means of E_a and E_η in the basic equations often used :

$$\ln k = \ln k_0 - E_a / RT, \quad (\text{in crystallization})$$

$$\log \eta = A + E_\eta / T, \quad (\text{in viscous flow}),$$

it suggest that larger E_a value corresponding to steep $\ln k$ - T curve. Similarly the high E_η (or small G) corresponds to steep $\log \eta$ - T gradient. The effects of E_a and E_η on the stability in "melt \rightarrow glass" cooling process are different from that in "glass \rightarrow fiber" heating process.

For low E_η and E_a glass melt, high critical cooling is required to jump the large unstable thermal zone. This wide temperature interval is caused from the slow decrease in viscosity determined by low E_η . In addition, the low E_a decreases crystallizing frequency (k) smoothly. It is clear that both low E_a and E_η values are of negative effect in glass formation. But they effect fiber drawing they in different ways. Low E_η needs high drawing temperature, meanwhile low E_a is beneficial in slow k

increase. This effect of low E_η does not bring any problem in silicate fiber drawing and just show wide working range as the glass is stable enough at a temperature well above this fiber drawing range. However low E_η may bring difficulty for fluoride glasses as they just have a limited thermal stable range for fiber drawing.

From the analysis made above, the advantages of low E_η ZBLAN glass are evident both in glass formation and in fiber drawing. Although its crystallization frequency factor k increases with temperature more rapidly, it should be rest at low level when fiber drawing is carried out at low temperature. The success of ZNLAN fiber drawing may also relates to its glass network constituted of $[\text{ZrF}_6]$ units as ZrF_4 content is high (>50 mole %). When glass is heated, this structure gives the crystal phases mainly in forms of MZrF_m [15] and therefore its DSC curve is very flat till to T_x . This character is beneficial to fiber drawing. However in CdFCl glass, the crystal phases are elemental fluorides and chlorides and the weak chlorides crystallize first at low temperature [16]. Its this nature and its smooth $\log \eta$ - T dependence make the critical problems to draw CdFCl fiber from preform process. Although fluorogallate and fluorindate glasses are much better than CdFCl glass in fiber fabrication, further optimizations on composition and making processes are needed for the requirement on low phonon energy fibers.

4. CONCLUSION

The temperature-viscosity dependence of ZrF_4 -, InF_3 - and CdF_2 -based fluoride glasses was obtained from Moynihan's relation by using the DSC data considering the width of glass transition region and from the parallel-plate measurement. The slope of the calculated $\log \eta$ - T (in 10^{7-9} Pa.s) decreases following a regularity: fluorozirconate glass (0.11) > fluorindate glasses (0.08) > cadmium fluorochloride glass (0.06). The same order of ($\log \eta$ - T) slope was observed in the measured results, e.g. 0.12, 0.09 and 0.08 respectively for the tetra-valence, the tri-valence and the di-valence fluoride glasses. This $\log \eta$ - T difference between the studied glasses is very closely related with their ionic characters. The Arrhenius activation energies of the shear viscosity are 27.4 for PGICZ and 15.3 kcal/mole for CdFCl . The influences of the activation energies of viscous flow and of crystallization on glass formation and on fiber drawing are different.

ACKNOWLEDGEMENT

The authors gratefully acknowledge Dr. M. Matecki at Laboratoire des Verres et Ceramiques, Université de Rennes 1 (France), for his helps in the viscosity measurement on the viscometer from Theta Industries Inc. and for useful discussion.

REFERENCE

- [1] E.H. Fontana, Amer. Ceram. Soc. Bull., **49** (6), pp594-597, 1970.
- [2] C.T. Moynihan, J. Amer. Ceram. Soc., **76** (5), pp1081-87, 1993.
- [3] S.J. Wilson and D. Poole, Mat. Sci. Forum, **6**, pp665-672, 1985.
- [4] A. Jha and J. M. Parker, Phys. And Chem. of Glasses, **30** (6), pp220-228, 1989.
- [5] A. Soufiane, Ph. D. Thesis, Rennes University, 1992.
- [6] F. Smektala, Ph. D. Thesis, Rennes University, 1992.
- [7] G. Zhang, Ph. D. Thesis Rennes University, 1996.
- [8] M. Matecki and M. Poulain, J. Non-Cryst. Solids, **140**, pp82-86, 1992.
- [9] G. Zhang, M. Poulain and A. Jha, J. Non-Cryst. Solids, **184**, pp72-78, 1995.
- [10] A.N. Gent, Brit. J. Appl. Phys., **11**, pp85-87, 1960.
- [11] A.V. Cardoso and A.B. Seddon, Glass Technology, **30** (5), 1991.
- [12] M.A. DeBolt, A.J. Eastale, P.B. Macedo and C.T. Moynihan, J. Amer. Ceram. Soc., **59** (1-2), pp16-21, 1976.
- [13] P. Baniel, A. Kober, Mat. Sci. Forum, Vol.19, 33, 1987.
- [14] M.P. Bansal, R.H. Doremus and C.T. Moynihan, Mat. Sci. Forum. Vol. 5, 211, 1985.
- [15] P. Baniel, C. Jacoboni and U. Unrau, Mat. Sci. Forum, Vol. 32-33, 601, 1988.
- [16] G.Zhang, J. Jiang, M.Poulain, J.R. Delben and A. Delben, SPIE, Quebec City, Canada, 1998.

PHYSICAL PROPERTIES AND RAMAN SPECTROSCOPY OF GeAs SULPHIDE GLASSES

B.G. Aitken and C.W. Ponader

SP-FR-05, Corning Inc., Corning, NY 14831, USA

ABSTRACT

Ternary GeAsS glasses have been investigated to determine the compositional dependence of selected physical properties. Although the latter show a linear variation with Ge:As ratio at a constant S content, many exhibit a nonlinear dependence on the S content at a fixed Ge:As ratio. The latter trends are consistent with the increasing formation of metal-metal bonds as the S concentration of these glasses is reduced below the stoichiometric value. Raman spectra of these glasses show a consistent evolution as a function of S content. The spectra of stoichiometric and S-excess glasses are dominated by a strong band at 345 cm^{-1} ; those of S-deficient glasses display bands associated with metal-metal bonds between $210\text{--}240\text{ cm}^{-1}$ that become more intense with increasing S deficiency.

INTRODUCTION

Rare-earth-doped chalcogenide glasses are promising materials for a variety of photonic applications, including optical amplification at $1.3\mu\text{m}$ and mid-IR fiber laser sources. The interest in these materials stems principally from their low maximum phonon energy and large refractive index, which result in low multiphonon relaxation rates and large stimulated emission cross-sections, respectively, for certain rare-earth $f\text{--}f$ transitions. Ge-rich sulphide glasses are particularly promising due to their broader transparency in the visible, permitting a greater range of excitation wavelengths, although they are relatively prone to crystallization. This devitrification tendency can be suppressed by partial replacement of As for Ge, resulting in glasses that have sufficient thermal stability to be drawn into optical fiber. Previous work has shown that an extensive glass-forming region exists in the Ge-As-S system [1]. This study was undertaken to determine the compositional dependence of physical properties relevant to fiber fabrication and to elucidate the structural origin thereof.

EXPERIMENTAL

GeAsS glasses were synthesized from the appropriate 36 gram mixtures of elements that had been loaded into fused silica ampoules under dry N_2 . The filled ampoules were evacuated to 10^{-6} Torr, flame sealed, and then heated at 925°C for at least 24 hours in a rocking furnace. Cylindrical 15 cm long glass rods were formed by quenching the hot ampoules in water and subsequently annealing the glass near the glass transition temperature (T_g).

Density was measured in water using the Archimedes method. T_g was determined by DSC at a heating rate of $10^\circ\text{C}/\text{min}$. The viscosity in the vicinity of the softening point (T_s , where viscosity = $10^{7.6}$ poise) was determined by the parallel plate technique using fused silica plates. Thermal expansion to 200°C was measured by dilatometry using Al_2O_3 as a reference. Refractive index was measured by the apparent depth method at 589 nm with

5mm thick samples. Optical absorption in the visible/near IR was measured using a Cary 5 spectrophotometer with a tungsten source. The Raman spectra were collected on an Instruments SA T64000 system using a single monochromator and holographic notch filter for Rayleigh scatter rejection. Scattering was collected in the 90° transmission configuration using 752.5 nm radiation from a Lexel Ramanlon laser. In some of the highly S-deficient samples spectra were collected in a backscattering arrangement due to the high absorption of these samples.

RESULTS

Stoichiometric GeAsS glasses, i.e. glasses whose chemical composition lies along the $\text{Ge}_{.33}\text{S}_{.67} - \text{As}_{.4}\text{S}_{.6}$ join, are characterized by an essentially linear dependence of properties on the Ge:As ratio (cf. Fig. 1). As can be seen in the following table, refractive index (n_D), and density (ρ) both decrease steadily as the Ge content of the glasses increases, whereas the glass transition temperature (T_g) and molar volume (V_{mol}) show a concomitant increase (note that V_{mol} is calculated on a constant atom basis using molecular formulae of the form $\text{Ge}_x\text{As}_y\text{S}_{1-x-y}$). In addition, the absorption edge (λ_{vis} = wavelength where the transmission is 50% of that at 1.0 μm for a 2mm thick sample) of these glasses shifts continuously to shorter wavelength with rising Ge:As ratio.

%Ge (Ge/Ge+As)	n_D	λ_{vis} (nm)	T_g (°C)	ρ (gm/cc)	V_{mol} (cc/mol)
0	2.58		~200	3.187	15.44
33.3		559.5	246	3.027	15.80
50	2.393	553.3	297	2.973	15.89
71.4	2.318	519.3	336	2.885	16.11
100	~2.20	~480	~493	~2.76	~16.5

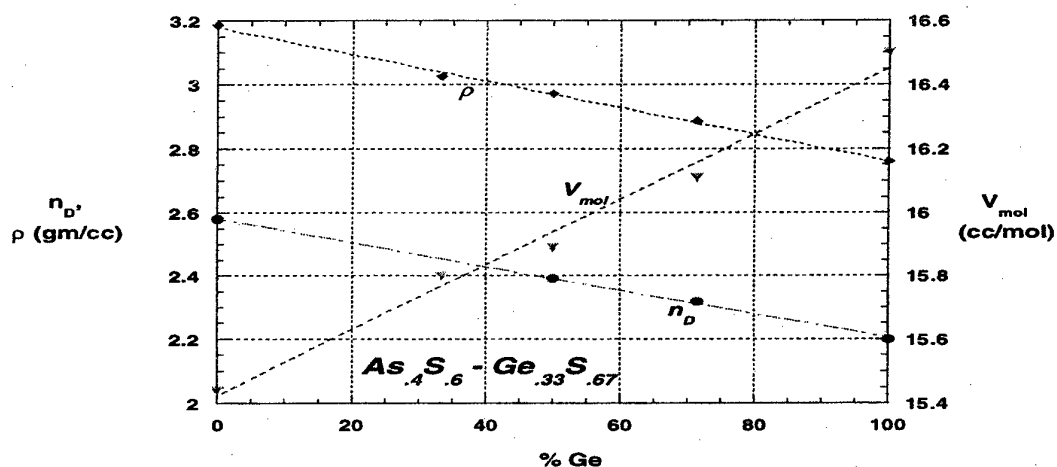


Fig. 1: Compositional dependence of refractive index (n_D), density (ρ) and molar volume (V_{mol}) of stoichiometric GeAsS glasses.

The following table lists properties for glasses with a constant atomic Ge:As ratio of 2.5:1, but with variable S content. In contrast to the behavior of stoichiometric GeAsS glasses, the properties of these glasses show a nonlinear dependence on composition, in this case as a function of S concentration (expressed as "% xs S", which corresponds to the percentage amount of S in excess of the stoichiometric quantity: i.e. $\text{Ge}_{25}\text{As}_{10}\text{S}_{65}$). Data for glasses with lower Ge:As ratios of 1:1 and 1:2 show similar trends as a function of S content.

% xs S	n_D	λ_{vis} (nm)	T_g ($^{\circ}\text{C}$)	T_s ($^{\circ}\text{C}$)	α (ppm/ $^{\circ}\text{C}$)	ρ (gm/cc)	V_{mol} (cc/mol)
20	2.306	523.0	281	414	19.96	2.802	16.01
15	2.309	522.6	295	426	18.53	2.824	16.01
10	2.310	522.6	311	439	17.62	2.844	16.04
5	2.316	518.0	328	456	16.24	2.866	16.06
0	2.318	519.3	336		15.35	2.885	16.11
-5	2.289	536.7	370	493	15.92	2.899	16.20
-10	2.297	551.4	368	490	16.07	2.923	16.24
-15	2.320	575.4	397	508	15.09	2.964	16.20
-20	2.351	598.6		520	13.88	3.005	16.18
-34.2	2.421	635.6	433		11.89	3.168	15.97
-46.2	2.534	702.6	436	512	10.49	3.348	15.73

The data show, for example, that λ_{vis} is essentially constant for S-excess and stoichiometric glasses, but shifts rapidly to longer wavelength as the glasses become increasingly S-deficient. A parallel trend is shown by the variation in n_D . On the other hand, at a given temperature, these glasses show a monotonic increase in viscosity as the sulphur content decreases, as indicated by the steadily rising isokom temperatures, T_g and T_s . Density also shows a steady increase with decreasing S content. However,

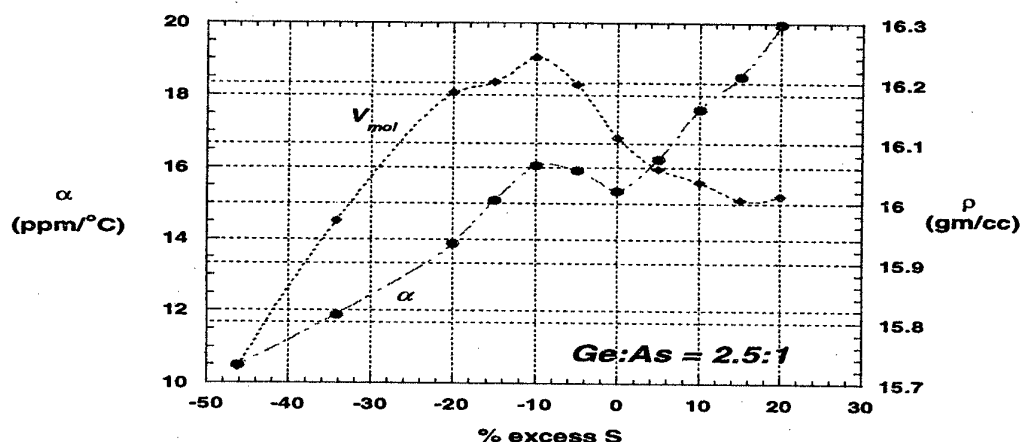


Fig. 2: Variation of thermal expansion coefficient (α) and molar volume (V_{mol}) with S content for ternary GeAsS glasses with Ge:As ratio of 2.5:1.

V_{mol} passes through a maximum in the S-deficient regime at a "xs S" value near -10%. The thermal expansion coefficient also attains a maximal value near this composition (Fig. 2).

The Raman spectra of all of the stoichiometric GeAsS glasses have a major peak at about 345 cm^{-1} (cf. Fig. 3). This peak also has shoulders on the high frequency side at approximately 367 cm^{-1} and 430 cm^{-1} . These shoulders become more pronounced as the Ge:As ratio increases from 1:2 to 2.5:1. Also apparent in the spectra of these glasses are weaker peaks at about 210 , 240 and 490 cm^{-1} . In S-excess glasses, the high frequency peak at 490 cm^{-1} increases in intensity, whereas the 210 and 240 cm^{-1} bands weaken and ultimately disappear with rising S content. As the S content of the glass is decreased below the stoichiometric value, there is a decrease in the intensity of the peaks in the $300\text{--}400\text{ cm}^{-1}$ region; in the most S-deficient glasses, the intensity of the 345 cm^{-1} peak decreases relative to that of the 367 cm^{-1} band. This is accompanied by the appearance of a new peak at approximately 240 cm^{-1} , as well as by an overall increase in intensity of the 210 and 240 cm^{-1} bands. In the 1:1 and 2.5:1 Ge:As glasses, the 240 cm^{-1} band initially strengthens with decreasing S concentration, but is ultimately surpassed by the 220 cm^{-1} band in the most S-deficient glasses. Finally, the 490 cm^{-1} peak observed in the spectra of stoichiometric glasses is not present in those of any S-deficient glass.

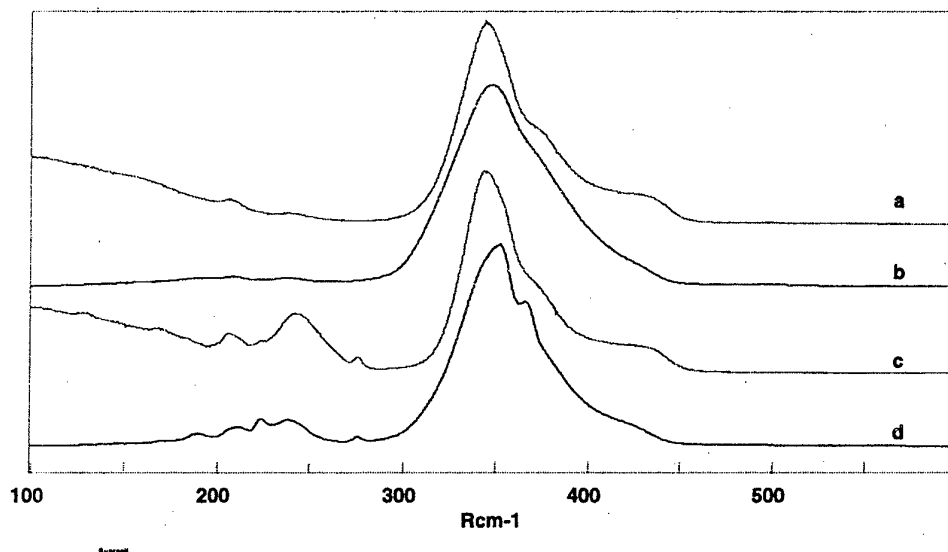


Figure 3. Raman spectra of stoichiometric Ge:As 2.5:1 and 1:2 glasses, a and b, and of -10% xs S 2.5:1 and 1:2 glasses, c and d.

DISCUSSION

The regular increase in n_D and redshift of λ_{vis} with rising As content in stoichiometric GeAsS glasses is expected in view of the higher polarizability, relative to Ge^{4+} , of As^{3+} with its lone $4s$ electron pair. The observed trend in density of the stoichiometric glasses is in agreement with the data of Ma et al. [9]. The greater density of As-rich glasses is, in part, a reflection of increasing average atomic mass. However, as indicated by the molar

volume data, the density of these glasses increases more rapidly than the latter with rising As content, resulting in a concomitant drop in molar volume and suggesting that an AsS_3 -based pyramidal network may be more efficiently packed than its GeS_4 -based tetrahedral counterpart.

For GeAsS glasses with a constant Ge:As ratio, the observed changes in the material properties are dominated by effects that can be attributed to the formation of "wrong", i.e. S-S, Ge-Ge, As-As or As-Ge, bonds. According to the model of binary Ge-S glasses proposed by Lucovsky et al. [3], glasses with S contents in excess of the stoichiometric value contain increasing numbers of S-S bonds and ultimately, at the highest S levels, S_8 rings. Conversely, S-deficient glasses are characterized by the formation of Ge-Ge bonds in the form of $\text{S}_3\text{Ge-GeS}_3$ tetrahedral dimers with falling S concentration. The compositional dependence of properties shown in the previous table suggests that it is reasonable to extend this model to describe these ternary GeAsS glasses. This is particularly supported by the observed variation of λ_{vis} . The latter is essentially constant with changing S content for S-excess glasses, but shifts rapidly to longer wavelengths, suggestive of increasing metallic character, as the S concentration drops below the stoichiometric value.

With regard to the Raman spectra of stoichiometric GeAsS glasses, the principal peak at 345 cm^{-1} is composed of overlapping bands associated with the vibration of AsS_3 pyramids and GeS_4 tetrahedra. The shoulders at 367 and 430 cm^{-1} may be related to Ge-S-Ge vibrations in rings [4] or other extended structures [5]. The high frequency peak at 490 cm^{-1} that is also observed in the spectra of S-excess glasses can be attributed to the formation of S-S bonds. The increasing intensity of this band with rising S concentration in excess of the stoichiometric amount, as well as its absence in the spectra of all S-deficient glasses is consistent with this assignment. The other weak peaks at 210 and 240 cm^{-1} are presumably due to the formation of metal-metal bonds. Peaks at similar frequencies (207 and 238 cm^{-1}) in As_2S_3 have been assigned to the vibrations of As-As bonds [6], and were also reported by Lucovsky et al. [7] in a stoichiometric 1:1 Ge:As glass. Thus, even in the stoichiometric glasses there is some disruption of the presumed network of AsS_3 pyramids and GeS_4 tetrahedra by the formation of "wrong" bonds and this occurs even in the 2.5:1 Ge:As glass where Ge is the predominant metal.

The Raman spectra of all S-deficient GeAsS are dominated by the appearance of bands between 210 - 250 cm^{-1} associated with metal-metal bonding which grow in intensity with decreasing S content. These structural changes are mirrored by the rapid redshift in absorption edge described above for the same glasses. In studies of $\text{As}_x\text{S}_{1-x}$, many of the peaks in the region below 300 cm^{-1} have been ascribed to As-As bonds in various configurations. For example, a peak at $\sim 230\text{ cm}^{-1}$ in the spectra of those glasses was attributed to As-As bonds in the network by Ewen and Owen [6] on the basis of resonance Raman experiments, while peaks around 215 and 180 cm^{-1} may be due to As_4S_4 molecules in the glass [8]. Lucovsky et al. [3] suggested that a broad feature at 250 cm^{-1} in sulfur-deficient $\text{Ge}_x\text{S}_{1-x}$ is associated with Ge-Ge bonds. In the glasses studied here, there is no distinct 250 cm^{-1} feature. However, the peak near 240 cm^{-1} shows an asymmetry towards higher frequency, which may be due to a broad feature centered around 250 cm^{-1} .

In the 2.5:1 Ge:As glasses at low S-deficiencies, the intensity of the 210 and 240 cm^{-1} bands increases more rapidly than the intensity in the 220 cm^{-1} region. However, in the

1:2 Ge:As glasses, the intensity increases first in the 220 cm^{-1} region and, in the 1:1 Ge:As glasses, the intensity appears to increase equally in both regions. These changes suggest that metal-metal bonds form first between the predominant cations in the glass. At the most S-deficient glasses, this effect seems to be reversed. In the 2.5:1 and 1:1 Ge:As glasses, the 220 cm^{-1} region has greater intensity than the 240 cm^{-1} region, whereas the intensity is higher in the 240 cm^{-1} region in the 1:2 Ge:As glasses. Although knowledge of the relative scattering cross-sections of As-As and Ge-Ge would be required to determine it absolutely, these results suggest that at high S-deficiencies a larger fraction of the minority metallic component forms metal-metal bonds than would be expected on the basis of bulk composition.

CONCLUSIONS

Physical properties of stoichiometric GeAsS glasses show a linear dependence on Ge:As ratio. However, at a fixed Ge:As ratio, a highly nonlinear dependence on the S concentration is observed. For example, the absorption edge is essentially insensitive to bulk composition for stoichiometric and S-excess glasses, but undergoes a rapid redshift with decreasing S content. Such a trend is consistent with the increasing formation of metal-metal bonds. This is supported by the Raman spectra of these glasses which show a consistent evolution as a function of S content at constant Ge:As ratio. The spectra of stoichiometric and S-excess glasses are dominated by a strong band at 345 cm^{-1} due to the vibration of GeS_4 tetrahedra and AsS_3 pyramids, with a weaker high frequency peak associated with the development of S-S bonds. Raman spectra of S-deficient glasses are characterized by lower frequency bands that become stronger with decreasing S content, and which are associated with the increased formation metal-metal bonds.

REFERENCES

- [1] R.L. Myuller, G.M. Orlova, V.N. Timofeeva and G.I. Ternova, in *Solid State Chemistry*, edited by Z.U. Borisova (Consultants Bureau, New York, 1966) 232.
- [2] J.A. Savage and S. Nielsen, *Infrared Phys.* 5 (1965) 195.
- [3] G. Lucovsky, F.L. Galeener, R.C. Keezer, R.H. Geils and H.A. Six, *Phys. Rev. B* 10 (1974) 5134.
- [4] R.J. Nemanich, S.A. Solin and G. Lucovsky, *Solid State Comm.* 21 (1977) 273.
- [5] G. Lucovsky, J.P. deNeufville and F.L. Galeener, *Phys. Rev. B* 9 (1974) 1591.
- [6] P.J.S. Ewen and A.E. Owen, *J. Non-Cryst. Solids* 35-36 (1980) 1191.
- [7] G. Lucovsky, R.J. Nemanich, S.A. Solin and R.C. Keezer, *Solid State Comm.* 17 (1975) 1567.
- [8] P.J.S. Ewen, M.J. Sik and A.E. Owen, *Solid State Comm.* 33 (1980) 1067.
- [9] D.S. Ma, P.S. Danielson and C.T. Moynihan, *J. Non-Cryst. Solids* 81 (1986) 61.

Crystallisation in $70\text{Ga}_2\text{S}_3$ - $30\text{La}_2\text{S}_3$ Glasses as a Function of Oxide/Hydroxide Concentration.

S. P. Morgan*, I. M. Reaney, R. Buckley, D. Furniss and A. B. Seddon.

The Centre for Glass Research, Department of Engineering Materials, University of Sheffield, Sheffield, S1 3JD, UK.

The crystallisation of $70\text{Ga}_2\text{S}_3$ - $30\text{La}_2\text{S}_3$ glasses has been studied using x-ray diffraction and transmission electron microscopy. Two of the glasses were prepared from raw materials with nominally different oxide concentrations. The third was prepared from raw materials aged in an oxygen depleted, argon flushed glove box for more than 1 yr. Their oxide/hydroxide/sulphate impurity content was qualitatively ranked using Fourier transform infrared spectroscopy. The lowest oxide content composition ($<0.5\text{wt}\%$, supplied information) devitrified readily close to T_g , forming crystallites of a new phase with a monoclinic Bravais lattice and a lath-like internal structure. Ga_2S_3 was observed in small quantities between the laths. Samples prepared from non-aged, higher oxide content precursors produced the most stable glass. On crystallisation, these samples exhibited spherulites which were composed of laths of $\text{La}_{3.33}\text{Ga}_6\text{S}_{14}$ and the new monoclinic GLS phase in a eutectic or eutectoid-like microstructure. Whiskers of Ga_2S_3 were found in the residual glass between crystallites. Samples prepared from aged raw materials produced spherulites of tetragonal, melilite-structured, $\text{La}_{3.33}\text{Ga}_6\text{S}_{14}$ on crystallisation with no identifiable regions of the new GLS phase.

* Now at, British Nuclear Fuels, Sellafield, Seascale, Cumbria, CA20 1PG, UK.

CRYSTALLIZATION DYNAMICS OF CHALCOGENIDE GLASS THIN FILMS UNDER NON-EQUILIBRIUM CONDITION

Fuxi Gan

Shanghai Institute of Optics and Fine Mechanics,
P. O. Box 800-211, Shanghai 201800, P. R. China.
Email: fxgan@srcap.stc.sh.cn

1. INTRODUCTION

Heat treatment of materials with laser beam has been developed rapidly in recent years. According to the theoretical estimation, the heating and cooling rate up to 10^{14} °C/s can be achieved by very short (ps) pulsed laser, which is much faster than we could get by common methods ($\sim 10^7$ °C/s).^[1,2] Therefore, the phase transition of the laser treated materials is under extra-nonequilibrium condition, and many new phenomena should be happened.

The reversible phase change (crystalline-amorphous) of chalcogenide alloy films irradiated by short pulse laser has been used for rewritable optical data storage. Among the chalcogenide alloy films the Ge-Sb-Te and In-Sb-Te were found to be the most suitable media for rewritable phase change recording. A great number of studies were performed concentrating on write, read and erase performances^[3-5], but not so much works were concerned with the basic understanding the mechanism and the kinetics of the phase change under such non-equilibrium condition. In this paper some of our experimental results of laser induced phase change of chalcogenide alloy films have been reviewed and discussed.

2. METASTABLE PHASE FORMATION AND STRUCTURE CHANGE CHARACTERISTICS

According to our series of research results it is worth noticing that many of the reported fast crystallization, amorphous chalcogenide materials crystallize into metastable phase at first, as shown in table 1.^[6]

The metastable phase are most likely a simple crystal structure, such as a cubic structure, and FCC structure is most favourable. The phase transition from amorphous to a simple lattice structure crystal can be completed by short distance diffusion of the constituent elements. Due to low crystallization activation energy and high entropy of metastable state, therefore, thermodynamically metastable state finally changes to stable phase. For example, in GeSb_2Te_4 it was found that the metastable FCC structure appeared at the first stage in the crystallization process, and finally changed to the stable Hex. structure. The crystallization activation energy for FCC and Hex. GeSb_2Te_4 phase are 1.94 eV and 2.34eV respectively by DSC measurement. Fig.1 gives the high magnification bright field TEM image and electron diffraction (ED) pattern of laser induced crystallization bit in GeSb_2Te_4 thin glass film, irradiated by the 100 ns, 9.6mW pulse of laser, operating at a wavelength of 632.8nm.

One of the most significant finding in our research is that crystallization of some alloy systems prefers to undergo a step-by-step sequence.

Table 1 Metastable phase in chalcogenide films

Compound	GaSb, InSb	In_3SbTe_2	GeTe	GeSb_2Te_4	SnSb_2Te_4	Sb_2Se	TeGeSnAg
Metastable phase	ZnS type FCC	FCC	distorted NaCl type FCC	FCC	FCC	?	Simple cubic

3. TRANSIENT PROCESS OF PHASE TRANSITION

The results of transient phase transition process are helpful to understand the thermal process in the film caused by short pulsed laser irradiation. The temporal reflectivity measurement is a useful method to explore the dynamic process in the thin film. [7] Fig.2 gives the reflectivity change at laser focusing spot of InSb thin film, according to our measurement results (irradiation laser pulse 10ns) the temperature rise time is 25~40 ns (interval b-c, Fig.2), the rising velocity is $1.3\sim2.0\times10^{10}$ K/s. The melting process can be taken place at 10~20 ns time interval (c-d, Fig.2), the liquid-solid (L-S) interface velocity is about $3.4\sim6.8\times10^3$ m/s in the melting process. The reflectivity drops, when resolidification occurs (d-e, Fig.2). The L-S interface velocity is $1.4\sim6.8\times10^2$ m/s in resolidification process. From here we can see that the melting speed is much faster than the resolidification speed.

The simple thermal melting—recrystallization model for laser induced phase change can be accepted. We here used an equation, which was based on an one-dimensional heat flow model. It is assumed to fit a thin film case. The computer simulated temperature rising profiles of $\text{Ag}_8\text{In}_{13.5}\text{Te}_{22.8}\text{Sb}_{55.7}$ film irradiated by laser beam with 10 mW laser power and 300ns pulse width are shown in Fig.3.

The increasing of peak temperature and widening of heated region with the heating time is obvious. The temperature reaches over 1200°C after the duration of 240ns. It leads to the inhomogeneous heating in the focusing. That is, the high centre peak temperature can lead to not only melt the materials, but violent splashing hence heavy tension or recoil pressure as well. The size of the hole may roughly represents this violently splashed region while the whole spot can be regarded as the irradiation effected area. It has also been observed that amorphous and crystalline phases can both present in the different part of the same irradiated spot in a long pulse irradiation. There must exist a certain region in the irradiated area where the rising temperature is between the materials phase transition temperature T_p and the melting temperature T_m , here the crystallization takes place.

Fig.4 shows the TEM image and ED pattern of laser irradiated bit of In-Sb-Te glass film. The central region is amorphous due to high temperature, the surrounding area is crystalline, the temperature at this area is between T_m and T_p . To achieve a fast amorphous-to-crystalline phase change, a careful choice of laser parameter is very critical although the materials itself is most important. To shorten the pulse duration for the crystallization, a fast crystallization property or low crystallization activity energy of the materials is required. One approach is to use the amorphous to metastable crystalline phase transition.

4. ACCELERATION OF CRYSTALLIZATION SPEED

For phase change (P-C) recording writing the crystalline state transforms to amorphous, therefore, the lifetime of data storage is related to the thermal stability of amorphous state of the P-C media. But for high speed erase, the amorphous state should be rapidly crystallized. This is the contradiction for choosing the chemical composition of P-C media. We proposed a concept on high speed erase and high stability of erasable P-C films. The elements with small values of T_g/T_m are found to be favourable to acceleration of erase speed of recording films, that means high crystallization speed, while those with large values of T_g are found to be useful to improvement of stability of the recording domain at amorphous state at room temperature. Therefore the elements with small values of T_g/T_m and large values of T_g can be used to enhance both the erase speed and stability. Table 2 lists the T_g and T_g/T_m values of some elements.

It can be seen that doping some elements with large T_g and low T_g/T_m values, such as Co, Cu, can accelerate the crystallization speed and improve the stability of glass state at room temperature. Table 3 shows the activation energy of crystallization (ΔE_a) of some chalcogenide thin films, the doping effect of Cu, Co is rather obvious.

Table 2 T_g , T_g/T_m values of some elements

element	Sb	Ag	Cu	Co	Pb	Te	Ge
T_g (K)	180	250	298	445	152	285	750
T_g/T_m	0.2	0.2	0.22	0.25	0.25	0.39	0.62

Table 3 Crystallization activation energy of some amorphous semiconductor films

composition	$\text{In}_{58}\text{Se}_{42}$	$\text{In}_{58}\text{Se}_{23}\text{Pb}_{19}$	$\text{In}_{58}\text{Se}_{23}\text{Pb}_{11}\text{Cu}_8$	$\text{In}_{58}\text{Se}_{23}\text{Pb}_{11}\text{Co}_8$
ΔE_a (eV)	1.20	1.61	2.90	3.64

5. CONCLUSION

The extremely quick heating and cooling process can be achieved by short pulse laser irradiation. The phase change of glass thin film materials is under extra-nonequilibrium condition, and takes place in sub-microsecond range. Metastable phases are always appeared in chalcogenide glass films during pulse laser induced crystallization process. Laser induced phase change in sub-micrometer domain is inhomogeneous. For achieving fast and homogeneous laser recording by amorphous to crystalline phase change, laser source with shorter pulse duration and lower power is needed. Some metallic elements doping in chalcogenide alloy films can accelerate the crystallization speed and stabilize the glass state.

REFERENCES

- [1] P. L. Lin, R. Yan and N. Bloembergen, Appl. Phys. Lett. 34 (1979) 864.
- [2] Fuxi Gan and Hao Wang, Bull. Chinese Sciences, 29 (1984) 1606.
- [3] M. Chen, K. A. Rubin, Marelo, U. G. Gerber and V.B. Jipson, Appl. Phys. Lett., 46 (1985) 734.
- [4] Fusong Jiang, Lisong Hou, Fuxi Gan and M. Okada, Jap. J. Appl. Phys. 28 (1989) 293.
- [5] Fuxi Gan, Proceedings SPIE, 1519 (1991) 530.
- [6] Fuxi Gan, Songsheng Xue and Zhengxiu Fan, Annalen der physic, 1 (1992) 392.
- [7] Yang Sun, He Deng and Fuxi Gan, Jap. J. Appl. Phys. 26 (1989) 291.

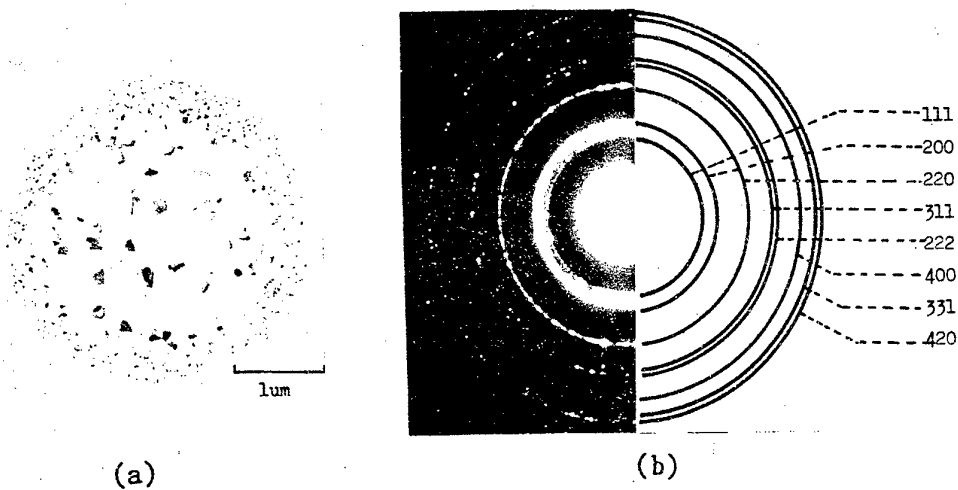


Fig.1 TEM image and ED pattern for the laser crystallized bit,
irradiated by a 100ns, 9.6mW laser pulse.

(a) TEM image (15400×); (b) ED pattern (camera const.: 34.384 mm · Å)

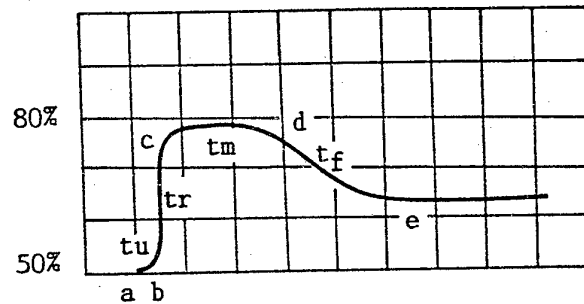
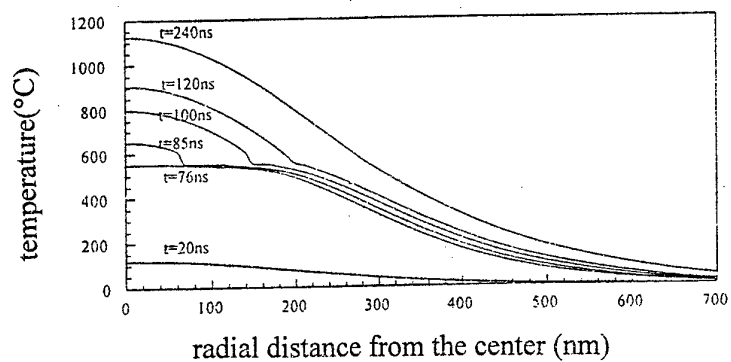
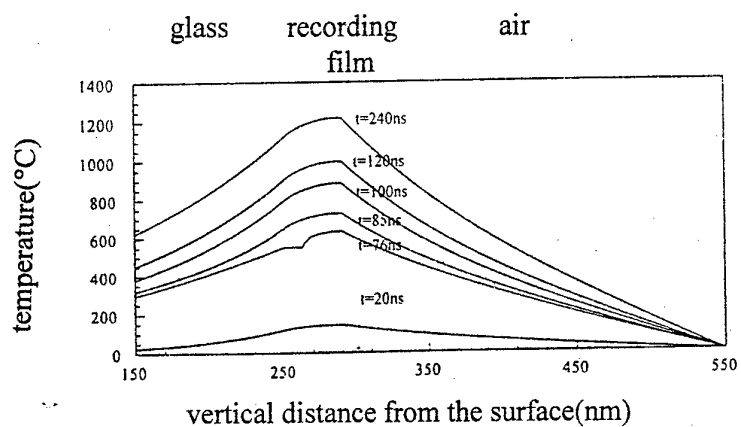


Fig.2 The transient reflectivity change of InSb film



(a)



(b)

Fig.3 Radial (a) and vertical (b) temperature distribution of the laser irradiated spot (bit) during heating with laser power 5mW and pulse duration 300ns

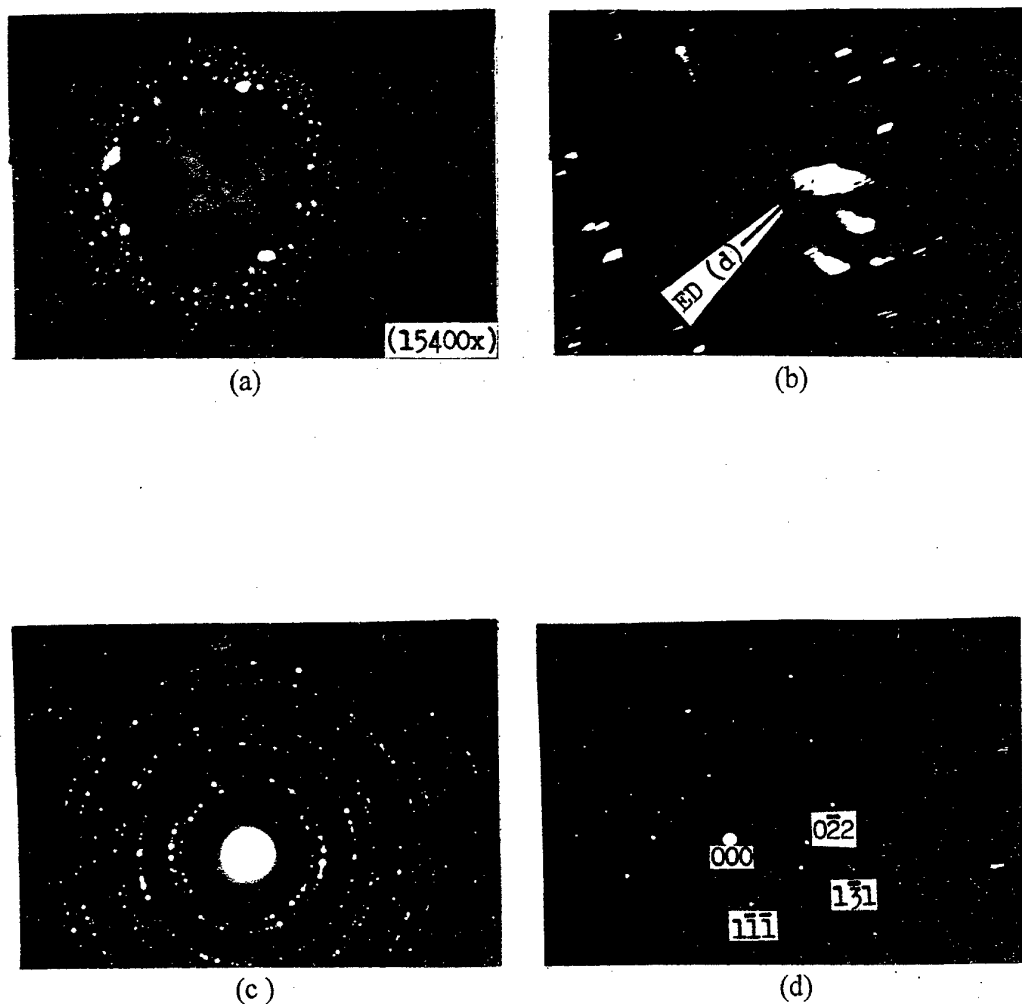


Fig.4 Shows the high magnification TEM images and ED patterns for the laser-crystallized bit irradiated by 200ns, 16mW laser pulse.
 (a) bright field TEM image; (b) dark field TEM image;
 (c) ED pattern of the bit; (d) single crystal ED mark for the biggest crystal shown in (b)

PHOTOINDUCED ACTIVE AND PASSIVE INTEGRATED-OPTIC ELEMENTS IN RAPID THERMALLY ANNEALED CHALCOGENIDE GLASSES

S. Ramachandran and S.G. Bishop

Microelectronics Laboratory, Dept. of Electrical Engineering
University of Illinois, Urbana, IL 61801, USA. email sid-r@uiuc.edu

ABSTRACT

Rapid thermal annealing of sputtered chalcogenide glasses yields films with enhanced photosensitive properties while tackling thermal stress related problems that have inhibited progress of thin film chalcogenide glass systems as candidates for photonic integrated circuits. Index changes of up to 5% are demonstrated. The superior quality of the films yields low loss ($\alpha \sim 0.27$ dB/cm) channel waveguides. The large index changes and high photosensitivity of this system are exploited to fabricate an index tapered waveguide for spot-size conversion. Investigation of Er doped chalcogenide glass films has revealed a novel, broad excitation band that arises from coupling between the mid gap states of the host glass and $4f$ shells of the Er ion. This allows novel pump wavelengths as well as geometries for pumping an Er doped planar waveguide.

INTRODUCTION AND BACKGROUND

Optical elements for applications in communications and interconnections such as waveguides and grating devices can be patterned in chalcogenide glasses by illumination with above band gap light, which causes photodarkening[1]. Photodarkening is a photo-induced red shift of the optical absorption edge and is accompanied by an increase in the index of refraction in the transparent spectral range below the absorption edge. A configurational model[2] describes photodarkening as an illumination induced transformation from a stable configuration to a quasi-stable configuration via an electronically excited state. Annealing close to the glass transition temperature (T_g) causes a direct structural relaxation from the quasi-stable to stable state.

A sputtered film of chalcogenide glass is in a quasi-stable state in the as-deposited form and closely corresponds to the photodarkened (PD) state. To utilize the photodarkening property and fabricate photonic devices, it is necessary to first change the film to its stable state from the as-deposited, PD state. This transition may be induced by either direct thermal annealing under an inert atmosphere[3] or by illuminating the film with high intensity light that causes local heating to give the same effect[3,4], called photobleaching. The optical annealing process will require uniform high intensity illumination over the film and is not technologically feasible. More importantly, illumination also contributes to photodarkening and thus competes with the photobleaching process. Chalcogenide glasses have high coefficients of thermal expansion (CTE) and thus thermal annealing must be performed with very low temperature gradients in order to avoid cracking the films due to thermal stress. Still, the quality of the film will depend on the CTE of the substrate, limiting the integration of these films with other opto-electronic devices.

RAPID THERMALLY ANNEALED FILMS OF CHALCOGENIDE GLASSES

We have demonstrated the use of Rapid thermal annealing (RTA) in obtaining high quality films of sputtered $\text{Ge}_{10}\text{As}_{40}\text{Se}_{25}\text{S}_{25}$ glasses. Bertolotti *et. al.*[4] have demonstrated that the electronic relaxation process has a 1-2 second time scale and thus a thermal anneal process of only a very short duration is needed for relaxing the glass structure. RTA has the advantage of providing just this kind of a thermal spike without allowing time for crack initiation due to thermal expansion to set in, eliminating the thermal stress problems with conventionally annealed chalcogenide glass films.

Fig. 1 contrasts SEM micrographs of a conventionally annealed chalcogenide film (Fig. 1(a)) with that of an RTA sample (Fig. 1(b)). The glass cracks under thermal stress and then reflows to trap N_2 bubbles in the film when conventionally annealed, as shown in Fig. 1(a), while RTA yields excellent surface smoothness (Fig. 1(b)).

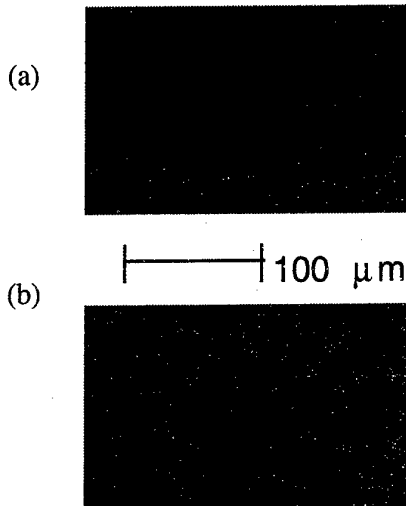


Fig. 1 SEM of films annealed at 235 C.
(a) Conventional oven anneal; (b) RTA
RTA yields films with excellent surface smoothness.

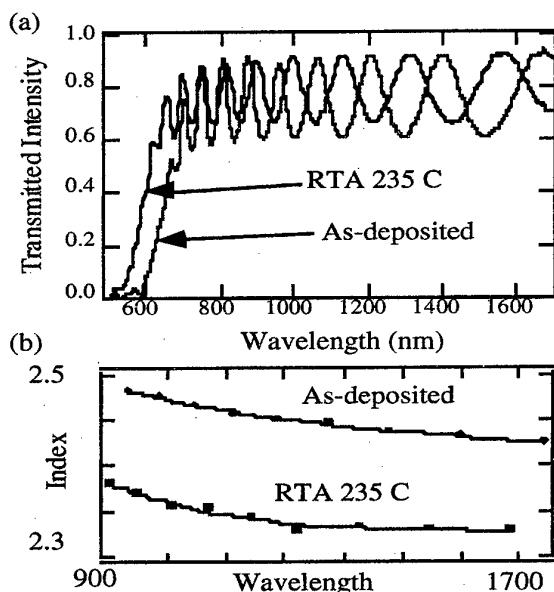


Fig. 2 (a) Transmitted intensity vs wavelength
(b) Index calculations. 5% photoinduced index changes possible.

Films for optical transmission measurements were 1.7 μm thick and were deposited on microscope glass slides. Figure 2(a) is a plot of the transmitted intensity as a function of wavelength for an as-deposited and RTA'ed sample respectively. A clear blue shift in the Urbach edge occurs when the sample is RTA'ed. The interference fringes at the transparent wavelengths can be used to extract the index of refraction for the film. Results from this calculation for as-deposited and RTA'ed films are plotted in Fig. 2(b); the index changes by 5% over the entire wavelength range, 900 - 1600 nm. Since the as-deposited films are similar to the photodarkened state, we infer that photoinduced changes as high as 5% are possible in RTA'ed chalcogenide glasses. This is twice the maximum change reported by Tada *et. al.*[5] and we attribute the difference to a more stable, lower index film due to RTA. The large index changes

indicate that these glasses are good candidates for high density optical interconnects.

Films deposited on cover glass substrates were used to characterize the efficiency of the PD process by holographic grating exposures. Spatially collimated light from an Argon ion laser at 514.5 nm was split and recombined at the film surface to fabricate 1 μm period gratings. Fig. 3 is a plot of the diffraction efficiency versus exposure time and we find that an index change of 0.001 (0.05%) is achieved with a 1 min. exposure. Fig. 3 indicates that longer exposures decrease the modulation depth of the gratings, possibly due to vibrations in the holographic set up and back reflection problems. Since up to 5% index changes are possible in RTA films of $\text{Ge}_{10}\text{As}_{40}\text{Se}_{25}\text{S}_{25}$ glass, the use of a phase mask and appropriate substrate will make possible the fabrication of much stronger gratings.

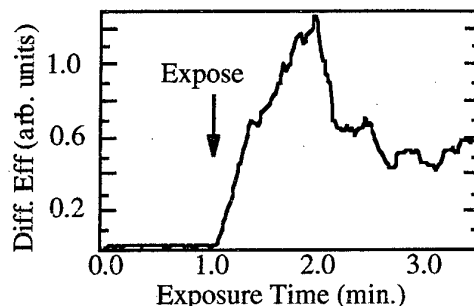


Fig. 3 Diffraction efficiency vs exposure time. $\Delta n \sim 10^{-3}$ in 1 min. exposure.

PASSIVE WAVEGUIDES AND DEVICES

Chalcogenide glass films for channel waveguides were sputtered on films of one micron thick SiN_x pre-deposited on Si wafers. The PECVD deposited SiN_x film has a refractive index of 2.2 in the 1500 nm range and serves as the bottom cladding layer separating the higher index Si substrate from the chalcogenide glass films ($\text{Ge}_{10}\text{As}_{40}\text{Se}_{25}\text{S}_{25}$ glass: $n \sim 2.3$ to 2.5, depending on dosage of photoinducing light). The glass film thickness was restricted to one micron to ensure single mode operation vertically. Horizontal confinement was achieved by exposing the films to spatially filtered and collimated Argon laser light at 488 nm, through an appropriately patterned mask. The resulting waveguides were excited by end-fire coupling light from a diode laser operating at 1566 nm or from a tunable laser operating between 1480 and 1570 nm. The excited mode patterns were obtained by imaging the output facet on to an IR Vidicon camera and the mode intensities were measured with a Ge PIN detector.

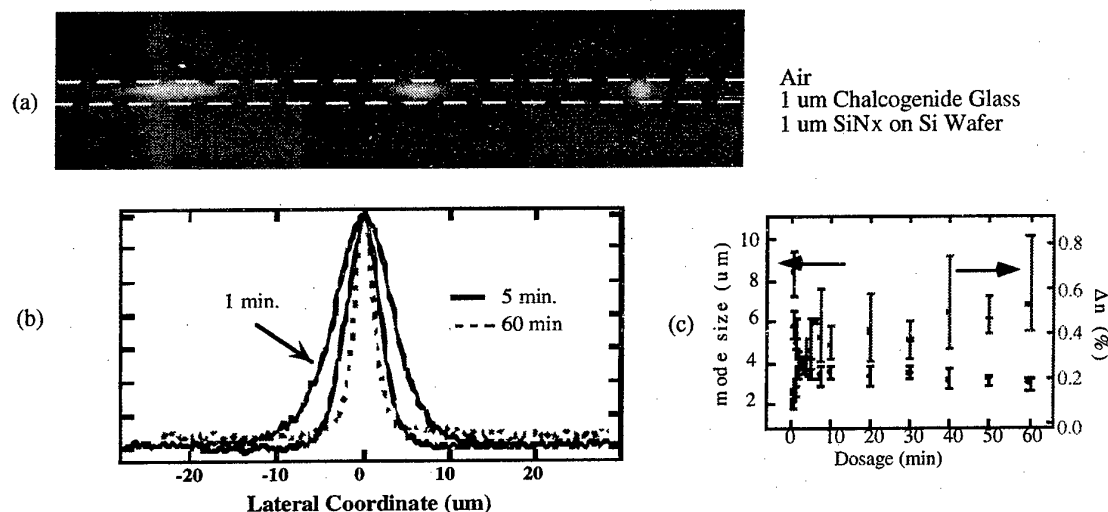


Fig. 4. Mode size control with exposure. (a) Output facet images of waveguides exposed for 1, 5 and 60 min. with 300 mW/cm^2 of 488 nm light from an Ar ion laser. (b) Mode profile intensity plots. (c) Variation of mode size and guide effective index with inducing light dosage. Guides excited by end-fire coupling 1566 nm light from a laser diode.

Waveguide losses were measured by performing Fabry-Perot resonance measurements over channel waveguide cavities of lengths ranging from 600 μm to 1000 μm . The losses in the waveguides can be calculated by measuring the ratio of the maxima and minima of the transmitted intensity for guides of different lengths. The calculated losses were 0.27 dB/cm

which is, to the best of our knowledge, the lowest loss figure reported[6] for planar waveguides in chalcogenide glass films. We believe that the RTA process is primarily responsible for decreasing interfacial stresses between the glass film and SiN_x cladding, thereby yielding low loss channel waveguides.

A mask with 2 μm wide lines was used to fabricate waveguides with exposure times ranging from one to 60 min. Figures 4 (a) & (b) (previous page) show that the lateral mode size changes from 10 μm for a 1 min. exposure to 3 μm for a 60 min. exposure. A typical photonic integrated circuit (PIC) would have components whose mode-sizes range from 3 μm (diode laser) to 10 μm (single mode fiber), and since this entire range is accessible for photoinduced waveguides in chalcogenide glasses, this technology would provide an attractive platform to build PICs. Also, spot sizes as small as 3 μm will allow interconnection densities as high as 2500 lines/cm with negligible crosstalk due to mode coupling. Fig. 4 (c) shows the variation of the mode size as function of exposure time for the aforementioned guide. The effective index method was used to extract the index change as a function of exposure time and Fig. 4 (c) indicates that the effect has not yet saturated, consistent with transmission measurements (Fig. 2) that revealed that index changes of up to 5% are possible.

We have used the large dynamic range of index changes possible in these films, to demonstrate an index tapered waveguide, whose guided mode size changes along the direction of propagation. The fabrication procedure involved adding a linearly varying neutral density filter in the beam path of the waveguide exposure scheme described earlier. This resulted in a variation of inducing light dosage along the waveguide pattern on the mask, leading to an index taper along the waveguide.

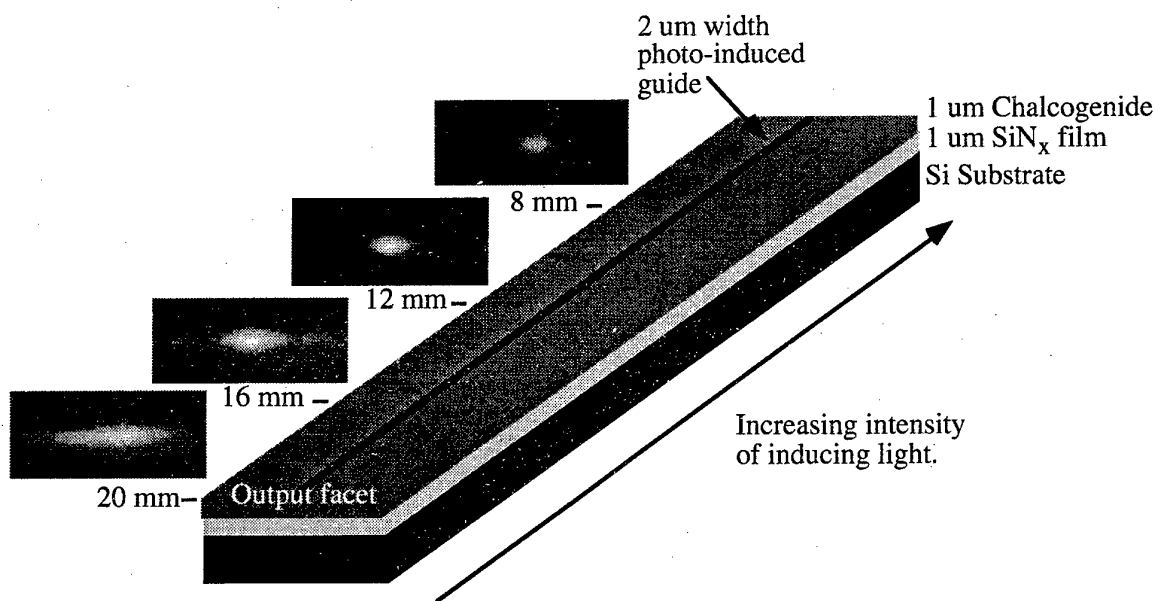


Fig. 5. Schematic of index tapered waveguide with mode profile images along the guide obtained by the cut-back technique.

Figure 5 (previous page) shows a schematic of the photoinduced waveguide, and the mode profiles at different longitudinal positions along a 20 mm long x 2 μm wide x 1 μm thick waveguide. The dosage of inducing light was constant at 846 J/cm² for 4 mm from the input end and thereafter, monotonically decreased to 233 J/cm² by the output end. The near field images of the guided mode shown in Fig. 5 clearly indicate that the mode size increases as the mode propagates away from the input facet. Figure 6 is a plot of the lateral mode size (1/e width) versus distance from the input facet, for the aforementioned guide. The most dramatic change in the mode size occurs for less confined modes, away from the input facet. The lateral mode size changes from 2.61 μm , 12 mm away

from the input facet, to 6.82 μm farthest away from the input facet (20 mm), translating to a spot-size conversion by a factor of 2.6 within a distance of 8 mm. Over the entire device length of 16 mm, the mode size changes by a factor of 3. The index contrast at different positions along the waveguide was extracted from the measured mode sizes using the effective index approximation, and was used to estimate the taper losses of this device. A beam propagation method simulation showed that the taper losses were below 0.1 dB for the 8 mm long tapered waveguide.

This fabrication technique eliminates the need for multi-step etching and developing processes common in defining tapers. The ease of fabrication, and the ability to sputter these glasses on any semiconductor substrate, makes this technology attractive for monolithic integration of tapers with semiconductor laser diodes, for efficient chip-to-fiber coupling.

ERBIUM DOPED FILMS FOR ACTIVE APPLICATIONS

Erbium doped films of these glasses were obtained by sputter deposition from a melt quenched target of Ge₁₀As₄₀Se₂₅S₂₅ glass with 0.5 wt% Er₂S₃ powder mixed in it. Photoluminescence (PL) and Photoluminescence Excitation (PLE) spectra reveal that in addition to the expected atomic absorption lines for Er, a broad excitation range exists[7] due to energy transfer between the photoexcited carriers of the host glass and the Er ions. This broad band PLE enables the excitation of the ~1550 nm Er PL with only a few microwatts of optical power, in the transverse geometry (normal incidence), with a sample thickness of only one micron. This capability could enable a variety of novel pumping schemes for rare earth-doped chalcogenide glass amplifiers and lasers.

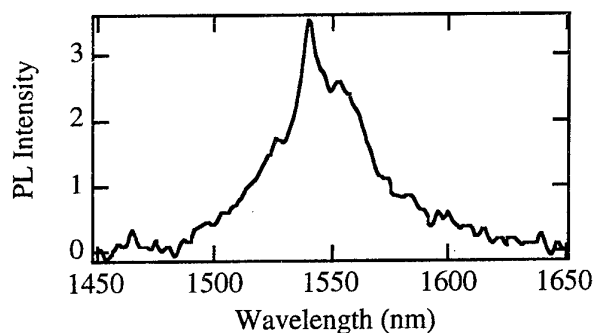


Fig. 7. PL lineshape of Erbium doped sputtered glass films. Pumped with 560 nm light from a xenon-lamp monochromator system.

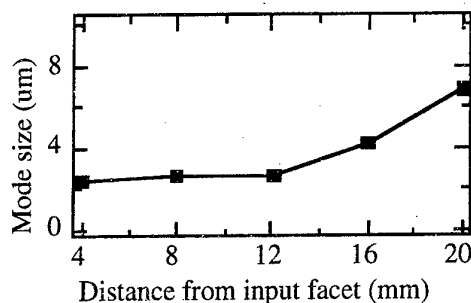


Fig. 6 Mode size evolution along the tapered waveguide. Mode size changes by factor of 2.6 over 8 mm taper.

Figure 7 shows the broad 1500-1600 nm $^4I_{13/2} \rightarrow ^4I_{15/2}$ Er³⁺ PL spectrum excited by 560 nm light from the xenon lamp-double monochromator system, for an as-deposited, sputtered film of Er-doped As₄₀Ge₁₀Se₂₅S₂₅ glass. The broad Er³⁺ PL spectra from the sputtered films are devoid of any sharp line Er³⁺ PL spectra characteristic of Er in a crystalline environment, indicating that the Er ions have been incorporated in the glassy film.

Figure 8 compares the line shapes of the Er^{3+} PLE spectra obtained in a sputtered Er-doped film, before and after the RTA process, and from the Er-doped bulk glass. Note that the peaks attributable to the direct Er^{3+} intra-4f shell absorptions at 980 and 810 nm are not observed in the PLE spectra of the Er-doped sputtered film. This is because only microwatts of pump power were used to excite a film that was only one micron thick. In contrast, a strong peak in 1550 nm fluorescence is observed in regions where the pump wavelength is highly absorbed by the host glass. This broad band excitation mechanism is attributed to optical absorption in the Urbach edge of the host glass, followed by carrier localization at native defects in the glass, and subsequent nonradiative energy transfer from the defects to the rare earth atoms[8]. The peak energy of the PLE is therefore expected to shift or track with the band gap of the host glass, and the "blue shift" in the PLE peak from the Er-doped sputtered film after the RTA process is consistent with the blue shift in the band gap (absorption edge) induced by the RTA (Fig. 2).

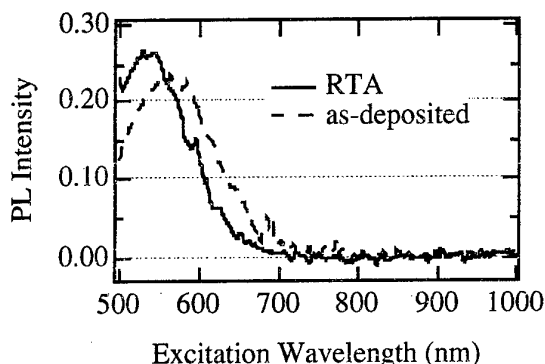


Fig. 8. Excitation spectrum. Detecting 1540 nm light as a function of pump wavelength.

ACKNOWLEDGMENTS

The authors would like to thank G.C. Papen, J.S. Sanghera and P.C. Taylor for many helpful discussions. This work has been supported by DARPA under the Center for Optoelectronic Science and Technology (Grant #MDA972-94-1-0004) Program.

References

- [1] Y. Utsugi and Y. Mizumisha, *Jpn. J. Appl. Phys.* **31**, Pt. 1, 3922 (1992).
- [2] G. Pfeiffer, M.A. Paesler and S.C. Agarwal, *J. Non-Cryst. Solids* **130**, 111 (1991).
- [3] T. Igo and Y. Toyoshima, *Supplement J. Jpn. Soc. Appl. Phys.* **43**, 106 (1974)
- [4] M. Bertolotti, F. Michelotti, V. Chumash, P. Cherbari, M. Popescu and S. Zamfira, *J. Non-Crystalline Sol.* **192&193**, 657 (1995).
- [5] K. Tada, N. Tanino, T. Murai, M. Aoki, *Thin Solid Films* **96**, 141 (1982).
- [6] S. Ramachandran and S.G. Bishop, submitted to *Appl. Phys. Lett.*
- [7] S. Ramachandran and S.G. Bishop, accepted for publication in *Appl. Phys. Lett.*
- [8] D.A. Turnbull and S.G. Bishop, *J. Non-Cryst. Sol.*, **223**, 105 (1998).

DESIGN AND FABRICATION OF PZG FLUORIDE GLASS CHANNEL WAVEGUIDES: THE STATE OF THE ART

**Y. Gao^(a), B. Boulard^(a), M. Lemiti^(b), R. Rimet^(c);
P. Loeffler^(d) and H. Poignant^(e)**

^(a) Laboratoire des fluorures, UPRES 6010, Faculté des sciences, Université du Maine, 72085
Le Mans Cedex 9, France. email brigitte.boulard@fluo.univ-lemans.fr

^(b) INSA, Bat. 502, 20 avenue A. Einstein, 69621 Villeurbanne, France.
email lemiti@insa.insa-lyon.fr

^(c) Laboratoire d'électromagnétisme micro-onde et optoélectronique, URA 833
ENSERG, BP 257, 38016 Grenoble Cedex France

^(d) P. LOEFFLER, Robert Bosch GmbH, dep. FV/FLD
Postfach 10 60 5070049 Stuttgart, Germany

^(e) France télécom, CNET Lannion, DTD/TSO Technopole Anticipa,
BP40 - 22307 Lannion, France. email poignant@lannion.cnet.fr

ABSTRACT

This paper describes rare earth doped PZG channel waveguides produced via mechanical, chemical and photosensitivity techniques. The geometry of the channel waveguides have been investigated and the near field pattern and optical loss have been measured.

1. INTRODUCTION

The development of integrated optical amplifiers or lasers opens a wide range of applications in telecommunication. Among all the glassy matrices, the fluoride glass host has significant advantages owing to decreased phonon energy and higher solubility for rare-earth dopants [1]. The lower phonon energy spectrum enables radiative transitions within rare earth ions which are quenched in other materials.

Optical glass channel waveguides can be fabricated by various techniques, such as vapor phase deposition, ion exchange, sol-gel synthesis [2,3,4]. The ability of rare earth doped PZG fluoride glass ($\text{PbF}_2\text{-ZnF}_2\text{-GaF}_3$) to be evaporated is attractive for applications in integrated optics. We have tested different techniques for achieving PZG glass channel waveguides: saw-cut, UV writing and photolithography.

- The mechanical profiling of the substrate prior to thin film deposition can be realized with a high precision wafer sawing machine.
- PZG thin films exhibit high photosensitivity both when doped with rare-earths and not [6]. The UV induced refractive index increase $\Delta n = 0.01$ is close to the one observed for hydrogen loaded germanosilicate fiber, the highest photosensitive material. A densification process can explain the refractive index modulation. Such a large Δn suggests the possibility of UV patterning of channel waveguides in PZG thin films.
- Photolithographic processes that are employed for silicon, silicate glasses are now standardized; they have been transferred and adapted to fluoride glasses [5].

2. EXPERIMENTAL

All the experiments are carried out in a clean room. The physical vapor deposition is conducted at 600°C under vacuum in a graphite crucible, and the PZG thin film is deposited on the substrate heated at 180°C. Rare earth doping of the thin film is made by coevaporation of PZG glass and rare earth fluoride at 1000-1100°C, depending on the doping rate and the rare earth. The typical thickness is 2-3µm for a 15 minute deposition, and the thin film is composed of roughly 37%PbF₂-21%ZnF₂-42%GaF₃ in mole %; the refractive index is about 1.58-1.59. The substrates are either CaF₂ single crystals or ZBLAN plates; the CaF₂ substrates are cleaved along the (110) plane and the ZBLAN end faces polished after thin film deposition to allow side light injection.

A short description of the different waveguides elaboration techniques is given below.

2.1. Mechanical sawing

We have used a high precision wafer sawing machine with an accuracy in parallelism lower than 1µm and resin bonded blades which is coated with synthetic diamonds of grit sizes lower than 3µm. The blade position can be adjusted better than 2µm vertically and laterally. Two parallel cuts, 100µm deep, 100µm large and separated by 10 µm, are sawed on a CaF₂ substrate. The cross section of the strip waveguide obtained after PZG thin film deposition should be 2x10µm².

2.2. U.V. laser writing

The UV laser is a frequency doubled argon ion laser system (FRED) operating at 244nm and delivering output powers up to 100mW. The focused UV beam (spot size 30x800µm²) is translated parallel to the surface of the sample: the speed of the spot varies from 1 to 4.5µm/s. The expected width of the channel waveguide is thus 30µm. The sample was a 0.3mole% ErF₃ doped, 3.5µm thick PZG thin film grown on a CaF₂ substrate. A scheme of the complete experiment is given in reference [7].

2.3. Photolithography and wet etching

The substrate, a ZBLAN polished plate, is spin coated with a photoresist and then exposed to UV light through a negative mask. After development, resist strips from 60 to 120µm separated from 1 to 80µm are obtained. The wet etching is performed under strong stirring by means of 0.4M ZrOCl₂-1M HCl attack solution for 4 minutes at 20°C. After the resist removal, a second attack is made (9mn at 5°C) in order to smooth and make more regular the resist edges. Finally, the PZG film is deposited on the top of the etched substrate.

The main steps of the process are shown on Fig. 1.

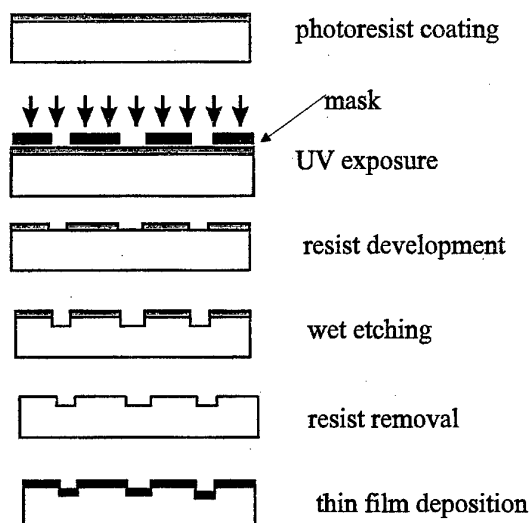


Fig.1: photolithography and wet etching process for channel waveguide fabrication

2.2. "Liftoff" photolithography

As in the first method, the substrate (CaF₂ plate: 10x20mm²) is coated with a photoresist. The resist is hardened (2mn at 120°C) on a heating plate, exposed to UV light, hardened again and developed. The "cap shape" expected resist profile allows the resulting deposited film to be noncontinuous between resist top and groove bottom. Different resists and thicknesses (from 2 to 4µm) have been tested to get the best profile for the strips.

During deposition, the substrate has to be kept at 60°C, to avoid any deformation of the resist. After this, the resist is dissolved with acetone in an ultra-sound tank.

A summary of the procedure is shown on Fig. 2.

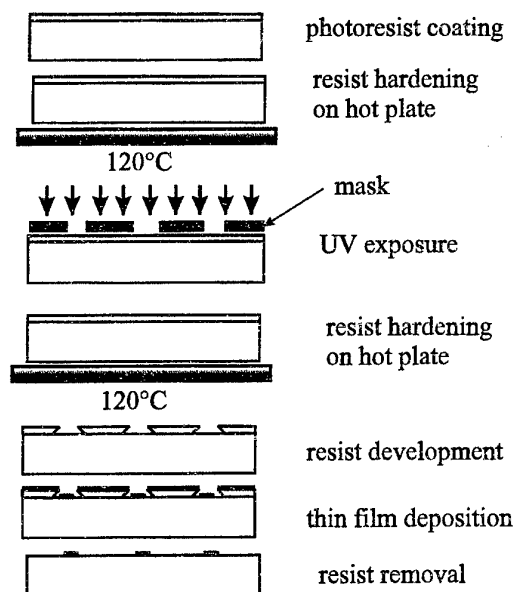


Fig.2 : photolithography and lift off process for channel waveguide fabrication

The near field pattern of the channel waveguides has been analyzed at 0.63µm with a camera connected to a video console. The He-Ne laser is injected in the end face of the channel waveguide using a single mode optical fiber. The fiber-guide coupling is optimized with a piezo-translation stage.

The propagation losses of the channel waveguides have been measured at 1.48µm using the OEC (Optimum End fire Coupling) method that consists of a double pass of the light.

3. RESULTS AND DISCUSSION

3.1. mechanical sawing

Fig. 3 shows the geometry of the substrate after sawing and the near field pattern of the channel waveguide. As can be seen on the right picture, the thin film is well localized at the top of the rib. Actually, the depth of the saw cut could be reduced to 10 or 20µm.

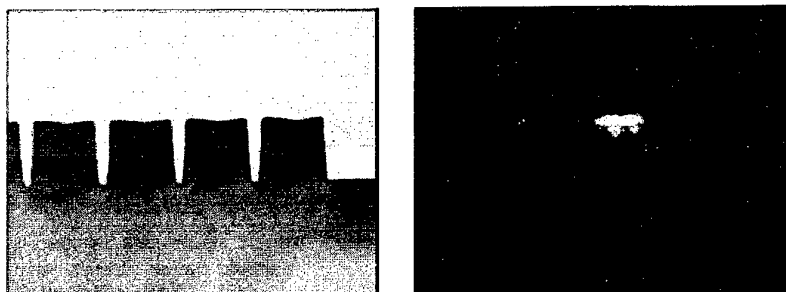


Fig. 3: side view of the substrate (light area) after saw cuts 100µm deep separated by 10µm, (left picture) and near field pattern of the channel waveguide created at the top of the rib at 0.63µm (right picture).

3.2. U.V. laser writing

The best confined channel waveguide, shown on Fig.4, was obtained for the highest fluence, i.e. the energy received per surface unit ($333\text{kJ}/\text{cm}^2$): the translation speed was $1\mu\text{m}/\text{s}$ and the UV spot power 100mW giving an irradiance of $420\text{W}/\text{cm}^2$. It appeared that for the same irradiance, the confinement was less for longer exposure: thermal diffusion induces an enlargement of the written waveguide, decreasing the confinement. The observed width of the channel is close to the beam width ($30\mu\text{m}$). Narrower channel waveguides may thus be achieved by reducing the spot size.

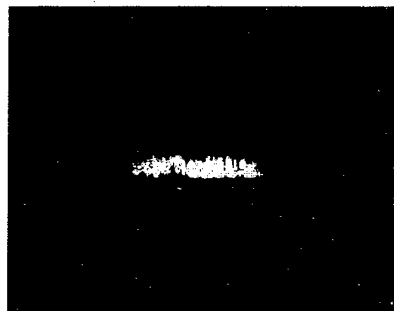


Fig. 4: near field pattern of a UV written channel waveguide ($30 \times 3.5\mu\text{m}$) at $0.63\mu\text{m}$

3.3. Photolithography and wet etching

We find that only the thin films deposited on the embossements can propagate light. The ZBLAN surface has lost its optical polishing at the bottom of the channel where the substrate was etched. Fig. 5 shows the near field pattern of two channel waveguides, the channel width varies from 1 to $80\mu\text{m}$; the smallest one we could fabricate is $10\mu\text{m}$ wide. In the left picture of Fig. 5, we can see that the confinement is not perfect, some light is injected in the thin film deposited on the grooves. The width of the embossment could be reduced to a few microns by increasing the time of the second attack but the walls would then be too smooth.



Fig. 5 : near field pattern $0.63\mu\text{m}$ of two channel waveguides at $0.63\mu\text{m}$ fabricated by wet etching. The cross sections are $50 \times 2\mu\text{m}^2$ (left picture) and $10 \times 2\mu\text{m}^2$ (right)

3.4. "liftoff" photolithography

Fig. 6a shows the best resist profile we could obtain, the resist wall being vertical. It appears that the resist has to be as twice as thick as the deposited film i.e. $4\mu\text{m}$, otherwise the step is not high enough to allow the film to brake at the top of the groove. The smallest channel width is $5\mu\text{m}$ (Fig. 6b); the adherence is very good even after ultra-sound tank treatment. For one channel waveguide (Fig. 6c), the thin film has not broken, creating "wings" along the edges of the waveguide. This may be due to the smoothing of the edges as the resist is heated during the deposition.

The near field test was negative because the substrate temperature was too low (60°C against 180°C for the standard deposition).

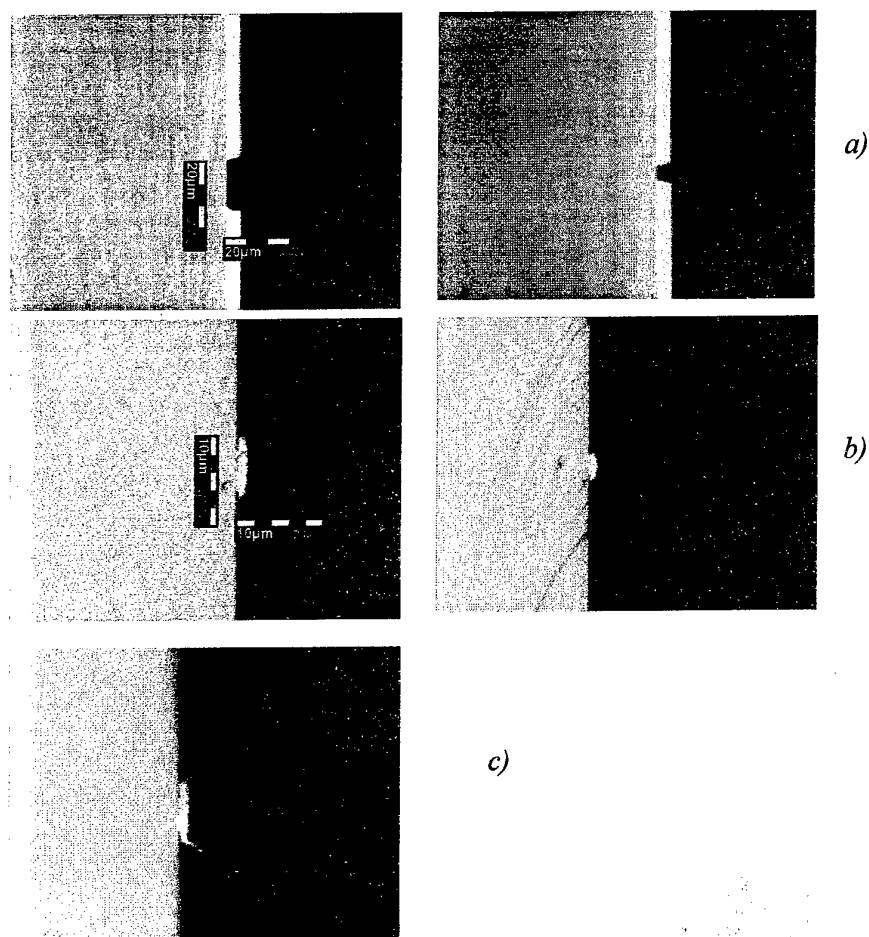


Fig. 6 : Optical micrograph of the channel waveguides obtained by lift-off process.

- a) resist profile obtained before thin film deposition ;*
- b) channel waveguides obtained after resist removal. The channel cross sections are : $10 \times 2 \mu\text{m}^2$ (left picture) and $5 \times 2 \mu\text{m}^2$ (right picture) ;*
- c) "wings" observed on a channel waveguide due to non vertical resist edges.*

Except for the U.V. writing method, the main problem consists of the profiling of the resist or substrate edge that must be vertical or better in cap shape. It appears that the wet etching process can not achieve this geometry. In addition, the confinement is decreased when the thin film is deposited on the whole surface of the substrate; there is some light leaking out of the channel waveguide. The problem is solved with the liftoff process since the film deposited on the resist is removed; only the thin film channels are left.

The measured loss is about 10 dB/cm for the doped channel waveguides fabricated by saw cut and wet etching. When not doped, the propagation loss decreases to 3dB/cm [5]. The deterioration of the guiding properties is probably due to thermal radiation emitted by the crucible heated at 1000-1100°C. Doping with rare earth chlorides, less volatile than their fluoride homologue (they can be evaporated at about 600°C), is now in progress.

4. CONCLUSION

We have demonstrated the feasibility in patterning channel waveguides obtained by vapor phase deposition. The best geometrical confinement is obtained with the liftoff process. However the potentiality of the technique is limited by the thermal properties of the resist that currently cannot be heated higher than 100°C. By comparison, it appears that the UV writing is the easiest process, especially for writing complex circuits but the control of the beam spot size is very difficult.

ACKNOWLEDGEMENT

This work is supported by the French company CNET under contract n°96-1B.

REFERENCE

- [1] B. Jacquier, J. of alloys and compounds 225 (1995) 15
- [2] E. Josse, J.E. Broquin, G. Fonteneau, R. Rimet and J. Lucas, J. of Non-Crystalline Solids 213&214 (1997) 152.
- [3] J. Ballato, M. Dejneka, R. E. Riman and E. Snitzer, J. Mater. Res. 11, N°4 (1996) 841
- [4] C. Jacoboni, O. Perrot and B. Boulard, J. of Non-Crystalline Solids 184 (1995) 184.
- [5] Y. Gao, O. Perrot, B. Boulard, J.E. Broquin, R. Rimet and C. Jacoboni, J. of Non-Crystalline Solids 213&214 (1997) 137.
- [6] W.X. Xie, P. Bernage, R. Ramecourt, M. Douai, T. Taunay, B. Boulard, Y. Gao, C. Jacoboni, A. Da Costa, H. Poignant and M. Monerie, Optics communications 134(1-6) (1997) 36
- [7] B. Boulard, L. Brilland and H. Poignant, electron. lett. 34(3) (1998) 267

PLANAR AND CHANNEL WAVEGUIDES ON FLUORIDE GLASSES

R. Sramek, G. Fonteneau, E. Josse and J. Lucas

Laboratoire Verres et Céramiques, UMR 6512, Université de Rennes 1,
Campus de Beaulieu, 35042 Cedex France
email ruth.sramek@univ-rennes1.fr

ABSTRACT

Fluoro-chloride glasses were studied. They have given information about density, specific temperatures and refractive index of planar and channel waveguides realised on ZBLA glass by exchange between fluorine and chlorine ions. In a second part, a second anionic exchange to reduce waveguides sensibility against moisture and optical losses, is presented.

INTRODUCTION

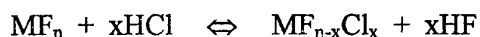
In the constant telecommunication spreading out, passive and active integrated optics take a large part, and are the subject of many studies.

Within its development, glass waveguides are today considered as excellent candidates for integrated optics applications due, in part, to the possibility of fabricating large number of devices at low cost. Various techniques such as thin film deposition or ion exchange [1-2] are used to fabricate waveguides in integrated optical systems. The simplicity and flexibility for designing waveguide dimensions make of the ion exchange an interesting technique.

An anionic exchange of a part of F^- ions by Cl^- ones, has been developed in our Laboratory to perform waveguides on fluorozirconate ZBLA glass. Such glass could be doped by rare earth ions (RE) for active applications which could be doped by rare earth ions (RE) for active applications ($57 ZrF_4$, $34 BaF_2$, $(5-x) LaF_3$, $4 AlF_3$, $x(RE)F_3$). That method is here quickly summarised, for more information take references 3 and 4.

The glass is treated during several hours by a gas mixing of HCl and Ar at a temperature below T_g ($T_g=307^\circ C$).

The chemical reaction at the glass surface is:



M symbolises glass cations.

In the first part, this paper presents a study of physical characteristics of waveguides created by that method.

The replacement of fluorine by chlorine increases the refractive index but, because weaker bondings and introduction of bigger ions, glass hygroscopicity, duration instability and surface deformations increase too. This paper presents a physical burial to isolate the guide from both atmosphere and humidity by a second anionic exchange. That treatment modifies the surface and by that, a pure fluoride glassy matrix overlays the waveguide.

PHYSICAL CHARACTERISTICS OF WAVEGUIDE:

The SIMS analysis on a glass treated 10.5 hours at $250^\circ C$, shows the profile of ionic concentrations in the waveguide (figure 1) [3]. It appears that the exchange of F^- by Cl^- involves 2 different phenomena in the glass: at the surface, in the depth of 1.5 to 2 μm , a chemical reaction substitutes the anions and deeper the exchange corresponds to a diffusion.

In the surfacing plateau, which depth depends of treatment duration, 18% of F^- are substituted by Cl^- .

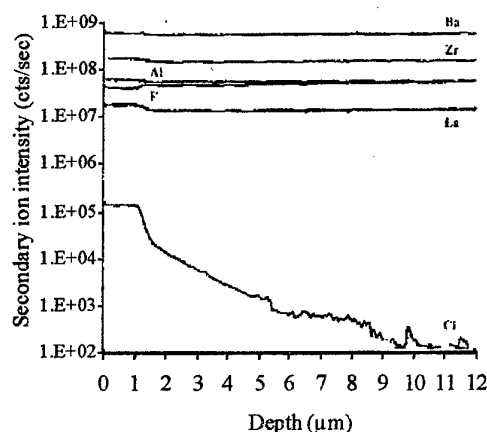


Figure 1: Profile shape of Cl^- : plateau 1.5 μm long followed by the diffusion to 10 μm deep.

The interest of F^- substitution by Cl^- is due to the increasing of local refractive index. Indeed that anion is more polarisable, bigger and weightier ($M_{Cl^-}=35.453$ g, $r_{Cl^-}=1.81$ Å against $M_{F^-}=18.9984$ g, $r_{F^-}=1.36$ Å), its presence creates compressive stress.

But it is known that chlorine in face of fluorine reduces thermal and mechanical properties of halide glasses [5-6] and, its presence generates more crystallisation. The bondings metal-chlorine being weaker than metal-fluorine [7], the sensibility to atmospheric moisture sensibly increases.

We were interested to know the physical characteristics of that "glass" structure.

Using the classical method, the synthesis of fluoro-chloride glasses is difficult. No sample with 18% of Cl^- could be realised, then glasses with less chlorine ions - 0, 5 and 10% - were synthesised. These chlorine percentages correspond to the introduction, respectively of 0, 8 and 16%, of $BaCl_2$ in substitution of BaF_2 .

Studying these glasses characteristics variations, the density, T_g and T_x , and refractive index of the plateau are estimated.

The variation of density (figure 2) shows a linear decreasing. Instead of Cl^- has bigger atomic weight, the density diminishes due to the increasing of molar volume.

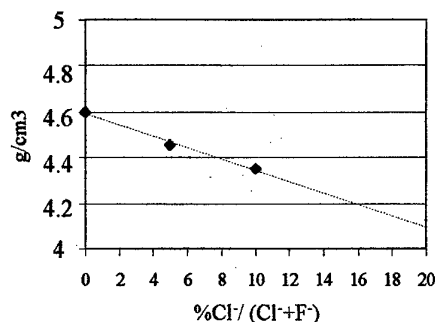


Figure 2: Fluoro-chloride glass density evolution in function of Cl^- percentage.

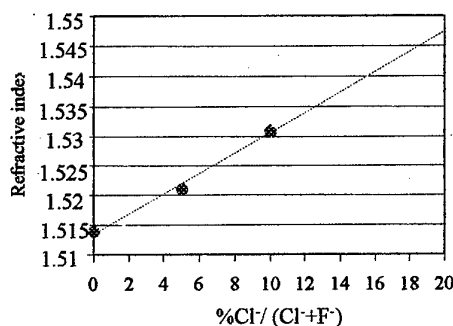


Figure 3: Refractive index evolution in function of Cl^- percentage.

As already shown, the exchange between fluorine and chlorine ions in ZBLA structure does not respond to a classical diffusion model as Fick laws. Then the refractive index profile could not be expressed by a erfc function. Both diffusion coefficient and surfacing refractive index could not be correctly calculated. The waveguides presenting a step-index profile, the WKB inverse method could not be used so either. Then Abbe refractometer was used for measurements on fluoro-chloride bulk glasses.

The curve of refractive index variations reveals a linear relationship with glass composition (figure 3). As allowed the refractive index increases with chlorine percentage [5]. At the surface, refractive index is estimated at 1.546. In comparison with pure fluoride ZBLA glass, the generated refractive index variation is approximately $3 \cdot 10^{-2}$.

Study on similar glasses [5] shows a linear decreasing too, that behaviour is also due to the difference in bondings energies. The estimated values of T_g and T_x are respectively 241 and $285 \pm 5^\circ\text{C}$ (figure 4).

Stability criterion $\Delta T = T_x - T_g$ falls from 85°C to 44°C . That fact is in accord with the difficulties to synthesise a bulk sample.

The table 1 summarises the physical characteristics of the chlorine richest part of the waveguide which were found be extrapolation from fluoro-chloride bulk glasses.

From waveguides plateau to substrate composition the chlorine percentage decreases, and described characteristics vary between these two limit compositions.

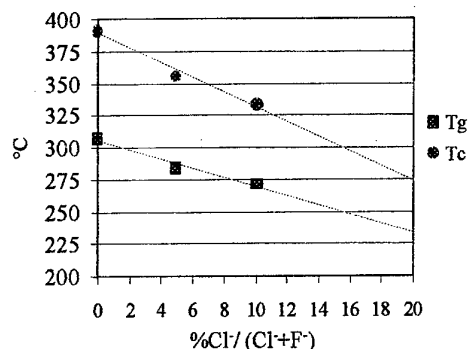


Figure 4: T_g and T_x evolution in function of Cl^- percentage.

Table 1: Comparison between substrate characteristics (0% Cl^-) and waveguide plateau.

% Cl ⁻	Density (g/cm ³)	Thermal characteristics		Refractive index
		T _g	T _x	
0	4.60	307 ± 1°C	392 ± 1°C	1.514 ± 0.001
18	4.15	241 ± 5°C	285 ± 5°C	1.546 ± 0.005

This study specifies the characteristics of waveguide glass structure. The refractive index increasing is approximately of $3 \cdot 10^{-2}$, and the specific temperatures T_g and T_x decrease. These results give indications on the structure during the heating and the buried treatment.

PRESENTATION OF BURIAL EXCHANGE

For channel waveguides, optical confinement was realised by deposition of a SiO_2 mask and remotes by RIE (Reactive Ion Etching) used in micro-electronic technologies. On such structure the better result for propagation losses was superior to 2 dB/cm^{-1} , that is too high. For applications, losses on waveguides ought to be smaller than 1 dB/cm^{-1} . To improve waveguide qualities it is needful to "bury" it. A good optical protection at 1.3 or $1.55 \mu\text{m}$ wavelengths ought to be deeper than these wavelengths. In this way, the evanescent wave, permits by Maxwell's equations, is kept in the guide.

We present here the treatment to protect and bury waveguides. The objective on ZBLA glass is to considerably reduce the waveguide sensibility against moisture and optical losses. That

study appears as needful prominent to the fabrication of optical devices, and before to study channel waveguides.

All the samples used for the burial were at first, treated 8 hours at 250°C by a gas mixture of HCl and argon. The HCl debit was equivalent to 0.02 mol/hour. These planar waveguides present 3 modes on m-lines at 633 nm.

The same kind of set up as used for the anionic exchange which leads to create the waveguide [3-4], was chosen (figure 5). After the exchange leading to the creation of the waveguide, the sample is protected from room atmosphere and introduced in the nickel tube. The set up is swept out by inert gas N₂ before and after the treatment, and by the mixture of HF and N₂ gases during exchange process. The HF gas is produced by heating KH₂HF up to 110°C, that vapour is carried away by a stream of N₂. For that second exchange the HF gas debit is approximately 0.08 mol/hour.

As HF is a very corrosive agent, all the set up in contact with it ought to be in Teflon or nickel.

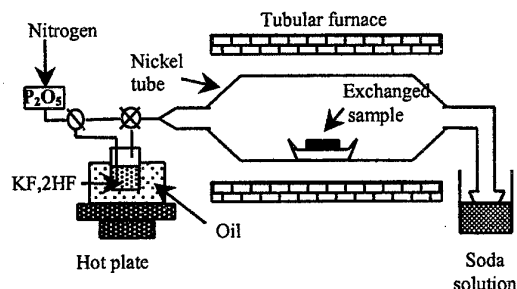


Figure 5: Set up for burial exchange: substitution of chlorine by fluorine on waveguides.

Table 2: Summarise of some buried treatments parameters and their m-lines results.

Temperature	Duration (Hours)	m-lines results
250°C	3	3 modes
270°C	3	3 modes
290°C	3	3 modes
305°C	3	0 mode
310°C	1	0 mode

Although the metal-chlorine bondings are weaker than metal-fluorine ones, the chlorine mobility at same temperature is reduced because it is bigger than fluorine. The study started at the same temperature as the first exchange: 250°C. Regarding to the estimated characteristics this temperature is up to T_g.

The moisture resistance is noticeably increase after each treatment from that temperature and for duration from 30 min. Although a heating up to guide plateau T_g, no crystallisation is observed under optic microscope. Some cracks are presented on the surface.

The buried treatment recreates substrate composition on the surface, then its action depth could not be measured by surface analysis methods. A simple method to improve the optical burial is the m-lines at 633 nm. As modes are observed, optic losses (evanescent wave) exist and then the optic burial is not achieved. The table 2 summarises the results. It appears that good burial needs more critical thermal conditions than the first exchange. It is due to the chlorine size and its low mobility. It is interesting to note that the modes visible by m-lines draw nearer.

To control that not all Cl⁻ ions have been substituted and the waveguides exist, other methods are needful. On sample treated 3 hours at 305°C, qualitative measurements by EDS show a diminishing of Cl⁻ concentration close to the surface, and near field analysis confirms the guiding.

CONCLUSION

The study of fluoro-chloride zirconate glasses precise waveguides characteristics. Such structures are realised by anionic exchange between F^- and Cl^- on ZBLA glass. The refractive index change is estimated to 3.10^{-2} . In such waveguide profile that information could not be easily found by other method. The experimental conditions of a burial by inverse anionic exchange, show that it is possible to protect the waveguide by a treatment under FH gas. The waveguides ought to be treated at temperatures close to bulk glass T_g , although its T_g is lower.

ACKNOWLEDGEMENTS

The authors would like to thank the CNET (Centre National d'Etude des Telecommunications) for support in this study and Miss Brigitte Boulard at the Université du Maine, Le Mans, France, for near field analysis.

REFERENCES

- [1] R.V. Ramaswamy, R. Srivastava, J. Lightw. Technol. 6 (1988) 984.
- [2] T. Findakty, Opt. Eng. 24 (1985) 244.
- [3] E. Josse, G. Fonteneau, J. Lucas, Mat. Research. Bull 9 (1997), n° 1139.
- [4] E. Josse, Thesis of University Rennes 1 n° 1797 (1997).
- [5] C. Henriel-Ricordel, Thesis of University Rennes 1 n° 1562 (1997).
- [6] J. Lucas, J.L. Adam, Optical properties of glass (D. R. Uhlmann, N. J. Kreidl, 1991).
- [7] P. Pascal, Nouveau traité de chimie minérale IV, VI, VII, IX (Masson et Cie, 1956 –1968).

PHYSICAL VAPOR DEPOSITION OF RARE-EARTH DOPED ZrF_4 -BASED PLANAR WAVEGUIDES

Paulo J. Morais *, M. Clara Gonçalves and Rui M. Almeida

Departamento de Engenharia de Materiais / INESC
Instituto Superior Técnico, Av. Rovisco Pais, 1000 Lisboa, Portugal
Email: pjgdm@eniac.inesc.pt

ABSTRACT

A series of $\text{ZrF}_4\text{-PbF}_2$ and $\text{ZrF}_4\text{-PbF}_2\text{-ErF}_3$ films of different composition have been prepared by thermal and electron beam evaporation, using microscope glass slides and single crystal silicon wafers as substrates. Several crystallization heat treatments were performed on these films at temperatures up to 300 °C. X-ray photoelectron spectroscopy was used to determine the film composition and the amorphous/crystalline nature of the samples was investigated by X-ray diffraction. After a heat treatment of 40 min, at 250 °C, the films are completely crystallized. The infrared absorption spectra of the films were recorded and the possible film structure is discussed and compared with that of ZrF_4 -based glasses. The optical propagation loss, measured for several waveguides at $\lambda = 632.8$ nm, varied between 1.9 and 3.5 dB/cm.

INTRODUCTION

In recent years, the main interest in heavy metal fluoride glasses has lied in their applications [1]. Because of their low phonon energy, fluoride glasses offer an advantage over silica for all-optical amplifiers, by decreasing the non-radiative emission probabilities of the rare earth ions. Recently, much effort has been dedicated to the development of planar and channel waveguides for integrated optics. The fabrication of fluoride channel waveguides has been achieved by ion exchange [2], chemical vapor deposition (MOCVD) [3 - 5], physical vapor deposition (PVD) (see ref. 6 for a review) and electron-beam deposition [7, 8].

Vapor deposition needs a good thermal stability for the glass to be evaporated [6] and similar vapor pressure values for the different glass constituents, in order to achieve the projected amorphous compositions [9, 10], which limits the systems to be prepared by this technique [4]. Almeida et al. [11, 12] have succeeded in preparing a series of glassy thin films based on ZrF_4 , some consisting of pure amorphous ZrF_4 (a- ZrF_4) and other of PbF_2 -modified binary glasses, some doped with Nd^{3+} . Bruce et al. [7, 8] are the only authors, to our knowledge, who have reported ZrF_4 -based glass films containing AlF_3 , NaF and BaF_2 , by electron-beam deposition. These authors have prepared glass films, up to 10 μm thick, outside the known range of bulk glass formation, and have demonstrated that the compositions of the films could be modified by using a multi-target deposition.

In this study, the preparation of fluorozirconate glass thin films by thermal evaporation and electron-beam deposition have been demonstrated. The glass structure of the films and the crystalline phases obtained by heat treatment were investigated by IR spectroscopy and XRD analysis.

EXPERIMENTAL

Zirconium fluoride based thin films were prepared in the $\text{ZrF}_4\text{-PbF}_2$ and $\text{ZrF}_4\text{-PbF}_2\text{-ErF}_3$ systems by two PVD methods: thermal evaporation and electron beam (e-beam) evaporation. Pure ZrF_4 , PbF_2 and ErF_3 films were also deposited by the two evaporation techniques. The films were deposited onto unheated single crystal silicon wafers or microscope glass slides, from the starting fluoride glass targets prepared by classic melting and quenching methods [13]. The pure films were prepared directly from the crystalline raw material powders. The distance from the target to the substrate and the pressure achieved during deposition were typically 3 cm and 3.5×10^{-5} mbar, respectively, for the thermal evaporation system; for the e-beam evaporation system, these were 5 cm and 1×10^{-5} mbar, respectively. After deposition, the thickness of these films was measured by mechanical profilometry (Tencor Alpha-Step 200).

Some of the films ($67\text{ZrF}_4\text{-}33\text{PbF}_2$) were subjected to selected crystallization heat treatments in a resistance furnace, at temperatures up to 300 °C, under a nitrogen atmosphere in a glove-box. The amorphous nature of the untreated samples and the crystalline phases present in the heat treated ones were determined by X-ray diffraction (XRD), with a Siemens D-5000 diffractometer ($\text{CuK}\alpha$ radiation), at grazing incidence (angle = 1°).

The film composition was determined by X-ray photoelectron spectroscopy (XPS), with a Auger/XPS spectrometer (Fisons Instruments Microlab 310F), using $\text{MgK}\alpha$ X-rays.

IR absorption spectra were recorded with a Nicolet 20F far IR Fourier transform spectrometer, for films deposited on Si wafers polished on both sides.

The optical loss was measured with a Spectra-Physics 105 He-Ne laser, at 632.8 nm, which was coupled to the waveguide, deposited on a glass slide substrate, using a high refractive index prism (SF_6 , $n_D = 1.80518$). The polarization of the laser beam was parallel to the plane of the waveguide (TE mode) and the scattered light was collected using a Cohu 2252-2340 CCD camera, in the direction perpendicular to the plane of the waveguides. The loss was measured through an exponential fit of the decaying scattered intensity.

RESULTS

The films obtained were stored in a dessicator, in order to avoid atmosphere contamination and it was found that the $67\text{ZrF}_4\text{-}33\text{PbF}_2$ and $50\text{ZrF}_4\text{-}50\text{PbF}_2$ compositions were the most stable within the studied ones, contrary to pure ZrF_4 films which are easily degraded by atmospheric air. The maximum thickness obtained by thermal evaporation, without cracking, was $\sim 4.5 \mu\text{m}$ for the ZrF_4 pure films [12] and $\sim 2.5 \mu\text{m}$ for the binary composition $\text{ZrF}_4\text{-PbF}_2$. Smaller thickness was obtained ($\sim 2 \mu\text{m}$) when depositing ZrF_4 and $\text{ZrF}_4\text{-PbF}_2$ films with e-beam evaporation.

Table 1 shows the surface composition, measured by XPS, of some of the films prepared by PVD. The peaks used for analysis were Zr 3d, Pb 4f, Er 4d and F 1s.

$\text{ZrF}_4\text{-PbF}_2$ films are easily deposited by the two PVD methods presented here, whereas films containing ErF_3 are more difficult to prepare, especially by thermal evaporation. In fact, for the doped films, due to the lower vapor pressure of ErF_3 , when compared to the ZrF_4 and PbF_2 vapor pressures, it was necessary to adjust the rare earth content of the starting batch in order to obtain adequate concentration levels in the waveguides. Pure ZrF_4 , PbF_2 and ErF_3 are easily prepared by both methods.

Table 1 – Compositions of starting batches and deposited films prepared by thermal and e-beam evaporation, measured by XPS.

Starting batch (mol%)	Film composition (mol%)	
	Thermal evaporation	E-beam evaporation
90ZrF ₄ -10PbF ₂	97ZrF ₄ -3PbF ₂	—
80ZrF ₄ -20PbF ₂	92ZrF ₄ -8PbF ₂	—
67ZrF ₄ -33PbF ₂	78ZrF ₄ -22PbF ₂	75ZrF ₄ -25PbF ₂
50ZrF ₄ -50PbF ₂	57ZrF ₄ -43PbF ₂	55ZrF ₄ -45PbF ₂
53ZrF ₄ -27PbF ₂ -20ErF ₃	68ZrF ₄ -7PbF ₂ -25ErF ₃	58ZrF ₄ -37PbF ₂ -5ErF ₃
60ZrF ₄ -30PbF ₂ -10ErF ₃	77ZrF ₄ -23PbF ₂	61ZrF ₄ -36PbF ₂ -3ErF ₃
63ZrF ₄ -32PbF ₂ -5ErF ₃	72ZrF ₄ -28PbF ₂	—

Typical amorphous X-ray diffraction patterns of a-ZrF₄-PbF₂ films are shown in fig. 1(a). Identical result is obtained for films containing ErF₃, with compositions such as those in table 1.

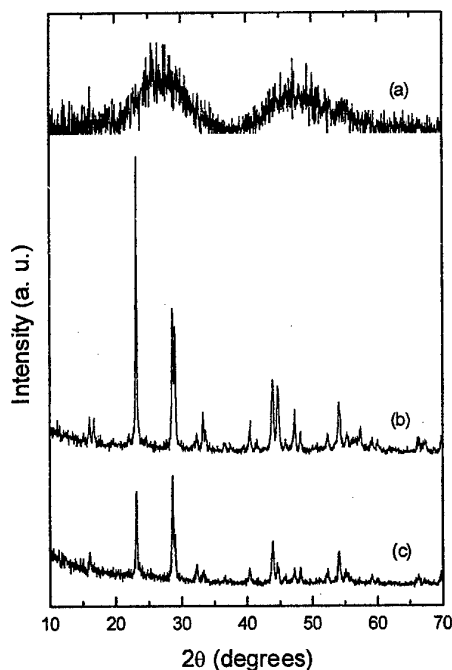


Fig. 1 – X-ray diffraction patterns of films deposited by thermal evaporation: (a) 78ZrF₄-22PbF₂ film (1.10 μ m thick); (b) same film, after 40 min of heat treatment at 250 $^\circ$ C, under N₂ atmosphere; (c) same, at 300 $^\circ$ C.

Fig. 2 shows the IR absorption spectra of several glassy films. The $\text{ZrF}_4\text{-PbF}_2$ and $\text{ZrF}_4\text{-PbF}_2\text{-ErF}_3$ compositions exhibit two principal bands at $\sim 470\text{ cm}^{-1}$ and $\sim 250\text{ cm}^{-1}$, plus a weak band at lower frequencies near 85 cm^{-1} . Pure ErF_3 films have two main bands at $\sim 420\text{ cm}^{-1}$ and $\sim 215\text{ cm}^{-1}$.

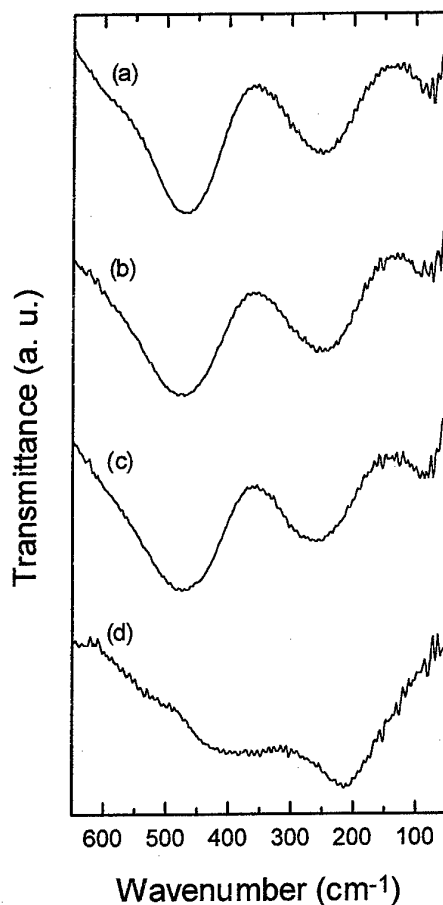


Fig.2 – Comparison of IR absorption spectra for different films (a) $78\text{ZrF}_4\text{-}22\text{PbF}_2$ film ($1.35\text{ }\mu\text{m}$ thick); (b) $75\text{ZrF}_4\text{-}25\text{PbF}_2$ film ($1.62\text{ }\mu\text{m}$ thick); (c) $58\text{ZrF}_4\text{-}37\text{PbF}_2\text{-}5\text{ErF}_3$ film ($1.05\text{ }\mu\text{m}$ thick); (d) 100ErF_3 amorphous film ($1.20\text{ }\mu\text{m}$). (Films (a) and (d) were prepared by thermal evaporation, films (b) and (c) were prepared by e-beam evaporation).

Figures 1 and 3 compare the results of XRD and IR absorption spectroscopy, respectively, for samples subjected to heat treatments. The films are completely crystallized after heated at $250\text{ }^\circ\text{C}$, during 40 min. Table 2 gives the optical loss at $\lambda = 632.8\text{ nm}$ of some of the waveguides.

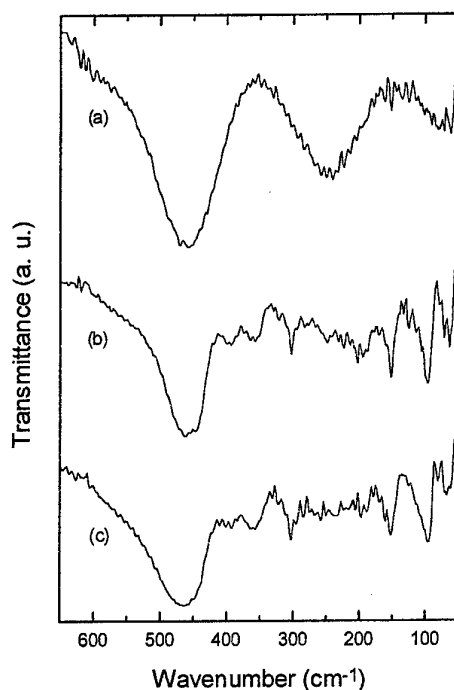


Fig. 3 – IR absorption spectra of films deposited by thermal evaporation: (a) a-78ZrF₄-22PbF₂ film (1.10 μm thick); (b) same film, after 40 min of heat treatment at 250 °C, under N₂ atmosphere; (c) same, at 300 °C.

Table 2 – Optical loss values at 632.8 nm (He-Ne laser) for some fluorozirconate waveguides, deposited on microscope glass slides.

Film composition (%mol)	Optical loss at 632.8 nm (dB/cm)
78ZrF ₄ -22PbF ₂ (thermal evap.)	3.5 ± 0.3
75ZrF ₄ -25PbF ₂ (e-beam evap.)	2.3 ± 0.3
61ZrF ₄ -36PbF ₂ -3ErF ₃ (e-beam evap.)	1.9 ± 0.1

DISCUSSION

The IR absorption spectra of fig. 2(a) and (b) are very similar to those of modified fluorozirconate ZrF₄-BaF₂ and ZrF₄-PbF₂ glasses [14]. In fact, the two IR fundamental bands at ~ 470 cm⁻¹ and ~ 250 cm⁻¹ are near the 496 cm⁻¹ and 245 cm⁻¹ found for the 70ZrF₄-30PbF₂ glass [15], as well the lower frequency band at ~ 85 cm⁻¹ which was found at 90 cm⁻¹ for the same glass composition. This indicates that the structure of films and modified ZrF₄-based

glasses are similar. Nevertheless, whereas the full width at half maximum is $\sim 120 \text{ cm}^{-1}$ for films prepared by thermal evaporation and $\sim 142 \text{ cm}^{-1}$ for films prepared by e-beam evaporation, the modified bulk glasses have broader peaks ($\sim 162 \text{ cm}^{-1}$ [16]), which is an indication of a more constrained structure in the films, especially those prepared by thermal evaporation. The relative simplicity of the IR spectra of these films suggests that there is essentially only one coordination number for the Zr atoms and, due to the similar vibrational frequencies being similar to those of the modified glasses, the average Zr coordination number probably remains the same, near 7. The absorption spectrum of the ErF_3 film, confirmed by XRD to have an amorphous structure, has two bands at $\sim 415 \text{ cm}^{-1}$ and $\sim 215 \text{ cm}^{-1}$, but its presence in the $\text{ZrF}_4\text{-PbF}_2\text{-ErF}_3$ films composition does not significantly affect the structure of the glass, as can be seen in fig. 2(c), for a final Er concentration of 5%.

XRD was used to check the amorphous nature of the vapor-deposited thin films, both as-prepared and after heat treatment in N_2 , as shown in Fig. 1, for the $78\text{ZrF}_4\text{-}22\text{PbF}_2$ composition. A thermal treatment up to 200°C did not change the amorphous character of the films, in good agreement with the characteristic temperatures determined by differential scanning calorimetry (DSC) for a quenched glass composition ($70\text{ZrF}_4\text{-}30\text{PbF}_2$), with a glass transition $T_g \sim 255^\circ\text{C}$ [13]. Although the crystallization temperature T_x of a melted and quenched $70\text{ZrF}_4\text{-}30\text{PbF}_2$ glass was $\sim 305^\circ\text{C}$ ($T_x - T_g = 50^\circ\text{C}$ only) [13], thermal treatments in N_2 at 250°C , for an evaporated thin film of slightly different composition ($78\text{ZrF}_4\text{-}22\text{PbF}_2$), caused complete crystallization. Further work is needed in order to identify the crystallization products.

The measured optical loss values were still high, but these preliminary measurements indicate that, with little improvements in processing, reasonable low losses ($\lesssim 1 \text{ dB/cm}$) may be obtained in waveguides prepared by e-beam evaporation.

CONCLUSIONS

$\text{ZrF}_4\text{-PbF}_2$ and $\text{ZrF}_4\text{-PbF}_2\text{-ErF}_3$ amorphous films, with thicknesses around $2 \mu\text{m}$, were prepared by thermal and electron beam evaporation methods. The doped composition is slightly more difficult to prepare by thermal than by electron beam evaporation. IR spectroscopy indicates that the film structures are similar to those of modified fluorozirconate bulk glasses, but a more constrained structure is apparent in the films, especially for those prepared by thermal evaporation. The heat treatments performed in the $\text{ZrF}_4\text{-PbF}_2$ films show that complete crystallization is achieved after 40 min at 250°C . The measured optical losses appear to be lower for waveguides prepared by electron beam evaporation ($\sim 2 \text{ dB/cm}$), than for those prepared by thermal evaporation.

ACKNOWLEDGEMENTS

The present work was supported by FCT, under contract No. PBICT/P/CTM/1915/95. We would also like to acknowledge the support of the PRAXIS XXI program (FCT) and ICEMS (Lisboa).

REFERENCES

- [1] J. Lucas, *Current Opinion Solid State Mater. Sci.* 2, 4 (1997) 405.
- [2] E. Josse, G. Fonteneau, J. Lucas, *Mater. Res. Bull.* 32, 9 (1997) 1139.

- [3] K. Fujiura, T. Kanamori, Y. Ohishi, Y. Terunuma, K. Nakagawa, S. Sudo, K. Sugii, Appl. Phys. Lett. 67, 21 (1995) 3063.
- [4] A. Sarhangi and D. A. Thompson, Mat. Sci. Forum V19-20 (1987) pp. 259-268.
- [5] L. Chia-Yen, F. Vladimir, Zhao Jing, C. Xuesheng, H. Seppo, P. Nasser, Proc. SPIE - Int. Soc. Opt. Eng. 2996 (Rare-Earth Doped Devices) 1997, 68.
- [6] M. C. Gonçalves, P. J. Morais and R. M. Almeida "Preparation of $\text{ZrF}_4\text{-PbF}_2\text{-NdF}_3$ Amorphous Thin Films by PVD" (to be published).
- [7] A.J. Bruce, G. Zydziec and M. Chui-Sabourin, "Electron-beam Deposition of Heavy Metal Fluoride Glass Films", ed. by B. V. Hiremath, Ceramic Transactions vol. 11 (1990), Am. Ceram. Soc., Ohio, pp. 281-290.
- [8] A. J. Bruce, G. Zydziec and M. Chui-Sabourin, Mat. Sci. Forum 67 & 68 (1991) 377.
- [9] H. Poignant, J. Le Mellot and Y. Bossis, Mater. Sci. Forum 5 (1985) 79.
- [10] C. Jacoboni, B. Boulard and P. Baniel, Mater. Science Forum V19-20 (1987) 253.
- [11] R. M. Almeida and P. J. Morais, J. Non-Cryst. Solids 184 (1995) 93.
- [12] R. M. Almeida, P. J. Morais and M. C. Gonçalves, J. Non-Cryst. Solids, 213-214 (1997) 251.
- [13] M. C. Gonçalves and R. M. Almeida, J. Non-Cryst. Solids 194 (1996) 180.
- [14] R. M. Almeida, Fluoride Glasses, in: Handbook on the Physics and Chemistry of Rare Earths, Vol. 15, ed. K. A. Gschneider Jr. and L. Eyring (Elsevier Science, Amsterdam, 1991) p. 287.
- [15] R. M. Almeida and J. D. Mackenzie, J. Phys. Colloq. (suppl. 12) 46 (1985) C8.
- [16] R. M. Almeida and J. D. Mackenzie, J. Chem. Phys. 74 (1981) 5954.

Chemical Etching of AlF-based Glasses

Y. D. West, E. R. Taylor, R. C. Moore, D. N. Payne
Optoelectronics Research Centre, University of Southampton
Highfield, Southampton, SO17 1BJ

Aluminium fluoride (AlF) based glass $[\text{AlF}_3\text{-M(II)F}_2]$, $\text{M}=\text{Mg, Ca, Ba, Sr}$ fibres produced from untreated preforms have low strength because there is surface contamination arising from their manufacture. Studies on ZBLAN have shown that fibre strength can be significantly improved when the outer surface of similarly produced preforms is removed by aggressive chemical etching. Therefore, to achieve an analogous result for AlF based glasses requires an etch capable of removing the contaminated skin at a realistic rate whilst generating an optical quality surface. However, the glass components are highly unreactive so, in spite of this essential fabrication requirement, few etching studies have been reported in the literature. After an extensive wide ranging program, two suitable multi component etches have been identified as highly efficient at dissolving AlF-based glass.

The first etch is an $\text{AlCl}_3\cdot 6\text{H}_2\text{O}/\text{HCl}$ composition, prepared by dissolving $\text{AlCl}_3\cdot 6\text{H}_2\text{O}$ in HCl . Etch rates are largely independent of component concentrations within the ranges $0.2\text{M} \leq [\text{AlCl}_3\cdot 6\text{H}_2\text{O}] \leq 1.2\text{M}$ and $0.5\text{M} \leq [\text{HCl}] \leq 12.0\text{M}$ but they are highly temperature dependent, enabling useful operation in the range 40°C ($\sim 0.2\mu\text{m}/\text{min}$) to 80°C ($\sim 3.5\mu\text{m}/\text{min}$) (or higher). Etches containing lower concentrations of the components more reproducibly yield optically polished preforms. A working composition of $0.4\text{M AlCl}_3\cdot 6\text{H}_2\text{O} / 1\text{M HCl}$ has been adopted which can be reused a minimum of 3 times with no resulting surface deterioration.

The second etch is a $\text{HF}/\text{HNO}_3/\text{H}_3\text{BO}_3$ composition. Etch rates are highly dependent on both the concentrations of HF and HNO_3 as well as the temperature [40°C ($0.1\text{-}0.5\mu\text{m}/\text{min}$) to 80°C ($3\text{-}8\mu\text{m}/\text{min}$)]. Optically polished preforms can be reproducibly produced provided a fresh etch solution is used. The optimum etch composition (by volume) is 50% HF (48%) / 30% HNO_3 (68%) / 20% H_2O plus 3M H_3BO_3 .

Fibre pulling trials reveal that both etches significantly improve the fibre strength and quality over fibre pulled from unetched / alternatively etched preforms. However the $\text{AlCl}_3\cdot 6\text{H}_2\text{O}/\text{HCl}$ composition tends, on average, to perform slightly better. The etching process is most effective if carried out immediately prior to fibre pulling.

Further fibre pulling investigations using the $\text{AlCl}_3\cdot 6\text{H}_2\text{O}/\text{HCl}$ composition concentrated on the etching procedure to give the best fibre ($125\mu\text{m}$ diameter) as analysed by bend testing the uncoated fibre and optical inspection. In order to completely remove the contaminated surface layer requires a two stage aggressive etch procedure ((1) 90 mins etch at 85°C , 60 mins ultrasonic rinse in methanol. (2) 60 mins etch at 55°C , 30 mins ultrasonic rinse in methanol) which must remove at least 1mm from the preform diameter. The subsequent fibre pulling is easily controlled and highly repeatable. The uncoated fibre has good strength ($\sim 1.0\%$ strain to failure) which is consistent along the total length (100m). Furthermore there is $<10\%$ loss in strength observed after leaving the fibre in an ambient atmosphere for two weeks.

COMPOSITIONAL INVESTIGATION OF Yb³⁺-DOPED HEAVY METAL FLUORIDE GLASSES FOR LASER-INDUCED FLUORESCENT COOLING APPLICATIONS

Michael T. Murtagh and George H. Sigel, Jr.

Fiber Optic Materials Research Program

Rutgers University, Piscataway, NJ 08854-8065. Email: murtagh@rci.rutgers.edu

James C. Fajardo

Corning Incorporated, Corning, NY 14831

Bradley C. Edwards and Richard I. Epstein

Los Alamos National Laboratory, Los Alamos, NM 87545

ABSTRACT:

A full-scale compositional analysis of Yb³⁺-doped heavy metal fluoride glasses (HMFG) has been undertaken to determine potential hosts for use in the development of a first-generation optical cryocooler for space-borne remote sensing applications. By pumping to the lower levels of the Yb³⁺ ²F_{5/2} manifold, followed by a thermally-driven population redistribution to higher levels within the manifold, net cooling can be achieved by anti-Stokes fluorescence back to the ground state. This will only occur, however, if the extrinsic absorptive component of the host glass is suppressed. This paper reports on fluoride glasses in the ZBLAN and BaF₂-InF₃-GaF₃ (BIG) families which have shown great promise for fluorescent cooling. ZBLANPb: Yb³⁺ is the first solid to actually exhibit net cooling due to anti-Stokes fluorescence. Temperature drops of 0.33 K in a bulk glass and 16 K in a fiber sample were obtained by infrared evaluation. Net cooling in ZBLANPb: Yb³⁺ could only be achieved once an electrochemical purification stage was successfully incorporated into the glass fabrication process to reduce the broad Fe²⁺ and Cu²⁺ absorption bands in the near-infrared region. Currently, due to the absence of concentration quenching of the Yb³⁺ ion and constraints on the dopant levels in ZBLAN glasses, hosts in the BIG family of fluoride glasses with higher rare earth concentration are being investigated as potential fluorescent coolers. The BIG-derived hosts have been determined to contain similar mean emission photon energies and larger long-wavelength absorption tails than that of ZBLANPb: Yb³⁺. These results indicate a strong potential for fluorescent cooling in these newly investigated hosts. Low-temperature absorption and fluorescence spectra have indicated that the Yb³⁺-containing BIG glasses should have a cooling efficiency more than twice that of ZBLANPb at temperatures below 80 K and may attain a minimum temperature of 45 K compared to 55 K expected for the ZBLANPb. In general, the great potential for high levels of net cooling makes these heavy metal fluoride hosts attractive candidates for the development of a first-generation optical cryocooler for astronomical remote sensing applications.

INTRODUCTION:

The continual cooling of matter by anti-Stokes fluorescence was first discussed in 1929 by Pringsheim.¹ After much controversy regarding the thermodynamic validity of such a phenomenon, L. Landau in 1946 established that optical cooling does not violate the second law

of thermodynamics through his introduction of radiation entropy.²⁻⁴ Much progress has been achieved in laser cooling free atoms to below one microKelvin;⁵⁻⁷ however, attempts to cool condensed phase material with light have only met with limited success.⁸ Laser cooling was recently achieved in solids for the first time in a ytterbium-doped ZBLANPb glass sample.⁹

The basic condition for optical refrigeration is that a material exhibit high quantum efficiency anti-Stokes fluorescence. Cooling via anti-Stokes fluorescence, where the emission energy is greater than that of the pump, may at first appear to contradict common sense: an intense monochromatic light irradiates a material, and the temperature of the material decreases. Figure 1 shows a general anti-Stokes fluorescence process and how it can result in cooling. Assume that a laser is tuned to the $1 \rightarrow 2$ transition and the separation between levels 2 and 3 is much less than the energy gap between 1 and 2. Phonon absorption follows the optical absorption such that the relative populations between the two upper levels equilibrate. Fluorescence from the $2 \rightarrow 1$ and $3 \rightarrow 1$ transitions will occur with a mean photon energy greater than the incident energy.

In order to obtain net cooling via the general anti-Stokes fluorescence process described in Figure 1, the following conditions must be satisfied. First there must be a radiative quantum efficiency close to unity. The nonradiative decay rate of a rare earth is approximated by

$$W_{mp} = W_o e^{-\alpha \Delta E}$$

where ΔE is the energy gap between levels 1 and 2 in Figure 1.¹⁰ A large ΔE would make the nonradiative decay rate negligible, and thus is desired for this application. Secondly, levels higher than level 2 must be accessible by absorption of the vibrational energy of the glass, and thermalization must be rapid compared to the relaxation time to the ground state. Thus, the spacing between levels in the excited state manifold should be at most a few times kT .¹¹

Of the various rare earths, trivalent ytterbium has the necessary characteristics described earlier. Ytterbium has only two available manifolds, the $^2F_{7/2}$ ground state and the $^2F_{5/2}$ excited state, separated by $\sim 10^4 \text{ cm}^{-1}$, with moderately strong electron-phonon coupling strength. In particular, the lack of three unwanted effects: multiphonon relaxation, concentration quenching, and excited state absorption make it unique as an activator for laser-induced fluorescent cooling. In a glass host, the energy levels of Yb^{3+} are also split due to Stark effects. Stark splitting is typically small ($\sim 200 \text{ cm}^{-1}$), thus levels within a manifold are accessible by thermalization should the relative populations of the manifold be perturbed.

Fluoride glasses in the ZBLAN and BIG (Barium-Indium-Gallium) glass families have been employed in this study for potential application in the area of laser-induced fluorescent cooling. The reasoning for the use of ZBLAN-derived hosts has been discussed previously.⁹ Compared with ZBLANPb hosts, BIG glasses allow substantially greater amounts of rare earth ions to be incorporated and offer improved chemical durability. These BIG-derived hosts also exhibit significant absorption extending to lower energies than the mean emission photon energy, which is the most fundamental spectroscopic requirement for optical cooling.

EXPERIMENTAL:

Ytterbium-doped ZBLANPb (in mol%: 53% ZrF_4 , 18% BaF_2 , 3% LaF_3 , 3% AlF_3 , 20% NaF , 2% PbF_2 , 1% YbF_3) and BIGaZYbTZr (in mol%: 30% BaF_2 , 18% InF_3 , 12% GaF_3 , 20% ZnF_2 , 10% YbF_3 , 6% ThF_4 , 4% ZrF_4) glass samples were fabricated using UHP starting materials

(EM Fluortran). 30 g batches were melted in a vitreous carbon crucible at 950°C for 1 h under an inert atmosphere. Reactive atmosphere processing was carried out with SF_{6(g)} for 1 h at 775°C for the elimination of reduced zirconium and residual moisture. Prior to casting, the liquid was placed into an electrochemical purification cell. The liquids were exposed to a voltage for 18 h at 600°C. The electrochemical purification process has been previously discussed in detail.⁹ Cast samples were cut and polished for optical measurements. The emission measurements were made using a tunable cw Ti-Sapphire laser (Spectra-Physics Model 3900S) pumped with an argon laser (Coherent INNOVA 20) and has a spectral bandwidth ≤ 30 GHz. A sample was placed in a cryostat (Infrared Lab. HDL-8) and the temperature was measured with a calibrated silicon diode. The absorption measurements were made with a similar setup, a calibrated white-light source replacing the laser.

RESULTS AND DISCUSSION:

Room temperature absorption and emission spectra of the two glasses are shown in Figure 2. The vertical dashed line indicates the mean emission wavelength (λ_f) that corresponds to the mean emission photon energy. λ_f is also the theoretical null wavelength, where when pumped with this wavelength the sample should neither heat nor cool. It was observed that the calculated null wavelength is the same regardless of where the excited state manifold was pumped between 940 nm and 1020 nm. The large integral overlap and absorption coefficient at wavelengths greater than λ_f are desired for efficient absorption for anti-Stokes fluorescence.

In comparison with the ZBLANPb glass sample, it is evident that absorptive and emissive properties of Yb³⁺ in the BIG-derived glass are very similar to those in the ZBLAN-based host. Due to the ability to incorporate greater Yb³⁺ into the BIG-derived hosts, a stronger absorption results. This enables Yb³⁺ to be pumped more effectively at longer wavelengths than for the ZBLANPb host, which may allow for a wider spectral range over which this composition will exhibit fluorescent cooling.

The absorption and emission spectra were measured from temperatures of ~ 10 to 300 K to assess the theoretical minimum operating temperatures and cooling efficiencies under optimum cooling conditions. Figure 3 shows the absorption and emission spectra for the BIG-derived sample as a function of temperature. Similar results were obtained for the ZBLANPb sample. The long-wavelength absorption tail, i.e. the cooling tail, shows a strong temperature dependence; the absorption coefficient rapidly falls with decreasing temperature. The short-wavelength blue tail of the emission also decreases at lower temperatures.

Based upon the low temperature absorption spectra and using the reciprocity method (not discussed here), theoretical cooling efficiencies were determined as a function of temperature. The data suggest that the BIG glass should have a cooling efficiency more than twice that of ZBLANPb at temperatures below 80 K and may attain a minimum temperature of 45 K compared to 55 K expected for the ZBLANPb.

In order to obtain fluorescent cooling in a solid, a high purity, high quality host must first be synthesized. Due to the fact that the absorption and fluorescence of the Yb³⁺ ion takes place in the 1.0 μ m region, one of the primary obstacles which must be overcome to successfully achieve fluorescent cooling is the suppression of the extrinsic absorption of the base glass in this region. Since transition metals have strong bands in the near IR and are common trace impurities in heavy metal fluoride glasses, the focus has been on the removal of these elements, specifically iron and copper. Purification via electrochemical processing has been undertaken to directly

remove the transition metal impurities from the melt. In a recent paper,⁹ Fajardo, et al. observed a substantial reduction in the transition metal impurity levels (particularly iron and copper) in a ZBLANPb host through the use of electrochemical purification techniques, potentially enabling fluorescent cooling to be obtained. Electrochemical purification studies are currently being performed on the BIG-derived hosts in order to similarly reduce transition metal levels to the extent where fluorescent cooling may be achieved.

The amount of cooling in the ZBLANPb glass sample was quantified via infrared evaluation. Temperature drops of 0.33 K and 16 K were observed in bulk and fiber samples, respectively. The higher Yb^{3+} concentrations in the BIG samples as well as continued improvements in the electrochemical purification process should result in greater levels of fluorescent cooling.

CONCLUSIONS:

Yb^{3+} -doped fluoride hosts in the ZBLAN and BIG glass families were examined to assess the potential for laser-induced fluorescent cooling. The assessment is based on the absorption and emission spectra as a function of temperature. The BIG and ZBLAN-derived glasses were determined to have theoretical minimum operating temperatures of 45 K and 55 K, respectively. The BIG glasses have the possibility of cooling more than twice as efficiently as ZBLANPb at temperatures below 80 K, largely due to its high tolerance of Yb^{3+} dopant concentration. Temperature drops of 0.33 K and 16 K were observed in bulk and fiber ZBLANPb samples via infrared evaluation. Electrochemical purification studies are currently ongoing on the BIG samples in order to eventually realize high levels of net cooling in these hosts.

ACKNOWLEDGMENTS:

The authors would like to acknowledge the generous support for this research granted by the Fiber Optic Materials Research Program at Rutgers University, the Institute of Geophysics and Planetary Physics at Los Alamos National Laboratory and the Department of Energy.

REFERENCES:

- [1] P. Pringsheim, *Zeitschrift fur Physik* 57 (1929) 739.
- [2] S. Vavilov, *J. Phys.* 9 (1945) 68.
- [3] P. Pringsheim, *J. Phys.* 10 (1946) 495.
- [4] L. Landau, *J. Phys.* 10 (1946) 503.
- [5] T.W. Hansch, A.L. Schawlow, *Opt. Commun.* 13 (1975) 68.
- [6] S. Chu, *Science* 253 (1991) 861.
- [7] M.H. Anderson, J.R. Ensher, M.R. Matthews, C.E. Wieman, E.A. Cornell, *Science* 269 (1995) 198.
- [8] T. Kushida, J.E. Geusic, *Phys. Rev. Lett.* 21 (1968) 1172.
- [9] J.C. Fajardo, G.H. Sigel, Jr., B.C. Edwards, R.I. Epstein, T.R. Gosnell, C.E. Mungan, *J. Non-Cryst. Solids* 213 & 214 (1997) 95.
- [10] C.B. Layne and M.J. Weber, *Phys. Rev. B* 16 (1977) 3259.
- [11] T.R. Gosnell, C.E. Mungan, B.C. Edwards, M.I. Buchwald, R.I. Epstein, *Postdeadline Abstracts of the 1995 Quantum Electronics and Laser Science Conference #QPD17 (1995).*

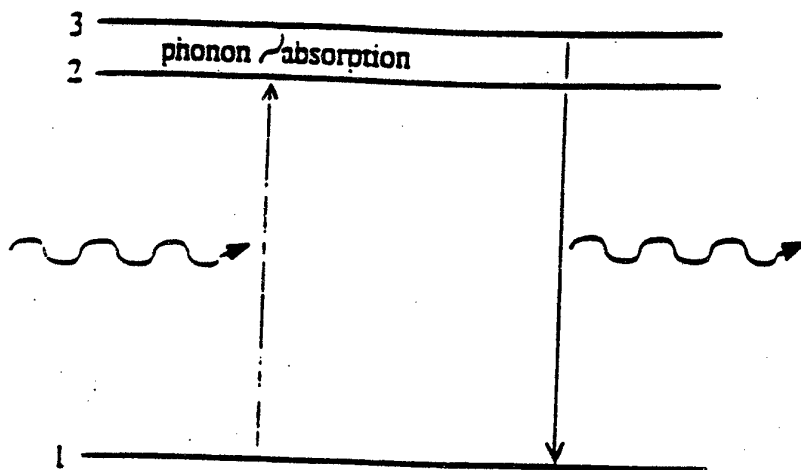


Figure 1. Anti-Stokes cooling cycle.

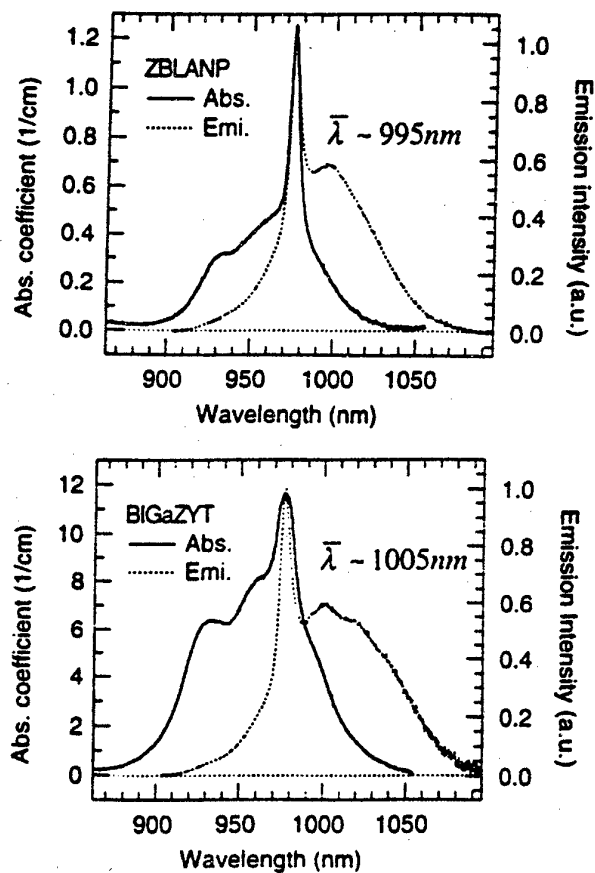


Figure 2. Room temperature absorption and emission spectra of Yb^{3+} in a) ZBLANP and b) BIG fluoride glass hosts.

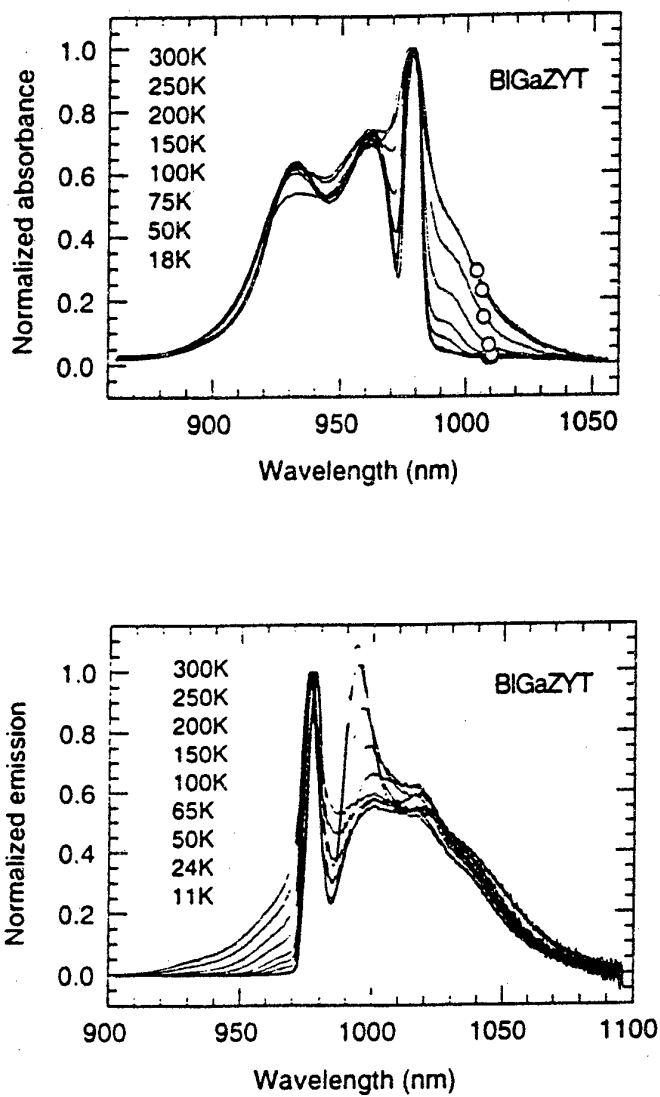


Figure 3. Normalized a) absorption and b) emission spectra of Yb^{3+} in a BIG fluoride glass host at different temperatures.

IONIC CONDUCTIVITY IN OPTIMIZED CHALCOGENIDE FIC GLASSES

Steve W. Martin

Department of Materials Science & Engineering, Iowa State University of Science & Technology, Ames, IA 50011, swmartin@iastate.edu

Fast ion conduction (FIC) in glass has been studied for some time and much effort has been directed at obtaining high conductivity in glass. Recent success in sulfide- and silver-doped glasses has pushed the maximum room temperature conductivity in glass up to $10^{-2} (\Omega\text{cm}^{-1})$ [1]. Concomitant with this success has been the clarification of the structural and dynamic models used to understand FIC in these "superionic" glasses. Our work for example has clearly identified the wide composition dependence of the ionic conductivity with both structural and conduction energetics features of these glasses [2]. Other work has shown the intimate interplay between composition, structure, and the dynamics of the FIC in these glasses [3]. In all of this work, the question still remains of how high the ionic conductivity can be pushed in these glasses. For example, does the limit of $10^{-2} (\Omega\text{cm}^{-1})$ represent a fundamental limit that will not be overcome, or do the calculations that have been made earlier [4], where a conductivity of 1 to 100 $(\Omega\text{cm})^{-1}$ at room temperature is predicted, still hold promise that more glass chemistry optimization must be done before the limit is reached?

In this contribution, we show that by using all the available knowledge that links ionic conductivity to glass chemistry and structure, a new feature in the composition and temperature dependence of ionic conductivity in glass arises that may well limit the maximum conductivity that is obtainable in glass. When all the features of the glass chemistry and composition have been carefully optimized to obtain highest conductivity in glass, the conductivity exhibits a strong non-Arrhenius temperature dependence that reduces the conductivity at room temperature some one to two orders of magnitude below that predicted from low temperature (sub-ambient) conductivities. We believe this behavior to be an as yet undiscovered ubiquitous behavior of all superionic FIC glasses and points to another feature of ionic conduction in glass that must be

fully understood in order to make any more progress in optimizing the conductivity in these glasses. Indeed, this behavior may well point to a fundamental device limitation for these glasses.

The purpose of this paper is to report new measurements on a series of new silver iodide-doped silver thioborosilicate glasses that were specifically designed to yield optimum ionic conduction in glass.

Glasses of general composition $z\text{AgI} + (1-z)[x\text{Ag}_2\text{S} + (1-x)\text{B}_2\text{S}_3:\text{SiS}_2]$ were prepared by batch melting AgI with previously prepared $x\text{Ag}_2\text{S} + (1-x)\text{B}_2\text{S}_3:\text{SiS}_2$ glasses in vitreous carbon crucibles in a high quality O_2 - and H_2O -free glove box at $\sim 850^\circ\text{C}$ and quenching into 1-2 mm x 25 mm discs in stainless steel molds held near the T_g of the glass, $\sim 350^\circ\text{C}$. The $x\text{Ag}_2\text{S} + (1-x)\text{B}_2\text{S}_3:\text{SiS}_2$ glasses were prepared from reagent grade Ag_2S and SiS_2 (99.9 %, Cerac, Inc.) and B_2S_3 prepared in this lab[5]. Conductivity measurements were made using a high quality Impedance Spectroscopy facility over the frequency range of 0.1 Hz to 32 MHz and from 100 to 600 K[4]. Complex plane analysis was used to determine the D.C. conductivity of these glasses. T_g s were determined using a PE-DSC 4 at $20^\circ\text{C}/\text{min}$.

It has been widely shown that due to their high electronic polarizability, silver cations always exhibit conductivities in glass some one to four orders of magnitude higher than any of the alkali ions[1]. Similarly, sulfide glasses, first discovered by Levasseur et al. [6], show conductivities some three to as many as ten orders of magnitude higher than any corresponding oxide glass. More recently, the effect of doping FIC glasses with halide salts, especially AgI, can increase the conductivity some two to three orders of magnitude[1]. Finally, it has also been shown that mixing different glass formers such as SiO_2 and B_2O_3 for reasons that are not completely understood produces non-linear increases in the conductivity and this has been termed the mixed-glass former effect[1]. Using these observations, it follows that high ionic conductivity in glass, if not the highest yet reported, should be found among glass compositions chosen in the series $\text{AgI} + \text{Ag}_2\text{S} + \text{SiS}_2 + \text{B}_2\text{S}_3$.

Although wide compositions of glass formation were not found, glasses in the ternary $\text{Ag}_2\text{S} + \text{SiS}_2 + \text{B}_2\text{S}_3$ could be prepared. It was observed that at the $\text{SiS}_2:\text{B}_2\text{S}_3$ ratio of 1:1, and a Ag_2S fraction of 60 mole %, the strongest glass former was observed. This glass was then used as host for the AgI doping and as in many other AgI-doped glasses[1], 40 mole% of AgI could be doped into the glass before devitrification was observed. The glasses reported in this paper therefore belong to the compositional series $y\text{AgI} + (1-z)[x\text{Ag}_2\text{S} + (1-x)\text{B}_2\text{S}_3:\text{SiS}_2]$, where $0 \leq z \leq 0.4$ and $x = 0.525$. Other glasses were prepared and studied and will be reported on separately. The present series is the highest conducting and most strongly glass forming.

Figure 1 shows the Arrhenius plots of the conductivity for these glasses along with a few other glasses both in this family and others to show the level of conductivity increase that the current series exhibits. Figure 1 shows that these glasses do indeed exhibit the highest yet reported of all conductivities in glass at room temperature, a result quite surprising in itself, except that the glass chemistry was specifically designed to yield this result. Another important finding about these glasses is that are exceptionally stable in both air and water. Even though they comprise some 50 atom % of SiS_2 and B_2S_3 , both of which are exceptionally chemically unstable, the resulting glasses are very chemically durable. These three features make these glasses particularly attractive for device fabrication and use.

Most dramatic about these glasses, however, is the fact that Figure 1 shows that their conductivities are exceptionally non-Arrhenius. A dashed line on the $z = 0.4$ glass data shows that the room temperature conductivity is some two to three orders-of-magnitude less than that predicted. This behavior has been reported before for other low T_g "oxysalt" FIC glasses, where the non-Arrhenius behavior was associated with the dynamic temperature dependent restructuring of the I^- anion "sub lattice"[7]. Such restructuring was proposed to be associated with the low T_g s of these glasses, $< 100^\circ\text{C}$. By annealing the glasses and presumably densifying the glass to the point where the I^- anions could not restructure, Ingram et al.[7] observed that they could remove the non-Arrhenius temperature dependence. In the present glasses, where T_g approaches 400°C and Figure 1 shows that the non-Arrhenius behavior persists even for glasses without AgI, it is clear that such a simple model may not be entirely correct. Indeed, Figure 1

also shows this behavior for a lithium ion FIC glass. For these reasons, it is argued that the non-Arrhenius temperature dependence is a ubiquitous feature of all FIC glasses that have optimized ionic conductivities. We believe this to be a new feature for FIC glasses that must be fully understood before any more significant increases in the conductivity of FIC glasses can be obtained. In the following, we propose a simple hypothesis that may account for this behavior that does not depend upon any unique features of glass chemistry or structure as the previous models.

The specific aim to obtain a glass with a maximum conductivity implies that the activation energy for conduction must be minimized. In this case, at high temperature the concept of ion conduction in glass being the result of infrequent individual ion hops over large energy barriers may not be appropriate. At low temperatures, however, where kT is far below the activation energy this is an appropriate picture of the conduction dynamics and the conductivity exhibits near but not completely Arrhenius temperature dependence. At higher temperatures and optimized glass compositions and minimized activation energies, it is very likely that a significant fraction indeed most if not all of the ions in the glass will be dissociated from their anionic potential energy wells and able to conduct in the glass. For example, kT at 500K is on the order of 0.04 eV, in the range, ~ 0.10 eV, observed for the activation energy for the most compositionally optimized glass studied here. In this case, the effect of temperature would no longer be to thermally create charge carriers for conduction but rather to increase the mobility of the carrier population. The hypothesis in this model would be that the conductivity has reached a mobile carrier concentration limit and further increases in conductivity depend upon increasing the mobility of the carriers. Such behavior is observed and well studied in electronic semiconductors, where even lower activation energies are observed. In these cases, of course, the charge carrier is the quantum-effects controlled electron, and the comparison to the "classical-limit" behavior of the mass and charge carrying ion conductors cannot be taken to far, however. None-the-less, the analogy is an important and may lead to a better understanding of these glasses and their anomalous behavior.

Such a hypothesis is in agreement with the oft cited notion that in glassy FICs, it is the carrier concentration that dominates the conductivity[8]. In the weak electrolyte model, this is seen as the dissociation energy required to create a mobile carrier. In the strong electrolyte Anderson-Stuart model, this is seen as the electrostatic binding (coulombic) energy barrier to conduction[9]. In both cases, the dominant energy barrier is believed to be associated with the electrostatic (coulombic) attraction between mobile cations and stationary anions in the glass. 1. If this is the case, the high temperature limit of the activation energy may well only be associated with the mobility part of the activation where all ions are participating equally in the conduction events.

If such a model were correct for these glasses, it would seem that at some temperature, below T_g , ion-ion interaction and scattering should become a major obstacle for conduction and the conductivity should begin to decrease with temperature in a manner seen in electronic band conductors. In the present case, the glasses appear to have not reached this limiting behavior. We are, however, using these base compositions to further optimize the glass chemistry to increase the T_g even further to observe whether such behavior occurs.

References

1. See for example S. W. Martin, J. Amer. Soc. 74[8](1991)1767.
2. H. K. Patel, S. W. Martin, Phys. Rev. B, 45(18)(1992)10292
3. C. A. Angell, Chem. Rev. 90(1990)523.
4. T. Minami, J. Non-Cryst. Sols. 73(1985)273.
5. J. Kincs, M. S. Thesis, Iowa State University, 1994.
6. Levasseur, A., Olazcuaga, R. Kballa, M., Zahir, M., Haggemuller, P., C.R. Acad. Sci. 293(1981)563.
7. M. Ingram, C. Vincent, A. Wandless, J. Non-Cryst. Sols. 53(1982)73.
8. J. L. Souquet, W. G. Perera, Solid State Ionics 40-41(1990)595.
9. S. W. Martin J. Amer. Ceram. Soc. 71[6](1988)438.

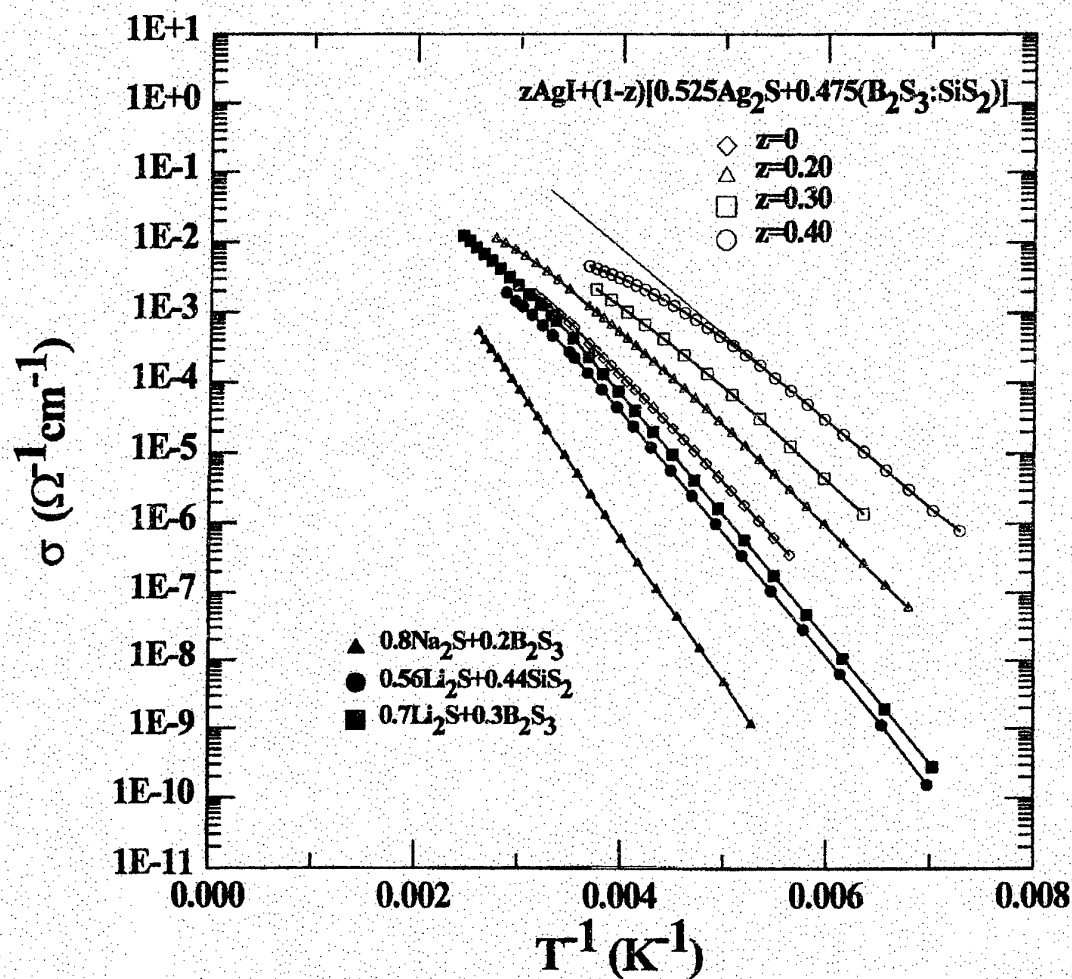


Figure 1. Arrhenius plots of the ionic conductivity for glasses studied in this work and compared to those for other Li and Na conducting glasses. Notice that for the poorer conducting glasses, the Arrhenius plots have a straight slope, whereas the optimized Ag conducting FIC glasses have significant curvature at highest temperatures.

GLASSFORMING ABILITY AND CATIONIC TRANSPORT IN GALLIUM CONTAINING CHALCOHALIDE GLASSES

Yu.S. Tver'yanovich, V.V. Aleksandrov, I.V. Murin, E.G. Nedoshovenko

St.-Petersburg State University, Dept. of Chemistry, St.-Petersburg, 198904, Russia.

email yuratver@yt2461.spb.edu

ABSTRACT

The glass formation regions are determined in the $\text{Ga}_2\text{S}_3\text{-GeS}_2\text{-MCl}$ ($\text{M}=\text{Li, Na, K, Cs, Ag, Tl}$) and $\text{GaI}_3\text{-NaCl}$ systems. It is noted that the formation of complex structural units is favourable for increasing the glass formation regions. Temperature dependencies of the electric conductivity of 60 glasses in the systems $\text{Ga}_2\text{S}_3\text{-GeS}_2\text{-MCl}$ were measured. All these glasses have significant cation conductivity. Activation energy of conductivity for all investigated systems is a linear function on the cubic root of the atomic fraction of cations. These results agree with the simple model of cation conductivity.

INTRODUCTION

It is possible to introduce a high concentration of NaCl into chalcogenide glasses containing gallium [1]. These glasses may contain even larger amounts of TlCl and AgCl [2]. They have a cation conductivity and can be used as ion selective electrodes [3,4]. The large number of other halides $\text{M}^{+n}\text{Hal}_n$ ($n=1,2$) can be also introduced into the chalcogenide glasses which consist of GeS_2 and Ga_2S_3 [5-7]. The possibility of formation of anions $(\text{GaS}_{3/2}\text{Cl})^-$ in glass network due to the high capability of Ga^{+3} to form complexes is mentioned in [1]. Further investigations of the glassforming process in systems $\text{GeS}_2\text{-Ga}_2\text{S}_3\text{-MCl}$ ($\text{M}=\text{Li, Na, K, Cs, (Cu), Ag, Tl}$) [2], Raman spectra [8], X-ray spectroscopy of Ga and Ge in glasses $\text{GeS}_2\text{-Ga}_2\text{S}_3\text{-NaF}$ (MnF_2) [7] confirm this supposition.

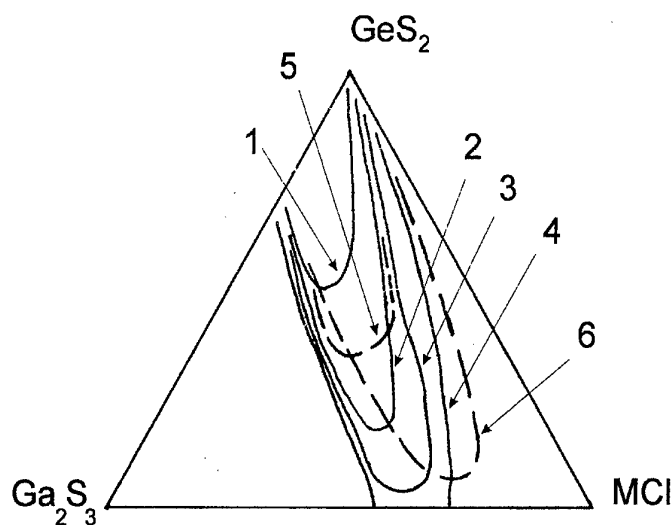


Fig. 1. Glass-forming regions with:
1 - LiCl; 2 - NaCl; 3 - KCl; 4 - CsCl; 5 - AgCl; 6 - TlCl.

RESULTS AND DISCUSSIONS

The melts with high chloride content (more than 15-20 mol %) are most readily synthesised. If the melt composition does not lie at the boundary of the glass formation region, a high cooling rate is not required to obtain the glass; it may even be down to the point of the furnace-cooled regime. The synthesis of glasses with a small chloride content is more complicated. Higher cooling rates are necessary for glass to be obtained, even to the point of quenching into water. The glasses lose their moisture resistance with an increase in the chloride content. Glasses containing 10 mol % chloride can be used as

membranes in ion-selective electrodes. At the maximum chloride concentrations, the glass ingots begin to crack after the tubes open up. Fig. 1 demonstrates the glass formation regions. The boundaries of glass formation region in the rubidium chloride system lie between those in

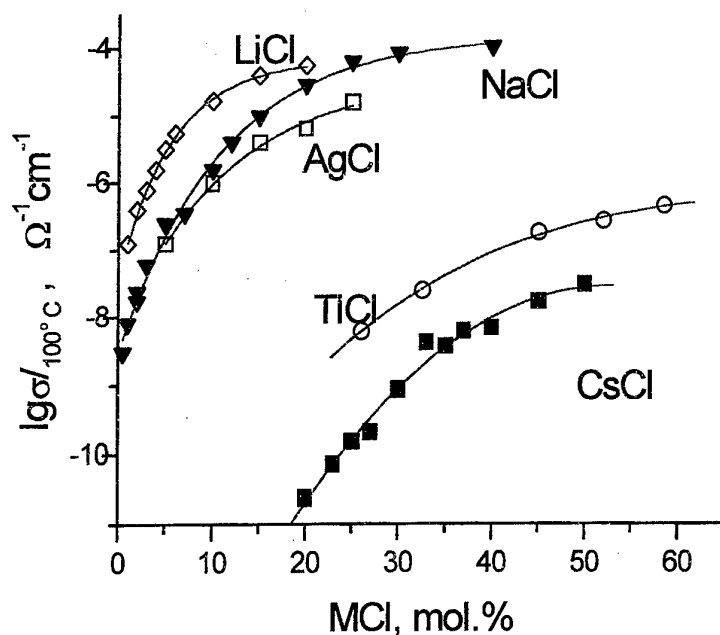


Fig. 2. Dependence of maximum chloride content in glasses of the $\text{GeS}_2\text{-Ga}_2\text{S}_3\text{-MCl}$ systems on cation radius.

the $\text{GeS}_2\text{-Ga}_2\text{S}_3$ system, the four fold co-ordination of Ga, along with the same co-ordination of germanium, produces a too high degree of glass-network connectivity, which hinders the glass formation. The introduction of chloride into the glass composition retains the fourfold co-ordination of gallium but decreases the degree of glass-network connectivity (Fig. 2). Therefore, the formation of the complex anion favours the glass formation. The insufficient stability of complex anion in the melt at temperatures when the glass network is formed can present a problem. It is known that the stability of the complex anion depends directly on the polarizability of outer-sphere cation, or inversely, on the field strength of this cation. To put it differently, the stability of the complex anion should increase with a rise in the radius of the outer-sphere cation. So, in fig. 2 it is shown the dependence of the maximum chloride content in glasses of the $\text{GeS}_2\text{-Ga}_2\text{S}_3\text{-MCl}$ systems on the outer-sphere cation radius. The points corresponded to Cu and Ag fall out of this dependence. The reason of this is the exchange chemical reactions, which take place in these systems [9].

Therefore, the concept of the formation of complex anions and their beneficial effect on the glass-forming ability of the melts should be used to explain the regularities of glass formation in the systems under consideration. It seems likely that an increase in the degree of covalence for the complexing agent metal bonds due to the complex formation is also favourable to glass formation. It was of interest to find a system that would be a totally halide system, but close in composition to the studied compounds, and where the role of complexing ability of the Ga^{+3} ions in the formation of glass network would be evident.

Such a system, namely, $(1-x)\text{GaI}_3\text{xNaCl}$, was found. The glass formation region extends from $x=0.05$ to $x=0.25$. The softening points for glasses were below room temperature. The

the systems with potassium and caesium chlorides. The glass formation region for the system with copper chloride is not depicted, because the glasses could be manufactured only when the CuCl content was less than 5 mol % and when the quenching was performed into water, by pouring the melt onto the tube walls. It is of interest that the concentration boundaries of all the glass formation regions are similar in shape: the boundaries are extended from the glass formation

region of the quasi-binary $\text{GeS}_2\text{-Ga}_2\text{S}_3$ system toward the $\text{MGaS}_{3/2}\text{Cl}$ composition. In the glass of

rate of glass hydrolysis in air is very high. The glasses are pale-yellow and become colourless with an increase in the sodium chloride content.

The compositions of glasses which conductivity was investigated lie in the following sections: 1. $(0.2\text{Ga}_2\text{S}_3 \cdot 0.8\text{GeS}_2)\text{-LiCl}$; 2. $(0.2\text{Ga}_2\text{S}_3 \cdot 0.8\text{GeS}_2)\text{-NaCl}$; 3. $(0.3\text{Ga}_2\text{S}_3 \cdot 0.7\text{GeS}_2)\text{-}(0.7\text{NaCl} \cdot 0.3\text{Ga}_2\text{S}_3)$; 4. $(0.2\text{Ga}_2\text{S}_3 \cdot 0.8\text{GeS}_2)\text{-}(0.67\text{KCl} \cdot 0.33\text{Ga}_2\text{S}_3)$; 5. $(0.11\text{Ga}_2\text{S}_3 \cdot 0.89\text{GeS}_2)\text{-}(0.67\text{CsCl} \cdot 0.33\text{Ga}_2\text{S}_3)$; 6. $(0.2\text{Ga}_2\text{S}_3 \cdot 0.8\text{GeS}_2)\text{-AgCl}$; 7. $(0.2\text{Ga}_2\text{S}_3 \cdot 0.8\text{GeS}_2)\text{-}(0.7\text{AgCl} \cdot 0.3\text{Ga}_2\text{S}_3)$; 8. $(0.2\text{Ga}_2\text{S}_3 \cdot 0.8\text{GeS}_2)\text{-}(0.65\text{TlCl} \cdot 0.35\text{Ga}_2\text{S}_3)$.

The examples of the concentration dependence of ionic conductivity are presented in fig.3. It should be noted that the investigated glasses possess a significant conductivity for practically all M^+ cations. The alloys with CuCl show no glassforming ability. The cation conductivity of glasses with RbCl has the values which are smaller than those for glasses with

KCl and are larger than those for glasses with CsCl . But the detailed investigations of glasses with RbCl were not carried out.

The main attention was spared to analyse the concentration dependencies of activation energy of cation conductivity (E_σ). These dependencies are presented in fig.4. It should be marked that the main orientation of all sections (1-8) in investigated systems is closed. Due to this fact it became possible to compare the concentration dependencies of E_σ , because deviation of orientation of sections does not influence on the dependencies $E_\sigma(\text{M}^{1/3})$ dramatically.

Fig. 3. Dependencies of conductivity of glasses from containing of halides at 100 °C .

$E_\sigma(\text{M}^{1/3})$ dependence for glasses with AgCl is plotted using the data for both sections 6 and 7 (fig. 4). Certainly, for sections with strong different orientations the nature of $E_\sigma(\text{M}^{1/3})$ dependencies is different.

We shall consider, that the conductivity is defined by the vacancy mechanism. The formation of vacancies is the result of the thermodissociation of the pairs cation-vacancy. The activation energy of the cationic conductivity consists of the three terms: the Column potential of the dissociation of cation-vacancy pairs, the Column barrier between two neighbouring vacancies and the elastic deformation of the glasses network due to the movement of cations with large radius. The latter is determined by multiplication of the deformed volume $(4\pi R_h(R_c - R_h)^2)$ and the modulus of the comprehensive compression (G) [10]. So, for E_σ we can write the following expression:

$$E_\sigma = 4\pi G R_h (R_c - R_h) + \frac{e^2}{8\pi\epsilon\epsilon_0 (R_c + R_a)} + \frac{e^2}{4\pi\epsilon\epsilon_0} \left(\frac{1}{R_c + R_a} - \frac{2}{r} + \frac{1}{2r} \right) \quad (1)$$

Or:

$$E_{\sigma} = \frac{3e^2 \left(\frac{1}{R_c + R_a} - \frac{1}{r} \right)}{8\pi\epsilon\epsilon_0} + 4\pi G R_h (R_c - R_h)^2 \quad (2)$$

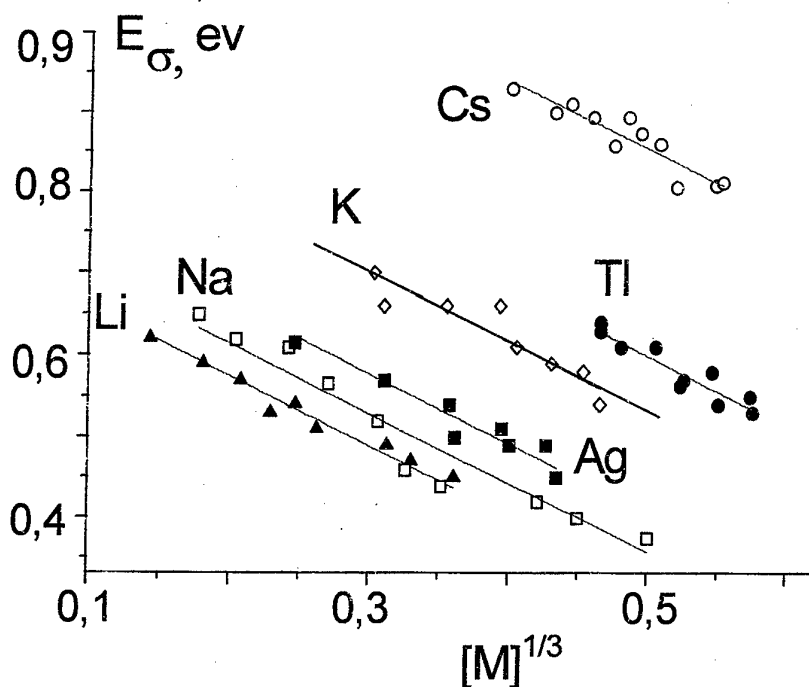


Fig.4. Dependence of E_{σ} on the cubic root of the atomic fraction of cations.

average distance between the cation positions in the glass network:

$$8r^3 \approx \frac{\bar{A}}{\rho N_A M} \quad (3)$$

\bar{A} is the average weight of the atoms, ρ is the glass density, M is the atomic fraction of the ion conductive cations in glass. The dependence of the factor $\frac{\bar{A}}{\rho N_A}$ on the composition is weak because the density of glasses is usually a linear function of an average weight of the atoms. Let us suppose that the dielectric constant ϵ does not depend on the composition of glasses in the investigated systems.

According to the model the $E_{\sigma}(M^{1/3})$ dependencies have the following peculiarities. All $E_{\sigma}(M^{1/3})$ dependencies under investigation should be linear. Their slope does not depend on the nature of the cation and is equal to

The length of ions' jump from one vacancy to another is marked by $2r$, the effective equilibrium distance between the anions' negative charge and the cations' positive charge is approximately the same as the sum of their radii ($R_c + R_a$). R_h is the radius of the channels among the atoms through which the cation moves ($R_h = 0.06$ nm [10]). Let us assume that $2r$ is equal to the

$$-\frac{dE_{\sigma}}{dM^{1/3}} = \frac{3e^2}{4\pi\epsilon\epsilon_0} \sqrt[3]{\frac{\rho N_A}{A}}. \quad (4)$$

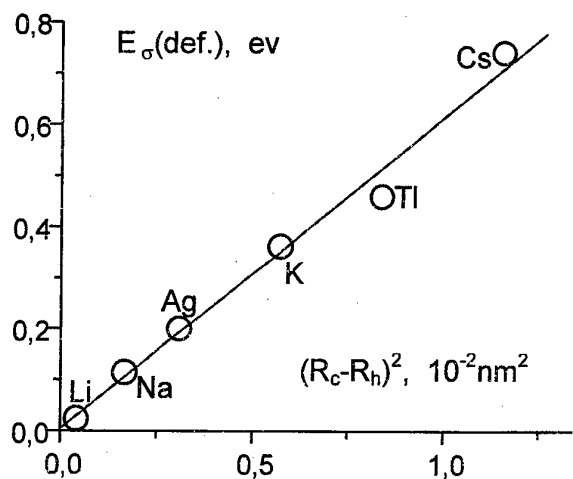


Fig. 5. Dependence of the deformation input into E_{σ} on $(R_c - R_h)^2$.

From this expression and according to the experimental data it can be estimated that ϵ has the value of about 10. The values of E_{σ} at $M \rightarrow 0$ (E_{σ}^0) are equal to:

$$E_{\sigma}^0 = \frac{3e^2}{8\pi\epsilon\epsilon_0(R_c + R_a)} + 4\pi G R_h (R_c - R_h)^2$$

This equation allows to find the part of E_{σ} which is determined by the deformation of the glass network due to the motion of the cations (E_{def}). According to the equation for E_{def} , it depends linearly on $(R_c - R_h)^2$ (fig. 5). So, it can be found from the slope of this dependence that $G \approx 1.3 \cdot 10^{10} \text{ J/m}^3$. According to the results of the sound velocity investigations it was established for various chalcogenide glasses that G

changes between 0.97 and $2.06 \cdot 10^{10} \text{ J/m}^3$ [11].

CONCLUSIONS

The new $\text{GeS}_2\text{-Ga}_2\text{S}_3\text{-MCl}$ and $\text{GaI}_3\text{-NaCl}$ glass-forming systems are identified. The complex $M^+[\text{GaS}_{3/2}\text{Cl}]^-$ structural units play a significant part in the formation of glass network. The occurrence of these units favours an increase in the limiting content of chlorides in the test glasses.

Glasses containing GeS_2 , Ga_2S_3 and chlorides of all M^+ cations, but for Cu, possess a significant cation conductivity. The dependencies of the activation energy of conductivity on the concentration of MCl and the cation radius are satisfactorily described with the help of the simple model. These facts allow to consider the discussed glasses as the convenient model objects for further investigations of the composition influence on the cationic conductivity of glasses.

ACKNOWLEDGEMENTS

This work has been supported by the Russian Fund of Basic Researches (Grant N98-03-32114a), by the Russian Programme "Integration" (Grant N326.47) and by the Competition Centre of S.-Petersburg State University (Grant N97-92-66).

REFERENCES

- [1] E.G. Nedoshovenko, E.Yu. Turkina, Yu.S. Tver'yanovich, Z.U. Borisova. Vestnik Leningradskogo universiteta. Ser. 4. №2. (1986). S.52.
- [2] Yu.S. Tver'yanovich, E.G. Nedoshovenko, V.V. Aleksandrov, E.Yu. Turkina, A.S. Tver'yanovich, I.A. Sokolov. Glass Physics and Chemistry. 22 (1996) 9.
- [3] Yu.S. Tver'yanovich, Z.U. Borisova, A.V. Pazin, E.Z. Klobukova. IIIth Vsesoyuznyi simposium "Tverdye elektrolity i ih analiticheskoe primeneniye". Minsk. 1990. S.28.

- [4] Z.U.Borisova, E.A. Bychkov, Yu.S.Tver'yanovich. Interaction of metals with chalcogenide glasses. Leningrad, 1991.
- [5] O.L. Baidakova, Yu.S.Tver'yanovich, S.V. Chernov, Z.U. Borisova. Vestnik Leningradskogo universiteta. Ser. 4. №18. S. 120. (1986).
- [6] T.N. Orkina., M.S. Gutenev, Yu.S. Tver'yanovich, V.V. Aleksandrov. In "Poluchenie i analiz chistykh veshestv". (Ed. G.Devyatyh). Nizhny-Novgorod. 1990. S.63.
- [7] N.D. Aksenov, M.S. Gutenev, T.N. Orkina, L.L. Makarov. Glass Physics and Chemistry. V.18. №2. (1992) S. 160.
- [8] A. Tverjanovich, Yu.S. Tver'yanovich, S. Loheider. J.Non-Cryst.Sol. 208 (1966) 49.
- [9] Kuznetsov S.L., Mikhailov M.D., Pecheritsyn I.M., Turkina E.Yu. J.Non-Cryst.Sol. 213&214 (1997) 68.
- [10] Physics of Electrolytes. Edited by J.Hladik. Academic Press. London - New-York. 1972.
- [11] Borisova Z.U. Glassy semiconductors. Plenum Press, New-York, 1981.

COMPARISON OF LOW-PHONON HOSTS FOR 1300 NM OPTICAL AMPLIFIER

R. S. Quimby

Department of Physics, Worcester Polytechnic Institute
Worcester, MA 01609 USA email rsquimby@wpi.edu

B.G. Aitken

Corning Incorporated, SP-DV-2-5
Corning, NY 14831

ABSTRACT

The measured spectroscopic properties of Pr^{3+} and Dy^{3+} doped into sulfide and fluoride hosts are used to predict the gain efficiency of a 1300 nm fiber amplifier. It is found that excited-state absorption from the long-lived $^3\text{H}_5$ level in Pr^{3+} doped sulfide glass causes a significant degradation in performance, especially at wavelengths shorter than 1320 nm. Pr^{3+} doped fluoride glass does not suffer significantly from this effect, although the maximum gain is smaller in the fluoride glass. The Dy^{3+} amplifier is predicted to be most efficient for wavelengths longer than 1330 nm.

INTRODUCTION

Low-phonon glasses such as the chalcogenides are widely recognized as ideal hosts for a rare-earth doped fiber amplifier, due to the lower nonradiative decay rates and consequent higher quantum efficiencies.¹⁻³ The higher refractive index of the low-bandgap chalcogenides also increases the radiative rates and emission cross sections, which further improves amplifier efficiency. Not widely recognized, however, is the detrimental effect of excited-state absorption (ESA) from certain long-lived levels in a chalcogenide-based amplifier. We show here how ESA from the $^3\text{H}_5$ level of Pr^{3+} limits the efficiency of a 1.3 μm sulfide-based fiber amplifier, and make a comparison between sulfide and fluoride hosts.

PR FIBER AMPLIFIER MODEL

Fig. 1 shows the relevant transitions for Pr^{3+} , with pumping into the $^1\text{G}_4$ (level 5) and amplification on the $^1\text{G}_4 \rightarrow ^3\text{H}_5$ (5 \rightarrow 2) transition. Levels $^3\text{H}_6$ and $^3\text{F}_2$ are thermally coupled and lumped into an effective level 3, and likewise for levels $^3\text{F}_3$ and $^3\text{F}_4$, which are lumped into level 4. The net gain coefficient is

$$\gamma = N_5\sigma_{52} - N_2\sigma_{25} \quad (1)$$

where N_j is the number of ions in level j per unit volume, and σ_{ij} is the cross section for the $i \rightarrow j$ transition. Although N_2 is usually assumed to be negligible, this assumption must

be re-examined for the chalcogenide glasses, where weak nonradiative relaxation leads to long level lifetimes.

The populations N_5 and N_2 were calculated under steady-state pumping on the $1 \rightarrow 5$ transition using a standard rate equation analysis. We consider only the small signal limit, but allow the pump power to be arbitrarily large. The fiber amplifier model is simplified to neglect amplified spontaneous emission (ASE) and overlap integrals between pump and signal modes. These simplifications are not expected to significantly affect the comparison of different glass hosts as presented here. After integrating the gain along a fiber long enough to absorb most of the pump power P_{in} , the gain efficiency is found to be

$$\frac{\text{dB gain}}{P_{in}} = \frac{10}{\ln 10} \frac{\tau_{eff} [x_5 \sigma_{52} - x_2 \sigma_{25}]}{A_{core} h \nu_p} \quad (2)$$

where A_{core} is the core area, $h \nu_p$ is the pump photon energy, and

$$\begin{aligned} \tau_{eff} &= T_2 + T_3 + T_4 + T_5 \\ T_5 &= \tau_5 \\ T_4 &= \beta_{54} \tau_4 \\ T_3 &= [\beta_{53} + \beta_{54} \beta_{43}] \tau_3 \\ T_2 &= [\beta_{52} + \beta_{54} \beta_{42} + \beta_{32} (\beta_{53} + \beta_{54} \beta_{43})] \tau_2 \end{aligned}$$

Also, τ_i is the fluorescence lifetime of level i , β_{ij} is the branching ratio for the $i \rightarrow j$ transition (including nonradiative decay), and $x_i \equiv T_i / \tau_{eff}$ is the fraction of all excited ions which are in level i . In the limit where level 5 is the only long-lived excited state, the gain in eq.(2) is simply proportional to $\sigma_{52} \tau_5$, which is the usual figure-of-merit for a four-level type amplifier.

Evaluation of x_5 and x_2 in eq.(2) requires knowledge of both radiative and nonradiative rates. Radiative rates were calculated from the Judd-Ofelt parameters (see table 1), and nonradiative rates were calculated using the energy gap law $W_{nr} = B(1+n)^p \exp(-\alpha \Delta E)$. In this expression, ΔE is the energy gap to the next lowest state, $p = \Delta E / \hbar \omega$, $\hbar \omega$ is the effective maximum phonon energy of the glass, $n = 1 / (e^{\hbar \omega / kT} - 1)$, and B and α are two phenomenological fitting parameters. We recently measured $\alpha = 3.2 \times 10^{-3} \text{ cm}$ and $B = 2 \times 10^6 \text{ s}^{-1}$ for the glass AsGaGeS, values similar to those previously obtained for LaGaS glass.⁴

Also needed in eq.(2) are the emission and ESA spectra, σ_{52} and σ_{25} . These are related by the McCumber transform $\sigma_{25}(\lambda) = \sigma_{52}(\lambda) \exp[\frac{\hbar c / \lambda - \epsilon}{kT}]$, where ϵ is an effective energy difference determined by the energies of all Stark components for the two levels. Knowledge of ϵ provides the scaling factor between σ_{52} and σ_{25} , and gives the ratio of absorption to emission oscillator strength f_{abs} / f_{em} . Since individual Stark components are not resolved in glasses at room temperature, an approximate method was used based on a simplified Stark level scheme,⁵ with the result $f_{abs} / f_{em} = 0.88$. Another method commonly used is based on the degeneracies of the two levels, which yields $f_{abs} / f_{em} = 0.82$. The small difference between these two values does not significantly impact the amplifier gain calculations.

PR AMPLIFIER RESULTS AND DISCUSSION

Eq.(2) was used to calculate the small-signal gain of a Pr:AsGaGeS fiber amplifier with 2 μm diameter core, pumped at 1027 nm. Fig. 2 compares the predicted gain spectra with and without considering the ESA from level 2. ESA becomes most important at shorter wavelengths because the absorption spectrum $\sigma_{25}(\lambda)$ is blue-shifted with respect to the emission spectrum $\sigma_{52}(\lambda)$.

To provide a comparison with other 1.3 μm amplifier hosts, the same calculation was performed for Pr³⁺ doped in a fluorozirconate glass (ZBLAN) and in a recently developed oxyfluoride transparent glass ceramic (TGC).⁶ The Judd-Ofelt parameters given in Table 1 for these hosts (as well as AsGaGeS) were determined using branching ratio as well as absorption measurements,⁷ and by minimizing the fractional deviations in oscillator strength.⁸ The values of α and $\hbar\omega$ for ZBLAN were taken from the similar glass ZBLA,⁴ with the value of B adjusted so the ¹G₄ lifetime agreed with the measured value of 110 μs . For TGC, values of α and $\hbar\omega$ were taken from SrF₂,⁹ with B adjusted so the radiative quantum efficiency of the 5 \rightarrow 2 transition agreed with the measured value of 8%.⁸

Fig. 3 shows the resulting calculated gain spectra for Pr doped in the three different hosts. ESA has much less effect in the fluoride hosts due to the shorter ³H₅ lifetime (1.8 μs in ZBLAN and 6.0 μs in TGC, compared with 125 μs in AsGaGeS). At wavelengths shorter than 1310 nm, TGC has a higher efficiency than the other two hosts, as well as a flatter gain spectrum. The peak efficiency of the three hosts is governed by the radiative quantum efficiency of the 5 \rightarrow 2 transition, and it is here where the sulfide host is clearly superior.

The calculated gain spectrum of a Pr:AsGaGeS amplifier is sensitive to the values chosen for the nonradiative decay parameters B and α . Fig. 4 shows how the gain at 1320 nm depends on B for a fixed α , with the vertical lines showing the best-fit value of B for each host. The gain is maximized at some optimum B value, due to two competing effects: at high B the quantum efficiency of the 5 \rightarrow 2 transition becomes small, reducing the gain, while at very low B ESA becomes important because of the long ³H₅ lifetime. It is seen that the actual value of B for AsGaGeS is close to optimum, while TGC and ZBLAN are some 2 orders of magnitude away from optimum. This implies that lower values of B are definitely preferred in the fluoride hosts, while for the sulfide hosts a lower B value may actually degrade amplifier performance, especially at the shorter wavelengths.

In addition to variations in B, the α parameter may vary from glass to glass. Fig. 5 shows how the gain at 1330 nm in a Pr:AsGaGeS fiber varies with B for a number of α values. Higher α yields a higher optimized gain because the ratio τ_5/τ_2 is larger, resulting in a smaller ESA contribution. At large α the optimized gain efficiency approaches 4 dB/mW, comparing favorably with the best erbium-doped amplifiers. It remains to be seen, however, whether chalcogenide glasses with these optimum values of α and B can be realized.

DY FIBER AMPLIFIER MODEL

An alternative 1.3 μm amplifier utilizes the Dy³⁺ transition shown in Fig. 1. Since this is a three-level system, the ground state must be significantly depleted in order for the gain coefficient $\gamma = N_4\sigma_{41} - N_1\sigma_{14}$ to be positive. The small-signal gain of a Dy:AsGaGeS

fiber amplifier was calculated using a modification of the simplified model described above, assuming a 2 μm core diameter, 10^{19} Dy^{3+} ions/ cm^3 , 100 mW of pump light at 1110 nm, and the α and B values of Table 1. Fig. 3 shows the gain spectrum obtained with an optimum fiber length calculated at each wavelength. The Dy^{3+} amplifier is seen to be most efficient around 1390 nm, with a very poor efficiency below 1320 nm.

One drawback of the Dy^{3+} amplifier is the long fiber lengths required for optimum gain. To achieve a gain of 25 dB at 1330 nm requires pumping at 100 mW with a fiber length of 50 m, compared to a power of 12 mW and fiber length of 4 m for the Pr:AsGaGeS amplifier. The long required fiber lengths in Dy are due to bottlenecking of population in levels 2 and 3. Only $\approx 2\%$ of the total excited-state population resides in level 4, so over 98% of the Dy ions must be pumped out of the ground state in order to achieve population inversion on the $4 \rightarrow 1$ transition. The pump transition is thus strongly bleached, requiring long fiber lengths to absorb most of the pump light. Co-doping with Tb^{3+} has been suggested as a way to reduce the lifetime of levels 2 and 3, thereby permitting shorter fiber lengths.¹⁰ Including Dy \rightarrow Tb energy transfer in the model confirms that the optimum fiber length is reduced upon co-doping with Tb, but this comes at the expense of a decreased gain efficiency.

The effect of varying B for fixed α is shown in Fig. 6. As in Pr^{3+} , there is an optimum value of B which optimizes the gain. However, the value of B for AsGaGeS is an order of magnitude larger than optimum for a Dy^{3+} amplifier. Therefore, hosts with even smaller nonradiative rates (such as selenide glasses) may improve the efficiency of a Dy fiber amplifier.

REFERENCES

- [1] D.W. Hewak, J.A. Medeiros Neto, B. Samson, R.S. Brown, K.P. Jedrzejewski, J. Wang, E. Taylor, R.I. Laming, G. Wylangowski, D.N. Payne, IEEE Photon. Technol. Lett. **6**, 609 (1994)
- [2] K. Wei, D.P. Machewirth, J. Wenzel, E. Snitzer, and G.H. Sigel Jr, Opt. Lett. **19**, 904 (1994)
- [3] Y. Ohishi, A. Mori, T. Kanamori, K. Fujiura, and S. Sudo, Appl. Phys. Lett. **65**, 13 (1994)
- [4] R. Reisfeld, ch. 58 in *Handbook on the Physics and Chemistry of Rare Earths*, ed. by K.A. Gschneidner and L. Eyring (Elsevier, 1987)
- [5] R.S. Quimby and W.J. Miniscalco, Opt. Lett. **16**, 258 (1991)
- [6] P.A. Tick, N.F. Borrelli, L.K. Cornelius and M.A. Newhouse, J. Appl. Phys. **78**, 6367 (1995)
- [7] R.S. Quimby and W.J. Miniscalco, J. Appl. Phys. **75**, 613 (1994)
- [8] R.S. Quimby, P.A. Tick, N.F. Borrelli, and L.K. Cornelius, J. Appl. Phys. **83**, 1649 (1998)
- [9] L.A. Riseberg and M.J. Weber, ch. III in *Progress in Optics XIV*, ed. E. Wolf (North-Holland 1976)
- [10] B.N. Samson, T. Schweizer, D.W. Hewak, and R.I. Laming, Opt. Lett **22**, 703 (1997)

TABLE I. Radiative and nonradiative parameters used in amplifier models.

Ion	Glass	$\hbar\omega$ (cm ⁻¹)	$\alpha(10^{-3}$ cm)	B (s ⁻¹)	$(\Omega_2, \Omega_4, \Omega_6)(10^{-20}\text{cm}^2)$
Pr	AsGaGeS	350	3.2	2×10^6	(10.4, 4.78, 10.4)
Pr	TGC	360	4.5	8×10^8	(1.41, 4.59, 7.88)
Pr	ZBLAN	500	5.2	2×10^{10}	(3.14, 3.65, 6.70)
Dy	AsGaGeS	350	3.2	2×10^6	(9.27, 3.19, 1.41)

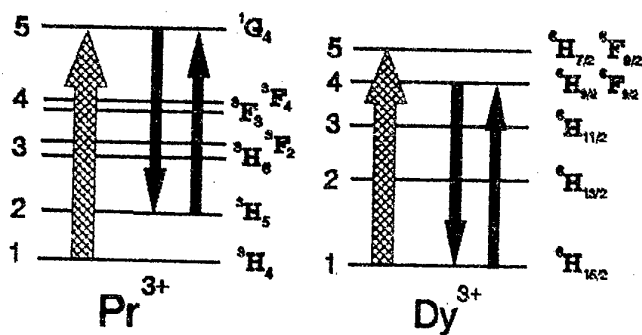


Fig. 1 Transitions for 1.3 μm amplifier

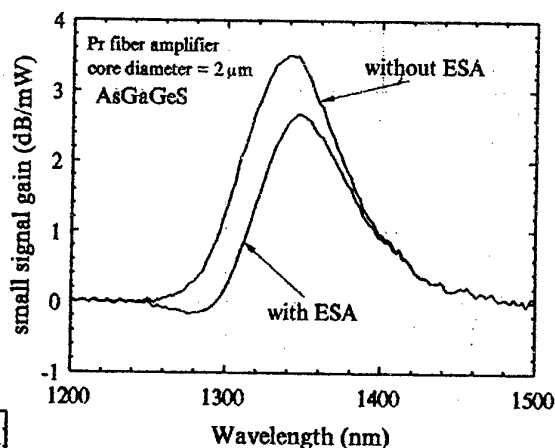


Fig. 2 Effect of including 3H5-1G4 excited-state absorption on the gain spectrum of a Pr:AsGaGeS fiber amplifier.

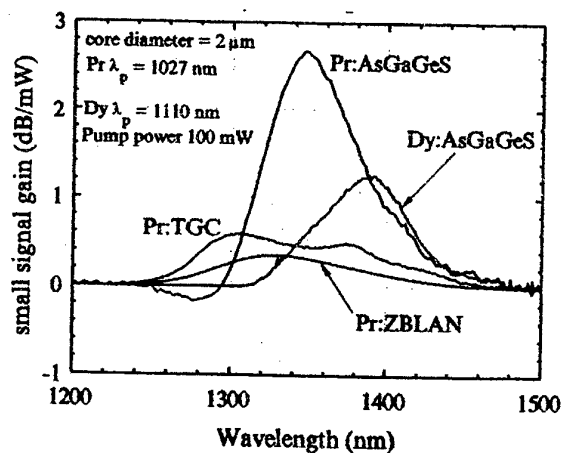


Fig. 3 Calculated gain spectra of Pr³⁺ and Dy³⁺ fiber amplifiers with sulfide glass (AsGaGeS), fluoride glass (ZBLAN) and oxyfluoride transparent glass ceramic (TGC) hosts.

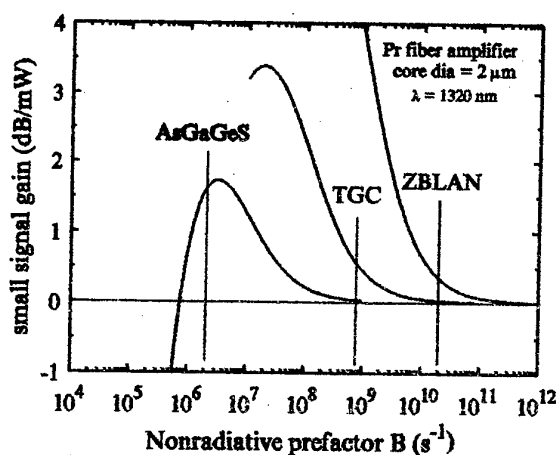


Fig. 4 Variation in calculated gain at 1320 nm in a Pr fiber amplifier with the assumed energy-gap law parameter B (α value given in Table 1).

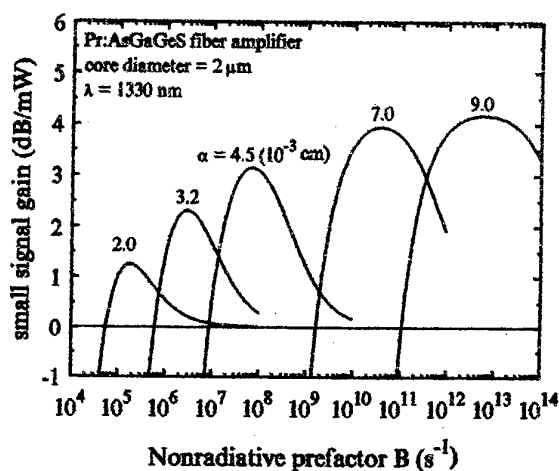


Fig. 5 Variation in calculated gain at 1330 nm in a Pr:AsGaGeS fiber amplifier with the assumed energy-gap law parameter B for different α values.

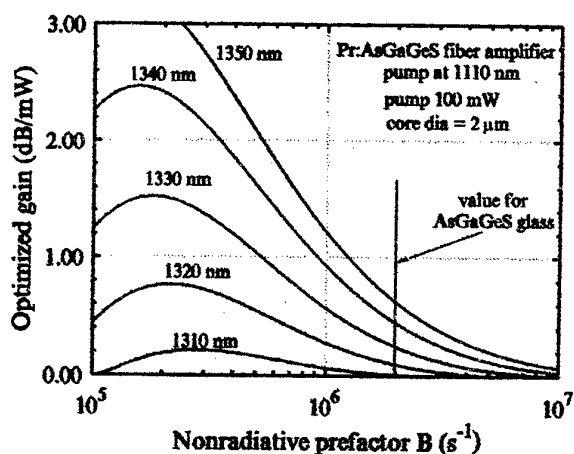


Fig. 6 Calculated gain in a Dy:AsGaGeS fiber amplifier vs. energy-gap law parameter B (α value given in Table 1).

SPECTROSCOPIC PROPERTIES OF Nd^{3+} IN FLUOROALUMINATE GLASSES FOR AN EFFICIENT $1.3\mu\text{m}$ OPTICAL AMPLIFIER

M. Naftaly*, A. Jha*, B.N. Samson** and E.R. Taylor**

*School of Materials, University of Leeds, Leeds LS2 9JT, UK; A.Jha@leeds.ac.uk

**ORC, University of Southampton, Southampton SO17 1BJ, UK

ABSTRACT

Nd^{3+} -doped $1.3\mu\text{m}$ fibre amplifier has many inherent advantages. Nonetheless, two major problems must be overcome in designing a device: long wavelength gain, and amplified spontaneous emission (ASE). In the majority of Nd^{3+} -doped glasses the gain is red-shifted out of the second telecom window as a result of long-wavelength emission and signal excited-state absorption (ESA). The ASE at 1050 nm clamps signal gain at low values due to its large branching ratio. In this paper we present new fluoroaluminate glasses developed as hosts for the $1.3\mu\text{m}$ Nd^{3+} -doped fibre amplifier. Nd^{3+} emission peaks at 1310-1317 nm were demonstrated in bulk glasses. Gain in the 1310-1320 nm region was measured in fibre, with evidence of significantly reduced ESA. ASE filtering is discussed, focusing on Bragg grating filters and on absorbing co-dopants. The paper also examines thermal and viscous properties of the core and cladding glasses for preform and fibre fabrication.

1. INTRODUCTION

The need to convert the second telecommunication window (1290-1330 nm) to all-optical operation has generated the demand for a $1.3\mu\text{m}$ optical fibre amplifier as an essential component required to support the explosion in telecommunications and the expected traffic associated with interactive video and multimedia services. At present the $1.3\mu\text{m}$ window has no device comparable to EDFA at $1.5\mu\text{m}$, i.e. efficient, low-noise, and broad-band. Currently available optical amplifiers at $1.3\mu\text{m}$ are of two types: semiconductor optical amplifiers (SOAs), and praseodymium-doped fibre amplifiers (PDFAs) based on fluorozirconate ZBLAN glass. SOAs suffer from several serious drawbacks, such as low gain, low saturation power level, and a high noise figure. PDFAs have low gain efficiency, require a large pump (~800 mW) at 1015 nm, and are very expensive. These disadvantages prevent a widespread deployment of either SOAs or PDFAs by the networks. However, commercial devices such as lasers, pre- and power amplifiers, and WDM devices are becoming available in the US.

Nd^{3+} is the preferred ion for the $1.3\mu\text{m}$ optical amplifier, enjoying several vital advantages. First, the Nd^{3+} -doped amplifier has a large small-signal gain. This is due to its large stimulated emission cross-section ($\sigma \sim 7 \times 10^{-21} \text{ cm}^2$)¹ and a relatively long lifetime ($\tau \sim 550 \mu\text{s}$). The figure-of-merit for gain ($\sigma\tau$) is therefore of the order of $4 \times 10^{-24} \text{ cm}^2\text{s}$; that is, more than 10 times larger than ZBLAN PDFA at approximately $0.3 \times 10^{-24} \text{ cm}^2\text{s}$. Furthermore, the pump is at 800 nm and is available from a laser diode; the pump absorption cross-section is also very large (170 dB/km.ppm, i.e. 50-100 times larger than for PDFA). Very high doping levels, over 1 mol% are possible, since quenching does not set in until concentrations exceed several mole percent. The amplifying transition is almost entirely radiative, with lifetimes of the order of 550 μs and a quantum efficiency of ~100%. These factors make possible a highly efficient amplifier only 1-2 cm in length. The short length of the Nd^{3+} -doped amplifier is particularly important, since it enables both fibre and planar waveguide devices.

To date, however, the development of a commercial Nd^{3+} -doped amplifier has been impeded by two obstacles arising from the spectroscopy of the Nd^{3+} ion (see Figure 1). The central problem of 1.3 μm Nd^{3+} amplifier is the long wavelength of the gain peak. In the majority of host glasses the emission peak lies at too long wavelengths¹⁻², largely outside the region of interest of second-window telecommunications. Moreover, excited state absorption (ESA) overlaps the short-wavelength part of the emission spectrum and cancels gain in that region, thus red-shifting the gain curve even further. Both emission and ESA are known to vary greatly among different glass hosts¹⁻⁶. In the past, the only host offering gain peak below 1.32 μm was fluoroberyllate glass, which is unacceptable due to its poor environmental stability and exceptionally high toxicity. In this paper we present new fluoroaluminate glasses exhibiting emission and gain at the centre of the second telecom window. Another problem of the Nd^{3+} amplifier is the competing ASE at 1050 nm (Figure 1).

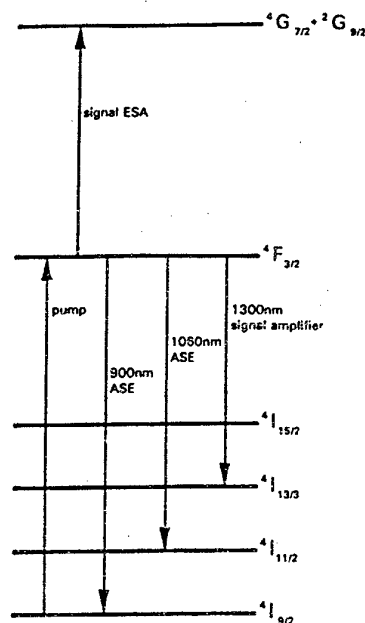


Figure 1. Energy levels of Nd^{3+} .

The branching ratio of this transition is five times larger than that of 1.3 μm signal emission¹. In a waveguide the 1050 nm ASE builds up to saturation, depopulating the lasing level, and thereby clamping signal gain at 1.3 μm to relatively low levels (<10 dB). The other ASE transition at 900 nm is three-level, and therefore does not pose a significant problem. In order to obtain high gain at 1.3 μm , the 1050 nm ASE must be filtered out. Continuous filtering is more effective than discrete filters; filtering schemes fall into two categories: fibre gratings that couple out the ASE radiation, and co-dopants that absorb it. The requirement for either type of filter is a rejection ratio of ≥ 30 dB at 1050nm ASE, with a 30nm bandwidth.

In the first part of this paper we describe the design of fluoroaluminate glasses for blue-shifting the emission at 1.3 μm and for reducing signal ESA, thereby extending the available gain to the centre of the second telecom window (1310-1320 nm). The second part of the paper discusses various methods of filtering ASE at 1050 nm. The third part looks at fluoroaluminate glass stability and viscous behaviour, and addresses fibre fabrication.

2. EXPERIMENTAL

Fluoroaluminate glasses were batched and melted under dry nitrogen atmosphere. Emission spectra were measured in bulk glass using a Ti-sapphire pump laser at 800 nm and a monochromator/detector assembly. The resolution was 1 nm. The fluorescence lifetime was observed using the same setup with the addition of a light chopper and a digital data recorder. Gain was measured in fibre geometry. The unclad fibres were 60 μm in diameter and 2 cm length, and were doped with 1 mol% of NdF_3 . The gain was measured in a pump-probe configuration, and was calculated as a pump-on/pump-off ratio. No steps were taken to suppress the 1050 nm ASE. The measured gain was low due to the large fibre diameter and the presence of ASE. Absorption spectra of Nd^{3+} in bulk glass samples were recorded by a Perkin-Elmer Lambda-19 spectrophotometer. The refractive indices of bulk glass samples were measured using an Abbe refractometer and a sodium light source at 589 nm. The characteristic temperatures of the glasses were determined by isochronal heating rate experiments (10 k min^{-1}) using a Perkin-Elmer differential scanning calorimeter (DSC-7). The viscosities were determined by the rotating bob technique⁷.

3. BLUE-SHIFTING THE GAIN CURVE

The new fluoroaluminate glass hosts for Nd^{3+} were designed to promote shorter-wavelength emission at 1.3 μm and to reduce signal ESA. The energy levels of Nd^{3+} ions in a glass host are subject to strong nephelauxetic effect⁸. As a result, in hosts where the Nd^{3+} dopant ions experience strong ionic bonding the emission appears at shorter wavelengths^{3,8}. The type of bonding, ionic or covalent, determines the character of ligand fields, thereby affecting the nephelauxetic shift and the spectral line-shape arising from the Stark splitting. It is a generally observed trend in rare-earth doped glasses that shorter-wavelength emission spectra are correlated with low refractive index⁸, which is indicative of strong ionic bonding. The new fluoroaluminate glasses were designed to have low refractive indices and to be strongly ionic, resulting in a shorter emission wavelength and a greatly reduced ESA. The nephelauxetic shift in Nd^{3+} -doped fluoroaluminate glasses is shown in Figure 2 where the peak of 1.3 μm emission is seen to shift to shorter wavelengths with decreasing refractive index.

Gain at 1.3 μm in two Nd^{3+} -doped fluoroaluminate glasses is shown in Figure 3 (the respective compositions are ALF70=37 AlF_3 :15 CaF_2 :12 MgF_2 :9 SrF_2 :6 BaF_2 :15 YF_3 :6 NaPO_3 and ALF123=40 AlF_3 :22 CaF_2 :6 MgF_2 :6 SrF_2 :6 BaF_2 :10 LiF :10 NaF). Comparing the two gain curves highlights two important features. The gain maximum shifts to shorter wavelength in the more ionic glass. The effect of ESA is also reduced, as seen in the extension of the short-wavelength side of the curve. Strongly asymmetric gain profiles with sharp short-wavelength cutoff are typical in Nd^{3+} -doped glasses, due to signal ESA cutting gain at these wavelengths. The gradual slope of gain on the blue side of the gain profile in ALF123 glass testifies to the greatly reduced influence of ESA. The gain requirements for a second-window amplifier are seen to be satisfied by glass ALF123 in Figure 3. The gain maximum is at 1317 nm. This is a substantially shorter wavelength than the 1323 nm obtained in fluorophosphate glass⁵, previously considered as the preferred Nd^{3+} host. Moreover, the wavelength of 1317 nm lies at the centre of the second telecom window, in the region of zero-dispersion of most installed fibre. Furthermore, signal ESA in ALF123 glass is greatly reduced. As a result, the gain remains above 0.5 dB level (90%) in the 1310-1320 nm region, with the 3dB (50%) point at 1305 nm. The reduction in ESA both allows an increase in available gain, and also improves the amplifier noise figure. At longer wavelengths in both glasses the gain is almost flat to 1360 nm, and is therefore suitable for WDM applications.

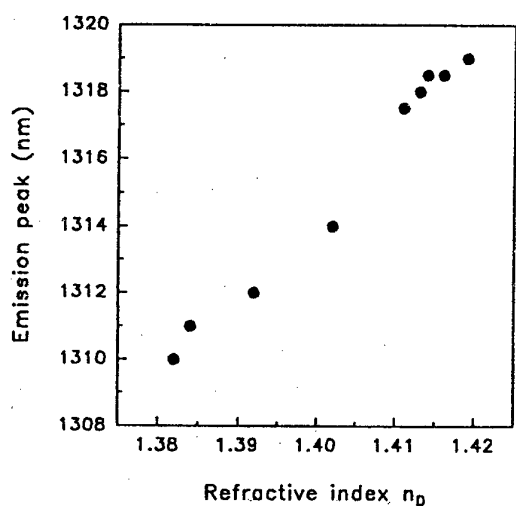


Figure 2: Nd^{3+} emission peak vs n_D .

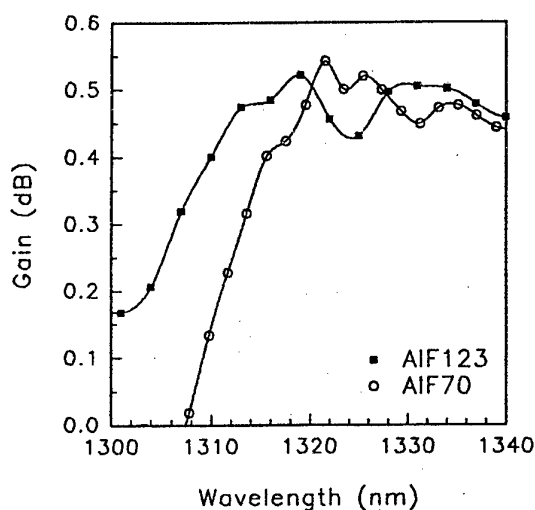


Figure 3: Nd^{3+} gain in new ALF glasses.

4. FILTERING 1050 nm ASE

The branching ratio of emission transitions at 1050 nm and 1300 nm is approximately 5:1¹. As a consequence, the 1050 nm ASE dominates the emission from the lasing level. In a waveguide, ASE is guided and amplified along with the signal, until it saturates the transition by depleting the lasing level. In the absence of ASE filtering, signal level will always be 1/5 of ASE level, leading to a highly inefficient amplifier. Therefore in order to obtain an efficient, high-gain amplifier it is essential to filter out the 1050 nm ASE radiation. Continuous filtering schemes are more effective than discrete filters, resulting in higher signal gain and lower noise. Continuous filtering can be of two types: fibre Bragg gratings, and absorbing co-dopants. In an amplifier device the ASE filter must have a rejection ratio of at least 30 dB at 1050 nm, with a bandwidth of around 30 nm.

Fibre Bragg gratings can be designed as narrow-band filters to couple out the ASE radiation. Gratings can be written in Ce³⁺-doped fluoroaluminate glass by a UV laser, such as excimer. The 250-300 nm absorption peak of Ce³⁺ matches the UV (electronic) edge of fluoroaluminate glasses. As a result, when exposed to UV light at these wavelengths, Ce³⁺ dopant facilitates band-gap absorption, giving rise to a significant change in the refractive index. Gratings can also be written in undoped fluoroaluminate glass using shorter-wavelength UV light below 200 nm. A grating-writing experiment using an excimer laser was carried out in Ce³⁺-doped fluoroaluminate bulk glass by exposing it to an interference pattern formed by the laser beam. This resulted in grating formation in the layer of the glass where the laser radiation was absorbed. The grating efficiency was measured as a change in glass reflectance, averaged over the glass area and thickness. This is shown in Figure 4, which plots grating efficiency as a function of laser exposure (total number of pulses). The grating was found to be persistent, with only a small reduction in efficiency observed after 8 months. It can be calculated⁹ that in order to obtain grating reflectivity of ≥ 30 dB in a short fibre (a few cm), such as the Nd³⁺-doped fluoroaluminate glass amplifier, the necessary change in the refractive index is of the order of 10^{-4} - 10^{-3} .

An alternative method of ASE filtering is co-doping with an ion having an appropriate absorption band. The difficulty here lies with finding a suitable co-dopant which will satisfy several critical requirements. First, absorption at 1050 nm must be very large. To achieve at least 30 dB absorption in several centimeters pathlength at dopant concentrations of ~ 1 mol%, the absorption coefficient must be of the order of 100 dB/km.ppm. Second, absorption around 1300 nm must be negligible, to avoid signal losses; and at 800 nm (pump wavelength) must be negligible or very low, to maintain pump efficiency. This implies a relatively narrow absorption peak. Third, there must be no energy transfer between Nd³⁺-ion and the co-dopant ion that can lead to Nd³⁺ fluorescence quenching and/or amplifier noise. One possible co-dopant that has been considered is Yb³⁺. The Yb³⁺ ion has a single absorption peak around 1 μ m, and has been successfully used for ASE filtering in Nd³⁺-doped silica fibres.

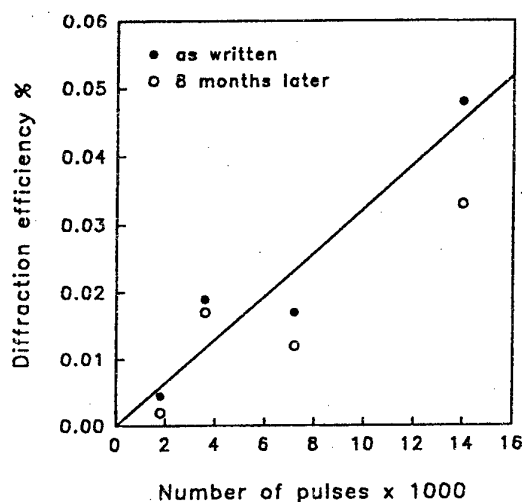


Figure 4. Grating writing in Ce³⁺-ALF.

5. THERMAL AND VISCOUS PROPERTIES OF FLUOROALUMINATE GLASSES

Successful fabrication of low-loss fibres requires stable core and cladding glasses. Preform fabrication and fibre drawing parameters are determined by the thermal and viscous properties of the glass. A matched pair of core and cladding glasses were examined in detail; the core glass was ALF70 ($\text{ALF70} = 37\text{AlF}_3 \cdot 15\text{CaF}_2 \cdot 12\text{MgF}_2 \cdot 9\text{SrF}_2 \cdot 6\text{BaF}_2 \cdot 15\text{YF}_3 \cdot 6\text{NaPO}_3$) and the cladding glass was ALF112 ($\text{ALF112} = 42\text{AlF}_3 \cdot 25\text{CaF}_2 \cdot 10\text{MgF}_2 \cdot 10\text{SrF}_2 \cdot 8\text{BaF}_2 \cdot 5\text{NaPO}_3$). The core/clad pair were matched as to their characteristic temperatures: both had $T_g = 435^\circ\text{C}$ and $T_x = 565^\circ\text{C}$, giving $T_x - T_g = 130^\circ\text{C}$ which implies a relatively large fibre-drawing range.

Figure 5 shows the TTT (time-temperature-transformation) curves of the two glasses. The core glass ALF70 is somewhat more stable than the cladding glass ALF112, since its TTT curve are shifted to longer times and higher temperatures. However, both glasses possess good stability. The fibre drawing temperature can be calculated¹⁰ from T_x and T_g , and for these glasses is $\sim 520^\circ\text{C}$. At this temperature the cladding glass will take 1 min to grow a 10^{-3} fraction of crystals; while the core glass in this time will grow only a 10^{-4} fraction of crystals.

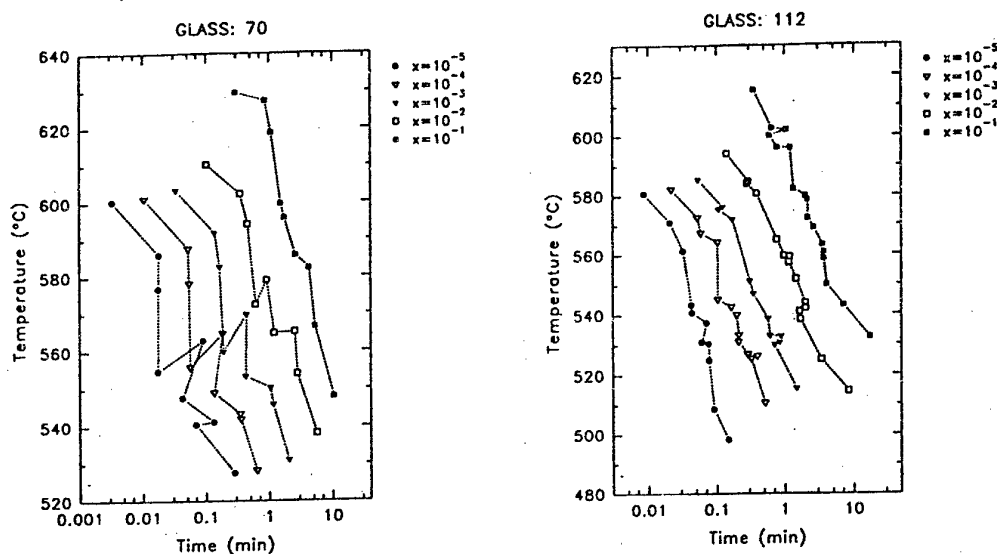


Figure 5. TTT curves of ALF core and cladding glasses.

The viscosity-temperature relation⁷ in fluoroaluminate glasses is highly nonlinear, as seen in Figure 6; the change in the core viscosity is somewhat less steep, indicating higher stability. The solid lines are fits to the Cohen-Grest equation. Figure 6 also shows the glass transition and crystallization temperatures (T_g and T_x) of the core and cladding glasses, defining the fibre-drawing range. The rapid drop in viscosity with increasing temperature causes difficulties in fibre drawing; when the temperature changes by 10°C , viscosity changes by a factor of 3. Therefore both temperature and fibre tension must be precisely monitored and controlled to maintain the desired fibre diameter.

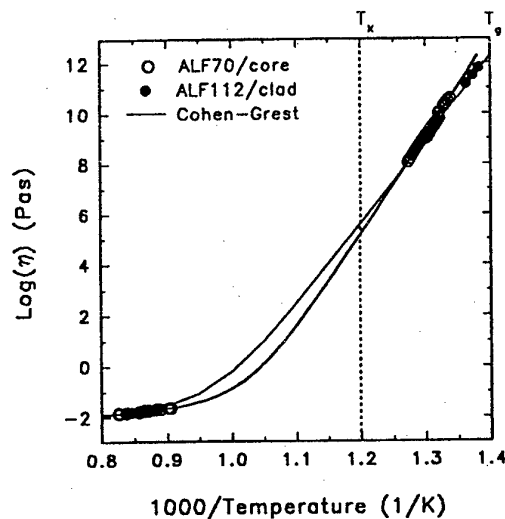


Figure 6. Viscosity in ALF glasses.

Recently fibre drawing experiments have been carried out, and will be reported elsewhere¹¹. A major advantage of the Nd³⁺-doped 1.3 μ m amplifier is its short length, which is due to high doping levels and large pump absorption. This reduces fibre loss requirement for device fabrication; the estimated upper limit on fibre loss is 1-10 dB/m.

6.CONCLUSIONS

New fluoroaluminate glasses have been designed as hosts for a 1.3 μ m Nd³⁺-doped amplifier in the second telecom window. The new glasses are highly ionic and have a low refractive index. Blue-shifted emission was observed, with peak emission at 1310 nm. Amplification in the centre of the second telecom window at 1310-1320 nm has been demonstrated in fibre, with peak gain at 1317 nm. The gain spectrum shows greatly reduced ESA, with 3 dB point at 1305 nm.

Persistent fibre grating has been written in Ce³⁺-doped fluoroaluminate glass. Analysis confirms that Bragg fibre gratings can be employed as filters for 1050 nm ASE radiation.

Crystallization behaviour of a matched core/clad fluoroaluminate glass pair was examined. The glasses were shown to be sufficiently stable to fabricate acceptable quality preforms and fibres. The viscosity-temperature relationship in fluoroaluminate glasses is highly nonlinear, indicating that precise control of fibre-drawing parameters is necessary to obtain low-loss fibre. For a realistic amplifier device, the upper limit on fibre loss is of the order of 10 dB/m.

New Nd³⁺-doped fluoroaluminate glasses were shown to be a highly promising candidate for an efficient, diode-pumped, high gain, broadband amplifier in the second telecom window.

ACKNOWLEDGEMENTS

The authors acknowledge the support of EU/ACTS and EPSRC in funding this work.

REFERENCES

1. W J Miniscalco, "Optical and Electronic Properties of Rare Earth Ions in Glasses", in *Rare Earth Doped Fibre Lasers and Amplifiers*, ed M J F Digonnet, Marcel Dekker, 1993, 19-133.
2. S Zemon, W J Miniscalco, G Lambert, B A Thompson, M A Newhouse, P A Tick, L J Button, D W Hall, *Proc. SPIE*, vol 1789, pp 53-60, 1993.
3. S. E. Stokowski, R A Saroyan, M J Weber, "Nd-doped laser glass spectroscopic and physical properties", *Lawrence Livermore National Laboratory Report M-095*, Rev. 2, 1981.
4. T Kogo et al.: *J. Non-Cryst. Solids*; 140 (1992) 223-231.
5. E Ishikawa, H Aoki, T Yamashita, Y Asahara, *Electr. Lett.*; 28 (1992) 1497-1498.
6. T Kogo, M Onishi, S Hirai, Y Chigusa, K Nakazato, M Shigematsu, S Suzuli, M Watanabe, *J. Non-Cryst. Solids*, 140 (1992) 233-237.
7. M Naftaly, A Jha, E R Taylor, K C Mills, *J. Non-Cryst. Solids*; 213&214 (1997) 106-112.
8. A Tesar, J Campbell, M Weber, C Weizapfel, *Opt. Materials*, 1 (1992) 217-234.
9. G Meltz, W W Morey, W H Glenn, *Opt. Lett.*, 14 (1989) 823-825.
10. C T Moynihan, *94th Meeting American Ceramic Society*, Minneapolis, USA, 1992.
11. E R Taylor et al.: *accepted for ECOC'98 - Madrid*; September 1998.

ROLE OF URBACH EDGE AND HOST GLASS DEFECTS IN BROAD BAND EXCITATION OF RARE EARTH DOPANTS IN CHALCOGENIDE GLASSES

D.A. Turnbull^a, V. Krasteva^b, J. Sanghera^c, G.H. Sigel Jr.^b and S.G. Bishop^a

^aMicroelectronics Laboratory, Depart. of Electrical and Computer Engineering
University of Illinois, Urbana, IL 61801 email sgbishop@uiuc.edu

^bFiber Optics Materials Research Program
Rutgers University, Piscataway, NJ 08855-0909

^cNaval Research Laboratory, Washington, DC 20375

ABSTRACT

The effects of altering the host glass bandgap, the host glass purity, and the sample temperature on the previously observed broad band optical excitation of emission from rare earth dopants in chalcogenide glasses have been investigated. The host bandgap was varied by altering both the glass composition and the sample temperature. In agreement with the predictions of a previously proposed model, it was found that the range of energy available to be transferred from the host glass to excite the rare earth dopants depends on the host glass bandgap and that there is a low energy cutoff to the transfer process. In addition, this range of transfer energies is found to be narrower than the width of the host glass photoluminescence (PL) band at liquid helium temperatures. The observation of the broad band excitation in a high purity Pr-doped $\text{As}_{12}\text{Ge}_{33}\text{Se}_{55}$ sample indicates that impurities do not play a crucial role in the broad band excitation process. Lastly, the thermal quenching behavior of the broad band excitation was measured and compared to that of the host glass PL. The behaviors were found to be quite similar, with both processes quenching with the same two activation energies.

BACKGROUND AND INTRODUCTION

Recently, chalcogenide glasses have become the subject of intensive investigation[1] as host media for rare earth (RE)-doped devices. In oxide or wide band gap chalcogenide glasses, RE emissions are usually pumped by direct optical excitation of intra 4f-shell transitions of the REs[2]. However, for chalcogenide glasses having band gaps in the visible or near infrared, the intrinsic optical transitions of the glass, including the interband absorption, the Urbach absorption edge, the below-gap weak absorption tail (WAT), and the broad mid-gap photoluminescence (PL) band, overlap some of the intra 4f-shell transitions of the RE dopants. Recent studies[3-8] of the PL and photoluminescence excitation (PLE) spectroscopy in RE-doped chalcogenide glasses have shown that these spectral overlaps lead to strong interactions between the optical absorption and emission processes of the rare earth dopants and the chalcogenide host glass. A remarkable, broad, near-band edge PLE band is observed in the excitation spectra of rare earth emission bands in chalcogenide glasses, superimposed on the expected 4f-RE PLE peaks.

Figure 1 shows the previously reported PL and PLE spectra obtained from 0.1 wt. % Er- and Pr-doped $\text{As}_{12}\text{Ge}_{33}\text{Se}_{55}$ glasses[3,5]. On the right are shown the PL spectra, pumped in the 980 nm Er^{3+} and 1040 nm Pr^{3+} absorption bands, respectively. These spectra show the characteristic rare earth emission bands at 1540 nm for the Er-doped sample and at 1340 and 1640 nm for the Pr-doped sample. The PLE spectrum shown on the bottom left, taken from the Er-doped sample while detecting at 1540 nm, shows the expected absorption bands of Er^{3+} at 980 and 810 nm. However, these bands are superimposed on a novel, strong, broad PLE band stretching from ~500 nm to beyond 900 nm. This broad PLE band is indicative of an absorption by the host glass, which subsequently transfers energy to the Er^{3+} , exciting the 1540 nm luminescence. A nearly identical broad PLE band is observed from the Pr-doped sample when detecting at 1640 nm, as shown by the solid line in the upper left of Fig. 1. The 1340 nm Pr emission, in contrast, shows only a very weak broad PLE band.

The energy level diagrams for the rare earth atoms shown in Fig. 2 suggest a possible

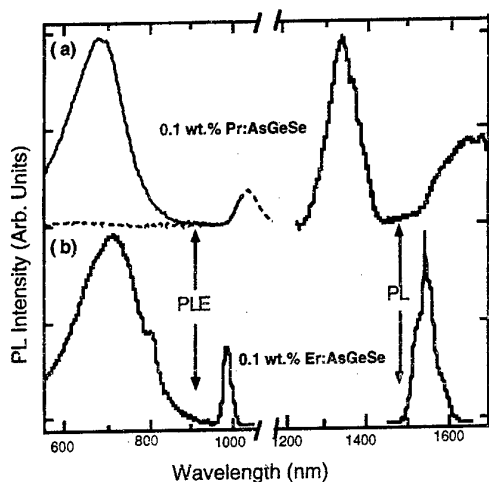


Fig. 1 PL (right) and PLE (left) spectra from 0.1 wt.% Er- (bottom) and Pr-doped (top) $\text{As}_{12}\text{Ge}_{33}\text{Se}_{55}$ glasses are shown.

energy, with the transitions lying above this point excited weakly or not at all by the broad band. Consistent with our previous results in Er- and Pr-doped glasses, the 1340 nm and 1700 nm Dy^{3+} transitions exhibited broad band PLE, while the higher lying 1150 and 1575 nm transitions which require energies of ~ 1 eV or higher to excite, are not excited by the broad PLE band [6].

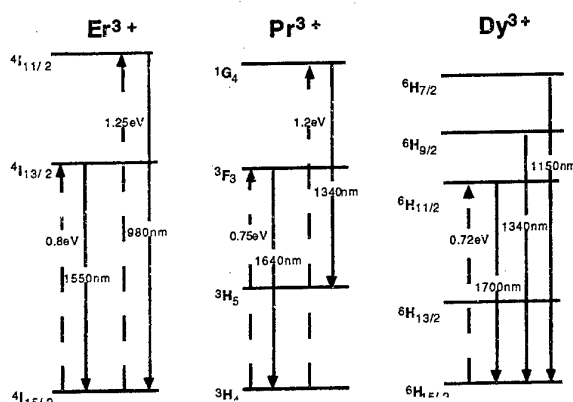


Fig. 2 Simplified energy level diagrams are shown for Er^{3+} , Pr^{3+} and Dy^{3+}

and of the involvement of native defects in the host glass in the energy transfer process. The Er PL and the mid-gap host glass PL exhibit nearly identical PLE lineshapes and PL fatiguing effects, indicating that the same native defects participate in the excitation of these two emission processes [8]. In addition, the effects on the broad band PLE of altering the host glass band gap and the host glass purity are consistent with this interpretation. Changing the band gap by altering either the glass composition or the sample temperature apparently alters the degree of resonance or overlap between the energy required to excite the RE ions and the energy available to be transferred from the optically excited host glass defects, thereby changing the strength or efficiency of the broad band PLE process. The observation of the broad PLE band in a high purity Pr-doped $\text{As}_{12}\text{Ge}_{33}\text{Se}_{55}$ glass presented here indicates that impurities do not play a crucial role in the broad band excitation process.

All of these results suggest a model for the energy transfer process from the host glass to the REs mediated by intrinsic defect states in the glass, and a model based on the Mott-Davis-Street (MDS) model [9,10] for the behavior of the chalcogenide glasses was proposed [6,8]. A

explanation for the contrasting strong and weak broad band PLE for the 1640 nm and 1340 nm Pr^{3+} emission bands, respectively. Both the 1540 nm Er^{3+} and the 1640 nm Pr^{3+} emission bands, which are strongly excited by broad PLE bands, terminate in the ground state and so require only ~ 0.8 eV to excite. In contrast, the 1340 nm Pr^{3+} emission terminates in an excited state of the Pr^{3+} , and so requires ~ 1.25 eV to excite. This observation led to the hypothesis [5] that there was a limit to the amount of energy which could be transferred to the rare earths through the broad band mechanism, and that transitions requiring higher energies to excite would not exhibit strong broad band PLE behavior. This hypothesis was confirmed by a study [6] of PL and PLE in a 0.1 wt.% Dy-doped $\text{As}_{12}\text{Ge}_{33}\text{Se}_{55}$ sample, the energy levels of which are also shown in Fig. 2. The Dy^{3+} has a ladder of levels of increasing energy, all of which terminate in the ground state, making it an ideal dopant to test this hypothesis. If there were a high energy cutoff to the transfer process, we should see the excitation of the Dy^{3+} bands up to a certain

These broad-band PLE spectra were originally attributed [3-7] to near-band edge absorption due to background impurities followed by non-radiative transfer of the excitation energy to the RE emitters. However, further investigations [8], including the work presented here, reveal that the broad RE PLE band is due to the absorption of light in the Urbach edge of the host glass and the subsequent transfer of this energy to the RE dopants. Comparative studies [8] of the properties of Er^{3+} PL in Er-doped $\text{As}_{12}\text{Ge}_{33}\text{Se}_{55}$ glass with those of the broad, mid-gap host glass PL observed at low temperature [9,10] provide strong evidence of the role of the Urbach edge absorption in the PLE of the Er emission,

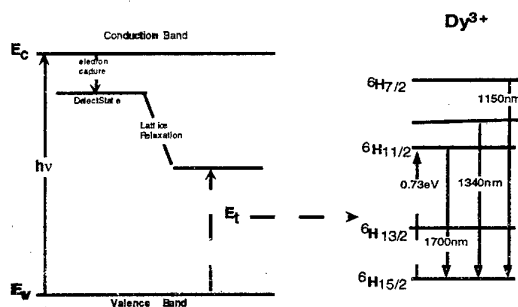


Fig. 3 A schematic of the proposed optical absorption, carrier localization, lattice relaxation, recombination, and energy transfer processes giving rise to the broad band excitation of the rare earth emission in chalcogenide glasses. (Based on the Mott-Davis-Street model of localized states in chalcogenide glasses.)

schematic of the proposed energy transfer mechanism is shown in Fig. 3. The initial exciting light creates an electron-hole pair in the glass. One of these carriers is subsequently captured by a nearby defect state. (The capture of an electron is shown in the figure, but capture of a hole is also possible.) The capture of the electron changes the charge state of the defect, which causes it to relax deeper into the gap due to the strong electron-phonon coupling in the chalcogenides. The hole can then recombine with the bound electron, emitting a photon (mid-gap host glass PL) or transferring its energy non-radiatively to a nearby rare earth dopant. In this model, the lattice relaxation explains the large Stokes shift observed between the initial excitation energy and the energy available for host glass PL or to be transferred to the rare earths. The high energy cutoff to the transfer process is also a direct consequence of this model. There

will be some range of recombination energies of the electron hole pair, determined by the energy distribution of the relaxed defect states in the gap and the vibrational broadening of the emission line [8,9]. Recombination at higher energies becomes less and less probable, resulting in a decrease in the host glass PL intensity and a declining transfer efficiency from the defect states in the glass to the rare earth dopants.

The investigations of the broad band excitation mechanism presented here were designed to test the predictions of this model. If, as hypothesized, the same local defect states in the glass are involved in both the broad band excitation of the rare earth dopants and the host glass PL, both processes should show similar thermal quenching behavior. Also, if native defects are responsible for the broad band PLE, then the presence or absence of impurities should not strongly affect the broad band excitation. Lastly, we wished to examine the effect which changing the host glass bandgap would have on the broad band excitation process.

EXPERIMENTAL PROCEDURE

Bulk samples of rare earth doped $\text{As}_{12}\text{Ge}_{33}\text{Se}_{55}$ glass were prepared at the Crystal Growth Laboratory at the University of Utah from a mixture of crystalline rare earth sulfides (e.g. Dy_2S_3) and commercially available, high purity $\text{As}_{12}\text{Ge}_{33}\text{Se}_{55}$ glass. The mixture was slowly heated (over 25 hours) in a quartz ampoule to 1000 C, rocked for 100 hours, and then slowly cooled to room temperature. Bulk samples of Pr-doped Ge-S-I glass were made at Rutgers from high purity commercially available materials. The powders were mixed, slowly heated in an etched quartz ampoule to a maximum temperature of 950 C, where the mixture was held for several hours. The glass melts were air quenched and annealed for 1 hour. A bulk sample of Pr-doped $\text{As}_{12}\text{Ge}_{33}\text{Se}_{55}$ was prepared at the Naval Research Laboratory by elemental doping of Pr into the melt, with additional distillation and purification steps taken to ensure the purity of the glass sample. Both the PL and PLE spectroscopy were carried out on these bulk samples (1-2 cm thick) using a tungsten lamp dispersed by a 0.25 m double grating monochromator as the excitation source. The luminescence was analyzed using a 1 m single grating monochromator and detected by a 77 K Ge pin photodiode. Exciting light was chopped mechanically and a lock-in amplifier provided phase sensitive detection.

RESULTS AND DISCUSSION

Figure 4 shows the PLE spectrum obtained from a high purity, 0.078 wt.% Pr-doped $\text{As}_{12}\text{Ge}_{33}\text{Se}_{55}$ glass, detecting in the 1640 nm Pr^{3+} emission band. A broad PLE band nearly identical to that previously observed is seen stretching from ~500-950 nm. Evidence for partial crystallization of the Pr in this sample can be seen in the relatively sharp PLE band at 1030 nm, due to crystallites, which lies on top of the broader Pr^{3+} *f*-band absorption around 1040 nm arising from the Pr^{3+} dissolved in the glass. Similar effects were observed in the PLE spectra of

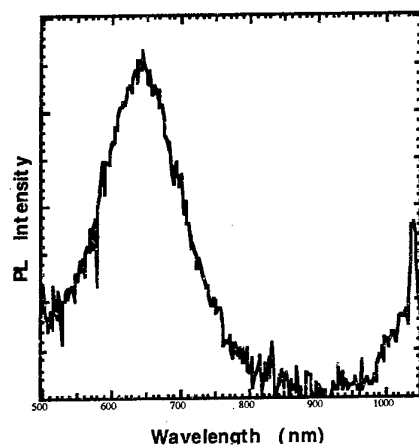


Fig. 4 A room temperature PLE spectrum from a high purity 0.078 wt.% Pr-doped $\text{As}_{12}\text{Ge}_{33}\text{Se}_{55}$, detecting at 1640 nm. The sharp PLE peak at ~ 1020 nm is attributed to crystallites of Pr_2S_3 in the sample.

Er-doped As_2S_3 glass [4] in which the Er_2S_3 dopant was not completely dissolved. The fact that a broad PLE band like those previously studied is observed even in a high purity sample is strong evidence that impurities do not play a crucial role in the broad band excitation process. This is consistent with the hypothesis that the states in the gap which mediate the transfer of energy to the rare earth dopants are intrinsic defect states of the host glass.

In order to determine whether the peak position of the broad band PLE spectrum would track with the bandgap of the host glass, the PLE spectra from a 0.1 wt.% Er-doped $\text{As}_{12}\text{Ge}_{33}\text{Se}_{55}$ sample were measured at both 300 K and 5 K. The results are plotted in Fig. 5 on a log scale versus energy. As can be seen from the figure, at low temperatures, when the bandgap of the glass is increased, the PLE peak position is also shifted to higher energy. Shown in an inset of the figure is a comparison of the 5K PLE from the Er-doped sample with a 5K PLE spectrum of the host glass emission from a pure $\text{As}_{12}\text{Ge}_{33}\text{Se}_{55}$ sample [8], both detecting at 1540 nm. As can be seen, the low energy sides of the two PLE spectra are nearly identical. It is known that the PLE spectrum of the host glass PL follows the exponential Urbach absorption edge of the glass [9], so this

comparison demonstrates that the PLE of the Er emission also follows the absorption edge of the host glass. This verifies that the initial absorption which gives rise to the broad band PLE is a band-to-band absorption, occurring in the Urbach tail absorption of the host glass.

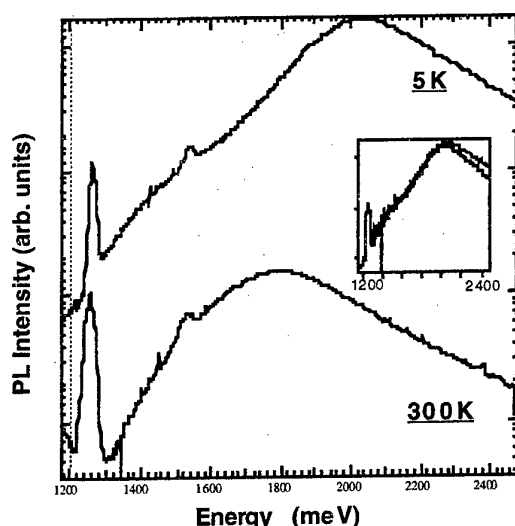


Figure 5 Room and low temperature PLE spectra taken from a 0.1 wt.% Er-doped $\text{As}_{12}\text{Ge}_{33}\text{Se}_{55}$ sample, detecting at 1540 nm, plotted on a log scale versus energy. Shown in the inset is a comparison of the PLE at 1540 nm from the Er-doped sample and from an undoped $\text{As}_{12}\text{Ge}_{33}\text{Se}_{55}$ sample.

In order to test whether or not the high energy cutoff of the broad band excitation of the rare earths would depend on the bandgap of the host glass a 0.1 wt.% Pr-doped Ge-S-I glass was investigated. The $\text{As}_{12}\text{Ge}_{33}\text{Se}_{55}$ glass has a bandgap of ~ 1.4 eV, while the Ge-S-I glass investigated here has a bandgap of ~ 2.2 eV. As discussed in the introduction and shown in Fig. 1, the 1340 nm Pr^{3+} emission band was not strongly excited [5] by the broad band PLE mechanism in $\text{As}_{12}\text{Ge}_{33}\text{Se}_{55}$. Figure 6 shows a PLE spectrum taken from the 0.1 wt.% Pr-doped Ge-S-I glass, detecting at 1342 nm. This spectrum shows the direct Pr^{3+} 4f absorption band at 1040 nm, as well as a weak, broad PLE band centered at ~ 550 nm. Thus, in the wider bandgap glass, the higher lying 1340 nm Pr^{3+} emission can be excited by the broad band mechanism, while in the narrower bandgap $\text{As}_{12}\text{Ge}_{33}\text{Se}_{55}$ glass, there was insufficient energy available to excite this transition.

Although the broad band excitation of the 1340 nm Pr emission in the Ge-S-I glass is much stronger than observed in the Pr-doped $\text{As}_{12}\text{Ge}_{33}\text{Se}_{55}$ glass, it is still much weaker than the broad band excitation of the 1640 nm Pr emission in the $\text{As}_{12}\text{Ge}_{33}\text{Se}_{55}$ glass. It is possible that the 1340 nm Pr^{3+} transition is still near the

edge of the available excitation energy range in the Ge-S-I glass studied. Alternatively, it is possible that the Ge-S-I glasses contain a lower concentration of the intrinsic defects that give

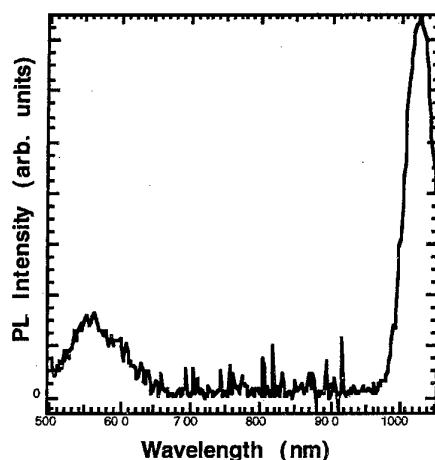


Fig. 6 PLE spectrum taken at 300 K, detecting at the 1340 nm Pr^{3+} emission, from a wider gap Pr-doped GeSI glass sample.

comparison. It can be seen that the 1700 nm Dy^{3+} PL emission is much weaker relative to the 1340 nm emission at 5 K than it is at 300 K, and this is consistent with the existence of a low energy cutoff to the energy transfer process. When the host glass bandgap is increased by the cooling of the sample, the range of available energies shifts to higher energy, moving out from underneath the 1700 nm band. At 5 K, it has almost shifted enough to quench the broad band PLE of the 1700 nm PL band. This shift also confirms that the low energy cutoff depends on the host glass bandgap. The strength of the broad band excitation of the 1700 nm band decreases when the bandgap of the host glass is increased by lowering the temperature.

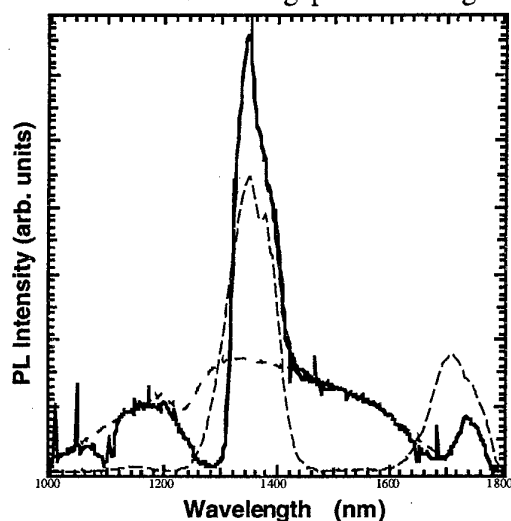


Fig. 7 Low temperature and 300K (dashed line) PL spectra from a 0.1 wt.% Dy-doped $\text{As}_{12}\text{Ge}_{33}\text{Se}_{55}$ sample, excited in the broad PLE band. Shown for comparison is a PL spectrum from an undoped $\text{As}_{12}\text{Ge}_{33}\text{Se}_{55}$ sample, also plotted as a dashed line. The Dy^{3+} spectra are normalized to the height of the 1340 nm emission band for comparison.

rise to the mid-gap host glass PL and mediate the transfer of energy to the rare earth atoms. The latter explanation is prompted by previous work in which it was found [9] that the strength of the host glass PL depended on the As concentration in $\text{As}_x\text{Se}_{1-x}$ glasses. The absence of As in the Ge-S-I glass might result in lower density of localized defect states which could explain both the absence of host glass emission and the weakness of the broad excitation band in the Ge-S-I glass.

In order to probe the possible existence of a low energy cutoff to the energy transfer process and its dependence on the bandgap of the host glass, the PL and PLE behavior of a 0.1 wt.% Dy-doped glass has been investigated at both 300 K and 5 K. The room temperature PL spectrum excited in the broad PLE band, at 740 nm, is compared in Fig. 7 with a PL spectrum excited at the same wavelength at 5 K in which the broad mid-gap host glass PL is superimposed on the Dy^{3+} emissions. The two spectra are scaled so that the intensities of the 1340 nm PL peaks are equivalent. The PL band from a pure $\text{As}_{12}\text{Ge}_{33}\text{Se}_{55}$ glass is also shown as a dotted line for

The final area investigated is the effect of changing the sample temperature on the strength of the broad band excitation of the rare earth dopants. Figure 9 (a) shows an Arrhenius plot of the temperature dependence of the host glass and Er PL intensity taken from a 1 wt.% Er-doped $\text{As}_{12}\text{Ge}_{33}\text{Se}_{55}$ sample while figure 9 (b) shows the host glass and Pr PL intensities from the NRL 0.078 wt.% Pr-doped $\text{As}_{12}\text{Ge}_{33}\text{Se}_{55}$ sample, with all PL bands excited at the peak of their respective PLE spectra at each temperature. The Arrhenius plot displays the log of the PL intensity versus the inverse of the temperature. In the temperature range where the PL is thermally quenched, the thermal activation energy is given by the slope of the curve on the Arrhenius plot. Qualitatively, both the host glass and the Er^{3+} and Pr^{3+} PL intensity show relatively constant efficiencies at low temperature with a thermally activated exponential quenching of the efficiency at high temperature. Both processes have similar activation energies (~ 42 meV), with the main difference in the two intensity curves being in the temperature at which the thermal quenching begins. The similar thermal activation energies are another link between the host glass PL and the broad band excitation of the rare earth dopants. The

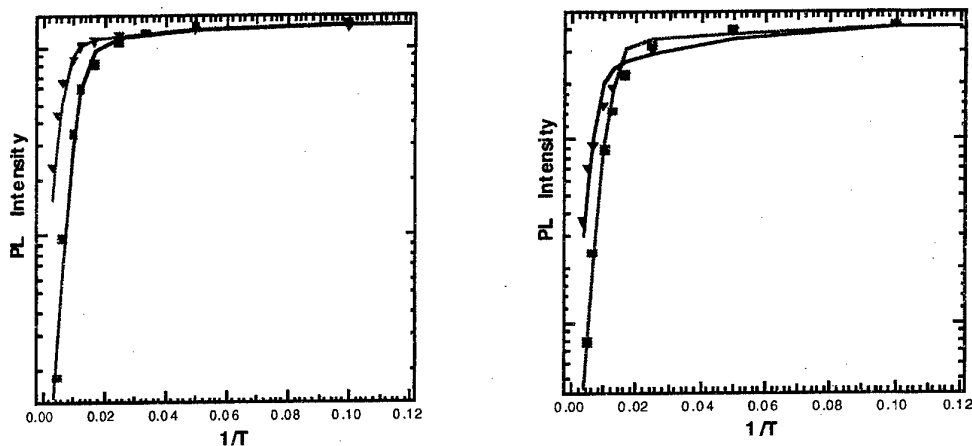


Fig. 8 Arrhenius plots of temperature dependence of the intensity of the host glass PL (squares) and rare earth PL (triangles) for the 1540 nm band from a 1 wt.% Er-doped $\text{As}_{12}\text{Ge}_{33}\text{Se}_{55}$ sample (left), and the 1640 nm band from a 0.078 wt.% Pr-doped $\text{As}_{12}\text{Ge}_{33}\text{Se}_{55}$ sample (right).

difference in roll-over temperatures explains why the broad band excitation of the rare earths still occurs at room temperature, while the host glass PL is completely thermally quenched at 300 K.

ACKNOWLEDGMENTS

The authors would like to thank M.C. Delong and the Crystal Growth Laboratory of the Department of Physics, University of Utah, for preparing the $\text{As}_{12}\text{Ge}_{33}\text{Se}_{55}$ glasses; and P.C. Taylor for many helpful discussions. This work has been supported by the NSF under the Engineering Research Centers (ECD-89-43166) and by DARPA under the Center for Optoelectronic Science and Technology (Grant #MDA972-94-1-0004).

REFERENCES

- [1] Proceedings of the Xth International Symposium on Non-Oxide Glasses, J. Non-Cryst. Sol., 213&214, (1997).
- [2] E. Desurvire, Erbium-Doped Fiber Amplifiers (Wiley-Interscience, New York, 1994), and references therein.
- [3] S.Q. Gu, S. Ramachandran, E.E. Reuter, D.A. Turnbull, J.T. Verdeyen, and S.G. Bishop, Appl. Phys. Lett. 66, 670 (1995).
- [4] S.Q. Gu, S. Ramachandran, E.E. Reuter, D.A. Turnbull, J.T. Verdeyen, and S.G. Bishop, J. Appl. Phys. 77, 3365 (1995).
- [5] D.A. Turnbull, S.Q. Gu, and S.G. Bishop, IEEE Photonics Tech. Lett. 8, 260-262 (1996).
- [6] D.A. Turnbull, S.Q. Gu, and S.G. Bishop, J. Appl. Phys. 80, 2436-2441 (1996).
- [7] D.A. Turnbull and S.G. Bishop, J. Non-Cryst. Solids, 1996, 213-214, 288-294 (1997).
- [8] D.A. Turnbull and S.G. Bishop, J. Non-Cryst. Solids, 223, 105-113 (1998).
- [9] R.A. Street, Adv. in Physics, 25, 397 (1976).
- [10] N.F. Mott, E.A. Davis, *Electronic Processes in Non-Crystalline Materials*, Clarendon, Oxford, 1979, ch. 9.

New rare-earth doped selenide and telluride glasses and fibers

B. Cole, L.B. Shaw, J.S. Sanghera, B.B. Harbison, P.C. Pureza, R. Miklos, V.Q. Nguyen, R. Mossadegh, D.T. Schaafsma, and I.D. Aggarwal.

In the past several years many advances have been realized in the search for stable rare earth doped chalcogenide glasses. Due to the reduced phonon energy of the chalcogenide glass host, rare earth transitions normally quenched in oxide and fluoride hosts become radiatively efficient. The need for efficient 1.3 μm amplification has fueled research into Pr^{3+} doped sulfide glasses including compositions based on GeGaS, GaLaS, AsS and GaNaS. Of these systems, Pr^{3+} doped GaNaS has produced fiber of sufficiently low loss to demonstrate amplification at 1.3 μm . Dy^{3+} has been proposed as an alternative to Pr^{3+} in chalcogenide glass for 1.3 μm amplifier applications. The absorption cross section for Dy^{3+} at 1.3 μm is about 10x that for Pr^{3+} at 1.1 μm , and the emission cross section for Dy^{3+} is calculated to be 2-3 times the cross section for Pr^{3+} . These larger cross sections allow for shorter device lengths thereby relaxing some of the requirements for low loss fiber.

We will report on the fabrication and characteristics of Dy^{3+} in GeAsSe based glass. Spectroscopy of Dy^{3+} in this glass system indicates that efficient operation at 1.3 μm should be feasible. The measured lifetime for the ${}^6\text{H}_{9/2}, {}^6\text{F}_{11/2} \rightarrow {}^6\text{H}_{15/2}$ (1.3 μm) transition is 310 μs for a glass doped with 1100 ppm Dy^{3+} . The radiative lifetime for the ${}^6\text{H}_{9/2}, {}^6\text{F}_{11/2}$ level as calculated by Judd Ofelt analysis is 325 μs . Using the measured and radiative lifetime, a quantum efficiency of greater than 90% was calculated for the 1.3 μm transition. This high quantum efficiency should reduce the degrading effects of ESA and bottlenecking from lower lying levels (${}^6\text{H}_{13/2}$, ${}^6\text{H}_{11/2}$) as may be problematic for sulfide based systems. The Dy^{3+} doped glass has been fiberized with a minimum loss of less than 1 dB/m at 6.63 μm . The core glass attenuation near 1.3 μm was measured to be less than 3 dB/m. We are currently in the process of fabricating fibers for single mode operation at 1.3 μm .

In addition to amplifier applications, rare earth doped chalcogenide glasses have many active transitions with high quantum efficiencies in the mid-IR. Mid-IR phosphors and fiber lasers developed from chalcogenide glasses have applications for chemical sensing and for Infrared Scene Simulation (IRSS) in the 3-5 μm and the 8-11 μm regions. We have already demonstrated mid IR emission (3-5 μm) for Pr^{3+} doped selenide glasses. We have recently drawn Pr^{3+} doped glass into multimode core/cladding fibers. The fiber attenuation showed a minimum loss of 1.54 dB/m at 2.69 μm . We have observed 3 μm emission from Tb^{3+} (${}^7\text{F}_4 \rightarrow {}^7\text{F}_6$) doped in a Ge-As-Te based glass. The 3 μm emission originates from the same level as the 8 μm transition (${}^7\text{F}_4 \rightarrow {}^7\text{F}_5$) indicating that this material could be active in the 8-11 μm region.

MID INFRARED EMISSIONS AND NONRADIATIVE RELAXATION IN Ge-Ga-S GLASS DOPED WITH Dy³⁺

Jong Heo * and Yong Beom Shin
Non-Crystalline Materials Laboratory
Department of Materials Science and Engineering
Pohang University of Science and Technology

Abstract

Effects of sulfur concentration in Ge-Ga-S glasses on the emission and nonradiative relaxation of the ⁶H_{11/2} and ⁶H_{13/2} levels in Dy³⁺ were investigated. Absorption and emission cross-sections of both levels increased with decreasing sulfur concentrations below the stoichiometric composition. Lifetimes of these two energy levels increased at the same time. Magnitude of the nonradiative interactions decreased as the amount of sulfur decreased. These changes in the emission characteristics suggest that a glass deficient in sulfur provide a better potential as a laser source compared to those with an excess sulfur. Calculation of the interaction parameters among rare-earths indicated the fast excitation migration phenomena accelerates the cross relaxation which directly quenches 2.9μm fluorescence from the ⁶H_{13/2} level.

1. Introduction

Electronic transitions between several pairs of the energy levels in Dy³⁺ are capable of emitting mid-infrared fluorescence. In fact, emissions at 2.9μm and 4.4μm in wavelength, which is due to the ⁶H_{13/2}→⁶H_{15/2} and ⁶H_{11/2}→⁶H_{13/2} transition, respectively have been reported[1]. However, the strong multiphonon relaxation due to the small energy separation among these levels resulted in the high nonradiative transition rates. As a result, efficiency of these mid-infrared emissions is low when oxides were used as hosts for Dy³⁺. This intrinsic characteristics of Dy³⁺ limit the host materials to non-oxide crystals and glasses. Fluorescences at the wavelength of 3μm also was reported from the BaY₂F₈ crystal[2] and a laser action at 4.34μm also was observed from the YLiF₄ crystal[3]. More recently, characteristics of the mid-infrared emissions at 2.9μm and 4.4μm have been reported by doping Dy³⁺ into several different sulfide glasses[4-7]. Low phonon energies of sulfide glasses[8] reduce the multiphonon relaxation and thereby, provide opportunities to obtain mid-infrared emissions.

However, most of the previous works mainly concerned with the measurement of the fluorescence in order to prove the potentials of Dy³⁺/non-oxide host combination as mid-infrared light sources. Compositions of the host glasses were not optimized even though small compositional changes in sulfide glasses can exert a significant influence on their optical properties. Current work reports the effect of sulfur concentration on the mid-infrared emission properties of Dy³⁺ doped into Ge-Ga-S glasses. Lifetimes of the ⁶H_{13/2} and ⁶H_{11/2} levels and the stimulated emission cross sections of 2.9μm and 4.4μm emissions were analyzed with a particular attention to their dependence on sulfur concentration. In addition, the variations in the multiphonon relaxation and nonradiative relaxation rates with sulfur content were analyzed.

2. Experimental procedures

2.1 Sample preparation

High purity(>99.999%) Ge, Ga and S were used as starting materials. Ga content was fixed at 5 at.%. In this case, a stoichiometric composition along the GeS₂-Ga₂S₃ tieline is Ge_{29.1}Ga₅S_{65.9}(referred to ST, hereafter). A glass with an excess amount of sulfur was prepared by substituting 3.3% of Ge with S. Composition of the glass in at.% is Ge_{25.8}Ga₅S_{69.2}(SE, sulfur excess). Substitution of an equal amount of S with Ge results in a sulfur-deficient glass with a composition of Ge_{32.4}Ga₅S_{62.6}(SD, sulfur deficient). These compositions were designed in order to investigate the effect of sulfur concentration on the emission properties of Dy³⁺. Dy₂S₃ was introduced into each composition so that the final concentrations of Dy³⁺ become 0.02, 0.04, 0.08, 0.16, 0.3, 0.5 and 0.6 at.%. Melting was done in a rocking furnace at 950°C for 12 hours using silica ampoules as crucibles. Melts were quenched in air and then annealed at near the glass transition temperature(~370 °C).

2.2 Optical measurements

Absorption spectra were recorded using a UV/VIS/NIR spectrophotometer in order to find the absorption cross sections of the excited states and initial parameters for the Judd-Ofelt analysis[9,10]. Room temperature fluorescence spectra at 2.9 μ m and 4.4 μ m wavelengths were measured using the Ti-sapphire tunable laser pumped by a Ar⁺ laser, 1/4 double monochromator and an InSb detector arrangement. Dy³⁺ ions in glasses were excited to the ⁶F_{7/2} level with the excitation beam of 914nm in wavelength. Position of the beam path through the sample was located immediately below the surface of the samples in order to minimize the reabsorption of fluorescence by the samples. Fluorescence lifetimes were measured from the first e-folding time of the emission intensities.

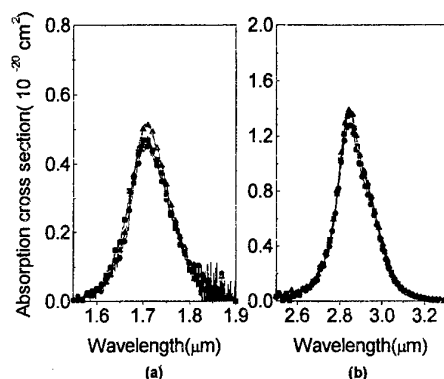


Fig.1 Absorption cross sections of the (a) ⁶H_{11/2} and (b) ⁶H_{13/2} level in Dy³⁺-doped Ge-Ga-S glasses. (▲) SD(Ge_{32.5}Ga₅S_{62.5}), (■) ST (Ge_{29.1}Ga₅S_{65.9}) (●) SE(Ge_{25.8}Ga₅S_{69.2})

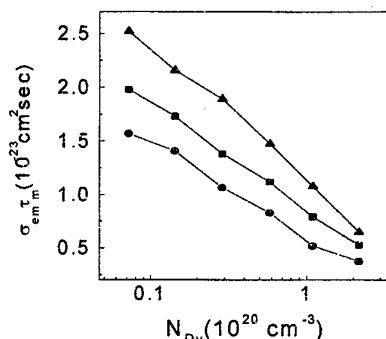


Fig.2 Values of $\sigma_{em}\tau_m$, a parameter representing the efficiency of a lasing, for the 4.4 μ m transition in Ge-Ga-S glasses doped with different Dy³⁺ concentrations. (▲) SD(Ge_{32.5}Ga₅S_{62.5}), (■) ST (Ge_{29.1}Ga₅S_{65.9}) (●) SE(Ge_{25.8}Ga₅S_{69.2})

3. Results

3.1 Absorption and emission cross-sections

Fig. 1 shows the absorption cross-sections(σ_{ab}) of the ⁶H_{11/2} and ⁶H_{13/2} manifolds for three glasses which increased slightly with decreasing sulfur concentration. This is mainly due to an increase in the refractive indices of the host glasses. This change in the refractive index also resulted in the enhanced radiative transition probabilities and consequently, the radiative lifetimes calculated from the Judd-Ofelt theory[9,10] decreased as in Table 1.

Table 1. Radiative transition rates, calculated lifetimes and Judd-Ofelt intensity parameters of Dy³⁺ in Ge-Ga-S glasses

Compositions	SE		ST		SD	
Transition	A(sec ⁻¹)	τ_R (ms)	A(sec ⁻¹)	τ_R (ms)	A(sec ⁻¹)	τ_R (ms)
⁶ F _{11/2} , ⁶ H _{9/2} → ⁶ H _{15/2}	3762	0.245	4209	0.219	4842	0.190
→ ⁶ H _{13/2}	290		312		367	
→ ⁶ H _{11/2}	29		32		36	
⁶ H _{11/2} → ⁶ H _{15/2}	256	3.38	278	3.12	283	2.98
→ ⁶ H _{13/2}	28		31		39	
⁶ H _{13/2} → ⁶ H _{15/2}	129	7.77	139	7.21	162	6.16

Emission cross-sections of the transitions responsible for the 2.9 μ m and 4.4 μ m fluorescences were also calculated. For the 2.9 μ m emission due to the ⁶H_{13/2} → ⁶H_{15/2} transition, cross-section were calculated from McCumber relation[11,12];

$$\sigma_{em}(\nu) = \sigma_{ab}(\nu) e^{[(\epsilon - h\nu)/kT]} \quad (1)$$

where h , ν , k and T is the Planck constant, frequency of fluorescence, Boltzmann constant and temperature, respectively. ϵ is the effective energy gap between the upper and lower manifold. On the other hand, the emission cross-section of the 4.4 μ m fluorescence could not be calculated from the McCumber relationship because of the difficulty in measuring the excited state absorption (ESA) from

the ${}^6\text{H}_{13/2}$ to ${}^6\text{H}_{11/2}$ level. Instead, it was derived from its spontaneous emission spectrum and Einstein relation[13];

$$\sigma_{em}(\nu) = \frac{c^2}{8\pi n^2 \nu^2} A \cdot g(\nu) \quad (2)$$

where A is a spontaneous emission rate of the $4.4\mu\text{m}$ fluorescence and ν is the frequency of the transition. $g(\nu)$ is a normalized line shape function.

From these calculated emission cross sections, it was possible to anticipate the threshold pumping power(P_{th}) for a lasing. It is inversely proportional to the lifetime(τ_m) multiplied by the emission cross section[14, 15] in case of a 4-level laser,

$$P_{th} = \frac{h\nu_p \delta A^*}{\sigma_{em} \tau_m} \quad (3)$$

Here ν_p , δ and A^* is the frequency of pumping light, single pass loss and effective pump area, respectively. Fig. 2 is the variation of $\sigma_e \tau_m$ values for the $4.4\mu\text{m}$ transition as a function of Dy^{3+} concentration for all three glasses. They decreased consistently with increasing Dy^{3+} concentration. Fig. 2 also indicates that a glass deficient in sulfur with SD ($\text{Ge}_{32.5}\text{Ga}_5\text{S}_{62.5}$) composition provides the most suitable condition for an efficient laser host provided that the other parameters remain constant.

3.2 Nonradiative transition rates

Measured fluorescence lifetime of the excited state is one of the most important properties to understand the relaxation processes.

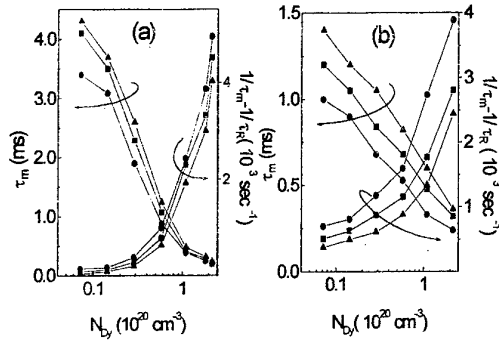


Fig.3 Measured lifetimes and the nonradiative transition rates for the (a) ${}^6\text{H}_{13/2}$ and (b) ${}^6\text{H}_{11/2}$ level in Ge-Ga-S glasses with different Dy^{3+} concentrations. (\blacktriangle) SD($\text{Ge}_{32.5}\text{Ga}_5\text{S}_{62.5}$), (\blacksquare) ST ($\text{Ge}_{29.1}\text{Ga}_5\text{S}_{65.9}$) (\bullet) SE($\text{Ge}_{25.8}\text{Ga}_5\text{S}_{69.2}$)

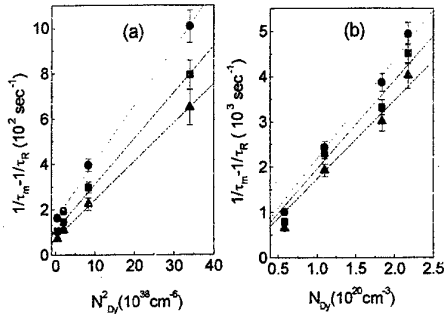


Fig.4 Nonradiative relaxation rates of the ${}^6\text{H}_{13/2}$ level for glasses with (a) low(<0.16%) and (b) high(>0.16%) Dy^{3+} concentration. (\blacktriangle) SD($\text{Ge}_{32.5}\text{Ga}_5\text{S}_{62.5}$), (\blacksquare) ST ($\text{Ge}_{29.1}\text{Ga}_5\text{S}_{65.9}$) (\bullet) SE($\text{Ge}_{25.8}\text{Ga}_5\text{S}_{69.2}$)

Fig. 3 shows the measured lifetimes(τ_m) of the ${}^6\text{H}_{13/2}$ and ${}^6\text{H}_{11/2}$ manifolds and nonradiative transition rate(W_n) calculated using the following relationship;

$$W_n = 1/\tau_m - 1/\tau_R \quad (4)$$

τ_R is the calculated radiative lifetime of the same manifold. Measured lifetimes(τ_m) of both manifolds in SD glass are the largest among three glasses for all Dy^{3+} concentration. It leads to the smallest values of W_n despite the smallest radiative lifetimes(τ_R). Differences in the measured lifetimes among three glasses were not trivial especially when the Dy^{3+} concentration is low. It is most likely from the changes in the multiphonon relaxation rates under a different sulfur concentration.

Nonradiative relaxation rate(W_n) from the ${}^6\text{H}_{13/2}$ level shows two different behaviors depending upon Dy^{3+} concentration as shown in Fig. 4. At low Dy^{3+} concentrations ($<5.8 \times 10^{19} \text{ cm}^{-3}$), it shows a quadratic dependence on the Dy^{3+} concentration [Fig. 4(a)]. If the fluorescence decays exponentially, the decay time constant long after the pump-off is equal to the measured lifetime(τ_m). In this case, the nonradiative relaxation can be divided into multiphonon relaxation(MPR) and energy transfer between ions as follows[16-18];

$$\frac{1}{\tau_m} - \frac{1}{\tau_R} = W_{mp} + K N_{Dy}^2 \quad (5)$$

Here, W_{mp} is the rate of the MPR, K is a constant and N_{Dy} is the concentration of Dy^{3+} . This is known

as a diffusion-limited or a migration-controlled regime [16,17]. Eq. (5) implies that rates of the nonradiative relaxation due to the ion-ion interaction depend on excitation migration between donors as well as cross relaxation between a donor and acceptor pair [16]. An excitation migration itself can not be a process to quench fluorescence, but it would accelerate the overall quenching rates by transferring the excitation energy to ions, the environments of which enable a more rapid quenching to take place. A slope in Fig.4(a), which indicates a constant K in eq.(5), is 1.80×10^{-37} and 1.50×10^{-37} and $1.13 \times 10^{-37} \text{ cm}^6 \text{ sec}^{-1}$ for the SE, ST and SD glass, respectively. These values of K suggest an increase in the nonradiative transition with increasing Dy^{3+} concentration and this increase occurs more rapidly as the amount of sulfur increases. The intercepts with the ordinate in Fig.4(a) provide MPR rates (W_{mp}) for each glass and they are 157, 107 and 71 sec^{-1} for the SE, ST and SD glass, respectively. As anticipated from the measured lifetimes, a glass deficient in sulfur shows the lowest MPR rate of all. An increase in the MPR rate for a SE glass is probably due to the existence of the homopolar S-S bonds with the vibrational frequency of 475 cm^{-1} which is higher than 365 cm^{-1} of the main Ge-S bonds [19]. The existence of the high frequency mode resulted in the increased phonon interaction with the host glasses.

As Dy^{3+} concentration increased, a fast excitation migration among donors takes place. In this case, total relaxation rates of the donor increases linearly with the acceptor concentration as in Fig. 4(b). This is a fast diffusion or supermigration regime [17,20] where

$$\frac{1}{\tau_m} - \frac{1}{\tau_R} = W_{mp} + K' N_{Dy} \quad (6)$$

Again, a glass deficient in sulfur concentration exhibited the lowest relaxation rate of all. A similar concentration dependence was also observed for the $\text{Nd}^{3+}: {}^4\text{F}_{3/2}$ level in the LaF_3 crystal [17].

In contrary to the ${}^6\text{H}_{13/2}$ level, a linear behavior was observed for the relaxation of the ${}^6\text{H}_{11/2}$ level over the entire Dy^{3+} concentration investigated (Fig.5). It indicates that the ion-ion interactions at the ${}^6\text{H}_{11/2}$ level follow a fast diffusion or supermigration. Pure MPR rate from the ${}^6\text{H}_{11/2}$ level for SE, ST and SD sample was 603, 462 and 328 sec^{-1} , respectively. Again, the nonradiative transition rate from the ${}^6\text{H}_{11/2}$ levels decreased with decreasing sulfur concentration.

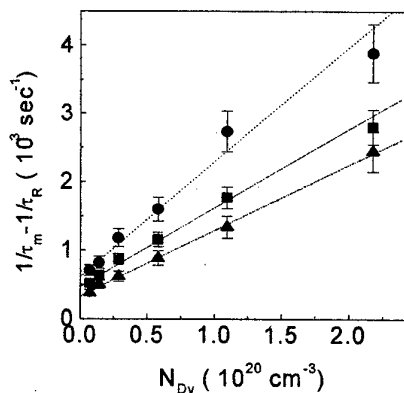


Fig.5 Nonradiative relaxation rates of the ${}^6\text{H}_{11/2}$ level in Dy^{3+} . (Δ) SD($\text{Ge}_{32.5}\text{Ga}_5\text{S}_{62.5}$), (\blacksquare) ST ($\text{Ge}_{29.1}\text{Ga}_5\text{S}_{65.9}$) (\bullet) SE($\text{Ge}_{25.8}\text{Ga}_5\text{S}_{69.2}$)

4. Discussion

In case of the electric dipole-dipole interaction, a time dependence of the normalized fluorescence intensity after a pulsed excitation is [21,22];

$$\Phi(t) = \exp(-t/\tau_R - W_{mp}t - \gamma t^{1/2} - \bar{W}t) \quad (7)$$

$\Phi(t)$ is the fluorescence intensity normalized by the intensity immediately before the pump-off. γ accounts for the donor-acceptor energy transfer causing the static disordered decay [23] and is given by

$$\gamma = \frac{4}{3} \pi^{3/2} N_A C_{DA}^{1/2} \quad (8)$$

$$C_{DA} = AR_{DA}^6$$

where R_{DA} is the distance between the donor-acceptor pair when the cross relaxation rate between them is equal to the radiative transition rate of the donor. \bar{W} is a cross relaxation enhanced by the

excitation migration among donors and from the hopping model [21,24],

$$\bar{W} = \pi(2\pi/3)^{5/2} N_A N_D \sqrt{C_{DA} C_{DD}} \quad (9)$$

where C_{DA} and C_{DD} is the energy transfer parameter for the cross relaxation and excitation migration, respectively. N_A and N_D is the concentration of acceptor and donor, respectively. In the particular case of the supermigration, \bar{W} changes a linearly with N_A [25], that is

$$\bar{W} = \frac{2}{3} \pi^2 \frac{C_{DA}}{R_{min}^3} N_A \quad (10)$$

where R_{min} means the possible minimum distance between rare-earth ions in a medium.

Since the fluorescence decay is mainly governed by the migration-enhanced cross relaxation long after a pump-off, eq.(7) can be reduced to the follows form;

$$\Phi(t) = \exp(-t/\tau_0 - \bar{W}t) \quad (11)$$

with $1/\tau_0 = 1/\tau_R + W_{mp}$. Therefore, a parameter K in eq.(5) becomes;

$$K = \pi(2\pi/3)^{5/2} (C_{DA} C_{DD})^{1/2} \quad (12)$$

and microparameter C_{DD} and C_{DA} can be expressed as follows[26] for the case of the dipole-dipole energy transfer;

$$C_{DD} = \frac{3c}{8\pi^4 n^2} \int \sigma_D^{em}(\lambda) \sigma_D^{ab}(\lambda) d\lambda \quad (13)$$

$$C_{DA} = \frac{3c}{8\pi^4 n^2} \int \sigma_D^{em}(\lambda) \sigma_A^{ab}(\lambda) d\lambda$$

where σ_D^{em} is the emission cross section of the donor and σ_D^{ab} and σ_A^{ab} is the absorption cross section of the donor and acceptor, respectively.

Fig. 6 illustrates the several possible routes for the nonradiative energy transfer from the ${}^6H_{13/2}$ level. Among these, microparameters C_{DD} for the excitation migration in Fig. 6(a) and C_{DA} for the cross relaxation of Fig. 6(b) can be calculated from eq. (13). Table 2 shows the calculated microparameters for glasses. For all glasses investigated, C_{DD} is considerably larger than C_{DA} . It suggests the rate of an excitation migration among donors is very faster than that of the cross relaxation between the donors and acceptors, leading to a spatial equilibrium within the donor system. In this case, the limiting step for the overall energy transfer process quenching the 2.9 μm fluorescence is the cross relaxation. Therefore, a slight variation in the transfer rates among different donor-acceptor pairs is effectively averaged out and the donors exhibit a simple exponential decay[16]. On the other hand, the magnitudes of these parameters were similar for all glasses and did not show any systematic changes. It is probably due to an increase in the refractive index of a glass deficient in sulfur even though it has the larger absorption and emission cross sections compared to ST and SE glasses.

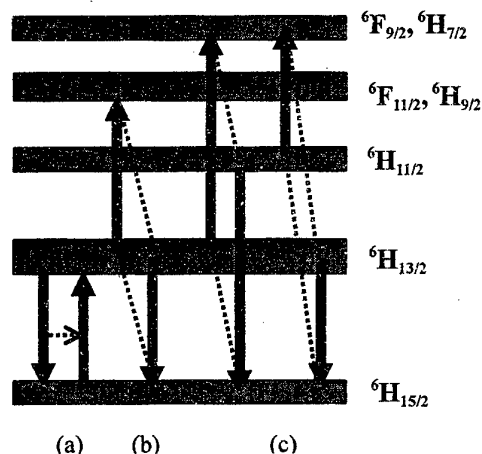


Fig.6 Possible nonradiative energy transfer occurring against the emission of the 2.9 μm fluorescence in Dy^{3+} -doped glasses; (a) excitation migration (b), (c) cross relaxation processes.

Table 2. Microparameters for excitation migration (C_{DD}) and for cross relaxation of Fig. 6(b) (C_{DA}) quenching the 2.9 μm fluorescence in Dy^{3+} -doped Ge-Ga-S glasses

Compositions Microparameter	SE	ST	SD
$C_{DD}(10^{-38} \text{ cm}^6 \text{ sec}^{-1})$	5.51 ± 0.24	5.53 ± 0.28	5.52 ± 0.21
$C_{DA}(10^{-41} \text{ cm}^6 \text{ sec}^{-1})$	2.31 ± 0.18	2.32 ± 0.20	2.32 ± 0.16

Calculated values of K using eq.(12) was almost constant with $2.25 \pm 0.12 \times 10^{-38} \text{ cm}^6 \text{ sec}^{-1}$, $2.26 \pm 0.14 \times 10^{-38} \text{ cm}^6 \text{ sec}^{-1}$ and $2.26 \pm 0.15 \times 10^{-38} \text{ cm}^6 \text{ sec}^{-1}$ for SE, ST and SD glasses, respectively. These calculated values show the considerable discrepancies from those derived from the slopes of lines in Fig.4(a). This calculation involves that the energy transfer occurs only through the excitation migration of 2.9 μm emission and cross relaxation of Fig. 6(b). Therefore, the difference is probably comes from the fact that the calculation of K using eq. (12) includes only the portion of the overall energy transfer processes. In addition, ${}^6H_{13/2}$, ${}^6H_{13/2} \rightarrow {}^6H_{15/2}$, $[{}^6F_{11/2}, {}^6H_{9/2}]$ and ${}^6H_{13/2}$, ${}^6H_{15/2} \rightarrow {}^6H_{15/2}$, ${}^6H_{13/2}$ transitions in Fig.6 appear to satisfy the condition of Dexter[26]. Therefore, the quenching processes in Dy^{3+} are also affected by the electric dipole-quadrupole and electric quadrupole-quadrupole interactions at least to a certain degree.

This discrepancy can also be explained from the difference in the rare-earth solubility among glasses with different sulfur concentration. A recent Raman study on the solubility mechanism of

La_2S_3 in $\text{GeS}_2\text{-Ga}_2\text{S}_3$ glass suggested that the most preferred site for rare-earths is the cation-cation bonds in Ge-Ga-S glass[27]. Formation of these cation-cation bonds was necessary due to the formation of GaS_4 tetrahedra from Ga_2S_3 which brings in the natural sulfur deficiency even at the stoichiometric $\text{GeS}_2\text{-Ga}_2\text{S}_3$ composition. This situation becomes pronounced in a SD glass and therefore, the solubility of rare-earths in a SD glass is higher than those in SE and ST glasses. Therefore, the clustering of Dy^{3+} in SD glass becomes less serious and the average distance among Dy^{3+} ions in SD glass is longer than that in SE or ST glasses even at the same Dy^{3+} concentration. It resulted in the reduced nonradiative interactions among Dy^{3+} and thereby, showed large K values with increasing sulfur concentration as in Fig. 4. A similar situation was found from the Ge-As-S glass system, where compositions containing less than 65 at.% of sulfur are favorable for rare-earth doping even if those compositions are less transmitting in the visible range[28].

V. Conclusions

Absorption cross-section of the $^6\text{H}_{11/2}$ and $^6\text{H}_{13/2}$ levels and emission cross-sections of the 2.9 and $4.4\mu\text{m}$ fluorescences in Dy^{3+} -doped Ge-Ga-S glasses increased with decreasing sulfur concentration. Measured lifetimes of the two energy levels also increased at the same time which is due to the reduced nonradiative relaxation rates. Rate of quenching the $2.9\mu\text{m}$ fluorescence from the $^6\text{H}_{13/2}$ level was enhanced by the fast excitation migration process. Magnitude in the nonradiative interactions among rare-earths decreased with decreasing sulfur concentration which is due to the enhanced solubility of rare-earths in the sulfur-deficient glass.

Reference

1. J. Heo, J. Mat. Sci. Lett. 14 (1995) 1014
2. L. F. Johnson and H. J. Guggenheim, Appl. Phys. Lett. 23 (1973) 96
3. N. P. Barnes and R. E. Allen, IEEE J. Quantum Electron. 27 (1991) 277
4. K. Wei, D. P. Machewirth, J. Wenzel, E. Snitzer and G. H. Sigel, Jr., Opt. Lett. 19 (1994) 904
5. S. Tanabe, T. Hanada, M. Watanabe, T. Hayashi and N. Soga, J. Am. Ceram. Soc. 78 (1995) 2917
6. J. Heo and Y. B. Shin, J. Non-Cryst. Solids 196 (1996) 162
7. T. Schweizer, D. W. Hewak, B. N. Samson and D. N. Payne, Opt. Lett. 21 (1996) 1594
8. Y. B. Shin, W. Y. Cho and J. Heo, J. Non-Cryst. Solids, 208 (1996) 29
9. B. R. Judd, Phys. Rev. 127 (1962) 750
10. G. S. Ofelt, J. Chem. Phys. 37 (1962) 511
11. D. E. McCumber, Phys. Rev. 136 (1964) A954
12. W. J. Miniscalco and R. S. Quimby, Opt. Lett. 16 (1991) 258
13. W. Koechner, Solid-state laser engineering, Springer-Verlag, New York, 1976
14. M. J. F. Digonnet and C. J. Gaeta, Appl. Opt. 24 (1985) 333
15. W. P. Risk, J. Opt. Soc. Am. B 5 (1988) 1412
16. M. J. Weber, Phys. Rev. B 4 (1971) 2932
17. Yu. K. Voron'ko, T. G. Mamedov, V. V. Osiko, A. M. Prokhorov, V. P. Sakun and I. A. Shcherbakov, Sov. Phys. JETP 44 (1977) 251
18. A. Brenier, C. Pedrini, B. Monie, J. L. Adam and C. Pledel, Phys. Rev. B 41 (1990) 5364
19. G. Lucovsky, F. L. Galeener, R. C. Keezer, R. H. Geils and H. A. Six, Phys. Rev. B 10 (1974) 5134
20. P. K. Watts and H. J. Richter, Phys. Rev. 136 (1972) 1584
21. M. V. Artamonova, Ch. M. Briskina, A. I. Burshtein, L. D. Zusman and A. G. Skleznev, Sov. Phys. JETP 35 (1972) 457
22. I. A. Bondar, A. I. Burshtein, A. V. Krutikov, L. P. Mezentseva, V. V. Osiko, V. P. Sakun, V. A. Smirnov and I. A. Shcherbakov, Sov. Phys. JETP 54 (1981) 45
23. T. Förster, Ann. Phys. (N.Y) 2 (1948) 55
24. A. I. Burshtein, Sov. Phys. JETP 35 (1972) 882
25. A. G. Avanesov, T. T. Basiev, Yu. K. Voron'ko, B. I. Dencker, A. Ya. Karasik, G. V. Maksimova, V. V. Osiko, V. F. Pisarenko and A. M. Prokhorov, Sov. Phys. JETP 50 (1980) 886
26. D. L. Dexter, J. Chem. Phys. 21 (1953) 836
27. J. Heo, J. M. Yoon and S. Y. Ryou, J. Non-Cryst. Solids, in press, 1998
28. K. Wei, Ph.D thesis, Rutgers, The state of University of New Jersey

SYNTHESIS AND OPTICAL PROPERTIES OF Ge-Sb-S: PrCl₃ SYSTEM GLASSES

B. Frumarová, P. Němec^a, M. Frumar^{a*}, J. Oswald^b and M. Vlček^a

Joint Laboratory of Solid State Chemistry of Acad. Sci. of Czech Rep. and of University of Pardubice, ^aDepartment of General and Inorganic Chemistry, University of Pardubice, 53210 Pardubice, ^bInstitute of Physics of Czech. Acad. Sci., Prague, Czech Republic. e-mail: Miloslav.Frumar@upce.cz

ABSTRACT

The (GeS₂)_{80-x}(Sb₂S₃)₂₀.xPrCl₃ and (GeS₂)_{60-x}(Sb₂S₃)₄₀.xPrCl₃ (x = 0.01, 0.1, 0.5) systems glasses were prepared from elements and PrCl₃ by thermal synthesis. The glasses were of orange to red colour, they were optically homogeneous up to 0.5 mol. % of PrCl₃, the samples with 1 mol. % of PrCl₃ were partly crystalline. The homogeneity was confirmed by optical methods and by electron microscopy. The T_g values are from the region 330-333 °C for (GeS₂)_{80-x}(Sb₂S₃)₂₀.xPrCl₃ glasses and from the region 256-274 °C for (GeS₂)_{60-x}(Sb₂S₃)₄₀.xPrCl₃ glasses, (x = 0.01, 0.1, 0.5). The short-wavelength absorption edge lies between 550 – 700 nm for (GeS₂)_{60-x}(Sb₂S₃)₄₀.xPrCl₃ glasses and between 500 – 650 nm for (GeS₂)_{80-x}(Sb₂S₃)₂₀.xPrCl₃ glasses. The long-wavelength absorption edge lies near 900-1000 nm⁻¹ and is apparently caused by multiphonon absorption of Ge-S and Sb-S vibration modes. Doping by Pr³⁺ ions leads to the creation of new absorption bands near 2100, 4980, 6370, 6640 and 9843 cm⁻¹, which can be assigned to the electron transitions from the ³H₄ level of Pr³⁺ to the ³H₅, ³H₆, ³F₂, ³F₃, ³F₄, ¹G₄ levels of the Pr³⁺ ion. The absorption bands corresponding to ³H₄ → ³H₆, ³F₂ and to ³H₄ → ³F₃, ³F₄ transitions are strongly overlapped.

The Raman spectra were deconvoluted into several bands, which can be assigned to the vibrations of GeS₄, SbS₃ and S₈ structural units. The structure of studied glasses is formed by the interconnected GeS₄ tetrahedra and SbS₃ pyramids with dissolved S₈ molecules and Pr³⁺ ions.

The luminescence spectrum consisted of two luminescence bands. The first one, ~ 1300 nm, can be assigned to ¹G₄ – ³H₅ electron transitions of the Pr³⁺ ions. The second luminescence band of lower intensity near 1600 nm can be assigned to the transitions between ³F₃ and ³H₄ electron levels of Pr³⁺.

1. INTRODUCTION

The rare-earth (RE) doped glasses and their luminescence have been studied extensively in the last time, partly due to fundamental science reasons, partly due to potential application of these phenomena and materials in optics and optoelectronics, e.g. in lasers, light amplifiers and light up-convertors [1, 2]. Silica telecommunication fibres exhibit a low-loss window in the wavelength region from 1290 nm to 1320 nm and Pr³⁺ ions seem to be a promising candidate for fibre amplifiers in this region. For such an application, the quantum and energy efficiencies of the

luminescence are important [3]. The quantum efficiency of the luminescence depends on energy of excitation and on the kind of RE ion. For the same RE ion it depends on the type of host matrix [2 - 5], because the non-radiative transitions to the lower electron energy states, when several lattice vibrations are generated, can compete with the radiative transitions and they can reduce the whole quantum efficiency [3, 4]. The emission from the 1G_4 level of Pr^{3+} can be, therefore, quenched because of the multiphonon relaxation to the underlying 3F_4 level [5]. As a consequence, the $^1G_4 \rightarrow ^3H_5$ radiative transition has low quantum efficiency in silica and other high phonon-energy glasses.

The chalcogenide glasses, due to heavier constituting elements, have lower phonon energies than oxide glasses and the probability of multiphonon relaxation can be lower because more phonons are required to bridge the energy gap between excited and next lower state.

The non-radiative decay rate, ω_p , due to multiphonon relaxation, depends on the energy gap between the electron levels, ΔE , and phonon energy, $\hbar\omega$, and is given by Miyakawa-Dexter equations [2]

$$\omega_p = \omega_0 \exp\left(\frac{-\alpha \Delta E}{\hbar\omega}\right), \quad (1)$$

$$\alpha = \ln(p/g) - 1,$$

where $p = \Delta E/\hbar\omega$, g is the electron-phonon coupling strength, and ω_0 is a host dependent constant. For glasses with a small maximum phonon energy, the number of phonons required to bridge the energy gap, ΔE , is large, leading to a smaller multiphonon relaxation rate [6].

The energy gap between 1G_4 and underlying 3F_4 level in Pr^{3+} ions is relatively large ($\sim 3500\text{cm}^{-1}$, [2]), which again decreases the multiphonon relaxation rate.

The RE compounds or elements are soluble in oxide and halide glasses, while their solubility in chalcogenides are generally less. The achievable density of RE ions in these materials is often too small for many possible applications [7]. A search for homogeneous chalcogenide glasses, which can contain larger amounts of RE elements and have low phonon energy, is, therefore, desirable. From this point of view, the glasses from the system Ge-Sb-S are promising similarly to the glasses of the Ge-Ga-S system [2]. The glasses are hard and non-hygroscopic, they can apparently dissolve larger amounts of RE elements or their compounds [7]. The justification of this suggestion will be given in part 3 of this paper.

2. EXPERIMENTAL

Samples were prepared from high purity elements (Ge, Sb, S, all of 5N-purity) and from praseodymium chloride ($PrCl_3$ per analysis, p.a.) in evacuated silica ampoules ($T \sim 960^\circ\text{C}$, 40 hrs) in a rocking furnace. The ampoules containing the melt were then annealed at 800°C for 8 hrs and quenched in the air.

The homogeneity of the samples was confirmed by optical and electron microscopy. The composition and its uniformity were measured by an energy-dispersive X-ray analyser. The absence of crystalline phase was checked by X-ray diffraction.

The thermal analysis (TA) was performed with the Mettler DSC 12E analyser. The optical spectra of cut and polished samples were measured using spectrophotometer (Perkin-Elmer Lambda 12 (UV, VIS), Jasco V 570 (VIS, NIR)) and FT spectrophotometer (BIO-RAD FTS 45 (IR)).

The luminescence spectra were measured at room temperature in the spectral region between 20000 - 6000 cm^{-1} (500 - 1670 nm). The Ar^+ ion laser lines 476.5, 488nm or YAG: Nd laser line 1064 nm were used for luminescence excitation.

The Raman spectra were measured by an FT Raman spectrometer (IFS55/FRA106, Bruker, Germany) using a backscattering method and Nd:YAG laser beam (1064 nm) as the excitation light. Temperature dependent population of individual phonon levels influences the intensities of individual Raman bands. This effect is most efficient at lower Raman frequencies. For correction of this effect, the reduced Raman spectra were calculated using Shuker-Gammon formula [8]

$$I^{\text{red}}(\omega) = (\omega_L - \omega)^{-4} \cdot \omega (1 - \exp(-\hbar\omega/kT)) \cdot I(\omega), \quad (2)$$

where ω_L and ω are the frequency of excitation light and of scattered light, respectively. T is the temperature, k is Boltzman constant and $I(\omega)$ is the measured Raman intensity.

3. RESULTS

The glassy samples of $(\text{GeS}_2)_{80-x}(\text{Sb}_2\text{S}_3)_{20} \cdot x\text{PrCl}_3$ and $(\text{GeS}_2)_{60-x}(\text{Sb}_2\text{S}_3)_{40} \cdot x\text{PrCl}_3$, ($x = 0.01, 0.1, 0.5$), were orange to red in colour. The glasses were optically homogeneous to the eyes and to the methods given above. Their X-ray diffraction patterns did not contain any peaks attributable to crystals. Several broad bands typical of the amorphous state were observed. The densities of samples were from the region, $d = 3.519 - 3.577 \text{ gcm}^{-3}$ for the glasses of the system $(\text{GeS}_2)_{60-x}(\text{Sb}_2\text{S}_3)_{40} \cdot x\text{PrCl}_3$ and from $3.223 - 3.258 \text{ g.cm}^{-3}$ for the glasses of the system $(\text{GeS}_2)_{80-x}(\text{Sb}_2\text{S}_3)_{20} \cdot x\text{PrCl}_3$.

The glass transition temperature, T_g , equals to $\sim 256 - 274^\circ\text{C}$ for $(\text{GeS}_2)_{60-x}(\text{Sb}_2\text{S}_3)_{40} \cdot x\text{PrCl}_3$ glasses. This temperature increases with increasing content of PrCl_3 . The T_g , equals to $\sim 330 - 333^\circ\text{C}$ for $(\text{GeS}_2)_{80-x}(\text{Sb}_2\text{S}_3)_{20} \cdot x\text{PrCl}_3$ glasses and it also slightly increases with increasing Pr content. There was not found any crystallisation at temperatures up to 400°C .

The short-wavelength absorption edge, as determined from optical transmissivity, lies between 550 - 700 nm for $(\text{GeS}_2)_{60-x}(\text{Sb}_2\text{S}_3)_{40} \cdot x\text{PrCl}_3$ glasses and between 500 - 650 nm for $(\text{GeS}_2)_{80-x}(\text{Sb}_2\text{S}_3)_{20} \cdot x\text{PrCl}_3$ glasses in their spectrum.

Doping of the samples with PrCl_3 creates new absorption bands near 4980, 6370, 6640, 9843 cm^{-1} , which are similar to the bands of Pr^{3+} in $\text{GeS}_2\text{-Ga}_2\text{S}_3$ glasses [2]. In the glasses with higher PrCl_3 content can be found a new absorption band near 2100 cm^{-1} which is probably created by electron transition between $^3\text{H}_4$ and $^3\text{H}_5$ electron levels of Pr^{3+} ion.

In the Raman spectrum of studied glasses can be seen a broad band with maximum near 340 cm^{-1} for $(\text{GeS}_2)_{80-x}(\text{Sb}_2\text{S}_3)_{20} \cdot x\text{PrCl}_3$ glasses, and a similar band with maximum near 330 cm^{-1} for $(\text{GeS}_2)_{60-x}(\text{Sb}_2\text{S}_3)_{40} \cdot x\text{PrCl}_3$ glasses (Fig. 1). These broad bands of both types of glasses can be deconvoluted into four or five bands. In the spectrum, there is also a low intensity broad band near 150 cm^{-1} and a weak band near 482 cm^{-1} (Fig.1). The Raman spectra of Pr^{3+} doped glasses are practically identical with the spectra of undoped glasses.

The long-wavelength absorption edge of the samples was found near 900 cm^{-1} and its position (in analogy with Pr-doped Ge-Ga-S glasses [2]) can be assigned to the multiphonon Ge-S and Sb-S vibrations. The amplitudes and band positions in this region are identical with these ones in the undoped samples. The absorption in the far IR region, behind this absorption edge, is strong. The analysis of the reflectivity spectra in this region will be given elsewhere [9].

The luminescence spectra of Pr^{3+} activated glasses are given in Figs. 2, 3. Two broad luminescence bands were observed with excitation by 1064 nm line. The luminescence was not observed when the samples were excited by 476.5 nm or 488 nm lines, probably due to high absorption in this region.

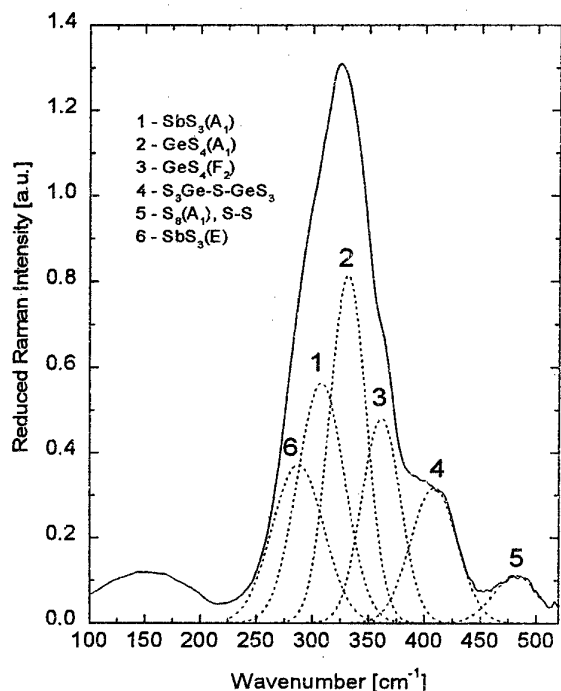


Fig. 1. Raman spectra of the $60\text{GeS}_2\text{-}40\text{Sb}_2\text{S}_3$ glass

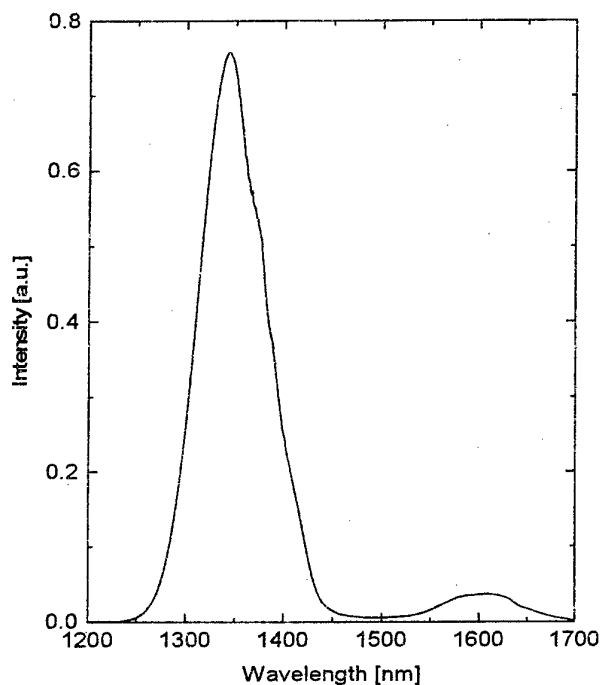


Fig. 2. Luminescence spectrum of $59.5\text{GeS}_2\text{-}40\text{Sb}_2\text{S}_3\text{-}0.5\text{PrCl}_3$ glass

4. DISCUSSION

The structure of studied glasses is reflected in the Raman spectra (Fig. 1). The broad band near 142 cm^{-1} in the spectrum of studied glasses can be also found in the spectrum of glassy GeS_2 (vibrations of GeS_4). There were found four weak bands with maxims near 130, 159, 195 and 241 cm^{-1} in the spectrum of crystalline Sb_2S_3 . The broad band of studied glasses with maximum near 142 cm^{-1} can be thus formed by overlapping of Raman bands of Sb_2S_3 and GeS_2 structural units which are broadened in glassy system of Ge-Sb-S. The weak band near 482 cm^{-1} of $(\text{GeS}_2)_{60-x}(\text{Sb}_2\text{S}_3)_{40-x}\text{PrCl}_3$ glasses can be assigned to the $\text{S}_8(\text{A}_1)$ ring vibration mode of sulphur. The individual bands obtained by deconvolution of the main broad Raman band of studied glasses (Fig. 1) can be assigned to $\text{SbS}_3(\text{E})$, 287 cm^{-1} and $\text{SbS}_3(\text{A}_1)$, $307 - 310\text{ cm}^{-1}$, pyramidal vibrations, to the $\text{GeS}_4(\text{A}_1)$, $330 - 333\text{ cm}^{-1}$, and to $\text{GeS}_4(\text{F}_2)$, $358 - 394\text{ cm}^{-1}$, tetrahedral vibrations, or to $\text{S}_3\text{Ge-S-GeS}_3$ structural units vibrations ($406 - 409\text{ cm}^{-1}$).

From the Raman spectra and from the spectral dependence of reflectivity in the far IR region can be thus judged that the structure of prepared glasses is formed by GeS_4 tetrahedra and by SbS_3 pyramids interconnected by sulphur bridging atoms. The S_8 ring vibrations can be also

found in some glasses. The results have also shown that the structure of Ge-Sb-S glasses is not practically influenced by small amounts of RE dopants.

In analogy with the paper [6], the new absorption bands introduced by Pr doping can be assigned to the electron transition from the level 3H_4 to the higher energy levels of Pr^{3+} ions 3H_5 , 3H_6 , 3F_2 , 3F_3 , 3F_4 and 1G_4 . The transitions $^3H_4 - ^3H_6$, 3F_2 , and $^3H_4 - ^3F_3$, 3F_4 formed unseparated absorption bands with strong overlapping of individual bands. The absorption bands corresponding to the transition $^3H_4 - ^1D_2$, $^3H_4 - ^3P_0$ and $^3H_4 - ^3P_1$ were partly hidden in the short-wavelength absorption edge.

In the luminescence spectrum of Pr^{3+} activated glasses (Figs. 2, 3) can be seen a dominant band near 1343 nm for $(GeS_2)_{60-x}(Sb_2S_3)_{40}xPrCl_3$ glasses and near 1346 nm for $(GeS_2)_{80-x}(Sb_2S_3)_{20}xPrCl_3$ glasses, which can be assigned to the radiative transition from $^1G_4 - ^3H_5$ levels of Pr^{3+} ions. From this 3H_5 level are the electrons transferred to the basic 3H_4 level by multiphonon relaxation. To the 1G_4 level mentioned above are the electrons excited directly from the 3H_4 level by the Nd:YAG laser light (1064 nm).

The luminescence band near 1600 nm is probably created by electron transitions between 3F_3 and 3H_4 levels (Fig. 4). This luminescence is of much lower intensity. The presence of electrons on the 3F_3 level is probably caused by multiphonon relaxation transition, when the depopulation of electrons on the 1G_4 level is received. The energy difference between 1G_4 and 3F_3 levels is relatively large ($\sim 3500\text{ cm}^{-1}$) and the probability of multiphonon relaxation is low. It results in low intensity of luminescence near 1600nm. It cannot be also excluded that there is some radiative transition between the 1G_4 and 3F_4 or 3F_3 levels with energy outside of sensitivity of our facility.

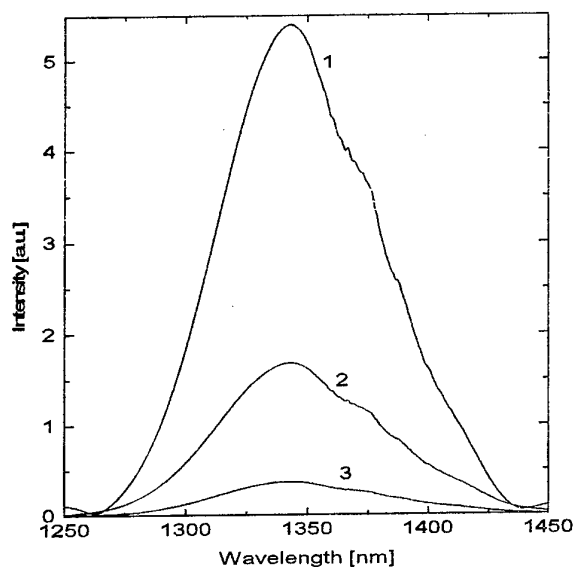


Fig. 3. Luminescence spectrum of $(GeS_2)_{60-x}(Sb_2S_3)_{40}xPrCl_3$. 1 $x = 0.5$, 2 $x = 0.1$, 3 $x = 0.01$.

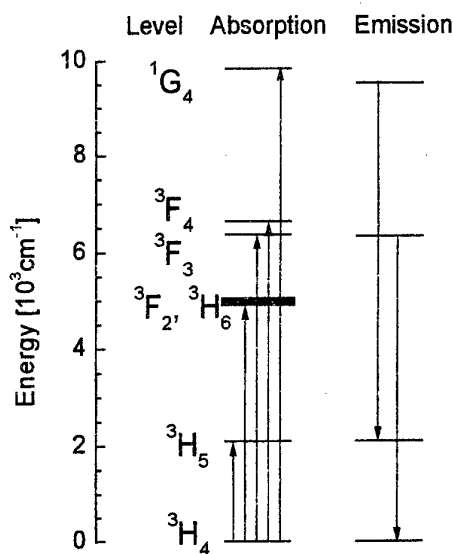


Fig. 4. Energy scheme of electron levels of Pr^{3+} ions in $79.5GeS_2-20Sb_2S_3-0.5PrCl_3$ glass

5. CONCLUSION

The $\text{GeS}_2 - \text{Sb}_2\text{S}_3$ glasses dissolve relatively large amounts of PrCl_3 and form stable glasses. Their properties are similar to Pr-doped Ge-Ga-S and also to Pr doped halide glasses. Due to lower phonon frequencies in sulphide glasses than in oxide or halide glasses, the Pr^{3+} doped chalcogenides may be good candidates for high efficiency light amplifiers and lasers.

ACKNOWLEDGEMENT

The work was partly supported by grants No.203/98/0103 and No. 203/96/0876 of Czech Grant Agency and by the "Key project 12/96" of Czech Acad. Sci., Prague, which are gratefully acknowledged.

REFERENCES

- [1] W.S. Brocklesby, A. Pearson: J.Luminesc. 59 (1994) 333.
- [2] B. Frumarová, J. Oswald, P. Krečmer, M. Frumar, V. Černý, V. Smrčka: Optical Materials, 6 (1996) 217.
- [3] D.R. Simons, A.J. Faber, F. Simonis, H. De Waal: Proc. 8th Internat. Symp. Halide Glasses, Perros Guirrec 992, CNET Lannion, France 1992, p.448.
- [4] D.W. Hewak, R.S. Deol, J. Wang, G. Wylangowski, J.A. Medeiros Neto, B.N. Samson, R.I. Laming, W.S. Brocklesby, D.N. Payne, A. Jha, M. Poulain, S. Otero, S. Surinach and M.D. Baro: Electronic Letters 29 (1993) 237.
- [5] H. Ebendorff-Heidepriem, W. Seeber, D. Ehrt: J. Non-Cryst. Solids 183 (1995) 191.
- [6] Deol R.S. et al.: J. Non-Cryst. Solids 161 (1993) 257.
- [7] B. Frumarová, P. Němec, M. Frumar, J. Oswald, Phys. Tech. Semiconductors, 1998, in press.
- [8] R. Shuker, R. W. Gammon: Phys. Rev. Lett. 25 (1970) 222.
- [9] P. Němec et al., to be published.

SITE-SELECTIVE SPECTROSCOPY OF Nd³⁺ IONS IN HEAVY METAL OXIDE GLASSES

R. Balda^a, J. Fernández^a, M. Sanza^a, A. Oleaga^a, A. de Pablos^b,
and J.M. Fernández-Navarro^b

^aDpto. de Física Aplicada I, E.T.S.I.I. y Telecom., Universidad del País Vasco, Alameda Urquijo s/n, 48013, Bilbao, Spain. email wupbacrr@bi.ehu.es

^bInstituto de Cerámica y Vidrio, 28500 Arganda del Rey, Madrid, Spain

ABSTRACT

Site-selective spectroscopy and time resolved fluorescence line narrowing experiments were performed in the $^4F_{3/2} \rightarrow ^4I_{9/2}, ^4I_{11/2}$ transitions of Nd³⁺ in six different compositions of heavy metal oxide glasses based on Bi₂O₃, GeO₂, and PbO. For all samples studied a strong line-narrowing of the $^4F_{3/2} \rightarrow ^4I_{11/2}$ emission has been observed when exciting at the long wave side of the $^4I_{9/2} \rightarrow ^4F_{3/2}$ transition. The lifetimes of the $^4F_{3/2}$ state do not show a monotonic variation with the excitation wavelength indicating large site-to-site variations in the local crystal field. Spectral migration of excitation among the Nd³⁺ ions has been studied from the time evolution of the $^4F_{3/2} \rightarrow ^4I_{9/2}$ spectra under resonant excitation. The results can be interpreted in terms of a dipole-dipole transfer mechanism.

INTRODUCTION

The discovery of heavy metal oxide (HMO) glasses has attracted interest because of their optical properties such as high refractive indices, high optical non-linearities and good infrared transmittance up to about 7-8 μm [1-3]. The wide infrared transmission window indicates that vibrational phonon energy of these glasses is small compared to other conventional oxide glasses. The maximum phonon energies of conventional oxide glasses such as silicate, borate, and phosphate are high; therefore the nonradiative relaxation due to multiphonon emission is the dominant process for transitions with small energy gaps. The reduced phonon energy in HMO glasses provides the possibility to develop more efficient lasers and fiber optics amplifiers. A knowledge about the most important laser parameters requires a detailed spectroscopic study of the optical properties of paramagnetic ions in these HMO matrices.

Among the various rare-earth ions, neodymium is the most widely studied ion in a variety of glasses not only because of its applications, but also because the variations with composition of its spectroscopic properties usually apply to other trivalent rare earth ions. The optical properties of rare-earth doped glasses are closely related to the local structure and bonding at the ion site [4] and for this reason have been commonly used as probes for local ordering. Although rare earths are not randomly distributed throughout the glass and they may or may not enter as former ions, their optical spectra show, even at low concentrations, an inhomogeneous broadening which is the evidence of large site-to-site crystal field variations. Several laser spectroscopic techniques, such as fluorescence line narrowing (FLN), spectral hole burning, etc., [5,6] are required to obtain detailed information on the local field and ion-ion and ion-host interaction processes.

In this work we report the optical properties of Nd³⁺ ions in six different compositions of HMO glasses based on Bi₂O₃, GeO₂, and PbO. In order to establish a correlation between

glass matrix composition and Nd^{3+} spectral properties, steady-state site selective and resonant time-resolved fluorescence line narrowing (TRFLN) spectroscopy were performed to obtain information about the site distribution of Nd^{3+} ions and the energy transfer between them.

EXPERIMENTAL

Batches of 20 g of glass have been prepared by mixing high purity reagents Bi_2O_3 (ALFA 99.999), GeO_2 (ALFA 99.999), PbO (ALFA 99.9995) and all glasses were doped with 1 % Nd_2O_3 (ALFA 99.999). This mixture was melted in a high purity alumina crucible placed in a vertical tubular furnace at temperature between 1100-1200 °C for 1 h and then poured onto a preheated brass plate, followed by 1 h annealing at 420 °C and cooling at 1.5 °C/min down to room temperature. Finally the samples were cut and polished for optical measurements. The composition and density of the glasses in the system Bi_2O_3 - GeO_2 - PbO are listed in Table 1.

Table 1.- Composition (mol%) and density (gr/cm^3) of the samples studied.

Glass	Composition (mol%)	d (gr/cm^3)
A	59 GeO_2 -41 PbO	6.21
B	25 Bi_2O_3 -62.5 GeO_2 -12.5 PbO	6.65
C	17.65 Bi_2O_3 -58.82 GeO_2 -25.53 PbO	6.63
D	11.11 Bi_2O_3 -55.56 GeO_2 -33.33 PbO	6.52
E	5.26 Bi_2O_3 -52.63 GeO_2 -42.11 PbO	6.53
F	25 Bi_2O_3 -75 GeO_2	6.22

As can be observed the density value slightly increases with the Bi_2O_3 concentration except for glass F. This effect has been observed in other HMO glasses and attributed to the weight of Bi_2O_3 compared to PbO and GeO_2 and the increase in the covalent bond character [7]. The densities are small compared to other bismuth and lead glass systems [8]. As expected a high refractive index for these HMO glasses is observed in the range 1.94 to 2.04.

The samples temperature was varied between 4.2 and 300 K with a continuous flow cryostat. The steady-state emission measurements were made with an Argon laser as exciting light and the medium wave tuning range (800-920 nm) of a Ti-Sapphire ring laser, pumped by an Argon laser. The fluorescence was analyzed with a 0.22 m SPEX monochromator, and the signal was detected by a Hamamatsu R7102 extended IR photomultiplier and finally amplified by a standard lock-in technique.

Lifetime measurements and time resolved resonant fluorescence line narrowed emission measurements were obtained by exciting the samples with a Ti-Sapphire laser, pumped by a pulsed frequency doubled Nd:YAG laser (9 ns pulse width), and detecting the emission with a Hamamatsu R7102 photomultiplier. Data were processed by an EGG-PAR boxcar integrator.

RESULTS AND DISCUSSION

Taking advantage of the tunability and narrow bandwidth of the Ti-sapphire ring laser as an excitation source for the ${}^4\text{I}_{9/2} \rightarrow {}^4\text{F}_{3/2}$ transition, we have performed the excitation spectra of this transition for all samples collecting the luminescence at different wavelengths along the ${}^4\text{F}_{3/2} \rightarrow {}^4\text{I}_{11/2}$ transition. Figure 1 shows, as an example, the low temperature steady-state excitation spectra for glass C obtained at two different emission wavelengths. As can be observed the spectrum narrows and blueshifts for emission at the high-energy wing of the ${}^4\text{F}_{3/2} \rightarrow {}^4\text{I}_{11/2}$ emission.

The steady-state emission spectra for the ${}^4\text{F}_{3/2} \rightarrow {}^4\text{I}_{11/2}$ transition were performed by exciting at different wavelengths in the low energy component of the ${}^4\text{I}_{9/2} \rightarrow {}^4\text{F}_{3/2}$ absorption band. Figure 2 shows the emission spectra of glasses A, C, and F obtained at different excitation wavelengths measured at 4.2 K. As can be observed as excitation wavelength increases along the low-energy Stark component of the doubled ${}^4\text{F}_{3/2}$, the shape of the emission band changes and a strong narrowing and redshift of the emission spectra occurs. For all samples the spectra are characterized by fluorescence bands having poorly resolved components and a large residue of inhomogeneous broadening. However, the fluorescence spectra of glass A show more resolved and slightly narrower lines which indicates a glass with a small site-to-site variation in the local field.

The decays of the ${}^4\text{F}_{3/2} \rightarrow {}^4\text{I}_{11/2}$ transition were performed by exciting the samples at different wavelengths along the low energy component of the ${}^4\text{I}_{9/2} \rightarrow {}^4\text{F}_{3/2}$ absorption band. They were found to be single exponential at all temperatures and compositions. This behaviour may be due to the use of narrow band laser excitation. Figure 3 shows that the lifetime displays a variation of about 20 % and does not show a monotonic variation with wavelength. The lifetime initially decreases with increasing wavelength but after reaching a minimum it increases again (this lifetime increasing at long wavelengths may be attributed to the presence of energy transfer between Nd^{3+} centers). The wavelength dependence suggests large site-to site differences in the local crystal field. The same behaviour was found at 4.2 K. The lifetime values are nearly independent of temperature in the 4.2 K-300 K range for all samples.

The existence of energy transfer between Nd^{3+} ions in these glasses can be studied by using time resolved fluorescence line narrowing (TRFLN) spectroscopy. If the laser source is pulsed and ion-ion interactions are present, the TRFLN technique provides us with a way to measure optical energy propagation from the initially excited subset of ions to other elements of the inhomogeneously broadened line. This is done by observing the emission characteristics of the system as a function of time. Resonant time-resolved fluorescence line narrowed emission spectra for the ${}^4\text{F}_{3/2} \rightarrow {}^4\text{I}_{9/2}$ transition were performed for all samples at 4.2 K by exciting the samples into the ${}^4\text{I}_{9/2} \rightarrow {}^4\text{F}_{3/2}$ absorption band at different time delays after the laser pulse. It is important to perform the measurements at low temperature to ensure that only the lowest energy Stark level of the ground state is excited. Typical results of these measurements are given in Figure 4, which shows the normalized spectra at two different time delays, 1 μs and 350 μs , for glass A. In the spectra we observe a simple FLN line and a broad emission which arise from the non-narrowed inhomogeneous line, and their evolution as time increases. In this case, a quantitative measure of the transfer is provided by the ratio of the intensity in the narrow line to the total intensity of the fluorescence in the inhomogeneous band.

Neglecting the dispersion in the radiative decay rate, and using the Förster formula for dipole-dipole energy transfer, one can write for the relationship between the integral intensities of the broad background emission I_B , and the narrow luminescence component I_N :

$$\text{Ln} \left(\frac{I_B}{I_N} + 1 \right) = \gamma(E_L) t_2^{\frac{1}{2}} \quad (1)$$

The macroscopic parameter $\gamma(E_L)$ has the meaning of an integral characteristic, reflecting the average rate of excitation transfer from donors to the ensemble of spectrally nonequivalent acceptors [9].

We have analyzed the time-resolved site-selective fluorescence spectra of the transition $^4F_{3/2} \rightarrow ^4I_{9/2}$ obtained at different time delays between 1 μs and 350 μs according to eq. (1). As an example, Fig. 5 shows the results for glasses A, C, and F doped with 1 mol% of Nd^{3+} at 4.2 K for an excitation wavelength of 882 nm. As can be observed a linear dependence of the $\ln[(I_B/I_N)+1]$ function on $t^{1/2}$ was found, indicating that a dipole-dipole mechanism of interaction among the Nd^{3+} ions dominates in this time regime. The values of the average transfer rate indicate that energy transfer among Nd^{3+} ions is weak at this concentration.

CONCLUSIONS

(i) The narrowing observed in the steady-state emission spectra of the $^4F_{3/2} \rightarrow ^4I_{11/2}$ transition when the exciting wavelength increases along the $^4I_{9/2} \rightarrow ^4F_{3/2}$ absorption band, together with the non monotonic dependence of the lifetimes on the excitation wavelength, reveal the existence of a broad distribution of Nd^{3+} sites in these HMO glasses. The spectral features and inhomogeneous broadening of the emission spectra for the glasses studied suggest that the addition of Bi_2O_3 contributes to a greater variation in the local crystal field.

(ii) Analysis of the time evolution of the $^4F_{3/2} \rightarrow ^4I_{9/2}$ emission spectra obtained at low temperature under resonant excitation shows that spectral migration of excitation among neodymium ions is weak at 1 mol% Nd^{3+} concentration.

ACKNOWLEDGMENTS

This work has been supported by the Spanish Government CICYT (Ref. MAT97-1009) and (DGICYT Ref. PB95-0512)

REFERENCES

- [1] W.H. Dumbaugh, Phys. Chem. Glasses 27 (1978) 121
- [2] J.E. Shelby, J. Am. Ceram. Soc. 71 (1988) C254
- [3] D.W. Hall, M.A. Newhouse, N.F. Borrelli, W.H. Dumbaugh, and D.L. Weidman, App. Phys. Lett. 54 (1989) 1293
- [4] M.J. Weber, J. Non-Cryst. solids 123 (1990) 208
- [5] M.J. Weber, *Laser Spectroscopy of Solids*, 49, edited by W.M. Yen and P.M. Selzer (Springer, Berlin) pp. 189-239 (1981), and references therein.
- [6] M.J. Weber, J. Non-Cryst. Solids 47, (1982) 117
- [7] V.C. Solano Reynoso, L.C. Barbosa, O.L. Alves, N. Aranha and C.L. Cesar, J. Mater. Chem. 4 (1994) 529
- [8] J.A. Ruller and J.E. Shelby, Phys. Chem. Glass 33 (1992) 177
- [9] T.T. Basiev, V.A. Malyshev and A.K. Prhevuskii, *Spectroscopy of Solids Containing Rare Earth Ions*, edited by A.A. Kaplyanskii and R.M. Macfarlane (North-Holland, Amsterdam) p.303 (1987), and references therein.

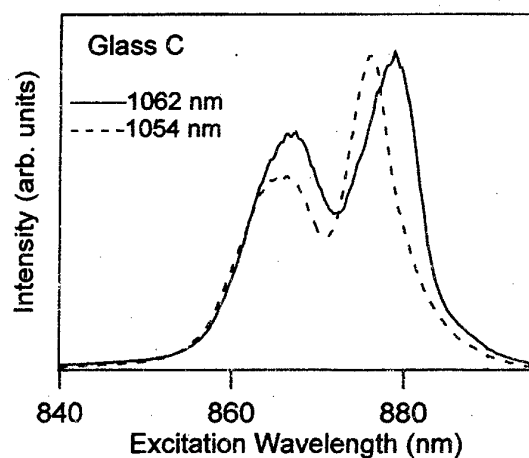


Fig. 1.- Steady-state excitation spectra of transition ${}^4I_{9/2} \rightarrow {}^4F_{3/2}$ in glass C for luminescence monitored at different wavelengths within the ${}^4F_{3/2} \rightarrow {}^4I_{11/2}$ emission band. Measurements were performed at 4.2 K.

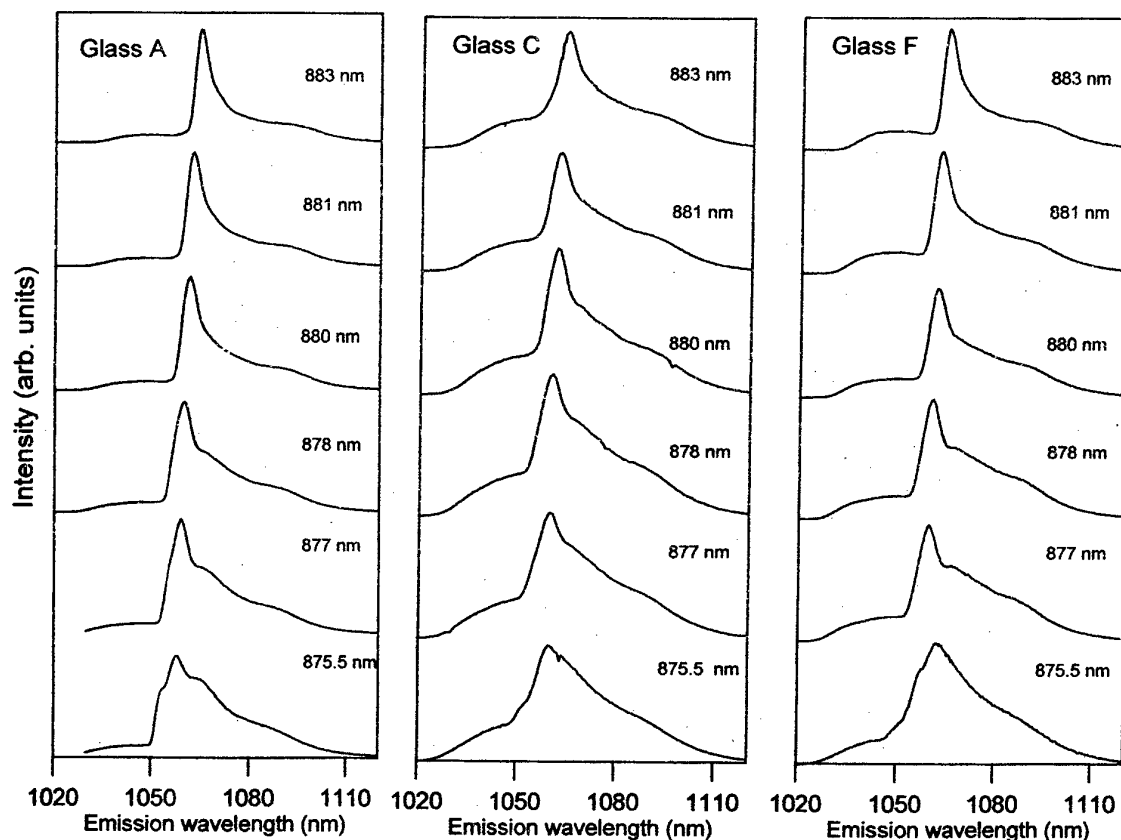


Fig. 2.- Steady-state emission spectra of transition ${}^4F_{3/2} \rightarrow {}^4I_{11/2}$ in glasses A, C, and F for different excitation wavelengths along the low energy Stark component of the ${}^4F_{3/2}$ level. Data correspond to 4.2 K.

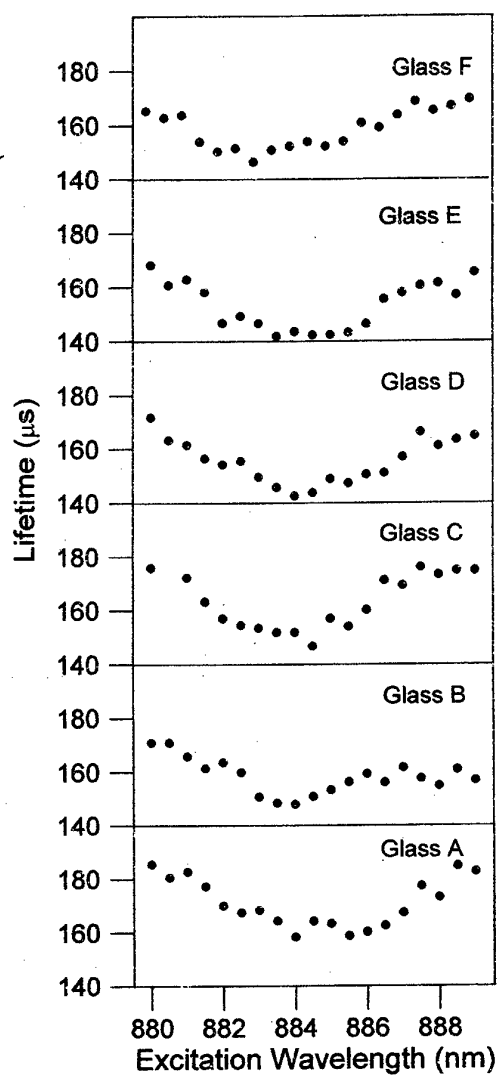


Fig. 3.-Lifetimes of the $^4F_{3/2}$ state as a function of excitation wavelength along the $^4I_{9/2} \rightarrow ^4F_{3/2}$ absorption band. Data correspond to 4.2 K

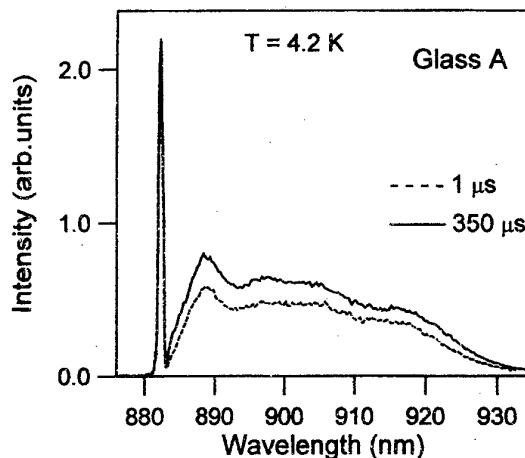


Fig. 4.- Time resolved fluorescence line narrowed spectra of the $^4F_{3/2} \rightarrow ^4I_{9/2}$ transition in glass A obtained for excitation at 882 nm at two different time delays after the laser pulse. Data correspond to 4.2 K.

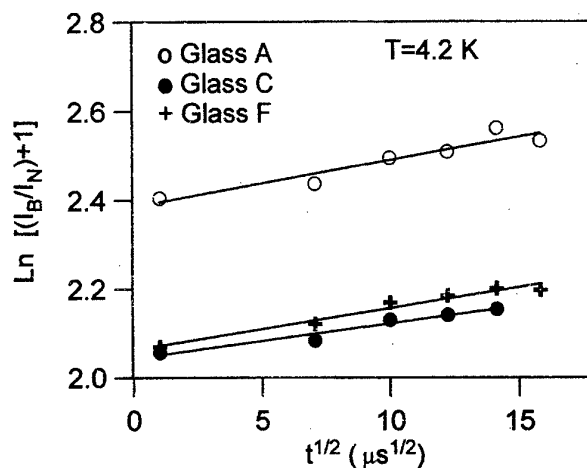


Fig. 5.- Analysis of the time evolution of the $^4F_{3/2} \rightarrow ^4I_{9/2}$ emission by means of eq. (1) for three different samples. Symbols correspond to experimental data and the solid lines are fits to eq. (1). Data correspond to 4.2 K.

STUDIES OF OPTICAL NONLINEARITIES OF CHALCOGENIDE AND HEAVY-METAL OXIDE GLASSES

F. W. Wise, I. Kang, and S. Smolorz

Department of Applied Physics
Cornell University
Ithaca, NY 14853
fwise@msc.cornell.edu

B. G. Aitken and N. F. Borrelli

Research, Development, and Engineering Division
Corning Incorporated
Corning NY 14831

INTRODUCTION

In recent years a considerable effort has been aimed at developing and characterizing glasses with large and fast optical nonlinearities, motivated largely by the potential application of these materials in all-optical switching devices. Several papers [1, 2, 3] offer thorough reviews of progress in this area up until the early 1990's and are highly recommended.

To be useful for applications in ultrafast switching and the generation of ultrashort pulses, glasses must have subpicosecond response times. However, most previous measurements of the optical nonlinearities of glasses were performed with pulses between 10 ps and 10 ns in duration. In addition, 2-photon absorption of nonlinear glasses was not thoroughly characterized. This is an important limiting factor in all-optical switching and in Kerr-lens modelocking of solid-state lasers.

These factors motivated us to investigate the optical nonlinearities of a variety of heavy-metal sulfide (LaGa sulfide, GeGa sulfide, and GeGaBa sulfide) and heavy-metal oxide (PbBi borosilicate, PbBi gallate, Pb tellurite, and TiBi gallate) glasses. Measurements were made using the z-scan technique, with 100-fs pulses at wavelengths between 600 nm and 1.25 μm [4]. Most of these glasses possess very good characteristics for photonics applications, including refractive nonlinearities among the largest reported for glasses and acceptable figures of merit for all-optical switching. The measured nonlinear refractive indices are predicted reasonably well by the semi-empirical Boling-Glass-Owyong formula [5], although the constant of proportionality relating the nonlinear to linear indices is smaller than is the case for glasses not containing heavy metals.

DISPERSION OF THE OPTICAL NONLINEARITIES

Virtually all previous measurements of the third-order optical nonlinearities of glasses have been made at one or two wavelengths. Our measurements constitute the first systematic study of the dispersion of the nonlinearities of glasses. Qualitatively similar variation was found for all samples: the nonlinearities increase rapidly below 900 nm, probably due to resonant enhancement given the proximity of the linear absorption edge. The third-order susceptibilities at 600 nm are among the largest values ever reported for

glasses, with $\text{Re } \chi^{(3)} > 10^{-11}$ esu. A weaker increase between 1250 and 900 nm can be understood from general principles: analysis of the quantum-mechanical expression for the second hyperpolarizability shows that it should deviate from the static value as a quadratic function of frequency far off resonance [6]. The expression for the off-resonant third-order susceptibility is qualitatively consistent with the experimental results.

NUCLEAR CONTRIBUTIONS TO THE THIRD-ORDER NONLINEARITIES

The magnitude of any nuclear contribution to the third-order optical nonlinearities of glasses was an unresolved issue for many years. Hellwarth and co-workers originally estimated the relative contributions of electronic and nuclear mechanisms to the third-order polarization of glasses by analyzing Raman-scattering spectra along with intensity-induced polarization changes [7]. The nuclear contribution was estimated to be 5-20% of the total nonlinear polarization. More recently, Hall *et al.* [8] and Kang *et al.* [4] attempted to assess the origin of the measured nonlinearities through their tensor properties. Away from an absorption resonance and for a purely electronic process, the ratio of the diagonal to off-diagonal elements of $\chi^{(3)}$ should be 3; this is known as Kleinman symmetry. Almost all glasses seem to obey Kleinman symmetry, and indeed the first femtosecond measurements of nonlinear refraction in glasses [9] indicated an instantaneous (i.e. electronic) response. These results directly contradict Hellwarth's conclusions. Despite the substantial nuclear polarizabilities of most glasses, there was no direct measurement of a nuclear contribution to $\chi^{(3)}$ until Kang *et al.* reported [10] the observation of the coherent nuclear response of glasses. The clear isolation of electronic and nuclear responses possible in the time domain allows for direct estimation of their relative strengths. The fractional nuclear contribution is ~10% in this case, quite similar to the values estimated previously [7] for different materials and elements of the response tensor. The experiments of Kang *et al.* also constitute the first observation of coherent phonons in a glass.

ADVANCES IN MEASUREMENT TECHNIQUES

Prior to 1990, almost all measurements of third-order susceptibilities of glasses were made using 3-wave mixing, 4-wave mixing, or third-harmonic generation. In 1989 the z-scan was introduced [11]. This is a simple, single-beam technique that provides the magnitude and sign of the real and imaginary parts of $\chi^{(3)}$. The z-scan is not particularly sensitive; it is difficult to measure nonlinear phase shifts ($\Delta\Phi$) less than 0.01 rad using it. The sensitivity is improved to $\Delta\Phi \sim 10^{-3}$ rad in the time-resolved z-scan, used in Reference [10]. Much greater sensitivity is possible using the optical-heterodyne-detected Kerr effect [12] or time-resolved interferometry [13]. Both of these techniques can resolve nonlinear phase shifts as small as 10^{-6} rad, but at a cost of significant complexity in the construction and operation of the experiment. Kang *et al.* recently demonstrated that equal sensitivity can be obtained in a very simple experiment based on spectrally-resolving a two-beam coupling signal [14]. This technique also gives the magnitude and sign of the real and imaginary parts of $\chi^{(3)}$ in a single experiment. Data from fused silica demonstrate a sensitivity $\Delta\Phi = 3 \times 10^{-6}$ rad.

REFERENCES

- [1] M. E. Lines, J. Appl. Phys. 69 (1991) 6876.
- [2] E. M. Vogel, M. J. Weber, and D. M. Krol, Phys. Chem. Glasses 32 (1991) 231.
- [3] N. F. Borrelli, B. G. Aitken, and M. A. Newhouse, J. Non-Cryst. Solids 185 (1995) 109.
- [4] I. Kang, T. D. Krauss, F. W. Wise, B. G. Aitken, and N. F. Borrelli, J. Opt. Soc. Am. B 12 (1995) 2053.
- [5] N. L. Boling, A. J. Glass, and A. Owyong, IEEE J. Quantum Electron. QE-14 (1978) 601.
- [6] D. M. Bishop, Phys. Rev. Lett. 61 (1988) 322.
- [7] R. Hellwarth, J. Cherlow, and T.-T. Yang, Phys. Rev. B 11 (1975) 964.
- [8] D. W. Hall, M. A. Newhouse, N. F. Borrelli, W. H. Dumbaugh, and D. L. Weidman, Appl. Phys. Lett. 54 (1989) 1293.
- [9] I. Thomazeau, J. Etchepare, G. Grillon, and A. Migus, Opt. Lett. 10 (1985) 223.
- [10] I. Kang, S. Smolorz, T. Krauss, F. Wise, N. F. Borrelli, and B. G. Aitken, Phys. Rev. B 54 (1996) R12641.
- [11] M. Shiek-Bahae, A. A. Said, and E. W. Van Stryland, Opt. Lett. 14 (1989) 955.
- [12] D. McMorro, W. T. Lotshaw, and G. A. Kenney-Wallace, IEEE J. Quantum Electron. QE-24 (1988) 443.
- [13] L. Sarger *et al.*, J. Opt. Soc. Am. B 11 (1994) 995.
- [14] I. Kang, T. Krauss, and F. Wise, Opt. Lett. 22 (1997) 1077.

BROADBAND 1.5 μm EMISSION IN Er^{3+} -DOPED TELLURITE GLASSES

S. Shen, M. Naftaly, A. Jha

Department of Materials, University of Leeds, Leeds LS2 9JT, UK

email: A.Jha@leeds.ac.uk

ABSTRACT

New Erbium-doped tellurite glass is presented as a host for broadband flat-gain Erbium amplifiers. The glass exhibits an exceptionally broad emission spectrum, a large stimulated emission cross-section, and a relatively long lifetime.

1. INTRODUCTION

The worldwide demand for bandwidth is urging an increase in the number of available wavelength-division-multiplexing (WDM) channels, especially in the 1.5 μm telecom window. Ultimately this can only be achieved by extending the gain bandwidth of Erbium-doped fibre amplifiers (EDFA) that enable long-distance optical transmission. Broadband flat-gain EDFAs are necessary for high-multichannel WDM operation. In this paper we present a new tellurite glass host for EDFA possessing exceptionally broad and flat 1.5 μm emission.

In 1997 NTT announced a flat-gain tellurite EDFA with 80 nm gain bandwidth. The full-width-at-half-maximum (FWHM) of emission in the NTT glass was 55 nm. In comparison, fluoride ZBLAN (Zr-Ba-La-Al-Na-fluoride) EDFA, which is the main broadband EDFA, has a broader emission of 65 nm FWHM, but a narrower gain bandwidth of only 40 nm. The broad gain of tellurite EDFA is due to its large stimulated emission cross-section (σ_{SE}) arising from its high refractive index. In the NTT glass σ_{SE} was $6.6 \times 10^{-21} \text{ cm}^2$, compared with $4.8 \times 10^{-21} \text{ cm}^2$ in ZBLAN. Tellurite glass also offers a large pump absorption cross-section and a good solubility for Er^{3+} ions, with doping levels of over 1 mol% being possible (10-20 times higher than in ZBLAN). These are important advantages, although in consequence of its high refractive index, the radiative lifetime (τ) in tellurite glasses is relatively short. The amplifier figure-of-merit $\sigma_{\text{SE}}\tau$ for NTT glass is $26 \times 10^{-24} \text{ cm}^2\text{s}$ ($48 \times 10^{-24} \text{ cm}^2\text{s}$ in ZBLAN).

2. RESULTS AND DISCUSSION

In this paper we investigate a new type of Er^{3+} -doped tellurite glass: $\text{TeO}_2\text{-Na}_2\text{O-ZnO}$. This glass exhibits emission with FWHM of 75 nm, implying exceptionally broadband gain. The emission cross-section is around $8 \times 10^{-21} \text{ cm}^2$, and the lifetime is around 5 ms. This gives a figure of merit of $40 \times 10^{-24} \text{ cm}^2\text{s}$ (comparable to ZBLAN). Due to its broad emission, large cross-section and large figure-of-merit, the new tellurite glass constitutes a highly promising glass host for a broadband flat-gain EDFA.

The Er^{3+} dopant in the new tellurite glass is sited in several different host environments. The width of Er^{3+} emission and absorption peaks in this glass indicates multiple sites with different ligand fields leading to varying Stark splittings. Moreover, Pr^{3+} emission from $^3\text{P}_0$ is also very broad, indicating similar multiple sites for Pr^{3+} ion. In addition, the OH^- absorption

peak is also unusually broad, signalling multiple OH⁻ sites. Other evidence for multiple sites arises from the behaviour of Er³⁺ emission with varying dopant concentration.

We investigate in detail the Er³⁺ spectroscopy in the new tellurite glasses, giving particular attention to aspects related to EDFA performance. The amplifier figure of merit is the product of stimulated emission cross-section and metastable lifetime. The available gain bandwidth, on the other hand, grows with emission cross-section. To achieve a large emission cross-section, and therefore broadband gain, our tellurite glasses were designed to have a high refractive index, as well as multiple dopant sites. Although the figure of merit decreases in high refractive index glasses, the preferred host glass has a good combination of a relatively long lifetime and a large cross-section.

Concentration quenching of Er³⁺ in the preferred tellurite host was studied. The optimum doping level was found to be around 10000 ppm wt. This is unusually high for EDFA, indicating the possibility of shorter fibre devices, as well as planar devices. The late onset of concentration quenching is due to the good solubility of Er³⁺ in this tellurite host, leading to a good dispersion of Er³⁺ ions. The lifetime of the feeding level was also measured to ascertain the efficiency of pumping at 980 nm, which is the preferred pumping scheme.

The effect of OH⁻ content on Er³⁺ lifetime was investigated to determine tolerance levels for OH⁻ content. It was found that tellurite glass with acceptably low OH⁻ concentration is relatively easy to produce, as compared with, for example, fluorozirconate glass hosts.

A range of tellurite glass compositions were studied to determine the optimum glass host. The relationship between the glass composition and Er³⁺ spectroscopy is considered in the light of glass structure.

¹ A Mori et al, OFC'97, paper PD1-1

RECENT DEVELOPMENTS IN As-S GLASS FIBRES

G.G. Devyatikh, M.F. Churbanov, I.V. Scripachev, G.E. Snopatin

Institute of Chemistry of High-Purity Substances of the Russian Academy of Sciences, 49 Tropinin St., GSP-75, Nizhny Novgorod, 603600, GSP-75, Russia,
email: hp@hp.nnov.su

E.M. Dianov & V.G. Plotnichenko

Scientific Centre of Fibre Optics, General Physics Institute of the Russian Academy of Sciences, 38 Vavilov St., Moscow, 117756, Russia, fax: (095) 135 81 39

ABSTRACT

Increase in degree of purity of As-S glasses and development of the drawing technique allowed to manufacture optical fibres with the improved parameters.

The minimum optical losses in the optical fibres were 23 - 45 dB/km, 50 - 70 dB/km, 200 - 300 dB/km and 300 - 500 dB/km at 2.2 - 2.7 μm , 3.2 - 3.6 μm , 4.0 - 4.5 μm and 5.0 - 5.5 μm , respectively.

The bending strength of optical fibres with diameter of 400 μm increased from 0.6 - 0.8 GPa to the values exceeding 1.2 GPa.

1. INTRODUCTION

There is a considerable interest to the optical fibres based on high-purity arsenic sulfide glasses. They have the best mechanical and optical parameters as compared with optical fibres based on chalcogenide glasses of other systems. A vitreous arsenic sulfide is the most stable to the crystallization. The previous investigations showed that the parameters of optical fibres can be improved in case the degree of purity of the studied glasses will be increased.

2. EXPERIMENTAL

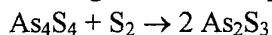
The experiments were carried out to increase the degree of purity of the glasses due to development of their production technique. The investigation of quantitative dependence of optical transmission of arsenic sulfide glasses on the content of the absorbing impurities was continued.

A conventional technique of production of high-purity glasses of $\text{As}_x\text{S}_{100-x}$ composition comprises melting of elements in evacuated silica ampoules. In contradistinction to previous methods a new process has been developed with using of arsenic monosulfide instead of elemental arsenic [1].

It is known that ultrapurification of arsenic from submicron particles, consisting mainly of carbon, by the method of vacuum sublimation is of low efficiency at the acceptable values of arsenic evaporation rates [2]. The particles accumulate on the surface of the sublimed arsenic which decreases during sublimation of the initial load. To produce the $\text{As}_x\text{S}_{100-x}$ glasses an arsenic monosulfide As_4S_4 was used as an arsenic-containing component of the charge for the glass preparation. Arsenic monosulfide is not a glass forming substance. It has rather high vapour pressure and low viscosity of the

melt and that is why there is no noticeable accumulation of submicron particles on surface and in the near-surface layer during distillation. For that reason As_4S_4 was purified by vacuum distillation at rather high evaporation rate (about $10^4 \text{ cm}^3/\text{cm}^2\text{s}$).

The glasses which had required composition, As_2S_3 for example, were obtained from the purified arsenic monosulfide by melting it with the required amount of sulphur, e.g.



A content of sumicron size particles in the glass obtained did not exceed $2 \cdot 10^4 \text{ cm}^{-3}$.

The values for extinction coefficients of the impurities of CO_2 , COS and CS_2 were found in As_2S_3 glass. The technique was used which had been previously developed to study the effect of hydrogen impurity on optical transmission of arsenic sulfide glasses [3]. The methods for production of the double-layered optical fibres were described earlier in [4]. Multimode optical fibres were drawn by the double-crucible technique. Single-mode fibers were obtained by the drawing of 1 mm diameter double-layer fibre which had been inserted into a tube made of cladding glass [5].

A primary coating of teflon dissolved in ketone with thickness of 10 mkm was applied to optical fibres in the process of drawing. A secondary coating with thickness of up to 100 mkm was applied by thermal solidification of PVC compound.

While drawing the optical fibres the main attention was given to reproducibility of the given ratio between the diameters of core and cladding, and to improvement in concentricity of the core position.

The content of inclusions of submicron size in glasses was determined by the laser ultramicroscopic method [6].

3.RESULTS AND DISCUSSION

Figures 1 and 2 show the merits of the new variant to produce high-purity glasses of As-S system as compared with those used previously.

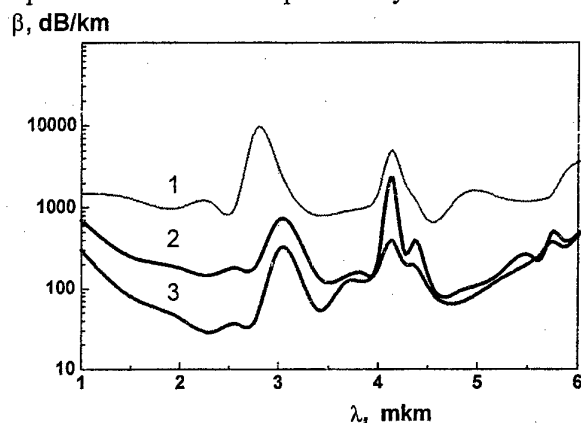


Figure 1. Spectra of the total optical losses in the optical fibres, based on As-S glass system, produced by different methods.

1 - distillation of the melt of commercial glass of special purity;
2 - synthesis from commercial elements of special purity with additional purification; 3 - synthesis from the purified arsenic monosulfide and sulfur

It is seen that the optical losses in the optical fibres, made of the glass by the suggested technique, are the lowest. The minimum optical losses in the optical fibres

were 23 - 45 dB/km, 50 - 70 dB/km, 200 - 300 dB/km and 300 - 500 dB/km at 2.2 - 2.7 mkm, 3.2 - 3.6 mkm, 4.0 - 4.5 mkm and 5.0 - 5.5 mkm, respectively.

The content of impurity inclusions of submicron size was decreased from $2 \cdot 10^6$ to $2 \cdot 10^4 \text{ cm}^{-3}$. The content of OH- and SH-groups in the glasses was also lowered as it can be seen from the optical loss spectra of the fibres. A substantial effect of submicron inclusions on the value of energy threshold of bulk damage of arsenic sulfide glass was found at pulse radiation of YAG:Er³⁺-laser ($\lambda = 2.94 \text{ mkm}$) [7]. The laser operated in a free-running mode and had the following parameters: a single-pulse energy is up to 1.8 J; pulse duration is 350 mks; pulse frequency is up to 4 Hz; the mean radiation energy is 2 Watts.

The threshold value of energy density of bulk damage increased from 100 J/cm^2 to 1500 J/cm^2 if the content of submicron size particles in the glass decreased from $2 \cdot 10^6 \text{ cm}^{-3}$ to $2 \cdot 10^4 \text{ cm}^{-3}$. This parameter reached the value of 3 kJ/cm^2 for the most pure glass samples.

The optical fibres with diameter of 460 mkm, made of more pure glass, were tested at the transmission of YAG:Er³⁺-laser radiation.

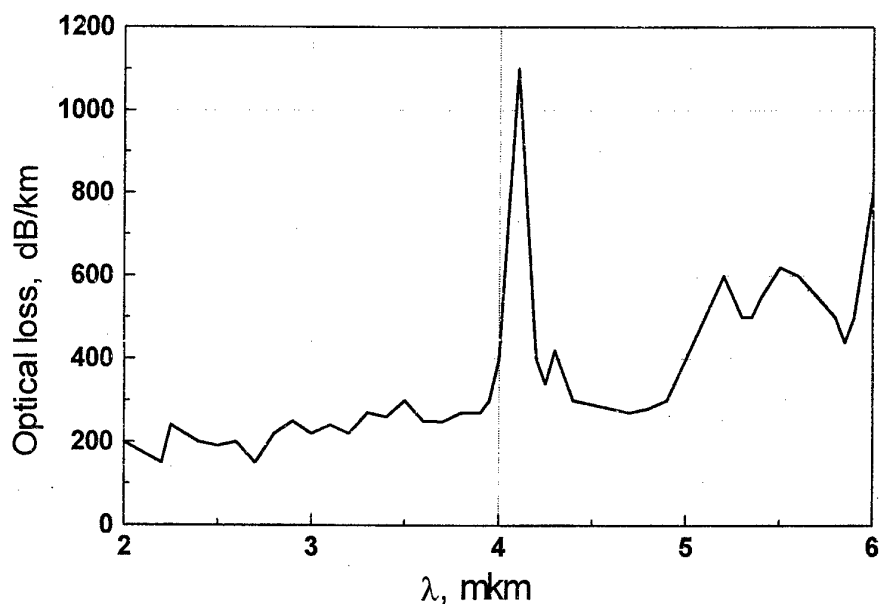


Figure 2. Spectra of the total optical losses of the optical fibre made of As-S glass with the content of particles less than $2 \cdot 10^4 \text{ cm}^{-3}$

The output energy in these fibers was up to 350 mJ after transmission of not less than 10^3 laser pulses. When a special technique for input of laser radiation into a fibre has been used the output energy at the end of the optical fibre attained 700 mJ. This parameter corresponds to the value observed in the IR-materials of high quality. No ageing of fibres was observed. In fibres kept in conventional atmosphere during a year damage threshold did not change.

Lowering in the concentration of microinclusions in the glasses also led to a substantial increase in the mean bending strength of the optical fibres from 0.4 - 0.6 GPa to 0.9 - 1.2 GPa (Figure 3).

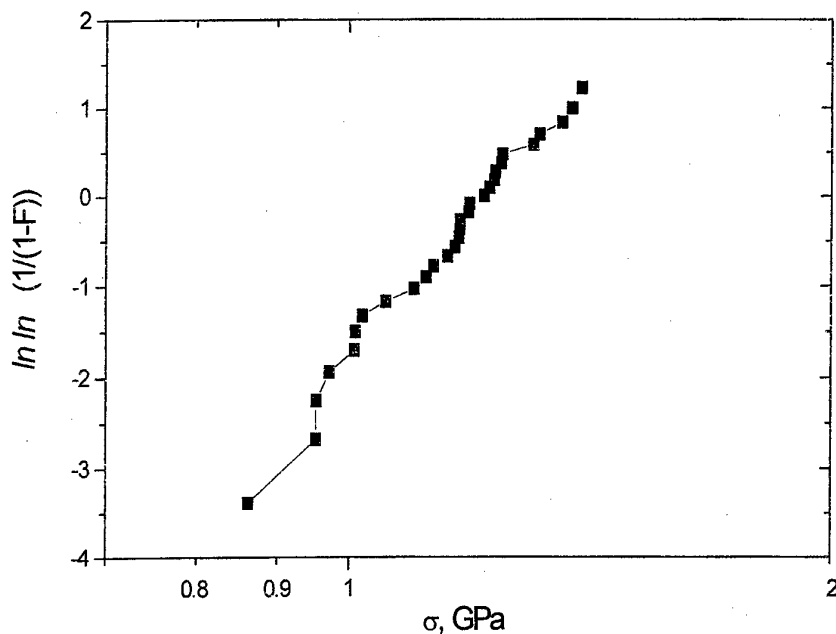


Figure 3. A Weibull distribution plot for the optical fiber made of As-S glass (the diameter of fibre is 400 mkm, the measurements were carried out at room temperature)

Table 1 gives the values for the extinction coefficient for the impurities of CO₂, COS and CS₂ dissolved in As₂S₃. The values for the concentrations of the impurities have been estimated in glasses which lead to the optical losses at the level of intrinsic ones.

Table 1
Values for the extinction coefficient for the maximum in intensity of absorption bands CO₂, COS and CS₂ in vitreous As₂S₃

Impurity	Position of band maximum, mkm	Range of studied concentrations, ppm.mol	Extinction coefficient cm ⁻¹ /ppm.mol	A content of the impurity which corresponds to intrinsic losses, ppb.mol
CO ₂	4,33	2 - 8	0,036 ± 0,005	0.004
COS	4,95	10 - 70	0,24 ± 0,7	0.006
CS ₂	6,68	1 - 6	1,1 ± 0,3	1

It can be seen that acceptable content of these impurities is at the level of several thousandth of ppb.

Table 2 gives the main parameters of the produced optical fibres.

Table 2

Main parameters of the optical fibres from high-purity As-S glasses

Type of optical fibre	Continuous length, m	Core/Clad diameter ratio	NA	Minimum losses at 2,2 - 4 mkm	Core concentricity, %	Bending strength, GPa	Notes
Multimode	Up to hundreds of meters	400/300, 250/130	0,2; 0,4	20 - 100	≥ 85	0,8-1,2	Intensity of OH < 0.3 dB/m SH < 1 dB/m
Single-mode	tens of meters	200/8	not measured	400	≥ 85	0,4-0,6	Cut-off wavelength : 1.1 - 1.5 mkm

4. CONCLUSION

Development of the method for preparation of high purity As-S glasses provided lowering in the concentration of heterophase impurity inclusions and of hydrogen-containing impurities by 2 - 3 orders of magnitude. It led to lowering in optical losses, to 2 - 3-fold increase in bending strength of optical fibres, and increased the output energy of erbium laser radiation, transmitted through the optical fiber, approximately by an order of magnitude.

Increase in the degree of purity of glasses should be considered the main way to improve the optical and operational parameters of the optical fibres.

REFERENCES

- [1] G.G.Devyatykh, M.F.Churbanov, I.V.Scripachev et.al., Russian Patent No.1721997, April 2, 1995.
- [2] M.F. Churbanov, V.S.Shiryaev, V.A. Fedorov et.al., Russian Journal «Vysokochistye Veshestva» (High-Purity Substances), No.6(1995), p.38.
- [3] V.G. Borisevich, V.G. Plotnichenko, I.V.Scripachev and M.F.Churbanov, Russian Journal «Vysokochistye Veshestva» (High-Purity Substances), No.2(1994), p.11.
- [4] I.V. Scripachev, V.G. Plotnichenko, G.E. Snopatin et.al., Russian Journal «Vysokochistye Veshestva» (High-Purity Substances), No.4(1994), p.34.
- [5] G.G.Devyatykh, E.M.Dianov, V.G.Plotnichenko et.al., Quantum Electronics, Vol.25, No.3(1995), p.270.
- [6] V.S. Shiryaev, I.V.Scripachev, G.E. Snopatin et.al., Russian Journal «Vysokochistye Veshestva» (High-Purity Substances), No.3(1995), p.114.
- [7] A.G.Antipenko, N.V.Artem'ev, A.A.Betin et.al., Quantum Electronics, Vol.25 No.5(1995), p.498.

Light Scattering from Coated Dielectric Particles in Fluorozirconate Glass

A. Edgar

School of Chemical and Physical Sciences, Victoria University of
Wellington, New Zealand
e-mail Andy.Edgar@vuw.ac.nz

ABSTRACT

We describe calculations of the optical extinction coefficient for spherical copper-coated dielectric particles in fluorozirconate glass. We show that as the coating thickness is reduced, the plasma resonance wavelength shifts from the visible region towards the infrared, and traverses the telecommunications windows. Such composite particles, with the appropriate coating thickness, can have a much larger effect on the extinction in the near infrared for a given volume of copper than can a particle which consists only of copper.

1. INTRODUCTION

The general theory of light scattering from a particle embedded in a homogeneous material was first developed by Mie [1], and comprehensive modern discussions of the theory are given in the books by Van der Hulst [2], and by Bohren and Huffman [3]. Light incident on a slab of glass containing particles will be attenuated by the combined effects of scattering and absorption; the attenuation is measured experimentally by the extinction coefficient α_{ext} which may be linked to Mie's scattering theory through the extinction, absorption and scattering efficiencies as follows,

$$\alpha_{\text{ext}} = n A Q_{\text{ext}} = n A (Q_{\text{abs}} + Q_{\text{sca}}), \quad (1)$$

where there are n particles per unit volume, each of cross sectional A . The cross-sectional efficiencies Q are defined as the ratio of the light intensity removed from the beam compared to that absorbed by a black disk of the same area. Their values may be computed from Mie's theory if the refractive indices of the particle and the host glass are known, and some model of the particle geometry is assumed. Analytical formulae [3] for the efficiencies can be deduced for some simple geometry's and when the particle diameter is small compared to the wavelength, but numeric computations must be performed in the general case.

In earlier work, we have reported the light scattering due to particles of metallic copper [4] and semiconducting cuprous chloride [5] in fluorozirconate glass. Figure 1, taken from reference 5, shows typical extinction spectra. The host glass had a composition close to that of the well-known ZBLAN20 formulation (53% ZrF_4 , 20% BaF_2 , 4% LaF_3 , 3% AlF_3 , and 20% NaF), and was prepared under mildly reducing conditions in a carbon crucible in an argon atmosphere. Copper particles with radii in the range of tens of nanometers strongly scatter red light due to a surface plasma resonance effect, whilst CuCl particles were found to be very strong scatterers in the exciton spectral region near 400 nm where the dielectric constant undergoes large and rapid changes. For both cases, the extinction is very strong in the visible/near UV portion of the spectrum, but at least for small particles, is substantially smaller in the near-infrared region, which contains the technically important telecommunications windows. Nonetheless, concentrations of just a

few parts per billion by volume of copper can still limit the optical transparency of optical fibers made from fluorozirconate glass to be less than for silica in the near-infrared region.

In electron microscopy investigations of fluorozirconate glass which were deliberately doped with copper, we have found some evidence for copper occurring as a decoration or coating on dielectric crystallites such as BaZrF_6 . The question then arises as to how the optical extinction spectra of glass containing such composite crystallites are modified from those containing crystallites of the pure dielectric, or pure copper. In this paper, we present the results of representative calculations of the extinction spectra for composite crystallites comprising a spherical dielectric core with a concentric spherical cap of copper.

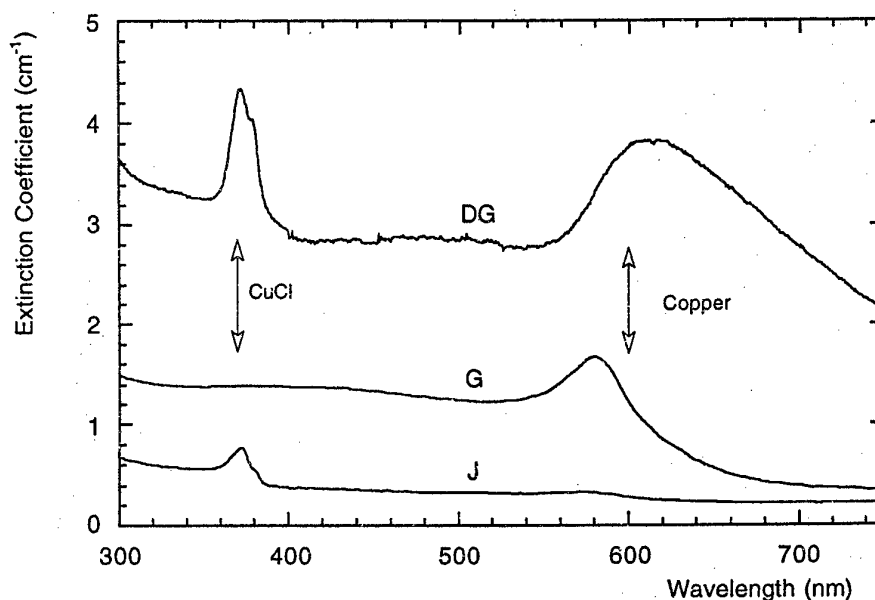


Figure 1: Optical extinction spectra for three samples labeled DG, G, J of fluorozirconate glass, showing extinction peaks due to metallic copper and cuprous chloride.

2. CALCULATIONS

We base our calculations on the analysis of a coated spherical particle presented by Bohren and Huffman [3]. In the present case we take the refractive index of the host glass to be 1.519 from Poulain et al. [6] and assume it to be wavelength independent, whilst we take the complex refractive index for copper from the collation by Lynch and Hunter [7] in the handbook of dielectric constants edited by Palik [7]. The data for copper must be used with some care, since there is a discontinuity at around 1.25μ where the source of data changes from one author to another. This abrupt discontinuity can give rise to artifacts in the computed extinction spectra if the refractive index data is used without modification; here we have numerically smoothed the interface between the two data sets. The choice of the refractive index of the core is arbitrary; as a representative value for typical heavy-metal fluoride crystallites such as BaZrF_6 we use the refractive index of ZBLAN itself.

We have adapted the FORTRAN program COAT published by Bohren and Huffman [3] to the Mathematica language, and tested the translated version of the program against earlier calculations for coated spheres by Fern and Oser [8], and Kerker et al [9]. We obtain satisfactory agreement to three significant figures for the extinction coefficients from the earlier works.

3. RESULTS

We show in figures 2 to 4 the computed extinction coefficients for coated particles of fixed outside radius of 32, 64, and 128 nm. In each case we present results for a coating of maximum thickness, i.e. a solid copper particle, and then for finite coating thicknesses of 32, 16, 8, 4, and 2 nm. We recognize that the use of the bulk copper dielectric constant for layers as thin as 2 nm is open to question, but include this result for the 32 nm radius particle case only so as to clearly indicate the trend with decreasing thickness. There is no point in calculations for coating thicknesses greater than about 40 nm because the resulting extinction spectrum is indistinguishable from that of a solid copper particle.

It is interesting to test the utility of effective medium theories for coated particles, since the computations for a uniform sphere are considerably more straightforward than for a coated sphere. In figure 5 we show the extinction spectra calculated for coated spheres compared with those for uniform spheres with effective dielectric constants ϵ_{eff} calculated from the Maxwell-Garnett theory [3],

$$\epsilon_{\text{eff}} = \epsilon_m [(\epsilon_d + 2\epsilon_m) + 2(1-f)(\epsilon_d - \epsilon_m)] / [(\epsilon_d + 2\epsilon_m) - (1-f)(\epsilon_d - \epsilon_m)], \quad (2)$$

where ϵ_m is the dielectric constant of the metallic copper, ϵ_d is the dielectric constant of the core, and f is the volume fraction of the copper with respect to the total particle volume. This formulation is equivalent to regarding the particle to be made of a medium comprising a copper host with embedded particles of dielectric.

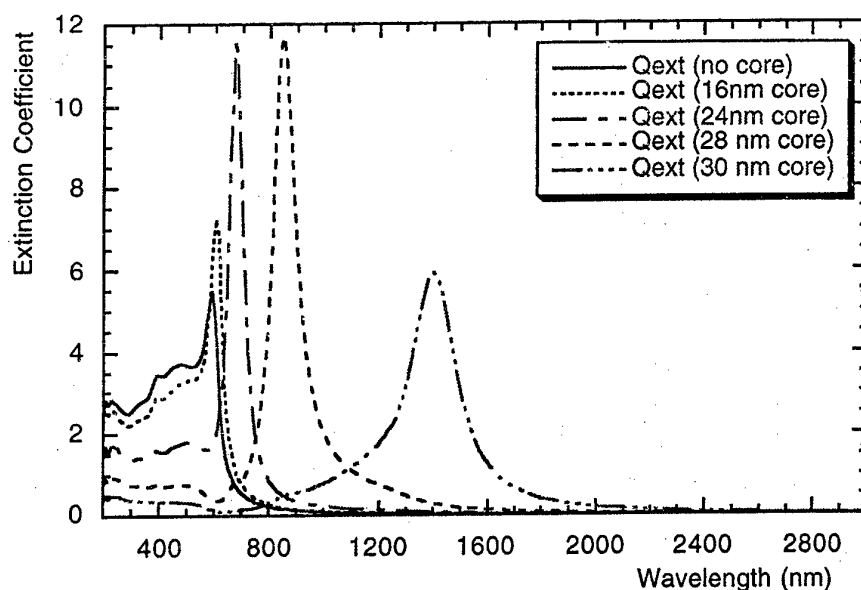


Figure 2: Calculated extinction spectrum for composite spherical particles of outside radius 32 nm, embedded in ZBLAN glass, comprising a copper coating on a ZBLAN dielectric core of variable radius.

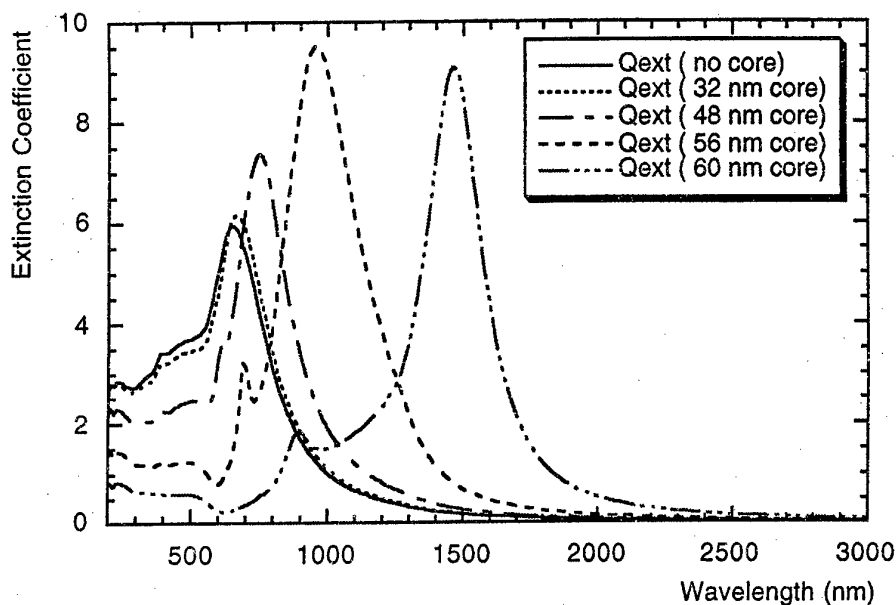


Figure 3: Calculated extinction spectrum for composite spherical particles of outside radius 64 nm, embedded in ZBLAN glass, comprising a copper coating on a ZBLAN dielectric core of variable radius.

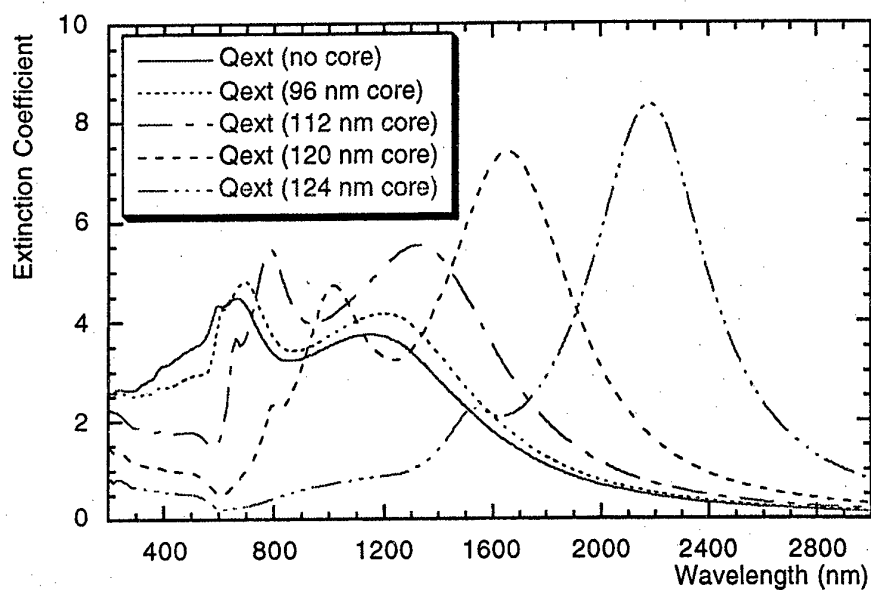


Figure 4: Calculated extinction spectrum for composite spherical particles of outside radius 128 nm, embedded in ZBLAN glass, comprising a copper coating on a ZBLAN dielectric core of variable radius.

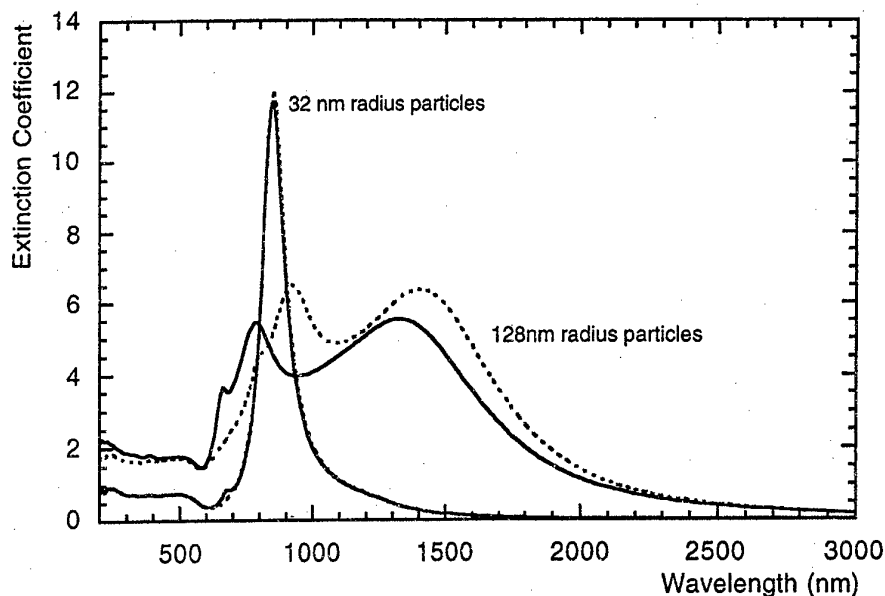


Figure 5: Calculated extinction spectrum (solid lines) for composite spherical particles of outside radii 32 and 128 nm, each comprising a copper coating on a ZBLAN dielectric core of radii 28 and 112 nm respectively, embedded in ZBLAN glass. The dashed lines are the calculated extinction coefficient for a uniform sphere of the same size, but with a single effective dielectric constant based on the Maxwell-Garnett theory. The volume fraction of dielectric is 67% in each case.

4. DISCUSSION

Turning first to figure 2 for particles of 32 nm radius, we note that the coated sphere calculation for an infinitesimally small core agrees with that using a different program [4] for a solid copper sphere. However, here we show the extinction spectrum over a greater wavelength range, including the near infrared region which includes the telecommunications windows. The dominant feature is a sharp peak near 600 nm, which corresponds to a surface plasma resonance [3,4]. This peak occurs for a small metallic sphere in a dielectric host when the condition,

$$\epsilon_{m1}(\lambda) + 2 \epsilon_h = 0, \quad (3)$$

is satisfied. In equation (3), $\epsilon_{m1}(\lambda)$ is the real part of the dielectric constant of the metal, and ϵ_h is the real dielectric constant of the host. The effect of reducing the coating thickness is that the plasma resonance moves towards long wavelengths, and initially at least the magnitude of the extinction peak increases. This implies that a given volume of copper is more effective in scattering light when present as a surface coating than in the form of solid copper spheres. Separate calculations of the scattering and absorption efficiencies shows that the dominant effect for thin coatings is absorption.

For spheres of 64 nm radius, the same general trends with coating thickness are evident, starting with a somewhat broader resonance peak for solid copper particles. However, for the 128 nm radius, the plasma resonance for solid particles has split into two peaks, which we believe represents the onset of higher order modes with increasing particle size [3].

In contrast to simpler metals such as aluminium, the surface plasma resonance in copper is complicated by the fact that equation 3 is satisfied in a region of the spectrum where an anomaly in the dielectric constant occurs: near 600 nm, there is a marked deviation from Drude-like behavior in copper due to an inter-band transition; this anomaly gives rise to the red colour of copper metal. For many of the spectra in figures 2-4, the effect of this dielectric anomaly near 600 nm is still evident, usually as a sharp dip in the extinction coefficient.

The comparison shown in figure 5 shows that effective medium theory is useful for particles small compared to the wavelength, although it is of decreasing accuracy as the size of the particle increases relative to the wavelength. To first order in f , i.e. for thin coatings, the Maxwell-Garnett (2) expression simplifies to,

$$\epsilon_{\text{eff}} = (1 - f/3) \epsilon_d + (2f/3) \epsilon_m. \quad (4)$$

This gives a qualitative insight into the shift of the plasma resonance for solid copper particles to longer wavelengths for copper-coated dielectric particles. The effective dielectric constant in (4) is a weighted linear combination of the dielectric constants of copper and the core. Since the real part $\epsilon_{m1}(\lambda)$ of the dielectric constant in the Drude model for a metal is negative and varies in magnitude as approximately λ^2 at sufficiently long wavelengths, the effect of a thin coating is to force the real part of ϵ_{eff} to be negative there, and for some particular wavelength the plasma resonance condition (1) will be satisfied with $\epsilon_{\text{eff}} + 2\epsilon_h = 0$. For thicker coatings, ϵ_{eff} will become more negative, and so the resonance will occur at a shorter wavelength; finally for a solid copper core the resonance will occur at the minimal wavelength around 600 nm.

5. CONCLUSIONS

Copper-coated spherical dielectric particles show a surface plasma resonance which is accentuated and shifted into the infrared as compared with a pure copper particle. The corresponding peak in the extinction spectrum means that a small volume fraction of copper, when present as a coating on a dielectric core, can strongly contribute to attenuation in the near infrared region of the spectrum.

REFERENCES

- [1] G. Mie, Ann. Phys. **25** (1908) 377.
- [2] H.C. Van der Hulst: Light Scattering by Small Particles, (Wiley, New York, 1957)
- [3] C.F. Bohren and D.R. Huffman, "Absorption and Scattering of Light by Small Particles", Wiley, New York, 1983.
- [4] A. Edgar, JNCS **220** (1997), 78.
- [5] A. Edgar and O. Pantoja, JNCS, to be published (1998).
- [6] M. Poulain, in Fluoride Glass Fibre Optics, edited by I. D. Aggarwal and G. Lu, (Academic Press, Boston, 1991).
- [7] D. W. Lynch and W. R. Hunter, in Handbook of Optical Constants of Solids, ed. by E.D. Palik (Academic Press, Orlando, 1985).
- [8] R.W. Fern and H. Oser, App. Optics **4** (1965) 1504
- [9] M.Kerker, J.P. Kratorvil and E. Matijevic, J. Opt. Soc. Am. **52** (1962) 551.

PHOTOINDUCED EFFECTS IN RARE-EARTH DOPED AND UNDOPED CHALCOGENIDE GLASSES.

Victor Tikhomirov

Department of Materials, University of Leeds, LS2 9JT Leeds, UK

e-mail: V.Tikhomirov@leeds.ac.uk

The mechanisms for vectoral (photoinduced anisotropy) and scalar (photorefractive and photodarkening) photoinduced effects in chalcogenide glasses are suggested. An enhancement of photosensitivity in chalcogenide glasses doped with Pr^{3+} is reported and the mechanism for this enhancement is proposed. Fatigues of edge, intrinsic defects and Pr^{3+} dopants photoluminescence and conditions for their appearance are discussed.

1. INTRODUCTION.

Interest in light induced effects in rare-earth doped and undoped glasses is motivated by recent applications of active waveguides for telecommunications, as well as by the fundamental interest in mechanisms of light-sensitivity in glasses. Earlier applications of light-sensitivity in glasses date back to ancient times. For instance, Iegova from Bethlehem used sunlight as an essential step in the manufacturing of glass vessels ¹. The importance of polarization state of light for generation of light induced effects was reported in ^{2,3}, where linear and circular dichroism were detected in photosensitive silver-halide emulsions, when induced by linearly ² and circularly ³ polarized beams, respectively.

Photoinduced anisotropy (PA) stimulated by linearly polarized light was reported in chalcogenide glasses (see, e.g. recent refs. 4,5). Impurities do not play a principal role in the mechanism of PA in chalcogenide glasses, where intrinsic structural elements (defects) are involved ⁴, however the dopants like Pr^{3+} magnify substantially the amplitude of PA ⁵.

Photorefractive and photodarkening in chalcogenide glasses were reported ⁶. It was shown by means of X-ray diffraction that reversible photodarkening is accompanied by light-stimulated reversible change in the glass structure ⁷: this light induced effect disappears upon annealing of the samples at the glass transition temperature and can be induced again by means of secondary irradiation with light. Mostly structural aspects of these effects were considered in ^{6,7}, while charge generation, separation and trapping probably were introduced in ⁴.

In this paper we shall report on our recent studies of light induced effects in chalcogenide glasses and propose the models for photoinduced anisotropy and photorefractive in undoped and rare-earth doped glasses. Fatigues of edge ⁸, intrinsic defect ⁹ and Pr^{3+} dopants ⁹ photoluminescence in chalcogenide glasses will be discussed together with conditions for their appearance.

2. VECTORAL AND SCALAR LIGHT-INDUCED EFFECTS.

While optical properties of isotropic media are equal in different directions, in anisotropic media these properties depend on the direction of light propagation. The

dielectric tensor $\epsilon_{jk}(\omega)$ consisting of nine components determines the anisotropy of medium and it is introduced by the equation

$$D_j = \sum \epsilon_{jk}(\omega) E_k \quad (j, k = x, y, z) \quad (1)$$

where D_j and E_k are the components of the internal electric induction vector \mathbf{D} and the electric vector of the light \mathbf{E} , respectively.

Gyrotropy (which is also called chirality, optical activity or spatial dispersion) appears in a medium where the link between \mathbf{D} and \mathbf{E} is not spatially local. In such a medium:

$$D_j = \sum \epsilon_{jk}(\omega) E_k + \gamma_{jkm}(\omega) \delta E_k / \delta x_m + \dots \quad (2)$$

where γ_{jkm} is the gyrotropic tensor.

PA appears in the course of prolonged irradiation of glasses with linearly polarized light when their dielectric tensor $\epsilon_{j,k}$ becomes an ellipsoid of revolution with its optical axis parallel to the electric vector of the inducing light. PA is also generated by unpolarized or circularly polarized light. In the latter case, the dielectric tensor becomes an ellipsoid of revolution with the optical axis parallel to the wavevector of inducing light^{1,10}. Light induced change of this tensor can proceed in two different ways: either due to the absolute change (decrease) of its component parallel to the electric vector of the inducing light or due to a re-orientation of the dielectric tensor, i.e. an increase of the orthogonal component at the expense of the parallel component. In both cases, the reaction of the medium will be vectorial, i.e. it will depend on the orientation of the electric vector of the inducing light. If a structural unit interacting with the light is intrinsically anisotropic, then it will preferably interact with light having a certain orientation of the electric vector. This means that only particularly oriented structural units can be changed with linearly polarized light thus accounting for the light induced macroanisotropy in the glass.

Metastable photoinduced gyrotropy appearing in glasses after prolonged irradiation by circularly polarized light was reported for the first time in¹¹. This effect is accounted for by changes in the gyrotropic tensor similar to the ones described above for the dielectric tensor. Well annealed glass is a racemic mixture of gyrotropic (chiral) units and does not possess macroscopic gyrotropy (optical activity). The left (right)-hand circularly polarized inducing light produces some excess of left (right)-hand structural units⁴ resulting in macroscopic gyrotropy, manifested in circular dichroism and birefringence/optical activity.

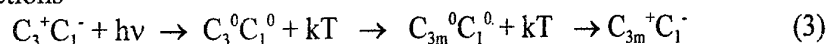
PA and gyrotropy are considered as vectorial photoinduced effects which are sensitive to the polarization state of light. This is in contrast to the scalar photoinduced effect, such as photorefraction and photodarkening, which are not sensitive to the polarization of light due to a different microscopic mechanism. This difference will appear when the excitation from the absorbing structural unit is passed onto another unit, which is randomly oriented with respect to the former one. In this case, no macroanisotropy (or gyrotropy) can be produced due to the lack of polarization memory⁴. This is the typical case for the normal photorefraction, where the carrier excited from one site is trapped by another site (non-geminate recombination). Geminate recombination of carriers is essential for vectorial effects.

3. VECTORIAL LIGHT-INDUCED EFFECTS.

It was mentioned in §2 that one has to look for anisotropic structural elements in the glass to account for PA. In this respect, a model of intrinsic (native) valence-alternation pairs (VAP's) in glassy chalcogenides was suggested^{12,13}. VAP's are denoted as $C_3^+C_1^-$.

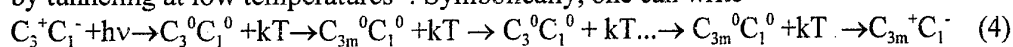
pairs, where C stands for a chalcogen atom, the subscript is the coordination number, and the superscript is the charge on the chalcogen. VAP's are anisotropic structural elements due to their electric-dipole moment. Lone pairs of the C_1^- atom contributing to the absorption of inducing light are p-orbital electrons which are sensitive to the polarization of the light. The mechanism of PA generally observed in all chalcogenide glasses was proposed⁴ to be based on the light induced re-orientation of VAP's (IVAP's) and their environments. Another reason for choosing IVAP's to model PA is that they strongly affect the surrounding atoms which adjust their positions around a C_3^+ center to compensate for the Coloumbic repulsion of electrons on the C_1^- atom^{12,13}. Thus the motion of charge inside an IVAP will strongly influence the structure in its vicinity, extending microstructural changes of IVAP's to medium-range structural changes in their environments.

When excited with linearly polarized light, IVAP's will be changed according to the following reactions⁴



To illustrate reaction (3) one can consider a four-well potential as it is shown in fig.1, with two wells corresponding to $C_3^+C_1^-$, $C_{3m}^+C_1^-$ charged, and two other wells $C_3^0C_1^0$ and $C_{3m}^0C_1^0$ corresponding to neutral states of IVAP's. (The symbol "m" means a mirror image of the C_3 atom in the plane determined by its three neighbors, as illustrated in fig.2). Since no room-temperature ESR- signal is observable in most of chalcogenide glasses¹⁴, the excited states will only have a transient population, and the energy barriers from $C_{3m}^0C_1^0$ ($C_3^0C_1^0$) to $C_{3m}^+C_1^-$ ($C_3^+C_1^-$) must be low. $C_{3m}^0C_1^0$ will decay either back to the initial $C_3^+C_1^-$ or to a new $C_{3m}^+C_1^-$ configuration. In the latter case the orientation of electric and magnetic dipoles (associated with the lone-pair chalcogen orbitals) of the IVAP' is changed and the original isotropic distribution of IVAP orientations is disturbed, thus producing macroanisotropy in the glass since only particularly oriented IVAP's can be excited with linearly polarized light.

It would also be possible to go back and forth many times between the two excited transient configurations of fig.1 via thermal excitation processes at high temperature, or by tunneling at low temperatures⁴. Symbolically, one can write



The configurational potential illustrated in fig.1 accounts for the observed stretched-exponentiality of the kinetics of PA generation⁴, since it was shown¹⁵ that motion between two low-lying energy levels and a multiplicity of iso-energetic excited levels (depicted in fig.1) leads to an expression of the type

$$t = -\tau' \text{Ln}(1-A(t)/A_s) + \Gamma A(t)/A_s \quad (5)$$

(where τ' and Γ are the constants, $A(t)$ and A_s are anisotropy at the time t and at saturation, respectively), which is difficult to distinguish experimentally from its stretched-exponential equivalent which fits the kinetics of PA.

$$t = \tau [-\text{Ln}(1-A(t)/A_s)]^{1/\beta} \quad (6)$$

A model for a structural change in chalcogenide glasses corresponding to reactions (3,4) is shown in fig.2a⁴. One of the reasons for considering such a 4-atom unit is that photoinduced circular dichroism and birefringence (optical activity) are observed in chalcogenide glasses¹¹ and it is known from the general theory of optical activity that asymmetric pyramids must be taken into consideration. Reactions (3,4) can thus be seen

as a simple flip of the pyramid $C_3^+C_1^-C_2^0C_2^0$ centred around the C_3^+ atom. The flip of this asymmetric pyramid is accompanied by a change of its anisotropy and chirality, producing linear or circular dichroism respectively. We note a similarity of this flip to that of the ammonia molecule NH_3 , which is historically the first example of a tunnelling entity.

Regarding the potential shown in fig.1 we note that light excitation of IVAP's at very low temperatures will produce a quite stable neutral configuration $C_3^0C_1^0C_2^0C_2^0$ (possessing light induced electronic spin resonance reported at very low temperatures¹⁴), where the tunneling of neutral C_3^0 atom between two mirror-image states may be responsible for the increased density of two-level systems in irradiated glasses at low temperatures, as reported in¹⁶.

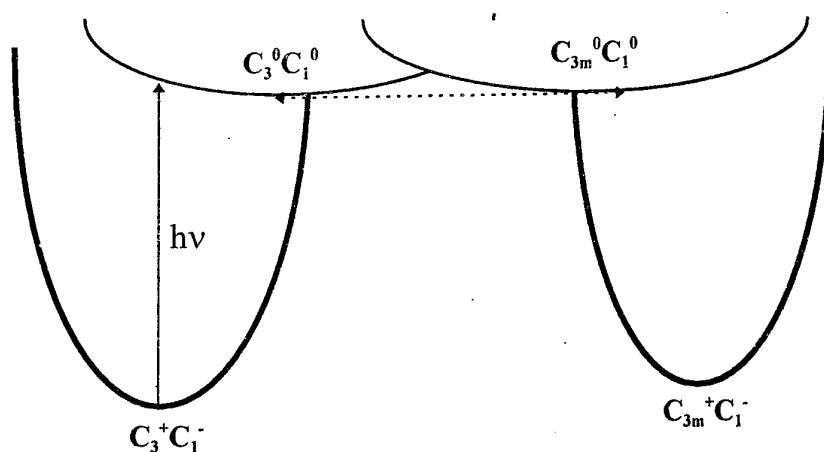


Fig.1. Configurational-coordinate potential-energy diagram of various states of IVAP's.

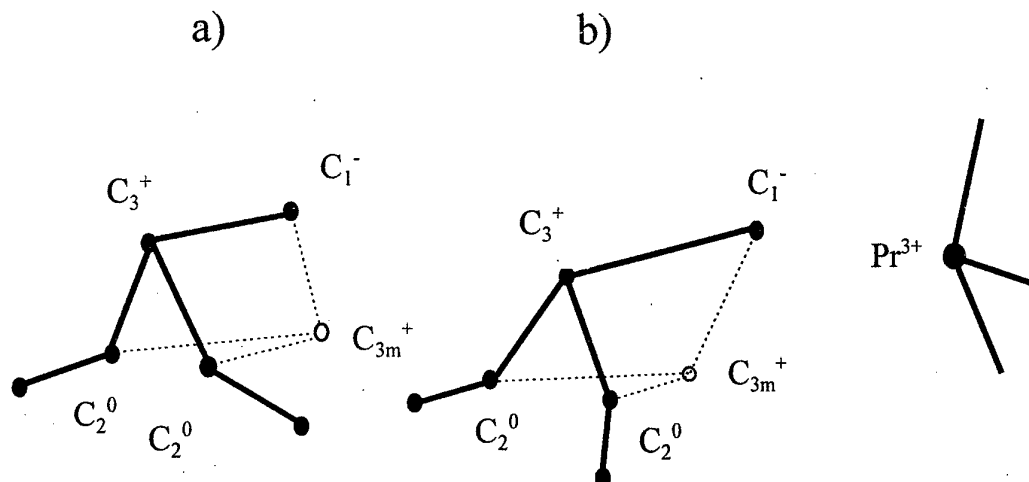


Fig.2. The flip of the pyramid involving an IVAP centered at a C_3^+ atom proposed to be responsible for PA, (a) in undoped (b) in Pr^{3+} doped chalcogenide glasses.

4. SCALAR LIGHT-INDUCED EFFECTS.

While the re-orientation of pre-existing intrinsic centers is responsible for the vectoral effect of PA, the photoinduced creation of metastable microscopic electric dipoles in the glass is a scalar effect⁴. In the latter case, photoexcited carriers will be trapped in the sites which are randomly situated with respect to the orientation of the electric vector of inducing light and the site where they were photoexcited. Note that the structural flexibility of centers (traps) responsible for the scalar effects is not essential, in contrast to the vectoral effects which are developed on the flexible centers.

Each resulting "photoinduced" dipole produces a frozen-in polarization field, which gives a local change of refraction $\Delta n \sim \chi^{(3)} E_{\text{dip}}^2$, where E_{dip} is the electric field of the dipole and $\chi^{(3)}$ is the cubic susceptibility term. Assuming that the total energy stored in this dipole field is comparable with the energy of the absorbed quantum of light $h\nu$ and that $\Delta n = f(\chi^{(3)}, N)$, where N is the number density of dipoles (or traps responsible for the creation of dipoles), we obtain according to¹⁷:

$$N = (\Delta n \sqrt{n_0 \epsilon_0 \epsilon_r}) / (3 \chi^{(3)} h\nu) \quad (7)$$

where Δn is the photorefractive index, n_0 the refractive index of unperturbed glass ($n_0 \gg \Delta n$) and ϵ_r the dielectric constant of the glass.

It is seen from (7) that Δn is determined mainly by N and $\chi^{(3)}$, while the other constants are not so different in different kinds of glass. For instance, $\chi^{(3)} = 6 \cdot 10^{-12}$ esu¹⁸ and $\Delta n = 0.01$ in sulfide glass As_2S_3 (at $\lambda = 633$ nm, where absorption coefficient is about 1 cm^{-1}), giving the $N = 3 \cdot 10^{19} \text{ cm}^{-3}$. $\chi^{(3)}$ is more than an order of magnitude larger in this glass as compared to $\chi^{(3)}$ in germanium-silica fibers in the transparent region of the spectrum¹⁸. This is the main reason why such a small concentration of dipoles (traps) leads to such a pronounced macroscopic Δn in sulfide glasses.

5. INFLUENCE OF Pr^{3+} ON LIGHT-INDUCED EFFECTS.

It was shown in⁵ that doping Ge-S-I glasses with Pr^{3+} ions caused an increase in PA. Moreover, PA did not show further enhancement at and above the doping level where clustering of Pr^{3+} ions occurred. Recently we have observed the analogous enhancement of PA in Pr-doped Ga-La-S glasses. First observation of PA and photorefractive index in Pr-doped chalcogenide glasses (Ge-Ga-S host) was reported at a previous Symposium on Non Oxide Glasses¹⁹, where different host compositions were used for different doping levels with Pr and thus qualitative influence of Pr^{3+} on PA could not be obtained.

Detailed experimental data on the influence of Pr^{3+} ions on PA and photorefractive index in different chalcogenide glasses will be reported at this Symposium. In this extended abstract we suggest a model for the enhancement of photosensitivity in chalcogenide glasses doped with Pr^{3+} . We note that Ce^{3+} ions also magnify photorefractive index in fluoride glasses²⁰ and we believe that the phenomenological reason for this magnification is the same as in chalcogenide glasses. Namely, a light-induced increase of polarizability of centers responsible for photosensitivity in these glasses with doping by rare earths is suggested to be the origin for enhanced photosensitivity of rare-earth doped glasses. However, the microscopic mechanisms for the increase of polarizability may be different in different kinds of glasses.

The model of PA shown in Fig.2 helps to understand an increase of polarizability of centers of $\text{C}_3^+ \text{C}_1^-$ type. Since Pr^{3+} ions influence PA when incorporated in the host already

at very low concentrations (~ 1000 ppm)^{5,21}, this means that Pr^{3+} ions effectively affect the centers responsible for PA. The concentration of dopants should be comparable to the concentration of centers responsible for PA²¹, which is indeed about 1000 ppm (according to estimates⁴ similar to that given by eq. (7)). Obviously, a positively charged Pr^{3+} ion is attracted by a C_1^- atom and is situated apart from the C_3^+ atom (Fig.2b). Due to Coloumbic interaction, the Pr^{3+} ion stretches the structural unit shown in Fig.2a thus increasing its polarizability and microanisotropy. Due to the large $\chi^{(3)}$ of chalcogenide glasses (eq. (7)), a large volume around the $\text{C}_3^+\text{C}_1^-\text{Pr}^{3+}$ unit in Fig.2b will also be polarized. This will result in enhanced components of the dielectric tensor ϵ_{jk} (eq.(1)) leading to enhanced PA according to considerations in §2.

Note that light beams used in our experiments (633 nm- He-Ne and 515 nm- Ar^+ lasers) could not excite Pr^{3+} ions directly and thus they were absorbed by the tail or defect states of the hosts.

6. FATIGUES OF PHOTOLUMINESCENCE.

Fatigues of edge⁸, intrinsic defects⁹ and Pr^{3+} dopants⁹ photoluminescence have been reported in some chalcogenide glasses when excited by light above or below gap. Fatigue of edge luminescence (both in undoped and doped samples) indicates a light stimulated appearance of non-radiative centers of recombination. Since this fatigue is suppressed in glasses exhibiting smaller photosensitivity (e.g. in Ga-enriched Ge-Ga-S glasses^{8,19}) we conclude that photocreated centers which are responsible for photorefraction are the same centers which cause non-radiative recombination. This is supported by the fact that photocreated centers responsible for photorefraction are charged (see §4) and thus effectively trap excited carriers.

Fatigue of intrinsic defects photoluminescence (which is Stokes-shifted for ~ 1 eV with respect to edge photoluminescence) can be explained similarly. Photocreated charged centers are efficient traps for photoexcited carriers in this case also. They provide a competitive non-radiative channel for carrier recombination, in contrast to intrinsic defects which seem to be more likely as a channel for radiative recombination.

Photocreated charged defects are an obvious competitor for Pr^{3+} dopants luminescence. Note that in⁹ photoluminescence from rare earths was excited via absorption of light by the host and followed by an efficient transfer of absorbed energy to the rare-earth ions. We suggest that fatigue of Pr^{3+} dopants photoluminescence excited via host absorption is due to photocreation of charged traps. These traps are a non-radiative competitor to Pr^{3+} dopants luminescence with respect to carriers excited in the host.

Remarkably, despite fatigue of edge luminescence, no fatigue of Pr^{3+} dopants luminescence was detected in⁸. This may indicate the fact that in high quality $80(\text{GeS}_3)20(\text{Ga}_2\text{S}_3):\text{Pr}^{3+}$ glasses studied^{8,19}, Pr^{3+} ions were excited by well below-gap light (blue line of Ar^+ laser, $\lambda=488$ nm) either directly into their ^3P term thus avoiding influence from the host or via absorption by intrinsic defects which are not an efficient channel for non-radiative recombination. Note that Pr^{3+} ions adhere very efficiently to intrinsic defects (Fig.2b), and that energy transfer from an intrinsic defect (which absorbs the light) to the Pr^{3+} ion (which emits the light) should proceed very easily in this case, without the participation of the host.

ACKNOWLEDGMENT.

It is a pleasure to acknowledge our colleagues Drs. A. Jha and M. Naftaly for support of this work. Drs. A. Seddon and R. Li (Sheffield University, UK) are gratefully acknowledged for providing us with Pr-doped Ga-La-S glasses, as well as Drs. V. Krasteva and G. Sigel (Rutgers University, USA) for providing with Pr-doped Ge-S-I glasses and Drs. A.J. Faber and D. Simmons (TU Eindhoven, The Netherlands) for providing with Pr-doped Ge-Ga-S glasses.

REFERENCES.

1. H. Fritzsche, J. Non-Cryst. Solids 164&166 (1993) 1169; unpublished.
2. F. Weigert, Verhandl. Deutschen Physik. Ges. 21 (1919) 479.
3. H. Zocher and K. Coper, Z. Phys. Chem. 132 (1928) 313.
4. V.K. Tikhomirov and S.R. Elliott, J. Phys.: Condens. Matter 7 (1995) 1737; V.M. Lyubin and V.K. Tikhomirov J. Non-Cryst. Solids, 114 (1989) 133; V.K. Tikhomirov, G.J. Adriaenssens, and S.R. Elliott, Phys. Rev. B 55 (1997) R660.
5. V.K. Tikhomirov, V. Krasteva, P.W. Hertogen, G.J. Adriaenssens, and G. Sigel, J. Non-Cryst. Solids 222 (1997) 296.
6. J.S. Berkes, S.W. Ing, and W.J. Hillegas, J. Appl. Phys. 42 (1971) 4908; S.A. Keneman, Appl. Phys. Lett. 19 (1971) 205; J.P. De Neufville, S.C. Moss, and S.R. Ovshinsky, J. Non-Cryst. Solids 13 (1973) 191.
7. Kazunobu Tanaka, Appl. Phys. Lett. 26 (1975) 243.
8. V. K. Tikhomirov, K. Iakoubovskii, P. Hertogen, and G.J. Adriaenssens, Appl. Phys. Lett. 71 (1997) 2740.
9. D.A. Turnbull and S.G. Bishop, J. Non-Cryst. Solids 223 (1998) 105.
10. V.K. Tikhomirov and S.R. Elliott, Phys. Rev. B 49 (1994) 17476.
11. V.M. Lyubin and V.K. Tikhomirov, JETP Lett. 52 (1990) 78; V.K. Tikhomirov and M.M. Chervinsky, Sov. Phys. Solid State 35 (1993) 566.
12. N. F. Mott, E.A. Davis, and R.A. Street, Phil. Mag. B 32 (1975) 961.
13. M. Kastner, D. Adler, and H. Fritzsche, Phys. Rev. Lett. 37 (1976) 1504.
14. S.G. Bishop, U. Strom, and P.C. Taylor, Phys. Rev. Lett. 36 (1975) 134.
15. C. Van de Walle, Phys. Rev. B 53 (1996) 11292.
16. D.L. Fox, B. Golding, and W.H. Haemmerle, Phys. Rev. Lett., 49 (1982) 1356.
17. D.P. Hand and P.St.J. Russel, Opt. Lett. 15 (1990) 102.
18. M. Asobe, K. Suzuki, T. Kanamori, and K. Kubodera, Appl. Phys. Lett. 60 (1992) 1153.
19. V.K. Tikhomirov, G.J. Adriaenssens, and A.J. Faber, J. Non-Cryst. Solids, 213&214 (1997) 174.
20. H. Poignant, S. Boj, E. Delevacue et al, Electron. Lett., 30 (1994) 1339.
21. V. K. Tikhomirov, P.W. Hertogen, G.J. Adriaenssens, V. Krasteva, G. Sigel, J. Kirchhof, J. Kobelke, and M. Scheffler, J. Non-Cryst. Solids, at print.

BRAGG GRATING INSCRIPTION IN RARE-EARTH DOPED FLUOROZIRCONATE GLASSES

R. Sramek ^a, F. Smektala ^a, J. Lucas ^a, W.X. Xie ^b, P. Bernage ^b, P. Niay ^b

^a Laboratoire des Verres et Céramiques, UMR 6512, Université de Rennes 1, Avenue du Général Leclerc, 35042 Rennes cedex, France.

^b Laboratoire de Dynamique Moléculaire et Photonique, Université des Sciences et Technologies de Lille, UFR de Physique, 59655 Villeneuve d'Ascq cedex, France

ABSTRACT

Bragg grating inscription experiments have been performed on fluorozirconate glasses. Two glass series were synthesised, one was melted under N₂ atmosphere, and the second was treated besides by NF₃ gas to reduce the Zr³⁺ traces. Inscription experiments show that traces of Zr³⁺ increase the photosensitivity. This result is compared to the influence of lead ion introduction in fluoride glasses.

1/ INTRODUCTION

Photosensitivity of glassy materials is studied for a few years because it could be used in numerous optical applications: filters, mode couplers, laser cavity, temperature captors...[1] Theories to explain photosensitivity of oxide glasses were already developed [2]. The interest of rare-earth doped fluoride glasses is due to the large number of possible infrared and visible radiations and thus they constitute interesting laser materials. Such glass photosensitivity has been demonstrated on PZG and ZBLA type glasses doped by Ce³⁺ ions. Mechanisms for this photosensitivity appear to be complex and are not yet well understood [3-5], but they are anyway different from those involved in oxide glasses. For example, no permanent formation of coloured centres can be observed. Densification of the matrix is not established until now. Molecular hydrogen diffusion in the matrix doesn't increase photosensitivity.

This paper presents Bragg gratings inscriptions in fluorozirconate glasses doped or not with 3 to 10 weight% Er³⁺ and Ho³⁺. A classical transverse holographic method was used for photoinscription.

2/ EXPERIMENTAL

2.1/ Glass synthesis

Compositions of tested fluoride glasses are summarised in table 1; some glasses are doped with 3 to 10 % of rare earth fluorine. Samples have been polished to optical quality and, their thickness is included between 0.4 and 1.1 mm.

Glass	Composition
ZBLA	57% ZrF ₄ , 34% BaF ₂ , 5% LaF ₃ , 4% AlF ₃
ZBLAN	54% ZrF ₄ , 30% BaF ₂ , 3.5% LaF ₃ , 2.5% AlF ₃ , 10% NaF
ZBLALi	54% ZrF ₄ , 30% BaF ₂ , 3.5% LaF ₃ , 2.5% AlF ₃ , 10% LiF

Table 1 : Fluoride glasses base compositions used in the study.

To study the influence of lead ion, which is polarisable and shifts the band gap, in a ZBLAN composition 2 % of BaF₂ were substituted by PbF₂.

Two series were synthesised by the classical method of oxide fluorination [6], but during the melting two different atmospheres were used.

The series n°1 was melted under N₂ atmosphere. To increase glassy quality the series n°2 was treated under N₂ in addition with NF₃, during several minutes at 650°C before the casting. This gas oxides reduced components as Zr³⁺. The presence of such impurities increases electronic transitions and though shift the band gap to longer wavelengths (figure 1) in function of Zr³⁺ quantity. A glass rich in Zr³⁺ presents a greyish tint and important optical losses in the visible and infrared spectra range. The band gap of the series n°1 moved between 230 and 255 nm while the series n°2 one is close to 200 nm. We define the "band gap wavelength" the wavelength for that the absorption coefficient is equal to 10 cm⁻¹. Other impurities than Zr³⁺ could be present in these glasses.

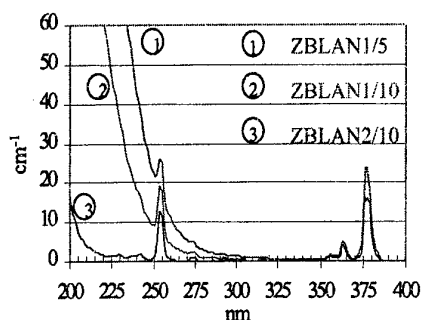


Figure 1: UV spectra of Er doped ZBLAN glass melted with NF₃ atmosphere (ZBLAN2/i), or without (ZBLAN1/i) (i gives the rare earth concentration in percent).

The rare earth ions, holmium and erbium, were chosen for this study because they have an absorption band close to the chosen UV light respectively at 240 nm (⁵I₈ → (³F, ⁵D)₄) and at 254 nm (⁴I_{15/2} → ⁴D_{7/2}). Both have only one valence degree, the +III. Moreover, with its transition at 1,55 μm erbium is very interesting as active ion for optics.

2.2/ Bragg gratings inscription

Bragg grating inscriptions were performed through the transverse holographic method [7-8] at 244 nm. The UV beam is produced by a pulsed, frequency doubled, XeCl pumped dye laser. The UV fringe pattern is realised by using a Lloyd's mirror type interferometer. The grating step is of 5 μm. The average fluence per pulse varied from 200 to 530 mJ/cm². The repetition rate was chosen equal to 30 or 40 Hz. The inscription dynamics were studied by measuring the Bragg diffraction efficiency of the grating η. A He-Ne laser linearly polarised along the TE direction was used as probe beam.

The intensity of the diffracted light I_{diff} by the grating is measured and gives the diffraction efficiency η (equation 1).

In the hypotheses of a pure phase grating, the intensity of diffracted light I_{diff}, is related to the maximum index modulation Δn by the relation :

$$\eta_{\max} = \frac{I_{\text{diff}}}{I_0} = \sin^2 \left[\frac{\pi \Delta n d}{\lambda \cos \alpha} \right]$$

where I₀ is the intensity of the incident probe light, d the grating thickness, λ the probe light wavelength, and α the angle of incidence for probe light.

The grating thickness is estimated through the grating angular selectivity.

3/ RESULTS AND DISCUSSION

Results at inscription experiments at 244 nm on glasses are summarised in table 2 and 3. All those gratings are permanent, no diffraction efficiency decreases have been observed 6 months after the inscription.

Glass sample	Absorption coefficient at 244 nm (cm ⁻¹)	Fluences (mJ/cm ²)	Number of pulses	Diffraction efficiency (%)	Refractive index change Δn (*10 ⁻⁵)
ZBLA (Z1)	6	300	50000	0.27	3.3
ZBLA 5%Er	15	420	100000	0.08	1.0
ZBLALi 3% Er	20	220	100000	0.1	2.5
		420	100000	0.21	3.7
ZBLALi 5% Er	32	420	100000	2.38	5.2
		210	100000	0.58	2.6
ZBLAN 5% Er	33	230	100000	2.31	6.3
		430	100000	5.53	9.7
ZBLA 5%Ho	3	350	86000	0.22	2.5
		200	85000	0.15	1.5
ZBLALi 5%Ho	9	440	100000	0.40	2.7
		220	100000	0.073	1.2
ZBLAN 5%Ho	12	230	76400	0.03	0.7
		350	52000	0.1	1.0

Table 2: Results of gratings inscriptions on glasses series n°1, melted without NF₃ gas addition.

From the efficiency of the Bragg grating photoinscribed inside the glasses of the series n°1, melted under N₂ atmosphere without NF₃ gas addition, we deduced that the refractive index modulation amplitude Δn is close to 10⁻⁴ (table 2).

Inside the glasses of the series n°2, melted in N₂ atmosphere with NF₃ gas addition, the modulation amplitudes are weaker (table 3).

From the results obtained with erbium doped glasses of series n°1, we can correlate Δn with the glass absorption at 244 nm. The most efficient grating was performed in 5%Er³⁺ doped ZBLAN glass, at an average fluence per pulse of 430 mJ/cm². After 100000 pulses, the refractive index modulation amplitude Δn is close to 10⁻⁴. With the same experimental conditions, the refractive index modulation amplitude observed in 5%Er³⁺ doped ZBLALi is close to 5*10⁻⁵ whereas the absorption coefficients of the two glasses are similar.

For all the studied samples, we have observed that the refractive index modulation amplitudes increase regularly versus the pulse number (figure 2). No saturation is noted until 100000 pulses.

Glass sample	Absorption coefficient at 244 nm (cm ⁻¹)	Fluences (mJ/cm ²)	Number of pulses	Diffraction efficiency (%)
ZBLA (Z2)	3	300	20000	0.076
ZBLAN 2%Pb	62	300	20000	0.024
ZBLAN 5%Er	1	210	49000	0.018
		525	30000	0.001
ZBLAN 10%Er	1	400	30000	0.01
		210	40000	0.001
ZBLALi 5%Er	1	210	32000	0.03
ZBLAN 5%Ho	1.5	210	30000	0.006
ZBLALi 5%Ho	1	255	30000	0.001

Table 3: Results of gratings inscriptions on glasses series n°2, melted under NF₃ atmosphere.

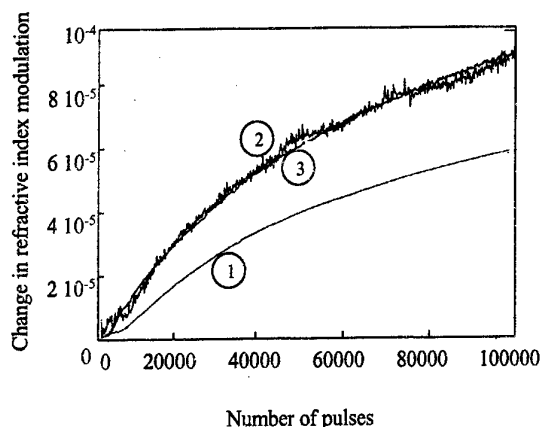


Figure caption :

- ① $Fl=230 \text{ mJ/cm}^2$, $\eta=2.2\%$, $\Delta n=6.2 \cdot 10^{-5}$
- ② $Fl=430 \text{ mJ/cm}^2$, $\eta=5.4\%$, $\Delta n=9.7 \cdot 10^{-5}$
- ③ $Fl=420 \text{ mJ/cm}^2$, $\eta=5.1\%$, $\Delta n=9.5 \cdot 10^{-5}$

Figure 2: Dynamic of grating inscription at 244 nm on Er doped ZBLAN of glasses series n°2 (grating step : 5 μm)

For holmium doped glasses of series n°1, the absorption coefficient vary from 3 to 12 cm^{-1} , the refractive index modulation amplitudes are approximately constant for similar experimental conditions.

For same glass compositions, but melted under N_2 with addition of NF_3 gas, inscription diffraction efficiencies are approximately 10 times weaker (table 3). The difference between the two glass series could not come from rare earth ion presence.

With a view to study the relationship between band gap location and laser wavelength used for Bragg grating inscriptions, experiments on undoped fluoride glasses by rare earth ions were performed.

Two undoped ZBLA glasses were synthesised under the two atmospheres, as explained previously. UV spectrum reveals a shift of the band gap wavelength from 232 nm, for glass series n°1, to 217 nm, for glass series n°2 (figure 3). Under the same experimental conditions (grating step : 5 μm , fluence : 300 mJ/cm^2) the UV induced refractive index modulation amplitude observed in Z2 sample (table 4) was two times smaller than Δn obtained in Z1. In addition, the index variation saturates in Z2 sample after 2500 shots (figure 4).

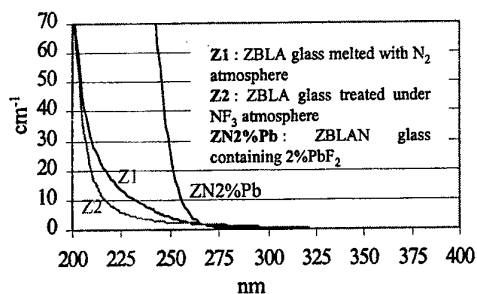


Figure 3: UV spectra of undoped glasses.

Sample name	Absorption coefficient at 244 nm	Number of pulses	Grating thickness	Diffraction efficiency η (%)	Refractive index change Δn
Z1	6 cm^{-1}	50000	500 μm	0.27	$3.3 \cdot 10^{-5}$
Z2	3 cm^{-1}	10000	330 μm	0.076	$1.4 \cdot 10^{-5}$
ZN2 %Pb	62 cm^{-1}	20000	500 μm	0.024	$6 \cdot 10^{-6}$

Table 4: Comparison of rare earth undoped sample characteristics and photoinduced changes after exposure at 244 nm.

It is known that lead ion is very polarisable, it shifts the band gap and increases refractive index. For this last reason 1 to 2% PbF_2 are usually introduced in fluoride fibre cores [9].

2% of PbF_2 were substituted to BaF_2 in ZBLAN composition. The glass melting was realised under NF_3 atmosphere. The band gap is located at 256 nm; thus the matrix absorbs the laser wavelength. A thick grating (500 μm) was inscribed (grating step : 5 μm , fluence : 300 mJ/cm²) inside this glass named ZN2%Pb (table 4). The inscription dynamic was followed as before (figure 5). Just after the inscription end, we have observed a drop of a half of diffraction efficiency. The refractive index modulation amplitude Δn measured after this drop is equal to 6.10^{-6} . We note that the glass absorption coefficient is 62 cm⁻¹ at 244 nm.

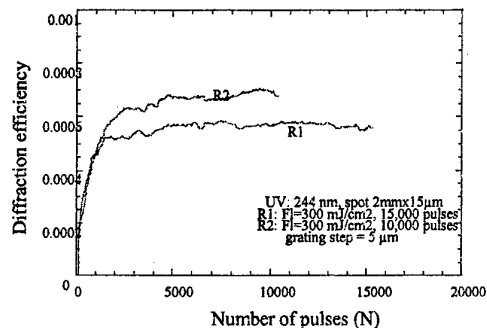


Figure 4: Curve of diffraction efficiency during grating inscriptions on ZBLA glass Z2.

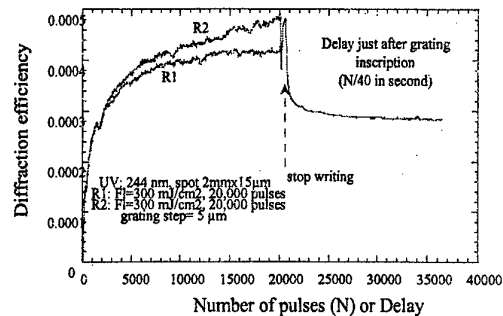


Figure 5: Curve of diffraction efficiency during and after grating inscriptions on ZBLAN 2%Pb glass.

Though the obtained Δn are too small for optical applications, these results are interesting because they show that photosensitivity in fluoride glasses is not expressly linked to rare earth ions as promote.

To see the influence of rare earth ions and glass matrix absorption, the glass samples were tested at longer wavelengths than band gap one. The chosen wavelengths correspond to holmium and erbium absorption, respectively at 360 nm ($^5\text{I}_8 \rightarrow (^5\text{G}, ^3\text{H})_5$) and at 364 nm ($^5\text{I}_8 \rightarrow ^5\text{G}_5$).

As expected an important fluorescence is observed, but no gratings were detected in samples of the both series. This result shows that pure excitation on absorption wavelengths, when the matrix is transparent, cannot induced any photosensitivity at these wavelengths.

In table 4, we observe that Δn obtained in Z1 sample is two times more important than in Z2 sample. Δn is nearly proportional to the absorption coefficient. In contrast, the absorption coefficient of ZN2%Pb is ten times greater than one of Z1 sample, but the obtained refractive index modulation amplitude is smaller than that of Z2 sample. It indicates that the photosensitivity is not directly linked to the matrix absorption level but to the present elements, which are susceptible to react and generate structural modifications as electron traps.

It is important to note that Zr^{3+} is known as a structural defect (an electron was trapped by Zr^{4+}). G.M. Williams *et al.* [10] have observed by electron spin resonance (ESR), on rare earth doped ZBLAN glass, after exposure to 248 nm light, a conversion of Zr^{4+} to Zr^{3+} . They

have advanced the theory of photoinduced generation of colour centres by Ce^{3+} bleaching and Zr^{3+} generating through a two photons absorption. Ce^{3+} has a strong 4f-5d transition centred at 248 nm. Without treatment under NF_3 atmosphere, a part of Zr^{3+} is present in the glassy matrix before the inscription. In this case, trace of Ce^{3+} as catalyser seems to be not so important for photoinscription because some electrons are already trapped. The presence of ions with several valence degrees seems to facilitate the reaction through the generation of colour centres.

Lead trace in glasses reduced Zr^{3+} generation in a competitive electron trapping between Zr^{4+} and Pb^{2+} [11]. Pb^{2+} in fluoride glass acts as electron and hole trap, and formed Pb^+ and Pb^{3+} . In tested Pb^{2+} doped glass Zr^{3+} is not present, thus the photosensitivity could only be attribute to lead traps formation. The decrease of diffraction efficiency after inscription, seems to come from trace of both hole and electron traps. A part of both defects disappears in cross relaxation phenomena.

3/ CONCLUSION

Bragg grating inscriptions were performed on fluoride glasses at 244 nm. Two series of samples were synthesised under N_2 and N_2 in addition with NF_3 atmospheres. Without treatment by NF_3 atmospheres, traces of reduced components as Zr^{3+} are present. On measured refractive index changes; it appears that in presence of such element the photosensitivity is increased. Bragg gratings were inscribed in undoped fluoride glasses too, but the Δn is only of several 10^{-5} .

With lead trace in such glass, weak grating was performed. The inscription dynamic shows that after the irradiation the diffraction efficiency drops. A relaxation phenomena acts.

Irradiation at 360 and 364 nm, on holmium and erbium electronic transitions, inscriptions had failed.

REFERENCES

- [1] R. Kashyap, Opt. Fiber Technol. 1 (1994) 17
- [2] B. Pommellec, P. Niay, M. Douay, J.F. Bayon, Proc. OSA Meeting 22 (1995) 112
- [3] H. Poignant, S. Boj, E. Delevaque, M. Monerie, T. Taunay, P. Niay, P. Bernage and W. X. Xie, J. Non-Cryst. Solids 184 (1995) 282
- [4] W.X. Xie, P. Bernage, D. Ramecourt, M. Douay, T. Taunay, P. Niay, B. Boulard, Y. Gao, C. Jacoboni, A. Da Costa, H. Poignant and M. Monerie, Opt. Comm. 134 (1997) 36
- [5] T. Taunay, P. Niay, P. Bernage, W.X. Xie, H. Poignant, S. Boj, E. Delevaque and M. Monerie, Opt. Lett. 19 (1994) 1269
- [6] M. Poulain, in "Fluoride glasses", (A.E. Comyns, 1989) 11
- [7] G. Meltz, W.W. Morey and W.H. Glenn, Optical Letters 144 (1989) 823
- [8] E. Fertein, S. Legoubin, M. Douay, S. Canon, P. Bernage, P. Niay, J.F. Bayon and T. Georges, Electron. Letters 27 (1991) 1838
- [9] H. Poignant, in "Halides glasses", (North-Holland, 1992) 192
- [10] G. M. Williams, T.E. Tsai, C. I. Merzbacher, E. J. Friebele, J. Lightw. Technol, 15 (1997) 1357
- [11] E. J. Friebele, D. C. Tran, J. Non-Cryst. Solids, 72 (1985) 221

Rare-earth doped transparent glass-ceramics with high cross-sections

Michel Mortier and François Auzel

Groupe d'Optique des Terres Rares,

CNRS-UPR 211, 1, place A Briand, 92195 Meudon Cedex, France

and France Telecom, CNET/DTD, 196, avenue Ravera, 92225 Bagneux Cedex, France.

Email : mortier@cnsr-bellevue.fr

INTRODUCTION

This study takes place in the framework of the optical amplifiers used in telecommunication systems and specially in the trend to look for more compact devices devoted to distribution networks. In this case, the goal is not to obtain a broad bandwidth but a high cross-section allowing the reduction of the system size. For that, we try to improve the maximum cross-sections of the rare earth (RE) ions in glassy systems by changing their surrounding in a crystalline one [1, 2] but taking care to keep the general properties of the glassy matrix. In this case, the glass-ceramic systems could be a promising solution provided that they stay optically isotropic and transparent.

Considering light scattering theory, two possibilities exist for producing transparent glass-ceramic or crystal-glass systems. Either the dispersed crystalline phase is small in size in comparison with the shortest wavelengths, or perfect optical isotropy is achieved within the composite system.

Two kinetic processes are well known in phase separation: nucleation and growth, spinodal decomposition. However, only nucleation-growth has been extensively studied in order to obtain transparent optical composite systems [3, 4]. Indeed, the liquid-liquid phase separation, so called spinodal decomposition, is generally viewed as a negative effect to avoid the loss of glass transparency. A precursor work has been done in our laboratory on such systems [5] and is still conducted to obtain highly transparent glass-ceramics.

With the success of the erbium doped fiber amplifiers (EDFA), it is well known that the fluoride environment is better than the oxide one mainly to avoid the non-radiative transitions. The solubility of the rare earth is also better in the fluoride medium than in the oxide one. Due to their sensitivity to oxygen and water traces, the fluoride compounds necessitate a complex synthesis under controlled atmosphere and are less durable. So, a good solution could be an

oxide glassy system in which Er^{3+} -doped fluoride crystallites would be embedded. For these reasons and from previous studies in the lab [2] in which the system was mainly crystalline by choice, and then of low transparency, due to the large amount of lead fluoride, we are now looking for a mainly glassy system [6] with a low PbF_2 amount in this family of germanate glasses : $50\text{GeO}_2, [40-x]\text{PbO}, x\text{PbF}_2 + y\text{ErF}_3$.

THERMAL ANALYSIS

The initiating mechanism of the glass devitrification in which immiscibility is thought to play an important role is studied. For this, the influence of the composition of the precursor glass is followed, with x and y varying, in thermal analysis by DTA. We studied the kinetics of phase change using Johnson-Mehl-Avrami model [7-9]. A non isothermal method, with different heating rates has been used to characterise the devitrification. The crystallised fractions $\chi(T)$ between the beginning of the crystallisation peak and given temperatures T have been evaluated. The Avrami parameter or reaction order is the slope of a linear law fitting $\ln(-\ln(1-\chi))$ versus $\ln(\alpha)$. The following values have been obtained for the different fixed temperatures ($T=390, 392, 394$ and 396°C) respectively ($n=2.55, 2.24, 2.08, 1.89$). Such values correspond to a three dimensional crystal growth controlled by the diffusion with a decreasing nucleation rate. It well describes our devitrification process in which the crystallites begin to grow quickly and then slow down their progression with time as shown by the X-ray estimated sizes of the crystallites versus time. This is explained by the progressive depletion of PbF_2 around the growing crystallites which involves more and more diffusion process. The decreasing nucleation rate reflects the progressive disappearance of the smallest crystallites in benefit of the largest ones.

The crystallisation apparent activation energy of the glass has been evaluated using Chen [9] and Ozawa methods. The Ozawa method gives a value of 228kJ/mol . The Chen method gives an energy of 239kJ/mol . For a very stable glass like ZBLAN, the activation energy is of 196kJ/mol [9]. A family of very unstable fluoride glasses [5] presenting a spinodal decomposition, has an activation energy of about 345kJ/mol . So, our value of about 233kJ/mol lies well between stable and unstable glass reflecting the tendency to partial devitrification.

The reheating temperature is fixed slightly above T_g and the composition is chosen in order to obtain the best stability of the glass. After thermal treatment, the vitreous transition is still observed but the exothermic peak associated to the precipitation of the lead fluoride has disappeared verifying the glassy nature of the matrix and the complete crystallisation of PbF_2 .

STRUCTURE AND MORPHOLOGY

Only one broad band, typical of an amorphous structure appears on the X-ray spectra of the as-melted samples. After treatment, the characteristic peaks of the βPbF_2 cubic phase appear and the feature of the glassy system remains, indicating a crystal glass system. The X-ray diffraction peak width and the Scherrer formula allows us to estimate the average size of the crystallites. The TEM measurements confirm the results as being of the order of 8 to 30nm as a function of the precursor composition. The crystallites appear spherical with a well defined contour and are not connected with each others. From TEM observations, the volume crystallised part is about 2%. The X-microanalysis shows an absolute lack of RE and lead fluorides in the glassy matrix reflecting the high segregation of the fluoride compounds in the crystallites.

OPTICAL MEASUREMENTS

We have studied the influence of thermal treatment on different absorption spectra from room temperature to 10K. The oscillator strengths of the involved transitions are deduced from the absorption cross-sections (σ_{abs}). This study has been done with the as-melted and reheated (10h at 360°C) glass with 3%ErF₃.

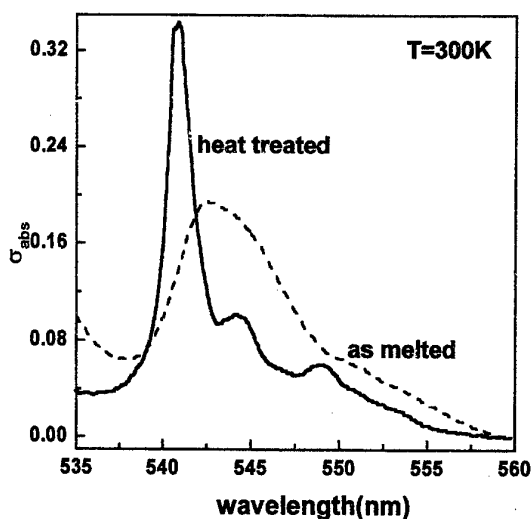


figure 1 : $\sigma_{\text{abs}}(^4\text{I}_{15/2} \rightarrow ^4\text{S}_{3/2})$ in 10^{-20}cm^2 at 300K

The absorption cross-section of the $^4\text{I}_{15/2} \rightarrow ^4\text{S}_{3/2}$ transition is reported at 300K on figure 1. The as-melted glass exhibits a clearly broader band than the reheated one for all

temperatures. The glass-ceramic has a higher intensity maximum respectively 4, 3 and 2 times more than the precursor glass at 10, 77 and 300K. The oscillator strengths increase when the temperature is lowered. So, a net benefit is obtained by the ceramming process on such a transition. The corresponding emission is also clearly improved after reheating.

We have measured the lifetime of the $^4I_{11/2} \rightarrow ^4I_{13/2}$ transition centred around 2.7 μ m which is the most sensitive to non radiative deexcitations. We have obtained a value of 360 μ s for the as-melted glass and 3ms for the reheated one. This strong difference corresponds to the drastic change of the rare earth surrounding induced by the heating treatment. In the as-melted glass, the surrounding medium is an oxide glass ; in the second one, it becomes a fluoride crystal. We have also synthetised polycrystalline PbF₂ doped with 1% ErF₃ in order to compare with the PbF₂ crystallites embedded into the glassy matrix. The lifetime in the polycrystalline PbF₂ is equal to 7ms. The difference with the treated glass results from the higher concentration of the rare earth due to its strong segregation during the nucleation and growth process.

REFERENCES

- [1] C.F. Rapp and J. Chrysochoos, J. Mat. Science **7**(1972)1090
- [2] F. Auzel, D. Pecile and D. Morin, J. of the Electrochem. Society **122**(1975)101
- [3] K. Hirao, K. Tanaka, M. Makita and N. Soga, J. Appl. Phys. **78**(1995)3445
- [4] R.S. Quimby, P.A. Tick, N.F. Borrelli and L.K. Cornelius, J. Appl. Phys. **83**(1998)1649
- [5] P.Santa-Cruz, D. Morin, J. Dexpert-Ghys, F. Glas, F. Auzel, J. Non-Cryst. Solids **190**(1995)238
- [6] M. Mortier and F. Auzel, 9th CIMTEC, Florence, June 1998
- [7] M. Poulain, J. Non-Cryst. Solids **140**(1992)1
- [8] Johnson W.A. and Mehl R.F., Trans. Am. Inst. Met. Eng. **135**(1939)416
- [9] M. Matecki, I. Noiret-Chiaruttini and J. Lucas, J. Non-Cryst. Solids **127**(1991)136

Nano-crystallite Fluorescence in Fluoride Glasses

D.R. MacFarlane¹, J. Javorniczky¹, P.J. Newman¹ and D.J. Booth²

¹Department of Chemistry, Monash University, Clayton Victoria 3168

²Department of Physics, Victoria University of Technology, Footscray
Victoria 3011

Fluorescence from rare earth ions such as Er(III) in a glass matrix is the origin of lasing phenomena in glass. The linewidth of the emission from glass hosts is often increased because of the multiplicity of sites in which the active ion can find itself. The intensity is therefore often reduced compared to emission from a crystal. In this work a series of erbium containing fluoroaluminate glasses have been prepared and characterized with respect to their stability towards nucleation and crystallization of Erbium containing phases. One of the compositions was then selected for further study in which the glass was subjected to thermal treatments designed to nucleate and grow crystallites of size well below the wavelength of visible light ie. <100 nm. The resultant material is transparent but has a significant fraction of crystallinity as discernible by DSC and small angle X-ray scattering. X-ray diffraction is unable to uniquely identify the phases however ErF₃ or an Er-rich mixed compound are likely. Er³⁺ fluorescence at 1530 nm as a result of 800 nm irradiation was measured and found to be approximately 40% greater than from the base glass.

Tungsten-tellurite glass: a new candidate medium for Yb^{3+} -doping

Xian Feng, Changhong Qi, Fengying Lin, Hefang Hu

Shanghai Institute of Optics and Fine Mechanics, Academia Sinica
P.O.Box 800-216 Shanghai, Shanghai 201800, P.R.China

ABSTRACT

Yb^{3+} -doped tungsten-tellurite glasses have been prepared in the $\text{TeO}_2\text{-WO}_3\text{-Li}_2\text{O}$, $\text{TeO}_2\text{-WO}_3\text{-BaO}$, $\text{TeO}_2\text{-WO}_3\text{-La}_2\text{O}_3$, $\text{TeO}_2\text{-WO}_3\text{-Bi}_2\text{O}_3$ and $\text{TeO}_2\text{-WO}_3\text{-Nb}_2\text{O}_5$ systems. Firstly, the thermal stability of these ternary tellurite glasses has been studied and the DTA data show that the $\text{TeO}_2\text{-WO}_3\text{-La}_2\text{O}_3$ and $\text{TeO}_2\text{-WO}_3\text{-Nb}_2\text{O}_5$ glasses have excellent thermal stability. Secondly, on the basis of the IR spectra, the glass structure has been analyzed. Then the absorption and emission properties of Yb^{3+} in these glasses have been investigated. Both the reciprocity method and F-L equation were employed to calculate the emission cross sections. It is found that the Yb^{3+} -doped ternary tungsten-tellurite glasses possess excellent absorption and emission properties, and show good promise as $1.02\text{ }\mu\text{m}$ laser source.

INTRODUCTION

Crystals and glasses doped with trivalent ytterbium ions exhibit highly efficient emission using InGaAs laser diodes as pump source. Yb^{3+} has ground configuration of $4f^{13}$, and there are only two manifolds in the Yb^{3+} energy level scheme, i.e., the $^2F_{7/2}$ ground state and the $^2F_{5/2}$ excited state, therefore, concentration quenching and multiphonon relaxation should not affect the lasing or the excitation wavelengths [1,2]. The Yb^{3+} -doped media are of interest in lasers for next generation nuclear fusion [3] and appear as a good candidate as a pump source for Pr^{3+} [4,5]. Additionally, the Yb^{3+} ion is also a sensitizer of energy transfer for infrared-to-visible upconversion and infrared lasers [6].

Tellurite glasses combine the attributes of (I) a reasonably wide transmission region ($0.35\text{-}5\mu\text{m}$), versus only $0.2\text{-}3\mu\text{m}$ for silicate glasses, (II) good glass stability and corrosion resistance, which present difficulties in fluoride glasses, (III) a relative low phonon energy among oxide glass formers (highest phonon energy $\sim 800\text{cm}^{-1}$), and (IV) high refractive index and high nonlinear refractive index, which are generally low in both fluoride and silicate glasses [7]. The high nonlinear refractive index and the low phonon energy make the tellurite glasses uniquely suitable for nonlinear and laser applications [7].

The objective of this work is to investigate the thermal stability and spectroscopic properties of Yb^{3+} -doped tungsten-tellurite glasses and to survey the feasibility of tungsten-tellurite glasses as the candidate for a new type of Yb^{3+} -doped media.

EXPERIMENTAL

Chemical-purity commercial oxides ($>99.5\%$ pure) were used as the starting materials. All ternary tungsten-tellurite glasses were doped externally with $1.0\text{mol.}\% \text{Yb}_2\text{O}_3$. Mixed batches were melted in a high-purity Al_2O_3 crucible at $800\text{-}950\text{ }^\circ\text{C}$ for $\sim 45\text{ min}$. In order to remove the $-\text{OH}$ groups in the glasses, the melts were bubbled with dry oxygen gas for 30 min while being melted. Each glass melt (in $\approx 50\text{ g}$ quantity) was cast into preheated stainless-steel molds and annealed for 2 h near the glass transition temperature. The obtained glasses were transparent, $\sim 6\text{ mm}$ in thickness and appeared yellow in color.

Thermal analysis was employed to determine the effect of glass composition on thermal stability. Each powdered sample weighing $\sim 100\text{ mg}$ was contained in a tiny Al_2O_3 crucible

and heated at a rate of 10 °C/min from ambient temperature to 800 °C in a LCP - 1 differential thermal analyzer (made in China).

IR spectra were measured via the KBr pellet technique with an infrared spectrophotometer (Model IR 435, Shimadzu Co., Kyoto, Japan) in the frequency of 4000-400 cm^{-1} .

Glass samples 3.5-4.5mm thick with four polished faces were used for absorption, density, and refractive index measurements. Absorption spectra were measured with a Perkin-Elmer UV/VIS/NIR Lambda 9 double beam spectrophotometer. Density was determined by the Archimedes method using distilled water as an immersion liquid. Refractive indexes were measured at 486.1, 589.3, and 656.3 nm, with a precision V-prism refractometer (made in China) using H_2 and Na lamps as spectral sources. The Cauchy dispersion equation, $n(\lambda) = a + b/\lambda^2$, was used to determine the refractive index at other wavelengths. For fluorescence lifetime measurement, a 970 nm laser diode was used as a pumping laser, and a R940-92 photomultiplier as a detector in the range 900 to 1150 nm. Glass samples were excited at a front surface and utilized for fluorescence spectra measurements to minimize the effect of radiation trapping due to reabsorption. The fluorescence lifetimes were measured on an oscilloscope, while the samples were pumped by pulsed LD laser.

RESULTS AND DISCUSSION

1. Thermal stability, IR spectra, and glass structure

Table 1 summarizes the measured DTA data of some tungsten-tellurite glasses. Fig.1(a)-(c) illustrate the DTA curves of $\text{TeO}_2\text{-WO}_3\text{-La}_2\text{O}_3$ and $\text{TeO}_2\text{-WO}_3\text{-Nb}_2\text{O}_5$ glasses with different composition, respectively. The IR spectra of some samples, as measured by the KBr pellet technique, are shown in Fig.2 from 400-1400 cm^{-1} (measured up to 4000 cm^{-1}).

From Table 1, it is clear that $\text{TeO}_2\text{-WO}_3\text{-La}_2\text{O}_3$ and $\text{TeO}_2\text{-WO}_3\text{-Nb}_2\text{O}_5$ glasses possess the largest difference of $\Delta T = T_x - T_g$ which are all larger than 160 °C (T_g : the glass transition temperature; T_x : the onset crystallization temperature). Because the quantity of $T_x - T_g$ has been frequently used as a rough measure of glass stability, and consequently it is desirable to have $\Delta T = T_x - T_g$ as large as possible in order to achieve a large working range during operations such as preform preparation for fiber drawing. Clearly, $\text{TeO}_2\text{-WO}_3\text{-La}_2\text{O}_3$ and $\text{TeO}_2\text{-WO}_3\text{-Nb}_2\text{O}_5$ glasses possess the highest thermal stability in Table 1. In Ref.[7], J.S.Wang chose the composition of $5\text{Na}_2\text{O-20ZnO-75TeO}_2$, whose difference of $\Delta T = T_x - T_g$ is only 118 °C, for their tellurite-based rare-earth-doped fiber; therefore, it can be concluded that $\text{TeO}_2\text{-WO}_3\text{-La}_2\text{O}_3$ and $\text{TeO}_2\text{-WO}_3\text{-Nb}_2\text{O}_5$ glasses should be superior to $\text{Na}_2\text{O-ZnO-TeO}_2$ glasses for waveguide fabrication. What is more, the La_2O_3 content in $\text{TeO}_2\text{-WO}_3\text{-La}_2\text{O}_3$ glasses can reach above 10mol.%; because La_2O_3 and Yb_2O_3 have similar solubility in glasses, and because high concentration of Yb_2O_3 does not lead to concentration quenching, the tungsten-tellurite-based fiber lasers or planar lasers doped with high concentration of Yb_2O_3 should be feasible if low-loss waveguide can be fabricated.

From the IR spectra of the samples No.2-5 (see Fig.2), it can be seen that there are a clear absorption shoulder at ~ 920 to 950 cm^{-1} , and a broad absorption band from ~ 500 to $\sim 900 \text{ cm}^{-1}$ with a minimum at ~ 600 to 650 cm^{-1} . The shoulder at ~ 920 to 950 cm^{-1} is assigned to the symmetry stretching vibration of W-O bond in the WO_4 tetrahedra which are connected with TeO_4 polyhedra [8]. The broad absorption band from ~ 500 to $\sim 900 \text{ cm}^{-1}$ is attributed to the overlap of the vibration of WO_4 tetrahedra (at $\sim 830 \text{ cm}^{-1}$) and TeO_4 polyhedra (at ~ 780 to 600 cm^{-1}). For the samples No.6 and 7, the shoulder at ~ 920 to 950 cm^{-1} does not appear in their IR spectra in spite of the increase of WO_3 content. According to Ref. [8], the network of binary tungsten-tellurite glass is built by both components, one from deformed TeO_4 polyhedra and the other from deformed WO_4 tetrahedra, which are incorporated in each other.

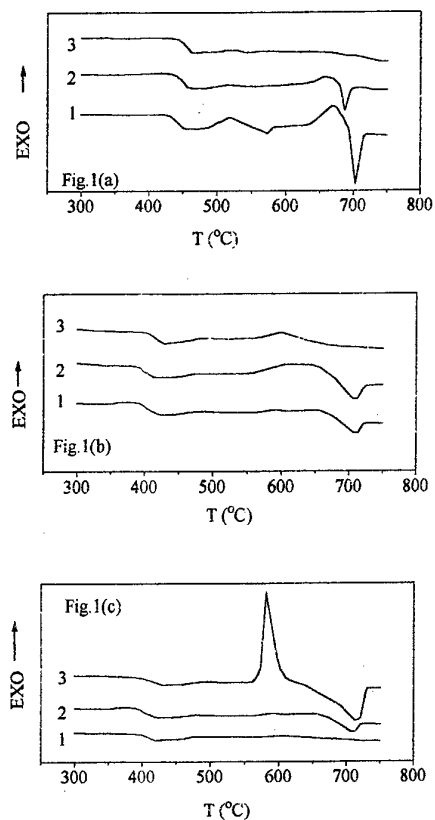


Fig.1 DTA curves of some Yb^{3+} -doped tungsten-tellurite glasses

- (a)1: $75\text{TeO}_2\text{-}15\text{WO}_3\text{-}10\text{La}_2\text{O}_3$;
 2: $70\text{TeO}_2\text{-}20\text{WO}_3\text{-}10\text{La}_2\text{O}_3$;
 3: $65\text{TeO}_2\text{-}25\text{WO}_3\text{-}10\text{La}_2\text{O}_3$;
 (b)1: $85\text{TeO}_2\text{-}5\text{WO}_3\text{-}10\text{Nb}_2\text{O}_5$;
 2: $82.5\text{TeO}_2\text{-}7.5\text{WO}_3\text{-}10\text{Nb}_2\text{O}_5$;
 3: $80\text{TeO}_2\text{-}10\text{WO}_3\text{-}10\text{Nb}_2\text{O}_5$;
 (c)1: $90\text{TeO}_2\text{-}5\text{WO}_3\text{-}5\text{Nb}_2\text{O}_5$;
 2: $85\text{TeO}_2\text{-}5\text{WO}_3\text{-}10\text{Nb}_2\text{O}_5$;
 3: $80\text{TeO}_2\text{-}5\text{WO}_3\text{-}15\text{Nb}_2\text{O}_5$

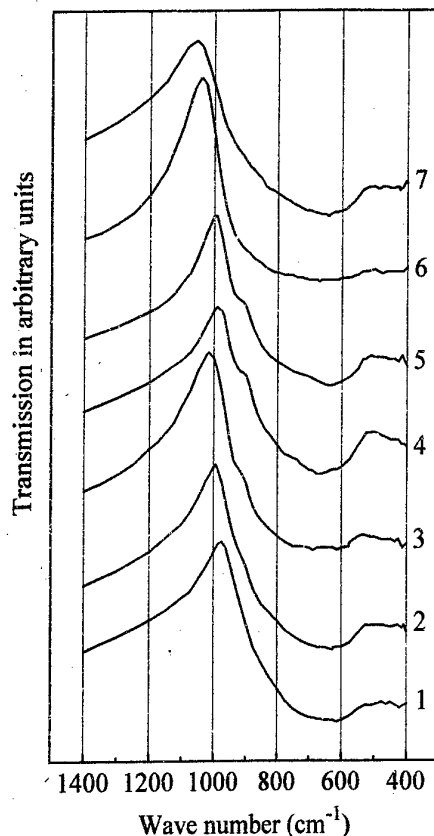


Fig.2 IR spectra of some Yb^{3+} -doped tungsten-tellurite glasses

- 1: $90\text{TeO}_2\text{-}10\text{BaO}$;
 2: $80\text{TeO}_2\text{-}10\text{WO}_3\text{-}10\text{BaO}$;
 3: $70\text{TeO}_2\text{-}10\text{WO}_3\text{-}20\text{Li}_2\text{O}$;
 4: $75\text{TeO}_2\text{-}15\text{WO}_3\text{-}10\text{La}_2\text{O}_3$;
 5: $65\text{TeO}_2\text{-}25\text{WO}_3\text{-}10\text{Bi}_2\text{O}_3$;
 6: $85\text{TeO}_2\text{-}5\text{WO}_3\text{-}10\text{Nb}_2\text{O}_5$;
 7: $80\text{TeO}_2\text{-}10\text{WO}_3\text{-}10\text{Nb}_2\text{O}_5$

Table 1 DTA data of some tungsten-tellurite glasses(all samples were externally doped with 1mol.% Yb_2O_3)

composition (mol.%)	T_g (°C)	T_x (°C)	$T_x - T_g$ (°C)	composition (mol.%)	T_g (°C)	T_x (°C)	$T_x - T_g$ (°C)
$90\text{TeO}_2\text{-}10\text{BaO}$	369	455	86	$85\text{TeO}_2\text{-}5\text{WO}_3\text{-}10\text{Nb}_2\text{O}_5$	396	563	167
$85\text{TeO}_2\text{-}5\text{WO}_3\text{-}10\text{BaO}$	371	458	87	$82.5\text{TeO}_2\text{-}7.5\text{WO}_3\text{-}10\text{Nb}_2\text{O}_5$	391	562	171
$80\text{TeO}_2\text{-}10\text{WO}_3\text{-}10\text{BaO}$	388	480	92	$80\text{TeO}_2\text{-}10\text{WO}_3\text{-}10\text{Nb}_2\text{O}_5$	404	566	162
$75\text{TeO}_2\text{-}15\text{WO}_3\text{-}10\text{La}_2\text{O}_3$	436	/	∞	$90\text{TeO}_2\text{-}5\text{WO}_3\text{-}5\text{Nb}_2\text{O}_5$	400	573	173
$70\text{TeO}_2\text{-}20\text{WO}_3\text{-}10\text{La}_2\text{O}_3$	438	/	∞	$85\text{TeO}_2\text{-}5\text{WO}_3\text{-}10\text{Nb}_2\text{O}_5$	396	563	167
$65\text{TeO}_2\text{-}25\text{WO}_3\text{-}10\text{La}_2\text{O}_3$	443	/	∞	$80\text{TeO}_2\text{-}5\text{WO}_3\text{-}15\text{Nb}_2\text{O}_5$	403	573	170
$60\text{TeO}_2\text{-}20\text{WO}_3\text{-}20\text{Li}_2\text{O}$	339	464	125	$60\text{TeO}_2\text{-}30\text{WO}_3\text{-}10\text{Bi}_2\text{O}_3$	392	490	98

In our opinion, similar to the structure of tungsten-phosphate glasses and phosphotellurite glasses, in ternary tungsten-tellurite glasses (except $\text{TeO}_2\text{-WO}_3\text{-Nb}_2\text{O}_5$ glasses), tellurite chains and tungstate chains can incorporate together easily because their structure is very similar, and this type of structure leads to loose structure and large solubility of other modifier oxides; in $\text{TeO}_2\text{-WO}_3\text{-Nb}_2\text{O}_5$ glasses, due to the large cationic field strength of Nb-O bond (the value of Z/a^2 is calculated in the order of $\text{W-O} > \text{Nb-O} > \text{Te-O} > \text{Bi-O} > \text{La-O} > \text{Ba-O} > \text{Li-O}$), NbO_6 octahedra connect the tellurite chains and tungstate chains, and consequently form three dimensional structure; because the cross-link structure of NbO_6 octahedra can not coordinate well with the loose chain structure of tungsten-tellurite glasses, the crystallization tendency is surely significant; this is the reason why $\text{TeO}_2\text{-WO}_3\text{-Nb}_2\text{O}_5$ glasses have a crystallization peak at $\sim 570^\circ\text{C}$ but $\text{TeO}_2\text{-WO}_3\text{-La}_2\text{O}_3$ glasses have not; and this is also the reason why for $\text{TeO}_2\text{-WO}_3\text{-Nb}_2\text{O}_5$ glasses the crystallization peak at $\sim 570^\circ\text{C}$ becomes significant with the increase of Nb_2O_5 content but it varies slightly with the increase of WO_3 content. Additionally, in $\text{TeO}_2\text{-WO}_3\text{-Nb}_2\text{O}_5$ glasses, weakly deformed WO_6 octahedra which are close to regular octahedra (according to the RDF data of Ref. [8]) exist instead of the strongly-deformed WO_4 tetrahedra, consequently, the stretching vibration of W-O bond at ~ 920 to 950 cm^{-1} becomes less active in IR spectra.

2. Calculation of the emission cross-section

The potential performance of an Yb^{3+} -doped glass laser may be assessed from the emission and absorption properties. The most important spectroscopic parameters required include the emission and absorption cross-sections of the $^2\text{F}_{7/2}\text{-}^2\text{F}_{5/2}$ transition and the upper laser level lifetimes of Yb^{3+} . The emission cross-section of Yb^{3+} is usually calculated from Fuchtbauer-Ladenburg equation [1] or by the reciprocity method [1,9].

In this paper, according to the reciprocity method [1,9], the emission cross-sections σ_{emi} of Yb^{3+} , were simply calculated from the measured absorption cross-section σ_{abs} , i.e.,

$$\sigma_{\text{emi}}(\lambda) = \sigma_{\text{abs}}(\lambda) \cdot \frac{Z_l}{Z_u} \cdot \exp\left(\frac{E_{zl} - hc\lambda^{-1}}{kT}\right), \quad (1)$$

where Z_l , Z_u , k , and E_{zl} represent the partition functions of the lower and the upper levels, Boltzman's constant, and the zero line energy which is defined to be the energy separation between the lowest components of the upper and lower states, respectively. Because the zero line energy E_{zl} is associated with the strong peak in the absorption spectrum of a Yb^{3+} -doped glass, it is very easy to determine the value of E_{zl} . Another parameter, the ratio of the partition functions of the lower and the upper levels of Yb^{3+} , Z_l/Z_u , can be obtained from the Yb^{3+} energy structure; in Ref [10], an approximate energy structure model of Yb^{3+} in oxide glasses was put forward to estimate the value of Z_l/Z_u . Additionally, according to the Fuchtbauer-Ladenburg equation [1], i.e.,

$$\sigma_{\text{emi}}(\lambda) = \frac{\lambda^4 g(\lambda)}{8\pi c n^2(\lambda) \tau_{\text{rad}}}, \quad (2)$$

where $g(\lambda)$ is the normalized line shape function of the $^2\text{F}_{7/2}\text{-}^2\text{F}_{5/2}$ transition for Yb^{3+} , $n(\lambda)$ is the refractive index, c is the velocity of light, and τ_{rad} is the radiative lifetime ($\tau_{\text{rad}} = 1/A$), the emission cross-sections were also obtained based on the measured fluorescence spectra.

3. Absorption and emission properties

Fig.3 shows the absorption cross-section spectra and the emission cross-section spectra of some Yb^{3+} -doped ternary tungsten-tellurite glasses studied here, respectively. Table 2 summarizes some important spectroscopic properties of the Yb^{3+} -doped tungsten-tellurite glasses studied.

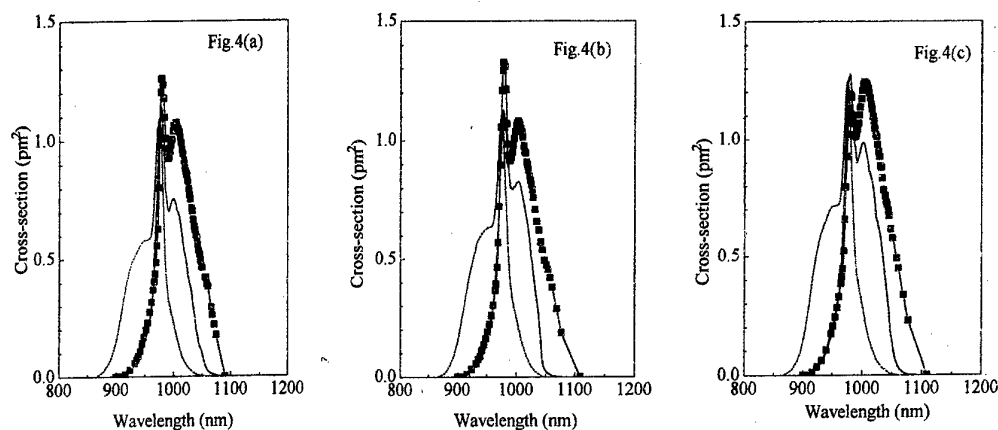


Fig.3 Absorption cross-section and emission cross-section spectra of Yb^{3+} in some tungsten-tellurite glasses: (a) $82.5\text{TeO}_2\text{-}7.5\text{WO}_3\text{-}10\text{Nb}_2\text{O}_5$; (b) $70\text{TeO}_2\text{-}20\text{WO}_3\text{-}10\text{La}_2\text{O}_3$; (c) $60\text{TeO}_2\text{-}30\text{WO}_3\text{-}10\text{Bi}_2\text{O}_3$

----- measured absorption cross-section spectra
 ———— emission cross-section spectra by reciprocity method
 —■—■— emission cross-section spectra from F-L equation

Table 2 Density(ρ), Wavelength of the prime absorption peak(λ_{21}), Refractive index at λ_{21} ($n(\lambda_{21})$), Integrated absorption cross section (Σ_{abs}), Radiative lifetime (τ_{rad}), Measured fluorescence lifetime (τ_f), Radiative quantum efficiency (η), Emission cross-section at subpeak (σ_s), Ratio of the emission cross-section at subpeak to that at prime peak (σ_s/σ_p), and Effective linewidth of the emission cross-section spectra ($\Delta\lambda_{\text{eff}}$) for the Yb^{3+} -doped ternary tungsten tellurite glasses (* Spectroscopic properties are calculated by reciprocity method.)

composition (mol.%)	ρ (g/cm ³)	λ_{21} (nm)	$n(\lambda_{21})$	Σ_{abs} ($\times 10^4 \text{ pm}^2$)	τ_{rad} (μs)	τ_f (μs) (± 20)	η (%)	σ_s (pm^2)	σ_s/σ_p (%)	$\Delta\lambda_{\text{eff}}$ (nm)
85TeO ₂ -5WO ₃ -10Nb ₂ O ₅	5.26	975.4	2.2	5.07	364	420	115	0.70	73	55.6
82.5TeO ₂ -7.5WO ₃ -10Nb ₂ O ₅	5.37	974.8	2.2	5.85	316	360	114	0.76	67	50.2
80TeO ₂ -10WO ₃ -10Nb ₂ O ₅	5.34	975.2	2.2	5.60	331	400	121	0.75	75	60.0
75TeO ₂ -15WO ₃ -10La ₂ O ₃	5.92	974.8	2.09	5.80	353	420	119	0.78	75	62.4
70TeO ₂ -20WO ₃ -10La ₂ O ₃	6.02	974.6	2.09	6.17	332	400	120	0.83	73	54.2
65TeO ₂ -25WO ₃ -10La ₂ O ₃	6.10	974.4	2.09	5.70	361	360	100	0.72	67	53.1
65TeO ₂ -25WO ₃ -10Bi ₂ O ₃	6.52	975.0	2.3	6.13	276	380	138	0.83	73	54.9
60TeO ₂ -30WO ₃ -10Bi ₂ O ₃	6.60	974.6	2.3	6.83	248	400	161	0.99	77	58.4
55TeO ₂ -35WO ₃ -10Bi ₂ O ₃	6.66	974.8	2.3	6.01	283	400	141	0.82	71	54.6
70TeO ₂ -10WO ₃ -20Li ₂ O	5.21	974.4	2.04	5.27	408	400	98	0.74	76	52.7
60TeO ₂ -20WO ₃ -20Li ₂ O	5.42	974.2	2.04	5.42	398	400	101	0.77	77	57.8
50TeO ₂ -30WO ₃ -20Li ₂ O	5.63	974.2	2.04	5.70	381	400	105	0.79	77	57.8
90TeO ₂ -10BaO	5.32	975.0	2.13	4.98	397	420	106	0.72	76	57.6
85TeO ₂ -5WO ₃ -10BaO	5.47	975.0	2.13	5.31	372	400	108	0.76	78	59.0
80TeO ₂ -10WO ₃ -10BaO	5.55	975.4	2.13	5.02	395	380	96	0.69	75	56.1

First of all, from Fig.3 and Table 2, it is seen that the effect of various composition upon the spectroscopic properties is relatively little for the Yb^{3+} -doped tungsten-tellurite glasses. And it is evident that the emission cross-sections calculated by the reciprocity method are in good agreement with the values obtained from F-L equation. The discrepancy of these two emission cross-section spectra is mainly caused by the radiation trapping due to the reabsorption. According to the opinion of Weber[11], due to the effect of radiation trapping, the absolute intensity of the measured fluorescence spectra at the prime peak decreases and consequently

the effective linewidth $\Delta\lambda_{\text{eff}}$ of the fluorescence spectra increases. On the other hand, by using the reciprocity method, the emission cross-sections of Yb^{3+} can be simply determined from the measured absorption spectrum and the effect of radiation trapping is not involved in the calculation. Accordingly, the emission cross-sections calculated by the reciprocity method should be closer to the actual values than the values obtained from F-L equation. Therefore, we adopt the reciprocity method to estimate the emission cross-sections of Yb^{3+} (see Table 2).

Also, from Fig.3 and Table 2, it is seen that all the emission cross-sections σ_s of Yb^{3+} -doped tungsten-tellurite glasses are very large, close to the reported maximum value of 1.1 pm^2 in the Yb^{3+} -doped glasses[3]. Moreover, it is interesting that all the ratios of σ_s/σ_p are larger than 65% and are much larger than those values reported in Ref.[3,5,11] (their σ_s/σ_p generally range between 40-50%); because the emission intensity is proportional to the ytterbium ion population contributing to the emission, large ratio of σ_s/σ_p implies that in tungsten-tellurite glass hosts, the ytterbium ion population taking part in the subpeak emission is very close to that taking part in the emission of the prime peak, and it is very helpful to the desirable emission at $\sim 1.02 \text{ }\mu\text{m}$. Finally, the radiative quantum efficiency $\eta = \tau_f/\tau_{\text{rad}}$ of Yb^{3+} in tungsten-tellurite glasses is also very high (close to unity).

Additionally, from the absorption cross-section profiles of Yb^{3+} in Fig.3, it is clear that there is a broad-and-flat terrace in the range between 940 and 960 nm for the Yb^{3+} -doped $\text{TeO}_2\text{-WO}_3\text{-La}_2\text{O}_3$ and $\text{TeO}_2\text{-WO}_3\text{-Nb}_2\text{O}_5$ glasses, and the absorption cross-sections in this range are between $\sim 0.5\text{-}0.6 \text{ pm}^2$; because high-power cw laser diodes operating at $\sim 940\text{nm}$ are becoming practical, large absorption cross-sections and the existence of the broad-and-flat absorption terrace at such wavelength range are favorable for 940nm-LD pumping.

In short, the excellent absorption and emission properties indicate that tungsten-tellurite glasses, including $\text{TeO}_2\text{-WO}_3\text{-La}_2\text{O}_3$ and $\text{TeO}_2\text{-WO}_3\text{-Nb}_2\text{O}_5$ glasses, show good promise for Yb^{3+} -doped media.

CONCLUSION

The thermal stability, the glass structure, and the absorption and emission properties of Yb^{3+} -doped ternary tungsten-tellurite glasses have been investigated; and the Yb^{3+} -doped $\text{TeO}_2\text{-WO}_3\text{-La}_2\text{O}_3$ and $\text{TeO}_2\text{-WO}_3\text{-Nb}_2\text{O}_5$ glasses exhibit good glass-forming ability, and excellent absorption and emission properties. To sum up, these two kinds of tungsten-tellurite glasses show good promise for Yb^{3+} -doped media as $1.02 \text{ }\mu\text{m}$ laser source.

REFERENCES

- [1] L.D.DeLoach, S.A.Payne, L.L.Chase, L.K.Smith, W.L.Kway, and W.F.Krupke, IEEE J.Quantum Electron., 29[4] (1993) 1179.
- [2] J.Y.Allain, M.Monerie, H.Poignant, and T. Georges, J.Non-Cryst. Solids, 161 (1993) 270.
- [3] H.Takebe, T.Murata, and K. Morinaga, J.Am.Ceram.Soc., 79[3] (1996) 681.
- [4] J.Y.Allain, M. Monerie, and H. Poignant, Electron.Lett., 28(11) (1992) 988.
- [5] X.Zou and H.Toratani, Proceeding of the XVII International Congress on Glass (Beijing, China, 1995), Vol.3 (1995) 648.
- [6] P.Laporta, S.Longhi, S.Taccheo, and O.Svelto, Opt. Lett., 18[1] (1993) 31.
- [7] J.S.Wang, E.M.Vogel, E.Snitzer, Optical Materials, 3 (1994) 187-203.
- [8] V.Kozhukharov, S.Neov, I.Gerasimova, P.Mikula, J.Mater. Sci. 21 (1986) 1707.
- [9] D.E.McCumber, Phys. Rev. 136 (1964) A954.
- [10] Xian Feng, Changhong Qi, Fengying Lin, Hefang Hu, submitted to *Materials Letters*.
- [11] M.J.Weber, J.E.Lynch, D.H.Blackburn, and D.J.Cronin, IEEE J.Quantum Electron., QE-19 [10] (1983) 1600.

Ultra-Transparent Glass-Ceramics for Photonic Applications

P. A. Tick

Introduction

In the broadest sense photonics may be defined as the technology of information transfer with light. At the moment, most of the demand for photonic devices is for telecommunications applications, but, because of the inherent advantages of light, other opportunities, such as optical computers, will eventually evolve. When this happens, the mainstay of today's photonics technology, CVD silica, may no longer be able to provide the properties necessary to support tomorrow's needs.

In reality, there are two aspects to developing a new optical technology. The first is to identify novel materials properties, but, of equal importance, is to develop the methods necessary to process those materials into functional devices. The dominance of silica is, in no small part, due to the versatility of CVD processing complex wave guiding structures, which are both inexpensive and low loss. Many other materials can have properties that are, at least in some respects, superior to silica, but, because the technology needed to build guided wave structures was not concurrently developed, most of these materials have not yet made any important impact upon photonics.

With today's rapidly changing technology it is probably not possible to predict the inventions that will shape the future of photonics, but it is possible to identify the kinds of materials advances that will be required to bring about such a revolution in optics. Most likely, materials with multi-active functionality and the ability to form precision three-dimensional nanostructures will represent key advances.

Given this premise, it would seem that glass-like materials offer the most attractive candidates. Redrawing glass can produce precision two-dimensional nanostructures and photorefractive or photosensitivity patterning for the third dimension. Doping with rare-earths or transition metals can provide the optical activity needed to generate or amplify light. Nonlinear optical behavior, dopant solubility, photorefractive and low passive losses are at least some of the properties that will also be needed. While silica does possess many of these characteristics, there are some inherent limitations. It is not a good nonlinear material, although some unusual second order nonlinearities have been observed after poling. It is also not a very versatile host for rare-earths because of their low solubility and its high phonon energy. Composition modifications to silica may well overcome some of these limitations and certainly there is a considerable effort to expand the capabilities of CVD processing, as well as to adapt that technology to building planar wave guiding systems. So, if a new material is to replace silica as a primary candidate for future photonic applications, it must have truly remarkable properties. Glass-ceramics may well have this potential.

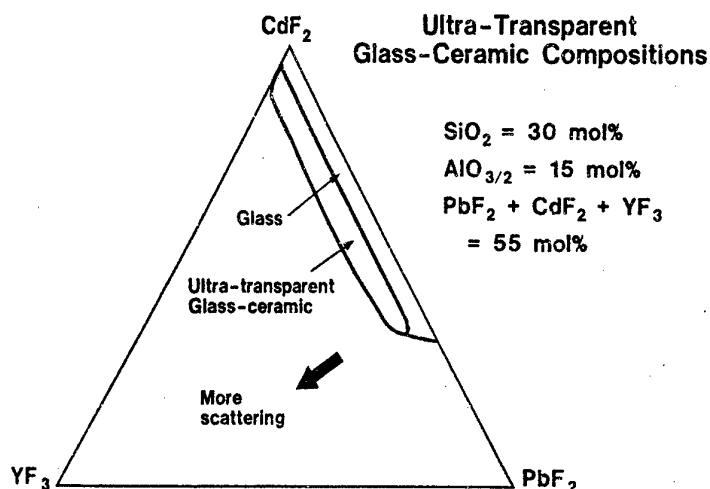
In 1993 Wang and Ohwaki described (1) a glass-ceramic system whose transparency was glass-like. Further examination (2) and expansion of similar composition fields revealed that this was indeed the case. Careful measurements were unable to distinguish between light scattering in the precursor glasses and the glass-ceramic structure. Despite these results, these materials, which can be called ultra-transparent glass-ceramics, have been largely ignored. The main reason for this is the mind set amongst optical scientists that transparency in two-phase systems can never meet even the most minimum passive

loss standards for photonic devices. One of the goals of this work is to show that this is not the case. To accomplish this, a method of fiberizing these glass-ceramics has been developed which can fabricate single mode fiber geometry's, with passive losses approaching at least some photonic device requirements. When the seemingly insurmountable obstacle of scattering loss is removed, ultra-transparent glass-ceramics offer a realistic opportunity to develop novel types of photonic devices, primarily due to the extra degree of freedom that the two active phases in glass-ceramic structures can offer.

Experimental Compositions and Methods Of Preparation

The base composition family in which much of the development work was done is comprised of 45 mol% aluminosilicate glass, along with a mixture of Cd, Pb and rare-earth fluorides. One example of the ultra-transparent glass-ceramic forming region is shown in Figure 1.

Figure 1



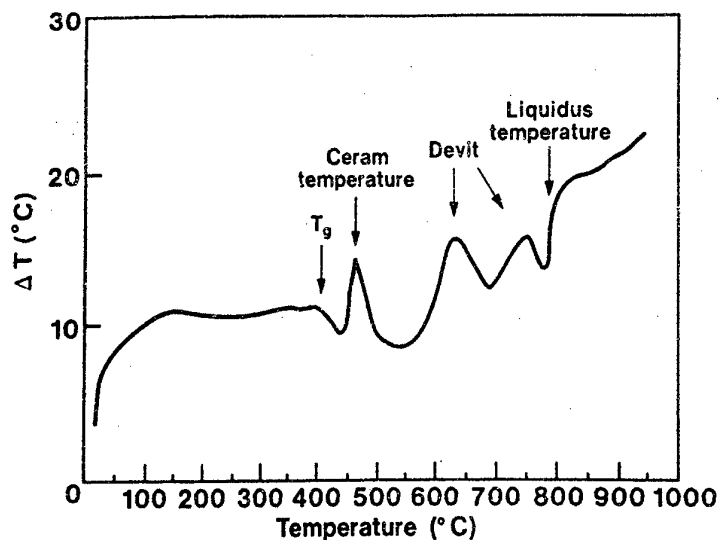
The composition used in most of these studies is 30 SiO₂-15 AlO_{3/2}-29 CdF₂-17 PbF₂-5 ZnF₂-4 YF₃ (in mol%). Increasing the silica or alumina, or removing the YF₃ will stabilize the glassy phase so that the desired glass-ceramic structure can longer be formed. Too much YF₃ causes the glass to devitrify upon cooling. ZnF₂ is not a necessary component, but helps stabilize the glass, without effecting the ceramming properties. The ratio of Cd to Pb is somewhat flexible; however, the Cd-rich compositions tend to be photochromic, which would be undesirable for a photonic device.

The precursor glass is melted from a mixture of the oxides and fluorides at 1000C, in covered platinum crucibles in air. During melting about 20% of the fluorine and 10% of the silica is lost, otherwise the remaining components are retained in essentially their original batched quantities. Once melting is complete, the hot glass can be cast into samples no more than 1 cm in thickness. If thicker samples are attempted, the slowly cooled region in the center of the patty will begin to spontaneously ceram.

Properties

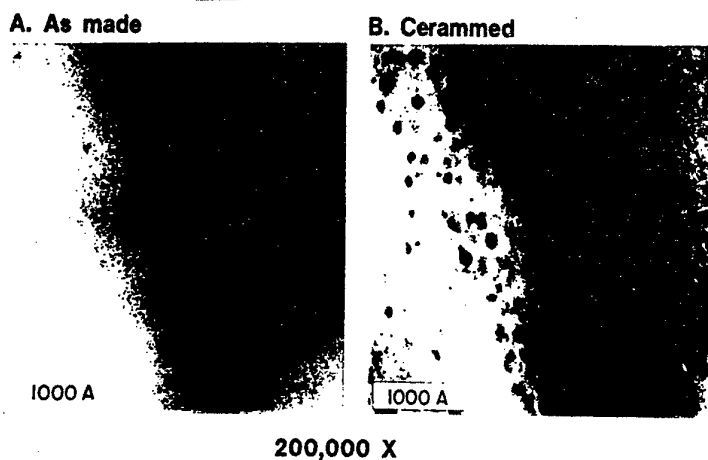
A DTA curve, shown in Figure 2, obtained at a heating rate of 10 C/min., illustrates the essential phase transition features necessary to form these ultra-transparent structures.

Figure 2
High Temperature Behavior Of Ultra-Transparent Glass-Ceramics



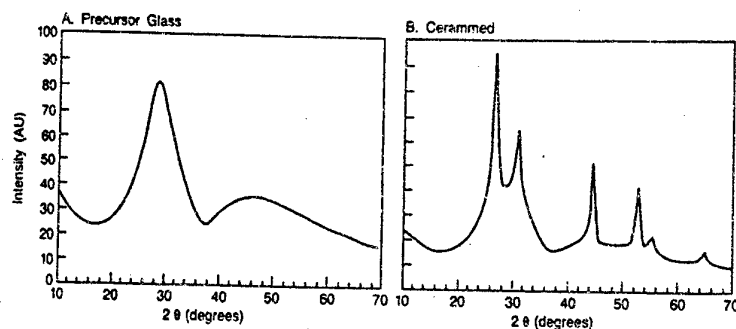
These are fluid glass melts with a liquidus temperature near 800 C. In order to form a glass, the melt must be rapidly cooled to the glass transition temperature (T_g), which is about 400 C, to avoid any high temperature crystallization reactions. The desired glass-ceramic structure may then be developed by reheating the precursor glass to a temperature near the sharp crystallization peak lying about 70 C above the T_g . Hold times at these temperatures of between 45 and 90 minutes are typical. The position of the ceramming peak is critical because the growth process must be done at a relatively high viscosity, usually above 10×10^8 poises. This insures that the kinetics of this process is slow enough to develop the proper nanostructure and that there will be minimal flow during processing.

Figure 3A
TEM Microstructures Of The Precursor Glass And Glass- Ceramic



Confirmation that the original material is entirely glassy and that the cerammed material contains two phases is shown by the transmission electron micrographs in Figure 3A and by the x-ray diffraction patterns in Figure 3B

Figure 3B
X-ray Diffraction Patterns Of The Precursor Glass And Glass-Ceramic



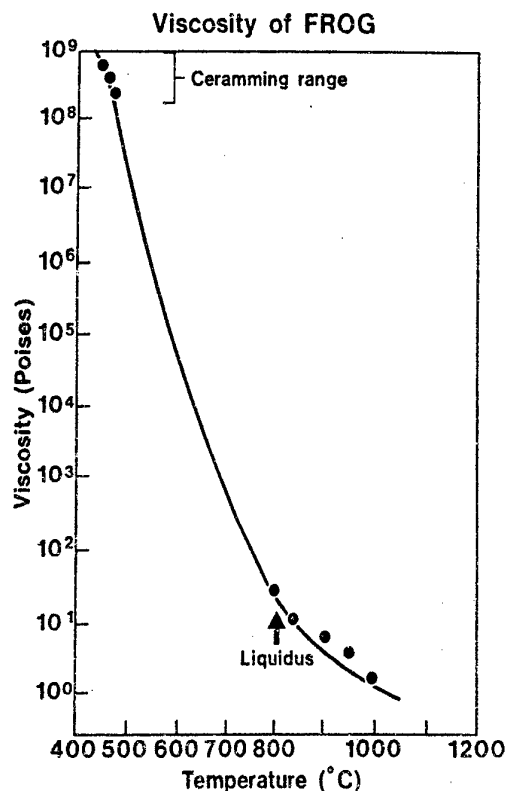
These data help define some of the critical aspects of the structure. It is essential that the periodic fluctuation of the refractive index, due to the presence of the two phases, be much smaller than the wavelength of light, so that the system may be treated as an effective medium (3). In this case the crystals are of the order of 10nm, as are the inter-crystal distances. This fixes the volume of crystals to between 5 and 30%. If the volume fraction falls below 5%, then the inter-crystal distances become too large and increased scattering can occur. If the volume fraction becomes much larger than 30% then the crystals can ripen, which can lead to a larger particle size distribution; that also results in increased scattering. When this type of nanostructure is achieved, i.e. 10nm particle size, 5-20nm inter-particle spacing, narrow particle size and uniform spatial distributions, then the conditions for ultra-transparency are satisfied. There are two other aspects of this particular glass-ceramic that are important. The first is that the refractive index difference between the two phases need not be small, in fact it is indirectly estimated to be about 0.05 in this system (4). The second feature is that the crystals are monophasic, with a cubic fluorite structure. When more than one phase appears, as can be induced by raising the concentration of Y too high, then ultra-transparency is lost. It is not known whether this is a peculiarity of this particular system, or whether this is a general rule. The spectral behavior of larger rare-earth dopants, like Er, Pr or Tm, unambiguously shows that the rare-earths are effectively partitioned into the crystal phase during ceramming and that the crystal is a pure fluoride. So for all practical purposes, this doped material behaves like an aluminosilicate glass in all respects except optically, where it behaves like a low phonon energy, fluoride crystal. These features are the basis of the property diversity

argument about the inherent uniqueness of ultra-transparent glass-ceramics compared to any mono-phase material and it is this diversity that may be able to provide at least some of the combinations of properties needed for the next generation of photonic devices.

Fiberization

Fiberization of this family of materials posed some unique challenges. The ability to melt without special atmospheres, moderate melting temperatures and compatibility with platinum are all significant advantages. However, these compositions do form fragile melts, as the viscosity curve in Figure 4 demonstrates.

Figure 4
Viscosity Of Ultra-Transparent GlassCeramics

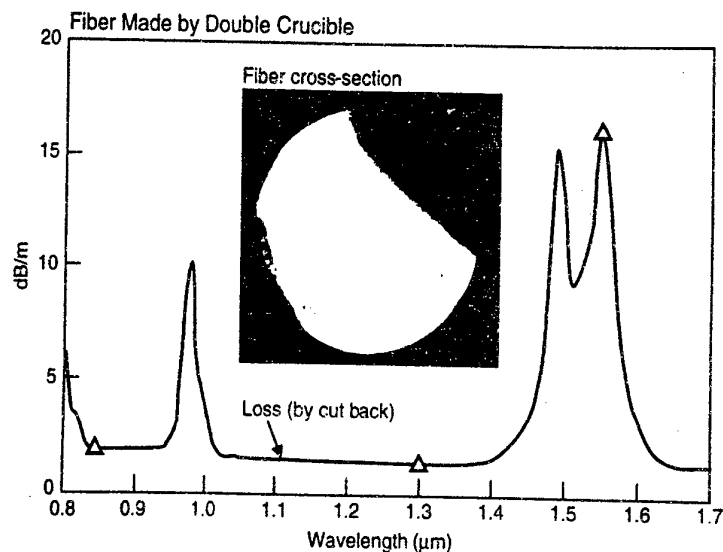


One of the traditional methods used to fiberize similar glasses is to first cast a core/cladding preform and then redraw into a fiber. That is not possible with this system because the material will over-ceram at the viscosities normally needed for redraw. Hence, a hot glass process seemed to be the most attractive alternative. But, as with other fragile systems, the high temperature properties do not easily lend themselves to hot forming. Small liquidus viscosity's (few poises), fast devitrification kinetics and the strong temperature dependence of the viscosity are amongst the primary reasons for this.

However, if ultra-transparent glass-ceramics are ever to be a legitimate candidate for future photonic devices there was really no choice. A hot fiberizing process needed to be developed. Using some ideas first proposed by Mimura (5), a double crucible process, capable of forming the fiber structures above the liquidus temperature of the core glass-

ceramic was developed. This process has produced, well centered cores whose dimensions are in the single mode regime. Losses, after ceramming, are near 1dB/m at 1300nm. A photograph of the core/cladding structure and a spectral loss curve are shown in Figure 5.

Figure 5
Ultra-Transparent Glass-Ceramic Fiber made By A Double Crucible Process



The loss measurement was made on a cerammed, 2m length of Er-doped fiber by a cut back method. There was essentially no difference in the measured loss between the precursor glass and cerammed fiber. There is 10 to 20 ppm of tramp iron in this particular sample, which is sufficient to account for much of the measured loss in the IR.

Conclusions

Ultra-transparent glass-ceramics offer a mix of properties not found in any monophase material. Mechanically, chemically and physically they exhibit aluminosilicate-like behavior. During ceramming any rare-earth dopants present are effectively partitioned into the crystal phase. This provides a low phonon energy, highly ordered environment for the rare-earth, which is reflected in the spectroscopy.

A hot glass process, capable of providing single mode fiber structures with passive losses near 1dB/m, has been demonstrated. These measurements also suggest that the intrinsic scattering losses, due to the glass-ceramic structure, have not yet been reached.

References

1. Y. Wang and J. Ohwaki, Appl. Phys. Lett., 63(24), 13 Dec. 1993, pp3268-70
2. P. A. Tick, N. F. Borrelli, L. K. Cornelius and M. A. Newhouse, J. Appl. Phys. 78(11), 1 Dec. 1995, pp6367-74
3. R. J. Gehr and R. W. Boyd, Chem. Mat., 8(8), Aug. 1996, pp1807-19
4. Tick unpublished data
5. Y. Mimura, International Comm. Res., No. 115, pp72-80, Jan. 1983

SECTION 2

POSTER PRESENTATIONS

REDOX STATES OF TRANSITION METAL IONS IN HEAVY METAL FLUORIDE GLASSES.

K J McKinlay¹ & J M Parker².

1. British Glass Manufacturers Confederation, Northumberland Road,
Sheffield, S10 2UA, UK: e-mail: k.mckinlay@britglass.co.uk

2. Department of Engineering Materials, University of Sheffield
Sheffield, S1 3JD, UK. e-mail: j.m.parker@sheffield.ac.uk

ABSTRACT

As part of a study of the effect of impurities in heavy metal fluoride glasses on scintillation yield, we have examined the effects of melting atmosphere and base glass composition on the redox equilibria of iron, titanium and copper. Certain oxidation states of these ions can absorb in the near UV and hence strongly affect the emission of the Ce^{3+} ion at 325nm. The interactions between the transition metal ions and other multivalent species, particularly indium and cerium, will be reported.

INTRODUCTION

There has been a considerable interest recently in heavy metal fluoride glasses for use as calorimeters in high energy particle physics experiments since their high density allows absorption of all incident energy in a relatively short distance of approximately 70 cm. By doping these glasses with cerium ions they become efficient scintillators and a reproducible fraction of the incident radiation which is incident on the glass becomes converted to UV radiation near 325 nm. Measurement of this light intensity therefore provides a measure of the intensity of radiation incident on the glass.

This application requires a large volume of glass. A key aim has therefore been to use raw materials of minimum cost. On the other hand optical transparency at the emission wavelength of 325 nm is vital for the operation of the device. The effect of impurities on optical properties, particularly UV transmission, is therefore a critical consideration. Indeed experiments have already shown that for this particular application melting under reducing conditions considerably improves the scintillation yield of these glasses [1].

In previous studies on redox in fluoride glasses the absorption spectra corresponding to a variety of transition metal and rare earth ions have been measured and the effects of the oxygen partial pressure in the melting atmosphere have been investigated [2]. Indeed for maximum infrared transmission oxidising conditions are usually preferred. The consequences of having more than one redox pair in the system have not been studied however although this has been of interest in oxide glass forming systems.

In particular Ce and In are both multivalent ions added to these glasses as the scintillating ion and to improve radiation hardness respectively. In this study the effect of these ions on the position of the Fe^{2+}/Fe^{3+} , Ti^{3+}/Ti^{4+} , and $Cu^0/Cu^{1+}/Cu^{2+}$ equilibria has been examined, the latter being ions which are likely to be present as impurities in low cost raw materials.

METHOD

For this study pure fluorides were used as raw materials and the transition metal fluorides were introduced as deliberate additions. Typical impurity levels used were 300 to 3000 ppm of transition metal cations. An example of the base glass composition used is given in Table 1.

The raw materials were batched in a dry glove box and transferred to the melting furnace in a sealed container. Melting was carried out in a silica liner sealed to a dry box but with a

separately controlled atmosphere so that the oxygen partial pressure above the melt could be varied. The glasses were melted in a platinum crucible when using oxidising or neutral melting atmospheres. Where reducing conditions were required however a vitreous carbon crucible was used. The glasses were melted from batch under oxidising conditions and then remelted in the neutral and reducing atmospheres to prevent the formation of reduced hafnium.

Table 1. Base glass composition (mol %) to which colouring agents have been added. Where CeF_3 was added, it completely replaced LaF_3 ; InF_3 only partially replaced AlF_3

HfF_4	CeF_3 or LaF_3	NaF	BaF_2	AlF_3 or InF_3
54	5	18	19	4

Fluoride glass melts have much lower viscosities than oxide melts and so can reach equilibrium much more quickly. However to aid the rate of equilibration, the melt was taken from the furnace and stirred by swirling once during the melting process. The melting schedule consisted of a two hour hold above the melting point (as followed by France [3]). For one case the melt schedule was extended to a seven hour hold to check that equilibrium was being achieved and the spectra obtained were very similar.

Glasses were prepared for optical absorption spectroscopy by grinding and polishing to plates approximately 4mm thick under paraffin to prevent corrosion. The specimens prepared were measured using a Perkin-Elmer IR Fourier transform spectrophotometer and a Perkin-Elmer UV/Vis spectrophotometer. The optical absorption spectra were corrected to a zero background by subtracting a linear baseline taken from the minimum absorption of the spectra. Typical background losses were near 8% as expected from reflection at two interfaces, but in a few cases deviations were present suggesting some sample inhomogeneity. Data points were output to a statistical analysis package and fitted to Gaussian curves; if required a background could be added and this was generally written in the form of a polynomial with up to three terms.

RESULTS

A typical fitted absorption spectrum for Fe^{2+} is shown in Figure 1. This spectrum has been corrected for reflection losses.

The iron absorption spectrum in the near infrared can be fitted by three Gaussians, which have been attributed to Fe^{2+} in a distorted octahedral site and in a tetrahedral site. The positions of these peaks are similar to those reported in an oxide glass but shifted to longer wavelengths. The widths of the fitted Gaussians change little with the glass compositions used in this work and hence we have taken peak height as a measure of the concentration of the species present. Melting under different atmospheres has a major effect on the quantity of Fe^{2+} present as illustrated in Table 2.

Table 2. Showing the amount of Fe^{2+} in the glass as a function of melting atmosphere for a Ce based glass with 3000ppm of Fe added

Melting atmosphere	Height of Fe^{2+} absorption peak
$p_{\text{O}_2} = 0.1$ atmospheres	0.0090
100% nitrogen (nominally)	0.0144
Nitrogen with 3% H_2	0.0346

Similar trends were also observed for Ti^{3+} and Cu^{2+} . For the case of titanium the height of the peak also depended on the form in which the Ti was added. If introduced as TiF_4 the amount of Ti^{3+} ions in the glass was much lower. This was attributed to the volatility of TiF_4 and its loss during the early stages of melting rather than to a failure to achieve equilibrium. Copper was easily reduced to the metallic state.

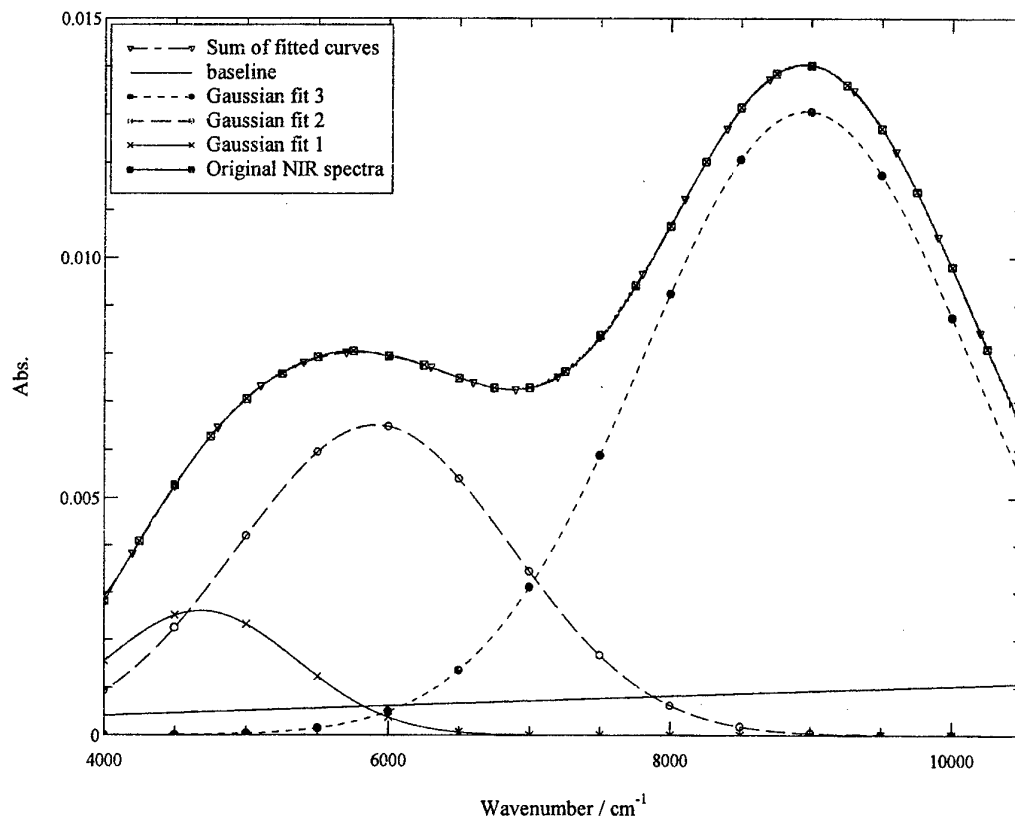


Figure 1. Fe^{2+} absorption spectrum in a glass of molar composition : $54\text{HfF}_4:19\text{BaF}_2:5\text{LaF}_3:4\text{AlF}_3:18\text{NaF} + 3000\text{ppm}$ of Fe melted in 100% N_2 atmosphere.

Doped glasses were melted in four principal groups: with LaF_3 added as the rare earth fluoride, with CeF_3 added in place of LaF_3 , and with 0.5 mol % InF_3 added replacing AlF_3 in both LaF_3 and CeF_3 glasses. LaF_3 exists in only one oxidation state but the Ce and In ions can both be present in more than one oxidation state. Table 2 below compares the height of the Fe^{2+} absorption peak for this series of compositions and for different melting conditions. The cerium containing melts clearly produce a slightly more reducing environment and the indium glasses a slightly more oxidising environment. This same pattern was reproduced for titanium and copper additions.

Table 2. Height of Fe^{2+} principal peak in the three glass series studied with 3000ppm Fe (arbitrary units).

Melting atmosphere	La glasses	Ce glasses	In + La glasses	In + Ce glasses
Oxidising	0.0056	0.0090	0.0064	0.0079
Neutral	0.0131	0.0144	0.0106	0.0137

DISCUSSION

Indium is added to these glasses to improve radiation hardness. Its action relies on its existence in two oxidation states so that it can act both as an electron trap and as an electron donor. It also has traditionally been used as an oxidising agent during melting in order to prevent the formation of reduced metal species. Clearly in this case its effects are similar; it shifts the $\text{Fe}^{2+} \leftrightarrow \text{Fe}^{3+}$ equilibrium towards the right. Previously indium fluoride has been found to reduce the scintillation yield of these glasses [1] although conferring radiation hardness. This may in part be the result of the oxidising action of the material since in general the scintillation yield shows significant improvements the more reduced are the melting conditions.

Cerium on the other hand produces more reduced glasses although the effects are very small. Higher concentrations of cerium may therefore not only enhance the scintillation yield as a simple concentration effect but may also help to eliminate some of the species responsible for reducing the emission yield in glasses which are too oxidised.

REFERENCES

- [1] P R Hobson, D C Imrie, T Price, S Salih, K W Bell, R M Brown, D J A Cockerill, P S Flower, G H Grayer, B W Kennedy, A L Lintern, M Sproston, K J McKinlay, J M Parker, D Bowen, T Cliff, R Hannay, R Smith, "Investigations into the possibilities of using fluoride glasses for the construction of homogeneous calorimeters in particle physics.", *J Non-Cryst Solids* **213 & 214** (1997) 147-151
- [2] P W France, S F Carter and J M Parker, "Oxidation states of 3d transition metals in ZrF_4 glasses", *Phys Chem Glasses*, **27** (1986) 32-41
- [3] P F France, Ph.D. thesis, University of Sheffield, UK (1988)

In-situ Generation of Eu^{2+} in Glass forming Melts

P. J. Newman¹, D. R. MacFarlane¹, J. D. Cashion² and A. Edgar³

¹ Department of Chemistry, Monash University, Clayton, Vic., Australia

² Department of Physics, Monash University, Clayton, Vic., Australia

³ School of Chemical and Physical Sciences, Victoria University
Wellington, New Zealand

Photostimulated luminescence from X-ray irradiated inorganic crystals and glasses is an important phenomenon from both a fundamental and practical point of view. Photostimulated luminescence has been demonstrated recently in cerium(III) and samarium(III) doped borate glass¹ and europium(II) doped BaFBr crystals² and fluoroaluminate glass³. The latter case presents a difficulty because the chemistry of the lanthanides is naturally dominated by the tendency to form the tripositive ion (Ln(III)) and EuF_3 is the normally encountered species. The fact that divalent europium can exist is thought to be correlated with the special stability associated with a half filled 4f orbital ($4f^7$).

Since Eu(II) compounds are not readily available and it is this oxidation state that is necessary for the phenomenon of photostimulated luminescence to be observed, we have begun a study to examine and compare different methods of generating Eu(II) in fluoride glasses. In this paper we report the reduction of Eu(III) to Eu(II) using a variety of chemical reductants and for the first time, the use of bulk electrochemical reduction of Eu(III) to Eu(II) in a fluoride melt. All glasses were characterized using a number of spectroscopic techniques including absorption, electron spin resonance and Mossbauer spectroscopy.

1. K. Tanaka, K. Hirao, H. Tanaka and N. Soga, Jpn. J. Appl. Phys. 35 (1996) 2170.

2. Y. Amemiya and I. Miyahara, Nature, 336 (1988) 89.

3. J. Qui, Y. Shimizugawa, Y. Iwabuchi and K. Hirao, Appl. Phys. Lett. 71 (1997) 759.

INFLUENCE OF FLUOROXIDIZERS ON SCINTILLATORS PROPERTIES OF FLUOROHAFNATE GLASS, DOPED WITH Ce³⁺

M.Brekhovskikh, V.Sukhoverkhov,¹ S.Batygov,

L.Dmitruk, N.Vinogradova,² E.Devitsin, V.Kozlov, A.Provorova³

¹Institute of General and Inorganic Chemistry, Russian Academy of Sciences, Leninsky pr., 31, Moscow 117907, Russia

²General Physics Institute, Russian Academy of Sciences, Vavilov str. 38, Moscow 117947, Russia

³Lebedev Physical Institute, Russian Academy of Sciences, Leninsky pr., 53, Moscow 117947, Russia

ABSTRACT

Presence of the reduced Hf²⁺ ions and oxygen impurities may cause the formation of radiation colouring centers and decrease of radiation hardness of scintillating HfF₄-based glasses, doped with Ce³⁺. A new technique of batch additional fluorination by chlorine trifluoride and xenon difluoride is proposed to obtain both oxygen-free and oxidised HfF₄ glasses. Radiation optical properties of the treated glasses are studied.

INTRODUCTION

Fluorohafnate glasses, doped with Ce³⁺, exhibit short life time, high density and small radiation length. In this connection they appear to be a perspective material for scintillating sensors that are used in high energy physics and nuclear physics [1,2]. Relatively low radiation hardness, compared with that of crystals CeF₃ and PbWO₄ is the main disadvantage of fluorohafnate glasses.

In this paper the influence of preliminary fluorination of the mixture for glass synthesis with fluoroxidizers (ClF₃, XeF₂) on radiation hardness of glasses is studied.

EXPERIMENTAL

The technique of batch additional fluorination by XeF₂ and ClF₃ is described in [3]. Fluorination of the mixture 51,5HfF₄-20-BaF₂-5CeF₃-2,5AlF₃-20NaF-1InF₃ with fluoroxidizers is held in the evacuated nickel reactor, connected with a vacuum line. Fluorinating agents are condensed into the reactor. The fluoroxidizing process proceeds in

gaseous and in liquid in the case of ClF_3 phases. To remove oxygen-containing impurities completely the reactor is heated from 20 upto 150°C at the pressure from 2,5 upto 6 atm. Fluorination time is equal to 50 hours. Excess of unreacted ClF_3 , XeF_2 and the gaseous products are eliminated in a dynamic vacuum at a room temperature and at 100°C . Sorbed water is eliminated with a marked rate at a room temperature.

Samples of glasses are synthesised from the starting fluorides of 99,5 purity in vitreous carbon crucibles in a dry argon atmosphere. After synthesis at $800\text{--}820^\circ\text{C}$ during 40 min the melt is cooled at a rate of $35\text{--}30^\circ/\text{min}$ within the crystallisation temperature range $440\text{--}340^\circ\text{C}$. To avoid the effect of synthesis conditions samples of glasses with preliminary treatment are synthesised together with the controls, i.e. glasses without preliminary fluorination.

Radiation hardness in the 280-800 nm region is estimated by the transmission spectra before and after γ -irradiation with $5 \cdot 10^5$ rad irradiation dose. The luminescence spectra of glasses under X-ray excitation and light yield under γ -irradiation as described in [4] are also measured.

RESULTS AND DISCUSSIONS

Conditions of preliminary treatment with fluoroxidizers influence to a great extent on the optical properties of glasses. The reactor being evacuated at a room temperature, the coloured opalescing glasses with absorption bands in the 440 and 690 nm region (fig.1) are obtained. The reactor being evacuated at 100°C , the transparent glasses with the transmission spectrum identical to that of controls are obtained.

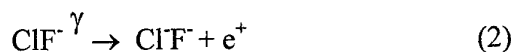
Some difference in the emission spectra of glasses, obtained from the fluorinated and traditional starting mixture, is observed (fig.2). The weak long-wave component appears along with the main luminescence band of Ce^{3+} at 310 nm in the luminescence spectra of the glass without fluoridation treatment. In [5] this component is attributed to luminescence of oxygen impurities in the glass. The absence of this band in the fluorinated glasses indicates indirectly the effectiveness of removing of oxygen impurities from the starting mixture.

Transmission spectra of some samples after γ -irradiation with the $5 \cdot 10^5$ rad dose are presented at fig. 3,4. As it follows from fig.3, transmission of glasses in the UV and visible range, obtained in the conditions of evacuation of the reactor at a room temperature, decreases sharply after γ -irradiation, compared with that of controls (curve 3, fig.3). Sharp

decrease of the radiation hardness is observed also in glasses, obtained in the reduction atmosphere (Ar+H₂) (curve 4, fig.4) and at doping of glasses with CeCl₃ (curve 3, fig.4). At the same time fluoridation treatment of the starting mixture with the following thermal evacuation enables to increase transmission in the UV and visible range after γ -irradiation (curve 2, fig.3). Increase of the radiation hardness is observed also at introducing into the starting mixture of small amounts of CeF₄ (curve 2, fig.4). In this case CeF₄ plays the role of the internal fluorinating agent that produces fluorine at 800°C in a dry atmosphere [6].

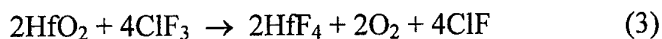
Absorption peaks in the visible range and intensive light scatter may be caused by the presence of the non-transparent colloid particles in the samples [7]. Coincidence of absorption bands at 440 and 690 nm with [7] and intensive red scattering in the samples, obtained from the starting mixture, evacuated at a room temperature, enables to consider the presence of non-transparent colloid particles in the samples. Such particles may appear as a result of the reaction of ClF₃, remained in the mixture, with carbon of the crucible at a high temperature. Obviously, the complete elimination of the excess of unreacted fluorinating agent is the necessary condition for obtaining of glasses with high optic quality.

Formation of several kinds of colouring centres under γ -irradiation of fluoride glasses is known [8]. The impurity colouring centres appear to be the most stable and are formed by the following schemes:



The defects of the first kind cause absorption bands in the near UV, the defects of the second type cause a broad band in the visible range.

Intensive colouring of the glasses, doped with CeCl₃, after γ -irradiation and increasing of the radiation hardness of the glasses suggest that introducing of chlorine in the fluorination process might not occur. The greater transmission of the fluorinated glasses in the UV range under γ -irradiation compared with that of controls might be connected with the lowering of oxygen-containing impurities in the starting mixture and firstly in the main component (HfF₄) by the reaction:



This reaction prevents forming of the colouring centres by (1).

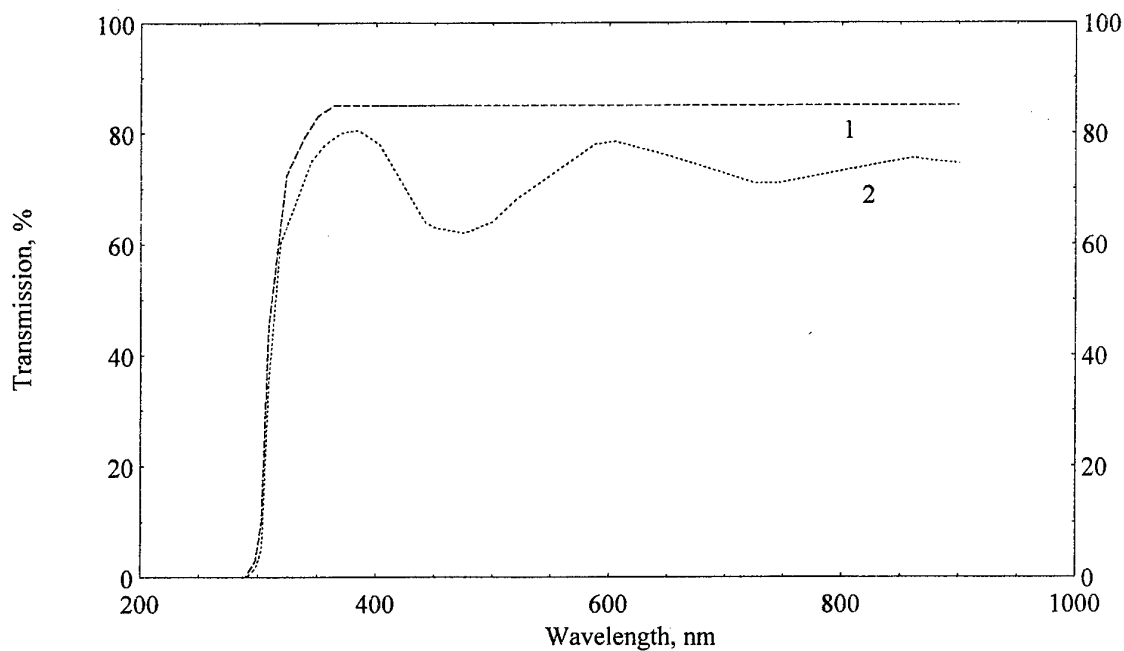


Fig.1 Transmission spectra of glasses: 1-glasses, obtained with the thermal evacuation of the reactor; 2-glasses, obtained with evacuation of the reactor at a room temperature

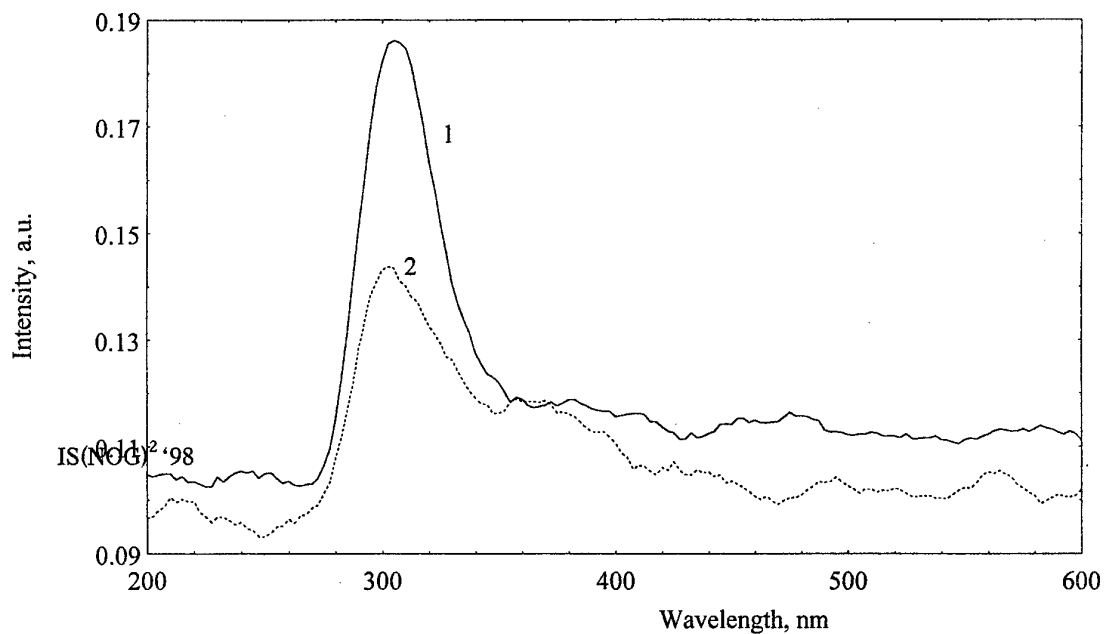
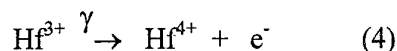


Fig.2 X-ray excited luminescence spectra of glasses prepared with the preliminary fluorination treatment (1) and without treatment (2)

Sharp decrease of the radiation hardness of glasses, obtained from the fluorinated starting mixture and synthesised in the reduction atmosphere (curve 4, fig.4) shows, that some other mechanisms of glass colouring take place. The formation of colouring centres is presumed to be connected with the presence of Hf^{3+} or Hf^{2+} ions :



The presence of reduced hafnium ions is discussed in [9]. Effective oxidation of reduced hafnium ions with such active fluoroxidizers as ClF_3 and XeF_2 should lead to the complete elimination of Hf^{3+} from the starting hafnium fluoride.

REFERENCES

- [1] L. Dmitruk, E. Devitsin, V. Kozlov, Proc. 9th Int.Symp. on Non-Oxide Glasses. Hangzhou, China. (1994) 90
- [2] P.R. Hobson et.al., Proc. Int. Conf. on Inorganic Scintillators and their Application. Delf, Netherland (1995) 317
- [3] M. Brekhovskikh, V. Fedorov, Proc. 9th Int.Symp. on Non-Oxide Glasses. Hangzhou, China (1994) 314
- [4] E. Devitsin et al., Further Progress in R&D of Scintillating Fluoride Glasses (Preprint 24, Lebedev Physical Institute RAS, Moscow, 1997)
- [5] L. Dmitruk, N. Vinogradova et al., Non-Cryst. Solids. 213&214 (1997) 311
- [6] M. Brekhovskikh, V. Fedorov, Proc. 10th Int.Symp. on Non-Oxide Glasses. Corning, USA (1996) 525
- [7] A. Edgar, Proc. 10th Int.Symp. on Non-Oxide Glasses. Corning, USA (1996) 191
- [8] A. Abgrall et al., Proc. SPIE. Vol.618 Infrared Optical Material 1V(1986) 63
- [9] A.J. Drehman, Mat. Sci. Forum 19&20 (1987) 483

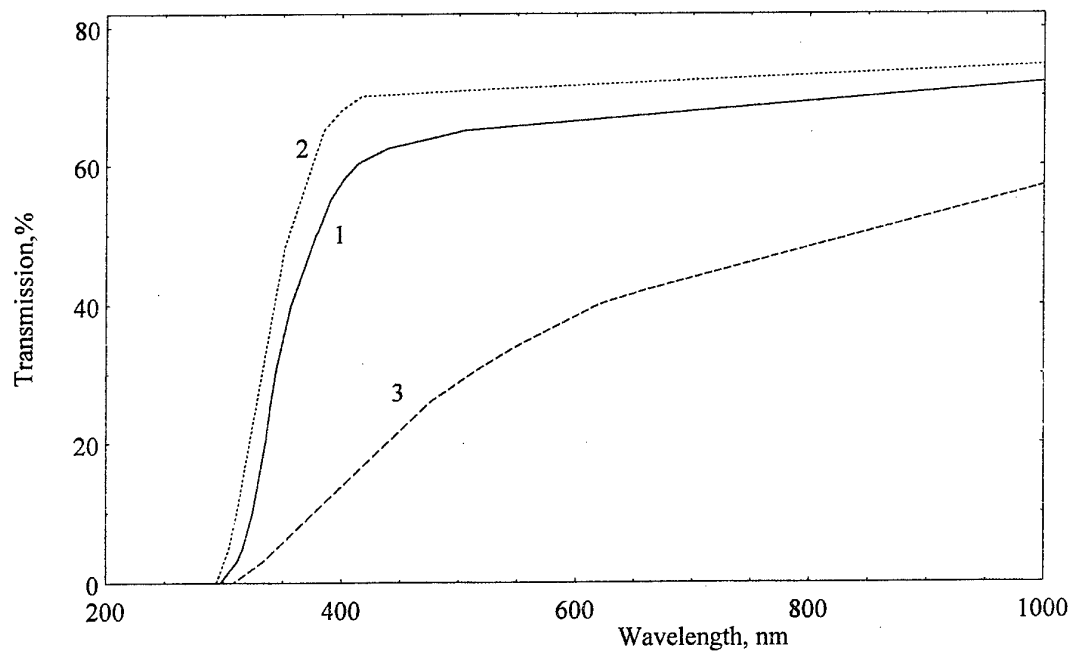


Fig.3 Transmission spectra of HBCeAln glasses after γ -irradiation with $5 \cdot 10^5$ rad dose; 1-control, 2-glass with preliminary fluorination treatment and thermal evacuation of the reactor, 3- glass with preliminary fluorination treatment and evacuation of the reactor at a room temperature.

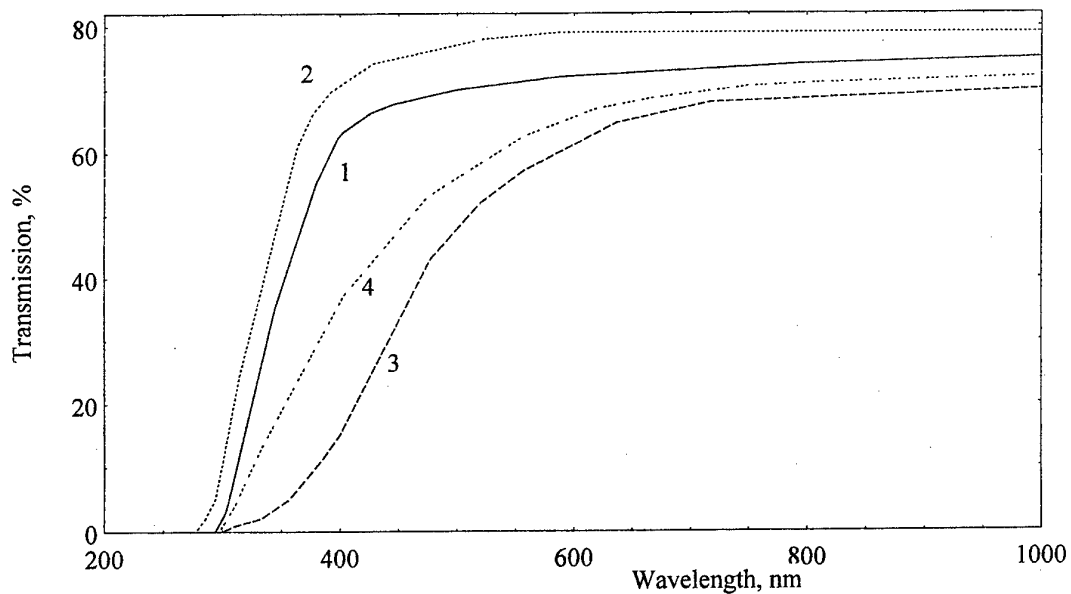


Fig.4 Transmission spectra of HBCeANIn glasses after γ -irradiation with $5 \cdot 10^5$ rad dose, 1-control, 2-glass addition of 0.5% wt of CeF_4 , 3 - glass with replacement of 5CeF_3 for 5CeCl_3 , 4- glass, synthesized in reduction ($\text{Ar}+4\%\text{H}_2$)

FLUORIDE GLASSES IN THE $\text{InF}_3\text{-GaF}_3\text{-YF}_3\text{-PbF}_2\text{-CaF}_2\text{-ZnF}_2$ SYSTEM

Ahmed BOUTARFAIA & Marcel POULAIN

Institut des Sciences Exactes, Université de Biskra, PB. 145, RP-Biskra, Algérie

Lab. Matériaux Photoniques, Université de Rennes 1, F35042 Rennes

ABSTRACT:

New glasses have been synthesized in a multicomponent system based on indium fluoride. Samples of a few mm in thickness were obtained. They are transparent and homogeneous. Main physical properties such as density, characteristic temperatures, density, thermal expansion and refractive index have been measured. Their evolution versus composition is reported for samples with the formula : $(35-x)\text{InF}_3 - x\text{GaF}_3 - \text{YF}_3\text{-PbF}_2 - \text{CaF}_2 - \text{ZnF}_2$. T_g lies between 260 and 296°C while melting starts around 480 °C. Glass samples are stable at room temperature. By comparison with other standard fluoride glasses, they exhibit higher refractive index and density.

1. INTRODUCTION

Fluoroindate glasses have been extensively studied because they extend the possibilities of the standard fluorozirconate glasses [1-4]. In particular they offer an extended infrared transmission range which directly derives from their lower phonon energy. In addition their intrinsic optical losses should be lower than those of the standard ZBLAN glass in the mid-IR. However nucleation and crystallization problems are far from being under control, which often results in high scattering losses. This paper reports attempts to optimize the glass stability in a multicomponent system based on the fluorides of In, Y, Pb, Ca, Zn and Ga. The influence of the Ga/In substitution on glass stability and physical properties has also been studied.

2. EXPERIMENTAL

Glass samples, usually 6 grams in weight, were synthesized in platinum crucibles using the ammonium bifluoride processing, with oxides and fluorides as starting materials. Fluorination was carried out for 1 hour at 300°C and 30 min. at 450°C and processing includes a 20 min. fining stage at 800-900°C after melting. Characteristic temperatures are T_g for glass transition, T_x for onset of crystallization and T_p for the maximum of the exothermic peak. They are measured using a Seiko 220 DSC at 10 Kmn⁻¹ heating rate. Assessment of glass stability is made from the value of the

stability range $\Delta T = T_x - T_g$ [5] or from the S factor $((T_x - T_g)(T_p - T_x)/T_g)$ [6]. Refractive index is measured using an Abbe refractometer and thermal expansion from a Seiko TMA/SS 120. Estimated accuracy is $\pm 1^\circ\text{C}$ for temperatures, ± 0.0005 for refractive index and $\pm 5 \cdot 10^{-7} \text{ K}^{-1}$ for thermal expansion. Archimedeian method used for density is expected to lead to an error margin of ± 0.01 .

3. RESULTS

Previous works aiming at the optimization of the InF_3 - YF_3 - PbF_2 ternary glasses showed that more stable compositions could be obtained incorporating calcium and indium fluorides as stabilizers [7]. A typical composition was 40 InF_3 - 5 YF_3 - 25 PbF_2 - 15 CaF_2 - 15 ZnF_2 . In a first step we have substituted indium by gallium, which is known to decrease devitrification rate in fluoroindate glasses. Glass samples were prepared with the general chemical formula: $(35-x) \text{ InF}_3$ - $x \text{ GaF}_3$ - 10 YF_3 - 25 PbF_2 - 15 CaF_2 - 15 ZnF_2 . The evolution of the stability criteria versus gallium content is reported in figure 1. This suggests that optimum composition corresponds to 15 to 30 mol % GaF_3 . In other words, fluorogallate glasses appear more stable in this multicomponent system than fluoroindates.

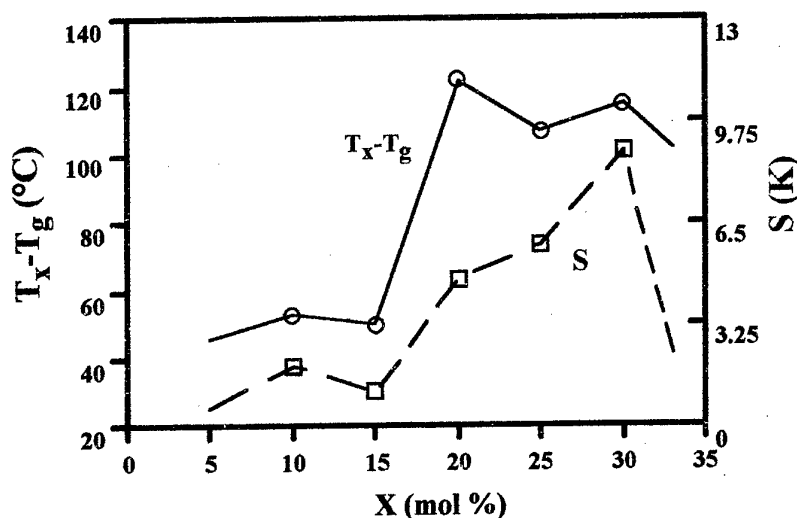


Figure 2 : Evolution of stability parameters ΔT and S versus GaF_3 content in $(35-x) \text{ InF}_3$ - $x \text{ GaF}_3$ - 10 YF_3 - 25 PbF_2 - 15 CaF_2 - 15 ZnF_2 glasses

When InF_3 is replaced by GaF_3 , glass transition temperature increases from 260°C to 296°C . The evolution of the other characteristic temperatures - T_x for onset of crystallization and T_f for the beginning of the fusion - is reported in figure 2.

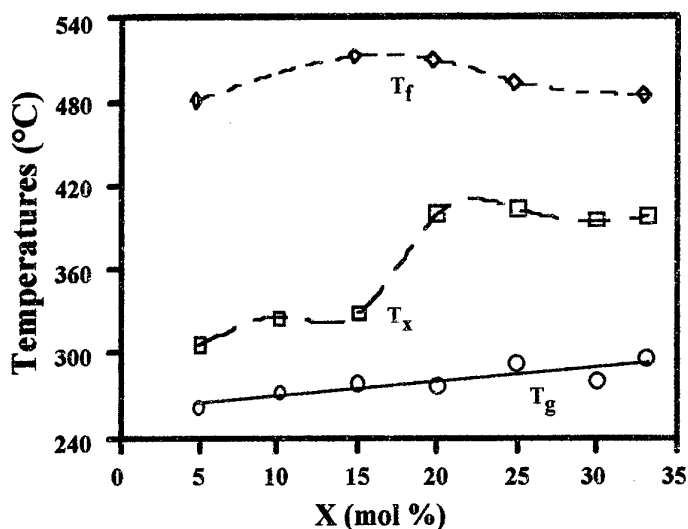


Figure 3 : Influence of GaF_3 on the value of the characteristic temperatures

T_g , T_x and T_f for glass transition, onset of crystallization and melting.

Density and refractive index decrease, while thermal expansion increases, when GaF_3 replace InF_3 . This evolution is exemplified by figures 3 to 5. These glasses are stable at room atmosphere and their chemical durability may be compared to that of fluorozirconate glasses.

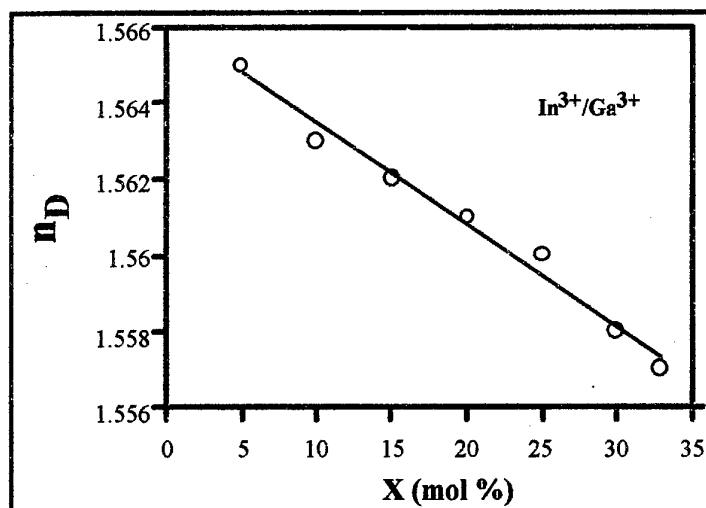


Figure 4 : Evolution of refractive index, n_D versus GaF_3 content

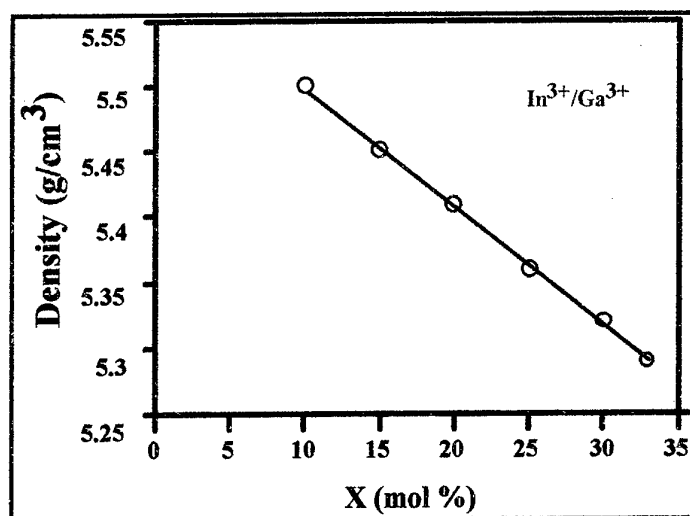


Figure 5 : Evolution of density versus GaF_3 content

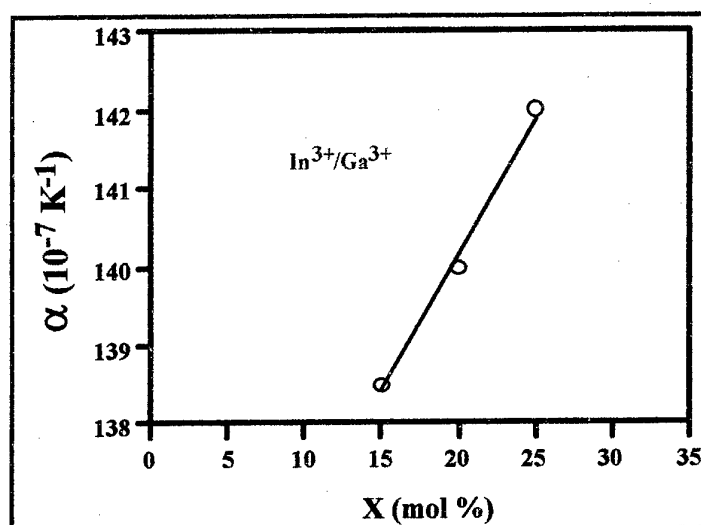
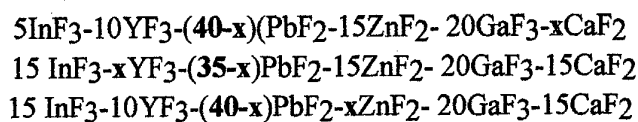


Figure 6 : Thermal expansion coefficient, α , as a function of GaF_3

The influence of the other glass components on glass stability and physical properties was also investigated. Various samples were prepared according to the general formulas :



The effect of the Pb/Y, Pb/Zn and Pb/Ca substitutions may be seen from the figures 7 to 10. Thermal stability range may reach 120°C , which is generally sufficient for casting large bulk samples. The evolution of the physical properties versus chemical composition is consistent with previous knowledge of fluoride glasses: refractive index and density are

correlated with lead content.

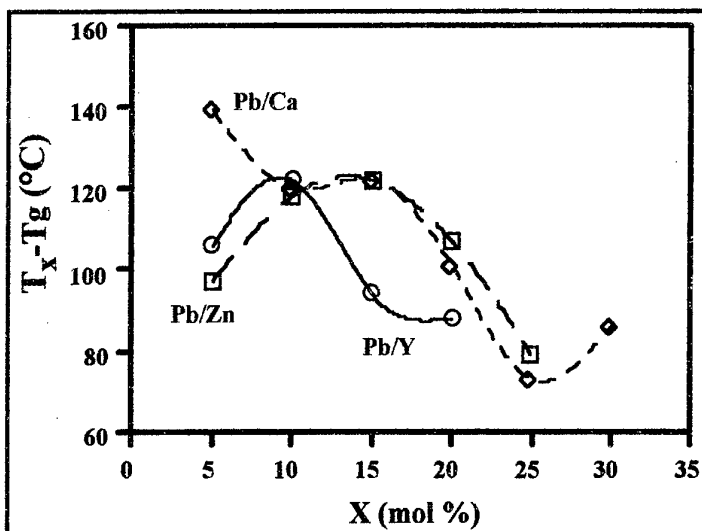


Figure 7 : Thermal stability range ΔT versus composition in the glasses:

15 InF_3 -10 YF_3 -(40-x)(PbF_2 -15 ZnF_2 - 20 GaF_3 -x CaF_2)

15 InF_3 -x YF_3 -(35-x) PbF_2 -15 ZnF_2 - 20 GaF_3 -15 CaF_2

15 InF_3 -10 YF_3 -(40-x) PbF_2 -x ZnF_2 - 20 GaF_3 -15 CaF_2

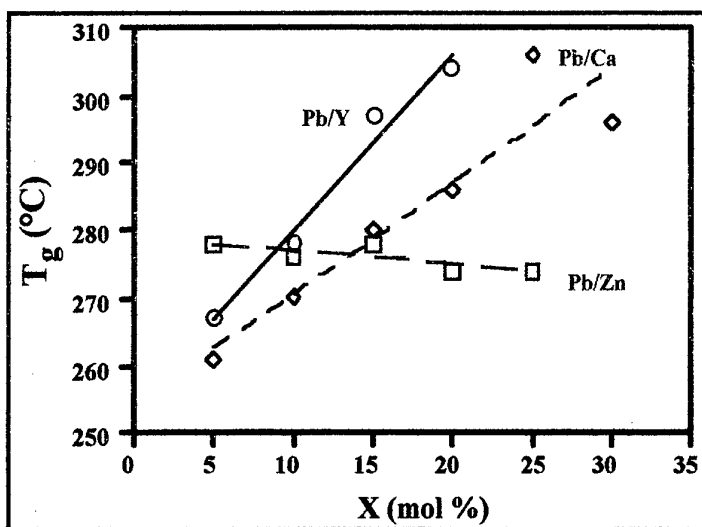


Figure 8 : Influence of Pb/Y, Pb/Ca and Pb/Zn substitutions on glass transition temperature T_g .

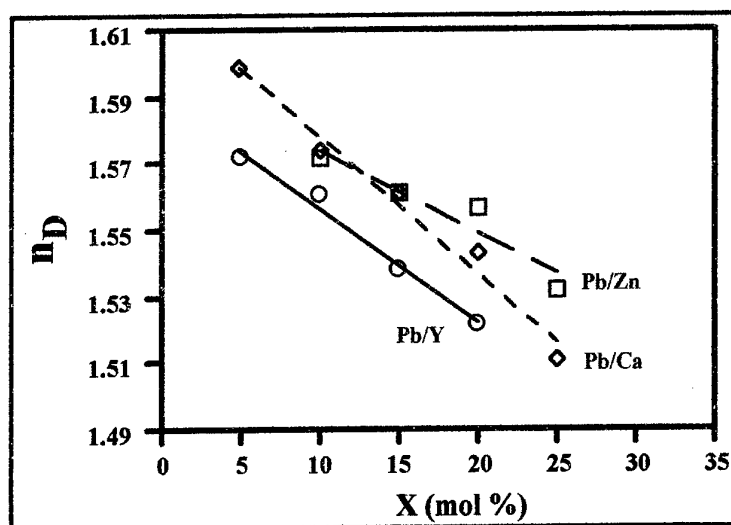


Figure 9 : Refractive index , n_D , versus ZnF_2 , CaF_2 and YF_3 content

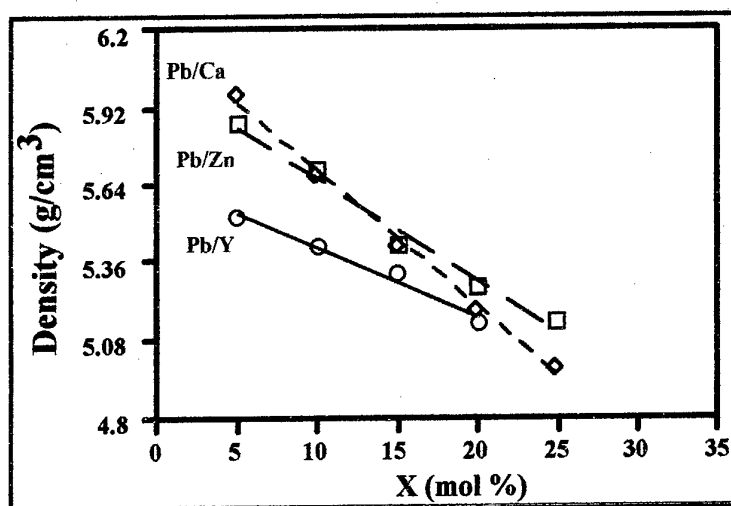


Figure 10 : Density versus ZnF_2 , CaF_2 and YF_3 content

4. DISCUSSION

These results show that more stable glasses could be obtained by convenient adjustments of chemical composition. It may be viewed as the illustration of the "confusion principle" which expressed that the stability of a multicomponent glass versus devitrification generally increases as the number of glass components increases. While numerous examples support this rule, current experience shows that it does not apply automatically. There is an optimum concentration range which cannot be predicted from theoretical considerations. In addition, processing has also to be adjusted in order to minimize the factors promoting heterogeneous nucleation. It is widely admitted that the diffusion processes involved for crystallization are more difficult when chemical species are more numerous. However this is only one of the factors ruling the whole devitrification process, and some glass forming melts may devitrify more rapidly when one additional

compound is incorporated.

Correlating glass forming ability to chemical composition and bonding has been a constant concern for glass scientists, and Zachariasen's rules [8] make the most famous - and perhaps the most successful - attempt in this way. Unfortunately most approaches fail on the point that devitrification first arises from nucleation and crystal growth which are not clearly influenced by chemical bonding. It is often assumed that any glass consists in a vitreous network which has a predominant covalent character. One may be tempted to conclude that glass stability will increase if network covalency is enhanced. This would explain why the substitution of indium fluoride by gallium fluoride which is more covalent improve glass formation; but it is contradictory with the fact that indium incorporation has a similar effect in fluorogallate glasses [9]. In a more general way, glass formation occurs in chemical systems having all types of bonding: covalent, ionic and metallic, and there is only one example of nitride glass - nitrides are covalent - while there are thousands of fluoride and predominantly ionic glasses.

As a consequence, glass science still remains largely empirical in this area of glass formation. Fortunately it is largely predictable as far as physical properties are concerned. The changes in the physical properties of the modified fluoroindate glasses are consistent with the observations in other fluoride systems: lead fluoride is known to increase density and refractive index and to decrease glass transition temperature. The respective influences of calcium and zinc fluorides appear different for glass transition. This could be explained by their different coordination numbers and the structural changes this substitution will induce. One may also point out that zinc is considered as a network former and calcium as a modifier.

Fluoroindate glasses may find practical applications to extend the possibilities of the standard fluorozirconate glasses [10] such as ZBLAN because they may transmit IR light at longer wavelength [11]. As an example, one may quote thermometry, remote spectroscopy and CO laser transmission. However, as most of these applications require optical fibers, the level of scattering and absorption losses should be reduced. Finally, active fibers made from fluoroindate glasses may have higher efficiency for various laser transitions, and also for optical amplification at 1.3 μm [12]. The fluoroindate glasses from this study have a high refractive index. Their association with lead-free glasses makes possible the design of optical fibers with a very large numerical aperture.

5. CONCLUSION

Numerous glass compositions have been investigated in the multicomponent systems based on the fluorides of In, Ga, Pb, Ca, Zn, Y. The influence of the composition on glass stability and physical properties has been investigated. Some of these glasses are stable enough against devitrification to be cast as thick samples from which preforms for fiber drawing experiments could be made.

REFERENCES

- [1] J. Nishii, Y. Kaite and T. Yamagishi, *Phys. Chem. Glasses* **30** (1989) 55
- [2] M. Poulain, M. Poulain, Y. Messaddeq and A. Soufiane, in: "Solid State Optical Materials"" Vol.28, Fluoroindate glasses, ed. A.J. Bruce and B.V. Hiremath, Am. Ceram. Soc., Westerville, USA (1992), p. 381
- [3] Y. Messaddeq, A. Delben, M. A. Aegerter, A. Soufiane and M. Poulain, *J. Mater. Res.* **8** (1993) 885
- [4] A. Boutarfaia, M. Poulain, M. Poulain and S. E. Bouaoud, *J. Non Cryst.Solids* **213-214** (1997) 36
- [5] A. Dietzel, *Glastech. Ber.* **22** (1968) 41
- [6] M. Saad and M. Poulain, *Mat. Sci. Forum* **19-20** (1987) 11
- [7] A. Boutarfaia, Thèse de Doctorat d'Etat, Constantine, 1997
- [8] W. H. Zachariasen, *J. Chem. Soc.* **54** (1932) 3841
- [9] A. Soufiane and M. Poulain, *Journal of Non-Crystalline Solids* **161** (1993) 206
- [10] G. Mazé, in: "Fluoride Glasses", Applications and prospects, ed. A. Comyns, John Wiley & Sons, Chichester (1989), p. 201
- [11] M. Poulain, *Proc. XVIII International Congress on Glass*, 1998, p. 1
- [12] G. Zhang, J. Jiang, M. Poulain, G. Maze, B. Kinsmann, E. Taylor, B. N. Samson and A. Jha, *Proc. XVIII International Congress on Glass*, 1998, p. 31

FLUOROZIRCONATE GLASS MATRIX OBTAINED BY SOL-GEL PROCESS

Orlando da S. Prado^a, Ricardo Fornazari^a, Doroteia F. Bozano^a, Angela S. T. Delben^a
*, José R. J. Delben^a, M. Ionashiro^b

^aDepartamento de Física/Universidade Federal de Mato Grosso do Sul, cx. p. 549, 79070-900,
Campo Grande, MS, Brazil

^bInstituto de Química / UNESP, cx. p. 355-14800-970 Araraquara, SP, Brazil¹

Abstract

Sol-gel process offers some advantages over fusion: glass can be obtained in various geometries, as thin films, and great homogeneity can be achieved for material production. For oxide glasses and ceramics sol-gel method is well developed, but production of fluoride glasses by sol-gel is not well established. In this paper we describe the preparation of precursor gels for fluorozirconate systems, from binary to five component gels. Acetic acid was used as complexing reagent and $\text{NH}_4\text{F}\cdot\text{HF}$ was used for fluorination. ZBLALi glasses with different contents of Li were obtained.

1-INTRODUCTION

The discovery of Heavy Metal Fluoride Glasses [1] had brought out great interest because of their ultra-low intrinsic loss and extended transmission in the infrared region. These properties assure potential applications in many optical devices as fibers for transcontinental telecommunication, fiber laser, optical amplifier and optical windows. The conventional preparation of fluoride glasses by fusion is not suitable to obtain fibers free of impurity as required for telecommunications. The CVD method presents limitations in use for multicomponent fluoride glass preparation due to the great differences of vapor pressure of the various fluorides [2]. Sol-gel may be an alternative for fluoride glass fabrication in various geometries, including planar devices [3], although some problems may be overcome to make possible obtaining glasses with improved quality. To obtain multicomponent system, as the matrix of glasses ZBLAN and ZBLALi, by the sol-gel process, the proper choice of precursors is very important due to homogeneity requirements of precursor solutions. As most metallic alkoxydes are very reactive for hydrolysis and condensation reactions they are the precursors most used. However, they need to be stabilized to avoid precipitation. The chemical control of these reactions is usually provided by the addition of complexing reagents that react with metallic alkoxyde in molecular level leading to new precursors with different structure, reactivity and functionality. The choice of complexing agent and the amount to be used are not unique for all the alkoxydes involved. In this way, the control of respective hydrolysis rates of the various alkoxydes as well as the proper sequence of introducing the divers precursors constitute a limiting stage since precipitation and phase separation must be avoided in order to obtain the oxide matrix of the fluoride glasses by sol-gel process. For compositions containing BaF_2 and LaF_3 , as in the case of ZBLAN and ZBLALi compositions that we have prepared, there is an additional problem: barium and lanthanum alkoxydes are not easily available commercially because they are chemically very instable and/or insoluble

¹ * Corresponding author - e-mail: propp@nin.ufms.br or delben@vip-cgr.com.br, Fax/phone: 55-67-7873093

in organic solvent. So it demands the replacement of alcoxides and we choose barium acetate and lanthanum hydroxide. These changes caused difficulties due to different reactivities of the acetate and hydroxide products related to the alcoxides of zirconium, aluminum, sodium and lithium. For sol-gel process each precursor change or addition implies a specific routine, so even though zirconate matrix has been prepared by other groups [4,5,6], we had to establish our own routine and it was achieved by using acetic acid as complexing agent and starting from binary compositions then ternary, quaternary and finally ZBLAN matrix gel, so that we could determine the best sequence to obtain homogeneous and stable solutions. Also, for ZBLALi we developed our own sol-gel routine and samples were prepared with various lithium concentrations.

2-EXPERIMENTAL

Precursors used were generally alcoxides (zirconium isopropoxide, lithium methoxide, aluminium butoxide, sodium ethoxide), except for lanthanum and barium, they were replaced by lanthanum hydroxide and barium acetate, acetic acid was used to convert lanthanum hydroxide in acetate and as complexing agent.

Gels obtained after drying solution were not constituted of fluoride, so they must be submitted to fluorination procedure to eliminate carbon and oxygen.

Gels were dried at 100 °C, then they were grided and $\text{NH}_4\text{F.HF}$ was added to the powder, the mass of $\text{NH}_4\text{F.HF}$ was twice the mass of gel. The batches were placed in platinum crucible for conventional fluorination at 350 °C and 500 °C for 30 min and one hour, respectively, in air atmosphere.

Melting of the products so obtained were performed in dry box at temperatures of 850 °C - 900 °C, depending on composition.

Gels and glass samples obtained were characterized by Differential Scanning Calorimetry in DSC-50, Shimadzu, under an N_2 atmosphere at 10 °C/min.

3-RESULTS

3.1 - Hydrolysis Rates

Zirconium isopropoxide is the main component and it develops hydrolysis with ambient moisture, resulting in $\text{Zr}(\text{OH})_4$, which is insoluble in water or isopropanol, so this reaction must be controlled in order to get a final homogeneous solution. Acetic acid was used to control the hydrolysis and $R_1 = n^\circ$ de moles of acetic acid/ n° de moles of zirconium alcoxide was varied, while keeping water and isopropanol content constant and gelification time measured, table I.

The complexation efficiency is related to time the solution takes to gelify: the greater the time the more efficient.

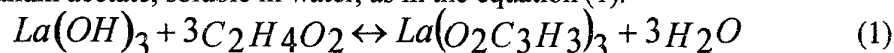
Table 1 shows that $R_1=2.5$ is suitable to control $\text{Zr}(\text{OC}_3\text{H}_7)_4$ hydrolysis rate and it was used in all compositions.

Table 1 - Zirconium isopropoxide gelification times for different molar rate R_1

Molar Rate, R_1	Gelification Time
0.5	5 min (without adding water, only ambient moisture)
1.5	8 min (without adding water, only ambient moisture)
2.5	solution stable for time, water was introduced for hydrolysis to occur

3.2 - Lanthanum Manipulation

Lanthanum hydroxide is insoluble in water and isopropanol, but is soluble in acid and the resulting salt may be soluble in water or isopropanol. The use of acetic acid results in the formation of lanthanum acetate, soluble in water, as in the equation (1):



This equation shows that molar rate, $R_2 = n^\circ$ of moles of acetic acid/ n° of moles of $La(OH)_3$, should be 3 for the complete reaction of lanthanum hydroxide with acetic acid. But acetic acid is a weak acid and the reaction velocity to the right decreases as some lanthanum hydroxide is converted into acetate, then there would be lanthanum hydroxide remaining in the solution and possibly precipitating. So R_2 must be determined, for this we prepared many solutions with different R_2 (Table II)

Table 2-Influence of acetic acid in homogeneity of solution.

R_2	Final solution
27	precipitation
41	precipitation and phase separation
55	homogeneous
103	homogeneous
137	homogeneous
171	homogeneous

R_2 should be equal or greater than 55 to provide homogeneous solution.

Since acetic acid would be used in excess to obtain lanthanum acetate, the remaining acid in the solution was suitable for hydrolysis control of the others components.

Precursors gels were obtained in binary systems (ZL,ZB,ZA), ternary (ZLA, ZLN, ZLB), quaternary (ZBNA) and five component systems (ZBLAN and ZBLALi). Details of preparation of gels of greatest complexity, are presented on Fig. 1. Since proportion of acetic acid must be controlled relating to zirconium isopropoxide, R_1 , and lanthanum hydroxide, R_2 , generally these two compounds were put in the solution in the beginning, so that the acetic acid added to them is used to stabilize the solution. The association of lanthanum hydroxide + barium acetate may also be included in the solution in the final stage.

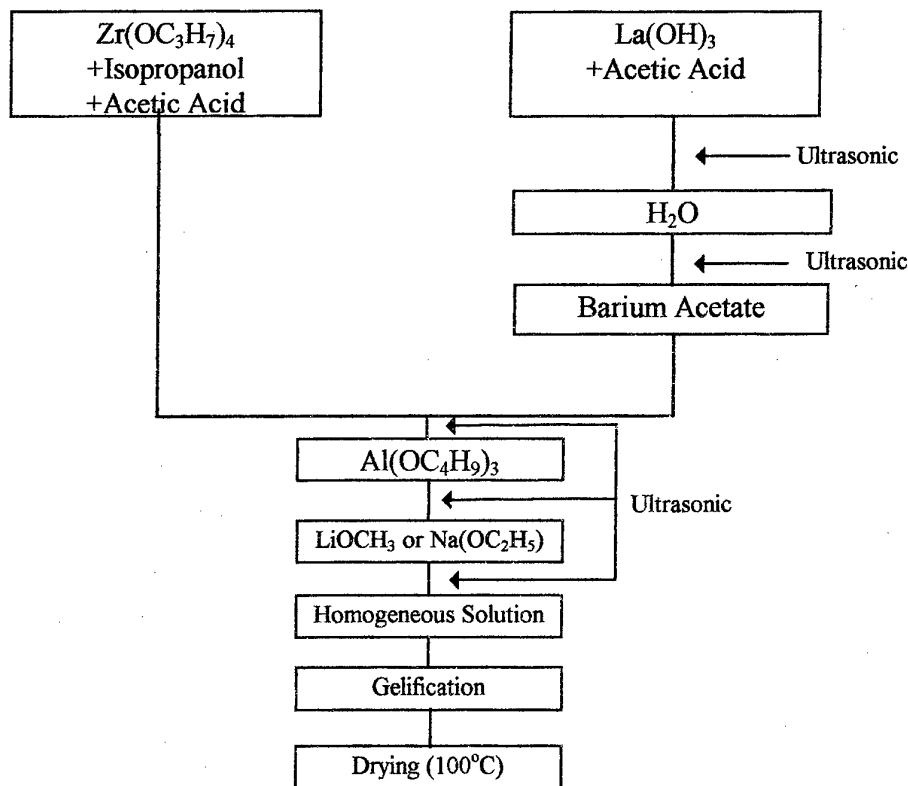


Fig. 1 - Diagram of preparation of five component precursor gels ZBLAN or ZBLALi. $R_1 = 2.5$ and $R_2 \geq 55$.

Gels of compositions ZBNA (57 Zr, 20 Ba, 3 Al, in mol%) ZBLAN (53 Zr, 20 Ba, 4 La, 3 Al, 20 Na), ZBLALi (47 Zr, 14 Ba, 5 La, 4 Al, 30Li ; 47 Zr, 8 Ba, 2 La, 3 Al, 40Li and 50 Zr, 20 Ba, 21 Li, 5 La, 4 Al) (for simplicity we represented only cations of compounds) were fluorinated and then melted. Gels containing Na couldn't be converted into glasses. Glasses of ZBLALi₃₀ composition, containing 30% of LiF, with different amount of acid acetic were obtained. Fig. 2 is a DSC curve for one sample, characteristics temperatures beeing $T_g=224^\circ\text{C}$, $T_x=294^\circ\text{C}$ and $T_p=304^\circ\text{C}$.

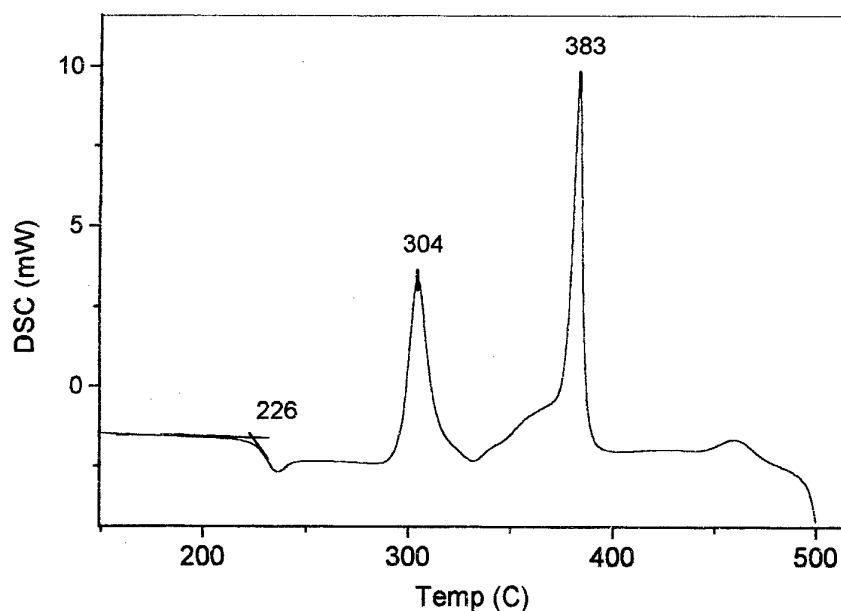


Fig. 2 - DSC curve of a ZBLALi₃₀ glass, obtained by sol-gel method.

4-CONCLUSIONS

Precursor gels for multicomponente fluorozirconate glasses were prepared, using acid acetic as complexing agent. NH₄F. HF was used for fluorination. ZBLALi glasses were obtained while the procedure was not proper to prepare glasses containing sodium.

REFERENCES:

- [1] M. Poulain, J. Lucas, Verre Réfract. 32 (1978) 276.
- [2] R. M. Almeida, P.J. Morais, J. Non-Cryst. Sol. 184 (1995) 93.
- [3] J. Ballato, R. E. Riman, E. Snitzer, J. Non-Cryst. Sol. 213&214 (1997) 126.
- [4] M. Dejneka, R. E. Riman, E. Snizer, J. Am. Ceram. Soc. 76 (1993) 3147.
- [5] J. Eamsiri, A.Elyamany, R. E. Riman, J. Non-Cryst. Sol. 163 (1993) 133.
- [6] P. J. Melling, M. Thomson, J. Mater. Res. 5 (1990) 1092.

SnO₂ CERAMIC CRUCIBLE FOR FLUORIDE GLASSES MELTING

R. Lebullenger¹, J.A. Cerri², I.M.G. dos Santos², A.C. Hernandez¹, E.R. Leite², E. Longo²

¹IFSC - Universidade de São Paulo - P.O 369 - 13560-970 São Carlos - Brazil

²LIEC - Universidade Federal de São Carlos - P.O.676 - 13565-905 São Carlos - Brazil

lebullen@ifsc.usp.br

ABSTRACT

Heavy metal fluoride glasses present a better optical transparency in the infrared region than silica based glasses. So, they have great potential as optical display devices for infrared applications (optical amplifiers, laser hosts, laser fibres, sensors, remote thermometry, etc.). The synthesis of high quality fluoride glasses for optical devices requires an extensive raw material purification and a drastic control of the all fusion process. To reduce crucible contamination, are commonly used platinum or vitreous carbon crucibles. In this work, were tested SnO₂ ceramic crucibles presenting a very low porosity (<0,5%). These crucibles were obtained by conventional slip casting and sintered at 1300 °C during 4 hours in air ambient. Various 10 grams batches of fluorozirconate glasses were melted in this SnO₂ ceramic crucible during one to four hours under controlled atmosphere. The low interaction between the crucible and the fused glass was evaluated by thermal (DSC) and optical technique. EPR analysis showed presence of manganese used as dopant for crucible preparation. However, chemical analysis by atomic absorption of the prepared glasses revealed that the manganese contamination level was about few ppm. SEM observation of the intern surface crucible was also realized.

INTRODUCTION

As well known since more than twenty years⁽¹⁾, heavy metal fluoride glasses present a good transmission window from UV up to the medium infrared and they allow to reach values of theoretical optical losses among 10^{-2} to 10^{-3} dB/km for wavelengths located between 2 and 4 μ m. However, the best results published are 0,45 dB/km for a 60 meters in length fiber⁽²⁾. Several factors limit the transparency of the fluoride glasses, as light absorption and/or its scattering by internal defects⁽³⁾. One of these scattering defects in the glass is crucible particles⁽⁴⁾. For platinum crucibles, oxygen can react with Pt to form PtO/PtO₂ that vaporizes for temperatures above 550°C. This material can incorporate the liquid glass after condensing in a colder area of the crucible⁽⁵⁾. On the other hand, the use of vitreous carbon crucible is limited when it is necessary to work under oxidizer atmosphere to avoid, for example, the reduction⁽⁶⁾ of Zr⁴⁺ in Zr³⁺ or In³⁺ in In²⁺ or In⁺. Another problem is the fluoride glasses synthesis involving a specific rare earth (Nd, Er, Yb and Tm), so, a drastic cleaning of the platinum crucible is necessary to avoid posterior contamination. The high price of these platinum crucibles does not allow to use a different crucible for each glass type. The SnO₂ ceramic crucible was already tested with success for the synthesis of heavy metal oxide glasses⁽⁷⁾, and in this work, we report the results obtained for the synthesis of fluorozirconate glasses.

EXPERIMENTAL PROCEDURE

Crucible preparation

Ceramic crucible were prepared by slip-casting using mold of plaster of Paris. The slurry is a mixture of SnO_2 (99.8% - CESBRA) with 0.5 mol% of MnO_2 (>99% - Aldrich), water and dispersing agent. Green crucibles were dried at 100°C for 12 hours and, then, sintered at 1300°C for 4 hours. The addition of MnO_2 helps the SnO_2 densificação, reaching densities up to 99,5% in relation to the theoretical⁽⁸⁾. Crucibles treated at 1300°C are named T1. A complementary heat treatment was performed on some T1 crucibles to reduce manganese content, they are named T2.

Glass synthesis

Raw materials were fluoride salts of high purity, such as ZrF_4 , BaF_2 , LaF_3 , AlF_3 , NaF and PbF_2 , supplied by BDH-Merck UK. The glass composition was (mol.%): 52 ZrF_4 - 28 BaF_2 - 4,5 LaF_3 - 3,5 AlF_3 - 10 NaF - 2 PbF_2 .

All the operations involved for the glass preparation were accomplished in a glove boxe with a controlled atmosphere. Initially, the necessary amounts for the synthesis of 10 grams glass were weighted and placed in the T1 and T2 crucibles. The mixture was gradually heated up to 800°C in an electric furnace. An affining step is necessary to obtain a good homogeneity of the liquid glass. Various affining duration steps (1,2,3 and 4 hours) were performed. Then, the liquid glass was poured in a brass mold preheated at about 260°C , and the annealing time was about 2 hours.

RESULTS & DISCUSSION

Glass samples

The ZBLANPb glass samples are denominated T1-x and T2-x, samples refined at 800°C during x hours, (x = 1, 2, 3 or 4) in crucible T1 and T2 respectively.

Thermal analysis

The thermal analysis of each sample is performed by DSC using a 2090 TA Instruments equipment with an heating rate of $10^\circ\text{C}.\text{min}^{-1}$. In the Table 1 are summarized the characteristic temperatures and calculated stability factors⁽⁹⁾ of the prepared T1-x samples with an accuracy of $\pm 1.5^\circ\text{C}$. (glass transition temperature (T_g), onset of crystallization temperature (T_x), crystallization peak maximum temperature (T_p))

Table 1: - Characteristic temperatures and stability factors

Name	T_g ($^\circ\text{C}$)	T_x ($^\circ\text{C}$)	T_p ($^\circ\text{C}$)	$T_x - T_g$ ($^\circ\text{C}$)	S ($^\circ\text{C}$)
T1-1	286	356	406	70	12,2
T1-2	283	358	407	75	13,0
T1-3	285	358	415	73	14,6
T1-4	286	355	411	69	13,5

We can note that the refining time at 800°C does not influence the glass stability, that is to say, (Tx-Tg) and S did not show any tendency. The same comportement is observed for the T2-x glass samples. These characteristic temperatures are the same as those obtained for samples prepared in the same conditions in platinum crucible.

Optical properties

UV-Visible transmission characterization of the glass samples (3 mm thick) were performed with a spectrophotometer Cary17. The infrared spectra were measured by using FTIR spectrophotometer Nicolet 850. The influence of melting ZBLANPb glass in SnO₂ crucible on its transparency window was evaluated between 200 and 10000 nm (Figure 1).

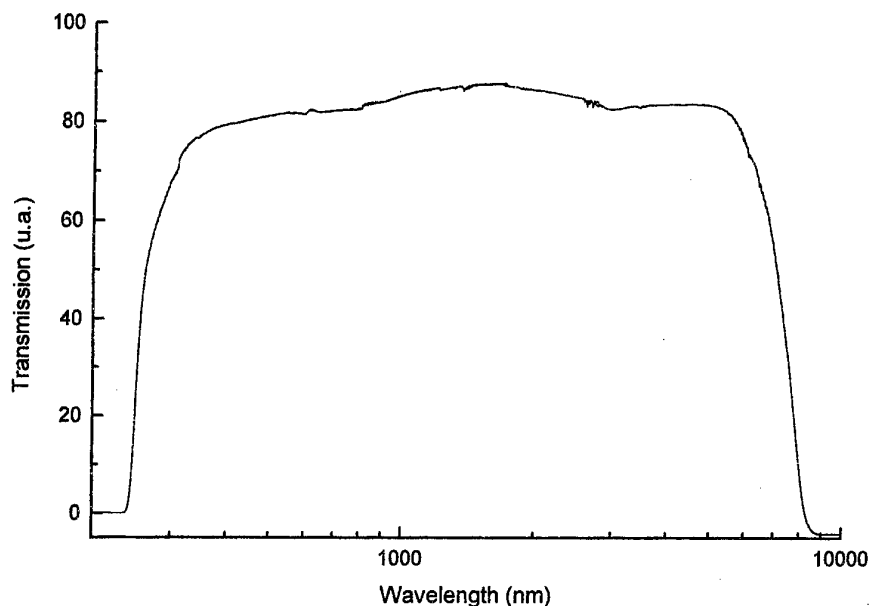


Figure 1: Transmission spectra of T1-4 sample in the UV-Visible-IR region

No appreciable characteristic bands due to the presence of Sn, Mn or O₂ were detected in the transmission window of the T1-4 prepared glass (4 hours melt at 800°C). In particular, Mn²⁺ holds an absorption band centred in 390nm⁽¹⁰⁾, which does not appear in our case.

EPR Analysis

EPR spectra were recorded at room temperature on spectrometer operating at x-band frequencies with a field modulation of 90 kHz. The microwave frequency was typically set at 9.6 GHz. The figure 2 shows a six-lines hyperfine structure due to the presence of Mn²⁺ ions in an environment close to octahedral symmetry. Similar EPR spectra have been reported in others fluoride glasses^(11, 12).

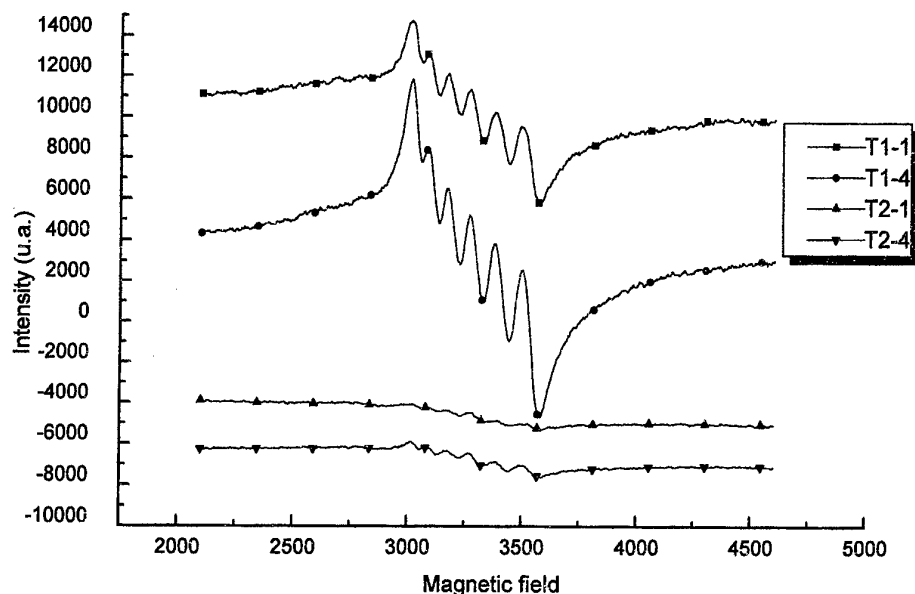


Figure 2: EPR spectra of ZBLANPb glasses melted 1 and 4 hours in T1 and T2 SnO₂ crucibles.

Glass composition analysis

The results obtained by EDX and X-ray fluorescence did not highlight the presence of Sn or Mn in the prepared vitreous material. We can suppose that their atomic concentrations are below the detection limit. Therefore, atomic absorption was used because it is an analytical technique efficient to measure contaminant presence at very low concentration. For the sample preparation, it was necessary to dissolve the T1-x and T2-x glasses in a solution of HCl and H₃BO₃ using H₂O milliQ. To avoid external contamination, pieces of PTFE and Teflon vessels were used. The equipment was an atomic absorption spectrophotometer GEMINI - INTRALAB AA12/1475. The table 2 summarizes the obtained results.

Table 2: Results of the analysis by atomic absorption

Sample	Mass (g)	Mn in the Glass (ppm wt.)
T1-1	0,153	63,5
T1-4	0,627	123,7
T2-1	0,480	9,7
T2-4	0,495	15,6

It can be observed that the amount of Mn present in the glasses elaborated in SnO₂ ceramic crucible is low, that is to say of the order of 100ppm. It can be noticed that the time of affining, or contact with the crucible, influences the amount of manganese which increases with the affining duration. For the glass melted during 4 hours (T2-4) in T2 type crucible, the manganese content is lower than 20ppm wt.

Crucible Characterization

After the synthesis of the two glass series T1x and T2x, with $x = 1, 2, 3$, and 4, it was observed a color change in the internal face of the crucible T1, indicating the possible elimination of the MnO_2 from SnO_2 ceramic. However, after an optical microscopy observation, no discernable alteration of the internal wall that was in contact with the melted glass was observed.

A transversal cut of the crucible (cf inserts in figure 3a and 3b) was performed for analysis by SEM using a ZEISS DSM 940A equipment. For the internal part, which was in contact with the melted glass, the fracture happens in way predominant intergranular, as showed in the Figure 3a. For the external part, that didn't suffer contact with the liquid glass, the fracture followed intragranular way, in agreement with figure 3b.

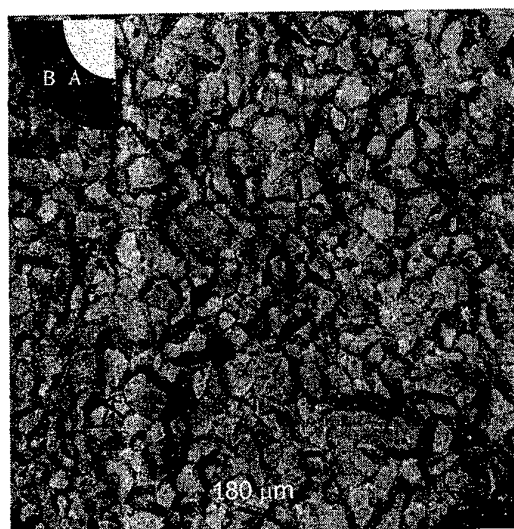


Figure 3: Internal part of the crucible wall (partA)



Figure 4: External part of the crucible wall (partB)

CONCLUSION

The melting of fluorozirconate glasses in dense SnO_2 ceramic crucible, did not prejudice the quality of the prepared vitreous samples compared with conventional platinum or vitreous carbon crucibles. The techniques involved to characterize the glasses and the crucible did not highlight any contamination of each one which prejudices both of them. For T2 type crucible, the higher Mn^{2+} contamination concentration does not ultrapass 20 ppm after 4 hours melting. Therefore, dense SnO_2 ceramic crucibles can be considered as an alternative support for the fluoride glasses research and fabrication. The low cost of this crucible permit the use of one crucible for one type glass preparation.

ACKNOWLEDGEMENTS

Brazilian financial agency, CNPq, FAPESP and FINEP for financial support
R.W.A.Franco (IFSC-USP) for E.P.R measurements,
J. Araujo (DQ-UFSCar) for atomic absorption analysis.
F. L. C. Rangel (LIEC- UFSCar) for SEM observation.

REFERENCES

- (1) M.Poulain, M. Poulain, J. Lucas, P. Brun, Mat. Res. Bull., 10, (1975), 243
- (2) D. Szebesta, S.T. Davey, J.R. Williams and M.W. Moore, J. Non-Cryst. Solids 161 (1993) 18
- (3) P.W. France, M.G. Drexhage, J.M. Parker, M.W. Moore, S.F. Carter and J.V. Wright, *Fluoride Glass Optical Fibres* (Blackie, London 1990) 132
- (4) M. Robinson, R.C. Pastor, R.R. Turk, D.P. Devor, M. Braunstein and R. Braustein, Mater. Res.Bull., 15 (1980) 735
- (5) G. Lu, I. Aggarwal and J.P. Bradley, J. Am. Ceram. Soc., 71 (3) (1988) C156-C157
- (6) S.F. Carter, P.W. France, M.W. Moore and E.A. Harris, Phys. Chem. Glasses, 28 (1987) 22
- (7) J.A. Cerri, I.M.G. Santos, E. Longo, E.R. Leite, R.M. Lebullenger, A.C. Hernandez, J.A. Varela, J. Am. Ceram. Soc. 81 (3) (1998) 705
- (8) J.A. Cerri, E.R. Leite, E. Longo and J.A. Varela, J. Am. Ceram. Soc. 79 (3) (1996) 799
- (9) M. Saad and M. Poulain, Mat. Sci. Forum 19-20 (1987) 11
- (10) L. N. Feuerhelm, S. M. Silbey and W.A. Silbey, J. of Solid State Chemistry 54, (1984) 164-169
- (11) B. Sreedhar, C. Sumalatha, K. Kojima, J. Non-Cryst. Solids 192-193 (1995) 203
- (12) C. Legein, J.Y. Buzaré, C. Jacoboni, J. Non-Cryst. Solids 161 (1993) 112

EFFECT OF OXIDE DOPING ON FLUOROHAFNATE GLASS LUMINESCENCE

S.Batygov, L.Dmitruk, L.Moiseeva, N.Vinogradova

General Physics Institute, Russian Academy of Sciences, Vavilov str.38, Moscow
117947, Russia

L.Popov

Lebedev Physical Institute, Russian Academy of Sciences, Leninsky pr., 53,
Moscow 117947, Russia

ABSTRACT

The X-ray excited luminescence of scintillating fluorohafnate glasses doped with different oxide compounds was investigated. The concentration of oxide compounds, added to the batch was in the 0.1-1.0 mol% range. The oxide addition resulted in many cases in the appearance of a broad luminescence band peaked at 360 nm, with lifetime ~ 12 ns. This band is found to be not connected with the presence of Ce^{3+} activator. So it can be attributed to structure defects induced by oxygen impurity, most probably to either O^{2-} ion substituting for F^- ion or F^- vacancy.

INTRODUCTION

Fluoride scintillators, glasses as well as crystals, always contain some amount of oxygen impurity depending on the purity of raw fluorides and the conditions of synthesis. Oxygen impurity can affect the luminescence yield and spectral characteristics of Ce-doped fluoride scintillators [1,2].

In this report the effect of different oxide additives on X-ray luminescence of HfF_4 - BaF_2 - CeF_3 (LaF_3)- AlF_3 - NaF - InF_3 glasses was investigated.

EXPERIMENTAL

At the initial stage two basic fluorohafnate batches were prepared: CeF_3 -containing batch (51.5HfF_4 - 20BaF_2 - 5CeF_3 - 2.5AlF_3 - 20NaF - 1InF_3) and LaF_3 -containing batch (52.5HfF_4 - 20BaF_2 - 4LaF_3 - 2.5AlF_3 - 20NaF - 1InF_3).

The glasses were melted in a glass carbon boat under Ar atmosphere. Then the glasses were powdered. The powders were used to prepare glass samples (~ 1.5 g) doped

with oxide compounds. Oxides (Ce_2O_3 , CeO_2 , La_2O_3) and complex oxides (BaCe_2O_4 , CeAlO_3 , Ce_2SiO_5 , $\text{Hf}_2\text{Ce}_2\text{O}_7$, CePO_4 , CeTaO_4 , $\text{Ce}_2(\text{WO}_4)_3$) with 0.1-1.0 mol% concentrations were added.

A series of glasses of different compositions was synthesized simultaneously in the sockets of a carbon boat under Ar flow. The glasses were melted at 840-860 °C for 60 min and then cooled to 620 °C. Then the boat was removed from the furnace and quenched at a fixed cooling rate.

Polished glass samples were used to measure X-ray excited luminescence spectra in 200-600 nm range. In some cases the light yield and decay time were measured.

RESULTS AND DISCUSSION

The typical X-ray excited luminescence spectra of CeF_3 - and LaF_3 - containing glasses doped with oxides are shown in Fig.1.

Only one band peaked at 310 nm, corresponding to 5d-4f transition of Ce^{3+} ion in fluorides, is present in the spectrum of CeF_3 - containing glass (curve 1). Appearance of an another band, centered at 360 nm is the characteristic feature of glasses doped with oxides (curve 2). The effect of oxide doping on the luminescence spectra is dependent on the kind and concentration of oxide added as well as on the Ce/O ratio. From oxides studied, the compounds of Ce_2O_3 with oxides of II, III, and IV groups show similar effect. In the case of CePO_4 the 360 nm band is less intense. The glasses doped with CeTaO_4 and $\text{Ce}_2(\text{WO}_4)_3$ do not show luminescence.

The luminescence spectra of LaF_3 -containing glasses, doped with different Ce concentrations at the same oxygen concentration are shown in Fig.2. One can see that at low Ce concentration, the 360 nm band is more intense than the 310 nm one. With increasing Ce content the intensity of 310 nm band increases while that of the 360 nm band decreases. As a result, at 0.5 at% Ce the 310 nm band dominates the emission spectrum. Such behavior of the 360 nm band does not agree with assumption that it is related with Ce^{3+} ion in the vicinity of defect sites. Moreover, the total luminescence intensity in oxide doped samples is comparable with that of the "standard" CeF_3 -containing glass (5 mol%) although the Ce concentration in oxide doped LaF_3 -containing glass is 10-100 times less than that of the CeF_3 -containing glass (Table 1). Relatively high luminescence intensity of glasses with small Ce^{3+} content contradicts

with known data on the CeF_3 concentration dependence of the light yield in fluorohafnate glasses [3]. It suggests the existence of some other luminescence centres in addition to Ce^{3+} in oxide doped fluorohafnate glasses.

To check this supposition the X-ray excited luminescence of oxide doped Ce-free glasses was studied. Luminescence spectra of such glasses are shown in Fig.3. It is evident that the 360 nm band appears in the absence of Ce^{3+} ions in the glass. So the defects of glass formed in the presence of oxygen rather than Ce^{3+} ions are the cause of the 360 nm band. The oxygen ions in the F^- sites or F^- vacancies may be responsible for this band. Luminescence decay times of some oxide doped Ce-free glasses for the time interval of 1 μs was measured. Slowly decaying components are absent in this time interval. Decay curve of oxide-doped Ce-free glass in comparison with Ce-containing glass is shown in Fig.4. It is evident that lifetime of «defect» centers is considerably shorter than that of Ce^{3+} ions.

In Table 1 the light yields of some kinds of fluorohafnate glasses under γ -excitation are presented.

Table 1.

Light yield of fluorohafnate glasses doped oxides under γ -excitation.

Glass composition	Additive	Light yield, %NaI (TI)
51.5HfF ₄ 20BaF ₂ 5CeF ₃ 2.5AlF ₃ 20NaF1InF ₃	none	0.64
«	0.2-0.3 mol% Ce ₂ O ₃	0.72
52.5HfF ₄ 20BaF ₂ 4LaF ₃ 2.5AlF ₃ 20NaF1InF ₃	0.2-0.3 at%Ce ₂ O ₃ or (silicate, aluminate)	0.46
«	0.3 mol% La ₂ O ₃ or (HfO ₂ , BaO)	0.42

CONCLUSION

The effect of oxygen impurity on the X-ray excited luminescence spectra of scintillator fluorohafnate glasses was investigated. The oxide doping of fluorohafnate glasses results in the appearance of the broad emission band at 360 nm with short decay time

~12 ns. The band is attributed to structure defects induced by oxygen, either O^{2-} ion substituting for F^- ion or F vacancy. The shift of luminescence band to long wavelength and short decay times of luminescence are promise properties of such glasses. Subsequent detailed investigations must show prospect of Ce-free fluorohafnate glass as fast scintillator.

ACKNOWLEDGMENTS

This work was supported by ISTF grant 256. We like to thank Prof. Yu.Voronko (GPI, Moscow) as well as Prof. R.Brown (RAL, Oxford) and Dr. J.Parker (Sheffield University) for help.

REFERENCES

1. A.J. Wojtowich et. al. IEEE Trans Nucl. Sci. NS-39 (1992) 494.
2. L. Dmitruk et. al. Journ. of Non-Crystalline Solids 213-214 (1997) 311-314.
3. P.R. Hobson et. al. Proceeding of the International Conference on Inorganic Scintillators and their Applications, Delft, The Netherlands, August 1995, 317-324.

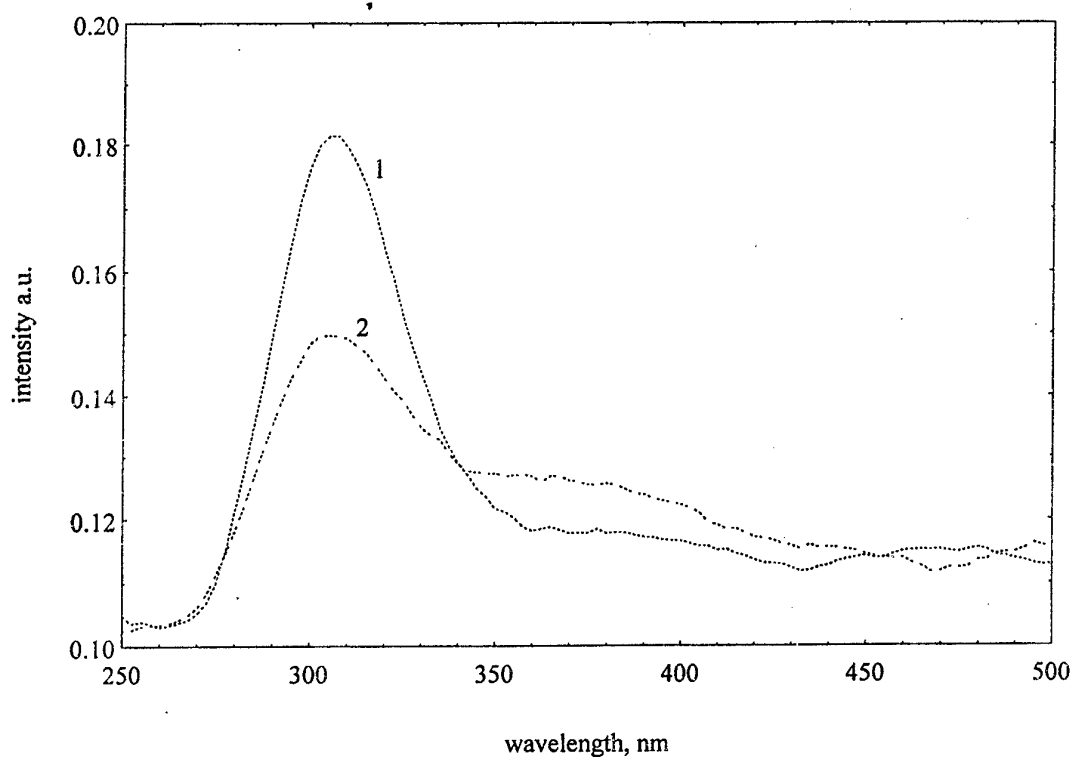


Fig.1 X-ray excited luminescence spectra of fluorohafnate glasses: 1- CeF_3 containing glass (5 mol% CeF_3); 2 - LaF_3 containing glass doped with 0.5 mol% Ce_2O_3 .

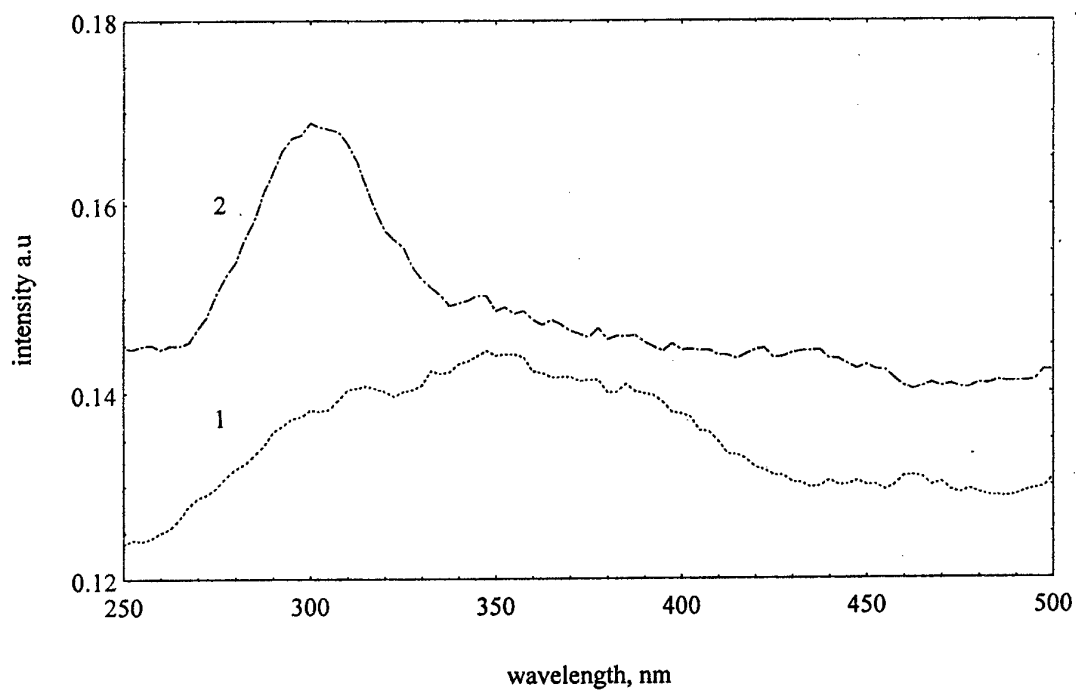


Fig.2 X-ray luminescence spectra of fluorohafnate glasses: 1- LaF_3 containing glass doped with 0.5 mol% $\text{Y}_{1.8}\text{Ce}_{0.2}\text{SiO}_5$; 2 - LaF_3 containing glass doped with 0.5 mol% Ce_2SiO_5 .

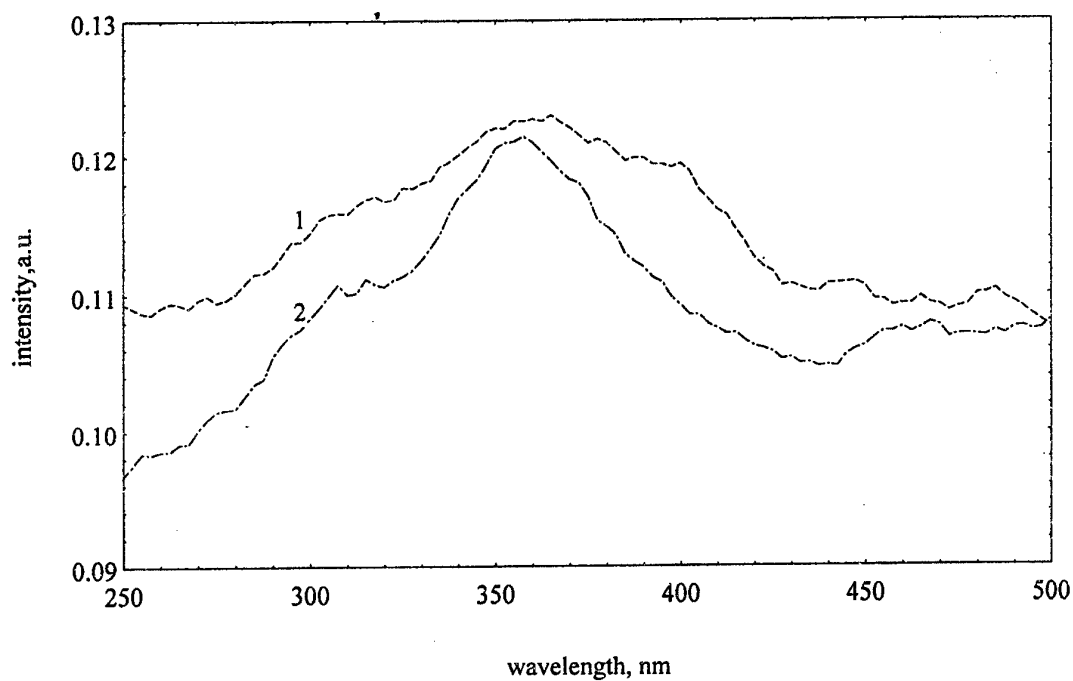


Fig.3 X-ray luminescence spectra of fluorohafnate glasses; 1- LaF_3 containing glass doped with 0.3 mol% HfO_2 ; 2- LaF_3 containing glass doped with 0.3 mol% La_2O_3 .

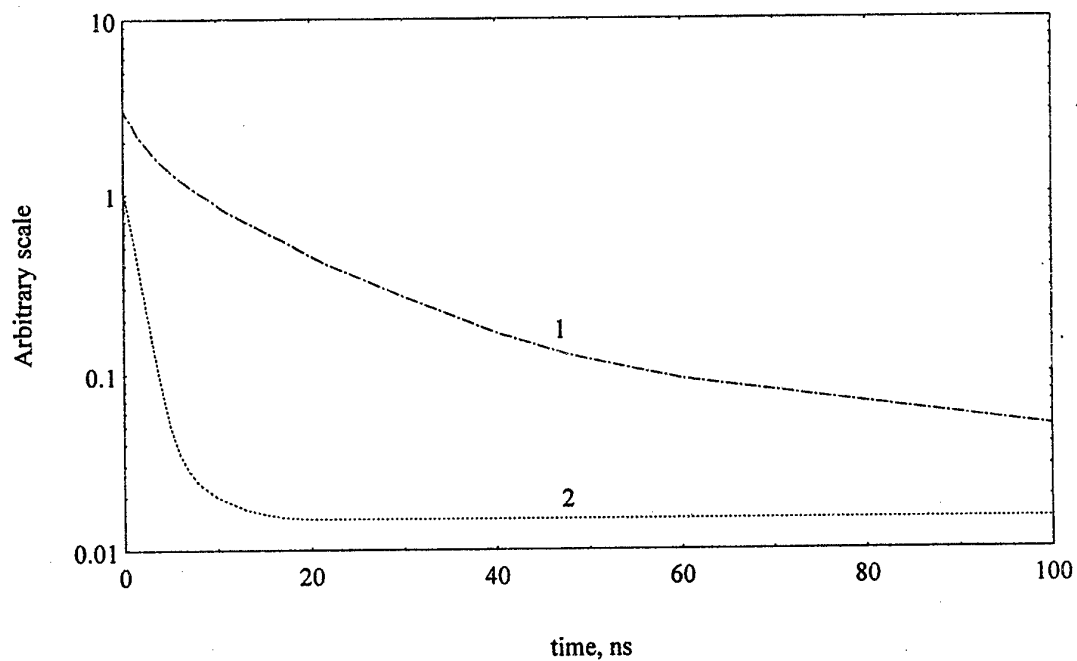


Fig.4 Decay time curves; 1 - CeF_3 -containing fluorohafnate glass with 5 mol% CeF_3 ; 2- LaF_3 -containing fluorohafnate glass with 0.3 mol% La_2O_3

ENHANCED RARE EARTH SOLUBILITY IN AS-S GLASSES

Michael Scheffler, Johannes Kirchhof, Jens Kobelke and Anka Schwuchow

Institut für Physikalische Hochtechnologie e.V. Jena
Department of Modern Optics, Helmholtzweg 4, 07743 Jena, Germany.
email: scheffler@main.ipht-jena.de

ABSTRACT

Since the beginning of this decade there are numerous activities in research and development of rare earth containing chalcogenide glasses and multi and singlemode fibers for 1.3 μm amplification. Compared to the fluoride glasses, the higher fluorescence lifetime of the Pr^3G_4 level and the higher refractive indexes of these glasses lead to a 3 to 4 times higher gain coefficient. First TAWARAYAMA [1] demonstrate the superiority of the chalcogenide glasses in the Ga-Na-S glass system.

The main problem in the field of chalcogenide glasses is the thermal behaviour in contrast to the rare earth solubility: glasses showing a good glass stability during thermal treatment and fiber drawing have a poor rare earth solubility [2] and glasses having a good rare earth solubility tend often strongly to crystallize [3, 4], resulting in high fiber losses. To overcome this contrast many groups are engaged with the modification of several chalcogenide glasses [5-9].

The arsenic sulfide glass possesses good thermal stability and mechanical and chemical durability. However, the rare earth solubility in pure As_2S_3 glass is only up to a few tens ppm. Higher contents cause crystallization and unacceptably high losses [2]. By co-doping of arsenic sulfide the rare earth solubility can be raised drastically maintaining the excellent glass stability and the mechanical and chemical properties [9].

Pure Pr^{3+} doped As-S glass, Ge, Ga and Ge/Ga co-doped As-S glasses were prepared by conventional melting procedure in evacuated and sealed quartz glass ampoules from high purity elements (7N As, Ga, Ge and 5N sulfur) and/or sulfides at 800...1.000°C for 12...24 hours in a rocking furnace, followed by air cooling.

From the chalcogenide glasses small parallel disks with 1...5 mm thickness were prepared and characterized by FTIR spectroscopy. Phase separation was investigated by XMA, SEM and light microscopy. Unstructured, uncladded testing fibers have been drawn by the crucible method. These fibers were characterized by attenuation measurements and spectral and time resolved fluorescence.

In previous studies we found gallium as an excellent co-dopant for praseodymium. To investigate the influence on fiber loss and crystallization behaviour we fixed the Pr content to 300 and to 600 ppm and varied the codopant / praseodymium ratio from 6 up to 20. Figure 1 shows fiber losses in dependence on the Ga content.

Without gallium $\text{Pr-As}_2\text{S}_3$ glass fibers show unacceptably high loss already with small Pr contents, combined with a weak absorption tail caused by crystallization effects and hetero phase separation. By introducing a small amount of Ga the loss decreases drastically. Increasing the Ga/Pr ratio, the loss decreases, passing a minimum at a Ga/Pr ratio of about 10...14 and rises again by further increasing the Ga content.

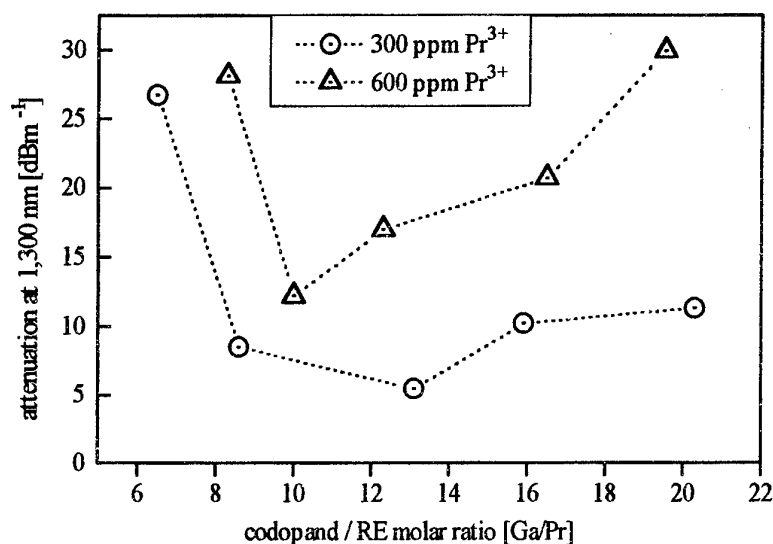


figure 1: fiber loss of Ga co-doped As_2S_3 glass fibers containing 300 and 600 ppm of Pr (the dot lines are guides to the eyes)

The significant higher loss minimum in the sample doped with 600 ppm Pr^{3+} points at a limit of the Pr doping concentration in arsenic sulfide glass. Attenuation minimum values at $1.3 \mu\text{m}$ amount about 4 and 10 dBm^{-1} for the 300 and 600 ppm Pr^{3+} containing Ga- As_2S_3 samples respectively. A further decrease of the loss can be achieved by adding germanium as a second co-dopant. Best arsenic sulfide fibers containing Ga and Ge show loss values of about 1.5 dBm^{-1} like shown in [10].

In fluorescence investigation under excitation at 1,017 nm by using a Ti:sapphire laser a shift of the emission peak from about 1,350 nm on Pr- As_2S_3 to 1,336 nm on Ga and Ga/Ge co-doped fibers could be observed. In Ga co-doped fibers with rising the Ga/Pr ratio a narrowing of the line width (FWHM) from about 80 to 65 nm is noticed. The fluorescence lifetimes of the $^1\text{G}_4$ level are of about 200...250 μs .

The RE solubility not only depends on the kind and concentration of the co-dopands. Moreover, the impurities of the starting elements, namely the -SH and the -OH content markedly influence the glass formation and glass stability.

For investigations of the -SH and -OH influence on the glass properties the glass composition was fixed at $\text{As}_{37.8}\text{Ge}_{1.3}\text{Ga}_{0.5}\text{S}_{60.4}$ containing 760 ppm Pr^{3+} . The concentrations of -OH and -SH were determined by FTIR spectroscopy using the $3.0 \mu\text{m}$ absorption band for -OH [11] and the $4.0 \mu\text{m}$ absorption band for the -SH [12]. The concentration of -OH and -SH impurities are in the range of 0.....4 and 30.....1,650 ppm respectively. In table 1 three glass pairs containing equal -OH and different -SH concentrations (D 112-D 091, D 113-D 083 and D 087-D105) are compared. Additionally, table 1 shows a sample containing a medium -OH and a medium -SH concentration (D 111). Surprisingly we found in all samples with equal -OH content or -OH free samples lower attenuation values at the higher -SH level. The lowest loss was obtained on fibers without -OH and about 1,650 ppm -SH (table 1, D 103 and also fig.2.). Samples with both, -OH and -SH in medium concentrations appear as opaque glasses, resulting in a high attenuation (D 111).

table 1: loss values at 1,300 nm on -OH and -SH containing As-Ge-Ga-S samples

sample	Pr [ppm]	OH [ppm]	SH [ppm]	Loss [1,300]
D 112	754	2.8	522	5.0
D 091	773	2.8	338	23.5
D 113	754	1.4	510	2.0
D 083	776	1.4	335	27.6
D 087	778	1.0	341	10.5
D 105	780	1.0	63	37.0
D 111	780	270	850	> 70

The presence of -SH furthermore influences the fluorescence lifetime. In figure 2 the lifetime of the Pr 1G_4 level (and the attenuation measured on -OH free samples) in dependence on the -SH concentration is shown. The lifetime rapidly decreases with the increase of the -SH content from about 250 μ s in the sample containing 35 ppm -SH to 170 μ s in the sample containing 1,650 ppm -SH.

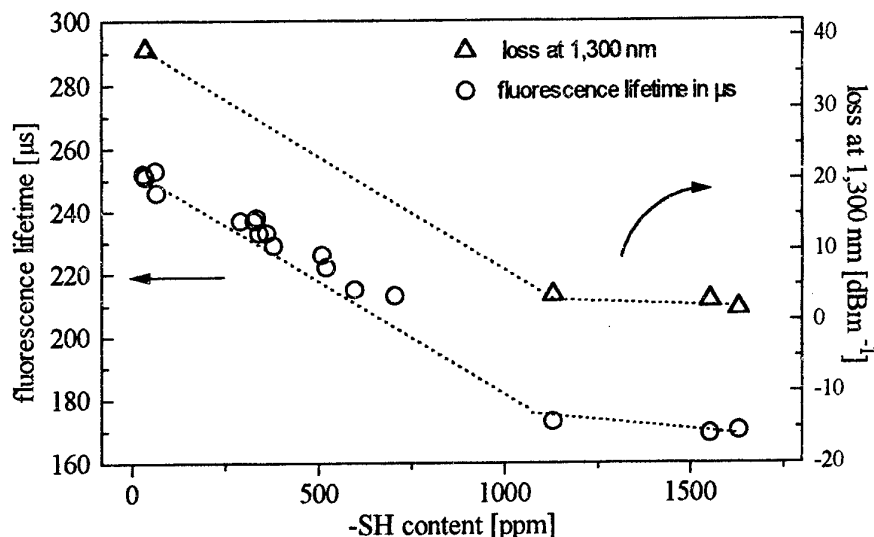


figure 2.: influence of the -SH concentration on fluorescence lifetime and loss in Ga/Ge co-doped As₂S₃ glasses (760 ppm Pr³⁺)

From the results of the fluorescence, loss and impurity measurements a model of the glass formation is developed and presented in fig.3. The model is based partly on facts mentioned above and partly on ideas of the glass formation in this system. It is necessary to support the first given interpretation by additional investigations. A helpful tool for clearing up the role of the -OH and the -SH groups is the 1H -MAS-NMR spectroscopy.

It is assumed, the glass consists of two glass forming regions: the first one is the usual arsenic sulfide glass (region A). This region is disturbed by the introduced gallium and praseodymium. From Ga₂S₃ and Pr₂S₃ the formation of crystals in a wide composition range is well known. This components form the second region (region B). The interaction of gallium sulfide and praseodymium sulfide is indicated by the line narrowing of the fluorescence peak by increasing the Ga/Pr ratio.

During thermal treatment (e.g. fiber drawing) the region B strongly tends to crystallize and causes high fiber loss. In presence of -SH in a sufficient amount the formation of Ga_2S_3/Pr_2S_3 mixed crystals will be avoided and the Ga_2S_3/Pr_2S_3 aggregates remain in the former state (amorphous or nano crystalline). For that, two mechanisms are discussed: the -SH groups are located in the region B and cause a link to sulfur from the region A via H-bond, or they cause an inter and intra aggregate push off. This effect changes the distance between the aggregates in such a way, that crystallization can not occur.

The germanium is able to form glasses with both, As_2S_3 and the Pr_2S_3/Ga_2S_3 . Here it acts as an "interlinker" between the both glass regions. By this effect the rare earth aggregates (region B) are fixed additionally on the region A.

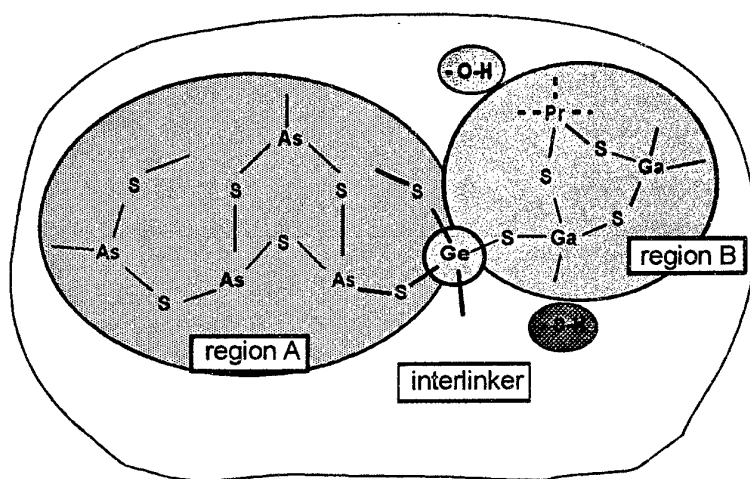


figure 3: drawing of the glass forming model in Ga/Ge codoped $Pr-As_2S_3$ glass

The disadvantage of these glass stabilization is the decrease of the fluorescence lifetimes. Otherwise, it is imaginable, that this effect also can be reached by the stronger interaction of -OH groups and a reduced amount of -SH groups. Here a fine tuning of this additional components is necessary.

We have shown that it is possible to increase the Pr^{3+} solubility in arsenic sulfide by co-doping with gallium and germanium up to a suitable level for optical active applications. Not only the co-dopants gallium and germanium are necessary, also the impurities play an important role. Mainly the -SH groups are responsible for the well distributed rare earth aggregates in a non or precrystalline state in the As_2S_3 matrix glass. By co-doping with Ga, Ge and thiol and / or hydroxyl containing substances the preparation of further rare earth element containing As-S glasses seems possible.

REFERENCES

- [1] H. Tawarayama, E. Ishikawa, K. Itoh, H. Aoki, H. Yanagita, K. Okada, K. Yamanaka, Y. Matsuoka and H. Toratani,
Proc. of the Int. Conf. on Optical Amplifiers and their Applications,
July 21-23, 1997, Victoria BC, Canada, Post Deadline Paper PD1-1

- [2] Y. Ohishi, A. Mori, T. Kanamori, K. Fujiura, S. Sudo,
Appl. Phys. Lett. **65** (1) (1994) 13
- [3] D.R. Simons, A.J. Faber, H. de Waal
Optics Letters **20** (5) (1995) 468
- [4] Y. Meresse, G. Fonteneau, J. Lucas
J. Non-Cryst. Solids **184** (1995) 254
- [5] J.A. Meideiros Neto, E.R. Taylor, B.N. Samson, J. Wang, D.W. Hewak, R.I. Laming,
D.N. Payne, E. Tarbox, P.D. Maton, G.M. Roba, B.E. Kinsman, R. Hanney,
J. Non-Cryst. Solids **184** (1995) 292.
- [6] R.S. Quimby, K.T. Gahagan, B.G. Aitken, M.A. Newhouse,
Optics Letters **20** (19) (1995) 2021
- [7] D.P. Machewirth, K. Wei, V. Krasteva, R. Datta, E. Snitzer, G.H. Sigel Jr.,
J. Non-Cryst. Solids **213 & 214** (1997) 295
- [8] L.B. Shaw, B.J. Cole, J.S. Sanghera, I.D. Aggarwal, D.T. Schaafsma,
OFC'98 OSA Tech. Dig. Series Vol. 2, (1998) 141
- [9] J. Kirchhof, J. Kobelke, M. Scheffler and A. Schwuchow,
Electronics Letters **32** (13) (1996) 1220
- [10] M. Scheffler, J. Kirchhof, J. Kobelke and A. Schwuchow,
to be published in *SPIE* Volume **3416**, paper No. [3416-11]
- [11] G. Fonteneau, Mat. Res. Bull. **19** (1984) 685
- [12] G.E. Devyatykh, M.F. Chorbanov, I.V. Scripachev, E.M. Dianov, V.G. Plotnichenko,
Int. J. Optoelectron **7** (1992) 237

COPPER HALOGENOANTIMONIATE GLASSES

Michel Poulain*, Marcel Poulain* and Josik Portier#

*Lab. Matériaux Photoniques, Université de Rennes I, F-35042 Rennes

ICMCB, Université de Bordeaux 1, Chateau Brivazac, F33600- Pessac

INTRODUCTION

Antimony oxyhalide glasses have been reported more than 12 years ago ¹, especially binary $\text{Sb}_2\text{O}_3\text{-PbX}_2$ glasses ($\text{X} = \text{F}, \text{Cl}, \text{Br}, \text{I}$). These glasses are fairly stable against devitrification and transmit IR light beyond $6\text{ }\mu\text{m}$ ^{1,2}. Their refractive index is larger than 2. This paper presents new vitreous compositions based on the $\text{Sb}_2\text{O}_3\text{-CuI}$ association.

EXPERIMENTAL

Powdered starting materials are weighted, carefully mixed and introduced in an oxide or vitreous carbon crucible. Processing includes the following steps: melting, homogenizing, casting and annealing. Synthesis is implemented at room atmosphere. Time and temperature are minimized in order to avoid the halogen loss which could result from halide evaporation. Samples, usually 1 to 2 grams in weight, are transparent and appear yellow or reddish.

RESULTS

A binary glass may form around 80 % and 20 % CuI. Melt must be quenched to prevent crystallization. Samples are yellow. Various attempts were made in order to assess which halides could be added to this binary system to improve the glass forming ability.

There series of vitreous samples were prepared:

- 1 - with lead halides PbCl_2 , PbBr_2 and PbI_2
- 2 - with cadmium halides CdCl_2 , CdBr_2 and CdI_2
- 3 - with alkali halides

The third element was incorporated at the expense of antimony oxide. A typical composition is 60 Sb_2O_3 - 20 CuI - 20 MX_2 or MX.

Other experiments were carried out with manganese and iron chlorides. Thick samples could be obtained from quaternary glasses such as 60 Sb_2O_3 - 10 CuI - 20 PbI_2 - 10 NaCl.

Main physical properties have been measured. They will be reported and compared to those of the glasses previously described. Glass transition temperature is lower than 300 °C and appear close to that of most fluoride glasses. Infrared transmission appears independent on composition as it is correlated to the O-Sb vibrations.

CONCLUSION

Numerous glasses may be formed with antimony oxide as the main glass progenitor in association with heavy halides. Such glasses are transparent in the infrared spectrum and show some similarities with fluorozirconate glasses, but with a much larger refractive index. For this reason optical losses could be more difficult to decrease. Potential applications relate to active fibers and components, and possibly to non linear properties.

¹ B. Dubois *et al.*, Mat. Res. Bull. 19, 1317-1323 (1984)

² M. M. Ahmed and D. Holland, Glass Techn. 28, 141-143 (1987)

LEAD ANTIMONIATE GLASSES

Michel Poulain, Marcel Poulain[#], Mauricio Silva^{*} and Sidney Ribeiro

^{*} Instituto de Química, UNESP, Araraquara, Brazil

[#] Lab. Matériaux Photoniques, Université de Rennes 1, F-35042 Rennes

INTRODUCTION

The glass forming ability of antimony sesquioxide has been reported in binary systems involving alkali and thallium oxides¹. To our knowledge, little work has been done on multicomponent systems. As antimony is close to tellurium in the periodic chart, one may expect some similarities in the optical properties, especially infrared transmission and high refractive index. This paper reports investigations in the Sb_2O_3 -PbO-ZnO ternary system.

EXPERIMENTAL

Glass synthesis is implemented from the mixture of the oxides or carbonates, by melting, homogenizing, casting and annealing at room atmosphere. Batches, usually 3 grams in weight, are processed. Melt is much more viscous than fluoride glass melts. It is poured onto brass molds at room temperature without additional quenching. Samples are characterized by visual and microscopic inspection, and by DSC.

RESULTS

The vitreous area was investigated first in the Sb_2O_3 -PbO-ZnO system with the oxides as starting materials. Then it was observed that the introduction of zinc as ZnCO_3 was beneficial to glass formation and the corresponding limits of vitreous composition have been determined. Binary glasses were found to exist around 10 mol % ZnO (starting from carbonate) and 20 mol % PbO. Quenching may extend these vitreous ranges. Lead concentration could be increased up to 50 % in glass compositions such as 40 Sb_2O_3 - 50 PbO - 10 ZnO. Samples are yellow colored.

Glass transition temperature T_g lies between 260 °C and 300 °C. Thermal stability range between T_g and the onset of crystallization T_x usually exceed 100 °C. The broad shape of the crystallization peak suggests that these glasses are rather stable against devitrification. The evolution of T_g and T_x with respect to lead content in the (90-x) Sb_2O_3 - x PbO - 10 ZnO glasses is reported.

Infrared transmission extends beyond 6 μm with a large OH absorption band around 3 μm in samples processed at room atmosphere without special care. Refractive index is larger than 2. Some other physical characterizations will be reported.

¹ See for example A. Winter, Verres Refract. 36, 353-355 (1982) and French patent N° 1,544,060 (December 18, 1967)

In(PO₃)₃ AS GLASS FORMER

D.Grando, P.Melnikov, Y.Messaddeq and S.J.L.Ribeiro

A cryo-thechnique approach has been used for the preparation of a pure indium polyphosphate. For this purpose conc. H₃PO₄. and In₂O₃ were mixed after being frizzed at liquid nitrogen temperature. The product was heated at 180°C until In(H₂PO₄)₃ crystallization, then fired at 900°C for 3 hours, allowing the formation of high purity In(PO₃)₃ . It does not contain neither In₂O₃ nor InPO₄. The heating of In(PO₃)₃ at 1400°C produce a transparent material. It's thermal and optical characteristics have been reported. elsewhere.

Glass compositions belonging to the ternary system In(PO₃)₃-BaF₂-InF₃ are being presented. Good optical quality and stable glass samples with up to 8 mm thickness could be prepared. Thermal analysis, Raman Scattering, IR spectroscopy have been performed and results presented. Studies comprising the used of rare -earth ions as dopants are in progress..

PROPERTIES OF LOW SILICA CALCIUM ALUMINATE GLASSES DOPED WITH Nd^{3+}

J. A. Sampaio, T. Catunda

Instituto de Física de São Carlos, Grupo de Espectroscopia de Sólidos, Universidade de São Paulo, Av. Dr. Carlos Botelho 1465, 13560-250, São Carlos - SP, Brazil.
e-mail jsampaio@ifqsc.sc.usp.br

M. L. Baesso, A. C. Bento

Departamento de Física, Universidade Estadual de Maringá, Av. Colombo 5790, 87020-900 Maringá - PR, Brazil.

S. Gama, F. C. G. Gandra

Instituto de Física Gleb Wataghin, Universidade Estadual de Campinas, Unicamp, 13083-970, Campinas - SP, Brazil.

ABSTRACT

Calcium aluminate glasses are a promising new laser materials host since they have high quantum efficiencies and good physical-chemical properties. In this work we describe the preparation and characterisation of the low silica calcium aluminate glasses doped with Nd^{3+} .

INTRODUCTION

Most of the works reported in the literature about calcium aluminate glasses are concerned to expand the glass-forming field, since these glasses have a strong tendency to devitrify easily [1-4]. To avoid this problem, it has been shown that the addition of small amounts of silica or barium oxide to the base composition increases the glass forming region in the phase diagram, without significant midinfrared (IR) transmission loss [4]. The great interest in these glasses is that they can be produced completely free of traditional glass-forming oxides [5,14]. Furthermore they have a better combination of properties, i.e., highly refractory nature, excellent chemical durability, high transformation temperature, good IR transmission, approximately 6 μm , phonon energy about 800 cm^{-1} [10] compared to 1000 cm^{-1} in silicate [23]. However very few papers have been devoted to calcium aluminate glasses doped with rare earth elements [6-11].

Rare earth doped glasses are interesting for many optical applications, including active media glass lasers. In this case is desirable to introduce large amounts of rare earth to glass host and to investigate the changes on its properties. In the current practice, the optimum rare earth doping is controlled by both of limit of vitrification and quenching of fluorescence [20-22]. Recent studies [6,7,9] have been shown that calcium aluminate glass doped with Nd^{3+} have a high quantum efficiencies, indicating that they have a great potential as a new laser material host. Although the base composition determines most properties of the glass, the rare earth concentration must also be taken into account because it induces structural changes on glass, modifying thermal expansion coefficient, density and molar volume [24-25].

The purpose of this work is to investigate the changes on the thermal properties of low silica calcium aluminate glasses doped with Nd_2O_3 , such as, glass transformation temperature (T_g), crystallization temperature (T_x), dilatometric softening temperature (T_d) and thermal diffusivity. Moreover microhardness vickers, density and refractive index as a function of doping is also studied.

EXPERIMENTAL

High purity CaCO_3 , Al_2O_3 , MgO , SiO_2 and Nd_2O_3 were used as a starting raw materials. The calcium aluminate glass sample compositions were (in wt. %): 47.4 CaO , (41.5 - X) Al_2O_3 , 7.0 SiO_2 , 4.1 MgO , X Nd_2O_3 , where X = 0.5, 1.0, 1.5, 2.0, 2.5, 3.0, 3.5, 4.0, 4.5, and 5.0 %. The batch was melted in 15 g quantities under vacuum condition at 1500 $^\circ\text{C}$, in graphite crucibles during 2 h. Afterwards the heater was switched off and the crucible was moved 60 cm upward to a cooled chamber close to room temperature. Depending of the composition it was also used a faster cooling rate by injecting argon gas to the chamber at the same time that the heater was switched off, and the crucible was moved up. The samples obtained were cut in three different shapes: disks of 10 mm diameter and around 3 mm in thickness, with optical polishing, for refractive index, microhardness and thermal lens measurements; disks of 6 mm diameter and 2 mm in thickness for thermomechanical analysis and specific heat measurements, and bulk shape about 150 mg for DTA/TG analysis. They were analysed by X-ray diffraction and optical microscopy. The doping concentration for all samples was verified by measuring the optical absorption coefficient in the peak of the absorption band at 590 nm. Measurements of refractive index was performed using a Abbe refractometer in the sodium D band (588.32 nm). The density was measured by the Archimedes method using CCl_4 as an immersion liquid at room temperature (24 $^\circ\text{C}$). Measurements of Vickers microhardness was performed by the same operator, using a Leitz Wetzlar Germany Microhardness Tester by measuring the diagonals at least 10 indentations, with a 200g load at room temperature, and calculated in kg/mm^2 by

$$H_v = 1854.4 \left(\frac{P}{d^2} \right) \quad (1)$$

where P (g) is the load and d (μm) is the diagonal length average of the indent. Linear thermal expansion coefficients, and dilatometric softening point were measured using a vertical Thermomechanical Analyzer TMA-50 Shimadzu, with a heat rate of 6 $^\circ\text{C}/\text{min}$. DTA/TG analysis were investigated using a Simultaneous Thermal Analyzer NETZSCH, STA 409-EP, with a heat rate of 10 $^\circ\text{C}/\text{min}$ until 1400 $^\circ\text{C}$, in alumina crucibles. Thermogravimetry shows that there is no loss of mass of the samples during heat process. Thermal Diffusivity measurements were conducted using the Thermal Lens Spectroscopy setup described in a previous work [6].

RESULTS AND DISCUSSION

The sample preparation procedure described in Experimental section provided us to obtain bubble free transparent glasses with high homogeneity. X- rays diffraction detect no crystal traces. Infrared spectra show that OH⁻ absorption was eliminated by melting the samples under vacuum. A faster cooling rate was needed since partial devitrification takes place above 2.0 wt.% of Nd_2O_3 doping, however this procedure enables crystal-free samples just up to 5.0 wt.% of Nd_2O_3 . Beyond this concentration there was total crystallization of the samples. We

also tried the replacement of CaO by Nd_2O_3 but the devitrification became more prominent. The optical absorption coefficients shown in Fig. 1 indicate no loss of Nd^{3+} during the melting.

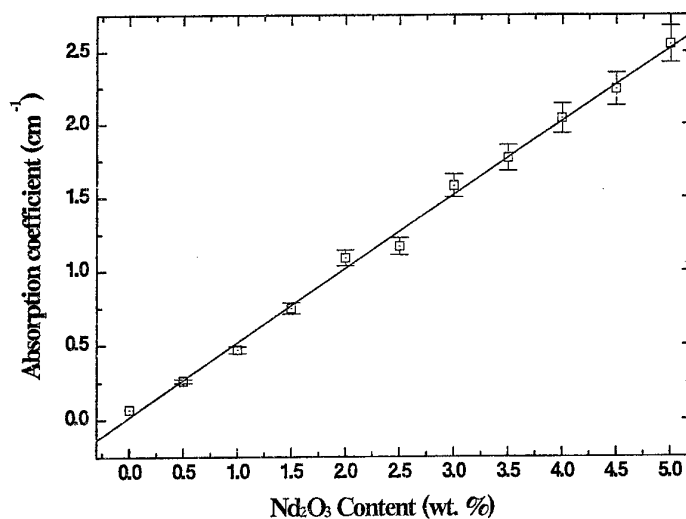


Figure 1. Optical absorption coefficients as a function of Nd^{3+} content.

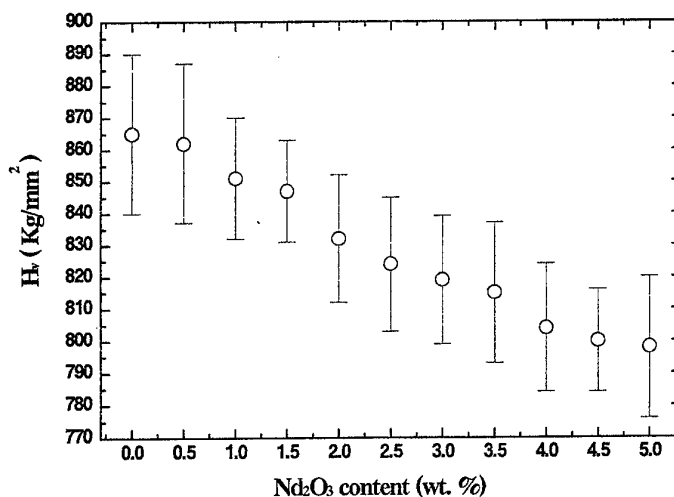


Figure 2 - Vickers microhardness to low silica calcium aluminate glasses when Nd_2O_3 replaces Al_2O_3 .

In order to minimise the error, measurements of Vickers microhardness (H_v), shown in Fig. 2, were conducted using different loads, i. e., 25 g, 50 g, 100 g, 200 g and 300 g. Loads below 200 g provided us some visual difficulty to measure diagonals values because they were very small. On the other hand, 300 g load resulted in cracking at the edges of the indentation. In Fig. 2 we can observe a slightly decrease of the H_v values as Al_2O_3 is replaced by Nd_2O_3 ($H_v = 867 \text{ Kg/mm}^2$ to undoped sample and $H_v = 798 \text{ Kg/mm}^2$ to 5.0 wt. % Nd_2O_3

doped sample). This behaviour can be explained by assuming that the rare earth ions disrupt the tetrahedral network characteristic of the calcium aluminate glasses.

The results of the measurements of the refractive index and density as a function of Nd^{3+} content are shown in Fig. 3A and 3B respectively. The refractive index is quite similar to all samples $n_D = 1.65$. These values are in good agreement with those reported by Oprea et. al [16]. The density increases slightly when Nd_2O_3 replaces Al_2O_3 which can be explained by simply considering the relative masses of the rare earth ions in comparison with those of the others ions in the glass.

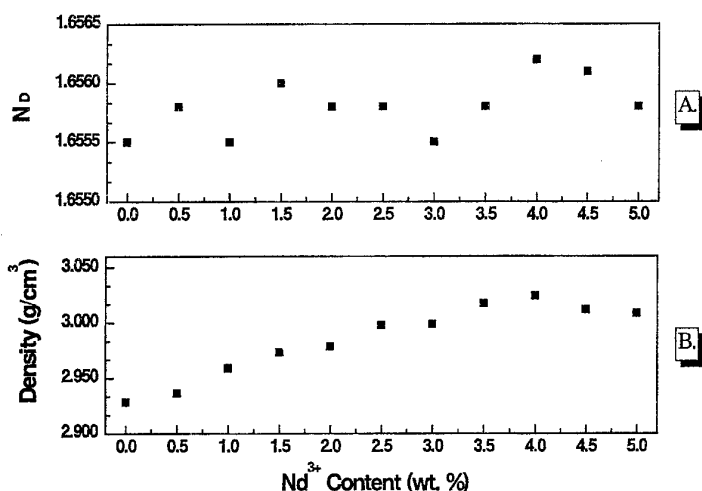


Figure 3. A. Behaviour of the refractive index at 588.3 nm B. Behaviour of the density as a function of the Nd_2O_3 content in low silica calcium aluminate glasses.

Figure 4 are shows the DTA curves of three glasses samples: undoped, 2.0 wt. % and 5.0 wt. % of Nd_2O_3 doped one. We can observe that the exothermal peaks shifted slightly toward smaller temperatures as the Nd_2O_3 content is increased. Glass transformation temperature (T_g), crystallisation temperature (T_x), and melting temperature (T_m) were determined by onset temperature of those curves. Dilatometric softening temperature (T_d) was obtained from TMA curves.

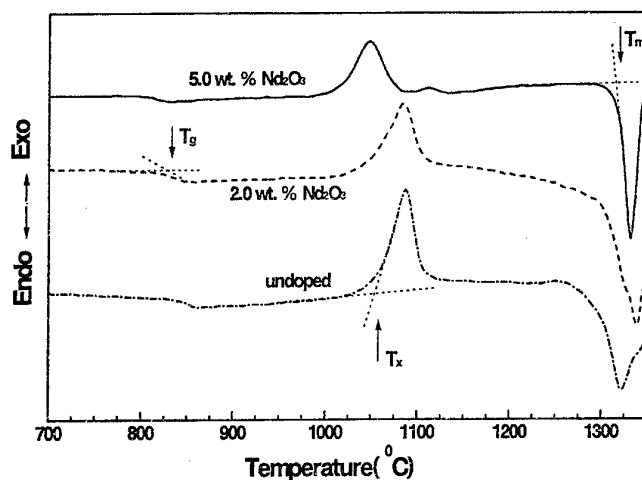


Figure 4. DTA curves showing the thermal events (T_g , T_x , T_m) of three different samples: undoped, 2.0 wt.% and 5.0 wt. % Nd_2O_3 doped

The thermal parameters data are plotted as function of Nd_2O_3 content in Fig. 5. Increasing the Nd_2O_3 content, we observed a slightly decrease on T_g and T_x and a slightly increase on T_d ; T_m values is the same for all samples.

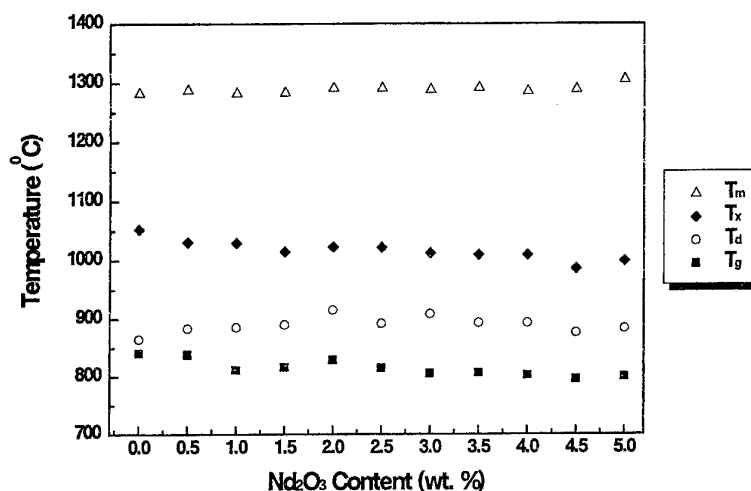


Figure 5. Behaviour of the thermal parameters T_g , T_d , T_x and T_m in low silica calcium aluminate glasses as Al_2O_3 is replaced by Nd_2O_3 .

Figure 6 shows that the thermal diffusivity decreases slightly as Nd_2O_3 replaces Al_2O_3 . These values changed from $5.69 \times 10^{-3} \text{ cm}^2 \text{ s}^{-1}$ for the undoped samples to $5.22 \times 10^{-3} \text{ cm}^2 \text{ s}^{-1}$ for the 5.0 wt.% Nd_2O_3 doped one.

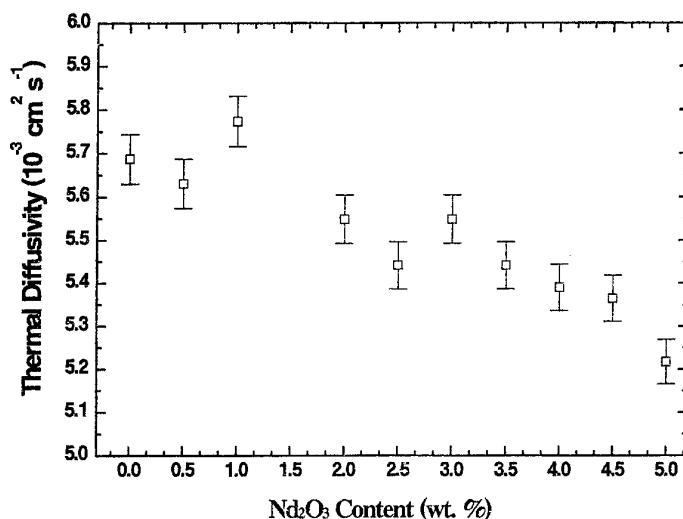


Figure 6. Behaviour of the Thermal Diffusivity in low silica calcium aluminate glasses doped with Nd₂O₃.

CONCLUSIONS

The replacement of Al₂O₃ by Nd₂O₃ in low silica calcium aluminate glasses became the glass forming field smaller. Furthermore the rare earth ions induces changes on its properties such as hardness, density, T_g, diffusivity. However is necessary to investigate the changes in its structural properties in order to know the role of the rare earth in these glass system.

ACKNOWLEDGEMENTS

We are thankful to Brazilian National Council (CNPq), CAPES and to FAPESP for the financial support of this work.

REFERENCES

- [1] J. M. Florence, F. W. Glaze and M. H. Black, J. Res. NBS 55 (4) (1955) 231.
- [2] H. C. Hafner, N. J. Kreidl and R. A. Weidel, J. Am. Ceram. Soc. 41 (8) (1958) 315.
- [3] G. Y. Onoda, JR. and S. D. Brown, J. Am. Ceram. Soc. 53 (6) (1970) 311.
- [4] J. R. Davy, Glass Technology 19 (2) (1978) 33.
- [5] J. E. Shelby, J. Am. Ceram. Soc. 68 (3) (1985) 155.
- [6] M. L. Baesso, A. C. Bento et al., Physical Review B 57 (17) (1998) 10545.
- [7] M. L. Baesso, A. C. Bento et al., J. Non-Cryst. Solids 219 (1997) 139.
- [8] W. J. Chung, J. R. Yoo, Y. S. Kim and J. Heo, J. Am. Ceram. Soc. 80 (6) (1997) 1485.
- [9] E. V. Uhlmann, M. C. Weinberg, N. J. Kreidl et al., J. Non-Cryst. Solids 178 (1994), 15.
- [10] S. Tanabe, T. Ohyagi, T. Hanada and N. Soga, J. Am. Ceram. Soc. Japan 101 (1993) 78.
- [11] X. L. Zou, T. Izumitani, Nippon Seram Kyo Gak 101 (1) (1993) 99.

- [12] P. L. Higby, R. J. Ginther, I. D. Aggarwal and E. J. Friebele, *J. Non-Cryst. Solids* 126 (1990) 209.
- [13] C. Huang and E. C. Behrman, *J. Non-Cryst. Solids* 128 (1991) 310.
- [14] W. A. King and J. E. Shelby, *Phys. Chem. Glasses* 37 (1) (1996) 1.
- [15] E. V. Uhlmann, M. C. Weinberg, N. J. Kreidl and A. A. Goktas, *J. Am. Ceram. Soc.* 76 (2) (1993) 449.
- [16] C. Oprea, D. Togan and C. Popescu, *Thermochimica Acta* 194 (1992) 165.
- [17] J. E. Shelby and R. M. Slilaty, *J. Appl. Phys.* 68 (7) (1990) 3207.
- [18] J. E. Shelby, C. M. Shaw and M. S. Spess, *J. Appl. Phys.* 66 (3) (1989) 1149.
- [19] J. E. Shelby and M. M. Wierzbicki, *Physics and Chemistry of Glasses* 36 (1) (1995) 17.
- [20] O. Deutschbein, M. Faulstich, W. Jahn, G. Krolla and N. Neuroth, *Appl. Opt.* 17 (1978) 2228.
- [21] J. Fernandes, R. Balda and M. A. Arriandiaga, *Optical Materials*, 4 (1994) 91.
- [22] H. Ebendorff-Heidepriem, W. Seeber and D. Ehrt, *J. Non-Cryst. Solids*, 183 (1995) 191.
- [23] K. Hirao, S. Todoroki and N. Soga, *Bol. Soc. Espan. Ceram. Vid*, 81 c (1992) 121.
- [24] J. T. Kohli and J. E. Shelby, *Phys. Chem. Glasses*, 32 (1991) 67.
- [25] J. E. Shelby, J. T. Kohli, *J. Am. Ceram. Soc.* 73 (1990) 39.

LOCAL STRUCTURE OF Pr IN FLUOROZIRCONATE GLASSES

M. Braglia, C. Bruschi, G. Dai, J. Kraus, S. Mosso,

CSELT Via Reiss Romoli 274 Turin ITALY

e-mail: marco.braglia@cse.lt.it

C. Meneghini, A. Balerna, F. Boscherini,

INFN, Laboratori Nazionali di Frascati, P.O.Box 13, I-00044 Frascati (Roma) Italy

S. Pascarelli

ESRF, BP220 F-38043 Grenoble, France

C. Lamberti

Dip. Chimica IFM, Università di Torino, Via P. Giuria 7, I-10125 Turin, Italy

ABSTRACT

Praseodymium activity for optical glass fibre amplifier efficiency is very sensitive to its structural environment, but up to now only few reports have been involved in this topic. The paper presents a study on the local atomic structure around Praseodymium in fluorozirconate glasses. Pr K-edge (at 42 keV) Extended Absorption Fine Structure (EXAFS) and Anomalous X ray Scattering (AXRS) data, both collected at the GILDA BM8 beamline at the ESRF (European Synchrotron Radiation Facility), and photoluminescence (PL) spectroscopy have been performed on two series of systems based on the composition $53 \text{ ZrF}_4 - 20 \text{ MF}_2 - 4 \text{ M}^*\text{F}_3 - 3 \text{ AlF}_3 - 20 \text{ NaF}$ (mol %)($\text{M}=\text{Sr}$, $\text{M}^*=\text{Y}$, ZSYAN; or $\text{M}=\text{Ba}$, $\text{M}^*=\text{La}$, ZBLAN). The first series were dealing with different doping contents of PrF_3 from 500 to 5000 ppmw and the second with different dopants such as PrF_3 , PrCl_3 , Pr_6O_{11} , Pr_2S_3 (5000 or 10000 ppmw). From our study three important results have been obtained: *) when the conventional method is used for the preparation of fluoride glasses, the local environment is independent of the doping precursor; **) no first shell Pr—Pr signal has been observed, even in the samples having a Pr^{3+} concentration of 10000 ppmw, i.e. ten times greater than what is generally recognized to be the concentration quenching limit (1000 ppmw); ***) preliminary analysis on AXRS, at the Pr K-edge, discards the presence of Pr—F—Pr contribution in the second shell signal in the samples doped with 10000 ppmw Pr.

INTRODUCTION

Rare earth doped optical fibres have been intensively studied in the last ten years because of the interest in the signal amplification in telecommunication systems at the wavelengths of 1.3 and 1.5 μm [1-4]. Among them, Er-doped SiO_2 fibres have been successfully used in the third window of telecommunications (1.5 μm) while Pr-doped ZBLAN ($\text{ZrF}_4\text{-BaF}_2\text{-LaF}_3\text{-AlF}_3\text{-NaF}$) fibres are considered one of the most promising candidate materials for the second window (1.3 μm).

In contrast to Er which exhibits a long excited state lifetime in silica glass (around 10 ms), Pr is inactive in this host at 1.3 μm wavelength due to the multi-phonon decay process. The lifetime of $^1\text{G}_4$ level of Pr in ZBLAN glasses is only around 110 μs , which translates to a low radiative quantum efficiency of less than 4%. Therefore, it is highly desirable to change the structural environment around Pr^{3+} in the glass hosts to depress effectively the multiphonon relaxation. One approach towards this gain goal, is to develop new glass hosts having lower phonon energy. Recent progress is focused on non-oxide glasses including fluoroindates [5], and chalcogenides [6,7].

Another possibility to increase the lifetime of the metastable 1G_4 level in Pr^{3+} could be to modify the local structure in a high phonon energy host by incorporating other dopants or phases with low phonon energy. Along this way, the group of research of Rennes University [8] doped Ga-In fluoride glass with different Praseodymium halides such as PrF_3 , PrCl_3 and PrI_3 , and observed that the lifetime increases as the mass of the doping anion becomes heavier [8].

On the other hand, the lifetime is also closely related to the concentration of Pr^{3+} in fluoride glass. It is generally believed that, at low concentration, Pr^{3+} is uniformly dispersed by non-bridging fluorine atoms in the glass. When the concentration of Pr^{3+} reaches 1000 ppmw, the lifetime of the excited level significantly decreases (concentration quenching effect [9]). Cross relaxation or/and co-operative up-conversion processes are possible mechanisms [9].

Although great progress has been made in the field of Pr^{3+} doped fluoride amplifiers, the local structure of Pr^{3+} in fluoride glasses is still unknown. In this paper, EXAFS and AXRS analyses were employed to investigate the short distance structure of Pr^{3+} in ZrF_4 -based fluoride glass. ZBLAN glasses doped with different concentrations of Pr were prepared to see if clustering occurs. Another objective was to assess the possible structural change of the Praseodymium surroundings in the glass when different Praseodymium dopants were used.

EXPERIMENTAL

Three ZBLAN glasses ($53\text{ZrF}_4\text{-}20\text{BaF}_2\text{-}4\text{LaF}_3\text{-}3\text{AlF}_3\text{-}20\text{NaF}$ (mol%)), two of them doped with PrF_3 (5000 and 10000 ppmw), the other left undoped for a blank AXRS experiment, have been prepared melting the precursors at about 850 °C in a Pt/Au crucible under N_2 and O_2 atmosphere and quenching the melt in a brass mould [10].

In addition, a second series of glasses $53\text{ZrF}_4\text{-}20\text{SrF}_2\text{-}4\text{YF}_3\text{-}3\text{AlF}_3\text{-}20\text{NaF}$ (mol%) (ZSYAN) was prepared in the same manner for EXAFS measurement. The composition was derived from the standard ZBLAN glass ($53\text{ZrF}_4\text{-}20\text{BaF}_2\text{-}4\text{LaF}_3\text{-}3\text{AlF}_3\text{-}20\text{NaF}$ (mol%)). By substituting BaF_2 with SrF_2 and LaF_3 with YF_3 , the interference from strong fluorescence lines of Ba and La, which overshadow the weak Pr fluorescence signal, could be avoided.

The glasses substituted were doped with PrF_3 , PrCl_3 , Pr_6O_{11} and Pr_2S_3 , respectively at concentrations of 500, 5000 and 10000 ppmw. Samples characteristics are summarized in Table 1.

Tab.1: Concentration of Pr^{3+} precursors in ZBLAN and ZSYAN samples.

	ZBLAN			ZSYAN						
Sample code	73	79	76	26	28	33	32	36	38	45
Precursor	-	PrF_3	PrF_3	PrF_3	PrF_3	Pr_6O_{11}	Pr_6O_{11}	Pr_2S_3	Pr_2S_3	PrCl_3
Conc. Pr^{3+} [ppmw]	-	5000	10000	500	5000	500	5000	5000	10000	5000

Pr K-edge EXAFS and AXRS spectra were recorded at 300 K, at the GILDA BM8 CRG beamline [11] (ESRF Grenoble). The Si(511) monochromator was operating in a dynamically sagittal focusing mode [11]. Harmonic rejection was obtained by detuning the crystals. Energy resolution was ~5 eV at 43 KeV, with an average photon flux on the sample of $\sim 5 \cdot 10^9$ photons s^{-1} and a spot size of $\sim 4 \text{ mm}^2$. The EXAFS measurements on model samples of PrF_3 , PrCl_3 , Pr_2S_3 and Pr_6O_{11} were performed in the transmission mode, using Kr filled ionisation chambers to monitor photon intensity before and after the sample. ZSYAN samples were measured in the fluorescence mode using a hyper-pure Ge detector to discriminate Pr fluorescence photons from the strongly predominant fluorescence of other atomic species in the sample and from the elastically scattered background. Integration times ranging between

20 and 60 s/pt has been adopted in order to obtain a S/N ratio of $\sim 10^{-3}$. The reader is reminded to ref. [12] for a more detailed description of the EXAFS experiment. Non anomalous XRS measurements were performed on both doped and undoped ZBLAN samples at 30 keV using a standard NaI scintillation detector. Its energy resolution was high enough to discern the Zr fluorescence from elastic scattering (Ba, La and Pr fluorescences are not excited at such energy). AXRS measurements were performed on doped ZBLAN sample at 41 and 41.995 keV, respectively. In such conditions, the principal drawback in scattering measurements near the Pr K edge is represented by the intense background fluorescences of La and Ba in the sample which cover the elastic signal. A Si(111) crystal analyzer (curved in Johnson geometry to enlarge its angular acceptance) was then used on the diffracted beam to remove this unwanted background from the NaI detector. XRS data were recorded in the q -range 0.1 - 23 \AA^{-1} , estimated statistical noise was kept better than 10^{-3} up to $q < 20 \text{ \AA}^{-1}$. For the normalisation of the data were treated using standard method to subtract Compton scattering, to make correction for volume and absorption effects [13].

The fluorescence spectra were recorded with PL Scantek equipped with diode laser source emitting at 1018 nm in the wavelength range from 1100 nm to 1600 nm with a resolution of 1 nm and an integration time of 1 s/pt.

RESULTS and DISCUSSION

A preliminary EXAFS analysis of the ZBLAN glass showed that the presence of Ba and La strongly interferes with the Pr K_{α} fluorescence emission, resulting in an unanalysable EXAFS signal. In order to eliminate this problem, the series of ZSYAN glass samples was prepared. According to the results of the thermal analysis, no difference was found in the glass transition temperatures of ZSYAN and ZBLAN glass ($269 \pm 1 \text{ }^{\circ}\text{C}$), but the substitution of BaF_2 with SrF_2 results in a strong tendency towards devitrification. We expect that the decrease in glass thermal stability does not bring significant change in the local structure around Pr^{3+} as documented by the fact that ZSYAN and ZBLAN show the same line-shape in the PL band at $1.31 \text{ }\mu\text{m}$ as shown in Fig. 1.

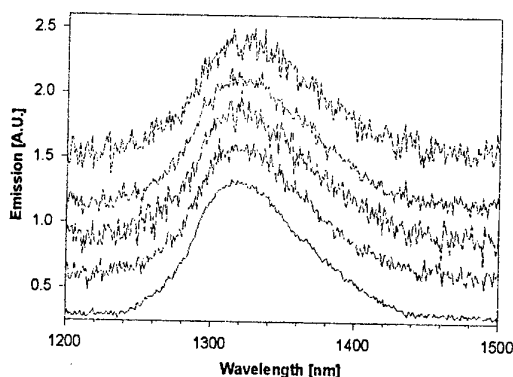


Fig. 1 : Normalised PL emission of, from the top to the bottom: ZSYAN 45 (PrCl_3), ZSYAN 36 (Pr_2S_3), ZSYAN 32 (Pr_6O_{11}), ZSYAN 28 (PrF_3), ZBLAN 79 (PrF_3) all the sample were doped with 5000 ppmw of Pr

A weak intensity of the emission fluorescence of ZSYAN with respect to ZBLAN sample was observed as expected due to the lower transparency of the samples at the pump wavelength of 1018 nm. The qualitative finding of PL spectroscopy is quantified by EXAFS data analysis. Fig. 2a reports the k -weighted Fourier transform (FT) of the EXAFS signals of the ZSYAN samples. From Fig. 2a, a great similarity of the first shell of Pr between the PrF_3 standard and

the glass samples is evident as well as the absence of significant second shell contribution in all ZSYAN samples.

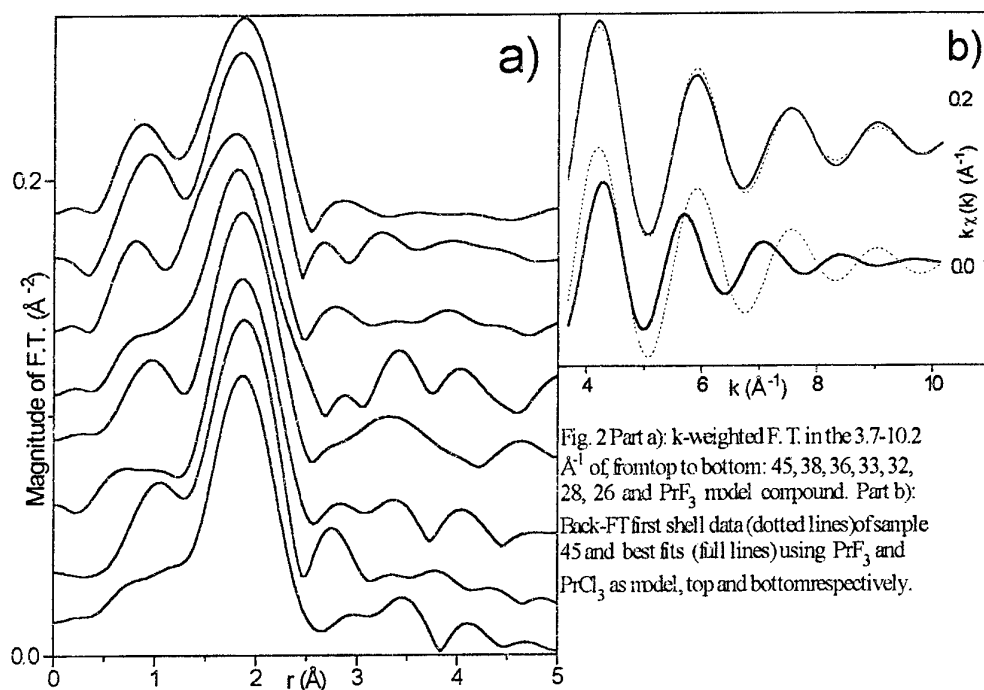


Fig. 2 Part a): k-weighted F. T. in the 3.7-10.2 Å⁻¹ of from top to bottom: 45, 38, 36, 33, 32, 28, 26 and PrF₃ model compound. Part b): Back-FT first shell data (dotted lines) of sample 45 and best fits (full lines) using PrF₃ and PrCl₃ as model, top and bottom respectively.

Quantitative EXAFS analysis (described in detail in ref. [12]) indicated that, for all the ZSYAN samples, the Pr first shell environment was identical to that found in PrF₃ (3 F atoms at 2.47 Å, 4 at 2.52 Å, 2 at 2.69 Å, with slightly higher Debye Waller factors). For all the samples, the quality of the first shell fit is good, as can be appreciated in Fig. 2b for sample 45 (top curves). For all samples prepared from other precursors, (32, 33, 36, 38 and 45) we have also tried to model the experimental EXAFS signal with local structure, phases and amplitudes of the corresponding PrCl₃, Pr₂S₃ and Pr₆O₁₁ standards. In no cases we were able to reproduce the experimental $k\chi(k)$ signal, as documented in Fig. 2b for sample 45 (bottom spectra), where the theoretical signal has been modelled with $N_1 = 6$ Cl atoms at $R_1 = 2.82$ Å and $N_2 = 3$ Cl atoms at $R_2 = 2.91$ Å. Results of the EXAFS study implies that, for all samples, the first shell local environment of Pr was the same as that in PrF₃ model compound. Similar results have been obtained for other rare-earth dopants in different glass hosts [14].

As for the second shell, AXRS measurements were performed in order to confirm and quantify the conclusion from the EXAFS data in which second shell signal was dumped by a limited signal to noise ratio [12]. Fig. 3a reports the total pair correlation functions, $G(r)$, of doped and undoped ZBLAN glasses obtained at 30 keV. In a first approximation [15], $G(r)$ can be expressed as a weighed sum of partial pairs correlation functions $g_{\alpha\beta}(r)$: $G(r) = \sum_{\alpha\beta} W_{\alpha\beta} g_{\alpha\beta}(r)$, where α and β represent the atomic species present in the sample. The $G(r)$ are characterized by three evident peaks at about 2.1, 2.6 and 4.1 Å, while for farther distances every correlation is smoothed out. From the evaluation of the $W_{\alpha\beta}$ factors and from structural considerations, the principal contributions to the three peaks in the $G(r)$ function (Fig. 3a) came from the bonds Zr-F at 2.1 Å, Ba-F at 2.6 Å and Zr-Ba, Zr-Zr and Ba-Ba at 4.1 Å. The differences between the $G(r)$ functions of doped and undoped samples are small as far as the peaks at 2.1 and 2.6 Å is concerned (due to the low Pr content) but a significant contribution around 4 Å is clearly observable. It is worth noticing that the first peak is nearly unchanged by doping. This

preliminary result suggests some changes of the host matrix induced by doping and an accurate analysis is in progress to quantify its extent.

In order to single out, from the total $G(r)$ function the partial $g_{Pr\beta}(r)$ function we performed an anomalous XRS experiment on Pr doped ZBLAN. AXRD is based on the principle that, for a specific element, a consistent variation of the dispersion corrections of the scattering amplitudes is observed in few eV across the absorption edge [16]. In this experiment the working energies (41 and 41.995 keV) were deliberately chosen in order to maximize the anomalous effect for Pr and minimize the effect for the other elements. This choice was particular critic for La and Ba having the K edge quite near to that of Pr. The differential correlation function $\Delta G_{Pr}(r)$, calculated following the procedure described in ref. [17], is reported in the upper part of Fig. 3b. The $\Delta G_{Pr}(r)$ shows two evident contributions at about 2.1 and 4 Å. The low r peak is strongly affected by the extraction procedures while the amplitude and position of the second one is stable. This effect is basically due to the lower anomalous effect on the first Pr coordination shell (coming from Pr-F correlations) that makes the effects of noise and small systematic errors larger than the anomalous one. In fact, the low r region is strongly affected by noise coming from the high momentum data (q).

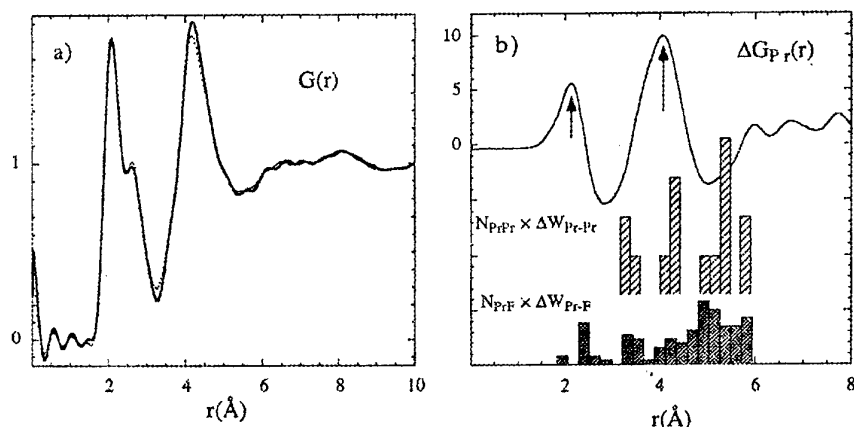


Fig 3: a) Experimental $G(r)$ of ZBLAN73 undoped (full line) and ZBLAN76 10000 ppmw of (dashed line) Pr^{3+}
b) The differential correlation function $\Delta G_{Pr}(r)$ of ZBLAN76 doped glass (full line) with the expected Pr-F and Pr-Pr shell structure in PrF_3 crystal. Pr-Pr and Pr-F are weighted to reproduce the effects of the dissimilar differential weight for the two pairs.

By contrast, the information obtained from the second peak is more reliable because the second Pr shell, composed of heavy elements, has larger differential effect. In addition, the information about the structure of the second neighbour shell is concentrated in the low momentum region where S/N ratio is higher. For these reasons we will only focus our attention on the second peak. This choice was also justified by the fact that the previous EXAFS study gave us a complete and quantitative description of the first coordination shell around Pr.

The EXAFS and AXRS techniques are largely complementary since the former probes with high accuracy the nearest neighbour distribution while the latter give more detailed information on medium range ordering.

The histograms reported in the lower part of Fig. 3b represent the Pr-Pr and Pr-F neighbour shells calculated within 6 Å on the basis of a PrF_3 crystalline structure and weighed by corresponding factors $\Delta W_{\alpha\beta}$ (similar to the $W_{\alpha\beta}$ taking into account for anomalous effect). According to these results, it is evident that cations located in the second shell around Pr in

ZBLAN are not Pr atoms in the same structural configuration found in PrF_3 , but the hypothesis that Pr cations can arrange in a consistent different configuration is very unlikely.

CONCLUSIONS

Some important results have been obtained:

- PL indicates that ZSYAN and ZBLAN have a very similar local environment around Pr.
- From EXAFS and PL measurements we observed that whatever is the Pr dopant (PrF_3 , PrCl_3 , Pr_2S_3 or Pr_6O_{11}), the first shell environment around Pr^{3+} in all ZSYAN samples is always identical to that in PrF_3 .
- By EXAFS measurements on ZSYAN, no first shell Pr-Pr signal has been observed, even in samples having a Pr^{3+} concentration of 10000 ppmw, i.e. ten times greater than what is generally recognised to be the concentration quenching limit.
- By AXRS measurements no evidence of second shell Pr-F-Pr contribution has been found in ZBLAN glass.

These results allow us to conclude that the quenching mechanisms cannot be due neither to first nor to second shell Pr clustering. If a conventional method is used for the preparation of fluoride glasses [10], the local Pr^{3+} environment is independent of the doping precursor. So it does not seem possible to increase the lifetime of $^1\text{G}_4$ level of Pr^{3+} in fluoride glass by only changing the anions.

REFERENCES

- [1] R.J. Mears, L. Reekie, I.M. Jauncy, D.N. Payne in Proc. Opt. Fibre Comm. (OFC1987) Reno, NV 1987, paper W12.
- [2] B. J. Ainslie, J. Ligth. Tech. **9**, (1991) 220.
- [3] W. J. Miniscalco, J. Ligth. Tech. **9**, (1991) 234.
- [4] T. J. Whitley, R. Wyatt, D. Szebesta, S.T. Davey, BT Technol. J. **11**, (1993) 115.
- [5] Y. Nishida, T. Kanamori, Y. Ohishi, M. Yamada, K. Kobayashi S. Sudo, IEEE Phot. Tech. Lett. **9**, (1997) 318.
- [6] B.G. Aitken, R.S. Quimby; J. Non-Cryst. Solids **213-214**, (1997) 281.
- [7] V. Krasteva, D. Machewirth, G.H. Sigel Jr.; J. Non-Cryst. Solids **213-214**, (1997) 304.
- [8] G. Zhang, Ph.D. Thesis, Université de Rennes1, (1996), pag. 115; G. Zhang, J. Jiang and M. Poulain, J. Non-Cryst. Solids **221**, (1997) 78.
- [9] Y. Ohishi, T. Kanamori, T. Nishi, S. Takahashi; IEEE Phot. Tech. Lett. **3**, 8, (1991) 715.
- [10] M. Braglia, J. Kraus, S. Mosso; J. Non-Cryst. Solids **201**, (1996) 237.
- [11] S. Pascarelli, F. Boscherini, F. D'Acapito, C. Meneghini, J. Hrdy and S. Mobilio, J. Synchrotron Rad., **3**, (1996) 147.
- [12] M. Braglia, G. Dai, S. Mosso, S. Pascarelli, F. Boscherini and C. Lamberti J. Appl. Phys. **83**, (1998) 5065.
- [13] M. Maggini, G. Licheri, G. Piccaluga, G. Pascina, and G. Pinna *X-Ray diffraction of ions in aqueous solutions*, CRC press. Inc. (1988).
- [14] P.M. Peters and S. N. Houde-Walter, Appl. Phys. Lett., **70**, (1997) 541; M. A. Marcus and A. Polman, J. Non-Cryst. Solids **136**, (1991) 260; D. T. Bowron, G. A. Saunders, R. J. Newport, B. D. Rainford and H. B. Senin, Phys. Rev. B **53**, (1996) 5268.
- [15] B. E. Warren, *X-Ray diffraction*, Addison-Wesley, Reading Mass. (1969)
- [16] P. H. Fuoss and P. Eiseberg, Phys. Rev. Lett. **46** (1981) 1537.
- [17] F. Buffa, A. Corrias, G. Licheri, G. Navarra, and D. Raoux, J. Non-Cryst. Solids, **151** (1992) 119.

AN INTERPRETATION OF THE BOSON PEAK IN RARE-EARTH DOPED GLASSES

V.K. Tikhomirov, M. Naftaly and A. Jha

Department of Materials, University of Leeds, Leeds LS2 9JT, UK

e-mail: V.Tikhomirov@leeds.ac.uk

ABSTRACT

The Boson peak is reported in a series of rare-earth doped sulfide, telluride and fluoride glasses. Doping with rare-earths, e.g. Pr^{3+} , at a level as low as 1000 ppm, increases intensity of the Boson peak, while the rest of Raman spectrum remains unchanged. This indicates that rare-earth ions are efficiently incorporated in the sites where vibrations give rise to the Boson peak. Further doping of up to 1-10 mol.% results in the formation of glassy alloys with Raman spectra entirely different from the corresponding spectra of undoped glasses. The large polarizability and atomic mass of rare-earths, such as Pr^{3+} , as well as the ionic character of their chemical bonding, are suggested as the origin of the Boson peak enhancement in rare-earth doped as compared to undoped glasses. It is further suggested that the presence of non-bridging anion atoms, such as S, O or F, determines the origin and intensity of the Boson peak, as well as the solubility of rare-earths in glasses. Rare-earth ions are therefore believed to be incorporated in sites where non-bridging anions are the principal component. Prolonged irradiation of sulfide glasses with near-gap laser light results in the enhancement of the Boson peak which is attributed to the accompanying metastable photorefractive effect and to the creation of additional non-bridging atoms (broken chemical bonds). This also indicates the principal contribution of non-bridging atoms to the intensity and origin of the Boson peak.

1. INTRODUCTION

Currently there is a great deal of interest in rare-earth doped glasses and fibers. In particular, it is urgent to develop low-cost Pr-doped optical fiber amplifiers/lasers for the 1.3 μm telecommunication window, where most installed fibers operate. The local environment of rare-earth ions embedded in glasses is of primary interest [1,2] although the number and range of techniques available for studying these environments is very restricted [2].

A universal feature of Raman scattering in glasses is the low-energy Boson peak situated close to the exciting laser line. This feature is not observed in crystals, and is therefore a characteristic of the glassy state. Recently we reported a well-resolved intense Boson peak in undoped and Pr^{3+} -doped Ge-S-I chalcogenide glasses with varying composition and Pr-content [3]. The strength of the Boson peak increased in glasses doped with small amounts of Pr^{3+} , indicating that Pr ions are efficiently incorporated in the sites whose vibrations are responsible for the Boson peak.

In this paper we will report on the influence of doping with rare-earths, such as Pr^{3+} , Ce^{3+} , Er^{3+} , Nd^{3+} , on the Raman spectra of different kinds of glasses with emphasis on changes in the intensity of the Boson peak. In particular, we have found that the intensity of the low-energy Raman scattering (in particular of the Boson peak) is much more sensitive to rare-earth

doping than the high-energy ($>100\text{ cm}^{-1}$) part of the Raman spectrum. We suggest that the large polarizability and atomic mass of rare-earths and the ionic character of their chemical bonds cause the enhancement of the Boson peak in rare-earth doped glasses. Hence the rare-earths can serve as a probe for sites where vibrations give rise to the Boson peak. We propose that non-bridging anion atoms, such as S, O or F, determine the origin of the Boson peak in glasses and act as attractors for rare-earths, thus enhancing their solubility. Prolonged irradiation of germanium sulfide-based glasses with near-gap laser light results in a remarkable enhancement of the Boson peak, which can be attributed to the accompanying metastable photorefractive effect and to the creation of additional non-bridging atoms (broken chemical bonds). Mechanisms for reported effects are suggested, and the origin of the Boson peak is discussed.

2. EXPERIMENTAL

High purity telluride, fluoride and sulfide glasses were fabricated by conventional methods [4]. Ga-La-S [5], Ge-S-I [6] and Ge-Ga-S [7] glasses, fabricated by techniques described in [5-7] respectively, were also examined.

A double grating monochromator with the spectral resolution of 2 cm^{-1} in the visible part of the spectrum was used to observe the Raman signal at 45° with respect to the pump beam direction, as described in [3]. In the majority of experiments the 647 nm line of a Kr laser (with 50 mW power) was used for the excitation of Raman scattering. More details regarding the experimental set-up and glass fabrication, as well as more extended results and discussion, will be published elsewhere [8].

3. RESULTS

A large variety of Raman scattering spectra in series of undoped sulfide, telluride and fluoride glasses will be presented at the Symposium. The position of the Boson peak and of the main optical-phonon related peaks will be correlated with changes in the glass composition. We confirmed that the doping with rare-earths, such as Pr^{3+} , at levels as low as 1000 ppm, increases intensity of the Boson peak in a variety of glassy hosts, as was reported in [3] for the case of Ge-S-I glassy host. The remaining part of Raman scattering spectrum remains unchanged in doped glasses. Experimental data on the influence of rare-earth dopants on Raman spectra in different glasses will be presented at the Symposium and elsewhere [8].

Doping telluride and fluoride glasses with up to 1-10 mol.% resulted in the formation of glassy alloys whose Raman spectra were essentially different from the corresponding spectra of undoped glasses. Experimental results regarding this change in the Raman spectrum will be presented at the Symposium and elsewhere [8].

Fig.1 illustrates the light-induced change in the Raman spectrum of $\text{Ge}_{24}\text{S}_{75}\text{Ga}_1$ glass, which shows a pronounced metastable photorefractive effect [9]. This glass was irradiated for 3 hours with an Ar^+ -laser at $\lambda=515\text{ nm}$ and 50 mW power, resulting in the saturation of the photorefractive effect.

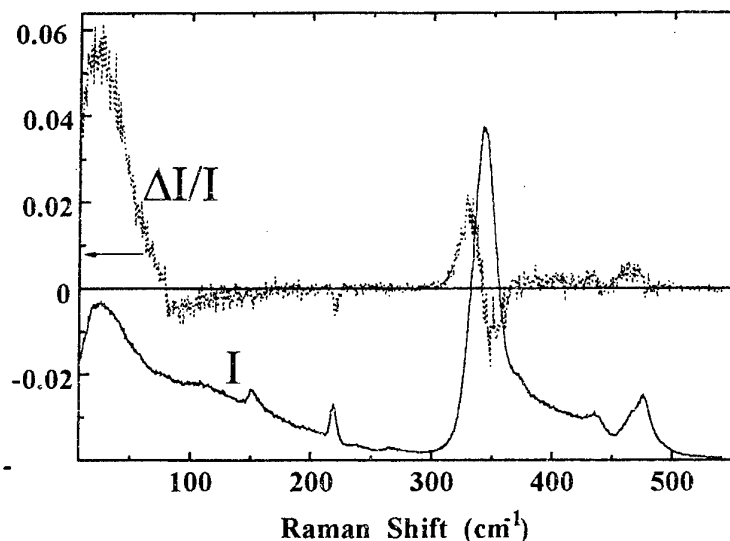


Fig. 1. The low-noise curve represents Raman spectrum of glass $\text{Ge}_{24}\text{S}_{75}\text{Ga}_1$ taken in 15 minutes (intensity I is in arbitrary units, excitation at 515 nm). The large-noise curve represents the difference $\Delta I/I$ in the Raman spectra of a fresh $\text{Ge}_{24}\text{S}_{75}\text{Ga}_1$ glass and of the same glass after 3-hour irradiation ($\Delta I/I=6\%$ at the maximum of the Boson peak (at 30 cm^{-1})).

4. DISCUSSION

According to the soft potential model [10], the vibrations responsible for the low-frequency light scattering in glasses are quasilocal harmonic oscillators with frequencies $\omega \sim (k/M)^{1/2}$ which is much lower than typical vibrational frequencies. Two parameters promote the quasilocal (or resonance) character of the vibrational modes: a weak effective elastic constant k (which is a property of bonds with large polarizability, such as ionic bonds), and a large effective mass M . Both conditions are satisfied by dopant sites of rare-earth ions in glassy hosts. As a result rare-earth doped glasses have a higher density of states of quasilocal harmonic oscillators compared with undoped glasses, which in turn enhances the Boson peak in these glasses. Note that doping with rare-earths influences the intensity of the Boson peak at dopant levels as low as 1000 ppm. This indicates that the concentration of sites which give rise to vibrations responsible for the Boson peak is also of a similar order.

We suggest that sites responsible for the Boson peak in glasses are related to non-bridging anions atoms (such as S, F or O), i.e. to broken bonds on anion atoms. This suggestion is confirmed by two main observations reported in this paper: the strength of the Boson peak is increased i) by rare-earth doping, and ii) by prolonged irradiation of photorefractive glasses with near-gap light.

i) It is known that stoichiometric glasses, such as SiO_2 [11] or GeS_2 [7], accept rare-earth only up to a limited amount 200-300 ppm. It was argued [see 11 and ref's therein] that rare-earth dopants are incorporated in the vicinity of non-bridging O atoms. Therefore glass modifiers

are added to stoichiometric glasses (such as Al to SiO₂ or Ga to GeS₂) to break the stoichiometric chemical order, thus increasing the number of non-bridging atoms and consequently the solubility of rare-earths. Chemical bonds between rare-earth ions and non-bridging anions have high ionicity and polarizability due to the large positive charge (+3) on rare-earths. These bonds possess lower elastic constants compared with the covalent network of the glassy host, and also have large effective vibrational mass due to the large atomic mass of rare-earths. According to relation $\omega \sim (k/M)^{1/2}$ for quasilocal vibrations, such bonds contribute very efficiently to the intensity of the low-energy Raman scattering, i.e. to the strength of the Boson peak.

ii) The mechanism of photorefractive effect in sulfide glasses was suggested to be due to the light-stimulated breaking of chemical bonds [12]. Following charge separation, the carriers are trapped, thus creating dipole moments leading to photorefractive effect due to the electro-optic effect [12]. The breaking of chemical bonds reduces the coordination number and consequently the elastic constants of atoms participating in the broken bonds, thus enhancing their polarizability. This in turn causes the enhancement of the Boson peak in glasses where prolonged irradiation resulted in the metastable photorefractive effect.

ACKNOWLEDGEMENT

The majority of the experiments were performed at the National Technical University of Athens (NTUA), Department of Physics during two visits of V. Tikhomirov, one of which was supported by a NATO scholarship. Hospitality and support of NTUA during these stays are gratefully acknowledged, as well as friendly help from graduate students I. Kotsalas, A. Perakis and post-doctoral assistant E. Sarantopoulou. The useful comments of Professor C. Raptis regarding this manuscript are gratefully acknowledged.

REFERENCES

1. V.K. Tikhomirov, M. Naftaly and A. Jha, Phys. Rev. Lett., to be published.
2. J. Wang, W.S. Brocklesby, J.R. Lincoln, J.E. Townsend, and D.N. Payne, J. Non-Cryst. Solids 163 (1993) 261.
3. V.K. Tikhomirov, I.P. Kotsalas, C. Raptis, and D.A. Parshin, Solid State Commun., 106 (1998) 145.
4. M. Naftaly and A. Jha, Proceedings of this Symposium.
5. A.B. Seddon and R. Li, to be published.
6. V. Krasteva, D. Hensley, and G. Sigel, J. Non-Cryst. Solids, 222 (1997) 218.
7. D.R. Simons, A.J. Faber, and H. De Waal, Optics Letters 20, (1995), 468.
8. V.K. Tikhomirov, A. Perakis, C. Raptis, M. Naftaly, A. Jha, R. Li, and A.B. Seddon, to be published.
9. V.K. Tikhomirov, G.J. Adriaenssens, and A.J. Faber, J. Non-Cryst. Solids, 213&214 (1997) 174.
10. V.L. Gurevich, D.A. Parshin, J. Pelous, and H.R. Schober, Phys. Rev. B 48 (1993) 16318.
11. D. Miniscalco, in: "Rare-earth doped glasses and fibers", ed. M. Digenet.
12. V.K. Tikhomirov and S.R. Elliott, J. Phys.: Condens. Matter, 7 (1995) 1737.

The Role of Surface and Strain Energies In The Stabilisation of Glassy Phases, and Their Importance In Designing New Types of Photonic Materials

A. Jha^{}, M. Naftaly and S. Shen**

*Department of Materials, The University of Leeds,
Clarendon Road, Leeds LS2 9JT, UK.*

Abstract

Traditionally glasses have been made via melt quenching route, during which the formation of crystals is kinetically suppressed due to large cooling rates. More recently, the sol-gel technique has been developed for designing and fabricating amorphous materials. Sol-gel amorphous materials, by contrast, are produced near room temperatures and have large internal surface area.

In this paper, using the classical nucleation model, we have computed the effect of surface energy on the nucleation rate for known glass-forming systems. The structural interpretation for enhancement in surface energy is elucidated by the reference of Eyring hole theory, and the effect of enhanced surface on the diffusion kinetics is explained on the basis of surface chemical potential model. Based on the classical approach, the effect of strain energy on the stability of glass-forming liquids to undergo crystallisation has been examined in view of a sub-microscopic capillary model. The influence of the sub-microscopic capillaries on the free-volume assisted viscous flow behaviour in weakly and strongly bonded liquids is described together with the stability of the glassy phases. The effect of strain on the structural relaxation of glassy phases is also exemplified.

Examples of the formation of glasses at the grain boundaries and within the sub-micrometer size pores are given in this paper for designing new ranges of photonic materials.

****:** Corresponding and presenting author
a.jha@leeds.ac.uk

MAGNETOCHEMICAL INVESTIGATION OF THE SECOND COORDINATION SPHERE OF TRANSITIONAL METALS IN GLASSES

Yu.S. Tver'yanovich, I.V. Murin

St.-Petersburg State University, Department of Chemistry, St.-Petersburg, 198904,
Russia. email yuratver@yt2461.spb.edu

ABSTRACT

Previously proposed simple model for low temperature paramagnetism of glasses is developed. The nonlinear temperature dependencies of the reciprocal paramagnetic susceptibility of glasses for systems *Ga-Ge-Mn-S* and *Ge-Sb-Fe-Se* are quantitatively described in terms of the model and detailed information about the composition of the second coordination sphere of transitional metals is obtained. This information is compared to the glassforming ability of the glasses.

INTRODUCTION

Recently considerable attention was concentrated on the studies of medium-range order in glasses. Unlike the short-range order determined by correlation in the positions of ions involved in the first coordination sphere, the medium-range order implies the existence of correlation in the ions arrangement in the second and other coordination spheres and the existence of structural groups several nanometers in size. The determinacy of correlation decreases with an increase in distance. Therefore, the medium-range order is determined, to a large extent, by the correlation in the arrangement of ions involved in the second coordination sphere. It is interesting to study some physicochemical property such as the one, that is governed by the second coordination sphere only and that can be sensitive to the type of metal ions located in the presented coordination sphere. Such property is the indirect exchange interaction.

Earlier the simple model for low temperature paramagnetism of glasses was presented [1]. Unlike the more complicated models for spin glasses it allow to obtain the concrete quantitative information about the structure of glasses. In the present paper this model was developed and applied to the interpretation of the experimental data on magnetic susceptibility of glasses in the systems *Ga-Ge-Mn-S* [1,2] and *Ge-Sb-Fe-Se* [4].

MODEL

Let us make four suppositions.

The first. Strong short-range order exists in the glass. All the metal cations are connected only with anions, and vice versa.

The second. The glass contains only one type of anions (*A*) and only one type of transition metal cations (*B*) with the magnetic moment which is independent on temperature. But the glass contains one or more types of diamagnetic metal cations *D*.

The third. The coordination number of cations *B* is equal to *Z*. The energy of indirect exchange interaction steeply decreases with increasing distance and with deviation of the angle of the bond from the straight direction. Therefore, *Z* cation sites exist in the second coordination sphere, that allows to form strong indirect exchange interactions with the energy significantly larger than those with all other cations. The cation *B* is marked as *B_i* if it has *i* cations *B* and (*Z-i*) cations *D* which are located in these *Z* sites.

And the last. θ_1 is the Weiss constant, which describes the behaviour of the magnetic moment of cations B_1 in exchangeable pairs $B-A-B$. θ_1 is equal to the θ_1 multiplied by i .

$$\theta = i \cdot \theta_1; \quad i=0,1,2,\dots,Z \quad (1)$$

Let us analyse the last supposition. The energy of the exchange interaction ($k\theta$) is smaller than that of any chemical bond. Therefore, the arrangement of electron density around B_i does not depend on the presence or absence of exchange interaction, or in other words, it does not depend on i . Thus, this equation is correct. However, it may be possible, that the electronegativity of B differs from the electronegativity of D . In this case, the replacement of a part of cations B in the second coordination sphere of the central cation B by cations D can lead to a the redistribution of the electron density and the change of the energy of single exchange interaction of the central cation B . Thus, θ_1 is not the linear function of i . For the studied glasses the electronegativity of B is close to the electronegativity of D , and so, we can use Eq. (1).

The maximum absolute value of θ_1 ($Z \theta_1$) can deviates from the Weiss constant of the crystalline compound in the $A-B$ system, in which cations B form Z exchange interaction bonds (θ_{ph}). The absolute value of θ_z is likely to be a bit smaller than θ_{ph} due to the distortion of the angles and lengths of the bonds, that is typical for the vitreous state.

So, the expression for the temperature dependence of the magnetic susceptibility is the following:

$$\chi = C \cdot \sum_{i=0}^Z \frac{g_i}{(T - \theta_i)}, \quad (T > \theta_i); \quad g_i = \frac{B_i}{\sum B_i} \quad (2)$$

where C is the Curie constant and g_i is the fraction of B_i . Function D may be introduced as follows:

$$D = \left[(T - \bar{\theta}) \cdot \sum_{i=0}^Z \frac{g_i}{(T - \theta_i)} \right] - 1 \quad (3)$$

where the average Weiss constant is equal to

$$\bar{\theta} = \sum_{i=0}^Z g_i \cdot \theta_i \quad (4)$$

Then equation (2) can be rewritten as the following

$$\chi = \frac{C}{(T - \bar{\theta})} \cdot (1 + D) \quad (5)$$

Expression (3) can be transformed in the following way

$$D = \sum_{j \neq i} g_i g_j \frac{(\theta_i - \theta_j)^2}{(T - \theta_i) \cdot (T - \theta_j)} \quad (6)$$

It can be concluded that the function (2) has the following properties

1. $D > 0$;
2. $D \rightarrow 0$ at $T \rightarrow \infty$;
3. $D \rightarrow \infty$ at $T \rightarrow \max \theta_i$; ($\max \theta_i = 0$ at $\theta < 0$ and $\max \theta_i = Z\theta_1$ at $\theta > 0$).

Therefore, the temperature dependencies of the reciprocal magnetic susceptibility have a general view as presented in Fig.1.

In absence of correlation between the type of the central cation and composition of its second co-ordination sphere the weight factors g_i can be calculated using the combinatorial relation.

$$g_i = \gamma_i b^i (1-b)^{Z-i}, \quad (8)$$

where b is the fraction of B among all the cations in glass and γ_i is the number of possible arrangements of i cations B and $(Z-i)$ cations D in Z positions. For the case of $Z=6$ γ_i has the following values $\gamma_0 = \gamma_6 = 1$; $\gamma_1 = \gamma_5 = 6$; $\gamma_2 = \gamma_4 = 15$; $\gamma_3 = 20$.

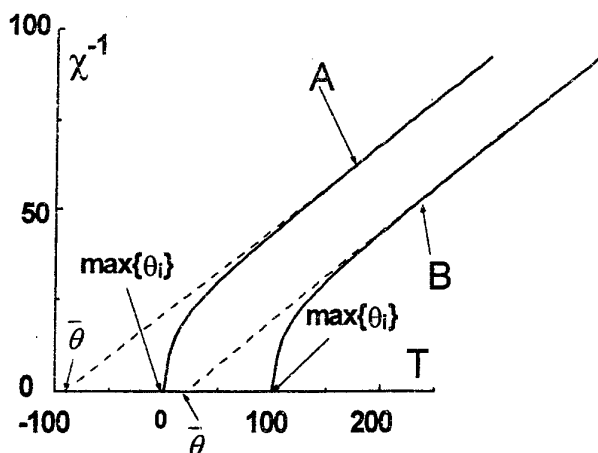


Fig. 1 Temperature dependencies of reciprocal magnetic susceptibility of glasses according to equation (2): A - with negative exchange interaction; B - with positive exchange interaction.

S is larger than unity if there is a tendency to the association of structural units containing cation B , and it is smaller than unity, if there is a tendency to the formation of complex structural units containing both B and D cations. In order to take into consideration S in equation (8) we introduce the effective concentration b^*

$$S \cdot \frac{b}{1-b} = \frac{b^*}{1-b^*}. \quad (12)$$

Table. 1 Compositions of the studied glasses.

N	MnS (b) (mol. part)	GeS ₂ (mol. part)	GaS _{1.5} (mol. part)
1	0.0384	0.6674	0.2942
2	0.0632	0.6215	0.3158
3	0.0873	0.5759	0.3368
4	0.1225	0.5102	0.3674
5	0.2308	0.3077	0.4615

Table 2. The results of the initial approximation step.

N	b^* (mol. part)	Θ_0 (K)	$-\Theta_1$ (K)
1	0.074 ± 0.001	-0.95 ± 0.03	46 ± 1.4
2	0.126 ± 0.002	-0.74 ± 0.07	39 ± 1.5
3	0.151 ± 0.002	-1.05 ± 0.09	59 ± 2.3
4	0.189 ± 0.002	-1.21 ± 0.08	61 ± 1.6
5	0.329 ± 0.01	1.17 ± 0.3	50 ± 2.6

This is the case of statistically uniform distribution of different structural units throughout the bulk of the glass (SUD). For this case it is shown that the following relation is absolutely correct:

$$\bar{\theta} = b \cdot (Z \cdot \theta_1). \quad (9)$$

For SUD the ratio between the probability for a vacant cation site being occupied by B or by any D cation is given by

$$P = b/(1-b). \quad (10)$$

The existence of the correlation in distribution of different cations among the cation sites is taken into consideration using the segregation factor S

$$P = Sb/(1-b) \quad (11)$$

When the concentration of B is equal to b^* and SUD takes place, the set of parameters $\{g_i\}$ is the same as for the glass under study, in which the concentration of B is equal to b and there exists the deviation from SUD. It is easy to verify that for any positive S , $0 \leq b^* \leq 1$.

As it was mentioned above, the energy of indirect exchange interaction steeply decreases with the increase of distance. This means that the exchange interactions with the other B cations, besides those Z cations which were considered above, can be neglected compared to $|\theta_1|$ and, so, $\theta_0 = 0$. However, if the exchange interaction is negative and the temperature of measurements is much

smaller than $|\theta_l|$ the value of θ_0 is not negligible compared to the temperature of measurements and it is necessary to introduce $\theta_0 \neq 0$. Thus, we can write the following equation for the magnetic susceptibility:

$$\chi = C \cdot \left[\frac{g_0}{T - \theta_0} + \sum_{i=1}^Z \frac{g_i}{T - i \cdot \theta_l} \right], \quad g_i = \gamma_i (b^*)^i \cdot (1 - b^*)^{Z-i}. \quad (13)$$

where b^* , θ_0 and θ_l are the free parameters. According to the model, θ_l is the same for all glasses with the same A , B and Z .

RESULTS AND DISCUSSIONS

The magnetic susceptibility of glasses $Ga_2S_3-GeS_2-MnS$ was investigated in [1,2]. The compositions of the glasses are presented in table 1. The results of the measurements are presented in Fig. 2.

The magnetic moment of manganese is calculated according to the model from the Curie constant at the high temperatures and it corresponds to the spin value of Mn^{2+} . The magnetic

Table 3. The results of the second approximation step.

N	b^* (mol.part)	Θ_0 (K)	S
1	0.0703 ± 0.0003	-1.05 ± 0.01	2.00
2	0.1109 ± 0.0008	-1.17 ± 0.05	1.89
3	0.1605 ± 0.0008	-0.74 ± 0.05	1.85
4	0.2030 ± 0.001	-0.70 ± 0.06	1.80
5	0.326 ± 0.002	1.08 ± 0.08	1.61

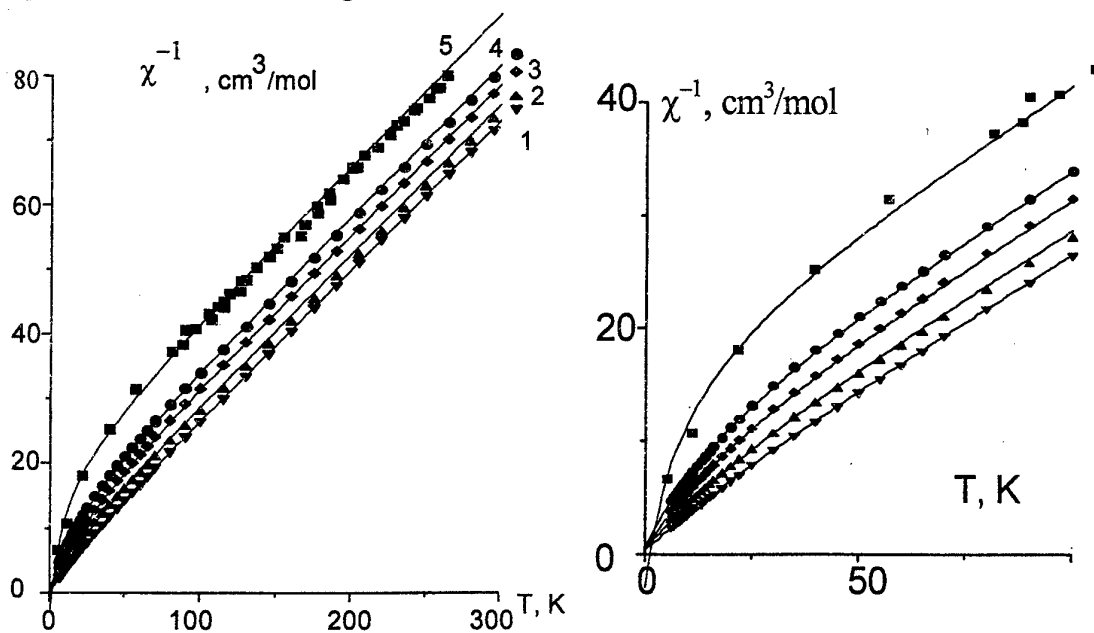


Fig. 2. Temperature dependencies of manganese reciprocal magnetic susceptibility in glasses of system $Ga_2S_3-GeS_2-MnS$. Experimental values were added by points. Results of simulations were added by unbroken lines. Figures correspond to ones in Table 1.

susceptibility of the glass of composition 5 has been measured by Barnier et. al. These authors found, that Mn has the coordination number equal to 6 in the glasses of the system $Ga_2S_3-GeS_2-MnS$ [2].

At the first step of fitting the experimental data with Eq.13 three parameters were varied (θ_0 , θ_l , b^*). The results are presented in Table 2. As it was supposed above, $|\theta_0| \ll |\theta_l|$. According to the model, the value of θ_l should be the same for all the studied glasses. From Table 2 it can be concluded that $\langle \theta_l \rangle = -51$ K.

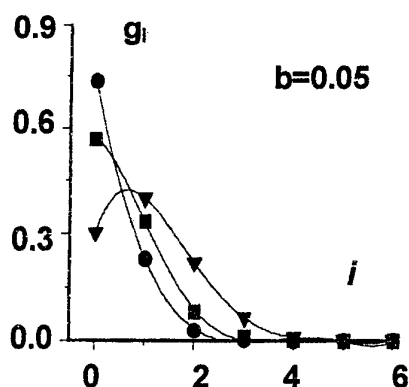


Fig. 3. Dependencies of the fraction of B_i on i . Circles mark the values calculated for the model glass structure with SUD; squares mark the values founded for the samples $Ga-Ge-Mn-S$; triangles mark the values founded for the samples $Ge-Sb-Fe-Se$.

At the second step of calculations θ_i is fixed and the values of b^* and θ_0 were varied. The results are presented in Table 3. The temperature dependencies of magnetic susceptibility and sets of parameters $\{g_i\}$ for all the glasses were calculated using these results and $\langle \theta_i \rangle = -51 \text{ K}$. The results of calculations of magnetic susceptibility are presented in Fig. 2 by the unbroken lines and the experimental results are given by points. The circles mark the values calculated for the model glass structure with SUD for the dependencies of the weight factor g on i for glasses with different compositions (Fig. 3). Squares mark values founded for the investigated glasses $Ga_2S_3-GeS_2-MnS$. The values of g for real glasses are slightly smaller than that for the model glasses with SUD for the small i and slightly larger for the large i . This means that the tendency to association of

structural units containing Mn exists in the glasses. The rate of this tendency can be characterized by the parameter S , which is about 1.5 or 2 (Table 3).

The value of S can be determined in another way. Fig. 4 shows the concentration dependence of $\bar{\theta}$. This dependence was plotted with the use of experimental values obtained directly from high temperature range of the temperature dependencies of reciprocal magnetic susceptibility. Experimental points, including $(Z \theta_i)$ at $b=1$ and 0 at $b=0$, are connected with the second-order curve. The function $S(b)$ (a dotted line) was calculated from this curve using Eq. (9) and (12):

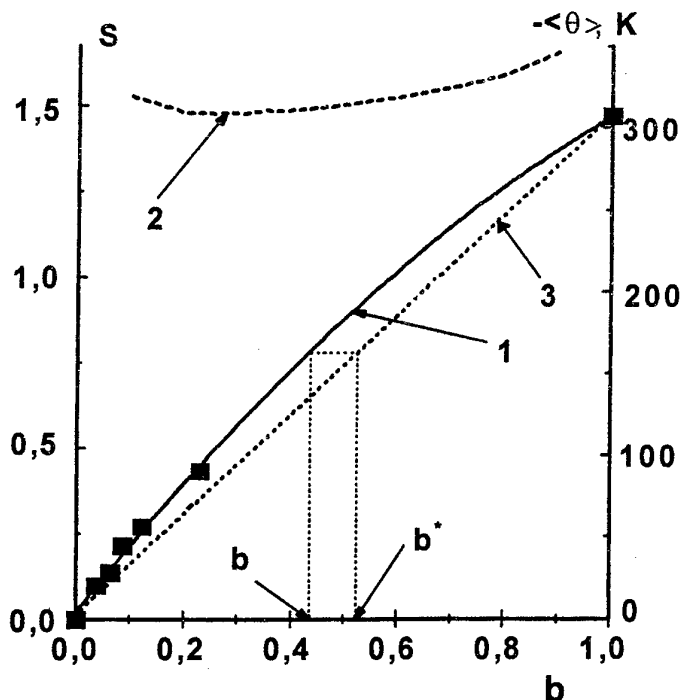


Fig. 4. Concentration dependencies of average Weiss constant (1) and segregation factor (2) for glasses $Ga_2S_3-GeS_2-MnS$. (3) - is the concentration dependence of $\langle \theta \rangle$ for model glasses with SUD.

$$S = \frac{\bar{\theta} \cdot (1 - b)}{(Z \theta_l - \bar{\theta}) \cdot b} \quad (14)$$

The results of the calculation using Eq.14 are given by curve 2 in Fig.4.

As it was mentioned above, the absolute value of $(Z \theta_l)$ is smaller than the absolute value of θ_{ph} which is equal to $-400K$ for MnS [3].

It is interesting to compare the results for the system $Ga_2S_3-GeS_2-MnS$ with the results for the glasses of the system $Sb-Ge-Se$ doped by Fe . The temperature dependencies of the reciprocal magnetic susceptibility for glasses with different concentration of Fe ($b = 0.05, 0.0125, 0.002$) were measured by Bychkov et. al. [4]. These authors found that Fe is present in the glasses in the state Fe^{+2} and its coordination number is equal to 6.

The sets of $\{g_i\}$ for the model glass with SUD, for the glass with Mn and for the glass with Fe are compared in Fig.3 ($b = 0.05$). All the glasses have the same value of b which is equal to 0.05. It can be seen that the tendency to the association of the structural units containing transition metal in the last system is more significant. S for glasses with Fe is equal to 4. It is interesting that maximum concentration of Mn in the glasses $Ga-Ge-S$ is six times larger than that of Fe in glasses $Sb-Ge-Se$.

CONCLUSIONS

The proposed model allows to describe the experimental data on magnetic susceptibility adequately and to obtain detailed information on composition of the second coordination sphere of a transition metal in glasses. It is found from the comparison of the glasses $Ga_2S_3-GeS_2-MnS$ with the glasses $Sb-Ge-Se-Fe$ that the tendency to association of the structural units containing a transition metal is smaller in the system with more extended glassforming region.

ACKNOWLEDGEMENTS

This work has been supported by the Russian Fund of Basic Researches (Grant N98-03-32114a), by the Russian Programme "Integration" (Grant N 326.47) and by the Competition Centre of S.-Petersburg State University (Grant N97-92-66).

REFERENCES

1. Yu.S.Tver'yanovich, W.Gunsser, H.Neuendorf, M.D.Bal'makov, I.V.Murin. Glass Physics and Chemistry (Russian). 23 (1997) 106.
2. S.Barnier, M.Guittard, M.Wintenberger, J. Flahaut. J. Non-Cryst. Solids. 56 (1983) 319.
3. J.J. Banewicz, R.F. Heidelberg, R. Lindsay. Phys.Rev. 117 (1960) 736.
4. E.A. Bychkov, Z.U. Borisova, Yu.G. Vlasov. Glass Physics and Chemistry. 10 (1984) 390 (in Russian).

COMPOSITION OF THE ENVIRONMENT OF Nd AND Sm IN CHALCOGENIDE GLASSES CONTAINED Ga AND Ge.

Yu. S. Tver'yanovich, S. V. Degtyarev, S. S. Pivovarov, V. B. Smirnov,
and A. V. Kurochkin

Russian Centre of Laser Physics, St. Petersburg State University (Petrodvorets Branch),
Ul'yanovskaya. 2, Petrodvorets, 198904 Russia. email yuratver@yt2461.spb.edu

ABSTRACT

The first coordination sphere of Nd and Sm in glasses of the germanium chalcogenide - gallium chalcogenide system is studied by analysing of optical transmission spectra of $0.85\text{GeCh}_2 \cdot 0.15\text{Ga}_2\text{Ch}_3$ glasses (where Ch = S, Se, or Te) doped with chalcogenide of these metals. It is shown that the spectral shift in absorption bands of Nd^{3+} is a linear function of the mean electronegativity of chalcogens involved in the glasses, which indicates the coincidence between the average composition of the first coordination sphere of neodymium ions and the composition of anionic subsystem in the glasses under investigation. Spectral shift in absorption bands of Sm^{3+} is non-linear function of the mean electronegativity of chalcogens involved in the glasses.

INTRODUCTION

At present, considerable interest has been aroused in the applications of vitreous semiconductors as luminescent media in optoelectronics [1-3]. On one hand, this interest is accounted for by absence of high-energy phonons in the vibrational spectra unlike most of the known laser materials and, as a result, by the low probability of multiphonon nonradiative relaxation in lanthanides. For example, the energy of phonons in silicate glasses is about 1100 cm^{-1} and, therefore, the emission of three phonons suffices to relax the Pr^{3+} ion from the $^1\text{G}_4$ level to $^3\text{F}_4$ [1]. The energy of phonons in chalcogenide glasses is equal to $250\text{-}350 \text{ cm}^{-1}$, and analogous nonradiative relaxation requires the simultaneous emission of at least ten phonons.

The second reason is that these materials exhibit a band gap close to the energy of laser transitions in lanthanides. This permits optical pumping through the interband absorption of a semiconductor matrix followed by the transmission of excitation to lanthanide ions. The most complex stage to be realized in the aforementioned mechanism of optical pumping includes the achievement of a highly efficient transmission of excitation from a vitreous semiconductor matrix to lanthanide ions. For lanthanide ions, which are implanted into a vitreous semiconductor, the efficiency of optical pumping depends, among other factors, on the chemical environment of these ions.

In order to accomplish the optical pumping of lanthanide atoms through the interband absorption of a glass matrix, it is important to take into account not only the relationship between the luminescent transition energy of lanthanide and band gap of vitreous semiconductors, but also the location of energy levels of lanthanide in the energy band structure of vitreous semiconductor. The energy-level position of extrinsic lanthanide centers in the energy band structure of a vitreous semiconductor depends on the composition of the anionic environment of lanthanide (that is, on the chemical composition of the first coordination sphere). Vitreous semiconductors provide a wide variation in the composition of anionic sublattice, which can incorporate not only S, Se, or Te, but also dopants of oxygen and all halogens. This allows a purposeful change in energy-level positions of lanthanide centers

in the energy band structure of the vitreous semiconductor and makes it necessary to control the composition of the first coordination sphere of lanthanide atoms.

The selected method of control over the composition of the first coordination sphere is based on the spectral shift observations in the absorption bands of lanthanides under changes in the degree of ionicity of the bond due to variations in the intensity of local electric fields at a lanthanide ion.

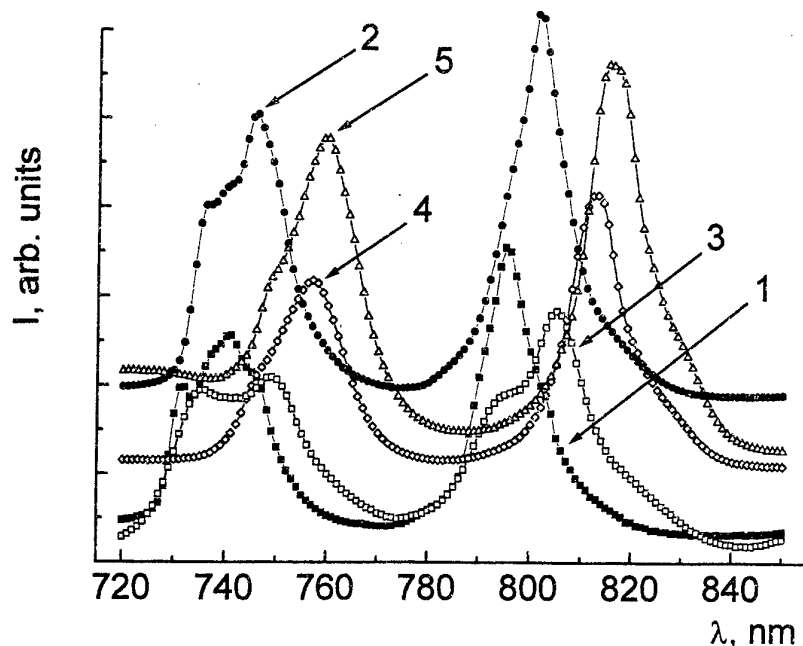


Fig.1. The absorption spectra of Nd^{3+} in (1) fluorozirconate, (2) phosphate, (3) aluminosilicate, (4) sulfide, and (5) selenide glasses.

EXPERIMENTAL

As is known, neodymium and other lanthanides can be introduced into glasses formed by gallium and germanium chalcogenides [4]. In the $\text{GeS}_2\text{-Ga}_2\text{S}_3$ system, the eutectic alloy of composition $0.85\text{GeS}_2 \cdot 0.15\text{Ga}_2\text{S}_3$ is most readily obtained in the vitreous state. Hence, the $0.85\text{GeCh}_2 \cdot 0.15\text{Ga}_2\text{Ch}_3$ glasses (where $\text{Ch}=\text{S}, \text{Se}, \text{or Te}$) were used as matrices in all the cases. Chalcogenide glasses were synthesized in evacuated (to 10^{-3} mm Hg) sealed silica ampules in rocking furnaces. For the synthesis, we used Se, Te, Ga, and Ge, in which the concentration of the major substance was no less than 99.9999 %. Sulfur (high-purity grade) was additionally distilled under vacuum. Metallic Nd and Sm were kept in sealed glass

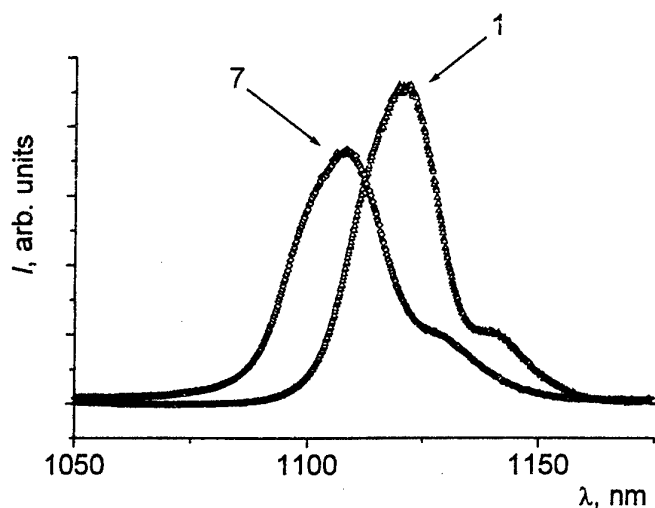


Fig.2. The absorption spectra of Sm^{3+} in (4) sulfide and (5) selenide glasses.

ampules and weighed immediately prior to evacuation of the ampule for synthesis. The synthesis was carried out upon continued rotation of the ampule at a temperature of 1150⁰ C for five hours. The concentration of Nd₂Ch₃ and Sm₂Ch₃ compounds in all samples was equal to 0.5 mol %.

Table 1.

Composition and spectral location of the Nd³⁺ absorption bands for chalcogenide glasses

Composition no.	Anionic composition of glass	α	E(II) \pm 5	E(III) \pm 5	E(V) \pm 5
			cm ⁻¹		
1	0.9Se-0.1Te	2.37	-	-	11177
2	Se	2.4	13169	12256	11192
3	0.97Se-0.03S	2.403	13174	-	-
4	0.7Se-0.3S	2.43	13180	12281	11216
5	0.5Se-0.5S	2.45	13194	12291	-
6	0.9S-0.1Te	2.46	-	12287	11236
7	0.7S-0.3Se	2.47	13189	12293	11230
8	S	2.5	13219	12312	11242
9	0.986S-0.014O	2.514	13233	12309	11261

In order to investigate the absorption spectra, glass samples were prepared in the form of plane-parallel polished plates 2 mm thick. To obtain information about changes in the spectral shift in absorption bands of Nd³⁺ and of Sm³⁺ as a function of the degree of ionicity of the bond in a wider range of the electronegativity values α of the anionic environment, we additionally studied the samples of fluorozirconate, phosphate, and aluminosilicate glasses doped with neodymium.

Table 2.

Composition and spectral location of the Sm³⁺ absorption bands for chalcogenide glasses

Composition no.	Anionic composition of glass	α	E(VI) \pm 5	E(VII) \pm 5
			cm ⁻¹	
1	Se	2.4	10327	9001
2	0.95Se-0.05S	2.405	10338	9024
3	0.8Se-0.2S	2.42	10380	9070
4	0.5Se-0.5S	2.45	10388	9068
5	0.8S-0.2Se	2.48	10402	9067
6	0.95S-0.05Se	2.495	10407	9050
7	S	2.5	10411	9045

The absorption spectra were taken at room temperature by using a universal spectrometric computer complex instrument (LOMO) based on an MDR-23 monochromator. Operation of the spectrometric complex, storage of information, and its preliminary processing were carried out on a PC. The spectra of the Nd-containing glasses were recorded in the wavelength range of 720-950 nm. The spectra of the Sm-containing glasses were recorded in the wavelength range of 800-1150 nm. All measurements were carried out with a step of 0.2 nm.

RESULTS

Figure 1 shows the absorption spectra of several neodymium-containing glasses: (1) fluorozirconate, (2) phosphate, (3) aluminosilicate, (4) sulfide, and (5) selenide. The last two

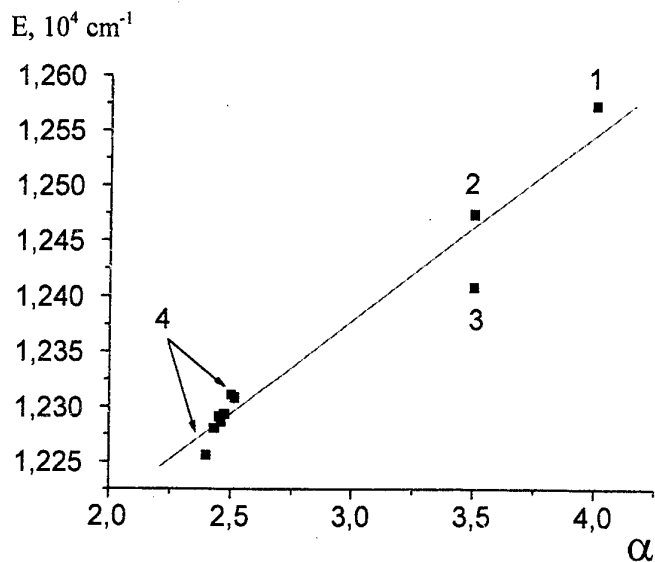


Fig.3. Spectral location of absorption band III plotted against the electronegativity of anions for (1) fluoride, (2) phosphate, (3) silicate, and (4) chalcogenide glasses.

glasses, which we synthesized, are included in the group of glasses under investigation (their compositions are presented in the table). Figure 3 displays the spectral location of absorption band at 790-820 nm as a function of the electronegativity of anions. These figures clearly demonstrate the general tendency in the spectral shift of absorption bands toward the long-wavelength range in going from anions with higher electronegativity to anions with lower electronegativity (F, O, S, and Se).

In addition to the two groups of absorption bands shown in Fig.1, we have studied the bands located at about 900 nm. Figure 4 depicts the total absorption spectrum of sulfide glass (see table 1, composition 8). For a detailed comparison, the intense bands (I, III, and V) were chosen from each group of the bands after resolution into components. The observed absorption bands I and II, III and IV are caused by the neodymium transitions $^4I_{9/2} \rightarrow ^4F_{7/2}$, $^4S_{3/2}$ and $^4I_{9/2} \rightarrow ^2H_{9/2}$, $^4F_{5/2}$, respectively. The absorption at about 890 nm is brought about by the $^4I_{9/2} \rightarrow ^4F_{3/2}$ transitions. Apparently, the complex structure of this part of the spectrum is determined by the Stark splitting of both states.

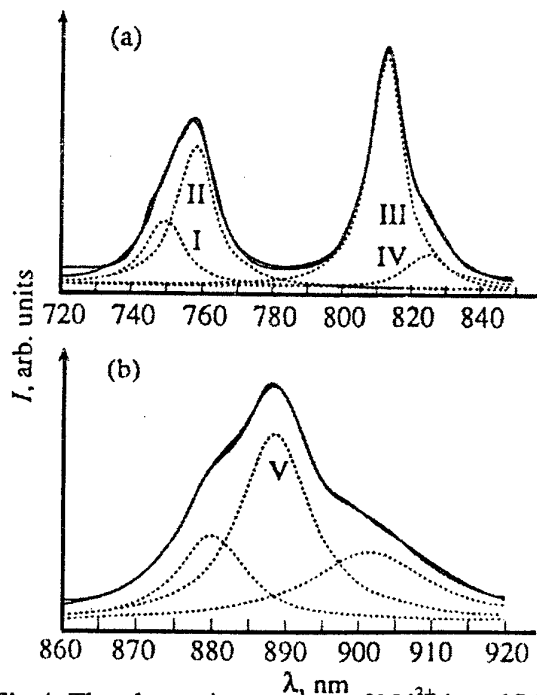


Fig.4. The absorption spectra of Nd^{3+} in sulfide glass (composition 8) in the wavelength ranges (a) 720-850 and (b) 860-920 nm. Roman numerals I-V denote the numbers of absorption bands.

Figure 5 presents the spectral locations of absorption band V as a function of the electronegativity of chalcogens, which from the anionic network of glass. In the case when the glass contains anions of different type, but analogous chemically (sulfur, selenium, and tellurium), the electronegativity (α) is treated as the mean value with allowance for the molecular

treated as the mean value with allowance for the molecular fraction of each type of anions. Generally speaking, the above dependence is rather a rough approximation, because the spectra shift is determined by the electric field strength at lanthanide ions, i.e., by the degree of ionicity of the chemical bonds. The latter quantity depends not only upon the electronegativity of anions, but also upon the chemical nature of the other elements involved in the formation of glass network. This is the reason why the absorption bands in phosphate and aluminosilicate glasses differ in location, even though both of these materials are oxide glasses. (We should not forget the concept of phosphate anion.) The studied glasses differ only in composition of the anionic subsystems. Therefore, the relationship between the spectral shift of absorption bands and the mean electronegativity of anions is not such a rough approximation.

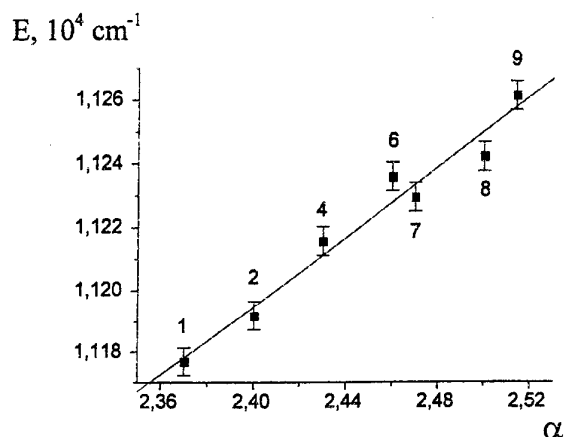


Fig.5. Spectral location of the Nd^{3+} absorption bands plotted against the mean electronegativity of anions in chalcogenide glasses.

and IV) plotted against the mean electronegativity of the anionic subsystem of chalcogenide glasses. However, the spectral locations of these bands are determined with a lower accuracy. This brings about a significant spread of the experimental points.

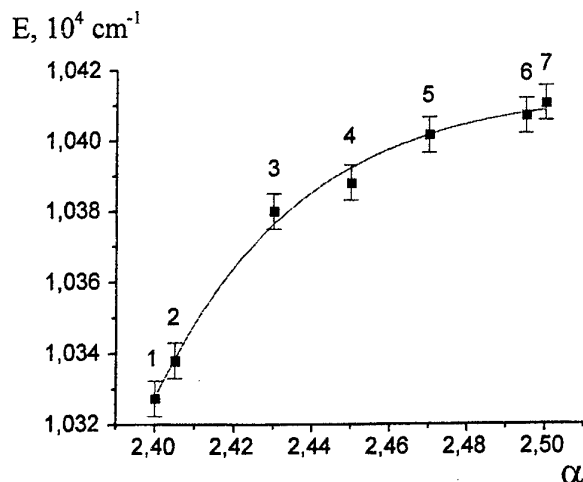


Fig.6. Spectral location of the Sm^{3+} absorption bands plotted against the mean electronegativity of anions in chalcogenide glasses.

In general, the ionicity of a bond is not a linear function of the difference in electronegativities when the latter quantity changes over a wide range. However, the mean electronegativity of chalcogens involved in the glasses under consideration varies within a rather narrow range. Hence, the linearity of the relationships represented in Fig.4 indicates the coincidence of the average composition of the anionic environment of neodymium ions in the first coordination sphere with the anionic composition of glass. A similar pattern is observed for the spectral location of weaker absorption bands (I

The spectral shift in absorption bands of Sm^{3+} is nonlinear function of average electronegativity of the anion sublattice (Fig.6). This may be the result of the two reasons. The first possible reason is the selectivity of Sm to the composition of the first coordination sphere, which manifests in enrichment of the first coordination sphere by S. Another possible reason is the existence of both Sm^{3+} and Sm^{2+} .

ACKNOWLEDGEMENTS

This work has been supported by the Programme "Integration" (Grant № 326.47).

REFERENCES

1. Wei, K., Machewirth, D.P., Wenzel, J., Snitzer, E., and Sigel, G.H., J. Non-Cryst. Solids, 1995, vol.182, pp.257.
2. Gu, S.Q., Ramachandran, S., Reuter, E.E., Turnbull, D.A., Verdeyen, J.T., and Bishop, S.G., Appl.Phys.Lett., 1995, vol.66, no.6, pp.670.
3. Mamedov, A.A., Noginov, M.A., Smirnov, V.A., Sokolov, V.V., and Shcherbakov, I.A., , Fiz.Khim.Stekla, 1991, vol.17, no.3, pp.446.
4. Vinogradova, G.Z., Moscow, Nauka, 1984.

RAMAN SPECTRA AND PHOTOSTRUCTURAL CHANGES OF SHORT RANGE ORDER IN AMORPHOUS As-S CHALCOGENIDES

M. Frumar, Z. Polák and Z. Černošek

Dept. General and Inorganic Chemistry, University of Pardubice, CZ 532 10 Pardubice, Czech Republic. e-mail: Miloslav.Frumar@upce.cz

ABSTRACT

Photoinduced changes of optical transmissivity, diffusion reflectivity, index of refraction and Raman spectra of $\text{As}_x\text{S}_{100-x}$ stoichiometric, ($x = 40$), as well as nonstoichiometric ($x = 38, 42$) glasses and thin films were studied. The irreversible photoinduced changes in thin films were larger than the reversible ones. Small photoinduced changes of optical properties and of the structure were also found in bulk glasses and glassy powders.

The reversible and irreversible changes of absorption edge and of index of refraction were accompanied by changes of Raman bands intensities and positions.

The Raman spectra of fresh-evaporated films as well as the spectra of As- rich bulk glasses contain some amount of As_4S_4 molecules. Their evaluated density (e.g. ~20 at % in $\text{As}_{42}\text{S}_{58}$ films, ~ 10 at. % for $\text{As}_{42}\text{S}_{58}$ bulk glasses) depends on the stoichiometry and state of the films and bulk glasses. The As_4S_4 content is lowered by exposure and also by annealing.

It was confirmed that the exposure changes not only the optical transmissivity, diffusion reflectivity and index of refraction but also the atomic structure of both fresh evaporated and annealed films of As-S system. A model was proposed in which the photoinduced changes of optical properties in As-S glasses are connected with photochemical reactions, which change the short-range-order, namely the densities of chemical bonds. The agreement between model assumptions and experimental results is reasonable.

1. INTRODUCTION

The irradiation of amorphous chalcogenides (AC) by ultraviolet or visible light, by electron- or γ - rays is often accompanied by changes of their atomic structure (see, e.g., ref. [1-3]). These changes are relatively large and irreversible in fresh-evaporated amorphous chalcogenide films (ACF) [1-4]. The illumination of fresh-evaporated ACF causes, e.g. in As-S films, some polymerisation and chemical interaction of molecular fragments (such as As_4S_4 , As_2S_3 , S_8 and others) which were formed in these films during thermal evaporation. The photoinduced process is accompanied by changes of many properties of ACF, including Raman bands intensities and positions [1, 2, 4]. The photoinduced effects (PE) in ACF were studied and reviewed many times, for the most recent see, e.g. [1, 3, 4]. In spite of a large experimental effort, controversial explanation of PE was obtained and the origin of many PE is still unclear.

In this paper, we have studied PE in as-evaporated and annealed films and bulk glasses of stoichiometric $\text{As}_{40}\text{S}_{60}$, and also in such films and bulk glasses containing excess sulphur or excess arsenic (e.g. in $\text{As}_{42}\text{S}_{58}$, or $\text{As}_{38}\text{S}_{62}$). The compositional dependence of individual properties and features can help to understand the Raman spectra, and help in elucidation of the nature of photoinduced effects. Thin evaporated films, bulk samples and glassy powders were studied. The comparison of the PE in As-S AC of identical composition and of different state gives again supplementing data for the description and discussion of PE.

For evaluation of photoinduced changes of atomic short-range order, which is apparently

behind many of photoinduced effects, the Fourier-transform (FT) Raman spectroscopy was used. This technique can "see" even small changes of short-range order, because the Raman bands intensities and positions are sensitive to the changes of the local structure including the densities of individual oscillators. The possibility of FT facility to scan the Raman spectra many times lowers effectively the noise and increases the sensitivity of this method.

2. EXPERIMENTAL

Bulk glasses were prepared by melting of high purity (5N) elements in evacuated quartz ampoules (650 - 700°C, 12 hrs). Thin films were prepared by vacuum thermal or flash evaporation ($p = 6 \times 10^{-4}$ Pa). The thickness of thin layers was measured using the dynamical weighing (quartz - crystal deposition monitor) and also by the Tolansky method (Na_D line interferometry of layers covered by semitransparent Ag layer). The fresh evaporated (= as-deposited) or annealed samples were exposed by high pressure mercury lamp light ($I = 0.014 \text{ W cm}^{-2}$, 1-2 hrs) in an inert atmosphere of pure Ar.

The Raman spectra were measured by FT Raman spectrometer IFS55/FRA106 (Bruker, Germany) using back-scattering method and Nd:YAG laser beam (1064 nm) as excitation light. The number of scans was usually $\leq 10^3$. In some experiments, the intensities of Raman lines from As-S thin films ($d \leq 500 \text{ nm}$) were too low. In such cases, the samples scratched from the larger area of glassy substrate were filled in a small ($\sim 0.5 \text{ mm}^3$) pit of a spectrometer target and then measured. The excitation light then penetrated several pieces of the film and Raman signal intensity was considerably improved. The powdered glasses were measured in the same pit of target. The reduced Raman spectra were obtained by the reduction method of Shuker and Gammon [5, 6] as modified by Kobliska and Solin [7]. The reduced spectra (their intensities) correspond to an approximate density of vibrational states $\rho(\omega)$ and were calculated using the equation

$$\rho(\omega) \sim I_{\text{red}} = (\omega_L - \omega)^{-4} [n(\omega, T) + 1]^{-1} \cdot I(\omega), \quad (1)$$

where $I(\omega)$ is measured intensity of Stokes part of the Raman spectrum, ω_L is incident photon frequency, ω is the vibrational frequency of Raman scattered light (in cm^{-1}). The Eq. (1) was modified by Bose-Einstein factor for distribution of phonons, $n(\omega, T) = [\exp(\hbar \omega/kT) - 1]^{-1}$, and Eq. 2 was used for corrections:

$$I_{\text{red}} = (\omega_L - \omega)^{-4} \cdot \omega [1 - \exp(-\hbar \omega/kT)] \cdot I(\omega), \quad (2)$$

where T is the temperature which enters through the Bose-Einstein occupation number for a phonon of energy ω .

The diffuse-reflectance spectra of powdered glasses were measured by JASCO V-570 spectrometer with Pulfrich integrating sphere. The evaluation of absorption coefficients from diffuse reflectance spectra was done by Kubelka and Munk method [8,9]. The Kubelka-Munk coefficient, (K/M) , of an "infinitely thick" layer may be written as

$$K/M = (f(R_\infty) = \frac{(1 - R_\infty)^2}{2R_\infty} = k / s,) \quad (3)$$

where R_∞ is absolute reflectance of the layer, $s \text{ (cm}^{-1}\text{)}$ is scattering coefficient and $k \text{ (cm}^{-1}\text{)}$ is the absorption coefficient. The scattering coefficient, s , depends on the size of particles and for fine powders is constant. The (K/M) is proportional to the absorption coefficient, k , and its spectral dependence can be used for evaluation of spectral dependence of k .

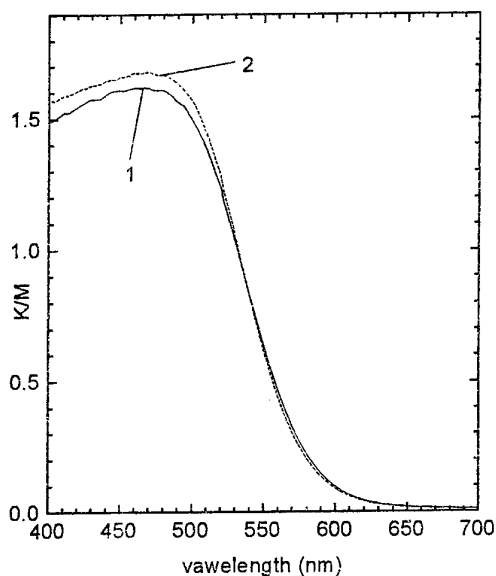


Fig. 5. The spectral dependence of K/M coefficient. 1 $\text{As}_{40}\text{S}_{60}$ powdered glass, 2 mixture of 0.8 $\text{As}_{40}\text{S}_{60}$ glass + 0.2 As_4S_4 powders

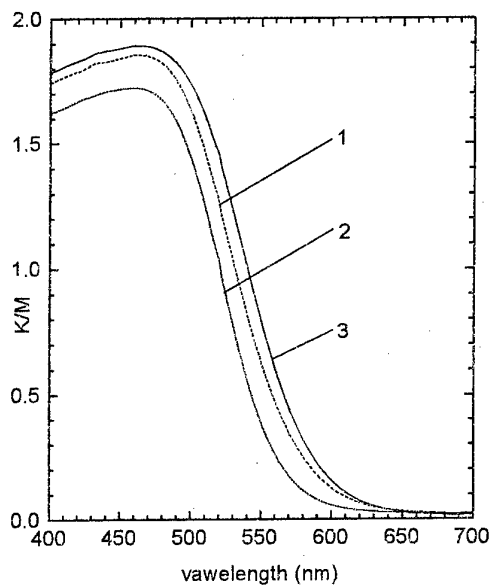


Fig. 6. The spectral dependence of K/M coefficient. 1 mixture of 0.5 $\text{As}_{38}\text{S}_{58}$ + 0.5 $\text{As}_{42}\text{S}_{58}$, powdered glasses, 2 $\text{As}_{38}\text{S}_{62}$ powdered glass, 3 $\text{As}_{42}\text{S}_{58}$ powdered glass

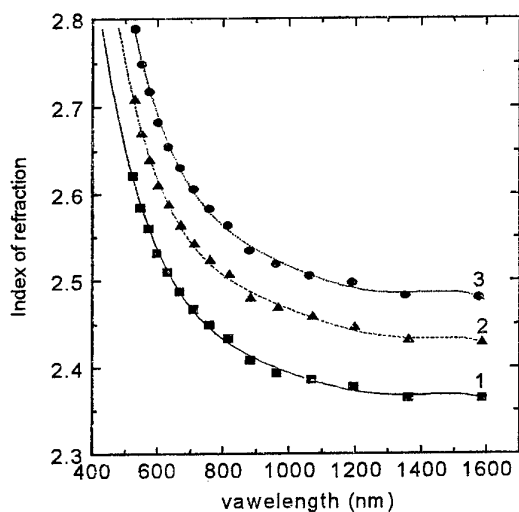


Fig. 7. Refractive index dispersion spectra of $\text{As}_{38}\text{S}_{62}$ films. The curves were determined according to polynomial fit. 1 fresh evaporated film, 2 exposed film, 3 annealed film.

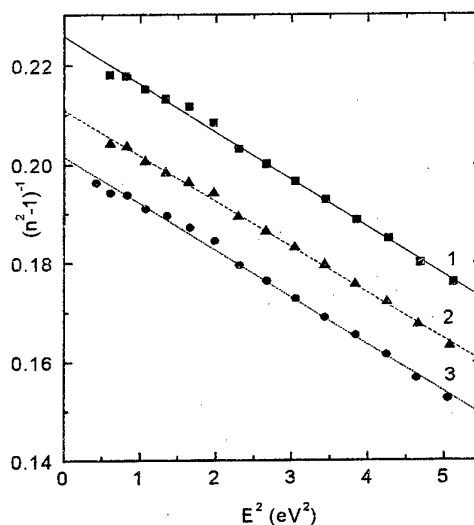


Fig. 8. Plot of refractive index factor $(n^2-1)^{-1}$ versus E^2 of $\text{As}_{38}\text{S}_{62}$ films. 1 fresh evaporated film, 2 exposed film, 3 annealed film.

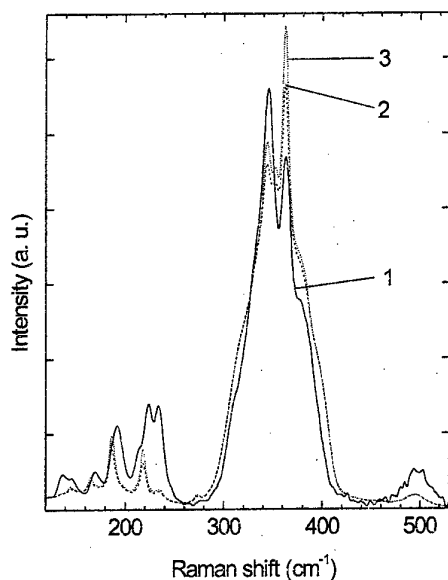


Fig. 1. Raman spectra of the As-S system samples. 1 $\text{As}_{42}\text{S}_{58}$ fresh evaporated film, 2 mixture of $0.85\text{As}_{40}\text{S}_{60}$ bulk + $0.15\text{As}_4\text{S}_4$ crystalline, 3 mixture of $0.2\text{As}_{40}\text{S}_{60}$ bulk + $0.8\text{As}_4\text{S}_4$ crystalline.

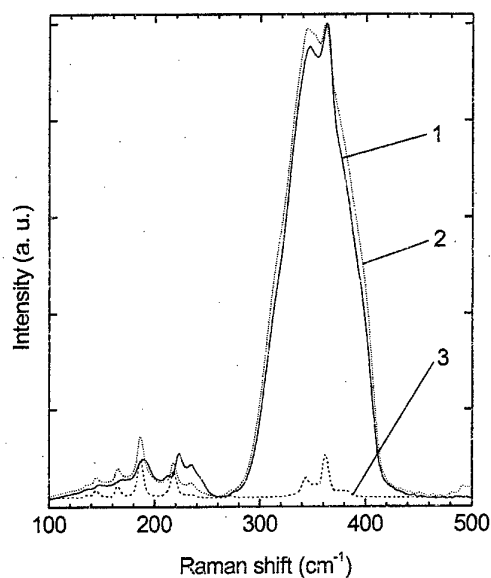


Fig. 2. Raman spectra of the As-S system glasses. 1 $\text{As}_{42}\text{S}_{58}$, 2 mixture of $\text{As}_{40}\text{S}_{60}$ bulk + crystalline As_4S_4 . 3 As_4S_4 crystalline. The background of spectra was corrected, the intensities were normalised to the intensity of 362 cm^{-1} band

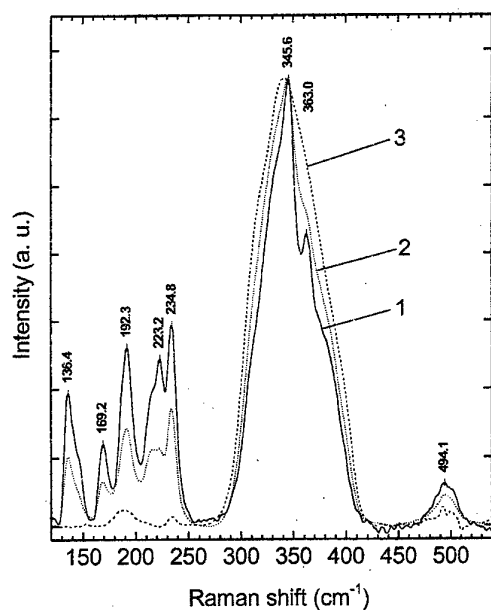


Fig. 3. Raman spectra of $\text{As}_{38}\text{S}_{62}$ films. 1 fresh evaporated film, 2 exposed film, 3 annealed film. The background was corrected, the intensities were normalised to the intensity of 345 cm^{-1} band.

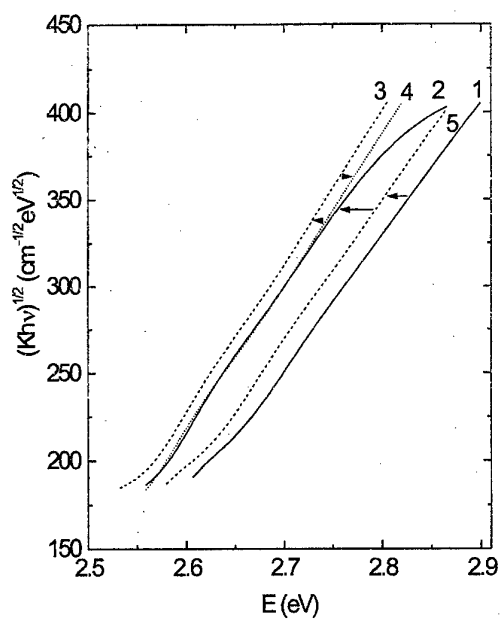


Fig. 4. Dependence of $(Kh\nu)^{1/2}$ on photon energy in $\text{As}_{40}\text{S}_{60}$ films. K is the absorption coefficient (cm^{-1}). 1 fresh evaporated film, 2 annealed film, 3 film exposed after annealing, 4 film was annealed, exposed and again annealed, 5 exposed film.

The spectral dependence of the index of refraction can be described Wemple-DiDomenico relationship for a single-oscillator model [11, 12]

$$n^2(\hbar\omega) - 1 = \frac{E_o E_d}{E_o^2 - (\hbar\omega)^2}, \quad (5)$$

where $\hbar\omega$ is photon energy, E_o is the single oscillator energy and E_d is the dispersion energy. The plot $1/(n^2-1)$ vs. $(\hbar\omega)^2$ is linear (Fig. 8).

The dispersion parameters obtained were following: The E_o was approximately $E_o \approx 2 E_g^{opt}$, where E_g^{opt} is the optical gap. The value of E_d obeys an empirical relation of Wemple DiDomenico [11, 12], $E_d = \beta N_c Z_a N_e$, (eV), where N_c is the co-ordination number of the cation nearest-neighbour to the anion. Z_a is formal chemical valence of the anion, N_e is the effective number of valence electrons per anion, and $\beta = 0.37 \pm 0.04$ for amorphous material [9,10].

The co-ordination number, N_c , probably increases by exposure, because As-S bonds replace some S-S bonds. The N_c should increase even more by annealing. Formal chemical valence of the anion, Z_a , should increase due to annealing. Its change by exposure is questionable. Some polymerisation is caused by exposure, and, also in the same time, formation of some S-S and As-As bonds can be supposed [2, 10]. The value of N_e (effective number of valence electrons per anion) is probably constant or nearly constant, because the sulphur can be bond either or to another S or to the As; both bonds are covalent. The ionicity of As-S bond is about 6% higher than the ionicity of the As-As bond. The highest number of unsaturated bonds should be probably found in fresh-evaporated films and the lowest one in the annealed films.

ACKNOWLEDGMENT

The work was supported by grants No. 203/96/0876 and No. 203/98/0103 of Czech Grant Agency Prague, which is gratefully acknowledged.

REFERENCES

- [1] M. Frumar, Z. Polák, Z. Černošek, B. Frumarová T. Wágner, Chem. Papers, 51 (1997) 310-327.
- [2] M. Frumar, M. Vlček, Z. Černošek, Z. Polák, T. Wágner, J. Non-Cryst. Solids, 213-214 (1997) 215-224.
- [3] K. Shimakawa, A. Kolobov, S. R. Elliott, Advances in Physics, 44 (1995) 475.
- [4] M. Frumar, Z. Polák, Z. Černošek, M. Vlček, and B. Frumarová, in Physics and Application of Non Crystalline Semiconductors in Optoelectronics (M. Bertolotti and A. Andriesh, Editors.) Pp.. 123-139. Kluwer Acad. Publ., London, 1997.
- [5] R. Shuker and R. W. Gammon, Phys. Rev. Lett. 25 (1970) 222.
- [6] G. Lucovsky, F. L. Galeener, R. C. Keezer, R. H. Geils and H. A. Six, Phys. Rev. B10 (1974) 5134.
- [7] R. J. Kobliska and S. A. Solin, J. Non-Crystalline Solids 8-10 (1972) 191.
- [8] P. Kubelka and E. Munk: Z. Tech. Phys. 12 (1931) 593.
- [9] G. Kortum, Reflexions – spektroskopie. Springer, Berlin 1969.
- [10] M. Frumar, A. P. Firth and A. E. Owen, Phil. Mag. B50 (1984) 463.
- [11] S. H. Wemple and W. DiDomenico, Phys. Rev. B3 (1971) 1338.
- [12] S. H. Wemple, Phys. Rev. B7 (1973) 3767.

3. RESULTS AND DISCUSSION

Fresh evaporated amorphous films of As-S system contain some amount of As_4S_4 and other molecular fragments (see, e.g. Fig. 1) which are formed during evaporation of As_2S_3 , e.g. according to the scheme: $2 \text{As}_2\text{S}_3 = \text{As}_4\text{S}_4 + \text{S}_2$. The reason for this dissociation is higher stability of As_4S_4 molecules than the stability As_2S_3 molecules at temperatures of evaporation.

The As_4S_4 molecules are apparently present not only in evaporated films but also in the glasses with excess of As, e.g. in $\text{As}_{42}\text{S}_{58}$ bulk glasses (Fig. 2). One can see that the most narrow features of the Raman spectrum of $\text{As}_{42}\text{S}_{58}$ bulk glass can be obtained by addition of the spectrum of crystalline As_4S_4 , which is a molecular solid, to the spectrum of $\text{As}_{40}\text{S}_{60}$ bulk glasses (Fig. 1). The glasses of the As-S system with excess of As can be considered as solid solutions of As_2S_3 and As_4S_4 , but the glass contains also some other As-As bonds built in the glassy matrix, not in As_4S_4 structural units (Fig. 2, band near 235 cm^{-1}).

The spectrum of fresh evaporated films of $\text{As}_{42}\text{S}_{58}$ (Fig. 1) contains some features which can be assigned to As_4S_4 molecules. The spectrum of fresh evaporated films can be again formed by addition of the spectrum of As_4S_4 and of As_2S_3 glass. The content of As_4S_4 is relatively high in fresh evaporated films. We evaluate, that the content is higher than 20 mol. % of As_4S_4 (Fig. 2).

In the Raman spectrum of fresh evaporated As-S films (Fig. 1, 3), there are also some other bands, which cannot be assigned to As_4S_4 and As_2S_3 , e.g. 138, 143, 214, 235 cm^{-1} . The intensities of As_4S_4 bands in As-S fresh evaporated films are changed and also their positions are shifted towards higher frequencies as compared with crystalline As_4S_4 (Figs. 1, 3) which is probably caused by more intensive interaction of dissolved As_4S_4 molecules with the amorphous matrix than in corresponding As_4S_4 crystals. In such crystals, the individual As_4S_4 molecules are bond together only by weak van der Waals bonds, in amorphous solid some covalent bonding is evidently present.

Exposure and even more annealing (Fig. 3) lower the content of As_4S_4 molecules in the fresh evaporated films. The exposure does not lower only the content of As_4S_4 and S-S bonds in such films (band near 495 cm^{-1}), the amplitudes of some Raman bands which can be assigned to the As-As bonds incorporated in the amorphous matrix (235 cm^{-1}) are relatively increased.

The absorption edge is shifted by exposure towards lower energies, further by annealing and even more by following exposure of annealed films (Fig. 4). The mechanism responsible for these shifts is not apparently connected with the content of As_4S_4 , as can be judged from the diffuse reflectivity of the powdered $\text{As}_{40}\text{S}_{60}$ and of the mixture of $0.8(\text{As}_{40}\text{S}_{60}) + 0.2(\text{As}_4\text{S}_4)$, (Fig. 5). The absorption edge is not practically shifted even by addition of 20 mol. % of As_4S_4 to $\text{As}_{40}\text{S}_{60}$, it becomes only sharper, because the As_4S_4 is a crystalline molecular solid. The photodarkening should be connected with the content of As-As bonds build in the amorphous matrix (but not in the form of As_4S_4) as can be judged from the Fig. 6. The increasing content of As and, therefore, of As-As bonds, in the bulk glasses (in which the content of As_4S_4 is low) lead to the "red" shift of the absorption edge (Fig. 6). The shift is analogous to the shift of the absorption edge due to exposure or annealing (Fig. 4). The results can be interpreted as the thermally and optically induced shift of the bond statistics [9].

$$2|\text{As-S}| = |\text{As-As}| + |\text{S-S}|, \quad (4)$$

where $|\text{M-X}|$ is for the chemical bonds between atoms M and X.

Together with the photoinduced change of structure, the index of refraction of As-S evaporated films are also changed. The exposure and even more the annealing increase the index of refraction (Figs. 7, 8).

STRUCTURE OF CHALCOGENIDE GLASSES IN As_2Se_3 - CuI SYSTEM.

S.Mamedov, A.Bolotov

Chemical Department, St.Petersburg University, Universitetski pr.2, Staryi Petergof,
198904, Russia. email: mamedov@physik.fu-berlin.de

L.Brinker, A.Kisliuk and M.Soltwisch

Institut für Experimentalphysik, Freie Universität Berlin, Arnimallee 14, 14195, Berlin,
Germany.

M.Vlcek, A.Sclenar

General and Inorganic Chemistry Department, Faculty of Chemical Technology
University of Pardubice, nam. Cs. ledii 565, 53210 Pardubice, Czech Republic.

ABSTRACT

X-ray diffraction, Raman and optical data have been obtained for glasses in the system As_2Se_3 - CuI . The position of first sharp diffraction peak is nearly independent from concentration of CuI . The experimental results indicate, that addition of CuI to glassy As_2Se_3 causes strong changes in the correlation length, in the slope of absorption edge, and in the transmission in near IR region, but there are no significant changes in the Raman spectra of these glasses. Results are discussed in the frame of the "layer structure" model of glassy As_2Se_3 . They support the picture of isolated and chemically non-reacting CuI -molecules between deformed As_2Se_3 -layers.

INTRODUCTION

The properties of chalcogenide glasses may change drastically when they are doped with transition metals such as Cu [1, 2]. The doping changes the electrical conductivity due to a change of the type of carriers in chalcogenide glasses. The system As_2Se_3 - CuI was already studied in [3-6]. Our previous X-ray measurements of the system As_2S_3 - CuI , which is a similar system from the chemical point of view, showed a strong influence of the dopant CuI on the First Sharp Diffraction Peak (FSDP) [7], but there are no changes in the Raman spectra of the glasses [10].

In the present report we study the nano structure of the chalcogenide glasses in As_2Se_3 - CuI using X-ray, Raman scattering and optical transmission experiments.

EXPERIMENTS

The chalcogenide glasses $(100-x) As_2S_3 - x CuI$ with different concentration of CuI ($x=0...90$) were prepared by the use of properly weighed analytical grade CuI and synthesised As_2Se_3 . The elemental arsenic and selenium as well as the copper-iodine were purchased from ALDRICH with a purity of $> 99.999\%$. To obtain glassy As_2Se_3 , pure selenium and arsenic (6N) were weighed and the mixture was vacuum sealed in a quartz tube. The tube was kept at 950K for 6 hours in a rocking furnace. The samples were quenched from the melt with rate 1 K/s. For each concentration, the mixture of As_2Se_3 and CuI was vacuum sealed in a quartz tube and kept afterwards at 1100K for 48 hours. During this time the liquid was stirred every 30 minutes in order to get a homogeneous melt. After this the mixture was cooled down to 700 °C with a rate of 1 °C/min and kept at this temperature for more than 10 hours. Next, the sample was rapidly quenched by plunging it into a water/ice mixture. No annealing was performed to prevent any micro crystallisation. For the X-ray and optical transmission

measurement plates of $10 \times 10 \times 0.5$ mm with polished surfaces were cut. For the Raman measurement samples of a thickness larger than 3 mm were used to insure bulk measurements.

X-ray measurements have been performed on a Debye-Scherrer goniometer (focusing-reflecting geometry; $\text{Cu K}\alpha$ radiation with $\lambda = 1.542 \text{ \AA}$; angular resolution 0.1°). The Raman spectra from 50 to 3500 cm^{-1} were measured by IFS 55 spectrometer with FHA 106 accessory (Bruker) using back-scattering geometry and Nd:YAG laser beam (1064 nm , 100 mW) as excitation light and a resolution of 4 cm^{-1} . Each dataset consists of 100 scans which results in a big signal noise ratio. There was no sign of signal deterioration due to photodarkening effect. For the transmission experiment we used a double beam spectrometer SF2 in the range of 750 nm to 1100 nm . The spectral slit gave result a 2 nm .

RESULTS

Figure 1 shows measured X-ray diffraction patterns for the investigated glasses (fig. 1) (strong lines at $30\text{--}35 \text{ nm}^{-1}$ are from the holder). The *FSDP* is disappeared for glasses with *CuI* concentration more 30%. As shown in Ref. [7,8,9] the *FSDP* can be approximated by a simple Lorentzian. Thus we used also a Lorentzian

approximation to evaluate the width ΔQ of the *FSDP*. The intensities $I(Q)$ on the side of small Q -values were fitted to a Lorentzian with a peak position Q_l and a width ΔQ . Figure 2 shows the calculated half width of the *FSDP* (ΔQ) (open circle), the correlation length (R_c) (solid circle) which was estimated from ΔQ using the relation $R_c = 2\pi/\Delta Q$. Note the strong increase of ΔQ with concentration, while the peak position Q_l changes only about 10%. Figure 3 shows the normalized Raman spectra of glasses in $(100-x)\text{As}_2\text{Se}_3-x\text{CuI}$ system. The spectral shape of the band between 200 and 300 cm^{-1}

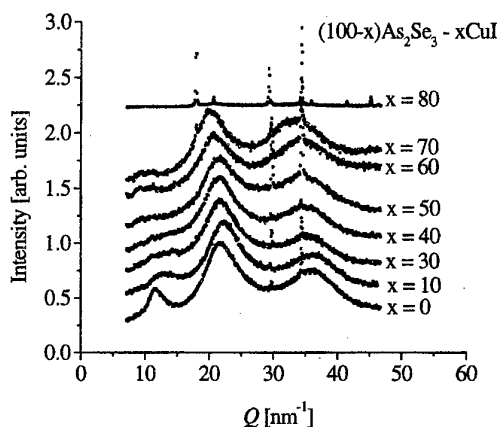


Figure 1.

does not significantly change up to 70% *CuI*. At the concentration of *CuI* more 70% the additional bands at are appeared. The peaks at 83 and 122 cm^{-1} are corresponds to the vibrational modes of crystalline *CuI*. The peaks at 106 , 171 , 215 , 228 and 247 cm^{-1} are corresponds to the crystalline As_2Se_3 . The transmission spectra are shown in Fig. 4 for pure As_2Se_3 and samples with different concentrations of *CuI*. The transmission of the glasses is drastically decreased with *CuI* concentration. From the transmission (T) spectra the absorption coefficient α was calculated using Equation

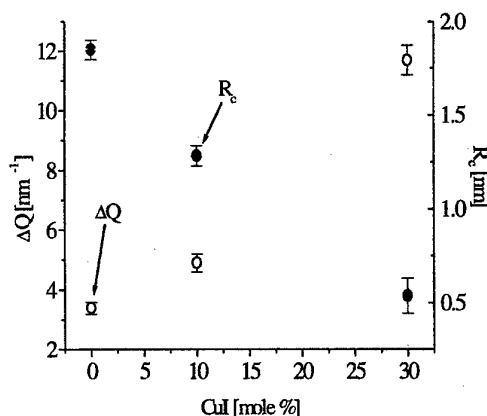


Figure 2.

$$\alpha(\lambda) = -\{\ln T(\lambda) - \ln(1-R^2)\}/d$$

here d , λ and R are thickness of the sample, wave length of light and reflection, respectively. From the energy-dependence of α the slope of the absorption edge (γ) using the Urbach-Equation

$$\alpha(h\nu) = \alpha_0 \times \exp[-(\gamma^f(E_0 - h\nu)/kT)]$$

and gap at $\alpha=100 \text{ cm}^{-1}$ were calculated. The slope of absorption edge (solid circle) and gap (open circle) in glasses of $(100-x) \text{As}_2\text{Se}_3 - x \text{CuI}$ system are shown in Fig 5. The slope of the edge is strong decrease with CuI concentration from 20.6 for pure As_2Se_3 to 7.6 for glass with 60% CuI , while the gap change only slightly (from 1.63 eV to 1.35 eV).

DISCUSSION

Let us discuss the experimental results in the frame of layer structure model for glassy As_2Se_3 [1,7,10]. Addition of CuI to glassy As_2Se_3 causes strong changes of $FSDP$, slope of the absorption edge and maximum transmission. The correlation length (R_c) which presents the scale of medium range order, is closely related to some characteristic distance between the underlying structural units which produce the $FSDP$. The width of this peak gives information about the distribution of structural fragments. Insertion of CuI molecules to glassy matrix cause a loss of the correlation between the As_2Se_3 layers and appeared as a broadening $FSDP$. The optical data suppose that the CuI molecules located between the layers destroy the As_2Se_3 network by introducing an additional disorder which cause scattering (or absorption) of the light into the glass and appears as a decreasing of transmission

(from 60% for pure As_2Se_3 to 17% for glass containing 60% CuI) and slope of absorption edge (from 21 to 7). It has been shown that in most glass-formers the slope of the absorption edge is between 16 and 20. Transmission for such materials in IR region is more 60% and it may be calculated from the refractive index. The addition of CuI causes only a disturbance of the As_2Se_3 -network without strong chemical interaction. This conclusion is consistent with Raman studies. The broad band at $200\text{--}300 \text{ cm}^{-1}$ which is connected with vibration modes of the AsSe_3 pyramid changes only slightly (i.e. structural changes of basic glassy As_2Se_3 matrix

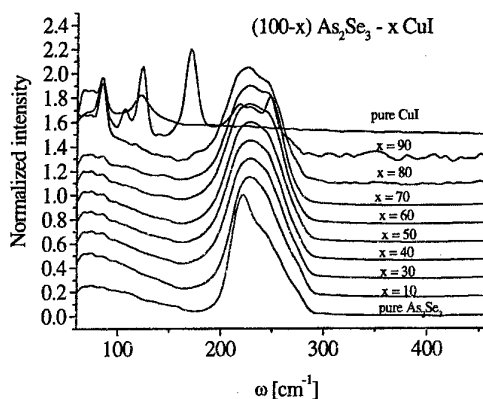


Figure 3.

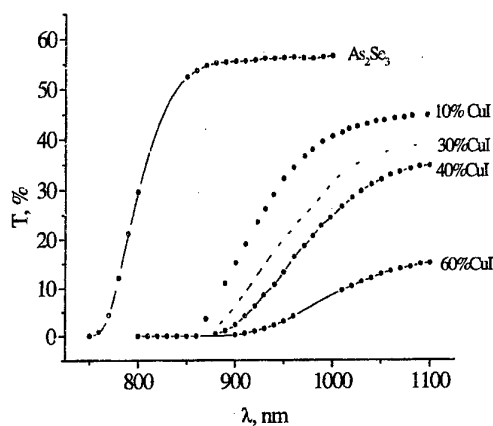


Figure 4.

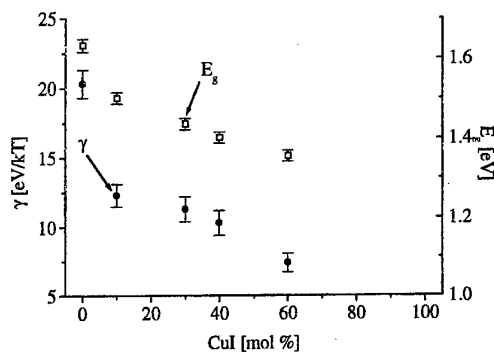


Figure 5.

are significantly lower than one would expect when 60% of other materials (*CuI*) is added) and new bands (from crystalline As_2Se_3 and *CuI*) can be seen but only for samples with 70% and more *CuI* (Fig.3). Thus we can conclude that *CuI* only destroys As_2Se_3 network by introducing an additional disorder and thus no chemical interaction between *CuI* and As_2Se_3 network takes place.

CONCLUSION

X-ray small angle scattering, Raman spectra, visible and near IR optical spectra glasses in As_2Se_3 -*xCuI* system have been measured. The experimental results indicate that *CuI* has strong effect on the width of *FSDP*, optical transmission and slope of the absorption edge. In contrast, the position of *FSDP* and Raman spectra caused by addition of *CuI* in concentration up to 60% shifts only slightly. This can be interpreted to mean that addition of *CuI* causes a disturbance of the As_2Se_3 network combined with the creation of an additional disorder (inhomogeneity). This conclusion has been confirmed by Raman spectroscopy, as the main bands at 200-300 cm^{-1} which corresponds to vibration modes of $AsSe_3$ pyramids has not been practically changed and no new bands were observed in spectra. At the concentration of *CuI* 60% and more the crystalline phase appears in the samples. It has been confirmed by X-ray diffraction and Raman measurements.

ACKNOWLEDGEMENTS

We are thankful to Prof.Dr.D.Quitmann (Institut für Experimentalphysik, FU-Berlin) for helpful discussion. The work was supported by DEG through Sfb 337.

REFERENCES

- [1] Z.U.Borisova, Glassy Semiconductors, Plenum Press, N.Y.,1981.
- [2] Tauc J., Menth A., J. Non-Cryst. Solids, 8-10 (1972), 569.
- [3] Lui C., Angell C.A., Solid State Ionics. 13 (1984), 2. 105.
- [4] Rivolta B., Bonino F., Scrosati B., Materials Chemistry and Physics. 19 (1988), 557.
- [5] Machida N., Chusho M., Minami T., J. Non-Cryst. Solids, 101 (1988), 70.
- [6] Kadono K., Mitani K., Yamashita M., Tanaka H., Kawamoto Y., Ohno K., Kanno R., J.Non-Cryst. Solids, 140 (1992), 103.
- [7] S.Mamedov, A.Bolotov, L.Brinker, A.Kisliuk, M.Soltwisch, J. Non-Cryst. Solids, 224 (1998), 89.
- [8] A.C.Wright, R.A. Hulme, D.J. Grimley, R.N. Sinclair, S.W. Martin, D.L. Price, F.L. Galeener, J.Non-Cryst. Solids, 129 (1991), 213
- [9] A.Sokolov, A.Kisliuk, M.Soltwisch, D.Quitmann, Phys. Rev. Lett., 69 (1992), 10, 1540.
- [10] S.Mamedov, A.Bolotov, L.Brinker, A.Kisliuk, M.Soltwisch, M.Vlcek, A.Sclenar, Phys.Rev. 1998 (in press).

HIGH TEMPERATURE STRUCTURE OF $K_2O \cdot TeO_2$ GLASSES

R. Akagi¹, K. Handa², N. Ohtori³, A.C. Hannon⁴, M. Tatsumisago⁵
and N. Umesaki⁶

1 Graduate School of Science and Technology, Kobe University, 1-1, Rokkodai-cho,
Nada-ku, Kobe 657-8501, Japan

2 Department of Photonics, Faculty of Science and Engineering, Ritsumeikan University,
Kusatsu, Siga 525-8577, Japan

3 Graduate School of Science and Technology, Niigata University, Igarashi 2-no cho,
Niigata 950-2102, Japan email ohtori@sc.niigata-u.ac.jp

4 ISIS, Rutherford Appleton Laboratory, Chilton, Didcot, Oxon OX11 0QX, UK email
ach@rl.ac.uk

5 Department of Applied Material Science, Osaka Prefecture University, Sakai, Osaka
599-8231, Japan email tatsu@chem.osakafu-u.ac.jp

6 Osaka National Research Institute (ONRI), AIST, 1-8-31, Midoriga-oka, Ikeda, Osaka
563-8577, Japan email umesaki@onri.go.jp

ABSTRACT

The local structure of tellurite glasses has attracted much interest in connection with their promising optical and electrical properties. It is well known that binary tellurite easily forms glass compared with the pure TeO_2 [1,2]. Incorporation of second components to TeO_2 glass is expected to extend the Te-O interatomic distance, which increases the mobility of the polyhedra and thereby provides a favorable condition necessary for tellurite vitrification [3]. The relationship between glass structure and added alkali ion composition has been discussed by means of Raman spectroscopy [4]. However, the exact form of the Te-O structural units in potassium tellurite glasses has not yet been established. Therefore, we have studied the structure of the $K_2O \cdot TeO_2$ glasses by using Raman spectroscopy, neutron diffraction and XAFS measurements. Furthermore, we have extended our study to the structure of the $K_2O \cdot TeO_2$ glasses at high temperature by high-temperature Raman spectroscopy and high XRD methods.

$xK_2O \cdot TeO_2$ ($x=5, 10, 15, 20, 25$ and $30mol\%$) glasses were prepared using a roller-quenching technique by a twin-roller apparatus with a thermal-image furnace [5].

Fig. 1 shows Raman spectra of the $xK_2O \cdot TeO_2$ ($x=5, 10, 15, 20, 25$ and $30mol\%$) glasses. The obtained Raman spectra for these glasses exhibited three broad Raman peaks at around $770, 670$ and $460cm^{-1}$ at room temperature. These peaks are ascribed to the stretching mode of the TeO_3 trigonal pyramid (*tp*) units containing terminal Te-O bonds such as $Te=O$ and $Te-O^-$ with non-bridging oxygen atoms (NBO), the stretching mode of TeO_4 trigonal bipyramid (*tbp*) units with bridging oxygen atoms (BO) and the bending mode of Te-O-Te or O-Te-O linkages, respectively [6,7]. The intensity of the $770cm^{-1}$ peak gradually becomes larger, and those of the $670cm^{-1}$ and $470cm^{-1}$ peaks become smaller as the ratio of K_2O content is raised. The Raman results indicate that the addition of K_2O increases the TeO_3 *tp* units with NBO in the $xK_2O \cdot TeO_2$ glasses. It is explained that potassium ion which is a network-modifying element stabilizes the TeO_3 *tp* units in the $xK_2O \cdot TeO_2$ glasses.

The detail of the K-O correlation and Te-O correlation in the $xK_2O \cdot TeO_2$ glasses were studied by XAFS measurements and neutron diffraction. Fig. 2 shows normalized XAFS spectra at the K K-edge of these glasses. The structural parameters for the K-O correlation in the $xK_2O \cdot TeO_2$ glasses have been obtained from a best-fit routine, as summarized on Table 1.

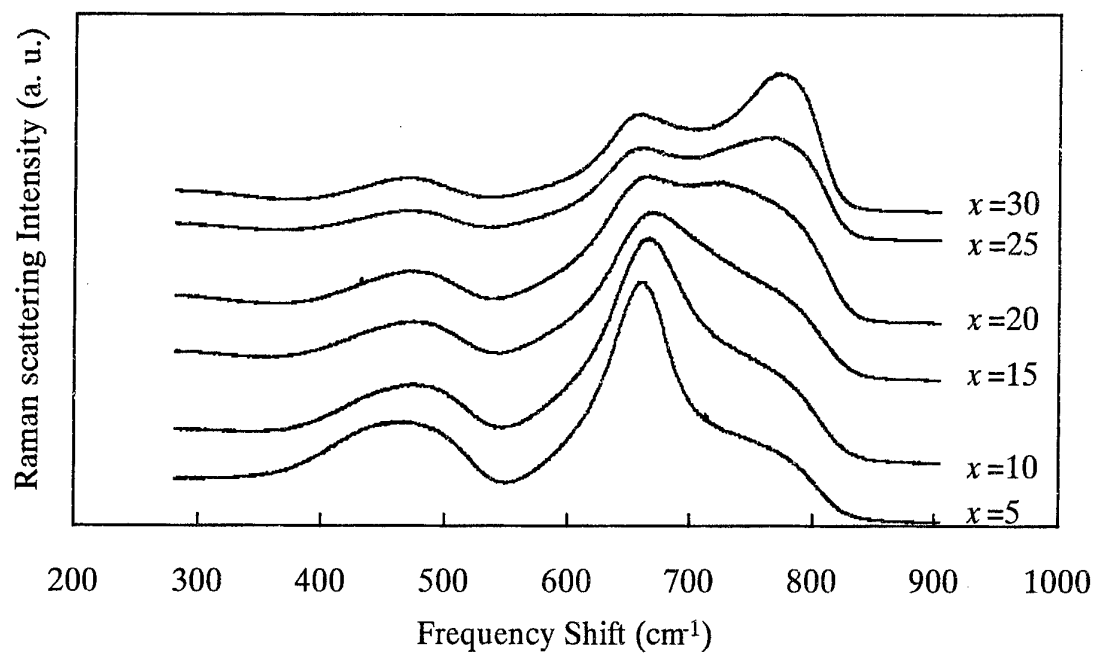


Fig. 1. Raman spectra for $x\text{K}_2\text{O} \cdot \text{TeO}_2$ ($x=5, 10, 15, 20, 25$ and $30\text{mol}\%$) glasses

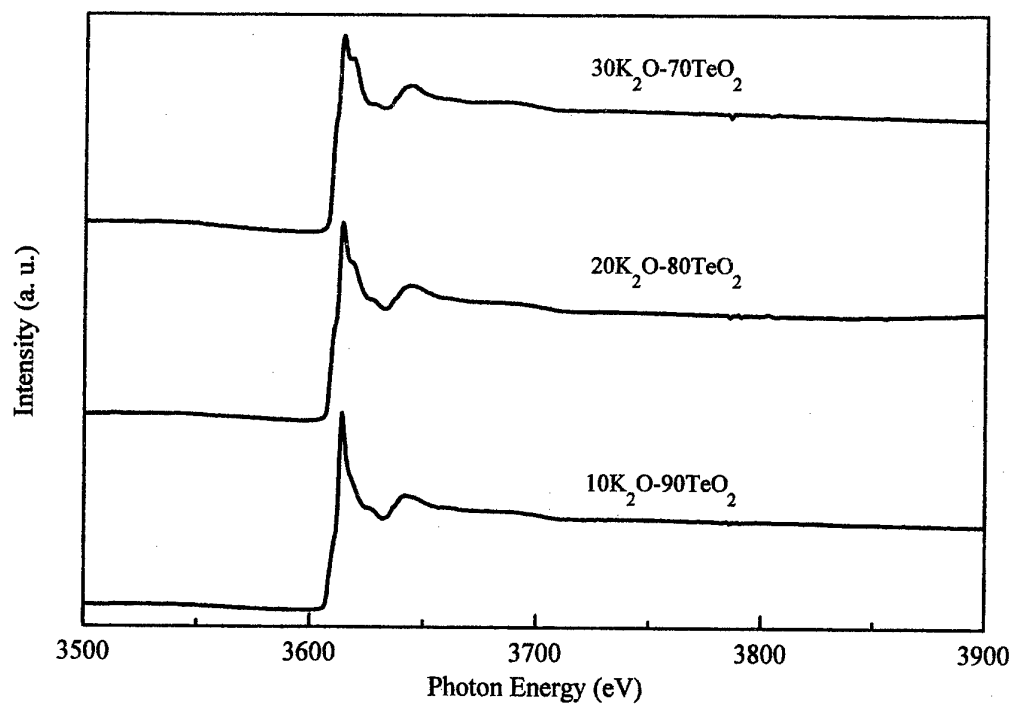


Fig. 2. Normalized K K-XAFS spectra for the $x\text{K}_2\text{O} \cdot \text{TeO}_2$ ($x=10, 20$, and $30\text{mol}\%$) glasses

The K-O distances are almost equal to the sum of the ionic radii K^+ and O^{2-} ($=2.73\text{\AA}$). Total coordination numbers ($N_{K/O}$ in Table 1) are almost six. A $k^3\chi(k)$ of the $30K_2O\cdot 70TeO_2$ glass is compared with a calculated $k^3\chi(k)$ of K_2TeO_3 [8] and $K_2Te_4O_{12}$ [9] crystals in Fig. 3. These $k^3\chi(k)$ spectra from experimental data are similar to the $k^3\chi(k)$ spectrum from FEFF calculation of K_2TeO_3 crystal [8] than that of $K_2Te_4O_{12}$ crystal [9]. It is considered that the local structure of potassium in $xK_2O\cdot TeO_2$ ($x=5, 10, 15, 20, 25$ and $30mol\%$) glasses is similar to that of K_2TeO_3 crystal in which the K atoms are octahedrally coordinated to six O atoms with distances ranging from 2.728 to 3.050 \AA [8]. On the other hand, the neutron diffraction results indicate the detailed Te-O correlation in the K_2O - TeO_2 glasses [10]. The well-defined low r component of the Te-O peak moves to lower r and becomes sharper as K_2O is added. Its coordination number falls from ~ 2.5 to ~ 2.2 . These neutron results are consistent with the expected increase in the number of non-bridging oxygen. The neutron results are in good agreement with our Te L3-edge XANES in $xK_2O\cdot TeO_2$ ($x=10, 20$ and $30mol\%$) as shown in Fig. 4.

Table 1. Structure parameters of short range order, mean distance R (\AA), coordination number N (atoms) and Debye-Waller factor σ (\AA) for $xK_2O\cdot TeO_2$ ($x=10, 20$ and $30mol\%$) glasses

Sample		$N_{K/O}$ (atoms)	$R_{K/O}$ (\AA)	$\sigma_{K/O}$ (\AA)
10 $K_2O\cdot 90TeO_2$	K-O	5.9	2.71	0.153
20 $K_2O\cdot 80TeO_2$	K-O	6.0	2.71	0.167
30 $K_2O\cdot 70TeO_2$	K-O	6.3	2.74	0.172

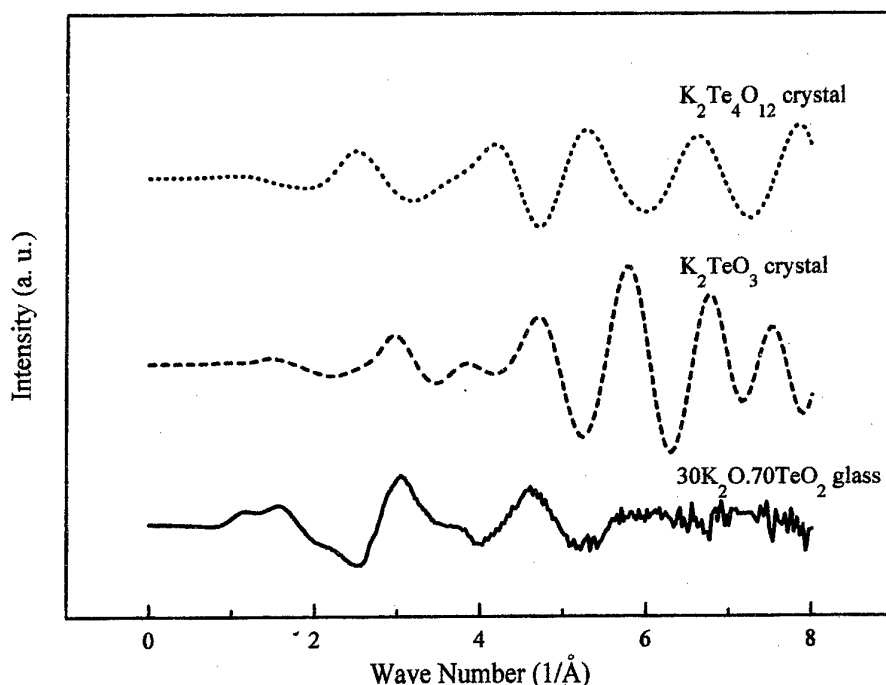


Fig. 3. $k^3\chi(k)$ spectrum from experiment data of $30K_2O\cdot 70TeO_2$ glass and spectra calculated using FEFF program for K_2TeO_3 crystal [8] and $K_2Te_4O_{12}$ crystal [9]

Fig. 5 shows the high-temperature Raman spectra for $20K_2O\cdot 80TeO_2$ glass. The intensity ratio of $770cm^{-1}$ peak and $670cm^{-1}, 470cm^{-1}$ peaks becomes larger with increasing temperature. The high-temperature Raman results indicate that Te-O-Te or O-Te-O linkage is cut with

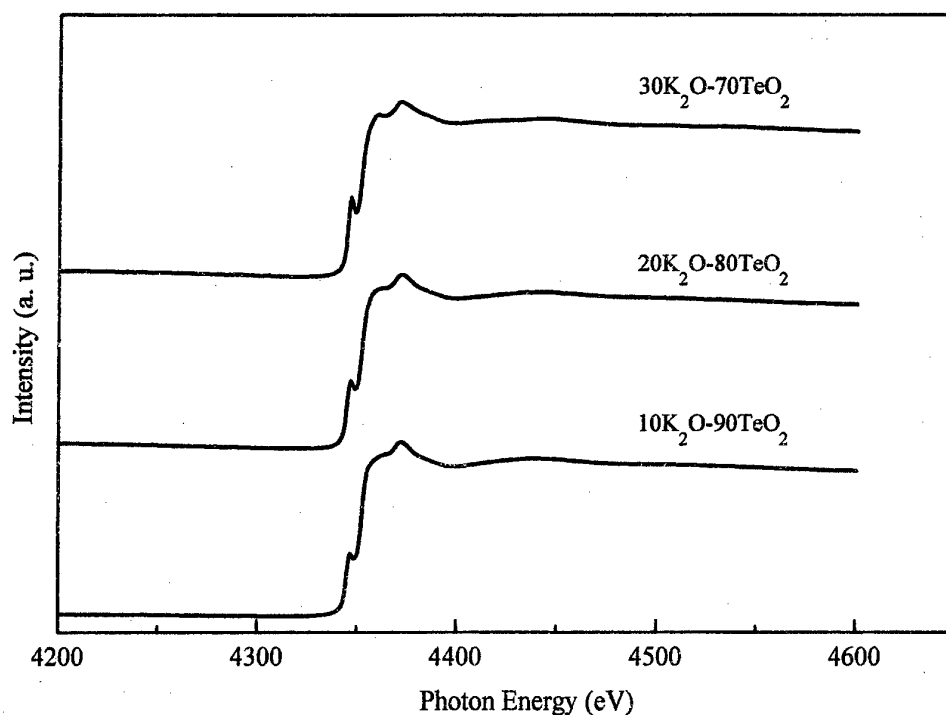


Fig. 4. Normalized Te L3-XAFS spectra for the $x\text{K}_2\text{O} \cdot \text{TeO}_2$ ($x=10, 20$ and $30\text{mol}\%$) glasses

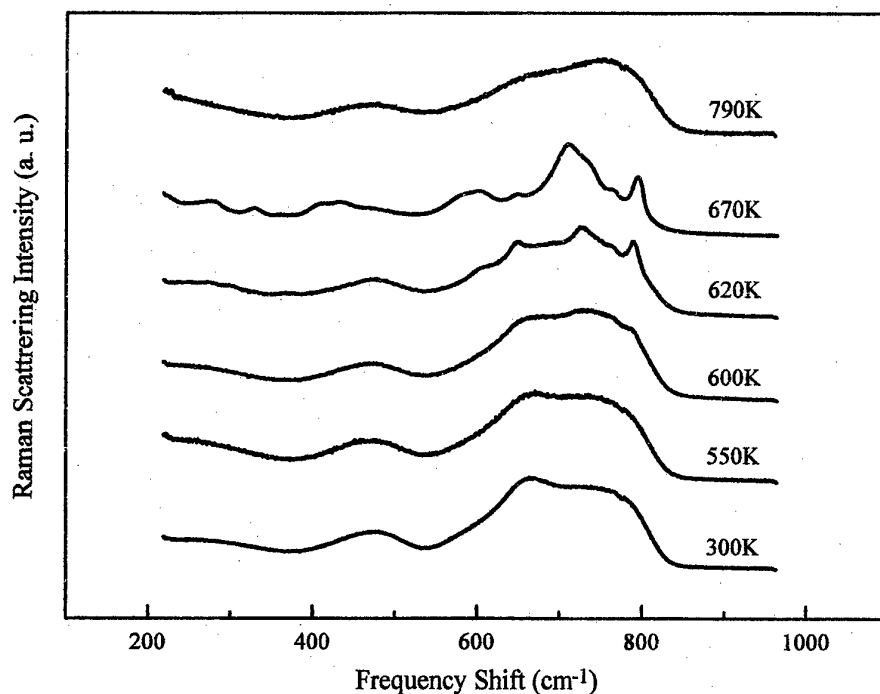


Fig. 5. High-temperature Raman spectra for $20\text{K}_2\text{O} \cdot 80\text{TeO}_2$

increasing temperature. And then, the glass melts through crystallization process. The intensity ratio of the 770cm^{-1} and $670, 470\text{cm}^{-1}$ reversed. It is considered that a part of TeO_4 *thp* units have changed to TeO_3 *tp* units. The Raman profile of $20\text{K}_2\text{O} \cdot 80\text{TeO}_2$ glass above glass transition temperature (T_g) is similar to that above melting temperature (T_m). At temperature above crystallization temperature (T_c), sharp peaks are observed at around 720cm^{-1} , and the

position of those peaks is similar to that of the peaks at temperature above T_m . This shows that a large portion of crystal structure consists of TeO_3 *tp* units. The network structure in the $20\text{K}_2\text{O}\cdot 80\text{TeO}_2$ melt is mainly made up of TeO_3 *tp* units.

Fig. 6 shows high-temperature XRD profiles of the $20\text{K}_2\text{O}\cdot 80\text{TeO}_2$ glass. In the temperature region from room temperature to 530K there are no peaks due to the crystal phase. At 590K many crystallization peaks were observed. And then diffraction peak patterns perfectly changed at 660K. At 690K diffraction profile was in fusion state. These crystallization behaviors correspond to DTA and high-temperature Raman results. The XRD profile of the $20\text{K}_2\text{O}\cdot 80\text{TeO}_2$ melt slightly differs from that of the correspond glass. This fact reflects the difference of network structure between $20\text{K}_2\text{O}\cdot 80\text{TeO}_2$ melt and glass suggested in high-temperature Raman spectroscopy. It is considered that the change of structure occurs accompanied by the change of network units.

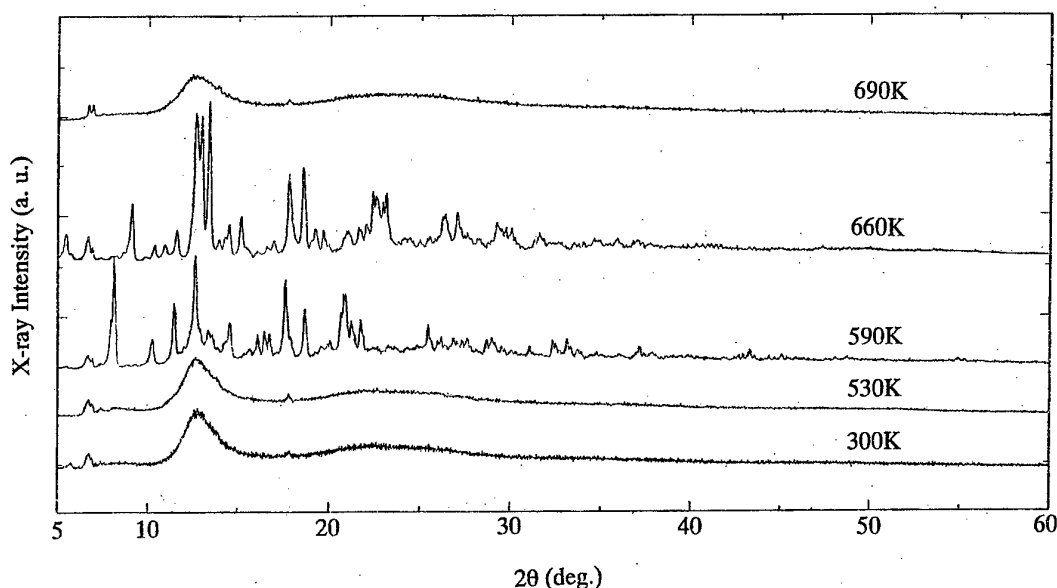


Fig. 6. High-temperature XRD profiles of the $20\text{K}_2\text{O}\cdot 80\text{TeO}_2$ glass

REFERENCES

- [1] T. Yoko, K. Kamiya, H. Yamada, and K. Tanaka, *J. Am. Ceram. Soc.* 71 (1988) C-70.
- [2] H. Burger, W. Vogel, V. Kozhukharov, and M. Marinov, *J. Mater. Sci.* 19 (1984) 403.
- [3] S. Neov, I. Gerassimova, K. Krezhov, B. Sydzhimov, and V. Kozhukharov, *Phys. Status Solidi A* 47 (1978) 743.
- [4] T. Sekiya, N. Mochida, A. Ohtsuka, and M. Tonokawa, *J. Non-Cryst. Solids* 144 (1992) 128.
- [5] M. Tatsumisago, T. Minami, and M. Tanaka, *J. Am. Ceram. Soc.* 64 (1981) C-97.
- [6] M. Tatsumisago, T. Minami, Y. Kowada, and H. Adachi, *Phys. Chem. Glasses* 35 (1994) 89.
- [7] J. Heo, D. Lam, G.H. Sigel Jr., E.A. Mendoza, and D.A. Hensley, *J. Am. Ceram. Soc.* 75 (1992) 277.
- [8] L. Andersen, V. Langer, A. Strömberg, and D. Strömberg, *Acta Cryst.* B45 (1989) 344.
- [9] F. Daniel, J. Moret, M. Maurin, and E. Philippot, *Acta Cryst.* B34 (1978) 1782.
- [10] N. Umesaki, A.C. Hannon, D.A. Cunningham, Y. Shimizugawa, and N. Kitamura, *ISIS Experimental Report*, No. 9151 (1998).

GLASS STRUCTURE AND 3rd NONLINEARITIES AT 1.5 μ m IN THALLIUM(I) TELLURIUM(IV) GLASSES

B. Jeansannetas, S. Blanchandin, P. Thomas, P. Marchet, J. C. Champarnaud-Mesjard, T. Merle-Méjean, B. Frit,

Laboratoire de Matériaux Céramiques et Traitements de Surface, ESA CNRS 6015, 123 Avenue A. Thomas, 87060 Limoges Cédex, France, email: pthomas@unilim.fr

V. Nazabal, E. Fargin G. Le Flem

ICMCB, UPR CNRS 9048, Avenue du Dr Schweitzer, 33608 Pessac cédex, France

M. O. Martin, B. Bousquet, L. Canioni, S. Le Boiteux, P. Segonds, L. Sarger
CPMOH, URA CNRS 283, Université de Bordeaux 1, 351 Cours de la Libération, 33405 Talence Cédex, France

INTRODUCTION

The development of new glasses for photonic devices or communication systems in the near infrared region (1.3 or 1.5 μ m communication wavelengths) requires to identify the microscopic origin of the optical nonlinearities in the spectral range of utilization. Up to now the third order nonlinearities were obtained with various techniques and at wavelengths (λ_m) more or less close to the fundamental absorption leading to a puzzling discrepancy between measured values for the same material (1). Moreover the resonant and nonresonant contributions are not always clearly isolated and strong reduction of the $\chi(3)$ values are observed as λ_m increases. Recently accurate values of $\chi(3)$ were obtained at 1.5 μ m for various metal oxides using a time resolved interferometric technique (2). The glasses, to be representative of a large scale of optical nonlinearities, was chosen on the basis of previous theoretical investigations analyzing the magnitude of the hyperpolarizability of ions or more complex structural entities identified in such materials (3,4). The largest nonlinear response are generated by heavy cations associated with ns^2 electron pairs (Te^{4+} , Bi^{3+} , Pb^{2+} , Tl^+). In contrast the lowest third order nonlinearity in oxyde glasses are found for the various forms of silica (1).

The origin of the nonlinearity in tellurite glasses was attributed to the Lewis $5s^2$ free doublet of electron on tellurium (5). In the present study the attention is focus on the effect of a second lone pair holder (Tl^+ and/or Bi^{3+}) upon the optical properties of tellurite glasses. This paper introduces the method of $\chi(3)$ measurement at 1.5 μ m, describes the structural features characterizing the new investigated glasses on the basis of the crystal chemistry of thallium(I) tellurite oxides and discusses the relations between the optical nonlinear response and the compositions and structures of the glasses.

EXPERIMENTAL

The elaboration of glasses has been previously reported (6). The Raman spectra were recorded using a Dilor X Y triple monochromator.

Optical measurements of thallium(I) tellurite glasses.

The non linear phase measurement relies on a Mach-Zehnder interferometer as displayed in fig (1). The laser used in this setup is an OPO pumped by a TiSa oscillator, (an OPAL and Tsunami from Spectra Physics) which delivers linearly polarized pulses of 150 fs (HWHM) at around 1.5 μ m with peak power of 10 Kw.

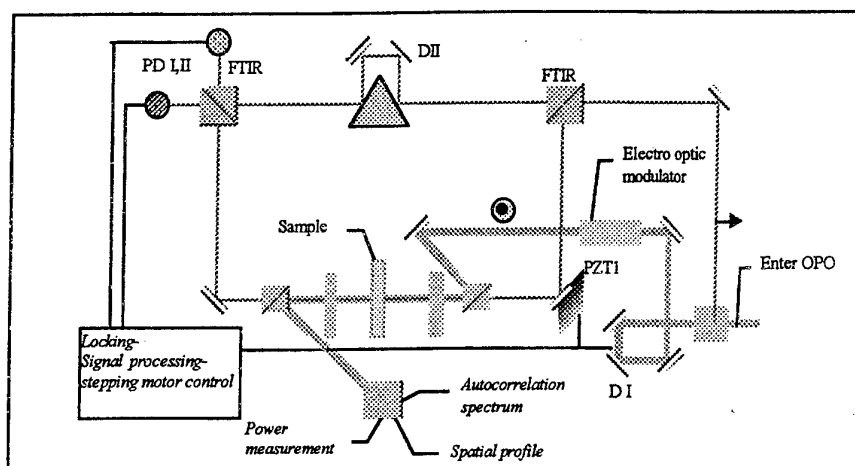


Figure 1 :Mach-Zhender interferometer used for the n_2 measurement

As the sample is located in the probe arm, the group index in the femtosecond regime at the operating wavelength is measured simply using the delayed reference arm. When the (stronger) collinear pump beam interacts, the analysis of the interferometric signal gives access to both ultra fast and slow nonlinearities. An afocal in the probe arm provides a convenient beam waist in the sample while great care is taken to insure a perfect overlap between both pump and probe beams. The signal from the two photodiodes PD_{1,2} is used as an error signal to lock the average phase between probe and reference beams and to measure the nonlinear phase shift induced by the electrooptically modulated pump beam(16). The resulting modulation of the signal is recorded using a spectrum analyzer and absolute values and dynamic of the non linear susceptibilities can be measured through the evolution in amplitude and phase of the relevant Fourier component recorded as a function of the pump-probe delay.

As expected for purely non-resonant glass sample, the response arises from a pure instantaneous electronic contribution, and in the collinear configuration, this leads to a signal whose average is due to the cross correlation between pump and probe fields and oscillations are due to third order coupling processes. The maximum average phase shift, free from any coherent contributions, is related to the nonlinear index by:

$$n_2 = \frac{\Delta\phi\lambda_p^2\sqrt{2}}{P_{pump}4\pi\arctan\left(\frac{I\lambda}{2\pi W_0^2}\right)}$$

In this orthogonally pump probe polarization scheme the determination of χ_{xyyy} will be sufficient to characterize the non linear response since the fourth rank tensor is totally symmetric among its indices (i.e. $3*\chi_{xyyy} == 3*\chi_{xyyx} = \chi_{xxxx}$) for isotropic materials.

The above linear relationship can be used to extract the sign and as every parameter in this expression is carefully controlled, an absolute value of the instantaneous nonlinear refractive index can be computed. The accuracy of all optical parameters limits the precision of our measurements to roughly 10%. The sensitivity of this interferometer is around 10^{-20} m²/watt mainly due to the moderate peak power of the OPO.

STRUCTURE OF THE THALLIUM (I) TELLURIUM (IV) GLASSES

Crystal chemistry of thallium(I) tellurite oxides

Some important points emerge from the careful analysis of structures of the various crystalline phases observed within the $\text{Tl}_2\text{O}-\text{TeO}_2$ system (i.e. α and β - TeO_2 , $\text{Tl}_2\text{Te}_3\text{O}_7$, $\text{Tl}_2\text{Te}_2\text{O}_5$, Tl_2TeO_3 and Tl_2O) (7-12).

1) In each structure the arrangement of anions around cations is highly anisotropic and characteristic of a strong stereochemical activity of the electronic lone pairs E of cations.
2) From TeO_2 to Tl_2TeO_3 , the anionic coordination polyhedron of Te^{4+} changes progressively from a TeO_4 disphenoid (in fact a TeO_4E trigonal bipyramid with two "relatively long" axial distances, two "relative short" equatorial distances, and the lone pair E so directed as to constitute the third equatorial corner (figure 2a)) to a TeO_3 trigonal pyramid (in fact a TeO_3E tetrahedron (figure 2c)), via an intermediate TeO_{3+1} polyhedron (figure 2b). The anionic polyhedra of Tl^+ cations show nearly the same kind of evolution with a progressive transformation of the TlO_4E trigonal bipyramids, observed in $\text{Tl}_2\text{Te}_3\text{O}_7$ (figure 2d), into the perfect TlO_3E tetrahedra of Tl_2O (figure 2e). Such evolutions clearly indicate that increasing thallium content enhances the anisotropic character of the anionic arrangement around cations and that the stereochemical activity of the lone pair of tellurium atoms is strengthened by the presence of a second lone pair holder.

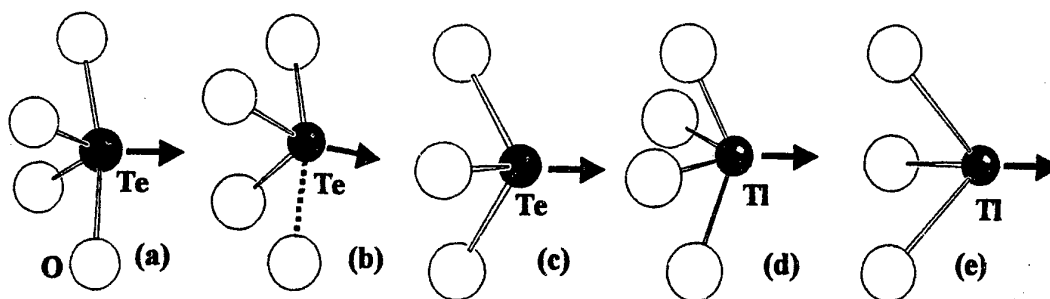


Figure 2 : The various cation coordination polyhedra observed in crystalline Tl-Te mixed oxides (arrows visualize the direction towards which the lone pairs E are directed).

Table 1 : The tellurium coordination polyhedra and their linking observed in crystalline Tl-Te mixed oxides

	TeO_x polyhedra	Te-O distances(Å)	TeO_x linking
$\text{TeO}_2 \alpha$	TeO_4	$2 \times 2.12 ; 2 \times 1.88$	3D: corner-sharing TeO_4
$\text{TeO}_2 \beta$	TeO_4	1.87/1.89/2.07/2.15	2D: edge and corner-sharing TeO_4
$\text{Tl}_2\text{Te}_3\text{O}_7$	$\text{Te}(2)\text{O}_3$	1.837/1.898/1.912	Te_3O_7 strips : edge and corner-sharing polyhedra
	$\text{Te}(1)\text{O}_{3+1}$	1.833/1.912/2.032/2.223	
	$\text{Te}(3)\text{O}_4$	1.834/1.943/2.108/2.154	
$\text{Tl}_2\text{Te}_2\text{O}_5 \alpha$	$\text{Te}(2)\text{O}_{3+1}$	1.870/1.873/2.041/2.327	Te_2O_5 sheets : edge and corner-sharing polyhedra
	$\text{Te}(1)\text{O}_4$	1.908/1.925/2.034/2.162	
Tl_2TeO_3	TeO_3	1.826/1.828/1.891	isolated TeO_3 groups

3) TeO_4E polyhedra are systematically connected via $\text{Te}^{\text{eq}}\text{O}^{\text{ax}}-\text{Te}$ bridges, which can be single bridges (corner sharing) or double bridges (edge sharing). Each double bridge leads

logically to short Te-Te (about 3.4 Å instead of 3.7 - 4 Å for a single bridge) and O-O distances (about 2.55 Å).

Raman investigation of thallium(I) tellurite glasses.

On the basis of these observations and of the analysis of the Raman spectra of homologous crystalline phases, the Raman spectra of $\text{Th}_2\text{O} - \text{TeO}_2$ glasses (see figure 3) can be interpreted. The pure TeO_2 glass spectrum is composed of two broad peaks. The peak at 650 cm^{-1} (noted G_{1s}) can be assigned to the totally symmetric stretching vibration of the "pseudo-molecular TeO_2 " entity of the TeO_4 polyhedron (short equatorial bonds) and its shoulder (noted G_{1as}) to the corresponding asymmetric vibration. The peak at 430 cm^{-1} (noted P) and its shoulder at about 460 cm^{-1} can be assigned to the stretching vibrations of respectively single or double $\text{Te}^{\text{eq}}\text{O}^{\text{ax}}\text{--Te}$ bridges.

The spectra of $\text{Th}_2\text{Te}_3\text{O}_7$ and $\text{Th}_2\text{Te}_2\text{O}_5$ glasses are nearly identical but exhibit noticeable differences with the pure TeO_2 spectrum. Addition of Th_2O leads to the appearance of two new bands (an intense one at about $710\text{--}720 \text{ cm}^{-1}$ and a small one at about 250 cm^{-1}) related to a progressive decrease of the intensity of the G_{1s} and P peaks. With respect to the Raman spectra of crystalline phases (13) and to the previous results of Sekyia et al. (14) and Dexpert et al. (15) on TeO_2 -based glasses, the peak at $710\text{--}720 \text{ cm}^{-1}$ (called G_2) has been assigned to the symmetric stretching vibrations of isolated TeO_3 groups. The peak at 250 cm^{-1} , which is not observed for the pure TeO_2 glass, could be assigned to $\text{Th}\text{--O}$ vibrations. After decomposition of the different peaks we observe that, with increasing thallium content, (i) the relative intensity of G_{1s} peak decreases and the ratio G_2/G_{1s} increases, (ii) the peaks ratio P/G_{1s} or $P/(G_{1s}+G_2)$, which determine the relative quantities of $\text{Te}\text{--O}\text{--Te}$ linkages with respect to TeO_3 , TeO_{3+1} or TeO_4 entities, decreases. This clearly indicates a progressive transformation of corner and/or edge-sharing TeO_4 polyhedra into isolated TeO_3 trigonal pyramids.

So thallium tellurite glasses are probably formed of TeO_x ($4 \leq x \leq 3$) structural units linked together both by single and double $\text{Te}^{\text{eq}}\text{O}^{\text{ax}}\text{--Te}$ bridges. These glasses show the same structural evolution than that observed with the corresponding crystalline phases : increasing thallium content leads to a depolymerization of the tellurium structural units framework due both to the transformation of TeO_4 entities to isolated TeO_3 polyhedra through TeO_{3+1} entities and to the decrease of the number of $\text{Te}\text{--O}\text{--Te}$ linkages.

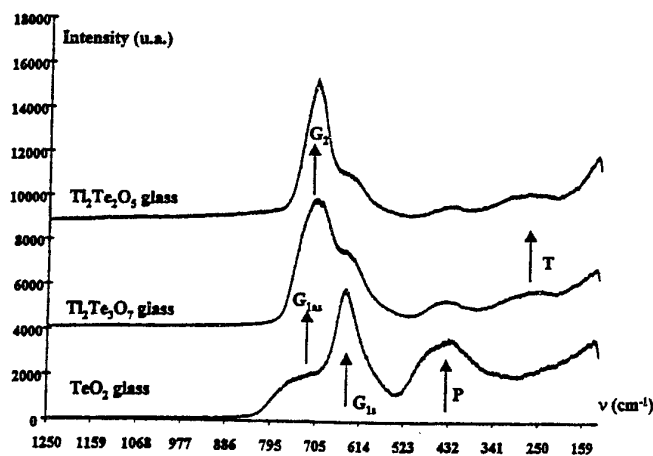


Figure 3 : Raman spectra of TeO_2 , $\text{Th}_2\text{Te}_3\text{O}_7$ and $\text{Th}_2\text{Te}_2\text{O}_5$ glasses.

DISCUSSION AND CONCLUSION

Table 2: Linear and nonlinear indices, $\chi^{(3)}$, at 1.5 μm .

Compounds	n_0	$n_2 (\text{m}^2/\text{W}) 10^{-19}$	$\chi^{(3)} (\text{V}^2/\text{m}^2) 10^{-21}$
Suprasil	1.422 ± 0.03	0.25 ± 0.2	0.089
Herasil	1.467 ± 0.01	0.121 ± 0.09	0.046
90 TeO_2 - 10 Al_2O_3	2.003 ± 0.06	5.38 ± 1.19	3.81
90 TeO_2 - 10 Nb_2O_5	2.144 ± 0.05	6.93 ± 0.72	5.63
80 TeO_2 - 20 Nb_2O_5	2.166 ± 0.05	5.94 ± 0.81	4.93
70 TeO_2 -30 $\text{TiO}_{0.5}$	2.125 ± 0.02	8.6 ± 1.0	6.87
65 TeO_2 -35 $\text{TiO}_{0.5}$	2.094 ± 0.02	8.9 ± 1.0	6.90
80 TeO_2 -10 $\text{TiO}_{0.5}$ -10 $\text{BiO}_{1.5}$	2.150 ± 0.07	7.17 ± 0.72	5.87
73.9 TeO_2 -23.5 $\text{TiO}_{0.5}$ - 2.6 $\text{BiO}_{1.5}$	2.156 ± 0.07	9.1 ± 1.7	7.48

As mentioned above the lower limits of n_2 for oxide glasses is provided by the various forms of silica. Only the introduction of fluorine in glasses can decrease n_2 . In contrast the addition of d^0 shell metal ions like Ti^{4+} or Nb^{5+} or metal ions with lone pair like Te^{4+} , Pb^{2+} , Bi^{3+} increases the nonlinear response. Recent theoretical approaches connected to the identification of the structural groups appearing in the glasses listed in table 2 allow the magnitude of n_2 to be explained.

In rich titanium glasses the tetragonal TiO_5 pyramids with a short Ti-O bond (1.7 Å) dominates as structural entity and the Ti-O arrangement, deduced from EXAFS investigation, is consistent with the creation of $\text{KTP}(\text{KTiOPO}_4)$ -like titanium oxygen chains i.e. with alternated short and long Ti-O distances. In rich niobium glasses, the niobium oxygen network can be described as made up of corner shared NbO_6 octahedra in which the Nb-Nb distances are typical of those found in tungsten bronze framework. The polarization of the M-O bond ($\text{M} = \text{Ti}, \text{Nb}$) with maximum p-d orbital overlap is the basic phenomenon at the origin of the nonlinear response but for the glasses with high titanium or niobium concentration, the additivity of the contribution of microscopic M-O bond polarization cannot be longer applied and the n_2 values are enhanced by the effect of the extended structural arrangement (17).

The theoretical approach of tellurium oxide glasses has been carried out through ab-initio calculations (5). The highest occupied molecular orbital (3a1) of both $(\text{TeO}_4)^{4-}$ and $(\text{TeO}_3)^{3-}$ groups is of the antibonding type and contains essentially the tellurium 5s atomic orbital and the 2p atomic orbital of oxygen and then correlated with the $5s^2$ non bonding doublet of Lewis. In addition the mean polarizability α was found about 20% higher for the TeO_4 cluster than for the TeO_3 one.

In the investigated tellurium oxide glasses the introduction of Al_2O_3 or Nb_2O_5 leads to the progressive transformation of TeO_4 trigonal bipyramids into TeO_3 trigonal pyramid through an intermediate TeO_{3+1} asymmetric polyhedron (5) and accordingly to a decrease of n_2 . This effect is less marked for tellurium niobium glasses due to the contribution of the niobium oxygen bond to the nonlinear response. In contrast the introduction of Ti_2O and/or Bi_2O_3

induces an increase of the nonlinear indice although the same structural transformation of the tellurium oxygen groups is observed. This evolution illustrates clearly the predominant contribution of the Tl(I) lone pairs which are strongly active in term of stereochemistry and consequently highly polarizable, assuming an identical environment of thallium atoms by oxygens in glasses and crystals.

In conclusion the nonresonant nonlinearities can be predicted in oxide glasses by analyzing the respective effect of high valence transition metal ions such as Ti(IV), Nb(V) and highly polarizable ions such as Te(IV), Tl(I), Bi(III). The two types glasses give rise to nonlinear response intensities which are respectively about 10 times and 30 times that of silica. The reported n_2 values can be correlated to the electronic polarizability (or hyperpolarizability) of individual metal oxygen entities in connection with the structural features of short range order appearing in the glasses. In such oxyde glasses the upper limit of nonresonant n_2 is about $10^{-18} \text{ m}^2/\text{W}$.

REFERENCES

- [1]. E. M. Vogel, M. J. Weber, E. M. Krol, Phys. Chem. Glasses, 32 (1991) 231.
- [2]. L. O. Canioni, M. O. Martin, B. Bousquet, L. Sarger, Optics Comm. (in press 1998).
- [3]. E. Fargin, A. Berthereau, T. Cardinal, J. J. Videau, A. Villesuzanne, G. Le Flem, Ann. Chim. Sci Mat., 23 (1998) 27.
- [4]. S. Le Boiteux, P. Segonds, L. Canioni, L. Sarger, T. Cardinal, C. Duchesne, E. Fargin, G. Le Flem, J Appl. Phys. 81, 3, (1997) 1481.
- [5]. A. Berthereau, E. Fargin, A. Villesuzanne, R. Olazcuaga, G. Le Flem, L. Ducasse J. Solid State Chem., 126 (1996) 143.
- [6]. B. Jeansannetas, P. Marchet, P. Thomas, J.C. Champarnaud-Mesjard, B. Frit, J. Mat. Chem. 8, 4 (1998) 1039.
- [7]. P. A. Thomas, J. Phys. C: Solid State Phys., 21 (1988) 4611.
- [8]. H. Beyer, Zeitschrift für Kristallographie, 124 (1967) 228.
- [9]. B. Jeansannetas, P. Thomas, J.C. Champarnaud-Mesjard, B. Frit, Mat. Res. Bull., 32 (1) (1997) 51.
- [10]. B. Jeansannetas, P. Thomas, J.C. Champarnaud-Mesjard, B. Frit, Mat. Res. Bull, to be published.
- [11]. B. Frit, D. Mercurio, Rev. Chim. Min., 17 (1980) 192.
- [12]. H. Sabrowsky, Zeitschrift für Anorg. und Allg. Chemie, 381 (1971) 266.
- [13]. B. Jeansannetas, Thesis of the University of Limoges (1998).
- [14]. T. Sekiya, N. Mochida, A. Ohtsuka, M. Tonokawa, J. Non-Cryst. Solids, 144 (1992) 128.
- [15]. J. Dexpert-Ghys, B. Piriou, S. Rossignol, J.M. Reau, B. Tanguy, J.J. Videau, J. Portier, J. Non-Cryst. Solids, 170 (1994) 167.
- [16]. L. Sarger, P. Segonds, L. Canioni, F. Adamietz, A. Ducasse, C. Duchesne, E. Fargin, R. Olazcuaga, G. Le Flem; JOSA B, Vol 11, N°6, (1994)
- [17]. T. Cardinal, E. Fargin, G. Le Flem, S. Le Boiteux, J. Non-Cryst. Solids 222, (1997), 228.

CRYOGENIC EXAFS INVESTIGATION ON THE STRUCTURAL ENVIRONMENT OF GALLIUM IN PbO-Ga₂O₃ GLASSES

Yong Gyu Choi^a, Vladimir A. Chernov^b, and Jong Heo^{a,*}

^a Non-Crystalline Materials Laboratory
Department of Materials Science and Engineering
Pohang University of Science and Technology
San 31, Hyoja-dong, Nam-gu, Pohang, Kyungbuk, 790-784, Korea
*e-mail : jheo@postech.ac.kr

^b Siberian Synchrotron Radiation Center
Budker Institute of Nuclear Physics
630090, Novosibirsk, Russia

ABSTRACT

Ga K-edge EXAFS spectra of PbO-Ga₂O₃ glasses were recorded at liquid-nitrogen temperature in order to understand the coordination scheme of gallium in glasses quantitatively. Enhanced spatial resolution of the experimental EXAFS functions at cryogenic temperature provides an opportunity to consider the distribution of Ga-O bond lengths. Four oxygens were bonded to each Ga forming GaO₄ tetrahedra at the average bond distance of 0.1855~0.1862 nm. A fitting assuming a non-Gaussian distribution of Ga-O bond distances provided better results with a smaller R-factor compared to the Gaussian counterpart. Two-subshell fitting suggested that oxygens with Ga-O bond distance of ~0.187 nm are bonded to three cations while the shorter ones are two-coordinated.

INTRODUCTION

Structure of PbO-Ga₂O₃ glasses has been subject of many research works, since they contain no traditional glass-former. Infrared, Raman and Nuclear Magnetic Resonance(NMR) spectroscopic studies suggested that most gallium ions are in a four-fold coordination of oxygens[1-3]. Quantitative analysis by the X-ray and neutron diffraction studies showed less than 10 % of total gallium ions are surrounded by six oxygens[4]. A recent EXAFS analysis also proved the four-fold coordination scheme of galliums with a negligible amount of six-fold coordination[5]. On the other hand, average Ga-O bond lengths of 0.1856~0.1861 nm in glasses were longer than 0.183 nm which is normally found in crystals with a similar coordination scheme. These long Ga-O bonds seemed to be associated with the three-coordinated oxygens. However, since the room-temperature EXAFS spectra provided only an average value of Ga-O distances for each glass, no quantitative information on the distribution of the bond lengths could be obtained.

The present study, therefore, aimed at detailed analysis on the oxygen coordination scheme around gallium in binary PbO-Ga₂O₃ glasses by analyzing the Ga K-edge EXAFS spectra recorded at liquid-nitrogen(LN₂) temperature. Ga-O correlation shells in these EXAFS spectra recorded within the photoelectron momentum(*k*) range of 30~145 nm⁻¹ were analyzed based on three different local structural models.

EXPERIMENTAL PROCEDURE

99.9% pure yellow PbO and β-Ga₂O₃ were mixed to yield a 10 g batch with the

composition of $(X)\text{PbO}-(1-X)\text{Ga}_2\text{O}_3$, where X is 0.7, 0.75 and 0.8 in mole fraction. Mixed starting materials were melted at 1000°C for 15 min in air using a platinum crucible. Yellow-orange colored samples were prepared by pouring the melts onto brass mold. Detailed sample preparation procedures can be found in the previous report[5].

Absorption spectra of Ga K-edge were recorded on the EXAFS beamline of VEPP-3 storage ring in Siberian Synchrotron Radiation Center at Budker INP, Novosibirsk, Russia. Energy and current of the electrons were 2.0 GeV and 80~120 mA, respectively. Measurements were done in the transmission mode with a Si(111) channel-cut monochromator at the fixed beam position. All spectra for glass samples were recorded at liquid nitrogen temperature. The monochromator was calibrated using LI, LII and LIII edges of a Ta metal foil to produce the energy resolution of approximately 2 eV at the Ga K-edge. A fused silica mirror was used to reject higher harmonics. Two ion chambers filled with Ar(5%) + He(95%) and Ar(100%) were used to detect the intensity of an incident and transmitted beam, respectively.

Extraction of EXAFS interference function from the raw absorption spectrum was done using the AUTOBK program[6] and explained in the previous publication[5]. Fourier transform of $\chi(k)$ was carried with a k^3 -weighting factor and a Hanning window function with a fixed window parameter(Dk) of 1.0 for all spectra. Two end points of Fourier transform, k_{\min} and k_{\max} were $30 \pm 10 \text{ nm}^{-1}$ and $145 \pm 20 \text{ nm}^{-1}$, respectively. Value of k_{\max} was larger in the present work compared to that of $120 \pm 30 \text{ nm}^{-1}$ for the room-temperature spectra[5] due to the increased amplitude and signal to noise ratio of spectra recorded at low temperature.

Validity of the theoretical Ga-O pair EXAFS function generated from FEFF6 program[7] was examined using the experimental EXAFS function recorded for the standard $\text{BaGa}_2\text{Ge}_2\text{O}_8$ crystal. Non-linear least-squares fitting was carried in R-space within the range of 0.09~0.22 nm, where the Ga-O partial distribution peak is located. All parameters used in the data reduction processes were kept constant for both glasses and crystals. Extraction of the EXAFS interference functions, Fourier transforms into K or R spaces as well as non-linear least-squares fitting were carried out using the UWXAFS 3.0 software package[8]. Again, more detailed descriptions on the data reduction and fitting procedure were given in the previous report[5].

METHODS OF FITTINGS AND RESULTS

Experimental Ga K-edge EXAFS spectra in K-space recorded from three glasses at LN_2 temperature are shown in Fig. 1. It revealed the larger amplitude and more regular variations of EXAFS oscillations above the k value of $\sim 120 \text{ nm}^{-1}$ compared to those recorded at room temperature[5]. They provide an opportunity for more precise fittings with different structural models including two-subshell fitting of Ga-O correlation peak. In case of a PbGa_2O_4

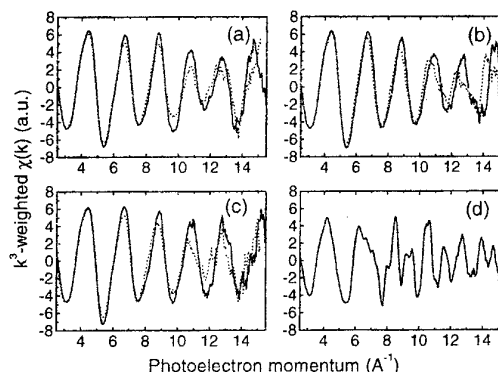


Fig. 1 k^3 -weighted Ga K-edge $\chi(k)$ spectra from three glasses with the composition of (a) 70PbO-30Ga₂O₃, (b) 75PbO-25Ga₂O₃, (c) 80PbO-20Ga₂O₃ and (d) crystalline standard of PbGa₂O₄. Solid lines and dotted lines represent the spectra recorded at LN_2 temperature and room temperature, respectively.

crystal, the room temperature EXAFS spectrum was good up to the k value of 145 nm^{-1} . Three different fitting models were used to attain the most reasonable fitting of Ga-O partial correlation peak in the EXAFS spectra recorded. The first model (Model I) assumes the Gaussian distribution of Ga-O bond lengths. Four independent fitting variables used for this fitting were the energy origin shift (E_0), Ga-O bond distance ($R_{\text{Ga-O}}$), coordination number (N) of oxygen around Ga and the EXAFS-type Debye-Waller factor (σ^2). Two additional fitting variables were used in Model II, which were the third (C_3) and the fourth (C_4) cumulants. This expansion on cumulants was used as a convenient way to express the disorder independent of the model chosen for the atomic distribution function[9]. Presence of a certain order of non-Gaussian distributions in Ga-O bond distances can be corrected by introducing these higher order cumulants[10]. A theoretical EXAFS interference function including higher order cumulants used in this analysis was[8];

$$\chi(k) = \text{Im} \left\{ \frac{A(k) N S_0^2}{k (R_0 + \Delta R)^2} \exp \left(-2 \frac{R_0}{\lambda(k)} - 2k^2 \sigma^2 - \frac{2}{3} k^4 C_4 \right) \right. \\ \left. \times \exp \left(i \left[2k \left(R_0 + \Delta R - 2 \frac{\sigma^2}{R_0} \right) + \delta(k) - \frac{4}{3} k^3 C_3 \right] \right) \right\}$$

where $A(k)$, $\lambda(k)$ and $\delta(k)$ are the functions of the back-scattering amplitude, the photoelectron mean-free path and phase shift, respectively. All of them were calculated from the FEFF6 code. R_0 and ΔR is the estimated Ga-O bond distance and the difference in bond length between the theoretical and the experimental EXAFS spectra, respectively.

In Model III, fittings with two different Ga-O distances (approximately 0.182 and 0.186 nm) in the GaO_4 tetrahedra were attempted using seven fitting variables. In fact, a PbGa_2O_4 crystal has a wide variation of Ga-O bond lengths of 0.181–0.187 nm[11]. In addition, the previous EXAFS investigation[5] gave an average bond length of ~ 0.186 nm which is longer than that found from the crystals with a uniform Ga-O distance. Therefore, it is reasonable to assume the presence of two groups of Ga-O bonds with significantly different lengths. After the coordination number ($N(I)$) of oxygens with a longer bond distance was calculated, the other $N(II)$ was obtained simply by subtracting $N(I)$ from four. Results of each fitting are listed in Table I along with the variables used for the calculation.

R-factor, calculated by normalizing the differences between experimental and

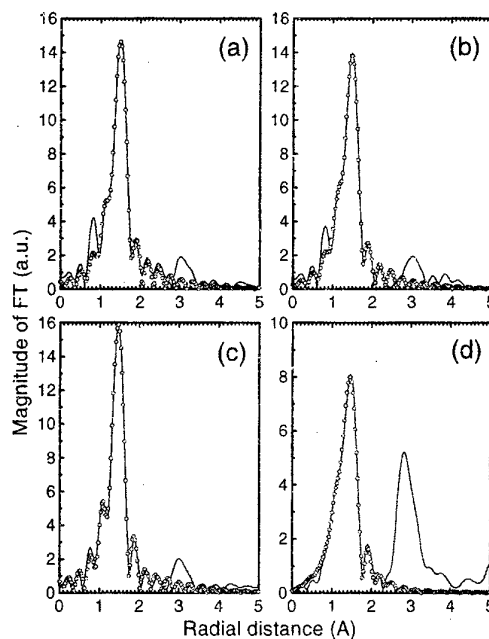


Fig. 2 Magnitude of Fourier transforms of k^3 -weighted $\chi(k)$ spectra for (a) 70PbO-30Ga₂O₃, (b) 75PbO-25Ga₂O₃, (c) 80PbO-20Ga₂O₃ glasses recorded at LN₂ temperature and (d) the standard crystal PbGa₂O₄ at room temperature. Solid lines and dots are from the experimental and the fitted with model II, respectively. The phase shifts were not corrected and only the nearest-neighboring peak was fitted.

theoretical values against the magnitude of experimental values, provides a measure of goodness of the fitting. It is the smallest in Model II for all glasses (Fig. 2). This cumulant fitting scheme of Model II seems to take the best snapshot of distribution of oxygens around Ga, being judged from the R-factor and coincidence of the fitted values with the structural informations obtained from other investigations (Table II). On the other hand, R-factor of Model I is the largest of all. Furthermore, Ga-O bond lengths obtained from Model I were somewhat different from those obtained from the previous room-temperature EXAFS and the neutron scattering analyses [4,5,12]. In addition, oxygen coordination numbers which were smaller than four in Model I, increased to approximately four in Model II. It suggests that the amplitude envelop of the Ga-O correlation peak should be analyzed by assuming the non-Gaussian distribution of Ga-O bond lengths in glasses especially when an EXAFS spectrum is taken at the cryogenic temperature.

Table I Fitting variables and results of each fitting scheme used to fit Ga-O pair correlation peak in Ga K-edge EXAFS taken at LN₂ temperature for glasses and room temperature for PbGa₂O₄ crystal

Variable	PbGa ₂ O ₄			70PbO-30Ga ₂ O ₃			75PbO-25Ga ₂ O ₃			80PbO-20Ga ₂ O ₃		
	Model I	Model II	Model III	Model I	Model II	Model III	Model I	Model II	Model III	Model I	Model II	Model III
R-factor	0.015	0.003	0.005	0.008	0.005	0.006	0.009	0.004	0.006	0.011	0.002	0.006
R _{Ga-O(I)} (Å)	1.874 (0.008)	1.851 (0.016)	1.868 (0.016)	1.867 (0.005)	1.857 (0.012)	1.871 (0.013)	1.864 (0.008)	1.855 (0.009)	1.873 (0.014)	1.846 (0.007)	1.862 (0.006)	1.876 (0.011)
N(I)	3.68 (0.49)	4.06 (0.45)	2.90 (0.74)	3.59 (0.47)	3.95 (0.33)	2.46 (0.68)	3.86 (0.36)	4.08 (0.38)	2.38 (0.54)	3.80 (0.42)	4.00 (0.31)	2.16 (0.73)
σ ² (I) (10 ⁻⁵ Å ²)	675 (114)	917 (68)	471 (274)	197 (55)	285 (79)	6.8 (321)	274 (61)	350 (112)	4.1 (317)	196 (83)	314 (87)	10 (442)
C ₃ (10 ⁻⁴ Å ³)		-3.85 (1.66)			-1.01 (2.16)			-1.02 (3.18)			1.90 (1.86)	
C ₄ (10 ⁻⁵ Å ⁴)		3.67 (710)			1.34 (721)			1.20 (821)			2.33 (519)	
R _{Ga-O(II)} (Å)			1.822 (0.08)			1.817 (0.06)			1.821 (0.06)			1.824 (0.05)
N(II)			1.10			1.54			1.62			1.84
σ ² (II) (10 ⁻⁵ Å ²)			316 (841)			10 (523)			10 (497)			6.2 (352)

* E₀ shifts are within -2-6 eV in all cases.

** Upper limit of σ² was set to 10⁻⁴ Å² in model III only for glasses.

*** Values in the parentheses are the estimated uncertainties.

Table II Average Ga-O bond lengths in PbO-Ga₂O₃ glasses

Source Composition	EXAFS* RT	EXAFS LN ₂ (Model I)	EXAFS LN ₂ (Model II)	Neutron Scattering	Neutron Scattering
	5	this study	this study	4	12
70PbO-30Ga ₂ O ₃	0.1856	0.1867	0.1857	0.186**	0.18587***
75PbO-25Ga ₂ O ₃	0.1858	0.1864	0.1855		
80PbO-20Ga ₂ O ₃	0.1861	0.1846	0.1862		0.18602

* single-shell fitting, R-range : 0.09 ~ 0.22 nm, K-range : 30 ~ 120 nm⁻¹, without higher order cumulants

** value for 50PbO-50Ga₂O₃(mole%) composition

*** value for 67PbO-33Ga₂O₃(mole%) composition

Model III assumes two different sets of Ga-O bond distances, i.e. one at around 0.182 nm and the other at 0.186 nm. Results of analysis showed that the longer Ga-O distances in glasses were in 0.1871~0.1876 nm, while the shorter ones were within 0.1817~0.1824 nm. The coordination number of longer Ga-O subshell was in the range of 2.16~2.46 and tends to increase with increasing Ga₂O₃ concentration. However, the R-factor calculated in the Model III was larger than that of Model II. It shows that a two-subshell fitting may not represent the best figures on the oxygen distribution around Ga since the Ga-O distance is not at two distinct values but within a wide range. Therefore, Model II with the assumption of wide non-Gaussian distribution of Ga-O bonds seems to provide more meaningful structural information.

DISCUSSION

It has been suggested that there exist oxygens bonded to three cations in these heavy metal oxide glasses[4,5,13]. Presence of the three-coordinated oxygens was speculated mainly from the formation of GaO₄ tetrahedra from Ga₂O₃. In other words, if all Ga₂O₃ forms GaO₄ tetrahedra, which seems to be the case for these glasses[2-5], there will not be enough number of oxygens available. Formation of three-coordinated oxygens is necessary in order to compensate this oxygen deficiency. Miyaji et al.[4] also predicted the formation of three-coordinated oxygens from the average coordination number of 2.8 around oxygens in 50PbO-50GaO_{1.5} glass. An average Ga-O distance of ~0.186 nm from the room-temperature EXAFS analysis[5] is longer than the average distance of ~0.183 nm in crystals and can be an another evidence for the presence of three-coordinated oxygens.

However, if Ga-O bond distance in glass is uniform at ~0.186 nm, this leads to a conclusion that almost all of oxygens bonded to Ga should be three-coordinated which will make the glass formation very difficult. In fact, Ga-O bond lengths are in-between 0.181~0.187 nm in PbGa₂O₄ crystal[11] and oxygens bonded to three cations have two Ga at the distance of 0.183~0.187 nm and one lead at ~0.235 nm. On the other hand, those bonded to two Ga only have shorter Ga-O distances of 0.181~0.183 nm. Therefore, the Ga-O bond lengths are asymmetrically distributed in PbGa₂O₄ crystal. The cumulant fitting scheme considering the non-Gaussian distribution(Model II) provided better results as evidenced from the smaller R-factor compared to the Gaussian case. This non-Gaussian distribution of oxygens around Ga seems to be attributed to the co-presence of two-coordinated and three-coordinated oxygens in glasses similar to that of a PbGa₂O₄ crystal.

Model III considering two distinct Ga-O bond lengths can be used to acquire quantitative figures despite of a slightly larger R-factor than Model II. Results of this two-subshell fitting(Table I) showed that the oxygen distributions of glasses are similar to PbGa₂O₄ crystal. More specifically, more than two out of four oxygens bonded to Ga have Ga-O distance of ~0.187 nm and they are most probably connected to three cations. On the other hand, the remaining oxygens are located at the distance of ~0.182 nm and form two-coordinated oxygens. Obviously, this kind of calculations employing only two distinct Ga-O distances can not reflect the precise structural scheme of the GaO₄ tetrahedra. In fact, Ga-O bond lengths in a crystalline PbGa₂O₄ can not be divided into two different sets. However, it is clear that bonds at the longer distances are associated with three-coordinated oxygens and vice versa. Therefore, the two-subshell calculation as in Model III can provide a crude idea on how many of those oxygens forming GaO₄ tetrahedra are bonded to three cations even though calculations using Model II may reflect the overall structure more precisely. In addition, two-subshell model calculation shows an increase in the number of three-coordinated oxygens with increasing Ga₂O₃ concentration.

CONCLUSIONS

Short-range order structural parameters around Ga in PbO-Ga₂O₃ glasses were analyzed from the Ga K-edge EXAFS spectra recorded at the liquid nitrogen temperature. Four oxygens were bonded to each gallium forming GaO₄ tetrahedra at the average bond distance of 0.1855~0.1862 nm. A fitting assuming a non-Gaussian distribution of Ga-O bond distance provided the best results with the smallest R-factor compared to the other cases. Fittings with two distinct Ga-O bond distances suggest that approximately 60 % of oxygens bonded to Ga is three-coordinated and the amount of which decreased with decreasing Ga₂O₃ concentration.

REFERENCES

1. A. A. Kharlamov, R. M. Almeida and J. Heo, *J. Non-Cryst. Solids*, 202 (1996) 233.
2. F. Miyaji and S. Sakka, *J. Non-Cryst. Solids*, 134 (1991) 77.
3. F. Miyaji, K. Tadanaga, T. Yoko, and S. Sakka, *J. Non-Cryst. Solids*, 139 (1992) 268.
4. F. Miyaji, T. Yoko, J. Jin, S. Sakka, T. Fukunaga, and M. Misawa, *J. Non-Cryst. Solids*, 175 (1994) 211.
5. Y. G. Choi, J. Heo, and V. A. Chernov, *J. Non-Cryst. Solids*, 221 (1997) 199.
6. M. Newville, P. Livins, Y. Yacoby, J. J. Rehr, and E. A. Stern, *Phys. Rev. B* 47[21] (1993) 14126.
7. J. J. Rehr, J. Mustre de Leon, S. I. Zabinsky, and R. C. Albers, *J. Am. Chem. Soc.* 113[14] (1991) 5135.
8. E. A. Stern, M. Newville, B. Ravel, Y. Yacoby, and D. Haskel, *Physica B* 209 (1995) 117.
9. G. Bunker, *Nuclear Instruments and Methods*, 207 (1983) 437.
10. E. D. Crozier, J. J. Rehr, and R. Ingalls, in: *X-Ray Absorption*, ed. D. C. Koningsberger and R. Prins (John Wiley & Sons, 1988) p. 373.
11. Von K. -B. Plotz and H. Muller-Buschbaum, *Z. Anorg. Allg. Chem.*, 488 (1982) 38.
12. A. C. Hannon, J. M. Parker, and B. Vessal, *J. Non-Cryst. Solids*, 196 (1996) 187.
13. J. C. Lapp, *American Ceramic Society Bulletin*, 71 (1992) 1543.

SURFACE ALTERATION OF ZINC ULTRAPHOSPHATE GLASS AT 140°C

C. Mercier, L. Montagne*, H. Sfihi⁽⁺⁾ and G. Palavit

Laboratoire de Cristallochimie et Physicochimie du Solide, URA CNRS 452,
Ecole Nationale Supérieure de Chimie de Lille, BP 108, 59652 Villeneuve d'Ascq Cedex,
France.

e-mail : Lionel.Montagne@univ-lille1.fr

⁽⁺⁾Laboratoire de Physique Quantique, URA CNRS 1428, ESPCI, 10 rue Vauquelin
75231 Paris Cedex 05 France.

* corresponding author

ABSTRACT

Infra-red spectroscopy, thermogravimetry, and conductivity measurements were used to monitor the mechanism of surface alteration of zinc ultraphosphate glass under moist air at 140°C. Water adsorption is followed with thermogravimetry. Infra-red spectroscopy shows that H₃PO₄ solution arising from the network hydrolysis appear on glass surface. Evolution of the surface conductivity gives evidence that this product concentrates with the exposition time.

INTRODUCTION

Ultraphosphate glasses containing large amounts of hydroxyl groups are of potential interest as matrix for protonic conduction [1]. We prepared zinc ultraphosphate glasses with large water content by melting of H₃PO₄-ZnO mixtures for short times [2]. Water content as high as 13 mole% could be obtained when melting time is less than one hour. It is then useful for the development of glassy matrix for protonic conductors to characterize the stability toward the atmospheric water. The mechanism of the phosphate glass network alteration was monitored with thermogravimetry, ³¹P NMR and surface conductivity measurements.

EXPERIMENTAL PROCEDURE

Zinc ultraphosphate glass containing large amount water was prepared by melting phosphoric acid and zinc oxide at 900°C for 1 hour. The glass was poured on a steel plate at room temperature. The molar composition is : 54.6 P₂O₅-34.2 ZnO-11.2 H₂O.

Thermogravimetric curve was recorded on a Dupont thermobalance. The increase in temperature from 20 to 140°C was carried out under argon, then air with 88% relative humidity was introduced. The conductivity was measured using the complex impedance method (Solartron 1170), with the same atmosphere schedule than the thermogravimetric analysis. Gold electrodes were sputtered on a polished glass sample. The infra-red spectra were recorded, using the KBr disc method, on samples previously heated at 140°C for the times shown on the spectra.

RESULTS

Figure 1 shows the thermogravimetric curve versus time at 140°C of a zinc ultraphosphate glass. After an induction period, an increase in weight is observed, that can be attributed to water adsorption. It occurs during 40 hours, then the weight tends to a constant value. The initial conductivity, measured at 140°C under argon is 1.6 10⁻¹⁰ S (Figure 2). It increases over seven orders magnitude during 40 hours, then decreases up to 100 hours and attains a constant value of 2 10⁻⁴ S.

The infra-red spectrum of the pristine zinc ultraphosphate glass (Figure 3) shows a set of bands in the 1400-700 cm⁻¹ region that are characteristics of the stretching vibrations of ultraphosphate compounds [3] : 1320 cm⁻¹ (vas P=O), 1050 cm⁻¹ (vs PO₂), 950 cm⁻¹ (vas P-O-

P) 700 cm^{-1} (vs P-O-P). Alteration of the ultraphosphate network by exposition under moist air at 140°C is clearly seen on the infra-red spectra : the band at 1320 cm^{-1} characteristic of P=O vibration in ultraphosphate compounds decreases in intensity together with P-O-P at 950 cm^{-1} , and a strong band at 1010 cm^{-1} appears. This last band is attributed to the stretching vibration of P-O bonds in PO_4 tetrahedra of orthophosphoric acid, as confirmed by the phosphoric acid spectrum (Figure 3). The presence of diphosphoric groups is difficult to be established on the infra-red spectra. The presence of $\text{ZnH}_2\text{P}_2\text{O}_7$ is however clearly shown on ^{31}P NMR spectra (not shown) [4].

DISCUSSION

The increase in weight monitored with 140°C isothermal thermogravimetric analysis can be attributed to water adsorption on the sample surface. Adsorption of water leads to a degradation of the ultraphosphate network by hydrolysis reactions, with the formation of acid phosphate compounds, mainly orthophosphoric acid and zinc dihydrogen pyrophosphate. The formation of these compounds is characterized with both infra-red spectroscopy (PO_4 groups of phosphoric acid) and ^{31}P NMR (Q^0 and Q^1).

The accumulation of the adsorbed water and hydrolysis products leads to the formation of a layer of concentrated acid zinc phosphate. The conductivity of this phase is very high, as reflected by the increase of conductivity over several orders of magnitude. Then, after 40 hours, the hydrated acid layer equilibrates with the atmospheric water, and the thermogravimetric curve reaches a constant level. The conductivity curve goes through a maximum at 40 hours, and decreases to a constant value after 100 hours. This behaviour is related to the change in the mechanism of protonic conductivity reported for H_3PO_4 solutions: when the acid solution becomes more and more concentrated, the conductivity increases and then decreases, as shown on Figure 4 [5,6]. The decrease in conductivity is indeed due to the decrease of proton concentration, then the proton mobility decreases owing to the formation of hydrogen bonds network.

CONCLUSION

Alteration of a zinc ultraphosphate glass containing 11.2% H_2O was followed at 140°C . Water adsorption occurs, followed by hydrolysis of the ultraphosphate network. It leads to the formation on the sample surface of a layer of an acidic phosphate solution. The conductivity of this layer is very high, and its evolution versus time can be explained by considering the effect of the concentration on a phosphoric acid solution.

REFERENCES

- [1] Y. Abe, G. Li, M. Nogami, T. Kasuga and L. Hench, *J. Electrochem. Soc.* 143[1] (1996) 144.
- [2] C. Mercier, L. Montagne, H. Sfihi, G. Palavit, J.C. Boivin and A.P. Legrand, *J. Non Cryst. Solids* 224 (1998) 163-172.
- [3] A. Rulmont, R. Cahay, M. Liegeois-Duyckaerts and P. Tarte, *Eur. Solids State Inorg. Chem.* 28 (1991) 207.
- [4] submitted
- [5] "Handbook of Chemistry and Physics" 62nd ed. (1982) CRS Press, Boca Raton.
- [6] J. Grondin, D. Rodriguez and J.C. Lassegues, *Solid State Ionics* 77 (1995) 70.

Weight variation (%)

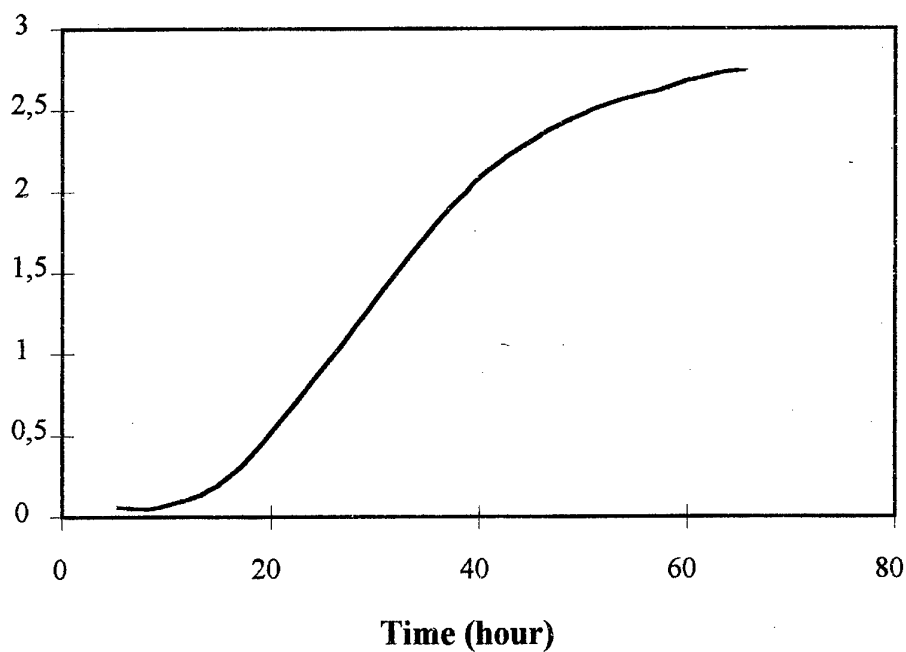


Figure 1 : Thermogravimetric curve, recorded at 140°C under moist air, of a zinc ultraphosphate glass containing 11.2 mole % H₂O

Conductance (S*10⁴)

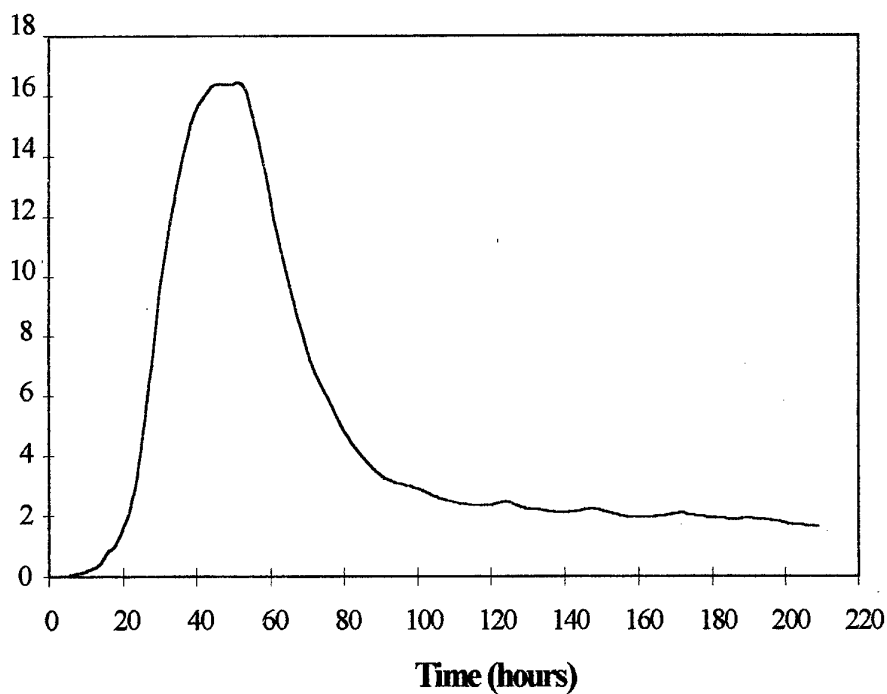


Figure 2 : Conductance versus time at 140°C under moist air, of a zinc ultraphosphate glass containing 11.2 mole % H₂O.

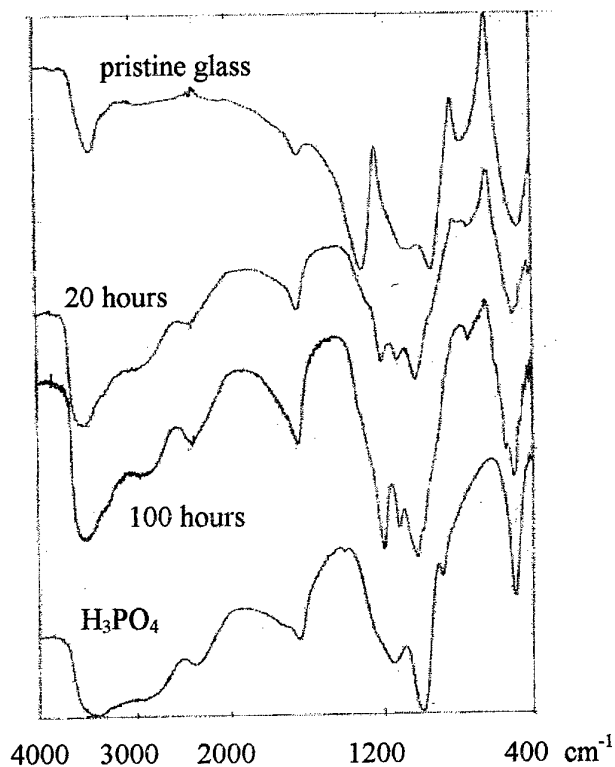


Figure 3 : Infra-red spectra of a zinc ultraphosphate glass containing 11.2 mole % H_2O , exposed for different times at 140°C under moist air. The spectrum of phosphoric acid is shown as a reference.

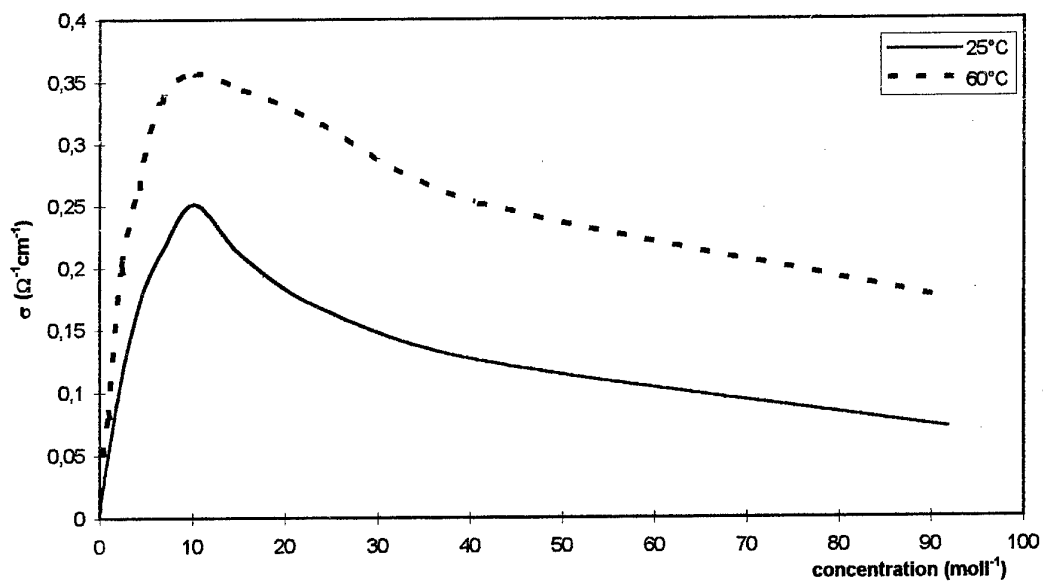


Figure 4 : Conductivity of H_3PO_4 solution versus the acid concentration [5,6].

PHYSICAL AND OPTICAL PROPERTIES OF Er^{3+} - Yb^{3+} CO-DOPED LEAD FLUOROINDOGALLATE GLASSES

R. Lebullenger, D. F. de Souza, L. F. C. Zonetti, A. C. Hernandes, L. A. O. Nunes

Instituto de Física de São Carlos - Universidade de São Paulo- Caixa Postal 369 -
13560-970 São Carlos -SP- Brazil

lebullen@ifsc.sc.usp.br

ABSTRACT

Lead fluoroindogallate glasses in the $30\text{PbF}_2\text{-}20\text{GaF}_3\text{-}15\text{InF}_3\text{-}15\text{ZnF}_2\text{-(}20\text{-x-y)}\text{CaF}_2\text{-xYbF}_3\text{-yErF}_3$ system (with x and y = 0,1,...12) were prepared in platinum crucible under controlled atmosphere. The principal physical characteristics of the PGIZCa glass matrix are: glass transition temperature T_g equal to 264°C , refractive index n_D of 1.564, and density of 5.57. Main physical properties as T_g and $(T_x\text{-}T_g)$, density vs dopant contents were measured. The substitution of CaF_2 by rare earth fluoride ErF_3 and/or YbF_3 does not damage glass stability. The difference $(T_x\text{-}T_g)$ for each glass is around 86°C , value also obtained for $x=y=0$. With regard to density, rare earth incorporation induced an increase of it. Optical properties, as absorption and emission in the UV-Vis-IR range, were also studied for these rare earth doped lead fluoroindogallate glasses. The transition $^4\text{I}_{11/2} \rightarrow ^4\text{I}_{13/2}$ (2700 nm) and upconversion process were observed, with emissions in 543 and 660 nm, using 980 nm diode laser pump. The visible emission intensities are highly increased with the presence of Yb^{3+} , while emission in mid-infrared region decreases.

INTRODUCTION

There is a great interest in compact lasers operating at mid infrared ($\approx 3\mu\text{m}$), for medical and eye-safe LIDAR applications[1,2], and in the visible region (blue-green), for use in data storage, undersea communications, etc. With the advent of powerful semiconductor lasers (up to 10 W) at 0.8 and $0.98\mu\text{m}$, diode pumped solid state lasers at mid infrared and visible (upconversion based lasers) became a reality. For diode pumped laser emission at mid infrared and visible regions, Er^{3+} seems to be a natural candidate because of its $\sim 2.8\mu\text{m}$ emission ($^4\text{I}_{11/2} \rightarrow ^4\text{I}_{13/2}$), its green emission at $\sim 0.543\mu\text{m}$ ($^4\text{S}_{3/2} \rightarrow ^4\text{I}_{15/2}$) and its absorption bands at ~ 0.8 and $\sim 0.98\mu\text{m}$, where exist cheap and powerful diode lasers. CW operation of the Er^{3+} at $\sim 2.8\mu\text{m}$ emission is observed in crystals [3,4], and also in glasses [5,6]. Among diverse techniques that are currently used to obtain compact visible lasers[7], upconversion lasing is the one of the most promising techniques as it does not require a non linear medium to second harmonic generation avoiding the problem of the spatial mode and lack of polarization of the semiconductor laser. Although upconversion laser performance of Er^{3+} has been observed in crystals[8,9] and glass fibers[10,11], it is not currently reported upconversion lasers using bulk glasses as active medium. Fluoride glasses offer an important advantage over more traditional oxide system for use as a laser host since the lifetime of the excited electronic states is longer in these systems. In order to study the laser performance of Er^{3+} in fluoride glasses, we realized a detailed investigation relating mid infrared ($2.8\mu\text{m}$) and upconversion results of Er^{3+} in single doped samples and Er^{3+} - Yb^{3+} codoped samples. We used a lead fluoroindogallate glass matrix as host to rare earth ions, its multiphonon edge is shifted by $1\mu\text{m}$ by comparison with fluorozirconate glasses[12,13]. This work was carried out to study the

spectroscopic properties of Er³⁺ and Er³⁺/Yb³⁺ in the PGIZCa glass. This glass is derived from the PGIZC composition[13], where CdF₂ was entirely substituted by CaF₂ to improve the chemical stability without altering the glass stability.

EXPERIMENTAL DETAILS

Were used two sets of samples, labelled PGIZCa-xEr and PGIZCa-2Er-xYb, which have the respective molar composition 30PbF₂ - 20 GaF₃ - 15InF₃ - 15 ZnF₂ - (20-x)CaF₂ - xErF₃ with x=0, 2, 4, 6 and 30PbF₂ - 20 GaF₃ - 15InF₃ - 15 ZnF₂ - (18-x)CaF₂ - 2ErF₃ - xYbF₃ with x=1, 2, 4, 8, 12. Starting materials were PbF₂, CaF₂, ZnF₂ from BDH - Merck UK and YbF₃ (3N) from Strem product. In, Ga, were available as oxide (4N) from PPM Pure Metals-Metaleurop and Er₂O₃ was an Aldrich (3N) product. Ammonium bifluoride NH₄F₂ from Aldrich was used to transform each oxide in anhydrous fluoride under dry atmosphere. All these anhydrous fluoride were then mixed in platinum crucible, all the classical steps of melting, refining, and casting were performed in a dry glove box in order to prevent hydrolysis. Sample were annealed for several hours at a few degrees celsius below glass transition, T_g, before cooling at room temperature. All the prepared samples are crystals free and are at least 4 mm thick.

Thermal analysis of the glass was carried out with a TA Instruments D.S.C. 2090. apparatus, using heating rate of 10°C.min⁻¹. We measured refractive index with an Abbe refractometer. The density as a function of dopant concentration was measured by the Archimedian method in CCl₄. The experimental error is equal to ± 2°C for temperatures, ± 0.005 g.cm⁻³ for density.

The experimental set-up used to upconversion and Stokes luminescence at near infrared and visible regions were already described in reference[14]. Mid infrared signal was measured using a nitrogen cooled InSb detector Judson model J10D coupled to a lock-in amplifier. The up-conversion intensity versus pump power was measured using green and red filters, in order to select the signal that reaches the power detector OPHIR model PD2-A, the pump was varied from 20 to 230 mW.

RESULTS- DISCUSSION

Glass physical characteristics

Characterisitic temperatures and density values of the prepared glasses are summarized in tables 1 and 2.

Table 1: Characteristic temperatures (°C) and density for PGIZCa-2Er-xYb samples

% Yb	T _g	T _x	T _p	T _x -T _g	d
0	269	351	400	82	5,64
1	268	352	405	84	5,68
2	267	357	415	90	5,704
4	261	348	407	87	5,789
8	272	363	426	91	5,92
12	275	379	426	104	6,02

Table 2: Characteristic temperatures (°C) and density for PGIZCa-xEr samples

% Er	T _g	T _x	T _p	T _x -T _g	d
0	264	350	380	86	5,57
2	269	351	400	82	5,68
4	269	361	410	92	5,74
6	270	356	406	86	5,77

The substitution of CaF_2 by fluoride rare earth ErF_3 or YbF_3 does not prejudice the glass stability when compared with the matrix glass IGPZCa. The (T_x-T_g) value for each sample is around 86°C . We can note that for high Yb concentration (12%) a notable stabilization is observed with $(T_x-T_g) > 100^\circ\text{C}$.

With regard to density, the incorporation of rare earth ions induces an increase of it. The density of YbF_3 and ErF_3 is $8,17$ e $7,81 \text{ g.cm}^{-3}$ respectively, whereas CaF_2 presents a density of $3,18 \text{ g.cm}^{-3}$. Thus, the substitution of calcium by a rare earth leads to a glass denser.

The refraction index of the matrix for the D line of the Na is $1,564$.

Absortion spectra

Raman scattering was performed on PGIZCa glass and showed a maximum phonon energy of 500 cm^{-1} . The transmission value from 0.3 up to $8\mu\text{m}$, is about 90% for samples 2mm thick.

The Er^{3+} fundamental level is $^4I_{15/2}$. The absorption bands showed in the 300 e 1600 nm spectral range (Figure 1) obtained for the sample PGIZCa₂Er₂Yb could be attributed to transition from ground level to excited level as shown in Table 3.

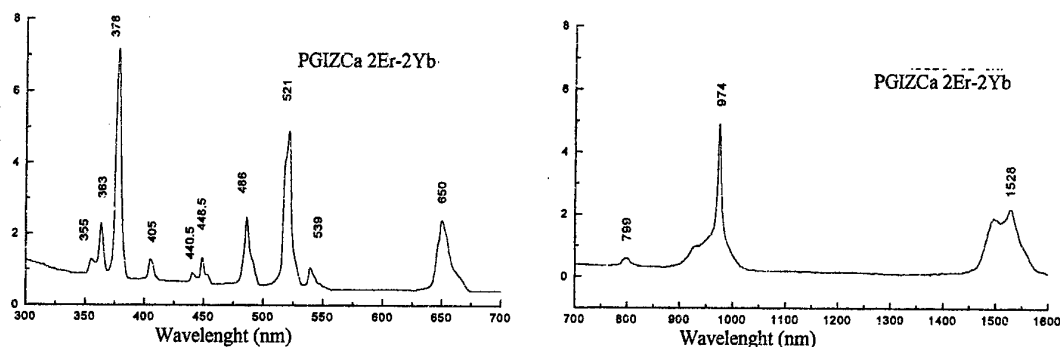


Figure 1: Absorption spectra for the PGIZCa-2Er₂Yb sample in the 300 to 1600nm range

Table 3: Absorption bands and their attribution $^4I_{15/2}$ (ground level) \rightarrow excited level.

Absorption band (cm^{-1})	Absorption band (nm)	Transition from $^4I_{15/2}$ to
28169	355	$^2G_{7/2}$
27548	363	$^2G_{9/2}$
26455	378	$^4G_{11/2}$
24691	405	$^2H_{9/2}$
22701	440	$^4F_{3/2}$
22296	448	$^4F_{5/2}$
20576	486	$^4F_{7/2}$
19193	521	$^2H_{11/2}$
18552	539	$^4S_{3/2}$
15384	650	$^4F_{9/2}$
12515	799	$^4I_{9/2}$
10266	974	$^4I_{11/2}$ (Yb^{3+}) $^2F_{7/2} \rightarrow ^2F_{5/2}$
6544	1528	$^4I_{13/2}$

Pump wavelength at 0.488 μm

Figures 2a and 2b show typical spectra of Er^{3+} luminescence from 0.5 up to 1.7 μm . The 8 transitions observed are identified by numbers.

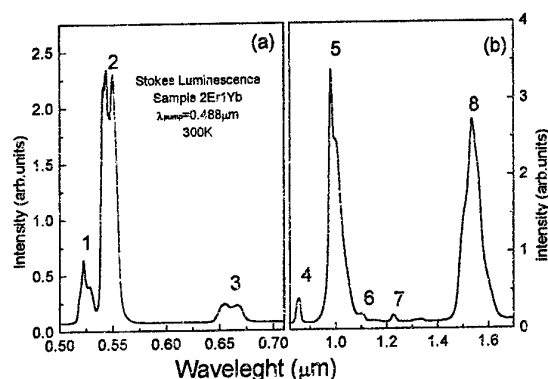


Figure 2a and 2b. Luminescence spectra of PGIZCa2Er1Yb sample

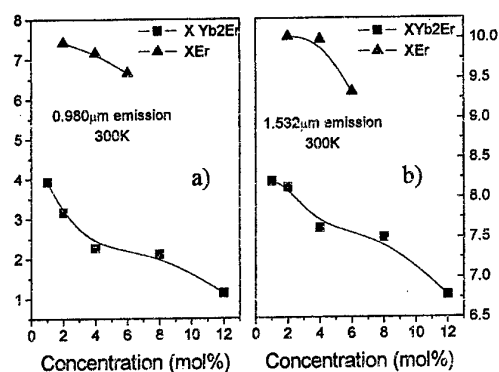


Figure 3a and 3b. Emission intensity versus rare earth concentration

These emission correspond to the following transitions: 1 at $\approx 0.523\mu\text{m}$ ($^2\text{H}_{11/2} \rightarrow ^4\text{I}_{15/2}$); 2 at $\approx 0.540\mu\text{m}$ ($^2\text{S}_{3/2} \rightarrow ^4\text{I}_{15/2}$); 3 at $\approx 0.650\mu\text{m}$ ($^2\text{F}_{9/2} \rightarrow ^4\text{I}_{15/2}$); 4 at $\approx 0.850\mu\text{m}$ ($^2\text{S}_{3/2} \rightarrow ^4\text{I}_{13/2}$); 5 at $\approx 1.0\mu\text{m}$ ($^2\text{I}_{11/2} \rightarrow ^4\text{I}_{15/2}$, $^2\text{F}_{5/2} \rightarrow ^2\text{F}_{7/2}$); 6 at $\approx 1.1\mu\text{m}$ ($^4\text{F}_{9/2} \rightarrow ^4\text{I}_{13/2}$); 7 at $\approx 1.23\mu\text{m}$ ($^2\text{S}_{3/2} \rightarrow ^4\text{I}_{11/2}$); and 8 at $\approx 1.532\mu\text{m}$ ($^4\text{I}_{13/2} \rightarrow ^4\text{I}_{15/2}$).

The intensity of 0.98 and 1.53 μm emission versus rare earth concentration are shown in figures 3a and 3b. The PGIZCa-xEr set of samples shows the best signal intensity when compared with the other. For the set PGIZCa2Er-xYb, there is a photoluminescence quenching process for the 0.98 μm emission in samples with Yb^{3+} concentration above $\sim 4\text{mol}\%$, also, this set exhibits the less intense signal for 1.532 μm emission.

Pump wavelength at 0.980 μm

Figure 4 shows the upconversion spectra of the PGIZCa-2Er1Yb sample.

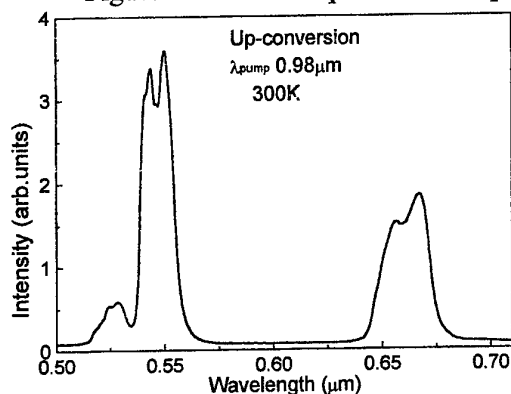


Figure 4. Upconversion spectra of PGIZCa2Er1Yb sample

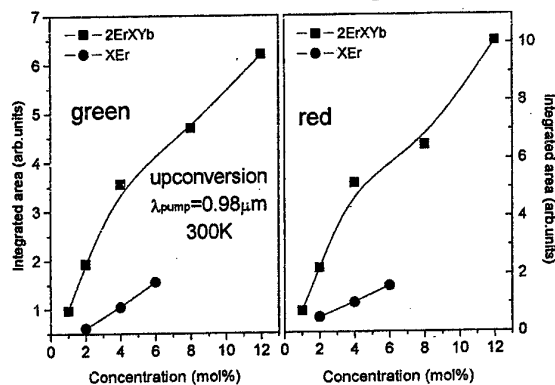


Figure 5. Upconversion intensity versus Er^{3+} concentration

Figure 6 shows the luminescence at 2.8 μm , this transition is an indirect one from $^4\text{I}_{11/2}$ to $^4\text{I}_{13/2}$ level.

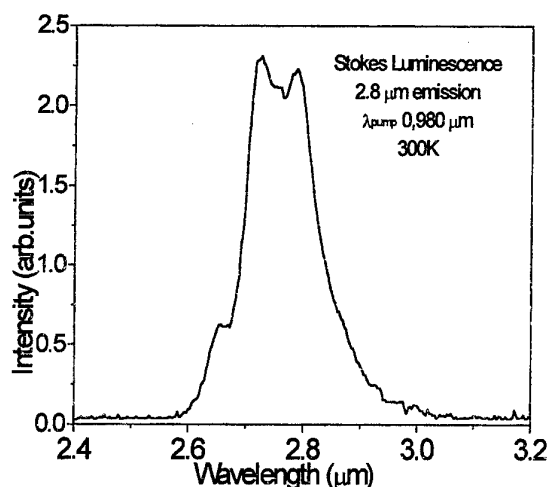


Figure 6. Luminescence spectrum of 2.8μm emission ($^4I_{11/2} \rightarrow ^4I_{13/2}$ transition) of the 2Er1Yb sample.

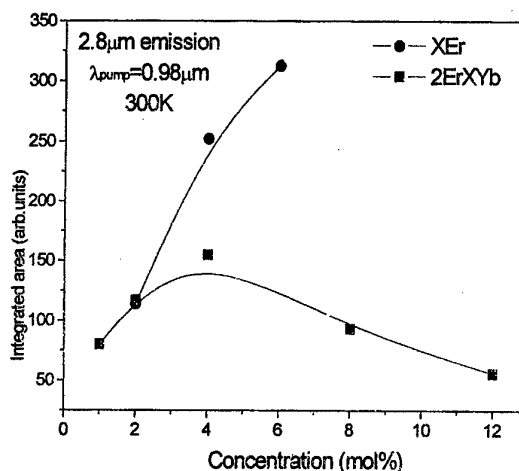


Figure 7. 2.8μm intensity against sample concentration

The intensity of the 2.8μm emission as a function of the dopant concentration is shown in figure 7. We can see that the best set of samples emitting at mid infrared is the single doped one (PGIZCa-xEr), which also has the less intense upconversion signal. The energy levels diagram in figure 8, shows us the mid infrared luminescence and upconversion mechanisms. In single doped samples, a pump photon excites an Er^{3+} to its $^4I_{11/2}$ level. From this level, it can decay to $^4I_{13/2}$ level, emitting a 1.532μm photon, or by means of a multiphonon relaxation. In codoped samples, the main absorbing channel is the Yb^{3+} , as represented. After an energy transfer process ET1, an erbium ion is excited to $^4I_{11/2}$ level, and become able to emit a 2.8μm photon going to $^4I_{13/2}$ level.

The upconversion processes that generate green emission are labeled (a) and (b) in figure 8. In process (a) one Er^{3+} is excited to $^4F_{7/2}$ state. Process (b) needs two Er^{3+} excited in $^4I_{11/2}$ level, two neighboring ions interact with each other.

In order to generate red light, we have three possible mechanisms (c), (d) and (e). In process (c), a single doped sample absorbs a new 0.98 μm photon after a radiative or non radiative decay from $^4I_{11/2}$ to $^4I_{13/2}$ excited state. In the case of a codoped sample, two non resonant energy transfer processes ET2 have to occur in order to excite an Er^{3+} . In process (d) are necessary two Er^{3+} , one of them excited in $^4I_{11/2}$ level and the other in $^4F_{7/2}$ level. The two ions interact, resulting that both ions go to $^4F_{9/2}$ level emitting red light. Finally, process (e) needs two Er^{3+} , the first one excited in $^4I_{9/2}$ and the second in $^4S_{3/2}$. After the interaction both are excited in $^4F_{9/2}$.

For the PGIZCa2Er-xYb set, which is the best one for upconversion applications (figure 5), we measured the upconversion intensity versus pump power. Upconversion intensity obeys a relation with pump power[15] given by $I \propto P^n$ where I is the signal intensity, P is the pump power and n is the ratio between the number of infrared photons and the number of visible photons involved. A small deviation from $n=2$ was observed for green emission (Table4). This can be due to the sharp focus of pump beam on the sample [16]. For red emission, processes (d) and (e) can be discarded because they depend on erbium concentration which is fixed in these samples, while the process (c) depends on Yb^{3+} concentration, this process has dependence $n=2$ which is in very good agreement with experimental results.

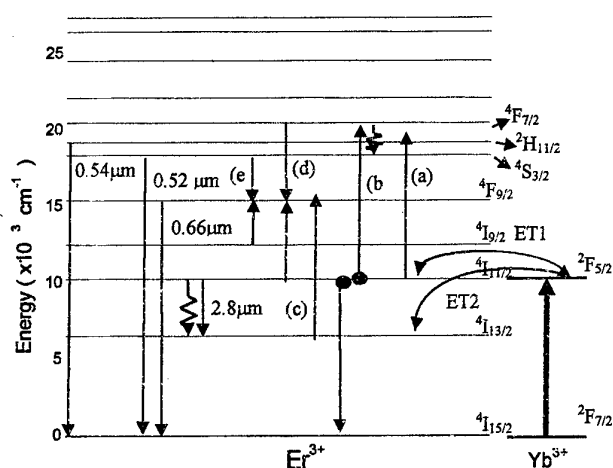


Table4. Slope of the upconversion intensity versus pump power (20-230mW) for 2ErXYb samples set.

2ErXYb	n (green)	n (red)
X=1	1.9	2
X=2	1.9	2
X=4	2	2
X=8	1.8	1.9
X=12	1.8	1.9

Figure 8: Energy levels of Er^{3+} and Yb^{3+} and Upconversion diagram.

CONCLUSION

PGZCa glass presents a good hability to incorporate rare earth fluoride as Er and Yb up to 14mol.% without altering its stability. 2.8 μm transition of Er^{3+} in this glass has been reported and its relation with upconversion processes was verified. From these results, we showed, as expected, that the increase of upconversion processes did not alter 2.8 μm emission in the same way. With a large amount of Yb^{3+} in the samples, the probability of two successive ET1 or ET2 mechanisms is so great and the erbium ion can not emit 2.8 μm radiation. The sample with 6%Er seems to be the best one for the 2.8 μm emission and, whereas, samples with a large amount of Yb^{3+} are indicated to enhance the upconversion efficiency.

ACKNOWLEDGEMENTS

Brazilian financial agencies CNPq-RHAE, FAPESP.and FINEP.

REFERENCES

- ¹ L. Esterowitz, C. A. Hoffman, D. C. Tran, K. Levin, M. Storm, R. F. Bonner, P. Smith and M. Leon, in SPIE, **605** Optical and Laser Technolgy in Medicine 32 (1986).
- ² N. P. Barnes, W. J. Rodriguez, B. M. Walsh- J. Opt. Soc. Am. **B13**, 2872 (1996).
- ³ Tso Yee Fan, G. Huber, Robert L. Byer and P. Mitzscherlich-IEEE J. Quan. Elect. **24**, 924 (1988).
- ⁴ G. J. Kintz, R. Allen and L. Esterowitz-Appl. Phys. Lett. **50**, 1553 (1987).
- ⁵ F. Auzel, D. Meichenin, H. Poignant - Elett. Lett., **24**, 1463 (1988).
- ⁶ H. Yanagita, I. Masuda, T. Yamashita, H. Toratani - Elett. Lett., **26**, 1836 (1990).
- ⁷ Derek W. Nam and Robert G. Waarts - Laser Focus World, **August**, 49 (19940).
- ⁸ A. J. Silversmith, W. Lenth, R. M. Macfarlane - Appl. Phys. Lett., **51**, 1977 (1987).
- ⁹ M. F. Joubert, S. Guy, and B. Jacquier - Phys. Rew. **B48**, 10031 (1993).
- ¹⁰ K. Hirao, S. Todoroki, N. Sogan - J. Non Cryst. Sol., **143**, 40 (1992).
- ¹¹ S. sanders, R. G. Waarts, D. G. Mehuys et al - Appl. Phys. Lett., **67**, 1815 (1995).
- ¹² J. Nishii, K. Kaite and T. Yamagishi, Phys. and Chem. of Glasses , 30(2) (1989) 55
- ¹³ G. Zhang, B. Friot, M. Poulain, J. Non-Cryst. Solids, 213 (1997) .
- ¹⁴ C. T. M. Ribeiro, A. R. Zanatta and L. A. O. Nunes - J. Appl. Phys., **83**, 2256 (1998).
- ¹⁵ S. Tanabe, K. Hirao and N. Soga-J. Non Cryst. Solids **122**, 79 (1990).
- ¹⁶ R. Reiche, L. A. O. Nunes, C. C. de Carvalho, Y. Messaddeq and M. A. Aegerter- Sol. State Commun, **85**, 773 (1993).

SURFACE PROTECTION OF FLUOROINDATE GLASSES BY SOL-GEL DIPCOATED SnO_2 THIN LAYER

A.P. Rizzato, S.H. Pulcinelli, C.V. Santilli, Y. Messaddeq and S.J.L. Ribeiro

Instituto de Química, UNESP, PO. Box 355,
14801-970, Araraquara, SP, Brazil

In the last decade, heavy metal fluoride glasses have received great attention and several technological applications can be frozen such as infrared devices and telecommunication. However, these glasses have a lower chemical durability specially fluorozirconate glasses which compromise some special applications.

In this purpose, glasses surface protection has been studied by coating with a thin film layer of tin oxide. The structural characteristics of sol-gel dip-coated samples were analyzed by FTIR spectroscopy, x-ray reflectometry and scanning electron microscopy. The layers present 55 nm in thickness, showing roughness of the order of 2 nm and transmittance higher than 80% in the IR region. Mass loss and IRFT measurements, have been carried out during etching with water at different pH. Samples coated with SnO_2 is five time resistant in acidic solution against corrosion.

ACTIVATION ENERGY OF RELAXATION TIME AND VISCOSITY OF CHALCOGENIDE GLASSES

A.Tverjanovich, M.D.Balmakov, Yu.S.Tveryanovich

Chemical Department, Saint-Petersburg State University, St.Petersburg, Russia

E-mail: andr@tver.usr.pu.ru

INTRODUCTION

Viscosity of glass-forming liquids and its interconnection with structural relaxation are principal problems of the vitreous state theory. Chalcogenide glasses having low glass transition temperature (T_g) and strong composition dependence of properties are most convenient materials for studying both temperature behaviour of viscosity in a wide range of viscosity values and peculiarities of properties' changes at T_g . All this is a reason to choose the subject and the objects of the investigation.

EXPERIMENTAL

Kinematic viscosity values lower than tens St were determined from the damping of free vibrations of cylindrical silica glass ampoule filled with the material to be investigated and suspended from fine silica glass filament. Dynamic viscosity (η) values were determined in the range $10^6 \div 10^{13}$ Ps by measuring the rate of indenting a cylindrical rod into a glass plate. Thermal expansion coefficient (α) was determined by quartz dilatometer.

RESULTS AND DISCUSSION

The dynamic viscosity logarithm of glass-forming liquids attains the value $-3 \div -4$ when temperature tends to $+\infty$. Small values of viscosity are limited by viscosity of gaseous state (temperature dependence of viscosity of liquid Se [1-6] and the calculated curve of viscosity for gaseous Se are shown in fig. 1). This fact is taken into account in activated viscosity theories by equating the pre-exponential factor η_0 to the value $\sim 10^{-3}$ in the equation of viscosity-temperature dependence (1).

$$\eta = \eta_0 \exp\left(\frac{E_\eta(T)}{RT}\right) \quad (1)$$

Usually, the free activation energy of viscous flow $E_\eta(T)$ is divided into two parts. The first one doesn't depend on temperature and corresponds to the activation energy in the classical two-minimum system. The second one depends on temperature and reflects the peculiarity of glass-forming liquids, namely the co-operative nature of viscous flow in the super-cooling range. Eyring proposed the following relationship for the free activation energy of viscous flow [7]:

$$E_\eta(T) = H_\eta + TS_\eta(T) \quad (2)$$

where H_η and S_η are the activation enthalpy and entropy of viscous flow.

Structural relaxation in the glass transition range can be well approximated within the framework of Moynihan's approach [8]. According to Moynihan, the activation energy of relaxation time h^* in the equation of temperature dependence of relaxation time (τ) is equated to the activation energy of viscous flow defined as the slope of the plot $\log \eta = f(1/T)$ that corresponds to H_η in the relationship (2).

$$\tau = \tau_0 \exp\left(\frac{xh^*}{RT} + \frac{(1-x)h^*}{RT_f}\right) \quad (3)$$

where x is a parameter and T_f is the fictive temperature,

$$T_f(T) = T_0 + \int_{T_0}^T dT' \left\{ 1 - \exp\left[-\left(\int_{T'}^T \frac{dT''}{q\tau}\right)^\beta\right] \right\} \quad (4)$$

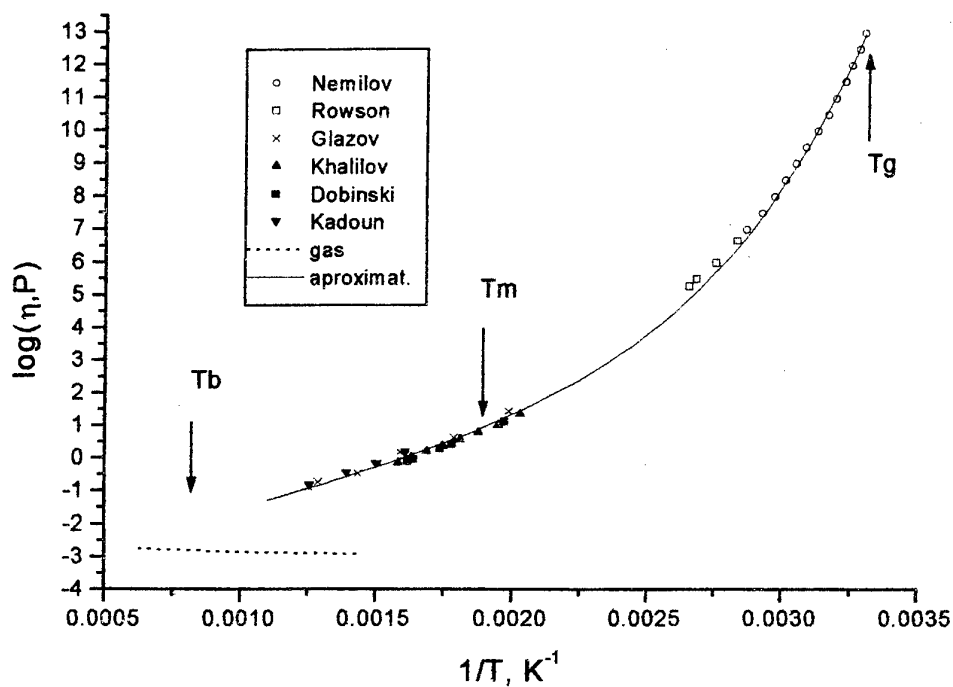


Fig. 1 Temperature dependence of logarithm viscosity of liquid Se: experiment [1-6] - dots, approximation - line; gaseous Se: calculation - dashed line.

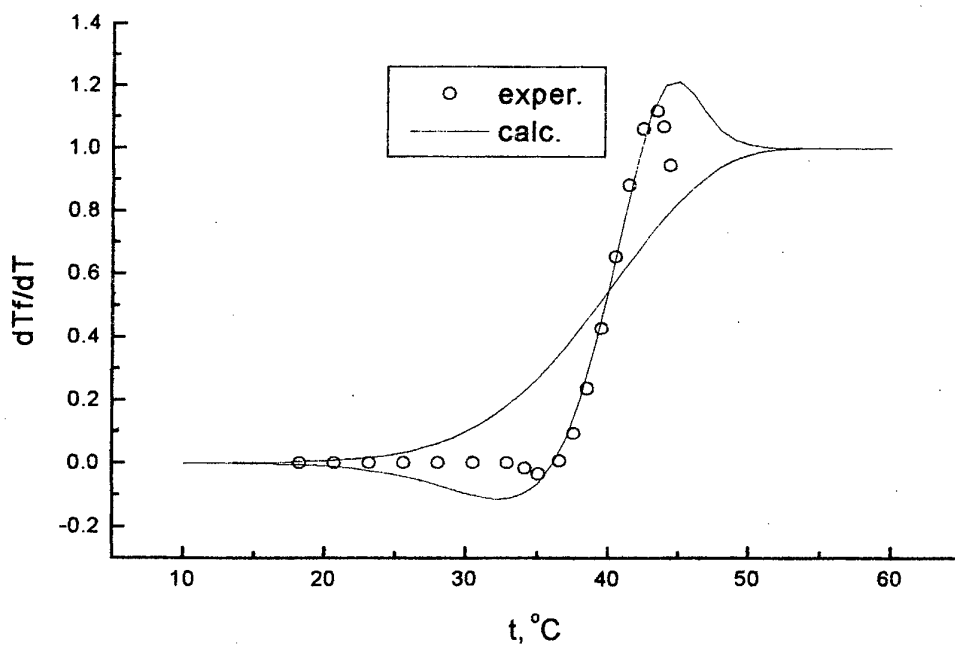


Fig. 2 Temperature dependence of temperature coefficient of the fictive temperature for Se for glass transition region. Dots is experimental data, line is approximation.

where T_0 is the temperature of the system in the equilibrium state, q is the cooling/heating rate, β is the exponent in Kolrausch's function which defines the relaxation time distribution, $0 < \beta \leq 1$.

Taking H_η instead of h^* in equations (3,4) leads to a τ_0 value much smaller than the time of thermal vibration of valence bonds (ν). For example, τ_0 values calculated for B_2O_3 and As_2Se_3 are $\sim 10^{-33}$ [8] and 10^{-39} [9] respectively, but the atom vibration frequency for As_2Se_3 is $7.3 \cdot 10^{12} \text{ s}^{-1}$ [10] (see Table 1). Besides, the calculated value of τ_0 strongly depends on the structure of the glass-forming liquid. For example, increasing the "fragility" of the structure results in a decrease of τ_0 value (τ_0 value for $AsSeI$ is $\sim 10^{-73}$ [9]).

The temperature dependence of dT_f/dT calculated from the experimental data on thermal expansion coefficient for Se is depicted in fig.2 by dots for the T_g region. The relationship between the fictive temperature and the experimental values of α can be expressed as follows:

$$\frac{dT_f}{dT} = \frac{\alpha_T - \alpha_g}{\alpha_m - \alpha_g} \quad (5)$$

where α_m and α_g are thermal expansion coefficients of a glass and a melt respectively. The solid line in fig.2 is the result of calculation carried out within the framework of Moynihan's approach. The calculation presents itself finding optimal values of τ_0 , h^* , β and x in equations (3,4) for the best fit of the experimental $dT_f/dT=f(T)$ curve. The free activation energy $E_\eta(T)$ was taken as h^* in equation (3) instead of the activation enthalpy of viscous flow. E_η was calculated from the experimental viscosity data using equation (1)¹. The η_0 value in equation (1) was chosen in the following two ways. The first one is according to [11]:

$$\eta_0 = N_A h / V_m; \quad E_\eta = F V_m; \quad F = \rho v_t \quad (6)$$

where N_A is Avogadro's number, h is Planck's constant, V_m is the molar volume of kinetic units overcoming the potential barrier, F is shear modulus, ρ is density, v_t is the transverse ultrasound velocity. Expressions (6) together with equation (1) enable us calculate η_0 *a priori*. The η_0 values calculated with the use of this approach are shown in the section I of Table 1. In the second approach, the temperature of a glass - metastable liquid transition on the calculated curve is determined by the values of τ_0 and η_0 at fixed cooling and heating rates. The η_0 value was taken for the calculated curve to approximate well the experimental data at τ_0 equated to the time of atoms vibration. The results are shown in the section II of Table 1. The same calculations were carried out for As_2S_3 , As_2Se_3 and $AsSeI$ (Table 1).

Table 1.

	I		II		
	$\log \eta_0$	τ_0, s	ν, s^{-1}	τ_0, s	$\log \eta_0$
Se	-3.89	$5 \cdot 10^{-14}$	$4.8 \cdot 10^{12}$	$2.08 \cdot 10^{-13}$	-3.3
As_2S_3	-3.81	$3 \cdot 10^{-14}$	$9.4 \cdot 10^{12}$	$1.06 \cdot 10^{-13}$	-3.2
As_2Se_3	-3.85	$1 \cdot 10^{-14}$	$7.3 \cdot 10^{12}$	$1.37 \cdot 10^{-13}$	-2.9
$AsSeI$	-3.87	$6 \cdot 10^{-14}$			

The calculated values of τ_0 presented in the section I of Table 1 are about the same order as the time of thermal vibrations of atoms, moreover the calculated data have weak

¹ Temperature dependence of E_η is approximated by the Jenckel's type equation

$$E_\eta = A + B \exp(C/T)$$

where A , B and C are parameters. The approximation curve $\log \eta = f(1/T)$ is shown as the solid line in fig.1.

dependence on the nature of a glass. The calculated values of η_0 are experimentally valid and they have weak dependence on the glass structure too. Therefore τ_0 can be excluded from the adjustable parameters in Moynihan's approach and it becomes possible to calculate the activation energy of viscosity and viscosity near T_g from the thermal expansion coefficient data or heat capacity data. Such calculations were carried out for As_2Te_3 , which has a high crystallisation ability prohibiting to measure viscosity in the metastable state.

The microscopic theory of viscosity is under development now. This can be explained by the fact that, on the one hand, the proposed approaches have been discussed well enough to hope to overcome their feeble sides and, on the other hand, they are yet far from description of the actual viscous flow phenomena. The solution can be found through an untraditional look at the problem.

Principal attention must be paid to the glass transition region. In this aspect the two factors are of great significance.

The first one is the configuration entropy $S^c(T)$ of fragments in which atoms' arrangements providing for the viscous flow take place. Above T_g the function $S^c(T)$ can be approximated by the expression [12]:

$$S^c(T) \approx \alpha_n m (1 - T_g^2/T^2) \quad \text{at } T \geq T_g \quad (7)$$

where m is the number of atoms in the fragment, α_n is the positive parameter defining the number J of all possible different structures of the fragment [13]

$$J = \exp(\alpha_n m + o(m)) \quad (8)$$

where the function $o(x)$ conforms to the relation $\lim_{x \rightarrow \infty} o(x)/x = 0$. The parameter α_n depends on chemical composition \mathbf{n} only (the components of the \mathbf{n} vector are relative concentrations of atoms of each kind which form the system, moreover $\sum_i n_i = 1$).

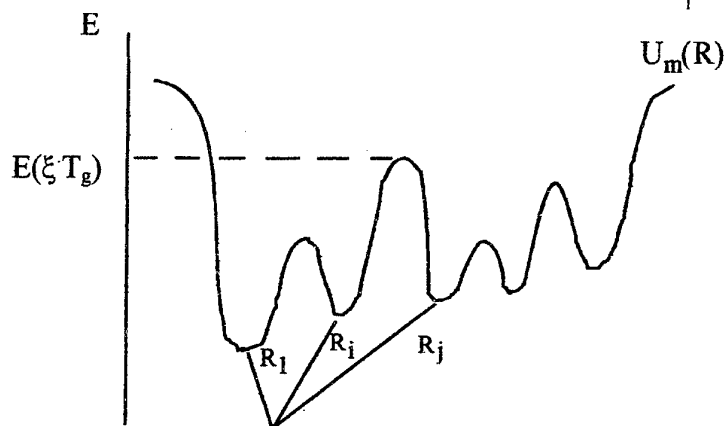


Fig.3 Symbolic picture of adiabatic electronic term $U_m(R)$

The second factor is the value of the coefficient of transition through the potential barrier which divides two equilibrium configurations [14] (two minima R_i and R_j of the adiabatic electronic term $U_m(R)$ [12,13], see fig.3). Indeed, the elementary act of viscous flow is the jump from one minimum to another available one. Certainly, the jumps take place over various barriers. The coefficients corresponding to these jumps also differ from one another. We introduce the concept of an averaged jump. As the first approximation, we suppose that the transition coefficient for this jump D^* is equal to all other D 's. Hence, taking into account that the number of minima available at temperature T is equal to $\exp(S^c(T))$ we obtain

$$\eta \sim [D^* \exp(S^c(T))]^I \quad (9)$$

The dependence of the transition coefficient $D^*(E)$ on energy E measured from the top of barrier is as follows [14]:

$$D^*(E) = [1 + \exp(-\delta E)]^{-1}, \quad \delta > 0 \quad (10)$$

The temperature dependence of internal energy E of the discussed fragment is well approximated by the following relation

$$E(T) \approx C(T - \xi T_g), \quad C > 0, \quad \xi > 1 \quad (11)$$

where ξT_g is the temperature when the energy $E(\xi T_g)$ of the fragment becomes equal to the energy corresponding to the top of the barrier (see fig.3). Within the framework of the above assumptions and after some transformations of relations (7,9-11) are made, equation (12) follows:

$$\lg \eta(T) = \lg \eta(T_g) + \left[\ln \left(\frac{1 + \exp(d(\xi - \frac{T}{T_g}))}{1 + \exp(d(\xi - 1))} \right) - g \left(1 - \left(\frac{T}{T_g} \right)^2 \right) \right] / \ln 10 \quad (12)$$

where $d = \delta C T_g \quad (13)$

$g = \alpha_n m \quad (14)$

Equation (12) approximates well the experimental data on $\lg \eta(T)$ for temperatures $T \geq T_g$. For example, for As_2Se_3 equation (12) approximates the experimental data with the deviation 0.1 with the following set of fitting parameters: $d=31.0$, $\xi=1.2$, and $g=30.2$. Extrapolation of the $\lg \eta(T)$ dependence calculated with equation (12) to high temperatures gives the value $\lg \eta(\infty) = -3.1$. Note that this value agrees with the data in Table 1. For As_2Se_3 the parameter α_n is equal to 1.3 [12]. The average number of atoms in the fragment of the elementary atom rearrangement which provides for the viscous flow can be calculated from equation (14). This number m is 23 for liquid As_2Se_3 . To estimate the number m one can use also the following expression (which results from the model approach proposed in [12])

$$m \approx 2g/\Delta c \quad (15)$$

where Δc is the jump of heat capacity at glass transition per one atom.

CONCLUSION

The calculation of temperature dependence of the temperature coefficient of fictive temperature within the framework of Moynihan's approach is modified, which results in the decrease of the number of fitting parameters.

The model of viscous flow for glass-forming liquids is set forth.

ACKNOWLEDGEMENTS

This work was supported by Russian Foundation for Basic Research grant No 98-03-32114a and Competitive Centre for Basic Natural Science of the St.Petersburg State University grant No 97-92.-66.

REFERENCES

1. S.V.Nemilov, G.T.Petrovskii, Zh. Prikl. Khim. (Leningrad), 36 (5) (1963) 977.
2. H.Rowson, Inorganic glass-forming systems, Academic Press, N.Y., 1967.
3. H.M.Halilov, Izv. Acad. Sci. Az.SSR, Ser. fiz.-mat. i tekhn. nauk, (6) (1959) 67.
4. S.Dobinski, J.Wesolowski, J.-Bull. Acad. Polon. Sci., (1-2A) (1937) 7.
5. A.Kadoun, G.Chanssemy, J.Fornasero, J.of Non-Cryst. Solids, 57 (1) (1983) 101.
6. V.M.Glazov, O.D.Shchelikov, Izv.Acad. Sci. USSR, Neorganicheskie Materialy, 10 (2) (1974) 202.
7. R.Ewell, H.Eyring J.Chem.Phys., 5 (1937) 726.

8. M.A.DeBolt, A.J.Easteal,P.B.Macedo, C.T.Moynihan, J.of Amer.Cer.Soc., 59 (1-2) (1976) 16.
9. A.Tverjanovich, Vagizova, J.of Non-Cryst. Solids, to be published.
10. E.V.Shkol'nikov, Stekloobraznoe sostoyanie (Glass State), Leningrad, Nayka, (1983) 131.
11. S.V.Nemilov, Fiz. Khim. Stekla, 4 (2) (1978) 129.
12. M.D.Bal'makov, Stekloobraznoe sostoyanie veshchestva (Glass state matter), St.Petersburg, St.P.St.Un., 1996.
13. M.D.Bal'makov, Glass Phys. and Chem., 22 (4) (1996) 344.
14. L.D.Landau, E.M.Lifshits, Kvantovaya mekhanika (Quantum mechanics), M. Fizmatgiz, 1963.

GLASS TRANSFORMATION, HEAT CAPACITY AND STRUCTURE OF $\text{Ag}_x(\text{As}_{0.4}\text{Se}_{0.6})_{100-x}$ GLASSES STUDIED BY TEMPERATURE MODULATED DIFFERENTIAL SCANNING CALORIMETRY (MDSC) EXPERIMENTS.

T. Wagner¹, M. Frumar¹ and S. O. Kasap²

1. Department of General of General and Inorganic Chemistry, University of Pardubice, Pardubice 532 10, Czech Republic. e-mail:tomas.wagner@upce.cz

2. Department of Electrical Engineering, University of Saskatchewan, Saskatoon S7N 5A9, Canada.

ABSTRACT

The recent novel temperature-modulated DSC (MDSC™ TA Instruments) technique has been applied to the measurement of the thermal properties of chalcogenide glasses of the $\text{Ag}_x(\text{As}_{0.4}\text{Se}_{0.6})_{100-x}$ systems in the glass transition. All samples in this work were exposed to the same temperature-modulated heating and cooling schedules with the average heating and cooling rate of 5 °C/min. The total heat flow (HF), modulated heat flow (MHF), reversing heat flow (RHF) and non-reversing heat flow (NHF) during heating schedules were measured. The values of the parameters T_g , ΔH , C_p and ΔC_p , which characterize the thermal events in the glass transition region, were also determined. The ability of determining the reversible heat flow (over the time scale of the experiment) in MDSC enables an accurate measurement of the true heat capacity (that normally associated with reversible heat flow), which could not be done hitherto in conventional thermal analysis where the detected heat flow is the total heat flow, sum of reversing and non-reversing heat flows. No such thermal analysis has been done in the Ag-containing chalcogenide glasses previously.

1. INTRODUCTION

Glasses in ternary systems Ag-As-X and Ag-Ge-X, where X is chalcogen (S, Se), are of considerable interest as infrared-transmitting and optical-recording materials [1]. The optimum compositions in terms of glass-forming ability, ease of fabrication, high softening temperature, and strength are of considerable interest. MDSC as a new experimental method has been described in more detail in the original papers [2-6] together with the results of measurements of various thermal events. The MDSC operates essentially in the same way as a typical heat flux DSC [7], but with an option that allows the sample temperature to be modulated sinusoidally about a constant ramp i. e. the temperature, T , at time t is given by

$$T = T_0 + rt + A \sin\left(\frac{2\pi t}{P}\right) \quad (1)$$

where T_0 is the initial (or starting) temperature, r is the heating rate (which may also be a cooling ramp, q), A is the amplitude of the modulation and P is the period. The resulting instantaneous heating rate, dT/dt , therefore varies sinusoidally about the average heating rate r . The apparatus measures the amplitude of the instantaneous heat flow and the average heat flow, called the total heat flow and then by carrying out a suitable Fourier deconvolution of the measured quantities (also incorporating the sinusoidal temperature signal) it determines two quantities: reversing heat flow (RHF) and nonreversing heat flow (NHF). The reader is referred to recent articles [8, 9] on the interpretation of MDSC and its application to various materials.

In an effort to elucidate the structure of these potentially important materials, T_g , ΔH , C_p

and ΔC_p , in the ternary $\text{Ag}_x(\text{As}_{0.4}\text{Se}_{0.6})_{100-x}$ system were studied. Ag-As-Se system forms glasses in two glass forming regions, with low and rather high silver content, respectively, separated by a non-miscibility region [10]. The compositions of all the studied glasses are placed on a composition span joining the pure components, $\text{As}_{40}\text{Se}_{60}$ and Ag in the ternary diagram, passing through glass-forming regions and immiscibility regions, as it is shown in Fig.1.

In the recent papers we were able to show the usefulness of the MDSC technique in correlating the thermal properties obtained from RHF and NHF to the structure of the chalcogenide glasses [11-13].

2. EXPERIMENTAL

The glasses of the ternary systems $\text{Ag}_x(\text{As}_{0.4}\text{Se}_{0.6})_{100-x}$, where $x = 0 - 42.5$ at.%, were prepared from pure elements. The elements Ag, As, Se of the purity 5N were weighed in a pre-cleaned and outgassed (heating under vacuum to 900 °C) quartz ampoules. Thus the ampoules were evacuated to a pressure of 1.10^{-3} Pa for 30 minutes and sealed. The synthesis was performed in the rocking furnace and exposed to the temperature 1000 °C for 8 hours. Following heating, the ampoules with glass melt were quenched in water to temperature 273 K.

The bulk samples were crushed into small pieces and immediately weighed into aluminum crimped pans and then sealed. A typical bulk and film sample weights were 20 mg and 18 mg, respectively. The MDSC experiments were carried as described previously [12]. Initially, the same thermal history was set up for all samples in the non-modulated regime. Thus modulated regime was applied to measure the modulated heat flow in heating and cooling schedules in the temperature region 20 - 250 °C. For the present experiments r or $q = 5$ °C/min, $A = \pm 1.061$ °C and $P = 80$ sec, in eqn.(1). The specific heat capacity C_p was calculated from the RHF. T_g and ΔC_p were determined from the step transition of heat capacity in the glass transition region. The quantity ΔH refers to enthalpy observed in the NHF observed in the glass transition region [14]. For each composition we carried out several experiments and all showed good reproducibility. The experimental points represent average values with typical errors bars comparable with the size of the plotted experimental point.

3. RESULTS

Figure 2 compares conventional DSC heat flow results for $\text{Ag}_x(\text{As}_{0.4}\text{Se}_{0.6})_{100-x}$ glasses in temperature region 30-450°C, where are also denoted important thermal events (e.g. glass transformation, crystallization and melting regions). Heat flow curves, in fig. 2, prove that all samples are glasses, apart of composition ($x=42.5$ at.% Ag), where the melting endotherm doesn't reflect crystallization exotherm in amount of the involved heat.

In our MDSC studies, we have focused our attention to glass transformation region and typical MDSC heating scan can be seen in Figure 3.

Figure 4 shows the dependence of the glass transition temperature, T_g , on the composition of bulk $\text{Ag}_x(\text{As}_{0.4}\text{Se}_{0.6})_{100-x}$ glasses. The T_g value at first decreases with increasing Ag concentration up to $x \approx 10$ at.% Ag and than staying almost constant and slightly increasing up to $x \approx 30$ at.% Ag.

Figure 4 also shows the compositional dependence of the relaxation enthalpy ΔH for $\text{Ag}_x(\text{As}_{0.4}\text{Se}_{0.6})_{100-x}$ glasses during glass transition. The composition dependence of relaxation enthalpies ΔH_h , ΔH_c and ΔH on the composition has a behavior similar to that of T_g . The ΔH_h was found by integrating the non-reversing heat flow (NHF) in heating scans as shown in Figures 3 and analogously ΔH_c value was established from cooling scan. If the ultimate interest is constructing a correlation curve for comparing the area of the relaxation endotherm with other "end-use" properties, then the error in non-reversing heat flow curve can be ignored because the same modulation period is used. To obtain an absolute measure of the heat of relaxation ΔH , we have to subtract the relaxation enthalpy (ΔH_c) obtained during the cooling scan from the relaxation enthalpy (ΔH_h) obtained during the heating scan as demonstrated for polyethylene [14]. The compositional dependence of ΔH ($\Delta H = \Delta H_h - \Delta H_c$) has a behavior similar to that of the glass transition temperature.

The specific heat capacities (C_p) were measured by MDSC in both heating and cooling scans in the temperature region $T = 20-250^\circ\text{C}$. The C_p dependence on the composition of the $\text{Ag}_x(\text{As}_{0.4}\text{Se}_{0.6})_{100-x}$ glasses at $T_f = 0.9T_g$ and $T_f = 50^\circ\text{C}$ is plotted in Figure 5. The C_p vs. composition plots in Figure 5, reveal an decrease of C_p with increasing content of Ag.

The specific heat capacity difference (ΔC_p) was determined for all the $\text{Ag}_x(\text{As}_{0.4}\text{Se}_{0.6})_{100-x}$ glass compositions and are plotted as a function of composition in Figure 5. The ΔC_p values, at first, decrease monotonically with increasing content of Ag in the glasses, and then change only a little.

4. DISCUSSION

There are a few models which can offer an explanation of the observed features in the compositional dependence of the various physical properties of network glasses. The notion that covalent bonding in glasses may be optimized when the average coordination number ($\langle r \rangle$) is 2.4 was advanced by Phillips [15] and As_2Se_3 glass is just a model structure as discussed also in our previous paper [12]. The IR and Raman spectroscopy results provide the additional information that the glass contains $\text{AsSe}_{3/2}$ pyramidal units [16]. This result was confirmed by numerous EXAFS (X-ray absorption fine structure spectroscopy) studies, e.g. [17]. Mastelaro [17] has also studied structure of As_2Se_3 modified by presence of Ag. He has clearly shown that arsenic atom is coordinated by three selenium atoms whatever the silver composition. Silver cation plays the role of the structure modifier. The addition of Ag in the binary As-Se matrix is possible by cutting the Se-As-Se chains or opening the As-Se-As rings. According to EXAFS studies [17, 18], the selenium atoms still remain two-coordinated with the addition of a small silver content, although selenium atoms become three-coordinated for enriched silver glasses. Also silver could be onefold, twofold or threefold coordinated with its increasing content in glass network. At first silver ions could work as a network depolymerizator and T_g and other structure sensitive parameters ΔH , C_p , ΔC_p are decreasing ($x \approx 1\text{at.\%Ag}$). Further addition of silver leads to a higher coordination in overall network (threefold coordinated Se and Ag atoms) and the T_g slightly increases up to $x \approx 30\text{at.\%Ag}$. Other structural sensitive parameters are not substantially influenced or slightly decrease their values.

Acknowledgments

The authors thanks NSERC (Canada) and grants 203/96/0876 and 203/98/0103 of the Grant Agency of Czech Republic for providing financial support for this project. One of the authors (T.W.) thanks NATO for an international research fellowship tenured between 1995-1997 at the University of Saskatchewan in Canada.

References

- [1] P. J. S. Ewen and A. E. Owen, In High-Performance Glasses, (Blackie Glasgow and London, 1992), Chap.14, pp.287-337 and references therein.
- [2] M. Reading, TRIP, 1 (1993) 248.
- [3] M. Reading, D. Elliott and V.L. Hill, Journal of Thermal Analysis, 40 (1993) 949.
- [4] M. Reading, A. Luget and R. Wilson, Thermochimica Acta, 238 (1994) 295.
- [5] B. Wunderlich, Y. Jin and A. Boller, Thermochimica Acta, 238 (1994) 277.
- [6] S. Sauerbrunn and L. Thomas, American Laboratory, January (1995) 19.
- [7] P. S. Gill, S. R. Sauerbrunn and M. Reading, Journal of Thermal Analysis, 40 (1993) 931.
- [8] L. Thomas, NATAS Notes (North American Thermal Analysis Society, Sacramento, CA, USA) 26 (1995) 48.
- [9] B. Hassel, NATAS Notes (North American Thermal Analysis Society, USA), 26 (1995) 54.
- [10] Z. U. Borisova, Glassy semiconductors, (Plenum Press, New York, 1981) Ch.1.
- [11] S. O. Kasap, T. Wagner and K. Maeda, Jpn. J. Appl. Phys., 35 (1996) L 1116.
- [12] T. Wagner and S. O. Kasap, Philos. Mag. B, 74 (1996) 667.
- [13] T. Wagner, S. O. Kasap and K. Maeda, J. Mater. Res., 12 (1997) 1893.
- [14] "Modulated DSC™ Compendium, Basic Theory & Experimental considerations", TA Instruments (TA Instruments Inc., Newcastle, DE, USA, 1996) pp.25-27.
- [15] J. C. Phillips, J. Non-Cryst. Sol., 34 (1979) 153.

- [16] G. Lukovsky and R. Martin, J. Non-Cryst. Solids, 8-10 (1972) 185.
 [17] V. Mastelaro, S. Benazeth and H. Dexpert, J. Non-Cryst. Solids, 185 (1995) 274.
 [18] V. Mastelaro, S. Benazeth, H. Dexpert, A. Ibanez and R. Ollitrault-Fichet, J. Non-Cryst. Solids, 151 (1992) 1.

FIGURES

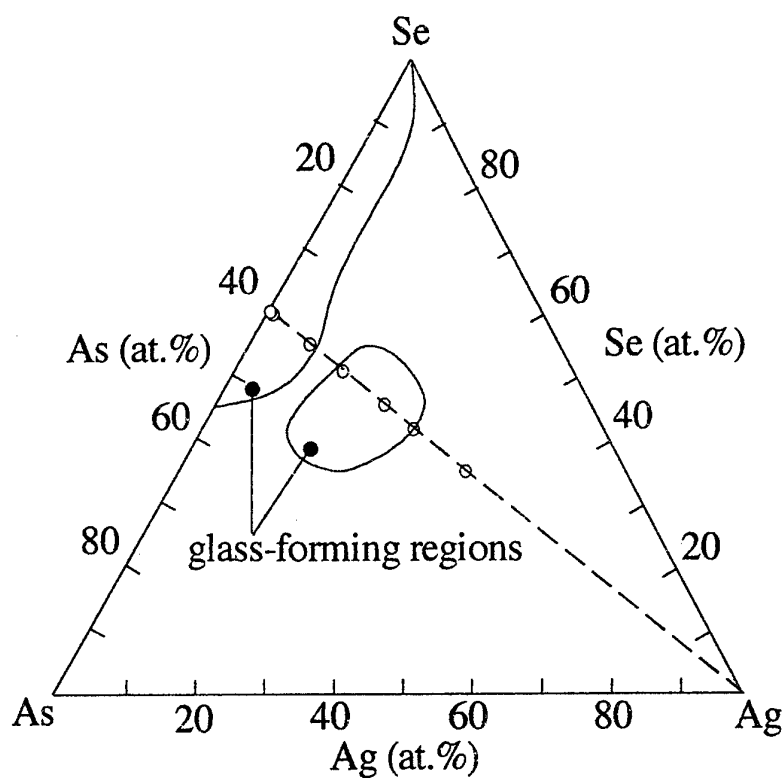


Figure 1.

Simplified phase diagram of Ag-As-Se system showing the glass-formation regions. Symbol (O) denotes composition of the studied samples.

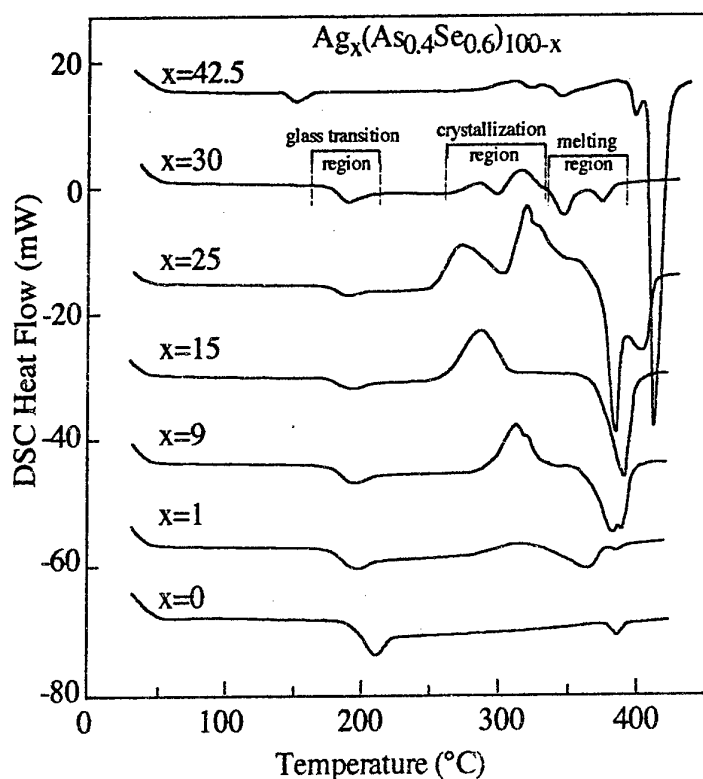


Figure 2.

Typical heating scan in non-modulated DSC regime at a rate $50^{\circ}\text{C min}^{-1}$ for all studied samples of the Ag-As-Se glass system. Sample with $x=42.5$ at. % Ag is a mixture of a crystalline and glassy phase.

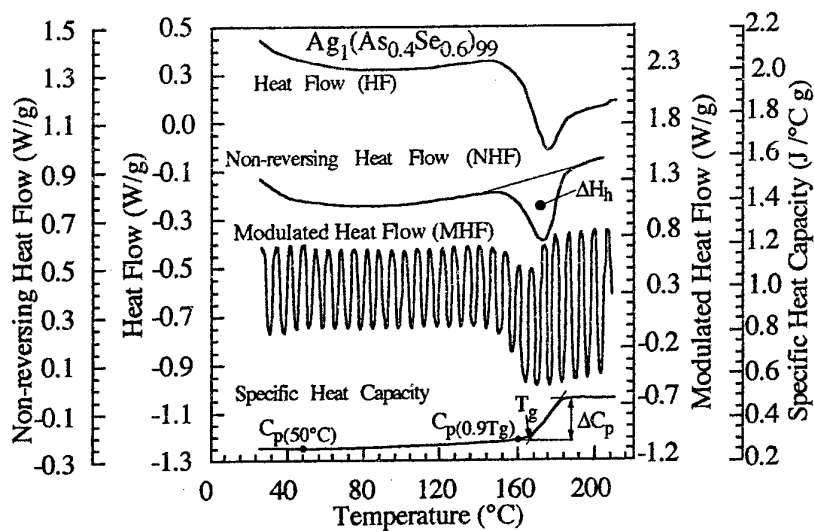


Figure 3.

Typical conventional DSC (HF) and MDSC (MHF, NHF, Heat capacity) results during a heating scan

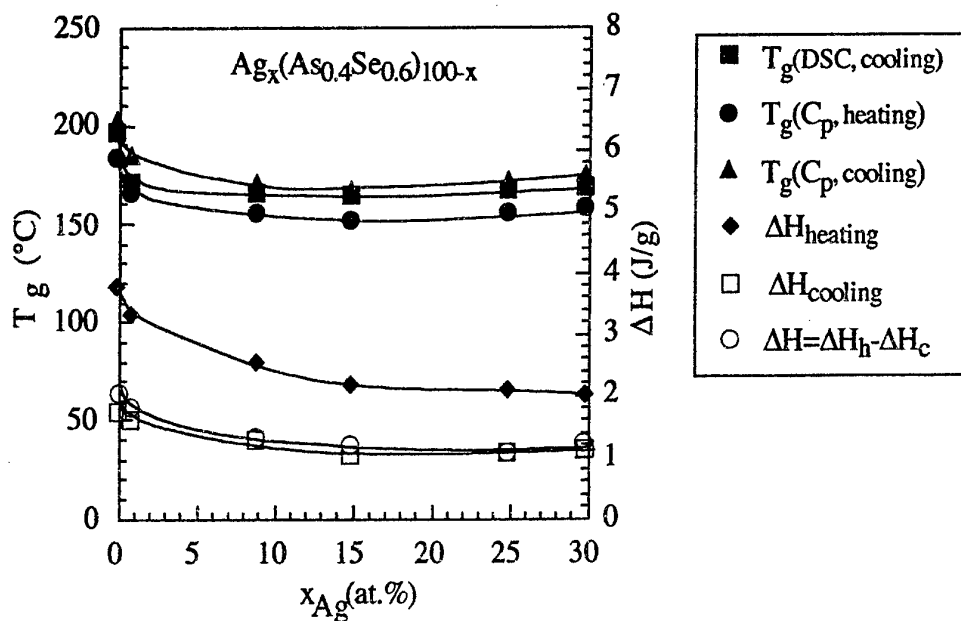


Figure 4

Dependence of the glass transition temperature T_g and relaxation enthalpy ΔH on composition of the Ag-As-Se glass system.

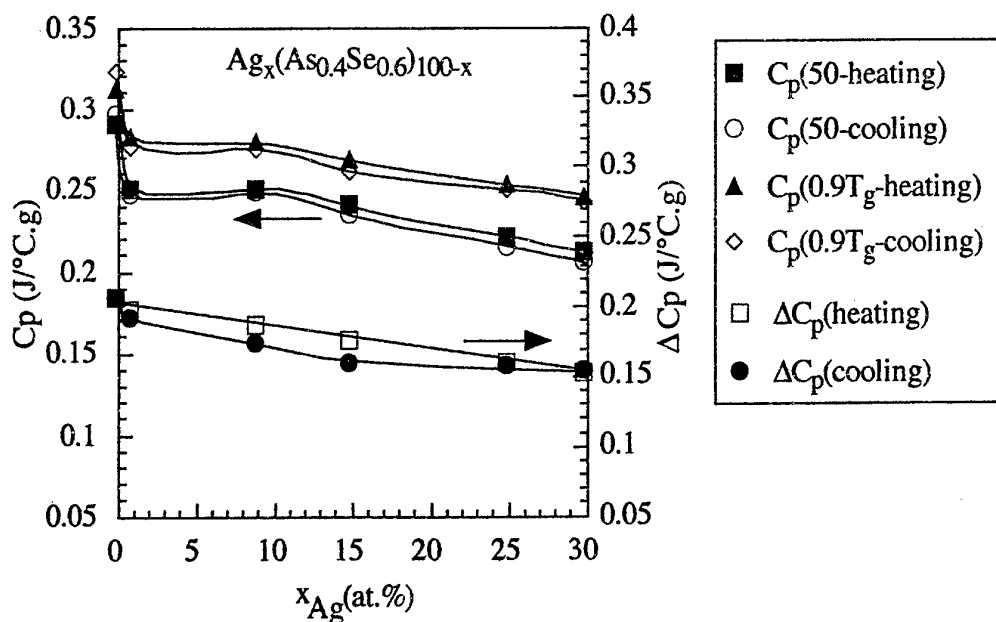


Figure 5.

Dependence of the specific heat capacity and change in specific heat capacity on composition for Ag-As-Se glass system.

Ga-Ge-Sb-Se BASED GLASSES AND INFLUENCE OF ALKALINE HALIDE ADDITION

H.L. Ma, Y. Guimond, X.H. Zhang and J. Lucas

Laboratoire des Verres et Céramiques, Université de Rennes I

Campus de Beaulieu, 35042 Rennes cedex, France. E-mail : ma.hong-li@univ-rennes1.fr

ABSTRACT

The quaternary Ga-Ge-Sb-Se system has been systematically studied and glass-forming region has been determined. It has been found that there is a domain in which glasses do not show any crystallisation when heated with a rate of 10°C/min. Some glass compositions have been selected inside this region for further studies. The stable glasses have a transition temperature of about 280°C.

Optical properties of these glasses have been determined, showing a good transmission from 0.9 μm up to 15 μm . The refractive index measurements have been performed between 2 and 14 μm by using the minimum deviation method. The values for the $\text{Ga}_5\text{Sb}_{10}\text{Ge}_{25}\text{Se}_{60}$ are, for example, 2.6709 at 2 μm and 2.6198 at 12 μm .

Other physical properties have been measured and the Young's module is typically about 24 GPa. Glasses from this system have much lower vapour pressure when heated. As an evidence, they can not be purified by distillation below 1000°C.

As mentioned above, these glasses do not show any visible transparency. Some attempts have been made in order to widen the band-gap by introducing some electronegative elements such as Cl_2 , Br_2 or I_2 in form of alkaline halides. The optical properties and chemical durability of these new glasses have been studied in detail.

Good results have been obtained with CsI and stable red glasses have been synthesised, which are still transparent up to 14 μm .

1. INTRODUCTION

Chalcogenide glasses have been widely studied since many years [1]. However, almost all of them have two common characteristics : high vapour pressure when melted and no visible transparency when the glass is transparent up to 12 – 14 μm .

This study is intent on overcoming partially these two problems.

The most promising and actual applications of chalcogenide glasses are for transmission in the second atmospheric window of 8 – 14 μm [2-3]. Our study will be limited to glasses which are transparent up to this wavelength region.

The well-known glass forming system Ge-Sb-Se [4] has been chosen because of their relatively low vapour pressure compared to the Ge-As-Se [5] system. Ga, which has very low vapour pressure when heated, has been introduced into the ternary system.

Chalcogenide glasses which are transparent up to 12 – 14 μm do not show any visible transparency. This characteristic is one of the problems limiting the use of these glasses, because it makes more complicated the quality control and IR system alignment. Some attempts have been made in order to widen the band-gap by introducing some electronegative elements such as Cl, Br or I in form of alkaline halides.

II. EXPERIMENTAL

Glasses for these experiments are synthesised by using the conventional methods : the appropriate quantities are weighed and introduced into silica ampoule which is then sealed under vacuum. The mixture is heated and homogenised in a rocking furnace at about 800°C for 12 hours. The ampoule is then cooled down in air for they determination of glass-forming region. Samples are annealed, cut and polished if necessary for measurements of different properties.

Samples are considered to be vitreous if they do not diffract the X rays and show a good optical transmission.

Thermal analysis has been performed by using a SETARAM DSC92 and the heating rate was 10°C/minute. Typical sample weight is about 10 mg.

Mechanical properties, especially Young's module, Poisson coefficient are obtained by measuring the ultrasonic propagation in the glass samples.

Optical transmission has been measured with a double beam spectrometer CARY5 in the visible and near IR region, and a Fourier Transform IR spectrometer BOMEM100. Samples are polished discs with a thickness of about 2 mm.

Refractive index has been obtained with the minimum deviation method by using a prism.

III. RESULTS

1. Glass-forming region

The glass-forming region in the Ga-Ge-Sb-Se system has been determined using the techniques described juste before. For visual convenience, the diagram is represented in figure 1 by two ternary systems Ge-Sb-Se with two different percentages of Ga (5% and 10%). It can be clearly seen that the addition of a metallic element, Ga, destabilise quickly the glasses. With more than 15% of Ga, it is hard to obtain glass samples which are big enough for real applications and even for some measurements.

With 5% of Ga, glasses are still stable enough in a relatively big region in which they do not show any crystallisation phenomena when heated with a rate of 10°C/minute (figure 1.a). This allows the preparation of big samples up to, for example, 100 mm in thickness.

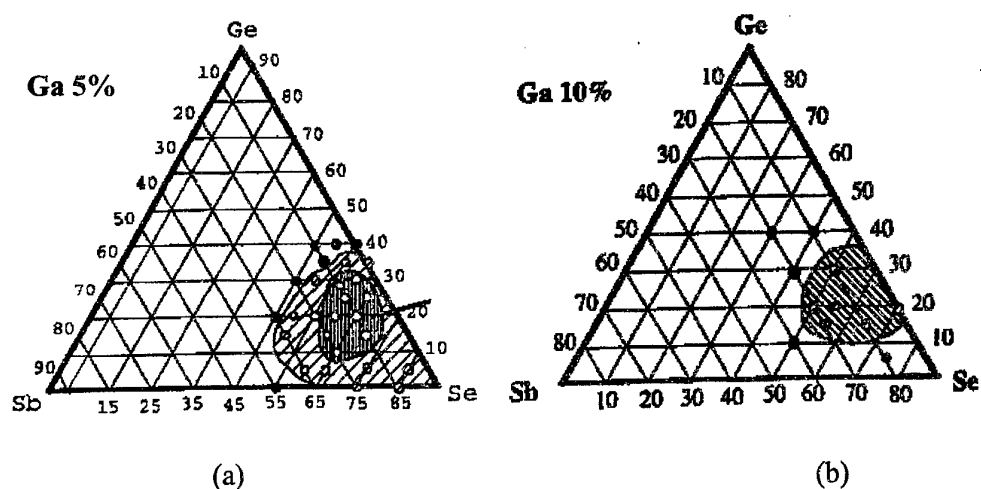


Figure 1. glass – forming region of the Ga-Sb-Ge-Se system

2. Thermal and mechanical properties

The DSC curves are used for the determination of glass transition temperature T_g , crystallisation temperature T_x (the beginning of crystallisation). Table I collects the data of these measurements for different glass compositions.

Table I: Thermal properties of different glasses in the Ga-Sb-Ge-Se system

glass composition (atom%)						
Ga	Sb	Ge	Se	T_g (°C)	T_x (°C)	$T_x - T_g$ (°C)
5	88	25	62	301	461	160
5	7	28	60	288	448	160
5	10	25	60	283	-	-
5	20	15	60	253	-	-
5	25	5	65	186	315	129
7	5	28	60	288	459	171
8	12	25	55	275	387	112
8	10	12	70	186	316	130
10	5	20	65	316	440	124
10	15	15	60	274	383	109

It is interesting to notice that two compositions do not show any crystallisation phenomena during the heating at a rate of 10°C/minute. Consequently, special attentions have been paid to these two glasses.

It is true that the other glasses are less stable, but they still have relatively large difference between the glass transition temperature and the crystallisation temperature. Large pieces of glass with a thickness of several centimetres can still be obtained.

Table II shows the mechanical properties of the $Ga_5Sb_{10}Ge_{25}Se_{60}$ glass. The values are typical for chalcogenide glasses.

Table II: Some properties of the $\text{Ga}_5\text{Sb}_{10}\text{Ge}_{25}\text{Se}_{60}$ glass

Elastic constant	Young's Module	Poisson's constant	Thermal expansion coefficient	Density
9.5 GPa	24 GPa	0.26	$155 \times 10^{-7} \text{K}^{-1}$	4.7 g/cm ³

Table III indicates the influence of CsI addition in the $\text{Ga}_5\text{Sb}_5\text{Ge}_{25}\text{Se}_{65}$ glass on different thermal and optical properties. It is clear that this addition of CsI decreases the glass transition temperature, but increases the thermal stability of this glass. In fact, the difference between T_g and T_x is significantly increased with the introduction of CsI up to 20 wt%.

Table III influence of CsI addition on the glass transition temperature, on the thermal stability of glass and on the band-gap of the $\text{Ga}_5\text{Sb}_5\text{Ge}_{25}\text{Se}_{65}$ glass

Wt% CsI	T_g (°C)	T_x (°C)	$T_x - T_g$ (°C)	Gap (nm)
0	331	483	152	705
5	319	490	171	700
10	316	478	162	680
20	292	460	168	665
30	271	395	124	660

3. Optical properties

Chalcogenide glasses are of particular interest especially because of the wide IR transmission. The spectrum for the $\text{Ga}_5\text{Sb}_{10}\text{Ge}_{25}\text{Se}_{60}$ glass is shown in figure 2, obtained with a thickness of 2 mm. The multiphonon absorption located in the long wavelength region is not sensitive

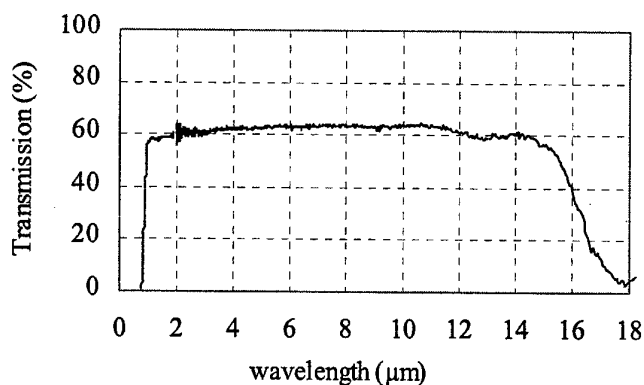


Figure 2. Transmission spectrum of the $\text{Ga}_5\text{Sb}_{10}\text{Ge}_{25}\text{Se}_{60}$ glass (thickness : 2 mm)

to the glass composition. The band-gap absorption located in the short wavelength region, is however largely influenced by the glass composition.

No glass in the Ga-Sb-Ge-Se system shows visible transparency and all glasses have a good transmission up to 14-15 μm region.

Figure 3 shows the influence of CsI addition in the $\text{Ga}_5\text{Sb}_{10}\text{Ge}_{25}\text{Se}_{60}$ glass. With 10 wt% of CsI, the beginning of transmission changes from about 820 nm to about 750 nm.

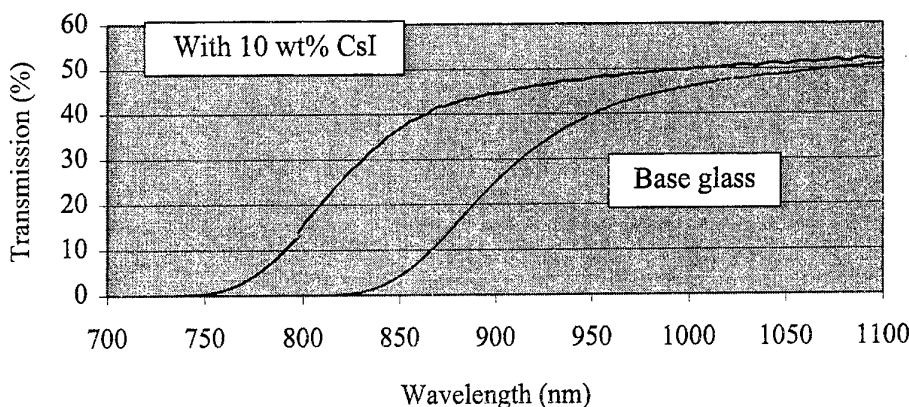


Figure 3. Influence of CsI addition on the band-gap absorption

Table III indicates the change of band-gap absorption of glasses with different percentages of CsI addition. It can be seen that several glasses begin to have significant transmission before 700 nm and their colour is deeply red.

The refractive index measurements have been performed between 2 and 14 μm by using the minimum deviation method. The values for the $\text{Ga}_5\text{Sb}_{10}\text{Ge}_{25}\text{Se}_{60}$ are, for example, 2.6709 at 2 μm and 2.6198 at 12 μm .

4. Chemical durability

All studied glasses are stable in normal air condition. No significant change is observed on the IR transmission spectra between freshly prepared glasses and after several months in air. Ga-Sb-Ge-Se glasses show good resistance even in hot water of 60°C for several hours.

Glasses containing alkali halides seem to be less stable and they are quickly corroded in hot water with appearance of absorption peaks at 2.9 μm and 6.2 μm due to respectively the presence of O-H and H_2O .

IV. Discussion

It is relatively difficult to perform measurements of vapour pressure of melted chalcogenide glass. There is no data concerning the influence of Ga addition in the Ge-Sb-Se glass on the vapour pressure. However, during the fabrication and shaping process (fibre drawing for example), observation shows that glasses containing Ga are less volatile. As a result, these glasses can not be purified by distillation even when heated up to 1000°C.

It has been demonstrated that large quantity of ionic compound such as CsCl, CsI can be dissolved in the covalent chalcogenide glasses to form a homogenous material with interesting properties. Thanks to the electronegative character of halogen which tends to widen the band-gap, chalcogenide glasses in the Ga-Sb-Ge-Se system can even show visible transmission if appropriate quantity of CsI is introduced. This should facilitate the application of chalcogenide glasses.

However, alkali introduction into the chalcogenide glasses generally induces poor thermal and mechanical properties. For example, the glass transition temperature and the microhardness of glasses are significantly decreased when the content of alkali halide increases. At the same time, the thermal expansion coefficient is also increased. Compromise should be found for applications.

Chalcogenide glasses containing halogens, which are called chalcohalide glasses, have been greatly studied [6-8]. In those cases, halogens are usually introduced in form of pure elements (Cl, Br or I). These glasses do not contain any alkali halide.

V. CONCLUSION

Glasses in the Ga-Sb-Ge-Se system have been systematically explored and very stable glasses have been found. Thermal, mechanical and optical properties have been measured for some glasses. These glasses have good IR transmission in the region of 0.8 μm – 15 μm . Some glasses do not show any crystallisation phenomena when heated with a rate of 10°C/minute.

Chemical durability studies indicate that these glasses are very stable in normal air conditions and even in hot water during several hours.

Introduction of alkali halide, especially CsI, into these glasses increase the width of band-gap, shifting the transmission region towards the visible region. Stable glasses with a deep red colour have been obtained and studied.

REFERENCES

- [1] J.A. Savage, Infrared Optical Materials and their antireflection coatings, Adam Hilger, Bristol, (1985).
- [2] J. Nishii, T. Yamashita and T. Yamagishi, Applied Optics, Vol.28, N°23 (1989) 5122.
- [3] M.F. Churbanov, J. Non-Cryst. Solids, 184 (1995) 25.
- [4] A.R. Hilton, C.E. Jones and M. Brau, Phys. Chem. Glasses, 7 (1966) 105.
- [5] B.T. Kolomiets Phys. Status Solidi, 7 (1964) 359.
- [6] T.E. Hopkins, R.A. Pasternak, E.S. Gould and J.R. Herndon, J. Phys. Chem., 66 (1962) 733.
- [7] J. Lucas, X.H. Zhang, J. Non-Cryst. Solids, 125 (1990) 1.
- [8] J.S. Sanghera, J. Heo and J.D. Mackenzie, J. Non-Cryst. Solids, 103 (1988) 155.

GLASS CERAMICS FOR OPTICAL AMPLIFIERS: RHEOLOGICAL, THERMAL AND OPTICAL PROPERTIES

M. Braglia, C. Bruschi, G. Dai, J. Kraus, S. Mosso,
CSELT Via Reiss Romoli 274 Turin ITALY.

M. Baricco, L. Battezzati, F. Rossi
Dip. Chimica IFM Università degli Studi di Torino/Unità INFM Torino ITALY
e-mail: marco.braglia@cse.lt.it

ABSTRACT

A glass ceramic system based on $\text{SiO}_2\text{-Al}_2\text{O}_3\text{-CdF}_2\text{-ZnF}_2\text{-YF}_3\text{-PbF}_2$ (TGC) doped with 500 ppmw of PrF_3 has been prepared and characterised in terms of structural, thermal, optical and rheological properties in order to verify a possible application in optical fibre amplifiers operating at 1.3 μm .

INTRODUCTION

There has been a recent, increasing interest in low phonon energy glasses containing rare earth elements. Great efforts have been devoted to this field in order to achieve a high efficiency in active optical fibre devices. One of these approaches is to develop novel glass hosts having low phonon energy for the amplification at 1.3 μm wavelength in telecommunication system. Fluorindate and chalcogenide glasses, for example, are considered as promising candidates for Pr^{3+} doped glass fibre amplifiers [1-2]. Another approach involves controlled ceramming of a rare earth doped glass. After ceramming, rare earth elements are preferentially coordinated with the low phonon energy phase therefore their active optical properties can be largely optimised.

In these years, several glass ceramic systems were reported for the applications in upconversion and amplification [3-5]. Wang and Ohwaki reported on properties of glass ceramics based on an aluminosilicate glass containing PbF_2 , CdF_2 and $\text{YbF}_3/\text{ErF}_3$ [4]. The green upconversion from this ceramic was found 10 times higher than that of fluoride glasses equally doped. The high upconversion efficiency was attributed to Er^{3+} enriched $\text{Pb}_x\text{Cd}_{1-x}\text{F}_2$ nanocrystals. Following up Wang and Ohwaki's work, Tick et al. [5] substituted Y^{3+} for Yb^{3+} and Pr^{3+} for Er^{3+} in the glass and exploited the two-phase system for Pr^{3+} doped amplifier applications. Pr^{3+} fluorescence lifetime at 1.3 μm was found to be longer in this glass ceramic than in a fluorozirconate glass.

In this report, we will consider some important aspects of the Pr^{3+} doped glass ceramic developed by Tick. Thermal, optical and rheological properties will be reported for this material in both glass and cerammed forms in order to assess the feasibility of fibre fabrication for 1.3 μm amplifiers.

EXPERIMENTAL PART

Several glasses were prepared in an induction furnace with Merck products 99% purity (see Table 1 for nominal composition). 20 g batches were melted in a platinum crucible at 1000°C for 30 minutes under N_2 and O_2/N_2 (20:80) atmosphere. The melt was then poured into a brass mould. Data will be reported here for two samples (named TGC A and TGC B): the former was poured in to the mould kept at room temperature whereas the latter was poured into the mould preheated at 350°C and annealed for 1 hour at the same

temperature for stress relief. Both materials were fully transparent. The glass composition was then determined by emission spectroscopy ICP (Optima 3000 P.E.) (Table 1).

Table 1 : Nominal composition of the glass and ICP analysis results.

Components	Nominal composition (mol %)	TGC A	TGC B
SiO ₂	32.4	21.0 ± 0.2	22.5 ± 0.3
Al ₂ O ₃	8.1	8.8 ± 0.2	8.7 ± 0.2
CdF ₂	31.4	38.1 ± 0.4	38.6 ± 0.1
PbF ₂	18.4	21.4 ± 0.3	18.9 ± 0.2
YF ₃	4.3	5.2 ± 0.1	5.5 ± 0.1
ZnF ₂	5.4	5.5 ± 0.1	5.8 ± 0.1
PiF ₃	500 ppmw	Not analysed	Not analysed

The loss of SiO₂ is manifestly due to the formation of volatile compounds such as SiF₄ during the synthesis implying difficulties in reproducibility of composition.

The thermal properties were measured by DSC-7 P.E. and DSC-2920 TA calorimeters. Crystallisation was studied with X-ray diffractometry (XRD) Philips PW 1830 and transmission electron microscopy (JEM 2000 EX). Fluorescence spectra were recorded with a PL Scantek in the wavelength range from 1100 nm to 1600 nm using a diode laser source emitting at 1018 nm. Infrared spectra were collected with FTIR 1760X P.E. Rheological properties were investigated with a parallel plate dynamic analyzer rheometer RDA II Rheometrics.

RESULTS AND DISCUSSION

X-ray Analysis

The x ray diffraction patterns of samples A and B are reported in figure 1.

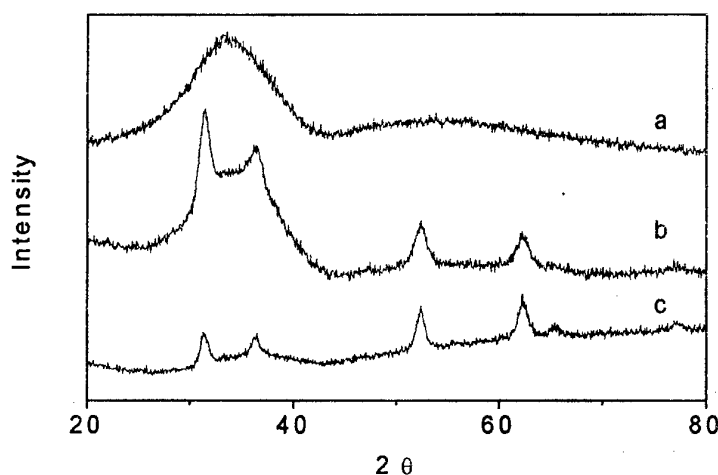


Figure 1: X-ray diffraction patterns of a) sample A, b) sample B, c) sample A annealed at 440 °C for 50 min.

Sample (A) is fully amorphous whereas sample (B) contains reflections that can be attributed to the Pb_xCd_{1-x}F₂ crystalline phase having fcc cubic symmetry, already identified by Tick [5]. The reflections are broad indicating a small size of the crystals.

XRD patterns of sample A heated at different temperatures between 420-550°C for different times display broad reflections due to the same phase. A Scherrer analysis was applied to determine the size of the crystals [6]. At 440 °C annealing for of 10 min, 50 min and 200 min resulted in sizes of 8 ± 2 nm, 12 ± 2 nm, 14 ± 3 nm respectively. Isochronal annealing of 100 min at 420 °C and 470 °C resulted in sizes of 8 ± 3 nm and 27 ± 4 nm respectively. For the as-prepared sample B, the crystal size is 8 ± 1 nm. After heating up to 420 °C, 470 °C and 550 °C it became 32 ± 4 nm, 31 ± 3 nm and 54 ± 5 nm, respectively. Isochronal and isothermal anneals show that the nuclei form rather quickly reaching a size of about ten nanometers, then growth slows down, e.g. at 440 °C, and after annealing for more than three hours the dimensions are still very limited. Even at higher temperature, e. g. 470 °C, coarsening of the crystals is slow, in fact a size of the order of thirty nanometers is reached for annealing as long as 100 minutes. The data obtained with sample B, which already contained nanocrystals, confirm this behaviour since a size of thirty nanometers was achieved for annealing in the range from 420 °C to 470 °C. Only at higher temperature, 550 °C, larger crystals are found.

TEM observations of these materials are difficult since they tend to decompose quickly under the beam. However, once crystallization has proceeded, the alumino-silicate matrix protects the embedded particles for times long enough to carry out microstructural analyses. Fig. 2 shows an image of sample B heated up to 550 °C. Most crystals are still well below the size obtained with the Scherrer analysis of XRD patterns to which a few larger particles contribute their scattered intensity. In summary, the two-phase state appears stable in a wide temperature range and for times long enough to devise processing of the material.

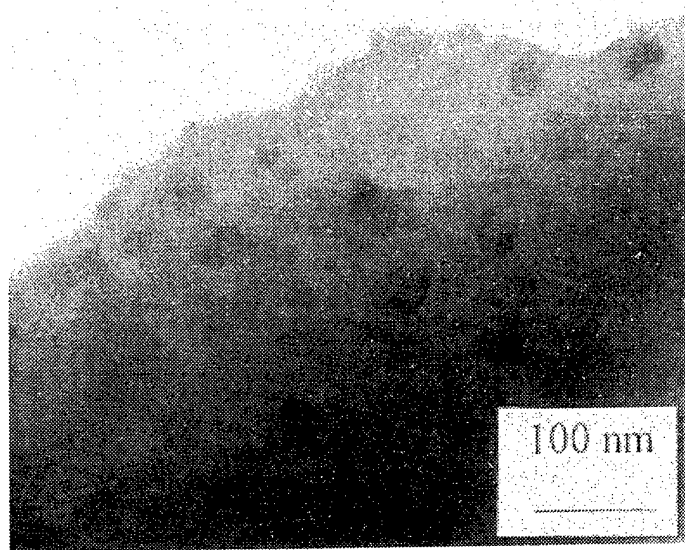


Figure 2: TEM micrograph of sample B heated up to 550 °C

DSC measurements

The glass transition temperature at 408 °C and the crystallisation onset at 457 °C were obtained for sample A by DSC using a heating rate of 10 °C/min under nitrogen flow (Fig.3).

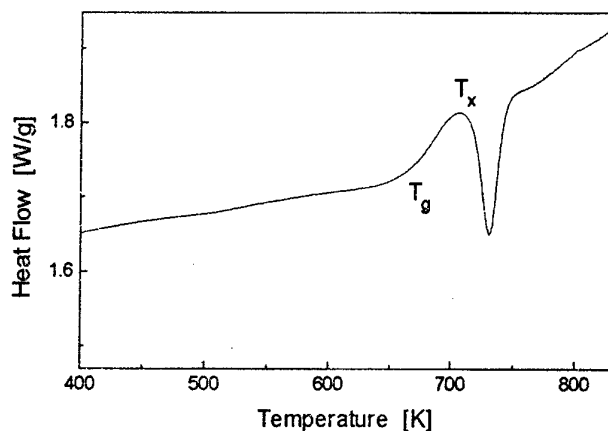


Figure 3: DSC trace of the sample A with a heating rate of 10 K/min

The crystallisation process was studied using 8 different heating rates (from 10 to 80 °C/min). An activation energy of 171 kJ/mol was calculated by Kissinger [7] method. These data guided the choice of temperatures and times for obtaining a controlled transformation to the two-phase state described in the previous section. The DSC trace of sample B has no exothermic signal but only an inflection around 450 °C.

Photoluminescence measurements

Figure 3 shows the photoluminescence spectra of sample B (already containing nanocrystals after the quench) and a ZBLAN glass doped with 500 ppmw of Pr. In order to compare them the two spectra were normalised to the same maximum intensity. Due to a shoulder at longer wavelength, sample B exceeded ZBLAN in fluorescence bandwidth.

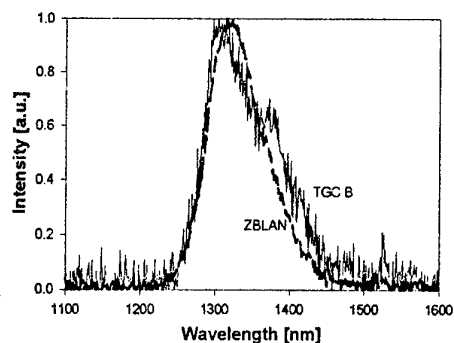


Figure 3: Fluorescence spectra of the sample B and ZBLAN glasses doped with 500 ppmw of Pr^{3+} .

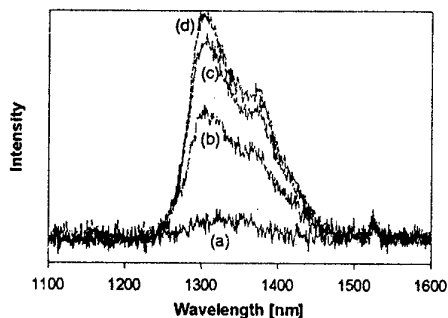


Figure 4: Photoluminescence spectra of amorphous a) and partially crystallised TGC A after annealing at 440 °C for 10 min b), 40 min c) and 200 min d) respectively.

In Fig. 4, the fluorescence spectra of sample A before and after ceramming at 440°C for different times are shown. Compared to the amorphous sample, the fluorescence intensity of cerramed samples was found to be six times higher after 10 min and ten times after 200 min at 440°C. Hence the photoluminescence intensity increased as the quantity of the nanocrystalline phase increased. This is an indication that the surroundings of Pr^{3+} ions are changed by migration into the nanocrystals or at their boundaries.

The IR spectra of samples A and B in Fig. 5 display two absorption bands, one centred around at 910 cm^{-1} and the other centred at 490 cm^{-1} for the cerammed sample and at 520 cm^{-1} for the amorphous sample, respectively. Both bands can be attributed to the aluminosilicate network [8], but oxyfluoride and/or fluoride bonds could also absorb in the in the wavenumbers region from 400 to 600 cm^{-1} as shown by the absorption peak of ZBLAN glasses (Fig.5). Since both CdF_2 and PbF_2 absorb at wavenumbers lower than 400 cm^{-1} , the $\text{Pb}_x\text{Cd}_{1-x}\text{F}_2$ phase is not likely to contribute to the absorption around 500 cm^{-1} .

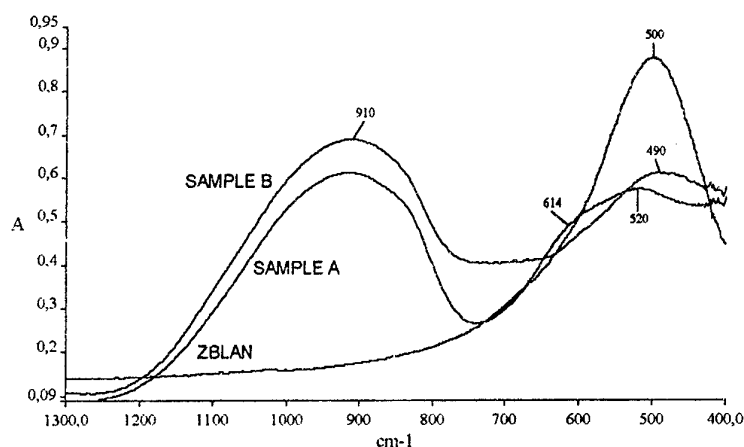


Figure 5: IR spectra of the samples TGC A a) and TGC B b) compared to that of a ZBLAN glass c)

Rheological measurements

In order to determine the range in which the viscosity does not depend on the applied strain, viscosity versus strain measurements were carried out at different temperatures. Sample B was used because it is constituted by the optically active two-phase microstructure. The strain γ is given by:

$$\gamma = \theta \cdot r / h$$

where θ is the rotation angle of the plates, and r (4 mm) and h (2-4 mm) are the radius and the thickness of the sample, respectively. Since the viscosity was constant for small strain values at each temperature, a γ values of 0.5 % was chosen for the following measurements.

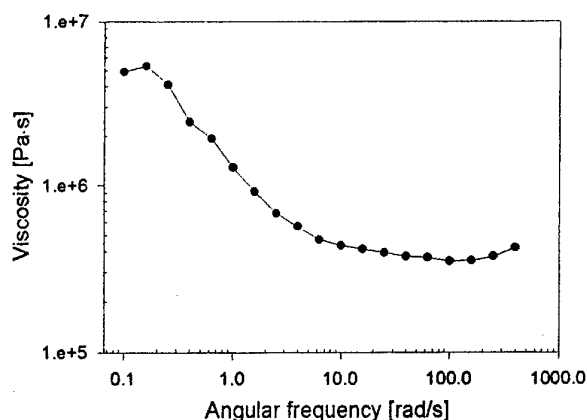


Figure 6: Frequency sweep test on the B sample at $550\text{ }^{\circ}\text{C}$. The line is drawn as guide for the eye.

In Fig. 6, the viscosity is reported as a function of the angular frequency. By increasing the angular frequency the viscosity drops to a fairly constant value in the range from 8 to 100 rad/s. This trend was alike that observed in fluorozirconate glasses [9]. So, a frequency of 10 rad/s was chosen for all measurements.

The measurements were performed on sample B in the temperature range between 480 and 560 °C. The experimental results were fitted with the Cohen-Grest [10] equation and are displayed in Fig. 7. From the fit, it emerges that the temperature range for fibre drawing (10^5 - 10^4 Pa.s) lies between 572 and 614 °C.

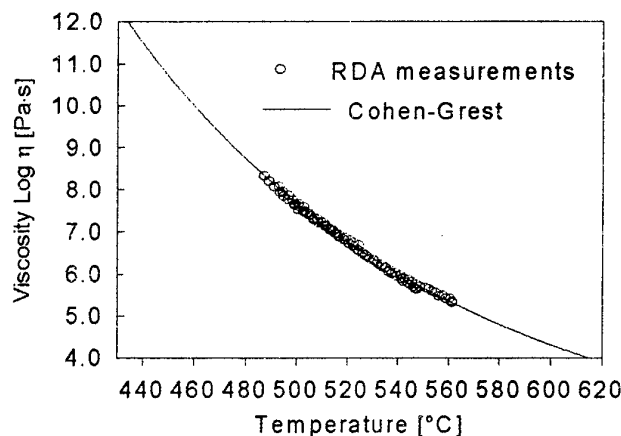


Figure 7: Viscosity measurements performed at 10 rad/s and $\gamma = 0.5$ % on the sample B fitted with the Cohen-Grest equation.

CONCLUSIONS

Glass transparent ceramic can be employed to draw fibres for amplifiers operating at 1.3 μm . A Pr^{3+} fluorescence band wider than that of fluorozirconate glasses has been found. A comparative analysis of vitreous and crystallised samples showed that the transformation to the two-phase active state can be performed in an ample temperature range where the crystal dimensions are kept constant or even during the quench. The drawing process can be performed in the temperature range from 572 to 614 °C.

ACKNOWLEDGMENTS

Work in the area of nanocrystalline materials at "Università di Torino" is supported by CNR-PF MSTA II.

REFERENCES

- [1] Y. Nishida et al. IEEE Phot. Tech. Lett. 9 (1997) 318
- [2] B.G. Aitken, R.S. Quimby.; J. Non-Cryst. Solids 213-214 (1997) 281.
- [3] F. Auzel, K. E. Lipinska-Kalita, P. Santa-Cruz, Opt. Mater. 5 (1996) 75-78
- [4] Y. Wang, J. Ohwaki, Appl. Phys. Lett. 63, (24), (1993) 3268-3270
- [5] P.A. Tick et al. J. Appl. Phys. 78 (1995) 11
- [6] B.D.Cullity, "Elements of X-ray diffraction", 2nd ed., Addison-Wesley Publishing Comp., Reading, MA, 1978, p. 102
- [7] H. E. Kissinger, J. Nat. Bur. Stand.(U.S.) 57 (4), (1956) 217
- [8] J.T. Kohli, R. A. Condrate, Snr & J. E. Shelby, Phy. Chem. Glasses 34 3 (1993) 81-87
- [9] M. Braglia et al. J. Non. Crys. Solids 213-214 (1997) 325-329
- [10] M. H. Cohen, G. S. Grest, Phys. Rev. B 20 (1979) 1077.

FORMATION OF 3-DIMENSIONAL OPTICAL MEMORY INSIDE VARIOUS GLASSES BY USING A FEMTOSECOND PULSED LASER

Jianrong Qiu ^{a,*}, K. Miura ^a, H. Inouye ^a, T. Mitsuyu ^a and K. Hirao ^{a,b}

^aHirao Active Glass Project, ERATO, Keihanna Plaza, Seika-cho, Kyoto 619-0237, Japan

^bDivision of Material Chemistry, Faculty of Engineering, Kyoto University, Sakyo-ku, Kyoto 606-8501, Japan

ABSTRACT

We report on the formation of 3-dimensional optical memory in various glasses by using a focused 800 nm, femtosecond pulsed laser. The glasses are transparent in the wavelengths ranging from 600 to 1000 nm. After the irradiation with the 800 nm tightly focused femtosecond laser, a refractive-index bit was formed in the glasses. The size of refractive-index bit increased with increasing average power of the laser. The threshold value of optical recording in the glasses decreased with an increase in the wavelength corresponding to the optical band gap of the glasses. The size of refractive index bit smaller than 400nm was obtained and a storage density of 10^{12} bit/cm³ can be attained. Writing 3-dimensional refractive-index bit inside the transparent glasses based on a multi-photon absorption process is expected to become a useful method used to fabricate optical memory with both an ultra-high storage density and an ultra-high recording speed.

* To whom all correspondence should be addressed. E-mail address: jrj@hap.jst.go.jp

1. INTRODUCTION

Optical memory using laser as a recording tool is one of the data storage methods which have high storage density. Compact disk is now widely used as a data storage medium. However, the laser beam spot used to record a bit of datum can never be smaller than the diffraction limit given by half of the illumination wavelength, thus the attainable storage density can never exceeds 10^9 bit/cm² if the wavelength of the laser is longer than 400nm [1]. To attain much higher storage density and storage capacity, many novel methods such as photochemical hole burning, holographic and 3-dimensional memory were proposed in the last decade [2-6]. Among these methods, 3-dimensional optical memory based on multiphoton absorption can be recorded and read out at room temperature, and has high storage density larger than 10^{12} bit/cm³. It has received great attentions recently.

Photorefractive crystals and photopolymers were usually used as 3-dimensional recording media [5-6]. However, few studies have been performed on 3-dimensional data storage inside glasses. In this paper, we report on the 3-dimensional optical storage inside transparent glasses by using a focused femtosecond pulsed laser. The mechanism of the formation of refractive index bit after the laser irradiation has also been discussed.

2. EXPERIMENTAL

Glass samples used in the present experiment were synthesized SiO₂ glass (SiO₂(s), supplied by Asahi Glass Co. Ltd., Japan), SiO₂ glass fabricated by VAD method (SiO₂(V)), supplied by Shinetsu Chemistry Co. Ltd., Japan), 53ZrF₄ · 20BaF₂ · 4LaF₃ · 3AlF₃ · 20NaF glass (ZBLAN), Macro slide glass (NCSO(M), supplied by Matsunami Industry Co. Ltd., Japan), White slide glass (NCSO(W), supplied by Takahashi Giken Co. Ltd. Japan), 20Na₂O · 80TeO₂ glass (NTO), 45Bi₂O₃ · 10ZnO · 15BaO · 10CaO · 20Li₂O glass (BiO

) and GeS_4 glass (GeS) (mol%). A regeneratively amplified 800 nm Ti:sapphire laser that emits a 120 fs, 200 kHz, mode-locked pulse was focused through 10-100X microscope objectives and injected inside the samples. By using an XYZ stage, it is possible to control the focused position inside the glasses. To study the structural changes in the glass samples induced by the laser irradiation, we wrote many damage lines inside the sample at room temperature. Then, ESR spectrum measurement was performed at liquid N_2 temperature for the samples before and after laser irradiation. The absorption spectrum was measured using a JASCO-570 spectrophotometer at room temperature.

3. RESULTS

Figure 1 shows the absorption spectra of the glass samples. The glasses are transparent in wavelengths ranging from 600 to 1000 nm. An absorption band peaking at 240 nm was observed in SiO_2 (v) glass. This band was due to the deficit of oxygen in the glass. The wavelength corresponding to the optical band gap of the glass, λ^* , was defined to be the crossing point of the two dotted lines as indicated in Fig. 1 for NTO sample.

When the average power of the laser exceeds a certain value, a refractive index bit which can be a bright or a colored spot in the glass samples after the laser irradiation through the observation of the microscope. If the average power of the laser increases further, microcrack will form in some of the glass samples after the laser irradiation.

Figure 2 (a) and (b) show results of the read out of the data stored inside the NACS (W) slide glass. The average laser power was 80 mW for (a) and 140 mW for (b), respectively. A 20X lens with an NA of 0.46 was used to focus the laser light. The irradiation duration of the laser was 1 s on one dot. The distance between the adjacent dots was 10 μm (a) and 20 μm (b), respectively. The size of dot formed in (a) and (b) was 4 and 10 μm , respectively. The size of the refractive index bit increases with an increase in the average power of the laser.

Figure 3 shows the relationship between the threshold value of optical recording and wavelength corresponding to the optical band gap of the glasses. The threshold value of the optical recording, V^* , is defined as the necessary minimum average power of the laser which can induce visible change in the focal point of the laser after the irradiation of the laser for 30 s. To focus the laser light, the 20X lens with the NA of 0.46 was used. The change usually is the formation of a bright spot. In the cases of NTO, BiO and GeS glasses, the change is the formation of a colored spot which can be observed through the objective microscope. The threshold value decreases with increasing wavelength of the optical band gap of the glass.

Figure 4 show a result of the refractive index bits induced by a single pulse of the femtosecond laser on one dot. A 50X lens with an NA of 0.80 was used to focus the laser light. The size of the refractive index bit was about 400 nm determined by a confocal laser microscope. The diameter of the refractive index bit is half of the wavelength of the laser.

Figure 5 shows the ESR spectrum of the SiO_2 (V) glass after the irradiation of the laser. The average power of the laser was 65 mW. No apparent signal was observed for the unirradiated glass. Therefore, SiE' , peroxy-radicals and non-bridge oxygen hole centers (NBOHC) were induced in the laser irradiated silica glass sample [7].

4. DISCUSSION

ESR spectra show that some defect centers, e.g. SiE' , peroxy-radicals and non-bridge oxygen hole centers have formed in SiO_2 (V) glass after the laser irradiation. Therefore,

permanent atomic displacements were created and electron transfer between atoms occurred during irradiation by the focused pulsed laser. Since the glass samples are transparent in 800nm, therefore, we suggest that a multiphoton absorption process occurred in the glasses when irradiated by the femtosecond pulsed laser.

We measured the refractive index profiles across the cross sections of the line, a continuous assembly of the refractive-index bits that was formed perpendicular to the laser beam [7]. A remarkable refractive-index increase was observed at the center of the irradiated region of a SiO_2 glass. The reasons of the increase in the refractive index are considered as follows.

Usually, the interaction of ultrashort pulsed laser with dielectrics is based on multiphoton ionization, Joule heating and collisional ionization [8]. The formation of defect centers induced by multiphoton and collisional ionization processes may be one of the reasons to cause the increase in refractive index at the center of the laser irradiated part. It is since the defect centers usually have absorption in the UV or shorter visible wavelength regions, resulting an increase of refractive index in the visible wavelength region. However, no apparent signal due to the formation of defect centers can be detected in some of laser irradiated glasses at liquid temperature. Therefore, other reason to cause the increase in refractive index also should be considered. The ultrafast energy deposition can also create high temperatures and pressures inside the glasses, and may cause densification of the melt around the focal point due to the high radiation pressure of the laser. After the removal of the laser, the melt may be froze, and the structural state of the melt is maintained, thus resulting in densification at the center of the irradiation region in the glasses.

The size of the refractive index bit increase with increasing the average power of the laser. Therefore, it is possible to adjust the size of the refractive index bit by controlling the laser power. The size of the refractive-index bit was observed to be approximately 400 nm after the irradiation of the single pulse of the laser, which is smaller than the wavelength of laser. It may be due to the self-focusing of the laser and non-linear effect of the glass, which resulted from the interaction between the laser and the glass. The result demonstrated that it is possible to record a bit of datum within two hundred femtoseconds by using a focused femtosecond laser. Moreover, using an objective with a long working distance, it is possible to record more than 1000 layers spaced by less than $1\mu\text{m}$ in a 1 mm thick disk. A recording density of approximately 10^{12} bits/cm³ can be attained.

We show that even slide glasses which are very cheap can be used as a media of 3-dimensional optical memory. The stored data in glasses have been examined to be stable below glass transition temperature. It is well known that glass is easy to be fabricated into a flat plate in large size. Therefore, we are convinced that writing three-dimensional spots inside the glasses will become a useful method to fabricate optical memory with both an ultrahigh storage density and an ultrahigh recording speed.

4. CONCLUSION

We have demonstrated 3-dimensional optical data storage inside various glasses using a focused 800 nm, 120 fs laser. The glasses were transparent in wavelengths ranging from 600 to 1000 nm. A refractive index bit was formed in the samples after irradiation by the 800 nm focused femtosecond laser. The size of the refractive-index increased with increasing the average power of the laser. ESR spectrum showed a significant increase in the concentration of color centers in some of the laser irradiated glass samples. A multi-photon absorption process is

considered to have occurred in the glasses when irradiated by the pulsed laser. Writing three-dimensional dots inside the glasses may become a useful method to fabricate optical memory with both an ultrahigh storage density and an ultrahigh recording speed.

ACKNOWLEDGEMENT

The authors thank Dr. J. Nishii of Department of Optical Materials, Osaka National Research Institute, Japan for his kind help in the measurement of ESR spectrum. The authors are also grateful to Drs. S. Fujiwara, T. Suzuki and Ms. T. Murase of the Hirao Active Glass Project, ERATO, JST, Japan for their cooperation in the experiments.

REFERENCES

- [1] T. Tanaka and S. Kawata, J. Opt. Soc. Am. A 13 (1996) 935.
- [2] K. Hirao, S. Todoroki, D. H. Cho and N. Soga, Opt. Lett. 18 (1993) 1586.
- [3] F. H. Mok, M. C. Tackitt and H. M. Stoll, Opt. Lett. 16 (1991) 605.
- [4] E. Bertzig, J. K. Trauman, R. Wolfe, E. M. Gyorgy, P. L. Finn, M. H. Kryder and C. H. Chang, Appl. Phys. Lett. 61 (1992) 142.
- [5] J. H. Stricker and W. W. Webb, Opt. Lett. 16 (1991) 1780.
- [6] Y. Kawata, T. Tanaka and S. Kawata, Appl. Opt. 35 (1996) 5308.
- [7] K. Davis, K. Miura, N. Sugimoto and K. Hirao, Opt. Lett. 21 (1996) 1729.
- [8] B. C. Stuart, M. D. Feit, A. M. Rubenchik, B. W. Shore and M. D. Perry, Phys. Rev. Lett. 74 (1995) 2248.

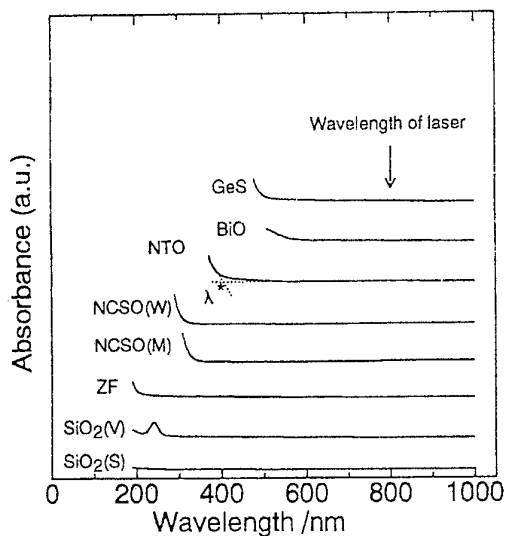


Figure 1 Absorption spectra of the glasses.

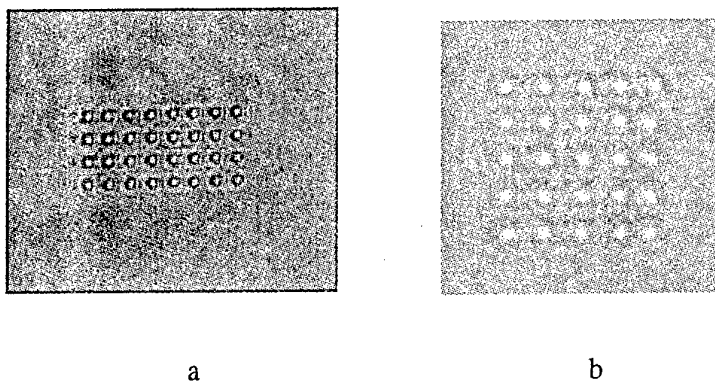


Figure 2 Results of the read out of the data information stored inside the NCSO(W) glass.

- a: The average power of the laser was 80 mW.
b: The average power of the laser was 140 mW.

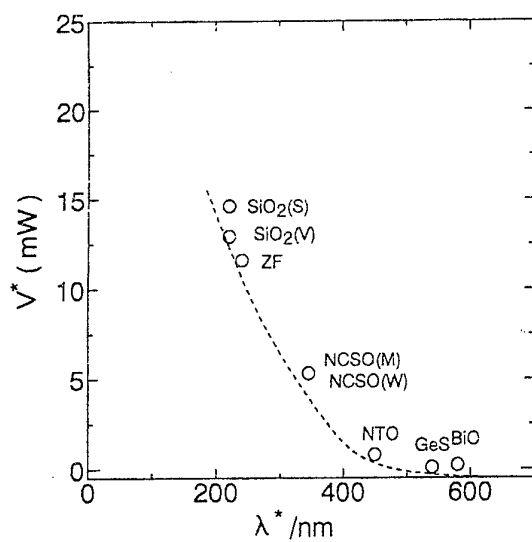


Figure 3 Relationship between the threshold value of the optical recording and wavelength corresponding to the optical band gap, λ^* , of the glasses. A microscope objective with an NA of 0.46 was used to focus the laser light.

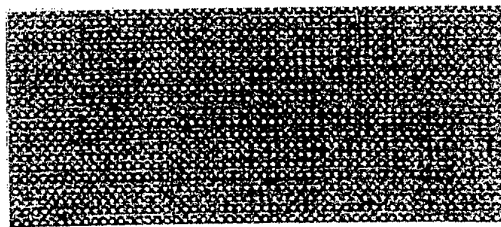


Figure 4 A result of the data stored in the $\text{SiO}_2(\text{S})$ glass by a single pulse of the femtosecond laser. The size of the refractive index bit is about 400 nm.

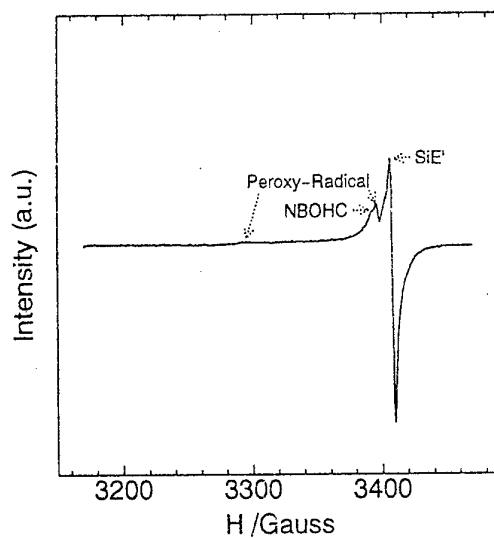


Figure 5 ESR spectrum of the $\text{SiO}_2(\text{V})$ glass after the laser irradiation.

TOWARDS PLANAR WAVEGUIDES FROM FLUOROZIRCONATE GLASSES

J. D. Shephard A. B. Seddon P.A.Houston#

Centre for Glass Research, Department of Engineering Materials,

#Department of Electronic and Electrical Engineering,

University of Sheffield, S1 3JD.

Tel: 0114 2225576 Fax: 0114 2225943 e-mail: mtp95jds@sheffield.ac.uk

A search for a viable process to produce integrated optical devices that will operate at 3-5 μ m is being conducted. Channel waveguides of a depth and width of 50 μ m are required for the devices that will operate at these wavelengths. A heavy metal fluoride glass based on the ZBLAN system has been selected as one candidate for the waveguide material. Techniques currently used for semiconductor manufacture and waveguide manufacture in silica will be modified for use on the ZBLAN glasses. One proposed manufacture route is to use a simple photolithographic technique involving a wet etch process.

A suitable etchant has been identified which is commonly used for the removal of defects from the surface of fluorozirconate glass preforms. A set of experiments has been performed on a ZBLAN based glass to determine the linear etch rate and the repeatability of the etchant. A series of steps of depth ranging from 20-120 μ m representing various etch times has been produced in the glass surface using temporary wax masks to define the topology. The linear etch rate was found to be repeatable up to depths of 120 μ m. Initial surface degradation problems have been overcome by changing the surface preparation prior to etching and adjusting the etchant agitation.

We are now investigating replacing the wax masks with a more defined photoresist to produce a series of etched channels in the glass surface and also aiming to produce core/clad waveguides. Glass melting, surface preparation and the controlled etching of surface features will be described together with the optical assessment of the waveguides.

Acknowledgements: Funding for JDS via EPSRC CASE Studentship with GEC-

Preparation and optical characterization of fluoride glass waveguides induced by laser pulses

K Miura, Jianrong Qiu, Y. Kondo, T. Mitsuyu

Hirao Active Glass Project, ERATO, Keihanna Plaza, 1-7 Hikaridai, Seika-cho, Kyoto 619-02, Japan

K. Hirao

Division of Material Chemistry, Faculty of Engineering, Kyoto University, Sakyo-ku, Kyoto 606-01, Japan

In an attempt to write optical waveguides in fluoride glasses, photo-induced refractive index changes were continuously created by focusing the pulse laser through a microscope objective and translating the sample parallel or perpendicular to axis of the laser beam. The ultra-short pulses (200 kHz, 800 nm) in Gaussian mode produced by a regeneratively amplified Ti:sapphire laser were utilized for the formation of photo-induced refractive index changes. The resulting, linear refractive index changes were written inside fluoride glasses along the path traversed by the focal point of laser. From field intensity distributions in the output of guided light for these, we demonstrated that permanent optical waveguides can be successfully formed in fluoride glasses. In addition, from the analysis of a near-field pattern by a CCD camera, it was confirmed that single mode waveguides of the graded index type can be formed by a writing technique using the ultra-short pulse laser.

Fabrication of High Numerical Aperture Fluoroaluminate Fibres

E.R.Taylor, R.C.Moore, J.A.Tucknott, D.W.J. Harwood, Y. West & D.N. Payne

Optoelectronics Research Centre
University of Southampton
Southampton SO17 1BJ

A family of fluoroaluminate glasses has been identified as the ideal host for doping with Nd^{3+} for use in the development of lasers and amplifiers in the second telecom window. For optimum performance, a fibre with high numerical aperture (NA), fibre length of 5cm and loss of 10dB/m is required. The high NA implies a core diameter of $3\mu\text{m}$ is needed and thus the core-to-clad interface represents greater than 50% of the core area. Crystallisation in the interface introduces large scattering losses. The critical step in the fabrication process is preform fabrication. We will present results comparing the different techniques employed and thermal and mechanical fabrication process modelling consistent with our experimental observations and detail the advantages and limiting parameters for the different processes.

Rod-in-tube is the simplest technique of preform fabrication and works exceptionally well for oxide glasses. Fluorides are highly prone to surface crystallisation. We have looked at the fibre losses as functions of polishing material, polishing time, and etching. It is a good first step to test the optical properties and performance in a fibre.

Rotational casting is usually employed in fluoride glasses. The high $T_g(450^\circ\text{C})$ and large expansion coefficient ($>150 \times 10^{-7}/^\circ\text{K}$) of fluoroaluminate glasses creates difficulties in rotational casting. We have modelled the thermal history and the stresses involved in the process. We have prepared glasses of varying expansion coefficients and find that the tolerances for core and clad expansion coefficients should be $<5 \times 10^{-7}/^\circ\text{K}$. We will compare the results of rotational casting with built-in-casting and the influence of processing time, thermal history and mould material (thermal conductivity).

Extrusion as a procedure for preform fabrication is specially suitable for fluoroaluminates. Extrusion allows one to operate at temperatures nearer T_g than T_x . Preforms can be prepared with small cores and thus avoid the thermal cycling involved in sleeving to get the singlemode fibre. To date our losses for fibres with $5\text{--}8\mu\text{m}$ cores vary from 100dB/m using rod-in-tube to 20dB/m using extrusion.

FABRICATION OF Er^{3+} -DOPED FLUORIDE FIBRES WITH SINGLE-MODE GEOMETRY BASED ON OVER-CLAD DRILLING

M. Braglia, C. Bruschi, E. Chierici, G. Dai, J. Kraus, S. Mosso
 CSELT, Via G. Reiss Romoli 274, I-10148 Turin, Italy.
 E-mail joerg.kraus@cse.lt.it

ABSTRACT

By a two-step method based on small-bore over-clad drilling as the key step, Er^{3+} -doped single-mode fluoride fibres have been fabricated. Best fibres have a loss of 0.48-0.80 dB/m at 1.3 μm , a LP_{11} cut-off of 1.35 μm and a bending strength of 0.83 GPa.

INTRODUCTION

With the establishment of wavelength-division multiplexing (WDM) technologies in existing transmission networks, the fluoride-based Er^{3+} -doped fibre amplifier (F-EDFA) has seen a revival because of its better gain flatness and longer amplification range compared with a silica-based one [1-3].

Er^{3+} -doped fluoride fibres usable for optical amplifiers operating at 1.55 μm have to be single mode at both the signal and the pump wavelength. The conditions for single mode operation are set by the normalised frequency, V , which, in case of a step-index fibre, is given by

$$V = \frac{\pi \cdot d \cdot \text{NA}}{\lambda} \leq 2.405$$

(NA, d , and λ are the numerical aperture of the fibre, its core diameter, and the operating wavelength, respectively).

If the fibre has a medium numerical aperture of 0.2, which has been shown to be sufficient for achieving high signal gain [4], a core diameter of less than 5.6 μm will be required. Hence, the core/clad ratio has to be at least 1/22.

Only recently, an insertion technique has been reported in which a fluoride glass preform with the ratio required has been achieved in single step [5]. Before that, multiple stretching and/or over-cladding has been the method of choice, thus, taking the risk of increasing the probability of crystallisation with each additional heating operation [6-8].

We now report on a simple two-step method based on small-bore over-clad drilling as the key step followed by a single stretching operation of a multimode preform down to a diameter which fits into the hole of the tube drilled. The resulting rod-in-tube preform could be successfully drawn into single-mode fibre.

EXPERIMENTAL

Core rods, clad tubes and over-clad rods used had outer diameters of 4 mm, 10 mm, and 10 mm, respectively, and a length of 145 mm. Core glasses were of ZBLyAl composition [9] and doped with 1000 ppm of Er^{3+} . Clad and over-clad glasses were of the ZBLyAN type [9]. From their refractive indices, a NA of 0.22 could be calculated.

Drilling was accomplished manually by using a drill press equipped with diamond impregnated core drills of 1.06 mm of nominal outer diameter and various lengths of up to 150 mm. Drills and equipment were supplied by Lunzer, Inc.

After drilling, both the inner and outer surfaces were etched separately with 1 l of an aqueous solution of 1 M HCl/0.04 M H_3BO_3 to the diameters desired, washed with

methanol and dried under vacuum. In detail, inner surface etching was carried out by continuously pumping the etching solution through the hole. The flow rate was about 0.7 l/min.

After jacketing the tubes with Teflon FEP and sealing them at one end, small-diameter rods obtained previously from the stretching of multimode preforms were inserted in the tubes and the resulting preforms drawn into fibres.

Measurements of the geometry of over-clad tubes and small diameter rods were made by an optical microscope equipped with a Polaroid camera. Non-circularity, NC, was expressed as $NC = [(a-b)/a] \cdot 100 \%$, with a and b being the major and the minor axis of an ellipse, respectively. Concentricity between two surfaces was taken as the distance between the centres of the best-fit circles of those surfaces, normally expressed in microns. Fibre geometry was measured by a Photon Kinetics 2400 instrument.

Optical loss spectra of the fibres were recorded in the range between 900 nm and 1600 nm by using the cutback technique. Attenuation coefficients were taken from the average loss spectrum of four cutback measurements.

Mechanical strength of the fibres was calculated from two-point bending tests on 25 samples of a length of 200 mm each. The platen velocity was 10 mm/min and the tests were performed within one week after drawing.

RESULTS

Preliminary trials showed that drilling of fluoride glass rods was feasible even by using standard solid twist drills. Unless drilled dry, rods of up to 50 mm length could be perforated by drilling from both ends. Since the maximum length of twist drills of 1 mm in diameter is about 55 mm, the achievable bore length is quite restricted. That can cause problems when it comes to drawing because of the close proximity of the preform fixing clamp to the drawing furnace. Moreover, drilling from both ends runs the risk of producing lateral misalignment of the two bores, which, in our case, turned out to be about 33 %. Additional attempts to do better if using an ultrasonic mill invariably led to the crack-up of the rods just after entering a few mm. Eventually, most of the problems mentioned above could be resolved by using diamond impregnated core drills. Table 1 gives an evaluation by listing the hole-overclad concentricity along the drill axis for each of the rods drilled, which had a final hole diameter of 1.11 mm.

Table 1 shows, that the deviation of the hole from the centre axis in the zone of the tube from which fibres were drawn lay in the range between 3.3 % and 9.4 %, with over-clad 4 being the best drilled. Generally, eccentricity doubled halfway through the rod. On the other hand, even a drill deflected can regain concentricity as evidenced by over-clad 2, whose concentricity improved in the last part from 9.4 % to 2.7 %.

Irregularly shaped vacuum bubbles scattered along the centre axis of a rod were seen to affect drilling a lot. If the edge of the bubble formed a sharp cone in drilling direction, the drill could gain concentricity, as seen from over-clad 3 which contained such a bubble between 60 mm and 75 mm. Concentricity improved from 4 % to 1.7 %. If the edge was round, though, the drill often started deflecting irreversibly from the centre axis.

Since the glass has come into contact with water, the wall of the hole after drilling was covered with a white hydrated layer and had to be cleaned by chemical etching prior to drawing. The hole diameter desired was obtained by controlling the etching time. Fig. 1 displays the calibration curve together with the corresponding data from the etching of the three over-clads. From a linear best fit of all data, an etching rate of $21.4 \mu\text{m}/\text{min}$ was obtained. Since the hole diameter also increased in pump direction, at a rate of $8 \pm 3 \mu\text{m}$

per 10 mm of tube length, all data in Fig. 1 referred to a distance of 20 mm from the solution entrance.

After the etching of the over-claddings, appropriate small diameter rods previously obtained from the stretching of multimode preforms were inserted, thus completing the new preforms from which fibres with single-mode geometry could be expected. From Table 2, which reports the geometry of the rods stretched, rod 2 emerged to be the best with 1.7 % of core non-circularity, 1.9 % of clad non-circularity and 3.3 % of core-clad concentricity. Of all the four rods employed, it was by far the least tapered as well.

In Table 3, the geometry of the fibres drawn are summarised and illustrated by a magnified cross-section of fibre 1 (Fig. 2.). For the sake of clearness, the number of a fibre and those of its over-clad and small diameter rod are corresponding. It can be seen that all the fibres obtained met the requirement of a core/clad ratio of less than 1/22. Whilst clad non-circularity was quite uniform except for fibre 4, and averaged 3.6 ± 0.3 %, core non-circularity varied strongly from about 6 % to 16 %. Core-clad concentricity was in the range from 1.7 μm (2.6 %) to 5.3 μm (7.9 %).

On fibres 1, 3, and 4, optical and, partly, mechanical properties were measured as well (Table 4). The mechanical properties of fibres 1 and 3 were nearly the same, averaging values of 0.81 GPa of bending strength and 6.1 of Weibull dispersion, respectively. In contrast to the mechanical properties, the optical ones were less homogeneous. With an optical loss of 0.48 dB/m and 0.80 dB/m at 1.3 μm , fibres 4 and 3 attenuated light five times and three times less than fibre 1, respectively. In case of fibre 3, the LP_{11} cut-off wavelength was found (at 1.35 μm), which corroborated that a real single-mode structure has been achieved.

DISCUSSION

The contribution of core and inner cladding to the total cross-sectional area of the fibre is just little more than 1 %. Therefore, it becomes clear that the core-clad concentricity achieved in the fibres (Table 3) was determined by the hole concentricity in the over-clad (Table 1) rather than by the core-clad concentricity of the small rods (Table 2). This could be demonstrated on fibres 2 and 4, whose corresponding small diameter rods represented best and worst case of core-clad concentricity with 3.3 % and 9.8 %, respectively. By sampling lengths from the last part of each drawing, where the hole-overclad concentricity in the rods drilled was approaching 9.4 % and 3.2 %, respectively (Table 1), a core-clad concentricity of 7.9 % and 2.6 % was measured (Table 3). Hence, the fibres closely followed the trend set by the drilling. On the other hand, core non-circularity in the fibres (Table 3) may depend on the gap between the width of the hole in the over-clad (Fig. 1) and the diameter of the small rod inserted (Table 2). Fibre 2, whose preform had the smallest gap (about 200 μm), turned out to have best core circularity if the error was taken into account.

The high clad non-circularity of fibre 4 may be attributable to the fact that preform 4 was jacketed with a FEP tube whose thickness was 40 % less than that normally used.

As mentioned above, the hole diameter was seen to increase in flow direction of the etching solution. This could be of practical use when it comes to match a tapered preform stretched.

To elucidate the enhanced optical loss of fibre 1, firstly, the core area of the stretched rod 1 was scanned by energy dispersive X-ray analysis (EDX). It should be stressed that the sample investigated had not undergone the drawing heat treatment. Crystals of AlF_3 , ranging from 0.10 μm to 0.15 μm in size, were detected throughout the

core region, whilst on the core-clad interface agglomerates of them were found with an average crystal size of $0.4\text{ }\mu\text{m}$, as reported previously [10]. Secondly, to assess the influence of drawing on the fibre loss, the remainder of the multimode preform of stretched rods 3 and 4 was drawn into multimode fibre using similar conditions as those employed for fibres 3 and 4. Fibre losses in the range of 0.28 dB/m to 0.46 dB/m were measured on lengths varying from 3 m to 25 m , respectively. Since the corresponding small-core fibres 3 and 4 had losses between 0.80 dB/m and 0.48 dB/m , it can be stated that the optical quality of the core glasses after stretching need not be compromised by the following drawing.

From cut-off measurements on fibre 3, an LP_{11} cut-off wavelength of $1.35\text{ }\mu\text{m}$ could be established, which is in good accordance with the theoretical one of $1.38\text{ }\mu\text{m}$ based on a NA of 0.22.

The question of how does the clad-clad interface affect the mechanical properties of the fibres, was not so easy to answer. In any case, compared with fibres 1 and 3, whose bending strengths averaged 0.81 GPa (Table 4), the corresponding multimode fibres were more fragile as shown by their bending strengths of 0.45 GPa and 0.58 GPa , respectively.

CONCLUSION

Small-bore over-clad drilling has been shown to be a valuable intermediate step in the fabrication of Er^{3+} -doped single-mode fluoride fibres affecting the optical properties of the core only geometrically in terms of core non-circularity and core-clad concentricity. Best values of around 6 % in the former case, and $1.7\text{ }\mu\text{m}$ in the latter, were obtained. Further improvements in hole concentricity and a proper match of the hole diameter with that of the rod to be inserted should be possible.

ACKNOWLEDGEMENTS

The authors wish to thank R. DeFranceschi for EDX analysis, A. Rossaro and M. Schiano for help with optogeometric fibre measurements, and R. Moore and LUNZER, INC. for technical assistance with drilling.

REFERENCES

- [1] H. Ono, M. Yamada, T. Kanamori, S. Sudo, Y. Ohishi, *Electron. Lett.* 33 (1997) 1471.
- [2] H. Masuda, S. Kawai, K.-I. Suzuki, K. Aida, *ECOC (1997) 73*, paper TH3C.
- [3] M. Chbat, S. Artigaud, D. Bayart, A. Jourdan, M. Sotom, J.-L. Beylat, *OFC (1997) 83*, paper TuP3.
- [4] F. Auzel, J. Chavignon, D. Meichenin, J. Fernandez, M. Potenza, Report on quantum efficiency and results on performance modelling, EEC RACE Project R2018 GAIN (1993).
- [5] A.R. Kortan, N. Kopylov, E. Özdas, R. Pafchek, *J. Non-Cryst. Solids* 213&214 (1997) 90.
- [6] T. Kanamori, Y. Terunuma, K. Fujiura, K. Oikawa, S. Takahashi, *NTT R&D* 39 (1990) 1352.
- [7] S.T. Davey, D. Szebesta, J.R. Williams, T. Whitley, R. Wyatt, *J. Non-Cryst. Solids* 161 (1993) 262.
- [8] C.G. Byrne, K.P. Clarke, D. Coulson, S.C. Goh, G. Rosman, R.S. Rowe, *Proc. 8th Int. Symp. on Halide Glasses*, Perros-Guirec, France (1992) 21.
- [9] M. Braglia, J. Kraus, S. Mosso, *J. Non-Cryst. Solids* 201 (1997) 237.

[10] H. Poignant, J. Le Mellot, A. Levé, P. Le Cabec, D. Rivière, J. Non-Cryst. Solids 161 (1993) 192.

Table 1: Hole concentricity of the over-claddings vs. length drilled

	Length drilled (mm)	Hole-overclad concentricity ¹⁾ (μm) / (%) ²⁾
Over-clad 1	5	190 / 3.9
	15	190 / 3.9
	77	380 / 8.1
Over-clad 2	8	160 / 3.3
	70	440 / 9.4
	80	460 / 9.4
	91	310 / 6.3
	100	130 / 2.7
Over-clad 3	60	190 / 4.0
	75	80 / 1.7
	89	160 / 3.3
Over-clad 4	14	200 / 4.1
	80	150 / 3.2
	93	230 / 4.7
	105	370 / 7.6

¹⁾ As measured on slices of the tubes left after drawing. The error was estimated to be 40 μm .

²⁾ Deviation from the centre axis of the over-cladding.

Table 2: Geometry of the small diameter rods obtained from the stretching of multimode preforms

	Rod 1	Rod 2	Rod 3 ¹⁾	Rod 4 ¹⁾
Total length (mm)	75	140	110	110
Core diameter ²⁾ (μm)	257 – 332	386 – 402	334 – 356	356 – 414
Clad diameter ²⁾ (μm)	734 – 935	1017 – 1021	844 – 972	980 – 1213
Average core/clad ratio	1/ 2.8	1/ 2.6	1/ 2.6	1/ 2.8
Core non-circularity (%)	5.2 \pm 0.8	1.7 \pm 0.7	1.9 \pm 0.4	2.2 \pm 0.3
Clad non-circularity (%)	2.0 \pm 0.8	1.9 \pm 0.4	1.8 \pm 0.5	1.5 \pm 0.2
Core-clad concentricity (%)	4.9	3.3	7.2 \pm 1.2	9.8

¹⁾ Rod 3 and 4 were derived from the same preform

²⁾ As measured at both ends

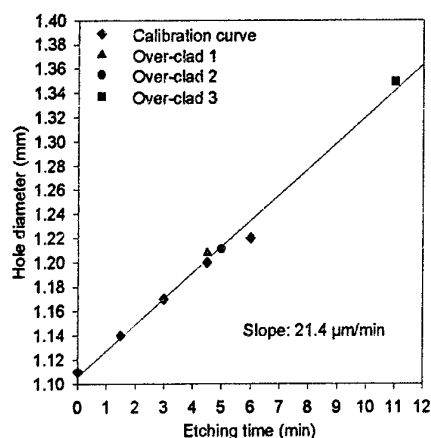


Fig. 1. Hole diameter vs. etching time.
The line is a best fit to the measured data.

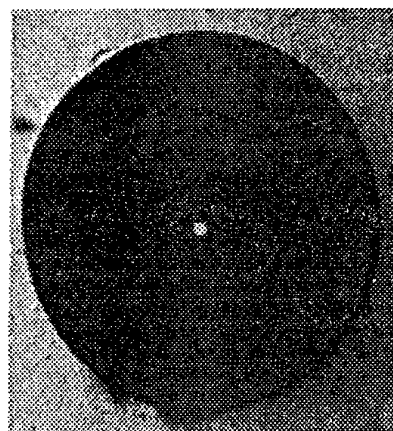


Fig. 2. Cross-section of fibre 1

Table 3: Geometry of the fibres drawn

	Fibre 1 ¹⁾	Fibre 2 ²⁾	Fibre 3 ³⁾	Fibre 4 ⁴⁾
Core diameter (μm)	4.6 ± 0.2	5.9 ± 0.1	4.8 ± 0.3	4.7 ± 0.2
Clad diameter (μm)	129.8 ± 1.4	134.4 ± 0.9	123.0 ± 0.1	133.2 ± 7.2
Core/clad ratio	1/28	1/23	1/26	1/28
Core non-circularity (%)	16.2 ± 7.6	6.6 ± 1.3	16.1 ± 15.8	5.9 ± 5.8
Clad non-circularity (%)	3.3 ± 0.8	3.7 ± 0.5	3.8 ± 0.1	6.2 ± 0.8
Core-clad concentricity (μm) / (%)	2.6 ± 0.3 / 4.0	5.3 ± 0.4 / 7.9	3.2 ± 0.3 / 5.2	1.7 ± 0.4 / 2.6

¹⁾ Average values and standard deviations of 5 measurements on 1 m of fibre

²⁾ Average values and standard deviations of 5 measurements on 2 m of fibre

³⁾ Average values and standard deviations of 10 measurements on 0.6 m of fibre

⁴⁾ Average values and standard deviations of 3 measurements on 0.6 m of fibre and 5 measurements on 1.1 m, respectively.

Table 4: Optical and mechanical properties of the fibres

	Fibre 1	Fibre 3	Fibre 4
Attenuation coefficient, α ¹⁾ (dB/m)	2.62 ± 1.30 ²⁾	0.80 ± 0.08 ³⁾	0.48 ⁴⁾
Cut-off wavelength, λ_c (μm)	-	1.35	-
Bending strength ⁵⁾ , σ_0 (GPa)	0.80 ± 0.01 ⁶⁾	0.83 ± 0.01 ⁷⁾	-
Weibull parameter, m	5.9 ± 0.3	6.2 ± 0.2	-

¹⁾ At 1.30 μm ²⁾ Average value of 4 lengths of fibre cut back ³⁾ Average value of 2 lengths of fibre cut

back ⁴⁾ 10 m of fibre cut back to 2.2 m ⁵⁾ At a failure probability of 63.2% ⁶⁾ Mean fibre diameter: 129

± 3 μm ⁷⁾ Mean fibre diameter: 126 ± 9 μm

A NEW CASTING TECHNIQUE FOR THE FLUORIDE GLASSES

L.Dmitruk, N.Vinogradova

**General Physics Institute, Russian Academy of Sciences, Vavilov str.38, Moscow
117947, Russia**

V.Fedorov, Yu.Efimov

All Russian Chemical Technology Institute, Moscow, Russia

ABSTRACT

The preparation of large size fluorozirconate and fluorohafnate glasses with increasing cooling rate of the melt was studied. Both external water cooling of the mould and «internal» cooling of the melt were employed to increase the cooling rate. Conditions to be needed to prepare glasses with $30 \times 30 \text{ mm}^2$ without crystallization and cracking were determined.

INTRODUCTION

Crystallization of fluoride glasses, particularly of those of non-trivial composition, e.g. of glasses with a high concentration of RE, complicates the production of large size samples. In particular the crystallization problem impedes a preparation of scintillating fluoride glass module with thickness more than 20 mm [1].

One of approachment to this problem could be increasing of the cooling rate of the melt during casting.

In this work the possibility of preparation of the fluorozirconate and fluorohafnate (ZBLAN type) glasses with $30 \times 30 \text{ mm}^2$ cross-section under forced cooling of the mould and «inner» cooling of the melt was studied.

RESULTS AND DISCUSSION

The matter of the proposed casting technique is illustrated in Fig.1. The melt is poured in thin thickness aluminum mould in which water cooling brass core is placed. On the outside the mould is cooled with water. During cooling the mould temperature is 100°C and the core one is about 20°C . As result of heat transfer solidified layers are formed both at core and mold surfaces. In present case the total heat towards mould and core considerably more in comparison with the usual casting technique due

to increasing of the temperature gradient in the melt and increasing of cooling surface. As a result cooling rates of the melt including one of the central part, where crystallization is most probable, are increased.

In some time the external cooling is removed and cooling core is taken out. Then the glass solidified on the core is submerged into the melt. In this stage the cooling of the unsolidified melt is continued due to heat transfer to solidified glass and last one is heated. After complete solidification the mould is transferred into the annealing furnace.

Experiment was performed in the set-up shown in Fig 2. The set-up consist of two main parts: the furnace for glass synthesis and the casting mould. The glasses were melted in the graphite crucible covered with glass carbon and placed in silica glass tube. The tube is hermetically tightened on the sides. Argon is passed through the silica glass tube. At the bottom part of the crucible, a nozzle fitted with a graphite cork is available. The mould represents an aluminum box with 0.8 mm walls. A water cooled core is introduced into the mould. From the outside the mould is cooled with water. The mould is hermetically connected with silica glass tube through flange.

The purpose of experiment was to determine the duration of enforced cooling, which ensures the increased cooling rate without cracking of glass ingot.

A batch of 600g of $52\text{ZrF}_4\text{-}20\text{BaF}_2\text{-}5\text{CeF}_3\text{-}2.5\text{AlF}_3\text{-}20\text{NaF-}0.5\text{InF}_3$ (mol.%) was melted under Ar flow at $820\text{-}840^\circ$ for 60 min, cooled to 580°C , then poured into the mould, with 30 mm width and 145 mm length. Two Pt-PtRh microthermocouples were inserted into the melt. They were 1 and 6 mm distant from the mould wall.

Some typical cooling curves corresponding to different duration of enforced cooling (t_1, t_2) are shown in Fig.3. The crystallization of the central part of melt at short cooling time (curve 1), and the cracking of the glass ingot at long cooling time (curve 2) took place.

Cracking it found to take place in the case of $(T_g - T_x)$ difference, where T_x is the temperature of the glass surface, more than 50°C .

Variation of «outer» and «inner» cooling times within the limits of 0.5-4 min allowed both to achieve high cooling rate of the central part of the melt and to prevent cracking of ingots. The typical cooling curves (3,4) for such case are shown in Fig.3. For this case $(T_g - T_x)$ is about 30°C and the minimum cooling rate in the temperature

range of 350-400°C is about 50°/min. Ingots with 30×30 mm² cross section and 145 mm length prepared in such a way did not show signs of crystallization and showed good optical quality.

ACKNOLEGMENT

This work was supported by ISTCF grant 256. We like to thank Prof. Brown and his colleagues (RAL,Oxford) and Dr.J. Parker and his colleagues (Sheffield University) for help.

REFERENCE

[1] P.R.Hobson, P.S.Flower et al. Proceedings of the International Conference on Inorganic Scintillators, Delft, The Netherlands, September, 1995, 505-507

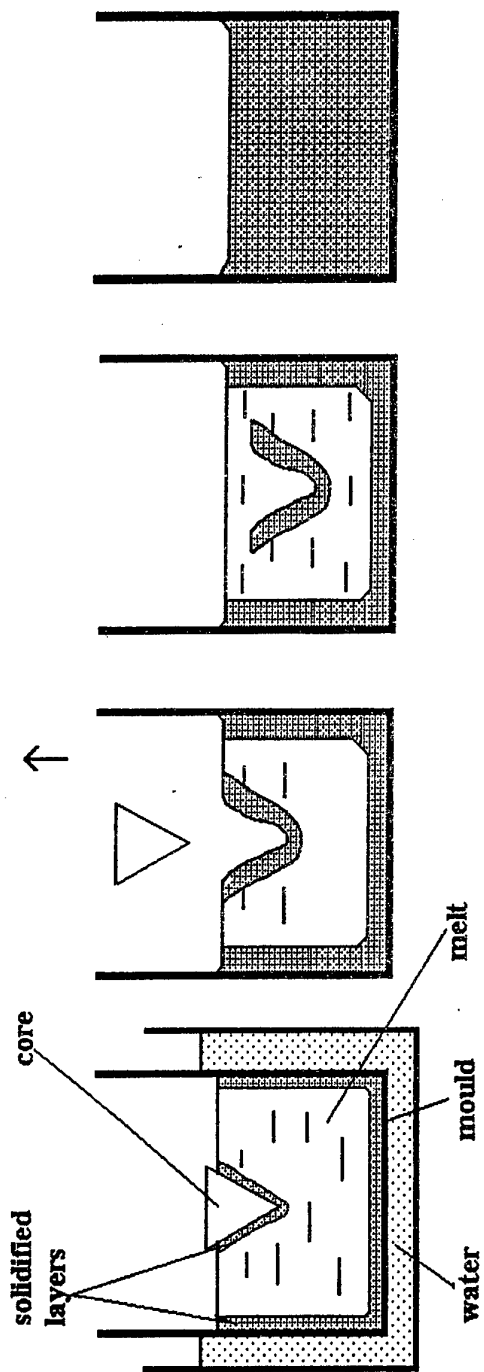


Fig.1 Scheme of casting technique

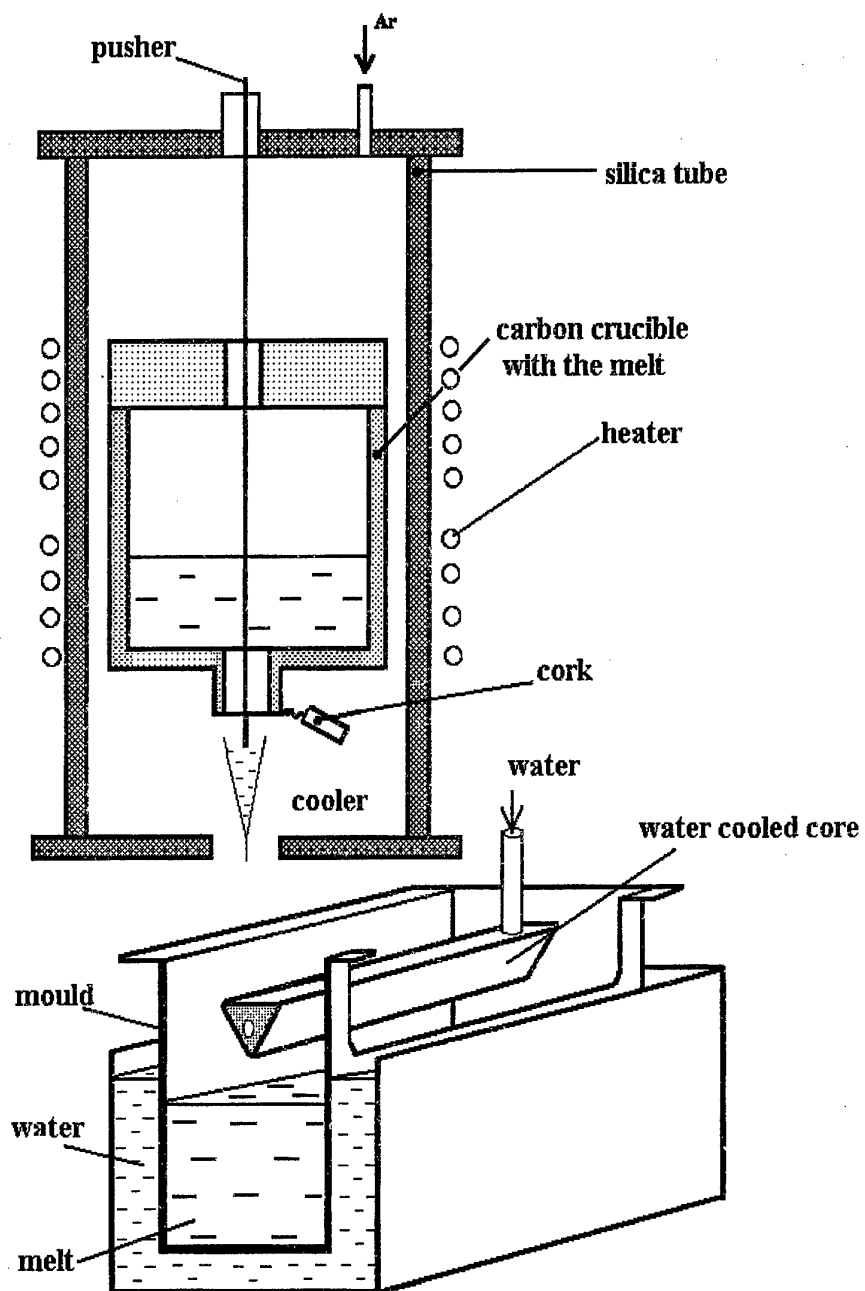


Fig.2 Set-up for preparation of fluoride glass

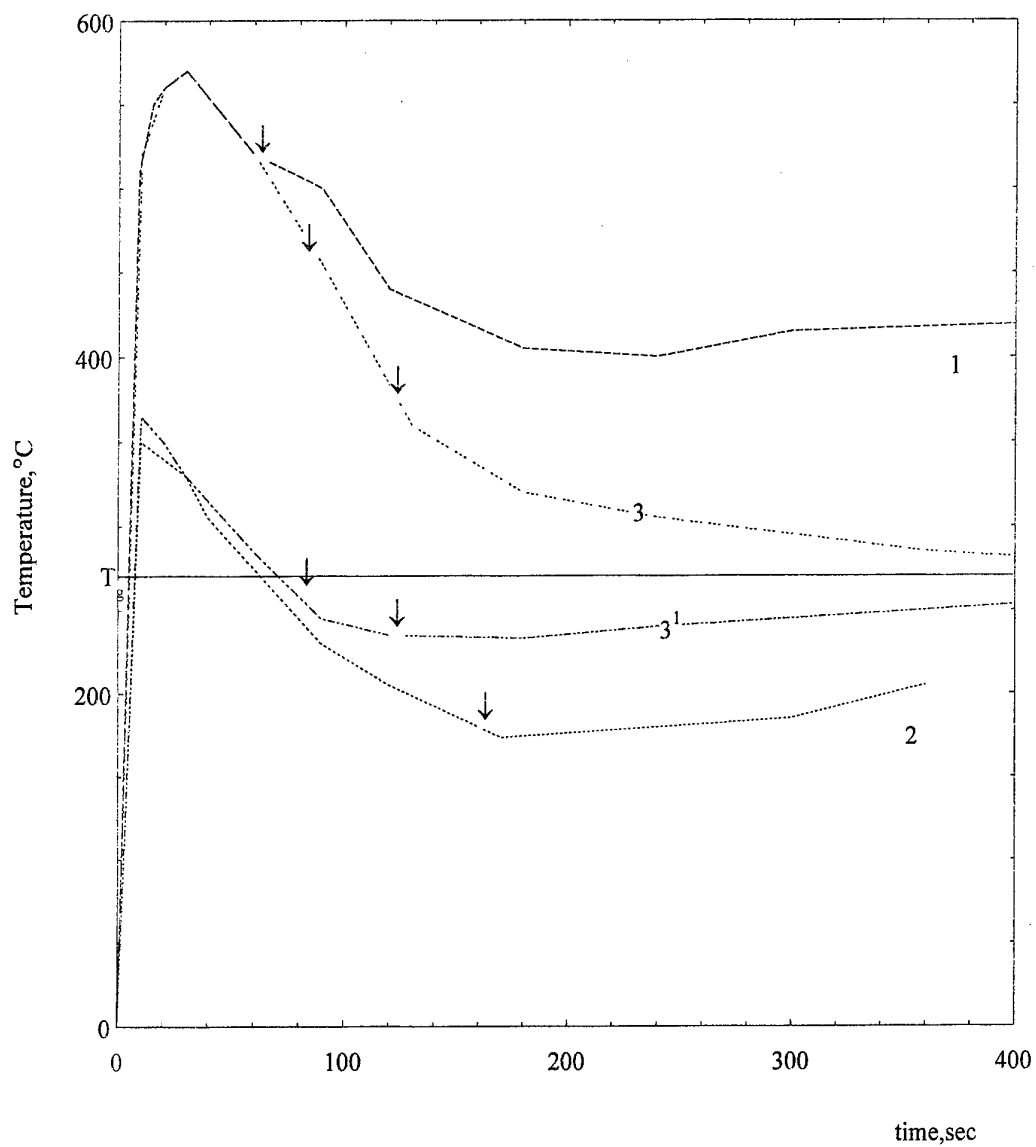


Fig.3 Cooling curves during casting: 1- thermocouple was 6 mm distant from the mould wall. External cooling time $t_1=60$ sec, internal cooling $t_2=60$ sec; 2- thermocouple was 1 mm distant from the mould wall, $t_1=t_2=160$ sec; 3- thermocouple was 6 mm distant from the mould wall $t_1=80$ sec, $t_2=120$ sec; 3'- thermocouple was 1 mm distant from the mould wall, $t_1=80$ sec, $t_2=120$ sec

Chalcogenide glass single mode fibres - preparation and properties

Jens Kobelke, Johannes Kirchhof, Michael Scheffler, Anka Schwuchow

Institut für Physikalische Hochtechnologie e.V. Jena
Helmholtzweg 4, 07743 Jena, Germany

ABSTRACT

For the first time we present a praseodymium doped arsenic sulfide based single mode fibre with low loss behaviour. The small core-high NA structure was realized by combination of double crucible method and rod-in tube processing. The fibre has a core-double clad structure. Based on a laminar model the parameters of viscous flow and the dimensions of concentric crucible tubes could be optimized. The favourable ratio of diameter relation innerclad-core is about 10:1. The main problem of single mode preparation is the quality of interface innerclad-overcladding. By high quality inner surface treatment the heterophase impurities could be considerably decreased. Best value of background loss is 3.3 dB m^{-1} at $1.3 \text{ }\mu\text{m}$.

INTRODUCTION

Chalcogenide glass single mode fibres are promising candidates for optical applications in the NIR- and MIR-range. Among their outstanding characteristics are the high refractive index and material dispersion. The high optical nonlinearity and large interaction length of fibres allow applications to all-optical switching. The low phonon energy marks chalcogenide glasses as suitable hosts for laser and amplifier applications.

Because of their low crystallization tendency and the high mechanical and chemical stability, glasses based on arsenic sulfide are favoured for passive and active fibre applications.

EXPERIMENTAL AND RESULTS

We prepared single mode fibers with double clad structure based on sulfide glass. The main point of view was their application for $1.3 \text{ }\mu\text{m}$ amplifiers. The fibres had a high Δn -small core structure. The praseodymium concentration in the core glass was chosen underneath 1000 wt.ppm , to exclude concentration quenching of lifetime of the excited level. The destination value of numerical aperture was about 0.4, the praseodymium doped core had a diameter of about $2 \text{ }\mu\text{m}$. The rare earth solubility was optimized by adding co-dopants, i.e. germanium, gallium, surplus-sulfur [1]. The solubility of rare earth elements was strongly influenced by the co-dopants. For praseodymium concentrations up to about a thousand wt.ppm we found an optimum molar concentration ratio germanium/gallium of about 2.6 [2].

The attenuation of the fibers was measured by cut back method at $1.02 \text{ }\mu\text{m}$ and $1.3 \text{ }\mu\text{m}$. The fluorescence behaviour and lifetime were measured by side light spectra method (exciting source: MOPA $1.020 \text{ }\mu\text{m}$). The refractive index of the several fiber glasses was estimated by prism coupling method at $1.3 \text{ }\mu\text{m}$. The mean viscosity under drawing conditions was estimated by measurement the drawing force. T_g gives a clue for viscosity in the glass transition region. It was estimated by DTA method. The thermal expansion coefficient of the different glasses

was estimated by length contraction by cooling unstructured fibres. The value for a stoichiometric arsenic sulfide fibre was $27.4 \cdot 10^{-6} \text{ K}^{-1}$.

We adjusted the difference of refractive index between core and innerclad by variation the germanium concentration. If refractive index was reduced by increasing the surplus-sulfur content this led to more streaky glasses. Probably it was caused due to higher vapourisation tendency in relation to stoichiometric or germanium doped arsenic sulfide. Additional surplus-sulfur led to an increase of the thermal expansion coefficient of innerclad glass of about 20 % in relation to core glass. In contrast the addition of germanium show an about 10 % decreased value in relation to core glass. Therefore, we doped the innerclad material with about 2.3 mol% additional germanium to core glass level. In consequence, the higher germanium concentration increases the viscosity of the innerclad in relation to the core glass about one order of magnitude. No crystallization was observed for the praseodymium doped core glass, innerclad or overcladding glass by DTA.

Table 1: Optical and thermal behaviour of typical core, innerclad and overcladding glasses:

	core glass	innerclad glass	overcladding glass
co-dopants	Ge, Ga, S _y	Ge, S _y	Ge
Pr ³⁺ typ. val.	760 wt.ppm	0	0
α_{OH} (2.9 μm) typ. val.	$< 0.1 \text{ cm}^{-1}$	$0.1 \dots 0.5 \text{ cm}^{-1}$	$0.1 \dots 0.5 \text{ cm}^{-1}$
α_{SH} (4.1 μm) typ. val.	0.9 cm^{-1}	$0.2 \dots 0.9 \text{ cm}^{-1}$	$0.2 \dots 0.9 \text{ cm}^{-1}$
refractive index (1.3 μm)	2.430	2.394	2.451 (0% Ge) 2.431 (3% Ge)
lowest attenuation of unstructured fibre (1.3 μm)	1.5 dBm^{-1}	2.9 dB m^{-1}	0.8 dB m^{-1}
T _g	191°C	215°C	202°C (0% Ge) 221°C (3% Ge)
mean viscosity (310°C))	$10^{5.5} \text{ dPas}$	$10^{6.0} \text{ dPas}$	$10^{5.0} \text{ dPas}$ (0% Ge) $10^{6.2} \text{ dPas}$ (3% Ge)
thermal expansion coeff. relat. to As ₂ S ₃	0.98	0.88	1.00 (0% Ge) 0.90 (3% Ge)

S_y: surplus-sulfur

*) typical crucible drawing temperature of As₂S₃

The single mode fibres were prepared by a modified rod-in-tube (RIT) drawing process. As a first step we pulled a rod core-innerclad structure by double crucible method. This rod was inserted into a hollow preform cylinder and drawn to a double clad fibre.

This method enabled the defined preparation of the fibre geometry and refractive index structure of the rod. To adjust the correct values of core and innerclad diameters we studied

the influence of thermal paramters of the glass composition and the double crucible dimensions on the drawing process by a laminar flow model. The diameter relation between cladding and core was determined by:

$$\frac{\phi_{clad}}{\phi_{core}} = \sqrt[4]{1 + \frac{\eta_{core} \cdot p_{clad}}{\eta_{clad} \cdot p_{core}} \cdot \frac{(c^2 - b^2) - c^4 + b^4}{\ln\left(\frac{c}{b}\right) \cdot a^4}}$$

η_{core} ; η_{clad} : viscosity of core; innerclad glass
 p_{core} ; p_{clad} : total pressure difference of core; innerclad glass
 a : inner radius of the core glass tube of the double crucible
 b : outer radius of the core glass tube
 c : inner radius of the innerclad glass tube

The influence of germanium and surplus-sulfur on the viscosity under crucible drawing condition was estimated by T_g and fiber elongation/tension force measurement:

$$\Delta \log \eta_{Ge} = 0.41 \cdot x_{Ge} \quad \text{and} \quad \Delta \log \eta_{Sy} = -0.13 \cdot x_{Sy}$$

$\Delta \log \eta_{Ge}$: difference in viscosity to As_2S_3 caused by added germanium (log units)
 $\Delta \log \eta_{Sy}$: difference in viscosity due to surplus-sulfur (log units)
 x_{Ge} : germanium concentration (mol%)
 x_{Sy} : surplus-concentration (mol%)

Table2 shows the relation between realized and expected ϕ_{clad}/ϕ_{core} by variation the germanium content of core and innerclad glass:

	NA	x_{Ge} core mol%	x_{Ge} clad mol%	$p_{clad} /$ p_{core}	$\eta_{clad} /$ η_{core}	$\phi_{clad} / \phi_{core}$	$\phi_{clad} / \phi_{core}$ (exper.)/ $\phi_{clad} / \phi_{core}$ (model)
A50-B47	0.121	0.000	2.256	1.00	8.57	9.32	0.74
D37-B27	0.253	0.868	2.910	1.00	7.00	2.22	1.06
D36-B26	0.326	0.880	2.519	1.00	4.77	2.70	1.07
D92-B49	0.368	1.344	3.969	1.00	12.91	4.26	1.32
D93-B57	0.416	1.318	3.618	1.18	8.67	10.81	1.59
D93-B52	0.436	1.318	3.626	1.00	8.98	5.05	1.31

Rods with high numerical aperture were inserted in overcladding hollow cylinders to draw single mode fibers by RIT-process. The fibres had a depressed innerclad structure:

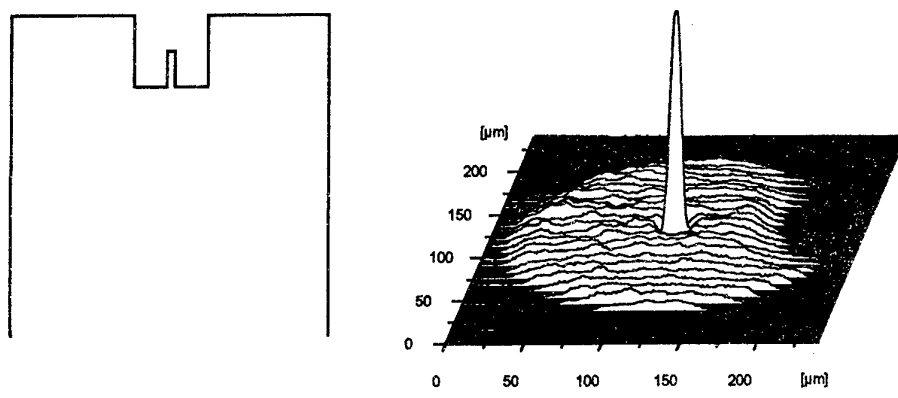


Figure 1: refractive index structure and intensity distribution of a single mode fibre at 1.02 μm

Single mode fibres with different refractive index overcladding were drawn by variation the germanium concentration of the hollow cylinders.

As one of the major problems of the preparation we found microscopic defects and inclusions. Obviously most of these imperfections were originated in the preform hollow cylinder inner surface quality. They could be mostly avoided by an improved inner surface treatment. We have drawn for the first time a praseodymium doped arsenic sulfide single mode fibre with a similar background loss like the unstructured multimode fibre.

Table 3: comparison of unstructured core glass fibre with single mode fibre

	unstructured core glass fibre	single mode fibre		
diameter	200 μm	core 2.5 μm	innerclad 20 μm	overclad 125 μm
refractive index (1.3 μm)	2.430	2.430	2.399	2.446
Pr ³⁺ concentration	754 wt.ppm	754 wt.ppm		
loss at 1.02 μm	6.7 dBm ⁻¹	6.7 dBm ⁻¹		
loss at 1.3 μm	2.0 dBm ⁻¹	3.3 dBm ⁻¹		
fluorescence peak maximum	1.337 μm	1.337 μm		
FWHV	74 nm	74 nm		

CONCLUSIONS

Praseodymium doped single mode fibers based on arsenic sulfide were drawn by combined double crucible and RIT-process. The fibres have a small core-high NA structure for amplifier application. The attenuation of single mode fibres was limited most by microscopic defects at innerface innerclad-overcladding. They could be decreased by high quality surface treatment of

the inner bore surface. Best attenuation values at 1.3 μm were now 3.3 dBm^{-1} . The test for amplifier application is in preparation.

ACKNOWLEDGEMENTS

This research was supported by the German Ministry of Education, Science, Research and Development under contract FKZ 01BP446/0.

REFERENCES

- [1] Johannes Kirchhof, Jens Kobelke, Michael Scheffler, Anka Schwuchow, "As-S based materials and fibres towards efficient 1.3 μm fibre amplification", *Electr. Lett.* 32 (13), (1996), 1220-1221

- [2] Michael Scheffler, Johannes Kirchhof, Jens Kobelke, Anka Schwuchow, "Pr³⁺ doped sulfide glasses for optical applications", *Proc. 10th Internat. Symp. On Non-Oxide Glasses*, Corning, N.Y., 18.06.-22.06. 1996, pp. 544-548

Further author information:

Email: Kobelke@main.ipht-jena.de, Tel. +49/3641-302 818

EXTRUSION OF GALLIUM LANTHANUM SULPHIDE GLASSES FOR FIBREOPTIC PREFORMS.

D. Furniss and *A.B. Seddon.

Centre for Glass Research, Department of Engineering Materials, University of
Sheffield, Sheffield S1 3JD, UK.

Glasses based on gallium lanthanum sulphide (GLS) are being developed as low phonon energy hosts for rare earth doping, potentially allowing the construction of waveguide devices for 1.3 μm all-optical amplification and for near- and mid-infrared lasing and sensing. The glasses can be prepared by melting the component sulphides at 1150°C. However the glass-forming liquids devitrify rapidly at the temperatures required for forming and shaping using the usual methods of hot working. This has led to the rod and tube geometries necessary for fibre preforms being manufactured by machining from a solid billet, so producing much waste and a poor surface finish.

In this work we report the use of an extrusion process in order to improve the quality and efficiency of the production of rods and tubes for fibre preforms. Extrusion utilises a relatively low forming temperature to shape the GLS glasses, so that the rate of crystallisation should be considerably reduced. In the extrusion process, a billet of GLS glass is forced at high pressure and high viscosity through a die of particular dimension, so imparting that dimension to the glass. The billet can be as-cast from the glass melting process, so eliminating any machining process.

* Corresponding author.

Tel: +44 (0)114 222 5516. Fax: +44 (0)114 222 5943. email: a.b.seddon@sheffield.ac.uk

STRUCTURE AND PROPERTIES OF ION-BEAM SPUTTERED $\text{As}_x\text{S}_{1-x}$ FILMS: FROM GLASS TO IDEAL AMORPHOUS STATE.

M.D. Mikhailov^{a*}, I.I. Kryzhanowsky^a, I.M. Petcherizin^b

^aS.I. Vavilov State Optical Institute, Babushkina str. 36, St. Petersburg, 193171, Russia.

Email mikhail@mmd.spb.su

^bInstitute of Chemistry, St-Petersburg State University, Universitetskaya emb. 7/9, St-Petersburg, 199034, Russia. Email Igor.Petcherizin@pobox.spbu.ru

INTRODUCTION

The problem of correlation between the structure and properties for amorphous films and bulk glasses is important because of many application of chalcogenide glasses as thin films. The investigations of thermally evaporated As_2S_3 films have shown that as-deposited films contain essential portion of homobonds that was explained as the existence of As_4S_4 , As_4S_3 , S_n molecules "frozen" at the time of condensation [1-4]. Annealing or light exposure cause the polymerization which sets to the formation of chemically ordered continuous Zachariasen's network.

Properties of the films prepared by three different methods of vacuum deposition, thermal evaporation from the opened surface, discrete evaporation and ion-beam sputtering, have been compared for As_2S_3 films [5]. Ion-beam sputtered (IBS) films were found not similar to the thermally evaporated films. Taking into account that the IBS-films possess such advantages as a high adhesion to a substrate and a low quantity of the defects, we have investigated the structure and properties of $\text{As}_x\text{S}_{1-x}$ IBS-films in more detail. In this paper, we shall describe some results of this studying.

EXPERIMENTAL

Glasses and crystals of As – S system with As content from 33 to 57 at.% were prepared by the standard method of synthesis in the silica ampoules.

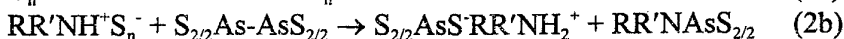
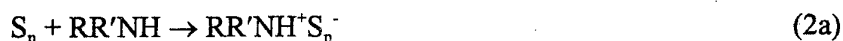
The sputtering setup was made using standard vacuum system. As an ion source the Kaufmanns's one with the tungsten cathode was entered to the vacuum system. Diameter of ion beam was 100 mm. The glassy or crystalline target was being on metal surface cooled by water. The angle of sputtering was 45°. The ion energy from 2 to 2.5 keV was used to sputter. The condensation rate was from 0.03 to 1 nm/s in dependence on the target composition, the energy and the ion current.

The films structure was investigated using the IR-spectroscopy in the range from 400 to 200 cm^{-1} where the characteristic vibrations of As-S containing fragments are located. IR spectra obtained were compared with the ones for glasses, crystals and thermally evaporated films with the same compositions.

The exposure of films was made by light of Hg-lamp. The annealing of films was made at from 120 to 150 °C. The etching rates were measured by standard interferometer method at $\lambda=633$ nm. Amine solutions were used as etchants. At the etching of films, two different reactions take place simultaneously [6].



* Present address: Corning Scientific Center in St. Petersburg, WESTPOST PO BOX 109, Lappeenranta, FIN-53101, Finland. Email corning@infopro.spb.su



To know a phase state of films before and after exposure and annealing the X-ray analysis was made.

RESULTS

Glasses and two crystalline molecular compounds, As_4S_4 and As_4S_3 , were chosen to sputter. All as-deposited films were obtained in amorphous state even their composition is outside of glass formation area. Let us consider at first the IR spectra and their change at annealing or after exposure.

For as-deposited films with arsenic content from 33 to 57 at.%, IR-spectra of IBS-films seem very similar: the most intensive absorption band is the one at 310 cm^{-1} , the bands at 340 and 370 cm^{-1} are displayed as shoulders. The relative intensities of the latter two bands increase with a growth of As concentration in the films. As

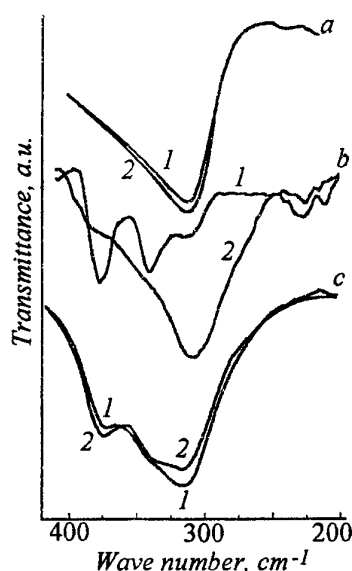


Fig. 1. IR spectra of (1) as-deposited and (2) exposed (a) IBS $As_{33}S_{67}$, (b) thermally evaporated and (c) IBS As_2S_3 films.

an illumination as an annealing of the films containing less than 40 at.% As results as some enlargement of intensity of the main absorption band at 310 cm^{-1} in their IR-spectra (fig. 1).

The intensity of the band at 310 cm^{-1} in IBS-films with As content more than 40 at.% decreases further after irradiation or annealing and an simultaneously the absorption at 340 and 370 cm^{-1} increases (fig 1, c). The most unexpected effects are obtained for As_4S_4 and As_4S_3 IBS-films. As example, IR-spectra of As_4S_3 IBS-films are presented in fig. 2. For as-deposited IBS-film, the spectrum distinguishes as from the one of thermally-evaporated As_4S_3 film as well as from the spectrum of crystalline dimorphite. The spectra of As_4S_3 IBS-films are similar to the ones of $As_{42}S_{58}$ and $As_{44}S_{56}$, and also to the IR-spectra of the bulk glasses enriched by As in relation to the stoichiometry of As_2S_3 . The absorption band at 320 cm^{-1} is the most intensive, the band at 344 cm^{-1} is displayed in a kind of a shoulder, the third band is observed at 370 cm^{-1} as a shoulder too. In contrast to the

light action, annealing of as-sputtered As_4S_3 films leads to the obtaining of the IR-spectrum characterized by another set of the bands. A presence of the strong band at $224\text{--}225\text{ cm}^{-1}$ (comparable on its intensity to the one at $202\text{--}206\text{ cm}^{-1}$) and the band at 344 cm^{-1} (more intensive than the one at 374 cm^{-1}) is agreed with the character features of the IR spectra for the bulk polycrystalline realgar As_4S_4 and for its annealed IBS-layers. After illumination by light of Hg-lamp as well as at annealing, the absorption edge of IBS-films is shifted to the short-wave spectral region. It corresponds to the photobleaching (fig. 3). Such influence of light and annealing on the absorption edge position is a contrary to the photodarkening which is typically obtained for thermally-evaporated As-S films. Earlier, the photobleaching of As-S layers induced by light exposure or by heating has been observed only if the forced evaporation methods are used ($T_{\text{evap}}=600\text{--}1000\text{ K}$) [7-9].

IBS-films that contain As less than 44 at. % are always stable to crystallization in the cycles "irradiation-annealing". It is suddenly that, starting from $\text{As}_{44}\text{S}_{56}$ composition, the sequence of both the light exposure and the annealing effects on the phase state of film. Namely, if as-deposited film is initially annealed it will remain transparent and amorphous after next "irradiation-annealing" cycles, whereas the films exposed previously will become to crystal-

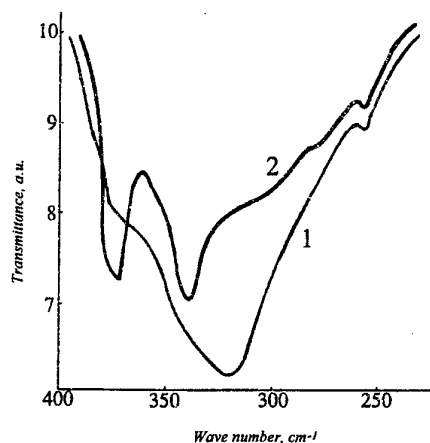


Fig. 2. IR spectra for (1) as-deposited and (2) exposed As_4S_3 IBS films.

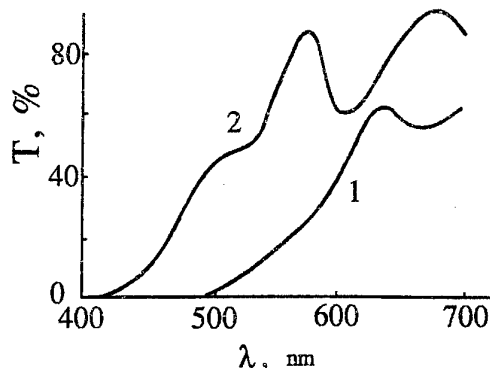


Fig. 3. Absorption edges for (1) as-deposited and (2) exposed As_4S_3 films.

line state at the annealing and be opaque.

Chemical properties of IBS-films are differed from the ones of thermally evaporated films and bulk glasses. IBS-films do not practically interact with the solutions of dialkylamines in aprotic solvents which had been proposed earlier to etch thermally evaporated As_xS_y films [10]. The dissolution rates were measurable (more than 0.01 nm/s) at the use of high-basic amines such as morpholine or primary amines in the solvents with high permittivity (dimethylsulfoxide, dimethylformamide). Thermally evaporated films dissolve instantaneously in these etchants.

It follows from interferometric measurements that the dissolution rates of as-deposited films do not change in the etching process. It testifies the uniformity of the film properties into its depth.

Fig. 4 presents the dependence of dissolution rates on the content of As in the IBS-films. The solution of 45% morpholine in dimethylformamide was used for these measurements. The minimal etching rate corresponds to As_2S_3 composition. This composition has the maximally-possible concentration of the heteropolar bonds As-S. The deviations from the stoichiometric composition lead to diluting of the disordered network with the homopolar bonds. Similar dependence of the dissolution rate on As content is characteristic also for the etching of bulk As-S glasses in the amine solutions [6]. Unlike bulk glasses and the products of their sputtering, the IBS-films of the compositions of As_4S_4 and As_4S_3 are stable to an action of the solutions of amines as well as the bulk molecular crystals As_4S_4 and As_4S_3 . To do them soluble in these etchants it was necessary to enter the suitable oxidant (the dissolved sulfur) into the amine solution. It let us to realize reaction (2). An application of the solutions of isopentylamine or morpholine in dimethylsulfoxide or dimethylformamide containing the dissolved sulfur, in concentration from 0.01 up to 0.1 mole/l, as an etchant allowed us to obtain the acceptable value of dissolution rates for As_4S_4 and As_4S_3 IBS-films.

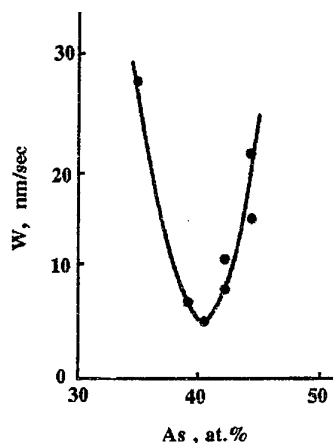


Fig. 4. Dependence of the dissolution rate of IBS $\text{As}_x\text{S}_{1-x}$ films on the As content.

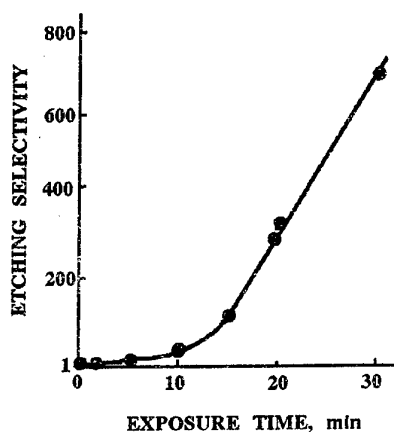


Fig. 5. The dependence of etching selectivity on exposure time for As_4S_3 films.

After exposure of As_4S_3 or As_4S_4 IBS-films, their dissolution rate increases, i.e. the positive photoresistive effect is observed. The obtained values of etching selectivity depend on the irradiation dose and amount to dozens and hundreds (fig. 5). Such values of selectivity were observed for the films deposited at condensation rate of 0.05-0.07 nm/sec. The photosensitivity of IBS $\text{As}_x\text{S}_{1-x}$ films is small. For continuous exposure with $\lambda=488$ nm, the energy more than 10 J/cm² is required to obtain phase hologram with relief depth about 0.3 μm .

DISCUSSION

A comparison of the properties for $\text{As}_x\text{S}_{1-x}$ IBS-films with the similar data for other amorphous and crystalline materials i.e. for bulk glasses, molecular crystals and thermally-evaporated films, allows us to make the following general conclusion.

The properties of IBS-films distinguish as from the thermally evaporated films as from the bulk analogs (glasses and crystals) of the same compositions. This difference shows itself as phenomenologically (amorphous state of As_4S_4 and As_4S_3 IBS-films, photo- and thermo-bleaching, high chemical stability) as spectrally.

For $\text{As}_x\text{S}_{1-x}$ glasses, the absorption band at 311-313 cm⁻¹ is connected with the vibrations of pyramidal $\text{AsS}_{3/2}$. Frequencies 340 and 370 1/cm are known as characteristic doublet in the spectra of the molecular crystals of As-S system, namely, of realgar As_4S_4 and dimorphite As_4S_3 . For all composition including As_4S_4 and As_4S_3 films, the spectral feature of as-deposited IBS-films is that frequency near 310 cm⁻¹ predominates in IR spectra. The exact position of this band depends on both film composition and deposition characteristics (ion current and energy), and it is shifted to lower frequencies if As concentration is decreased (see Table). It means that polymer network is formed at condensation, even if the sputtering of molecular crystal takes place. Frequency shift can be explained as a result of formation of disordered network which contains various structural units, $\text{As}(\text{As}_{3/3})_3$, $\text{As}_{2/3}\text{AsS}_{1/2}$, $\text{As}_{1/3}\text{AsS}_{2/2}$, $\text{AsS}_{3/2}$ etc. The displacement of the oscillation frequency of pyramidal $\text{AsX}_{3/2}$ structural units which is occurred at a change of As content in IBS-films is similar to the phenomenon known for the IR-spectra of SiO_x IBS-films [11, 12]. The structure of as-deposited As_4S_3 and As_4S_4 films is characterized by the covalent disordered network of the pyramids $\text{AsX}_{3/2}$, with the molecular fragments partially bonded into it.

Table. Oscillation frequencies of $\text{AsS}_{3/2}$ pyramids for as-deposited IBS-films.

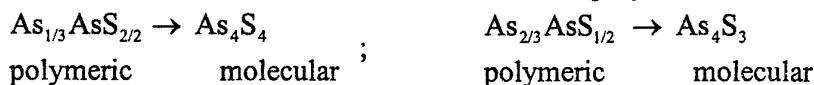
As, at. %	The peak position, $1/\text{cm}$
33	310-312
40	310-320
42	310-320
44	314-315
50	318-320
57	318-320
Glassy As_2S_3	311

* the peak position depends on condensation regime.

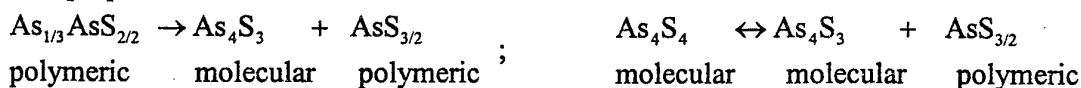
The features of photostructural changes in IBS-films can be interpreted as follows. For films enriched by sulfur, the continuous covalent network is the predominant structural element. This network consists of the polymer structural units of type $\text{AsS}_{3/2}$ being observable in the spectra as a band near 310 cm^{-1} and the polymer ones $\text{SS}_{2/2}$ not displaying themselves in the investigated spectral range. After exposure or annealing, any new IR absorption bands do not appear, but the intensity of the main absorption band near 310 cm^{-1} increases in a little degree (by 2-4% of its absolute size). In these films, the photostructural changes are directed to structural perfection of this disordered network.

Starting from As_2S_3 composition, other type of photostructural changes is observed. In these cases, the spectral features of photostructural changes can be explained on the basis of representations about the photostimulated partial depolymerization of the disordered network resulting to the isolation of the molecular fragments which are similar in its structure and composition to As_4S_4 and As_4S_3 . It is interesting that, for As_2S_3 , the photodepolymerization can be seen from IR spectra also in reversible cycles exposure – annealing at T_g .

The mechanism of photostructural changes in IBS-films may be understand as chemical relaxation (ordering) of the nearest neighbors. At that, the change leads to the formation of stable fragment closed to the nearest fragment which is stable or metastable in bulk form. The direction of the processes of the transformations of the statistically-random structural units can be presented by the following schemes of the reactions of depolymerization:



and of disproportionation:



The processes of the structural-chemical ordering in $\text{As}_x\text{S}_{1-x}$ IBS-layers are in agreement with the known Ostwald's rule of step for chemical reaction, accordingly to which "at chemical processes, at the first stage will be formed not the most stable substances, but the substances which are the nearest to the initial system" [13]. Probably, this conclusion is correctly as for photoinduced as for thermoinduced changes in the investigated IBS-films. Only using this approach we can explain the spectrally observed presence of the As_4S_3 - like molecular fragments in the exposed As_4S_4 films as well as the spectrally-observed appearance of the As_4S_4 -like ones in the annealed As_4S_3 films.

Comparison of the IR-spectra of the As_2S_3 films deposited by different methods shows that a structure of as-deposited films is determined not by the method to transfer As_2S_3 to a vapor phase itself, but by the molecular composition of the vapor. Only the stable molecular fragments having a crystalline analog might be frozen in the film. At condensation, non-saturated molecules will form the polymer atomic network characterized by the distribution of bonds which is closed to the random one [5]. For ion-beam sputtering, we can assume that non-defined fragments of glassy or crystalline target are knocked out to vacuum. As a result, the chemically non-saturated particles form the random polymer network at the condensation.

The results of the investigations of dissolution kinetics for $\text{As}_x\text{S}_{1-x}$ IBS-films agree with the spectroscopic data and confirm the thesis about the difference in structural-chemical ordering between thermally evaporated films and IBS-layers. This difference is expressed as the following experimentally-observed facts:

-IBS-layers are more chemically-stable than thermally-evaporated ones, it confirms the conclusion made above concerning to a high degree of polymerity of IBS-films;

-the direction of the photoresistive effect depends on the As concentration in the film, it changes from negative to positive when As content passes the stoichiometry of As_2S_3 ;

CONCLUSION

The structure and properties of $\text{As}_x\text{S}_{1-x}$ IBS-films are considered as experimental realization of the model of the network chemically and structurally disordered and closed to the pure-statistic kind of ordering where only coordination numbers are permanently. This kind of ordering corresponds to the following situation: the continuous covalent structural network is built of the structural units, the forms of which are determined by coordination numbers of the atoms, but their chemical composition is random. The structural individuality in the investigated concentration region is the trigonal-pyramidal unit of type $\text{AsAs}_{n/3}\text{S}_{(3-n)/2}$ ($n = 0, 1, 2, 3$) of statistically-random chemical composition.

REFERENCES

- [1] H. Strom, T.P. Martin, Solid State Comm. 29 (1979) 527.
- [2] R.J. Nemanich, G.A.N. Connel, T.M. Hayes, R.A. Street, Phys. Rev. B 18 (1978) 6900.
- [3] T. Takahashi, Y. Hamada, Solid State Comm. 33 (1980) 191.
- [4] S. Onari, K. Asai, T. Arai, J. Non-Crystall. Sol. 86 (1985) 243.
- [5] I.M. Petcherizin, I.I. Kryzhanowsky, M.D. Mikhailov, Sov. J. Phys. and Chem. of Glass 1988 in press.
- [6] S.A. Zenkin, S.B. Mamedov, M.D. Mikhailov, E.Yu. Turkina, I.Yu. Yusupov, Sov. J. Phys. and Chem. of Glass, 23 (1997) 560.
- [7] I.I. Turyanitsa, A.A. Kikineshi, D.G Semak, Sov. Ukrainish Phys. J. 24 (1979) 534 .
- [8] B.T. Kolomiets, V.M. Lyubin, V.A. Fedorov, Sov. J. Techn. Phys. Lett. 5 (1979) 3.
- [9] I.M. Petcheritsin, M.D. Mikhailov, M.D. Balmakov, Sov. J. Inorganic Materials. 17 (1981) 909.
- [10] A.S. Dneprovskii, S.B. Mamedov, M.D. Mikhailov, K.A. Stepanov, R.R. Gerke, O.A. Yakovuk. USSR Inventor's Certificate N 1230145(1986) (unpublished).
- [11] L.Schumann, A. Lehmann, H. Sobotta, V. Riede, U. Teschner, K. Hubner, Phys. Stat. Sol.(b) 110 (1982) 69.
- [12] A.P. Dostanko, E.S. Akulich, V.Ya. Shiripov, S.A. Sobolev, Sov. J. Appl. Spectr. 50 (1989) 436.
- [13] B.V. Nekrasov, General Chemistry (Goshimisdat, Moskow, 1955).

IONIC CONDUCTION AND STRUCTURAL INVESTIGATIONS IN PbO-PbCl₂-CdCl₂ GLASSES

S. Donze, , L. Montagne*, H. Hareux, G. Palavit

Laboratoire de Cristallochimie et Physicochimie du Solide, URA CNRS 452,

Ecole Nationale Supérieure de Chimie de Lille, BP 108,

59652 Villeneuve d'Ascq cedex - France.

e-mail : lionel.montagne@univ-lille1.fr

* corresponding author

ABSTRACT

We have investigated the electrical conductivity of the PbO-PbCl₂-CdCl₂ oxychloride glasses by impedance spectroscopy. All glasses exhibit Arrhenius behaviour in log (conductivity) versus reciprocal temperature plots. The observation of a polarisation effect for a fixed applied voltage indicates that the electrical conductivity in PbO-PbCl₂-CdCl₂ glasses is due to the migration of ions rather than electrons. The evolution of the isothermal ionic conductivity with the glass composition can be described considering both chloride ions or Pb²⁺ ions as charge carriers. Structural characterisation of Pb environment in PbO-PbCl₂-CdCl₂ glasses has been achieved using ²⁰⁷Pb NMR spectroscopy. Local environment of lead atoms becomes more ionic as PbCl₂ is substituted for PbO. Ionicity of lead coordination is not affected by the substitution of PbCl₂ for CdCl₂. Our aim was to elucidate the local environment of Pb atoms in such a disordered system in order to explain the evolution of the conductivity with the glass composition.

INTRODUCTION

A large interest has developed in anionic conduction and particularly in halide conducting materials for sensors. The halide anionic conductivity in lead halosilicate glasses was first reported by Schultz and Mizzoni [1] and then, by Horton and Shelby [2]. Sundar et al. [3] have investigated ionic conduction in lead halide - lead metaphosphate glasses and have reported that the conduction was principally due to halide ions rather than to the Pb²⁺.

In this work, we have studied the electrical conductivity of PbO-PbCl₂-CdCl₂ glasses. The high chloride content of these glasses is of potential interest for the elaboration of chloride conducting glasses. Moreover the high polarisability of heavy metals is favourable to enable the mobility of large charge carriers.

The modification of the polarisable cations environment will influence the electrical conductivity of PbO-PbCl₂-CdCl₂ glasses. We have used ²⁰⁷Pb NMR spectroscopy to elucidate the local environment of atoms in a such disordered system in order to explain the evolution of the conductivity with the glass composition.

EXPERIMENTAL PROCEDURE

Glass preparation

The PbO - PbCl₂ - CdCl₂ oxychloride glasses are prepared from PbO, PbCl₂, CdCl₂ as raw materials. Batches of 5 g are melted in quartz crucibles covered with a lid in an electric furnace for 30 min. between 600°C and 700°C, depending on the PbO content. The melts are poured into a cooled brass mould to avoid their devitrification. The glasses are annealed at T_g for two hours and allowed to cool in the furnace.

Weight loss measurements and chemical analysis of chlorine indicate that no significant volatilisation of chlorinated species occurs during melting.

Glass transformation (T_g) temperatures were determined using a differential scanning calorimeter (Setaram D.S.C. 141) at a heating rate of 10 °C/min.

Structural analysis

²⁰⁷Pb NMR spectra are very broad because the polarizability of Pb^{2+} electronic cloud leads to very large chemical shift anisotropy. Moreover, in glassy materials, the disorder also increases the chemical shift anisotropy owing to lead environment distribution. In such conditions, MAS can not improve spectrum resolution. ²⁰⁷Pb NMR spectra were obtained with the variable offset cumulative spectrum method VOCS : the spectrum results in the sum of 5 static echos recorded with 80 kHz offset. The pulse sequence is $(\pi/2 - \tau - \pi - \text{acq})$ with $\pi/2 = 3 \mu\text{sec}$, $\tau = 60 \mu\text{sec}$, $\pi = 6.5 \mu\text{sec}$. Recycling delay is 30 sec, sufficient to enable spin relaxation. The spectra were recorded at 83.71 MHz (9.4T). Chemical shifts are referenced to a 0.5 M aqueous solution of lead nitrate at -2941 ppm vs tetramethyl lead at 0 ppm.

Electrical measurements

For electrical measurements, gold electrodes were deposited by sputtering on each face of polished glass samples of approximately 1 mm thickness. A.C. electrical conductivity measurements were carried out using impedance spectroscopy in the 20°C - 250°C temperature range by varying the measurement frequency from 1 to 10^6 Hz.

Application of a 900 mV DC voltage with a regulated power supply leads to a decrease of the intensity toward zero within a few minutes. The observation of this polarisation effect can be taken as an evidence that the electrical conductivity is due to the migration of ions rather than electrons.

RESULTS

Glass formation and Glass Transition temperature

Figure 1-a represents the glass forming region described by Fue-Jie et al. []. We can notice on figure 1-b that the use of quartz crucible enables glass formation thanks to dissolution of silica during glass melting. We have measured the amount of SiO_2 in the oxychloride glasses by X-ray fluorescence spectroscopy and it appears that the amount of silica dissolved in the melt during glass melting is low (less than 6 mol. %). We have treated SiO_2 as primarily an impurity and given the compositions of glasses in terms of batch composition. $(80-x) \text{PbO} - x\text{PbCl}_2 - 20\text{CdCl}_2$ glasses, i.e. glasses with constant cationic fraction in batch composition, are located among line A on figure 1-b. On the same figure, line B represents glasses of $30 \text{PbO} - x\text{PbCl}_2 - (70-x)\text{CdCl}_2$ composition, i.e. glasses with constant anionic fraction.

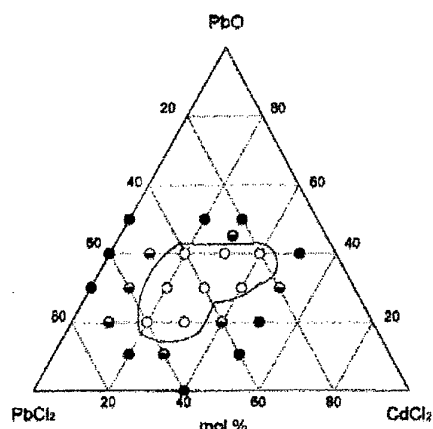


Figure1-a

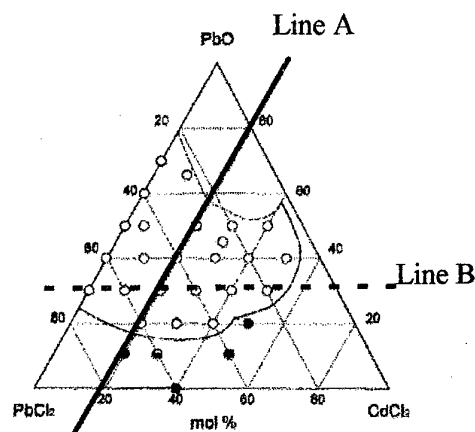


Figure1-b

Figure1-a : Glass forming region described previously by Fue-Jie et al. [5].

Figure 1-b : Glass forming region extended thanks to dissolution of silica during the glass melting.

The effect of PbCl_2 substitution for PbO in $(80-x)\text{PbO} - x\text{PbCl}_2 - 20\text{CdCl}_2$ on the glass transition temperature is illustrated on figure 2. We can observe a 100°C decrease as PbCl_2 concentration varies from 30 to 60 mol. %. This evolution of T_g is characteristic of a weakened and expanded network as PbCl_2 replaces PbO , i.e. as one O^{2-} is substituted by two larger chloride anions [6].

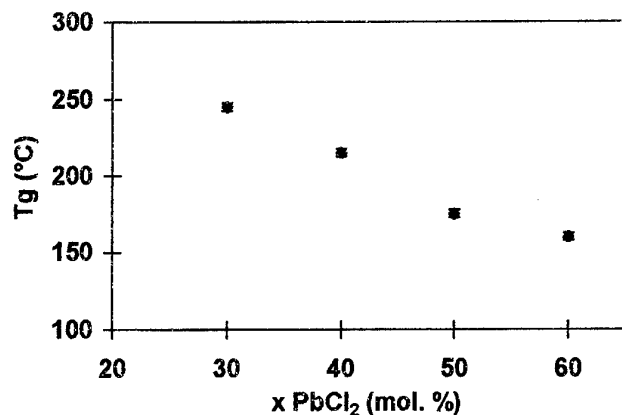


Figure 2 : Effect of the glass composition on the glass transformation temperature of $(80-x)\text{PbO} - x\text{PbCl}_2 - 20\text{CdCl}_2$ glasses.

No significant evolution of T_g with composition along line B on figure 1-b for $30\text{PbO} - x\text{PbCl}_2 - (70-x)\text{CdCl}_2$ glasses can be deduced from figure 3. We can then affirm that the substitution of CdCl_2 for PbCl_2 does not modify the glass network. The small variation in the T_g values may be due to differences in glass density owing to the close values of Pb^{2+} and Cd^{2+} ionic radii ($r_{\text{Pb}^{2+}} = 1.18 \text{ \AA}$; $r_{\text{Cd}^{2+}} = 0.95 \text{ \AA}$, values given by Shannon [6] for a six fold coordination state).

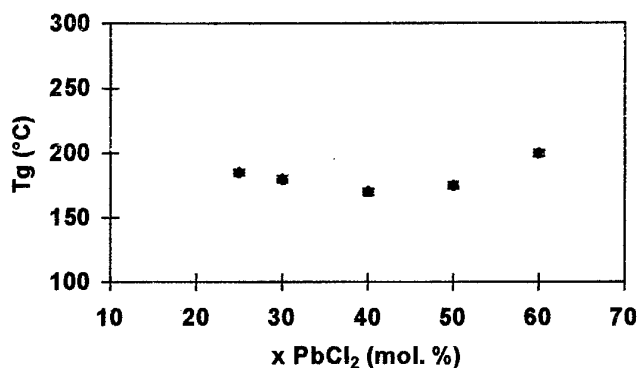


Figure 3 : Effect of the glass composition on the glass transformation temperature of $30\text{PbO} - x\text{PbCl}_2 - (100-x)\text{CdCl}_2$ glasses.

Ionic conductivity

As all glasses studied exhibit Arrhenius behaviour in $\log(\text{conductivity})$ versus reciprocal temperature plots, the effect of the glass composition on the electrical conductivity will be discussed by considering the isothermal conductivity. The results obtained at 160°C are reported in Figures 4 and 5. Figure 4 plots the evolution of the isothermal conductivity as PbO replaces PbCl_2 in glasses containing a fixed amount of CdCl_2 ($(80-x)\text{PbO} - x\text{PbCl}_2 - 20\text{CdCl}_2$.) The effect of the substitution of PbCl_2 for CdCl_2 in $30\text{PbO} - x\text{PbCl}_2 - (70-x)\text{CdCl}_2$ glasses is shown on Figure 5. In both cases (Figures 4 and 5), we can observe that the isothermal

conductivity is function of the PbCl_2 content. We can note that $\sigma_{160^\circ\text{C}}$ rises of nearly two orders of magnitude as PbCl_2 concentration varies from 30 to 60 mol. %.

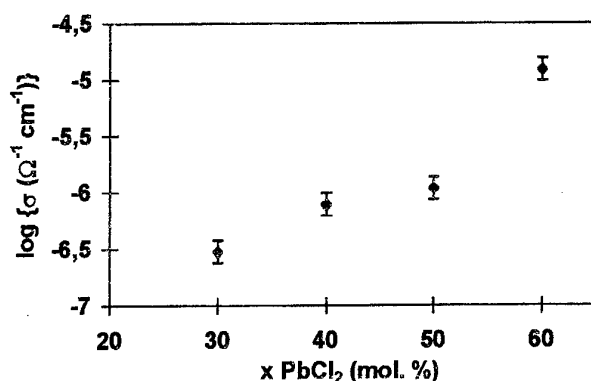


Figure 4 : Effect of the glass composition on the isothermal (160°C) electrical conductivity of (100-x) PbO- x PbCl₂ - 20 CdCl₂ glasses.

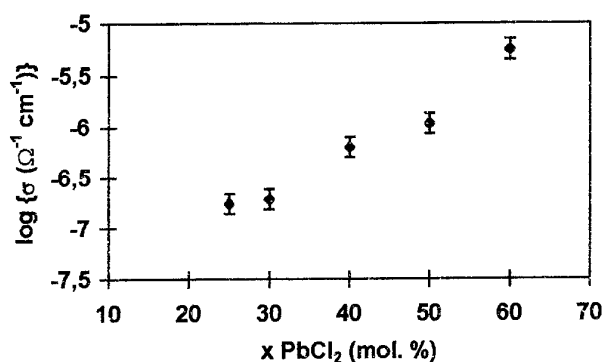


Figure 5: Effect of the glass composition on the isothermal (160°C) electrical conductivity of 30 PbO- x PbCl₂ - (100-x) CdCl₂ glasses.

Structural analysis

The ^{207}Pb spectra of (80-x)PbO -xPbCl₂ -20CdCl₂ glasses are presented on figure 6. They reflect the evolution of the shielding on lead nuclei as PbO is substituted for PbCl₂ in the glasses (line A on Figure 1-b). The spectrum of the 53.33PbO-26.67PbCl₂-20CdCl₂ glass is very broad, it is spread from -2000 to 2000 ppm, thus it reflects a very strong chemical shift anisotropy. The spectrum of the 30PbO-50PbCl₂-20CdCl₂ glass tends toward more negative chemical shifts and shows less chemical shift anisotropy. Although isotropic chemical shift can not be measured accurately on such spectra, the comparison with the spectra of crystalline PbO and PbCl₂ reveals that the spectra of the oxychloride glasses are consistent with a lead environment containing both oxygen and chlorine.

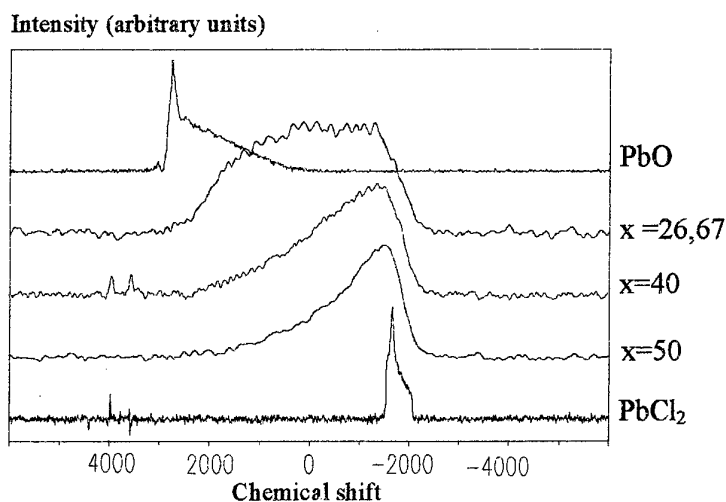


Figure 6 : ^{207}Pb NMR spectra of crystalline PbO , and $(80-x)\text{PbO}-x\text{PbCl}_2-20\text{CdCl}_2$ glasses.

The ^{207}Pb NMR spectra of $30\text{PbO}-x\text{PbCl}_2-(70-x)\text{CdCl}_2$ glasses (Figure 7) remain similar as PbCl_2 is substituted for CdCl_2 (line B on Figure 1-b).

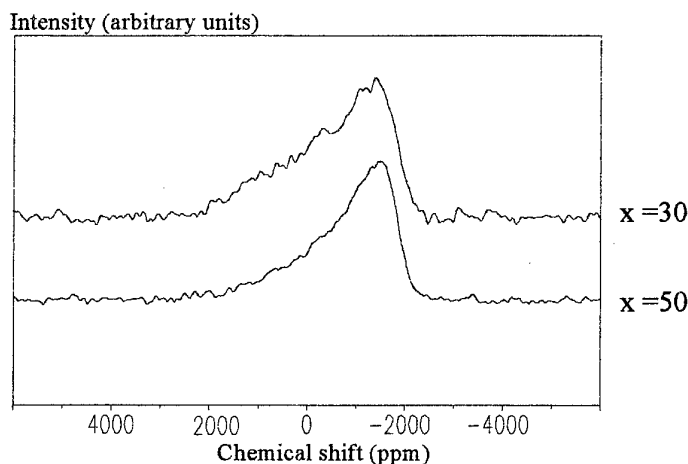


Figure 7 : ^{207}Pb NMR spectra of $30\text{PbO}-x\text{PbCl}_2-(70-x)\text{CdCl}_2$ glasses.

DISCUSSION

The polarisation effect on glasses observed at fixed applied voltage allows us to state that the $\text{PbO}-\text{PbCl}_2-\text{CdCl}_2$ glasses are ionic conductors. Two hypotheses can be proposed to support this observation. In the first one, we'll suppose that the electrical conductivity is due to the migration of chloride ions, and in the second one, Pb^{2+} ions will be considered as charge carriers.

The evolution presented on Figure 4 supports the first hypothesis. In this case, the improvement of the conductivity can be attributed to an increase of the quantity of charge carriers by the substitution of PbCl_2 for PbO . We can also correlate this assumption with the results shown on Figure 5. If we consider the replacement of CdCl_2 by PbCl_2 the amount of

chloride ions (n_{Cl^-}) remains constant. The enhancement of the electrical conductivity is attributed to the introduction of a more polarisable cation in the glass structure. The electronic structure of Pb^{2+} ions, and particularly the presence of an electronic lone pair can actually enhance the mobility of large charge carriers like Cl^- ions through the glass structure.

Let's now consider the second hypothesis : Figure 5 shows the improvement of the electrical conductivity as PbCl_2 replaces CdCl_2 , while n_{Cl^-} remains constant, i.e. as the amount of lead ions ($n_{\text{Pb}^{2+}}$) in the glass network arises. Thus, the enhancement of the cationic conductivity, due to the Pb^{2+} ions, is associated to the increased number of charge carriers. This second hypothesis is also supported by the open network structure model which has been used by El-Damrawi [5]. According to this model, it is considered that the glassy network structure becomes weakened and expanded as PbCl_2 replaces PbO . The decrease of T_g as PbCl_2 is substituted for PbO illustrates this model. We can deduced from the characterisation of local Pb environment by ^{207}Pb NMR and according to the empirical correlations reported by Fayon et al. [7] that the ionicity of lead-chloride and lead-oxygen bonds increases as PbO is replaced by PbCl_2 (line A on Figure 1-b). In such an environment with weaker bonds, Pb^{2+} charge carriers can leave their sites more easily and move through the network. So, the evolution presented on Figure 4 can be regarded as the enhancement of the cationic conductivity by the expansion of a more ionic glassy network.

CONCLUSION

The electrical conductivity reported for oxychloride $\text{PbO} - \text{PbCl}_2 - \text{CdCl}_2$ glasses has been found to be due to the migration of ions. The evolution of the isothermal ionic conductivity with the glass composition can be explained either considering Cl^- ions or Pb^{2+} ions as charge carriers. Measurements of current for a fixed applied voltage with lead electrodes (non blocking electrodes to Pb^{2+} ions) lead to a residual steady state current. This can be considered as an evidence of the participation of Pb^{2+} ions into the conduction mechanism.

Other experiments using impedance spectroscopy have shown rapid and reversible reactions at the electrodes (at low frequency) under a Cl_2 atmosphere. It can be assumed that the electrical conductivity is also due to the migration of Cl^- ions in the glass structure. Transport number measurements will be achieved by coulo-dilatometry to quantify the role of both possible charge carriers in the electrical conduction observed in the $\text{PbO} - \text{PbCl}_2 - \text{CdCl}_2$ oxychloride glasses.

REFERENCES

- [1] P.C. Schultz, M.S. Mizzoni, *Journal of The American Ceramic Soc.*, 56 [2], 65-68 (1973).
- [2] M. Horton, J.E. Shelby, *Physics and Chemistry of Glasses*, 34 [6], 238-243 (1993).
- [3] H.G.K. Sundar, S.W. Martin, C.A. Angell, *Solid State Ionics*, 18&19, 437-441 (1986).
- [4] Fu Jie, H. Yatsuda, *Journal of Materials Science Letters*, 14, 580-581(1995).
- [5] G. El Damrawi, *Journal of Non Crystalline Solids*, 176, 91-97 (1994).
- [6] R.D. Shannon, *Acta Crystallogr., Sect. A*, 32, 751-67 (1973)
- [7] F.Fayon, I. Farnan, C. Bessada, J. Coutures, D. Massiot, J.P. Coutures, *Journal of American Chemical Society*, 119 (29), 1997

Optical measurements of the electronic energy gap and structural implications for alkali tellurite glasses

W. Ash D.B. Hollis

Department of Electronic Engineering & Physics
University of Paisley
Paisley PA1 2BE

Introduction

A series of alkali tellurite glasses of formula $XR_0O \cdot (1-X) TeO_2$, where $X = 0$, and 10 to 33.3 molar percent was prepared by melting together the alkali carbonates of lithium, sodium, or potassium with tellurium oxide in the correct molar proportions at 850°C for 30 minutes. After casting into disks the glasses were annealed at 250°C for 30 minutes, then cooled at 1°C per minute to ambient. For the melting, recrystallised alumina crucibles were used. Electron microscope analysis by secondary electron emission indicated take-up of about 2% of Al_2O_3 on the glass allowed us a larger range of alkali content than is usually reported for these glasses in the literature.

Density measurements were carefully made by Archimedes principle with toluene as the immersion fluid.

Ultraviolet-visible absorption spectra were taken over the range 340-540 nm, using the glass disks in a Hitachi U3501 spectrometer.

The electronic energy gap and the density of a glass are related to structure by the coordination of the tellurium ions by the oxygens. Of particular significance is the number of non-bridging oxygens coordinating to each tellurium ion. This last parameter is strongly affected by the alkali oxide content.

From the densities, molar volumes for the oxygens, alkali ions, and tellurium ions were determined. Trends with alkali content will be discussed in terms of the changes in the network forming structure of the glass with alkali content from a 3-dimensional network of TeO_4 trigonal bipyramids linked in chains. As the modifier oxide is added, non bridging oxygens are formed in the structure. Additionally it is believed that the TeO_4 trigonal bipyramids change to TeO_{3+1} tetrahedra. Since non bridging oxygens bind electrons less strongly than bridging oxygens we expect the optical absorption cut off to move to longer wavelengths as alkali is added. However, the change from TeO_4 to TeO_{3+1} is also expected to affect the absorption spectra, by shortening the cutoff wavelength, as the alkali content increases. These effects are interpreted in terms of the number of non-bridging oxygens per TeO_4 polyhedron. For no alkali, all four corners will be joined to other tetrahedra by bridging oxygens (Q4). As alkali is added, an increasing number of non-bridging oxygens is formed, and tetrahedra become joined by only 3 corners (Q3). One might expect a random mixture of Q4 and Q3 with even Q2 tetrahedra. However, M.A.S. N.M.R. experiments reported in the literature by R. Dupree and D. Holland (University of Warwick) and computer simulations by CRA Catlow and co-workers (Royal Institution and Keele University)

suggest a "constrained" model in which no Q2 are formed until all Q4 are converted to Q3. Our results show otherwise. The change in energy gap with alkali content is rapid around several molar compositions, notably 20% and 30%. This implies that some Q3 are changing to Q2 while some Q4 still remain. Full analysis and interpretation will be reported at the glass congress.

Estimation of the electronic energy gap from the optical spectra was done in three ways, to yield information about the structure of the electronic energy bands on either side of the bandgap. A visual extrapolation of the steep absorption edge to the wavelength axis was supplemented by Tauc and Urbach curve fits to the optical spectra. Urbach showed that impurity states in semiconductors just above the valence band, or just below the conduction band would lead to a thermalised energy gap narrowing, and give an absorption curve of form $\alpha(\lambda) = \alpha(0) \exp(hc / \lambda / E_0)$ where E_g is the gap energy. This relation has been found for many glasses as well as semiconductors. Changes in the Urbach energy E_0 as well as the energy gap obtained by extrapolation of the Urbach plot to the wavelength axis will be discussed in terms of disorder in the glassy structure.

Tauc showed that if the variation of density of electronic states with energy for the valence and conduction bands departs from the usually assumed parabolic function, then near the centre of the electronic absorption band, a tailing effect will exist, of the form $\alpha(\lambda) = A^2 (hc / \lambda - E_T)^2 / (hc / \lambda)$

That is,

$$[\alpha(\lambda) \cdot hc / \lambda]^{\frac{1}{2}} = A(hc / \lambda - E_T)$$

Again, an extrapolation to the wavelength axis gives a value for the energy gap, and the value of E_T - the tailing effect can be found by estimating the slope coefficient A , and the intercept - AE_T . These values will also be discussed in terms of the structural units present, and the disordering of the glass network.

Roger F. Bartholomew, Dianna M. Young and Adam J. G. Ellison
Corning Incorporated, Sullivan Park, FR-05, Corning, NY 14831, USA.

ABSTRACT

High-density energy systems such as lithium-ion batteries have a very promising future. To improve on the present technology requires an understanding of the electrode materials and identification of new electrolytes. For safety reasons, solid state electrolytes are preferred. A number of lithium-ion conductors have been reported in the literature. This study builds on those results, based on the $\text{Li}_2\text{S-SiS}_2$ system. AC Impedance Spectroscopy was used to determine the ionic conductivity of glasses where additions were made of IVA, VA, VB or VIA sulphides to 60/40 $\text{Li}_2\text{S-SiS}_2$ (mol %). These additions improved the stability of these glasses, so much so that thick samples (>2 mm) could be prepared by cooling without quenching. Addition of lithium halides further improved conductivity. Ionic conductivity values $> 2 \times 10^{-3}$ S/cm at room temperature were measured, amongst the highest values reported in the glass literature. The temperature coefficients of these glasses will be reported.

INTRODUCTION

Sahami et al. [1] reported on fast-ion conduction in lithium sulphide based systems in 1985, followed by Pradel [2] in 1986. Since then, many patents and literature references have appeared outlining the potential of lithium-ion conducting glasses as solid electrolytes for secondary battery applications. The base glass contains Li_2S and SiS_2 as major components and the glass forming region has been established to be $x\text{Li}_2\text{S}-(1-x)\text{SiS}_2$, over the range $0.3 < x < 0.6$. Ionic conductivities are typically 1×10^{-3} S/cm. Properties such as light weight, high energy density, high voltage stability, high ionic conductivity, and solid state, make the sulfide glasses an attractive alternative as an electrolyte.

There are several drawbacks in processing the lithium sulfide glass. One particular undesirable characteristic is that the glasses spontaneously devitrify unless quenched rapidly, e.g., splat or roller-quench methods [2], or sputtering. These fabrication methods produce glass flakes or powders, and conductivity measurements must be conducted on pressed pellets. Measurements on pressed pellets are suspect because of grain boundary effects. Ideally, glass samples for conductivity measurements should be solid annealed solid pieces. For this and for more practical reasons, such as building working devices, it is desirable to identify means of stabilizing the glasses without impacting conductivity.

High ionic conductivity coupled with high stability is a difficult balance with the lithium silicon sulfide glasses. It has been established that lithium carbonates, sulphates, phosphates and silicates stabilize lithium silicon sulfide glasses [3], but generally at the expense of ionic conductivity. By contrast, addition of lithium halides such as LiI improves conductivity, but has a neutral or negative effect on glass stability. We report significant improvements in stability and ionic conductivity in the lithium silicon sulfide glass system by adding various Group IVA, VA, VIA and VB sulfides or compounds. These components include SnS , SnS_2 , TaS_2 , BiI_3 , As_2S_3 ,

Sb_2O_3 , and TeO_2 . These additions stabilize the glass sufficiently that melts can be cooled to glass in the crucible, with no heroic quench needed, a major improvement over the base glass. As a result, we are able to obtain homogeneous solid glass patties of various thicknesses that can be easily annealed and their ionic conductivity measured. Moreover, in a few cases the conductivities at room temperature are amongst the highest reported. In these materials, ionic conductivity is further improved by addition of LiX ($\text{X} = \text{Br}, \text{I}$).

EXPERIMENTAL

Because of the extreme hygroscopic nature of the batch materials and resulting glasses all batching, melting, and quenching procedures, as well as the conductivity measurements were carried out in an argon-filled drybox. Starting materials were ground powders readily available from Aldrich, Aesar, or Cerac, with as high purity as could be obtained. Powders were weighed out in 5g batches, mixed, placed in a vitreous carbon crucible, and melted in a furnace at 900°C for 10-15 minutes. The fluid melts were removed from the furnace and quenched on a steel plate. Glasses were flattened with another steel plate to form flat patties for conductivity measurements. Patties of various thicknesses, 1-9 mm, may be formed by this method. All glasses were annealed at approximately 300°C for half an hour, then cooled at furnace rate to room temperature. Compositions are reported as $40\text{Li}_2\text{S}-60\text{SiS}_2\text{-XMS}_y$ where X is the moles of MS_y added to the base glass (S can be oxide in a few examples).

The ionic conductivity measurements were made using a specially designed fixture, using a two-electrode set-up. Both indium discs and lithium discs (0.7cm diameter) were used. Fresh discs of lithium were used in each experiment. There was no difference in the resistivity data recorded using the two different electrode materials. An AC impedance method, using an EG&G 283 Potentiostat and a 1025 EG&G Frequency Response Detector, was used to measure the conductivity of the samples. Reproducibility of the conductivity data was 5% in the worst case sample to sample, but in most samples was better than 1%. A frequency range of 10^6 Hz to 1 Hz was used. The equivalent circuit which best described the data is shown in Figure 1a, with a schematic of the response shown in Figure 1b.

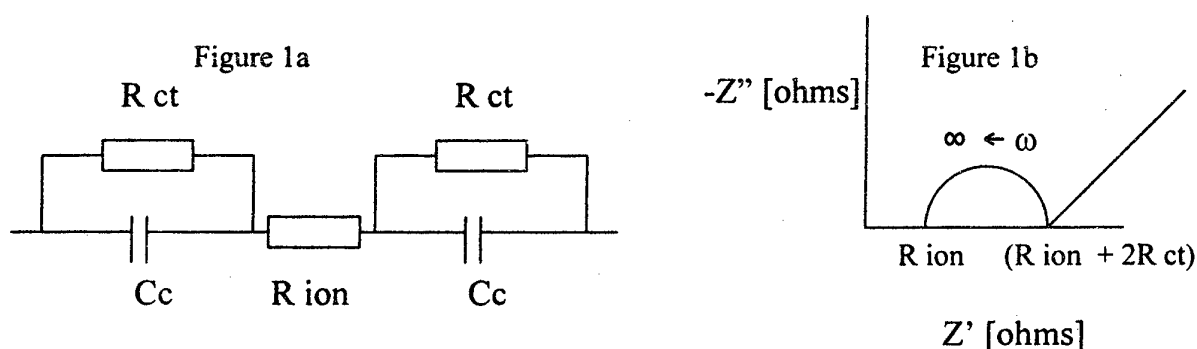


Figure 1 a: Equivalent circuit: R_{ion} is the glass resistance; R_{ct} is the charge transfer resistance, C_{cc} is the capacity of the charge transfer layer. Figure 1b: Complex impedance plot

Experimental error in the conductivity data is estimated to be 5%, mostly due to changes in the area of the ductile metal electrodes. Another possible error arises from the roughness of the glass

surface. In one case the sample was measured, then the surface ground and polished and the sample measured again. There was no significant difference between the two sets of data.

The T_g and T_x data were obtained using a TA 2920 instrument, at a $10^\circ\text{C}/\text{min.}$ heating rate from room temperature to 575°C. Aluminum pans were used, with Al_2O_3 as the reference. The T_g values were determined at the mid-point of the transformation range, and the T_x values were obtained from the start of the crystallization event.

RESULTS

The conductivity data on the base glass, 60/40 $\text{Li}_2\text{S-SiS}_2$ was measured first on different samples, using the lithium disc electrodes. The room temperature conductivity of that sample is $1.36 \pm 0.22 \times 10^{-3} \text{ S/cm.}$ This is higher than values reported on pressed discs of $5 \times 10^{-4} \text{ S/cm}$ [4], but compares well with those reported by Aotani et al. [5] who claim that the electrical conductivity of sulphide glasses prepared by the pelletization method depends on the packing density. We are reporting measurements on annealed glass discs.

Various sulphides and oxides of IVA, VA, VB or VIA groups were added to the base glass. Of particular interest are the additions of TaS_2 and the sulphides of tin (+2 and +4). Figure 2 shows conductivity data measured at room temperature. The tin-containing glasses were a straw yellow color, while the tantalum-containing glasses were a deep reddish-brown in color.

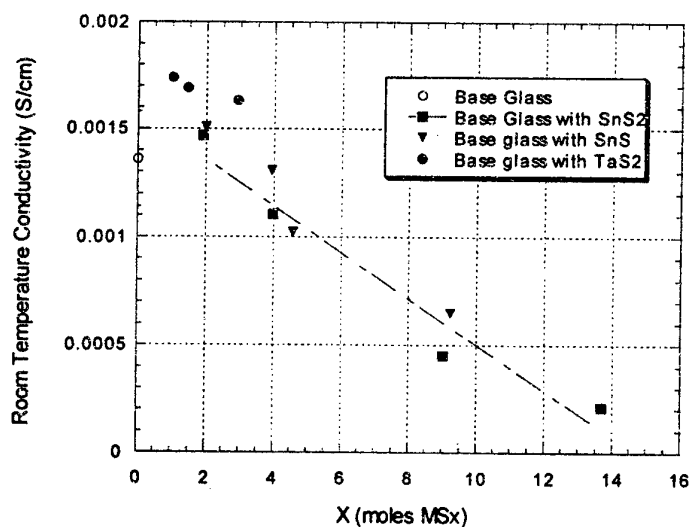


Figure 2: Ionic conductivity of base glass containing SnS_2 , SnS or TaS_2 . (Line to guide the eye.)

The TaS_2 additions above approximately $X=4$ lead to devitrification of the glass. However, additions of the Sn(II) or Sn(IV) sulphides can be made to much higher levels, up to $X=14$. It should be noted that the initial additions of TaS_2 result in an increase in ionic conductivity, while the additions of the tin sulphides (both valence states) leads to a decrease in the conductivity below $X=3$. There appears to be a linear relationship between the conductivity and the

concentration of tin. The highest conductivity, 2.1×10^{-3} S/cm at room temperature, was obtained on the composition 60 LiS₂-40 SiS₂-2.79 TaS₂-4.02 LiI. This is the highest value recorded for lithium ionic conductivity in a solid at room temperature [2]. Table I lists the room temperature conductivity of some ternary lithium sulphide-silicon sulphide glasses. There was a measurable, but not significant electronic contribution to the ionic conductivity of the glasses described in this paper.

TABLE I

Values Of Room Temperature Conductivity for Additions to Base Glass

Additions	X	Conductivity(mS/cm)
PbS	3.80	0.63
As ₂ S ₃	5.46	0.82
Sb ₂ S ₃	1.04	0.75
BiI ₃	3.94	0.90
Sb ₂ O ₃	2.38	0.97
ZnS	7.21	1.12
Base Glass	0.00	1.36
Ti ₂ S ₃	3.30	1.48
TiS ₂	3.87	1.63

In addition to these examples, the multi-component glass 60Li₂S-40SiS₂ with 1.95 SnS₂-4.38LiI and 2.02 TaS₂ additions had a room temperature conductivity of 1.62×10^{-3} S/cm.

The effect of temperature on the ionic conductivity was determined for several glasses-see Figure 3. This Figure also shows that the ionic conductivity determined for a sample of the base glass with 2.77 TaS₂ additions for sample of two thicknesses, 1.70 mm and 8.70 mm, agreed very well. This demonstrates that the interpretation of the impedance data is correct.

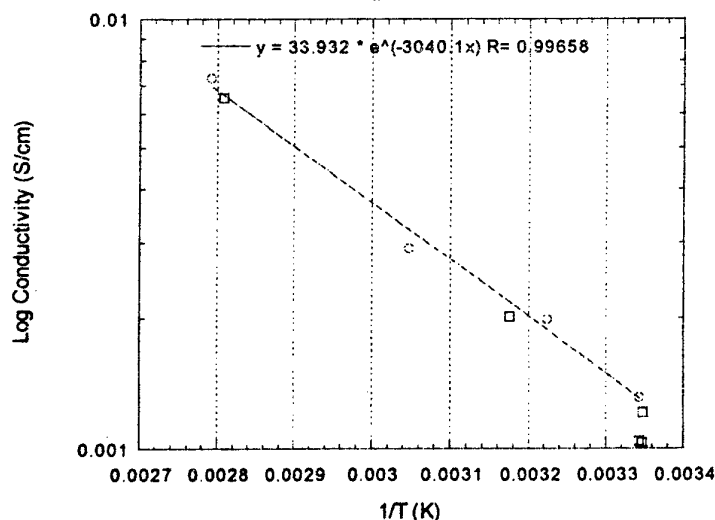


Figure 3 Conductivity of Glass 60Li₂S-40SiS₂-2.77TaS₂ obtained from impedance results using two sample thicknesses.
(Circle=1.70mm; Square 8.7 mm)

Table II lists activation energies for several glasses. Kennedy and Yang [4] reported a value of 0.33 eV as the activation energy for the base glass on a pressed pellet. Our value is lower, however, we measured an annealed sample. The different additions did not cause significant changes in the activation energy, indicative of the transport mechanism being the same in all systems.

Table II
Activation Energies for Selected Compositions

Added Component	X	Activation Energy (eV)	R
Base Glass	0.00	.307 (16.3kcal)	.996
As ₂ S ₃	5.46	.280 (14.9kcal)	.984
TaS ₂	2.77	.262 (13.9kcal)	.996
SnS ₂ /LiI	4.9/3.04	.295 (15.7kcal)	.999
SnS ₂ /LiBr	4.93/4.71	.284 (15.1 kcal)	.991
BiI ₃	2.29	.270 (14.3 kcal)	.998
PbS	4.80	.317 (16.9 kcal)	.955

A sense of a lack of stability for a glass can be strongly influenced by the conditions under which it is melted and formed. We found that 40Li₂S-60SiS₂ base glass was prone to spontaneous devitrification when melted for 30 minutes at 950 and splat quenched, even for patties as thin as 1 mm. By lowering the melting temperature and decreasing the melt duration, we were able to quench an 8 g melt into a 2 mm thick patty with no devitrification at all. The melt that remained in the crucible devitrified, however, showing that rapid quench is still required. By contrast, standard batches of certain of the doped glasses cool to clear glass even when cooled in the crucible, and poured patties did not require pressing to form good glass. This stabilization is manifest in T_g, T_x and (T_x-T_g) data for SnS₂ and SnS-containing glasses, as shown in Figure 4.

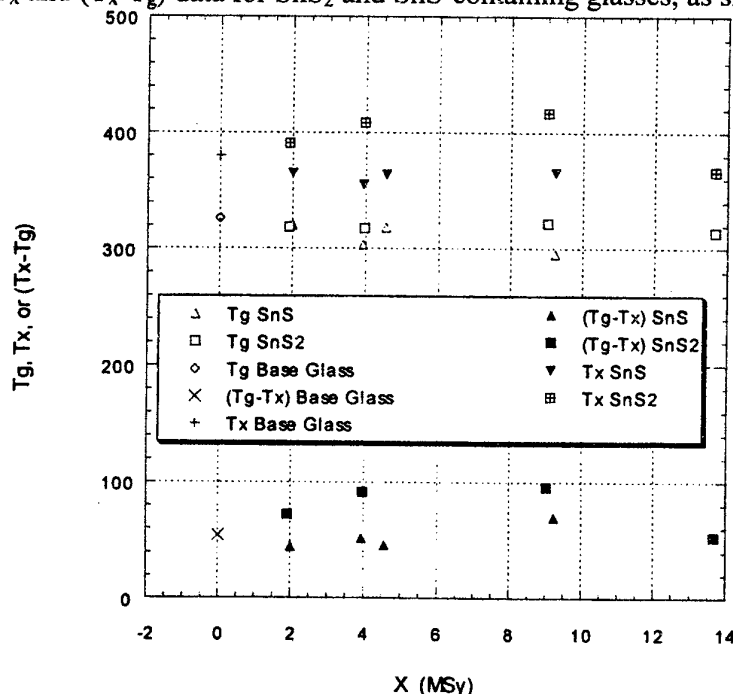


Figure 4: T_g, T_x and (T_x-T_g) data for additions of SnS₂ or SnS to the Base Glass

DISCUSSION

Glasses based on additions of group IVA or VB sulphides, and in some instances oxides, show the same fast ion-conduction as the binary lithium sulphide-silicon sulphide glasses. Additions of TaS_2 and TaS_2+LiI , increase lithium ion conductivity, in the latter glass to $> 2 \times 10^{-3} \text{ S/cm}$ at room temperature. This is the highest reported value for lithium mobility in a glass [2]. The UV-edge in these systems shifts due to TaS_2 additions, producing a reddish brown color. This probably indicates color center formation arising from the impetus for Ta^{4+} to lose an electron. This in turn might facilitate the mobility of the lithium ions by reducing the depth of the potential well between Li sites. Tin is more amphoteric than tantalum, and produces effects on conductivity and glass stability intermediate between those of tantalum and group IVA sulfides.

As mentioned previously, TaS_2 additions $> X=4$ cause the glasses to spontaneously devitrify, but at lower levels the Ta-doped glasses more readily form glass than the base glass. Paradoxically, the T_x-T_g of Ta-doped glasses is quite small, 59.9°C for $X=2.69$. In tin-doped glasses, T_g shows little variation with addition of tin sulfides (SnS_x , Fig. 4), but there are significant changes in T_x , which translate into a net increase in T_x-T_g . Thus we see two aspects of glass stabilization. Seen as the tendency of a final glass to devitrify on re-heating, SnS_x additions stabilize the glass, but TaS_2 additions do not. In this case, nucleation of crystals from the glass is inhibited by the presence of tin ions. This might arise because tetrahedrally coordinated tin interferes with formation of SiS_2 or binary lithium sulfides. Neutron diffraction data [6] indicates that all Si atoms occupy corner-sharing tetrahedra in $\text{Li}_2\text{S}-\text{SiS}_2$ glasses, so introducing a comparatively large tetrahedral species might increase the jump distance and lower conductivity. When stability is seen as a tendency to suppress crystallization on cooling of a melt, then both SnS_x and TaS_2 additions improve glass stability. This effect might arise from interference with crystal nucleation or, perhaps more likely, from a reduction in the free energy of the melt relative to any crystalline phases. The latter only requires that the component added does not show large positive deviations from ideal mixing to produce the desired effect.

CONCLUSIONS

New glass-forming regions in the lithium sulphide-silicon sulphide field have been identified. Stable glasses were obtained in ternary systems with additions of group IVA, VA, VB or VIA sulphides or oxides. Room temperature ionic conductivity exceeding $2 \times 10^{-3} \text{ S/cm}$ is reported. NMR studies are in progress to elucidate the lithium-ion environment in these glasses.

REFERENCES

- [1.] S. Sahami, S. Shea, J. Kennedy, J. Electrochem. Soc. 132 (1985) 985.
- [2.] A. Pradel and M. Ribes, Solid State Ionics 18 & 19 (1986) 351.
- [3.] K. Hirai, M. Tatsumisago and T. Mimami, Solid State Ionics 78 (1995) 269.
- [4.] J. Kennedy and Y Yang, J. Electrochem. Soc., 133 (1986) 2437.
- [5.] N. Aotani, K. Iwamoto, K. Takada and S. Kondo, Solid State Ionics 68 (1994) 35.
- [6.] D.L. Price and A.J.G. Ellison, J. Non-Crystall. Solids, 177 (1994) 293.

EXCITED STATE ABSORPTION AT 1.3 μm IN Nd^{3+} -DOPED FLUORIDE AND SULFIDE GLASSES

Jean-Luc Adam^a, Jean-Louis Doualan^b, Laurent Griscom^a, Sylvain Girard^b,
and Richard Moncorgé^b

^aLaboratoire des Verres et Céramiques, UMR-CNRS 6512
Université de Rennes 1, Campus de Beaulieu, 35042 Rennes Cedex, France
jean-luc.adam@univ-rennes1.fr

^bLaboratoire de Spectroscopie Atomique, UPRES A-CNRS 6084
Institut Supérieur de la Matière et du Rayonnement, Université de Caen
Bd. Du Maréchal Juin, 14050 Caen Cedex, France

ABSTRACT

Excited-state absorption and emission spectra are recorded from the $^4\text{F}_{3/2}$ level of Nd^{3+} ions in ZBLAN (Zr-Ba-La-Al-Na) and BIG (Ba-In-Ga) fluoride glasses and in GGSC (Ge-Ga-S-Cs-Cl) chlorosulfide glass. Special attention is paid to the 1.3 μm region.

The pump-probe technique utilized in this study is able to predict the gain profile as a function wavelength in optical fibers. Gain is expected at wavelengths greater than 1.31 μm with ZBLAN and BIG, and 1.35 μm with GGSC. An evaluation of the ratio between stimulated emission and excited-state absorption processes is obtained by Judd-Ofelt calculations.

INTRODUCTION

Low-phonon-energy glasses have received a great deal of interest for optical amplification at 1.3 μm with Pr^{3+} ions [1], and, in a lesser extent, with Dy^{3+} ions [2]. Nd^{3+} is another rare-earth ion emitting in the 1.3 μm region. However, a major drawback with Nd^{3+} is the absorption of the 1.3 μm signal from the $^4\text{F}_{3/2}$ excited-state (ESA). Thus no gain can be obtained around this wavelength with Nd^{3+} -doped silica fibers, and, in ZBLAN fluoride fibers, gain is achieved at 1.34 μm [3], too far away from the 1.31 μm wavelength required for telecommunications.

ESA processes may strongly vary from host to host. The immediate environment of rare-earth ions in a given material modifies the position of the energy levels involved in emission and ESA transitions. It may also change significantly the probabilities of such transitions.

In the present paper, we report on a comparative study of the effect of ESA on stimulated emissions (SE) from the $^4\text{F}_{3/2}$ level of Nd^{3+} ions in bulk ZBLAN (Zr-Ba-La-Al-Na) and BIG (Ba-In-Ga) fluoride glasses, as well as in a germanium-based chlorosulfide glass. Direct measurements of both ESA and SE are carried out by a pump-probe technique. This procedure has the capability to determine, from measurements with a bulk material, whether net gain is to be expected in fiber configuration.

EXPERIMENTAL PROCEDURES.

Glass synthesis and characterization

Two neodymium-doped fluoride glasses were synthesized for this study: ZBLAN and BIG, whose compositions are: 53 ZrF_4 – 20 BaF_2 – 3 LaF_3 – 3 AlF_3 – 20 NaF – 1 NdF_3 , and 30 BaF_2 – 18 InF_3 – 12 GaF_3 – 20 ZnF_2 – 6 ThF_4 – 4 ZrF_4 – 9 YF_3 , – 1 NdF_3 , respectively. They were prepared from oxides and fluorides carefully mixed together with a fluorinating

agent (NH_4 , HF). The method is well described in the literature [4]. After fluorination around 300 °C and melting around 800 °C under controlled dry atmosphere, the glasses are cooled down to the glass transition temperature (T_g). They are finally annealed nearly T_g (270 °C for ZBLAN and 320 °C for BIG) before being cut and polished for optical measurements.

The chlorosulfide glass, referred to as GGSC, is of the following composition: 50 GeS_2 – 25 Ga_2S_3 – 25 CsCl with Nd_2S_3 substituting for the whole composition. It was prepared from high purity 5N elements (Ge, Ga, S) and 3N CsCl introduced in a silica ampoule under vacuum. The procedure is presented in details in a complementary paper in these proceedings [5].

The Nd^{3+} concentration was 1.91, 1.96, and 0.98 10^{20} ions cm^{-3} in ZBLAN, BIG and GGSC glasses, respectively.

Optical measurements

For ground state absorption measurements, a Varian Cary 5 spectrophotometer that operates from 175 nm to 3300 nm was utilized.

Direct measurements of both ESA and SE were carried out by a pump-probe technique [6]. A Ti:sapphire laser pumps the $^4\text{F}_{3/2}$ level, and a white lamp probes the transmission from 0.82 to 1.44 μm . Both the pump and the probe are modulated, at frequencies of 10 Hz and 1 kHz, respectively. Special care was taken for measurements with GGSC glass that experiences self-defocusing with high pump powers.

RESULTS

In the 1.3 μm region, ESA is expected to occur from the $^4\text{F}_{3/2}$ level of Nd^{3+} to the ($^2\text{K}_{13/2}$, $^4\text{G}_{7/2}$, $^4\text{G}_{9/2}$) group of levels, as shown in Figure 1. In order to identify precisely the energy of the levels involved, we have recorded the ground state absorption (GSA) spectrum of Nd^{3+}

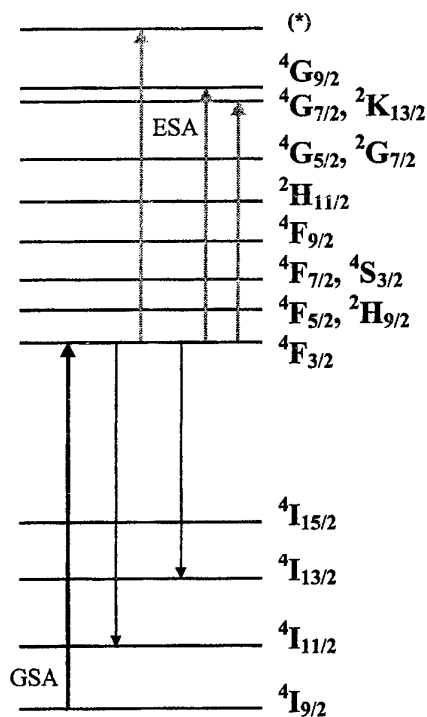


Figure 1 : Energy-level diagram of Nd^{3+} ions. (*) = ($^2\text{D}_{3/2}$, $^2\text{G}_{9/2}$, $^4\text{G}_{11/2}$, $^2\text{K}_{15/2}$) levels.

ions in ZBLAN, BIG and GGSC glasses. The results are shown in Figure 2, on a normalized scale, for ZBLAN and GGSC glasses. The BIG spectrum, which is very similar to ZBLAN, is not shown. One should notice the red shift observed for GGSC: Nd^{3+} , due to the nephelauxetic effect. Both spectra present two components with the main peak located in the low-energy side of the band.

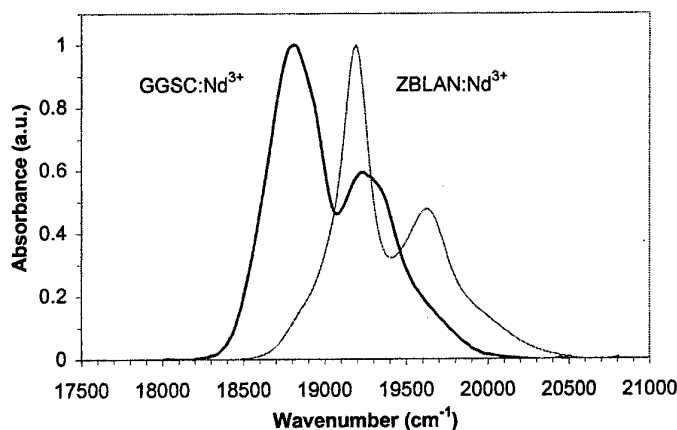


Figure 2 : Normalized GSA spectra to the ($^2\text{K}_{13/2}$, $^4\text{G}_{7/2}$, $^4\text{G}_{9/2}$) levels in Nd^{3+} -doped ZBLAN and GGSC glasses.

Table I : Electric-dipole line strength (in 10^{-40} esu² cm² units) and energy (cm⁻¹) of ground-state absorptions to the (²K_{13/2}, ⁴G_{7/2}, ⁴G_{9/2}) group of levels of Nd³⁺.

Transition	Nd ³⁺ aquo	ZBLAN : Nd ³⁺		GGSC :Nd ³⁺	
	Energy	S _{ed}	Energy	S _{ed}	Energy
⁴ I _{9/2} → ² K _{13/2}	19018	3.21	19194	4.79	18815
→ ⁴ G _{7/2}	19103	15.8		39.0	
→ ⁴ G _{9/2}	19544	7.89	19627	18.1	19286

The absorption line strength, S_{ed}, for electric dipole transitions can be calculated by the following equation:

$$S_{ed} = e^2 \sum_{t=2,4,6} \Omega_t \left(\langle SLJ \| U^{(t)} \| S' L' J' \rangle \right)^2 \quad (1)$$

where e is the electron charge. The Judd-Ofelt parameters Ω_t ($t = 2, 4, 6$), determined in previous reports, are equal to 2.20 – 2.82 – 3.94 for ZBLAN [7], and 7.09 – 8.99 – 5.03 for GGSC [5], in (10^{-20} cm²) units. The $U^{(t)}$ matrix elements were those calculated by Kaminskii et al. [8]. The results are listed in Table I. Considering the energy of the transitions (as compared to Nd³⁺ aquo [9]) and the relative intensity of the line strengths, the low-energy component in Figure 2 must be attributed to absorption to the (²K_{13/2}, ⁴G_{7/2}) levels and the ⁴I_{9/2} → ⁴G_{9/2} transition is assigned to the high-energy component. This is summarized in the energy-level diagram in Figure 1.

The emission and absorption spectra of transitions from the ⁴F_{3/2} excited state are shown in Figure 3 for ZBLAN and BIG fluoride glasses. The spectra are calibrated to the ground state absorption cross-section of the ⁴I_{9/2} → ⁴F_{3/2} transition by means of the Einstein reciprocity method [10]. Both spectra show an ESA band located at nearly 970 nm. This band, attributed to the ⁴F_{3/2} → (²D_{3/2}, ²G_{9/2}, ⁴G_{11/2}, ²K_{15/2}) transition, has no influence on the ⁴F_{3/2} → ⁴I_{11/2} emission at 1050 nm. On the contrary, ESA processes affect the ⁴F_{3/2} → ⁴I_{13/2}

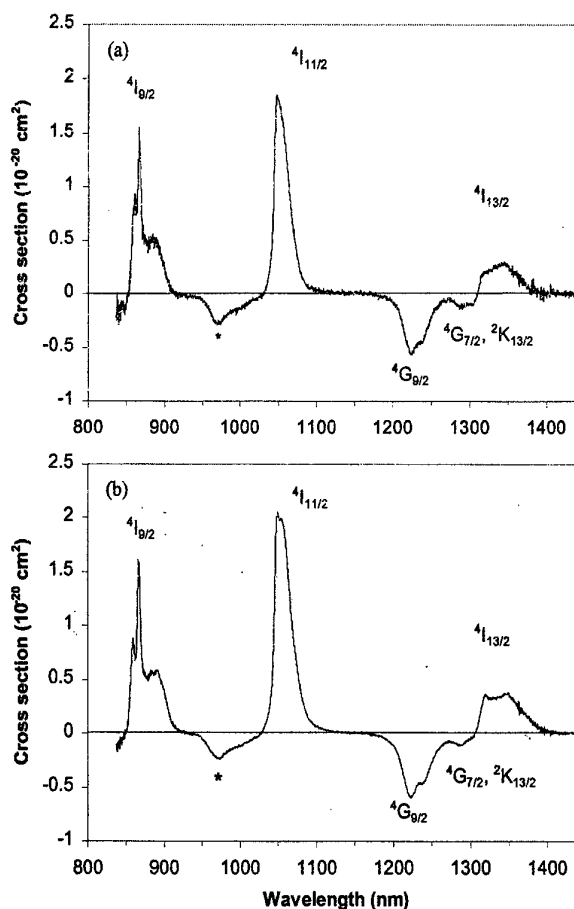


Figure 3 : Excited state spectrum from the ⁴F_{3/2} level of Nd³⁺ ions in (a) ZBLAN and (b) BIG fluoride glasses. (*) = (²D_{3/2}, ²G_{9/2}, ⁴G_{11/2}, ²K_{15/2}) levels.

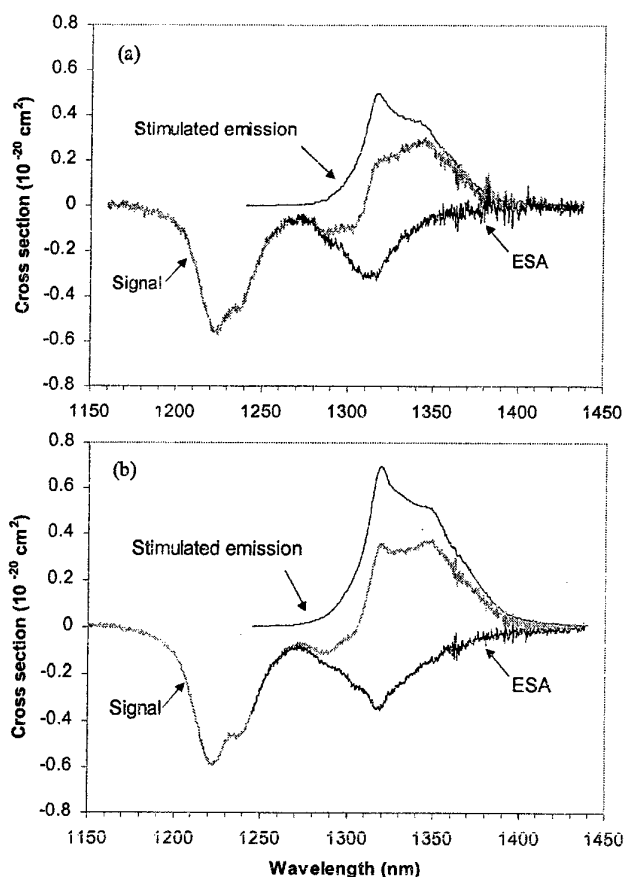


Figure 4 : Stimulated emission and excited-state absorption in the 1.3 μm region in Nd^{3+} -doped (a) ZBLAN and (b) BIG fluoride glasses.

the higher SE cross-section of BIG glass results in an increase of the signal at 1320 nm, as compared to ZBLAN.

Similar measurements were carried out for GGSC: Nd^{3+} chlorosulfide glass. The full excited-state spectrum is shown in Figure 5. Contrary to fluoride glasses, there is no evidence of ESA processes in the 1000 nm region. However, in the 1300 nm region, strong ESA transitions to $^4\text{G}_{9/2}$ and $(^2\text{K}_{13/2}, ^4\text{G}_{7/2})$ are observed. In the detailed spectrum, in Figure 6, one should remark that the most intense ESA band is at ≈ 1330 nm and that the SE peak is shifted at ≈ 1350 nm. Therefore, a positive cross-section is attained only in the 1350-1410 nm range with a maximum at 1375 nm.

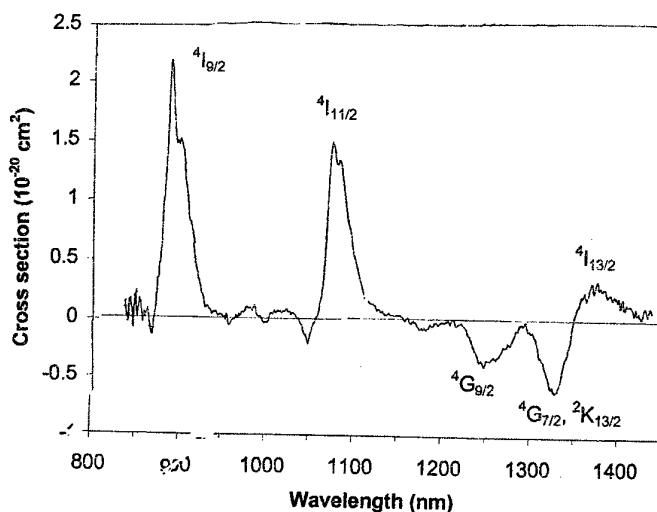


Figure 5 : Excited state spectrum from the $^4\text{F}_{3/2}$ level of Nd^{3+} ions in GGSC chlorosulfide glasses.

transition around 1.3 μm . Detailed spectra in this wavelength region are given in Figure 4. The stimulated-emission spectra are calculated by the Fuchtbauer-Ladenburg equation:

$$\sigma_{SE} = \frac{1}{8\pi n^2 c} \frac{\beta}{\tau_R} \frac{\lambda^5 I(\lambda)}{\int \lambda I(\lambda) d\lambda} \quad (2)$$

where c is the light velocity. Refractive indices (n), branching ratios (β) and radiative lifetimes (τ_R) are reported in the literature [7]. The excited-state absorption bands in the 1.3 μm region are obtained by subtracting the calculated stimulated emission profile from the recorded spectrum. The short-wavelength component, around 1230 nm, corresponds to the $^4\text{F}_{3/2} \rightarrow ^4\text{G}_{9/2}$ transition. Despite its intensity, this band is not broad enough to alter the $^4\text{F}_{3/2} \rightarrow ^4\text{I}_{13/2}$ stimulated emission. Conversely, the long-wavelength ESA component, around 1320 nm ($^4\text{F}_{3/2} \rightarrow (^2\text{K}_{13/2}, ^4\text{G}_{7/2})$), coincides with the maximum of the stimulated emission peak, resulting in a negative signal at wavelengths below 1310 nm for both ZBLAN and BIG glasses. However,

DISCUSSION

The first conclusion that can be drawn from the results is that none of ZBLAN, BIG or GGSC glass is suitable for optical amplification with Nd^{3+} in the second telecommunication window. This was already known for ZBLAN from measurements on Nd^{3+} -doped fibers. It must be mentioned that our results are in excellent agreement with those reported for fibers in terms of ESA profiles, and in terms of overall excited-state spectrum as compared to optical gain response [3]. Thus, a second information is that gain profiles in rare-earth-doped fibers can efficiently be predicted by means of excited-state spectroscopy applied to simple parallel-plate samples.

By comparison with ZBLAN, a higher gain should be achieved with BIG glass at wavelengths greater than 1310 nm, due to higher SE cross-section. For GGSC: Nd^{3+} glass, no amplification is expected at wavelengths below 1350 nm. Above that wavelength, the remaining part of the signal is weak anyway, due to a decreasing stimulated emission in this region.

We have investigated the possibility to predict, in some way, the effect of excited-state absorption on stimulated emission by Judd-Ofelt calculations. The results are given in Table II. For each composition, the integrated SE and ESA cross-sections, ($\int \sigma_{\text{SE}} d\nu$) and ($\int \sigma_{\text{ESA}} d\nu$), were determined around 1.3 μm from the spectra in Figures 4 and 6. The ratio of the emission to the absorption is given as R_{σ} in Table II. Similarly, the electric-dipole line strengths and the R_S ratio between them were calculated by means of Eq. (1) and parameters available in the literature [5, 7, 8].

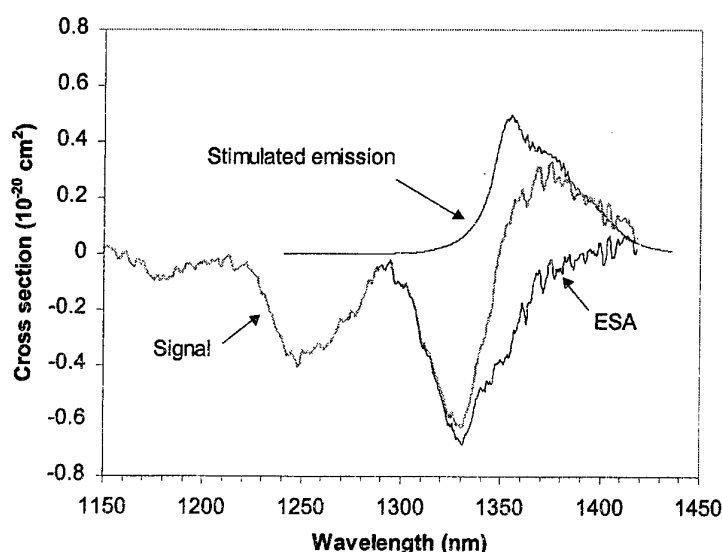


Figure 6 : Stimulated emission and excited-state absorption in the 1.3 μm region in GGSC chlorosulfide glasses.

Table II : Experimental integrated cross-sections and calculated electric-dipole line strengths for transitions from the $^4\text{F}_{3/2}$ level, in (10^{-20} cm) and (10^{-40} esu 2 cm 2) units, respectively. R_{σ} and R_S are the emission / absorption ratios.

Glass	$^4\text{F}_{3/2} \rightarrow ^4\text{I}_{13/2} / (^4\text{G}_{7/2}, ^2\text{K}_{13/2})$						$^4\text{F}_{3/2} \rightarrow ^4\text{G}_{9/2}$
	Experimental			J-O calculation			J-O calc.
	$\int \sigma_{\text{SE}} d\nu$	$\int \sigma_{\text{ESA}} d\nu$	R_{σ}	$S_{\text{ed}}(\text{em})$	$S_{\text{ed}}(\text{ESA})$	R_S	$S_{\text{ed}}(\text{ESA})$
ZBLAN	141.1	86.6	1.63	18.9	9.5	1.99	16.7
BIG	215.8	113.3	1.90	19.3	7.2	2.68	17.6
GGSC	122.5	157.6	0.78	24.2	29.1	0.83	30.0

By comparing R_σ and R_s , one observes that the relative probabilities of emission and absorption processes obey the same ordering sequence ($BIG > ZBLAN > GGSC$). In addition, R_σ and R_s are in fairly good agreement, considering the approximation generated by the Judd-Ofelt treatment. So, the relative intensities of SE and ESA for the 1.3 μm spectrum of Nd^{3+} can be evaluated with good consistency by simple Judd-Ofelt calculations.

We have also calculated the ESA line strength for the $^4F_{3/2} \rightarrow ^4G_{9/2}$ transition. For ZBLAN and BIG, it is found to be nearly twice as large as the line strength for the $^4F_{3/2} \rightarrow (^2K_{13/2}, ^4G_{7/2})$ transition. This is in good agreement with the spectra in Figure 4 where the $^4G_{9/2}$ component is noticeably more intense. For GGSC glass, the agreement is not as good: according to Table II, the line strengths should be the same for both components, which is not verified in the spectrum in Figure 6. This is possibly due to less applicable conditions for the Judd-Ofelt theory, in the case of GGSC. Because of an optical gap located in the blue, only six transitions were utilized for determining the Judd-Ofelt parameters in that glass [5].

CONCLUSION

In summary, we have established the excited-state emission and absorption spectra from the $^4F_{3/2}$ level of Nd^{3+} ions in ZBLAN, BIG and GGSC glasses. Measurements were carried out by a pump-probe technique. This technique, which necessitates simple parallel-plate glass specimens, can predict optical gain profiles in fibers. Analysis of the spectra shows that, in the 1.3 μm region, optical gain is expected at wavelengths greater than 1.31 μm with ZBLAN and BIG, and 1.35 μm with GGSC. In addition, we have shown that Judd-Ofelt calculations permit to evaluate the ratio between stimulated emission and ESA.

REFERENCES

- [1] T.J. Whitley, J. Lightw. Technol. 13 (1995) 744.
- [2] J.-L. Adam, Y. Guimond, A.-M. Jurduc, L. Griscom, J. Mugnier, and B. Jacquier, S.P.I.E. 3280 (1998) 31.
- [3] J.E. Pedersen, M.C. Brierley, S.F. Carter, and P.W. France, Electron. Lett. 26 (1990) 329.
- [4] C. Henriel-Ricordel, J.-L. Adam, B. Boulard, and C. Sourisseau, Eur. J. Solid State Inorg. Chem. 34 (1997) 125.
- [5] L.S. Griscom, J.-L. Adam, and K. Binnemans, (1998) (this proceeding) .
- [6] P. Le Boulanger, PhD thesis, Université de Caen, France (1998).
- [7] J.-L. Adam, N. Rigout, E. Dénoue, F. Smektala, and J. Lucas, S.P.I.E. 1581 (1991) 155.
- [8] A.A. Kaminskii, G. Boulon, M. Buoncristiani, B. Di Bartolo, A. Kornienko, and V. Mironov, Phys. Status Solidi A - Appl. Res. 141 (1994) 471.
- [9] W.T. Carnall, P.R. Fields, and K. Rajnak, J. Chem. Phys. 49 (1968) 4424.
- [10] S.A. Payne, L.L. Chase, L.K. Smith, W.L. Kway, and W.F. Krupke, IEEE J. Quant. Electron. 28 (1992) 2619.

SPECTROSCOPIC STUDIES ON MULTIPHOTON PROCESS IN ERBIUM DOPED FLUORIDE AND OXIDE GLASSES

Setsuhisa TANABE

Faculty of Integrated Studies, Kyoto University, Sakyo-ku, Kyoto 606-8501, Japan
email: tanabe@chem.h.kyoto-u.ac.jp

ABSTRACT

Spectroscopic analyses of the multiphoton process in erbium doped glasses are described by monitoring the upconversion luminescence. The two-step upconversion mechanisms by excited state absorption and by energy transfer with excitation spectra and time-resolved luminescence decay are represented. Under CW excitation, the excited state absorption was dominant in oxide glasses. In fluoride glasses the excitation profile of the Er^{3+} green emission was superposed with the squared absorption spectra. In tellurite glasses, the ESA from the $^4\text{I}_{13/2}$ level was dominant, since the excited energy relax rapidly to the $^4\text{I}_{13/2}$ level.

Under pulse excitation, the energy transfer upconversion was dominant in both glasses. To clarify the dominant energy transfer scheme contributing the green upconversion, the luminescence decay curves were analyzed with proper rate equations in Er^{3+} doped systems. The intermediate level was found to be the $^4\text{I}_{11/2}$ in both tellurite and fluoride glasses.

INTRODUCTION

Due to its characteristic energy level structures, the multiphoton processes of Er^{3+} in doped glasses occurs in several ways and characterizes the material performances. Even if we restricted to the case of III-V group diode laser pumping, the Er^{3+} doped materials show various behaviors, such as upconversion[1], negative nonlinear absorption (NNA) effect[2], and gain saturation in EDFA's. In fluoride glasses, considered to be an excellent host for green upconversion, the optimum Er^{3+} content for efficient 550nm emission is often higher than that for UV excited Stokes emission. By 800nm pumping, it sometimes reaches up to 15mol% ErF_3 in ZBN glasses[3], although the concentration quenching of Stokes 550nm emission usually starts around 1mol% because of monotonic decrease of lifetime of the $^4\text{S}_{3/2}$ with concentration, largely due to cross relaxations. However, in most oxide glasses, the optimum content by infrared pumping is very low even in well dispersed states[4]. This difference can be due to the difference of dominant mechanism of two photon excitations between low- and high-phonon energy hosts. This paper describes the observed data and reasonable analyses, which explain the different mechanisms of Er^{3+} upconversions in fluoride and oxide glasses. The change of mechanisms of a doped tellurite by CW pumping and by pulse laser pumping are also shown.

A. Difference in Er^{3+} Luminescence Spectra

Fig.1 shows the 800nm pumped upconversion spectra of Er^{3+} doped fluoride glasses ($50\text{MF}_n-30\text{BaF}_2-15\text{YF}_3-5\text{ErF}_3$; $\text{M} = \text{Zr, Hf, In, Ga, Al, Sc, or Zn}$)[5]. The 410nm emission due to the $^2\text{H}_{9/2} \rightarrow ^4\text{I}_{15/2}$ is very weak, though it has stronger intensity by uv (380nm) excitation in all the glasses. This indicates that the successive two-step excitation through the $^4\text{I}_{9/2}$ level ($E = 12500 \text{ cm}^{-1}$) to the $^2\text{H}_{9/2}$ is not a conceivable process for the green upconversion in fluo-

ride glasses.

B. Elucidation of Excited State Absorption

Generally for the upconversion by the energy transfer (*APTE*, Addition de Photons par Transfert d'Energie [1]) mechanisms in singly doped systems, the incident light is absorbed only in the transition from the ground state and the energy transfer occurs between adjacent excited ions. Thus the wavelength dependence of upconversion efficiency should vary similarly with the ground state absorption profile. In the case of excited state absorption (*ESA*) mechanisms, the efficiency depends both on the ground state (*GSA*) and *ESA* profiles[6]. The *ESA* cross section does not usually vary with wavelength in exactly the same way as the ground state absorption. Thus, to distinguish *ESA* and *APTE* mechanism it is effective to see how the upconversion efficiency varies with the wavelength of the pump light[6]. Tunable dye (DCM) lasers was used as a pumping source to verify the upconversion mechanism of tellurite and fluoroaluminate glasses doped with 1mol% Er. The CW-pumped excitation spectra of the 550nm upconversion in the fluoride and tellurite glasses are shown by white dots in FIG.2. Also the squared profile of the $^4F_{9/2}$ absorption spectra of the corresponding glass are shown. It is seen that both profiles are similar in the fluoride, whereas those are different in the tellurite glass. In the two-photon process, the excitation efficiency should become proportional to the square of the first step pumping, which is proportional to the absorption cross section. The deviation in Fig.2(b) is due to the contribution of the *ESA* from the $^4I_{13/2}$, which has a large energy gap ($E=6600\text{cm}^{-1}$). The lifetime, τ_f of the $^4I_{13/2}$ level are 9ms and 4ms, while the τ_f of the $^4I_{11/2}$ level ($E=10200\text{cm}^{-1}$) are 6.5ms and 210 μs in the fluoride and tellurite glass, respectively. Due to the difference of the energy gap, the τ_f ($^4I_{13/2}$) is dominated by the radiative decay, while the τ_f ($^4I_{11/2}$) is sensitive to the phonon energy. By pulse laser excitation of 650nm light, the green intensity of the tellurite became weaker. It is interesting that the excitation profile in the tellurite glass becomes almost similar to the squared absorption by pulse laser excitation as shown in Fig.3. Under the pulse (5ns) excitation, the *ESA* hardly occurs from the $^4I_{13/2}$ level, since there should be a time lag for multiphonon relaxation from the $^4F_{9/2}$ level.

C. Time Resolved Spectra by Pulse Excitation

To see what's going on, the time resolved spectra were measured and analyzed for both glasses. The dynamics were investigated with decay curves by Stokes and anti-Stokes excitation ($^4F_{7/2}=488\text{nm}$, $^4F_{9/2}=650\text{nm}$). The time resolved spectra (Fig.4.) and the decay curves of Er^{3+} : 550nm luminescence due to the $^4S_{3/2} \rightarrow ^4I_{15/2}$ in the tellurite and fluoride glasses are shown in Figs. 5 and 6, respectively. The white circles indicate the decay data of the upconversion luminescence ($\lambda_{\text{ex}}=650\text{nm}$) and the squares the Stokes luminescence ($\lambda_{\text{ex}}=488\text{nm}$). It is seen that the decay curve of upconversion differs from that of Stokes one. The Stokes luminescence decays with a single exponential whose time constants are shorter, whereas the decay curve of the upconversion has two exponential components. One component has a longer time constant than another. This can be explained by a set of rate equations which bases on a model assuming a simple mechanisms. This model is simplified by some assumptions that the relaxation rates from the $^4F_{9/2}$ level to the intermediate level(1) and from the higher lying level than the $^4S_{3/2}$ level to the $^4S_{3/2}$ level(2) are rapid enough, which are valid because of their energy gap structure. The rate equations which satisfy the model are (1) and (2);

$$\frac{dn_1}{dt} = -\frac{n_1}{\tau_{1f}} - W_{ET} n_1^2 \quad (1)$$

$$\frac{dn_2}{dt} = -\frac{n_2}{\tau_{2f}} + \frac{W_{ET}}{2} n_1^2 \quad (2)$$

where the suffix denotes the level in Fig. 2, n means the population, τ_{if} indicates the fluorescence lifetime of the level i and W_{ET} is defined as the energy transfer rate.

The intrinsic decay rate (the radiative decay + multiphonon relaxation) is determined with the decay of 488nm pumped emission as follows;

$$\frac{dn_1}{dt} = -\frac{n_1}{\tau_{1f}} \quad (3).$$

Solving the Eqs. (3) and (2) gives n_2 as a function of t ;

$$n_2 = \left\{ n_{2(0)} - \frac{C}{\tau_{2f}^{-1} - 2\tau_{1f}^{-1}} \right\} \exp\left(-\frac{t}{\tau_{2f}}\right) + \frac{C}{\tau_{2f}^{-1} - 2\tau_{1f}^{-1}} \exp\left(-\frac{2t}{\tau_{1f}}\right) \quad (4)$$

$$\text{with } C = \frac{W_{ET} n_{1(0)}^2}{2},$$

where $n_{1(0)}$ and $n_{2(0)}$ is the population of the intermediate level and the $^4S_{3/2}$ level when $t=0$, respectively. Eq. (4) shows that the decay curve of the upconversion luminescence consists of two components whose time constants are τ_{2f} , the lifetime of the emitting level, and half of τ_{1f} , the intermediate level. The fitting of Eq. (4) to Fig. 4 results in the good agreement, where the lifetime for the Stokes luminescence of the $^4S_{3/2}$ level is employed as the value of τ_{2f} . The values of τ_{1f} obtained by the fitting are 215 μ m for the tellurite and 7.35ms for the fluoroaluminate glass.

To deduce the intermediate level, the multiphonon relaxation rate is considered, which is dependent on the energy gap ΔE to the next lower lying level and given by the form[7],

$$W_{MP} = W_0 \exp(-\alpha \Delta E / \hbar \omega) \quad (5)$$

where W_0 is the transition probability extrapolated to zero energy gap, $\hbar \omega$ is the phonon energy and α is a function of the electron-phonon coupling constant. The Eq.(5) indicates that W_{MP} is related to the ΔE and also to the phonon energy.

Since there holds the relation of Eq. (6) among the fluorescent lifetime τ_f , spontaneous emission probability A and multiphonon relaxation rate W_{MP} , τ_{1f} obtained by the fitting and A 's can give W_{MP} of each level.

$$\tau_f^{-1} = \sum A + W_{MP} \quad (6)$$

The A was calculated by three J-O parameters ($\Omega_2=7.14\text{pm}^2$, $\Omega_4=1.74\text{pm}^2$, $\Omega_6=0.92\text{pm}^2$ for tellurite; $\Omega_2=2.27\text{pm}^2$, $\Omega_4=1.31\text{pm}^2$, $\Omega_6=0.98\text{pm}^2$ for fluoride). For the Er^{3+} : 4I_J ($J=9/2, 11/2, 13/2$), possible intermediate levels, the values of W_{MP} obtained from Eq. (6) are plotted in Fig. 5 versus energy gap. Fig. 5 also includes W_{MP} of other levels which have been obtained in our previous works[8]. Since W_{MP} changes exponentially with the ΔE for a given matrix as mentioned above, the $^4I_{11/2}$ level can be the APTE intermediate level of Er^{3+} : 550nm upconversion. Fig. 6 shows the values of W_{MP} of the Er^{3+} : $^4I_{11/2}$ level against the inverse phonon energy of each host[9-11]. As expected from Eq. (5), W_{MP} decreases exponentially as phonon energy decreases in Fig. 6, where W_{MP} of the $^4I_{11/2}$ level in the tellurite and fluoride

glasses fit to the trend. Thus, the APTE between the $^4I_{11/2}$ is the dominant process in both glass samples under pulsed-excitation.

CONCLUSIONS

The mechanism of Er^{3+} green upconversion under CW excitation depends on the phonon energy of host. The excitation spectra around 650nm in the oxide glasses deviate to a higher energy side than the absorption profile of the $^4F_{9/2}$, whereas that in the fluoride glasses becomes identical to the square of this GSA, indicating the ESA and APTE upconversion, respectively. However, it is to be noted that under a pulsed laser excitation the spectra in both glasses become superposed to their (GSA)². The ESA in the oxide glass can hardly occur simultaneously with GSA. The dominant intermediate level for upconversion under pulse excitation was the $^4I_{11/2}$ for both glasses.

Acknowledgment

This work was partially supported by Nippon Sheet Glass Materials Engineering Foundation.

REFERENCES

- [1] F. E. Auzel, *Proc. IEEE*, 61 (1973) 758.
- [2] Y. Maeda, *J. Appl. Phys.* 83 (1998) 1187.
- [3] D.R. MacFarlane, et al., *J. Non-Cryst. Solids* 213&214 (1997) 158.
- [4] S. Tanabe, in *RARE EARTHS*, No.23, (ed. by G. Adachi, The Rare Earth Society of Japan, 1993) pp.67-94.
- [5] S. Tanabe, et al., *J. Opt. Soc. Am. B* 12, (1995) 786.
- [6] S. Tanabe, et al., *Phys. Rev. B* 47, (1993) 2507.
- [7] T. Miyakawa and D. L. Dexter, *Phys. Rev. B* 1, (1970) 2961.
- [8] S. Tanabe, K. Suzuki, N. Soga, and T. Hanada, *J. Opt. Soc. Am. B* 11, (1994) 933.
- [9] C. B. Layne, W. H. Lowdermilk and M. J. Weber, *Phys. Rev. B* 11, (1977) 10.
- [10] S. Tanabe, S. Yoshii, K. Hirao and N. Soga, *Phys. Rev. B* 45, (1992) 4620.
- [11] S. Tanabe and S. Todoroki, *New Glass* 7, (1992) 189.

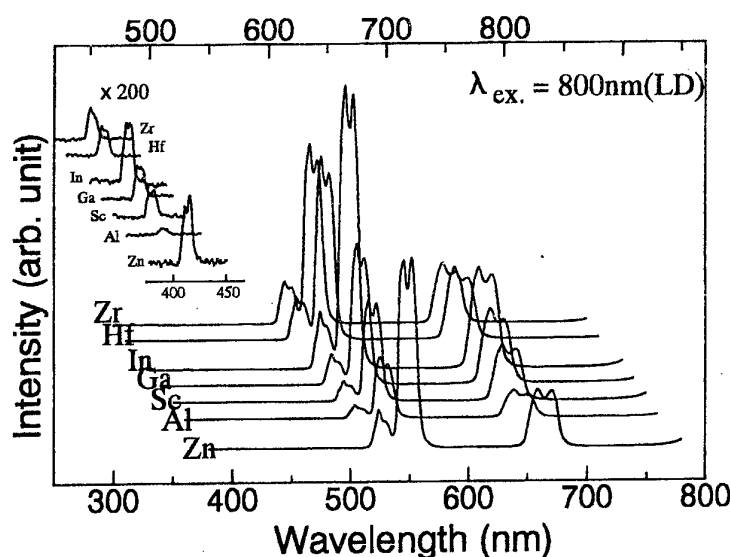


FIG.1. Upconversion spectra of Er^{3+} in MF_n - BaF_2 - YF_3 glasses by 800nm excitation.

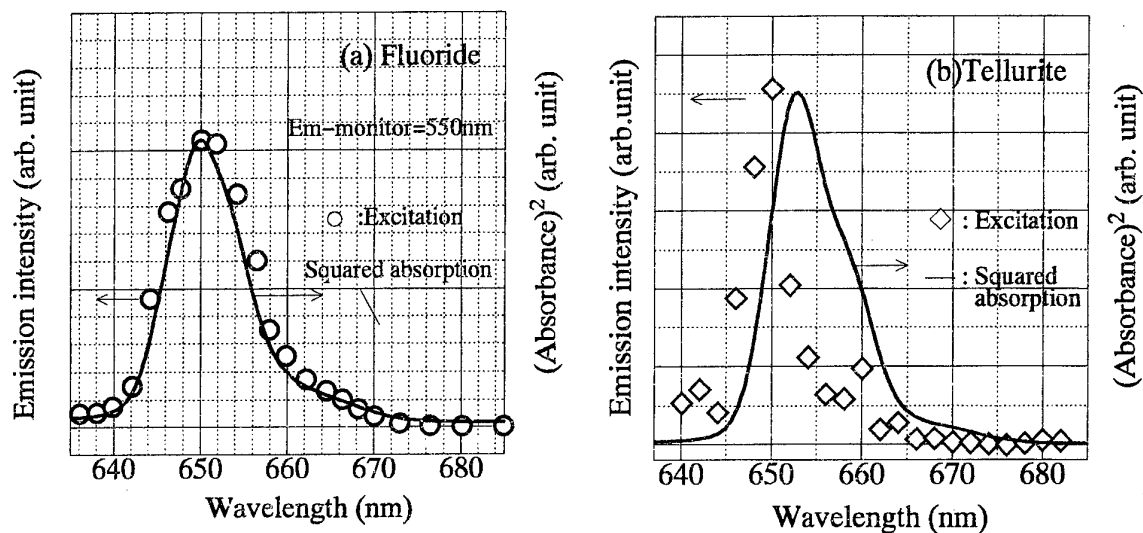


Fig. 2. Excitation spectra of Er^{3+} :550nm upconversion luminescence under CW-excitation and the squared absorption spectra of (a)Fluoride and (b)Tellurite glasses.

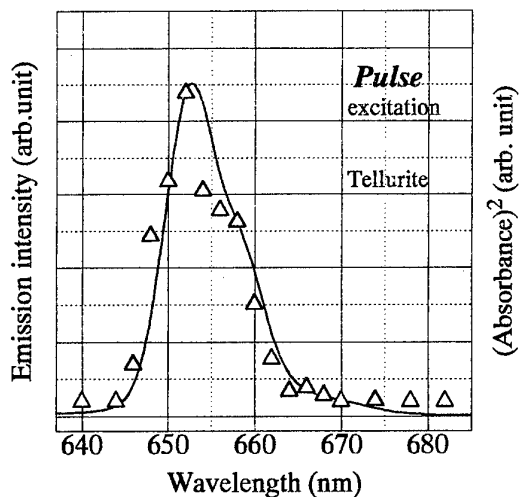


Fig. 3. The excitation spectrum of Er^{3+} :550nm upconversion luminescence under **pulse**-excitation and the squared absorption spectrum of the tellurite glass.

△ : Excitation — : Squared absorption

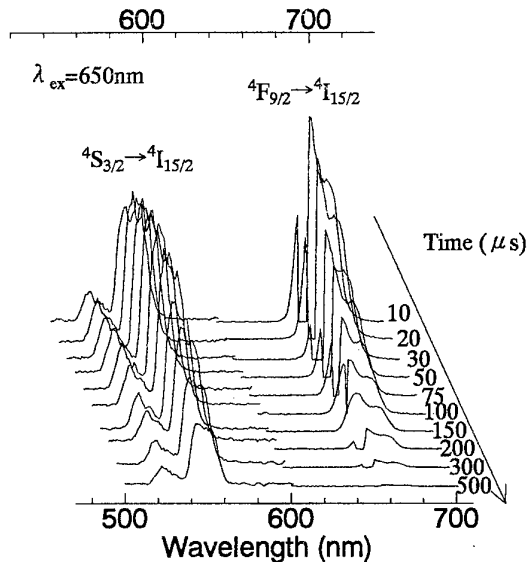


Fig. 4. Time resolved luminescence spectra of Er^{3+} doped fluoride glass by 650nm pumping.

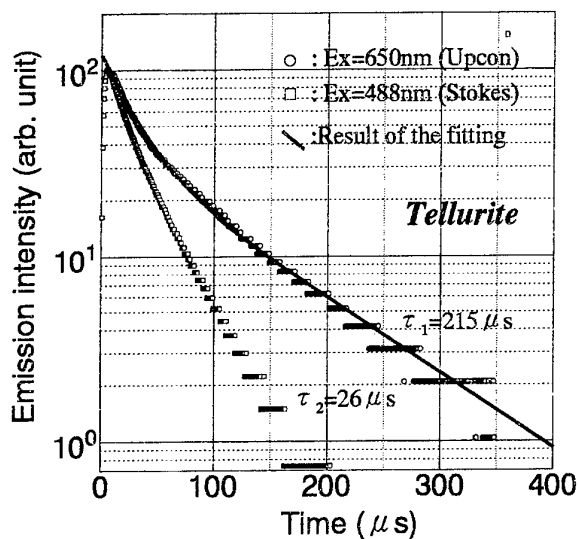


Fig. 5. Decay curves of Er^{3+} :550nm luminescences in tellurite glass.
Results of LSQ fitting is also shown.

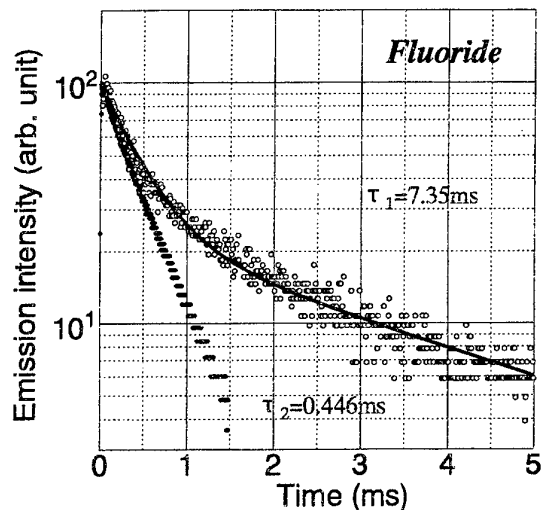


Fig. 6. The decay curves of Er^{3+} :550nm luminescence of the fluoride glass.
● :Stokes lumine. ○ :Upcon. lumine.
— :Result of LSQ fitting

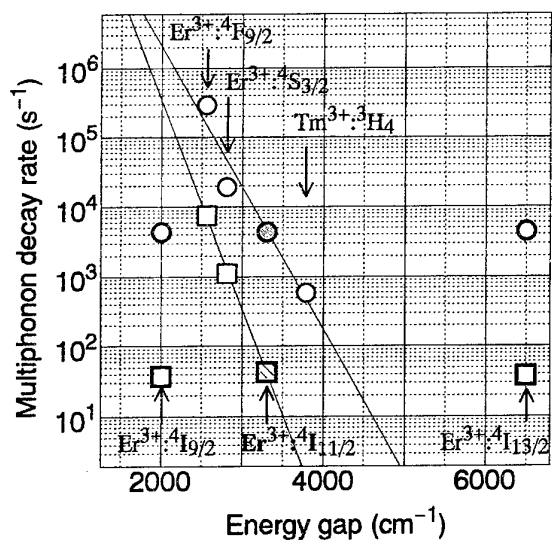


Fig. 7. Plots of W_{MP} of some levels versus energy gap.
○ :Tellurite glass □ :Fluoride glass

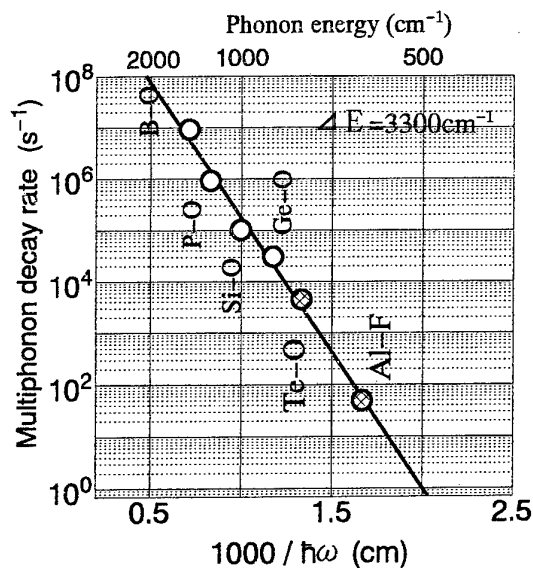


Fig. 8. Multiphonon decay rate of the Er^{3+} : $^4I_{11/2}$ level as a function of $(\hbar\omega)^{-1}$ for various glass matrices.
○ :previous work ⊗ :present work

ENERGY EXCHANGE PROCESSES IN Er^{3+} - DOPED FLUOROZIRCONATE GLASSES

V. K. Bogdanov, W. E. K. Gibbs, D.J. Booth

Optical Technology Research Laboratory, Victoria University, Melbourne, Australia.

Fax: +61-3-9688-4698, email : david=booth@vut.edu.au

J.S. Javorniczky, P.J. Newman, D.R. MacFarlane

Monash University, Department of Chemistry, Clayton, Victoria 3168, Australia

ABSTRACT

A comprehensive study has been conducted of the effects of high erbium dopant concentration on the fluorescence properties of the three lowest energy levels which are significant for infrared emission in Er^{3+} -doped fluorozirconate glasses. Pulsed pump radiation at wavelengths of 800 nm, 980 nm and 1.5 μm was used to measure fluorescence rise and decay waveforms for Er^{3+} concentrations between 0.2 mol% and 18 mol%. A rate-equation model has been developed for the relevant levels and the fitting of this model to the experimental results has enabled the contribution of various ion-ion energy exchange processes to be identified and quantified. These processes are significant in determining the population dynamics, especially for the high dopant concentrations used.

INTRODUCTION

In recent years there has been considerable interest in compact laser-diode-pumped rare-earth laser sources for a range of medical, sensor, spectroscopic and communications applications. For compact bulk laser configurations, such as with microchip lasers, relatively high doping concentrations are normally required to obtain sufficient absorption of the pump radiation in a thin sample. We have discussed the attractiveness of erbium-doped fluorozirconate glasses for this application and presented [1] fluorescence measurements at concentrations of up to 18 mol% which was higher than any previously reported dopant levels in these materials. The present paper reports further measurements of fluorescence rise and decay times together with rate-equation modelling that identifies and quantifies ion-ion energy exchange processes important to the population dynamics of the relevant levels.

GLASS PREPARATION

Samples of Er^{3+} -doped ZBAN glass ($\text{ZrF}_4\text{-BaF}_2\text{-AlF}_3\text{-NaF}$) with Er^{3+} concentrations from 0.2 to 18 mol% were prepared by methods described previously [2]. For Er concentrations up to 4 mol%, the glass contained some La^{3+} . Above this level of erbium doping, the La^{3+} concentration was zero and the glasses could be described as ZBEAN.

FLUORESCENCE MEASUREMENTS

The samples were pumped using a Spectra-Physics optical parametric oscillator (MOPO) with a 10 ns, 30 mJ, output at wavelengths appropriate to the $^4\text{I}_{9/2}$ (800 nm), $^4\text{I}_{11/2}$ (980 nm) and $^4\text{I}_{13/2}$ (1.5 μm) levels. Rise and the decay waveforms of the fluorescence from these levels were measured as described previously [1].

ENERGY LEVELS

The basic energy level diagram for Er^{3+} in ZBAN is shown in Fig.1. As the present work is primarily concerned with 800 nm pumping, most of the excited ions are considered to be in the three lowest levels ($^4\text{I}_{9/2}$, $^4\text{I}_{11/2}$, $^4\text{I}_{13/2}$), although the $^4\text{S}_{3/2} + ^2\text{H}_{11/2}$ levels are included for completeness. The levels considered in the modelling are designated as: $0(^4\text{I}_{15/2})$, $1(^4\text{I}_{13/2})$,

$2(^4I_{11/2})$ and $3(^4I_{9/2})$. The co-operative processes are designated as either two-ion(W) or three-ion (T), followed by up to six numbers indicating (starting levels, finishing levels).

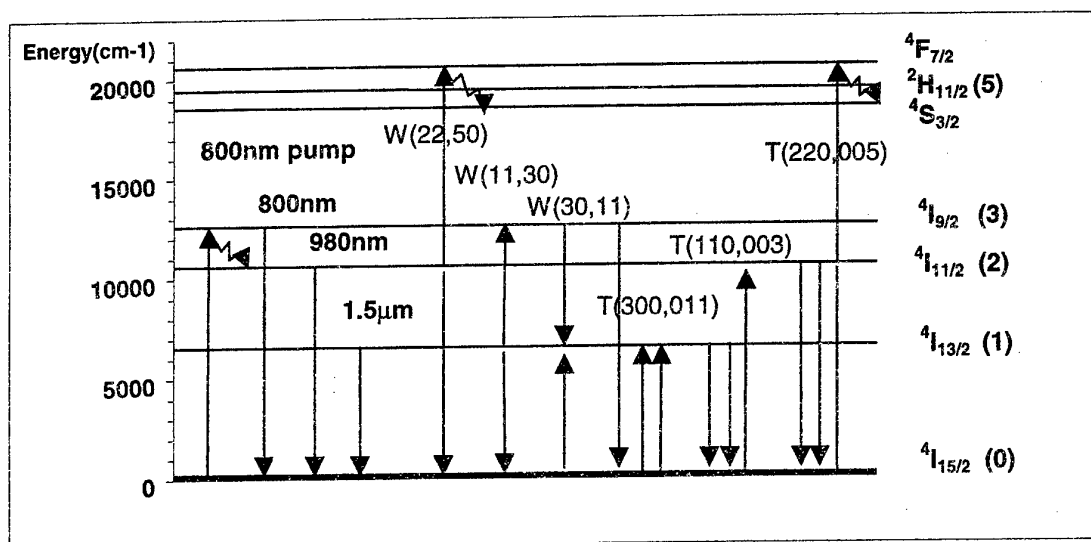


Figure1. Energy level diagram, fluorescence transitions and co-operative processes in $Er^{3+}/ZBAN$ glasses

The radiative transitions under consideration are shown together with the important multiphonon decays from the $^4I_{9/2}$, $^4F_{7/2}$ and $^2H_{11/2}$ levels. The co-operative processes examined in the modelling of the observed fluorescence rise and decay waveforms are also shown and are detailed below:

W(22,50): $[2(^4I_{11/2}) \rightarrow ^4S_{3/2} + ^4I_{15/2}]$, W(11,30): $[2(^4I_{13/2}) \rightarrow ^4I_{9/2} + ^4I_{15/2}]$,
W(30,11): $[^4I_{9/2} + ^4I_{15/2} \rightarrow 2(^4I_{13/2})]$, T(300,011): $[^4I_{9/2} + 2(^4I_{15/2}) \rightarrow ^4I_{15/2} + 2(^4I_{13/2})]$,
T(110,002): $[2(^4I_{13/2}) + ^4I_{15/2} \rightarrow 2(^4I_{15/2}) + ^4I_{9/2}]$, T(220,005): $[2(^4I_{11/2}) + ^4I_{15/2} \rightarrow 2(^4I_{15/2}) + ^4S_{3/2}]$

EXPERIMENTAL RESULTS

The rise and decay waveforms of most of the fluorescence lines were fitted with exponentials and a summary of the results is presented in Table1. Although each fit had a standard error of less than 5%, the repeatability of the measurements was about 20%, due to variations in the pulse-to-pulse spatial distribution of the pump source. The non-exponential (NE in Table1) behaviour of the decay of the $^4I_{11/2}$ and $^4I_{13/2}$ levels at high concentrations was characterised by instantaneous rate changes of a factor of between 3 and 10 during the time of the decay. The fluorescence at 801nm from the $^4I_{9/2}$ level could be detected only with direct pumping into this level. The measured decay times (not shown in Table 1) varied between 9 μs and 6 μs over the concentration range. As multiphonon processes dominate the $^4I_{9/2}$ decay, it would be expected that the rise times of the $^4I_{11/2}$ level would be similar to these decay times. Table 1 shows this to be the case. Table 1 also shows some substantial variations in rise and decay times of the various levels with concentration. This variation is a good indication of the existence of ion-ion interaction processes. Another interesting feature was the observation of a fast component in the rise of the population of the $^4I_{13/2}$ level with 800 nm pumping. Although the measurement of this fast component (Fast in Table1) was detector limited ($\sim 10\mu s$), the most noticeable feature was its contribution to the overall rise of the level population. Whilst this fast contribution was virtually nonexistent at low concentration, it completely dominated the rise waveform at the highest concentration used.

Table 1. Measured fluorescence rise and decay times for the pump wavelengths as shown.
NE – non-exponential, Fast – Fast component (see text)

Fluor. λ (Level)	Er (mol%)	800nm pump			980nm pump		1.5 μ m pump	
		Rise (μ s)	Decay (ms)	Decay (ms)	Rise (ms)	Decay (ms)	Rise (ms)	Decay (ms)
980nm ($^4I_{11/2}$)	0.4	7.7		7.7				
	0.8					7.8		
	1.6	7.8		8.0			3.9	10.4
	4	7.5		8.3		8.2	1.7	12.8
	8	6.9		NE				
	10	6.9		NE		NE	1.3	12.3
	14	6.2		NE				
	18	5.8		NE		NE	0.3	7.4
1.5 μ m ($^4I_{13/2}$)	0.2							9.3
	0.4		8.0	8.7				9.5
	0.8		8.0	9.1	11.1	12.7		10.0
	1.6		8.0	10.4				10.3
	4		8.0	10.0	10.0	16.5		9.0
	8	Fast +	3.9	11.6				NE
	10	Fast +	2.9	15.5	2.3	16.3		NE
	14	Fast +	1.0	15.0				NE
	18	Fast Only		7.4	0.61	7.7		NE

RATE-EQUATION MODELLING

General

The modelling is based on the processes shown in Fig.1. The level populations in the rate-equations are normalised to the total ion concentration C [3] and the normalised initial population $n(0)$ of each pumped level was determined from

$$n(0) = \sigma E / h\nu S,$$

where σ is the absorption cross-section, E is the energy of the pump pulse, $h\nu$ is the pump photon energy and S is the pumped area of the sample. The calculated initial populations were:

$$\begin{aligned} n_1(0) &= (2 \pm 0.4) \times 10^{-3} \quad (\text{for } \sigma_{1.5\mu\text{m}} = 4.6 \times 10^{(-21)} \text{ cm}^2, E_{1.5\mu\text{m}} = 6\text{mJ}, S = 10\text{mm}^2) \\ n_2(0) &= (1 \pm 0.2) \times 10^{-3} \quad (\text{for } \sigma_{980\text{nm}} = 1.8 \times 10^{(-21)} \text{ cm}^2, E_{980\text{nm}} = 14\text{mJ}, S = 13\text{mm}^2) \\ n_3(0) &= (5 \pm 0.1) \times 10^{-4} \quad (\text{for } \sigma_{800\text{nm}} = 6.4 \times 10^{(-22)} \text{ cm}^2, E_{800\text{nm}} = 5\text{mJ}, S = 2.5\text{mm}^2) \end{aligned}$$

The cross-sections were determined from appropriate absorption measurements. It can be seen that the ground state population was not significantly perturbed by the pump energy density used.

Direct pumping

The population dynamics of levels $^4I_{13/2}$ and $^4I_{11/2}$ under direct pumping was modelled to examine the contribution of the co-operative processes W(22,50) and W(11,30) in Fig.1. The rate-equations incorporating these processes are nonlinear, and this could explain the observed non-exponential decay of these levels under direct pumping. Both processes are well known [3]; however, no estimates of the cross-relaxation coefficients in fluoride glasses have been published. The behaviour of both $^4I_{13/2}$ and $^4I_{11/2}$ levels was modelled by the equation:

$$\frac{dn(t)}{dt} = -\frac{n(t)}{\tau} - 2Kcn^2(t)$$

where τ is the measured decay time in low concentrations and K is the cross-relaxation coefficient corresponding to W(22,50) or W(11,30). The normalised initial level populations, $n(0)$, used were those detailed above. The explicit solution of these equations was fitted to the experimental waveforms to obtain estimates of the two parameters as shown in Table 2.

Table 2. Cross-relaxation coefficients for co-operative processes in Er/ZBAN glasses

Er (mol%)	0.8	4	10	14	18
W(11,30)($\times 10^{(-17)}\text{cm}^3\text{s}^{(-1)}$)		1.0	2.3	4.0	4.3
W(22,50) ($\times 10^{(-17)}\text{cm}^3\text{s}^{(-1)}$)	1.7		3.0	7.1	

Although the values in Table 2 are subject to the uncertainties in the initial populations used in the fitting, there is an obvious trend to increased values at higher concentrations. One possible reason for this could be the presence of additional co-operative processes such as T(110,002) and T(220,005) (Fig.1). Although three ions are needed for these interactions, their probability could be appreciable since only the ground level and relatively highly-populated levels are involved in the case of direct pumping. However, inclusion of the three-ion processes with the limited data set results in fairly large uncertainties in the fitted parameters. Whilst a more detailed analysis of these processes is needed, the coefficients in Table 2 were sufficient to use as a starting point for the modelling of $^4\text{I}_{13/2}$ and $^4\text{I}_{11/2}$ levels with 800nm pumping.

800nm pumping

For 800 nm pumping (see Table1) the decays of the $^4\text{I}_{13/2}$ and $^4\text{I}_{11/2}$ levels are less concentration dependent than with direct pumping. This could be due to the reduced importance of the three-ion processes T(110,002) and T(220,005) resulting from the relatively smaller populations of these levels caused by the smaller number of initially excited ions (see $n_1(0)$, $n_2(0)$, $n_3(0)$ above). For this reason these processes were not included in the present model. However, all of the other processes in Fig.1 were considered. The fast rise of the population of $^4\text{I}_{13/2}$ level, dominant at high concentrations, has already been described. This observation would suggest a co-operative process originating from the $^4\text{I}_{9/2}$ level and hence the well-known [4] two-ion process W(30,11) (Fig.1) was included in the model. However, as discussed below, good agreement with the measured waveforms over the whole range of concentrations, requires the inclusion of the three-ion process T(300,011) instead of W(30,11). The full rate equations, describing the behaviour of the system with 800 nm pump are as follows:

$$\begin{aligned} \frac{dn_1(t)}{dt} &= -(A_1 + \omega_1^{mph})n_1(t) + (b_{21}A_2 + \omega_2^{mph})n_2(t) + b_{31}A_3n_3(t) + 2W(30,11)Cn_0(t)n_3(t) + \\ &\quad + 2T(300,011)C^2n_3(t)n_0^2(t) - 2W(11,30)Cn_1^2(t) \\ \frac{dn_2(t)}{dt} &= -(A_2 + \omega_2^{mph})n_2(t) + (b_{32}A_3 + \omega_3^{mph})n_3(t) - 2W(22,50)Cn_2^2(t) \\ \frac{dn_3(t)}{dt} &= -(A_3 + \omega_3^{mph})n_3(t) + W(11,30)Cn_1^2(t) - W(30,11)Cn_3(t)n_0(t) - T(300,011)C^2n_3(t)n_0^2(t) \end{aligned}$$

In these equations, n_1, n_2, n_3 are the normalised populations of levels $^4\text{I}_{13/2}$, $^4\text{I}_{11/2}$ and $^4\text{I}_{9/2}$; A_i is the radiative decay rate and ω_i^{mph} is the multiphonon decay rate of the i -th level; b_{ij} is the

branching ratio from i-th to j-th level; C is the concentration of the sample and W(30,11), W(11,30), W(22,50) and T(300,011) are the cross-relaxation coefficients for the ion-ion interaction processes shown in Fig.1. The equation for the ground level has not been presented since the number of excited ions is very small and thus $n_0 \approx 1$. The values of the parameters used are given in Table 3.

Table 3. Parameters, used in the rate-equation modelling (ow-our work)

Parameter	$A_1(s^{-1})$	$A_2(s^{-1})$	$A_3(s^{-1})$	$\omega_1(s^{-1})$	$\omega_2(s^{-1})$	$\omega_3(s^{-1})$	b_{21}	b_{31}	b_{32}
Value:	102	115	154	0	8	125000	0.12	0.22	0.01
Source:	5,6,7,ow	5, 6	5	5,7,ow	5,6,7, ow	5,ow	5, 6	5, 6	5, 6

Numerical solutions to the rate equations were obtained by the Fehlberg fourth-fifth order Runge-Kutta method and these were used to examine the importance of the various co-operative processes by fitting these solutions to the experimental waveforms. The most challenging task was the modelling of the fast rise of $^4I_{13/2}$ level. The inclusion of the two-ion process W(30,11) and the exclusion of the three-ion process T(300,011) gave good fits to the data over the range of concentrations but required a value of W(11,30) that was ten times that determined from direct pumping at 1.5 μm . However, inclusion of T(300,011) and the exclusion of W(30,11) gave good agreement and a value of W(11,30) consistent with that determined from direct pumping. The necessity of including the three-ion process is a significant result of the modelling. The values of the cross-relaxation coefficients that produced the best fits to the experimental waveforms are given in Table 4

Table 4. Cross-relaxation coefficients for Er/ZBEAN glasses

Parameter:	W(22,50)	W(11,30)	W(30,11)	T(300,011)
Value(cm^3/s)	$5 \times 10^{(-17)}$	$4 \times 10^{(-17)}$	0	$0.4 \times 10^{(-38)}$

Because of the use of numerical routines, it is difficult to give an estimate of the uncertainties in the values of these coefficients. However, a study of the sensitivity of the fits to changes in the values of coefficients, indicated an uncertainty of about 50%. Some of the measured waveforms together with the model predictions are presented in Figure 2. The good agreement indicates that a satisfactory model has been developed.

CONCLUSION

Fluorescence waveforms were studied for ZBEAN glasses having Er^{3+} concentration of up to 18 mol% using a number of pumping wavelengths. A rate-equation model for the population dynamics of the $^4I_{13/2}$, $^4I_{11/2}$ and $^4I_{9/2}$ levels has been developed and good agreement with the experimental data has been obtained. The model incorporates a number of co-operative processes and estimates of the corresponding cross-relaxation coefficients have been obtained. A previously unreported three-ion process has been found to be necessary to explain the observed fast rise in the population of the $^4I_{13/2}$ level.

REFERENCES

- [1] V.K.Bogdanov, W.E.K.Gibbs, D.J.Booth, J.S.Javorniczki, P.J.Newman and D.R.MacFarlane, Opt. Commun.132 (1996) 73
- [2] J.S.Javorniczki, P.J.Newman, D.R.MacFarlane, D.J.Booth and V.K.Bogdanov, J. Non-Cryst. Solids, 184 (1995) 249
- [3] D.R.MacFarlane, J.S.Javorniczki, P.J.Newman, V.K.Bogdanov, D.J.Booth and W.E.K.Gibbs, J. Non-Cryst. Solids 213 & 214 (1997) 158
- [4] W.Q.Shi, M.Bass and M.Birnbaum, J. Opt. Soc. Am. B, 7 (1990) 1456

- [5] X.Zou and T.Izumitany, J. Non-Cryst. Solids, 162 (1993) 68
 [6] L.Wetenkamp, G.F.West and H.Tobben, J. Non-Cryst. Solids, 140 (1992) 35
 [7] M.D.Shinn, W.A.Sibley, M.G.Drexhage and R.N.Brown, Phys. Rev. B, 27 (1983) 6635

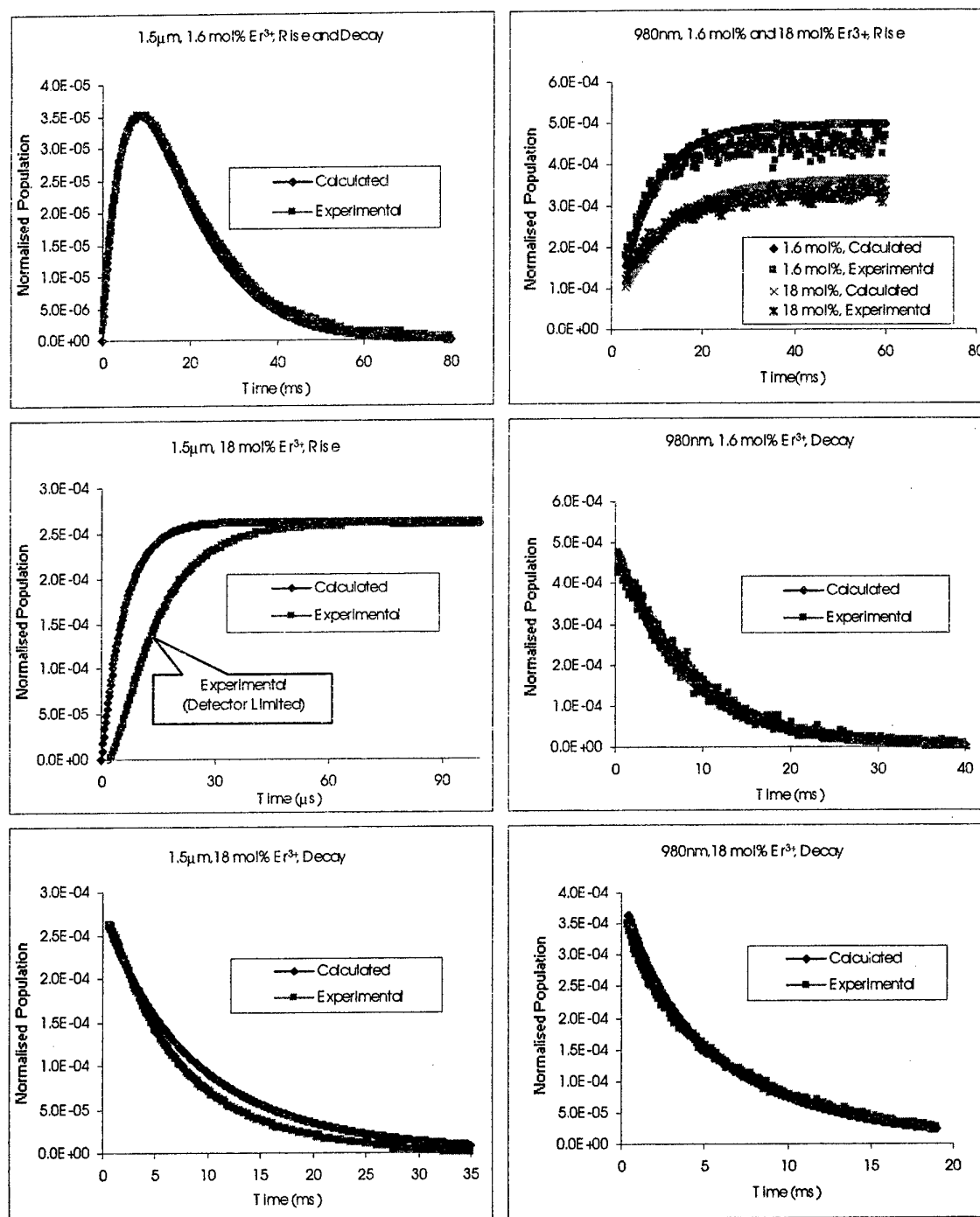


Figure 2. Calculated populations and experimental fluorescence waveforms for the $^4\text{I}_{13/2}$ (1.5 μm) and $^4\text{I}_{11/2}$ (980 nm) levels for Er-concentrations of 1.6 mol% and 18 mol%.

REDUCTION OF OH-RELATED PHOTOLUMINESCENCE QUENCHING IN Pr-DOPED GeS₂-BASED GLASSES BY MEANS OF PURIFICATION

X. Liu*, B. B. Kale**, V. K. Tikhomirov*, and A. Jha*

*Department of Materials, University of Leeds, Leeds LS2 9JT, UK; A.Jha@leeds.ac.uk

**CMET Laboratory, Pashan-NDA Road, Pune 411021, India

ABSTRACT

Pr-doped germanium sulphide glasses are one of the most promising candidates for an efficient 1.3 μm fibre amplifier. The major problem in designing this amplifier is the presence of OH⁻ impurities and oxides which quench the ¹G₄ metastable state. A chemical method of removal of OH⁻ impurities from GeS₂ powder is investigated in this paper. Thermodynamic conditions for the purification of GeS₂ by vapour phase reaction were established by controlling the reactive atmosphere, mixed with Ar - 5 vol % H₂ - 10 vol % HCl, at different temperatures (250 - 470 °C). The glasses made from the purified powders were characterised using FTIR to estimate the concentration of OH⁻ ions. The equilibrium condition for the removal of OH⁻ impurities from GeS₂, Ga₂S₃, and CsI starting powders is discussed by considering the Gibbs free energy minimisation condition in an atmosphere of Ar - H₂ - HCl. The roles of vapour species GeX₄, GaX₃ (X: Cl, I) are particularly discussed in view of the removal of OH⁻ ions and oxide impurities by considering the partial pressure-temperature diagram.

The lifetimes of ¹G₄ level in Pr-doped purified glasses were measured. The relationships between the quenching of ¹G₄ photoluminescence and OH⁻ ion concentration is discussed in view of the energy transfer model. The effect of the presence of OH⁻ ion on the solubility of Pr-ions in the glass is also briefly discussed.

1. INTRODUCTION

Germanium sulphide glasses are promising hosts for Pr³⁺ ions for optical fibre amplifiers in the 1.3 μm telecommunication window^[1]. However, a major problem in making these glasses is the existence of OH-related impurities in the glasses, which result in the photoluminescence quenching. It is reported that the concentration quenching of photoluminescence results from the poor solubility of Pr³⁺ in the glasses and the presence of OH⁻ ion impurities in the glasses has strongly affected the solubility of Pr³⁺ in the glasses^[2]. For example, more than 400 ppmw Pr³⁺ can produce the complete self-quenching for unary GeS₂ glasses, 1000 ppmw Pr₂S₃ for GeGaS glasses, and 2000 ppmw Pr³⁺ for GeS₂-Ga₂S₃-CsI glasses. It is argued that the emission lifetime of ¹G₄ level of Pr³⁺ in GeS₂-based glasses decreases with increasing hydroxyl- and oxygen-content and both oxygen bonds and hydroxyl groups could be the acceptors^[3-5].

In this investigation, the combined physical and chemical method of removal of OH⁻ impurities from GeS₂ powder and mixed compositions was studied. Thermodynamic conditions for purification of GeS₂ powder by vapour phase reaction were established by regulation of the atmosphere and temperatures. The equilibrium condition for the removal of OH⁻ impurities from GeS₂, Ga₂S₃, and CsI starting powders are discussed by considering the Gibbs free energy minimisation condition in an atmosphere of Ar + H₂ + HCl. The roles of vapour species GeX₄, GaX₃ (X: Cl, I) are particularly discussed in view of the removal of OH⁻ ions and oxide impurities by considering the partial pressure-temperature diagram.

The glasses made from the purified powders were characterised using FTIR to estimate the concentration of OH⁻ ions. The lifetimes of ¹G₄ level in Pr-doped purified glasses were measured. The relationships between the quenching of ¹G₄ photoluminescence and OH⁻ ion concentration is discussed in view of the energy transfer model. The effect of the presence of OH⁻ ion on the solubility of Pr-ions in the glass is also quantitatively discussed.

2. EXPERIMENTAL

The starting materials were elemental and compound chemicals with 99.99 - 99.999% purity. The glass composition was 79 mol % GeS₂, 15 mol % Ga₂S₃, and 6 mol % CsI, doped with 2000 ppmw and 700 ppmw. The procedure of making Pr-doped GeS₂-based glasses was described in earlier papers^[2,5,6].

Germanium sulphide powder was purified by using a silica glass reactor, shown in figure 1. The powder mixed with a ratio of GeS₂ : S = 5 : 1 was heated slowly from room temperatures to 100 °C and then to 200 - 500 °C in an atmosphere of 4 vol % H₂ + 10 vol % HCl + Ar gas mixture for several hours (6 - 12 h). After purification, the mixture was cooled to room temperatures in the Ar + H₂ atmosphere, and it was quickly withdrawn from the reactor to minimise the contact with the surrounding air. The purified chemical was then transferred inside glove box where it was used for making glass.

The presence of OH⁻ ions in the glasses was characterised by measuring the strength of the OH⁻ peak at a wavenumber of ~ 3500 cm⁻¹ using FTIR. The concentration of OH⁻ ions in the glasses was estimated by using the molar extinction coefficient (ε_{OH}), which is about 14.5 l·mol⁻¹·cm⁻¹ for germanium sulphide glasses^[6]. The Pr-ion absorption in doped glasses was determined using a UV-VIS-NIR spectrophotometer operating in the 300-3200 nm range. The lifetimes of ¹G₄ level in Pr-doped purified glasses were measured in the same way mentioned in elsewhere^[5].

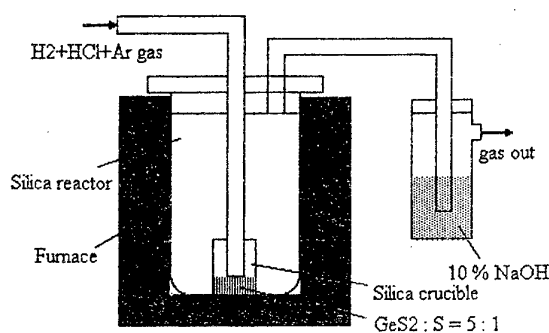
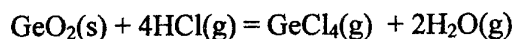


Figure 1: Process of purification of GeS₂

3. RESULTS AND DISCUSSION

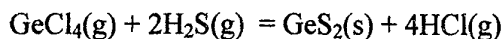
1) Purification of GeS₂

The GeS₂ powder and the mixed compositions were purified by maintaining a reactive atmosphere of HCl + H₂ + Ar gas mixture in this investigation. Figure 2 shows that the strong OH⁻ absorption exists in the glass made from GeS₂ powder. This implies that the existence of OH-related impurities in the GeS₂ powder is in the form of GeO₂(GeOH) and water adsorbed on the surface of the powder. The OH-related impurities was mainly reduced through the following reactions.



$$\Delta G^\circ_T = -48468 + 79.5T \text{ J mol}^{-1}, \quad T_{\text{eq}} = 610 \text{ K},$$

$$K_P = P_{\text{H}_2\text{O}}^2 \cdot P_{\text{GeCl}_4} / P_{\text{HCl}}^4 \quad (1)$$



$$\Delta G^\circ_T = 25995 - 85.3T \text{ J mol}^{-1}, \quad T_{\text{eq}} = 305 \text{ K},$$

$$K_P = P_{\text{HCl}}^4 / P_{\text{H}_2}^2 P_{\text{GeCl}_4} P_{\text{S}_2} \quad (2)$$

The free energy changed with temperatures in the reaction (1) and (2) can be calculated from thermodynamic data^[7]. The gas phase at 600 -1000 K and a pressure of 1 atm is assumed in equilibrium. The partial pressures of germanium halides in the equilibrium are plotted in figure 3. For example, in an atmosphere of $\text{H}_2 + \text{HCl} + \text{Ar}$ reactive gas mixture, reaction (1) will occur and, GeCl_4 gas will form together with steam. The equilibrium partial pressures of H_2O and GeCl_4 are compared with the reacting gas HCl . The equilibrium computation confirms that the HCl partial pressure will have the highest value compared to H_2O , GeCl_4 , H_2S , SO_2 and S_2 gaseous species. We have also compared the partial pressures of GeS and GeCl_2 , which are less significant gaseous species but are important for considering the overall mass balance of Ge in the reactor. For sustaining the purification reactions (1) and (2), the conditions imposed by Le Chatelier's principle must be satisfied. Figure 2 shows that the strength of OH^- absorption band in the purified unary GeS_2 glass was much lower than that in the unpurified glass. Reaction (1) is exothermic and undergoes a major reduction in gaseous phase molar volume from 4 moles on the left hand side of the reaction to 2 moles in the forward direction. This means that a higher equilibrium partial pressure of HCl will shift the equilibrium in the forward direction. The exothermic nature of this reaction demands that the temperature must be kept below the equilibrium temperature 610 K, which was derived by equating ΔG , to zero in equation (1). On the other hand, reaction (2) is mildly endothermic and undergoes a major increase in the molar volume in the forward direction. The signs of enthalpy and entropy changes for reaction (2) impose conditions that the temperature of the reactor must be kept above the equilibrium temperature of 305 K, and the gaseous reaction product, HCl must be removed. Since HCl is consumed in the reaction (2), the equilibrium in reaction (1) is never achieved. In the same way, the backward equilibrium in reaction (1) never dominates because GeCl_4 is continuously used by reaction (2). Table 1 summarises the results of the purification reaction under reactive atmosphere. From this table, it is apparent that the purification process is also dependent on time. This is not unexpected.

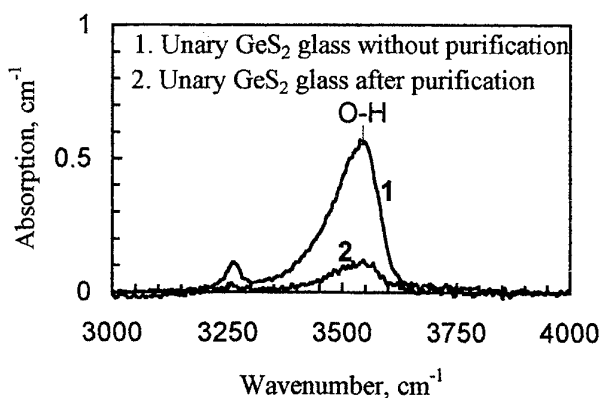


Figure 2: Comparison of OH^- absorption bands in the glass before and after purification

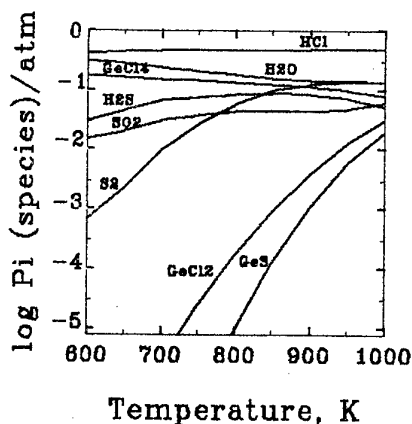


Figure 3: Plot of partial pressure in $\log (p_i / \text{atm})$ via temperature in K.

Table 1: Purification reaction and OH concentration, c in ppmw, in the glass.
Glass composition: 79 mol % GeS₂, 15 mol % Ga₂S₃, and 6 mol % CsI.
Purification conditions: T = temperature in °C and t = time in hours.

Sample	Reaction conditions	$\alpha_{\lambda, \text{cm}^{-1}}$	c, ppmw
S-24	unary GeS ₂ glass without purification	1.28	250
P ₇	100 mol % GeS ₂ , T = 475, t = 5	0.34	60
S-0	without purification	2.82	470
P ₁	T = 375, t = 8, GeS ₂ powder	1.61	270
P ₂	T = 375, t = 16, GeS ₂ powder	1.86	310
P ₄	T = 275, t = 24, GeS ₂ powder	1.80	300
P ₈	T = 475, t = 6, glass composition	0.83	140
P ₉	T = 350, t = 6, glass composition	2.01	340

2) Estimation of OH⁻ concentration in the glass

The molar extinction coefficient, ϵ_{OH} , for germanium sulphide glasses was characterised and found to be 14.5 l·mol⁻¹·cm⁻¹[6]. Estimation of OH concentration in the glasses can be made from the OH⁻ absorption band using Lambert-Beer law ($I = I_0 \exp[-\alpha d]$, where α_{λ} is the absorption coefficient in cm⁻¹, I_0 and I are incident and transmitted light intensity at wavelength λ respectively, and d is the sample thickness in cm). The concentration of OH⁻, c (in ppmw), is related to the absorption coefficient according to the following equation:

$$c = \frac{1000}{\ln(10)} \cdot \frac{M}{\rho} \cdot \frac{\alpha_{\lambda}}{\epsilon_{\text{OH}}} \quad (3),$$

where M is the molar weight of an OH⁻ ion, ρ is the density of the glass ($= 3.05 \text{ g/cm}^3$). The concentrations of OH⁻ ions in the purified and unpurified glasses are tabulated in table 1, from which it can be seen that the purification reaction by using HCl and H₂ gas mixture with excess sulphur contributes to a significant reduction in the OH⁻ concentration of the unary and ternary glasses.

3) OH⁻ photoluminescence quenching

The presence of OH⁻ in the Pr-doped GeS₂-based glasses has resulted in a strong ¹G₄ fluorescence quenching by decrease of solubility of Pr³⁺ in the glasses and by impurities quenching mechanism^[2-6]. It is argued that the ¹G₄ lifetime quenching in the GeS₂-based glasses mainly results from the existence of OH⁻ impurities which compete with Pr-ions for sharing structure sites in the germanium sulphide glasses. The presence of OH⁻ ions, as stated in reaction (1) where H₂O gas is involved in the reaction, contributes to the formation of GeO₂ in the glass. As a result [GeO₄]⁴⁻ tetrahedra are expected to form and adversely influence the non-radiative rate from ¹G₄ level of Pr-ions. Furthermore, a [GeO₄]⁴⁻ unit is smaller in size than a [GeS₄]⁴⁻ tetrahedron, consequently the overall packing of the glass structure results in a further reduction in the solubility of Pr-ions.

The relationship between solubility of Pr³⁺ ions in the glass structure and OH⁻ absorption coefficient, α_{λ} , was quantitatively studied by characterisation of Pr³⁺ absorption spectra at the range of 1200 - 1800 nm and by the corresponding integrated absorption coefficients. The integrated absorption coefficient, α_i in cm⁻¹·s⁻¹, is defined as^[9]:

$$\alpha_i = \int f(\nu) d\nu = c \int f(\nu) d\nu \quad (4)$$

where $f(\nu)$ is the absorption coefficient in cm^{-1} at frequency ν , ν is the wavenumber in cm^{-1} and c is the speed of light. The overlapping 3F_4 and 3F_3 absorption bands were chosen to calculate the integrated absorption coefficient, shown in figure 4(a). The plots of the integrated absorption coefficient for 700 ppmw and 2000ppmw Pr-ion concentrations versus

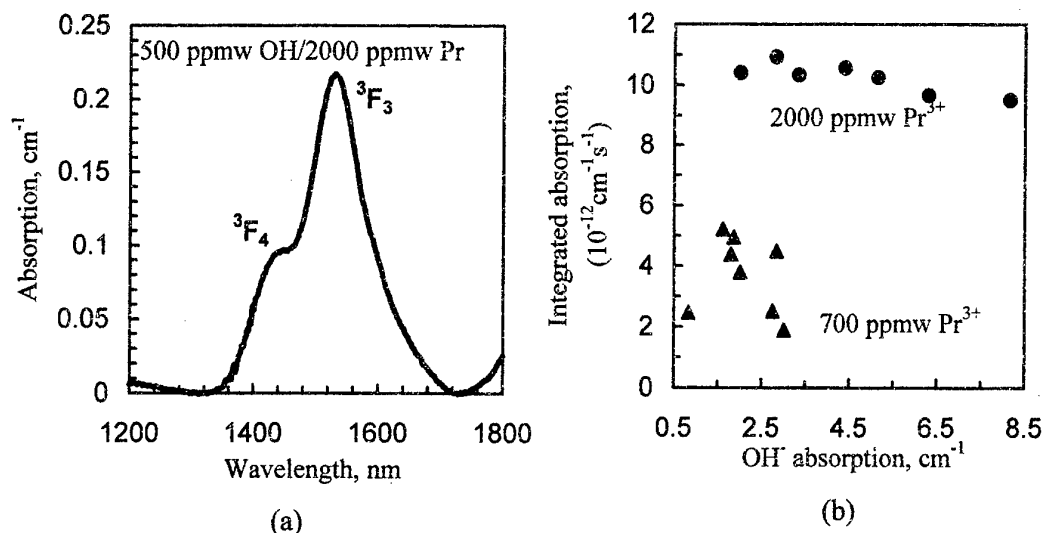


Figure 4: (a) Absorption spectra of 500 ppmw OH⁻ and 2000 ppmw Pr³⁺ doped glass sample. (b) Integrated absorption of overlapping 3F_4 and 3F_3 absorption bands as a function of OH⁻ absorption coefficient in the glass samples.

OH⁻ absorption are shown in Figure 4(b). It can be estimated from figure 4(b) that α_i is $11.2 \times 10^{12} \text{ cm}^{-1} \cdot \text{s}^{-1}$ for 2000 ppmw and $3.6 \times 10^{12} \text{ cm}^{-1} \cdot \text{s}^{-1}$ for 700 ppmw Pr³⁺-doped glasses without OH⁻ impurities. These data are consistent with those reported for I⁻ ion modified GeS₂ glasses^[8], which are $\sim 11.7 \times 10^{12} \text{ cm}^{-1} \cdot \text{s}^{-1}$ for 2000 ppmw and $\sim 3.8 \times 10^{12} \text{ cm}^{-1} \cdot \text{s}^{-1}$ for 700 ppmw. From figure 4(b), it is evident that the solubility of Pr³⁺ in the decreases with increased OH⁻ absorption.

The measured 1G_4 lifetimes (τ , μs) in 2000 ppmw Pr³⁺ doped glasses were tabulated in Table 2. In view of the energy transfer mechanism, the inverse measured lifetime, (τ , μs), increases with OH⁻ concentration according to equation $\tau_{\text{tot}}^{-1} = \tau_{\text{max}}^{-1} + k c_{\text{OH}}$, where k is constant and c_{OH} is OH⁻ concentration in ppmw^[6-9].

Table 2: Measured 1G_4 lifetime in the GeS₂ based glasses with different OH⁻ concentrations

Sample	OH⁻ concentration, ppmw	τ (μs) $^1G_4 - ^3H_5$
L₁	360	190
L₂	200	110
L₃	110	195
L₄	110	140
L₅	100	155
L₆	100	210
L₇	80	160
L₀	10	360

4. CONCLUSIONS

Thermodynamic conditions for OH⁻ ion removal from the starting powder were studied. The equilibrium conditions determined by equation (1) and (2) require that the purification temperature should not be maintained well above 610 K. The presence of excess sulphur while purifying GeS₂ starting powder is essential for reducing the OH⁻ concentration. The process is also temperature and time dependent. The lifetime of ¹G₄ level in Pr-ion is adversely affected by the presence of oxygen and OH⁻ ions.

ACKNOWLEDGEMENTS

The authors acknowledge the financial support of the Ph.D. studentship from Galileo Corporation in Massachusetts, USA.

REFERENCES

1. P. N. Kumta and S. H. Risbud, J. Materials. Sci., 29 (1994) 1135-1158.
2. D. Marchese and A. Jha, J. Non-cryst. Solids, 213 & 214 (1997) 381-387.
3. D. P. Machewirth, K. Wei et al., J. Non-cryst. Solids, 213 & 214 (1997) 295-303.
4. D. R. Simons, A. J. Faber and H. de Waal, J. Non-cryst. Solids, 185 (1995) 283-288.
5. D. Marchese, G. Kakarantzas and A. Jha, J. Non-cryst. Solids, 196 (1996) 314-319.
6. B. B. Kale, X. Liu, M. Naftaly and A. Jha, 18th International Congress on Glass, CA, USA, 1998 (in press).
7. I. Barin and O. Knacke, Thermochemical Properties of Inorganic Substances, 1973 & 1977 (supplement).
8. V. Krasteva et al, J. Non-cryst. Solids, 213 & 214 (1997) 304-310.
9. L. A. Riseberg, Progress in Optics, vol. XIV (1976) 91-157.

**Mechanism of self quenching of fluorescence
of thulium in tellurite glasses**

GP14

D.B. Hollis

Department of Electronic Engineering & Physics

University of Paisley

Paisley PA1 2BE

M.J. Payne

DRA Malvern

St. Andrew's Road

Great Malvern Worcs WR14 3PS

Thulium has been used as a potential laser ion in crystals, but not in glasses. A strong self quenching mechanism exists for thulium in glasses, which does not exist for thulium in crystals. Two possible mechanisms could be active:- distortion of sites leading to relaxed selection rules and loss of energy via phonon-assisted routes, and/or self-quenching by clusters of thulium ions. We have investigated these for the fluorescence band centred at $1.8\mu\text{m}$.

Pulsed 20mW, 10ns, excitation from a Ti-sapphire laser at 795 nm, and whole band (1600-2100 nm) fluorescence decay curves have been obtained using a doped InGaAs diode, custom built by Plessey, such that it detects over the range 1500-3000 nm. The diode detector operated at room temperature.

C.W. excitation using the monochromated output of a xenon lamp - $795\text{ nm} \pm 5\text{ nm}$ - has been used to obtain spectral intensity - wavelength profiles of the fluorescence over the range 1600-2100 nm, using an EG and G Judson type PbS, dry CO_2 cooled photo-conductive cell which detects over the range 1200-2600 nm.

A series of alkali tellurite glasses of form $\text{XR}_2\text{O} \cdot (1-\text{X})\text{TeO}_2$ with 0.1 to 5.0 mol % of Tm_2O_3 was made, for $\text{R} = \text{Li}, \text{Na}, \text{K}$, with X covering the range 10, 15, 20 and 30 mol%. The dry alkali carbonate, thulium oxide, and tellurium oxide were weighed in the correct proportions and mixed thoroughly before transfer to crucibles made of recrystallised alumina. The glasses were melted at 850°C in air for 30 minutes, poured into disk molds, and annealed at 250°C for 30 minutes, then cooled at 1°C per minute to ambient. The top surfaces and sides of the disks were sufficiently smooth to not require further polishing. The spectral measurements, including ultraviolet - visible - infrared absorption, and measurements of disk thickness were taken.

The results all indicate a quantum yield which falls with concentration of thulium above 0.5 mol%. By expressing the fluorescence signal intensity under c.w. excitation in units of intensity per unit of excitation absorbed per mole of thulium we obtain a falling signoid plot of quantum yield with concentration indicative of Forster-Dexter type multipole - multipole interactions. Dipole - dipole interactions seem to be ruled out, on grounds of the relatively low concentrations on thulium ions needed to produce that type of interaction. Instead, dipole-quadrupole interactions appear to be active. The fluorescent lifetime measurements for pulsed excitation show a similar behaviour, again indicating dipole-quadrupole interactions. Both of these would suggest that the ions are in close proximity to each other i.e. clustered. If site/
 $\text{IS}(\text{NOG})^2$ '98

distortion and relaxation of selection rules were the only determinant, one would expect dipole-dipole interactions to be the dominant quenching mechanism at both low and high concentrations. The "background" quenching at low concentrations is an indication of the effect of site distortion/vibronic coupling, and can be compared to that seen in the more regular ion sites of crystals doped with low concentrations of thulium.

Research described elsewhere in this conference in which EXAFS studies of thulium in glasses is reported, shows possible clustering of thulium ions in alkali rich parts of the glassy network. Studies by us on densities and electronic energy gaps of undoped alkali tellurite glasses, also reported at this conference, indicate the presence of inhomogeneity on a microscopic scale. This may indicate presence of alkali rich regions in the glass structure, into which the thulium ions migrate and cluster.

ENERGY TRANSFER AND FREQUENCY UPCONVERSION IN Pr³⁺-DOPED FLUOROPHOSPHATE GLASS

R. Balda^a, J. Fernández^a, J.L. Adam^b, A. Mendioroz^a, and
M.A. Arriandiaga^c

^aDpto. de Física Aplicada I, E.T.S.I.I. y Telecom., Universidad del País Vasco, Alameda Urquijo s/n, 48013, Bilbao, Spain. email wupbacrr@bi.ehu.es

^bLaboratoire des Verres & Céramiques, U.R.A.-C.N.R.S. No 1496, Campus de Beaulieu, Université de Rennes I, 35042 Rennes, Cedex, France

^cDpto. Física Aplicada II, Facultad de Ciencias, Universidad del País Vasco, Apartado 644, Bilbao, Spain

ABSTRACT

We have investigated the process of fluorescence quenching from the ¹D₂ state of Pr³⁺ ions in fluorophosphate glasses of composition (in mol%) 60NaPO₃-15BaF₂-(25-x)GdF₃-xPrF₃ (x= 0.1, 0.2, 0.5, 1, 2, 5, and 10) due to energy transfer among Pr³⁺ ions. The fluorescence of the ¹D₂ level shows a strong concentration quenching for Pr³⁺ concentrations higher than x=0.1 mol% even at 4.2 K. The non-exponential character of the decays of the ¹D₂ level when increasing concentration, together with the behaviour of the effective decay rates as a function of Pr³⁺ concentration, indicate the presence of a dipole-dipole quenching process in the framework of a limited diffusion regime. Anti-Stokes emission from the ³P₀ level following excitation of the ¹D₂ state is also observed. This anti-Stokes emission is attributed to up-conversion by energy transfer.

INTRODUCTION

Fluorophosphate glasses are promising host materials for optical applications because of their optical properties, low refractive indices, low dispersion, and good transparency from the ultraviolet to the infrared regions of the optical spectra [1,2]. In general, highly concentrated rare earth glasses are difficult to synthesize because they are very unstable materials. However, recently new fluorophosphate glasses in the NaPO₃-BaF₂-REF₃ system have been obtained which are very stable and able to accept huge amounts of rare earth ions [3]. Among these latter, trivalent praseodymium is a very attractive laser activator because its optical spectrum from ultraviolet to near infrared contains a large number of metastable multiplets from which laser action has been shown. But unfortunately, concentration quenching of the Pr³⁺ emission is a common phenomenon in many systems [4-7]. Among the energy transfer mechanisms responsible for the quenching of the emitting levels of Pr³⁺, cross-relaxation and upconversion are very important. Both contribute to a non-exponential behaviour of the decay curves, but upconversion is particularly interesting since it may lead to the observation of anti-Stokes fluorescence.

In this work we report the results of the concentration quenching of the ¹D₂ state in Pr³⁺-doped fluorophosphate glasses of composition (in mol%) 60NaPO₃-15BaF₂-(25-x)GdF₃-xPrF₃ (x= 0.1, 0.2, 0.5, 1, 2, 5, and 10). The generation of anti-Stokes fluorescence from

the $^3P_0 \rightarrow ^3H_4$ transition under excitation of the 1D_2 level is studied. This anti-Stokes emission varies quadratically with the laser intensity indicating that the up-converted fluorescence is due to the interaction between two excited Pr^{3+} ions in the 1D_2 state.

EXPERIMENTAL TECHNIQUES

The fluorophosphate glasses used in this study were prepared at the Laboratoire de Verres et Céramiques of the University of Rennes (France). Glasses were synthesized in the $NaPO_3$, BaF_2 , (GdF_3/PrF_3) system with the following compositions in mol% : $60NaPO_3$ - $15BaF_2$ -($25-x$) GdF_3 - $xPrF_3$ ($x = 0.1, 0.2, 0.5, 1, 2, 5$, and 10), and designated as NBGdPr $_x$. Details on the entire glass forming diagram may be found in Ref. [3]. Rare-earth oxides were processed by a fluorinating agent NH_4F, HF . The fluorination of the rare-earth oxides was carried out at $300^\circ C$ in a vitreous carbon crucible under argon atmosphere during four hours. Then, the excess of NH_4F, HF was eliminated at $800^\circ C$, and the newly formed rare-earth fluoride was cooled down to room temperature. At this stage, the phosphate and fluorides were mixed together and the batch was heated up to $1100^\circ C$ for melting and refining for 15 minutes, then cooled down to $750^\circ C$, and poured onto a brass mold preheated at the glass transition temperature, T_g . Finally, the samples were annealed at T_g before being appropriately cut and polished for the optical measurements.

The samples temperature was varied between 4.2 K and 300 K with a continuous flow cryostat. The steady-state emission measurements were made with an argon laser as exciting light. The fluorescence was analyzed with a 0.25 monochromator, and the signal was detected by a Hamamatsu R928 photomultiplier and finally amplified by a standard lock-in technique.

Lifetime measurements were performed by exciting the samples with a pulsed frequency doubled Nd:YAG pumped tunable dye laser of 9 ns pulse width and 0.08 cm^{-1} linewidth. The fluorescence was analyzed with a 1 m Spex monochromator, and the signal was detected by a Hamamatsu R928 photomultiplier. Data were processed by a EGG-PAR boxcar integrator.

Experiments under pulsed excitation on the 1D_2 level were performed by using a high-power optical parametric oscillator (MOPO, Spectra Physics model 730) which provides 10 ns pulses of about 35 mJ of average energy with a repetition rate of 10 Hz. The luminescence was dispersed by a 500 M SPEX monochromator (spectral resolution $\approx 0.05\text{ nm}$) and detected with a cooler photomultiplier. The signals were recorded by using a SR400 two-channel gated photon counter. The decay time measurements were performed using the averaging facilities of a Tektronix 2400 digital storage oscilloscope.

RESULTS AND DISCUSSION

The room temperature steady-state emission spectra were obtained for all concentrations in the 470-800 nm spectral range by exciting with an argon laser. After excitation in the 3P_2 level (454 nm) there is emission from 3P_0 and 1D_2 levels. The emission lines are related to transitions $^3P_0 \rightarrow ^3H_{4,5,6}$, $^3P_0 \rightarrow ^3F_{2,3,4}$ and $^1D_2 \rightarrow ^3H_{4,5}$. At low concentration, the most intense emission corresponds to the $^1D_2 \rightarrow ^3H_4$ transition. However, as concentration rises this transition shows a strong quenching and at high concentration, the most prominent one is the emission from the 3P_0 level. This strong concentration quenching of the 1D_2 emission is often observed in the emission spectra of Pr^{3+} and has been attributed to cross-relaxation between Pr^{3+} ions [4-7].

In order to obtain additional information on the luminescence properties of Pr^{3+} ions in these glasses, the fluorescence dynamics of the $^3\text{P}_0$ and $^1\text{D}_2$ emitting levels were investigated as a function of Pr^{3+} concentration at different temperatures. Decay curves for all samples were obtained under laser pulsed excitation at 486 nm, and collecting the luminescence at different emission wavelengths between 490 and 720 nm. Table 1 shows the lifetime values of the $^3\text{P}_0$ and $^1\text{D}_2$ levels as a function of concentration at 4.2 K, 77 K and 295 K. As can be observed the lifetimes of the $^3\text{P}_0$ level are nearly independent on concentration up to 5 mol%; however, the lifetimes of the $^1\text{D}_2$ level become shorter with increasing concentration even at low temperature. The decays of the $^1\text{D}_2$ level can be described at low concentration (0.1 mol%) by an exponential function in the 4.2 K-295 K temperature range. As concentration increases the decays become non-exponential and a rapid lifetime decrease occurs. This variation of fluorescence with concentration indicates the presence of energy transfer processes at concentrations higher than 0.1 mol%. The same behaviour was observed at 77 K and 295 K. As in other Pr^{3+} systems investigated, the $^1\text{D}_2$ emission is affected much more strongly by quenching than is $^3\text{P}_0$, so we will focus the discussion on the $^1\text{D}_2$ level and its fluorescence dynamics.

Table 1. Lifetimes (μs) of the $^3\text{P}_0$ and $^1\text{D}_2$ levels as a function of Pr^{3+} concentration at three different temperatures.

	$^3\text{P}_0$			$^1\text{D}_2$		
x (mol%)	4.2 K	77 K	295 K	4.2 K	77 K	295 K
0.1	5.5	5.5	5.4	275	260	238
0.2	5.5	5.4	5	225	211	200
0.5	5.5	5.3	5.1	118	112	105
1	5.3	5.4	4.5	47	40	40
2	4.1	3.9	3.4	12.3	11.2	10.3
5	3.5	3.2	3.2	4.7	4.6	4.1
10	3	2.7	2.7	3	2.9	2.7

The lifetime of $^1\text{D}_2$ state of Pr^{3+} ion should be governed by a sum of probabilities for several competing processes: radiative decay, nonradiative decay by multiphonon emission, and by energy transfer to other Pr^{3+} ions. Nonradiative decay by multiphonon emission from the $^1\text{D}_2$ level is expected to be small because of the large energy gap to the next $^1\text{G}_4$ lower level ($\approx 7100 \text{ cm}^{-1}$) as compared with the highest energies of the phonons involved ($\approx 1300 \text{ cm}^{-1}$) [9]. Hence, at low temperature and low concentration (0.1 mol%) the measured lifetime, which is single exponential, should approach the radiative lifetime of the $^1\text{D}_2$ level. As the concentration rises, the lifetime decreases even at 4.2 K (see Table 1) indicating that Pr-Pr relaxation processes are present at concentrations higher than 0.1 mol%.

Concentration quenching of fluorescence leading to a fast lifetime decrease at high concentration can be due to one or both of the following processes: (i) cross relaxation between

Pr³⁺ ions, (ii) migration of the excitation energy due to resonant energy transfer among Pr³⁺ ions and finally to a quencher center. Energy migration has been described either as a diffusion process or as a random walk (hopping model) [9]. In the diffusion model, in the case of dipole-dipole interaction, at long times the fluorescence of the donors decay exponentially with an effective decay time given by:

$$\frac{1}{\tau} = \frac{1}{\tau_0} + VC_A C_D \quad (1)$$

where V is a constant involving donor-donor and donor-acceptor transfer constants and C_A and C_D are the acceptor and donor concentrations respectively. The donor decay regime described by relation (1) is known as diffusion-limited decay [9]. In our case the donors and acceptors are the Pr³⁺ ions, and the equation gives the effective decay as a function of the square of concentration. Hence a logarithmic plot of the effective decay versus concentration should show a slope equal to two if the ¹D₂ decay is diffusion limited.

Figure 1 shows a logarithmic plot of the effective fluorescence decay times as a function of the Pr³⁺ concentration. As can be observed, in this concentration range, the slope is 1.85, which indicates that the behaviour is close to a dipole-dipole quenching mechanism in the framework of a limited-diffusion regime.

The quenching of fluorescence from the ¹D₂ level can be associated with different kinds of cross relaxation processes. One of these processes is attributed to the following transitions between two Pr³⁺ ions: (¹D₂, ³H₄) → (¹G₄, ³F_{3,4}). This process results obviously in un-conversion to the ³P₀. However, ions in the ¹D₂ state can upconvert back to the ³P₀, leading to the observation of anti-Stokes fluorescence [10-14]. Two energy transfer mechanisms have been proposed to account for this upconversion. In one kind of process, there are two ¹D₂ ions, with one making a transition to the ¹G₄ while the other goes to the ³P₂: (¹D₂, ¹D₂) → (³P₂, ¹G₄). The second process is an ion from the ¹D₂ going to the ³H₄, while an ion from the ³H₆ goes to the ³P₁: (¹D₂, ³H₆) → (³H₄, ³P₁). In both cases the ³P₀ is then populated by fast nonradiative decay [10].

To investigate the possibility of up-converted fluorescence in this system we have excited directly the ¹D₂ level and we have observed anti-Stokes fluorescence from the ³P₀ → ³H₄ transition in the 4.2 K-295 K temperature range for different Pr³⁺ concentrations. Figure 2 shows the up-converted emission for the sample doped with x= 5 mol% at 4.2 K. The broad line is due to large site-to-site variations of the crystal field strength.

The intensity of the anti-Stokes emission shows a quadratic dependence with the excitation laser energy indicating that the up-conversion fluorescence is due to the interaction between two excited Pr³⁺ ions in the ¹D₂ state [12,14]. Figure 3 shows the integrated emission intensity of the up-converted fluorescence as a function of the square of the laser energy. This process has been observed in borate [12] and fluoroindate [14] glasses and has been attributed to a redistribution of energy between two ions according to: ¹D₂ + ¹D₂ → ³P₀ + ¹G₄ + phonons.

Up-conversion by energy transfer leads to a decay curve for the anti-Stokes emission which shows a rise time and a lifetime longer than that of the ³P₀ level under direct excitation. These effects become more pronounced as the ¹D₂ lifetime increases [11]. Figure 4 shows the experimental decay of the ³P₀ level obtained by exciting at 486 nm and at 590 nm for the sample doped with x= 5 mol%. As can be observed the lifetime values are similar with a small rise time in the case of the anti-Stokes emission. This is probably due to the lifetime value of the ¹D₂ level which at this concentration, is similar to that of ³P₀. In samples with low

concentration where the lifetime of the 1D_2 level is longer, the up-converted emission is too weak to measure accurately the decays. Therefore, it seems that this up-conversion energy transfer process has a very low efficiency to account for the observed quenching of the 1D_2 level.

CONCLUSIONS

From the above results, the following conclusions can be reached:

(i) Fluorescence quenching from the 1D_2 state has been demonstrated to occur for Pr^{3+} concentrations higher than 0.1 mol% even at 4.2 K. This can be attributed to a cross relaxation process.

(ii) A weak anti-Stokes fluorescence from the $^3P_0 \rightarrow ^3H_4$ transition under excitation of the 1D_2 level was observed. This anti-Stokes emission varies quadratically with the laser intensity, which shows that the up-converted fluorescence is due to the interaction between two excited Pr^{3+} ions in the 1D_2 state. A rise time was found to be associated with the 3P_0 decays showing that this level is populated from lower lying levels and supporting the argument that energy transfer is the responsible for the upconversion process.

ACKNOWLEDGEMENTS

This work has been supported by the Spanish Government (DGICYT Ref. PB95-0512), CICYT (Ref. MAT97-1009), and Acción Integrada HF1997-0063.

REFERENCES

- [1] D. Ehrt and W. Seeber, J. Non-Cryst. Solids 129 (1991) 19.
- [2] M.J. Weber, C. Layne, R. Saroyan, and D. Milam, Opt. Commun. 18 (1976) 171.
- [3] M. Matecki, N. Duhamel, and J. Lucas, J. Non-Cryst. Solids 184 (1995) 273.
- [4] J. Hegarty, D.L. Huber, and W.M. Yen, Phys. Rev. B 25 (1982) 5638.
- [5] H. Dornauf, and J. Heber, J. Lumin. 22 (1980) 1.
- [6] C. de Mello Donegá, H. Lambaerts, A. Meijerink, and G. Blasse, J. Phys. Chem. Solids 54 (1993) 873.
- [7] C. de Mello Donegá, A. Ellens, A. Meijerink, and G. Blasse, J. Phys. Chem. Solids 54 (1993) 293.
- [8] C. B. Layne, W.H. Lowdermilk, and M.J. Weber, Phys. Rev. B 16 (1977) 10.
- [9] M.J. Weber, Phys. Rev. B4 (1971) 2932.
- [10] J. Ganem, W.M. Dennis, W.M. Yen, J. Lumin. 54 (1992) 79.
- [11] O.L. Malta, E. Antic-Fidancev, M. Lemaitre-Blaise, J. Dexpert-Ghys, B. Piriou, Chem. Phys. Lett. 129 (1986) 557.
- [12] E. M. Pacheco and C.B. Araujo, Chem. Phys. Lett. 148 (1988) 334.
- [13] X.Wu, W.M. Dennis, and W.M. Yen, Phys. Rev. B 50 (1994) 6589.
- [14] L.E.E. de Araujo, A.S.L. Gomes, Cid B. de Araujo, Y. Messaddeq, A. Florez, and M.A. Aegerter, Phys. Rev. B 50 (1994) 16219.

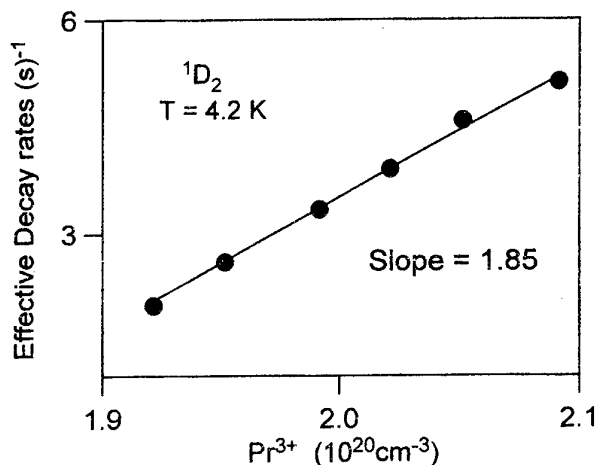


Fig. 1.- Logarithmic plot of the effective decay rate of the 1D_2 emission as a function of Pr^{3+} concentration at 4.2 K.

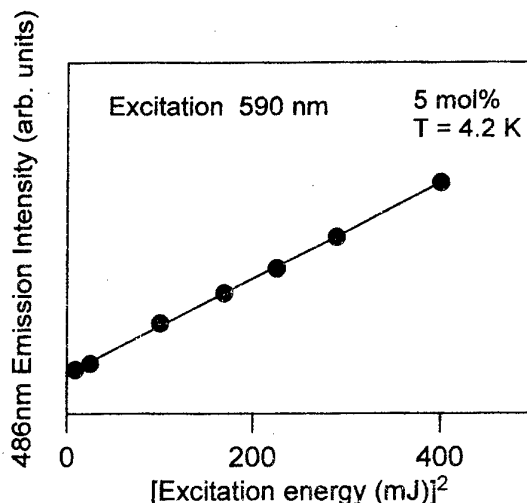


Fig. 3.- Fluorescence intensity of the up-converted $^3P_0 \rightarrow ^3H_4$ emission as a function of the square of the excitation energy. Data correspond to 4.2 K and 5 mol% of Pr^{3+} .

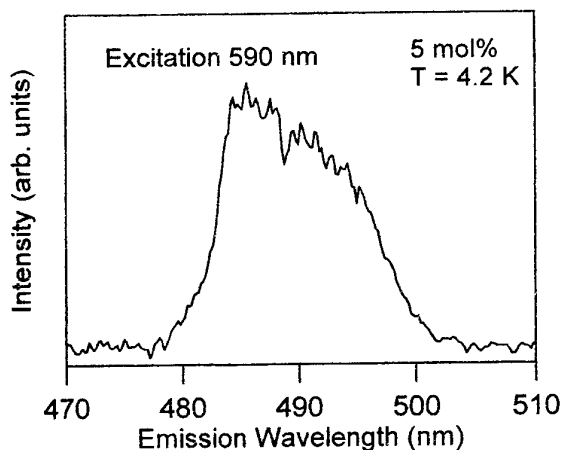


Fig. 2.- Fluorescence spectrum corresponding to the $^3P_0 \rightarrow ^3H_4$ transition at 4.2 K. The excitation wavelength (590 nm) was in resonance with the transition $^3H_4 \rightarrow ^1D_2$. (Sample with $x = 5$ mol%)

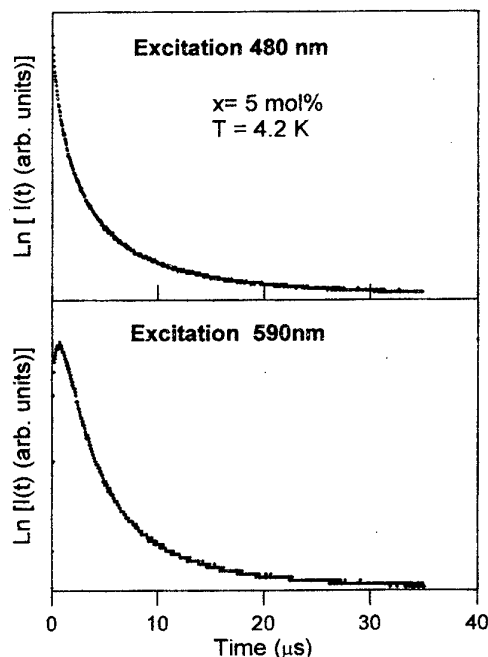


Fig. 4.- Experimental emission decay curves of level 3P_0 obtained under direct excitation (486 nm) and under excitation in resonance with the transition $^3H_4 \rightarrow ^1D_2$ (590 nm) for the sampled doped with 5 mol% of Pr^{3+} . Data correspond to 4.2 K.

Study of thermal and optical properties of $\text{Pr}^{3+}/\text{Yb}^{3+}$ -codoped ZBLAPN glasses

Zhong Jia-cheng, Zan Ling, Huang Lin, Luo Qirong

(IR Materials Lab, Wuhan University, Wuhan 430072 P. R. China)

Huang Dahai, Li Chengfang

(Phys. Dep. Wuhan University. Wuhan 430072 P. R. China)

ABSTRACT

Different concentrations of $\text{Pr}^{3+}/\text{Yb}^{3+}$ -codoped ZBLAPN glasses are prepared. The relationships of different concentration of PbF_2 -doped with thermal stability are studied. The absorption spectras are measared. The fluorescent properties are calculated by using the Jadd-ofelt theory. The energy trasfer rates between Pr^{3+} and Yb^{3+} are calculated. It is shwon that the use of Yb^{3+} intensify the absortion of Pr^{3+} .

I INTRODUCTION

Fluoride glass fiber is the most promising candidate for use in infrared optical amplifi-er because of the low phonon frequency characteristics. It has already been confirmed that a Pr^{3+} -doped fluoride fiber amplrfier operating at $1.3\mu\text{m}$ has the potential for a high gain, a high saturated output power and a large bandwidth^[1]. This gain characteristic has been achieved by developing low-loss high-NA fluoride single-mode fibers and codoping with other rare earth ions.

Among RE ions, Yb^{3+} has the simplest energy diagram which removes detrimental complications, such as excited state absorption. Its long fluorescence lifetime and low thermal loading is quite benefital for energy transfer source. In order for high NA fiber to be got, the most effective and common means for raising the refractive index of the core is to substitute some of the Ba^{2+} with Pb^{2+} . Every mole percent of substitutional Pb^{2+} raises the refractive index by 0.003, but with increasing Pb^{2+} doping the glass becomes unstable; beyond 10%, it readily devitrifies^[2]. The goal of this study is to investigate the absorption spectra and fluorescent properties of $\text{Pr}^{3+}/\text{Yb}^{3+}$ codoped ZBLAPN glasses, it is shown that the use of Yb^{3+} intensify the absorption of Pr^{3+} . In other way we present the thermal stability of ZBLAPN glasses under the influence of Pb^{2+} dopant concentration.

II EXPERIMENTAL

Glasses were made from high purity anhydrous metal fluorides, which were batched under dry nitrogen in platinum crucibles. Melting was carried out around 850°C for 1.5h in an electrothermal furnace with a silica liner tube attached to the side of a nitrogen purged dry-box. The glass melts were then poured into brass moulds held just below the glass

transition temperature (T_g), typically 240°C and annealed for 8 h. In the present work, nine samples have been examined. Five samples were codoped with Pr^{3+} and Yb^{3+} of 0.1%, 0.2%, 0.3%, 0.4%, 0.5% and 1%, 2%, 3%, 4%, 5% in weight. Four samples were doped with Pb^{2+} of 4%, 4.5%, 7.5%, 9.5% in molo concentration.

The UV/visible absorption spectra were measured by using a UV — 3400 Spectrophotometer (HITACHI). The glass thermal stability has been evaluated using DTA analysis With a 10°C/min heating rate values.

In the Judd-Ofelt theory^[3] the linestrength S_{ed} by neglect electric quadrupole and magnetic dipole transitions is given:

$$S_{ed} = e^2 [\Omega_2 \| U^{(2)} \|^2 + \Omega_4 \| U^{(4)} \|^2 + \Omega_6 \| U^{(6)} \|^2] \quad (1)$$

Ω_t ($t=2,4,6$) is phenomenological intensity parameter, $U^{(t)}$ ($t=2,4,6$) is the matrix element, which were calculated with datum in the literatur^[4].

Integral of the electric dipole absorption intensity is shown:

$$\int K(\lambda) d\lambda = \rho \frac{8\pi^3 e^2 \bar{\lambda}}{3hc(2J+1)} \frac{1}{n} \frac{(n^2+2)^2}{9} S_{ed} \quad (2)$$

ρ is the concentration of Pr^{3+} , $\bar{\lambda}$ is average wavelength, $n=n(\bar{\lambda})$ is index of refraction at $\bar{\lambda}$.

A least-squares fitting from the measured absorption linestrengths were used to predict the Judd-Ofelt parameters Ω_{tA} of Pr^{3+} by equations (1), (2).

Due to the weak absorption band from $^3\text{H}_4$ to $^1\text{G}_4$ of Pr^{3+} and the high concentration of Yb^{3+} in the host, the absorption band at 1.0 μm can be approximate to the absorption of Yb^{3+} . Using $^2\text{F}_{5/2} \rightarrow ^2\text{F}_{7/2}$ line strength of Yb^{3+} , one can calculate the S_{ed} of Yb^{3+} and $\sum_i \Omega_{it} < J_s \| U^{(t)} \| J_s' >$

We can calculate the spontaneous emission probability from j energy level to j' level A (j, j'), a branching ratio β and a radiative lifetime τ_0 of Pr^{3+} :

$$A(j, j') = \frac{64\pi^4 \nu^3}{3hc^3(2J+1)} \frac{n(n^2+2)^2}{9} \sum_{t=2,4,6} \Omega_{it} (< 4f^n j \| U^{(t)} \| 4f^n j' >)^2 \quad (3)$$

$$\beta = \frac{A(j, j')}{\sum_j A(j, j')} \quad (4)$$

$$\tau_0 = [\sum_j A(j, j')]^{-1} \quad (5)$$

Where h is Planck's constant, n is the index of refraction, γ is the frequency.

Using Judd-ofelt analysis KUSHIDA calculated energy transfer rates from electric dipole moment — electric dipole moment, electric dipole moment — electric quadrupole moment, electric quadrupole moment — electric quadrupole moment^[5].

$$\begin{aligned} \overline{P}_{SA}^{dd} = & \frac{1}{(2J_s+1)(2J_A+1)} \left(\frac{2}{3}\right) \left(\frac{2\pi}{h}\right) \left(\frac{e^2}{R^3}\right)^2 [\sum_i \Omega_{it} < J_s \| U^{(t)} \| J_s' >^2] \\ & [\sum_i \Omega_{itA} < J_A \| U^{(t)} \| J_A' >^2] S \end{aligned} \quad (6)$$

$$\overline{P}_{SA}^{dq} = \frac{1}{(2J_S + 1)(2J_A + 1)} \left(\frac{2\pi}{h}\right) \left(\frac{e^2}{R^4}\right)^2 \left[\sum_i \Omega_{ii} \langle J_S \| U^{(i)} \| J_S' \rangle^2 \right] \\ \langle 4f \| \gamma_A^2 \| 4f \rangle^2 \langle f \| C^{(2)} \| f \rangle^2 \langle J_A \| U^{(2)} \| J_A' \rangle^2 \overline{S} \quad (7)$$

$$\overline{P}_{SA}^{dq} = \frac{1}{(2J_S + 1)(2J_A + 1)} \left(\frac{14}{5}\right) \left(\frac{2\pi}{h}\right) \left(\frac{e^2}{R^5}\right)^2 \langle 4f \| \gamma_A^2 \| 4f \rangle^2 \\ \langle 4f \| \gamma_A^2 \| 4f \rangle^2 \langle f \| C^{(2)} \| f \rangle^4 \langle J_S \| U^{(2)} \| J_S' \rangle^2 \\ \langle J_A \| U^{(2)} \| J_A' \rangle^2 \overline{S} \quad (8)$$

S presents the sensitizer, ion, A is the acceptor ion. $\overline{S} = 10^{-3} \text{cm}^{-1}$ [6], R is distance between ions. $R = \sqrt{\frac{1}{N_{Yb} + N_{Pr}}}$, N_{Yb} and N_{Pr} is unit particle number of Yb^{3+} and Pr^{3+} .

III RESULTS

1. Absorption spectrum of $\text{Pr}^{3+}/\text{Yb}^{3+}$ co-doped flouride glasses were given in Fig 1.

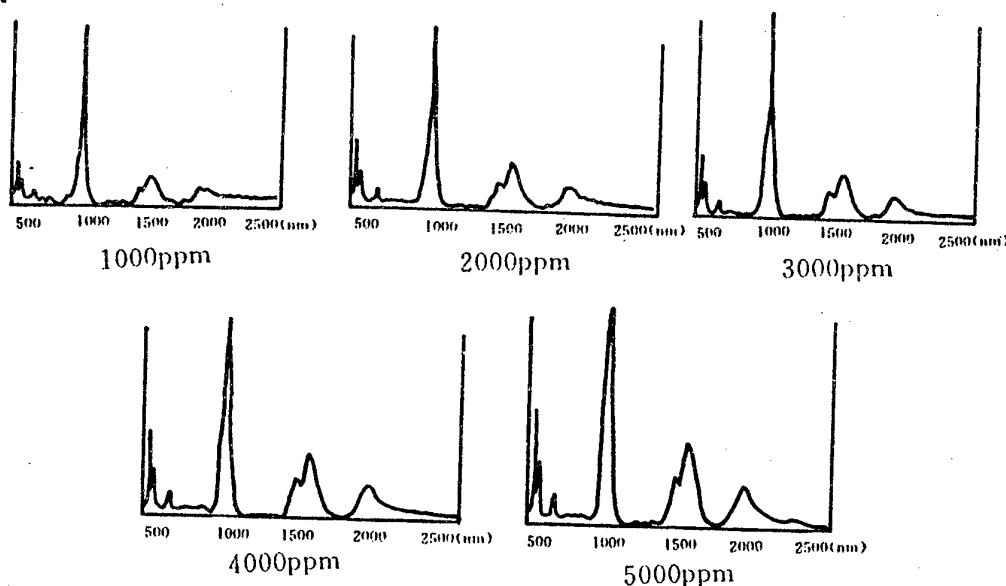


Fig:1 Absorption spectrum of $\text{Pr}^{3+}/\text{Yb}^{3+}$ co-doped flouride glasses

2. Values of $\Omega_{iA} (\times 10^{-20} \text{cm}^2)$ of Pr^{3+} were fitted:

	Ω_{2A}	Ω_{4A}	Ω_{6A}
1000ppm	4.2	4.9	5.8
2000ppm	2.8	4.8	5.7
3000ppm	1.9	5.0	5.1
4000ppm	1.2	6.4	5.0
5000ppm	1.3	5.8	5.1

Table 1 Values of $\Omega_A (\times 10^{-20} \text{cm}^2)$ by fitting diferent energy levels

3. Values of $\sum_i \Omega_{ii} \langle J_i \| U^{(n)} \| J_i' \rangle^2 (\times 10^{-20} \text{cm}^2)$ were measured.

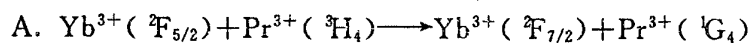
$\sum_i \Omega_{ii} \langle J_i \ U^{(n)} \ J_i' \rangle^2$	
1000ppm	3.26
2000ppm	2.89
3000ppm	3.18
4000ppm	2.79
5000ppm	3.16

Table 2 Measured values of $\sum_i \Omega_{ii} \langle J_i \| U^{(n)} \| J_i' \rangle^2 (\times 10^{-20} \text{cm}^2)$

4. Values of $A(j, j')$ were calculated:

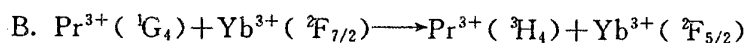
	1000ppm	2000ppm	3000ppm	4000ppm	5000ppm
$^3\text{H}_5\text{-}^3\text{H}_4$	10.00	9.53	8.68	8.97	8.87
$^3\text{H}_6\text{-}^3\text{H}_5$	8.99	8.59	7.85	8.16	8.05
$^3\text{H}_4$	13.18	12.95	11.89	12.30	12.23
$^3\text{F}_2\text{-}^3\text{H}_6$	0.50	0.49	0.44	0.44	0.44
$^3\text{H}_5$	62.77	61.63	57.64	61.81	60.47
$^3\text{H}_4$	290.10	244.08	217.07	229.08	218.22
$^3\text{F}_3\text{-}^3\text{F}_2$	0.26	0.23	0.23	0.27	0.25
$^3\text{H}_6$	21.46	21.08	19.60	20.80	20.45
$^3\text{H}_5$	111.94	88.34	75.54	76.71	72.97
$^3\text{H}_4$	522.00	504.97	469.62	501.76	490.30
$^3\text{F}_4\text{-}^3\text{F}_3$	0.68×10^{-2}	0.62×10^{-2}	0.61×10^{-2}	0.60×10^{-2}	0.61×10^{-2}
$^3\text{F}_2$	0.69	0.68	0.61	0.60	0.61
$^3\text{H}_6$	37.57	33.37	30.26	32.17	30.95
$^3\text{H}_5$	125.67	122.10	114.81	124.95	121.19
$^3\text{H}_4$	252.44	246.33	222.60	223.72	225.22
$^3\text{G}_4\text{-}^3\text{F}_4$	16.36	15.48	14.13	14.73	14.49
$^3\text{F}_3$	2.67	2.59	2.33	2.31	2.34
$^3\text{F}_2$	2.24	2.19	2.21	2.70	2.50
$^3\text{H}_6$	118.82	105.90	95.50	100.27	97.05
$^3\text{H}_5$	271.06	261.65	237.70	242.82	242.07
$^3\text{H}_4$	23.26	22.26	20.37	21.22	20.93
$^3\text{D}_2\text{-}^3\text{G}_4$	377.21	288.21	225.86	192.08	194.91
$^3\text{F}_4$	1026.80	697.38	481.98	317.19	341.25
$^3\text{F}_3$	106.83	84.52	72.48	73.90	70.23
$^3\text{F}_2$	330.81	311.54	314.84	391.26	356.61
$^3\text{H}_6$	317.42	311.04	319.62	401.12	366.49
$^3\text{H}_5$	16.35	16.02	16.27	20.05	18.46
$^3\text{H}_4$	803.04	782.91	722.31	757.169	747.42

5. Energy transfer rates between Yb^{3+} and Pr^{3+} were calculated:



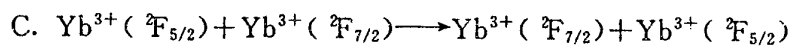
	$\overline{\text{P}}^{\text{dd}}$	$\overline{\text{P}}^{\text{dq}}$	$\overline{\text{P}}^{\text{qq}}$
1000ppm	15.2	4.0	0.45
2000ppm	53.0	23.1	4.7
3000ppm	116.9	72.2	17.5
4000ppm	191.9	138.4	46.5
5000ppm	328.0	276.3	94.5

Table 4 Energy transfer rates from $\text{Yb}^{3+} ({}^2\text{F}_{5/2})$ to $\text{Pr}^{3+} ({}^3\text{H}_4)$ (S^{-1})



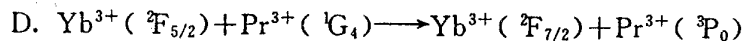
	$\overline{\text{P}}^{\text{dd}}$	$\overline{\text{P}}^{\text{dq}}$	$\overline{\text{P}}^{\text{qq}}$
1000ppm	11.4	1.3	0.34
2000ppm	39.8	8.2	3.6
3000ppm	87.6	21.3	13.1
4000ppm	143.9	48.4	34.9
5000ppm	246.0	81.4	72.8

Table 5 Energy transfer rates from $\text{Pr}^{3+} ({}^1\text{G}_4)$ to $\text{Yb}^{3+} ({}^2\text{F}_{7/2})$ (S^{-1})



	$\overline{\text{P}}^{\text{dd}}$	$\overline{\text{P}}^{\text{dq}}$	$\overline{\text{P}}^{\text{qq}}$
1000ppm	455.6	48.2	5.1
2000ppm	1442.5	273.7	51.9
3000ppm	3869.7	869.9	195.6
4000ppm	5230.0	1616.7	499.8
5000ppm	10625.7	3380.4	1075.4

Table 6 Energy transfer rates from $\text{Yb}^{3+} ({}^2\text{F}_{5/2})$ to $\text{Yb}^{3+} ({}^2\text{F}_{7/2})$ (S^{-1})



	$\overline{\text{P}}^{\text{dd}}$	$\overline{\text{P}}^{\text{dq}}$	$\overline{\text{P}}^{\text{qq}}$
1000ppm	32.6	0	0
2000ppm	112.8	0	0
3000ppm	285.4	0	0
4000ppm	578.3	0	0
5000ppm	927.6	0	0

Table 7 Energy transfer rates from $\text{Yb}^{3+} ({}^2\text{F}_{5/2})$ to $\text{Pr}^{3+} ({}^1\text{G}_4)$ (S^{-1})

6 Fig 2 shows the DTA curves of those samples doped with Pb^{2+} .

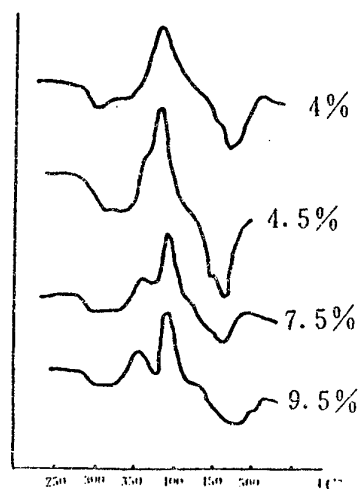


Fig. 2 DTA curves of glasses

IV DISCUSSION:

1. Comparing $\Omega_{\text{Pr}^{3+}}$ and $A(j, j')$ of $\text{Pr}^{3+}/\text{Yb}^{3+}$ co-doped glass with $\Omega_{\text{Pr}^{3+}}$ and $A(j, j')$ of Pr^{3+} doped glass [7] one can note that the influence of Yb^{3+} doped on energy levels of Pr^{3+} is less.

2. Table 3 shows that with the increase of concentration, every $A(j, j')$ gradually decreases but changes a little. The results prove that the ion concentration of Pr^{3+} alone doped can be more than 1000ppm, but table 3 shows when Yb^{3+} ions are added, the energy transfer rate from $\text{Yb}^{3+} (^2\text{F}_{5/2})$ to $\text{Pr}^{3+} (^3\text{H}_4)$ following increase of $\text{Pr}^{3+}/\text{Yb}^{3+}$ concentrations rises doubly. Energy transfer rate may compensate absorptivity reducing due to concentration increase, it is shown that it is perfectly possible to increase concentration of Pr^{3+} .

3. Table 6 shows the energy transfer rate from $\text{Pr}^{3+} (^1\text{G}_4)$ to $\text{Pr}^{3+} (^3\text{P}_0)$ is large, this is harmful to making amplifier but favourable to manufacturing upconversion laser.

4. Fig. 2 presents the thermal stability of glasses containing PbF_2 concentration being greater than 4.5%mol begins changing badly, in glasses containing PbF_2 over 4.5%mol separated phases show up.

V CONCLUSION

Using the Judd-Ofelt theory the fluorescent properties of $\text{Pr}^{3+}/\text{Yb}^{3+}$ codoped ZBLAPN glasses and the energy transfer rates between Pr^{3+} and Yb^{3+} were calculated. It is shown that the use of Yb^{3+} intensify the absorption of Pr^{3+} . This predicts that the concentration of Pr^{3+} doped may increase direct ratio with Yb^{3+} codoped.

Over 4.5%mol of PbF_2 doped separated phases appear, this will increase transit wastage of optical fibre.

REFERENCES

- [1] Y. Ohishi. T. Kanamori etc; IEEE Photo. Technol Lett. 3(1991) 715
- [2] K. Fujiura. T. Kanamori etc; Appl. Phys. Lett. 67(1995) 3063.
- [3] B. R. Judd; Optical absorption intensities of rare-earth ions. Phys. Rev. Vol. 127 P. 750, 1962.
- [4] W. J. Weber; Spontaneous emission probabilities and quantum efficiencies for excited states of Pr^{3+} in LaF_3 . J. Chem. Phys. Vol. 48. P. 4774, 1968
- [5] T. Kushida. Energy transfer and cooperative optical transitions in rare-earth doped inorganic materials. J. Phys. Soc(Japan), Vol. 34, P. 1318, 1973
- [6] R. Reisfeld; Lasers and Excited States of Rare Earths (Springer-Verlag Berlin Heidelberg New York 1997)
- [7] M. Eyal, E. Greenberg and R. Reisfeld. Spectroscopy of Praseodymium (III) in Zirconium fluoride glasses. Chem. Phys. Lett, Vol. 117, P. 108, 1985

The emission properties and energy transfer of Yb-Tm codoped fluoride glass

Maohe Li Changhong Qi Fengying Lin Hefang Hu
Shanghai Institute of Optics and Fine Mechanics, CAS
P.O.BOX 800-216, Shanghai 201800, China

Abstract

In this paper a series of Yb-Tm codoped fluorozirconate glass with different dopant content was prepared. The upconversion fluorescence properties of glasses were measured using 970nm LD as a exciting source. A strong blue upconversion fluorescence band at 478nm due to $1G_4-3H_6$ transition and two other weak upconversion fluorescence bands at 647 and 792nm due to $3F_2-3H_6$ and $3F_4-3H_6$ transition, respectively, were observed. The relationship between the upconversion fluorescence intensity and dopant concentration were studied. The glass containing high Yb^{3+} and low Tm^{3+} concentration exhibits most strong upconversion fluorescence intensity. The energy transfer mechanism from Yb^{3+} to Tm^{3+} was also discussed.

TIME-RESOLVED THERMAL LENS MEASUREMENTS OF THERMAL DIFFUSIVITY AND FLUORESCENCE QUANTUM EFFICIENCY IN ION DOPED FLUORIDE GLASSES

S.M. Lima, T. Catunda, R. Lebullenger and A.C. Hernandez,
Instituto de Física de São Carlos, Universidade de São Paulo, C.P. 369, CEP 13560-970,
São Carlos, SP, Brasil. E-mail: tomaz@ifqsc.sc.usp.br

M.L. Baesso and A.C. Bento
Departamento de Física, Universidade Estadual de Maringá, Maringá, PR, Brasil

The time-resolved mode-mismatched thermal lens technique has been used to determine an absolute value for the optical path change with temperature (ds/dT), thermal diffusivity (D) and conductivity (K) in ion doped fluoride glasses. We present, for the first time, thermal diffusivity and conductivity results for fluoride glasses. The method is simple and can be applied to a wide range of fluorescent materials.

INTRODUCTION

The thermal lens (TL) technique¹ has proved to be valuable to study transparent materials²⁻⁷. Since the first report of the TL effect, the sensitivity of the technique has been improved by changing the experimental configuration. The two-beams mode-mismatched method is the most sensitive one.

The TL effect is caused by the deposition of heat via a non-radiative decay process after the laser energy has been absorbed by the sample. In this situation a transverse temperature gradient is established, owing to the temperature coefficient of refractive index (dn/dT), a refractive index gradient is produced, creating a lens-like optical element, the so-called TL. As the probe laser beam passes through the sample, its propagation is affected resulting in a spreading or focusing of the beam center. By measuring its beam center intensity variation in the far field, the thermo-optical properties of the sample can be determined. The time-resolved method is used to study the temporal evolution of the TL effect, allowing the determination of sample thermal diffusivity.

The thermal diffusivity of a material is known to be dependent upon the effects of compositional and microstructural variables as well as processing conditions. In this study, we apply the TL technique in several fluoride glasses to determine an absolute value for the optical path change with temperature (ds/dT), thermal diffusivity (D) and conductivity (K).

The fluoride glasses are very transparent, presenting very low absorption coefficient ($\sim 10^{-3} - 10^{-4} \text{ cm}^{-1}$) in the visible and even lower in the mid infrared. Consequently the TL signal from undoped matrixes are very low. To improve the signal to noise ratio of our experiment, we doped the glasses with low concentrations of Cobalt.

THEORY

The theoretical treatment of TL is done using Fresnel diffraction theory⁸. An analytical expression can be obtained for probe beam intensity $I(t)$ ³:

$$I(t) = I(0) \left\{ 1 - \frac{\theta}{2} \operatorname{atan} \left[\frac{2 m V}{\left[(1+2 m)^2 + V^2 \right] t_c / 2 t + 1 + 2 m + V^2} \right] \right\}^2 \quad (1)$$

where

$$m = \left(\frac{\omega_{1p}}{\omega_{oe}} \right)^2 ; V = \frac{Z_1}{Z_c} \text{ when } Z_c \ll Z_2. \quad (2)$$

Here, Z_c is the confocal distance of the probe beam, Z_1 is the distance between the probe beam waist and the sample, Z_2 is the distance between the sample and the detector (2), ω_{1p} is the probe beam radius at the sample, ω_{oe} is the excitation laser beam radius at the sample, t_c is the characteristic thermal lens time constant, θ is approximately the phase difference of the probe beam at $r = 0$ and $r = \sqrt{2} \omega_e$ induced by the thermal lens, and $I(0)$ is the value of $I(t)$ when the transient time t or θ is zero.

The TL effect can be treated through the calculation of the temporal evolution of the sample temperature profile $\Delta T(r, t)$, caused by a Gaussian beam. The TL transient signal amplitude is proportional to its phase shift given by³

$$\theta = - \frac{PAL}{K \lambda_p} \phi \frac{ds}{dT} \quad (3)$$

where P is the excitation laser power, K is the thermal conductivity, λ_p is the probe beam wavelength, L is the sample thickness, ds/dT is the optical path temperature coefficient, A is the absorption coefficient and $\phi = 1 - \eta \lambda_e / \langle \lambda_{em} \rangle$ is the fraction of absorbed energy converted into heat per photon, where ϕ is the sample radiative quantum efficiency, λ_e is the excitation beam wavelength, and $\langle \lambda_{em} \rangle$ is the average wavelength of the fluorescence. In the case of Cobalt doped samples, we supposed that all absorbed energy is converted into heat so $\eta = 0$ and $\phi = 1$.

The optical path change with temperature is given by

$$\frac{ds}{dT} = (n-1)(1+\nu)\gamma + \frac{dn}{dT} \quad (4)$$

where n is the refractive index, ν is the Poisson ratio and γ is the linear temperature expansion coefficient.

The characteristic TL signal response time t_c is given by

$$t_c = \frac{\omega_{oe}^2}{4D} \quad (5)$$

where $D = K/\rho C$ is the thermal diffusivity, ρ is the density, C is the specific heat and K is the thermal conductivity.

We performed time-resolved TL experiments in several fluoride glasses, using the two-beams mode mismatched TL configuration. Parameters θ and t_c can be determined by the proper fitting of the transient TL signal and then the thermal diffusivity D and conductivity K and the optical path change with temperature ds/dT can be obtained.

EXPERIMENT

The starting materials used for the preparation of the glasses were fluorides (BDH and Strem products), and oxides such as In_2O_3 and Ga_2O_3 (MetalEurop). The ammonium bifluoride was used to transform oxides in fluorides. The mixture was heated in a crucible for melting and refining. Finally, the melt was poured into a brass mold preheated at few degrees below the T_g temperature to prepare samples with 4mm of thickness. All these operations were made in glove boxes with controlled inert atmosphere whose relative moisture was below 10ppmv.

Table 1: Concentration of glasses (wt %).

Acronym	ZrF ₄	YF ₃	LaF ₃	AlF ₃	GaF ₃	InF ₃	CaF ₂	SrF ₂	BaF ₂	ZnF ₂	PbF ₂	NaF
ZBLAN	53		4.5	3.5					29			10
YABC		20		40			20		20			
IGPZCa					20	15	20			15	30	
ISZn					6	34		20	16	20		4
InSBZnGdN					2GdF ₃	40		20	16	20		2

The mode-mismatched thermal lens experimental setup used is showed in Figure 1.

We used an Ar^+ laser as an excitation beam and a HeNe laser as probe beam. The sample was positioned at the waist of the excitation laser beam, where the power density was maximum.

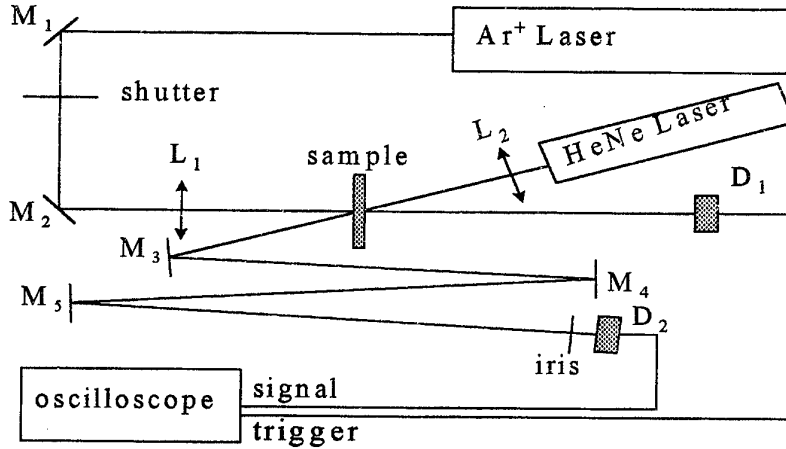


Figure 1: A schematic diagram of the mode-mismatched thermal lens experimental apparatus, where M_1 , M_2 , M_3 , M_4 and M_5 are mirrors, D_1 and D_2 are detectors, and L_1 and L_2 are lenses.

The excitation beam was focused with a $f_1 = 15\text{cm}$ lens (L_1), and the sample was put at its focal plane. The exposure of the sample to the excitation beam was controlled by means of a shutter or a mechanical chopper. The probe laser beam was a HeNe laser at 632.8nm. It was focused by a converging lens (L_2) with focal length $f_2 = 25\text{cm}$ at an angle $\alpha < 1.5^\circ$ which refers to the excitation beam and centered to pass through the thermal lens to maximize the TL signal. The excitation beam, was incident on a detector (D_1) and used as a trigger, after having

passing through the sample. These adjustable mirrors M_3 , M_4 and M_5 were used to get a long optical length ($\sim 2\text{m}$) from the sample to an iris mounted before the detector (D_2). An iris was put in front of the detector in order to select the beam central part.

The optical absorption coefficients were determined using the same experimental configuration applied to the TL measurements. The transmitted light of the Ar^+ laser at 514.5nm was recorded for different incident power.

The experimental parameters used are summarized in Table 2.

Table 2: The experimental parameters for TL measurements.

λ_p	$632.8 \times 10^{-7} \text{ cm}$
Z_{op}	$21.6 \pm 0.04 \text{ cm}$
Z_{cp}	$4.27 \pm 0.07 \text{ cm}$
λ_e	$514.5 \times 10^{-7} \text{ cm}$
Z_{oe}	$14.47 \pm 0.002 \text{ cm}$
Z_{ce}	$0.34 \pm 0.003 \text{ cm}$
ω_{oe}	$2.35 \times 10^{-3} \text{ cm}$
Z_1	4 cm
ω_p	$12.7 \times 10^{-3} \text{ cm}$
$m = (\omega_p / \omega_{oe})^2$	29.22
$V = (Z_1 / Z_{cp})$	0.937

We also performance measurements in a soda lime sample in order to check our diffusivity value with the literature one [3].

RESULTS AND DISCUSSION

Figure 4 shows a typical TL signal, for the ZBLAN with 0,3% of Cobalt. We fitted the experimental data with Eq. (1) and obtained $\theta = 0.23 \pm 0.0004$ and $t_c = 0,52 \pm 0.004\text{ms}$. Using Eq. (5) from t_c and ω_{oe} (Table 2) we calculated $D = 2.6 \times 10^{-3} \text{ cm}^2/\text{s}$.

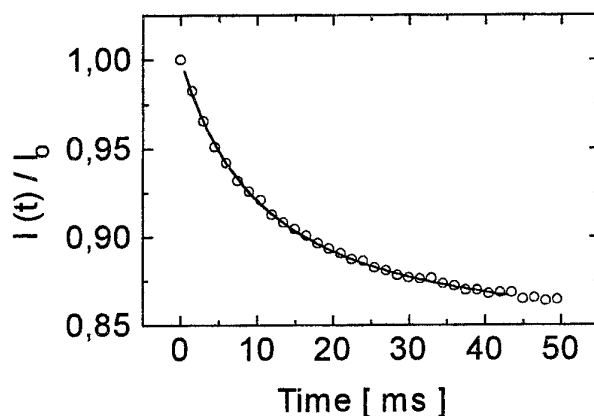


Figure 4: Transient Thermal Lens signal for the 0.3% Cobalt ZBLAN sample in a $P = 42.2\text{mW}$ ($\lambda = 514.5\text{nm}$). The line indicates the fitting made with Eq. (1).

We studied 4 ZBLAN samples doped with 0.1, 0.2, 0.3 and 0.375 wt% of Cobalt. Figure 5 shows that, in this Cobalt concentration range, the thermal diffusivity was practically constant (within our experimental uncertainty): $D = (2.6 \pm 0.14) \times 10^{-3} \text{ cm}^2/\text{s}$. From this D value we calculated $K = (7.4 \pm 0.4) \times 10^{-3} \text{ W/kcm}$ using the ρC value for ZBLAN from ref. [10].

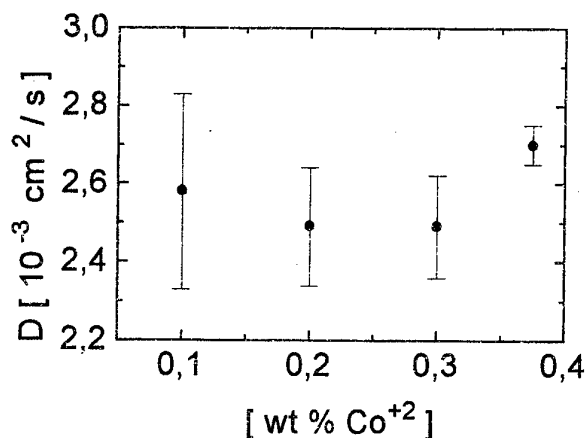


Figure 5: Thermal diffusivity versus Cobalt concentration in ZBLAN

Figure 6 shows that $\theta P/L$ increases linearly with the absorption coefficient A , so by Eq. (3) this behavior indicates that the product $K^{-1}ds/dT$ remains constant in the Cobalt concentration range studied.

The same procedure was adopted for the other samples. For these glasses we do not have the ρC value. However, Bruce⁹ analyzed 12 kinds of fluoride glasses and concluded that, at 300k, the molar specific heat is almost constant $\sim 21.3 \text{ k}^{-1} \text{ mol}^{-1}$ (86% of the Dulong-Petit value). For instance, using this value for ZBLAN we obtained $\rho C = 2.7 \text{ Ws/kcm}^3$ in a good agreement with the experimental value $\rho C = 2.8 \text{ Ws/kcm}^3$ from ref. [10]. We estimated ρC for all the samples and calculated K from our experimental D datas as shown in the Table 3.

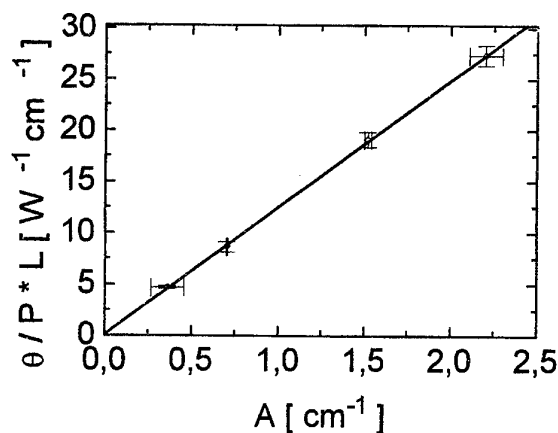


Figure 6.: This graphic shows the linear behavior of the product $K^{-1}ds/dT$.

CONCLUSIONS

All fluorides we studied presented negative ds/dT values. We remark that $ds/dT \propto [\phi - \eta\beta]$, where ϕ and β are the temperature coefficients of the electronic polarizability and volume expansion respectively, and η is a constant that depends on the glass refractive index and the Poisson ratio ν . Therefore the negative ds/dT values are an indication of the small ϕ values of fluorides.

For laser applications, the thermal parameters are very important. High thermal conductivity is desired to dissipate the heat from the laser action region. It is well known that fluoride glasses do not have thermo-optical properties suitable for high power laser applications. However we observed that fluorindate glasses, which have very good optical properties, presented thermal conductivity $\sim 18\%$ and diffusivity $\sim 23\%$ greater than the one of ZBLAN.

Table 3: Results of thermal diffusivity and conductivity and the optical path change with temperature ds/dT .

Samples	A (cm^{-1})	D ($10^{-3} \text{ cm}^2/\text{s}$)	K (10^{-3} W/kcm)	ds/dT (10^{-6} K^{-1})
IGPZ 0,2% Co	0.9 ± 0.04	2.9 ± 0.14	8.0 ± 0.39	-1.8 ± 0.14
ISZn 0,2% Co	1.0 ± 0.10	3.1 ± 0.06	8.4 ± 0.16	-1.2 ± 0.20
InSBZnGdN 0,29% Co	0.8 ± 0.02	3.2 ± 0.07	8.6 ± 0.19	-1.7 ± 0.14
YABC 0,377% Co	1.8 ± 0.03	3.3 ± 0.06	8.1 ± 0.15	-1.9 ± 0.13
ZBLAN 0,1% Co	0.4 ± 0.09	2.6 ± 0.25	7.4 ± 0.71	-6.1 ± 1.79
ZBLAN 0,2% Co	0.7 ± 0.003	2.5 ± 0.15	7.1 ± 0.43	-5.5 ± 0.43
ZBLAN 0,3% Co	1.5 ± 0.02	2.5 ± 0.13	7.1 ± 0.37	-5.6 ± 0.37
ZBLAN 0,375% Co	2.2 ± 0.10	2.7 ± 0.05	7.6 ± 0.14	-6.0 ± 0.52

ACKNOWLEDGMENTS

This research was supported by FAPESP and CNPq.

REFERENCES

- [1] J.P. Gordon, R.C.C. Leite, R.S. More, S.P.S. Porto, and J.R. Whinnery, *J. Appl. Phys.* 36, 3 (1965).
- [2] M.L. Baesso, J. Shen, and R.D. Snook, *Chem. Phys. Lett.* 197, 255 (1992).
- [3] M.L. Baesso, J. Shen and R.D. Snook, *J. Appl. Phys.* 75 (1994) p.3732-7.
- [4] T. Catunda, M.L. Baesso, Y. Messaddeq, M.A. Aegerter, *J. Non-Cryst. Solids.* (1997) 1-6.
- [5] M.L. Baesso, A.C. Bento, A.A. Andrade, T. Catunda, J.A. Sampaio, S. Gama. *J. Non-Cryst. Solids.* 219 (1997) 165-169.
- [6] M.L. Baesso, A. C. Bento, A.A. Andrade, J.A. Sampaio, E. Pecoraro, L.A.O. Nunes, T. Catunda, S. Gama. 57 (1998) 10545-10550.
- [7] R.C. Powell, D.P. Neikirk and D. Sardar, *J. Opt. Soc. Am.*, 70, 486, (1980).
- [8] S.J. Sheldon, L.V. Knight, and J.M. Thorne, *Appl. Opt.* 21, 1663 (1982).
- [9] A.J. Bruce, in *NATO on Halide Glasses for Infrared Optica Fiber optics* (Portugal), ed. by R.M. Almeida, Martinus Nijhoff, Dordrecht (1987) p. 149-62.
- [10] G. ROSMAN: 'Dynamics of glass cooling applied to preform fabrication', *J. Non-Cryst. Solids*, 1992, 140, pp. 255-258.

**PHOTOINDUCED NONLINEAR OPTICAL PHENOMENA
IN Sb_2Se_3 - BaCl_2 - PbCl_2 GLASSES**

J.Wasyłak, J.Kucharski, I.V.Kityk* and J.Kasperczyk*

University of Mining and Metallurgy, Al. Mickiewicza 30, PL - 30-059 Kraków, Poland

*Physics Institute, Pedagogical University, AL.Armi Krajowej 13/15, PL - 42 201

Częstochowa, Poland

Abstract

Photo-induced changes have been investigated in new synthesized Sb_2Se_3 - BaCl_2 - PbCl_2 glasses using a CO_2 pulse laser ($\lambda = 10.6 \mu\text{m}$). A source beam from the same IR laser was split into a probe and pump beam which have been mutually delayed in time and possessed different intensities. It was revealed that such illumination by continuous CO laser ($\lambda = 5,5 \mu\text{m}$, $W = 45 \text{ W/cm}^2$) during several hours leads to an increase of output optical second harmonic generation signal. We have also observed an influence of external mechanical uniaxial stresses on the output photoinduced optical SHG. We have found that the time delay between the probe and pump beam, CO photon time exposure and temperature strongly influence behaviour of corresponding nonlinear optical susceptibilities. Time-resolved measurements indicate existence of at least three short-time components, which can be connected with different mechanisms of the observed phenomenon. It was clearly shown that degree of a noncentrosymmetry of corresponding chemical bonds corresponds to the time of the CO-laser light exposure, temperature and mechanical stresses.

TIME-RESOLVED THERMAL LENS MEASUREMENTS OF THERMAL DIFFUSIVITY AND FLUORESCENCE QUANTUM EFFICIENCY IN ION DOPED FLUORIDE GLASSES

S.M. Lima, T. Catunda, R. Lebullenger and A.C. Hernandez,
Instituto de Física de São Carlos, Universidade de São Paulo, C.P. 369, CEP 13560-970,
São Carlos, SP, Brasil. E-mail: tomaz@ifqsc.sc.usp.br

M.L. Baesso and A.C. Bento
Departamento de Física, Universidade Estadual de Maringá, Maringá, PR, Brasil

The time-resolved mode-mismatched thermal lens technique has been used to determine an absolute value for the optical path change with temperature (ds/dT), thermal diffusivity (D) and conductivity (K) in ion doped fluoride glasses. We present, for the first time, thermal diffusivity and conductivity results for fluoride glasses. The method is simple and can be applied to a wide range of fluorescent materials.

INTRODUCTION

The thermal lens (TL) technique¹ has proved to be valuable to study transparent materials²⁻⁷. Since the first report of the TL effect, the sensitivity of the technique has been improved by changing the experimental configuration. The two-beams mode-mismatched method is the most sensitive one.

The TL effect is caused by the deposition of heat via a non-radiative decay process after the laser energy has been absorbed by the sample. In this situation a transverse temperature gradient is established, owing to the temperature coefficient of refractive index (dn/dT), a refractive index gradient is produced, creating a lens-like optical element, the so-called TL. As the probe laser beam passes through the sample, its propagation is affected resulting in a spreading or focusing of the beam center. By measuring its beam center intensity variation in the far field, the thermo-optical properties of the sample can be determined. The time-resolved method is used to study the temporal evolution of the TL effect, allowing the determination of sample thermal diffusivity.

The thermal diffusivity of a material is known to be dependent upon the effects of compositional and microstructural variables as well as processing conditions. In this study, we apply the TL technique in several fluoride glasses to determine an absolute value for the optical path change with temperature (ds/dT), thermal diffusivity (D) and conductivity (K).

The fluoride glasses are very transparent, presenting very low absorption coefficient ($\sim 10^{-3} - 10^{-4} \text{ cm}^{-1}$) in the visible and even lower in the mid infrared. Consequently the TL signal from undoped matrixes are very low. To improve the signal to noise ratio of our experiment, we doped the glasses with low concentrations of Cobalt.

THEORY

The theoretical treatment of TL is done using Fresnel diffraction theory⁸. An analytical expression can be obtained for probe beam intensity $I(t)$ ³:

$$I(t) = I(0) \left\{ 1 - \frac{\theta}{2} \operatorname{atan} \left[\frac{2 m V}{\left[(1 + 2 m)^2 + V^2 \right] t_c / 2t + 1 + 2 m + V^2} \right] \right\}^2 \quad (1)$$

where

$$m = \left(\frac{\omega_{lp}}{\omega_{oe}} \right)^2 ; V = \frac{Z_1}{Z_c} \text{ when } Z_c \ll Z_2. \quad (2)$$

Here, Z_c is the confocal distance of the probe beam, Z_1 is the distance between the probe beam waist and the sample, Z_2 is the distance between the sample and the detector (2), ω_{lp} is the probe beam radius at the sample, ω_{oe} is the excitation laser beam radius at the sample, t_c is the characteristic thermal lens time constant, θ is approximately the phase difference of the probe beam at $r = 0$ and $r = \sqrt{2} \omega_e$ induced by the thermal lens, and $I(0)$ is the value of $I(t)$ when the transient time t or θ is zero.

The TL effect can be treated through the calculation of the temporal evolution of the sample temperature profile $\Delta T(r, t)$, caused by a Gaussian beam. The TL transient signal amplitude is proportional to its phase shift given by³

$$\theta = - \frac{PAL}{K \lambda_p} \varphi \frac{ds}{dT} \quad (3)$$

where P is the excitation laser power, K is the thermal conductivity, λ_p is the probe beam wavelength, L is the sample thickness, ds/dT is the optical path temperature coefficient, A is the absorption coefficient and $\varphi = 1 - \eta \lambda_e / \langle \lambda_{em} \rangle$ is the fraction of absorbed energy converted into heat per photon, where ϕ is the sample radiative quantum efficiency, λ_e is the excitation beam wavelength, and $\langle \lambda_{em} \rangle$ is the average wavelength of the fluorescence. In the case of Cobalt doped samples, we supposed that all absorbed energy is converted into heat so $\eta = 0$ and $\varphi = 1$.

The optical path change with temperature is given by

$$\frac{ds}{dT} = (n-1)(1+\nu)\gamma + \frac{dn}{dT} \quad (4)$$

where n is the refractive index, ν is the Poisson ratio and γ is the linear temperature expansion coefficient.

The characteristic TL signal response time t_c is given by

$$t_c = \frac{\omega_{oe}^2}{4D} \quad (5)$$

where $D = K/\rho C$ is the thermal diffusivity, ρ is the density, C is the specific heat and K is the thermal conductivity.

We performed time-resolved TL experiments in several fluoride glasses, using the two-beams mode mismatched TL configuration. Parameters θ and t_c can be determined by the proper fitting of the transient TL signal and then the thermal diffusivity D and conductivity K and the optical path change with temperature ds/dT can be obtained.

EXPERIMENT

The starting materials used for the preparation of the glasses were fluorides (BDH and Strem products), and oxides such as In_2O_3 and Ga_2O_3 (MetalEurop). The ammonium bifluoride was used to transform oxides in fluorides. The mixture was heated in a crucible for melting and refining. Finally, the melt was poured into a brass mold preheated at few degrees below the T_g temperature to prepare samples with 4mm of thickness. All these operations were made in glove boxes with controlled inert atmosphere whose relative moisture was below 10ppmv.

Table 1: Concentration of glasses (wt %).

Acronym	ZrF ₄	YF ₃	LaF ₃	AlF ₃	GaF ₃	InF ₃	CaF ₂	SrF ₂	BaF ₂	ZnF ₂	PbF ₂	NaF
ZBLAN	53		4.5	3.5					29			10
YABC		20		40			20		20			
IGPZCa					20	15	20			15	30	
ISZn					6	34		20	16	20		4
InSBZnGdN					2GdF ₃	40		20	16	20		2

The mode-mismatched thermal lens experimental setup used is showed in Figure 1.

We used an Ar^+ laser as an excitation beam and a HeNe laser as probe beam. The sample was positioned at the waist of the excitation laser beam, where the power density was maximum.

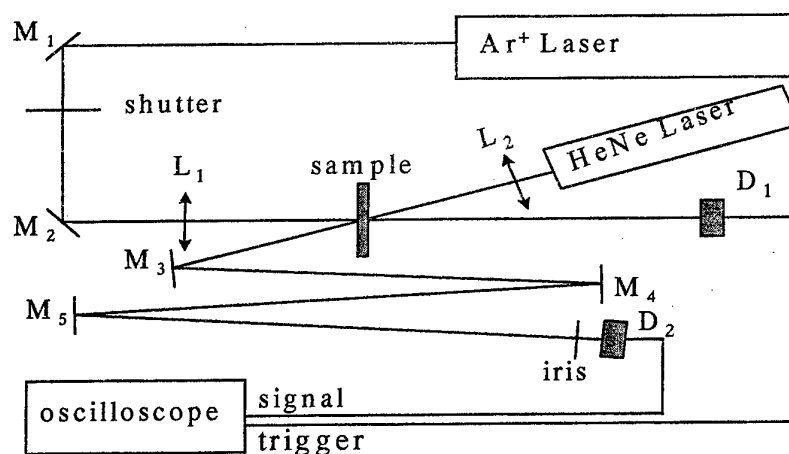


Figure 1: A schematic diagram of the mode-mismatched thermal lens experimental apparatus, where M_1 , M_2 , M_3 , M_4 and M_5 are mirrors, D_1 and D_2 are detectors, and L_1 and L_2 are lenses.

The excitation beam was focused with a $f_1 = 15\text{cm}$ lens (L_1), and the sample was put at its focal plane. The exposure of the sample to the excitation beam was controlled by means of a shutter or a mechanical chopper. The probe laser beam was a HeNe laser at 632.8nm. It was focused by a converging lens (L_2) with focal length $f_2 = 25\text{cm}$ at an angle $\alpha < 1.5^\circ$ which refers to the excitation beam and centered to pass through the thermal lens to maximize the TL

signal. The excitation beam, was incident on a detector (D_1) and used as a trigger, after having passing through the sample. These adjustable mirrors M_3 , M_4 and M_5 were used to get a long optical length ($\sim 2m$) from the sample to an iris mounted before the detector (D_2). An iris was put in front of the detector in order to select the beam central part.

The optical absorption coefficients were determined using the same experimental configuration applied to the TL measurements. The transmitted light of the Ar^+ laser at 514.5nm was recorded for different incident power.

The experimental parameters used are summarized in Table 2.

Table 2: The experimental parameters for TL measurements.

λ_p	$632.8 \times 10^{-7} \text{ cm}$
Z_{op}	$21.6 \pm 0.04 \text{ cm}$
Z_{cp}	$4.27 \pm 0.07 \text{ cm}$
λ_e	$514.5 \times 10^{-7} \text{ cm}$
Z_{oe}	$14.47 \pm 0.002 \text{ cm}$
Z_{ce}	$0.34 \pm 0.003 \text{ cm}$
ω_{oe}	$2.35 \times 10^{-3} \text{ cm}$
Z_1	4 cm
ω_p	$12.7 \times 10^{-3} \text{ cm}$
$m = (\omega_p / \omega_{oe})^2$	29.22
$V = (Z_1 / Z_{cp})$	0.937

We also performance measurements in a soda lime sample in order to check our diffusivity value with the literature one [3].

RESULTS AND DISCUSION

Figure 4 shows a typical TL signal, for the ZBLAN with 0,3% of Cobalt. We fitted the experimental data with Eq. (1) and obtained $\theta = 0.23 \pm 0.0004$ and $t_c = 0,52 \pm 0.004ms$. Using Eq. (5) from t_c and ω_{oe} (Table 2) we calculated $D = 2.6 \times 10^{-3} \text{ cm}^2/s$.

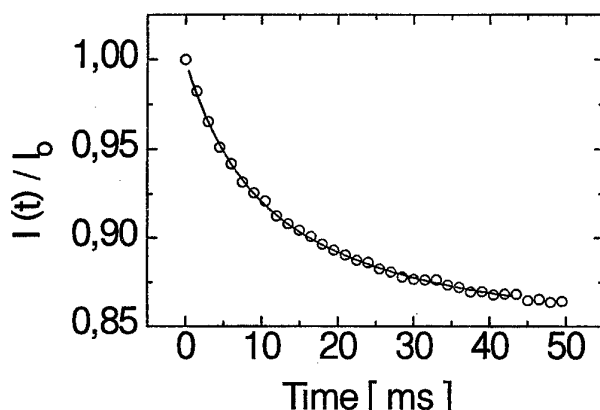


Figure 4: Transient Thermal Lens signal for the 0.3% Cobalt ZBLAN sample in a $P = 42.2mW$ ($\lambda = 514.5nm$). The line indicates the fitting made with Eq. (1).

We studied 4 ZBLAN samples doped with 0.1, 0.2, 0.3 and 0.375 wt% of Cobalt. Figure 5 shows that, in this Cobalt concentration range, the thermal diffusivity was practically constant (within our experimental uncertainty): $D = (2.6 \pm 0.14) \times 10^{-3} \text{ cm}^2/\text{s}$. From this D value we calculated $K = (7.4 \pm 0.4) \times 10^{-3} \text{ W/kcm}$ using the ρC value for ZBLAN from ref. [10].

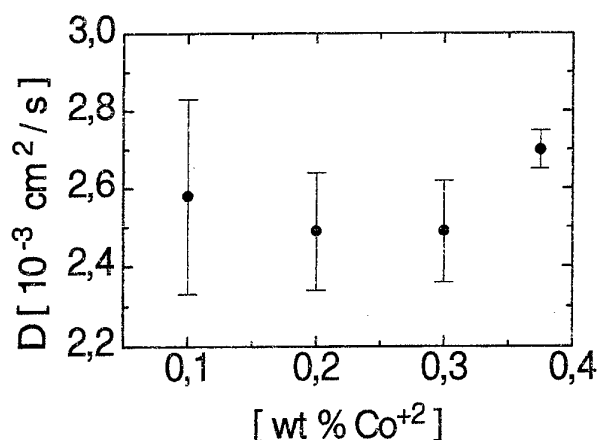


Figure 5: Thermal diffusivity versus Cobalt concentration in ZBLAN

Figure 6 shows that $\theta P/L$ increases linearly with the absorption coefficient A , so by Eq. (3) this behavior indicates that the product $K^{-1}ds/dT$ remains constant in the Cobalt concentration range studied.

The same procedure was adopted for the other samples. For these glasses we do not have the ρC value. However, Bruce⁹ analyzed 12 kinds of fluoride glasses and concluded that, at 300k, the molar specific heat is almost constant $\sim 21.3 \text{ k}^{-1} \text{ mol}^{-1}$ (86% of the Dulong-Petit value). For instance, using this value for ZBLAN we obtained $\rho C = 2.7 \text{ Ws/kcm}^3$ in a good agreement with the experimental value $\rho C = 2.8 \text{ Ws/kcm}^3$ from ref. [10]. We estimated ρC for all the samples and calculated K from our experimental D datas as shown in the Table 3.

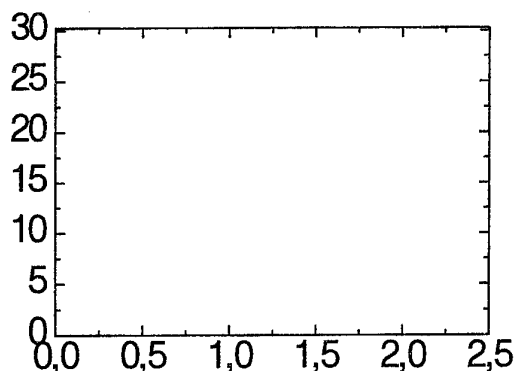


Figure 6: This graphic shows the linear behavior of the product $K^{-1}ds/dT$.

CONCLUSIONS

All fluorides we studied presented negative ds/dT values. We remark that $ds/dT \propto [\phi - \eta\beta]$, where ϕ and β are the temperature coefficients of the electronic polarizability and volume expansion respectively, and η is a constant that depends on the glass refractive index and the Poisson ratio ν . Therefore the negative ds/dT values are an indication of the small ϕ values of fluorides.

For laser applications, the thermal parameters are very important. High thermal conductivity is desired to dissipate the heat from the laser action region. It is well known that fluoride glasses do not have thermo-optical properties suitable for high power laser applications. However we observed that fluoroindate glasses, which have very good optical properties, presented thermal conductivity $\sim 18\%$ and diffusivity $\sim 23\%$ greater than the one of ZBLAN.

Table 3: Results of thermal diffusivity and conductivity and the optical path change with temperature ds/dT .

Samples	A (cm^{-1})	D ($10^{-3} \text{ cm}^2/\text{s}$)	K (10^{-3} W/kcm)	ds/dT (10^{-6} K^{-1})
IGPZ 0,2% Co	0.9 ± 0.04	2.9 ± 0.14	8.0 ± 0.39	-1.8 ± 0.14
ISZn 0,2% Co	1.0 ± 0.10	3.1 ± 0.06	8.4 ± 0.16	-1.2 ± 0.20
InSBZnGdN 0,29% Co	0.8 ± 0.02	3.2 ± 0.07	8.6 ± 0.19	-1.7 ± 0.14
YABC 0,377% Co	1.8 ± 0.03	3.3 ± 0.06	8.1 ± 0.15	-1.9 ± 0.13
ZBLAN 0,1% Co	0.4 ± 0.09	2.6 ± 0.25	7.4 ± 0.71	-6.1 ± 1.79
ZBLAN 0,2% Co	0.7 ± 0.003	2.5 ± 0.15	7.1 ± 0.43	-5.5 ± 0.43
ZBLAN 0,3% Co	1.5 ± 0.02	2.5 ± 0.13	7.1 ± 0.37	-5.6 ± 0.37
ZBLAN 0,375% Co	2.2 ± 0.10	2.7 ± 0.05	7.6 ± 0.14	-6.0 ± 0.52

ACKNOWLEDGMENTS

This research was supported by FAPESP and CNPq.

REFERENCES

- [1] J.P. Gordon, R.C.C. Leite, R.S. More, S.P.S. Porto, and J.R. Whinnery, J. Appl. Phys. 36, 3 (1965).
- [2] M.L. Baesso, J. Shen, and R.D. Snook, Chem. Phys. Lett. 197, 255 (1992).
- [3] M.L. Baesso, J. Shen and R.D. Snook, J. Appl. Phys. 75 (1994) p.3732-7.
- [4] T. Catunda, M.L. Baesso, Y. Messaddeq, M.A. Aegerter, J. Non-Cryst. Solids. (1997) 1-6.
- [5] M.L. Baesso, A.C. Bento, A.A. Andrade, T. Catunda, J.A. Sampaio, S. Gama. J. Non-Cryst. Solids. 219 (1997) 165-169.
- [6] M.L. Baesso, A. C. Bento, A.A. Andrade, J.A. Sampaio, E. Pecoraro, L.A.O. Nunes, T. Catunda, S. Gama. 57 (1998) 10545-10550.
- [7] R.C. Powell, D.P. Neikirk and D. Sardar, J. Opt. Soc. Am., 70, 486, (1980).
- [8] S.J. Sheldon, L.V. Knight, and J.M. Thorne, Appl. Opt. 21, 1663 (1982).
- [9] A.J. Bruce, in NATO on Halide Glasses for Infrared Optica Fiberoptics (Portugal), ed. by R.M. Almeida, Martinus Nijhoff, Dordrecht (1987) p. 149-62.

[10] G. ROSMAN: 'Dynamics of glass cooling applied to preform fabrication', *J. Non-Cryst. Solids*, 1992, **140**, pp. 255-258.

PHOTOINDUCED DICHROISM IN CHALCOGENIDES: INFLUENCE OF TEMPERATURE AND LIGHT INTENSITY

P.Hertogen ^a, V.K. Tikhomirov ^b, G.J. Adriaenssens ^a

^a **Laboratorium voor Halfgeleiderfysica, Department of Physics, K.U.Leuven, Celestijnenlaan 200D, B-3001 Heverlee, Belgium.**

E-mail: Peter.Hertogen@fys.kuleuven.ac.be

^b **Department of Materials, University of Leeds, Leeds LS2 9JT, U.K.**

ABSTRACT

The results of an experimental study of high-temperature and light intensity dependence measurements of photoinduced linear dichroism of amorphous As₂S₃ are given. At temperatures close to the glass transition temperature a light intensity dependence of the saturation value of the photoinduced dichroism (PDi) is observed. In addition, it is shown that the build-up kinetics of the PDi are temperature and light intensity dependent. These new data show that the so-called reciprocity law is limited to a certain temperature range (below the glass transition temperature). As a consequence, the model that tries to explain the PDi and that makes use of this law, will also have the limitation to that particular temperature range.

INTRODUCTION

Chalcogenide glasses exhibit good transmittance in the near infrared and have other promising qualities to serve as glass host materials for rare earth doping (Er, Pr, Ny...), leading to efficient optical fiber amplifiers^{1,2,3}. At the same time, these semiconducting glasses (both films and bulk), become metastable optically anisotropic solids, with the optical axis parallel to the electric vector of the inducing light, on being exposed to linearly polarized light⁴. When exposed to unpolarized light the optical axis appears with respect to the propagation direction of the inducing beam⁵. This photoinduced anisotropy (PA) is already commercially exploited in so-called Bragg reflectors and rocking-filters^{6,7,8,9}. The study of the underlying microscopic mechanism of this behaviour, which is still not well understood, is also very important from fundamental point of view since it is based on intrinsic defects of the glassy state¹⁰.

PA of chalcogenide glasses (e.g. As₂S₃, Se, GeS₂...) has already been extensively investigated the last 15 years, giving rise to some 'universal' observations: a slow build-up of the anisotropy is observed (seconds to minutes, and even hours) with an even slower dark relaxation¹¹. The effect is optically reversible and it does not show fatigue after many cycles of changing the polarization state of the inducing light¹². The saturation value of the anisotropy does not depend on the inducing light intensity well below the glass-transition temperature, and its corollary: the slowing down of the kinetics when lower light intensities are used¹⁰. This observation has been referred to as the *reciprocity law*^{13,14}.

Relatively few measurements of the temperature dependence have been performed. What is known up to now is that decreasing temperature increases the saturation value of the PA in an apparently activated way between the glass transition temperature, T_g , and about $T_g - 100$ K, followed by a relatively insensitivity to the temperature at lower temperatures^{15,16}. In these papers, the observed decrease in the anisotropy with rising temperature is ascribed to thermal relaxation processes.

However, based on a simple and general mathematical model, Baranovskii *et al.*¹⁷ showed that latter assumption is in conflict with the observed independence from the light-intensity of the steady-state anisotropy. The model is looked at in two extreme cases: the rate of aligning the already present dipoles is very fast compared to the relaxation rate and vice versa. It is concluded that the only possibility of explaining the temperature dependence of the saturation level of the PA (and staying consistent with the reciprocity law) is to allow a temperature dependence of the number of dipoles available for orientation. Indirect support for that conclusion was seen in the experimentally observed temperature independence of the kinetics of the anisotropy build-up and the independence of the saturation level of the PA on the generation rate (which is directly proportional to the light intensity).

In this paper we show that, based on new data on As₂S₃ films that the kinetics of the PA build-up are indeed temperature dependent. We also present some data showing that the light-intensity independence of the PA (and as a result the reciprocity law) is only valid within a certain temperature region. The validity of the reciprocity law within a given temperature interval is defined with respect to the glass transition temperature of the material under study. These new results define the limits within which the experimental data can be explained by the Baranovskii *et al.*¹⁷ model.

EXPERIMENTAL

The experiments were performed on fresh As₂S₃ and Se films prepared by thermal vacuum evaporation under a $5 \cdot 10^{-5}$ Torr atmosphere. Starting materials for evaporation were As₂S₃ powder and Selenium metal grey (99.995% purity). An air-cooled Ar⁺ laser ($\lambda=514$ nm) and a HeNe laser ($\lambda=632.8$ nm) were used to induce the effect in respectively As₂S₃ and Se. Inserting neutral density filters in the light path gave the desired light intensities. The linear dichroism, defined as $2(I_{||}-I_{\perp})/(I_{||}+I_{\perp})=(\alpha_{\perp}-\alpha_{||}) \cdot h/A$ with $I_{||,\perp}$ respectively the intensity of the transmitted beam parallel and perpendicular to the polarization direction of the inducing beam, h the thickness of the sample and $\alpha_{\perp,||}$ respectively the absorption coefficients perpendicular and parallel to the polarization direction of the inducing beam. The value of the denominator was detected with a lock-in amplifier by modulating the polarization state of the laser beam between two mutually orthogonal directions. A detailed description on measuring linear dichroism is given elsewhere¹⁸. The samples were heated in an optical thermostat, filled with nitrogen gas to serve as contact gas and to avoid sample contamination at high temperatures. Because chalcogenide glasses exhibit both scalar (e.g. photodarkening, photobleaching) and vectoral (e.g. dichroism, birefringence) photoinduced effects¹⁹, care was taken to bring the photodarkening in the samples to saturation before measuring the linear dichroism.

RESULTS

Figure 1 shows the typical build-up kinetics and reversibility of the PA in amorphous chalcogenides. The build-up is a relatively slow process: depending on the temperature and light intensity used, it can take up to 1 hour to reach saturation. When changing the polarization state of the inducing laser beam to its orthogonal state, the PA is broken down quite fast (compared to the build-up) and again a build-up process will start, but this time it will induce anisotropy with the opposite sign. This kind of experiment was done at different temperatures up to T_g , which is around 180°C for As₂S₃ films, and at light intensities of 5 and

50 mW. Typically between four and six reorientation cycles were recorded and analysed in order to obtain reliable fit data. Each of these cycles was fitted with the stretched exponential:

$$A(t) = A_s \left(1 - \exp \left[- \left(\frac{t}{\tau} \right)^\gamma \right] \right)$$

with A the value of the PA, A_s its saturation value, τ a typical relaxation parameter and γ a parameter which characterizes the stretched exponential behaviour.

The data can also be fitted with the same function, but with $-t'/\tau'$ in the exponent. Then the relation $\tau' = \tau^\gamma$ holds. The values presented below refer to τ . Figure 2 shows the variation of the parameter τ with temperature and light intensity. This parameter is clearly dependent on the

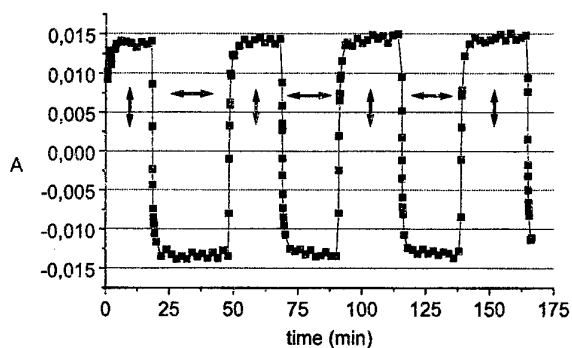


Figure 1: Anisotropy A versus time (min) for an As_2S_3 film at 125°C with a 50 mW inducing laser beam (Ar^+ 514 nm line).

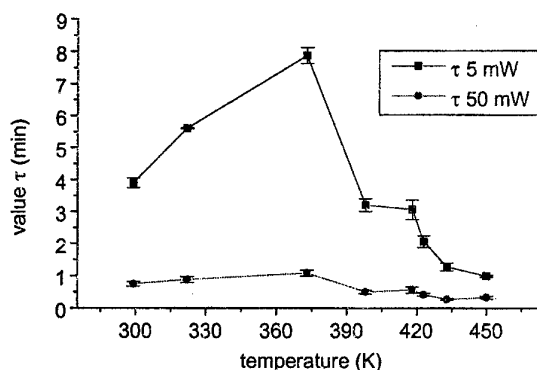


Figure 2: Value of the fit parameter τ versus temperature (K) for a 5 mW (squares) and a 50 mW (circles) inducing laser beam (Ar^+ 514 nm line).

temperature and the light intensity. Higher light intensities will speed up the process, and this for all temperatures investigated. From 373 K on, increasing the temperature also results in faster kinetics for both light intensities. We also note the peculiar behaviour at lower temperatures (from 373 K to 298 K): decreasing the temperature will increase the speed of the processes! In figure 3, the second parameter γ is plotted for different temperatures and light intensities. Within the experimental uncertainty, there was no dependency found on the temperature or light intensity. Close to T_g , it seems there may be some strong increase of γ , but due to the large experimental uncertainty it is difficult to make this conclusion.

The natural logarithm of A_s (the saturation value of the PA) versus the reciprocal temperature is plotted in figure 4, for the two light intensities investigated. The typical dependence of A_s on temperature was already published elsewhere¹⁵, but it also shows for the first time the limited validity of the so-called reciprocity law. There is indeed light intensity dependence at higher temperatures, therefore violating the reciprocity law. This is better shown in a 3D graph in figure 5, showing the temperature dependence for both 5 and 50 mW.

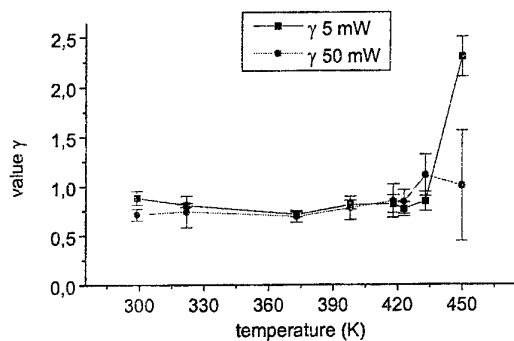


Figure 3: Value of the fit parameter γ versus temperature (K) for a 5 mW (squares) and a 50 mW (circles) inducing laser beam (Ar⁺ 514 nm line).

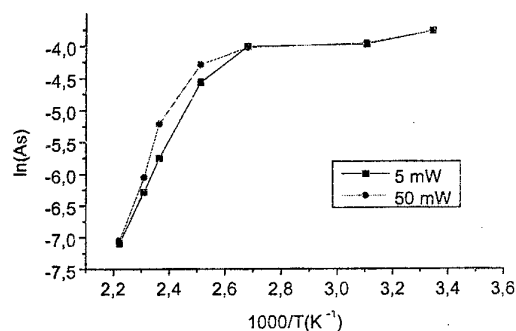


Figure 4: Natural logarithm of A_s versus the reciprocal temperature, for a 5 mW (squares) and a 50 mW (circles) inducing laser beam (Ar⁺ 514 nm line).

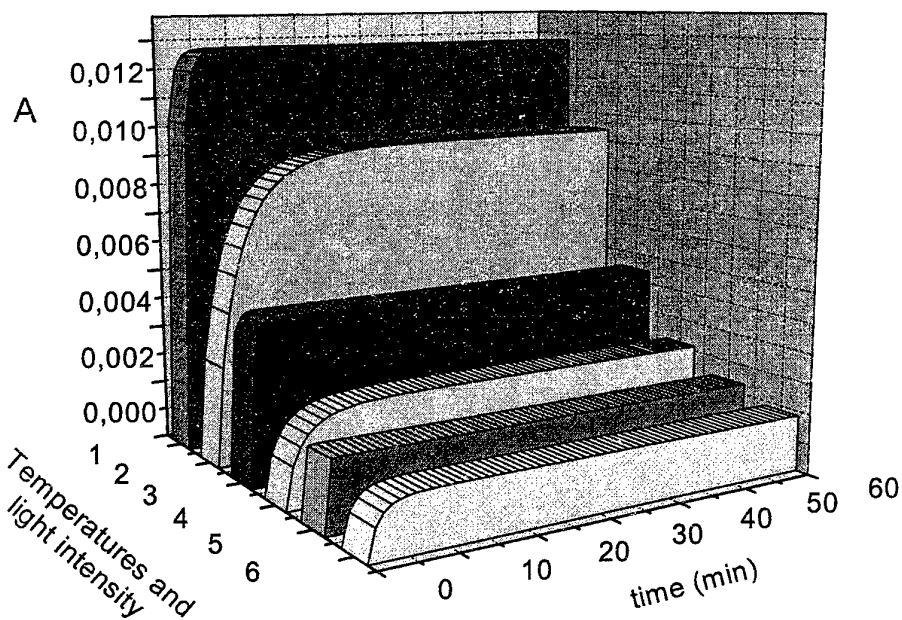


Figure 5: 3D representation of the temperature and light intensity dependence of PA. On the x-axis we see time (min), on the y-axis per temperature two light intensities are shown, and on the z-axis the anisotropy A is plotted. The labels correspond to the following: 1 (125°C, 50mW), 2 (125°C, 5mW), 3 (150°C, 50mW), 4 (150°C, 5mW), 5 (160°C, 50mW), 6 (160°C, 5mW).

Following the notion that the PA can be explained on the basis of a reorientation of intrinsic defects¹⁰, the idea was conceived that measurability near T_g might be improved by making use of samples with an increased density of native defects. It was thought that oblique deposition would give such material with more defects, and thus a higher value of PA. In addition, oblique deposition at large angles will give columnar growth, making the material more porous²⁰. We evaporated some As₂S₃ films at an angle of 80° with respect to the plane perpendicular to the evaporation direction. The PA was measured at room temperature with a 15mW strong inducing laser beam. As shown in figure 6, and compared to the saturation value of the normal films at room temperature, two remarks can be made: 1) the saturation value of the PA does not seem to be enlarged considerably, 2) the films show strong “structural” anisotropy, which can be changed by the photoinduced anisotropy. These experiments were also performed on oblique deposited Se films, showing an increase of A_s by a factor of 2,5. The structural anisotropy was not seen in those samples, indicating that probably no columns were formed during evaporation. This was confirmed by AFM surface scans, showing no difference between oblique and normal evaporated samples.

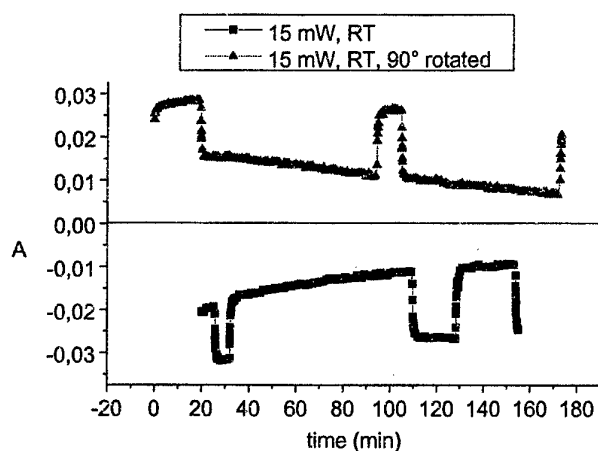


Figure 6: Anisotropy A versus time (min) for an oblique deposited As₂S₃ film at room temperature (squares) and induced with a 15mW Ar⁺ 514 nm line. Rotating the sample with 90° gives the triangles-signal.

DISCUSSION

The behaviour of the fit parameters can be explained to some extent. The parameter τ is clearly dependent on light intensity. The higher the light intensity, the smaller the values of τ , hence the faster the kinetics. The dependency of τ on temperature from 373 K to 450 K is also logical: higher temperatures will give smaller values of τ and therefore faster kinetics. In the first case, more optical stimuli will be given to the microscopic units responsible for PA such that the kinetics become faster when more intense light is used. In the latter case, the supply of more thermal energy to those units makes it easier to realign them. The temperature

dependence of τ in the temperature region 298 K to 373 K is less obvious: increasing the temperatures in that region will lead to *higher* values of τ with a slowing down of the kinetics as a consequence. This is rather a puzzle and needs further investigation.

As pointed out before, the parameter γ is independent on temperature and light intensity within the experimental uncertainty. γ is also less than 1, except possibly very close to T_g , which shows that the simple exponential rate equation used in Baranovskii *et al.*¹⁷ is an oversimplification. Clearly, in amorphous materials a distribution of rate constants can be expected, and a γ value below 1 is the natural consequence. From the constancy of γ with respect to temperature and light intensity, we may conclude that that distribution directly relates to the frozen-in disorder of the amorphous structure. This distribution will not considerably change with temperature and light intensity, explaining the behaviour of γ . The strong structural anisotropy in the oblique deposited films most probably comes from the presence of columns in the film. This assumption was confirmed by turning the sample 90° with respect to the electric field vector of the inducing beam. This gives a structural anisotropy in the opposite direction (triangles in figure 6). The fact that this structural anisotropy can be lowered by photoinduced anisotropy, is another confirmation that the photoinduced changes in chalcogenide materials are correlated with structural changes in the material¹⁹.

CONCLUSIONS

In the paper of Baranovskii *et al.*¹⁷, it is shown that to obtain temperature dependence in A_s , it would be either through the temperature dependence of τ , or through a temperature dependence of the concentration of centers (defects) which are responsible for PA. The new data presented in this paper show that both conditions are fulfilled only in a certain temperature range. Therefore, the new observations define the limits within which the experimental data can be explained by the Baranovskii *et al.*¹⁷ model.

¹ Y. Ohishi, T. Kanamori, T. Kitagawa, S. Takahashi, Opt. Lett. 16 (1991) 1747.

² K. Wei, D.P. Machewirth, J. Wenzel, E. Snitzer, G.H. Sigel Jr., J. Non-Cryst. Solids 182 (1995) 257.

³ J. Kirchhof, J. Kobelke, M. Scheffler, A. Schwuchow, Electron. Lett. 32 (1996) 1220.

⁴ V.M. Lyubin, V.K. Tikhomirov, J. Non-Cryst. Solids 114 (1989) 133.

⁵ V.K. Tikhomirov, S.R. Elliott, Phys. Rev. B 49 (1994) 17476.

⁶ R.H. Stolen, A. Ashkin, W. Pleibel, J.M. Dziedzic, Opt. Lett. 9 (1984) 300.

⁷ K.O. Hill, F. Bilodeau, B. Malo, D.C. Johnson, Electron. Lett. 27 (1991) 1548.

⁸ P. ST.J. Russell, D.P. Hand, Electron. Lett. 26 (1990) 1846.

⁹ C.H. Kwak, S.Y. Park, H.M. Kim, E.H. Lee, Opt. Commun. 88 (1992) 249.

¹⁰ G.J. Adriaenssens, V.K. Tikhomirov, S.R. Elliott, J. Non-Cryst. Solids, proc. icams17, to be published.

¹¹ V.K. Tikhomirov, S.R. Elliott, Phys. Rev. B 51 (1995) 5538.

¹² V.M. Lyubin, V.K. Tikhomirov, J. Non-Cryst. Solids 135 (1991) 37.

¹³ V. Lyubin, M. Klebanov, V. Tikhomirov, G. Adriaenssens, J. Non-Cryst. Solids 198-200 (1996) 719.

¹⁴ H. Fritzsche, Phys. Rev. B 52 (1995) 15854.

¹⁵ V.K. Tikhomirov, G.J. Adriaenssens, S.R. Elliott, Phys. Rev. B 55 (1997) R660.

¹⁶ P. Krecmer, M. Vleck, S.R. Elliott, J. Non-Cryst. Solids, proc. icams17, to be published.

¹⁷ S.D. Baranovskii, V.K. Tikhomirov, G.J. Adriaenssens, Phil. Mag. Lett. 77 (1998) 295.

¹⁸ V.M. Lyubin, V.K. Tikhomirov, Sov. Phys. Solid State 32 (1990) 1069.

¹⁹ K. Shimakawa, A. Kolobov, S.R. Elliott, Adv. in Physics 44 (1995) 475.

²⁰ K. Starbova, J. Dikova, N. Starbov, J. Non-Cryst. Solids 210 (1997) 261.

INFLUENCE OF IMPURITIES ON OPTICAL PROPERTIES OF As-Se-Te GLASSES

M.F. Churbanov, V.S. Shyriaev

Institute of Chemistry of High-Purity Substances of the Russian Academy of
Sciences, 49 Tropinin St., GSP-75, Nizhny Novgorod, 603600, GSP-75, Russia,
email: hp@hp.nnov.su

V.G. Plotnichenko

Scientific Centre of Fibre Optics, General Physics Institute of the Russian
Academy of Sciences, 38 Vavilov St., Moscow, 117756, Russia, fax: (095) 135 81 39

ABSTRACT

The qualitative and quantitative aspects of the impurities influence on the optical transmission of As-Se-Te glasses in the 4-12 mkm wavelength region are considered in the paper.

INTRODUCTION

High-purity glasses of As-Se and As-Se-Te systems are promising optical materials. They have a high transparency in the wide spectral region and low optical losses in the middle IR range.

The theoretically predicted minimum of optical losses is equal to $5 \cdot 10^{-2}$ dB/km at 6.1 mkm for As_2Se_3 glass. The optical loss value less than 0.1 dB/m is expected between 2 and 8 mkm and about 0.8 dB/m at wavelength 10.6 mkm. Optical losses at 10.6 mkm in the glass of As-Se-Te system may be lower than in As_2Se_3 glass because of a shift of multiphonon absorption edge into the long-wave range.

The real optical losses in the glasses are higher than theoretically predicted as a result of impurities presence. These impurities are oxygen, carbon, sulfur and hydrogen bounded with each other or with the elements-macrocomponents of glass. Absorption bands due to these compounds are within the transparency region of chalcogenide glasses.

The quantitative and qualitative data on the effect of these impurities on optical losses in the As-Se and As-Se-Te glass systems at 4-12 mkm are limited.

The purpose of this work was the investigation of the impurities in the As-Se and As-Se-Te glasses by IR spectroscopy of bulk samples and fibres and of the impurity effect on the optical losses of glasses.

EXPERIMENTAL

The experiment included the preparation of the glasses with the known content of impurities of sulfur, carbon and oxygen and with investigation of transmission spectra of the samples.

We investigated the impurities influence using glasses of As_2Se_3 and $\text{As}_2\text{Se}_{1.5}\text{Te}_{1.5}$ compositions.

Synthesis of As_2Se_3 and $\text{As}_2\text{Se}_{1.5}\text{Te}_{1.5}$ glasses carried out by melting the purified elements (As, Se and Te) in the vacuumed and sealed reactors from silica. To preclude contamination of their surface and oxidation the starting substances were loaded into the reactor by vacuum distillation or sublimation from the intermediate vessels in the all-soldered set-up.

Purity of glasses obtained by the direct synthesis from the elements is depended by the degree of purity of the elements used and by the temperature-time conditions of the synthesis.

In an initial arsenic the content of carbon was 0.6 ppm and the concentration of submicron particles did not exceed $1 \cdot 10^6 \text{ cm}^{-3}$. In an initial selenium the content of carbon was 10 ppm, the content of hydrogen in the form of SeH was less than 1 ppm.at. and the concentration of particles with sizes of $0.07 \div 0.1 \text{ mkm}$ did not exceed $5 \cdot 10^6 \text{ cm}^{-3}$. In an initial tellurium the content of carbon was 0.7 ppm and the concentration of submicron particles with sizes of $0.07 \div 0.1 \text{ mkm}$ did not exceed $3 \cdot 10^6 \text{ cm}^{-3}$.

The melting of mixture was carried out in the rocking furnace at 750°C for 7 hours. To form the bulk glass samples we cooled the melt of As_2Se_3 glass in the range of $750 \div 400^\circ\text{C}$ and of $\text{As}_2\text{Se}_{1.5}\text{Te}_{1.5}$ glass in the range of $750 \div 500^\circ\text{C}$ at the rate of about 1 K/min, then quenched it in air, separated the glass rod from the walls of silica ampoule and annealed. The content of impurities in glasses was determined by the reactive gas chromatography technique, laser mass-spectrometry, laser ultramicroscopy and IR-spectroscopy.

The given quantity of impurity (carbon, oxygen or sulfur) were added to the samples of base glasses. Then the glass was melted and homogenized again.

The samples with thickness of 1, 3 and 14 mm were made from prepared glasses, their transmission spectra were registered in the wavenumber range of $5000 \div 350 \text{ cm}^{-1}$ using IR-spectrometer Bruker IFS-113V.

Optical fibers with diameter of $200 \div 500 \text{ mkm}$ were drawn from these glasses by a single crucible, a double crucible and a «rod-in-tube» technique. The total optical loss spectra of fibres were measured by a well-known two-point method.

RESULTS

The prepared glasses contained $1 \div 3 \text{ ppm}$ of carbon, $10^6 \div 10^7 \text{ cm}^{-3}$ of particles with sizes of $0.07 \div 0.11 \text{ mkm}$ and 1 ppm.at of hydrogen in the form of Se-H groups. The transmission spectra of the tested glass samples were obtained in the $5000 \div 350 \text{ cm}^{-1}$ spectral region. The transmission spectra of the best glass samples had no absorption bands, caused by As-O and Se-O bonds at $1 \div 15 \text{ mm}$ optical way.

The transmission spectra were the primary information about the quality of glasses prepared and about the impurities which present in the glass.

The transmission spectra were convert to the absorption spectra taking into account of the sample thickness and using a base line method. A program has been used for analyzing of complex shape absorption bands to determine their parameters and to evaluate their contribution to total absorption at various wavelengths.

Figure 1 shows spectral dependence of the absorption coefficient for high-purity of As_2Se_3 and $\text{As}_2\text{Se}_{1.5}\text{Te}_{1.5}$ glasses composition in the $1800 \div 400 \text{ cm}^{-1}$ wavenumber range. It is seen the essential shift of multiphonon absorption edge into the short wavenumber range after partial substitution of selenium by tellurium.

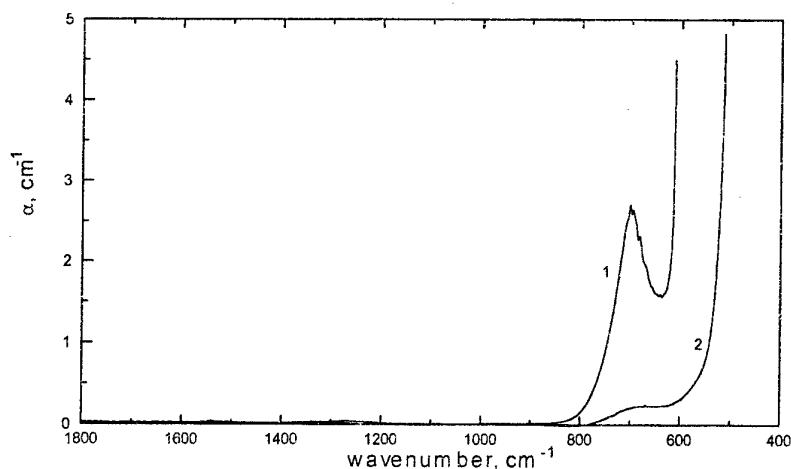


Fig.1 Absorption spectra of As_2Se_3 (1) and $\text{As}_2\text{Se}_{1.5}\text{Te}_{1.5}$ (2) glasses

The spectral dependence of the extinction coefficient of sulfur in As_2Se_3 (1) and $\text{As}_2\text{Se}_{1.5}\text{Te}_{1.5}$ (2) glasses in the $1400\div 500\text{ cm}^{-1}$ wavenumber range is given in the figure 2. This dependence was obtained from absorption spectra of glasses doped by the elementary sulfur up to 10 at.% with respect to a stoichiometric ratio of arsenic/chalcogen.

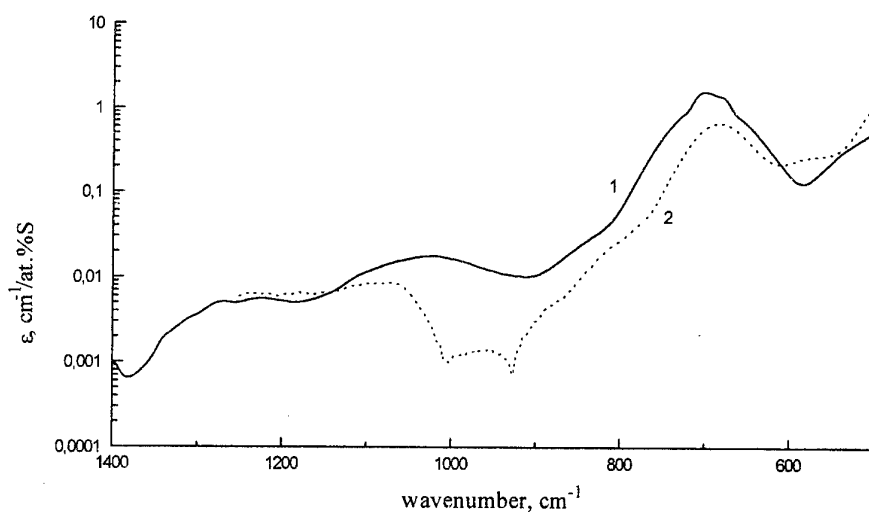


Fig.2. Spectral dependence of the extinction coefficients of sulfur in As_2Se_3 (1) and $\text{As}_2\text{Se}_{1.5}\text{Te}_{1.5}$ (2) glasses

Figure 3 shows absorption spectra of high-purity As_2Se_3 (1), As_2S_3 (2) glasses and of $(\text{As}_2\text{Se}_3)_{0.95}(\text{As}_2\text{S}_3)_{0.05}$ glass composition, prepared by melting of given amounts of As_2Se_3 and As_2S_3 . A remarkable effect is a transfer of hydrogen from SeH-groups to sulfur atoms, caused by more higher bond strength of SH in comparison with SeH bond.

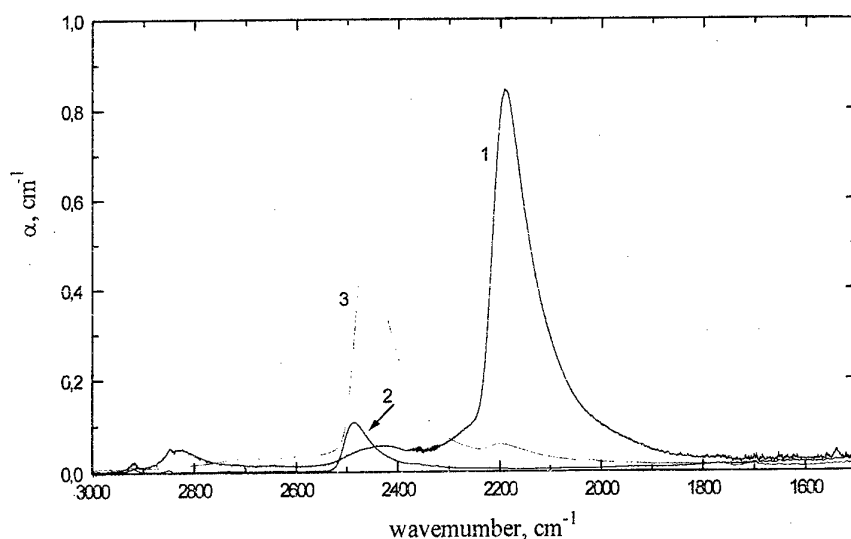


Fig.3. A hydrogen transfer from Se to S in the mixed As_2S_3 - As_2Se_3 glasses. 1,2,3 - absorption spectra of As_2Se_3 , As_2S_3 and $(\text{As}_2\text{Se}_3)_{0.95}(\text{As}_2\text{S}_3)_{0.05}$ glasses, respectively

Figure 4 shows transmission spectra of As_2Se_3 before (1) and after (2) adding of 100 ppm carbon powder. It can be seen the essential decrease of intensity of oxides bands, of initial glass, increase of intensity of carbon dioxide band and appearance of new band with maximum at 2190 cm^{-1} in the spectrum of the glass doped by 100 ppm of carbon.

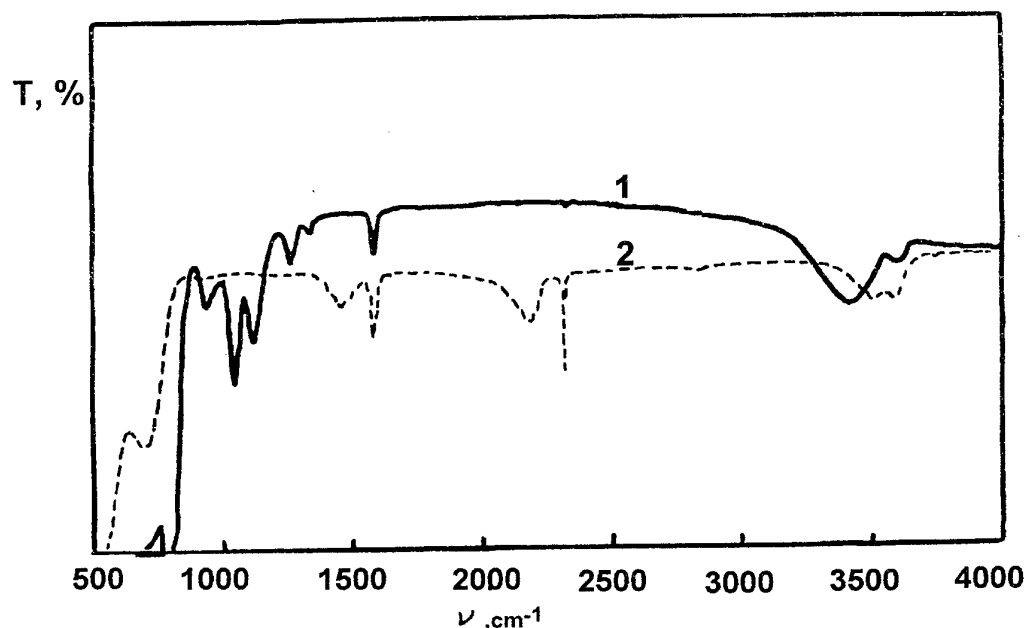


Fig.4. Transmission spectra of As_2Se_3 before (1) and after (2) adding of 100 ppm carbon. The depth of samples is 2 mm

Figure 5 shows spectra of total optical losses for monolayer fibers of As-Se-Te glass system, prepared at different conditions. The glass composition: 1 - $\text{As}_2\text{Se}_{1.5}\text{Te}_{1.5}$, 2 - $\text{Ge}_3\text{As}_{36}\text{Se}_{51}\text{Te}_{10}$, 3 - $\text{As}_2\text{Se}_{1.5}\text{Te}_{1.5}$.

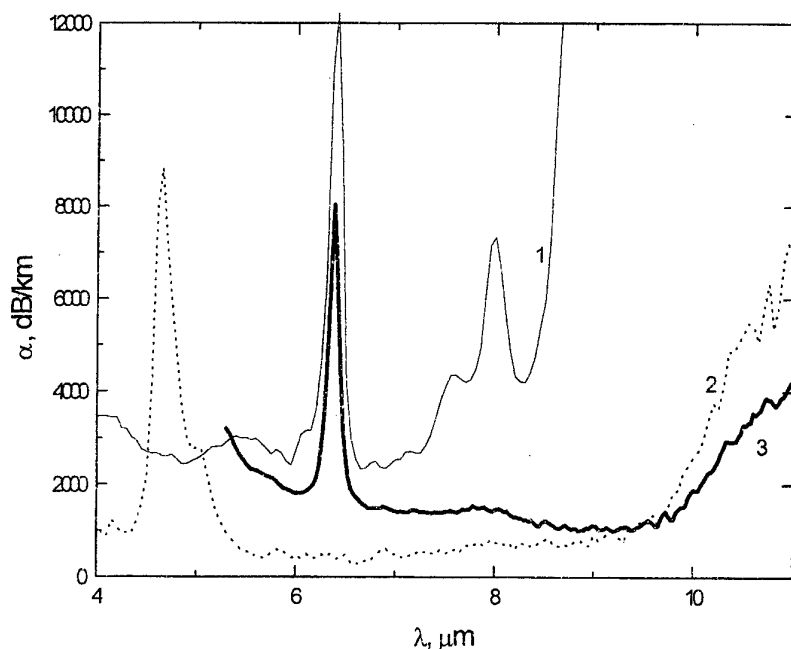


Fig.5. Total optical loss spectra of fibers based on glass compositions: 1 - $\text{As}_2\text{Se}_{1.5}\text{Te}_{1.5}$, 2 - $\text{Ge}_3\text{As}_{36}\text{Se}_{51}\text{Te}_{10}$, 3 - $\text{As}_2\text{Se}_{1.5}\text{Te}_{1.5}$

DISCUSSION

The impurities of oxygen, hydrogen and sulfur have an essential influence on the optical transparency of As-Se and As-Se-Te glass systems in the $2500\div 700\text{ cm}^{-1}$ region. Compounds of these impurities with the elements-macrocomponents of glass and with each other are responsible for an appearance of absorption bands (fundamental bands, overtones and their superpositions). If the impurities content is high, these bands are resolved the spectra only of thin samples (Fig.4). In total optical loss spectra of fibers they are overlapped and are registered as a continuous absorption bands in wide spectral region (Fig.5).

As appears from the experimental results, the sulfur has an influence on optical transparency of As-Se-Te glasses in $1000\text{-}500\text{ cm}^{-1}$. Its content which causes the loss closed to intrinsic one is equal to about 1000 ppm for $1200\text{-}850\text{ cm}^{-1}$. This level is essentially lower in the long wavelength region. The influence of oxygen impurity is much more stronger (by several orders of magnitude greater). The value of the acceptable concentration of oxygen impurity is estimated as $\sim 0.1\div 0.01\text{ ppm.at}$. The content of hydrogen also should not exceed parts of ppm.at.

The impurities of oxygen, carbon, hydrogen and sulfur interact during synthesis of glass-forming compounds not only with the elements-macrocomponents, but also with each other. For that reason their initial chemical form is changed. Therefore, the optical loss spectra of fibres and transmission spectra of bulk samples can not be reproduced,

even if glasses and fibres were prepared from the same initial substances and at the same conditions. Fig.5 confirms this statement.

The source of gas-formation impurities in the glasses are initial substances, material of a container, in which glass melt is prepared, gas environment, including vacuum residual gases. Because of high values of extinction coefficients of these impurities small variations in impurity content in initial substances and in the conditions of synthesis affects strongly on the optical characteristics of glasses.

CONCLUSION

The optical losses of As-Se-Te glasses in the 4-12 mkm spectral region are very sensitive to the presence of oxygen, hydrogen, carbon and sulfur. The impurities content in the glasses with intrinsic optical losses should not exceed the level of tens of ppb.at. to tens ppm.at.

THERMALLY INDUCED CHANGES IN REFRACTIVE INDEX OF As-S AND Ag-As-S THIN FILMS

G. Dale, P.J.S. Ewen and A.E. Owen

Department of Electronics & Electrical Engineering,
University of Edinburgh, Edinburgh, EH9 3JL, UK. email gd@ee.ed.ac.uk

ABSTRACT

Reflection measurements at infrared (IR) wavelengths are used to measure thermally induced changes in the optical thickness of as-deposited and annealed As-S and Ag-As-S amorphous thin films. For annealed As-S films the values for the change in optical thickness corresponded to the expansion coefficient for the bulk material between room temperature and $\sim 160^\circ\text{C}$, indicating that the refractive index, n , has a negligible dependence on temperature. In contrast, the Ag-As-S system was found to have thermal coefficients ~ 2.5 times those for the As-S films, and this was not reduced by annealing.

INTRODUCTION

Chalcogenide glasses such as the arsenic sulphides (As-S) are well known IR transmitting materials which have been under investigation for many years because of the range of photo-induced effects they exhibit such as photodarkening and metal-photodoping [1,2]. Potential applications include diffractive optical element (DOE) and photonic band gap (PBG) devices. PBG structures need to have high resolution with large refractive index modulation, both of which can be achieved by metal-photodoping. Though devices using the bulk material are of interest, structures in thin films are also important.

A feature of As-S glasses which is sometimes overlooked is the thermal coefficient of the refractive index (dn/dT). For example, for bulk $\text{As}_{40}\text{S}_{60}$ (the most stable As-S glass), the figure for dn/dT is lower than for most of the other commonly used IR materials such as Ge, ZnS, NaCl etc. [3]. Any device fabricated in an IR material will therefore deteriorate in performance with changes in ambient temperature; diffractive structures, for example, can exhibit sharp angular/wavelength dependence and would become 'de-tuned'. Similarly, thermal imaging systems would suffer defocusing at different temperatures. This problem has led to the routine use of hybrid (refractive/diffractive) structures which have an athermalising effect whilst minimising cost and weight of the optical system [4]. Other work has investigated the use of $\text{As}_{40}\text{S}_{60}$ for a hybrid single element lens which is both achromatic and athermal when set in an aluminium mount [5].

EXPERIMENTAL PROCEDURES

The As-S films were deposited on glass slides from thermally evaporated As-S fragments in a quartz crucible heated via a wire coil. The deposition rate was kept stable at $\sim 0.1\text{nm s}^{-1}$ since this is known to yield films with composition matching the source [6,7]. The thicknesses of the films were checked independently with a surface profilometer (Dektak IIA). Ag-As-S films were prepared from bilayers of $\text{Ag}/\text{As}_{33}\text{S}_{67}$ which were heated for a prolonged period well beyond the complete exhaustion of the Ag into the As-S glass matrix. The resulting composition was estimated as $\text{Ag}_{21}\text{As}_{26}\text{S}_{53}$.

The reflection spectrum of the thin films was recorded with the sample in a temperature cell (Specac P/N 21.520). As temperature is increased the spectral features shifted due to the change in optical thickness (nt) of the film, where t is the geometric thickness of the film. The measurements were restricted to the relative shift of the spectrum, for which the absolute instrumental accuracy is less important than the repeatability of the recorded spectra. Small changes in n over this small spectral shift could be neglected because the materials are non-dispersive ($dn/d\lambda \approx 0$) in the wavelength region considered [8]. The average measured shifts in the spectra were found to be reproducible and reversible during several annealing cycles, except where indicated.

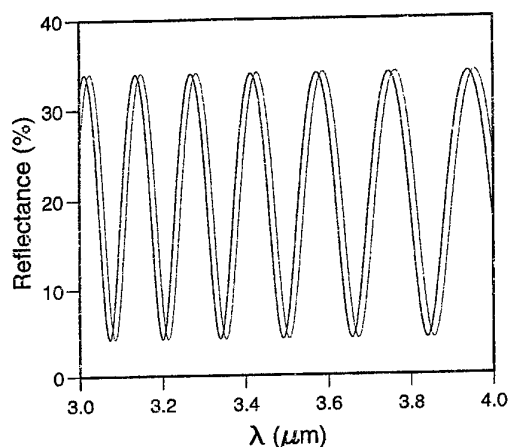


Figure 1: theoretical reflectance spectrum for a thin film on a glass substrate. The dashed line is at an elevated temperature, where: $n_{\text{film}} = 2.4$, $t = 16\mu\text{m}$, $n_{\text{substrate}} = 1.52$, $\delta n/n = 10 \times 10^{-6}^\circ\text{C}^{-1}$, $\delta t/t = 25 \times 10^{-6}^\circ\text{C}^{-1}$ and $\Delta T = 120^\circ\text{C}$.

If the thermal coefficients of expansion and refractive index are small, it can be shown that [9]:

$$\theta = \frac{\delta t}{t} + \frac{\delta n}{n}, \quad (1)$$

where $\theta = (\lambda_{\text{[hot]}} - \lambda_{\text{[cold]}})/(\lambda_{\text{[hot]}})$ and δt and δn are the thermally induced increments in t and n . $\lambda_{\text{[hot]}}$ and $\lambda_{\text{[cold]}}$ are wavelengths corresponding to equivalent spectral features for the upper and lower temperatures respectively. Hereafter values of θ are given averaged over a temperature range. A calculated example of these effects is shown above in figure 1.

RESULTS AND DISCUSSION

ANNEALING $\text{As}_{40}\text{S}_{60}$ FILMS

An as-deposited $16.1\mu\text{m}$ thick film of $\text{As}_{40}\text{S}_{60}$ was heated to 135°C and the shift in the spectrum recorded. The shifts at various wavelengths were used to calculate values for θ which are plotted as squares in figure 2. Though neither of the coefficients could be calculated independently from this data, previous literature gives coefficients of $dn/dT < 3 \times 10^{-6}^\circ\text{C}^{-1}$ for a similar wavelength range [1], and $dt/dT = 20 - 25 \times 10^{-6}^\circ\text{C}^{-1}$ [3,10]

which is consistent with smaller values of θ than those given here. The differences are explained by the fact that the present data relates to as-deposited films rather than the bulk material.

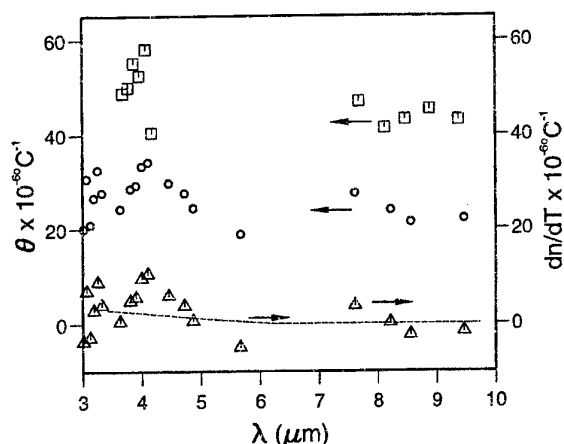


Figure 2: Effect of heat on the optical thickness of a $16.1\mu\text{m}$ thick $\text{As}_{40}\text{S}_{60}$ layer. \square 's represent values of θ after annealing the as-deposited film at 135°C , o 's represent values after film has been annealed at 160°C and Δ 's represent the estimated dn/dT for the annealed films assuming an expansion coefficient for the annealed film equal to that for the bulk $\text{As}_{40}\text{S}_{60}$.

Subsequently, the same sample was raised to the annealing temperature for $\text{As}_{40}\text{S}_{60}$ glass, i.e. 10°C below the glass transition temperature of $T_g = 170^\circ\text{C}$. The data obtained on re-heating after annealing is plotted as circles in figure 2, whilst the triangles represent calculated values for dn/dT assuming a film expansion coefficient equal to that of $\text{As}_{40}\text{S}_{60}$, i.e. $23.7 \times 10^{-6}^\circ\text{C}^{-1}$. Annealing has reduced the thermal coefficients of the film such that they are closer to the values for the bulk material [7] given by the dashed line which represents dn/dT obtained by Rodney [1] for a more limited temperature range (19 – 31°C). An average value for dn/dT across the wavelength range for the present data is $3.3 \times 10^{-6}^\circ\text{C}^{-1}$. In comparison, Young [11] gives $dn/dT \sim 5 \times 10^{-6}^\circ\text{C}^{-1}$ for thin films of the same material at $\lambda = 2.5\mu\text{m}$ and with $T = -196$ to 90°C after correcting for the thermal expansion coefficient which was taken as $23.7 \times 10^{-6}^\circ\text{C}^{-1}$.

ANNEALING OF $\text{As}_{33}\text{S}_{67}$ AND $\text{Ag}_{21}\text{As}_{26}\text{S}_{53}$ FILMS

The thin films samples of these materials had layer thicknesses of 1.4 – $1.5\mu\text{m}$. The reduced thickness meant that fewer oscillations were present in the reflection spectra and hence the data generated is for a more restricted wavelength range. For the $\text{As}_{33}\text{S}_{67}$ film the values of θ at λ – $3.4\mu\text{m}$ are given in table 1 below, where the sequence reading from top to bottom corresponds to the order in which the heating cycles were carried out.

It is apparent that annealing at the higher temperature produces a reduction in θ compared with the as-deposited film. The average values for θ are 42.1 and $23.7 \times 10^{-6}^\circ\text{C}^{-1}$ for the as-deposited film and the film after annealing at 154°C respectively. The values of θ for this composition are in the same range to those found for the annealed $\text{As}_{40}\text{S}_{60}$ film, where dn/dT is very small and θ is accounted for by the expansion coefficient of the bulk material.

Table 1: values of θ for $\text{As}_{33}\text{S}_{67}$ and $\text{Ag}_{21}\text{As}_{26}\text{S}_{53}$ films following annealing at the indicated temperatures.

	$\text{As}_{33}\text{S}_{67}$	$\text{Ag}_{21}\text{As}_{26}\text{S}_{53}$
$T^{\circ}\text{C}$	$\theta \times 10^{-6}^{\circ}\text{C}$	$\theta \times 10^{-6}^{\circ}\text{C}$
140	40.04	
140	34.91	65.47
140	45.26	70.33
154	47.65	62.55
154	25.70	66.44
154	21.46	74.88
154	23.96	

In diffractive optical elements produced in these glasses the Ag-As-S phase is a secondary grating material having greater refractive index and etch resistance compared with the As-S glass. Values of θ for this material are given in the table 1 above, for $\lambda = 2.7 - 3.9\mu\text{m}$. The coefficients do not appear to be reduced by annealing, and this can be explained by the fact that the sample was effectively annealed by heating the original bilayer system to induce Ag diffusion into the $\text{As}_{33}\text{S}_{67}$ layer. The average value of θ is $67.9 \times 10^{-6}^{\circ}\text{C}^{-1}$, which is ~ 2.5 times larger than the figure for the As-S compositions. This indicates a stronger dependence of refractive index and/or film expansion on temperature for the Ag-containing films. It is known that the effect of introducing Ag into the As-S glass matrix results in a material with a larger refractive index and a shift in the dispersion curve towards longer wavelengths [8,12]. Optical devices in the form of Ag structures dissolved in As-S glasses would have different thermal coefficients for each material phase.

CONCLUSIONS

The thermal properties of As-S and Ag-As-S films have been investigated using reflectance measurements at IR wavelengths. For $\text{As}_{40}\text{S}_{60}$ the measured change in optical thicknesses are essentially the same as with the coefficients for the bulk material once the films are annealed at 160°C . In the wavelength range $3-10\mu\text{m}$ the estimate of $\delta n/n$ is $3.3 \times 10^{-6}^{\circ}\text{C}^{-1}$ between room temperature and 160°C . For $\text{As}_{33}\text{S}_{67}$, the sum of the thermal coefficients of film expansion and refractive index change is $23.7 \times 10^{-6}^{\circ}\text{C}^{-1}$ for a similar temperature range. This figure can be accounted for by the expansion coefficient of the $\text{As}_{33}\text{S}_{67}$ alone, where dn/dT is negligible. In both cases annealing reduced the thermal coefficients of the as-deposited films to the values given. The $\text{Ag}_{21}\text{As}_{26}\text{S}_{53}$ layer had thermal coefficients ~ 2.5 times those given for the As-S layers for a similar wavelength and temperature range. These values are not reduced by annealing which effectively takes place during the prior thermal diffusion of Ag into the As-S layer. These low coefficients give the annealed As-S films good potential in athermalising optics.

ACKNOWLEDGEMENTS

This work has been supported by EPSRC.

REFERENCES

- [1] W. S. Rodney, I. H. Malitson and T. A. King, *J. Opt. Soc. Am.* 48(9) (1958) 633.
- [2] P.J.S. Ewen and A.E. Owen, Photo-induced changes in chalcogenide glasses and their applications, in *High Performance Glasses* edited by M Cable and J.M. Parker (Blackie & Sons, London, 1992).
- [3] As₂S₃ Material Data Sheet, Amorphous Materials Inc., 31030 Benton Street, Garland Texas 75402, USA.
- [4] P.J. Rogers, Current Developments in Optical Design and Engineering V, *Proc. SPIE* 2540 (1995) 13.
- [5] P. Conway, D. Pain, C. Slinger, P. Rogers, A. Zekak and P.J.S. Ewen, *Proc. SPIE* 3061 (1997) 396.
- [6] D. Goldschmidt and P.S. Rudman, *J. Non-Cryst. Solids* 22 (1976) 149.
- [7] A. Zekak, PhD Thesis, University of Edinburgh (1993).
- [8] T.I. Kosa, T. Wagner, P.J.S. Ewen and A.E. Owen, *Int. J. Electron. (UK)* 76(5) (1994) 845.
- [9] G. Dale, PhD Thesis, University of Edinburgh (1996).
- [10] S.S. Ballard and J.S. Browder, *App. Opt.* 5(12) (1966) 1873.
- [11] P.A. Young, *J. Phys. C: Solid St. Phys.* 4 (1971) 93.
- [12] M. Ohto, M. Itoh and K. Tanaka, *J. App. Phys.* 77 (1995) 1034.

ELECTRON PARAMAGNETIC RESONANCE, OPTICAL AND PHYSICAL PROPERTIES OF $R_2B_4O_7$ - PbO - CuO - TeO₂ (R = Li, Na or K) GLASSES

A.Murali and J.Lakshmana Rao

Department of Physics, Sri Venkateswara University, Tirupati - 517 502, A.P., INDIA.

ABSTRACT

Electron paramagnetic resonance, optical and physical properties of copper ions in $(85-x/2) R_2B_4O_7 - x PbO - y CuO - (15 - x/2 - y) TeO_2$ ($x = 0, 10$; $y = 0.1 - 1.5$; $R = Li, Na$ or K) glasses were studied. EPR spectra of all the glasses show resonance peaks characteristic of Cu^{2+} ions. The number of spins participating in the resonance were measured as a function of temperature and the activation energy was calculated. The optical absorption spectra of all the samples show a broad absorption band; the position of the band head varies from 14500 cm^{-1} to 12700 cm^{-1} for glasses with different alkali ions. By correlating the EPR and optical data, the molecular orbital coefficients were evaluated. The optical energy gap E_{opt} and Urbach energy ΔE were calculated for all the glass samples from their ultraviolet absorption edges. The optical energy gap varies between $3.4 - 2.7\text{ eV}$ and increases from Li to K glasses. Also it was observed that as copper ion concentration is increased E_{opt} decreases while ΔE increases. This was explained as due to change in non-bridging oxygen content.

1. INTRODUCTION

Tellurite glasses were considered to be important because of their optical and electrical properties, and as potential optical CD memory devices. The distinguishing factor about the matrix of this glass is that the tellurium atoms have unshared pairs of electrons which do not take part in bonding. On the other hand, their relatively low temperature of crystallization and melting makes these types of glass an active candidate for CD memory devices. Further these glasses are characterized by low glass transition temperature, high refractive index and high transmittance from ultraviolet to near-infrared. Yet the knowledge of the structure of tellurite glasses is limited [1].

It is known that TeO_2 in combination with modifiers, like PbO , form stable glasses at cooling rates typical of glass preparation ($< 1\text{ K/min.}$). Recently, the tellurite glasses drawn the attention of many investigators for their optical, electrical, Raman, structural, infrared, XPS and EPR & magnetic susceptibility properties [2-9].

Electron paramagnetic resonance (EPR) spectrum of transition metal ions in glasses is an interesting research subject [10] and affords a method to investigate glass structure. The ability to characterize the local structure of a paramagnetic centre and sensitive detection of structural changes form the basis for the increasing number of application of ESR technique to glasses [11].

The present study describes the Electron paramagnetic resonance, optical and physical properties of $R_2B_4O_7 - TeO_2 - PbO - CuO$ and $R_2B_4O_7 - TeO_2 - CuO$ glasses ($R = Li, Na$ or K).

2. EXPERIMENTAL TECHNIQUES

The glass samples were prepared by melt quenching method with the compositions given in Table 1. The densities of all glasses were measured at room temperatures using

Table 1
Composition of the Glasses studied in the present work

Glass	Li ₂ B ₄ O ₇	Na ₂ B ₄ O ₇	K ₂ B ₄ O ₇	TeO ₂	PbO	CuO	Melting Temperature (°C)
LPT1	80	---	---	9	10	1.0	943
NPT1	---	80	---	9	10	1.0	852
KPT1	---	---	80	9	10	1.0	852
LT1	85	---	---	14	---	1.0	943
NT1	---	85	---	14	---	1.0	852
KT1	---	---	85	14	---	1.0	852
NPT0.1	---	80	---	9.9	10	0.1	852
NPT0.5	---	80	---	9.5	10	0.5	852
NPT0.75	---	80	---	9.25	10	0.75	852
NPT1.5	---	80	---	8.5	10	1.5	852

Archimedes' principle with Toluene as the immersing liquid. The refractive indices of the glass samples were measured using an Abbe's refractometer at sodium yellow wavelength (5893 Å).

Electron paramagnetic resonance spectra were recorded at room temperature on an EPR spectrometer (JEOL-FE-1X) operating in the X-band frequencies with a modulation frequency of 100 kHz. EPR spectra of KPT1 glass sample was recorded at different temperatures (103 - 294 K) using a variable temperature controller (JES-UCI-2AX).

Optical absorption spectra of all the glass samples were recorded at room temperatures on an Hitachi U-3400 UV-VIS-NIR Spectrophotometer from 200 to 1300 nm

3. RESULTS AND ANALYSIS

3.1 ELECTRON PARAMAGNETIC RESONANCE STUDIES

No EPR signal is observed in the undoped glasses confirming that the starting materials used in the present work were free from transition metal impurities. All other glasses doped with copper ions show resonance peaks. Figure 1 shows the EPR spectrum of Cu²⁺ ions in

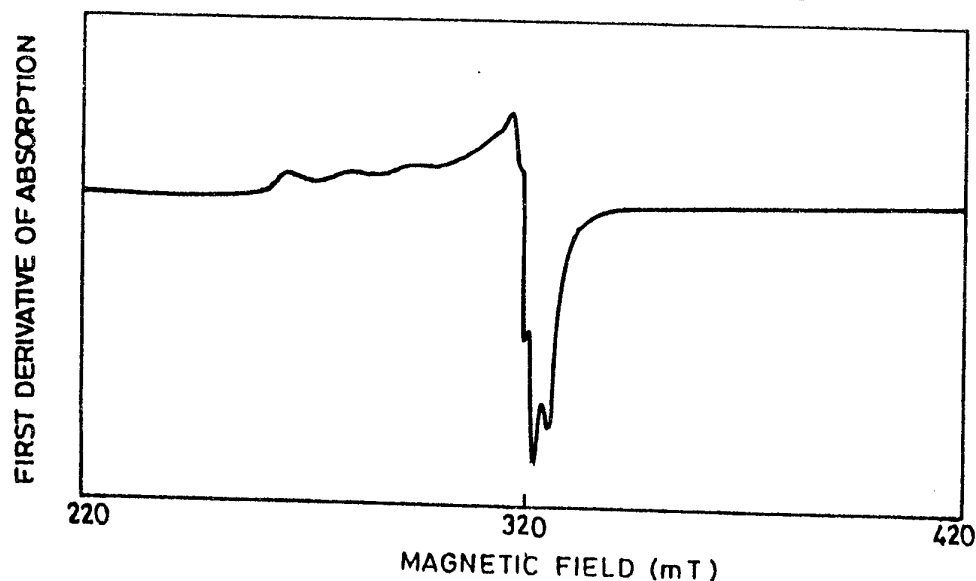


FIGURE 1
EPR Spectra of LPT1 glass at room temperature.

lithium lead borotellurite glasses at room temperature. The EPR spectra of all other samples are similar to Figure 1 and are similar to those reported earlier for Cu^{2+} ions in literature [12-16].

The number of spins can be calculated with the help of a reference ($\text{CuSO}_4 \cdot 5\text{H}_2\text{O}$) by using the formula [17]:

$$N = [\text{std}] \{A_x (\text{Scan}_x)^2 G_{\text{std}} (B_m)_{\text{std}} (g_{\text{std}})^2 [S(S+1)]_{\text{std}}\} / \{A_{\text{std}} (\text{Scan}_{\text{std}})^2 (B_m)_x (g_x)^2 [S(S+1)]_x\} \quad (1)$$

where A is the area under the absorption curve which can be obtained by double integrating the first derivative absorption curve; Scan is the magnetic field corresponding to the unit length of the chart; G is the gain; B_m is the modulation field width; g is the g factor; S is the spin of the system in its ground state. The subscript 'x' and 'std' represent the corresponding quantities for Cu^{2+} sample and the reference ($\text{CuSO}_4 \cdot 5\text{H}_2\text{O}$) respectively.

The number of Cu^{2+} ions in KPT1 glass sample were calculated at various temperatures from the EPR spectra of their sample recorded at different temperatures. Figure 2 shows a plot of $\log N$ vs. $1/T$ for this glass sample.

3.2 PHYSICAL PROPERTIES

The optical dielectric constant $p\delta\epsilon/\delta p$ can be calculated using the formula [18]:

$$(p\delta\epsilon/\delta p) = \epsilon - 1 = (n^2 - 1) \quad (2)$$

where n is the refractive index of the glass sample.

The polaron radius r_p can be calculated using the formula [19]:

$$r_p = (1/2) (\pi / 6N)^{1/3} \quad (3)$$

where N is the number of copper ions per unit volume and the inter ionic separation can be estimated using the relation [19]:

$$r_i = (1/N)^{1/3} \quad (4)$$

The electronic polarizability α_e can be evaluated using the formula [20]:

$$\alpha_e = (3/4\pi N) [(n^2 - 1) / (n^2 + 2)] \quad (5)$$

Table 2 lists the densities, molar volumes, refractive indices, number of Copper ions per unit volume, the optical dielectric constants, polaron radii, inter ionic distances and electronic polarizabilities calculated from the above relations for the glasses studied in the present work.

3.3 OPTICAL ABSORPTION SPECTRUM

Figure 3 shows the optical absorption spectrum of LPT1 glass sample at room

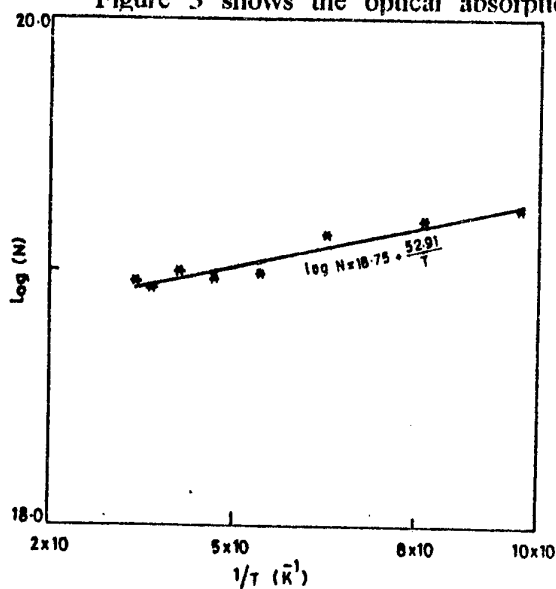


FIGURE 2

A plot of $\log N$ vs. $1/T$ for KPT1 glass sample.

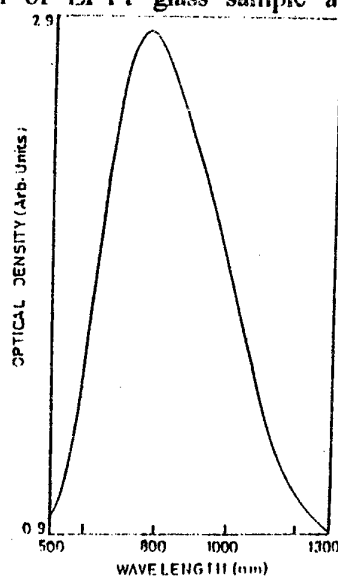


FIGURE 3

Optical absorption spectrum of LPT1 glass

temperature observed between 500 nm and 1300 nm. From the figure we can observe that there is only one broad absorption band centered at 766.3 nm (13045 cm^{-1}). This band has been assigned to $^2B_{1g} \rightarrow ^2B_{2g}$ transition of Cu^{2+} ions in a distorted octahedral site.

3.4 OPTICAL ENERGY GAP AND URBACH ENERGY

A main feature of the absorption edge of amorphous semiconductors is an exponential increase of the absorption coefficient $\alpha(\nu)$ with photon energy ($h\nu$) in accordance with an empirical relation [3]:

$$\alpha = \alpha_0 \exp(h\nu/E_0) \quad (6)$$

where α_0 is a constant, E_0 is the Urbach energy which indicates the width of the band tails of the localized states and ν is the frequency of radiation.

Optical absorption measurements were made as a function of photon energy at room temperature. The absorption coefficient $\alpha(\nu)$ can be determined near the edge using the formula:

$$\alpha(\nu) = [\ln(I_0/I)]/d \quad (7)$$

where d is the thickness of the glass sample, I_0 and I are the intensities of the incident and transmitted beams respectively. For absorption by indirect transitions, the equation takes the form:

$$\alpha(\nu) = A(h\nu - E_{\text{opt}})^2/h\nu \quad (8)$$

where A is a constant, E_{opt} is band gap and this relation applies to many oxide glasses [3]. Plots were drawn between $(\alpha h\nu)^{1/2}$ with $h\nu$. The values of E_{opt} is determined from these plots by extrapolating the linear parts of the curves to $(\alpha h\nu)^{1/2} = 0$. Figure 4 shows a plot of E_{opt} vs mol % of copper ions in sodium lead borotellurite glasses.

Plots were also drawn with $\ln \alpha$ vs $h\nu$. From these plots, the reciprocal of the slopes gives the Urbach energy. Figure 4 also shows a plot of Urbach energy as a function of copper ion concentration.

4. DISCUSSION

4.1 EPR STUDIES

For Cu^{2+} ions in a regular octahedral site may not exist, because the cubic symmetry is disturbed by electronic hole in the degenerate $d_{x^2-y^2}$ orbital and this produces the tetragonal

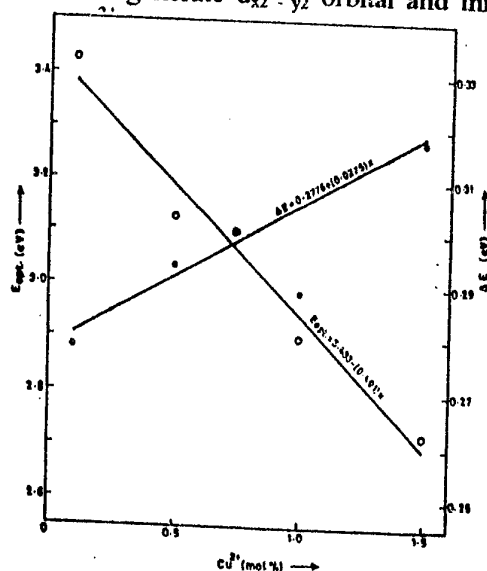


FIGURE 4

Variation of E_{opt} and ΔE with mol % of Cu in NPT glass samples.

distortion. The EPR spectra of Cu^{2+} ions in the present glasses can be analysed by using an axial spin-Hamiltonian of the form :

$$\mathcal{H} = \beta g_{\parallel} H_z S_z + \beta g_{\perp} (H_x S_x + H_y S_y) + A_{\parallel} S_z I_z + A_{\perp} (S_x I_x + S_y I_y) \quad (9)$$

The symbols in the above equation have their usual meanings; the nuclear quadrupole and nuclear Zeeman interaction terms are ignored.

The solution of the spin-Hamiltonian gives the expression for the peak position of the principal g and A tensors as [21]

$$h\nu = g_{\parallel} \beta H + m A_{\parallel} + (15/4 - m^2) [A_{\perp}^2 / (2 g_{\parallel} \beta H)] \quad 10(a)$$

$$h\nu = g_{\perp} \beta H + m A_{\perp} + (15/4 - m^2) [(A_{\parallel} + A_{\perp}^2 / (4 g_{\parallel} \beta H))] \quad 10(b)$$

for parallel and perpendicular hyperfine peaks respectively. Here m is the nuclear magnetic quantum number of the copper nucleus with values 3/2, 1/2, -1/2 and -3/2 and ν is the microwave frequency at resonance. Using equation 10(a) and 10(b), the spin-Hamiltonian parameters were evaluated for all glasses presented in Table 3. From Table 3, we observe that g_{\parallel} and g_{\perp} values are decreasing from Li to K glasses. This confirms that the copper ions are surrounded by alkali ions. There is no significant change in the spin-Hamiltonian parameters as the copper concentration is increased.

Figure 2 shows a plot of $\log N$ vs. $1/T$. From the graph the activation energy can be calculated. The activation energy thus calculated was found to be 7.305×10^{-22} J.

The number of copper ions [shown in table 2] calculated from density measurements will be the sum of copper ions in +2 oxidation state (N_2) and +1 oxidation state (N_1). Since EPR technique is sensitive for copper ions in +2 oxidation state, the number of spins obtained from EPR spectra refers to those in +2 oxidation state (N_2) only. From these two numbers it is possible to calculate the ratio of number of copper ions in +1 state to +2 state (i.e. N_1/N_2).

(4.2) OPTICAL ABSORPTION SPECTRUM

Table 3 lists the absorption bands observed for different glasses reported in the present work. Each of these bands was assigned to the transition ${}^2B_{1g} \rightarrow {}^2B_{2g}$ as given in Table 3. From the table, we can observe that the band positions fall at higher energies for glasses with lead content than that for glasses without lead content for each alkali ion. This indicates that the crystalfield around the central metal ion (Cu^{2+}) will have the influence of lead ions in glasses. Table 3 also lists the molecular orbital coefficients β_1^2 , α^2 , $\Gamma \Pi$ (%), $\Gamma \sigma$ (%) calculated from the formulas given in literature [22,23]. From the table, it was observed that the β^2 value decreases and α^2 value increases from Li to K (for glasses with and without lead content). This indicates that the in-plane σ bonding and the in - plane Π bonding are dependent on the type of alkali ion present in the glass. This supports the conclusion drawn from spin-Hamiltonian parameters.

Table 2
Physical parameters for the glasses studied in the present work

Glass Sample	Density (g cm^{-3})	Refractive Index	Number of Cu ions (10^{20} ions cm^{-3})	Optical Dielectric Constant	Polaran radius r_p (\AA)	Interionic distance r_i (\AA)	Electronic polarizability (10^{-22} cm^3)
LPT1	3.4777	1.481	1.2227	1.1934	8.120	20.148	5.5565
NPT1	3.2972	1.329	1.0081	0.7662	8.659	21.486	4.8180
KPT1	3.8287	1.489	1.0352	1.2171	8.583	21.297	6.6559
LT1	3.8722	1.441	1.4236	1.0765	7.718	19.152	4.4284
NT1	6.7405	1.332	2.1243	0.7742	6.754	16.760	2.3053
KT1	4.3507	1.477	1.1993	1.1815	8.172	20.278	5.6246

Table 3
Spin Hamiltonian parameters, optical band positions and molecular orbital coefficients
for the glasses studied in the present work

Glass Sample	g_{\parallel}	g_{\perp}	$A_{\parallel} (10^{-4}$ $\text{cm}^{-1})$	$A_{\perp} (10^{-4}$ $\text{cm}^{-1})$	${}^2B_{1g} \rightarrow {}^2B_{2g}$ (cm^{-1})	β_1^2	α^2	$\Gamma \Pi$ (%)	$\Gamma \sigma$ (%)
LPT1	2.323	2.067	128.7	22.1	13045	0.9086	0.6944	18.28	66.60
NPT1	2.293	2.056	136.4	23.0	14480	0.8804	0.7210	23.92	60.80
KPT1	2.291	2.051	129.9	26.3	12915	0.8598	0.6540	28.04	75.40
LT1	2.310	2.063	117.1	25.5	12870	0.9445	0.6323	11.10	80.13
NT1	2.303	2.060	122.4	23.8	12710	0.8892	0.6480	22.16	76.71
KT1	2.294	2.056	128.7	24.7	12910	0.8646	0.6567	27.08	74.81

(4.3) OPTICAL ENERGY GAP AND URBACH ENERGY

The values of optical energy gap observed in the present work for different glasses were listed in Table 4. The values obtained in the present case were of the same order for those of copper tellurium oxide glasses [3], PbO - TeO₂ glasses [6] and tellurium borate glasses [4] reported in literature.

Figure 4 shows a plot of optical energy gap (E_{opt}) and Urbach energy (ΔE) as a function of the copper ion content in the glass. From the figure we can observe that the energy gap increases with CuO content while Urbach energy decreases with increasing CuO content. Similar behaviour was observed by Hasan and Hogarth [3]. They have attributed this as a consequence of the increase in non-bridging oxygen ion content with increasing CuO content.

Table 4
Optical band gap energies and Urbach energies
for the glasses studied in the present work

Glass System	Optical Energy Gap (eV)	Urbach Energy ΔE (eV)
LPT1	2.875	0.3688
NPT1	2.900	0.2884
KPT1	3.320	0.2510
LT1	2.875	0.2783
NT1	3.000	0.2506
KT1	3.125	0.3033
NPT0.1	3.425	0.2780
NPT0.5	3.125	0.2934
NPT0.75	3.100	0.3001
NPT1.5	2.725	0.3175

5. CONCLUSIONS

- 1) From the EPR and optical absorption spectra of Cu²⁺ ions in alkali lead borotellurite glasses it was observed that the copper ions were occupied in octahedral site with tetragonal distortion and that they were surrounded by alkali ions and lead ions in the glasses studied.
- 2) The EPR spectra of copper ions at different temperatures show a linear dependence between $\log N$ and $1/T$. The activation energy was calculated and found to be 7.305×10^{-22} J.
- 3) The optical energy gap (E_{opt}) and the Urbach energies (ΔE) were found to be dependent upon the type of alkali ion and the presence of lead ions.

- 4) E_{opt} and ΔE were found to be changing with CuO content which was assigned to the increase in non-bridging oxygen content with increase in CuO.
- 5) By correlating EPR and optical data, it was observed that in-plane σ bonding decreases and in plane π bonding increases from Li to K (for glasses with and without lead content).

ACKNOWLEDGEMENTS

One of the authors (AM) is thankful to the Council of Scientific and Industrial Research (New Delhi) for the award of Senior Research Fellowship. The authors are thankful to Society of Glass Technology for providing the Financial Assistance to present the paper at the Symposium.

REFERENCES

- [1] H.Burger, K.Kneipp, H.Hobert, W.Vogel, V.Kozhukharov and S.Neov, *J.Non-Cryst. Solids*, 151 (1992) 134.
- [2] C.S.Sunandana and K.S.Rao, *Phys. Stat. Solidi (a)*, 90 (1985) 681.
- [3] M.A.Hassan and C.A.Hogarth, *J.Mater. Sci.*, 23 (1988) 2500.
- [4] A.I.Sobry and M.M.El-Samanoudy, *J.Mater. Sci.*, 30 (1995) 3930.
- [5] T.Komatsu, H.G.Kim and H.Mohri, *J.Mater. Sci. Lett.*, 15 (1996) 2026.
- [6] M.Vithal, P.Nachimuthum T.Banu and R.Jagannathan, *J.Appl. Phys.*, 81 (1997) 341.
- [7] I.Ardelean, M.Peteanu, S.Filip, V.Simon and G.Gyosffy, *Solid St. Commun.*, 102 (1996) 2026.
- [8] Z.D.Pan and S.H.Morgan, *J.Non-Cryst. Solids*, 210 (1997) 130.
- [9] Y.Himeji, Y.Miura, T.Nanda and A.Osaka, *J.Non-Cryst. Solids*, 211 (1997) 64.
- [10] D.L.Griscom, *Glass Sci. Technol.*, 4(B), (1990) 151.
- [11] R.Stober and M.Nofz, *Glasstech. Ber. Glass Sci. Technol.*, 67 (1994) 156.
- [12] H.Hosono, H.Kawazoe and T.Kanazawa, *J.Non-Cryst. Solids*, 29 (1978) 173.
- [13] A.K.Bandyopadhyay, *J.Mater. Sci.*, 15 (1980) 1605.
- [14] A.S.Rao, J.Lakshmana Rao and S.V.J.Lakshman, *J.Phys. Chem. Solids*, 53 (1992) 1221.
- [15] I.Ardelean, O.Coazar, S.Filip, V.Pop and I.Cenan, *Solid St. Commun.*, 100 (1996) 609.
- [16] R.P.Sreekanth Chakradhar, A.Murali and J.Lakshmana Rao, *J.Alloys Comp.*, 265 (1998) 29.
- [17] J.A.Weil, J.R.Bolton and J.E.Wertz, *Electron paramagnetic resonance - Elementary Theory and Practical Applications* (John Wiley & Sons, New York, 1994) p.498.
- [18] J.Schroeder, *J.Non-Cryst. Solids*, 40 (1980) 549.
- [19] M.M.Ahmed, C.A.Hogarth and M.N.Khan, *J.Mater. Sci. Lett.*, 19 (1984) 4040.
- [20] A.Klonkowski, *J.Non-Cryst. Solids*, 72 (1985) 117.
- [21] B.Bleaney, K.D.Bowers and M.H.L.Pryce, *Proc. Roy. Soc. A*, 228 (1955) 147.
- [22] H.A.Kuska, M.T.Rogers and R.E.Durlinger, *J.Phys. Chem.*, 71 (1967) 109.
- [23] D.Kivelson and R.Nieman, *J.Chem. Phys.*, 35 (1961) 145.

LONG LASTING PHOSPHORESCENCE IN Eu^{2+} -DOPED STRONTIUM ALUMINOSILICATE GLASSES

Jianrong Qiu^{a,*}, K. Tanaka^b, Y. Shimizugawa^c, K. Kojima^d, T. Mitsuyu^a and K. Hirao^{a, b}

^aHirao Active Glass Project, ERATO, Keihanna Plaza, Seika-cho, Kyoto 619-0237, Japan

^bDepartment of Material Chemistry, Graduate School of Engineering,
Kyoto University, Kyoto 606-8501, Japan

^cDepartment of Optical Materials, Osaka National Research Institute,
Osaka 563-0026, Japan

^dFaculty of Science and Engineering, Ritsumeikan University, Shiga 525-8577, Japan

ABSTRACT

We report on bright and long lasting phosphorescence in Eu^{2+} -doped glasses based on $\text{SrO-Al}_2\text{O}_3\text{-SiO}_2$. After irradiation by a white-color fluorescent lamp, a visible light (peaking at 510 nm) can be seen with the naked eye in the dark even 24 hours after the removal of the activating light. Thermal luminescence curve, X-ray absorption and ESR spectra have been measured. The long lasting phosphorescence in the Eu^{2+} -doped glasses is suggested to result from the recombination of electrons and holes at shallow traps in the glass matrix which can be thermally released at room temperature, and energy transfer between the recombination centers and Eu^{2+} ions.

*To whom correspondence should be addressed. E-mail: jrqr@hap.jst.go.jp

1. INTRODUCTION

Defects are usually a negative factor for the realization of functions in materials. However, in fiber gratings [1, 2] and photostimulated luminescence [3-5], defects artificially introduced by using external fields such as UV light and X-ray play important roles. In the formation of Bragg fiber gratings, the increase in refractive index of Ge-doped silica glasses after the irradiation by UV light is suggested to arise from the formation of various color centers e.g. GeE' and local densification of the glasses. Fiber gratings have been used as optical filter which can be directly connected to optical communication system. In the case of photostimulated luminescence, defect centers e.g. F centers act as electron trapping centers. The electron trapped by the F-center after the X-ray irradiation is released after the excitation by a visible or an infrared laser, and recombines with a trapped hole, leading to emitting a light whose intensity is proportional to the irradiated dose of X-ray. Photostimulable luminescence phosphors have been used as materials for 2-dimensional X-ray sensor.

In this paper, we report on a novel, defect-concerned phenomenon in Eu^{2+} -doped aluminosilicate glasses. After the irradiation by UV or visible lights with wavelengths shorter than 450nm, the glasses show bright and very long lasting phosphorescence. The mechanism of the long lasting phosphorescence has also been discussed.

2. EXPERIMENTAL

Compositions of the glass samples used in this study were $x\text{Al}_2\text{O}_3 \cdot 40\text{SrO} \cdot (60-x)\text{SiO}_2 \cdot 0.05\text{Eu}_2\text{O}_3 \cdot 0.05\text{Dy}_2\text{O}_3$ ($x=0, 10, 30$) ($x\text{ED}$) and $40\text{SrO} \cdot 30\text{Al}_2\text{O}_3 \cdot 30\text{SiO}_2 \cdot 0.05\text{Eu}_2\text{O}_3$ (30E) (mol%). Dy^{3+} ions were introduced into some of our samples and we

expected them to act as hole traps as they act in SrAl_2O_4 crystal doped with Eu^{2+} and Dy^{3+} [6]. Reagent-grade Al_2O_3 , SrCO_3 , SiO_2 , Eu_2O_3 and Dy_2O_3 were used as starting materials. Approximately 30 g batches were mixed and then melted in Pt crucibles at 1550°C for 60 min under an ambient atmosphere. The crucibles containing the melts were then taken out of the furnace, and cooled to room temperature. The obtained colorless and transparent glasses were then pulverized into pieces, put into glassy carbon crucibles and remelted under an $\text{Ar}+\text{H}_2$ (5 vol%) atmosphere at 1550°C for 60 min. The melts were then quenched to the room temperature. Transparent glasses in dark green color were obtained. The glass samples were cut, polished and subjected to the optical measurements. Absorption spectra of the samples were measured by a spectrophotometer (JASCO V-570). Normal fluorescence spectra of the samples were measured by a fluorescence spectrophotometer (Hitachi 850) using 394 nm UV light from a xenon lamp as the excitation source. For the phosphorescence spectrum and decay curve of phosphorescence measurements, glass samples were first irradiated by an UV lamp with a power of 300 W for 30 s. Thermoluminescence glow curves of the irradiated glass samples were measured with a thermoluminescence detector reader (made by Kasei Optonics Co Ltd., Japan) at a heating rate of 2°C/s . X-ray absorption spectra of the Eu^{2+} - Dy^{3+} co-doped 30ED sample irradiated by 6.981 keV X-ray for Eu ions and by 7.790 keV for Dy ions for various durations were measured at the photon factory of the National Laboratory for High Energy Physics, with an electron beam energy of 2.5 GeV and a maximum stored current of about 400 mA. The absorption spectra of Eu_2O_3 , EuF_2 , EuF_3 , EuS , Dy_2O_3 , DyF_3 and Dy_2S_3 crystals were also measured as references.

All measurements were carried out at room temperature except for the thermal luminescence curve.

3. RESULTS

Figure 1 shows the photoluminescence spectra of the glass samples. The excitation wavelength was 394 nm. An emission band at 510 nm due to the $5d-4f$ transition of Eu^{2+} was observed [7]. No emission peaks due to the 5D_i ($i=0,1$) \rightarrow 7F_j ($j=0\sim4$) transitions of Eu^{3+} were observed [7]. Therefore, most of the Eu ions are present as divalent state in the reduced samples.

Figure 2 shows the excitation spectra of the $x\text{Al}_2\text{O}_3 \cdot 40\text{SrO} \cdot (60-x)\text{SiO}_2 \cdot 0.05\text{Eu}_2\text{O}_3 \cdot 0.05\text{Dy}_2\text{O}_3$ ($x=0, 10, 30$) glass samples when the emission at 510 nm is monitored. All bands can be ascribed to the transitions of Eu^{2+} ions. The intensity of the band at 425 nm decreases with increasing Al_2O_3 concentration.

After irradiation by a white-color fluorescent lamp with a power density of 2×10^4 lx for 30 min, no phosphorescence was observed in the samples fabricated under the ambient atmosphere, while glass samples remelted under the reducing atmosphere showed a bright and long lasting phosphorescence. The phosphorescence in 30ED sample can still be seen with the naked eye in the dark even 24 hours after the removal of the exciting lamp. The emission spectra of the phosphorescence have similar appearances to the photoluminescence spectra excited by 394 nm light. Figure 3 shows the decay curves of the phosphorescence at 510 nm in glass samples after the irradiation by an UV lamp with a power of 300 W for 30 s. The emission decays quickly at first and then the intensity decreases slowly. The decay curves of

30ED and 30E samples overlap with each other. Figure 4 shows the thermal luminescence curves of the glass samples irradiated by the UV lamp for 30 s. There is a broad band with the maximum at about 50°C, ranging from room temperature to 230°C.

Figure 5 (a) and (b) show the X-ray absorption spectra due to the absorption of Eu and Dy ions of 30ED sample doped with Eu^{2+} and Dy^{3+} X-ray irradiated for various durations. The X-ray absorption spectra of Eu^{2+} , Eu^{3+} and Dy^{3+} doped crystals are also shown in Figure 5(a) and (b) for comparison. The bands at 6.973 keV and 6.981 keV are assigned to the absorption due to the Eu^{2+} and Eu^{3+} , respectively. A new band should appear in the wavelength regions shorter than 6.973 keV if Eu^+ ($\text{Eu}^{2+} + \text{electron}$) is formed after the X-ray irradiation. However, little difference can be found between the absorption spectra of 30ED before and after the X-ray irradiation.

Figure 6 shows the ESR spectra of 10ED sample. a is the spectrum of the sample after the irradiation by the UV lamp for 5 min, b is the spectrum of the sample 5 min after the measurement of a, c is the spectrum of b was further heat-treated at 80°C for 2 min and d is the spectrum after c was further irradiated by the UV lamp for 2 min. The signals ranging from 500 to 2600 Gauss are ascribed to Eu^{2+} ions and the sharp signal at about 3400 Gauss ($g \approx 2.0$) is attributed to the defect centers [8].

4. DISCUSSION

The long lasting phosphorescence is suggested to be due to the thermostimulated recombination of electrons and holes at traps which leave electrons or holes in a metastable state at room temperature [9]. Usually, incorporation of rare earth ions such as Eu^{2+} , Sm^{3+} , Dy^{3+} into phosphors can largely change the phosphorescence properties of the phosphors, therefore, such rare earth ions are proposed to act as electron or hole trapping centers [10]. The mechanism of the long lasting phosphorescence in Eu^{2+} - Dy^{3+} doped strontium aluminate phosphor has been investigated by Matsuzawa et al [6]. Based on the photoconductivity measurements, Matsuzawa et al. proposed that Dy^{3+} ion acts as hole traps ($\text{Dy}^{3+} + \text{hole} \rightarrow \text{Dy}^{4+}$) and Eu^{2+} acts as electron traps ($\text{Eu}^{2+} + \text{hole} \rightarrow \text{Eu}^+$). Introduction of Dy^{3+} into the Eu^{2+} -doped strontium aluminate results in the creation of a highly dense trapping level which locates at a suitable depth so that the trapped hole is thermally released with a proper rate at room temperature. Thus bright and long lasting phosphorescence takes place.

However, no evidence has been obtained for the conversion of Eu^{2+} to Eu^+ and Dy^{3+} to Dy^{4+} up to now. From Fig. 5(a) and (b), little difference can be observed between the absorption spectra of Eu and Dy ions in 30ED sample doped with Eu^{2+} and Dy^{3+} before and after X-ray irradiation, though long lasting phosphorescence was observed after the X-ray irradiation. In addition, the photoluminescence spectrum, decay curve of phosphorescence and thermal luminescence curve in 30ED sample were observed to be nearly the same as those in 30E sample. Moreover, little difference can be observed in the signals due to Eu^{2+} ions from ESR spectra of the glass sample (10ED) before and after the irradiation of UV light. Therefore, we suggest that Eu^{2+} and Dy^{3+} ions do not directly act as hole and electron traps.

ESR spectra in Fig. 6 show that color centers have been formed after the UV irradiation.

(1997) 266.

[8] H. Hosono, N. Asada and Y. Abe, J. Appl. Phys. 67 (1990) 2840.

[9] E. Nakazawa, Handbook of Phosphors, edited by Keikoutai Dougakukai (Ohm Press, Tokyo, 1987), p. 65.

[10] A. Yamamoto, Handbook of Phosphors, edited by Keikoutai Dougakukai (Ohm Press, Tokyo, 1987), p. 138.

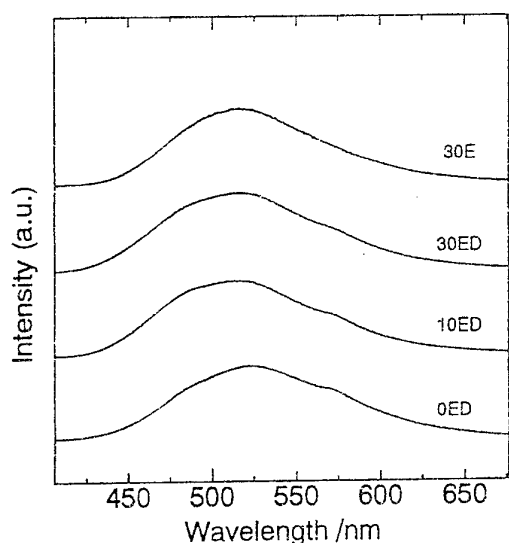


Fig. 1. Photoluminescence spectra of glass samples. The excitation wavelength is 394 nm.

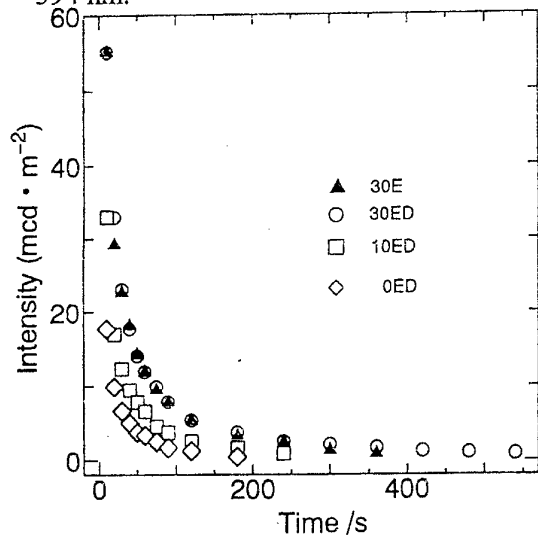


Fig. 3. Decay curves of the long lasting phosphorescence at 510 nm in glass samples after irradiation by the UV lamp for 30 s.

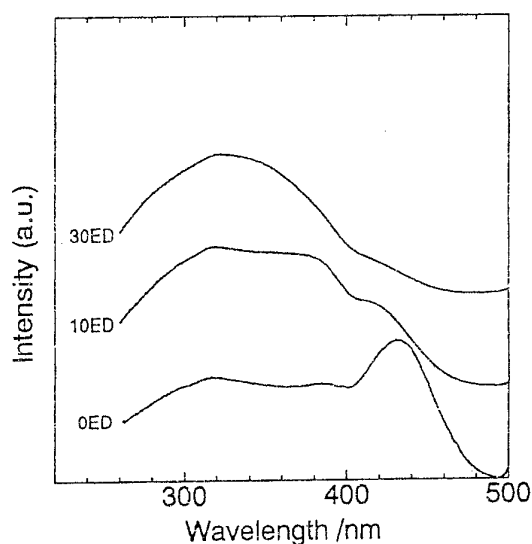


Fig. 2. Excitation spectra of glass samples. The emission at 510 nm is monitored.

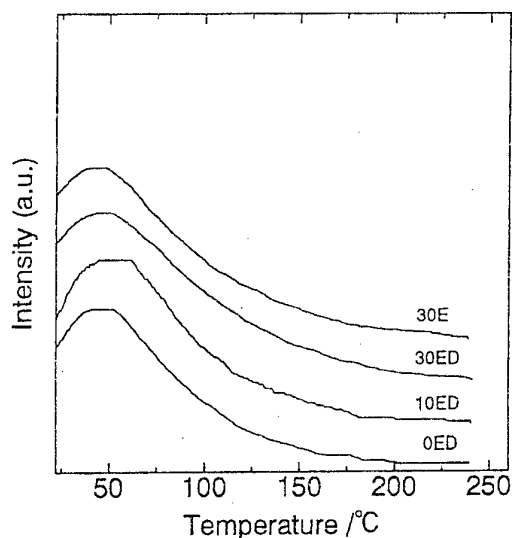


Fig. 4. Thermal luminescence glow curves of the glass samples after irradiation by the UV lamp for 30 s.

After removal of the activating UV light, the intensity of the signal due to the color centers decreases with time, which agrees well with the decay of phosphorescence. The partially enlarged ESR spectrum at about $g=2.0$ showed that the signal is a combined results of electron ($g<2.00$) and hole ($g>2.00$) trapping centers. Hosono et al found that calcium aluminate glasses without any rare earth ions melted under a reducing atmosphere show photochromism [8]. Upon exposure to ultraviolet radiation, broad absorption with an apparent peak of around 2 eV and a shoulder around 3.5 eV were induced, and after interrupt of the light illumination, both bands faded at room temperature. The photochromism is suggested to originate from an electron trapped at the site of oxygen vacancy surrounded by Ca^{2+} ions. The oxygen vacancy in the glasses was formed due to the strong reduction in the reducing atmosphere. We suggest that such oxygen vacancies surrounded by Sr^{2+} ions also exist in the glass samples fabricated under the reducing atmosphere and may act as electron trapping centers, since the physicochemical behaviors of Ca^{2+} and Sr^{2+} are very similar. After irradiation by the white-color fluorescent lamp, electrons and holes are formed in the samples. Part of the electrons are trapped by oxygen defects and part of the holes are captured by other defects in the glass matrix. Since the electron trap depth is broadly distributed and shallow, the electrons can be thermally released at room temperature, recombine with the trapped holes. The released energy due to the recombination of electron and hole is transferred to the Eu^{2+} ions, and long lasting phosphorescence is brought about. The question what the concrete hole trapping center is still remains. Further study is in progress.

5. CONCLUSIONS

In conclusion, the bright and very long lasting phosphorescence in Eu^{2+} -doped glasses based on $\text{SrO-Al}_2\text{O}_3\text{-SiO}_2$ was observed. Based on the thermal luminescence, X-ray absorption and ESR spectra, the long lasting phosphorescence in the Eu^{2+} -doped glasses is suggested to result from the recombination of electrons and holes at shallow traps in the glass matrix which can be thermally released at room temperature. These glasses can absorb lights in UV and visible regions with shorter wavelength region to emit light at 510 nm, which fits well with the wavelength region corresponding to a larger conversion efficiency of the conventional amorphous silicon solar cells. They may be promising materials for energy-saving display and useful for the enhancement of the conversion efficiency of solar cells.

REFERENCES

- [1] K. O. Hill, Y. Fujii, D. C. Johnson and B. S. Kawasaki, Appl. Phys. Lett. 32 (1978) 647.
- [2] H. Hosono, Y. Abe, D. L. Kinser, R. A. Weeks, K. Muta and H. Kawazoe, Phys. Rev. B46 (1992) 11445.
- [3] Y. Amemiya, K. Wakabayashi, H. Tanaka, Y. Ueno and J. Miyahara, Science 237 (1987) 164.
- [4] J. Qiu, Y. Shimizugawa, Y. Iwabuchi and K. Hirao, Appl. Phys. Lett. 71 (1997) 43.
- [5] J. Qiu, Y. Shimizugawa, Y. Iwabuchi and K. Hirao, Appl. Phys. Lett. 71 (1997) 759.
- [6] T. Matsuzawa, Y. Aoki, N. Takeuchi and Y. Murayama, J. Electrochem. Soc. 143 (1996) 2670.
- [7] J. Qiu, Y. Shimizugawa, N. Sugimoto and K. Hirao, J. Non-Cryst. Solids 213&214

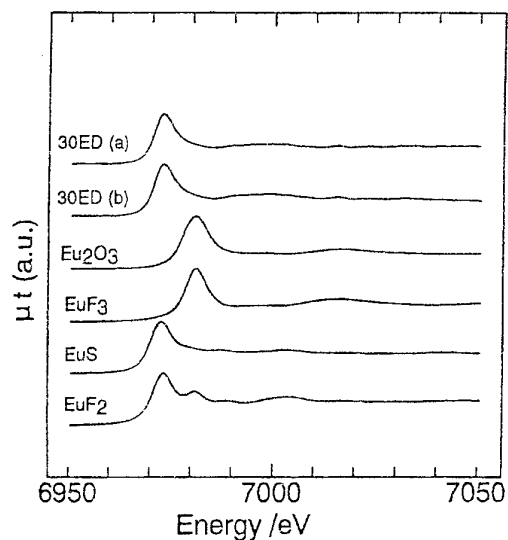


Fig. 5(a) X-ray absorption spectra of Eu ions in 30ED sample X-ray irradiated for various durations. The wavelength of the irradiated X-ray is 6.981 keV.

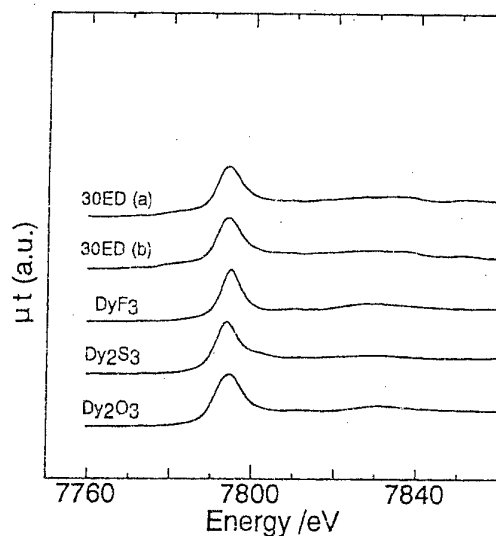


Fig. 5(b) X-ray absorption spectra of Dy ions in 30ED sample X-ray irradiated for various durations. The wavelength of the irradiated X-ray is 7.790 keV.

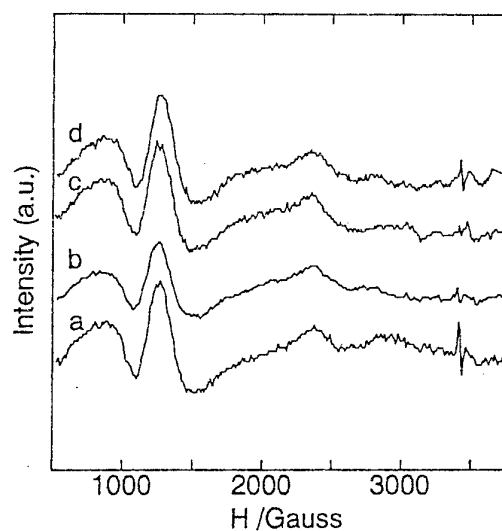


Fig. 6 ESR spectra of the 10ED glass sample. a: after the irradiation by the UV lamp for 5 min. b: 5 min after the measurement of a. c: b was further heat-treated at 80°C for 2 min. d: c was further irradiated by the UV lamp for 2 min.

PHOTO-INDUCED ABSORPTIVE CHANGES IN GERMANIUM SELENIDE GLASSES

Craig Schardt and Joseph H. Simmons

University of Florida, P.O. Box 116400

Gainesville, FL 32611, USA, e-mail: simmons@silica.mse.ufl.edu

Pierre Lucas

Arizona State University

Tempe, AZ 85287, USA

Lydia Le-Neindre and Jacques Lucas

University of Rennes I

Laboratoire des Verres et Ceramiques

Campus de Beaulieu, 35042 Rennes, France

ABSTRACT

Photo-induced increases in absorption near the band-gap edge have been investigated in a series of germanium selenide glasses using 150 fs pulses from a Ti-sapphire laser at 800 nm. The observed changes appear as a red shift in the band-gap absorption edge. Illumination using polarized light shows the formation of both isotropic and anisotropic components, with the latter aligned in the direction of polarization. An associated index change is observed and acts to form a radial gradient index due to the Gaussian cross-sectional intensity profile of the laser pulse. Reversibility and dependence of the effect on germanium concentration are investigated.

INTRODUCTION

Photo-induced changes in the optical properties of chalcogenide glasses have been observed both with unpolarized [1] and polarized [2] light. These changes are associated with a photodarkening process [3] which appears as a red-shift in the absorption edge of the glass. Studies in arsenic chalcogenide glasses have demonstrated that the photodarkening is reversible and results from structural changes in the glass [3]. While measurements indicate that the structural changes correspond to modifications of the short and medium range order of the glass, the nature of the structural change, however, is still not fully understood. The photodarkening is only one of several changes in physical and chemical properties that result from band-gap light exposure, including density [4], viscosity [5], chemical durability [6], electronic transport properties [7] and crystallization [8].

This work examines the behavior of a series of $\text{Ge}_x\text{Se}_{1-x}$ glasses (with x varied between 0.10 and 0.25). These glasses have structures that span a broad range of different geometries, including the $\text{Ge}_3\text{Se}_{17}$ and the GeSe_4 compositions that represent the maximum connectivity [9] and the rigidity percolation [10] compositions. The goal of this research is to separate the photo-induced absorption and refractive index changes, and to relate them to structural

changes through IR absorption, photoluminescence and Raman scattering measurements.

SAMPLE PREPARATION

Raw materials of Se and Ge were purified before melting into glasses. Selenium was heated at 250°C to eliminate oxide impurities. The purified compounds were sealed in a dehydrated silica ampoule under vacuum. The ampoule was then heated in a rocking furnace at 600°C for several hours [11]. The ampoule was cooled vertically to form a 1 cm diameter rod from which disks 1-2 mm thick were cut. The samples were then polished on both faces. Sample compositions tested were GeSe_9 , $\text{Ge}_3\text{Se}_{17}$, GeSe_4 and GeSe_3 .

OPTICAL MEASUREMENTS

The optical set up consisted of pump and probe optical paths passing through the sample in the same 4 mm² spot. The low intensity probe beam is monochromatic and wavelength selected by a grating in a UV-visible spectrometer. The high intensity pump beam is generated by a titanium-sapphire laser operating at 76 kHz, producing 150 fs pulses. The pump beam power was varied up to 1.5 Watts, corresponding to 20 $\mu\text{J}/\text{pulse}$ and an average power of 130 MW/pulse. Most of the experiments were conducted at a power of 1 W and exposures were varied by changing the total fluence.

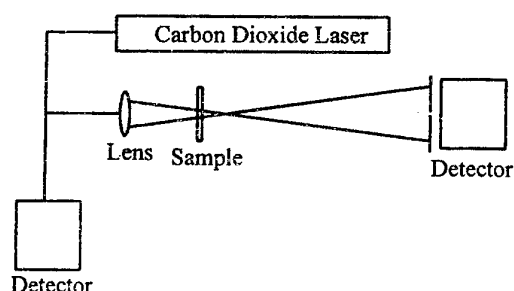


Figure 1 - Sketch of z-scan apparatus. The sample is scanned along the beam axis and its position spans across the focal point of the lens. Both carbon dioxide and titanium-sapphire lasers have been used.

A second set of measurements was conducted using the method of open aperture z-scan. The test set up was designed following the z-scan method of Sheik-Bahae and co-workers [12]. A diagram of the apparatus is shown in Fig. 1. The laser beam is divided into two equal beams, one for reference and the other for the measurement. The light from the second beam is focused by a lens and passes through the sample on its way to an aperture and a detector. In the normal z-scan test, as the sample is positioned along the path of the beam, first before the focal point, then past the focal point, the refractive index of the sample will deflect

and move the actual focal point, thus increasing or decreasing the intensity of the light at the detector. If the sample has a negative NLO coefficient, it will move the focal point closer to the aperture when located before the focal point and thus increase the intensity. If the sample has a positive NLO coefficient, the opposite case occurs. The z-scan tests conducted used both a carbon dioxide laser (as shown in the figure) and the pulsed titanium-sapphire laser. In an open-aperture test, the aperture ahead of the detector is removed. Using the latter method, absorptive changes may be distinguished from changes in refractive index. If the sample undergoes changes in refractive index without absorption, then no change in intensity is seen at the detector as the sample is scanned through focus. In the case of absorptive changes,

there will be an increased loss as the sample is scanned through focus.

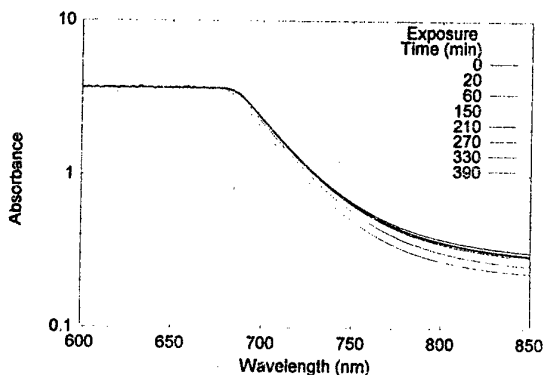


Figure 2 - Band-gap absorption edge for different times of pump-beam exposures to near-band-gap light.

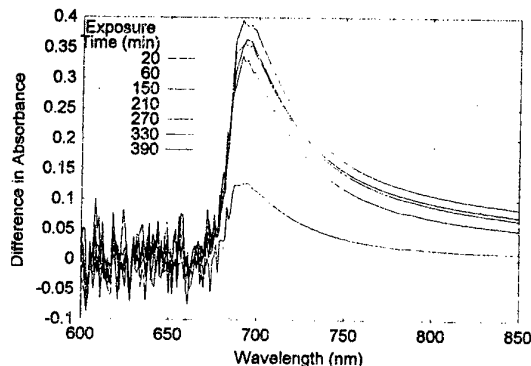


Figure 3 - Difference in absorbance from an unexposed sample near the band edge of the glass for the same exposure times of Fig. 2.

RESULTS

Plots of the measured absorption edge for the $\text{Ge}_{20}\text{Se}_{80}$ glass as a function of wavelength for different fluence levels are given in Fig. 2. As the fluence is increased, the sample absorbance near the band-gap increases. This is more evident in plots of the difference in absorbance for the same fluence values as shown in Fig. 3. The difference in absorbance is calculated from the unexposed absorption edge. The largest difference appears at the band edge.

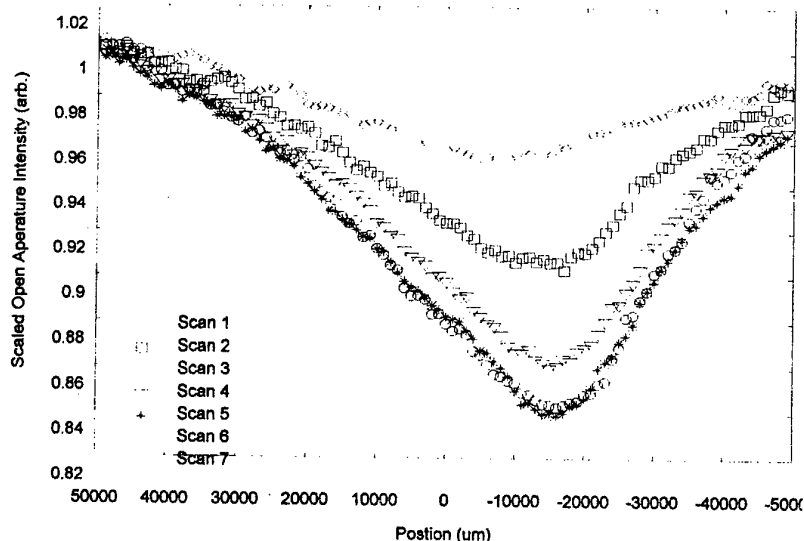


Figure 4 - Open-aperture intensity measurement showing the increase in loss with exposure to near-band-gap light.

band-gap light. Measurements with the carbon dioxide laser at much higher powers showed no permanent damage.

Figure 4 shows the variation in transmitted intensity in an open-aperture z-scan measurement. The successive scans show a more pronounced decrease in intensity through focus. This clearly indicates that the absorptive processes dominate the response of this material to light. This effect was evident only under exposure to near-

DISCUSSION

The photo-induced changes caused by near band-gap light in chalcogenide glasses involve both an increase in absorption and a change in refractive index. These are related to each other through Kramers-Kronig relations [13]. The studies presented here have mostly concentrated on absorptive changes. For example, the pump-probe set up and the open-aperture z-scan tests only examine the absorptive changes. We have observed the effects of index changes in examinations of the transmitted beam through the formation of refractive interference rings or Fabry-Perot fringes about the beam's central axis and through closed aperture z-scan tests which show the intensity dependence of the refractive index of the exposed material.

However, in the analysis of the underlying processes, it is useful to determine the fundamental causative process in order to identify the microscopic mechanism, whether it is the formation of color centers or regional changes in the polarizability of the material. Our studies indicate that the change in absorption dominates. It appears to result from the formation of sub-band-gap defect states possibly through the formation of a donor-acceptor band that may result from valence-alternation pairs [14]. Ongoing studies of the photoluminescence behavior of these material may help elucidate the nature of the donor and acceptor states involved.

REFERENCES

- [1] V. K. Tikhomirov and S. R. Elliott, Phys. Rev. B49 (1994) 17476.
- [2] H. Fritzsche, Phys. Rev. B52 (1995) 15854.
- [3] G. Pfeiffer, M. A. Paesler and S. C. Agarwal, J. Non-Crystalline Solids 130 (1991) 111.
- [4] K. Tanaka, J. Non-Crystalline Solids 35 & 36 (1980) 1023.
- [5] J. S. Berkes, Ss. W. Ing and W. J. Hillegas, J. Appl. Phys. 42 (1971) 4908.
- [6] S. R. Elliott, J. Non-Crystalline Solids 81 (1986) 71.
- [7] K. Shimakawa and S. R. Elliott, Phys. Rev. B38 (1988) 122479.
- [8] S. A. Keneman, J. Bordogna and J. N. Zemel, J. Appl. Phys. 49 (1978) 4663.
- [9] S. R. Elliott, Physics of Amorphous Materials, Longman (London, 1983) 49.
- [10] M. Tatsumisago, Bb. L. Halfpap, J. L. Green, S. M. Lindsay and C. A. Angell, Phy. Rev. Lett. 13 (1990) 1549.
- [11] L. Le Neindre, PhD dissertation, University of Rennes, 1997.
- [12] M. Sheik-Bahae, A. A. Said, T. H. Wei, D. J. Hagan and E. W. Van Stryland, IEEE J. Quant. Electronics 26, 760 (1990).
- [13] A. Yariv, Optical Electronics in Modern Communications, Oxford University Press (Oxford, 1997) 723.
- [14] V. K. Tikhomirov and S. R. Elliott, Phys. Rev. B51 (1995) 5538.

Linear and Nonlinear Optical Characterization of As-S-Se glasses

T. Cardinal, K. Richardson, H. Shim, S. Park G. Stegeman, R. Beatty and A. Villeneuve*
 CREOL, University of Central Florida
 4000 Central Florida Blvd.
 Orlando FL 32826
 Email: kcr@creol.ucf.edu

*Laval Universite,
 Centre d'Optique, Photonique et Laser
 Cite Universitaire, Pavillon A.-Vachon
 Quebec, Canada G1K 7P4

Abstract

We report results of a systematic study examining the relationship of bond type and concentration to the linear and nonlinear optical properties of As-S-Se glasses. The effects of iso-structural substitution of Se for S, and intrinsic and extrinsic impurity level as characterized by linear and nonlinear absorption processes, are discussed. Nonlinear optical properties of chalcogenide glasses in the system As-S-Se measured at 1.6 μm was reported. The nonlinearities measured reach 400x the value for pure silica. The enhancement of the kerr effect for small As/(S+Se) molar ratio is interpreted to be due to the formation of S-Se bonds. The applicability of these materials in planar waveguides is reported.

Optical glasses exhibiting large nonresonant nonlinearity are good candidates for optical switching devices. Glasses have the advantage in comparison with semiconductors, polymers to have a fast response time, a low linear and multi photon absorption in the range of wavelength of interest. In comparison with crystals they are low cost materials and more easily compatible to fiber or thin film processing.

Chalcogenide are very promising materials. They have been studied first for IR transmission due to their low phonon energy at these wavelengths. The interest reported on chalcogenide for optical devices is recent (1). Recent studies have reported the possibility to use these materials as optical memories, grating and switching devices. As_2S_3 glasses have been demonstrated to have a third order nonlinear susceptibility 80 times higher than pure silica (1). Their ability to be integrated in devices has been demonstrated. Nevertheless the nonlinear optical properties have yet to be completely understood.

This paper reports results of a study performed on chalcogenide glasses in the ternary system As-S-Se suitable for optical devices. The interest of such glasses has been previously discussed (2). In this paper a systematic study of the linear and nonlinear optical properties of these glasses and a correlation between the molecular and the optical properties is discussed. Local structural investigations have been carried out on such glasses (3) but the influence of the different molecular entities on the linear and the nonlinear optical properties of these glasses is not well understood. The glass compositions examined in this study are shown in the ternary diagram in Figure 1.

Two variations of composition within the ternary have been studied. First, compositions along the line $x \text{As}_2\text{S}_3 - (1-x) \text{As}_2\text{Se}_3$ have been investigated in order to keep the molar ratio $\text{As}/(\text{S} + \text{Se}) = 2/3$ constant and carry out an iso-structural replacement of sulfur by selenium. Secondly the compositions corresponding to the molar ratio $\text{Se}/\text{S}=1$ while decreasing the molar ratio $\text{As}/(\text{S} + \text{Se})$ have been examined. Shown in Table 1 are the measured glass transition temperature and density for these samples.

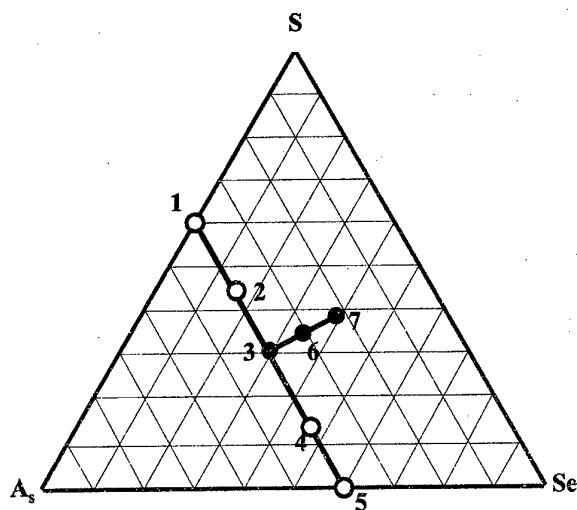


Figure 1 : Ternary diagram As-S-Se of studied glass compositions
 1 $\text{As}_{40}\text{S}_{60}$; 2 $\text{As}_{40}\text{S}_{45}\text{Se}_{15}$; 3 $\text{As}_{40}\text{S}_{30}\text{Se}_{30}$; 4 $\text{As}_{40}\text{S}_{15}\text{Se}_{45}$; 5 $\text{As}_{40}\text{Se}_{60}$;
 6 $\text{As}_{32}\text{S}_{34}\text{Se}_{34}$; 7 $\text{As}_{24}\text{S}_{38}\text{Se}_{38}$

Glass number	Glass composition	Density (g/cm^3) (± 0.01)	Glass transition temperature T_g (± 2 °C)
1	As_2S_3	3.20	215
2	$\text{As}_{40}\text{S}_{15}\text{Se}_{45}$	3.56	207
3	$\text{As}_{40}\text{S}_{30}\text{Se}_{30}$	3.92	202
4	$\text{As}_{40}\text{S}_{45}\text{Se}_{15}$	4.27	196
5	$\text{As}_{40}\text{Se}_{60}$	4.59	191
6	$\text{As}_{32}\text{S}_{34}\text{Se}_{34}$	3.74	154
7	$\text{As}_{24}\text{S}_{38}\text{Se}_{38}$	3.63	135

Table 1 : Glass composition, density and glass transition temperature

Samples of chalcogenide (ChG) glasses were prepared from a batch of 15g of high purity metals, arsenic, sulfur and selenium (Cerac, 99.999 %). The batch was transferred and sealed under vacuum in quartz ampoules. The ampoule was transferred to a rocking furnace and heated up to a temperature between 700°C and 900°C, to obtain a good fluidity, for 24 hrs. To insure good homogeneity of the melt, the ampoule was rocked for two hours. The glass was then quenched by removing the ampoule from the furnace to air, and annealed at 30°C degrees below the glass transition temperature under vacuum for 1 hour. Glass samples were then cut and optically polished. Upon addition of the selenium to the glass, a change in glass color is observed from red to dark. As this glass exhibits a very good stability, the melt could be kept in the furnace during the cooling of the furnace without showing any signs of crystallization, but the quench was necessary to avoid the breakage of the tube and the glass rod during cooling.

Numerous physical and optical properties of the melted glass samples were measured. The density of the different vitreous compositions has been measured using the Archimedes method in diethyl Phtalate. The accuracy was better than $\pm 0.3\%$. The glass transition temperature was investigated using a Differential Thermal Analysis, DTA (TA Instrument SDT 2960) following a ramp of 10 °C/min. The glass transition temperature is taken at the inflection point of the endotherm with an accuracy of ± 2 °C.

Linear optical absorption spectra were recorded on a Perkin-Elmer spectrophotometer 330. The nonlinear optical properties were measured by using a standard Z-Scan set up as described by Sheik- Bahae and co-workers (4). The laser system was a Spectra-Physics optical parametric amplifier combination with a Ti:sapphire source and a generative amplifier. The measurements were done at 1.6 μm with 100 fs pulses and microjoule pulse energies. The spectral width and the temporal envelope were monitored during the experiments. The measurements were carried out for intensities around $20\text{GW}/\text{cm}^2$.

Table 1 summarizes the measured glass densities. In the system $x\text{As}_2\text{S}_3 - (1-x)\text{As}_2\text{Se}_3$ the density increase linearly from the density of the glass As_2S_3 ($3.2\text{ g}/\text{cm}^3$) to the density of the glass As_2Se_3 ($4.59\text{ g}/\text{cm}^3$) as indicated on Figure 2. This linear evolution shows a replacement of the sulfur by the selenium without a strong structural change. This observation is in agreement with prior Raman studies on glasses of this system which pointed out that the selenium substitute the sulfur in the pyramidal site AsZ_3 ($Z=\text{S}$ or Se) without structural change or site segregation. (3, 5). On the contrary as shown on figure 4, the decrease of the density of the glass when the ratio $\text{As}/(\text{S}+\text{Se})$ decrease versus the molar percentage of arsenic is also linear with the molar percentage of arsenic.

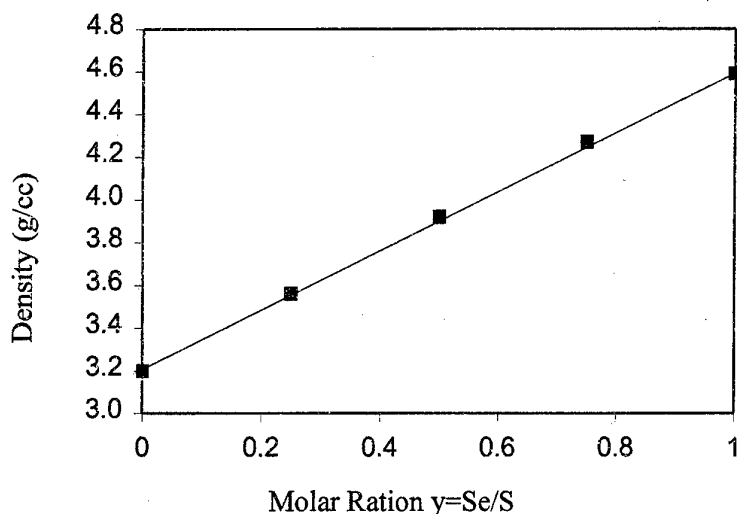


Figure 3 Density of glasses in the system $x\text{As}_2\text{S}_3 - (1-x)\text{As}_2\text{Se}_3$ versus the molar ratio,

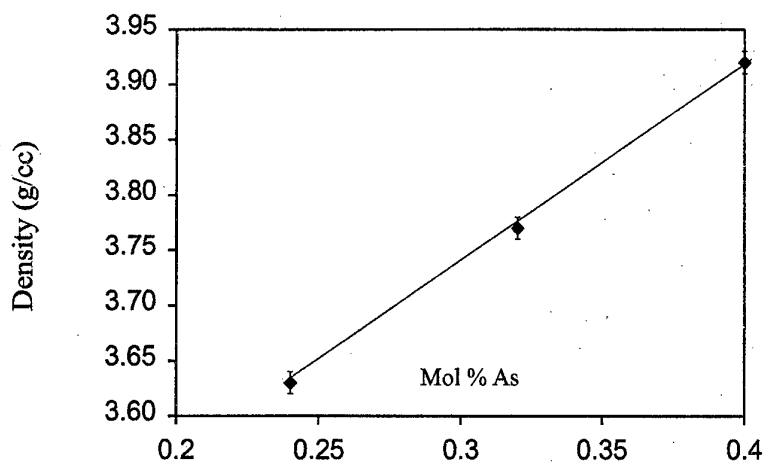


Figure 4 : Density of glasses for modification of the ratio $\text{As}/(\text{S}+\text{Se})$ versus the molar percentage of Arsenic introduced

The glass transition temperatures taken at the inflection point are also reported in the table 1. For the glass system $x \text{As}_2\text{S}_3 - (1-x) \text{As}_2\text{Se}_3$ the transition glass temperature decrease as the selenium content increase from 215°C (As_2S_3) to 191°C (As_2Se_3). When the ratio $\text{As}/(\text{S}+\text{Se})$ decrease the glass transition temperature T_g decrease dramatically. The T_g drop from 202 °C for the glass $\text{As}_{40}\text{S}_{30}\text{Se}_{30}$ to 135°C for the glass $\text{As}_{24}\text{S}_{38}\text{Se}_{38}$.

The linear absorption spectra of glasses are reported on the figures 5 and 6. As soon as the sulfur is substituted by the selenium in the glass system $x \text{As}_2\text{S}_3 - (1-x) \text{As}_2\text{Se}_3$, the optical bandgap shifts progressively to the near infra-red as shown in Figure 5. The decrease of the molar ratio $\text{As}/(\text{S}+\text{Se})$ doesn't significantly affect the linear absorption, as can be seen in Figure 6 where the tail of the band edge remains in the same wavelength range for the three glasses 3, 6, 7. Results on nonlinear absorption and index will be presented.

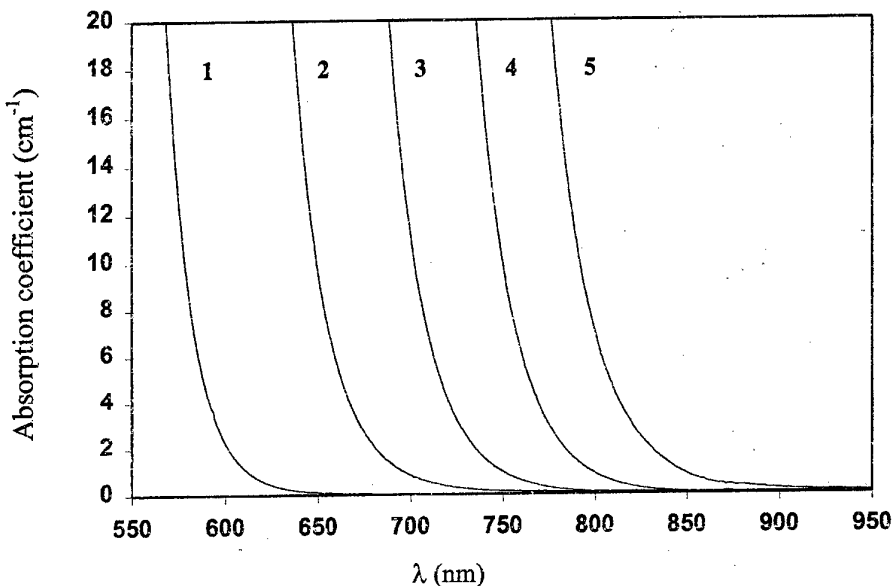


Figure 5 : Absorption spectra of glasses 1, 2, 3, 4, 5

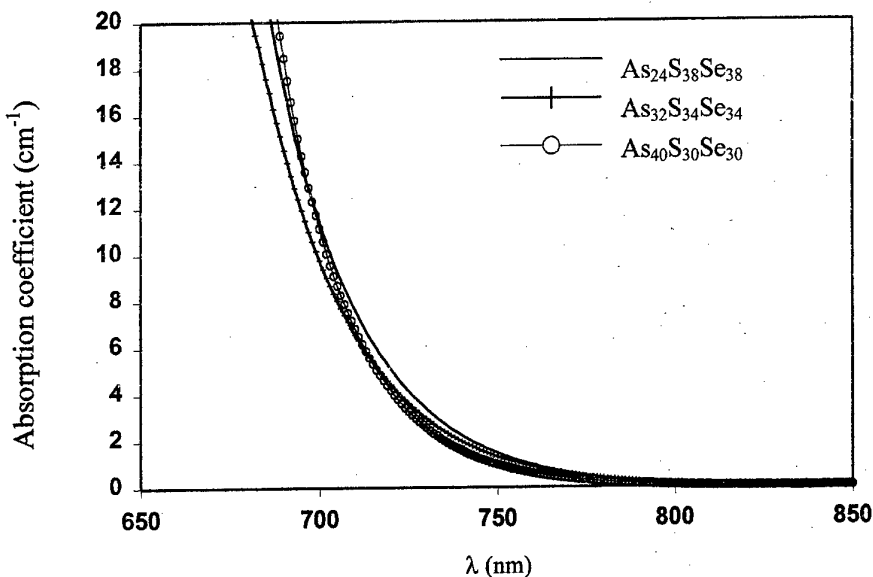


Figure 6 : Absorption spectra of glasses 3 , 6, 7

References

- 1 H. Nasu, Y. Ibara, K. Kubora, J. Non-Cryst. Solids, 110, (1989), 229.
- 2 K. A. Cerqua-Richardson, J. M. McKinley, B. Lawrence, S. Joshi, A. Villeneuve, J. Optical Materials, 12, 4 (1998).
- 3 J. A. Freitas, Jr. & U. Strom, J. Non-Cryst. Solids, 59 & 60, (1983), 875.
- 4 M. Sheik-Bahae, A. A. Said, T. H. Wei, D. J. Hagan, E. W. Van Stryland, IEEE J. Quantum Electron., 26, (1990), 760.
- 5 D. J. Treacy, S. G. Greenbaum, U. Strom, P. C. Taylor, J. Non-Cryst. Solids, 59 & 60, (1983), 847.

NON-LINEAR OPTICAL PROPERTIES IN CHALCOGENIDE VITREOUS SYSTEMS.

C. Quémard^a, F. Smektala^a, J. Lucas^a, C. Couderc^b, A. Barthélémy^b.

^a Laboratoire des Verres et Céramiques, Université de Rennes 1, Avenue du Général Leclerc, 35042 Rennes cedex, France

^b Institut de Recherches en communications Optiques et Microondes, Université de Limoges, 87060 Limoges, France.

ABSTRACT

Chalcogenide glasses of different systems have been tested by the z-scan technique in regard with their third-order non-linear optical properties. Non-linear refractive index is measured in the glass transparency region with a pulsed Nd-Yag at low level energy and low repetition rate to avoid thermal effect and measure ultrafast electronic nonlinearity. Values of non-linear refractive index as high as 700 times the non-linearity of silica glass have been obtained for a Ge-As-Se glass.

1. Introduction.

Laser appearance allowed strong intensities and put forward non-linear phenomena into materials. Among the different third-order effects observed in glasses, the variation of the refractive index (n) with the intensity (I) of an electromagnetic wave is of interest for applications in ultra-fast, all optical switching devices. Indeed, n can be expressed as $n = n_0 + n_2 I$, where n_0 is the linear index of refraction and n_2 the non-linear index of refraction. Glass could be a good material to realize this kind of device. But silica glass, used for telecommunications transmission, has a small non-linear refractive index ($2.7 \cdot 10^{-20} \text{ m}^2/\text{W}$ at $1.06 \mu\text{m}$) [1]. This nonlinearity is not sufficient for real application in ultra-fast switching device. Oxide, fluoride and chalcogenide glasses have been tested by different technics. Among these different glasses families, the chalcogenide one exhibits the greatest nonlinearities. The literature presents As_2S_3 as a good non-linear material with n_2 values ranging from $n_2 = 0.9 \cdot 10^{-18} \text{ m}^2/\text{W}$ measured by the Kerr Shutter method at $1.55 \mu\text{m}$ [2] to $n_2 = 25 \cdot 10^{-18} \text{ m}^2/\text{W}$ measured by the THG technique at $2.1 \mu\text{m}$ [3]. We have focused our attention on other chalcogenide glasses, especially in Ge-Se, Ge-As-Se and Ge-As-Se-Sn systems. Non-resonant non-linear refractive indices, n_2 , and non-linear absorption coefficients β have been quantified by the Z-scan technique.

2. Experimental procedure

2.1 Glass synthesis.

The elements (5N purity) are evacuated under vacuum to remove oxygen. Se and As elements are purified by the oxide volatilization method. The oxides, (SeO_2) and (As_2O_3) present vapor pressures over than those of the elements Se and As respectively. Then, the sealed silica tube is introduced into a rocking furnace. The raw material is melted at 900°C and quenched in air to

room temperature. The glasses are polished to obtain a two plane and parallel faces disc for z-scan measurements.

2.2 Measurement technique.

The measurement technique used is the z-scan technique [4]. A Nd-Yag laser, emitting 50 Ps at 1064 nm pulses with a repetition rate of 10 Hz is used. The pulses average energy of the order of the mJ, doesn't induce thermal effect, whereas the pick intensity closed to 2 GW/cm² allows the observation of non-linear phenomena. Measurements are made in the glass transparency area (fig. 1). There are different contributions to n_2 , the electronic effect, which is an intrinsic glass property with a very fast response time but a small effect. The nuclear effect is a molecular reorientation but doesn't occur in glasses. The thermic effect appears when too much energy is used, then the n_2 is exalted and the response time is smaller

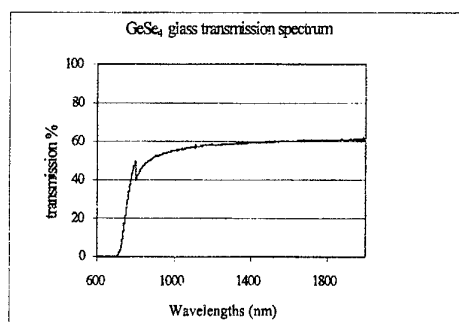


Figure 1: transmission spectrum of GeSe₄glass

The laser beam is focused by a convergent lens. The sample is first placed at the focal point ($Z=0$) then it is moved here and there along the axial laser beam ($-Z$ and $+Z$). The sample transmittance is registered through a diaphragm. When non-linear absorption (TPA) is present, we record an open diaphragm curve to quantify non-linear coefficient absorption, β . Then a closed diaphragm z-scan curve is registered and normalized from the non-linear absorption.

3. Results and discussion.

The bench has been calibrated by the liquid CS₂ measurement. The value found for n_2 is $2.8 \cdot 10^{-18} \text{ m}^2/\text{W}$. The difference observed with the literature is 7% ($n_2 = 3 \cdot 10^{-18} \text{ m}^2/\text{W}$ [4]).

Then, Ge-Se, Ge-As-Se and Ge-As-Se-Sn glasses have been characterized. For each glass two measurements were performed. For the non-linear absorption coefficient, the curve presents a characteristic valley shape (fig.2). β is proportionnal to the valley amplitude. Then for the non-linear refractive index, the z-scan curve, normalized from the non-linear absorption presents a valley-pick shape (fig.3) characteristic of a positive n_2 . The non-linear refractive index is proportional to the valley-pick amplitude. The transmittance variations are dominated by electronic effects. All the experimental conditions have been chosen to avoid thermal contribution. Typical z-scan curves are presented in fig. 2 and 3 for GeSe₄glass. Results for n_2 and β are presented in table 1. The experimental error is around 15-20 %

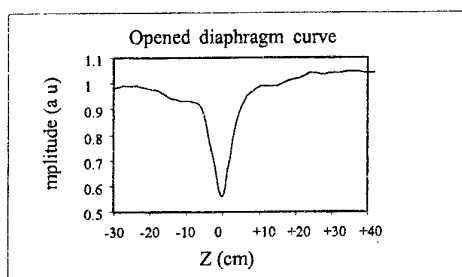


Figure 2: non-linear absorption curve for GeSe₄ glass

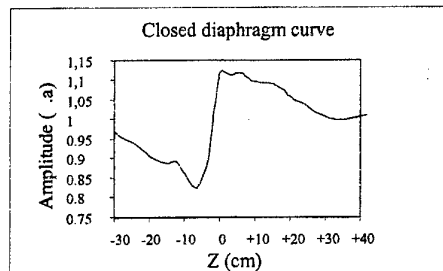


Figure 3: z-scan curve corrected from non-linear absorption for GeSe₄ glass.

Table 1: Non-linear characteristics of several chalcogenide glasses.

Compositions	λ_{gap} (nm)	T _g (°C)	$\lambda_{\text{gap}}/\lambda_{\text{Laser}}$	n_2 ($10^{-18} \text{ m}^2/\text{W}$)	β (10^{-11} m/W)	Thickness (mm)
Ge ₅ Se ₉₅	748	81	0.703	12.9	1.7	2
Ge ₁₀ Se ₉₀	746	102	0.701	14.7	1.8	1.9
Ge ₂₀ Se ₈₀	745	165	0.700	12.9	1.8	1
Ge ₂₀ As ₄₀ Se ₄₀	839	316	0.79	18.5	5.9	1.18
Ge ₂₇ As ₁₃ Se ₆₀	680	315	0.64	20	1.5	1.16
Ge ₂₇ As ₁₃ Se ₅₅ Sn ₅	945	292	0.89	17.7	4.6	1.2

Among the different chalcogenide glasses tested, Ge_x-Se_{1-x} glasses, where $x = 0.05, 0.1, 0.2$, don't exhibit non-linear refractive index significant variation. All the n_2 values are around $13 \cdot 10^{-18} \text{ m}^2/\text{W} \pm 15\text{-}20\%$. The measurement experimental error is too important to conclude for small n_2 variations. The non-linear absorption coefficient is similar for the three compositions, that is in relationship with the wavelength band-gap. Indeed, between λ_{gap} and $2\lambda_{\text{gap}}$, non-linear absorption is present, scales as λ_{gap}^3 and is maximum for $\lambda_{\text{gap}}/\lambda_{\text{Laser}} = 0.7$ [5].

We have also studied the influence of different elements on the non-linearity. First, 40% Se have been substituted by 40% As in the GeSe₄ glass, to characterize the As influence against Se. The non-linear refractive index measured is stronger for Ge₂₀As₄₀Se₄₀ ($18 \cdot 10^{-18} \text{ m}^2/\text{W}$) than for GeSe₄ ($13 \cdot 10^{-18} \text{ m}^2/\text{W}$). This points out the positive effect of arsenic on n_2 . The introduction of As in Ge-Se systems leads to increase the linear refractive index n_0 [6]. Considering that n_2 increases with n_0 [7], this result is not surprising. The higher non-linear absorption coefficient observed for Ge₂₀As₄₀Se₄₀ glass is consistent with the two-band model established for semiconductor materials [5], since β scales as λ_{gap}^3 .

For Ge₂₇As₁₃Se₆₀ glass a high n_2 ($20 \cdot 10^{-18} \text{ m}^2/\text{W}$) is also obtained. This glass presents the advantage of a smaller λ_{gap} and smaller non-linear absorption by comparison with Ge₂₀As₄₀Se₄₀.

Tin has been introduced in the Ge₂₇As₁₃Se₆₀ glass by substitution of 5% Se. This leads to the apparition of trigonal structures [Sn Se_{2/2} Se_{1/3}] where one tin atom is linked with three selenium atoms. Two selenium bonds are bridging ones, the third one being a donor-acceptor bond from selenium to tin. Thus, one tin atom presents one lone pair and is linked with two selenium atoms presenting each other two lone pairs and selenium atom presenting one lone pair [8]. Thus by

comparison with $\text{Ge}_{27}\text{As}_{13}\text{Se}_{60}$ glass, with have substituted 5% of Se presenting two electronic lone pairs by 5% of Sn presenting one electronic lone pair higher in energy. In the same time, 5% of selenium presenting two lone pairs is replaced by 5% of selenium presenting one lone pair because of the donor-acceptor bonds. No significant variation of the non-linear refractive index has been noticed. This seems to indicate a positive effect of the polarizable electronic lone pair of tin on n_2

5. Conclusion.

Different chalcogenide glasses have been tested in order to see different contributions to the nonlinearity. We could see that the substitution of Se by As in Ge-Se systems increases the nonlinearity. As increases the linear refractive index and so the non-linear refractive index. n_2 increases. $\text{Ge}_{27}\text{As}_{13}\text{Se}_{60}$ glass appears to be a good candidate for an all optical ultrafast switching device. It presents a strong non-linear refractive index ($20 \cdot 10^{-18} \text{ m}^2/\text{W}$) 700 times higher than those of silica, and a small non-linear absorption. Despite the higher energy level of the Sn electronic lone pair, the substitution of Se by Sn has not lead to an increase in n_2 values.

Aknowledgments.

The authors wish to thank the CNET (Centre National d'Etudes des Télécommunications) for support in this study.

REFERENCES

- [1] E. M. Vogel, M. J. Weber, D. M. Krol, *Physics and Chemistry of Glasses*, 32 (1991) 231.
- [2] M. Asobe, H. Kobayashi, H. Itoh, T. Kanamori, *Opt. Lett.* 18 (1993) 1056.
- [3] H. Kobayashi, H. Kanbara, M. Koga, K. Kubodera, *J. Appl. Phys.* 74 (1993) 3683.
- [4] M. S. Bahae, A. A. Said, T. Wei, D. J. Hagan, E. W. Van Stryland, *IEEE J. Quantum Electron.* 26 (1990) 760.
- [5] M. S. Bahae, D. C. Hutchings, D. J. Hagan, E. W. Van Stryland, *IEEE J. Quantum Electron.* 27 (1991) 1296.
- [6] J. A. Savage, *Infrared Optical Materials and their Antireflection Coatings* (Adam Hilger, Bristol, 1985)
- [7] H. Nasu, J. S. Lin, J. Lau, J. D. Mackenzie, *SPIE Advances in Optical Materials* 505 (1984) 75.
- [8] V. F. Kokorina, *Glasses for Infrared Optics* (CRC press INC, 1996).

INTERACTION IN $\text{ZnBr}_2\text{-HgBr}_2\text{-CsBr}$ TERNARY SYSTEM

I.Kuznetsova, I.Kovaleva, V.Fedorov

Kurnakov Institute of General and Inorganic Chemistry, Russian Academy of Sciences,
Leninsky pr.,31, Moscow, Russia

ABSTRACT

The study of interaction and glass formation in the $\text{ZnBr}_2\text{-HgBr}_2\text{-CsBr}$ ternary system was performed to search for and synthesize new vitreous halide phases for use in IR optics. This system is studied by differential thermal analysis (DTA) and X-ray powder diffraction (XRD) methods. Liquidus surface projection and coordinates of non-variant points of the $\text{ZnBr}_2\text{-HgBr}_2\text{-CsBr}$ ternary system are determined. The condition for the synthesis of glasses, the glass formation region, and glass transition, crystallization and liquidus temperatures of synthesized glasses are examined. Devitrification stabilities and the T_g/T_l ratio are calculated. The obtained results are used to determine the most promising compositions for synthesis of stable glasses in the $\text{ZnBr}_2\text{-HgBr}_2$ and the $\text{ZnBr}_2\text{-CsBr}$ binary systems, and the $\text{ZnBr}_2\text{-HgBr}_2\text{-CsBr}$ ternary system.

INTRODUCTION

Recently, much attention has been paid to non-fluoride halide glasses. The cut-off wave lengths of these halide glasses are much longer than those of fluoride glasses and therefore these glasses are considered to be useful for transmission of CO_2 laser [1,2]. ZnBr_2 glass is a potentially useful optical material with low losses, if the glass can be protected from atmospheric moisture [3]. However, ZnBr_2 -based glasses have been rather less investigated. The glasses were obtained in the systems RBr-ZnBr_2 ($\text{R}=\text{Li, Na, K, Rb, Cs, Tl}$) in the concentration range from ~50 to 100 mol % ZnBr_2 [4]. Glass formation has been examined for the $\text{ZnBr}_2\text{-KBr-MBr}_2$ systems in which $\text{M}=\text{Mg, Ca, Sr, Ba, Mn, Fe, Co, Ni, Cd, Pb}$ [5-8]. Interaction and glass formation in the $\text{ZnBr}_2\text{-CdBr}_2\text{-CsBr}$ ternary system were investigated in our earlier papers [9,10]. Glass formation in the $\text{ZnBr}_2\text{-CdBr}_2$ and the $\text{ZnBr}_2\text{-HgBr}_2$ binary systems was investigated [9,11]. Replacement of Cd by Hg shifts the cut-off wavelength to the farther IR region. Information about the $\text{ZnBr}_2\text{-HgBr}_2\text{-CsBr}$ ternary system is absent. The binary systems

limiting the $\text{ZnBr}_2\text{-HgBr}_2\text{-CsBr}$ system were investigated [11,12,13]. Before studying glass formation in the $\text{ZnBr}_2\text{-HgBr}_2\text{-CsBr}$ ternary system, we studied the interaction of components of this system [14]. Knowledge of phase diagrams allows to predict glass formation in systems [15].

EXPERIMENTAL

The $\text{ZnBr}_2\text{-HgBr}_2\text{-CsBr}$ ternary system was investigated by DTA and XRD methods. The equipment for DTA and XRD has been described previously in [11]. The starting ZnBr_2 , HgBr_2 and CsBr were synthesized, purified and dried. The emission spectral analysis of purified bromides showed the purity of each reagent of 99,999 wt %. All operation with ZnBr_2 were done in a dry argon box to avoid hydration of ZnBr_2 . Batch mixtures of 0,5 g with appropriate compositions of the initial bromides were melted in vacuum quartz crucibles at temperatures of 300° higher than their melting points for about 20 min and quenched in water-ice mixture with NaCl . The quenching rate was $\sim 200\text{-}250^\circ/\text{sec}$. Glass formation was determined by the transparency of samples by eye observation. All glasses were colourless. Specific temperatures of the glasses were measured by DTA at heating rate of $8\text{-}10^\circ/\text{min}$.

RESULTS AND DISCUSSIONS

Six compounds are formed in these binary systems, viz. Cs_3ZnBr_5 , Cs_2ZnBr_4 , CsZn_2Br_5 , Cs_2HgBr_4 , CsHgBr_3 and CsHg_2Br_5 . All compounds melt congruently except CsZn_2Br_5 which melts incongruently. Compounds Cs_2HgBr_4 and Cs_3ZnBr_5 as well as Cs_2HgBr_4 and Cs_2ZnBr_4 form continuous solid solutions. Liquidus surface of the $\text{ZnBr}_2\text{-HgBr}_2\text{-CsBr}$ system consists of 8 initial crystallization fields of the following phases: ZnBr_2 , HgBr_2 , CsBr , CsZn_2Br_5 , Cs_2ZnBr_4 , CsHg_2Br_5 , CsHgBr_3 and continuous solid solutions (Fig.). Coordinates of non-variant points were determined [14].

Glass formation of the $\text{ZnBr}_2\text{-HgBr}_2\text{-CsBr}$ system has been examined. In the $\text{ZnBr}_2\text{-HgBr}_2$ binary system good transparent glasses were obtained in the concentration range 60-100 mol % ZnBr_2 , and in the $\text{ZnBr}_2\text{-CsBr}$ system 75-100 mol % ZnBr_2 . The DTA results for the quenched vitreous samples of the $\text{ZnBr}_2\text{-HgBr}_2$ and the $\text{ZnBr}_2\text{-CsBr}$ binary systems and the $\text{ZnBr}_2\text{-HgBr}_2\text{-CsBr}$ ternary system are listed in the table, showing the compositions of the samples; glass transition (t_g), crystallization (t_c) and liquidus (t_l) temperatures; and the calculated devitrification stabilities $(T_c - T_g)/T_g$ and T_g/T_l ratios (T is the absolute temperature).

Table. DTA for quenched vitreous samples of ZnBr₂-HgBr₂-CsBr ternary system

Composition, mol % ZnBr ₂ HgBr ₂ CsBr			t, °C			(T _c -T _g)/T _g	T _g /T _l
			t _g	t _c	t _l		
100	0	0	150	230	395	0.19	0.64
95	5	0	80	205	390	0.35	0.63
90	10	0	105	150	385	0.12	0.57
80	20	0	40	235	370	0.62	0.48
70	30	0	55	220	360	0.50	0.51
60	40	0	40	-	355	-	0.50
90	0	10	-	160	375	-	-
75	0	25	110	160	315	0.13	0.65
50	30	20	105	130	315	0.07	0.64
45	35	20	90	120	280	0.09	0.65
45	30	25	80	215	235	0.40	0.69

In the ZnBr₂-HgBr₂ binary system stable glasses can be obtained at the HgBr₂ concentration less than 15 mol%, because in this concentration range, $t_g > 80^\circ\text{C}$; the devitrification stability $(T_c - T_g)/T_g$ is relatively low (< 0.35), and $0.57 < T_g/T_l < 0.65$. Note that the sample 90ZnBr₂ - 10HgBr₂ is especially promising for synthesis of stable glass, because this sample has a comparatively high t_g value (105°C) and the lowest devitrification stability (0.12) in this system. and $T_g/T_l = 0.57$. The devitrification stability of this sample is lower than that for the ZnBr₂ glass. The glass 75ZnBr₂ - 25CsBr ($t_g = 110^\circ\text{C}$, $(T_c - T_g)/T_g = 0.13$; $T_g/T_l = 0.65$) is of interest for the same reason. Analysis of obtained results allows to determine the glass formation region (Fig.) and to choose compositions of the most stable glasses which have relatively high t_g ($> 80^\circ\text{C}$), low devitrification stability $(T_c - T_g)/T_g$ (< 0.20), and $0.57 < T_g/T_l < 0.65$. This agrees well with the "rule of two-thirds", which is a criterion of glass formation [15].

REFERENCES

- [1] M. Poulain, J. Non-Cryst.Solids. 56 (1983) 1
- [2] M.F.Ding, J. Lau, J.D.Mackenzie, J. Non-Cryst.Solids . 80 (1986) 538
- [3] H.Hu, F.Ma, J.D.Mackenzie, J. Non-Cryst.Solids . 55 (1983) 169

- [4] H.Hu, F.Ma, J.D.Mackenzie, J. Chin. Silic. Soc. 12 (1984) 307
- [5] M.Yamane, H.Kawazoe, S.Inoue, K.Maeda, Mat. Res. Bull. 20 (1985) 905
- [6] K.Kadono, H.Nakamichi, M.Nogami, Mat.Sci. Forum. 19&20 (1987) 63
- [7] K.Kadono, M.Nogami, J. Non-Cryst.Solids. 95&96 (1988) 473
- [8] K.Kadono, A.Yasuyoshi, T.Tarumi, H.Tanaka, H.Nakamichi, M.Nogami, Mat. Res. Bull. 23 (1988) 785
- [9] I. Kuznetsova, I.Kovaleva, V.Fedorov, Zh. Neorg. Khim. 35 (1990) 2625
- [10] I. Kuznetsova, I.Kovaleva, V.Fedorov, Zh. Neorg. Khim. 35 (1990) 756
- [11] I. Kuznetsova, I.Kovaleva, V.Fedorov, Zh. Neorg. Khim. 38 (1993) 371
- [12] V.Pakhomov, P.Fedorov, Yu. Polyakov, V.Kirilenko, Zh. Neorg. Khim. 22 (1977) 188
- [13] I.Kovaleva, I.Kusnetsova, V. Fedorov, Zh. Neorgan. Mater. 31 (1995) 1584
- [14] I. Kuznetsova, I.Kovaleva, V.Fedorov, Zh. Neorg. Khim. 38 (1993) 2049
- [15] H. Rawson, Inorganic Glass-Forming Systems (Academic Press. London and New York. 1967)

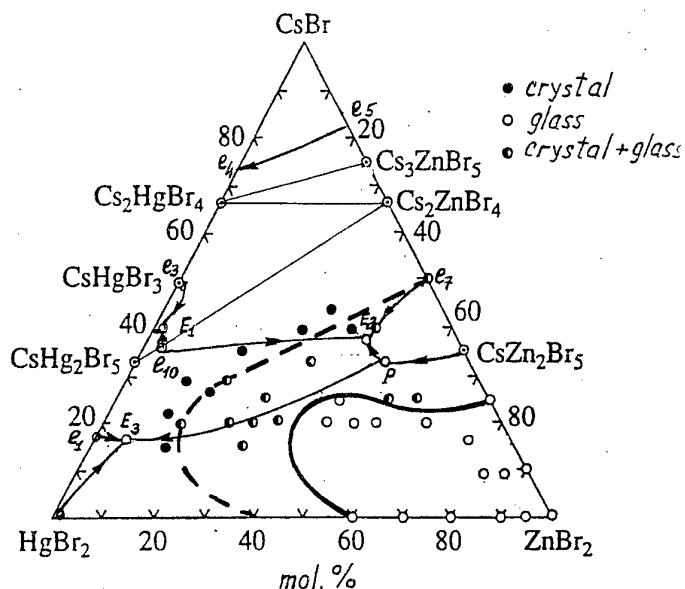


Fig. Liquidus surface projection and glass formation region in ZnBr₂-HgBr₂-CsBr ternary system

OPTICAL PROPERTIES OF ANTIMONY-STABILISED GLASSES DOPED WITH Dy^{3+} AND Er^{3+} IONS

Yann Guimond^a, Jean-Luc Adam^a, Anne-Marie Jurduc^b, Hong Li Ma^a,
Jacques Mugnier^b, and Bernard Jacquier^b

^aLaboratoire des Verres et Céramiques, UMR-CNRS 6512
Université de Rennes 1, Campus de Beaulieu, 35042 Rennes Cedex, France
E-mail : guimond@univ-rennes1.fr

^bLaboratoire de Physico-Chimie des Matériaux Luminescents, UMR-CNRS 5620
Université Claude Bernard-Lyon 1, 42 Bd. du 11 novembre 1918,
69622 Villeurbanne Cedex, France

ABSTRACT

Sulphide glasses based upon the ternary system GeGaS were stabilised by addition of antimony. Their thermal stability is very good, indicating a promising ability for fibre drawing. These new glasses show a good transparency from 0.6 to 11 μm . The 1.3 μm emission of Dy^{3+} could be observed because of the low phonon energy of these glasses. A Judd-Ofelt analysis was conducted, and the 1.3 μm transition was characterised in terms of emission cross section and quantum efficiency. The emission properties of Er^{3+} at 1.55 μm were also studied, especially the lifetimes at different temperatures.

1. INTRODUCTION

The search of new hosts for rare-earth ions is of prime importance for the development of optical fibre amplifiers in the 2nd and 3rd telecommunication windows. The emission of Dy^{3+} has been already studied in low phonon energy germanium sulphide glasses at 1.3 μm [1, 3] and recently Er^{3+} has been investigated at 1.55 μm in GaLaS [4]. But in order to develop fibres with reasonable losses, it is necessary to work with very thermally stable glasses.

In this paper we will describe the spectroscopic properties of Dy^{3+} and Er^{3+} ions in a new matrix based upon the ternary system GeGaS stabilised by addition of antimony. These new glasses are characterised by an excellent resistance towards water even at 60°C for several hours, the infrared spectra showing no significant changes. They show a relatively high glass transition temperature and, contrary to GeGaS and GaLaS glasses, the crystallisation peak is very weak (with a heating rate of 10°C min⁻¹).

2. EXPERIMENTAL PROCEDURE

GeGaSbS glass samples were prepared by weighing pure elements (5-6N) in a dry glove box. Then, the mixture was placed in a fused silica ampoule and pumped under vacuum for a few hours. At this stage, the tube was sealed, heated in a rocking furnace at 1000 °C for 6 hours, and cooled down to room temperature. About 3 mm - thick glass plates containing 0.05, 0.1, 0.2, 0.5 and 1 at.% Dy^{3+} and Er^{3+} were obtained. An undoped GeGaSbS glass prism was also fabricated.

Thermal analyses were carried out on single glass chips, about 50 mg, in sealed aluminium pans. The measurements were performed at a heating rate of $10^{\circ}\text{C min}^{-1}$ by means of a Setaram 92 differential scanning calorimeter. The accuracy of the measurement is $\pm 2^{\circ}\text{C}$.

The refractive index of GeGaSbS glass was measured by two independent methods at 632.8 nm using a He-Ne laser. First, by the prism-coupling method with a rutile prism optically coupled to a GeGaSbS glass plate and, second, by the minimum deviation method applied directly to the GeGaSbS prism.

For rare-earth emission measurements, continuous excitation in the infrared was obtained with a Coherent CW ring titanium-sapphire laser (2 GHz linewidth) pumped by a Coherent 310 argon ion laser. Fluorescence at 90° was analysed through a Jobin-Yvon double monochromator (HR320). Laser light was modulated through a mechanical chopper and the output signal of a germanium photodiode (ADC, 403 L, Low Speed), cooled to liquid nitrogen temperature, was fed into a lock-in amplifier. The fluorescence data were corrected by the response of the detection system obtained with a calibrated standard lamp.

Selective pulsed laser excitation was used for lifetime measurements. The visible beam of a pulsed dye laser pumped by a Nd:YAG from BM Industry was shifted towards the infrared range by stimulated Raman scattering through an H_2 cell and delivers pulses of about 10 ns duration and 0.04 cm^{-1} spectral width. The fluorescence was then analysed with a Jobin-Yvon monochromator (H25) and a high-speed germanium photodiode (ADC, 403 HS, High Speed) cooled to liquid nitrogen temperature. The fluorescence time evolution was then recorded with a Lecroy 9410 digital oscilloscope.

3. RESULTS

3.1 Thermal and physical properties

The results of thermal analysis obtained for standard GeGaS and 80GeS_2 , $20\text{Ga}_2\text{S}_3$ glasses compared to our stabilised GeGaSbS glass are shown in table 1. The glass transition temperatures are equal to 333, 432 and 305°C and the crystallisation temperatures are 506, 513 and 494°C , respectively. There is a good agreement between our measurements and previously reported data [5, 6]. The temperature difference between crystallisation (T_c) and glass transition (T_g) is the largest for GeGaSbS glass with a value of 189°C . This is to be compared with 81°C and 173°C for standard glasses and to 129°C in GaLaS for which T_c and T_g are respectively 681°C and 552°C [7]. In addition, the crystallisation peak is significantly less intense for GeGaSbS glass.

Table 1 : Thermal properties of different sulphide glasses and corresponding refractive indices

Glass	$T_g (^{\circ}\text{C})$	$T_x (^{\circ}\text{C})$	$T_x - T_g (^{\circ}\text{C})$	n	Ref.
GeGaS	333	506	173	2.15	[8]
$80\text{GeS}_2 - 20\text{Ga}_2\text{S}_3$	432	513	81	2.15	[9]
GeGaSbS	305	494	189	2.3657	This work
GaLaS	552	681	129	2.38	[10]

GeGaSbS glass shows a high refractive index, as expected. Two different methods were used to measure the index. First, we used the prism coupling technique [11]. The measurements

were performed three times, with a very good reproducibility, leading to a mean refractive index of $2.3657 \pm 5 \times 10^{-4}$ at 632.8 nm. This result was confirmed by direct measurement using the minimum deviation technique with a GeGaSbS prism. The refractive index was found to be $2.368 \pm 2 \times 10^{-3}$ which is in good agreement with the previous measurement.

GeGaSbS glasses are transparent from 0.6 μm in the visible to 11 μm in the infrared. The long wavelength limit is due to the absorption of the first harmonic of Ge-S and Ga-S vibrations located at 13.0 μm . This absorption increases rapidly with the thickness of the sample.

A Raman scattering spectrum recorded for undoped glass with excitation at 676 nm is shown in Fig. 1. The main band, which peaks at 340 cm^{-1} , is due to the A_1 vibration mode, also known as the breathing mode of the GeS_4 and GaS_4 groups.

The shoulder located at 430 cm^{-1} is attributed to $\text{S}_3\text{Ge-S-GeS}_3$ and $\text{S}_3\text{Ga-S-GaS}_3$ vibration modes while the structure observed at 470 cm^{-1} is due to the presence of some -S-S- bonds, the glass composition being non-stoichiometric. As can be seen on the expanded-scale spectrum, there is a weak signal in the $600\text{--}800 \text{ cm}^{-1}$ region. This is explained by the presence of residual oxygen within the glass leading to some high-energy metal-oxygen vibration modes.

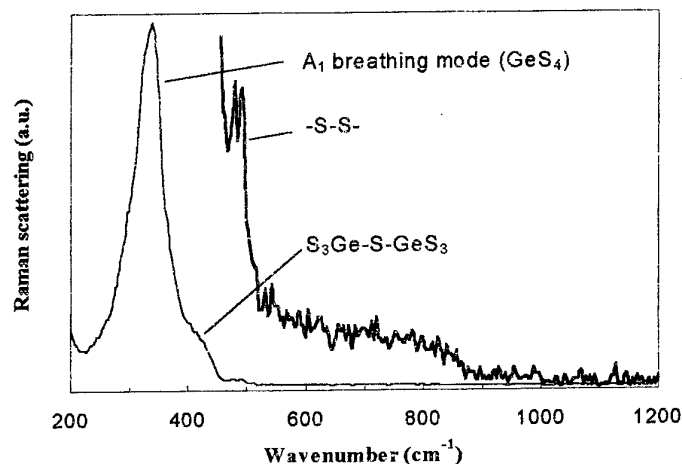


Figure 1: Raman spectrum of GeGaSbS sulfide glass. (—): expanded scale.

3.2. Optical properties of Dy^{3+} at 1.3 μm

As reported in a previous paper [12], the Judd-Ofelt parameters have been determined as $\Omega_2 = 8.49$, $\Omega_4 = 2.29$, $\Omega_6 = 1.79$, in (10^{-20} cm^2) units. Considering that the 1.3 μm emission originates from two overlapping levels, ${}^6\text{F}_{11/2}$ and ${}^6\text{H}_{9/2}$, we have defined an effective spontaneous emission rate for this transition. This effective rate, which is a combination of the individual radiative rates as referred in [13], is equal to 2641 s^{-1} . The corresponding effective lifetime is 379 μs , apparently higher than usual reported lifetimes for GeGaS ternary glasses [1, 3]. This point will be discussed later.

The 1.3 μm emission for the 0.1 at.% Dy^{3+} sample, expressed in terms of emission cross-section, is displayed in Fig. 2. The $({}^6\text{H}_{9/2}, {}^6\text{F}_{11/2}) \rightarrow {}^6\text{H}_{15/2}$ emission band is centred at 1.336 μm and has a bandwidth of 95 nm. We assumed that there is no re-absorption of the emission neither from the ground state nor from excited states.

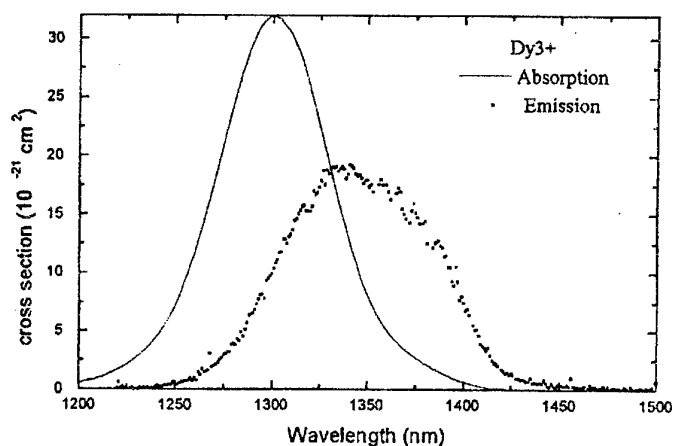


Figure 2 : 1.3 μm absorption and emission cross sections of Dy^{3+} ions in GeGaSbS glass

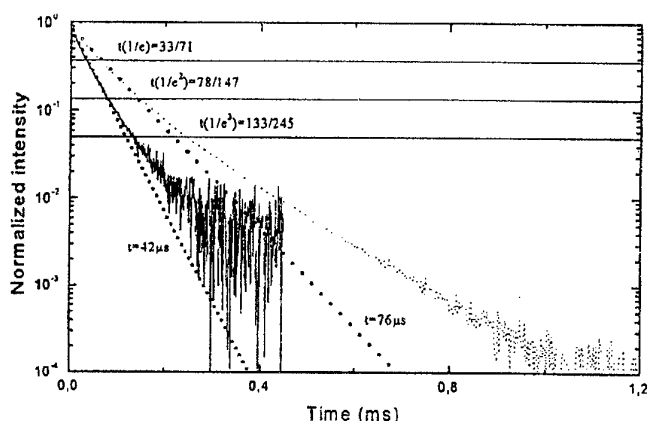


Figure 3 : (${}^6\text{H}_{9/2}$, ${}^6\text{F}_{11/2}$) decays at 10 K and room temperature for GeGaSbS glass doped with 0.1 % Dy^{3+} . (•): exponential fits.

10 K. The results are displayed in Fig. 3. Even at low temperature, decays remain largely non-exponential. The difference between 10 K and room temperature lifetimes (e.g. 71 μs and 33 μs at $1/e$) clearly indicates that non-radiative relaxations occur.

3.3. Optical properties of Er^{3+} at 1.55 μm

Considering the limited transparency of these glasses in the visible, only 4 optical transitions of Er^{3+} ions can be observed. The 1.55 μm emission of a 0.2% Er^{3+} sample is displayed in fig. 4. As reported in GaLaS [4], the peak is centred at 1.54 μm . Meanwhile, the shoulders located at 1519 nm and 1555 nm in our glass are more intense than in GaLaS. This results in a full width at half maximum as large as 50 nm in

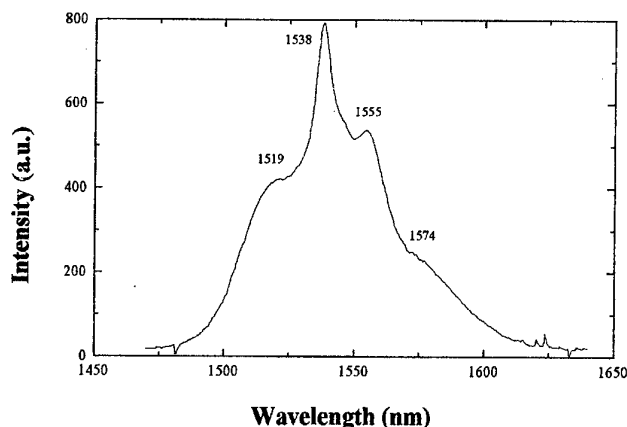


Figure 4 : 1.54 μm emission of Er^{3+} ions in GeGaSbS glass

Lifetime measurements around 1.3 μm were performed with pulsed excitation at 1110 nm (${}^6\text{H}_{15/2} \rightarrow {}^6\text{H}_{7/2}$, ${}^6\text{F}_{9/2}$) for various Dy^{3+} concentrations. For 0.1 and 0.05 at.% Dy^{3+} , the decays are identical. So, we can conclude that there is no luminescence quenching for these concentrations.

For concentrations above 0.1 %, decays start shortening due to $\text{Dy}^{3+} - \text{Dy}^{3+}$ interactions. Whatever the Dy^{3+} concentration is, the decays are markedly non-exponential. It is then necessary to estimate a measured lifetime. For the lowest concentrations, the first e-folding time of the decay curve is found to be 33 μs and the zero-order momentum is equal to 38.5 μs . For the 0.2 and 1 at. % Dy^{3+} samples, the first e-folding time drops to 24.3 and 3.5 μs , respectively. Using those results, the total quantum efficiency, is 10% for the 0.1 % doped sample.

For the 0.1 % doped sample, decays were also recorded at

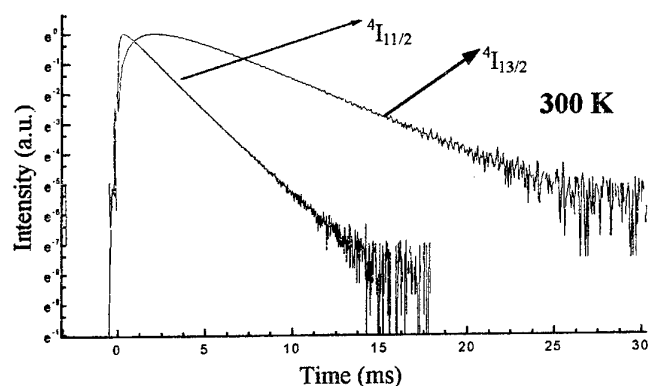


Figure 5 : ${}^4I_{11/2}$ and ${}^4I_{13/2}$ decays at 300 K GeGaSbS :Er³⁺ (0.05 at. %) glass

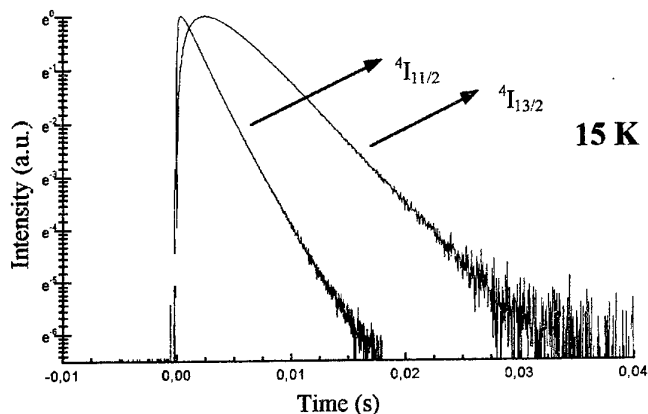


Figure 6 : ${}^4I_{11/2}$ and ${}^4I_{13/2}$ decays at 15 K GeGaSbS :Er³⁺ (0.05 at. %) glass

GeGaSbS glasses. Thus, these glasses presents a better potential than GaLaS for broadband amplification in the 1.55 μm spectral domain.

Lifetimes measurements were performed for the lowest concentration (0.05 at. %) at room temperature and 15 K by pumping at 979 nm (${}^4I_{15/2} \rightarrow {}^4I_{11/2}$). All the decays curves could be fitted by single exponentials at long times.

At room temperature, the fluorescence decay time is measured to be 4.0 ms and 1.7 ms respectively for the 1.54 μm and 985 nm emissions. This is in the same order of magnitude as the one obtained in GaLaS (3.0 ms for the 1.54 μm transition).

The same measurements, carried out at 15 K, show that the lifetimes for ${}^4I_{13/2}$ and ${}^4I_{11/2}$, increase to 4.6 ms and 2.3 ms as displayed in fig. 6. This indicates that as observed in the case of dysprosium, non-radiative relaxations occur.

4. DISCUSSION

We mentioned in the previous section that the effective lifetime (379 μs) for the 1.3 μm emission of dysprosium in GeGaS was apparently longer than the lifetime reported for GeGaS (227 μs) [1, 3]. This is actually due to a different method of calculation. In our case, the individual radiative rates of ${}^6H_{9/2}$ and ${}^6F_{11/2}$ were balanced by their respective degeneracies. In ref. [1, 3], the two contributions were simply added. In the former case, the effective decay time is intermediate between the two radiative lifetimes. In the latter, the overall decay is found to be more rapid than the fast component, which has no physical meaning in our opinion. After recalculation of the effective lifetime of the 1.3 μm transition in standard GeGaS glasses, a value of 417 μs has been found, which leads to a quantum efficiency of 9 % instead of 17 % previously reported. This is to be compared with 10 % for our stabilised GeGaSbS glass.

In the same way, one must also pay attention to the emission cross-section, which must be calculated from effective emission rates and effective branching ratios. The use of effective emission rates leads to an estimated value of $2 \times 10^{-20} \text{ cm}^2$ for conventional GeGaS glass,

which is similar to the cross-section of $1.9 \times 10^{-20} \text{ cm}^2$ obtained in this work for GeGaSbS glass.

For Dy^{3+} and Er^{3+} doped glasses, lifetime decreases with increasing temperature, even at low rare-earth concentrations indicating the presence of non-radiative relaxations. For Dy^{3+} doped samples, considering the weak energy gap of 1900 cm^{-1} between (${}^6\text{H}_{9/2}$, ${}^6\text{F}_{11/2}$) and (${}^6\text{H}_{11/2}$), one may attribute these relaxations to multiphonon emission. According to the Raman spectrum in fig. 1, the main vibration mode is located at 340 cm^{-1} . The non-radiative process is, then, in a 5-6 phonon regime which is consequently very probable. With an energy gap to the lower level of more than 6000 cm^{-1} , intrinsic non-radiative relaxations can not occur from the ${}^4\text{I}_{13/2}$ level of Er^{3+} . In that case, the decrease of the lifetime with increasing temperature can be explained by the presence of traces of impurities which generate high energy metal-oxygen bondings, as suggested by the Raman spectra in fig. 1.

5. CONCLUSION

The $1.3 \mu\text{m}$ emission of Dy^{3+} was observed in a new generation of GeGaS glasses stabilised by addition of antimony. The lifetime of this transition is found to be $379 \mu\text{s}$ which leads to a quantum efficiency of 10 % and an emission cross section of $1.9 \times 10^{-20} \text{ cm}^2$. This is comparable to the results obtained in standard GeGaS glass. For Er^{3+} , the $1.55 \mu\text{m}$ emission lifetime has been measured to be 4.0 ms and the width at half maximum is significantly broader than for GaLaS. The main interest of these new glasses lies in their good thermal stability towards devitrification, and their consequent potential to the realisation of rare-earth doped fibres with reasonable low optical attenuation.

REFERENCES :

- [1] K. Wei, D.P. Machewirth, J. Wenzel, E. Snitzer, and G.H. Sigel, *Opt. Lett.* 19 (1994) 904.
- [2] B.N. Samson, J.A. Medeiros Neto, R.I. Laming, and D.W. Hewak, *Electron. Lett.* 30 (1994) 1617.
- [3] J. Heo and Y.B. Shin, *J. Non-Cryst. Solids* 196 (1996) 162.
- [4] C.C. Ye, D.W. Hewak, M. Hempstead, B.N. Samson, D.N. Payne, *J. Non-Cryst. Solids* 208 (1996) 56.
- [5] G. Saffarini, *Solid State Commun.* 91 (1994) 577.
- [6] Mao Xilai, Zhang Mingli, Yang Peihong, and Gan Fuxi, in *Proc. XIVth Int. Cong. On Glass* (New Delhi, India) (1986) 118.
- [7] D.W. Hewak, *Opto Laser Europe* 22 (1995) 17.
- [8] P Löffler, T. Schwartz, H. Sautter, *ECIO 97* (Stockholm, Suede) (1997).
- [9] D.R. Simmons, Thesis of the University of Eindhoven (1995).
- [10] J. Flahaut, M. Guittard, A.M. Loireau-lozac'h, *Glass Technology* (1979) 24 149.
- [11] H. Onodera, I. Awai and J. Ikenoue, *Appl. Optics* 22 (1983) 1194.
- [12] J.L. Adam, Y. Guimond, A.M. Jurdy, L. Griscom, J. Mugnier and B. Jacquier, *Photonics West '98* (San José, USA) SPIE 3280 (1998) 31.
- [13] J.L. Adam, M. Matecki, H. L'Helgoualch, and B. Jacquier, *Eur. J. Solid State Inorg. Chem.* 31 (1994) 337.

OPTICAL STUDY OF HALIDE MODIFIED SULFIDE GLASSES CONTAINING NEODYMIUM IONS

L. S. Griscom, J.L. Adam, K. Binnemans*

Laboratoire des Verres et Céramiques, Université de Rennes-1
Campus de Beaulieu, 35042 RENNES Cedex FRANCE
email Laurent.Griscom@univ-rennes1.fr

*Coordination Chemistry Division, Department of Chemistry,
K.U. Leuven, Celestijnenlaan 200F, B-3001 Heverlee, Belgium

ABSTRACT

Optical properties of different halide modified Germanium Gallium Sulfide glasses doped with Nd^{3+} ions are presented. Halide modifiers can change the physical and optical properties of the glasses. Absorption spectra were measured and oscillator strengths calculated. Judd-Ofelt parameters were determined and compared with sulfide glasses of varying halide content. Excited state emission lifetimes were calculated by the Judd-Ofelt theory and compared with the measured lifetime. The halide modified glasses have been found to present a curious reversible water sensitivity.

INTRODUCTION

With the development of integrated optical amplifiers and techniques such as Wavelength Division Multiplexing in large demand in the telecommunications industries, a great amount of research has been undertaken to find new glass matrices containing rare earth ions. Optimization of the physical and optical properties of such glasses can lead to important advances in amplifier quantum efficiencies. A low multiphonon glass can greatly improve amplification performance in the $1.3\mu\text{m}$ telecommunications transmission window, where rare-earth doped fluoride and chalcogenide glasses are currently the best candidates. Chalcogenide glasses are highly transparent in the infrared and have large oscillator strengths necessary for excitation. However, one drawback to these glasses is that the reduced short-wavelength transmission can limit the choice of high energy transition levels of rare-earths for population inversion in the glasses. Modifying chalcogenide glasses with halides can shift the absorption bandgap to shorter wavelengths without significantly reducing the infrared transmission and rare-earth absorption coefficients.

The Germanium Gallium Sulfide glass system has been well studied in its potential as a low multiphonon glass for laser and fiber optic amplifier applications. [1-5] Various studies have incorporated halides into chalcogenide based glasses [6-9]. This work concentrates on the physical and optical qualities of glasses recently developed by Yu. S. Tver'yanovich et al [10] who incorporated metal chlorides into the Ge-Ga-S ternary system. The halides, when added to the system, act as network modifiers. It was found that using a cation of large radius, such as cesium opens up the basic tetrahedral structure and forms the most stable glasses.

In this work it is found that some of these glasses can incorporate significant amounts of rare-earth ions. Changing the chemical composition of the glass host can significantly affect the optical characteristics of rare earth ions. Neodymium ions which have been the most extensively studied laser ions [2, 11-14] are added to the glass matrix whose physical and optical qualities are measured under varying halide content. The composition $\text{Ge}_{25}\text{Ga}_5\text{S}_{70}$, a chalcogenide glass commonly used as a rare-earth host, was synthesized in the laboratory for reference to the halide modified glasses.

EXPERIMENTAL PROCEDURES

Starting materials of high purity 5N elements for the synthesis of glass were weighed and batched in a dry box under an argon atmosphere. For halide modified glasses 3N purity

CsCl, CsBr or CsI was used. Neodymium was incorporated as Nd_2S_3 . The method for synthesizing the glasses was a standard one. In the dry box, the products were transferred into a silica ampoule which was then put under vacuum for several hours at 10^{-3} torr and sealed. The sealed ampoules were then put in a rocking furnace and heated to 925°C at 1.5°C per minute. Before the ampoules were taken out, the rocking was stopped and the temperature was reduced to 800°C . This allows the reduction of bubbles in the glass and a gentler cooling. The glasses were cooled in air and annealed at the glass transition temperature, T_g , for several hours.

It had been noted that often the ampoule and subsequently the glass sample would break during annealing. Breakage occurs because air cooled samples would often stick to the sides of the ampoule walls and break as the glass relaxes. This problem is avoided by very quickly dipping the ampoules in water while cooling. This allows the exterior to solidify quickly and unstick to the ampoule walls. The samples are then placed in the annealing oven without breakage.

After annealing, the samples were cut and polished using $0.5\mu\text{m}$ aluminum oxide powder and water. Samples containing halides polished this way did not show any initial sensitivity to water. The glass transition temperature and crystallization points, T_x , were measured by differential scanning calorimeter (DSC) using a Setaram 92 DSC.

To obtain the Judd-Ofelt parameters, the density and index of refraction of the glasses were needed. Density was measured in CCl_4 using the Archimedes principle. The index of refraction was measured at 632.8nm with a He-Ne laser using the prism coupling technique. To obtain the oscillator strengths of the neodymium 4f-4f transitions, absorption spectroscopy was measured from 350nm to 3000nm using a Cary 5 Vis-IR spectrometer. Infrared spectroscopy was performed using a Bomem-Michelson M100 FT-IR. Fluorescence emissions and radiative lifetime measurements were carried out by directly pumping the $^4\text{F}_{3/2}$ transition at 880nm using a Ti:Sapphire laser. The measurements were taken at the Universidad del Pais Vasco, Spain, by J. Fernandez with an accuracy of $\pm 3\%$.

RESULTS

Glass compositions

Work by Tver'yanovich et al. showed that in the $\text{GeS}_2\text{-Ga}_2\text{S}_3\text{-MCl}$ (where M is a metal) ternary system, stable glasses are found when chlorides are added along the $\text{GaS}_{1.5}$ tie-line. Having no glass formation with GeS_2 , it was suggested that the halides form a gallium-halide complex which serves as a network terminator. Halides with the largest cation radius such as cesium open up the glass forming network and form the most stable glasses. In this study all compositions contained 25% cesium halides, giving a composition of $50\text{GeS}_2\text{ } 25\text{Ga}_2\text{S}_3\text{ } 25\text{CsX}$ (X being a halogen Cl, Br, or I). These were found to give the most thermally stable glasses. Higher halide content would break too many of the network forming bonds and give a very fragile glass. For reference purposes the glasses are coded GGSC for CsCl modified glasses, GGSB for CsBr, GGSi for CsI, and GGS for the unmodified $\text{Ge}_{25}\text{Ga}_5\text{S}_{70}$ glass.

Table 1: Physical Properties of Halide Modified Chalcogenide Glasses

Glass Composition	Nd^{3+} (10^{19} cm^{-3})	$T_g \pm 2^\circ\text{C}$	$T_x \pm 2^\circ\text{C}$	$T_x - T_g \pm 4^\circ\text{C}$	d (g cm^{-3})	n_D	
GGSC 25 5 70		333	506	173	2.798	2.1603	± 0.0005
GGS 25 5 70 0.5% Nd^{3+}	5.69	330	513	183			
GGSC		347	-	-	3.06	2.016	± 0.001
GGSC 0.5% Nd^{3+}	5.41	348	492	144			
GGSB		347	-	-	3.197	2.031	± 0.001
GGSB 0.5% Nd^{3+}	5.39	348	-	-			
GGSi		347	-	-	3.279	2.0559	± 0.0005
GGSi 0.5% Nd^{3+}	5.99	342	-	-			

Physical Properties

Table 1 lists T_g , T_x , the density d , and the index of refraction n_D of the glasses. DSC measurements of undoped samples containing cesium halides show no crystallization peaks up to 550°C , the limit of the apparatus. Halide modified glasses were stable enough to be placed

directly in the annealing oven from the synthesis furnace without crystallization. The GGS glass showed a crystallization peak at 506°C but the separation, $T_x - T_g$, is large enough to give a stable glass and remains relatively stable when Nd^{3+} ions are added. However in the GGSC glass, a strong crystallization peak appears as soon as a small amount of Nd_2S_3 is added, and is limited to 0.25% Nd_2S_3 (0.5 cat.% Nd^{3+}). Compositions containing CsI, on the other hand, show no crystallization even with higher amounts of rare earth ions; up to 1.0 cat.% Nd^{3+} was incorporated with no sign of crystallization ($9.8 \times 10^{19} \text{ cm}^{-3}$). Higher concentrations were not attempted.

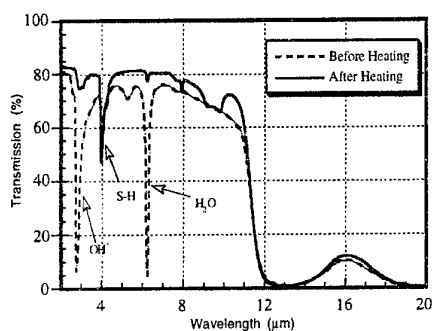


FIG 1: Infrared transmission of GGS glass after 3 months exposure to air; and after 24hrs. heated at 300°C under an argon atmosphere

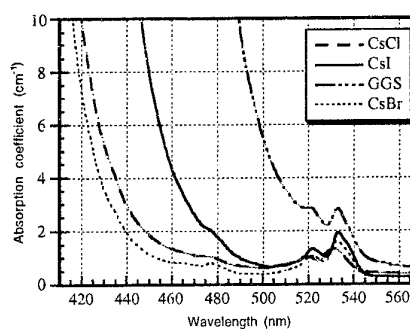


FIG 2: Visible bandgap absorption in GGS, GGSi, GGSe, GGSC, glasses. $^4\text{I}_{9/2} \rightarrow ^4\text{G}_{7/2}$, $^4\text{G}_{7/2}$ transition is visible at 535nm

Infrared optical transmission measurements were made to monitor the sensitivity of these glasses to atmospheric moisture. GGS glass is totally insensitive to humidity, but halide modified glasses samples showed large absorption bands corresponding to H_2O and OH^- , and it was initially supposed to come from a mistake in the synthesis of the glass. However these bands were found to increase over time showing no visible degradation to the glass. This effect is due to a curious phenomena where the glass absorbs molecular water like a sponge on the surface without any apparent chemical modification. The water could then be removed simply by heating the glasses above 100°C in a dry atmosphere. This reversible surface effect should not affect the radiative performance of the rare-earth ions incorporated into the glass. However an absorption band corresponding to S-H vibrations remains unchanged and is found in the bulk of the glasses. This is a common problem associated with sulfide glasses, and is found also in the GGS glasses.

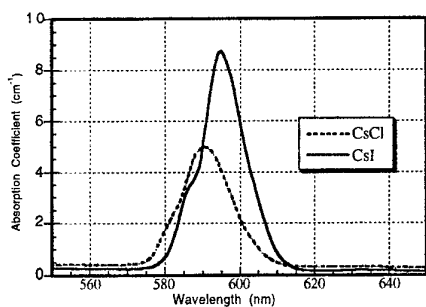


FIG 3: Absorption of the $^4\text{I}_{9/2} \rightarrow ^4\text{G}_{5/2}, ^2\text{G}_{7/2}$ transition in GGSi and GGSC glasses.

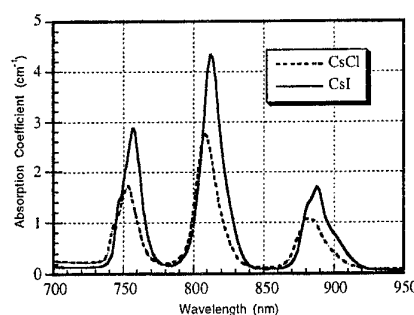


FIG 4: $^4\text{I}_{9/2} \rightarrow ^4\text{F}_{7/2}, ^4\text{S}_{3/2}, ^4\text{F}_{5/2}, ^2\text{H}_{9/2}, ^4\text{F}_{3/2}$ Transitions in GGSi and GGSC glasses

Rare-Earth Spectroscopy

When halides are added to sulfide glasses the band gap is progressively shifted to shorter wavelengths with increasing halide content and goes from light orange for the GGS

glass to a pale yellow for the GGSC glass. The band gap taken arbitrarily at 5 cm^{-1} gives a value of 502nm for GGS glass, 458nm for GGSI glass and 431nm for GGSC and 426nm for GGSB glasses (Fig 2). It is to be noted that glasses modified with bromide and chlorine have similar bandgaps.

With neodymium doping these glasses turn slightly green. The glasses used for rare-earth spectroscopy were doped at 0.5% Nd^{3+} ; the concentrations are listed in table 1. The oscillator strengths for the neodymium 4f-4f transitions when compared to oxide or fluoride glasses are several times stronger, giving elevated Judd-Ofelt parameters. The largest oscillator strengths are found in the GGSI glasses with only slightly weaker transitions for the GGS and GGSC glasses. However, when CsCl is incorporated into the glass the oscillator strengths are reduced almost by half when compared with the other glasses (Figs 3,4). Transitions in the CsCl modified glass are also blue-shifted due to the nephelauxic effect and a higher ionicity of the glass matrix.

For Judd-Ofelt calculations, oscillator strengths (Table 2) were obtained in the Nd^{3+} doped samples by integrating the effective cross section of the transitions and used in the equation:

$$f = \frac{mc}{\pi e^2 N} \int \alpha(\nu) d\nu$$

where m is the electron mass, e the electron charge, c the speed of light and N is the concentration in cm^{-3} of Nd^{3+} all in cgs units. The Judd-Ofelt parameters were determined using the reduced matrix elements $U^{(i)}$ for Nd^{3+} in NdF_3 calculated by Argonne National Labs [15]. The values of the index of refraction was assumed to be constant, and only electric dipole transitions were taken into consideration such that a transition of average frequency ν from a level J to J' is:

$$f(J;J') = \frac{8\pi^2 m \nu}{3h(2J+1)e^2 n^2} \frac{n[n^2+2]^2}{9} S_{ed}(J;J'),$$

where S_{ed} is the electric dipole line strength:

$$S_{ed}(J;J') = e^2 \sum_{t=2,4,6} \Omega_t \left\langle 4f^n J \left\| U^{(t)} \right\| 4f^n J' \right\rangle^2$$

The Judd-Ofelt Ω_t parameters were then calculated by fitting using a least squares method. The root mean square deviation (rms) are an order of magnitude larger than the values found in the literature for fluoride glasses, however the oscillator strengths are much larger and smaller a number of transitions were used for fitting. The Judd-Ofelt parameters for the studied glass compositions are given in table 2. The average wavelengths for transitions were the same for all the sulfide glasses except GGSC which is blue shifted. As compared to fluoride glasses, the Ω parameters are larger due to the increased oscillator strengths. However, in fluoride glasses the Ω_2 parameter is small in relation to the Ω_4 and Ω_6 parameters [16].

Table 2: Judd-Ofelt Parameters and Calculated Radiative lifetime for Halide Modified Chalcogenide Glasses

Oscillator Strengths (10^{-8})									
$^4I_{9/2} \rightarrow$	GGS		GGSI				GGSC		
	λ (nm)	Measured	Calculated	Measured	Calculated	Measured	Calculated	λ (nm)	Measured
$^4G_{7/2} \rightarrow ^4G_{9/2}$	528			1404	1739	1643	1817	526	1061
$^4G_{5/2} \rightarrow ^4G_{7/2}$	595	6756	6757	6922	6900	6905	6894	591	4634
$^4F_{7/2} \rightarrow ^4S_{3/2}$	756	1425	1536	1446	1660	1333	1483	753	949
$^4F_{5/2} \rightarrow ^2H_{9/2}$	814	2154	2010	2251	1892	2099	1846	810	1557
$^4F_{3/2}$	890	828	968	878	766	829	837	886	605
$^4I_{15/2}$	1662	74	41	67	47	61	41	1659	38
$^4I_{13/2}$	2533	367	294	374	323				
δ RMS (10^{-8})		141	(1.21%)	275	(2.06%)	198	(1.54%)		195
Judd-Ofelt Parameters (10^{-20} cm^2)									
Ω_2		8.06		11.3		10.8			7.09
Ω_4		13.7		11.3		13.1			8.99
Ω_6		6.16		7.58		6.79			5.03

In this work, the calculated Ω_2 parameter relies largely on the $^4I_{9/2} \rightarrow ^4G_{5/2}$ hypersensitive transition. It is found that this transition has significantly larger oscillator strengths relative to other transitions in the sulfide glasses resulting in stronger Ω_2 parameters. This transition is thought to be an indicator of the overall covalency of the ligands surrounding the rare earth ion. Accordingly, in the GGSC glass the Ω_2 parameter is reduced.

The Judd-Ofelt parameters allow us to calculate the excited state emission probabilities and the branching ratio of Nd^{3+} transitions in the glass host (table 3). The $U^{(2)}$ reduced matrix element is zero, in the $^4F_{3/2} \rightarrow ^4I_{15/2}, ^4I_{13/2}, ^4I_{11/2}, ^4I_{9/2}$ transitions giving that the over all lifetimes are only dependent on the Ω_4 and Ω_6 parameters, and the index of refraction. The total emission probabilities are strongest in the GGS glasses due to the higher index of refraction, but the GGSI glass gives the largest branching ratio and emission probability at the important 1.3 μm telecommunications window. The $U^{(4)}$ reduced matrix element is zero for the $^4F_{3/2} \rightarrow ^4I_{13/2}$ transition, so that it is only reliant on the Ω_6 parameter and the index of refraction.

The radiative probabilities of the GGS glass varies slightly with that found in the literature, but are similar. Abe et al. found Judd-Ofelt parameters of 10.6, 9.29, 7.08 ($\Omega_{2,4,6}$ respectively) for Nd^{3+} in a glass of the same composition resulting in a calculated radiative lifetime of 74 μs [2].

The measured radiative lifetime in GGSC glass was exponential indicating no competing decay phenomena. However, the value for the measured lifetime (121 μs) was longer than that predicted by the Judd-Ofelt theory (104 μs). This normally cannot occur since any competing non-radiative decay shortens the total radiative lifetime, but this falls within the accuracy of the Judd-Ofelt theory.

Table 3: Calculated spontaneous emission probabilities for sulfide glasses; Measured radiative lifetime for GGSC glass

	λ (nm)	GGS			GGSI			GGSB			GGSC		
		A (s^{-1})	B		A (s^{-1})	B		A (s^{-1})	B		A (s^{-1})	B	
$^4F_{3/2} \rightarrow$													
$^4I_{15/2}$	1916	47	0.003	48	0.004	41	0.003	1897	31	0.003			
$^4I_{13/2}$	1372	962	0.056	983	0.071	842	0.061	1364	617	0.064			
$^4I_{11/2}$	1080	6830	0.394	5973	0.433	5629	0.407	1074	4004	0.417			
$^4I_{9/2}$	890	9483	0.547	6808	0.493	7304	0.529	888	4954	0.516			
$A_{total} (s^{-1})$		17322		13812		13816				9606			
$\tau_{calc} (\mu s)$		58		72		72				104			
Measured $\tau (\mu s)$										121 \pm 4			

DISCUSSION

Electric dipole transitions in rare earths are sensitive to their environment in that covalent polarizable bonds allow greater movement of the 4f electrons during the transition. Since iodine and sulfur are highly polarizable, oscillator strengths are increased proportionately, and are only slightly reduced when CsBr is added (Table 2). However, when CsCl is added to the composition, the oscillator strengths are significantly reduced, more so than one would suppose given the ratio of sulfur to chlorine in the composition. In this composition there are 7 sulfurs for every chlorine atom. The significant reduction in transition intensity indicates that the neodymium cations show a preference for chlorine anions. This is in agreement with the theory that rare-earth trivalent ions are considered to be "hard" acids which are preferentially coordinated with "hard" bases [12]. The so called "hard" bases are low polarizable ligands that have high electron affinities such as F and Cl; Br and I are considered to be "soft" bases. In the CRC Handbook of Chemistry and Physics the listed electron affinities are 3.61, 3.36 and 3.05 eV for Cl, Br and I respectively. On comparison with the electron affinity of sulfur at 2.08 eV, Nd^{3+} would show a preference for all the halides. However what is most likely to explain the reduction in oscillator strength in the CsCl modified glasses is the polarizability. Chlorine has a polarizability of 2.18, in units $10^{-24} cm^3$, where as sulfur has higher polarizability of 2.90 and 3.05 for Br and 5.35 for I. This would indicate that if Nd^{3+} has a preference for anions

with a larger electron affinities, the absorption intensities are largely influenced by the polarizability of the ligands.

The total radiative probabilities in the halide glasses are reduced mostly due to the reduction of the refractive index as compared to the GGS glass. However, the large absorption coefficients and favorable Judd-Ofelt parameters give similar lifetime to the GGSB and GGSB glasses. Only the CsCl modified glass has a significantly lowered radiative probability which can be attributed to lowered Ω_4 and Ω_6 parameters.

CONCLUSION

Chalcogenide glasses are a well researched medium for use in for rare-earth doped amplifiers. Halide modified chalcogenide glasses can be used to control some of the parameters which need to be optimized for efficient amplification. In this way a compromise in glass attributes can be envisioned such that rare-earth absorption coefficients remain strong while expanding the short wavelength window of the glass host. In this case Ge-Ga-S glasses modified with CsBr present the best compromise for high transparency and strong rare-earth absorption coefficients.

For glasses containing halides there are often problems associated with atmospheric moisture, as is the case for the current glasses studied. However, since the effect is a priori a surface phenomena where there is no degradation to the transparency, optical systems could still be envisioned. The diffusion rate of into the glass is still unknown, but it has been noted that the diffusion rate follows the concentration of halides in the glass.

ACKNOWLEDGMENTS

The authors would like to thank the Comité Régional de Bretagne for support in this study and to express thanks to Joaquin Fernandez at the universidad del Pias Vasco, Bilbao, Spain, for the excited state lifetime measurements, and also Jacques Mugnier at the Université de Lyon for index of refraction measurements.

REFERENCES

- [1] B. Frumarová, M. Frumar, J. Oswald, J. Non-Cryst. Solids 213&214 (1997) 58
- [2] K. Abe, H. Takebe, K. Morinaga J. Non-Cryst. Solids 212 (1997) 143
- [3] Gan Fuxi; J. Non-Cryst. Solids 140 (1992) 184
- [4] K. Wei, D.P. Machewirth, J. Wenzel, E. Snitzer, G.H. Siegel Jr. J. Non-Cryst Solids 182 (1995) 257
- [5] D. Simons, Doctoral Thesis, University of Eindhoven, Holland, 1995
- [6] A.B Seddon, M.A. Hemmingway, Phys. Chem. Glasses 35(1994) 5
- [7] Z.G. Ivanova, V.S. Vassilev, K.G. Vassileva, J. Non-Cryst. Solids 162 (1993) 123
- [8] B. Petrova M. Frumar E. Cernosková, V. Cerny, J. Non-Cryst. Solids 161 (1993) 316
- [9] L. Koudelka, M. Pisarcik, O. Baidakova, J. Mat. Sci. Lett. 8 (1989) 1161
- [10] Yu. S. Tver'yanovich, E.G. Nedoshovenko, V.V. Aleksandrov, E. Yu. Turkina, A.S. Tver'yanovich, I.A. Sokolov. Glass Phys. Chem. 22 (1996) 9
- [11] A. Bornstein, R. Reisfeld, J. Non-Cryst Solids 50 (1982) 23
- [12] M.J. Weber, D.C. Ziegler, C.A. Angell J. Appl. Phys. 53 (1992) 6
- [13] B. Viana, M. Palazzi, O. LeFol J. Non-Cryst. Solids. 215 (1997) 96
- [14] A. Belykh, L. Glebov, C. Lermiaux, S. Lunter, M.Mikhailov. A. Plyukhin, M.Prassas, A. Przhnevuskii, J. Non-Cryst. Solids. 213&214 (1997) 238
- [15] W.T Carnall, H. Crosswhite, H.M. Crosswhite, Argonne National Labs Publication (1977)
- [16] K. Binnemans, D. Verboven, C. Görrler-Walrand, J. Lucas, N. Duhamel-Henry, J.L. Adam, J. Non-Cryst Solids 204 (1996) 178

SYNTHESIS AND PROPERTIES OF Ge-Sb-S: NdCl₃ GLASSESP. Němec, B. Frumarová^a, M. Frumar and J. Oswald^b

Department of General and Inorganic Chemistry, University of Pardubice,
 53210 Pardubice, ^aJoint Laboratory of Solid State Chemistry of Acad. Sci. of
 Czech Rep. and of University of Pardubice, ^bInstitute of Physics of Czech Acad.
 Sci., Prague, Czech Republic. e-mail: Miloslav.Frumar@upce.cz

ABSTRACT

High purity (GeS₂)_{80-x}(Sb₂S₃)₂₀. xNdCl₃, x = 0, 0.01, 0.1, 0.5, glasses were prepared and their optical properties determined. The Ge-Sb-S system dissolves up to 0.5 mol. % of NdCl₃. The structure of these glasses is formed by interconnected GeS₄ tetrahedra and SbS₃ pyramids as it follows from the Raman spectra. The glasses are optically well transparent in the range from 15400 cm⁻¹ to 1000 cm⁻¹. Doping with Nd creates new absorption bands which can be assigned to electron transfer from the ⁴I_{9/2} level to ²G_{5/2}, ²G_{7/2}, ²H_{11/2}, ⁴F_{9/2}, ⁴F_{7/2}, ⁴S_{3/2}, ²H_{9/2}, ⁴F_{5/2}, ⁴F_{3/2}, ⁴I_{13/2} and ⁴I_{11/2} levels. The oscillator strengths and Judd-Ofelt parameters were evaluated. Their values are close to the values of those of Nd³⁺ in another chalcogenide hosts. The long-wavelength absorption edge was found near 1000 cm⁻¹ and is due to multiphonon Ge-S and Sb-S vibrations. In doped glasses, several broad luminescence bands, near 890, 1080, 1370 and 1540 nm, were found, which can be assigned to the transitions from ⁴F_{3/2} to ⁴I_{9/2}, to ⁴I_{11/2}, to ⁴I_{13/2} and ⁴I_{15/2} electron levels. The 890nm luminescence band was excited also by 1064nm line and represents probably the upconversion of light.

1. INTRODUCTION

The luminescence of rare earth (RE)- doped glasses have been studied frequently for potential application in lasers, light amplifiers and light up-convertors (see, e.g. [1-7]). For such applications, the quantum efficiency, which is different for the same RE ion placed in different hosts, is important [3 - 5]. The non-radiative transitions to the lower electron energy state, when several lattice vibrations are generated, compete with the radiative transitions. The emission from the ⁴F_{3/2} level of Nd³⁺ ion to the underlying ⁴I_{15/2} level can be quenched because of the above mentioned multiphonon relaxation [6,7]. The whole quantum efficiency is then reduced [3,4].

The non-radiative decay rate, ω_p , due to multiphonon relaxation, depends on the energy gap, ΔE , and phonon energy, $\hbar\omega$, and is given by Miyakawa-Dexter equations [8]

$$\omega_p = \omega_0 \exp\left(\frac{-\alpha\Delta E}{\hbar\omega}\right), \quad \alpha = \ln(p/g) - 1, \quad (1)$$

where $p = \hbar \omega$, g is the electron-phonon coupling strength, and ω is a host dependent constant.

For glasses with a small maximum phonon energy, the number of phonons required to bridge the energy gap, is large, leading to a smaller multiphonon relaxation rate [8]. The chalcogenide glasses, because of the larger atomic weights of their constitutive elements, have smaller phonon energies than do oxide glasses and the probability of multiphonon relaxation can be less. The energy gap between $^4F_{3/2}$ and underlying $^4I_{15/2}$ level in Nd ions is relatively large ($\sim 6500\text{cm}^{-1}$ [9]). Its value, in combination with low phonon energies, decreases the probability of multiphonon relaxation.

The RE compounds or elements are well soluble in oxide and halide glasses, while their solubility in chalcogenides, e.g. in Ge-S system glasses, is generally less and is often too small for many possible applications [5]. From this point of view, the glasses from the system, Ge-Sb-S, similarly to the Ge-Ga-S glasses studied earlier [6], are promising because they can dissolve larger amounts of RE elements or their compounds.

2. EXPERIMENTAL

Samples were prepared from high purity elements (Ge, Sb, S, all of 5N-purity) and from neodymium chloride (NdCl_3 per analysis, p.a.) in evacuated silica ampoules ($T \sim 960^\circ\text{C}$, 40 hrs) in a rocking furnace. After the synthesis, the ampoules were annealed at 800°C for 8 hrs and then air quenched. The homogeneity of the samples was confirmed by optical and electron microscopy and by X-ray diffraction. The composition and its uniformity was also checked by an energy dispersive X-ray analyzer (EDAX).

The optical spectra of cut and polished planparallel plates were measured using spectrophotometer (JASCO V-570 (VIS, NIR)) and FT spectrophotometer (BIO-RAD FTS 45 (IR)).

The Raman spectra were measured at room temperature by FT Bruker IFS 55/FRA106 spectrophotometer, the YAG:Nd line (1064 nm) was used for excitation of Raman spectra. The Ar^+ ion laser lines (476.5, 488nm) and YAG:Nd laser line (1064 nm) were used for luminescence excitation.

3. RESULTS

The samples $(\text{GeS}_2)_{80-x}(\text{Sb}_2\text{S}_3)_{20} \cdot x\text{NdCl}_3$, ($x = 0, 0.01, 0.1, 0.5$) were orange in color. The glasses were optically homogeneous to the eyes and to the methods given above. Their X-ray diffraction patterns did not contain any peaks attributable to crystals. Several broad bands typical of the amorphous state were observed. The densities of samples were increasing a little with increasing Nd^{3+} content ($d = 3.22\text{--}3.26\text{ g cm}^{-3}$).

The short-wavelength absorption edge lies between 500 and 600 nm in the visible region of the spectrum. Doping of the samples with NdCl_3 (Fig. 1) creates new absorption bands near 16892, 16447, 14493, 13333, 12315, 11312 cm^{-1} (Fig. 1), which

are similar to the bands of Nd^{3+} in fluoride glasses [10,11] and in $\text{GeS}_2\text{-Ga}_2\text{S}_3$ glasses [6]. In the spectra of glasses with higher Nd content (~ 0.5 mol.%) can be seen a weak absorption band near 1950 cm^{-1} which can be assigned to electronic transitions between the level $^4\text{I}_{9/2}$ and $^4\text{I}_{11/2}$ of Nd^{3+} ion. The long-wavelength absorption edge of the samples was found near 1000 cm^{-1} and its position can be assigned to the multiphonon Ge-S and Sb-S vibrations.

The reduced Raman spectrum of $(\text{GeS}_2)_{80}(\text{Sb}_2\text{S}_3)_{20}$ glass was given and discussed in [10]. In accordance with [11] the main bands can be assigned to the vibrations of SbS_3 pyramids, to the vibrations of GeS_4 tetrahedra and to vibrations of $\text{S}_3\text{Ge} - \text{S} - \text{GeS}_3$ structural units. It does mean that the structure of host glass is formed mainly by the "lattice" of GeS_4 tetrahedra and SbS_3 pyramids, which are interconnected by bridging sulfur atoms. An identical result was received also from the analysis of IR reflectivity spectra.

The doping of Ge-Sb-S glass by Nd does not influence the IR and Raman spectra as can be expected, because the density of NdCl_3 dissolved molecules in glassy matrix is low.

In the luminescence spectra of Nd-activated glasses (Figs. 2a,b) were observed four broad luminescence bands, which can be assigned to the transitions between the discrete electron levels of Nd^{3+} ions.

4. DISCUSSION

In analogy with Ref. [6, 7, 10], the absorption bands introduced by Nd doping in visible (VIS) and near infrared (NIR) region of spectrum can be assigned to the electron transitions from the ground $^4\text{I}_{9/2}$ level to the $^2\text{G}_{5/2}$, $^2\text{G}_{7/2}$, $^2\text{H}_{11/2}$, $^4\text{F}_{9/2}$, $^4\text{F}_{7/2}$, $^4\text{S}_{3/2}$, $^2\text{H}_{9/2}$, $^4\text{F}_{5/2}$ and $^4\text{F}_{3/2}$ higher energy levels. The transitions from the $^4\text{I}_{9/2}$ level to ($^4\text{G}_{7/2}$, $^4\text{G}_{9/2}$, $^2\text{K}_{13/2}$) are hidden in short wavelength absorption edge, the transition to ($^2\text{H}_{11/2}$, $^2\text{G}_{5/2}$, $^2\text{G}_{7/2}$), to ($^4\text{F}_{7/2}$, $^4\text{S}_{3/2}$) and to ($^2\text{H}_{9/2}$, $^4\text{F}_{5/2}$) levels are forming absorption with overlapping of individual bands (Fig. 1).

The oscillator strength f depends on the intensity of absorption bands and can be calculated from

$$f = \frac{mc}{\pi e^2 N} \int \sigma(\nu) d\nu, \quad (2)$$

where m and e are electron mass and charge, respectively, $\sigma(\nu)$ is absorption cross-section, N is the density of Nd^{3+} ions. The absorption cross-section is given by $\sigma(\nu) = \alpha(\nu)/N$, where α is absorption coefficient and N is the density of Nd^{3+} ions (cm^{-3}). The obtained values of oscillator strengths are given in Table I.

A set of f_{exp} data served as the basis for calculation of the Judd-Ofelt parameters [12, 13], Ω_t , using Eq. (3).

$$f_{\text{exp}}(aJ, a'J') \cong f_{\text{calc}}(aJ, a'J') = \frac{8\pi^2 m \nu}{3h(2J+1)} \left[\frac{(n^2+2)^2}{9n} \sum_{t=2,4,6} \Omega_t \left| \langle aJ \| U^{(t)} \| a'J' \rangle \right|^2 \right], \quad (3)$$

where f_{exp} and f_{calc} are experimental and calculated oscillator strengths, respectively. The h is Planck's constant, m is electron mass, ν is mean wavenumber of the absorption band, J is the ground-state total angular momentum of Nd^{3+} ($J=9/2$), n is the refractive index of the material, Ω_t are the Judd-Ofelt phenomenological intensity parameters and the $\langle aJ \| U^{(t)} \| a'J' \rangle$ are the reduced matrix elements of the tensor operator, $U^{(t)}$ of rank t , which have been taken from [12, 13]. The obtained values of the Judd-Ofelt parameters are $\Omega_2 = (3.1 \pm 0.07) \times 10^{-20} \text{ cm}^2$, $\Omega_4 = (3.2 \pm 0.1) \times 10^{-20} \text{ cm}^2$, $\Omega_6 = (7 \pm 3) \times 10^{-20} \text{ cm}^2$. The Ω_t parameters obtained are similar to these ones for Nd^{3+} in Ga-Ge-As-S glasses [7].

Table I.

Experimental (f_{exp}) and calculated (f_{calc}) oscillator strengths for transitions from $^4I_{9/2}$ level of Nd^{3+} ion to the level given in table

Level	Wavenumber [cm ⁻¹]	f_{exp} (10 ⁻⁸)	f_{calc} (10 ⁻⁸)
$^4F_{3/2}$	11312	281	286
$^4F_{5/2}, ^2H_{9/2}$	12315	711	705
$^4F_{7/2}, ^4S_{3/2}$	13333	619	624
$^4F_{9/2}$	14493	59	54
$^2H_{11/2}, ^2G_{5/2}, ^2G_{7/2}$	16447, 16892	2548	2550

The luminescence spectrum of Nd-activated glasses (Figs. 2a, b) consists of four broad luminescence bands which we assign to the transitions between discrete electron levels of Nd^{3+} ions: $^4F_{3/2} - ^4I_{9/2}$ or $^4F_{7/2} - ^4I_{11/2}$ (890 nm); $^4F_{3/2} - ^4I_{11/2}$ (1080 nm); $^4F_{3/2} - ^4I_{13/2}$ (1370 nm); and $^4F_{3/2} - ^4I_{15/2}$ (1540 nm). The different shape of individual luminescence bands of $NdCl_3$ doped glasses may be caused by difference in the coordination sphere of Nd^{3+} ions.

The luminescence band with maximum near 890 nm has higher energy than the excitation light (1064 nm) and it is probably caused by an upconversion effect. The exciting light can transfer electrons of Nd^{3+} ions from fundamental level $^4I_{9/2}$ to the excited level $^4F_{3/2}$ or to the $^4F_{7/2}$ ($^4S_{3/2}$) level in two steps. The difference of energy between $^4F_{3/2}$ and $^4I_{9/2}$ level is higher (Fig. 3) than the energy of excitation light (9398 cm⁻¹) and the process of excitation can not proceed by absorption of one photon only. The slope, k , of linear dependence of $\log I_{lum}$ vs. $\log I_{exc}$ is $k = 1.82$, where I_{lum} is intensity of luminescence and I_{exc} is the excitation power. The quadratic dependence of the intensity of luminescence with the laser power indicates that the two photons participate in this process. The value of k is rather less than 2, which can be expected, because the downward electron transitions tend to equalize the populations of the pumped initial and final states. Such an effect is commonly observed in two-photon upconversion processes [14].

It is also possible to explain the presence of luminescence band with maximum near 890 nm (when excited by 1064 nm light) as an anti-Stokes band excited with contribution of several phonons. The energy difference between the excitation and luminescence light maxims is $\sim 1950 \text{ cm}^{-1}$, the highest energy of phonons in this type of

glasses can be evaluated as $\sim 400 \text{ cm}^{-1}$ [5]. It does mean that ~ 5 phonons should be absorbed for such luminescence excitation, which seems to be less probable.

5. CONCLUSION

The GeS_2 - Sb_2S_3 glasses dissolve relatively large amounts of Nd^{3+} and form stable and homogeneous glasses. Their properties are similar to Nd-doped Ge-Ga-S and Ge-Ga-As-S glasses [6, 7]. Due to lower phonon frequencies in sulfide glasses than in oxide or halide glasses, the Nd doped chalcogenides may be good candidates for high efficiency light amplifiers, up-convertors, lasers and other optoelectronic devices.

ACKNOWLEDGMENT

The work was supported by grants No. 203/96/0876 and No. 203/98/0103 of Czech Grant Agency and by the "Key project 12/96" of Czech Acad. Sci., Prague, which are gratefully acknowledged.

REFERENCES

- [1] A.C. Tropper, J.N. Carter, R.D.T. Lauder, D.C. Hanna, S.T. Davey, D. Szebesta, *J. Opt. Soc. Am. B - Opt. Phys.*, 11, 886 (1994).
- [2] W.S. Brocklesby, A. Pearson, *J. Luminesc.*, 59, 333 (1994).
- [3] D.W. Hewak, R.S. Deol, J. Wang, G. Wylangowski, J.A. Medeiros Neto, B.N. Samson, R.I. Laming, W.S. Brocklesby, D.N. Payne, A. Jha, M. Poulain, S. Otero, S. Surinach and M.D. Baro, *Electronic Letters*, 29, 237 (1993).
- [4] D.R. Simons, A.J. Faber, H. De Waal, *Proc. 8th Internat. Symp. On Halide Glasses*, Perros-Guirec, France 1992. CNET, Lannion, France 1992, p.448.
- [5] B. Frumarová, J. Oswald, P. Krečmer, M. Frumar, V. Černý, V. Smrčka, *Optical Materials*, 6, 217 (1996).
- [6] B. Frumarová, M. Frumar, J. Oswald, *J. Non-Cryst. Solids* 213-214, 58 (1997).
- [7] A. Belykh, L. Glebov, C. Lermniaux, S. Lunter, M. Mikhailov, A. Pliukhin, M. Prassas, A. Przhevuskii, *J. Non-Cryst. Solids* 213-214, 238 (1997).
- [8] R.S. Deol, D.W. Hewak, S. Jordery, A. Jha, M. Poulain, M.D. Baro, D.N. Payne, *J. Non-Cryst. Solids* 161, 257 (1993).
- [9] H. Ebendorff-Heidepriem, W. Seeber, D. Ehrt, *J. Non-Cryst. Solids* 183, 191 (1995).
- [10] B. Frumarová, P. Němec, M. Frumar, J. Oswald, *Phys. Tech. Semiconductors (St. Peterburgh)*, 1998, in press.
- [11] L. Koudelka, M. Frumar, M. Pisárčik, *J. Non-Cryst. Solids* 41, 171 (1980).
- [12] B.R. Judd, *Phys. Rev.* 127, 750 (1962).
- [13] G.S. Ofelt, *J. Chem. Phys.* 37, 511 (1962).
- [14] A.T. Stanley, E.A. Harris, T.M. Searle and J.M. Parker, *J. Non-Cryst. Solids* 161, 235 (1993).

New Heavy Metal Oxide Glasses

D. R. MacFarlane and P. J. Newman

Department of Chemistry, Monash University, Clayton, Vic., Australia

An important means of monitoring the curing of advanced polymer resins, for example those involved in graphite fibre composites, for aerospace applications involves evanescent wave spectroscopy using optical fibre technology. In order to obtain the most sensitive probe, the optical fibre must transmit in the near infrared, have a high refractive index and a glass transition temperature in excess of 350° C.

We report here a new series of heavy metal oxide glasses, based on the oxides of lead, bismuth and gallium with the addition of germanium oxide, designed to have the required properties. The multicomponent mixture system investigated was $(25-x/3)\text{Bi}_2\text{O}_3-(57-x/3)\text{PbO}-(18-x/3)\text{Ga}_2\text{O}_3-x\text{GeO}_2$, $x=0$ to 15 mol%. The glasses were prepared by melting the appropriate amounts of pure oxides in a gold crucible in air and splat quenching the resulting viscous liquid. All the glasses were deep yellow/orange.

The addition of GeO_2 was found to improve the thermal stability of the glass. The glass transition temperature increased from 330°C for the germanium free glass to 364° C for a glass containing 15 mol% GeO_2 . This improvement in glass stability is thought to be due to the enhancement of network formation in the glass brought about by the presence of GeO_2 . Addition of GeO_2 improved the mid-infrared region of transparency, the transparency cut-off shifting from ca. 6 microns at $x=0$ to 8 microns at $x = 15$ mol%.

TeO₂ based glasses and glass ceramics materials

F.C.Cassanjes, D.Matai, M.A.Zagheti, J.A.Varela, Y.Messaddeq and S.J.L.Ribeiro

Institute of Chemistry- UNESP-

PoBox355- Zip 14801-970, Araraquara-SP-Brazil

key-words- ferroelectrics, glass-ceramics, TeO₂ glasses, non-linear optical devices

TeO₂ based glasses have received great attention in the last years mainly because of the potential applications either as non-linear optical devices or as laser hosts for lanthanide containing materials. With these two guide lines we have been studying glasses in the system (Li₂O-K₂O)-Nb₂O₅-TeO₂. The vitreous domain has been established and the role of the crucibles material on the preparation conditions has been stressed. SnO₂ and gold crucibles have revealed to be well adapted materials for these highly corrosive melts. Tripositive lanthanide ions (Pr, Nd, Eu, Ho, Er and Tm) have been added to the most stable compositions and their spectroscopic properties studied under the Judd-Ofelt formalism for f-f electronic transitions. The role of Eu₂O₃ as a nucleating agent has been established by Differential Thermal Analysis. With the knowledge of nucleation temperatures glass ceramics have been obtained from two-stage heat treatments. In an alternative way composite materials have been obtained by incorporation at T_g of ferroelectric phases as LiNbO₃:Ln and PLZT:Ln (Ln= Nd and Eu) in the glasses. These composite materials have been characterised by x-ray diffraction and electronic spectroscopy and they are suggested as potential candidates as laser hosts or non-linear optical devices.

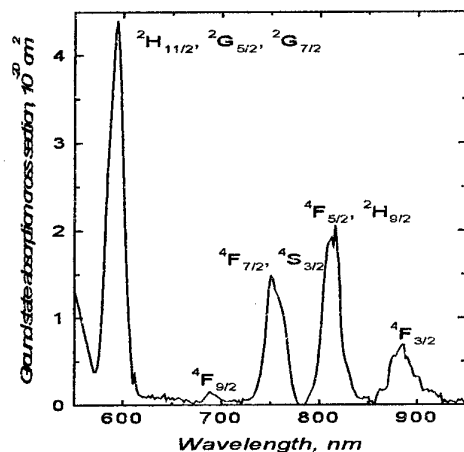


Fig. 1. Ground state absorption cross section of Nd^{3+} ions in $(\text{GeS}_2)_{79.5}(\text{Sb}_2\text{S}_3)_{20}(\text{NdCl}_3)_{0.5}$ glass.

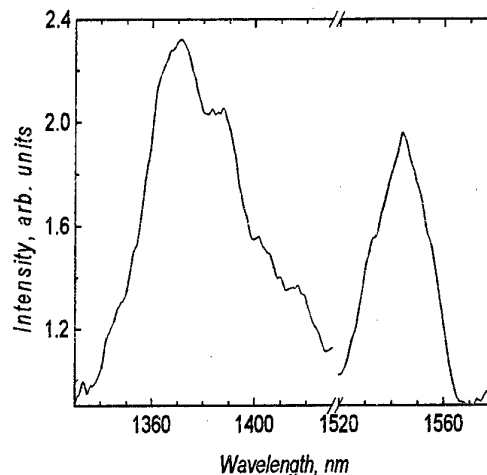


Fig. 2a. Luminescence spectrum of the glass $(\text{GeS}_2)_{79.9}(\text{Sb}_2\text{S}_3)_{20}(\text{NdCl}_3)_{0.1}$. The bands with maximum near 1370 and 1540 nm (excitation line 1064 nm)

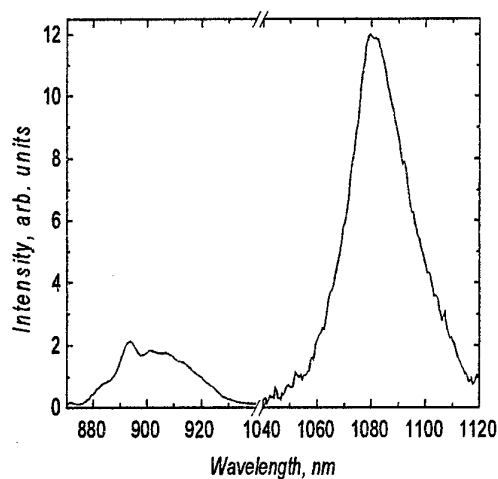


Fig. 2b. Luminescence spectrum of the glass $(\text{GeS}_2)_{79.9}(\text{Sb}_2\text{S}_3)_{20}(\text{NdCl}_3)_{0.1}$. The bands with maximum near 890 and 1080 nm. The band with maximum near 890 nm was excited by 1064 nm laser line. The luminescence band near 1080 nm was excited by Ar^+ laser lines (476.5 or 488 nm).

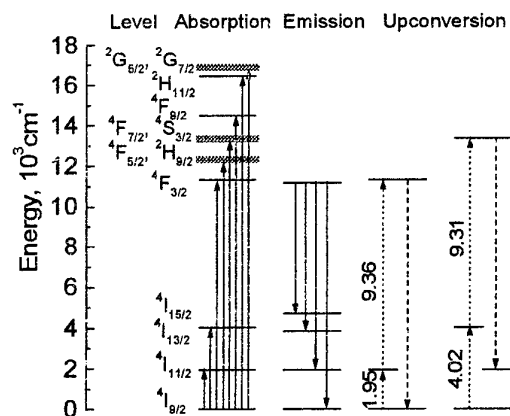


Fig. 3. Energy scheme of electron transitions in Nd^{3+} ion in $(\text{GeS}_2)_{79.5}(\text{Sb}_2\text{S}_3)_{20}(\text{NdCl}_3)_{0.5}$ glass. Possible upconversion transitions are given by dotted lines, corresponding luminescence transitions by dashed lines.

GLASS COMPOSITIONS CONTAINING ErPO_4 AT HIGH CONTENTS.

C.M.Moya, C.A.S.Barbosa, P.Melnikov, S.J.L.Ribeiro and Y.Messaddeq

Institute of Chemistry - UNESP

PoBox355-Zip 14801-970, Araraquara-SP-Brazil

e-mail younes@iq.unesp.br

key-words: erbium phosphate glass, infrared emission.

Glasses containing ErPO_4 are not known. The present work deals with the study of ternary system $\text{ErPO}_4\text{-BaF}_2\text{-InF}_3$ (mol %), where their formation has been discovered. It is to be noted that a strict condition for glass stabilization is the usage of high purity ErPO_4 . That is why a special technique for the synthesis of this precursor has been developed and implemented. It consists of Er(OH)_3 precipitation and its further conversion into ErPO_4 by addition of stoichiometric quantity of H_3PO_4 , at room temperature. After dehydration at 180°C , the product is fired at 900°C during 2 hours. High purity ErPO_4 samples were obtained and used for glass preparation. Glass compositions up to 30% mol Er^{3+} have been obtained in this system and their characterization performed by Thermal Analysis, X - ray Diffraction and Vibrational Spectroscopy (IR Absorption and Raman Scattering). Data on binary system with glass composition 70% InF_3 - 30% ErPO_4 are also reported. Special attention has been paid to the infrared emitting properties of the obtained glasses which may be considered as promising materials for the preparation of advanced optical devices.

SPECTROSCOPY OF Nd³⁺ IONS IN NEW RARE-EARTH-RICH FLUOROARSENATE GLASSES

J.-L. Adam^a, R. Balda^b, I. Melscoët^a, F. Smektala^a,
L.M. Lacha^b and J. Fernández^b

^aLaboratoire des Verres et Céramiques, UMR-CNRS 6512
Université de Rennes 1, Campus de Beaulieu, 35042 Rennes Cedex, France
jean-luc.adam@univ-rennes1.fr

^bDepartamento de Física Aplicada 1, E.T.S.I. Industriales y Telecomunicación
Universidad del País Vasco, Alameda Urquijo s/n, 48013 Bilbao, Spain

ABSTRACT

Rare-earth-rich fluoroarsenate glasses are synthesized in the Na₂O, As₂O₅, BaF₂, YF₃ system. Physical constants are given for the most stable compositions. The behavior of neodymium ions in the (40 Na₄As₂O₇ - 30 BaF₂ - 30 YF₃) glass is investigated in terms of emission spectroscopy and lifetime measurements as a function of temperature and concentration. Time-resolved line-narrowed fluorescence spectra of the ⁴F_{3/2} → ⁴I_{9/2} transition show that energy transfer occurs between non-resonant sites. A quantitative measure of the transfer as a function of time indicates that a dipole-dipole mechanism dominates. In addition, the transfer rate is found to increase with increasing excitation energy, that is with increasing number of possible energy acceptors.

INTRODUCTION

New glasses were recently discovered in the Na₄As₂O₇, BaF₂, YF₃ system [1]. Stable compositions with YF₃ content as high as 40 mol % were synthesized. These glasses are parent materials with fluorophosphate glasses of the NaPO₃, BaF₂, YF₃ system [2]. While optical properties of some active ions have been already investigated in fluorophosphates [3-6], the behavior of rare-earth ions in fluoroarsenate glass is unknown.

The optical properties of rare-earth ions depend on the chemical composition of the host. From a fundamental point of view, the investigation of such properties gives important information on the structure of the glass, and on energy transfer that occurs between rare-earth sites.

In this paper, after a brief description of the basic physical properties of undoped fluoroarsenate glasses, the optical properties of Nd³⁺ ions are investigated by means of time-resolved fluorescence line narrowing (TRFLN) measurements.

EXPERIMENTAL PROCEDURES

The raw materials are commercial BaF₂, Y₂O₃, and Na₂HAsO₄·7H₂O. The yttrium and neodymium oxides are fluorinated by a classical reaction with ammonium bifluoride NH₄F, HF at 300°C in an open platinum crucible. The arsenate compound is obtained by dehydration

of $\text{Na}_2\text{HAsO}_4 \cdot 7\text{H}_2\text{O}$, in a vitreous carbon crucible heated at 300°C for 3 hours under nitrogen flow. A thermal gravimetric analysis confirms the dehydration. After this stage, the arsenate compound is introduced into a dry glove box where the various compounds are weighed.

The use of vitreous carbon crucible for glass melting is not possible because reduction of As^{V} into As^{III} , and even As^0 , occurs. Thus, melting of fluoroarsenate glasses must take place in a platinum crucible heated at 900°C for 15 minutes in air. The risk of reaction between platinum and arsenic is real, but only in reducing conditions, which is not the case in the present experiment.

Then, the melt is cast into a brass mould, either at room temperature for vitreous domain investigations, or preheated at a temperature close to the glass transition temperature (T_g) to obtain bulk pieces. Finally, the samples are annealed at T_g and cooled down to room temperature before being cut and polished for optical measurements.

Neodymium-doped samples are prepared by substituting NdF_3 for YF_3 in the initial batch. Glasses containing 0.1, 0.5, 2 and 5 mol % NdF_3 were synthesized.

Thermal analyses were performed with 30-mg samples at a heating rate of $10^\circ\text{C}/\text{min}$, from room temperature to 550°C . A Setaram model 92 Differential Scanning Calorimeter was employed. Densities (d) were measured at room temperature in carbon tetrachloride by the Archimedean method. Refractive index (n_D) measurements were performed at sodium D-line with an Abbe refractometer.

The samples temperature was varied between 4.2 K and 300 K with a continuous flow cryostat. Time resolved fluorescence line narrowing spectroscopy for the $^4\text{F}_{3/2} \rightarrow ^4\text{I}_{9/2}$ transition were performed by exciting the samples with a Ti-Sapphire laser, pumped by a pulsed frequency doubled Nd:YAG laser (9 ns pulse width). The emission was detected with a Hamamatsu R5108 photomultiplier provided with a gating circuit designed to enable gate control from external applied TTL level control signal. Data were processed by an EGG-PAR boxcar integrator.

RESULTS

Glass compositions and physical characterization

The glass-forming diagram obtained for the $(\text{Na}_4\text{As}_2\text{O}_7 - \text{BaF}_2 - \text{YF}_3)$ system is given in Figure 1. The limits correspond to samples quenched in a brass mould at room temperature, in air.

A wide forming area of colorless glasses is found. They are referred to as NAsBY glasses. The limits of the glassy domain are : $\text{Na}_4\text{As}_2\text{O}_7$: 15-75 %, BaF_2 : 0-55 %, YF_3 : 5-55 %. The most stable compositions are found in the central part of the domain. Stability parameter ΔT is

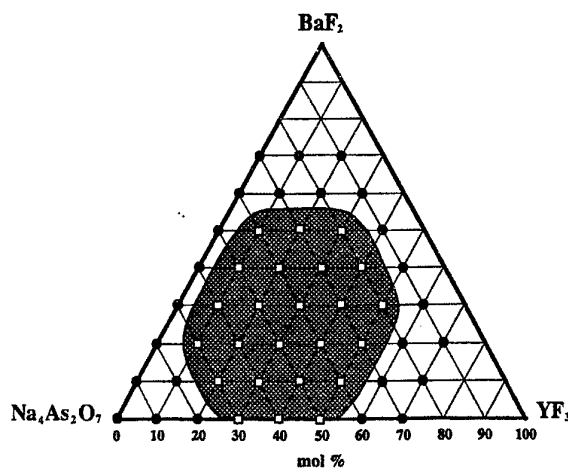


Figure 1 : Glass forming diagram in the the $(\text{Na}_4\text{As}_2\text{O}_7 - \text{BaF}_2 - \text{YF}_3)$ system

Table I : Physical properties of undoped fluoroarsenate glasses

Glass composition	T_g (± 2 °C)	T_c (± 2 °C)	ΔT (± 4 °C)	n_D (± 0.001)	d (± 0.01 g.cm ⁻³)
(NAs) ₃₀ B ₃₀ Y ₄₀	269	420	151	1.548	3.88
(NAs) ₄₀ B ₃₀ Y ₃₀	277	390	113	1.555	3.72
(NAs) ₅₀ B ₃₀ Y ₂₀	272	353	81	1.554	3.60

as high as 151 °C for (NAs)₃₀B₃₀Y₄₀ glass, as reported in Table I. Such compositions can easily be cast in bulk pieces, a few millimeters thick. In this central area, we have observed that, for a given BaF₂ content, the glass stability decreases with increasing Na₄As₂O₇ concentration. Thus, the data in Table I show that ΔT drops to 113 °C for (NAs)₄₀B₃₀Y₃₀ glass, and 81 °C for (NAs)₅₀B₃₀Y₂₀. In addition, it is to be noted that glasses can be synthesized in the Na₄As₂O₇-YF₃ binary system. They exhibit a good stability, with a ΔT parameter of about 100°C for the (NAs)₆₀Y₄₀ glass.

Optical properties of Nd³⁺ ions

With a full transparency from 400 nm to 2700 nm, Nd³⁺-doped (NAs)₄₀B₃₀Y₃₀ glasses show as many as thirteen optical transitions in their absorption spectrum. In a previous report [7], we have determined the J-O parameters: $\Omega_2 = 4.04$, $\Omega_4 = 4.31$, and $\Omega_6 = 6.65$, in (10⁻²⁰ cm²) units. It is well established that Ω_2 increases with the covalent nature of the host. In fluoroarsenate glass, Ω_2 is intermediate between the values reported for fluorophosphate glasses (2.4 – 3.7) and pure phosphates (> 4.0) [8]. This is consistent with the facts that arsenates are more covalent than phosphates and that fluorine increases the ionic character of the glass.

By means of the J-O parameters, the radiative lifetime is found to be 301 μ s for the ⁴F_{3/2} level. At room temperature, the upper-lying ⁴F_{5/2} (²H_{9/2}) levels are weakly thermalized. We have checked that thermalization had no influence on the ⁴F_{3/2} lifetime, so that experimental and calculated lifetimes can be directly compared.

The time-resolved line-narrowed excitation spectrum was recorded for the ⁴I_{9/2} → ⁴F_{3/2} transition of Nd³⁺ ions in (NAs)₄₀B₃₀Y_{29.9}Nd_{0.1} glass. The spectrum, shown in Figure 2, is obtained at 77 K with a time delay of 1 μ s after the laser pulse by monitoring the ⁴F_{3/2} → ⁴I_{11/2} emission. Two components, as expected with low-symmetry sites, are found for the ⁴F_{3/2} level of Nd³⁺. There are located at 863 and 872.5 nm.

Lifetime measurements of the ⁴F_{3/2} level were performed at 4.2 K, 77 K and room temperature by monitoring the ⁴F_{3/2} → ⁴I_{11/2} emission at 1053.6 nm. The ⁴F_{3/2} level was directly excited at 873.6 nm, that is in the low-energy Stark component of the ⁴I_{9/2} → ⁴F_{3/2} excitation profile shown in Figure 2. All decays were single exponentials, probably because of the use of narrow line excitation. The results are shown in Figure 3. Since there is no non-radiative relaxation from ⁴F_{3/2}, the lifetime measured at low concentration is the pure radiative lifetime. Within the experimental error of 3%, the lifetime is similar for 0.1 and 0.5 % Nd³⁺, whatever

dependence of the $\ln[(I_B/I_N)+1]$ function on $t^{1/2}$ was found, indicating that a dipole-dipole mechanism of interaction among the Nd^{3+} ions dominates in this time regime. The values of the $\gamma(E_L)$ parameter for the two excitation energies were found to be $23 \text{ s}^{-1/2}$ ($E_L = 11442 \text{ cm}^{-1}$) and $45 \text{ s}^{-1/2}$ ($E_L = 11481 \text{ cm}^{-1}$). The increase of the energy migration rate with increasing excitation energy (E_L) is due to the increasing number of possible energy acceptors.

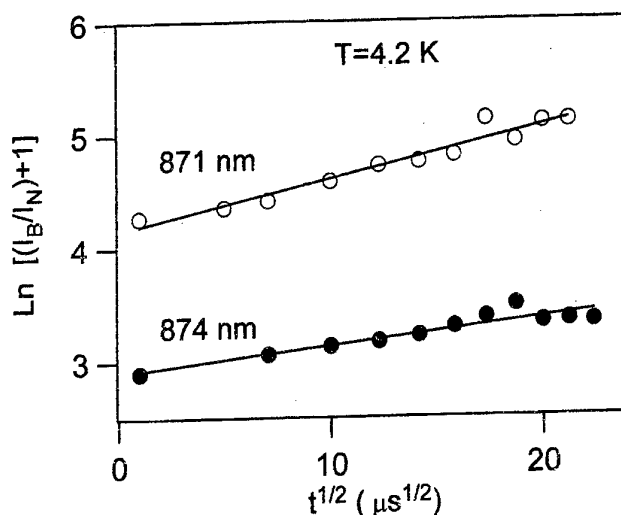


Figure 5 : Time evolution analysis of the ${}^4\text{F}_{3/2} \rightarrow {}^4\text{I}_{9/2}$ emission spectrum in NAsBY:Nd^{3+} (5 mol %) by means of Eq. (1).

CONCLUSION

In summary, rare-earth rich fluoroarsenate glasses have been synthesized in the $\text{Na}_2\text{O-As}_2\text{O}_5\text{-BaF}_2\text{-YF}_3$ system with $M = \text{Na}$ or K . The behavior of Nd^{3+} ions was studied in this new material. Good agreement between calculated (301 μs) and measured lifetimes (284 μs) was found for the ${}^4\text{F}_{3/2}$ level, indicating favorable conditions for applying the Judd-Ofelt theory to this new neodymium-doped glass system.

Study of the lifetime as a function of Nd^{3+} concentration indicates that energy transfer due to Nd-Nd interactions takes place above 0.5 % NdF_3 . Analysis of time-resolved fluorescence line-narrowing spectra of the ${}^4\text{F}_{3/2} \rightarrow {}^4\text{I}_{9/2}$ transition show that energy transfer occurs between non-resonant sites and that dipole-dipole mechanisms dominate in the 1 μs – 350 μs time regime.

REFERENCES

- [1] F. Smektala, I. Melscoët, G. Fonteneau, and J. Lucas, *J. Non-Cryst. Solids* (1998) accepted.
- [2] M. Matecki, N. Duhamel, and J. Lucas, *J. Non-Cryst. Solids* 184 (1995) 273.
- [3] N. Duhamel-Henry, J.L. Adam, B. Jacquier, and C. Linares, *Opt. Mater.* 5 (1996) 197.
- [4] J.L. Adam, N. Duhamel-Henry, and J.Y. Allain, *J. Non-Cryst. Solids* 213-214 (1997) 245.
- [5] R. Balda, J. Fernández, J.L. Adam, and M.A. Arriandiaga, *Phys. Rev. B* 54 (1996) 12076.
- [6] K. Binnemans, R.van Deun, C. Görller-Walrand, and J.L. Adam, *J. Alloys and Comp.* (1998) accepted.
- [7] J.L. Adam, F. Smektala, I. Melscoët, R. Balda, and J. Fernández, *S.P.I.E.* 3280 (1998) 143.
- [8] C. Görller-Walrand and K. Binnemans, *Spectral Intensities of f-f Transitions*, in *Handbook on the Physics and Chemistry of Rare Earths*, K.A. Gschneidner and L. Eyring, Editors. 1998, Elsevier Science B.V.: Amsterdam. p. 101.
- [9] T.T. Basiev, V.A. Malyshev, and A.K. Prhevuskii, in *Spectroscopy of Solids Containing Rare Earth Ions*, A.A. Kaplyanskii and R.M. Macfarlane, Editors. 1987, North-Holland: Amsterdam. p. 303.

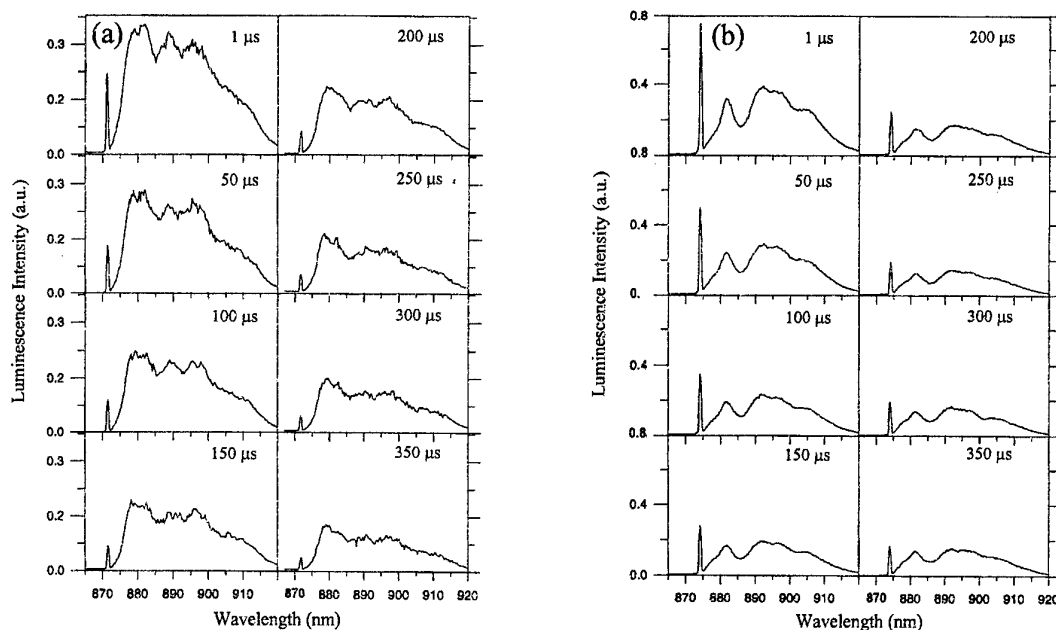


Figure 4 : TRFLN spectra of the ${}^4F_{3/2} \rightarrow {}^4I_{9/2}$ emission in NAsBY:Nd $^{3+}$ (5 mol %). Resonant excitation at (a) 871 nm and (b) 874 nm.

DISCUSSION

From the results in Figure 3, we can conclude that there is no concentration quenching for 0.5 % Nd $^{3+}$ (4.67×10^{19} ions cm $^{-3}$). As a result, the experimental radiative lifetime is defined as the average of the lifetimes measured for 0.1 % and 0.5 % -doped samples. It is equal to 284 μ s. This is in good agreement with the calculated lifetime of 301 μ s, which shows the validity of the Judd-Ofelt theory for neodymium ions in fluoroarsenate glasses.

Above 0.5 %, energy transfer between Nd $^{3+}$ ions is responsible for the decrease of the lifetime. Energy transfer processes account also for the shortening of the lifetime with increasing temperature, as observed for the 2% and 5% -doped samples.

A quantitative measure of the transfer is provided by the ratio of the intensity in the narrow line to the total intensity of the fluorescence in the inhomogeneous band shown in Figure 4.

Neglecting the dispersion in the radiative decay rate, and using the Förster formula for dipole-dipole energy transfer, one can write for the relationship between the integral intensities of the broad background emission I_B , and the narrow luminescence component I_N :

$$\ln \left(\frac{I_B}{I_N} + 1 \right) = \gamma(E_L) t^{1/2} \quad (1)$$

The macroscopic parameter $\gamma(E_L)$ has the meaning of an integral characteristic, reflecting the average rate of excitation transfer from donors to the ensemble of spectrally nonequivalent acceptors [9].

We have analyzed the time-resolved site-selective fluorescence spectra of the ${}^4F_{3/2} \rightarrow {}^4I_{9/2}$ transition obtained at different time delays between 1 μ s and 350 μ s according to Eq. (1). Figure 5 shows the results for two excitation energies. As can be observed, a linear

the temperature is. Above 0.5 % Nd^{3+} , the lifetime decreases down to 126 μs at room temperature for 5 mol % NdF_3 .

The existence of energy transfer between Nd^{3+} ions in these glasses can be studied by using time resolved fluorescence line narrowing (TRFLN) spectroscopy. If the laser source is pulsed and ion-ion interactions are present, the TRFLN technique provides us with a way to measure optical energy propagation from the initially excited subset of ions to other elements of the inhomogeneously broadened line. This is done by observing the emission characteristics of the system as a function of time. Resonant time-resolved fluorescence line narrowed emission spectra for the ${}^4\text{F}_{3/2} \rightarrow {}^4\text{I}_{9/2}$ transition were performed for the 5 % Nd^{3+} -doped sample, at 4.2 K. Excitation was at different wavelengths into the ${}^4\text{I}_{9/2} \rightarrow {}^4\text{F}_{3/2}$ absorption band and spectra were recorded at different time delays after the laser pulse. It is important to perform the measurements at low temperature to ensure that only the lowest energy Stark level of the ground state is excited. Typical results of these measurements are given in Figure 4, which shows the spectra

at time delays between 1 μs and 350 μs , for two different excitation wavelengths, 871 nm (high energy wing of the low energy component ${}^4\text{I}_{9/2} \rightarrow {}^4\text{F}_{3/2}$ absorption band) and 874 nm (energy at the peak of the low energy component of ${}^4\text{I}_{9/2} \rightarrow {}^4\text{F}_{3/2}$ absorption band),

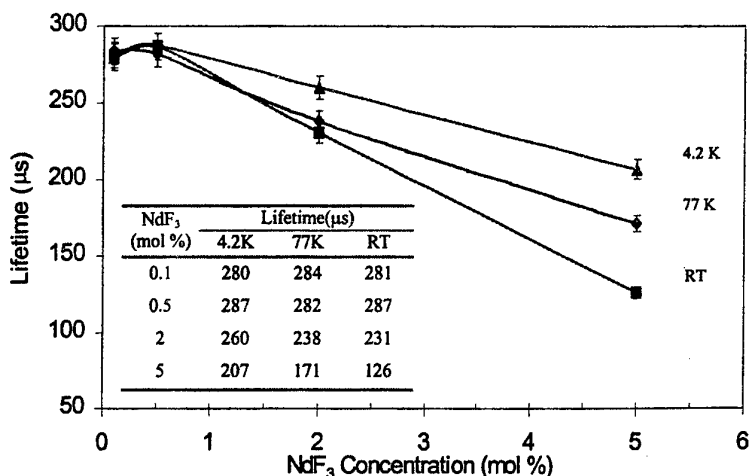


Figure 3 : Lifetime of the ${}^4\text{F}_{3/2}$ level as a function of Nd^{3+} concentration and temperature. The lines are only guides for the eye.

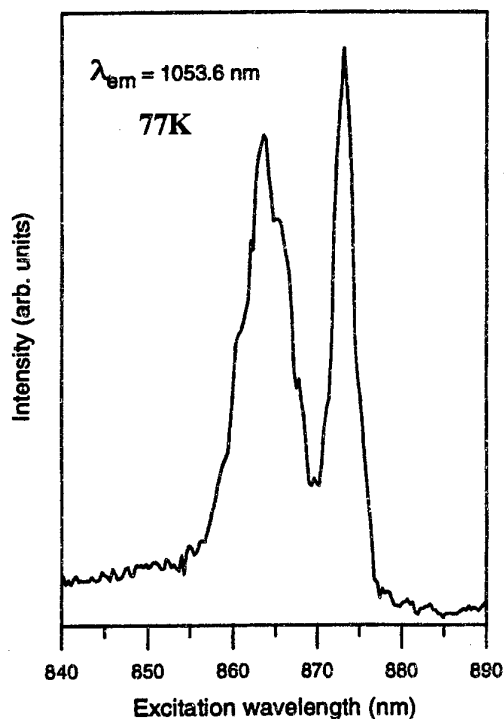


Figure 2 : Time-resolved line-narrowed excitation spectrum of the ${}^4\text{I}_{9/2} \rightarrow {}^4\text{F}_{3/2}$ transition of Nd^{3+} ions in $(\text{NaAs})_{40}\text{B}_{30}\text{Y}_{29.9}\text{Nd}_{0.1}$ glass. Time delay of 1 μs after the laser pulse by monitoring the ${}^4\text{F}_{3/2} \rightarrow {}^4\text{I}_{11/2}$ emission.

respectively. In the spectra, we observe a simple FLN line and a broad emission which arise from the non-narrowed inhomogeneous line. As time delay increases, the relative intensity of the narrow line and the broad (non selected) emission change. The latter becomes stronger indicating the existence of energy transfer between discrete regions of the inhomogeneous broadened profile.

IP 13 : FLUOROARSENATE GLASSES : SYNTHESIS AND CHARACTERISTICS OF A NEW RARE EARTH RICH GLASSY MATRIX

F. Smektala*, I. Melscoet, S. Chauvel, G. Fonteneau.

Laboratoire des Verres et Céramiques, UMR 6512, Université de Rennes 1,

Avenue du Général Leclerc, 35 042 Rennes Cédex, France

e-mail : Frederic.Smekkala@univ-rennes1.fr

ABSTRACT.

Fluorophosphate systems can lead to a large variety of glasses with high concentrations of rare earths. In order to study the glass forming behavior of arsenic pentoxide in similar oxyfluoride systems, glass formation has been studied in new rare earth rich oxyfluoride systems $M_2O-As_2O_5-BaF_2-YF_3$, where $M = Li, Na$ or K . Physical, thermal and optical properties have been measured in these new glasses. A particularly large glass forming region has been found in the sodic system. Stable glasses can be cast with glass transition temperatures around $270^\circ C$. Fluoride rare earth concentrations as high as 36 % molar can be introduced in these matrixes. The introduction of lithium in the glasses significantly improves their chemical durability.

1. INTRODUCTION.

Because large concentrations of rare earths can be introduced into the $NaPO_3-BaF_2-LnF_3$ system ($Ln =$ rare earth) [1], we have studied glass formation in similar oxyfluoride systems, and in particular in fluoroarsenate systems. The glass forming role of phosphorous pentoxide P_2O_5 is well known, and similar behavior has been demonstrated for arsenic pentoxide As_2O_5 [2-5]. Hence we have begun studying systems containing arsenic pentoxide (As_2O_5) as glass former, alkali metal oxide M_2O ($M = Li, Na$ or K) and barium fluoride (BaF_2) as modifiers, and yttrium fluoride (YF_3) as a model for the behavior of fluoride rare earths in these systems. The interest of this kind of glassy host is for example for visible light sources, since fluoride glasses are very good materials for these types of applications [6]. When a rare earth such as terbium is introduced into the glass, faraday rotator properties are enhanced and an optical isolator application can be envisaged [7-8]. Thus, the aim of this work has been to establish the glass formation in rare earth rich fluoroarsenate systems, to identify glass forming regions, and to characterize these glasses with regard to their transparency range, thermal behavior, densities and refractive indices.

2. EXPERIMENTAL PROCEDURES.

2-1. Glass synthesis.

The raw materials used for these studies are commercial grade BaF_2 , Y_2O_3 , $\text{Na}_2\text{HAsO}_4 \cdot 7\text{H}_2\text{O}$, KH_2AsO_4 , As_2O_5 and Li_2CO_3 . Yttrium oxide is fluorinated with ammonium bifluoride NH_4FHF at 300°C in an open platinum crucible and is converted to yttrium fluoride [9-10]. Arsenate compounds $\text{Na}_4\text{As}_2\text{O}_7$ and KAsO_3 are obtained by dehydration of $\text{Na}_2\text{HAsO}_4 \cdot 7\text{H}_2\text{O}$ and KH_2AsO_4 respectively. Reaction between As_2O_5 and Li_2CO_3 in aqueous solution leads to precipitation of Li_3AsO_4 . After filtration and drying, Li_3AsO_4 is mixed with As_2O_5 . Heating at 600°C leads to LiAsO_3 . The fluoroarsenate glasses are prepared by mixing the different compounds required amounts, and melting them in a platinum crucible heated at 900°C for 15 minutes, in air. Typically 15 g batches are melted. The melt is then either cast into a brass mold at room temperature, or preheated near glass transition temperature (T_g) to obtain bulk pieces, which are then annealed before cooling to room temperature.

2.2. Glass analysis.

In order to confirm the glass composition after synthesis, because compounds such as AsF_3 or AsF_5 can volatilize, and also to verify the arsenic oxidation state, the glass is dissolved in 10 N non-oxidizing cold chlorhydric acid. This solution is then used for fluorine and arsenic proportioning. Fluoride ions are titrated using a specific electrode and a millivoltmeter coupled with an automatic proportioning device, whose precision is 10^{-2} cm^3 , calibrated with NaF solutions. Proportioning is obtained by the addition method [11]. In order to establish the presence or absence of As^{III} in the dissolved glass solution, an excess of an oxidizing agent, such as $\text{K}_2\text{Cr}_2\text{O}_7$, is added to the solution, in order to oxidize all of the arsenic to As^{V} . Any remaining Cr^{VI} is titrated by Fe^{II} . The measurement of the arsenic present is realized by reduction of As^{V} to As^{III} with an excess of an iodide solution, which is then titrated by $\text{Na}_2\text{S}_2\text{O}_3$. The methods were checked with KH_2AsO_4 and KAsO_2 standards solutions.

2.3. Physical characterizations.

Densities were measured by the Archimedean method. Refractive indices were determined with an Abbe refractometer at the sodium D light. Thermal analyses have been performed on 30 mg samples, at a heating rate of 10K/mn , from room temperature to 550°C .

3. RESULTS.

3.1. Glass synthesis and physical characterisations.

The glass forming regions obtained in the $\text{Na}_4\text{As}_2\text{O}_7$ - BaF_2 - YF_3 and KAsO_3 - BaF_2 - YF_3 systems are given figure 1.

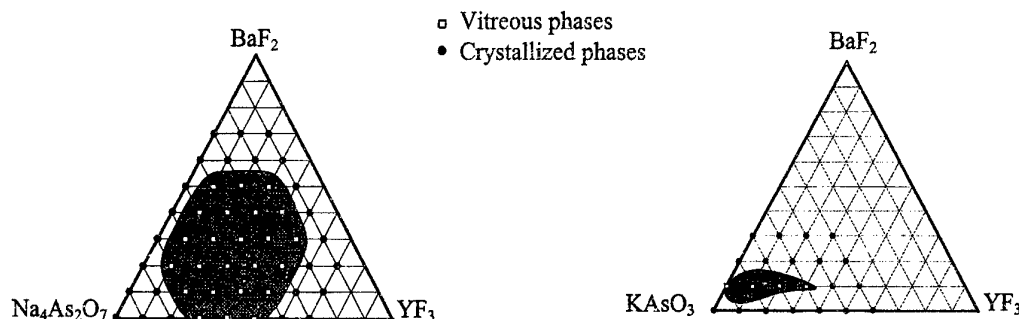


Figure 1: Glass forming regions in $\text{Na}_4\text{As}_2\text{O}_7$ - BaF_2 - YF_3 and KAsO_3 - BaF_2 - YF_3 systems.

The boundaries correspond to samples poured in a brass mold at room temperature, in air. The glass transition temperatures (T_g) and crystallization temperatures (T_x) were determined from thermal analysis. Data for some of these glasses are presented in Table 1.

Table 1: Physical properties of some fluoroarsenate glasses.

Glass composition	T_g ($^{\circ}\text{C}$) (± 2 $^{\circ}\text{C}$)	T_x ($^{\circ}\text{C}$) (± 2 $^{\circ}\text{C}$)	$T_x - T_g$ ($^{\circ}\text{C}$) (± 4 $^{\circ}\text{C}$)	n_D (± 0.001)	ρ (g.cm^{-3}) (± 0.01)
$\text{A}_{30}\text{B}_{30}\text{Y}_{40}$	269	420	151	1.548	3.88
$\text{A}_{30}\text{B}_{40}\text{Y}_{30}$	284	412	128	1.545	3.92
$\text{A}_{40}\text{B}_{30}\text{Y}_{30}$	277	390	113	1.555	3.72
$\text{A}_{40}\text{B}_{20}\text{Y}_{40}$	288	397	109	1.549	3.68
$\text{K}_{70}\text{B}_{10}\text{Y}_{20}$	230	340	110	-	-

$\text{A}_a(\text{K}_k)\text{B}_b\text{Y}_y$, glass composition in molar percentages a, k, b, y; A, $\text{Na}_4\text{As}_2\text{O}_7$; K, KAsO_3 ; B, BaF_2 ; Y, YF_3 ; T_g , glass transition temperature; T_x , crystallisation temperature; n_D , refractive index at sodium D radiation; ρ , density.

A representative transmission spectrum is presented figure 2.

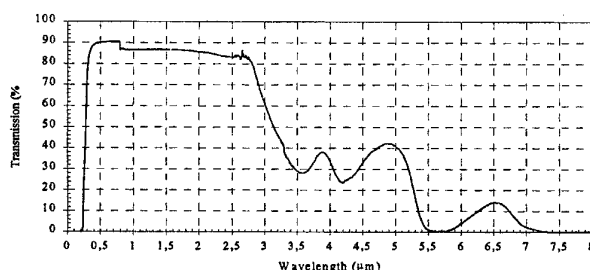


Figure 2: Transmission spectrum of $\text{A}_{40}\text{B}_{20}\text{Y}_{40}$ glass (1.82 mm thickness).

Composition analysis by proportioning shows that essentially no fluorine is lost during melting (table 2). So there is no formation of volatile compounds such as AsF_3 or AsF_5 . However, there is a small deviation in the arsenic concentration as well as a presence of reduced arsenic. This is explained by the observed accelerated aging of platinum crucibles, which suggests a reaction between arsenate compounds and platinum. The reducing agent involved is assumed to be residue from the NH_4FHF used in the fluorination of Y_2O_3 .

Table 2: Fluorine, As^{III} and As^{V} proportioning results for some fluoroarsenate glasses.

Glass composition	Present As^{III} % (± 0.3) %	Present As^{V} % (± 0.3) %	Total As present % (± 0.6) %	Present fluorine % (± 0.3) %
$\text{A}_{60}\text{B}_{20}\text{Y}_{20}$	2.8	96.4	99.2	99.8
$\text{A}_{50}\text{B}_{30}\text{Y}_{20}$	2.3	97.2	99.5	99.9
$\text{A}_{40}\text{B}_{30}\text{Y}_{30}$	4.3	95.2	99.5	100.0

$\text{A}_a\text{B}_b\text{Y}_y$, glass composition in molar percentages a, b, y; A, $\text{Na}_4\text{As}_2\text{O}_7$; B, BaF_2 ; Y, YF_3 .

As shown figure 1, a wide glass forming region of colorless glasses occurs in $\text{Na}_2\text{O}-\text{As}_2\text{O}_5-\text{BaF}_2-\text{YF}_3$ system. Compositions near the center are stable (Tc-Tg can be as high as 150°C for $\text{A}_{30}\text{B}_{30}\text{Y}_{40}$ glass for example) and they can easily be cast into bulk pieces (30 x 10 x 10 mm). In the case of $\text{KAsO}_3-\text{BaF}_2-\text{YF}_3$ system, the glass forming region is smaller. Nevertheless a stable glass is obtained for the $\text{K}_{70}\text{B}_{10}\text{Y}_{20}$ composition with a difference in Tc-Tg of 110°C . The chemical durability of these glasses is poor. The measurement of an infrared spectrum after few hours of exposure to room atmosphere shows the apparition of a strong absorption band at $2.9\text{ }\mu\text{m}$ (OH vibration). Surface devitrification occurs because of a reaction with atmospheric water. In order to improve the chemical durability of these new fluoroarsenate glasses, some compositions have been investigated in the sodic system with the aim of reducing the sodium amount present in the glass. The most stable glass ($\text{A}_{30}\text{B}_{30}\text{Y}_{40}$) of the $\text{Na}_4\text{As}_2\text{O}_7-\text{BaF}_2-\text{YF}_3$ system has been chosen as a basis. In this composition, $\text{Na}_4\text{As}_2\text{O}_7$ has been partially substituted by LiAsO_3 and glasses have been synthesized in the $\text{LiAsO}_3-\text{Na}_4\text{As}_2\text{O}_7-\text{BaF}_2-\text{YF}_3$ system (table 3). The higher ratio Li/Na allowing glass synthesis is 1.25. The chemical durability of these Li-containing glasses is considerably better than these of previous ones. After 24 h of exposure to room atmosphere, their infrared spectrum shows no modification. What's more, for sodic glasses, the transmission falls down to 65% after 6 minutes in water. For lithium containing glasses, it must be wait 90 minutes before seeing a small alteration in the infrared spectrum (figure 3).

Table 3 : Incorporation of lithium in fluoroarsenate glasses.

Glass composition	T _g (°C) (± 2 °C)	T _x (°C) (± 2 °C)	T _x -T _g (°C) (± 4 °C)
L ₂₅ A ₅ B ₃₀ Y ₄₀	308	366	58
L ₂₀ A ₁₀ B ₃₀ Y ₄₀	310	360	50
L ₁₀ A ₂₀ B ₃₀ Y ₄₀	293	368	75
L _{5.5} A _{24.5} B ₃₀ Y ₄₀	298	403	105

L₁A_aB_bY_y, glass composition in molar percentages l, a, b, y; L, LiAsO₃; A, Na₄As₂O₇; B, BaF₂; Y, YF₃; T_g, glass transition temperature; T_x, crystallisation temperature.

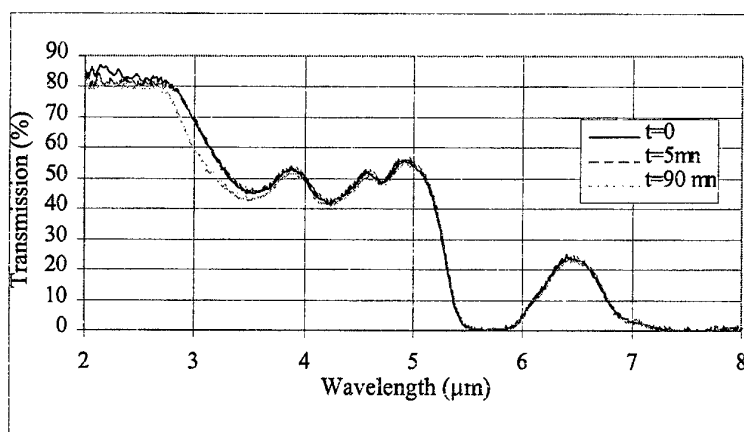


Figure 3 : Infrared spectra of a lithium containing fluoroarsenate glass.
a : just polished – b : after 5 mn in water - c : after 90 mn in water

4. DISCUSSION.

These new fluoroarsenate glasses are singular compare to classical fluorophosphate glasses. Their composition is particular. They present a high concentration in rare earth. The most stable composition, 18.75% As₂O₅, 25% YF₃, 37.5% Na₂O, 18.75% BaF₂, contains 25 % mol rare earth. Since this composition is leading to glass, the melt is highly polymerized, with a high connectivity between polyhedrons. Then, yttrium must play a glass former role. Indeed, when we examine the ratio anion (O+F) on former cation, we are in a particular situation. If arsenic is the only glass former, then this ratio is equal to 6.5. A seven-fold coordination should be envisaged. This is highly unlikely for the chemistry of arsenic. With yttrium as glass former, the ratio anion (O+F) on former cation (As+Y) is pretty close to four. It must be also noted that the ratio oxygen on fluorine is close to 1 and that the concentration in modifier cations (sodium and barium) is particularly high (BaF₂ + Na₂O = 56.25 % mol). In

front of this situation and to account chemical singularity of these glasses, we propose two structural hypotheses. They are based on two possible coordinations for arsenic, 4 and 6. On one hand, on the basis of a 4-fold coordination, it could be envisaged $[\text{AsO}_3\text{F}]$ tetrahedrons, as observed for phosphorous in fluorophosphate glasses [12-13]. These tetrahedrons could be connected with $[\text{YO}_5\text{F}_3]$ polyhedrons. All oxygen atoms are bridging, except one for yttrium and arsenic. Thus, the chemical characteristics of the composition are respected. The high concentration of modifier cations is in favor of this opened structure. But the connectivity of yttrium polyhedrons is low (four bridging oxygen for yttrium 8-fold coordination). On the other hand, on the basis of a 6-fold coordination for arsenic, it can be obtained a higher connectivity for yttrium polyhedrons. Indeed, in this case, $[\text{AsO}_4\text{F}_2]$ polyhedrons connected with $[\text{YO}_5\text{F}_2]$ ones could be envisaged, with all bridging oxygen atoms. Then, five oxygen atoms are bridging for yttrium seven-fold coordination. Also, combination of 4-fold and 6-fold coordination for arsenic could be possible.

5. CONCLUSION.

A new family of glasses has been identified. These glasses are rare earth rich fluoro-arsenate glasses. They are synthesized in $\text{M}_2\text{O}-\text{As}_2\text{O}_5-\text{BaF}_2-\text{YF}_3$ systems where $\text{M} = \text{Li}, \text{Na}$ or K . A large glass forming region was found in the sodic system, where stable glasses can be cast, with glass transition temperatures around 270°C . Rare earth contents as high as 36 % molar can be introduced in these glasses. Introduction of lithium in the composition significantly improves the chemical durability. Considering the chemical singularity of these glasses, two structural models are proposed, according to arsenic coordination.

REFERENCES.

- [1] M. Matecki, N. Duhamel, J. Lucas, J. Non-Cryst. Solids **184** (1995) 273-277.
- [2] L. G. Van Uitert, W. H. Grodkiewicz, J. Am. Ceram. Soc. **64** [12] (1981) 690-692.
- [3] W. H. Grodkiewicz, H. M. O'Bryan, G. A. Pasteur, L. Pressman, S. Singh, L. G. Van Uitert, and G. J. Zydzik, Mater. Res. Bull. **16** [4] (1981) 373-76,
- [4] W. H. Grodkiewicz, H. M. O'Bryan, S. Singh, L. G. Van Uitert, and G. J. Zydzik, J. Non-Cryst. Solids **44** [2-3] (1981) 405-8.
- [5] L.G. Van Uitert, W.H. Grodkiewicz, A.J. Bruce, J. Am. Ceram. Soc. **70** [3] (1987) 133-6.
- [6] J. L. Adam, F. Smektala, J. Lucas, Opt. Mat. **4** (1994) 85-90.
- [7] V. Letellier, A. Seignac, A. Le Floch, M. Matecki, J. Non-Cryst. Solids **111** (1989) 55.
- [8] M. Matecki, S. Jordery, J. Lucas, J. Mater. Sci. Lett. **11** (1992) 1431.
- [9] J. L. Adam, F. Smektala, E. Denoue, J. Lucas, SPIE Proc., Int. Soc. Opt. Eng., Glasses for Optoelectronics II **1513** (1991) 150-7.
- [10] J. Lucas, I. Chiaruttini, G. Fonteneau, P. Christensen, S. Mitachi, SPIE Proc. **1228** (1990) 56-62.
- [11] D. Tregoeat, Thesis, Université de Rennes 1, (1985).
- [12] R. K. Brow, C. C. Phifer, X. J. Xu and D. E. Day, Physics and Chemistry of Glasses **33** 2 (1992) 33-39.
- [13] M. Anma, T. Yano, A. Yasumori, H. Kawazoe, M. Yamane, H. Yamanaka, M. Katada, J. Non-Cryst. Solids **135** (1991) 79-85.

NEW OXYSULPHIDE GLASSES FROM THE

Sb_2O_3 - Sb_2S_3 - MxS System

Ling Zan, Jia-Shen Zhong, Qi-rong Luo,

Ling Huang, Wei Zhao

IR. Mat. Lab. Wuhan Univ. China 430072

Email: ZhanLin@public.wh.hb.cn.

ABSTRACT

New oxysulphide glasses involving Sb_2O_3 , Sb_2S_3 and MxS which have different features from classical oxide glasses and pure chalcogenides glasses have been prepared. Glass forming regions have been shown in the Sb_2O_3 - Sb_2S_3 , Sb_2O_3 - MxS binary systems and ternary systems. These glasses are easy to prepare and chemically stable. The thermal and optical properties of the glasses have been measured and compared with the glass of Sb_2O_3 and the glasses of Sb_2O_3 - RX_2 . The glasses are transparent ranging from 0.7 μm up to 7.0 μm and $\Delta T > 90^\circ\text{C}$. The glasses are potential candidates for IR transparent glass around 0.7-7.0 μm . The value of σ (100-200 $^\circ\text{C}$) of the glasses is about $10^{-5} \Omega^{-1} \text{cm}^{-1}$.

INTRODUCTION

The oxysulphide and oxyhalide glasses, chalcohalide glasses containing oxide and sulfide or halide components have been studied intensively in recent times [1]. Their glass-forming ability are often better than pure oxides and chalcogenides [2]. For some properites they are even better than that of pure oxide glasses. Sb_2O_3 is considered as a glass former. But pure single component glass is too difficult to prepare. Kordes who prepared a few milligrammes of the glass was the first to succeed in overcoming the problems of preparation. Dubois [3] prepared Sb_2O_3 - RX_m oxyhalide glasses. It was expected that, by adding the sulfide as a modifier, the glass-forming ability of Sb_2O_3 would have been improved. In this paper new oxysulphide glasses involving Sb_2O_3 and Sb_2S_3 , MxS are reported. Glass-forming regions have been shown. The characteristic temperature, the IR, UV transmission spectras and the electrical conductivity of the glasses sample have been measured.

EXPERIMENTAL

The starting materials are AR Sb_2O_3 , Sb_2S_3 , MxS . A mixture of Sb_2O_3 and Sb_2S_3 or MxS was put into a covered quartz crucible in an argon atmosphere and

rapidly heated to a temperature between 800 and 850°C. The mixture was completely melted and quenched in air after melting homogeneously for several minutes. Glass flakes with the thickness of 0.5–2mm were found. The melt was poured into a bass mould at 280°C, then cooled slowly down to room temperature. 30(mm)×30(mm)×5mm thick pieces of glass were obtained.

The glass-forming region of the system was determined by X-ray diffractometry. The thermal properties of these glasses were measured using a DT-3013 with a heating rate of 10 Ks⁻¹. The IR spectra were recorded by a spectrophotometer (Nicolet SX-107). The UV spectra were recorded by a spectrophotometer (Hitachi U-3400).

RESULTS

Binary glasses may be formed by combining Sb₂O₃ and Sb₂S₃, K₂S, Na₂S, ZnS. The composition ranges are shown in Fig. 1. Numerous ternary glasses are derived from these binary associations. The vitreous areas are shown in Fig. 2. The results of DTA are given in table 1. The influences of Sb₂S₃ content on T_g and ΔT are shown in Fig. 3. Fig. 4. Typical transmission curves are shown in Fig. 5, Fig. 6 for a glass sample of 2mm thickness.

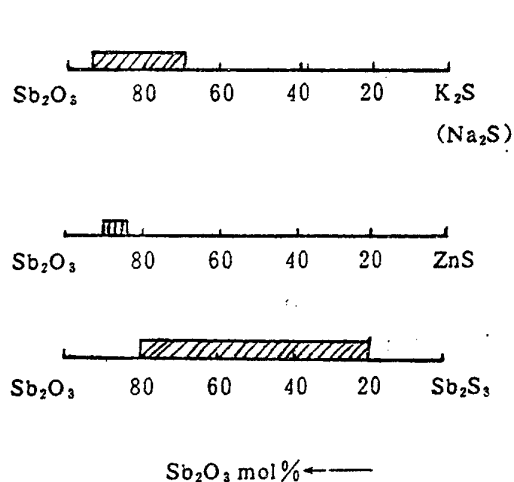


Fig. 1. Glass-forming range in the binary system.

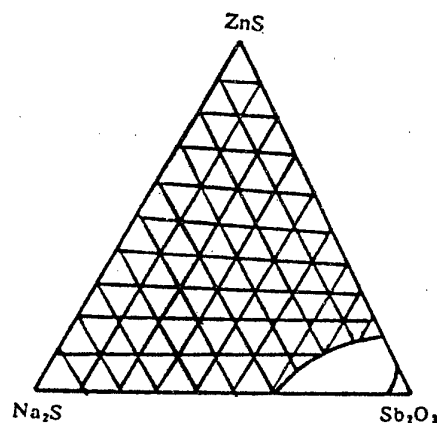


Fig. 2. Glass forming range in the ternary system.

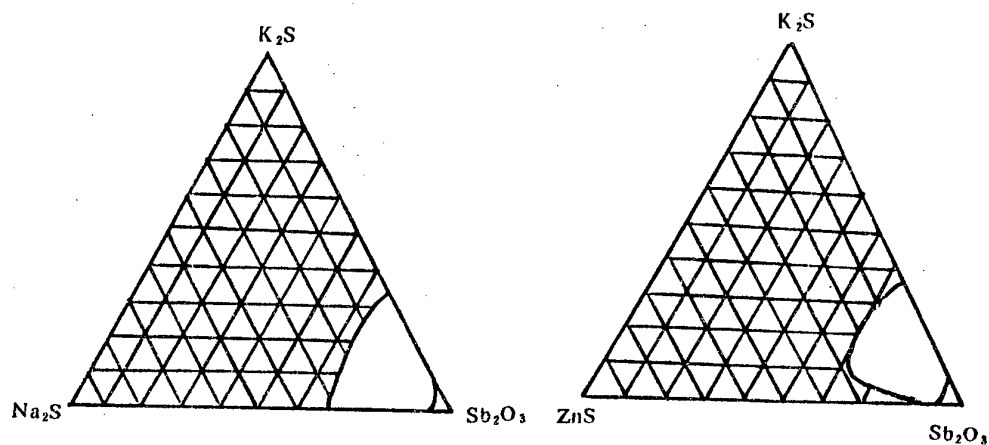


Fig. 2. Glass forming range in the ternary system

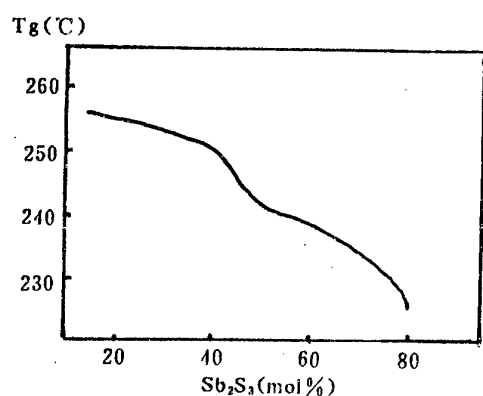


Fig. 3. Influence of Sb_2S_3 content on T_g (°C)

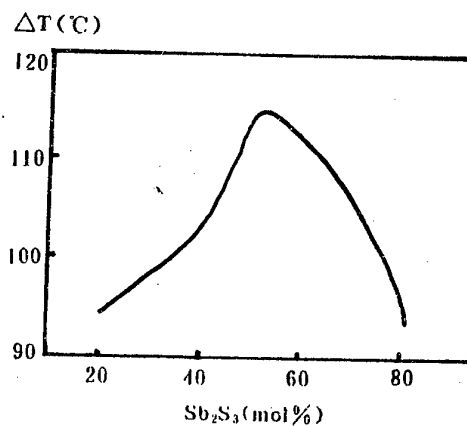


Fig. 4. Influence of Sb_2S_3 content on ΔT .

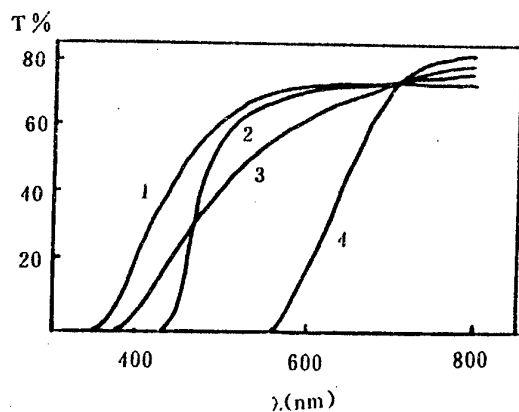


Fig 5. UV transmission spectra of glass.

1. Sb_2O_3 - PbCl_2 (70 : 30)
2. Sb_2O_3 - K_2S - ZnS (80 : 10 : 10)
3. Sb_2O_3
4. Sb_2O_3 - Sb_2S_3 (80 : 20)

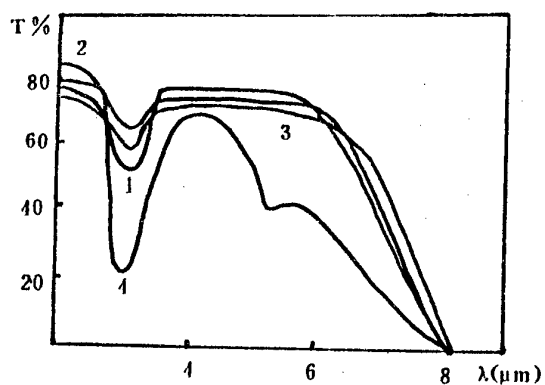


Fig 6. IR transmission spectra of glasses.

1. Sb_2O_3 - PbCl_2 (70 : 30)
2. Sb_2O_3 - Sb_2S_3 (80 : 20)
3. Sb_2O_3 - K_2S - ZnS (80 : 10 : 10)
4. Sb_2O_3

Table 1. The characteristic temperature of the glasses

System	Composition (mol%)	T _g (°C)	T _c (°C)	T _c -T _g (°C)
Sb ₂ O ₃ ^{<4>}	100	245	296	51
Sb ₂ O ₃ -Sb ₂ S ₃	80 : 20	225	349	94
	60 : 40	250	351	101
	50 : 50	241	356	115
	40 : 60	238	350	112
	20 : 80	225	318	93
Sb ₂ S ₃ ^{<5>}	174	174	174	0
Sb ₂ O ₃ -K ₂ S	80 : 20	246	404	158
Sb ₂ O ₃ -Na ₂ S	90 : 10	257	363	106
Sb ₂ O ₃ -ZnS	90 : 10	265	368	103
Sb ₂ O ₃ -K ₂ S-ZnS	80 : 10 : 10	285	398	113
Sb ₂ O ₃ -K ₂ S-Na ₂ S	80 : 10 : 10	270	390	120
Sb ₂ O ₃ -ZnS-Na ₂ S	80 : 10 : 10	275	390	115
Sb ₂ O ₃ -PbCl ₂ ^{<4>}	70 : 30	264	340	76
Sb ₂ O ₃ -ZnF ₂	80 : 20	203	265	62

The electrical conductivity of these glasses was measured (Tab. 2). The electrical conductivity of the oxysulphide glasses is similar to chalcogenide glasses, is greater than the multicomponent chalcogenide glasses. The conduction mechanism requires further study.

Table 2. Electrical conductivity of glasses

System	Composition (mol%)	T (°C)	$\sigma(\Omega^{-1}\text{cm}^{-1})$
Sb ₂ O ₃ -K ₂ S	80 : 20	100—200	2×10^{-5}
Sb ₂ O ₃ -Sb ₂ S ₃	60 : 40	100—200	3.1×10^{-5}
Sb ₂ S ₃ -Na ₂ Cl ^[1]	80 : 20	100—200	4×10^{-5}
Sb ₂ S ₃ -Tl ₂ S ^[6]	80 : 20	180	6.8×10^{-7}

DISCUSSION

From table 1, we can see, comparing with Sb₂O₃ glass, the values of T_g increase with adding MxS. The values of T_g first increase then decrease with adding Sb₂S₃. The values of T_c and ΔT increase greatly with adding MxS and Sb₂S₃. In the Sb₂O₃-Sb₂S₃ binary glasses, the value of ΔT is up to the maximum when the contents of Sb₂O₃ and Sb₂S₃ is same. Comparing with single component Sb₂O₃ glass and 70 Sb₂O₃-30PbCl₂ glass, shown in Tab. 1, the oxysulphide glasses have bigger value of ΔT .

It is difficult to prepare glass by using pure single component Sb_2O_3 . But oxysulphide glasses can be easy to prepare. The glass forming ability of Sb_2O_3 has been greatly improved by adding MxS , and Sb_2S_3 . T_c - T_g can reach up 158°C , permitting the preparation of preforms of considerable size. From Fig. 5. we can see, the transparent domain is expanded as PbCl_2 or MxS is added to Sb_2O_3 and turns into narrow as Sb_2S_3 is added to Sb_2O_3 . From this experiment we know the UV-vis cut-off wavelength shift to longer wavelength with increasing Sb_2S_3 . The color of glasses are yellow as adding MxS . It change from deep red to black with the increase of Sb_2S_3 content. In Fig. 6. the absorption band at $3.0\mu\text{m}$ results from traces of hydroxyl groups and water. The transparent domain is expanded and the absorption at $3.0\mu\text{m}$ is decreased when the MxS and Sb_2S_3 were introduced as a modifier. The new oxysulphide glass has broader transparent domain than Sb_2O_3 glass. IR transparent range of the new glasses is similar to halide as a modifier.

CONCLUSION

In this work, new oxysulphide glasses involving Sb_2O_3 and Sb_2S_3 , MxS have been prepared. The glass-forming areas have been investigated. The glass transition temperature lies between 225 and 285°C , T_c - T_g between 93 and 158°C . The IR-transparent wavelength extends up to $7.0\mu\text{m}$. These glasses are potential candidates for IR-transparent glasses 0.7 - $7\mu\text{m}$.

REFERENCES

1. Z. Ling, H. Ling, Z. Cheng shan, J. Non-Cryst. Solids 184(1995)1.
2. Z. Ling, Z. Jia-shen, J. Of Functional Materials. 26(1995)79
3. Z-B. Dubsis, H Aomi and J. J. Videau, Mat. Res. Bull. 19(1984)317
4. J. F. Bednarik and J. A. Neely, Phys and Chem. Of Glasses 239(1979)204
5. L. Cervinka, A. Hruby, J. Non-Cryst. Solids 48(1982)231
6. J. Olivier-Fourcade, A. Bouaza. and J. C. Jamas, J. Non-Cryst. Solids. 111 (1989)277

AUTHORS INDEX

AUTHORS INDEX

A

Adam, J.-L. *GP8, GP17, IP6, IP7, IP12*
 Adriaenssens, G. J. *HP10*
 Aggarwal, I. D. *A4, B3, G4*
 Aitken, B. G. *C2, D3, G1, H1*
 Akagi, R. *CP13*
 Aleksandrov, V. V. *F2*
 Almeida, R. M. *B2, E5*
 Aoki, H. *A3*
 Arriandiaga, M. A. *GP17*
 Ash, W. *FP4*
 Auzel, F. *I1*

B

Baesso, M. L. *BP18, HP7, HP9*
 Balda, R. *G7, GP17, IP12*
 Balerna, A. *CP6*
 Balmakov, M. D. *DP7*
 Barbosa, C. A. S. *IP11*
 Baricco, M. *DP10*
 Barthelemy, A. *HP17*
 Bartholomew, R. *FP5*
 Battezzati, L. *DP10*
 Batygov, S. *BP9, BP13*
 Bayya, S. *B3*
 Beatty, R. *HP16*
 Bell, K. W. *B5*
 Bento, A. C. *BP18, HP7, HP9*
 Bernage, P. *H6*
 Binnemans, K. *IP7*
 Bishop, S. G. *E2, G3*
 Blanchandin, S. *CP14*
 Bogdanov, V. K. *GP11*
 Bolotov, A. *CP12*
 Booth, D. J. *I2, GP11*
 Borrelli, N. F. *H1*
 Boscherini, F. *CP6*
 Boulard, B. *E3*
 Bousquet, B. *CP14*
 Boutardaia, A. *BP10*
 Bozano, D. F. *BP11*
 Braglia, M. *CP6, DP10, EP12*
 Brekhovskikh, M. *BP9*

Brinker, L. *CP12*
 Brown, R. M. *B5*
 Bruschi, C. *CP6, DP10, EP12*
 Buckley, R. *D4*

C

Canioni, L. *CP14*
 Cardinal, T. *HP16*

Cashion, J. D. *B4, BP8*
 Cassanjes, F. C. *IP10*
 Catunda, T. *BP18, HP7, HP9*
 Cernosek, Z. *CP11*
 Cerri, J. A. *BP12*
 Champarnaud-Mesjard, J. C. *CP14*
 Chauvel, S. *IP13*
 Chernov, V. A. *CP15*
 Chierici, E. *EP12*
 Choi, Y. G. *CP15*
 Churbanov, M. F. *H3, HP11*
 Clare, A. G. *C4*
 Cockerill, D. J. A. *B5*
 Cole, B. *G4*
 Couderc, C. *HP17*

D

da S Prado, O. *BP11*
 Dai, G. *CP6, DP10, EP12*
 Dale, G. *HP12*
 de Pablos, A. *G7*
 de Souza, D. F. *DP5*
 Degtyarev, S. V. *CP10*
 Delben, A. S. *D2, BP11*
 Delben, J. R. J. *D2, BP11*
 Denis, J. B. *B6*
 Dersch, O. *D1*
 Devitsin, E. *BP9*
 Devyatykh, G. G. *H3*
 Dianov, E. M. *H3*
 Dmitruk, L. *BP9, BP13, EP13*
 Donze, S. *FP3*
 dos Santos, I. M. G. *BP12*
 Doualan, J.-L. *GP8*

E

Edgar, A. *B4, H4, BP8*
 Edwards, B. C. *E7*
 Efimov, Yu. *EP13*
 Ellison, A. J. G. *FP5*
 Epstein, R. I. *E7*
 Ewen, P. J. S. *HP12*

F

Faber, A. J. *A2(I)*
 Fajardo, J. C. *E7*
 Fargin, E. *CP14*
 Federov, V. *EP13, IP5*
 Feng, X. *I3*
 Fernandez, J. *G7, GP17, IP12*
 Fernandez-Navarro, J. M. *G7*

Firth, L. D. *C5*
 Flower, P. *B5*
 Fonteneau, G. *E4, IP13*
 Fornazari, R. *BP11*
 Frischat, G. H. *D1*
 Frit, B. *CP14*
 Frumar, M. *G6, CP11, DP8, IP8*
 Frumarova, B. *G6, IP8*
 Furniss, D. *D4, EP15*

G

Gama, S. *BP18*
 Gan, F. *E1(I)*
 Gandra, F. C. G. *BP18*
 Gao, Y. *E3*
 Gibbs, W. E. K. *GP11*
 Girard, S. *GP8*
 Goncalves, M. C. *E5*
 Grando, D. *BP17*
 Griscorn, L. S. *GP8, IP7*
 Guimond, Y. *DP9, IP6*
 Handa, K. *CP13*
 Hannon, A. C. *C2, CP13*
 Harbison, B. B. *G4*
 Hareux, H. *FP3*
 Harwood, D. W. J. *EP11*
 Heo, J. *G5, CP15*
 Hernandez, A. C. *BP12, DP5, HP7, HP9*
 Hertogen, P. *HP10*
 Hirao, K. *EP8, EP10, HP14*
 Hobson, P. R. *B5*
 Hollis, D. B. *C5, FP4, GP14*
 Houston, P. A. *EP9*
 Hu, H. *I3, GP19*
 Huang, D. *GP18*
 Huang, L. *IP14*
 Hueber, B. *D1*

I

IľChenko, O. V. *C3*
 Inouye, H. *EP8*
 Ionashiro, M. *BP11*
 Ishikawa, E. *A3*
 Itoh, K. *A3*

J

Jacquier, B. *IP6*
 Javorniczky, J. S. *I2, GP11*
 Jeansannetas, B. *CP14*
 Jha, A. *G2, H2, CP7, CP8, GP12*
 Jiang, J. *D2*
 Josse, E. *E4*
 Jurdyc, A.-M. *IP6*

K

Kale, B. B. *GP12*
 Kanamori, T. *A1*
 Kang, I. *H1*
 Kasap, S. O. *DP8*
 Kasperczyk, J. *HP8*
 Kennedy, B. W. *B5*
 Kirchhof, J. *BP14, EP14*
 Kisliuk, A. *CP12*
 Kityk, I. V. *HP8*
 Kobayashi, K. *A1*
 Kobelke, J. *BP14, EP14*
 Kojima, K. *HP14*
 Kondo, Y. *EP10*
 Kovaleva, I. *IP5*
 Kozlov, V. *BP9*
 Krasteva, V. *G3*
 Kraus, J. *CP6, DP10, EP12*
 Kryzhanowsky, I. I. *EP16*
 Kucharski, J. *HP8*
 Kurochkin, A. V. *CP10*
 Kuznetsova, I. *IP5*

L

Lacha, L. M. *IP12*
 Lamberti, C. *CP6*
 Le Flem, G. *CP14*
 Le Boiteux, S. *CP14*
 Lebullenger, R. *BP12, DP5, HP7, HP9*
 Leite, E. R. *BP12*
 Lemit, M. *E3*
 Le-Neindre, L. *HP15*
 Li, C. *GP18*
 Li, R. *B1, D4*
 Li, M. *GP19*
 Lima, S. M. *HP7, HP9*
 Lin, H. *GP18*
 Lin, F. *I3, GP19*
 Lintern, A. L. *B5*
 Liu, X. *GP12*
 Loeffler, P. *E3*
 Longo, E. *BP12*
 Lucas, J. *E4, H6, DP9, HP15, HP17*
 Lucas, P. *HP15*
 Luo, Q. *GP18, IP14*

M

Ma, H. L. *DP9, IP6*
 MacFarlane, D. R. *B4, I2, BP8, GP11, IP9*
 Maldener, A. *D1*
 Mamedov, S. *CP12*
 Marchet, P. *CP14*
 Martin, M. O. *CP14*

Martin, S. W. *F1(I)*
 Martins, O. *B2*
 Matai, D. *IP10*
 Matsumoto, Y. *A3*
 Matsuoka, Y. *A3*
 McKinlay, K. J. *B5, BP7*
 Melnikov, P. *BP17, IP11*
 Melscoet, I. *IP12, IP13*
 Mendioroz, A. *GP17*
 Meneghini, C. *CP6*
 Mercier, C. *CP16*
 Merle-Mejean, T. *CP14*
 Messaddeq, Y. *BP17, DP6, IP10, IP11*
 Mikhailov, M. D. *EP16*
 Miklos, R. *G4*
 Mitsuyu, T. *EP8, EP10, HP14*
 Miura, K. *EP8, EP10*
 Moiseeva, L. *BP13*
 Moncorge, R. *GP8*
 Montagne, L. *CP16, FP3*
 Moore, R. C. *E6, EP11*
 Morais, P. J. *E5*
 Morgan, S. P. *D4*
 Mori, A. *A1*
 Mortier, M. *I1*
 Mossadegh, R. *G4*
 Mossellmans, F. W. *C5*
 Mosso, S. *CP6, DP10, EP12*
 Moya, C. M. *IP11*
 Mugnier, J. *IP6*
 Murali, A. *HP13*
 Murin, I. V. *F2, CP9*
 Murtagh, M. T. *E7*
 Mutolo, P. *C1*

N

Naftaly, M. *G2, H2, CP7, CP8*
 Nazabal, V. *CP14*
 Nedoshovenko, E. G. *F2*
 Nemec, P. *G6, IP8*
 Newman, P. J. *B4, I2, BP8, GP11, IP9*
 Nguyen, U. Q. *G4*
 Niay, P. *H6*
 Nishida, Y. *A1*
 Nunes, L. A. O. *DP5*

O

Ohishi, Y. *A1*
 Ohtori, N. *CP13*
 Okada, K. *A3*
 Oleaga, A. *G7*
 Oswald, J. *G6, IP8*
 Owen, A. E. *HP12*

P

Palavit, G. *CP16, FP3*
 Park, S. *HP16*
 Parker, J. M. *B5, BP7*
 Pascarelli, S. *CP6*
 Payne, M. J. *GP14*
 Payne, D. N. *Keynote, E6, EP11*
 Petcherizin, I. M. *EP16*
 Pivovarov, S. S. *CP10*
 Plotnichenko, V. G. *H3, HP11*
 Poignant, H. *E3*
 Polak, Z. *CP11*
 Ponader, C. W. *D3*
 Popov, L. *BP13*
 Portier, J. *BP15*
 Poulain, Marcel. *B6, D2, BP10, BP15, BP16*
 Poulain, Michel *BP15*
 Provorova, A. *BP9*
 Pulcinelli, S. H. *DP6*
 Pureza, P. C. *G4*

Q

Qi, C. *I3, GP19*
 Qiu, J. *EP8, EP10, HP14*
 Quemard, C. *HP17*
 Quimby, R. *G1(I)*

R

Ramachandran, S. *E2*
 Rao, J. L. *HP13*
 Rauch, F. *D1*
 Reaney, I. M. *D4*
 Regelsky, G. *C1*
 Ribeiro, S. *BP17, DP6, IP10, IP11*
 Richardson, K. *HP16*
 Rimet, R. *E3*
 Rizzato, A. P. *DP6*
 Rossi, F. *DP10*

S

Sampaio, J. A. *BP18*
 Samson, B. N. *G2*
 Sanghera, J. S. *A4(I), B3, G3, G4*
 Santilli, C. V. *DP6*
 Sanz, M. *G7*
 Sarger, L. *CP14*
 Schaafsma, D. T. *G4*
 Schardt, C. *HP15*
 Scheffler, M. *BP14, EP14*
 Schmedt, J. *C1*
 Schrader, A. B. *C4*

Schwuchow, A. *BP14, EP14*
 Sclenar, A. *CP12*
 Scotto, C. *B3*
 Scripachev, I. V. *H3*
 Seddon, A. B. *B1, D4, EP9, EP15*
 Segonds, P. *CP14*
 Sfihi, H. *CP16*
 Shaw, L. B. *G4*
 Shen, S. *H2, CP8*
 Shephard, J. D. *EP9*
 Shim, H. *HP16*
 Shimada, T. *A1*
 Shimizu, M. *A1*
 Shimizugawa, Y. *HP14*
 Shirakawa, A. *A3*
 Shyriaev, V. S. *HP11*
 Sigel Jr, G. H. *E7, G3*
 Silva, M. *BP16*
 Simmons, J. H. *HP15*
 Smektala, F. *H6, HP17, IP12, IP13*
 Smirnov, V. B. *CP10*
 Smolorz, S. *H1*
 Snopatin, G. E. *H3*
 Soltwisch, M. *CP12*
 Sproston, M. *B5*
 Sramek, R. *E4, H6*
 Stegeman, G. *HP16*
 Sukhoverkhov, V. *BP9*

T

Tanabe, S. *GP10*
 Tanaka, K. *HP14*
 Tatsumisago, M. *CP13*
 Tawarayama, H. *A3*
 Taylor, E. R. *E6, G2, EP11*
 Thomas, P. *CP14*
 Tick, P. *I4(I)*
 Tikhomirov, V. K. *H5(I), CP7, GP12, HP10*
 Toratani, H. *A3*
 Tucknott, J. A. *EP11*
 Turnbull, D. A. *G3*
 Turner, D. P. *C5*
 Tverjanovich, A. *DP7*

Tver'yanovich, Yu. S. *C3, F2, CP9, CP10, DP7*

U

Umesaki, N. *CP13*

V

Varela, J. A. *IP10*
 Villeneuve, A. *HP16*
 Vinogradova, N. *BP9, BP13, EP13*
 Vlcek, M. *G6, CP12*

W

Wagner, T. *DP8*
 Wasylak, J. *HP8*
 West, Y. D. *E6, EP11*
 Wise, F. W. *H1(I)*
 Witschas, M. *C1*

X

Xie, W. X. *H6*
 Xu, J. *B2*

Y

Yamada, M. *A1*
 Yamanaka, K. *A3*
 Yanagita, H. *A3*
 Yong, B. S. *G5*
 Young, D. M. *FP5*

Z

Zagheti, M. A. *IP10*
 Zan, L. *GP18, IP14*
 Zhang, G. *D2*
 Zhang, X. H. *DP9*
 Zhao, W. *IP14*
 Zhong, J. *GP18, IP14*
 Zonetti, L. F. C. *DP5*

LIST OF SPONSORS OF IS(NO²G)

- **Corning SA, France.**
- **Galileo Corporation, USA.**
- **Hoya Co. Ltd., R & D Centre, Japan.**
- **Merck Ltd., UK.**
- **European Commission,
Directorate General XII,
Science, Research & Development.
Directorate C:
Industrial and Materials Technologies.**
- **USARDSG,
United State Army,
European Research Office.**
- **ONREUR,
United States Navy,
European Office of Naval Research.**
- **Society Of Glass Technology.**
- **Sheffield City Council.**
- **University of Sheffield.**